

Secondary Organic Aerosol Composition Studies
Using Mass Spectrometry

Thesis by
Katherine Ann Schilling

In Partial Fulfillment of the Requirements for the degree of
Doctor of Philosophy



CALIFORNIA INSTITUTE OF TECHNOLOGY

Pasadena, California

2015

(Defended May 18, 2015)

© 2015

Katherine Ann Schilling

All Rights Reserved

ACKNOWLEDGEMENTS

A. A. Milne wrote, “Piglet noticed that even though he had a Very Small Heart, it could hold a rather large amount of Gratitude.” I am so thankful to so many people; it is hard to put it all in words.

I would like to thank John Seinfeld, my thesis advisor, for his guidance, support, and mentoring, which have been absolutely vital to my growth and success. I am so grateful for his advice and insight over the years. John is a gifted scientist, and it has been an honor to do research with him and be a part of his academic legacy.

Many thanks to my thesis committee, Jack Beauchamp (chair), Geoff Blake, and Mitchio Okumura, for their valuable time, great insight, and fascinating discussions. It has been a privilege to have such talented and knowledgeable scientists make themselves available to me for research discussions and mentoring. Special thanks to Jack for allowing me to be an informal group member and helping me stay connected to the worlds of chemical physics and instrumentation innovation.

I am honored and delighted to have wonderful people in my professional and personal circles. Nathan Dalleska, Chithra Krishnamurthy, Kaitlyn Lucey, MK Dean, Lara Huppert, April Padilla, Karen Van Dusen, Mary Monks, Denise LaSonde, Portia Harris, Lee Coleman, Felicia Hunt, Natasha Hodas, Jill Craven, ManNin Chan, Xerxes Lopez-Yglesias, Jason Gamba, Jason St. Clair, Jim House, Mona Shahgholi, Candice Bridge, Kim Mooney, Anthony Koertner, Henry Swofford, Molly Hall, Amanda Atkins, Anna Deakin, Derek Dorrien, Jeff Dake, and Ed Sisco: thank you for making my world a better place.

Many thanks go to the members of the greater Seinfeld-Flagan lab, past and present, for their scientific insights, hard work, dedication, and for weathering the good and tough times with me. Matt Coggon, Hanna Lignell, Mandy Grantz, Johannes Leppa, Paula Popescu, Lindsay Yee, Christine Loza, Puneet Singh, Joey Ensberg, Scott Hersey, Andi Zuend, Manabu Shiraiwa, Jean Chen, Renee McVay, Andrew Metcalf, Andrew Downard, Becky Schwantes, Xuan Zhang, as well as Jill, ManNin, Natasha, Xerxes, and Jason. Thank you for all the science cakes, coffee, and camaraderie. It’s been an honor.

Finally, thank you to my parents, Michael and Cherrie, to my brother Nick and his wife Rhiannon, and to my best friend Laura Kaufmann. Your constant love, well-developed senses of humor, and heartfelt encouragement keep me going, even when things get tough. This thesis is dedicated to you.

ABSTRACT

Trace volatile organic compounds emitted by biogenic and anthropogenic sources into the atmosphere can undergo extensive photooxidation to form species with lower volatility. By equilibrium partitioning or reactive uptake, these compounds can nucleate into new aerosol particles or deposit onto already-existing particles to form secondary organic aerosol (SOA). SOA and other atmospheric particulate matter have measurable effects on global climate and public health, making understanding SOA formation a needed field of scientific inquiry. SOA formation can be done in a laboratory setting, using an environmental chamber; under these controlled conditions it is possible to generate SOA from a single parent compound and study the chemical composition of the gas and particle phases. By studying the SOA composition, it is possible to gain understanding of the chemical reactions that occur in the gas phase and particle phase, and identify potential heterogeneous processes that occur at the surface of SOA particles. In this thesis, mass spectrometric methods are used to identify qualitatively and quantitatively the chemical components of SOA derived from the photooxidation of important anthropogenic volatile organic compounds that are associated with gasoline and diesel fuels and industrial activity (C_{12} alkanes, toluene, and *o*-, *m*-, and *p*-cresols). The conditions under which SOA was generated in each system were varied to explore the effect of NO_x and inorganic seed composition on SOA chemical composition. The structure of the parent alkane was varied to investigate the effect on the functionalization and fragmentation of the resulting oxidation products. Relative humidity was varied in the alkane system as well to measure the effect of increased particle-phase water on condensed-phase reactions. In all systems, oligomeric species, resulting potentially from particle-phase and heterogeneous processes, were identified. Imines produced by reactions between $(NH_4)_2SO_4$ seed and carbonyl compounds were identified in all systems. Multigenerational photochemistry producing low- and extremely low-volatility organic compounds (LVOC and ELVOC) was reflected strongly in the particle-phase composition as well.

TABLE OF CONTENTS

Acknowledgements	iii
Abstract.....	v
Table of Contents.....	vii
List of Tables.....	ix
List of Figures.....	xi
List of Schemes	xvi
Chapter 1: Introduction.....	1
Motivation.....	1
Research Objectives	2
Approach.....	3
References	4
Chapter 2: Secondary Organic Aerosol Composition from C ₁₂ Alkanes	5
Abstract.....	6
Introduction.....	6
Experimental Section.....	7
Results and Discussion	11
Conclusions	19
Acknowledgements	20
References	20
Chapter 3: Chemical Composition of Toluene and Cresol Secondary Organic Aerosol: Effect of NO Level.....	23
Abstract.....	24
Introduction.....	25
Experimental Section.....	29
Results and Discussion	33
Acknowledgements	43
References	43
Chapter 4: Conclusions and Future Work.....	47
Conclusions.....	48
Heterogeneous Chemistry in Secondary Organic Aerosol	50
References	53
Appendices	
A: Molecular Corridors and Kinetic Regimes in the Multiphase Chemical Evolution of Secondary Organic Aerosol	56
B: Size Distribution Dynamics Reveal the Importance of Particle-Phase Chemistry in Organic Aerosol Formation.....	76
C: The Pasadena Aerosol Characterization Observatory (PACO): Chemical and Physical Analysis of the Western Los Angeles Basin Aerosol	92
D: Effect of Chemical Structure on Secondary Organic Aerosol Formation from C ₁₂ Alkanes	120
E: Secondary Organic Aerosol Formation from Low-NO _x Photooxidation of Dodecane: Evolution of Multigeneration Gas-Phase Chemistry and Aerosol Composition	141
F: Secondary Organic Aerosol Formation from Biomass Burning Intermediates: Phenol and Methoxyphenols.....	171

G: Secondary Organic Aerosol Yields of 12-Carbon Alkanes	197
H: Influence of Aerosol Acidity on the Chemical Composition of Secondary Organic Aerosol from β -Caryophyllene	215
I: α -Pinene Photooxidation under Controlled Chemical Conditions – Part 2: SOA Yield and Composition in Low- and High-NO Environments	233
J: Analysis of Secondary Organic Aerosol Formation and Aging Using Positive Matrix Factorization of High-Resolution Aerosol Mass Spectra: Application to the Dodecane Low-NO _x System.....	249
K: Role of Ozone in SOA Formation from Alkane Photooxidation.....	273
L: Organic Aerosol Formation from the Reactive Uptake of Isoprene Epoxydiols (IEPOX) onto Non-Acidified Inorganic Seeds	295
M: A Chemically Relevant Artificial Fingerprint Material for the Cross Comparison of Mass Spectrometry Techniques	310
N: Supporting Information from “Secondary Organic Aerosol Composition from C ₁₂ Alkanes.....	332
O: Supporting Information from “Chemical Composition of Toluene and Cresol Secondary Organic Aerosol”.....	355

LIST OF TABLES

<i>Number</i>	<i>Page</i>
2.1 Prior alkane SOA composition studies	7
2.2 C ₁₂ compounds studied	8
2.3 Summary of alkane experimental conditions	9
2.4 Alkane SOA mean molecular weights and mean O:C and H:C ratios	14
3.1 Summary of toluene and cresol experimental conditions	29
4.1 Isoprene nitroxy epoxydiol SOA organosulfate content.....	51
A.1 Summary of analysis of identified SOA oxidation products.....	60
C.1 Previous Los Angeles air quality studies and major findings relative to SOA	95
C.2 PACO sampling regimes (2009)	96
C.3 OC/EC concentrations for representative days from each regime.....	101
D.1 C ₁₂ compounds studied.....	122
D.2 Experimental conditions	124
D.3 Selected ions monitored by CIMS for <i>n</i> -dodecane and 2-methylundecane	127
D.4 Selected ions monitored by CIMS for hexylcyclohexane and cyclododecane.....	127
D.5 Selected ions monitored by AMS for <i>n</i> -dodecane and 2-methylundecane	128
D.6 Selected ions monitored by AMS for hexylcyclohexane	128
D.7 Selected ions monitored by AMS for cyclododecane	129
E.1 Dodecane low-NO _x experiments	144
E.2 Reactions included in the gas-phase photochemical model.....	146
E.3 CIMS signals and their suggested assignments	150
F.1 Chemical properties of phenol, guaiacol, and syringol.....	173
F.2 Experimental conditions and aerosol yields.....	174
F.3 Proposed structures for CIMS ions in the phenol low-NO _x system.....	179
F.4 Proposed structures for CIMS ions in the guaiacol low-NO _x system.....	180
F.5 Guaiacol SOA products observed in the offline UPLC/(-)ESI-MS analysis	181
F.6 Proposed structures for CIMS ions in the phenol low-NO _x system.....	185
G.1 Alkane SOA precursor and aerosol properties	200
G.2 High-NO _x experimental details	203
G.3 Low-NO _x experimental details	205
H.1 Experimental details for β-caryophyllene/NO _x irradiation experiments.....	218

H.2 β -Caryophyllene SOA species detected by (+)-ESI-MS	221
H.3 β -Caryophyllene SOA species detected by (-)-ESI-MS	222
H.4 β -Caryophyllene SOA N-containing species detected by (-)-ESI-MS.....	224
H.5 β -Caryophyllene SOA organosulfate species detected by (-)-ESI-MS	225
I.1 SOA yields from low- and high-NO _x photooxidation of α -pinene	238
I.2 Raw UPLC peak areas for α -pinene SOA components	240
I.3 Scaled UPLC peak areas for α -pinene SOA components	240
J.1 Experimental conditions for dodecane low-NO _x photooxidation	252
J.2 Ion fragment identifications	258
J.3 HR-ToF-AMS ions with best correlations	259
J.4 Distinct ions present in early C ₁₈ SOA formation	265
K.1 Experimental conditions for the photooxidation of dodecane	276
K.2 Proposed structures for CIMS ions unique to dihydrofuran chemistry.....	285
L.1 Summary of results from representative reactive uptake experiments.....	301
M.1 Artificial sweat components.....	329
M.2. Artificial sebum components.....	330
N.1 Components of dodecane low-NO SOA	339
N.2 Components of dodecane high-NO SOA	341
N.3 Components of cyclododecane low-NO SOA	343
N.4 Components of cyclododecane high-NO SOA.....	345
N.5 Components of hexylcyclohexane low-NO SOA.....	347
N.6 Components of hexylcyclohexane high-NO SOA.....	350
O.1 Components of toluene low-NO SOA	361
O.2 Components of toluene high-NO SOA	361
O.3 Components of toluene high-NO SOA with Na ₂ SO ₄ seed	362
O.4 Components of toluene high-NO SOA with NaCl seed.....	364
O.5 Components of toluene high-NO SOA with MgSO ₄ + H ₂ SO ₄ seed	365
O.6 Components of <i>o</i> -cresol high-NO SOA.....	367
O.7 Components of <i>m</i> -cresol high-NO SOA	369
O.8 Components of <i>p</i> -cresol high-NO SOA	370

LIST OF FIGURES

<i>Number</i>	<i>Page</i>
2.1 Exemplar data from C ₁₂ alkane secondary organic aerosol (SOA) analysis by gas chromatography/mass spectrometry with electron impact ionization and chemical ionization, and by direct analysis in real time mass spectrometry (DART-MS).....	10
2.2 Chemical composition of <i>n</i> -dodecane-derived secondary organic aerosol	12
2.3 Van Krevelen diagram for <i>n</i> -dodecane SOA produced under dry, high-NO Conditions with (NH ₄) ₂ SO ₄ seed	15
2.4 Chemical composition of cyclododecane-derived SOA.....	16
2.5 Van Krevelen diagram of cyclododecane SOA produced under dry, high-NO Conditions with (NH ₄) ₂ SO ₄ seed	17
2.6 Chemical composition of hexylcyclohexane-derived SOA.....	18
2.7 Van Krevelen diagram of hexylcyclohexane SOA produced under dry, high-NO Conditions with (NH ₄) ₂ SO ₄ seed	19
3.1 Gas-phase mechanism for toluene oxidation proceeding by OH addition, based on the Master Chemical Mechanism (MCM).....	25
3.2 Mechanism the gas-phase oxidation of the bicyclic peroxy radical under low- and high-NO conditions based on the MCM	26
3.3 Gas-phase mechanism for <i>o</i> -cresol oxidation proceeding by OH addition, based on the Master Chemical Mechanism (MCM).....	27
3.4 Chemical composition of toluene and cresol SOA as measured by offline DART-HR-MS analysis, displayed by general molecular formula category.....	33
3.5 Three-factor PMF solution comparing toluene and <i>o</i> -cresol SOA produced under high-NO conditions in the presence of (NH ₄) ₂ SO ₄ seed.....	35
3.6 Van Krevelen diagram of species identified by DART-HR-MS analysis of toluene SOA produced under low- and high-NO conditions in the presence of (NH ₄) ₂ SO ₄ seed.....	37
3.7 Van Krevelen diagram of species identified by DART-HR-MS analysis of <i>o</i> -, <i>m</i> -, and <i>p</i> -cresol SOA produced under high-NO conditions in the presence of (NH ₄) ₂ SO ₄ seed.....	38

3.8	Chemical composition of toluene and cresol SOA, displayed as a function of C number, derived from offline DART-HR-MS analysis.....	40
3.9	Toluene SOA formation graphical abstract	42
A.1	Molecular corridors of SOA evolution for different precursors.....	59
A.2	Molecular processes of SOA evolution.....	60
A.3	Kinetic regimes and limiting cases of SOA evolution.....	61
A.4	Ensemble of molecular corridors and kinetic regimes of SOA evolution.....	62
A.5	Evolution of dodecane reaction pathways over the molecular corridor	63
B.1	Modeling SOA formation from dodecane photooxidation	78
B.2	Evolution of particle number size distributions	79
B.3	Relative contribution and distribution of gas- and particle-phase products	80
C.1	Characteristic measurements for regimes 1, 2 and 3	98
C.2	Average diurnal DMA number concentrations for regimes 1, 2, and 3.....	100
C.3	Bulk AMS diurnal mass averages for regimes 1, 2, and 3.....	102
C.4	AMS bulk mass fractions for AM, midday, PM and night.....	102
C.5	WSOC magnitude and % of AMS organic.....	104
C.6	Mass spectra for the three factors identified in PMF analysis	105
C.7	Mass fraction of total organic from each PMF factor.....	106
C.8	Plot of f_{44} versus f_{43} for PACO	107
C.9	Growth factors at 74, 85, and 92% RH versus organic mass fraction.....	108
C.10	K and critical dry diameter plotted against organic mass fraction.....	109
D.1	General alkane mechanism under low-NO conditions	124
D.2	General mechanisms for particle-phase chemistry.....	126
D.3	Gas-phase trends of major species formed in early photooxidation.....	127
D.4	HR mass spectrum of dodecane SOA at different time points.....	130
D.5	HR mass spectrum of 2-methylundecane SOA at different time points.....	130
D.6	HR mass spectrum of hexylcyclohexane SOA at different time points.....	131
D.7	HR mass spectrum of cyclododecane SOA at different time points	131
D.8	Gas-phase trends displaying PHA formation from key precursors.....	133
D.9	Organic fraction attributed to PHA tracer ions	134
D.10	Characteristic ions from alkane SOA measured by AMS.....	135
D.11	Van Krevelen diagram for low-NO alkane photooxidation	136
E.1	Dodecane low-NO _x mechanism.....	145

E.2 Simulated and observed compositional time evolution	148
E.3 Carboxylic acids.....	151
E.4 Acids or hydroperoxides.....	151
E.5 Span of O:C values verses log of vapor pressure.....	154
E.6 Scheme for formation of PHA types.....	155
E.7 Aerosol growth correlated to carbonyl hydroperoxide and acid formation	156
E.8 AMS and CIMS ion time trends for key PHA species and precursors	157
E.9 Estimated mass contributions from semivolatiles to SOA.....	159
F.1 Aerosol organic mass yields for phenol, guaiacol, and syringol.....	177
F.2 Phenol low-NO _x gas and particle chemical development.....	178
F.3 Proposed mechanism for acid formation in the phenol low-NO _x system.....	182
F.4 Proposed mechanism for guaiacol low-NO _x oxidation.....	182
F.5 Selected traces in guaiacol low-NO _x gas- and particle-phase development	183
F.6 Common chemical routes in the phenol and guaiacol	183
F.7 Selected traces in syringol low-NO _x gas- and particle-phase development.....	186
F.8 Possible routes of methoxy loss in syringol gas-phase chemistry	187
F.9 Enthalpy differences between products indicating methoxy loss	187
F.10 Evolution of average carbon oxidation state for studied systems	189
G.1 Temporal trends of gas-phase species and SOA mass concentration.....	201
G.2 Alkane SOA yields under high- and low-NO _x conditions.....	202
G.3 Comparison of SOA yields as a function of organic mass concentration.....	204
G.4 SOA yield upper limit as a function of estimated SVOC-particle collisions.....	205
G.5 SOA average carbon oxidation state as a function of OH exposure	206
G.6 Contributions of AMS ion families to bulk organic mass under high NO _x	207
G.7 Contributions of AMS ion families to bulk organic mass under low NO _x	207
G.8 Comparison of gas-phase products measured by CIMS under high NO _x	209
H.1 β-caryophyllene SOA product concentrations, detected by (+)-ESI/MS.....	228
H.2 β-caryophyllene SOA product concentrations, detected by (-)-ESI/MS	228
H.3 β-caryophyllene SOA product concentrations, detected by (+)-ESI/MS.....	229
H.4 β-caryophyllene SOA product concentrations, detected by (-)-ESI/MS.....	229
H.5 β-caryophyllene SOA product concentrations, detected by (-)-ESI/MS.....	229
I.1 SOA yield as a function of OH exposure of α-pinene	237
I.2 Time evolution of SOA growth and gas-phase chemical composition	239

I.3 SOA yield as a function of OH exposure with variations in seed acidity.....	239
I.4 Structures of identified SOA components.....	241
I.5 UPLC/(-)ESI-ToF-MS chromatograms of α -pinene low-NO _x SOA.....	241
I.6 UPLC/(-)ESI-ToF-MS chromatograms of α -pinene high-NO _x SOA	242
I.7 Time traces of aerosol volume as a result of gas-particle partitioning	244
I.8 CIMS traces of α -pinene OH oxidation	244
I.9 CIMS traces of α -pinene OH oxidation	245
J.1 Total organic aerosol mass and elemental ratios.....	253
J.2 Simplified mechanism for dodecane low-NO _x photooxidation	254
J.3 Time series of m/z 183 for the early and most oxidized growth phases	255
J.4 Time series of m/z 215 for the early and most oxidized growth phases	255
J.5 Time trends of C ₁₂ backbone ions with varying degrees of oxygenation	256
J.6 Three-factor PMF solution for dodecane low-NO _x SOA.....	256
J.7 Three-factor mass spectral profiles, highlighting ion families.....	257
J.8 Factor time series with three best-correlated AMS ions.....	258
J.9 Mass spectrum of octadecane aerosol before and after irradiation.....	260
J.10 HR-ToF-AMS factor time series with CIMS tracer ions.....	260
J.11 Time trends of MOVI-ToF-CIMS aerosol tracer ions	261
J.12 Time trends for carbonyl hydroperoxide tracer ions	262
J.13 Aerosol mass distribution as a function of SOA exposure	262
J.14 Mass distributions and time series described as two PMF factors.....	263
J.15 Van Krevelen diagram for low-NO _x photooxidation of dodecane.....	264
K.1 Schematic mechanism for dodecane photooxidation.....	277
K.2 Proposed mechanism for OH oxidation of dihydrofuran.....	280
K.3 Model-predicted abundance of first-generation oxidation products	282
K.4 Time profiles of key tracer ions from AMS and CIMS measurements.....	282
K.5 Time profiles of key tracer ions from AMS and CIMS measurements.....	283
K.6 Time profiles of time trends from CIMS measurements.....	284
K.7 Time profiles of key tracer ions from AMS measurements.....	286
K.8 SOA evolution as a function of OH exposure versus ozone exposure.....	287
K.9 SOA oxidation state and a van Krevelen diagram of dodecane SOA.....	287
K.10 Time profiles of CIMS tracer ions in negative mode.....	288
K.11 Comparison of dodecane decay and SOA growth.....	289

K.12 Regimes of dominance of ozonolysis versus OH oxidation	290
L.1 Time trend of a typical uptake experiment under dry and humid conditions	300
L.2 Reactive partitioning coefficients during IEPOX injection.....	301
L.3 Reactive partitioning coefficients for trans β -IEPOX isomer	302
L.4 Ratio of organic aerosol produced to IEPOX injected.....	303
L.5 ToF-MS normalized difference spectra showing organic fragments.....	304
L.6 ToF-AMS difference spectra showing amine fragments	305
M.1 Negative secondary ion SIMS spectrum of actual and artificial fingerprints.....	331
M.2 Positive secondary ion SIMS spectrum of actual and artificial fingerprints.....	331
M.3 Negative DESI-MS spectrum of actual and artificial fingerprints	331
M.4 Positive LDI-MS spectrum of actual and artificial fingerprints	331
M.5 Examples of chemical imaging of artificial fingerprints by MS.....	331
M.6 Comparison of real and artificial developed fingerprints.....	331
N.1 (+)-DART mass spectrum of PPG	334
N.2 (+)-DART mass spectrum of a randomly chosen five-dollar bills	335
N.3 (+)-DART mass spectrum of t-butyl peroxybenzoate	335
N.4 CI mass spectrum showing water loss from a polyhydroxylated species	337
O.1 MCM mechanism for benzyl peroxy radical oxidation	356
O.2 MCM mechanism for epoxy muconaldehyde oxidation.....	357
O.3 (+)-DART mass spectra for toluene and cresol SOA	360
O.4 Van Krevelen diagram for toluene low- and high-NO SOA.....	372
O.5 Van Krevelen diagram for <i>o</i> -, <i>m</i> -, and <i>p</i> -cresol high-NO SOA	373
O.6 $Q/Q_{expected}$ vs. the number of factors.....	374
O.7 Maps for one, two, three, and four factor solutions	376
O.8 Comparison of factor mass spectra between 3-, 4-, and 5-factor solutions.....	376
O.9 $Q/Q_{expected}$ vs. f_{peak} values and vs. seed number.....	377
O.10 Factor profiles for a 3-factor solution with varying f_{peak} values.....	378
O.11 High-resolution mass spectrum of pyridine	379
O.12 Variation of the Chichibabin synthesis of pyridine.....	379

LIST OF SCHEMES

<i>Number</i>	<i>Page</i>
2.1 Proposed mechanism for the formation of hemiacetals (<i>m/z</i> 431) in dodecane SOA formed under low-NO conditions.....	13
2.2 Proposed mechanism for the formation of peroxyhemiacetals (<i>m/z</i> 432) in dodecane SOA formed under low-NO conditions.....	13
2.3 Proposed mechanism for formation of furan (<i>m/z</i> 209) and imine (<i>m/z</i> 208) species in <i>n</i> -dodecane SOA generated under low-NO conditions.....	14
2.4 Proposed mechanism for the formation of hemiacetals (<i>m/z</i> 458) in dodecane SOA formed under high-NO conditions	15
2.5 Proposed mechanism for the formation of carboxylic acids in the presence of ozone under high-NO conditions, following Ziemann <i>et al.</i> 2005.....	15
2.6 Proposed mechanism for the formation of hemiacetals (<i>m/z</i> 391) in cyclododecane SOA under low-NO conditions.....	17
2.7 Proposed mechanism for the formation and detection by DART-MS of peroxyhemiacetals (<i>m/z</i> 412) in hexylcyclohexane SOA under low-NO conditions	18
2.8 Proposed mechanism for the formation of hemiacetals (<i>m/z</i> 472) in hexylcyclohexane SOA Formed under High-NO Conditions.....	22
H.1 Proposed reaction pathways of β -caryophyllene leading to SOA	219
H.2 Proposed reaction pathways of β -caryophyllon aldehyde leading to SOA	220
H.3 Proposed reaction pathways of β -hydroxycaryophyllon aldehyde	226
H.4 Proposed reaction pathways of β -oxycaryophyllon aldehyde	226
H.5 Proposed reaction pathways of β -norcaryophyllon aldehyde	227
L.1 Formation of IEPOX isomers in low-NO photooxidation.....	297
L.2 Addition of weak nucleophiles in ring-opening of IEPOX.....	306

Chapter 1

Introduction

1.1 Motivation

While the composition of the atmosphere is predominantly gaseous, the atmosphere contains aqueous and solid phase particulate matter (aerosols) with important roles in atmospheric processes that lead to climate and visibility effects.¹ Aerosol particles have both direct and indirect effects on the atmosphere and climate. An example of a direct effect of aerosol particles is their interaction with solar radiation: atmospheric aerosol can absorb and scatter solar radiation, affecting the radiative transfer of energy and influencing climate directly. The scattering of visible light by aerosol particles is commonly recognized as the haze in urban environments, including Los Angeles. An indirect effect of aerosol particles is their role in cloud production: aerosols are known to act as cloud condensation nuclei (CCN) and ice nuclei (IN), which form clouds and thereby affect the global climate.¹ Aerosol particles are composed of organic and inorganic compounds, originate from anthropogenic or biogenic sources, and can become airborne as particles (primary organic aerosol, POA; e.g. pollen) or develop in the atmosphere as the result of chemical and physical processes (secondary organic aerosol, SOA).² The chemical compositions of POA and SOA affect their physical properties, which in turn determine their direct and indirect climate effects.

Organic compounds compose 20-90% by mass of ambient aerosol. Volatile organic compounds (VOCs) in the atmosphere originate from both anthropogenic and biogenic sources; the most abundant non-methane hydrocarbon in the atmosphere is isoprene, which is biogenic in origin.³ The atmosphere contains highly reactive radicals, predominantly OH and NO₃, which drive the oxidation of atmospheric organic compounds. As organic compounds undergo oxidation, they can decrease in volatility through the addition of polar functional groups (e.g. carbonyl and hydroxyl groups) or increase in volatility through decomposition into smaller C-chain compounds. Gas/particle partitioning of these semi- and low-volatility compounds leads to SOA formation. Ambient aerosol is often chemically complex due to the variety of ambient sources of organic compounds and the diverse products from atmospheric photooxidation of these species.⁴ Reduction of aerosol burdens and prediction of CCN efficacy and climate effects require identification of major SOA sources; this effort requires understanding of the chemistry leading to SOA formation and measurements of the chemical composition of ambient aerosol to identify the parent organic compounds.

SOA particles exist in a chemical and physical state of flux: the constituent molecules can continue to condense, evaporate, and be chemically transformed through reactions and photochemistry. The dynamic nature of gas/particle partitioning dictates that compounds can freely partition between the phases, driven by concentration gradients and temperature. Chemical reactions and photochemical reactions can occur within the bulk and at the surface of aerosol. Oxidation in the particle-phase can occur at the surface or from unique bulk processes like photo-Fenton reactions. Oligomerization is a key process in particle formation and growth; it has been shown to be important to anthropogenic and biogenic compounds. These transformative processes occur on an atmospherically relevant timescale.

Detailed chemical characterization of SOA composition at a molecular level is typically conducted using solvent extraction and electron impact ionization (EI) in order to conduct a mass spectrometric analysis. These techniques are highly useful in identifying molecules by fragmentation patterns, which indicate structural details. Analysis method artifacts arise with the use of these methods, however; less stable compounds like peroxides, epoxides, and acid-cleavable, high-boiling oligomers are not readily detectable in their native state. Derivatization and gas chromatographic/mass spectrometric (GC/MS) analysis, and liquid chromatography/mass spectrometry (LC/MS) are powerful techniques for the separation of complex mixtures and identification of components, but like all techniques, they need to be used alongside auxiliary techniques to gain a fuller view of SOA chemical composition that includes more fragile or low-volatility species. Recent advancements in ambient ionization methods including direct analysis in real time mass spectrometry (DART-MS) have shown promise in measuring sensitive compounds in complex matrices.

1.2 Research Objectives

The principal objectives of this research are to study the formation of SOA from anthropogenic marker compounds (C_{12} alkanes, toluene, and *o*-, *m*-, and *p*-cresol) under simulated urban and rural atmospheric conditions using comprehensive characterization of SOA composition using GC/MS and DART-MS, and to explore the extent of particle-phase chemistry to SOA chemical composition, specifically the importance of oligomer formation to SOA growth.

1.3 Approach

This section provides an overview of the research presented in the following chapters.

Chapter 2 describes the study of the effect of structure, NO_x conditions, relative humidity, and acidity on the chemical composition of SOA generated from the photooxidation of the C₁₂ alkanes *n*-dodecane, cyclododecane, and hexylcyclohexane. Alkanes are an important anthropogenic VOC in urban areas, and known precursors to SOA. The gas-phase oxidation of alkanes is known to lead to peroxide formation and oligomers including hemiacetals and peroxy hemiacetals.⁵ The findings presented in Chapter 2 originate from the offline analysis of alkane SOA collected via filtration by solvent extraction and GC/MS analysis paired with on-filter DART-MS analysis. In the GC/MS analysis, electron impact ionization was used along with chemical ionization by methanol to obtain structural and molecular information about the analytes. GC/EI-MS with a high-resolution time-of-flight mass spectrometer was used to obtain accurate mass measurements of the ion fragments. DART-MS analysis was performed on a commercial high-resolution system to obtain accurate mass measurements of the pseudomolecular ions and ion clusters, as well as on an experimental source coupled to an ion trap mass spectrometer to use reactive methods to identify ion clusters and the target analyte contained within the cluster. The products identified in this research show the influence of particle-phase oligomerization, cyclization, and imine formation on alkane SOA chemical composition, as well as the impact of NO_x and parent alkane structure.

Chapter 3 describes the study of toluene SOA formation under low- and high-NO conditions, and explores the influence of the cresol pathway on determining the chemical composition of toluene SOA. Toluene is known to undergo photooxidation through a bicyclic peroxy radical intermediate as well as through a cresol intermediate; those two major pathways account for 83% of the photooxidative fate of toluene. Low and extremely low volatility organic compounds (LVOC and ELVOC) are known to be important to aromatic SOA formation, as well as oligomeric species, particularly those derived from glyoxal. In this research, the extent to which LVOC and ELVOC comprise aromatic SOA is explored, as well as ascertaining the nature of those compounds to determine the contributions of oligomerization and multigenerational photooxidation to the formation of these low-volatility species and toluene SOA. To this end, toluene and *o*-, *m*-, and *p*-cresol were directly photooxidized under comparable conditions to allow for the comparison of SOA chemical compositions and the estimation of the contribution of the cresol pathway to toluene SOA. In this study, chemical analysis of SOA was conducted by using high-resolution aerosol mass spectrometry (HR-AMS) and high-resolution direct analysis in real time mass spectrometry (DART-HR-MS). The

mass spectral datasets for toluene and *o*-cresol SOA produced under high-NO conditions were qualitatively analyzed using positive matrix factorization to draw out commonalities and differences between the different growth periods of toluene and cresol SOA. The chemical compositions measured by offline DART-HR-MS analysis were examined in van Krevelen space to identify overall trends in functionalization and fragmentation over the course of the photooxidation experiment.

To close, chapter 4 summarizes the main findings of this research and provides future directions for extensions of this work. Additional applications of offline analysis of SOA to the addressing of major chemical questions involving biogenic SOA, anthropogenic SOA, and ambient SOA are located in the Appendices.

1.4 References

1. Boucher, O.; Randall, D.; Artaxo, P.; Bretherton, C.; Feingold, G.; Forster, P.; Kerminen, V.-M.; Kondo, Y.; Liao, H.; Lohmann, U.; Rasch, P.; Satheesh, S. K.; Stevens, B.; Zhang, X. Y., Clouds and Aerosols. In *Climate Change 2013: The Physical Science Basis. Contribution of Working Group I to the Fifth Assessment Report of the Intergovernmental Panel on Climate Change*, Stocker, T. F. Q., D.; Plattner, G.-K.; Tignor, M.; Allen, S. K.; Boschung, J.; Nauels, A.; Xia, Y.; Bex, V.; Midgley, P. M., Ed. Cambridge University Press: Cambridge, United Kingdom and New York, NY, USA, 2013.
2. Seinfeld, J. H.; Pandis, S. N. *Atmospheric Chemistry and Physics*; Wiley: New York, 1998.
3. Guenther, A.; Karl, T.; Harley, P.; Wiedinmyer, C.; Palmer, P. I.; Geron, C. Estimates of Global Terrestrial Isoprene Emissions Using Megan (Model of Emissions of Gases and Aerosols from Nature). *Atmos. Chem. Phys.* **2006**, *6*, 3181-3210.
4. Hall, W. A.; Johnston, M. V. Oligomer Content of α -Pinene Secondary Organic Aerosol. *Aerosol Sci. Technol.* **2011**, *45*, 37-45.
5. Ziemann, P. J. Formation of Alkoxyhydroperoxy Aldehydes and Cyclic Peroxyhemiacetals from Reactions of Cyclic Alkenes with Ozone in the Presence of Alcohols. *J. Phys. Chem. A* **2003**, *107*, 2048-2060.

Chapter 2

Secondary Organic Aerosol Composition from C₁₂ Alkanes¹

¹ This chapter is reproduced by permission from “Secondary Organic Aerosol Composition from C₁₂ Alkanes” by K. A. Schilling, F. H. Fehsenfeld, L. D. Yee, C. L. Loza, M. M. Coggon, R. Schwantes, X. Zhang, N. F. Dalleska, J. H. Seinfeld. *J. Phys. Chem. A*, Article ASAP, DOI: 10.1021/jp501779w, 9 May 2014. Copyright 2006 American Chemical Society.

Secondary Organic Aerosol Composition from C₁₂ Alkanes

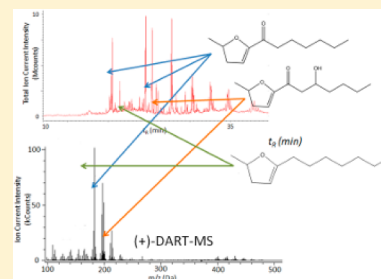
Katherine A. Schilling Fahnestock,[†] Lindsay D. Yee,^{‡,§} Christine L. Loza,^{†,||} Matthew M. Coggon,[†] Rebecca Schwantes,[‡] Xuan Zhang,[‡] Nathan F. Dalleska,[‡] and John H. Seinfeld^{*,†,‡}

[†]Division of Chemistry and Chemical Engineering, California Institute of Technology, Pasadena, California 91125, United States

[‡]Division of Engineering and Applied Science, California Institute of Technology, Pasadena, California 91125, United States

Supporting Information

ABSTRACT: The effects of structure, NO_x conditions, relative humidity, and aerosol acidity on the chemical composition of secondary organic aerosol (SOA) are reported for the photooxidation of three C₁₂ alkanes: *n*-dodecane, cyclododecane, and hexylcyclohexane. Acidity was modified through seed particle composition: NaCl, (NH₄)₂SO₄, and (NH₄)₂SO₄ + H₂SO₄. Off-line analysis of SOA was carried out by solvent extraction and gas chromatography–mass spectrometry (GC/MS) and direct analysis in real-time mass spectrometry. We report here 750 individual masses of SOA products identified from these three alkane systems and 324 isomers resolved by GC/MS analysis. The chemical compositions for each alkane system provide compelling evidence of particle-phase chemistry, including reactions leading to oligomer formation. Major oligomeric species for alkane SOA are peroxyhemiacetals, hemiacetals, esters, and aldol condensation products. Furans, dihydrofurans, hydroxycarbonyls, and their corresponding imine analogues are important participants in these oligomer-producing reactions. Imines are formed in the particle phase from the reaction of the ammonium sulfate seed aerosol with carbonyl-bearing compounds present in all the SOA systems. Under high-NO conditions, organonitrate products can lead to an increase of aerosol volume concentration by up to a factor of 5 over that in low-NO conditions. Structure was found to play a key role in determining the degree of functionalization and fragmentation of the parent alkane, influencing the mean molecular weight of the SOA produced and the mean atomic O:C ratio.



INTRODUCTION

Secondary organic aerosol (SOA) formation generally proceeds by the multigeneration gas-phase oxidation of volatile organic compounds (VOCs) followed by condensation of the oxidized products into the aerosol phase.¹ It has been well-established that once in the particle phase, oxidation products may undergo additional chemistry, including oligomerization reactions.^{2–8} A dominant issue in a particular VOC system is the extent of particle-phase chemistry in its SOA formation. Oligomerization has in some cases been observed to occur within seconds of the onset of particle formation and, in addition, can be sensitive to the presence of acidic species.^{3,4,8} Low-volatility, high-molecular weight oligomers can influence the particle's phase state.^{9–11} The molecular characterization of the particle phase holds the key to identifying particle-phase chemistry in SOA formation.

Cyclic, branched, and linear alkanes constitute a large fraction of gasoline and diesel fuel.¹² Moreover, alkane combustion and photooxidation products are known to be important contributors to urban and transportation-related SOA.^{12–15} Alkane SOA composition has been reported in a number of studies (Table 1).^{15–30}

These studies encompass both flow tube and environmental chamber photooxidation of C₆ to C₂₇ alkanes with cyclic, linear, and branched structures under high- and low-NO conditions. Observed photooxidation products are hydroxycarbonyls, alcohols, aldehydes, and carboxylic acids, as well as more complex species such as furans, lactones, and peroxyhemiac-

tals. Combined experimental and modeling studies point to the importance of oligomer formation under low-NO oxidation of *n*-dodecane.^{32,35,36} Targeted studies showed that peroxyhemiacetals can be important contributors to alkane SOA formation under low-NO conditions when both aldehydes and hydroperoxides are present in the gas phase.^{25,36}

Particle-phase chemistry of carbonyl groups is known to lead to relatively complex structures; for example, 1,4-substituted hydroxycarbonyl compounds form cyclic hemiacetals that can dehydrate to form dihydrofurans.³⁷ 1,4-hydroxycarbonyls are found in both the gas and particle phases and when additionally substituted may participate in further particle-phase chemistry. Aldehydes are known to undergo imine formation in the presence of amines, but none of the studies to date has investigated nitrogen incorporation in the organic aerosol phase, other than the nitration of secondary alkane sites under high-NO conditions.^{38–40} Imines are an important constituent of “brown carbon”, a broad category of chromophoric organic material that impacts the optical properties of atmospheric aerosol.⁴¹ Gas- and particle-phase chemical analyses employed in these previous studies provide a foundation for interpreting

Special Issue: Mario Molina Festschrift

Received: February 19, 2014

Revised: May 8, 2014

Table 1. Prior Alkane SOA Composition Studies

alkane system	experimental conditions	technique employed	types of products identified	reference
cholestone ($C_{27}H_{48}$)	flow tube reactor, OH-initiated heterogeneous oxidation	2D-GC/ToF-MS (EI or VUV)	ketones, aldehydes, alcohols, hydroxyketones	Zhang et al. ¹⁵
C_5 - C_8 <i>n</i> -alkanes	chamber-based OH oxidation with NO	SPME/GC-FID	hydroxyketones	Reisen et al. ¹⁶
hydroxy-aldehydes	chamber-based OH oxidation	Tenax and SPME/GC-FID	alcohols, aldehydes	Baker et al. ¹⁷
squalane ($C_{30}H_{62}$), octacosane	flow tube reactor, OH-initiated heterogeneous oxidation	2D-GC/ToF-MS	carbonyls, alcohols, lactones, hydroxyketones, carboxylic acids	Ruehl et al. ²¹
$C_{15,16}$ <i>n</i> -alkanes, $C_{12,15}$ cyclic alkanes, 2,6,10-trimethyldodecane	chamber-based high- NO_x OH oxidation	thermal desorption particle beam MS (TDPB-MS)	dihydrofurans, alkyl nitrates, hydroxyketones	Lim et al. ²²
C_{6-17} linear alkanes, $C_{6-8,10,12,15}$ cyclic alkanes, C_{6-11} branched alkanes	chamber-based high- NO_x OH oxidation	TDPB-MS	dihydrofurans, alkyl nitrates, hydroxyketones	Lim et al. ²³
C_{8-15} alkanes	chamber-based high- NO_x OH oxidation	TDPB-MS	hydroxy-nitrates, dinitrates, substituted tetrahydrofurans	Lim et al. ²⁴
$C_{6,7,8,10}$ cyclic monoalkenes	chamber-based ozonolysis, reaction of alcohols with stabilized Criegee intermediates	TDPB-MS	alkoxy hydroperoxy aldehydes, peroxyhemiacetals (PHA)	Ziemann ²⁵
<i>n</i> -dodecane	chamber-based OH oxidation	chemical ionization MS (CIMS), aerosol MS (AMS)	hydroxycarbonyls, hydroperoxycarbonyls, hydro-peroxides, peracids, PHA	Yee et al. ²⁸ Craven et al. ³¹
<i>n</i> -dodecane, 2-methylundecane, hexylcyclohexane, cyclododecane	chamber-based OH oxidation	CIMS, AMS	hydroxycarbonyls, hydroperoxides, hydroperoxy carbonyls, acids, PHA	Yee et al. ³²
$C_{10,15,17}$ <i>n</i> -alkanes tricyclo[5.2.1.0] -decane, diesel fuel, crude oil	PAM flow reactor with OH oxidation	AMS	no speciation; O:C ratios 0.13–1.33	Lambe et al. ³³
cyclo $C_{8,10,15}$, pentyl- and decylcyclohexane, pristane ($C_{19}H_{40}$), 7-methyltridecane, 2-methylundecane, <i>n</i> -dodecane	environmental chamber, OH oxidation under high- NO_x conditions	AMS	no speciation; O:C ratios from 0.1 to 0.5	Tkacik et al. ³⁴

dependence of alkane SOA composition resulting from changes in reaction conditions or parent compound structure.

We report characterization of the chemical composition of SOA generated in the low- and high- NO oxidation of three C_{12} alkanes: *n*-dodecane, hexylcyclohexane, and cyclododecane. We also report the first application of direct analysis in real-time mass spectrometry (DART-MS) to off-line filter samples to determine SOA composition; this method allows us to identify intact compounds, including species prone to reactive loss and decomposition. Off-line analysis of SOA allows the application of a variety of softer ionization conditions, preserving functionalities not detected in aerosol mass spectrometry (AMS). Reactive DART-MS using ion trap mass spectrometry allowed the confirmation of hydroperoxide and peroxide functional groups. Gas chromatography – mass spectrometry enabled the resolution of isomeric species and provided structural information. We address the evidence for particle-phase chemistry in each of these three alkane systems through detailed analysis of the particle-phase composition. By the combination of these two mass spectrometry approaches, we are able to report close to 100% identification and quantification of the particle phase for each of the three alkane systems. In all, 750 individual mass spectral features are identified, and 324 isomers are resolved. We begin with a description of the experimental techniques applied, followed by a discussion of the compositions for each of the three alkane systems. Plausible reaction mechanisms associated with the key identified species are presented.

EXPERIMENTAL SECTION


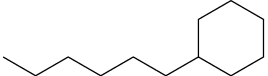
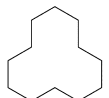
SOA formation from oxidation of three C_{12} alkanes (Table 2) was studied in the dual 24 m³ Teflon reactors in the Caltech Environmental Chamber, which is described elsewhere.^{28,29,42}

Hydroxyl radicals were generated via photolysis of hydrogen peroxide using black lights with a peak wavelength of 350 nm. H_2O_2 (280 μ L of 50% wt. solution, Sigma-Aldrich) was measured with a glass syringe (Hamilton) and injected into a glass trap, which was then immersed in a water bath (35–38 °C) while 5 L min⁻¹ of filtered air flowed through the trap into the chamber. H_2O_2 was volatilized over the course of 90 min under these conditions, producing an initial mixing ratio of approximately 4 ppm. An aqueous solution of ammonium sulfate was prepared from solid ammonium sulfate (>99.9%, Sigma-Aldrich) and water (18 M Ω , Milli-Q). Ammonium sulfate seed aerosol was produced by atomizing a 0.015 M aqueous solution into the chamber, providing a 15–20 μ m³ cm⁻³ volume concentration. Atomization of aqueous solutions of 0.015 M NaCl (Sigma-Aldrich, >99%) and $(NH_4)_2SO_4$ mixed with H_2SO_4 (Sigma-Aldrich, 18 M) produced seed aerosol at similar volume concentrations in selected experiments (Table 3).

Teflon filters (Pall Life Sciences, 47 mm, 1.0 μ m pore size), on which SOA was collected, were cleaned prior to aerosol collection by sonication in a 50/50 (v/v) mixture of heptane (Aldrich, Chromasolv, >99%) and acetone (EMD, Omnisolv, 99.5%). The filters were dried in glass Petri dishes under a gentle stream of UHP nitrogen on an aluminum block heated to 35 °C. Once dry, the filters were stored in glass scintillation vials with Teflon-lined caps prior to use. Aerosol was collected on filters in parallel at flow rates of 17 ± 1 and 23 ± 1 L min⁻¹ for 2 h.

Analysis of SOA by DART-MS. Filter samples were analyzed using two different DART-MS systems: a JEOL

Table 2. C₁₂ Compounds Studied

Parent Compound	Structure	P _{vap} ^a at 25 °C (atm)	k _{OH} × 10 ¹² ^b (cm ³ molec ⁻¹ s ⁻¹)
<i>n</i> -Dodecane		2.59 × 10 ⁻⁴	13.9
Hexylcyclohexane		4.1 × 10 ⁻⁴	13.1
Cyclododecane		1.64 × 10 ⁻⁴	14.7

^aUsing EVAPORATION.⁴³ ^bCalculated using relative rate from *n*-dodecane k_{OH} in the University of Leeds' Master Chemical Mechanism (MCM).⁴⁴

AccuToF DART-MS and the custom-built Caltech mini-DART source on a Thermo LTQ ion trap mass spectrometer. The combination of both instruments provided both accurate mass measurements and MS/MS data to confirm adduct identities.

The JEOL DART-MS was operated with the discharge electrode set to +5 kV and subsequent electrodes set to +150 and +250 V. Helium flow was set at 1 L min⁻¹, and the source was heated to 200 °C. Mass calibration was performed for accurate mass measurement in both positive and negative modes by the analysis of a standard solution of PEG-600 in methanol. Solids were analyzed by placing a small piece in the DART stream with stainless steel forceps. Solutions were analyzed by dipping a glass capillary in the solution and placing the capillary tip in the DART stream. A 1 cm wide swath was cut from the center of each filter using clean stainless steel surgical scissors. The filter membrane piece was wrapped around the tip of clean stainless steel forceps and placed in the path of the DART stream until the ion current began to decline after reaching a maximum, indicating that most of the available organic material had been removed during analysis.

The mini-DART source that we employed offers flexibility in the ionizer configuration as well as the ability to conduct MS² experiments with the ion trap mass spectrometer. The needle electrode was operated at a DC potential of 3–5 kV with a current between 0.2 and 1.0 mA. The filter electrode was maintained at a potential of +110–250 V, based on prior studies with other DART systems.^{45–48} The helium flow was 1.0 L min⁻¹, and the source temperature was 200 °C. The outlet of the mini-DART was oriented for direct flow into the mass spectrometer inlet at a distance of 1–3 cm; the sample, prepared identically to those analyzed on the JEOL instrument, was manually introduced into this space. Additional standard analyses using the mini-DART to assess analyte response across a broad range of vapor pressures using polypropylene glycol, cocaine, and heroin are included in the Supporting Information.

Homologous compound standards were analyzed under conditions identical to those of chamber SOA samples to identify ionization artifacts and to validate interpretation of DART mass spectra. A precleaned Teflon filter was spiked with 100 μL of a 4 ppm standard containing *n*-dodecane (Sigma-Aldrich, 99+%), 2-dodecanol (Aldrich, 99%), 2-dodecanone (Aldrich, ≥97%), 1,12-dodecanediol (Aldrich, 99%), and dodecanoic acid (Sigma, ≥99%) in heptane/acetone (50/50, v/v). The filter was analyzed in the same manner as the chamber samples. For calibration of liquid samples, a clean glass capillary was dipped into the 4 ppm standard mixture and analyzed. Benzoyl peroxide, lauroyl peroxide, and *tert*-

butylperoxy benzoate were analyzed individually by dipping a clean glass capillary into an aliquot of each neat compound then passing it through the DART stream. For confirmation of the presence of primary amines (in this case, ammonia), a syringe with a 2 mM solution of 18-crown-6 in methanol was primed to load a droplet onto the needle tip. The 18-crown-6 droplet was cointroduced into the DART stream with the peroxide liquid sample. Ammonium ion adducts disappear with introduction of 18-crown-6 and are replaced by proton adducts ([M + H]⁺). Further discussion of this procedure as well as example mass spectra appear in the Supporting Information.

Targeted quantitative analysis by DART-MS requires the presence of an internal standard, typically one that is isotopically labeled so as to have the same vapor pressure and proton affinity as the analyte.⁴⁹ Choosing an internal standard is more difficult in the case of a complex mixture of unknown compounds with a range of vapor pressures. The ideal internal standard for SOA analysis would be an organic compound with a vapor pressure and proton affinity similar to that of the projected components, be present solely in the particle phase at a mixing ratio near that of the photochemical products, but be nonparticipatory in particle-phase reactions. Such an ideal standard has not been identified, so an alternative internal standard was chosen. Dibutyl phthalate is present in the Teflon filters used to collect the particles; it can be considered to be in excess with respect to individual SOA components. It is also assumed that its ion current intensity is proportional to the DART stream spot size and other transient ionization conditions.

Vapor pressures and proton affinities must be similar for the internal standard and average predicted analyte. Semivolatile compounds have vapor pressures between 10⁻⁵ and 10⁻¹¹ atm, and compounds composing aerosol have vapor pressures below about 10⁻¹¹ atm.⁵⁰ Dibutyl phthalate has a vapor pressure of 5.93 × 10⁻⁹ atm at 298 K.⁵¹ This vapor pressure is within the range of expected analyte vapor pressures but biased toward the semivolatile range. Dibutyl phthalate forms a proton adduct ([M + H]⁺, *m/z* 279.1591) in positive-mode DART ionization.^{52,53} Proton affinity (PA) is defined by the reaction of M + H⁺ → MH⁺, where ΔH_{rxn} = -PA, and PA is reported in kilojoules per mole.⁵⁴ The estimated PA for the average predicted alkane SOA compound is on the order of ~839 kJ mol, based on the PA values for homologous compounds (4-methylcyclohexanone (844.9 kJ mol⁻¹), ethyl methyl carbonate (842.7 kJ mol⁻¹), *n*-propyl acetate (836.6 kJ mol⁻¹), *n*-dipropyl ether (837.9 kJ mol⁻¹), 4-heptanone (845.0 kJ mol⁻¹), tetrahydro-2-methylfuran (840.8 kJ mol⁻¹), and 2,5-dihydrofur-

Table 3. Summary of Experimental Conditions^a

parent VOC	[VOC] ₀ (ppb)	oxidant precursor	[NO] ₀ (ppb)	[NO ₂] ₀ (ppb)	[O ₃] ₀ (ppb)	T (°C)	RH (%)	seed	seed volume (μm ³ cm ⁻³)	total organic volume (μm ³ cm ⁻³)
<i>n</i> -dodecane	321	H ₂ O ₂	ND	ND	ND	24.11	3.3	(NH ₄) ₂ SO ₄	20	167
<i>n</i> -dodecane	359	H ₂ O ₂	ND	ND	ND	23.9	54.1	(NH ₄) ₂ SO ₄	35	56
<i>n</i> -dodecane	245	H ₂ O ₂ + NO	97.5	ND	ND	23.2	5.6	(NH ₄) ₂ SO ₄	15	376
<i>n</i> -dodecane	342	H ₂ O ₂	7.9	ND	ND	23.9	2.8	MgSO ₄ + H ₂ SO ₄	14	74
<i>n</i> -dodecane	366	H ₂ O ₂	ND	ND	ND	23.6	59.7	NaCl	32	80
<i>n</i> -dodecane	339	H ₂ O ₂	ND	ND	ND	24.0	2.4	NaCl	15	138
hexylcyclohexane	457	H ₂ O ₂	ND	ND	ND	24.1	3.3	(NH ₄) ₂ SO ₄	21	265
hexylcyclohexane	332	H ₂ O ₂ + NO	120.1	ND	ND	23.1	4.5	(NH ₄) ₂ SO ₄	16	748
cyclododecane	330	H ₂ O ₂	ND	ND	ND	24.0	5.1	(NH ₄) ₂ SO ₄	19	144
cyclododecane	293	H ₂ O ₂ + NO	102.1	ND	ND	22.5	4.0	(NH ₄) ₂ SO ₄	14	767

^aAerosol samples collected by filtration during final 2 h of photooxidation. ND = not detected (limit of detection is 5 ppb). In the fourth *n*-dodecane experiment, 7.9 ppb of NO was not added deliberately and did not affect the experimental outcome significantly. Total organic volume is wall-loss corrected.

an (823.4 kJ mol⁻¹).⁵⁵ The proton affinity of dibutyl phthalate can be estimated from its homologue, dimethyl *p*-phthalate (843.2 kJ mol⁻¹).⁵⁵ The difference between the estimated PA for the internal standard, dibutyl phthalate, and the average predicted alkane SOA compound is ~0.5%. There is good agreement between the internal standard and predicted analyte PA, and the assumption that the ratio of the internal standard and analyte PA is ~1 holds for this predicted system.

A relationship between analyte concentration and ion current must be established next. For DART-MS, the ion current intensity *I* of any species is proportional to the concentration *C*, vapor pressure *P*_{vap}, and proton affinity *A*: $I = AP_{\text{vap}}C$. This equation is written for both the analyte (*A*) and the internal standard (*IS*) and then ratioed, allowing for the cancellation of the proton affinity term. Analyte vapor pressures were estimated by using the EVAPORATION model; imine functional groups are not included in the EVAPORATION model, but their vapor pressures were estimated from their carbonyl analogues because of the first-order similarity in bond polarity between carbon and oxygen or nitrogen.⁴³ When rewritten to solve for the ratio of the concentration of analyte to the concentration of the internal standard, the equation becomes

$$\frac{C_A}{C_{\text{IS}}} = \frac{P_{\text{vap,IS}} I_A}{P_{\text{vap,A}} I_{\text{IS}}}$$

The dominance of one or a few compound classes makes it preferable to use the log of the ratio of concentrations of analyte to internal standard for each compound and summed for each compound class. The relative concentrations for each compound class allows for comparison between functional group abundances. To calculate the mean molecular weight for each chamber SOA sample, these relative concentrations were summed to obtain the total. Using the total, a percentage contribution for each compound was obtained, and that was used as the weighting factor for each compound in calculating the mean molecular weight. A further discussion of this calculation procedure appears in the Supporting Information.

From the formulas obtained by DART-ToF-MS analysis, H:C and O:C ratios were calculated and plotted on a van Krevelen diagram⁵⁶ to depict the trends in functionalization and fragmentation for each chamber SOA sample. Typically, a van Krevelen diagram is generated from high-resolution aerosol mass spectrometry data, where each data point on the diagram corresponds to the bulk SOA chemical composition at a specific time point. Here, each data point represents a specific compound detected by DART-MS. The van Krevelen diagram has been developed as an interpretation of HR-MS data to visualize the functionalization of complex organic mixtures.^{30,33,56-62} The slope of a line drawn between or through points in a van Krevelen diagram represents the extent of addition or loss of C, H, or O atoms, which when interpreted with the source HR-MS data obtained by soft ionization, translates to the net differences in functionality between the detected compounds.^{33,60} From this type of analysis, the distribution of products from a chamber SOA sample can be visualized and interpreted along the lines representing hydration, peroxide formation or alcohol addition, ketone or aldehyde formation, carboxylic acid formation, or nitrate addition. The line with slope = -1, for example, can represent both a carboxylic acid group addition or the addition of both a carbonyl group and a hydroxyl group to the same compound;

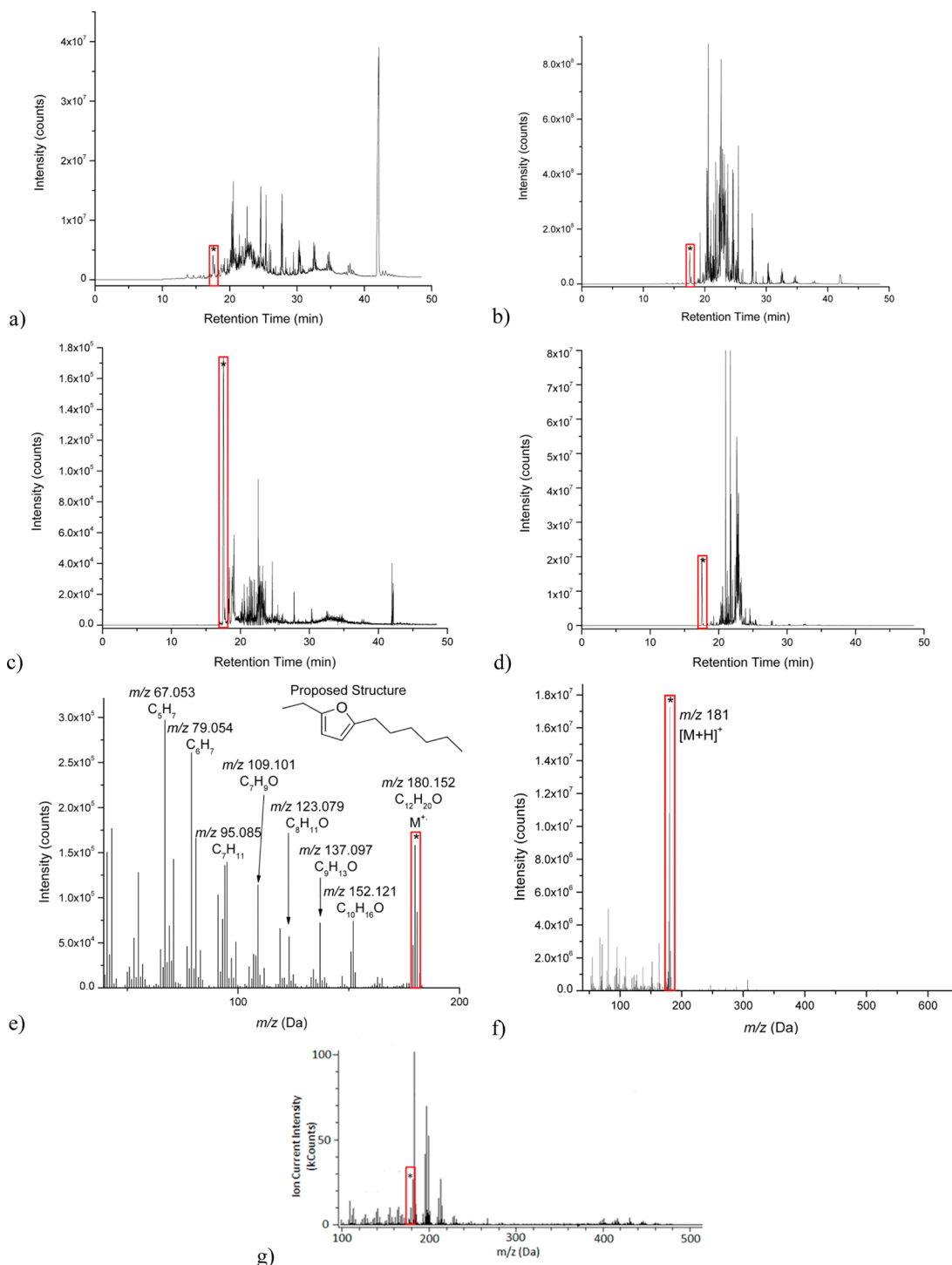


Figure 1. (a) Total ion chromatogram (EI-MS) of *n*-dodecane SOA produced under low-NO conditions with ammonium sulfate seed aerosol. The starred peak at 17.5 min corresponds to the target analyte with a molecular weight of 180 amu. (b) Total ion chromatogram (CI-MS) of *n*-dodecane SOA produced under low-NO conditions. The starred peak at 17.5 min corresponds to the target analyte with a molecular weight of 180 amu. (c) Extracted ion chromatogram (EI-MS) for m/z 180. The starred peak at 17.5 min corresponds to the target analyte with a molecular weight of 180 amu. (d) Extracted ion chromatogram (CI-MS) for m/z 180. The starred peak at 17.5 min corresponds to the target analyte with a molecular weight of 180 amu. (e) Electron impact mass spectrum at 17.5 min, with m/z values labeled from the high-resolution GC/ToF-MS analysis, along with assigned fragment formulas. (f) Chemical ionization mass spectrum at 17.5 min, with methanol as the reagent gas. (g) (+)-DART mass spectrum of *n*-dodecane SOA produced under low-NO conditions with ammonium sulfate seed aerosol. The starred peak corresponds to the target analyte with a molecular weight of 180 amu.

therefore, hydroxycarbonyl formation and carboxylic acid formation appear along the same line on a van Krevelen diagram.

Analysis of SOA by GC/MS. Filter extracts were analyzed by a Varian Saturn 2200 gas chromatograph (GC) ion trap mass spectrometer. The GC was equipped with an autosampler, a programmed temperature vaporization (PTV) injector

(Varian 1079) lined with a deactivated glass single-gooseneck liner with a deactivated glass frit (Restek, Sky, 3.4 mm ID), and a DB5-MSUI column (0.25 $\mu\text{m} \times 0.25 \text{ mm} \times 30 \text{ m}$). The PTV inlet temperature program was (i) 45 $^{\circ}\text{C}$ for 0.50 min, (ii) 180 $^{\circ}\text{C min}^{-1}$ to 300 $^{\circ}\text{C}$, and (iii) hold at 300 $^{\circ}\text{C}$ for 46.58 min. The oven temperature program was (i) 65 $^{\circ}\text{C}$ for 10 min, (ii) 10 $^{\circ}\text{C min}^{-1}$ to final temperature of 300 $^{\circ}\text{C}$, and (iii) 300 $^{\circ}\text{C}$ for 15 min. Electron impact and chemical ionization (CI) mass spectra were collected for each sample. The GC/CI-MS analysis was conducted with methanol as the reagent gas, generating protonated analyte species ($[\text{M} + \text{H}]^+$). These protonated species are not stable and dehydrate to form $[\text{M} + \text{H} - n\text{H}_2\text{O}]^+$. Additional analysis by GC/CI-MS/MS using methanol as the reagent gas was conducted to obtain additional structural information for compounds detected in CI mode. Additional discussion of standards analysis and measures taken to minimize method artifacts is provided in the Supporting Information.

Samples were also analyzed on a Waters GCT Premier in electron impact (EI) ionization mode. The GCT Premier combines an Agilent 6890N GC with a Waters orthogonal acceleration time-of-flight mass spectrometer (resolution 7000 fwhm). The GC was equipped with an autosampler (Agilent 7683), a split/splitless injector held at 275 $^{\circ}\text{C}$ and lined with a deactivated glass single-gooseneck liner with a deactivated glass wool plug (Restek, Sky, 4.0 mm ID), and a DB5-MS column (0.25 $\mu\text{m} \times 0.25 \text{ mm} \times 30 \text{ m}$). The oven temperature program was (i) 65 $^{\circ}\text{C}$ for 10 min, (ii) 10 $^{\circ}\text{C min}^{-1}$ to final temperature of 300 $^{\circ}\text{C}$, and (iii) 300 $^{\circ}\text{C}$ for 15 min. Continuous introduction of perfluorotributylamine (PFTBA) to the ion source enabled accurate mass determination. Postprocessing of centroid mass spectra was carried out by linear interpolation between PFTBA peaks on either side of the analyte peak of interest.

The GC/MS data set comprises unit-mass resolution data acquired in both EI and methanol CI mode on the Varian Saturn GC/IT-MS and high-resolution data acquired in EI mode on the Waters GCT Premier. By using nearly identical temperature programs and identical columns, compounds were linked across ionization modes and instruments by retention time. A database was assembled of retention time and mass spectral data (ions formed under CI, EI-MS fragments, and molecular ions) for all samples tested. Through these correlations of molecular responses to the different ionization conditions and the use of high-resolution mass spectral data, molecular formulas were obtained using the elemental composition tool in MassLynx (Waters).

SOA samples generated under high- and low-NO conditions with ammonium sulfate seed were analyzed by high-resolution mass spectrometry with positive mode DART ionization (DART-MS). For DART-MS data, all mass spectral peaks over 1% relative intensity (approximately 1000 counts, signal-to-noise ratio ≈ 7) were included in the analysis. Assignments were made by choosing the minimum error for a formula that fits within the expected range of elemental compositions ($\text{C}_1\text{--}\text{C}_{50}$, $\text{H}_1\text{--}\text{H}_{100}$, $\text{O}_0\text{--}\text{O}_{50}$, $\text{N}_0\text{--}\text{N}_5$); the mass tolerance was 15 ppm. The DART-MS analysis was complemented by adding the dimension of chromatographic separation (GC/MS) with its sensitivity to structural differences. Chromatograms with unit-mass resolution electron impact and chemical ionization, as well as high mass resolution electron impact mass spectral data, were acquired for each sample. Chromatographic peak intensity was judged relative to the most intense peak present,

and all chromatographic peaks over 5% relative intensity were included in the analysis.

RESULTS AND DISCUSSION

Chromatographic retention times were used as identifiers for compounds in GC/EI-MS (high- and unit-mass resolution) and GC/CI-MS data. GC/CI-MS peaks were paired by retention time to GC/EI-MS data acquired on the same instrument. Retention times were repeatable to ± 0.01 min between chromatographic runs. Retention time indexing enabled the linking of molecular weight (obtained from the measured $[\text{M} + \text{H}]^+$) to the fragmentation pattern produced by electron impact ionization. $[\text{M} + \text{H}]^+$ unit mass values were used in conjunction with the DART-MS data to identify intact molecules outside of GC/MS analysis and to obtain molecular formulas from the high-resolution DART mass spectra. Figure 1 shows the progression of data analysis from a total ion chromatogram, which is composed of the signal of all ions as a function of retention time, for both EI- and CI-MS (Figure 1a,b), to an extracted ion chromatogram (Figure 1c,d), which targets a specific ion's signal as a function of retention time, to the mass spectrum of a compound at a specific time point (Figure 1e,f), representing a single compound. The DART mass spectrum for the same sample is depicted in Figure 1g.

Interpretation of GC/EI-MS Data. Unit-mass resolution GC/EI-MS data were linked by retention time to high-mass resolution GC/EI-MS data. The high-resolution mass spectra were the combination of the analyte and the mass calibrant, PFTBA, so the unit-mass resolution EI mass spectra were used as a reference to identify analyte peaks. The accurate masses of ions were converted to formulas through the use of Waters' Mass Lynx software. Fragmentation patterns were interpreted for structural information with the assistance of the National Institute of Standards and Technology programs MS Search and MS Interpreter.

Interpretation of GC/CI-MS Data. Methanol CI mass spectra with a pattern of peaks spaced by 18 Da were observed for many chromatographic peaks. These losses of water masses are explained as the result of dehydration reactions arising from the protonation of a hydroxylated compound; the peaks then represent $[\text{M} + \text{H}]^+$ ions and, in the case of polyhydroxylated compounds, $[\text{M} + \text{H} - n\text{H}_2\text{O}]^+$ ions. An example mass spectrum that demonstrates the dehydration that can occur when a polyhydroxylated compound undergoes chemical ionization is included in the Supporting Information.

Interpretation of DART Mass Spectra. Positive mode DART ionization uses ambient gases to execute proton transfer or form ion adducts with analyte molecules. Accurate mass measurements allowed the determination of ion formulas, and interpretation of the ion's identity as a proton, water, or ammonium adduct was done by interpreting MS/MS data from the Caltech mini-DART coupled to a Thermo LTQ ion trap mass spectrometer and by evaluating the most reasonable structure from a given formula derived from accurate mass measurements made with the JEOL AccuToF DART. $[\text{M} + \text{H}]^+$ and $[\text{M} + \text{H} - n\text{H}_2\text{O}]^+$ m/z values from DART-MS were correlated with GC/CI-MS values and thereby linked with their chromatographic retention times and electron impact mass spectra acquired with unit-mass and high resolution. Multiple occurrences of $[\text{M} + \text{H}]^+$ and $[\text{M} + \text{H} - n\text{H}_2\text{O}]^+$ m/z values at different retention times were interpreted as different structural isomers (see Figure 1c).

Reactive DART-MS methods were used with the Caltech mini-DART to differentiate nitrates, imines, and hydroperoxide-ammonium adducts. The flexible ionizer configuration allowed for the inclusion into the DART gas stream of 1,4,7,10,13,16-hexaoxacyclooctadecane (abbrev. 18-crown-6), a reagent that strongly complexes with primary amines. An important analytical goal was to differentiate ammonium ion adducts from imine or nitrate compounds by monitoring the decrease and disappearance of even m/z compounds from the mass spectrum upon the introduction of 18-crown-6. The decline of ammonium ion adducts with peroxides in the presence of 18-crown-6 is caused by the more favorable formation of 18-crown-6 ammonium ion adducts. Proton adducts of peroxides are then detected once the ammonium ion-peroxide adducts are not produced in high abundance. Spectra that illustrate this method of analysis are provided in the Supporting Information.

SOA Composition. The experiments were targeted at exploring the effects of structure (cyclic versus linear alkane) on SOA composition, and for each structure, the effects of the $\text{RO}_2 + \text{HO}_2$ pathway (low NO) versus the $\text{RO}_2 + \text{NO}$ pathway (high NO). For the *n*-dodecane system, the additional effects of relative humidity and seed type on SOA composition were investigated.

***n*-Dodecane SOA Composition.** *n*-Dodecane Low-NO SOA Composition. *n*-Dodecane, when oxidized in the $\text{RO}_2 + \text{HO}_2$ regime, forms hydroperoxides and hydroxyl- and carbonyl-bearing compounds (Figure 2).^{28,32} These functional additions can occur sequentially on the full C_{12} backbone or on smaller carbon chains if fragmentation reactions are occurring. Products of sufficiently low volatility appear in the particle phase.

The dominant species in *n*-dodecane SOA under the low-NO regime are functionalized hemiacetals and peroxyhemiacetals, which together constitute over 98% of the assigned SOA mass (Figure 2a). These compounds form from particle-phase reactions that are traditionally considered to be acid-catalyzed; we propose that ammonium ions from the seed are involved because of their abundance and activity (Scheme 1). Under ~4% RH conditions, ammonium sulfate seed is minimally hydrated with physisorbed monolayers of water. Ammonium sulfate seed has been shown for other hydrocarbon systems to promote oligomer formation under dry conditions from pathways that are traditionally acid-catalyzed.^{3,4,63} The presence of these oligomers is consistent with the activity of an acid catalyst, but we cannot unequivocally establish that ammonium ions and surface monolayers of water are responsible for the products we found.

Peroxyhemiacetals form from the reaction of an aldehyde or ketone and a hydroperoxide group (Scheme 2).²⁵ The formation of oligomeric species such as peroxyhemiacetals has been shown via kinetic gas-particle modeling to be consistent with the observed evolution of the size distribution of alkane SOA.³⁶ Hydroperoxides and alcohols are ~8 orders of magnitude lower in relative concentration than hemiacetals and ~6 orders of magnitude lower than peroxyhemiacetals; this suggests that oligomer formation is favored. The mean molecular weight for *n*-dodecane low-NO SOA was calculated to be $429.01 \text{ g mol}^{-1}$ (Table 4), reiterating the important role of oligomeric species in *n*-alkane SOA formation.

Hydroxycarbonyls are the most abundant monomeric species, a finding that is consistent with previous alkane studies (Figure 2a).^{28,32,37,39} These hydroxycarbonyls, when substituted

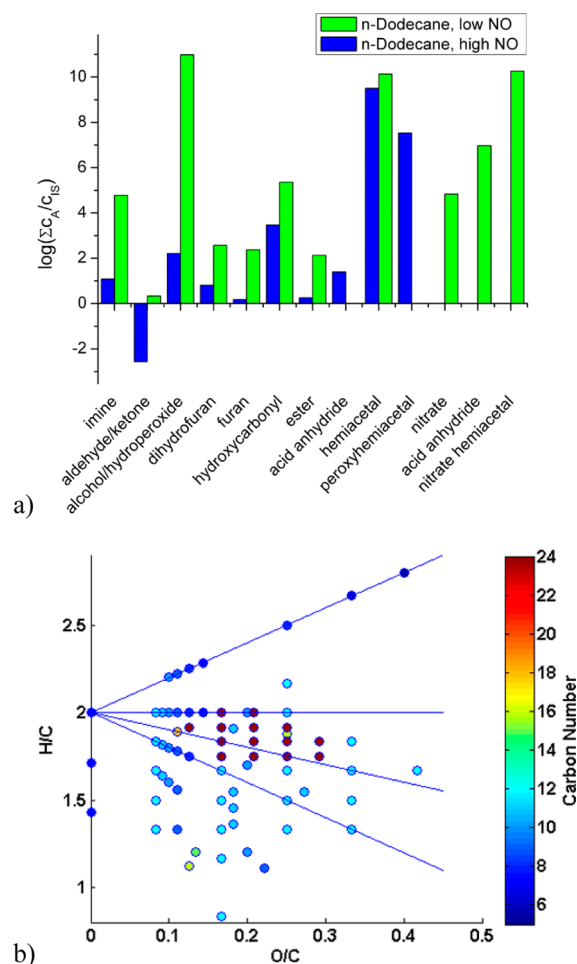


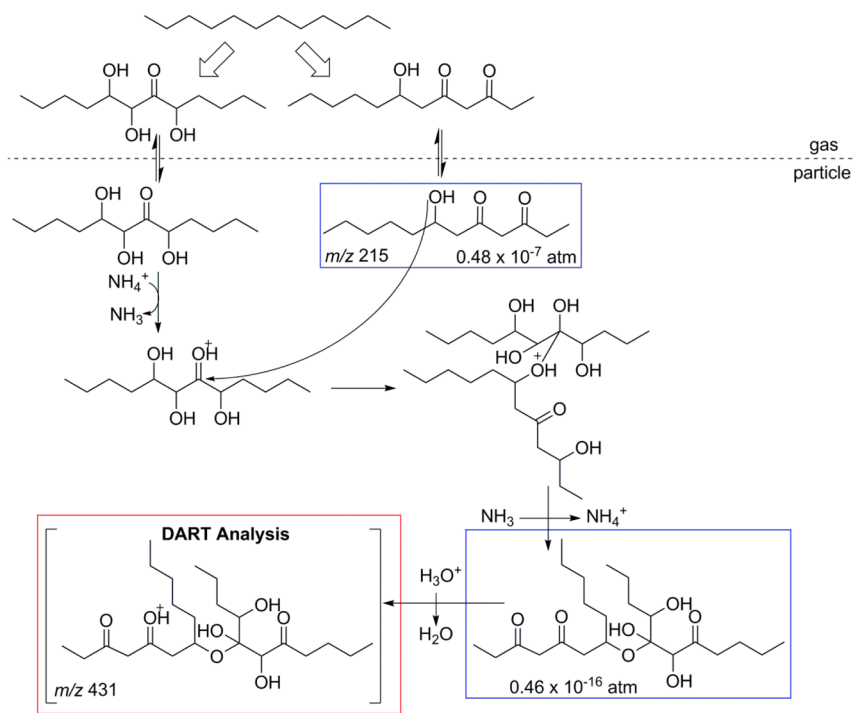
Figure 2. (a) *n*-Dodecane SOA composition under dry, low- and high-NO conditions with $(\text{NH}_4)_2\text{SO}_4$ seed. (b) Van Krevelen diagram for *n*-dodecane SOA produced under dry, low-NO conditions with $(\text{NH}_4)_2\text{SO}_4$ seed. A slope of 2 can be interpreted to represent hydration reactions. A slope of 0 can be interpreted to represent the formation of a hydroxy or peroxy group. A slope of -1 can represent the formation of a carboxylic acid group or the addition of a hydroxy group and a carbonyl group on the same molecule. A slope of -2 can represent the addition of a carbonyl group.

in a 1,4 configuration, can undergo intramolecular cyclization to form cyclic hemiacetals, which in the presence of a suitable acid catalyst are dehydrated to form dihydrofurans (Scheme 3).^{37,64,65} If these dihydrofurans carry additional hydroxyl groups on the ring, they may undergo an additional dehydration step to form a furan. Both dihydrofurans and furans were detected in this study, with dihydrofurans being more prevalent than furans in the particle phase.

A carbonyl can be converted to an imine in the particle phase in the presence of an amine or ammonium ions and ammonia, as is the case in this study (Scheme 3).^{38,66} The imine population is measured here to be larger than the purely aldehyde and ketone components, suggesting that the majority of ketones and aldehydes are converted to imines. The carbonyl population upon which the imine formation process draws includes hydroxycarbonyls, ketones, aldehydes, and functionalized furans and dihydrofurans.

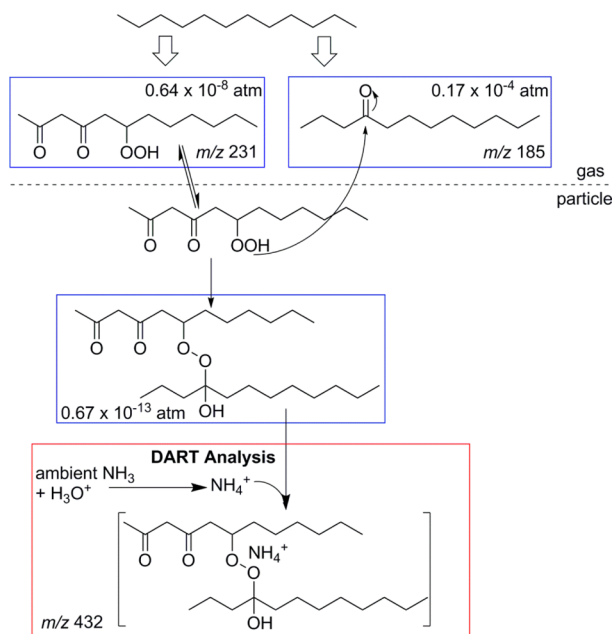
The van Krevelen diagram for *n*-dodecane low-NO SOA (Figure 2b) indicates that hydration reactions and the formation of alcohols, peroxides, carbonyls, and hydroxycar-

Scheme 1. Proposed Mechanism for the Formation of Hemiacetals (m/z 431) in Dodecane SOA Formed under Low-NO Conditions^a



^aLarge arrows indicate several gas-phase photooxidation steps. Proposed structures are boxed in blue. Ion clusters as measured by mass spectrometry are boxed in red. Vapor pressures are estimated by EVAPORATION.⁴³

Scheme 2. Proposed Mechanism for the Formation of Peroxyhemiacetals (m/z 432) in Dodecane SOA under Low-NO Conditions^a



^aLarge arrows indicate several gas-phase photooxidation steps. Proposed structures are boxed in blue. Ion clusters as measured by mass spectrometry are boxed in red. Vapor pressures are estimated by EVAPORATION.⁴³

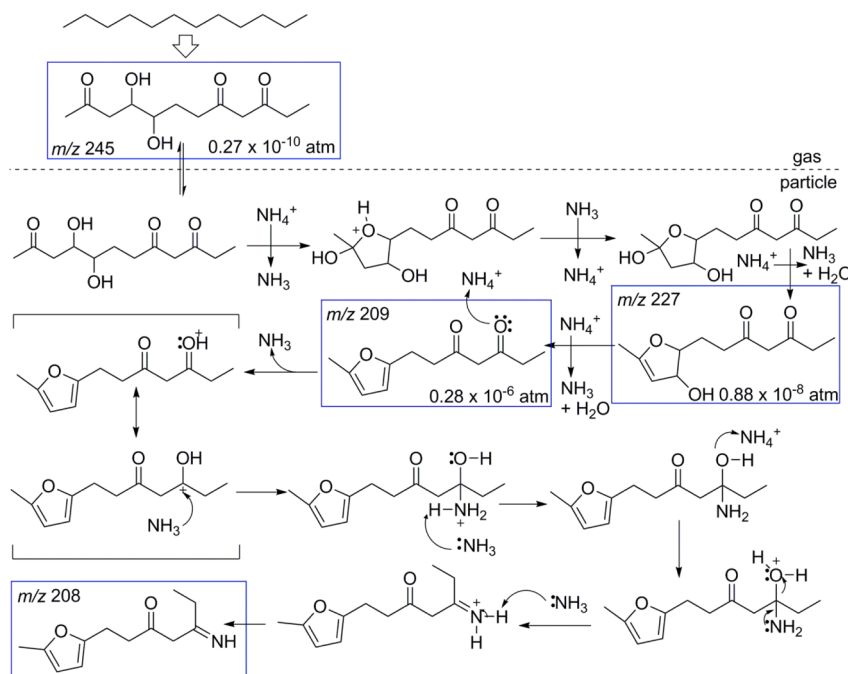
photooxidation products, such as furans and dihydrofurans, and would most likely occur at a hydrated surface layer of a particle or the chamber wall. At <4% RH, the gas phase would be an unlikely place for hydration to occur. The majority of data points trend in the space between the ketone/aldehyde slope and the alcohol/peroxide slope; this space is bisected by the hydroxycarbonyl slope, which is consistent with the importance of hydroxycarbonyl-bearing compounds in the quantitative analysis.

Some of the compounds measured here are estimated to have relatively high volatility, a property that is consistent with facile DART-MS detection. It is possible that these relatively high volatility compounds are, in fact, present at a concentration lower than that of the C_{12} products but undergo more facile detection by DART-MS, even though their concentration may be below the effective method limit of detection for extraction-GC/MS analysis. Shiraiwa et al.³⁶ suggest that particle growth in the dodecane low-NO system is driven by oligomerization and that the resultant particles are semisolid in phase. That reasoning is consistent with the presence of these products as oligomers that are destabilized upon ionization and are measured as their monomers; a semisolid nature of the aerosol phase possibly explains why these relatively volatile compounds could remain trapped in the particle phase as well. Additional explanation for the apparent discrepancy could also be found in the negligible sample preparation required for DART-MS analysis versus the extensive sample preparation and elevated temperatures necessary for GC/MS analysis. Both sample preparation and elevated temperature can lead to losses of sensitive or thermally labile compounds in GC/MS; by comparison, DART-MS provides a more comprehensive breadth of analysis by

bonyls are all key processes in directing the chemical composition. Hydration processes occur for unsaturated

Table 4. Alkane SOA Mean Molecular Weights and Mean O:C and H:C Ratios

parent VOC	NO conditions	% speciation	mean molecular weight of SOA (g mol^{-1})	mean atomic O:C ratio	mean atomic H:C ratio
<i>n</i> -dodecane	low	92	429.01	0.25	1.93
	high	95	495.33	0.47	2.07
cyclododecane	low	99	384.52	0.18	1.61
	high	99	458.38	0.35	1.72
hexylcyclohexane	low	95	310.49	1.09	1.53
	high	98	418.06	0.30	1.65

Scheme 3. Proposed Mechanism for Formation of Furan (m/z 209) and Imine (m/z 208) Species in *n*-Dodecane SOA Generated under Low-NO Conditions^a

^aVapor pressures are estimated by EVAPORATION.⁴³

preserving even highly unstable and reactive molecules for detection.

***n*-Dodecane High-NO SOA Composition.** Under dominant $\text{RO}_2 + \text{NO}$ gas-phase chemistry, the photooxidation proceeds through the formation of alkoxy radicals, which undergo decomposition to aldehydes or isomerization to form alcohols.^{23,24,27} Further oxidation of aldehydes by ozone present under high-NO conditions produces carboxylic acids, facilitating the production of esters and serving as a reaction catalyst.⁶⁷ Organonitrates are also expected products in the particle phase.²⁷ Expected oligomers, given these starting materials and conditions, are esters and ethers carrying other pendant groups as well as carboxylic acid anhydrides.

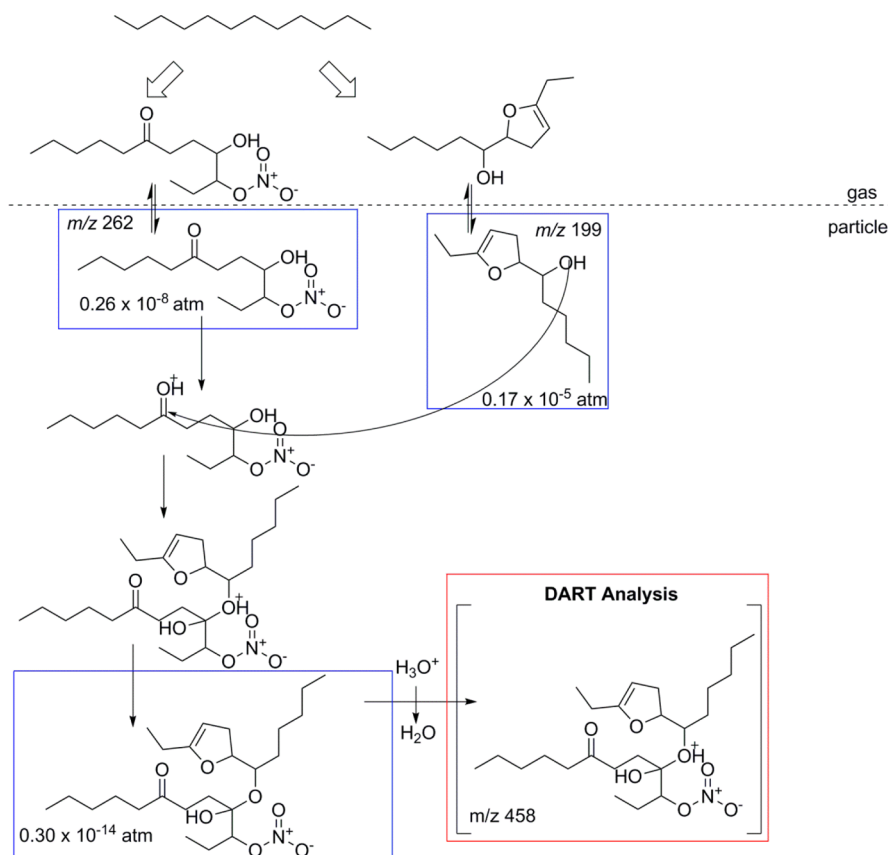
Figure 2a gives an overview of the chemical composition of *n*-dodecane SOA from high-NO conditions. The dominant species are alcohols, hemiacetals, nitrate-bearing hemiacetals, and acid anhydrides. The majority of monomers are alcohols, hydroxycarbonyls, imines, and nitrates, with a smaller proportion of dihydrofurans, furans, and ketones present. Imines, dihydrofurans, and furans result from particle-phase chemistry, as do hemiacetals and acid anhydrides (Schemes 2–4). The van Krevelen diagram (Figure 3) shows the importance of oxygenated smaller carbon chain compounds as well as the presence of highly substituted alcoholic species. The atomic O:C ratio reaches 1 in this system, as opposed to

the atomic O:C ratio of 0.5 under low-NO conditions. Sub- C_{12} compounds that result from fragmentation comprise aldehydes and hydroxycarbonyls, which have vapor pressures higher than those of compounds normally attributed to exist in the particle phase. Shiraiwa et al.³⁶ predict a semisolid particle phase for dodecane low-NO SOA, which implies that higher volatility material can be trapped between layers of less volatile material during the particle accretion process.

The presence of a series of C_{13} compounds with high degrees of oxygenation (O:C of 0.38–0.62) can be explained as the formation of C_{13} oligomers from a combination of sub- C_{12} hydroxycarbonyl compounds. These monomers are multifunctional, including β -hydroxycarbonyls, and therefore could combine to form oligomers via aldol condensation or ether or ester formation. Aldol condensation has been found to occur in the presence of amines, so ammonia from the seed could potentially serve to enable the condensation of aldehydes and β -hydroxycarbonyls in the particle phase.⁶⁸ Additional compounds with backbones $>\text{C}_{12}$ but $<\text{C}_{24}$ are also consistent with oligomerization of dissimilar monomers.

The oligomers formed under high-NO conditions are predominantly hemiacetals, nitrate hemiacetals, with smaller concentrations of carboxylic acid anhydrides and esters (Scheme 4). An ester would form via an acid group from an aldehyde, which is known to form through the chain

Scheme 4. Proposed Mechanism for the Formation of Hemiacetals (m/z 458) in Dodecane SOA Formed under High-NO Conditions^a



^aLarge arrows indicate several gas-phase photooxidation steps. Proposed structures are boxed in blue. Ion clusters as measured by mass spectrometry are indicated in the red box. Vapor pressures are estimated by EVAPORATION.⁴³

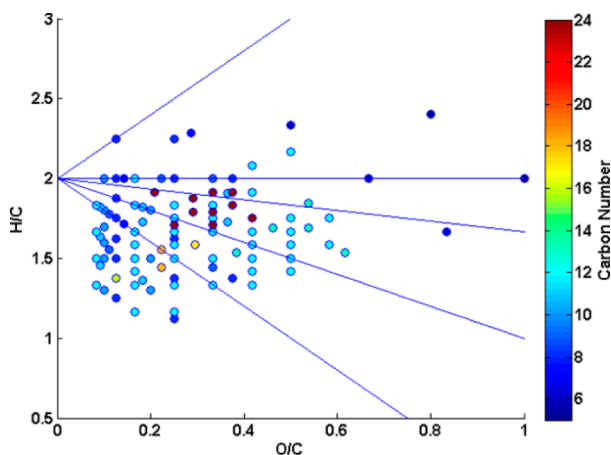
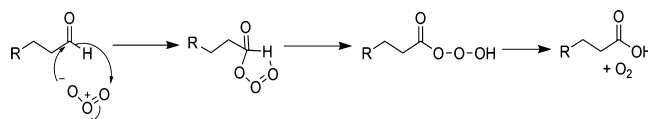


Figure 3. Van Krevelen diagram for *n*-dodecane SOA produced under dry, high-NO conditions with $(\text{NH}_4)_2\text{SO}_4$ seed. A slope of 2 can be interpreted to represent hydration reactions. A slope of 0 can be interpreted to represent the formation of a hydroxy or peroxy group. A slope of -1 can represent the formation of a carboxylic acid group or the addition of a hydroxy group and a carbonyl group on the same molecule. A slope of -2 can represent the addition of a carbonyl group. A slope of $-1/3$ can represent the addition of a nitrate group.

fragmentation pathway. Aldehyde ozonolysis under high-NO conditions is known to produce carboxylic acids (Scheme 5).⁶⁹ On the basis of the retention of all 12 carbons by both monomer units, the C_{24} oligomers are likely linked through

Scheme 5. Proposed Mechanism for the Formation of Carboxylic Acids in the Presence of Ozone under High-NO Conditions, Following Ziemann et al. 2005⁶⁷



hemiacetal groups. Lim and Ziemann^{23,24,52} have proposed the particle-phase formation of cyclic hemiacetals or full acetals. Hemiacetals, including those bearing nitrate groups, are present at ~ 8 orders of magnitude higher concentrations than esters. Hemiacetals are much more abundant under high-NO conditions for *n*-dodecane than under low-NO conditions; this is consistent with the large increase in alcohol formation due to $\text{RO}_2 + \text{NO}$ reactions.

It is also important to note that the organic aerosol loading increased by a factor of 2.3 from the low-NO to the high-NO case (Table 2) and that the mean molecular weight increased from 429.01 to 495.33 g mol^{-1} (Table 4). The production of secondary nitrates under these conditions, along with drastically increased ether formation from the large alcohol population, is the simplest route to this increase in organic aerosol production and increase in compounds with high molecular weights. In comparison to hexylcyclohexane and cyclododecane, the linear structure of *n*-dodecane offers no tertiary sites and ring sites for

nitration; thus, the volume concentration enhancement is less than for the other structures.

Cyclododecane SOA Composition. *Cyclododecane Low-NO SOA Composition.* Cyclododecane low-NO SOA is dominated by ethers and peroxyhemiacetals and contains contributions of hydroxycarbonyls, hydroperoxides, and alcohols that are more significant than those in *n*-dodecane low-NO SOA. The cyclododecane product distribution under low-NO conditions clearly exhibits both functionalization and fragmentation (Figure 4). The stable molecules that result from fragmentation of cyclododecane are highly oxidized, especially when compared to the *n*-dodecane products.

Yee et al.²⁹ report that cyclododecane undergoes two characteristic periods of chemical development: the early formation of hydroperoxides, hydroxy hydroperoxides, and dicarbonyl hydroperoxides, followed by the formation of ring-

opened products, which include an aldehyde group. The rapid addition of oxygenated groups observed by Yee et al.,²⁹ in conjunction with aldehyde formation associated with ring-opening, is consistent with the observations here of elevated functionality and fragmentation of these highly oxidized structures. The atomic O:C ratio for cyclododecane extends to 1.25, but the H:C ratio indicates the compound remains saturated, reflecting the importance of hydroperoxyl and hydroxyl groups in the oxidation of cyclododecane; for *n*-dodecane, the atomic O:C ratio did not exceed 0.45.

The C₁₂ and sub-C₁₂ compounds (Figure 4) constitute a mixture of hydroperoxides, hydroxy hydroperoxides, carbonyl hydroperoxides, carbonyl hydroxy hydroperoxides, hydroxycarbonyls, ketones, and aldehydes. These compounds are the building blocks of the oligomeric species that dominate the aerosol composition, and they also are responsible for increasing the atomic O:C ratio range occupied by cyclododecane SOA components. They constitute a sufficient amount of the SOA mass to also decrease the mean molecular weight as compared to that of *n*-dodecane low-NO SOA (Table 4).

Imines are present at a comparable concentration in cyclododecane and *n*-dodecane low-NO SOA. This result is expected because the total relative amounts of carbonyl-bearing species are approximately equivalent and ammonia from the aerosol seed is abundant and not limiting in either case.

Oligomers in cyclododecane low-NO SOA are, in decreasing order by concentration, hemiacetals, esters, peroxyhemiacetals, and carboxylic acid anhydrides. The contribution of esters in this system is 5 orders of magnitude higher than that for *n*-dodecane, and this can be attributed to the ring structure breaking to form C₁₂ dialdehydes, which can react with OH radicals to form carboxylic acids. The presence of hemiacetals, which arise through an acid-catalyzed reaction, suggests the sufficiency of the ammonium ion and carboxylic acid populations to serve as catalysts for other acid-catalyzed processes (Scheme 6). These oligomeric species, combined with the smaller-chain but highly oxygenated compounds, produce a mean molecular weight of 384.52 g mol⁻¹.

Cyclododecane High-NO SOA Composition. Cyclododecane SOA produced under high-NO conditions is primarily composed of ethers with or without pendant nitrate groups, esters, hydroxycarbonyls, alcohols, and nitrates (Figure 4a). The majority of the aerosol is formed of oligomeric species, particularly hemiacetals (combined relative concentration of ~10¹⁹). The mean molecular weight for this system is 458.48 g mol⁻¹, which reflects the large contributions of oligomers and increased molecular weights from nitration.

Cyclododecane oxidized under high-NO conditions shows the same propensity toward extensive functionalization and fragmentation that opens the ring or breaks the C₁₂ backbone as under low-NO (Figure 5). The high-NO composition is characterized by an abundance of nitrated compounds that are also extensively oxygenated. Lim and Ziemann^{22,24,70} note that an alkoxy radical formed on a cyclododecane ring is prone to rapid decomposition compared with the linear form because of high ring strain and suggested that a cyclic alkyl nitrate may be more volatile than a linear alkyl nitrate because the nitrate is never in a terminal chain position. If the vapor pressures of the cyclododecane nitrates were sufficiently high, they would remain in the gas phase and continue to undergo gas-phase OH oxidation, generating these highly functionalized compounds, including the dinitrate. Cyclododecane reaches a

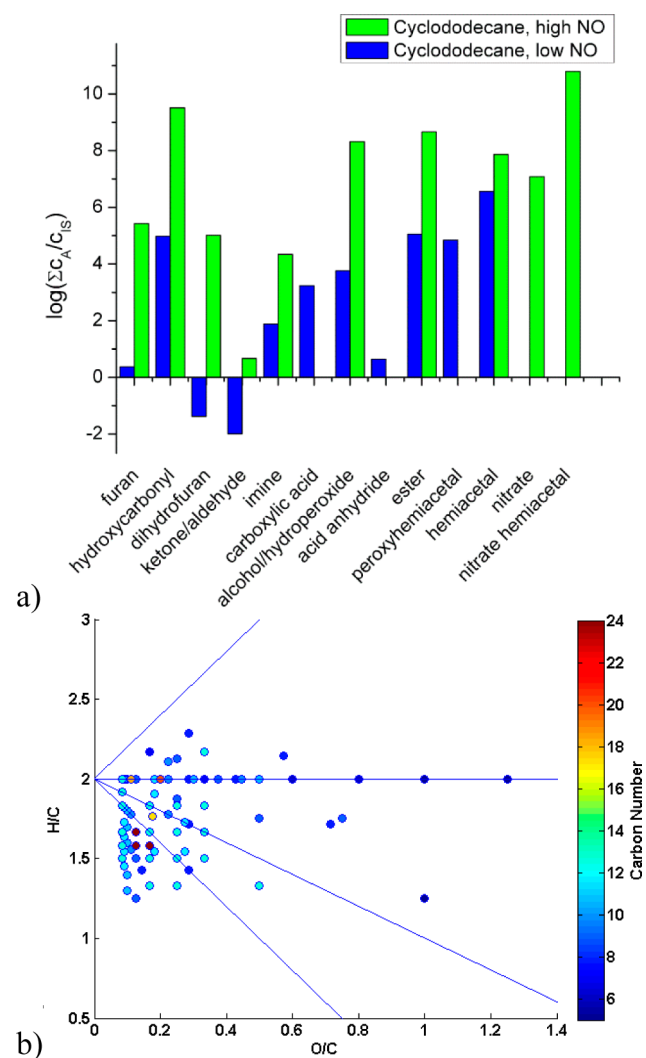
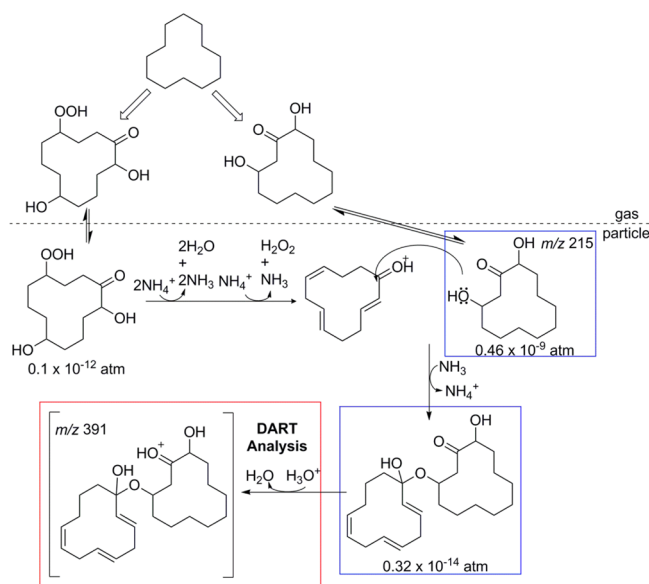


Figure 4. (a) Composition of cyclododecane SOA produced under dry, low- and high-NO conditions, with $(\text{NH}_4)_2\text{SO}_4$ seed. (b) Van Krevelen diagram for cyclododecane SOA produced under dry, low-NO conditions, with $(\text{NH}_4)_2\text{SO}_4$ seed. A slope of 2 can be interpreted to represent hydration reactions. A slope of 0 can be interpreted to represent the formation of a hydroxy or peroxy group. A slope of -1 can represent the formation of a carboxylic acid group or the addition of a hydroxy group and a carbonyl group on the same molecule. A slope of -2 can represent the addition of a carbonyl group.

Scheme 6. Proposed Mechanism for the Formation of Hemiacetals (m/z 391) in Cyclododecane SOA under Low-NO Conditions^a



^aLarge arrows indicate several gas-phase photooxidation steps. Proposed structures are boxed in blue. Ion clusters as measured by mass spectrometry are indicated in the red box. Vapor pressure calculated for ether was performed for the proxy compound without carbon-carbon double bonds. Vapor pressures are estimated by EVAPORATION.⁴³

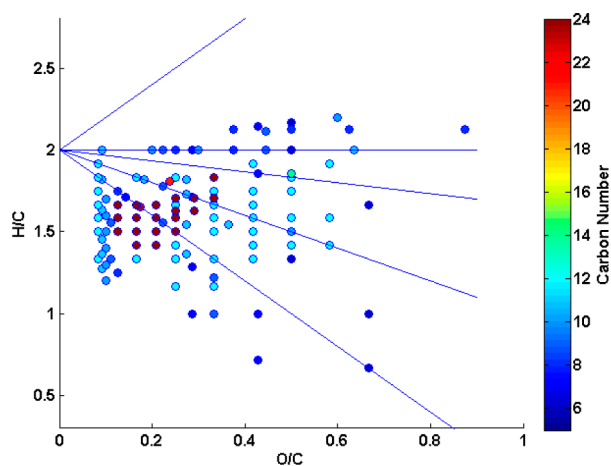


Figure 5. Van Krevelen diagram for cyclododecane SOA produced under dry, high-NO conditions, with $(\text{NH}_4)_2\text{SO}_4$ seed. A slope of 2 can be interpreted to represent hydration reactions. A slope of 0 can be interpreted to represent the formation of a hydroxy or peroxy group. A slope of -1 can represent the formation of a carboxylic acid group or the addition of a hydroxy group and a carbonyl group on the same molecule. A slope of -2 can represent the addition of a carbonyl group. A slope of $-1/3$ can represent the addition of a nitrate group.

comparable maximum atomic O:C as *n*-dodecane under high-NO conditions (Figures 4b and 5). The product distribution density is greater toward the carboxylic acid and hydroxycarbonyl slope and the carbonyl slope, which is consistent with past studies.^{22,24} From the van Krevelen diagram representation, the production of hydroxycarbonyls, dihydrofurans, and furans is greatly increased under high-NO conditions as compared to that under low-NO conditions. Furans and

dihydrofurans, along with their cyclic hemiacetal precursor, carry side-chains with a variety of degrees of functionalization by hydroxyl, ketone, and nitrate groups.

Cyclododecane shows a far greater propensity toward oligomer generation under high-NO conditions than under low-NO conditions. Nitrate hemiacetals are the dominant species, and nitrates are the third most abundant monomeric species in the particle phase. These oligomers comprise cyclic, straight-chain, and furan monomer units that carry additional oxygenated groups as well as imine groups. The organic aerosol volume concentration for cyclododecane under high-NO conditions was found to be a factor of 5 higher than that under low-NO conditions (Table 2). The enhancement of volume concentration and high mean molecular weight (Table 4) under high-NO conditions suggests the importance of nitrate groups to decreasing oxidation product volatility and increasing partitioning to the particle phase.

Hexylcyclohexane SOA Composition. *Hexylcyclohexane Low-NO SOA Composition.* Hexylcyclohexane SOA generated under low-NO conditions is composed predominantly of hydroperoxides, peroxyhemiacetals, hemiacetals, and hydroxycarbonyls (Figure 6a); this composition spectrum is in contrast to those of *n*-dodecane and cyclododecane, with particle-phase compositions dominated by oligomeric species. Some of the hydroxycarbonyls and ketones are converted to imines, as in the other alkane systems.

The concentration of hydroxycarbonyls in hexylcyclohexane SOA is a factor of 10^3 higher than in *n*-dodecane and cyclododecane aerosol. The imine concentration for hexylcyclohexane SOA is a factor of 10^4 higher than that for *n*-dodecane and cyclododecane aerosol, as well. The increase in imine concentration can be attributed to the larger concentration of carbonyl compounds available to be converted into imines through reaction with ammonium in the seed aerosol.

The hexylcyclohexane low-NO SOA clearly reflects the gas-phase oxidation mechanism. The sub- C_{12} products are either ring-retaining C_6 or from the *n*-hexyl chain, which has been cleaved from the cyclohexane ring. Cleavage of the cyclohexyl ring from the *n*-hexyl chain can occur through decomposition of an alkoxy radical formed at the tertiary carbon site. Radical formation at the tertiary site is favored for its stability. *n*-Hexane and cyclohexane products can be differentiated by the additional degree of unsaturation of cyclohexane due to its structure. The *n*-hexyl chain can be further fragmented along with being substituted with carbonyl, hydroperoxide, or hydroxyl groups. This substitution pattern upon these two frameworks can be seen in the pattern visible in the van Krevelen diagram (Figure 6b).

Oligomeric species feature prominently in the hexylcyclohexane system, particularly peroxyhemiacetals (Scheme 7) and hemiacetals, but they are not the most abundant molecules in the resulting SOA. The peroxyhemiacetal concentration for hexylcyclohexane is 10 times higher than that for *n*-dodecane and a factor of 10^3 higher than that for cyclododecane. The concentration of hemiacetals in hexylcyclohexane low-NO SOA is equivalent to that for cyclododecane but is less than that for *n*-dodecane. The increased production of peroxyhemiacetals in hexylcyclohexane is linked with the highest concentration of hydroperoxides out of the three systems ($\sim 10^{12}$). The asymmetry of hexylcyclohexane produces more structurally distinctive compounds than either *n*-dodecane or cyclododecane for the same set of chemical reactions. The tertiary carbon in hexylcyclohexane becomes the most stable peroxy

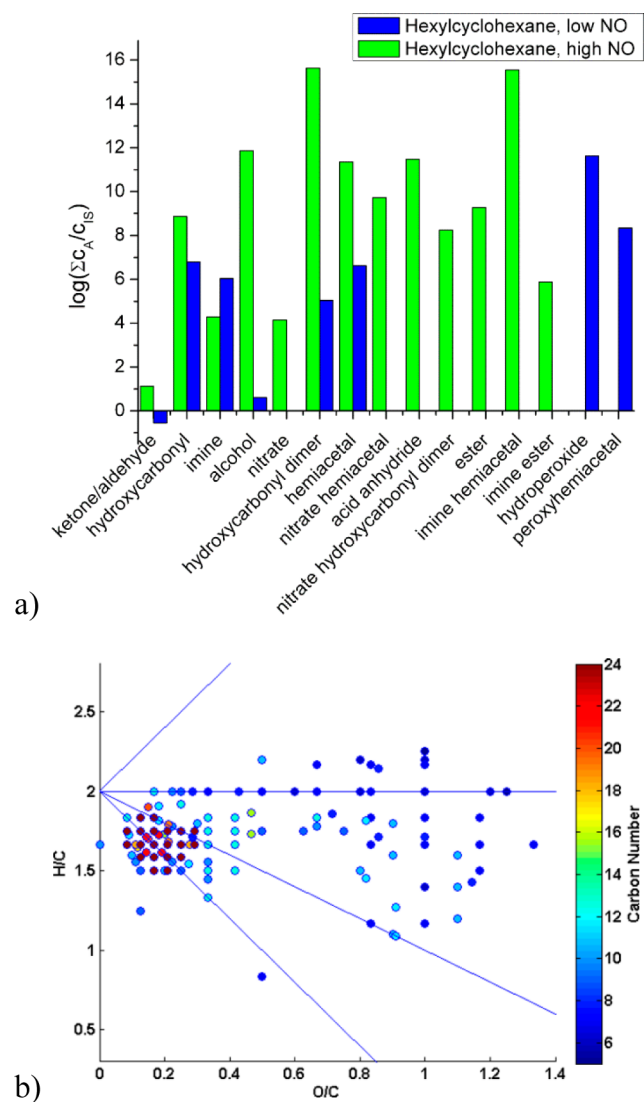
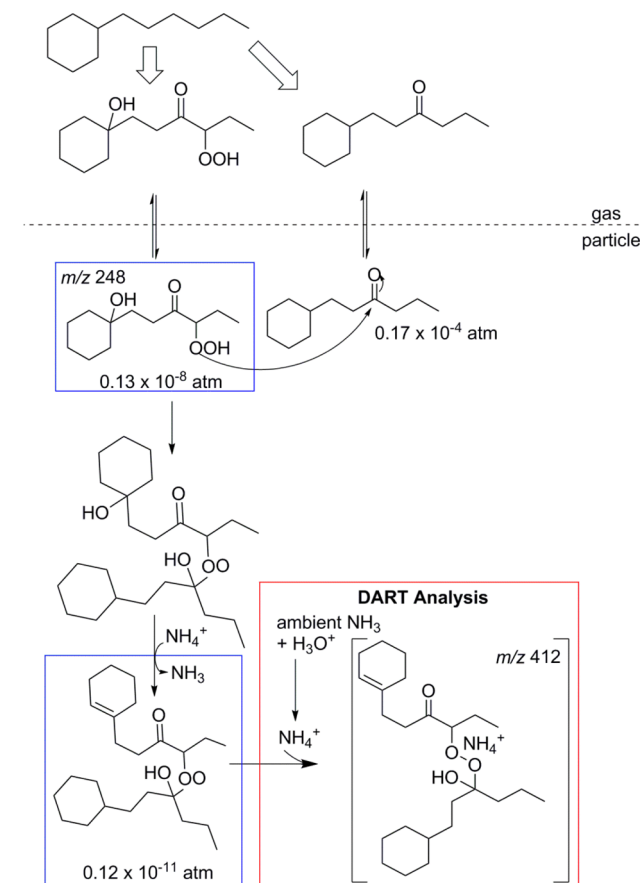


Figure 6. (a) Composition of hexylcyclohexane SOA produced under dry, low- and high-NO conditions, with $(\text{NH}_4)_2\text{SO}_4$ seed. (b) Van Krevelen diagram for hexylcyclohexane SOA produced under dry, low-NO conditions, with $(\text{NH}_4)_2\text{SO}_4$ seed. A slope of 2 can be interpreted to represent hydration reactions. A slope of 0 can be interpreted to represent the formation of a hydroxy or peroxy group. A slope of -1 can represent the formation of a carboxylic acid group or the addition of a hydroxy group and a carbonyl group on the same molecule. A slope of -2 can represent the addition of a carbonyl group.

radical out of these three alkanes, leading to a more enduring contribution to SOA mass. The mean molecular weight, $310.49 \text{ g mol}^{-1}$, is the lowest among the three parent structures and points to the important presence of low-volatility monomers in the particle phase (Table 4).

Hexylcyclohexane High-NO SOA Composition. Under high-NO conditions, alkoxy radicals drive the chemistry, fragmentation, functionalization, and oligomerization in hexylcyclohexane SOA formation (Figure 7). The uniquely stable cyclohexyl ring allows the formation of C_6 species that can be fully substituted with hydroxyl groups. A C_6 nitrate is also detected, but it is likely on the straight-chain or at the tertiary site that serves as the juncture of the cyclohexane ring and n -hexyl chain, based on Lim and Ziemann's conclusion that cyclic alkyl nitrates are more volatile than straight-chain alkyl nitrates.^{23,70} Nitrates are observed from C_5 to C_{12} , most of

Scheme 7. Proposed Mechanism for Formation and Detection by DART-MS of Peroxyhemiacetals (m/z 412) in Hexylcyclohexane SOA Generated under Low-NO Conditions^a



^aLarge arrows indicate several gas-phase photooxidation steps. Proposed structures are boxed in blue. Ion clusters as measured by mass spectrometry are indicated in the red box. Vapor pressures are estimated by EVAPORATION.⁴³

which do not bear additional oxygen atoms. The lack of additional oxygenation suggests that these nitrates condense into the particle phase directly and do not undergo additional cycles of oxidation. The variance in chain length suggests alkyl chain cleavage due to alkoxy radical formation and decomposition into an aldehyde and an alkyl radical, which becomes a RO_2 radical that reacts with NO . These smaller RO_2 are less prone to form a nitrate in $\text{RO}_2 + \text{NO}$.

Hexylcyclohexane SOA produced under high-NO contained an abundance of oligomeric compounds: hydroxycarbonyl dimers, with and without pendant nitrate groups, formed through aldol condensation; hemiacetals with and without pendant nitrate or imine groups; and esters with and without pendant imine groups (Figure 6a). Esters were more abundant in this system than for any of the other parent structures, likely because of the ease of aldehyde and carboxylic acid formation through the oxidation of n -hexyl chain cleavage products and the presence of ozone due to the high-NO conditions. Hemiacetals and aldol condensation products are present in the particle-phase because of the existence of alcohols and β -hydroxycarbonyls (Scheme 8). The pronounced presence of imines in the oligomer products is related to the large number of carbonyl-bearing compounds, as seen in the van Krevelen

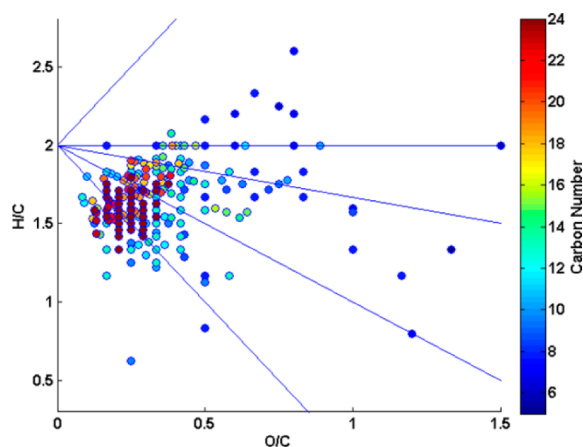


Figure 7. Van Krevelen diagram for hexylcyclohexane SOA produced under dry, high-NO conditions, with $(\text{NH}_4)_2\text{SO}_4$ seed. A slope of 2 can be interpreted to represent hydration reactions. A slope of 0 can be interpreted to represent the formation of a hydroxy or peroxy group. A slope of -1 can represent the formation of a carboxylic acid group or the addition of a hydroxy group and a carbonyl group on the same molecule. A slope of -2 can represent the addition of a carbonyl group. A slope of $-1/3$ can represent the addition of a nitrate group.

diagram (Figure 7). Dominant trends occur along the hydroxycarbonyl slope and ketone/aldehyde slope. The maximum atomic O:C ratio for this system (1.5) is higher

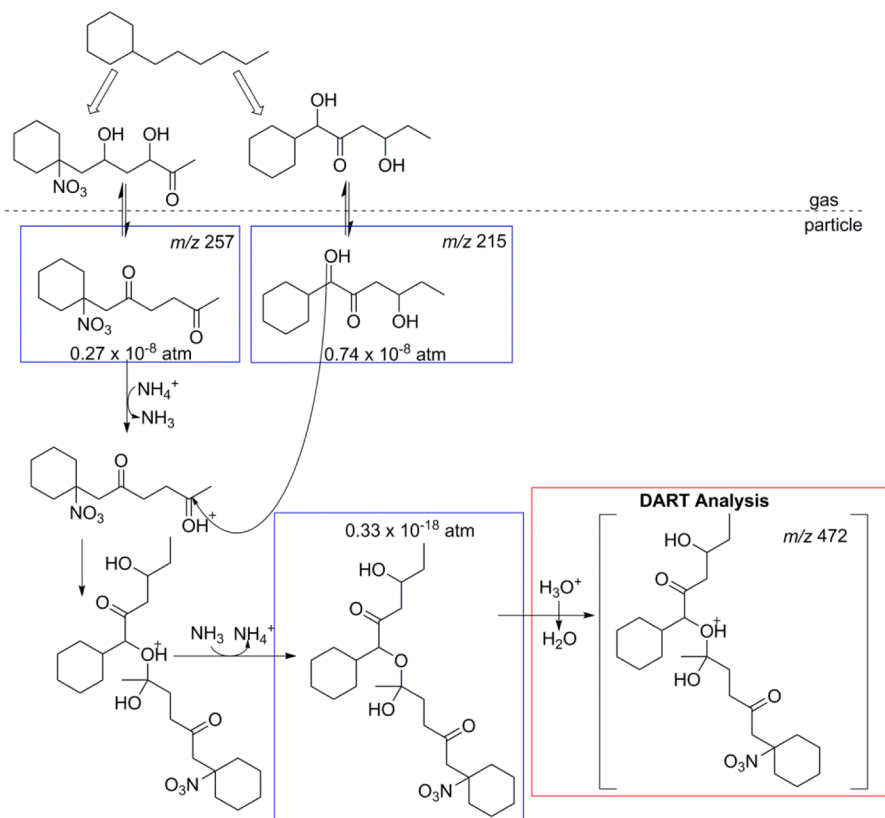
than for any of the other parent compounds under either NO condition.

The organic aerosol volume concentration (see Table 2) is found to increase by a factor of 2.8 from low- to high-NO conditions, an increase that can be attributed primarily to the presence of nitrates in the aerosol phase. The increase in hexylcyclohexane SOA volume concentration from low- to high-NO conditions is higher than that for *n*-dodecane but less than that for cyclododecane. This trend in NO-related volume concentration increase underlies the importance of cyclic structure and increased secondary sites for the particle-phase partitioning of alkyl nitrates. The mean molecular weight of $418.06 \text{ g mol}^{-1}$ is the largest increase in mean molecular weight in this study when going from low- to high-NO conditions for a given system (Table 4). High degrees of functionalization and oligomerization in high-NO hexylcyclohexane-derived SOA lead to its large mean molecular weight.

CONCLUSIONS

SOA formed in the *n*-dodecane, cyclododecane, and hexylcyclohexane systems is largely the result of particle-phase chemistry. The contribution of oligomeric compounds to alkane SOA has been reported previously (Table 1).^{15,28,32} We demonstrate here the importance of peroxyhemiacetals in generating aerosol mass from alkane photooxidation under low-NO conditions and the relevance of ether formation across NO conditions. These findings underscore the importance of NO-induced chemistry and parent compound structure in

Scheme 8. Proposed Mechanism for the Formation of Hemiacetals (m/z 472) in Hexylcyclohexane SOA Formed under High-NO Conditions^a



^aLarge arrows indicate several gas-phase photooxidation steps. Proposed structures are boxed in blue. Ion clusters as measured by mass spectrometry are indicated in the red box. Vapor pressures are estimated by EVAPORATION.⁴³

determining the chemical structure and functionality of SOA oligomeric species. Under high-NO conditions, organic aerosol volume can vary by a factor of 2.3–5, depending on the structure of the parent C₁₂ alkane. This variation in aerosol mass reflects the importance of nitrate formation in the alkane system. In addition, nitrogen incorporation from the ammonium seed aerosol into the organic component of the aerosol through the formation of imines is reported here for the three alkane systems. Imine concentration is correlated with the amount of carbonyl-bearing compounds, as expected, and is therefore an important component of alkane SOA, which is rich in ketones, aldehydes, and hydroxycarbonyls.

The complex compositional data presented here demonstrate the relevance of particle-phase chemistry in alkane-derived SOA and the importance of the ammonium ion as a source of nitrogen incorporation into organic aerosol. The data reinforce the understanding that, for long-chain alkanes, there exist a large number of oxidation products, each of which is present at a relatively low concentration. This finding is an important consideration in generating mechanisms for SOA formation that can eventually be included in atmospheric models.

■ ASSOCIATED CONTENT

● Supporting Information

Additional information and example data for the DART-MS and GC/MS analytical methods; the equations to describe the weighted averaging procedure to obtain mean molecular weights; quantitative compositional data; proposed structures and calculated vapor pressures using the EVAPORATION model for *n*-dodecane, cyclododecane, and hexylcyclohexane SOA. This material is available free of charge via the Internet at <http://pubs.acs.org>.

■ AUTHOR INFORMATION

Corresponding Author

*E-mail: seinfeld@caltech.edu.

Present Addresses

[§]C.L.L.: 3M Environmental Laboratory, 3M Center, Building 260-05-N-17, St. Paul, MN.

^{||}L.D.Y.: Environmental Science, Policy, and Management at University of California, Berkeley, CA.

Notes

The authors declare no competing financial interest.

■ ACKNOWLEDGMENTS

The authors thank Mark S. Andersen of the Jet Propulsion Laboratory and Kathleen T. Upton and Jesse L. Beauchamp of the California Institute of Technology for experimental assistance with DART-MS. This research was funded by U.S. Department of Energy Grant DE-SC 0006626 and National Science Foundation Grant AGS-1057183. K.A.S.F. acknowledges support from a Department of Defense Science, Mathematics, and Research for Transformation Fellowship.

■ REFERENCES

- (1) Molina, M. J.; Ivanov, A. V.; Trakhtenberg, S.; Molina, L. T. Atmospheric Evolution of Organic Aerosol. *Geophys. Res. Lett.* **2004**, *31*, L22104.
- (2) Kalberer, M.; Paulsen, D.; Sax, M.; Steinbacher, M.; Dommen, J.; Prevot, A. S. H.; Fisseha, R.; Weingartner, E.; Frankevich, V.; Zenobi, R.; et al. Identification of Polymers as Major Components of Atmospheric Organic Aerosols. *Science* **2004**, *303*, 1659–1662.

- (3) Gao, S.; Ng, N. L.; Keywood, M.; Varutbangkul, V.; Bahreini, R.; Nenes, A.; He, J.; Yoo, K. Y.; Beauchamp, J. L.; Hodyss, R. P.; et al. Particle Phase Acidity and Oligomer Formation in Secondary Organic Aerosol. *Environ. Sci. Technol.* **2004**, *38*, 6582–6589.

- (4) Gao, S.; Keywood, M.; Ng, N. L.; Surratt, J.; Varutbangkul, V.; Bahreini, R.; Flagan, R. C.; Seinfeld, J. H. Low-Molecular-Weight and Oligomeric Components in Secondary Organic Aerosol from the Ozonolysis of Cycloalkenes and α -Pinene. *J. Phys. Chem. A* **2004**, *108*, 10147–10164.

- (5) Tolocka, M. P.; Jang, M.; Ginter, J. M.; Cox, F. J.; Kamens, R. M.; Johnston, M. V. Formation of Oligomers in Secondary Organic Aerosol. *Environ. Sci. Technol.* **2004**, *38*, 1428–1434.

- (6) Loeffler, K. W.; Koehler, C. A.; Paul, N. M.; De Haan, D. O. Oligomer Formation in Evaporating Aqueous Glyoxal and Methylglyoxal Solutions. *Environ. Sci. Technol.* **2006**, *40*, 6318–6323.

- (7) Baltensperger, U.; Kalberer, M.; Dommen, J.; Paulsen, D.; Alfara, M. R.; Coe, H.; Fisseha, R.; Gascho, A.; Gysel, M.; Nyeki, S.; et al. Secondary Organic Aerosols from Anthropogenic and Biogenic Precursors. *Faraday Discuss.* **2005**, *130*, 265–278.

- (8) Heaton, K. J.; Dreyfus, M. A.; Wang, S.; Johnston, M. V. Oligomers in the Early State of Biogenic Secondary Organic Aerosol. *Environ. Sci. Technol.* **2007**, *41*, 6129–6136.

- (9) Virtanen, A.; Joutsensaari, J.; Koop, T.; Kannosto, J.; Yli-Pirilä, P.; Leskinen, J.; Mäkelä, J. M.; Holopainen, J. K.; Pöschl, U.; Kulmala, M.; et al. An Amorphous Solid State of Biogenic Secondary Organic Aerosol Particles. *Nature (London, U.K.)* **2010**, *467*, 824–827.

- (10) Koop, T.; Bookhold, J.; Shiraiwa, M.; Pöschl, U. Glass Transition and Phase State of Organic Compounds: Dependency on Molecular Properties and Implications for Secondary Organic Aerosols in the Atmosphere. *Phys. Chem. Chem. Phys.* **2011**, *13*, 19238–19255.

- (11) Renbaum-Wolff, L.; Grayson, J. W.; Bateman, A. P.; Kuwata, M.; Sellier, M.; Murray, B. J.; Shilling, J. E.; Martin, S. T.; Bertram, A. K. Viscosity of α -Pinene Secondary Organic Material and Implications for Particle Growth and Reactivity. *Proc. Natl. Acad. Sci. U.S.A.* **2013**, *110*, 8014–8019.

- (12) Ensberg, J. J.; Hayes, P. L.; Jimenez, J. L.; Gilman, J. B.; Kuster, W. C.; de Gouw, J. A.; Holloway, J. S.; Seinfeld, J. H. Emission Factor Ratios, SOA Mass Yields, and the Impact of Vehicular Emissions on SOA Formation. *Atmos. Chem. Phys.* **2013**, *14*, 2383–2397.

- (13) Bahreini, R.; Middlebrook, A. M.; de Gouw, J. A.; Warneke, C.; Trainer, M.; Brock, C. A.; Stark, H.; Brown, S. S.; Dube, W. P.; Gilman, J. B.; et al. Gasoline Emissions Dominate over Diesel in Formation of Secondary Organic Aerosol Mass. *Geophys. Res. Lett.* **2012**, *39*, L06805.

- (14) Gentner, D. R.; Isaacman, G.; Worton, D. R.; Chan, A. W. H.; Dallmann, T. R.; Davis, L.; Liu, S.; Day, D. A.; Russell, L. M.; Wilson, K. R.; et al. Elucidating Secondary Organic Aerosol from Diesel and Gasoline Vehicles through Detailed Characterization of Organic Carbon Emissions. *Proc. Natl. Acad. Sci. U.S.A.* **2012**, *109*, 18318–18323.

- (15) Zhang, H.; Ruehl, C. R.; Chan, A. W. H.; Nah, T.; Worton, D. R.; Isaacman, G.; Goldstein, A. H.; Wilson, K. R. OH-Initiated Heterogeneous Oxidation of Cholestane: A Model System for Understanding the Photochemical Aging of Cyclic Alkane Aerosols. *J. Phys. Chem. A* **2013**, *117*, 12449–12458.

- (16) Reisen, F.; Aschmann, S. M.; Atkinson, R.; Arey, J. 1,4-Hydroxycarbonyl Products of the OH Radical-Initiated Reactions of C₅–C₈ *n*-Alkanes in the Presence of NO. *Environ. Sci. Technol.* **2005**, *39*, 4447–4453.

- (17) Baker, J.; Arey, J.; Atkinson, R. Formation and Reaction of Hydroxycarbonyls from the Reaction of OH Radicals with 1,3-Butadiene and Isoprene. *Environ. Sci. Technol.* **2005**, *39*, 4091–4099.

- (18) Schauer, J. J.; Kleeman, M. J.; Cass, G. R.; Simoneit, B. R. T. Measurement of Emissions from Air Pollution Sources. 2. C₁ through C₃₀ Organic Compounds from Medium Duty Diesel Trucks. *Environ. Sci. Technol.* **1999**, *33*, 1578–1587.

- (19) Schauer, J. J.; Kleeman, M. J.; Cass, G. R.; Simoneit, B. R. T. Measurement of Emissions from Air Pollution Sources. 5. C₁–C₃₂

Organic Compounds from Gasoline-Powered Motor Vehicles. *Environ. Sci. Technol.* **2002**, *36*, 1169–1180.

(20) Isaacman, G.; Wilson, K. R.; Chan, A. W. H.; Worton, D. R.; Kimmel, J. R.; Nah, T.; Hohaus, T.; Gonin, M.; Kroll, J. H.; Worsnop, D. R.; et al. Improved Resolution of Hydrocarbon Structures and Constitutional Isomers in Complex Mixtures Using Gas Chromatography-Vacuum Ultraviolet-Mass Spectrometry. *Anal. Chem.* **2012**, *84*, 2335–2342.

(21) Ruehl, C. R.; Nah, T.; Isaacman, G.; Worton, D. R.; Chan, A. W. H.; Kolesar, K. R.; Cappa, C. D.; Goldstein, A. H.; Wilson, K. R. The Influence of Molecular Structure and Aerosol Phase on the Heterogeneous Oxidation of Normal and Branched Alkanes by OH. *J. Phys. Chem. A* **2013**, *117*, 3990–4000.

(22) Lim, Y. B.; Ziemann, P. J. Chemistry of Secondary Organic Aerosol Formation from OH Radical-Initiated Reactions of Linear, Branched, and Cyclic Alkanes in the Presence of NO_x. *Aerosol Sci. Technol.* **2009**, *43*, 604–619.

(23) Lim, Y. B.; Ziemann, P. J. Effects of Molecular Structure on Aerosol Yields from OH Radical-Initiated Reactions of Linear, Branched, and Cyclic Alkanes in the Presence of NO_x. *Environ. Sci. Technol.* **2009**, *43*, 2328–2334.

(24) Lim, Y. B.; Ziemann, P. J. Products and Mechanism of Secondary Organic Aerosol Formation from Reactions of *n*-Alkanes with OH Radicals in the Presence of NO_x. *Environ. Sci. Technol.* **2005**, *39*, 9229–9236.

(25) Ziemann, P. J. Formation of Alkoxyhydroperoxy Aldehydes and Cyclic Peroxyhemiacetals from Reactions of Cyclic Alkenes with Ozone in the Presence of Alcohols. *J. Phys. Chem. A* **2003**, *107*, 2048–2060.

(26) Tkacik, D. S.; Presto, A. A.; Donahue, N. M.; Robinson, A. L. Secondary Organic Aerosol Formation from Intermediate-Volatility Organic Compounds: Cyclic, Linear, and Branched Alkanes. *Environ. Sci. Technol.* **2012**, *46*, 8773–8781.

(27) Presto, A. A.; Miracolo, M. A.; Donahue, N. M.; Robinson, A. L. Secondary Organic Aerosol Formation from High-NO_x Photooxidation of Low Volatility Precursors: *n*-Alkanes. *Environ. Sci. Technol.* **2010**, *44*, 2029–2034.

(28) Yee, L. D.; Craven, J. S.; Loza, C. L.; Schilling, K. A.; Ng, N. L.; Canagaratna, M. R.; Ziemann, P. J.; Flagan, R. C.; Seinfeld, J. H. Secondary Organic Aerosol Formation from Low-NO_x Photooxidation of Dodecane: Evolution of Multigeneration Gas-Phase Chemistry and Aerosol Composition. *J. Phys. Chem. A* **2012**, *116*, 6211–6230.

(29) Yee, L. D.; Craven, J. S.; Loza, C. L.; Schilling, K. A.; Ng, N. L.; Canagaratna, M. R.; Ziemann, P. J.; Flagan, R. C.; Seinfeld, J. H. Effect of Chemical Structure on Secondary Organic Aerosol Formation from C₁₂ Alkanes. *Atmos. Chem. Phys.* **2013**, *13*, 11121–11140.

(30) Craven, J. S.; Yee, L. D.; Ng, N. L.; Canagaratna, M. R.; Loza, C. L.; Schilling, K. A.; Yatavelli, R. L. N.; Thornton, J. A.; Ziemann, P. J.; Flagan, R. C.; et al. Analysis of Secondary Organic Aerosol Formation and Aging Using Positive Matrix Factorization of High-Resolution Aerosol Mass Spectra: Application to the Dodecane Low-NO_x System. *Atmos. Chem. Phys.* **2012**, *12*, 11795–11817.

(31) Craven, J. S.; Yee, L. D.; Ng, N. L.; Canagaratna, M. R.; Loza, C. L.; Schilling, K. A.; Yatavelli, R. L. N.; Thornton, J. A.; Ziemann, P. J.; Flagan, R. C.; Seinfeld, J. H. Analysis of Secondary Organic Aerosol Formation and Aging Using Positive Matrix Factorization of High-Resolution Aerosol Mass Spectra: Application to the Dodecane Low-NO_x System. *Atmos. Chem. Phys.* **2012**, *12*, 11795–11817.

(32) Yee, L. D.; Craven, J. S.; Loza, C. L.; Schilling, K. A.; Ng, N. L.; Canagaratna, M. R.; Ziemann, P. J.; Flagan, R. C.; Seinfeld, J. H. Effect of Chemical Structure on Secondary Organic Aerosol Formation from C₁₂ Alkanes. *Atmos. Chem. Phys.* **2013**, *13*, 11121–11140.

(33) Lambe, A. T.; Onasch, T. B.; Croasdale, D. R.; Wright, J. P.; Martin, A. T.; Franklin, J. P.; Massoli, P.; Kroll, J. H.; Canagaratna, M. R.; Brune, W. H.; et al. Transitions from Functionalization to Fragmentation Reactions of Laboratory Secondary Organic Aerosol Generated from the OH Oxidation of Alkane Precursors. *Environ. Sci. Technol.* **2012**, *46*, 5430–5437.

(34) Tkacik, D. S.; Presto, A. A.; Donahue, N. M.; Robinson, A. L. Secondary Organic Aerosol Formation from Intermediate-Volatility Organic Compounds: Cyclic, Linear and Branched Alkanes. *Environ. Sci. Technol.* **2012**, *46*, 8773–8781.

(35) Zhang, X.; Schwantes, R. H.; Coggon, M. M.; Loza, C. L.; Schilling, K. A.; Flagan, R. C.; Seinfeld, J. H. Role of Ozone in SOA Formation from Alkane Photooxidation. *Atmos. Chem. Phys.* **2013**, *14*, 1733–1753.

(36) Shiraiwa, M.; Yee, L. D.; Schilling, K. A.; Loza, C. L.; Craven, J. S.; Zuend, A.; Ziemann, P. J.; Seinfeld, J. H. Size Distribution Dynamics Reveal Particle-Phase Chemistry in Organic Aerosol Formation. *Proc. Natl. Acad. Sci. U.S.A.* **2013**, *110*, 11746–11750.

(37) Lim, Y. B.; Ziemann, P. J. Kinetics of the Heterogeneous Conversion of 1,4-Hydroxycarbonyls to Cyclic Hemiacetals and Dihydrofurans on Organic Aerosol Particles. *Phys. Chem. Chem. Phys.* **2009**, *11*, 8029.

(38) De Haan, D. O.; Tolbert, M. A.; Jimenez, J. L. Atmospheric Condensed-Phase Reactions of Glyoxal with Methylamine. *Geophys. Res. Lett.* **2009**, *36*, L11819.

(39) Lim, Y. B.; Ziemann, P. J. Chemistry of Secondary Organic Aerosol Formation from OH Radical-Initiated Reactions of Linear, Branched, and Cyclic Alkanes in the Presence of NO_x. *Aerosol Sci. Technol.* **2009**, *43*, 604–619.

(40) De Haan, D. O.; Corrigan, A. L.; Smith, K. W.; Stroik, D. R.; Turley, J. J.; Lee, F. E.; Tolbert, M. A.; Jimenez, J. L.; Cordova, K. E.; Ferrell, G. R. Secondary Organic Aerosol-Forming Reactions of Glyoxal with Amino Acids. *Environ. Sci. Technol.* **2009**, *43*, 2818–2824.

(41) Nguyen, T. B.; Laskin, A.; Laskin, J.; Nizkorodov, S. A. Brown Carbon Formation from Ketoaldehydes of Biogenic Monoterpenes. *Faraday Discuss.* **2013**, *165*, 473–494.

(42) Loza, C. L.; Craven, J. S.; Yee, L. D.; Coggon, M. M.; Schwantes, R. H.; Shiraiwa, M.; Zhang, X.; Schilling, K. A.; Ng, N. L.; Canagaratna, M. R.; et al. Secondary Organic Aerosol Yields of 12-Carbon Alkanes. *Atmos. Chem. Phys.* **2014**, *14*, 1423–1439.

(43) Compernelle, S.; Ceulemans, K.; Müller, J. F. EVAPORATION: A New Vapour Pressure Estimation Method for Organic Molecules Including Non-Additivity and Intramolecular Interactions. *Atmos. Chem. Phys.* **2011**, *11*, 9431–9450.

(44) Jenkin, M. E.; Saunders, S. M.; Pilling, M. J. The Tropospheric Degradation of Volatile Organic Compounds: A Protocol for Mechanism Development. *Atmos. Environ.* **1997**, *31*, 81–104.

(45) Cody, R. B.; Laramee, J. A.; Durst, H. D. Versatile New Ion Source for the Analysis of Materials in Open Air under Ambient Conditions. *Anal. Chem.* **2005**, *77*, 2297–2302.

(46) Cody, R. B. Observation of Molecular Ions and Analysis of Nonpolar Compounds with the Direct Analysis in Real Time Ion Source. *Anal. Chem.* **2009**, *81*, 1101–1107.

(47) Shelley, J. T.; Wiley, J. S.; Chan, G. C. Y.; Schilling, G. D.; Ray, S. J.; Hieffje, G. M. Characterization of Direct-Current Atmospheric Pressure Discharges Useful for Ambient Desorption/Ionization Mass Spectrometry. *J. Am. Soc. Mass Spectrom.* **2009**, *20*, 837–844.

(48) Harris, G. A.; Fernandez, F. M. Simulations and Experimental Investigation of Atmospheric Transport in an Ambient Metastable-Induced Chemical Ionization Source. *Anal. Chem.* **2009**, *81*, 322–329.

(49) Nilles, J. M.; Connell, T. R.; Durst, H. D. Quantitation of Chemical Warfare Agents Using the Direct Analysis in Real Time (DART) Technique. *Anal. Chem.* **2009**, *81*, 6744–6749.

(50) Goldstein, A. H.; Galbally, I. E. Known and Unknown Organic Constituents in the Earth's Atmosphere. *Environ. Sci. Technol.* **2007**, *41*, 1514–1521.

(51) Taylor, J.; Hall, C. R. L.; Thomas, H. The Thermochemistry of Propellant Explosives. *J. Phys. Colloid Chem.* **1947**, *51*, 580–592.

(52) Self, R. L.; Wu, W.-H. Rapid Qualitative Analysis of Phthalates Added to Food and Nutraceutical Products by Direct Analysis in Real Time/Orbitrap Mass Spectrometry. *Food Control* **2012**, *25*, 13–16.

(53) Rothenbacher, T.; Schwack, W. Rapid Identification of Additives in Poly(vinyl chloride) Lid Gaskets by Direct Analysis in Real Time Ionisation and Single-Quadrupole Mass Spectrometry. *Rapid Commun. Mass Spectrom.* **2010**, *24*, 21–29.

(54) Lias, S. G.; Bartmess, J. E. *Proton Affinity and Gas Phase Basicity*. <http://webbook.nist.gov/chemistry/ion/#GB> (accessed 01/27/2014).

(55) Hunter, E. P. L.; Lias, S. G. Evaluated Gas Phase Basicities and Proton Affinities of Molecules: An Update. *J. Phys. Chem. Ref. Data* **1998**, *27*, 413–656.

(56) Van Krevelen, D. W. Graphical-Statistical Method for the Study of Structure and Reaction Processes of Coal. *Fuel* **1950**, *24*, 269–284.

(57) Kim, S.; Kramer, R. W.; Hatcher, P. G. Graphical Method for Analysis of Ultrahigh-Resolution Broadband Mass Spectra of Natural Organic Matter: The Van Krevelen Diagram. *Anal. Chem.* **2003**, *75*, 5336–5344.

(58) Wu, Z.; Rodgers, R. P.; Marshall, A. G. Two- and Three-Dimensional Van Krevelen Diagrams: A Graphical Analysis Complementary to the Kendrick Mass Plot for Sorting Elemental Compositions of Complex Organic Mixtures Based on Ultrahigh-Resolution Broadband Fourier Transform Ion Cyclotron Resonance Mass Measurements. *Anal. Chem.* **2004**, *76*, 2511–2516.

(59) Heald, C. L.; Kroll, J. H.; Jimenez, J. L.; Docherty, K. S.; DeCarlo, P. F.; Aiken, A. C.; Chen, Q.; Martin, S. T.; Farmer, D. K.; Artaxo, P. A Simplified Description of the Evolution of Organic Aerosol Composition in the Atmosphere. *Geophys. Res. Lett.* **2010**, *37*, L08803.

(60) Ng, N. L.; Canagaratna, M. R.; Jimenez, J. L.; Chhabra, P. S.; Seinfeld, J. H.; Worsnop, D. R. Changes in Organic Aerosol Composition with Aging Inferred from Aerosol Mass Spectra. *Atmos. Chem. Phys.* **2011**, *11*, 6465–6474.

(61) Chhabra, P. S.; Ng, N. L.; Canagaratna, M. R.; Corrigan, A. L.; Russell, L. M.; Worsnop, D. R.; Flagan, R. C.; Seinfeld, J. H. Elemental Composition and Oxidation of Chamber Organic Aerosol. *Atmos. Chem. Phys.* **2011**, *11*, 8827–8845.

(62) Lambe, A. T.; Onasch, T. B.; Massoli, P.; Croasdale, D. R.; Wright, J. P.; Ahern, A. T.; Williams, L. R.; Worsnop, D. R.; Brune, W. H.; Davidovits, P. Laboratory Studies of the Chemical Composition and Cloud Condensation Nuclei Activity of Secondary Organic Aerosol and Oxidized Primary Organic Aerosol. *Atmos. Chem. Phys.* **2011**, *11*, 8913–8928.

(63) Hall, W. A., IV; Johnston, M. V. Oligomer Formation Pathways in Secondary Organic Aerosol from MS and MS/MS Measurements with High Mass Accuracy and Resolving Power. *J. Am. Soc. Mass Spectrom.* **2012**, *23*, 1097–1108.

(64) Dibble, T. S. Cyclization of 1,4-Hydroxycarbonyls Is Not a Homogeneous Gas-Phase Process. *Chem. Phys. Lett.* **2007**, *447*, 5–9.

(65) Atkinson, R.; Arey, J.; Aschmann, S. M. Atmospheric Chemistry of Alkanes: Review and Recent Developments. *Atmos. Environ.* **2008**, *42*, 5859–5871.

(66) De Haan, D. O.; Corrigan, A. L.; Smith, K. W.; Stroik, D. R.; Turley, J. J.; Lee, F. E.; Tolbert, M. A.; Jimenez, J. L.; Cordova, K. E.; Ferrell, G. R. Secondary Organic Aerosol-Forming Reactions of Glyoxal with Amino Acids. *Environ. Sci. Technol.* **2009**, *43*, 2818–2824.

(67) Ziemann, P. J. Aerosol Products, Mechanisms, and Kinetics of Heterogeneous Reactions of Ozone with Oleic Acid in Pure and Mixed Particles. *Faraday Discuss.* **2005**, *130*, 469–490.

(68) Markert, M.; Mulzer, M.; Schetter, B.; Mahrwald, R. Amine-Catalyzed Direct Aldol Addition. *J. Am. Chem. Soc.* **2007**, *129*, 7258–7259.

(69) Liu, S.; Day, D. A.; Shields, J. E.; Russell, L. M. Ozone-Driven Daytime Formation of Secondary Organic Aerosol Containing Carboxylic Acid Groups and Alkane Groups. *Atmos. Chem. Phys.* **2011**, *11*, 8321–8341.

(70) Lim, Y. B.; Ziemann, P. J. Kinetics of the Heterogeneous Conversion of 1,4-Hydroxycarbonyls to Cyclic Hemiacetals and Dihydrofurans on Organic Aerosol Particles. *Phys. Chem. Chem. Phys.* **2009**, *11*, 8029–8039.

Chapter 3

Chemical Composition of Toluene and Cresol Secondary Organic Aerosol:

Effect of NO Level¹

¹ This chapter is reproduced by permission from “Chemical Composition of Toluene and Cresol Secondary Organic Aerosol: Effect of NO” by K. A. Schilling, H. Lignell, M. M. Coggon, R. H. Schwantes, X. Zhang, and J. H. Seinfeld. In submission to *Environmental Science and Technology*, 2015.

ABSTRACT

The NO_x effect on toluene SOA formation was studied under dry low- and high-NO conditions, and with varied seed: $(\text{NH}_4)_2\text{SO}_4$, Na_2SO_4 , $\text{MgSO}_4 + \text{H}_2\text{SO}_4$, and NaCl . *o*-, *m*-, and *p*-Cresol SOA was produced under high-NO conditions to compare cresol and toluene SOA chemical compositions and assess the contribution of the cresol path to toluene SOA. Online aerosol mass spectrometry (HR-AMS, Aerodyne, Inc.) and offline direct analysis in real time mass spectrometry (DART-HR-MS, JEOL, Inc.) were used to chemically characterize SOA. Oxygenated compounds with general formulae $\text{C}_x\text{H}_y\text{O}_{5+}$ and $\text{C}_x\text{H}_y\text{O}_4$ together constitute a relative mass fraction > 0.9 of all toluene SOA components identified here. Oligomers are found to be important contributors to cresol-derived SOA (relative mass fractions: ortho, 0.13; meta, 0.03; para, 0.99). $\text{C}_{10}\text{H}_{10}\text{O}_4$ is the principal oligomeric species identified in toluene SOA formed under dry low-NO conditions, with a relative mass fraction of 3.0×10^{-5} . Under dry high-NO conditions, toluene SOA has a relative mass fraction of $0.99 \geq \text{C}_7$ species, including $\text{C}_x\text{H}_y\text{O}_{5+}$, $\text{C}_x\text{H}_y\text{O}_4$, $\text{C}_x\text{H}_y\text{NO}_{5+}$, $\text{C}_x\text{H}_y\text{NO}_4$. A relative mass fraction of 0.84 of toluene SOA is estimated to be attributable to the cresol pathway, specifically $\text{C}_7\text{H}_8\text{O}_4$ (0.7) and $\text{C}_7\text{H}_6\text{O}_4$ (0.1) species, with the remainder composed of $\text{C}_x\text{H}_y\text{O}_2$, $\text{C}_x\text{H}_y\text{NO}_2$, $\text{C}_x\text{H}_y\text{NO}_3$, and $\text{C}_x\text{H}_y\text{O}$.

INTRODUCTION

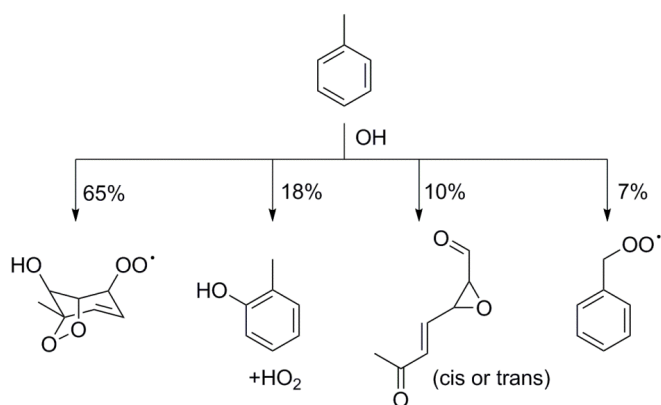


Figure 1. Gas-phase mechanism for toluene oxidation proceeding by OH addition, based on the Master Chemical Mechanism (MCM).⁷

Aromatic compounds are well-established precursors of secondary organic aerosol (SOA), and the gas-phase photooxidation chemistry of toluene and early aromatic oxidation products including cresol is the subject of numerous studies.¹⁻³⁰ Toluene photooxidation occurs through four channels leading to the formation of bicyclic peroxy radicals, cresols, epoxy muconaldehydes, and peroxy methyl benzene radicals under low- and high-NO conditions (Fig. 1).⁷ Here, we address toluene photooxidation by the major channels: the bicyclic peroxy radical and cresol pathways. Mechanisms for the minor pathways, taken from the Master Chemical Mechanism (MCM), are given in the Supporting Information.

Low- and extremely low-volatility compounds (LVOC and ELVOC) are of substantial interest in the study of SOA formation, and emerging technologies are enabling their detection.³¹ Important related questions are the extent to which toluene and cresol SOA comprise LVOC and ELVOC, and the extent to which LVOC and ELVOC originate from multigenerational photooxidation and oligomerization under dry conditions. Oligomers, which include dimers up to polymers in excess of 500 amu, have been established as important compounds in aromatic SOA.^{6, 28-29, 32-33} Glyoxal, a volatile oxidation product of aromatic compounds, can form oligomers in aromatic SOA, with its contribution related to the presence of particle-phase water.^{26, 28} Hygroscopic seed and humid

conditions facilitate partitioning of glyoxal to the particle phase.²⁶ In the present study, we expect minimal contributions from glyoxal to SOA growth due to the dry experimental conditions, and if oligomerization occurs, we anticipate other routes.

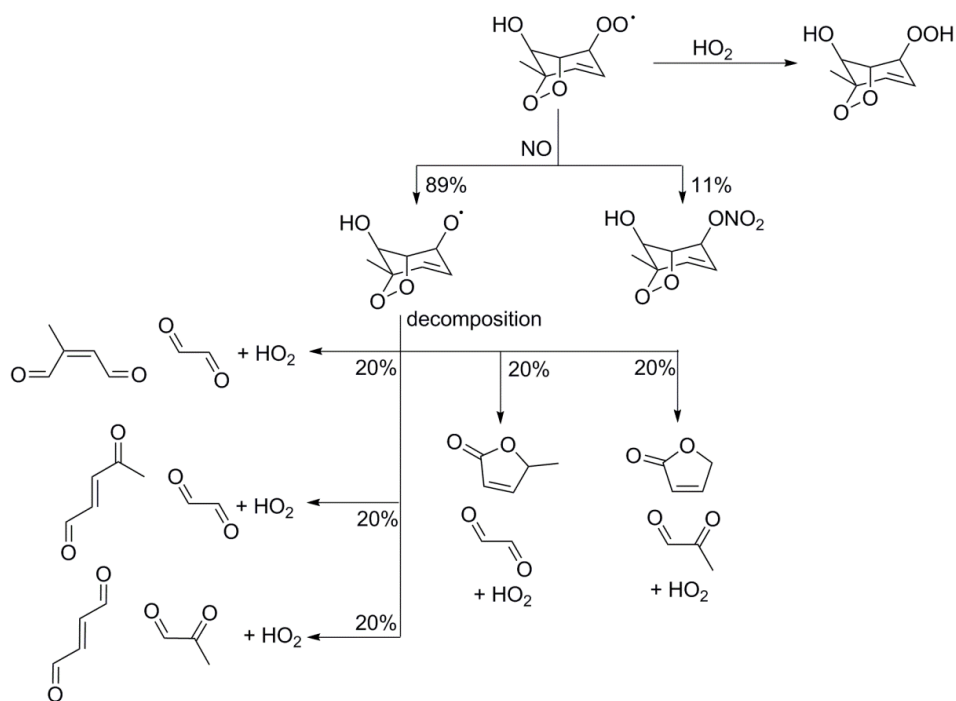


Figure 2. Mechanism for the gas-phase oxidation of the bicyclic peroxy radical under low- and high-NO conditions based on the Master Chemical Mechanism (MCM).⁷

The toluene-derived bicyclic peroxy radical pathway results primarily in ring-opening during decomposition of the bicyclic alkoxy radical formed from reaction with NO (Fig. 2). The decomposition products include unsaturated dicarbonyls of various chain lengths (e.g., glyoxal and methyl glyoxal), and lactones.⁷ Symmetric species like glyoxal are capable of forming extensive oligomer networks, as linking groups are present on both ends of the molecule. Oligomers formed by dissimilar compounds may not span a large molecular weight range, as the monomers may not contain multiple functional groups capable of linking molecules. The bicyclic peroxy radical pathway can be considered a major contributor to toluene SOA when high concentrations of aldehydes and

aldehyde-based oligomers are found in the particle phase, especially under humid conditions and with hygroscopic seed.

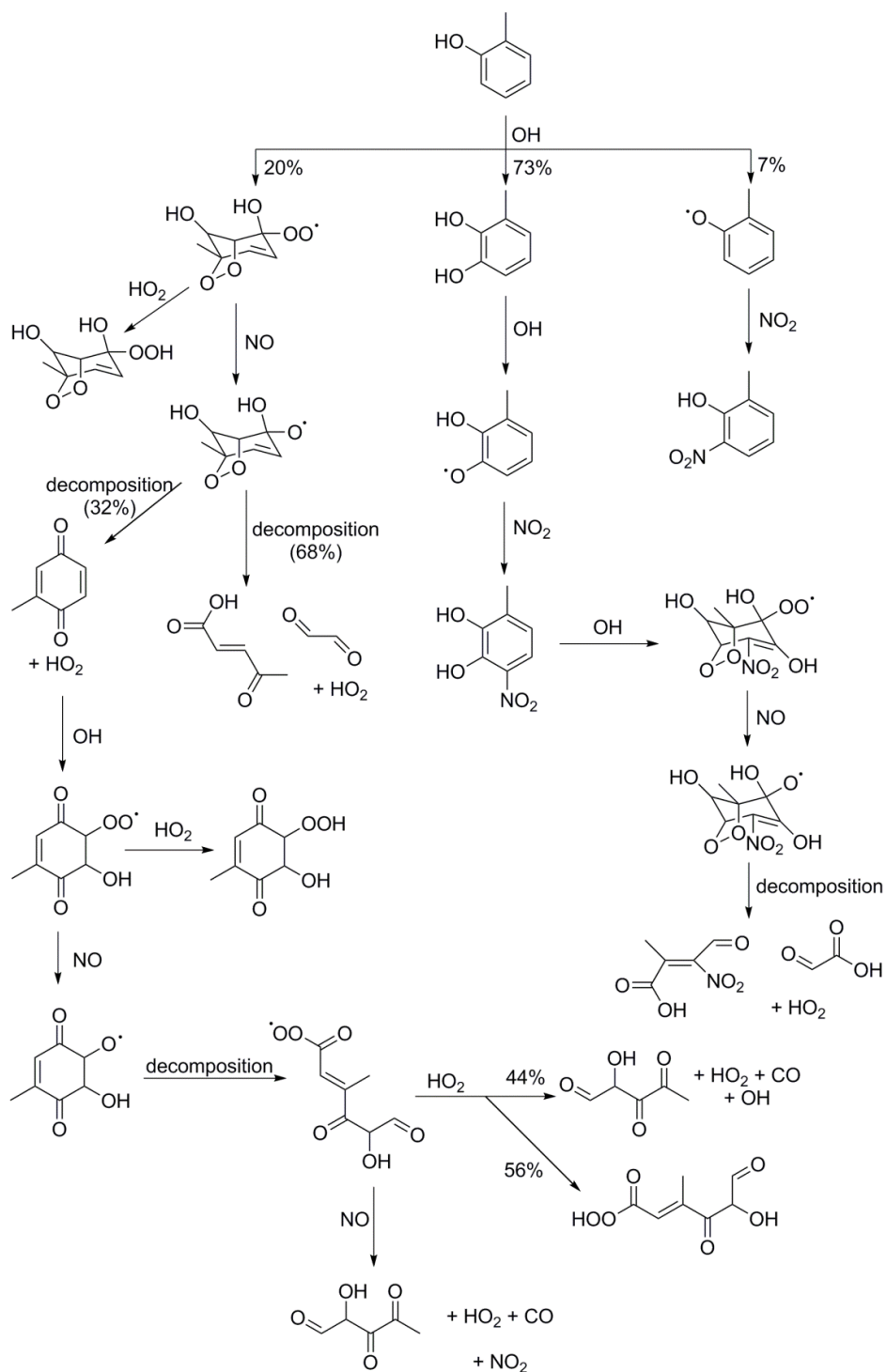


Figure 3. Gas-phase mechanism for *o*-cresol oxidation proceeding by OH addition, based on the Master Chemical Mechanism (MCM).⁷

The cresol pathway leads to its own bicyclic peroxy radical and polyhydroxylated toluene species which can retain the aromatic ring structure in subsequent oxidation steps or undergo a ring-opening step and decompose (Fig. 3). Methyl-*p*-benzoquinone is estimated to form at a 32% yield from the cresol-derived bicyclic alkoxy radical, and its continued oxidation produces both ring-retaining species and ring-opened products that form from alkoxy radical decomposition. These unsaturated carbonyl compounds can form lactones, furans, and oligomeric species, and resemble the later-stage products of toluene photooxidation along non-cresol channels. Unique chemical markers for the cresol pathway include ring-retaining polyhydroxylated and benzoquinone-based species, the presence of which demonstrates the relevance of the cresol pathway to toluene SOA chemical composition.

In this study, we characterize comprehensively toluene SOA composition by utilizing both online high-resolution aerosol time-of-flight mass spectrometry (HR-AMS) and offline direct analysis in real time high-resolution mass spectrometry (DART-HR-MS). We present chemical compositions for SOA produced by the photooxidation of toluene under low- and high-NO conditions in the presence of a variety of inorganic seeds: $(\text{NH}_4)_2\text{SO}_4$, Na_2SO_4 , $\text{MgSO}_4 + \text{H}_2\text{SO}_4$, and NaCl . We also report the chemical composition of SOA from the photooxidation of *o*-, *m*-, and *p*-cresol under high-NO conditions with $(\text{NH}_4)_2\text{SO}_4$ seed aerosol. By producing and analyzing cresol-derived SOA under the same conditions as toluene SOA, we assess the role of cresol as an SOA precursor produced through the photooxidation of toluene. To assist in the comparison of the chemical composition of toluene and cresol SOA, we present results from the application of positive matrix factorization to the HR-AMS datasets for toluene and *o*-cresol high-NO SOA.

EXPERIMENTAL

Environmental Chamber Photooxidation Experiments

The hydroxyl radical-initiated photooxidation of toluene, *o*-, *m*-, and *p*-cresol produced SOA under low- and high-NO conditions in the dual California Institute of Technology environmental chambers, described elsewhere and in the Supporting Information (Table 1).³⁴⁻³⁵ Low-NO conditions are defined here as NO mixing ratios < 5 ppb; high-NO conditions are defined as > 80 ppb NO. Seed composition was varied by using different inorganic salts: (NH₄)₂SO₄, Na₂SO₄, MgSO₄ + H₂SO₄, and NaCl. All cresol isomers were oxidized under similar high-NO and seed conditions to those of toluene to enable the comparison of the resulting SOA chemical compositions, thereby evaluating the contribution of the cresol pathway to toluene SOA formation. All experiments were conducted at 25.0 ± 0.5 °C and ≤ 3% relative humidity.

Table 1. Summary of Experimental Conditions.^{a,b}

Code	Parent VOC	[VOC] ₀ (ppb)	Oxidant Precursor	[NO _x] ₀ (ppb)	Seed	Bulk O:C	Bulk H:C	Bulk N:C	Offline O:C	Offline H:C	Offline N:C
A	toluene	286	H ₂ O ₂	ND	(NH ₄) ₂ SO ₄	0.78	1.34	0.00	0.71	1.14	2.4×10 ⁻¹¹
B	toluene	313	H ₂ O ₂ +NO	96	(NH ₄) ₂ SO ₄	0.81	1.26	0.04	0.60	1.21	0.07
C	toluene	295	H ₂ O ₂ +NO	103	Na ₂ SO ₄	0.80	1.30	0.03	0.67	1.23	9.4×10 ⁻⁵
D	toluene	290	H ₂ O ₂ +NO	102	MgSO ₄ +H ₂ SO ₄	0.78	1.26	0.04	0.71	1.21	9.2×10 ⁻⁵
E	toluene	319	H ₂ O ₂ +NO	91	NaCl	0.90	1.22	0.04	0.59	1.31	0.04
F	<i>o</i> -cresol	105	H ₂ O ₂ +NO	86	(NH ₄) ₂ SO ₄	0.89	1.15	0.05	0.65	1.00	1.2×10 ⁻⁴
G	<i>m</i> -cresol	151	H ₂ O ₂ +NO	73	(NH ₄) ₂ SO ₄	0.73	1.19	0.03	0.86	1.99	4.1×10 ⁻⁷
H	<i>p</i> -cresol	158	H ₂ O ₂ +NO	95	(NH ₄) ₂ SO ₄	0.92	1.21	0.04	0.88	1.75	7.7×10 ⁻⁷

^aND = not detected. Limit of NO and NO₂ detection is 5 ppb. Limit of RH measurement is 3%. Bulk elemental ratios are derived from HR-AMS measurements. Uncertainty estimates for bulk O:C and H:C are 20% and 12%, respectively. Uncertainty estimates for bulk N:C ratios are not reported. Offline elemental ratios are derived from DART-HR-MS measurements.

^bAll ions of intensity ≥ 5% of the base peak in a DART-HR-MS mass spectrum are assigned a molecular formula. Background ions are not included.

Chemical Analysis of SOA by HR-AMS

Aerosol composition was recorded online using a high-resolution time-of-flight aerosol mass spectrometer (HR-AMS, Aerodyne Research, Inc.). The HR-AMS was operated switching every 1 min between the high-resolution W-mode and the lower-resolution, higher-sensitivity V-mode. The data were analyzed with Igor Pro (Wave Metrics, Inc.), utilizing the Squirrel 1.53G and PIKA 1.12G analysis toolkits. Air interference corrections were made to the fragmentation table by applying correction factors determined by in-line filter runs prior to the experiments.³⁶ Bulk SOA elemental composition was calculated following the methods and recommendations of Aiken *et al.* and Canagaratna *et al.*³⁶⁻³⁷

Positive matrix factorization analysis (PMF) was used to investigate qualitatively the differences in aerosol compositions between toluene and o-cresol SOA produced under high-NO conditions with $(\text{NH}_4)_2\text{SO}_4$ seed. A detailed description of PMF application to chamber HR-AMS data can be found in Craven *et al.*³⁸ Details of the PMF application procedure and support for the solutions presented here appear in the Supporting Information.

Chemical Analysis of SOA by DART-HR-MS

SOA was collected by filtration over the final 4 h of experiments at 24 L min^{-1} with a Teflon membrane filter (47 mm, $1.0 \mu\text{m}$ pore size, Pall Life Sciences) and analyzed by high-resolution direct analysis in real time mass spectrometry (DART-HR-MS, JEOL, Inc.). A DART source is a low-temperature He plasma that generates primarily pseudomolecular $([\text{M}+\text{H}]^+)$ ions in positive mode through proton transfer reactions between the analyte, M, and ionized ambient water vapor (H_3O^+).³⁹⁻⁴⁰ Samples are introduced for analysis directly into the DART stream, between the end of the DART source and the mass spectrometer inlet. In this study, a portion of the filter membrane was cut free from the support ring using a clean stainless steel scalpel and wrapped in a spiral around the barrel of a clean glass Pasteur pipet. The pipet was rotated slowly in the DART stream to warm

the glass and desorb organic material gently from the Teflon filter. Each sample was cut and analyzed in triplicate. Intrasample peak intensity variability was < 3%. Additional analysis details, mass spectra for each SOA sample, and tabulated interpreted mass spectral data corrected to remove background ions are provided in the Supporting Information.

The accurate m/z of each ion $\geq 5\%$ of the base peak intensity was fit to a chemical formula, adjusted to its neutral form, and given a proposed structure based on MCM toluene photooxidation and previously reported components of toluene SOA.^{1-5, 7, 12, 17, 19, 21, 23, 30, 41} The Estimation of Vapor Pressure of Organics, Accounting for Temperature, Intramolecular, and Non-additivity Effects (EVAPORATION) model was used for each proposed structure, given in Simplified Molecular-Input Line-Entry System (SMILES) notation, to estimate the vapor pressure of the compound.⁴² The EVAPORATION model is compatible with molecules containing oxygen-based functional groups and nitrates. To fit within these parameters, the vapor pressures of species proposed to be imines and N-containing heterocycles were estimated by using their oxygenated equivalent, and the vapor pressures of compounds containing nitro groups were estimated by substituting with a nitrate group.

DART-generated ion signal intensity for a given species is proportional to its vapor pressure, proton affinity, and concentration.⁴³⁻⁴⁴ Targeted quantitative DART-MS analysis is performed by co-analyzing a compound with its isotopically labeled counterpart. In broad-spectrum quantitative analyses, such as those in this study, an internal standard must be chosen within the expected range of proton affinities and vapor pressures. The application of a droplet of internal standard solution to filtered SOA may lead to undesirable side reactions and alteration of SOA composition. Dibutyl phthalate (DBP) was chosen as an internal standard, as it is found in the Teflon filters used in this study, and its proton affinity and vapor pressure are within the expected range of proton affinities and vapor pressures for toluene and cresol SOA components. DBP and typical SOA components

have proton affinities that are estimated to be comparable, leading to an analyte: standard proton affinity ratio of approximately 1.⁴⁴ With a proton affinity ratio of 1, analyte concentrations relative to DBP were arrived at by multiplying the ratio of vapor pressure of DBP to the analyte vapor pressure predicted by EVAPORATION by the ratio of the intensity of the analyte pseudomolecular ion to the intensity of the DBP pseudomolecular ion. Mixing ratios, also called relative mass fractions here, were calculated by dividing an analyte or analyte class by the sum of all measured SOA compounds for that given sample. The maximum propagated uncertainty in relative mass fractions for all species, based on 3% intensity variation, is 3×10^{-14} ; this uncertainty holds for all reported relative mass fractions. Weighted average values for elemental ratios from offline analysis results were obtained by summing the products of each species mixing ratio by the H:C, O:C, or N:C for each species molecular formula (Table 1).

RESULTS AND DISCUSSION

Quantitative Analysis of Toluene and o-, m-, and p-Cresol SOA

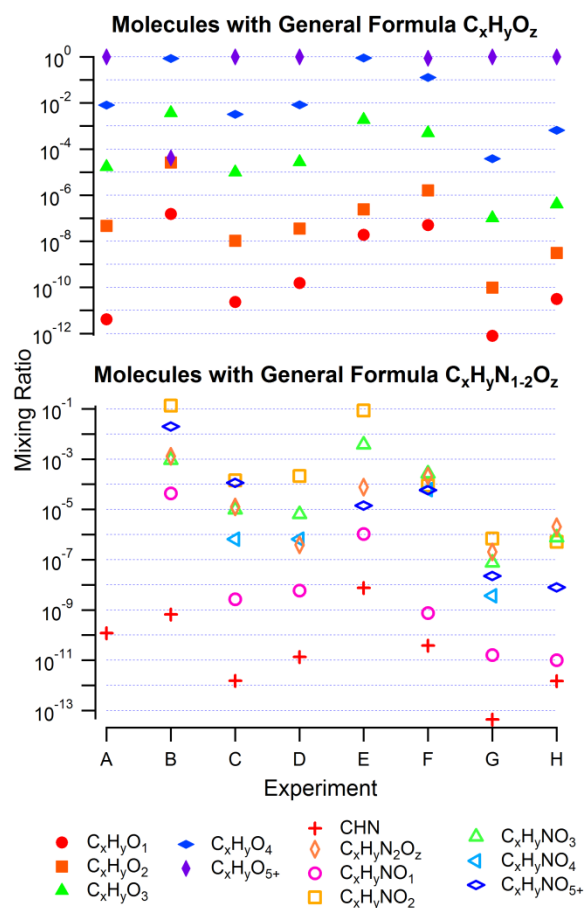


Figure 4. Chemical composition of SOA produced in current toluene and cresol photooxidation experiments as measured by offline DART-HR-MS analysis, displayed by general molecular formula category. Table 1 contains the key with experimental details.

The composition of both high- and low-NO SOA derived from toluene is dominated by species with the general formulae $C_xH_yO_{5+}$ and $C_xH_yO_4$, and N incorporation is significant only under high-NO conditions (Fig. 4). The SOA compositions reported here are consistent with multigenerational photooxidation through the bicyclic peroxy radical and cresol pathways as the primary routes to toluene SOA formation under low- and high-NO conditions. Toluene low-NO SOA does not feature significant N incorporation, indicating the expected lack of nitrate and nitro group formation as well as the inhibition of seed-related processes like imine formation, which can occur with high

concentrations of carbonyls in the presence of ammonium sulfate (Table 1 and Fig. 4).⁴⁴ Pyridine formation, while minor, is ubiquitous in these experiments and potentially attributable to artifactual chemistry on the chamber walls (see Supporting Information).

Under high-NO conditions, the most highly oxygenated compounds ($C_xH_yO_{5+}$) constitute relative mass fractions of 0.99 for toluene- and cresol-derived SOA; no clear seed effect related to O number is observed. The next most abundant general molecular formulae are $C_xH_yO_4$ and $C_xH_yO_3$. $C_xH_yO_2$ compounds, including glyoxal, constitute $\leq 1\%$ by mass of toluene and *o*-, *m*-, and *p*-cresol SOA under these dry, high-NO conditions. The most abundant nitrogenous species are oxygenated nitro compounds or nitrates, $C_xH_yNO_{5+}$. The bulk N:C ratios for all high-NO SOA systems studied are consistent across seed types, supporting gas-phase reactions with NO to form nitrates and nitro compounds as the origins of the N functionality (Table 1). The difference between the bulk and offline N:C ratios can be attributed to uncertainty in the estimated vapor pressures of compounds with N-containing functional groups, which fall outside the present scope of the EVAPORATION model (e.g., imines, nitro groups). For broad-spectrum quantitation by DART-HR-MS, accurate vapor pressures are necessary.

Species found in *o*-cresol high-NO SOA constitute a relative mass fraction of 0.84 of toluene high-NO SOA in this study. $C_7H_8O_4$, interpreted as tetrahydroxytoluene (estimated vapor pressure 9.0×10^{-14} atm), comprises a relative mass fraction of 0.70 in toluene high-NO SOA. $C_7H_6O_4$, corresponding to trihydroxybenzaldehyde (estimated vapor pressure 8.3×10^{-9} atm) contributes a relative mass fraction of 0.10 to toluene high-NO SOA. $C_7H_6O_3$, proposed to be dihydroxybenzaldehyde, contributes a relative mass fraction of 2.5×10^{-5} to toluene high-NO SOA. The additional 0.04 is composed of molecules with general formulae $C_xH_yNO_2$, $C_xH_yNO_3$, C_xH_yO , and $C_xH_yO_2$ (see Supporting Information). The particle-phase measurement of modest

concentrations of these moderate- to high-volatility oxidation products is attributed to the proposed trapping of condensing volatiles during the rapid accumulation of organic material in the growth phase.^{45,46} Partial re-partitioning of volatile species occurs, possibly because the expected glassy nature of SOA may trap trace amounts of volatiles.

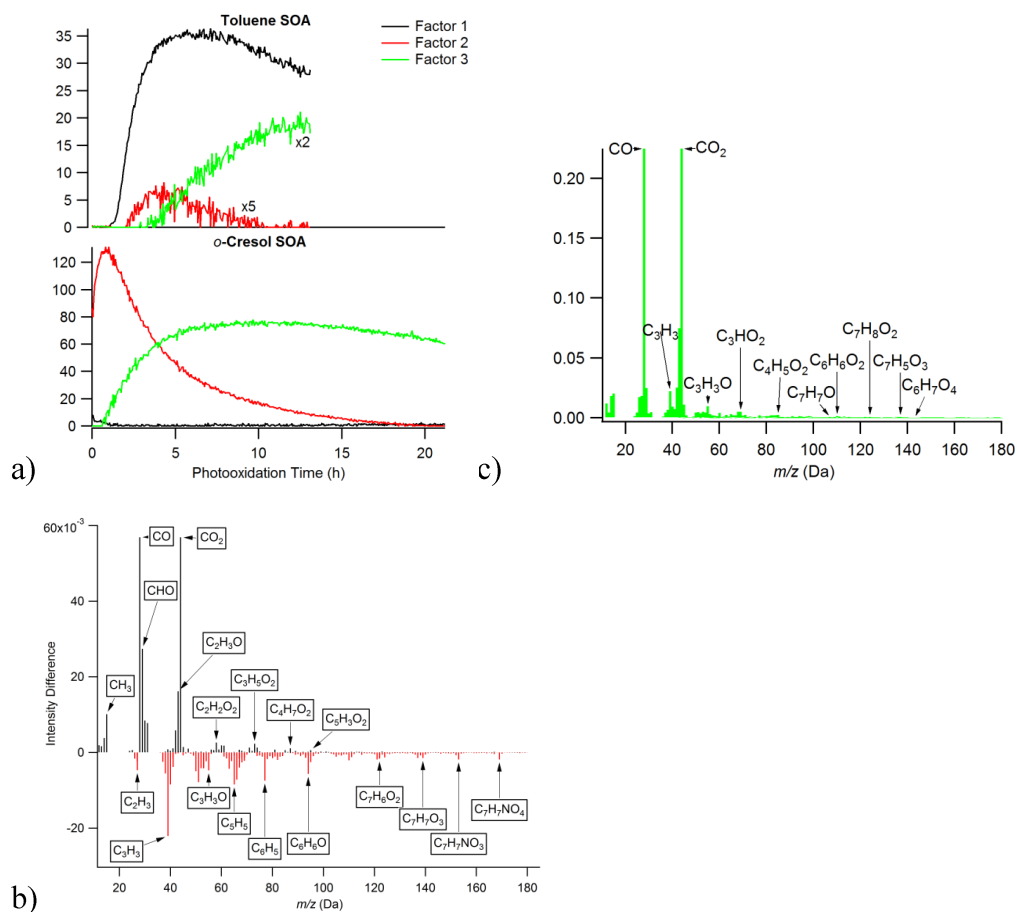


Figure 5. Three-factor PMF solution comparing toluene and *o*-cresol SOA produced under high-NO conditions in the presence of $(\text{NH}_4)_2\text{SO}_4$ seed. (a) Factor time trends: factor 1, distinct ions characterizing toluene SOA (black); factor 2, ions common to both toluene and cresol SOA related to early-generation cresol oxidation, multiplied by 5 for clarity (red); factor 3, ions from later-generation toluene and cresol oxidation (green), multiplied by 2 for clarity. (b) The difference between factor 1 (black) and factor 2 (red) mass spectral profiles. (c) Factor 3 mass spectral profile (green).

Detailed PMF analysis of the HR-AMS spectra of toluene and cresol SOA was conducted to assess qualitatively the chemical pathways leading to SOA formation under high-NO conditions. A three-factor fit is the simplest solution that captures the variation of the HR-AMS data within the

known uncertainties of HR-AMS spectra (Fig. 5a). Toluene high-NO SOA has a distinctive factor (factor 1, shown in black); this is expected, given that no toluene is present in the cresol experiment. A shared factor (factor 2) describes early-generation *o*-cresol high-NO SOA and a small fraction of toluene high-NO SOA. The later, gradual decrease of factor 2 can be attributed to partial repartitioning of higher-volatility early-stage oxidation products back to the gas phase. Another shared factor (factor 3) describes the later-generation high-NO toluene and *o*-cresol SOA. Figure 5b shows the difference spectrum obtained by subtracting the mass spectral profile of factor 1 from that of factor 2. The difference spectrum shows enrichment in the unique toluene SOA profile (factor 1) of marker ions for highly oxidized species (e.g. CO_2^+) and unsaturated ketones and aldehydes (e.g., $\text{C}_2\text{H}_2\text{O}_2^+$, $\text{C}_4\text{H}_7\text{O}_2^+$, $\text{C}_3\text{H}_5\text{O}_2^+$, $\text{C}_5\text{H}_3\text{O}_2^+$). Marker ions for ring-retaining aromatic oxidized species (e.g. C_3H_3^+ , $\text{C}_7\text{H}_7\text{O}_3^+$, $\text{C}_6\text{H}_6\text{O}_2^+$) are observed in early generation *o*-cresol SOA (factor 2). Factor 3 describes the late stages of multigenerational photooxidation, in which toluene and *o*-cresol SOA compositions converge, and features marker ions for aromatic ring-retaining oxidation products (e.g., $\text{C}_7\text{H}_8\text{O}_2^+$, $\text{C}_7\text{H}_8\text{O}_2^+$, $\text{C}_6\text{H}_7\text{O}_4^+$) (Fig. 5c). The measurement of a family of shared chemical species is expected based on the MCM for toluene and cresol photooxidation (Figs. 1-3).

Elemental Ratios as Descriptor of Toluene and Cresol Chemical Composition

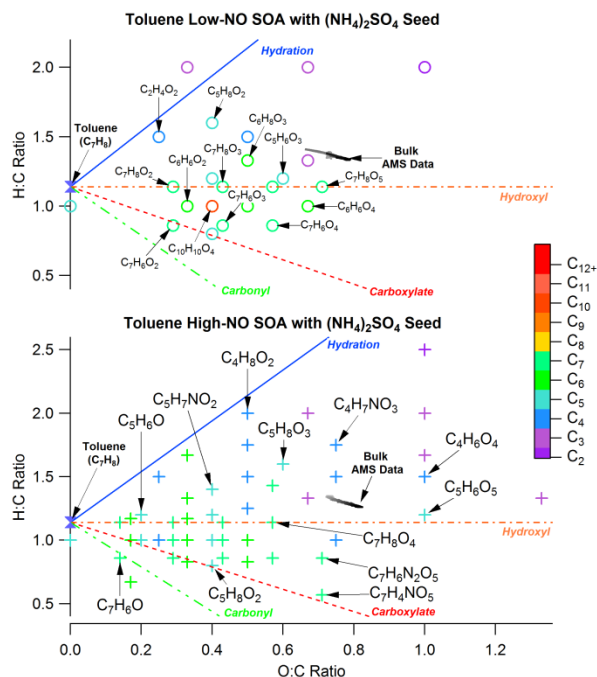


Figure 6. Species identified by DART-HR-MS analysis in the present study of toluene SOA produced under low- and high-NO conditions with $(\text{NH}_4)_2\text{SO}_4$ seed are displayed in van Krevelen space. Data markers are colored by the molecular formula C number. The bulk H:C and O:C elemental ratios derived from HR-AMS measurements are shown in grayscale for both low-NO and high-NO conditions.

Van Krevelen diagrams depict concisely variations in the functionalization of a complex organic mixture.⁴⁷⁻⁴⁹ Figure 6 displays in van Krevelen space the elemental ratios for species measured by DART-HR-MS in the present study of toluene SOA generated under dry, low-, and high-NO conditions in the presence of $(\text{NH}_4)_2\text{SO}_4$ seed aerosol. Lines representing various functionalization pathways are shown. Not all measured species have a unique coordinate in van Krevelen space, as redundancies in H:C and O:C ratios may occur with nitrogen incorporation.

Multigenerational oxidation chemistry is evident in the polyfunctional species measured in these experiments. The majority of compounds in both high- and low-NO toluene SOA are C_7 : $\text{C}_7\text{H}_8\text{O}_4$ in high-NO conditions and $\text{C}_7\text{H}_8\text{O}_5$ under low-NO conditions. These formulae are consistent with tetra- and pentahydroxytoluene, which are suggestive of oxidation following the cresol pathway.

Toluene high-NO SOA in this study is also characterized by $< C_7$ compounds, which are attributed to decomposition of toluene- and cresol-derived bicyclic peroxide intermediates (Fig. 2, 3, 6). Carboxylate formation (or the equivalent addition of carbonyl and hydroxyl groups on different sites within the same molecule) occurs on C_7 and C_5 backbones in toluene SOA, supporting the contribution from ring-opening non-cresol pathways (72% yield, by MCM). Bulk SOA H:C and O:C HR-AMS data have a slope of -2, supporting the relevance of carbonyl functionalization to toluene SOA formation under both low- and high- NO conditions.

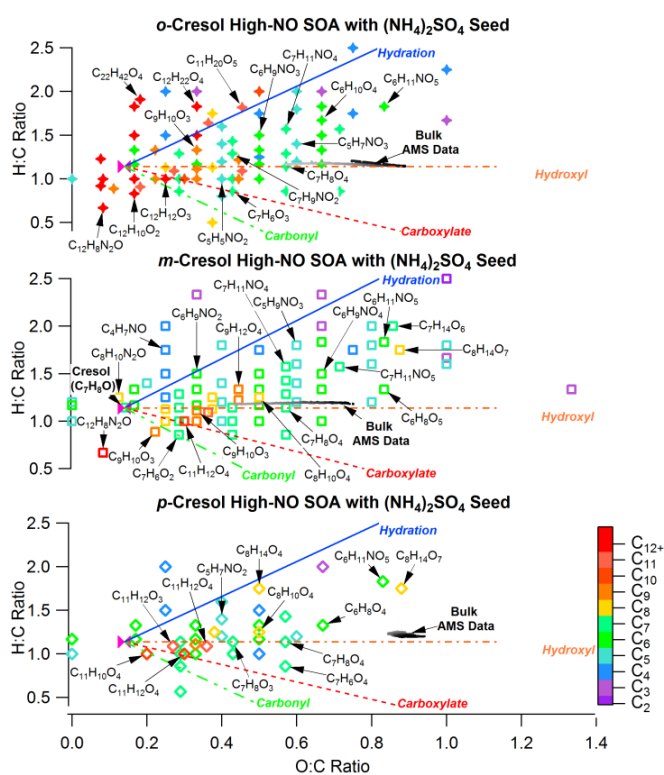


Figure 7. Van Krevelen diagram depicting chemical compositions of cresol SOA produced under high-NO conditions with $(NH_4)_2SO_4$ seed, as measured by offline DART-HR-MS. Data markers are colored by the molecular formula C number. The bulk SOA H:C and O:C elemental ratios derived from HR-AMS measurements are shown in grayscale.

Figure 7 displays the chemical composition of individual *o*-, *m*-, and *p*-cresol SOA formed under high-NO conditions with $(NH_4)_2SO_4$ seed. *o*- and *m*-Cresol SOA span a much larger O:C range than *p*-cresol SOA does, yet the final bulk O:C and H:C values for all three cresol isomers are similar

(Table 1). The close proximity of the electron-rich hydroxyl group to the methyl group in *o*- and *m*-cresol may affect ring-opening pathways and further functionalization in ways that do not occur for *p*-cresol.

Both offline and online SOA chemical characterization suggest repeated hydroxylation is an important process for SOA formation from all cresol isomers (Fig. 7). This finding is consistent with the MCM-estimated 73% of cresol undergoing further OH addition (Fig. 3). The majority of SOA mass for all cresol isomers is attributable to C₇₋₁₀ compounds; oligomerization through hemiacetal formation from C₇ compounds and small carbonyl species may be the source of these products. Increased H:C ratios and decreased C number are consistent with the expected decomposition products of the bicyclic alkoxy radical formed from continued high-NO photooxidation of cresol. These unsaturated oxidized species are measured as monomeric and oligomeric species, ranging from C₅ to C₁₁ in chain size, and in the case of *o*-cresol up to C₂₂.

Species Carbon Number as a Descriptor of Toluene and Cresol SOA Composition

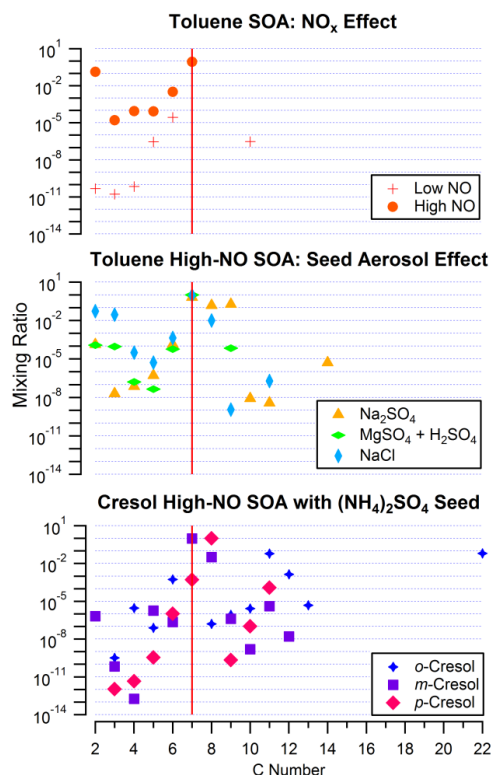


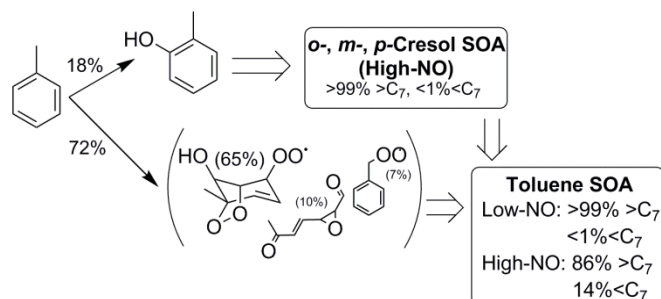
Figure 8. Chemical composition of toluene and cresol SOA, displayed as a function of C number, derived from offline DART-HR-MS analysis. The red line represents the C_7 threshold.

Toluene SOA formed under dry, low- and high-NO conditions with $(\text{NH}_4)_2\text{SO}_4$ seed comprise high relative mass fractions of highly oxygenated C_7 compounds. The abundance of C_7 oxidation products in toluene SOA suggests the cresol pathway is influential in toluene SOA formation, since fragmentation is a major early-generation mechanism for the bicyclic peroxy radical, epoxy muconaldehyde, and toluene peroxy pathways (Figs. 1-4 and 8, and Supporting Information). $\text{C}_{10}\text{H}_{10}\text{O}_4$ is the principal oligomeric species identified in toluene SOA formed under dry low-NO conditions, with a relative mass fraction of 3.0×10^{-5} , and is potentially a hemiacetal formed between a C_7 polyhydroxylated species and a C_3 carbonyl compound. Extensive oligomerization is not found in this case possibly because of the abundance of highly oxidized, bulky, ring-retaining C_7 compounds relative to the modest amount of sub- C_7 compounds.

In the present study, a seed effect is observed in the increased C chain lengths ($> C_7$) in the presence of Na_2SO_4 , $\text{MgSO}_4 + \text{H}_2\text{SO}_4$, and NaCl seeds (Fig. 8). We report here high oligomer C numbers and relative mass fractions in toluene high-NO SOA formed in the presence of Na_2SO_4 (0.34) and NaCl (0.01) seeds relative to that formed in the presence of $\text{MgSO}_4 + \text{H}_2\text{SO}_4$ (7.1×10^{-5}) and $(\text{NH}_4)_2\text{SO}_4$ (0) seeds. Seed effects have been observed in previous studies as the shifting of oligomer distributions in SOA to higher molecular weights as seed acidity is increased.^{6,33} The abundance of lower molecular weight oligomers observed by Gao *et al.* did not change with increased acidity, implying that oligomer types may have different acid sensitivities, which is consistent with observations here.³³ In this study, toluene high-NO SOA has an abundance of polyhydroxylated C_7 species, and these species may have potential to produce an oligomer type that is less responsive to acidic seed. Additionally, the continuity of the oligomer C atom range (C_8 , C_9 , C_{10} , etc.) suggests that oligomers may be forming between C_7 particle-phase compounds and small gas-phase oxidation products. Hall and Johnston observed the independence of monomer abundance in SOA and monomer vapor pressure and suggested reactive uptake between a monomer colliding and reacting with the particle surface as a potential scenario for oligomer formation in SOA.⁵⁰

In this study, *o*-, *m*- and *p*-Cresol SOA contain abundant oligomeric species (relative mass fractions: 0.13, 0.03, and 0.99, respectively). *o*- and *m*-Cresol-derived oligomeric species have the general forms $\text{C}_x\text{H}_y\text{O}_{4-5+}$, with $< 1\%$ of the oligomeric relative mass fraction composed of $\text{C}_x\text{H}_y\text{NO}_{3-5+}$ and $\text{C}_x\text{H}_y\text{O}_{2-3}$. *p*-Cresol SOA contains one identified oligomer, $\text{C}_8\text{H}_{14}\text{O}_7$. The position of the hydroxyl group in the cresol isomer is observed here to affect oligomer formation as well as monomer composition and bulk H:C and O:C trends.

GRAPHICAL ABSTRACT



ASSOCIATED CONTENT

Supporting Information. The supporting information includes additional details for the environmental chamber experiments, Master Chemical Mechanisms for non-cresol pathway toluene photooxidation, details on SOA collection by filtration, experimental details from the offline analysis of SOA by DART-HR-MS, tabulated interpreted offline mass spectral data, van Krevelen diagrams of DART-HR-MS and HR-AMS data, details on the qualitative PMF analysis performed in this study and evidence of the solution robustness, as well as HR-AMS data supporting the identification of pyridine and the Chichibabin mechanism for pyridine synthesis.

AUTHOR INFORMATION

Corresponding Author

*Correspondence should be addressed to John H. Seinfeld, seinfeld@caltech.edu.

Author Contributions

The manuscript was written by KAS and JHS. The experiments were performed by KAS, HL, MMC, RHS, and XZ. Data were analyzed by KAS, HL, and MMC.

ACKNOWLEDGMENTS

The authors thank Jill Craven for helpful data discussions and Jeffrey Dake of the United States Army Criminal Investigation Laboratory, Trace Evidence Branch, for experimental assistance with DART-HR-MS analysis. This research was funded by U.S. Department of Energy grant DE-SC0006626. KAS acknowledges support from a Department of Defense Science, Mathematics, and Research for Transformation Fellowship.

REFERENCES

1. Yu, J.; Jeffries, H. E.; Sexton, K. G. Atmospheric Photooxidation of Alkylbenzenes - I. Carbonyl Product Analyses. *Atmos. Environ.* **1997**, *31*, 2261-2280.
2. Yu, J.; Jeffries, H. E., Atmospheric Photooxidation of Alkylbenzenes – II. Evidence of Formation of Epoxide Intermediates. *Atmos. Environ.* **1997**, *31*, 2281-2287.
3. Calvert, J. G.; Atkinson, R.; Becker, K. H.; Kamens, R. M.; Seinfeld, J. H.; Wallington, T. J.; Yarwood, G. *The Mechanisms of Atmospheric Oxidation of Aromatic Hydrocarbons*; Oxford University Press: New York, 2002.
4. Cao, G.; Jang, M. Effects of Particle Acidity and UV Light on Secondary Organic Aerosol Formation from Oxidation of Aromatics in the Absence of NO_x. *Atmos. Environ.* **2007**, *41*, 7603-7613.
5. Jang, M.; Kamens, R. M. Characterization of Secondary Aerosol from the Photooxidation of Toluene in the Presence of NO_x and 1-Propene. *Environ. Sci. Technol.* **2001**, *35*, 3626-3639.
6. Tolocka, M. P.; Jang, M.; Ginter, J. M.; Cox, F. J.; Kamens, R. M.; Johnston, M. V. Formation of Oligomers in Secondary Organic Aerosol. *Environ. Sci. Technol.* **2004**, *38*, 1428-1434.
7. Jenkin, M. E.; Saunders, S. M.; Wagner, V.; Pilling, M. J. Protocol for the Development of the Master Chemical Mechanism, MCM v3 (Part B): Tropospheric Degradation of Aromatic Volatile Organic Compounds. *Atmos. Chem. Phys.* **2003**, *3*, 181-193.
8. Wagner, V.; Jenkin, M. E.; Saunders, S. M.; Stanton, J.; Wirtz, K.; Pilling, M. J. Modelling of the Photooxidation of Toluene: Conceptual Ideas for Validating Detailed Mechanisms. *Atmos. Chem. Phys.* **2003**, *3*, 89-106.
9. Klotz, B.; Barnes, I.; Becker, K. H.; Golding, B. T. Atmospheric Chemistry of Benzene Oxide/Oxepin. *J. Chem. Soc., Faraday Trans.* **1997**, *93*, 1507-1516.
10. Klotz, B.; Barnes, I.; Golding, B. T.; Becker, K. H. Atmospheric Chemistry of Toluene-1,2-Oxide/2-Methyloxepin. *Phys. Chem. Chem. Phys.* **2000**, *2*, 227-235.
11. Klotz, B.; Sorensen, S.; Barnes, I.; Becker, K. H.; Etzkorn, T.; Volkamer, R.; Platt, U.; Wirtz, K.; Martin-Reviejo, M. Atmospheric Oxidation of Toluene in a Large-Volume Outdoor Photoreactor: In-Situ Determination of Ring-Retaining Product Yields. *J. Phys. Chem. A* **1998**, *102*, 10289-10299.

12. Olariu, R. I.; Klotz, B.; Barnes, I.; Becker, K. H.; Mocanu, R. FT-IR Study of the Ring-Retaining Products from the Reaction of OH Radicals with Phenol, *o*-, *m*-, and *p*-Cresol. *Atmos. Environ.* **2002**, *36*, 3685-3697.
13. Volkamer, R.; Klotz, B.; Barnes, I.; Imamura, T.; Wirtz, K.; Washida, N.; Becker, K. H.; Platt, U. OH-Initiated Oxidation of Benzene: Part I. Phenol Formation under Atmospheric Conditions. *Phys. Chem. Chem. Phys.* **2002**, *4*, 1598-1610.
14. Birdsall, A. W.; Elrod, M. J. Comprehensive NO-Dependent Study of the Products of the Oxidation of Atmospherically Relevant Aromatic Compounds. *J. Phys. Chem. A* **2011**, *115*, 5397-5407.
15. Birdsall, A. W.; Andreoni, J. F.; Elrod, M. J. Investigation of the Role of the Bicyclic Peroxy Radicals in the Oxidation Mechanism of Toluene. *J. Phys. Chem. A* **2010**, *114*, 10655-10663.
16. Baltaretu, C. O.; Lichtman, E. I.; Hadler, A. B.; Elrod, M. J. Primary Atmospheric Oxidation Mechanism for Toluene. *J. Phys. Chem. A* **2009**, *113*, 221-230.
17. Edney, E. O.; Driscoll, D. J.; Weathers, W. S.; Kleindienst, T. E.; Conner, T. S.; McIver, C. D.; Li, W. Formation of Polyketones in Irradiated Toluene/Propylene/NO_x/Air Mixtures. *Aerosol Sci. Technol.* **2001**, *35*, 998-1008.
18. Edney, E. O.; Driscoll, D. J.; Speer, R. E.; Weathers, W. S.; Kleindienst, T. E.; Li, W.; Smith, D. F. Impact of Aerosol Liquid Water on Secondary Organic Aerosol Yields of Irradiated Toluene/Propylene/NO_x/(NH₄)₂SO₄/Air Mixtures. *Atmos. Environ.* **2000**, *34*, 3907-3919.
19. Kleindienst, T. E.; Smith, D. F.; Li, W.; Edney, E. O.; Driscoll, D. J.; Speer, R. E.; Weathers, W. S., Secondary Organic Aerosol Formation from the Oxidation of Aromatic Hydrocarbons in the Presence of Dry Submicron Ammonium Sulfate Aerosol. *Atmos. Environ.* **1999**, *33*, 3669-3681.
20. Hildebrandt, L.; Donahue, N. M.; Pandis, S. N. High Formation of Secondary Organic Aerosol from the Photooxidation of Toluene. *Atmos. Chem. Phys.* **2009**, *9*, 2973-2986.
21. Smith, D. F.; McIver, C. D.; Kleindienst, T. E. Primary Product Distribution from the Reaction of Hydroxyl Radicals with Toluene at ppb NO_x Mixing Ratios. *J. Atmos. Chem.* **1998**, *30*, 209-228.
22. Smith, D. F.; Kleindienst, T. E.; McIver, C. D. Primary Product Distributions from the Reaction of OH with *m*- and *p*-Xylene, 1,2,4- and 1,3,5-Trimethylbenzene. *J. Atmos. Chem.* **1999**, *34*, 339-364.
23. Forstner, H. J. L.; Flagan, R. C.; Seinfeld, J. H. Secondary Organic Aerosol from the Photooxidation of Aromatic Hydrocarbons: Molecular Composition. *Environ. Sci. Technol.* **1997**, *31*, 1345-1358.
24. Baltensperger, U.; Kalberer, M.; Dommen, J.; Paulsen, D.; Alfarra, M. R.; Coe, H.; Fisseha, R.; Gascho, A.; Gysel, M.; Nyeki, S.; Sax, M.; Steinbacher, M.; Prevot, A. S. H.; Sjogren, S.; Weingartner, E.; Zenobi, R. Secondary Organic Aerosols from Anthropogenic and Biogenic Precursors. *Faraday Discuss.* **2005**, *130*, 265-278.
25. Cocker, D. R.; Mader, B. T.; Kalberer, M.; Flagan, R. C.; Seinfeld, J. H. The Effect of Water on Gas-Particle Partitioning of Secondary Organic Aerosol: II. *m*-Xylene and 1,3,5-Trimethylbenzene Photooxidation Systems. *Atmos. Environ.* **2001**, *35*, 6073-6085.
26. Nakao, S.; Liu, Y.; Tang, P.; Chen, C. L.; Zhang, J.; Cocker, D. R. Chamber Studies of SOA Formation from Aromatic Hydrocarbons: Observation of Limited Glyoxal Uptake. *Atmos. Chem. Phys.* **2012**, *12*, 3927-3937.

27. Song, C.; Na, K.; Warren, B.; Malloy, Q.; Cocker, D. R. Secondary Organic Aerosol Formation from *m*-Xylene in the Absence of NO_x. *Environ. Sci. Technol.* **2007**, *41*, 7409-7416.
28. Kalberer, M.; Paulsen, D.; Sax, M.; Steinbacher, M.; Dommen, J.; Prevot, A. S. H.; Fisseha, R.; Weingartner, E.; Frankevich, V.; Zenobi, R.; Baltensperger, U. Identification of Polymers as Major Components of Atmospheric Organic Aerosols. *Science* **2004**, *303*, 1659-1662.
29. Kalberer, M.; Sax, M.; Samburova, V. Molecular Size Evolution of Oligomers in Organic Aerosols Collected in Urban Atmospheres and Generated in a Smog Chamber. *Environ. Sci. Technol.* **2006**, *40*, 5917-5922.
30. Sato, K.; Hatakeyama, S.; Imamura, T. Secondary Organic Aerosol Formation During the Photooxidation of Toluene: NO_x Dependence of Chemical Composition. *J. Phys. Chem. A* **2007**, *111*, 9796-9808.
31. Ehn, M.; Thornton, J. A.; Kleist, E.; Sipila, M.; Junninen, H.; Pullinen, I.; Springer, M.; Rubach, F.; Tillmann, R.; Lee, B.; Lopez-Hilfiker, F.; Andres, S.; Acir, I.-H.; Rissanen, M.; Jokinen, T.; Schobesberger, S.; Kangasluoma, J.; Kontkanen, J.; Nieminen, T.; Kurten, T.; Nielsen, L. B.; Jorgensen, S.; Kjaergaard, H. G.; Canagaratna, M.; Dal Maso, M.; Berndt, T.; Petaja, T.; Wahner, A.; Kerminen, V.-M.; Kulmala, M.; Worsnop, D. R.; Wildt, J.; Mentel, T. F. A Large Source of Low-Volatility Secondary Organic Aerosol. *Nature* **2014**, *506*, 476-496.
32. Gao, S.; Keywood, M.; Ng, N. L.; Surratt, J.; Varutbangkul, V.; Bahreini, R.; Flagan, R. C.; Seinfeld, J. H. Low-Molecular-Weight and Oligomeric Components in Secondary Organic Aerosol from the Ozonolysis of Cycloalkenes and α -Pinene. *J. Phys. Chem. A* **2004**, *108*, 10147-10164.
33. Gao, S.; Ng, N. L.; Keywood, M.; Varutbangkul, V.; Bahreini, R.; Nenes, A.; He, J.; Yoo, K. Y.; Beauchamp, J. L.; Hodyss, R. P.; Flagan, R. C.; Seinfeld, J. H. Particle Phase Acidity and Oligomer Formation in Secondary Organic Aerosol. *Environ. Sci. Technol.* **2004**, *38*, 6582-6589.
34. Zhang, X.; Cappa, C. D.; Jathar, S.; McVay, R. C.; Ensberg, J. J.; Kleeman, M. J.; Seinfeld, J. H. Influence of Vapor Wall-Loss in Laboratory Chambers on Yields of Secondary Organic Aerosol. *Proc. Natl. Acad. Sci. USA* **2014**, *116*, 5802-5807.
35. Loza, C. L.; Craven, J. S.; Yee, L. D.; Coggon, M. M.; Schwantes, R. H.; Shiraiwa, M.; Zhang, X.; Schilling, K. A.; Ng, N. L.; Canagaratna, M. R.; Ziemann, P. J.; Flagan, R. C.; Seinfeld, J. H. Secondary Organic Aerosol Yields of 12-Carbon Alkanes. *Atmos. Chem. Phys.* **2014**, *14*, 1423-1439.
36. Aiken, A. C.; De Carlo, P. F.; Kroll, J. H.; Worsnop, D. R.; Huffman, J. A.; Docherty, K. S.; Ulbrich, I. M.; Mohr, C.; Kimmel, J. R.; Sueper, D.; Sun, Y.; Zhang, Q.; Trimborn, A.; Northway, M.; Ziemann, P. J.; Canagaratna, M. R.; Onasch, T. B.; Alfarra, M. R.; Prevot, A. S. H.; Dommen, J.; Duplissy, J.; Metzger, A.; Baltensperger, U.; Jimenez, J. L. O/C and OM/OC Ratios of Primary, Secondary, and Ambient Organic Aerosols with High-Resolution Time-of-Flight Aerosol Mass Spectrometry. *Environ. Sci. Technol.* **2008**, *42*, 4478-4485.
37. Canagaratna, M. R.; Jimenez, J. L.; Kroll, J. H.; Chen, Q.; Kessler, S. H.; Massoli, P.; Hidebrandt Ruiz, L.; Fortner, E.; Williams, L. R.; Wilson, K. R.; Surratt, J. D.; Donahue, N. M.; Jayne, J. T.; Worsnop, D. R. Elemental Ratio Measurements of Organic Compounds Using Aerosol Mass Spectrometry: Characterization, Improved Calibration, and Implications. *Atmos. Chem. Phys. Discuss.* **2014**, *14*, 19791-19835.
38. Craven, J. S.; Yee, L. D.; Ng, N. L.; Canagaratna, M. R.; Loza, C. L.; Schilling, K. A.; Yatavelli, R. L. N.; Thornton, J. A.; Ziemann, P. J.; Flagan, R. C.; Seinfeld, J. H. Analysis of Secondary Organic Aerosol Formation and Aging Using Positive Matrix Factorization of High-Resolution Aerosol Mass Spectra: Application to the Dodecane Low-NO_x System. *Atmos. Chem. Phys.* **2012**, *12*, 11795-11817.

39. Cody, R. B. Observation of Molecular Ions and Analysis of Nonpolar Compounds with the Direct Analysis in Real Time Ion Source. *Anal. Chem.* **2009**, *81*, 1101-1107.
40. Cody, R. B.; Laramée, J. A.; Durst, H. D. Versatile New Ion Source for the Analysis of Materials in Open Air under Ambient Conditions. *Anal. Chem.* **2005**, *77*, 2297-2302.
41. Liu, X.; Jeffries, H. E.; Sexton, K. G. Atmospheric Photochemical Degradation of 1,4-Unsaturated Dicarboxyls. *Environ. Sci. Technol.* **1999**, *33*, 4212-4220.
42. Compernelle, S.; Ceulemans, K.; Müller, J. F., Evaporation: A New Vapour Pressure Estimation Method for Organic Molecules Including Non-Additivity and Intramolecular Interactions. *Atmos. Chem. Phys.* **2011**, *11*, 9431-9450.
43. Nilles, J. M.; Connell, T. R.; Durst, H. D. Quantitation of Chemical Warfare Agents Using the Direct Analysis in Real Time (DART) Technique. *Anal. Chem.* **2009**, *81*, 6744-6749.
44. Schilling Fahnestock, K. A.; Yee, L. D.; Loza, C. L.; Coggon, M. M.; Schwantes, R.; Zhang, X.; Dalleska, N. F.; Seinfeld, J. H. Secondary Organic Aerosol Composition from C₁₂ Alkanes. *J. Phys. Chem. A* **2014**, Articles ASAP. <http://dx.doi.org/10.1021/jp501779w>.
45. Virtanen, A.; Joutsensaari, J.; Koop, T.; Kannosto, J.; Yli-Pirilä, P.; Leskinen, J.; Mäkelä, J. M.; Holopainen, J. K.; Pöschl, U.; Kulmala, M.; Worsnop, D. R.; Laaksonen, A. An Amorphous Solid State of Biogenic Secondary Organic Aerosol Particles. *Nature* **2010**, *467*, 824-827.
46. Bones, D. L.; Reid, J. P.; Lienhard, D. M.; Krieger, U. K. Comparing the mechanism of water condensation and evaporation in glassy aerosol. *Proc. Nat. Acad. Sci. USA* **2012**, *109*, 11613-11618.
47. Chhabra, P. S.; Ng, N. L.; Canagaratna, M. R.; Corrigan, A. L.; Russell, L. M.; Worsnop, D. R.; Flagan, R. C.; Seinfeld, J. H. Elemental Composition and Oxidation of Chamber Organic Aerosol. *Atmos. Chem. Phys.* **2011**, *11*, 8827-8845.
48. Ng, N. L.; Canagaratna, M. R.; Jimenez, J. L.; Chhabra, P. S.; Seinfeld, J. H.; Worsnop, D. R. Changes in Organic Aerosol Composition with Aging Inferred from Aerosol Mass Spectra. *Atmos. Chem. Phys.* **2011**, *11*, 6465-6474.
49. Heald, C. L.; Kroll, J. H.; Jimenez, J. L.; Docherty, K. S.; DeCarlo, P. F.; Aiken, A. C.; Chen, Q.; Martin, S. T.; Farmer, D. K.; Artaxo, P. A Simplified Description of the Evolution of Organic Aerosol Composition in the Atmosphere. *Geophys. Res. Lett.* **2010**, *37*, L08803.
50. Hall, W. A.; Johnston, M. V. Oligomer Formation Pathways in Secondary Organic Aerosol from MS and MS/MS Measurements with High Mass Accuracy and Resolving Power. *J. Amer. Soc. Mass Spectrom.* **2012**, *23*, 1097-1108.

Chapter 4

Conclusions and Future Work

4.1 Conclusions

This thesis discusses insights into anthropogenic SOA formation by extensive analysis of SOA chemical composition using complementary mass spectrometry methods. Environmental chamber experiments enable the detailed study of SOA formation from a single parent compound. In this work, the formation of SOA from C₁₂ alkanes, toluene, and *o*-, *m*-, and *p*-cresol was studied by applying a combination of mass spectrometric methods to analyze the SOA chemical composition.

Gasoline and diesel fuel contain significant amounts of cyclic, branched, and linear alkanes.¹ Moreover, the combustion and photooxidation products of alkanes are major contributors to urban and transportation-related SOA.²⁻⁴ The effects of parent alkane structure, NO_x conditions, relative humidity, and aerosol acidity on SOA formation and composition were studied in Chapter 2. The composition of alkane SOA produced in these studies was characterized strongly by particle-phase chemistry, including oligomerization reactions. The monomeric species participating in these reactions are chiefly hydroxycarbonyl compounds in linear and cyclized forms (e.g., furans, dihydrofurans). Imines are another monomeric species forming potentially from reactions of carbonyl compounds with ammonia present in the seed aerosol. The oligomers that are formed from these monomers include peroxyhemiacetals, hemiacetals, esters, and aldol condensation products. Peroxyhemiacetals are the major contributor to alkane SOA mass under the low-NO conditions studied here; under high-NO conditions, ether formation is significant to SOA formation, as is the generation of alkyl nitrates. The NO_x effect on alkane SOA composition, specifically oligomer structure and functionality, is shown to be important in Chapter 2. Alkane structure affected the degree of functionalization and fragmentation of the parent compound as it progressed through multigenerational photooxidation; the final outcome of this was a variation in organic aerosol volume produced. Nitrogen incorporation from the ammonium sulfate seed aerosol into the organic fraction by imine formation occurred for all alkane structures studied in Chapter 2. Overall, the composition of alkane SOA is found to be

attributable to a large number of oxidation products, each of which is present at a relatively low concentration.

Aromatic compounds are a major component of anthropogenic and biogenic emissions; they appear in fuels as well as in biomass burning emissions, among other sources.¹ Toluene is an important industrial VOC and SOA precursor. Its gas-phase photooxidation and the photooxidation of its early-generation product, cresol, have been studied extensively, as discussed in Chapter 3. Open questions center on the extent to which low- and extremely-low volatility organic compounds (LVOC and ELVOC) comprise toluene SOA, and the proportions of the LVOC and ELVOC which arise from oligomerization and multigenerational photooxidation. Given that glyoxal and other volatile dicarbonyls are major fragmentation products in aromatic systems, the role of relative humidity and seed hygroscopicity is important to determining the chemical composition of toluene- and cresol-derived SOA. The experiments described in Chapter 3 were conducted under dry conditions to promote SOA formation from other channels. Highly oxygenated compounds were found to be the major contributors to toluene SOA under dry low- and high-NO conditions. The NO_x effect was primarily seen in the production of nitro and nitrate compounds that partitioned to the particle phase. Heterogeneous chemistry is implied by the chemical formulae of oligomeric species produced by toluene and all cresol isomers; the range of C number in these molecules is continuous, suggesting small, volatile aldehydes are reacting with highly-oxygenated C₇ compounds already present in the particle phase. This is different to oligomer formation in the alkane systems, where dimerization occurred between C₁₂ oxidized species. For toluene- and cresol-derived SOA, the LVOC and ELVOC components arise from both multigenerational oxidation and oligomer formation. Through comparison of SOA chemical compositions, a relative mass fraction of 0.84 of

toluene SOA is estimated to be attributable to the cresol pathway, specifically $C_7H_8O_4$ (0.7) and $C_7H_6O_4$ (0.1) species, with the remainder composed of $C_xH_yO_2$, $C_xH_yNO_2$, $C_xH_yNO_3$, and C_xH_yO .

4.2 Future Work: Exploring Heterogeneous Reactions Leading to Oligomerization in Secondary Organic Aerosol

SOA formation is commonly predicted by equilibrium partitioning models, but there is evidence in certain chemical systems that reactive uptake can be important to SOA formation. Reactive uptake as a phenomenon involves the collision of a gas-phase molecule with a surface, resulting in the incorporation of that molecule into the surface because of a chemical reaction. Some examples of reactive uptake include isoprene epoxydiols, glycolaldehyde, and glyoxal and simple carbonyl compounds.⁵⁻⁸

There is evidence for oligomerization, in some cases, occurring in the manner of reactive uptake as opposed to equilibrium partitioning and condensed-phase reactions.^{5,9} If monomer abundance in the particle phase, leading to oligomerization through equilibrium reactions, was driven by equilibrium partitioning, there would be a correlation between monomer abundance and vapor pressure. In the case of SOA formed from α -pinene ozonolysis, Hall and Johnston used a Fourier transform ion cyclotron resonance mass spectrometer with an electrospray ionization (ESI) interface to identify over 1000 distinct oligomer elemental formulae, and find independence between monomer abundance and vapor pressure.¹⁰ The classes of oligomers included in that study included aldol condensation products, hemiacetals, ethers, esters, and carboxylic acid anhydrides; this system covers all major oligomer types one would find, with, perhaps, the exception of the peroxyhemiacetal, which is known to be important under low-NO conditions in some cases.¹⁰⁻¹¹

Table 4.1. Compounds measured in SOA formed from isoprene nitroxy epoxydiol uptake onto $(\text{NH}_4)_2\text{SO}_4$ seed aerosol by filtration and extraction in methanol for analysis by reverse-phase ultra-high performance liquid chromatography/(-)ESI-MS. Compounds are indexed by retention time (t_R).

t_R (min)	Measured m/z (Da)	Calculated m/z (Da)	Error (mDa)	Formula [M-H] ⁻
2.61	346.007	346.008	1.0	$\text{C}_8\text{H}_{12}\text{NO}_{12}\text{S}^-$
2.61	283.0111	283.0124	1.3	$\text{C}_8\text{H}_{11}\text{O}_9\text{S}^-$
2.68	241.9962	241.9971	0.9	$\text{C}_5\text{H}_8\text{NO}_8\text{S}^-$
2.88	304.9921	304.9927	0.6	$\text{C}_5\text{H}_9\text{N}_2\text{O}_{11}\text{S}^-$
2.95	304.9921	304.9927	0.6	$\text{C}_5\text{H}_9\text{N}_2\text{O}_{11}\text{S}^-$
3.02	304.9916	304.9927	1.1	$\text{C}_5\text{H}_9\text{N}_2\text{O}_{11}\text{S}^-$
3.1	304.9916	304.9927	1.1	$\text{C}_5\text{H}_9\text{N}_2\text{O}_{11}\text{S}^-$
3.15	304.9924	304.9927	0.3	$\text{C}_5\text{H}_9\text{N}_2\text{O}_{11}\text{S}^-$
3.4	302.9757	302.9771	1.4	$\text{C}_5\text{H}_7\text{N}_2\text{O}_{11}\text{S}^-$
3.52	365.9716	365.9727	1.1	$\text{C}_5\text{H}_8\text{N}_3\text{O}_{14}\text{S}^-$
3.61	318.9702	318.972	1.8	$\text{C}_5\text{H}_7\text{N}_2\text{O}_{12}\text{S}^-$
3.61	493.024	493.0248	0.8	$\text{C}_{12}\text{H}_{17}\text{N}_2\text{O}_{17}\text{S}^-$
3.69	390.9918	390.9931	1.3	$\text{C}_8\text{H}_{11}\text{N}_2\text{O}_{14}\text{S}^-$
3.89	327.9962	327.9975	1.3	$\text{C}_8\text{H}_{10}\text{NO}_{11}\text{S}^-$
3.89	390.9919	390.9931	1.2	$\text{C}_8\text{H}_{11}\text{N}_2\text{O}_{14}\text{S}^-$
3.89	448.9969	448.9985	1.6	$\text{C}_{10}\text{H}_{13}\text{N}_2\text{O}_{16}\text{S}^-$
3.97	349.9767	349.9778	1.1	$\text{C}_5\text{H}_8\text{N}_3\text{O}_{13}\text{S}^-$
4.06	349.9763	349.9778	1.5	$\text{C}_5\text{H}_8\text{N}_3\text{O}_{13}\text{S}^-$
4.06	138.9684	138.9701	1.7	$\text{C}_2\text{H}_3\text{O}_5\text{S}^-$
4.14	349.9771	349.9778	0.7	$\text{C}_5\text{H}_8\text{N}_3\text{O}_{13}\text{S}^-$
4.14	138.9686	138.9701	1.5	$\text{C}_2\text{H}_3\text{O}_5\text{S}^-$
4.34	372.9789	372.9825	3.6	$\text{C}_8\text{H}_9\text{N}_2\text{O}_{13}\text{S}^-$

Evidence from recent experiments to study SOA formation from isoprene nitroxy-epoxydiols as well as that presented in Chapter 3 shows that the reaction of small, gas-phase carbonyl compounds and alcohols with particle-phase species to form oligomers is possible (Table 4.1). This is expected, based on what is known about the reactivity of these compound types, but it would be compelling to explore the limits of the SOA mass contribution of this kind of reactive uptake, as well as its sensitivities to relative humidity, seed hygroscopicity, seed composition, and parent compound type.

A fundamental chamber experiment would be to atomize a solution of a functionalized alkane sulfonate and introduce into the gas phase a compound proposed to react with that functional group. This experiment would simply target reactive uptake without accounting for any photochemistry or diverse range of products. An example of this type of experiment would be to use sodium dodecanal

sulfonate as the seed aerosol and to introduce a hydroperoxide, such as cumene hydroperoxide or tert-butyl hydroperoxide, into the chamber by blowing clean air through a tube containing the peroxide. Peroxyhemiacetal formation should occur in the particle phase between the aldehyde functionality on the surfactant seed and the gas-phase peroxide. The vapor pressures of cumene and tert-butyl hydroperoxides (5.5×10^{-6} and 7.4×10^{-3} atm, respectively) are such that they should not condense onto the particles significantly. Control experiments measuring the partitioning of cumene and tert-butyl hydroperoxide to the chamber walls and to an inert seed such as NaCl would also need to be conducted.

A common question in SOA compositional analysis is on the origin of high-volatility compounds detected in offline analysis of SOA. Some have explained the modest concentrations of high-volatility species through equilibrium partitioning: when these are present in high concentration in the gas phase, they are driven into the particle phase, and as oxidation proceeds in the gas phase and these species are consumed, they partition back into the gas phase and are reacted away. A small amount remains in the particle, perhaps due to the presumed glassy nature of SOA.¹² Another scenario is that these high-volatility species are present in the particle-phase as oligomers, but revert back to their monomeric state during sample preparation for analysis. Given the invasiveness of solvent extraction, it is not implausible that oligomers were reverted back to monomeric species, but there is no means at present to verify this scenario in the suspended aerosol. A potential means of tagging the surface-available reactive organic compounds is to conduct a photooxidation experiment on a well-known system (e.g. dodecane or toluene), stop the photooxidation by turning off the black lights initiating OH generation, and introduce a unique marker compound that is not known to occur naturally in the system at a ppb-level mixing ratio. A volatile, halogen-labeled aldehyde (e.g. trifluoromethyl butyraldehyde) would be a potential tag for hemiacetal and peroxyhemiacetal formation, as well as

aldol condensation. The tag molecule concentration would be monitored by either GC or gas-phase chemical ionization mass spectrometry, and any change in particle composition and volume would be measured by online aerosol mass spectrometry and differential mobility analyzer. SOA samples would also be collected by filtration and analyzed using noninvasive, soft ionization methods like direct electrospray ionization (DESI) or DART coupled to a high-resolution mass spectrometer, as well as by complementary techniques that provide structural information (e.g. GC/MS or LC/MS).

References

1. Ensberg, J. J.; Hayes, P. L.; Jimenez, J. L.; Gilman, J. B.; Kuster, W. C.; de Gouw, J. A.; Holloway, J. S.; Seinfeld, J. H. Emission Factor Ratios, SOA Mass Yields, and the Impact of Vehicular Emissions on SOA Formation. *Atmos. Chem. Phys.* **2013**, *14*, 2383-2397.
2. Bahreini, R.; Middlebrook, A. M.; de Gouw, J. A.; Warneke, C.; Trainer, M.; Brock, C. A.; Stark, H.; Brown, S. S.; Dube, W. P.; Gilman, J. B.; et al. Gasoline Emissions Dominate over Diesel in Formation of Secondary Organic Aerosol Mass. *Geophys. Res. Lett.* **2012**, *39*, L06805.
3. Gentner, D. R.; Isaacman, G.; Worton, D. R.; Chan, A. W. H.; Dallmann, T. R.; Davis, L.; Liu, S.; Day, D. A.; Russell, L. M.; Wilson, K. R.; et al. Elucidating Secondary Organic Aerosol from Diesel and Gasoline Vehicles through Detailed Characterization of Organic Carbon Emissions. *Proc. Nat. Acad. Sci. USA* **2012**, *109*, 18318-18323.
4. Zhang, H.; Ruehl, C. R.; Chan, A. W. H.; Nah, T.; Worton, D. R.; Isaacman, G.; Goldstein, A. H.; Wilson, K. R. OH-Initiated Heterogeneous Oxidation of Cholestane: A Model System for Understanding the Photochemical Aging of Cyclic Alkane Aerosols. *J. Phys. Chem. A* **2013**, *117*, 12449-12458.
5. Lin, Y.-H.; Budisulistiorini, S. H.; Chu, K.; Siejack, R. A.; Zhang, H.; Riva, M.; Zhang, Z.; Gold, A.; Kautzman, K. E.; Surratt, J. D. Light-Absorbing Oligomer Formation in Secondary Organic Aerosol from Reactive Uptake of Isoprene Epoxydiols. *Environ. Sci. Technol.* **2014**, *48*, 12012-12021.
6. Kroll, J. H.; Ng, N. L.; Murphy, S. M.; Varutbangkul, V.; Flagan, R. C.; Seinfeld, J. H. Chamber Studies of Secondary Organic Aerosol Growth by Reactive Uptake of Simple Carbonyl Compounds. *J. Geophys. Res.* **2005**, *110*, D23207.
7. Liggio, J.; Li, S.-M.; McLaren, R. Reactive Uptake of Glyoxal by Particulate Matter. *J. Geophys. Res.* **2005**, *110*, D10304.
8. Nguyen, T. B.; Coggon, M. M.; Flagan, R. C.; Seinfeld, J. H. Reactive Uptake and Photo-Fenton Oxidation of Glycolaldehyde in Aerosol Liquid Water. *Environ. Sci. Technol.* **2013**, *47*, 4307-4316.
9. Hall, W.A.; Johnston, M. V. Oligomer Formation Pathways in Secondary Organic Aerosol from MS and MS/MS Measurements with High Mass Accuracy and Resolving Power. *J. Amer. Soc. Mass Spectrom.* **2012**, *23*, 1097-1108.
10. Yee, L. D.; Craven, J. S.; Loza, C. L.; Schilling, K. A.; Ng, N. L.; Canagaratna, M. R.; Ziemann, P. J.; Flagan, R. C.; Seinfeld, J. H. Secondary Organic Aerosol Formation from Low-Noxphotooxidation of Dodecane: Evolution of Multigeneration Gas-Phase Chemistry and Aerosol Composition. *J. Phys. Chem. A* **2012**, *116*, 6211-6230.

11. Ziemann, P. J. Formation of Alkoxyhydroperoxy Aldehydes and Cyclic Peroxyhemiacetals from Reactions of Cyclic Alkenes with Ozone in the Presence of Alcohols. *J. Phys. Chem. A* **2003**, *107*, 2048-2060.
12. Virtanen, A.; Joutsensaari, J.; Koop, T.; Kannosto, J.; Yli-Pirilä, P.; Leskinen, J.; Mäkelä, J. M.; Holopainen, J. K.; Pöschl, U.; Kulmala, M.; et al. An Amorphous Solid State of Biogenic Secondary Organic Aerosol Particles. *Nature* **2010**, *467*, 824-827.

Appendices

Appendix A

Molecular Corridors and Kinetic Regimes in the Multiphase Chemical Evolution of Secondary Organic Aerosol³

³ Reproduced by permission from “Molecular corridors and kinetic regimes in the multiphase chemical evolution of secondary organic aerosol” by M. Shiraiwa, T. Berkemeier, K. A. Schilling-Fahnestock, J. H. Seinfeld, and U. Poschl. *Atmos. Chem. Phys.* **2014**, *14*, 8323-8341.



Molecular corridors and kinetic regimes in the multiphase chemical evolution of secondary organic aerosol

M. Shiraiwa¹, T. Berkemeier¹, K. A. Schilling-Fahnestock², J. H. Seinfeld², and U. Pöschl¹

¹Multiphase Chemistry Department, Max Planck Institute for Chemistry, 55128 Mainz, Germany

²Division of Chemistry and Chemical Engineering, California Institute of Technology, Pasadena, CA 91125, USA

Correspondence to: M. Shiraiwa (m.shiraiwa@mpic.de)

Received: 21 February 2014 – Published in Atmos. Chem. Phys. Discuss.: 6 March 2014

Revised: 15 July 2014 – Accepted: 16 July 2014 – Published: 20 August 2014

Abstract. The dominant component of atmospheric, organic aerosol is that derived from the oxidation of volatile organic compounds (VOCs), so-called secondary organic aerosol (SOA). SOA consists of a multitude of organic compounds, only a small fraction of which has historically been identified. Formation and evolution of SOA is a complex process involving coupled chemical reaction and mass transport in the gas and particle phases. Current SOA models do not embody the full spectrum of reaction and transport processes, nor do they identify the dominant rate-limiting steps in SOA formation. Based on molecular identification of SOA oxidation products, we show here that the chemical evolution of SOA from a variety of VOC precursors adheres to characteristic “molecular corridors” with a tight inverse correlation between volatility and molar mass. The slope of these corridors corresponds to the increase in molar mass required to decrease volatility by one order of magnitude ($-dM/d\log C_0$). It varies in the range of 10–30 g mol⁻¹, depending on the molecular size of the SOA precursor and the O : C ratio of the reaction products. Sequential and parallel reaction pathways of oxidation and dimerization or oligomerization progressing along these corridors pass through characteristic regimes of reaction-, diffusion-, or accommodation-limited multiphase chemical kinetics that can be classified according to reaction location, degree of saturation, and extent of heterogeneity of gas and particle phases. The molecular corridors and kinetic regimes help to constrain and describe the properties of the products, pathways, and rates of SOA evolution, thereby facilitating the further development of aerosol models for air quality and climate.

1 Introduction

Organic aerosol is ubiquitous in the atmosphere and its major component is secondary organic aerosol (SOA) (Jimenez et al., 2009). Reaction of atmospheric volatile organic compounds (VOCs) with oxidants such as OH, O₃, and NO₃ initiate the formation of semi-volatile organic compounds (SVOCs), which can undergo further gas-phase oxidation to form low-volatility organic compounds (LVOCs) that will preferentially partition into the particle phase (Kroll and Seinfeld, 2008; Hallquist et al., 2009; Donahue et al., 2012; Murphy et al., 2014). A fraction of the SVOCs partitions into the particle phase, wherein they can be transformed into LVOCs such as dimers, oligomers, and other high molecular mass compounds (Jang et al., 2002; Kalberer et al., 2006; Ervens et al., 2011; Ziemann and Atkinson, 2012; Shiraiwa et al., 2013a). Some portion of the LVOCs can be transformed back to (semi-)volatile compounds or CO / CO₂ by fragmentation reactions triggered by OH or other oxidants at the particle surface or in the particle bulk (Bertram et al., 2001; Kroll and Seinfeld, 2008; Jimenez et al., 2009). SOA partitioning is also affected by particle-phase state, non-ideal thermodynamic mixing, and morphology (Chang and Pankow, 2006; Zuend and Seinfeld, 2012; Shiraiwa et al., 2013b).

SOA consists of a myriad of organic compounds, of which only 10–30 % have been identified (Goldstein and Galbally, 2007). Common techniques applied for the analysis of SOA are gas chromatography/electron impact ionization mass spectrometry (GC/EI-MS) and liquid chromatography/electrospray ionization mass spectrometry (LC/ESI-MS) (e.g., Surratt et al., 2006). Hard ionization, such as electron impact ionization, generally causes significant fragmentation

of organic molecules, which makes molecular identification challenging, but can provide molecular structural information. The recent advent of soft ionization methods such as electrospray ionization (ESI), matrix-assisted laser desorption ionization (MALDI), atmospheric pressure chemical ionization (APCI), and direct analysis in real time (DART) ionization has facilitated the identification of the dominant fraction of the compounds constituting SOA by preserving analytes as intact or nearly intact during ionization (Kalberer et al., 2006; Williams et al., 2010; Laskin et al., 2012a, b; Chan et al., 2013; Nguyen et al., 2013; Vogel et al., 2013; Schilling-Fahnestock et al., 2014). Taking advantage of such data, here we present a new, 2-D map for SOA evolution of molar mass vs. volatility, which can be linked to kinetic regimes and reaction pathways of formation and aging of SOA that is currently poorly constrained and a major limitation in the understanding and prediction of atmospheric aerosol effects.

2 Molecular corridors for different SOA precursors

Figure 1 shows 2-D maps of molecular weight or molar mass (M) plotted against volatility or saturation mass concentration (C_0) for organic compounds in SOA from a range of anthropogenic and biogenic precursors: dodecane (Fig. 1a, b) (Yee et al., 2012), cyclododecane (Fig. 1c, d), hexylcyclohexane (Fig. 1e, f) (Schilling-Fahnestock et al., 2014), α -pinene (Fig. 1g) (Docherty et al., 2005; Claeys et al., 2007, 2009; Zuend and Seinfeld, 2012; Kahnt et al., 2014; Kristensen et al., 2014), limonene (Fig. 1h) (Jaoui et al., 2006; Kundu et al., 2012), isoprene (Fig. 1i) (Surratt et al., 2006; Surratt et al., 2010; Lin et al., 2012, 2013), glyoxal and methylglyoxal (Fig. 1j) (Lim et al., 2010; Sareen et al., 2010; Zhao et al., 2012). Experimental conditions including oxidants, NO levels, and seed particles used in earlier studies are summarized in Table A1. The experimental conditions and methods applied in this study to analyze the formation and composition of SOA from C_{12} alkanes under low and high NO conditions are detailed in Appendix A and Schilling-Fahnestock et al. (2014). DART is a soft ionization technique of atmospheric pressure ionization that has recently been used for the analysis of a variety of organic compounds with minimal fragmentation (Chan et al., 2013). SOA compounds identified include alcohols, ketones, aldehydes, hydroxycarbonyls, organic hydroperoxides, and nitrates, which are generated in the gas phase (open markers), as well as dihydrofuran, furan, ether, ester, peroxyhemiacetal, hemiacetal, dimer, and imine, which are likely particle-phase products (Ziemann and Atkinson, 2012) (solid markers). Through the combination of an aerosol mass spectrometer (AMS) and DART-MS, close to 100 % identification and quantification of the particle phase for each of the three alkane systems was achieved (Schilling-Fahnestock et al., 2014). Thus, alkane SOA are plotted for low and high NO conditions in separate panels due to large

number of identified products, whereas biogenic SOA data are shown in one panel due to the relatively small number of data points.

Vapor pressures and saturation mass concentrations of organic compounds were estimated using the “estimation of vapor pressure of organics, accounting for temperature, intramolecular, and non-additivity effects” (EVAPORATION) model, (Compernelle et al., 2011). The EVAPORATION model estimates vapor pressure of molecules with the following functionalities: aldehyde, ketone, alcohol, ether, ester, nitrate, acid, peroxide, hydroperoxide, peroxy acyl nitrate, and peracid. Organosulfates and imidazoles are not covered and were thus not included in our analysis, although they have been identified in SOA from biogenic precursors and glyoxal (Iinuma et al., 2007; Surratt et al., 2008; Ervens et al., 2011).

The markers in Fig. 1 are color-coded with atomic O : C ratio. Generally, volatility decreases and molar mass increases with chemical aging of SOA both in the gas and particle phases. Consequently, molar mass of oxidation products tightly correlates with volatility with high coefficient of determination (R^2), as summarized in Table 1. The 95 % prediction intervals (dashed lines in Fig. 1) can be regarded as molecular corridors, within which additional unidentified oxidation products are likely to fall. The negative slope of the fit lines corresponds to the increase in molar mass required to decrease volatility by one order of magnitude, $-dM / d\log C_0$. It increases from $\sim 10 \text{ g mol}^{-1}$ for glyoxal, and methylglyoxal to $\sim 25 \text{ g mol}^{-1}$ for dodecane and cyclododecane, depending on the molecular size of the SOA precursor and the O : C ratio of the reaction products, as will be discussed below. The mean value of $-dM / d\log C_0$ average over all investigated systems is $20 \pm 4 \text{ g mol}^{-1}$.

The composition of SOA may vary depending not only on the organic precursor, but also on the oxidant and other reaction conditions of formation and aging (Presto et al., 2005; Surratt et al., 2006; Lin et al., 2012, 2013; Kristensen et al., 2014; Loza et al., 2014; Xu et al., 2014). The atomic O : C ratio tends to be higher at high NO concentrations, partly due to the formation of organonitrates (Nguyen et al., 2011; Schilling-Fahnestock et al., 2014). Even though Fig. 1g, h, and i contain biogenic SOA oxidation products measured under different conditions, as specified in Table A1, the molecular corridors are relatively tight with $R^2 > 0.85$. The molecular corridors of alkane SOA formed under low and high NO conditions are also quite similar (Fig. 1a–f). Thus, the molecular corridors of SOA formation appear to be determined primarily by the organic precursor, and the extent to which they are influenced by reaction conditions warrants further studies.

3 Kinetic regimes and limiting cases

Traditionally, SOA formation has been modeled based on instantaneous gas-particle equilibrium partitioning, implicitly

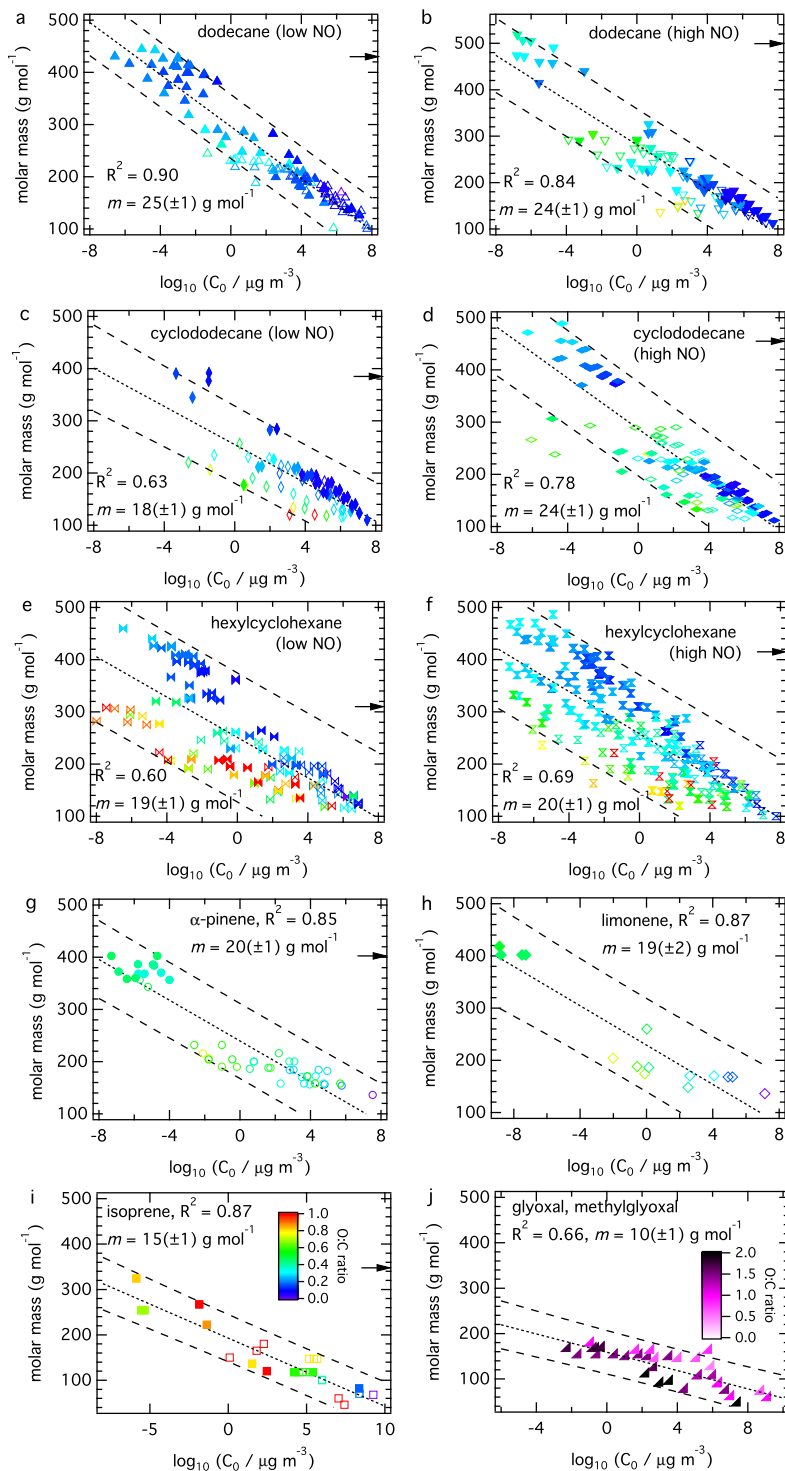


Figure 1. Molecular corridors of SOA evolution for different precursor compounds. Molar mass vs. volatility (saturation mass concentration, C_0) at 298 K for oxidation products of dodecane at (a) low and (b) high NO condition, cyclododecane at (c) low and (d) high NO condition, and hexylcyclohexane at (e) low and (f) high NO condition and (g) α -pinene, (h) limonene, (i) isoprene, and (j) glyoxal and methylglyoxal. The open and solid markers correspond to the gas- and particle-phase products, respectively, color-coded by atomic O : C ratio (note different color scale for j). With a linear regression analysis, the coefficient of determination (R^2), fitted lines (dotted lines) and their slopes (m), and prediction intervals with 95 % confidence (dashed lines) are shown. The arrows on the right axis indicate average molar mass for isoprene and α -pinene (Kalberer et al., 2006), as well as for alkanes, as measured in this study.

Table 1. Summary of analysis of identified SOA oxidation products. Number of identified oxidation products N , average molar mass M_{ave} , negative slope ($-dM/d\log C_0$) of fitted lines in Fig. 2 of molar mass vs. logarithm of volatility, coefficients of determination R^2 , as well as R^2 for O : C vs. logarithm of volatility.

Precursor	N	M_{ave} (g mol $^{-1}$)	$-dM/d\log C_0$ (g mol $^{-1}$)	R^2 (molar mass)	R^2 (O : C)
Dodecane, low NO	116	429	25(\pm 1)	0.90	0.22
Dodecane, high NO	106	495	24(\pm 1)	0.84	0.29
Cyclododecane, low NO	77	384	18(\pm 1)	0.63	0.08
Cyclododecane, high NO	122	458	24(\pm 1)	0.78	0.08
Hexylcyclohexane, low NO	137	310	19(\pm 1)	0.60	0.05
Hexylcyclohexane, high NO	230	418	20(\pm 1)	0.69	0.00
α -pinene	47	400*	20(\pm 1)	0.85	0.13
Limonene	17	–	19(\pm 2)	0.87	0.38
Isoprene	29	350*	15(\pm 1)	0.87	0.09
Glyoxal, methylglyoxal	35	–	10(\pm 1)	0.66	0.16

* Kalberer et al. (2006).

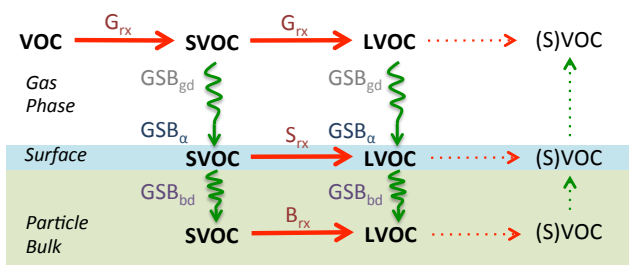


Figure 2. Molecular processes of SOA evolution: schematic outline of formation and aging. Red and green arrows denote chemical reactions and mass transport, respectively. Sequential and parallel reactions in the gas phase, at the particle surface, and in the particle bulk lead to multiple generations of volatile, semi-volatile and low-volatile organic compounds (VOC, SVOC, LVOC). Dotted arrows denote revolatilization resulting from fragmentation reactions. Labels on arrows relate to kinetic regimes outlined in subsequent figure.

assuming that gas-phase reactions are the rate-limiting step of SOA formation and growth (Pankow, 1994; Donahue et al., 2006; Hallquist et al., 2009). Recent studies, however, have shown that mass transport and chemical reaction in the particle phase may also play an important role (Fig. 2) (Ervens et al., 2011; Ziemann and Atkinson, 2012; Shiraiwa et al., 2013a). Recently, Berkemeier et al. (2013) provided a conceptual framework which enables the characterization of heterogeneous reactions and gas uptake in atmospheric aerosols and clouds through a well-defined set of distinct kinetic regimes and limiting cases. We extended this framework to cover the complex interplay of gas- and particle-phase reactions in the evolution of SOA and to enable a systematic classification of rate-limiting processes in the analysis and interpretation of laboratory chamber data and ambient measurements, as well as in the comparison of experimental results with theoretical predictions.

Different types of kinetic behavior can be characterized by three basic criteria as detailed in the Appendix B: (1) the location of the chemical reaction leading to SOA formation or aging (gas phase, particle surface, particle bulk); (2) the saturation ratio of the reactants (ratio of ambient concentration to saturation concentration); and (3) the extent of spatial heterogeneity of the gas and particle phases (concentration gradients). The kinetic regimes and limiting cases defined by these criteria can be visualized on a “kinetic cuboid”, in which each axis corresponds to one of the three classification parameters, as shown in Fig. 3a. The symbols “G”, “S”, and “B” indicate the predominant reaction location: gas phase, particle surface, or particle bulk, respectively. A subscript denotes the rate-limiting process for SOA formation and aging: “rx” indicates chemical reaction; “bd” indicates bulk diffusion; “ α ” indicates mass accommodation; “gd” indicates gas-phase diffusion. Depending on atmospheric composition and reaction conditions, which vary widely in space and time, the chemical evolution of organic compounds and SOA particles can progress through any of these regimes.

The left part of the cuboid can be regarded as a particle-phase chemistry regime, and the right side as a gas-phase chemistry regime. As shown in Fig. 3b, the particle-phase chemistry regime (SB, including surface (S) or bulk (B) reaction) can be further subdivided into a reaction-diffusion regime (SBrd), where the system is limited by reaction or diffusion in the particle-phase, and a mass-transfer regime (SB^{mt}) limited by mass accommodation at the interface or diffusion through the gas phase (Berkemeier et al., 2013). The gas-phase chemistry regime (G) comprises the traditional scenario of SOA formation determined by a rate-limiting chemical reaction in the gas phase, followed by quasi-instantaneous gas-particle partitioning of the reaction products (G_{rx}), corresponding to so-called quasi-equilibrium growth (Shiraiwa and Seinfeld, 2012; Zhang et al., 2012). The rest of the gas-phase chemistry regime is mass-transport-limited and corresponds to so-called non-equilibrium growth

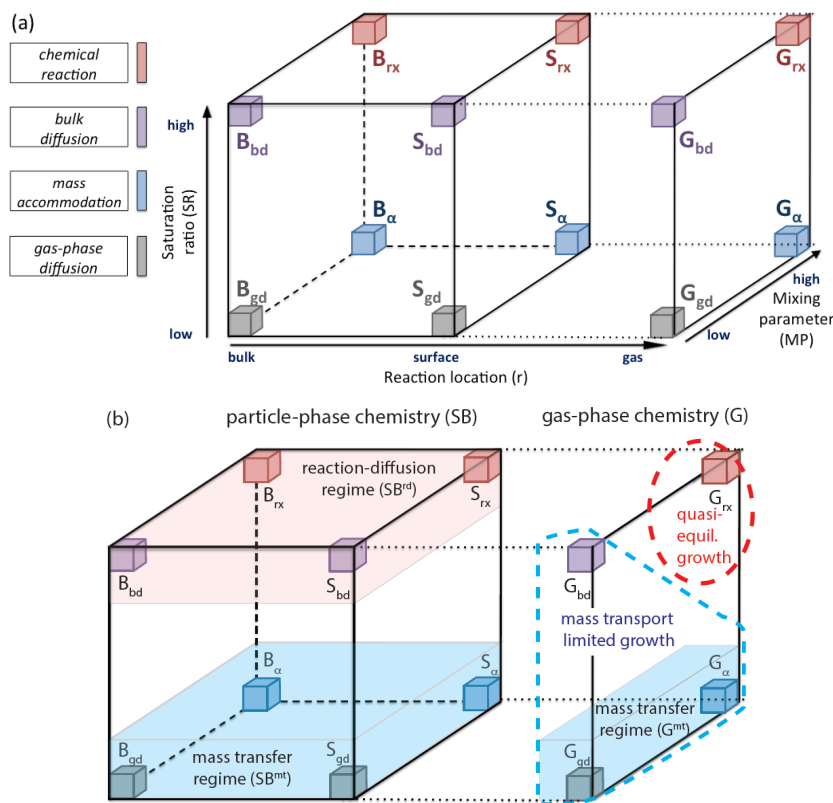


Figure 3. Kinetic regimes and limiting cases of SOA evolution mapped onto the axes of a cuboid representing reaction location, saturation ratio, and mixing parameter. **(a)** Horizontal edges of the cuboid (left to right) correspond to four regimes governed by chemical reaction (“rx”, red), bulk diffusion (“bd”, purple), mass accommodation (“ α ”, blue), or gas-phase diffusion (“gd”, grey). Each of these regimes includes three distinct limiting cases characterized by a single rate-limiting process and a dominant reaction location (particle bulk, B; surface, S; gas phase, G). **(b)** The left side of the cuboid can be regarded as a particle-phase chemistry regime (SB) and subdivided into a reaction-diffusion regime (SB^{rd}) and a mass transfer regime (SB^{mt}). The right side of the cuboid can be regarded as a gas-phase chemistry regime (G) and subdivided into a traditional scenario of “quasi-equilibrium growth”, limited only by a gas phase reaction, followed by quasi-instantaneous gas-particle partitioning (G_{rx}) and a mass-transport limited regime of “non-equilibrium growth” that may be kinetically limited by gas-to-particle mass transfer (G^{mt}) or diffusion in the particle (G_{bd}).

(Perraud et al., 2012; Zaveri et al., 2014), which can be kinetically limited by gas-to-particle mass transfer (gas-phase diffusion and accommodation at the interface; G^{mt}) or retarded diffusion in the particle phase (G_{bd}).

4 Characteristic pathways and properties

Figure 4a shows the ensemble of molecular corridors from Fig. 1 with a total of 909 identified oxidation products from seven different SOA precursors. They are constrained by two boundary lines corresponding to the volatility of n -alkanes C_nH_{2n+2} and sugar alcohols $C_nH_{2n+2}O_n$. These lines illustrate the regular dependence of volatility on the molar mass of organic compounds; the different slopes of 30 g mol^{-1} for C_nH_{2n+2} and 12 g mol^{-1} for $C_nH_{2n+2}O_n$ reflect that the decrease of volatility with increasing molar mass is stronger for polar compounds (see Fig. D2 for alternative representation).

Many early generation gas-phase oxidation products of alkanes, as well as dimers or oligomers with low O:C ratio (LOC), fall into a molecular corridor close to the C_nH_{2n+2} line, which we designate as LOC corridor ($-dM/d\log C_0 \geq \sim 25 \text{ g mol}^{-1}$, blue shaded area). Aqueous-phase reaction and autoxidation products with high O:C ratio (HOC), on the other hand, tend to fall into a corridor near the $C_nH_{2n+2}O_n$ line, which we designate as HOC corridor ($-dM/d\log C_0$ of $\leq \sim 15 \text{ g mol}^{-1}$, red shaded area). The area in between is characterized by intermediate O:C ratios and accordingly designated as IOC corridor ($-dM/d\log C_0 \approx \sim 20 \text{ g mol}^{-1}$). Among the SOA systems investigated in this study, the small precursor VOCs glyoxal, methylglyoxal, and isoprene (C_2 – C_5) evolve through the HOC corridor, and the terpenes α -pinene and limonene (C_{10}) through the IOC corridor. The alkanes dodecane and cyclododecane (C_{12}) evolve through the LOC corridor, while hexylcyclohexane exhibits a branching between the LOC and

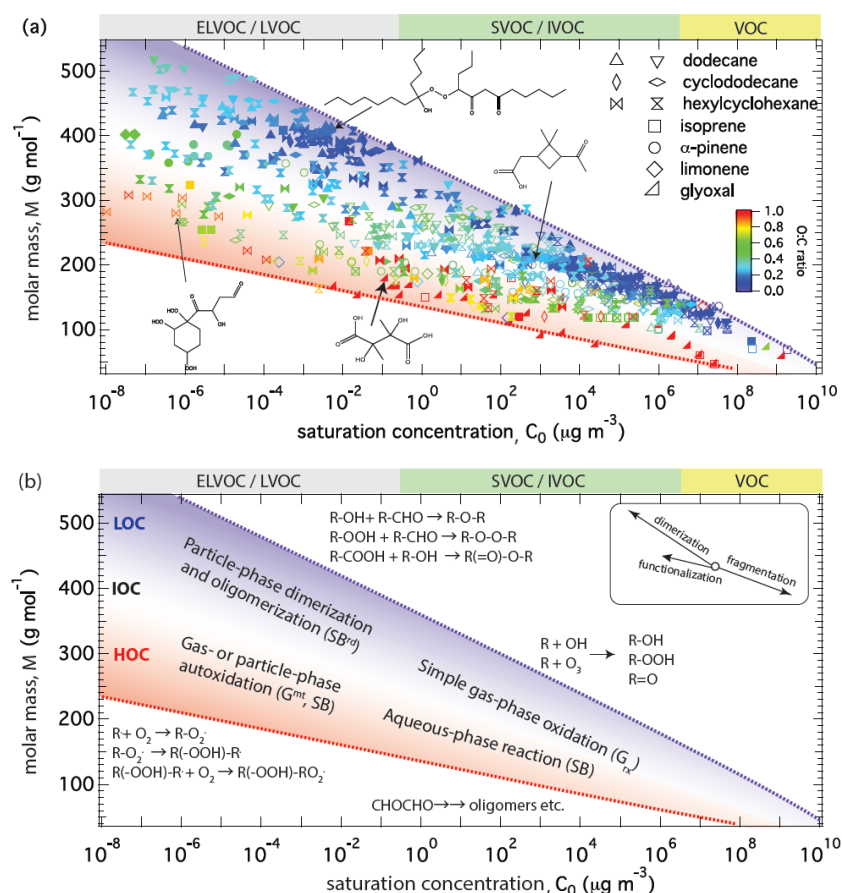


Figure 4. Ensemble of molecular corridors and kinetic regimes of SOA evolution. **(a)** Molar mass vs. volatility (C_0) at 298 K for gas-phase (open) and particle-phase (solid) oxidation products of anthropogenic precursors (dodecane, cyclododecane, hexylcyclohexane) under low/high NO conditions, biogenic precursors (α -pinene, limonene, isoprene) and aqueous-phase reaction products of glyoxal and methylglyoxal. The dotted lines represent linear alkanes C_nH_{2n+2} (purple with O : C = 0) and sugar alcohols $C_nH_{2n+2}O_n$ (red with O : C = 1). Chemical structures of some representative products are shown. **(b)** Characteristic reaction pathways with most probable kinetic regimes. Molecular corridors consists of high, intermediate and low O : C corridors (HOC, red shaded area; IOC, white area; LOC, blue shaded area). SOA products evolve over the molecular corridor driven by three key reaction types of functionalization, oligomerization, and fragmentation, as illustrated in the insert (note different lengths of arrows indicating different intensities of effects on volatility).

HOC corridors, suggesting the involvement of different reaction pathways. For unidentified SOA products, the molecular corridor ensemble in Fig. 4a and alternative representations (Fig. D2a) may also be used as a look-up plot to obtain a rough estimate of volatility by comparison of molar mass and O : C ratio (e.g., from soft-ionization high-resolution mass spectrometry) to the data in the plot.

Characteristic reaction pathways and relevant kinetic regimes are outlined in Fig. 4b. SOA precursor VOCs with high volatility and low molar mass are located in the lower right corner of the molecular corridor ensemble. As illustrated in the insert in Fig. 4b, single-step functionalization usually leads to a small increase in molar mass, corresponding to one order of decrease in volatility (Donahue et al., 2006), while dimerization and oligomerization tend to multiply molar mass, and thus decrease volatility by multiple orders of magnitude (Trump and Donahue, 2014) (e.g., three

to four orders of magnitude for alkane and terpene SOA, see Fig. 1). Fragmentation, on the other hand, can lead to a substantial decrease of molar mass and increase in volatility (Bertram et al., 2001; Yee et al., 2012; Schilling-Fahnestock et al., 2014). As a result, simple gas-phase oxidation products are confined to the lower right area in the 2-D space. Such oxidation products ($C_0 > 10 \mu\text{g m}^{-3}$) tend to fall into the gas-phase reaction limiting case G_{rx} (quasi-equilibrium growth), as their gas-particle equilibration timescale is on the order of seconds to minutes (Shiraiwa and Seinfeld, 2012) (see Appendices C and D).

Particle-phase dimerization and oligomerization involving two or more molecules usually leads to the formation of compounds with low volatility and high molar mass lying in the upper left area in the 2-D space. The formation of such particle-phase products is likely limited by reaction or diffusion in the particle bulk (SBrd), as rate coefficients for dimer

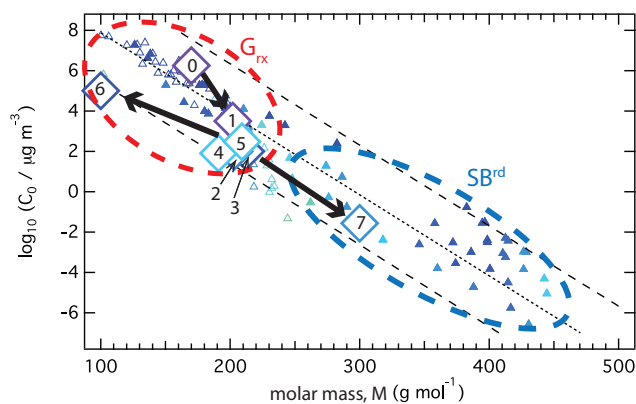


Figure 5. Evolution of reaction pathways over the molecular corridor of dodecane SOA under low NO condition. The large diamonds indicate the surrogate compounds used in the kinetic multi-layer model for gas-particle interactions (KM-GAP) simulations (Appendix D; Shiraiwa et al., 2013a), including the precursor (dodecane, 0), 1st–5th generations of surrogate products of gas-phase oxidation (1–5), gas-phase fragmentation (aldehydes, 6), and particle-phase dimerization products (7). The smaller symbols indicate identified individual products (as shown in Fig. 1a).

formation are relatively low ($< 10 \text{ M}^{-1} \text{ s}^{-1}$) (Ziemann and Atkinson, 2012) and large molecules tend to diffuse slowly (Pfrang et al., 2011; Shiraiwa et al., 2011; Abramson et al., 2013; Zhou et al., 2013). An example of reaction pathways leading to dimerization is shown in Fig. 5 for dodecane SOA (Appendix D, Shiraiwa et al., 2013a). Within the molecular corridor of dodecane SOA evolution, Fig. 5 illustrates a specific trajectory from the precursor (dodecane, 0) through multiple generations of surrogate products of gas-phase oxidation and functionalization (multifunctional alcohols, ketones, and peroxides, 1–5), gas-phase fragmentation (aldehydes, 6), and particle-phase dimerization between aldehydes and peroxides to peroxyhemiacetals (7). Numerical model results shown in Figs. 5 and D1 indicate that the trajectory of chemical evolution passes through different kinetic regimes, i.e., from limitation by gas-phase reaction (G_{rx}) to particle-phase reaction and diffusion (SB^{rd}). Note that particle-phase reactions may also be limited by gas-to-particle mass transfer (e.g., accommodation, supply of reactive gases into the particle), when they are sufficiently fast, i.e., catalyzed by acids (Jang et al., 2002; Iinuma et al., 2004; Offenberg et al., 2009; Surratt et al., 2010).

Aqueous-phase processing of glyoxal and methylglyoxal is an efficient pathway for formation of low volatility and semi-volatile HOC compounds (Liggio et al., 2005; Carlton et al., 2007; Lim et al., 2010; Ervens et al., 2011; Zhao et al., 2012). Uptake of glyoxal into the particle phase leads to hydration and acid catalysis to form hemiacetals, aldols, imines, anhydrides, esters, and organosulfates (Lim et al., 2010). Reactive uptake of isoprene epoxydiols (IEPOX) and subsequent formation of oligomers (Surratt et al., 2010; Lin

et al., 2012, 2013) also progresses over the HOC corridor. Whether multiphase chemistry of glyoxal and IEPOX is limited by mass transfer or chemical reactions may depend on various factors including reaction rate coefficients, relative humidity, particle pH, and Henry's law constant (Ervens and Volkamer, 2010; McNeill et al., 2012; Kampf et al., 2013).

Recently, highly oxidized, extremely low volatility organic compounds (ELVOC) have been detected in field and chamber experiments (Ehn et al., 2012; Schobesberger et al., 2013; Ehn et al., 2014). Such compounds may populate the upper left corner of the HOC corridor. It has been shown that such compounds can be formed via autoxidation (inter- and intramolecular hydrogen abstraction by peroxy radicals) in the gas and particle phases (Crouse et al., 2013). When they are formed in the gas phase, the equilibration timescale of partitioning is long due to their low volatility, and the SOA growth is limited most likely by mass transfer (gas-phase diffusion and accommodation; G^{mt}) (see Appendix C and Fig. C1) (Pierce et al., 2011; Riipinen et al., 2011; Shiraiwa and Seinfeld, 2012). Note that kinetic limitation by retarded bulk diffusion (G_{bd}) is also possible for semi-volatile and low-volatility products when organic particles adopt amorphous, solid state (Virtanen et al., 2010; Cappa and Wilson, 2011; Shiraiwa et al., 2011; Vaden et al., 2011; Kuwata and Martin, 2012; Perraud et al., 2012; Shiraiwa and Seinfeld, 2012; Renbaum-Wolff et al., 2013; Zaveri et al., 2014). Indeed, recent observation found that some SVOCs do not necessarily adhere to equilibrium partitioning (Vogel et al., 2013).

Formation of high molecular weight SOA compounds from oligomerization or autoxidation results in high average molar mass for the biogenic systems of isoprene and α -pinene (Kalberer et al., 2006), as well as the anthropogenic C_{12} alkanes (Fig. 1 and Table 1; Schilling-Fahnestock et al., 2014). Figure 4a shows that most identified oxidation products with molar masses higher than 300 g mol^{-1} are particle-phase products (solid markers). Thus, the relatively high average molar mass observed for laboratory-generated SOA points to the importance of particle-phase chemistry in these systems. Some SOA compounds with higher molar mass are gas-phase oxidation products including ELVOC and ester dimers observed in α -pinene oxidation (Ehn et al., 2014; Kristensen et al., 2014), and there are also some particle-phase products with relatively low molar mass, including furans and dihydrofurans in dodecane and cyclododecane SOA (Yee et al., 2012; Loza et al., 2014), as well as glyoxal and IEPOX products in isoprene SOA (Lim et al., 2010; Surratt et al., 2010). Nevertheless, the clustering of identified reaction products in molecular corridors may facilitate estimation of the relative importance of gas- vs. particle-phase routes to SOA formation (Fig. 1).

Molar mass and O:C ratio also correlate with the glass transition temperature of organic compounds, which tends to rise with increasing molar mass and O:C ratio (Koop et al., 2011). As elevated glass transition temperatures are indicative of semi-solid or amorphous, solid states, SOA evolution

represented in molecular corridors allows one to infer the regime in which particles are likely to become highly viscous. For example, recent experiments have shown an order of magnitude increase in the viscosity of oleic acid particles upon reaction with ozone owing to formation of oligomers (Hosny et al., 2013), and model calculations indicate that this may lead to the formation of surface crusts (Pfrang et al., 2011).

In summary, presenting identified SOA products in a molecular corridor encapsulates fundamental aspects of SOA formation and aging: volatility, molar mass, O : C ratio, and phase state. Such a representation can be used to constrain and/or predict the properties of unidentified SOA oxidation products. The kinetic regimes, within which SOA evolution is occurring along the molecular corridor, facilitate the specification of the rate of progression to higher generation products. Thus, molecular corridors may serve as a basis for compact representation of SOA formation and aging in regional and global models of climate and air quality.

Appendix A: Product analysis of alkane SOA

Photo-oxidation and subsequent SOA formation of *n*-dodecane, cyclododecane, and hexylcyclohexane was conducted in the 28 m³ Teflon reactors in the Caltech environmental chamber (Yee et al., 2012; Loza et al., 2014; Schilling-Fahnestock et al., 2014). Aqueous H₂O₂ solution was evaporated into the chamber as the OH source, followed by the atomization of an aqueous ammonium sulfate solution generating seed particles, which were subsequently dried. Experiments were conducted under low NO conditions, in which alkyl peroxy radicals (RO₂) react primarily with HO₂, and under high NO conditions, in which RO₂ react primarily with NO (Loza et al., 2014).

SOA particles were collected on Teflon filters (Pall Life Sciences, 47 mm, 1.0 μm pore size). Off-line analysis of collected particles was conducted by solvent extraction and gas chromatography time-of-flight mass spectrometry (GC-TOF-MS, GCT Premier, Waters) and GC/ion trap mass spectrometry (Varian Saturn 2000, Agilent), and by direct analysis in real time (DART) time-of-flight and ion trap mass spectrometry (DART-AccuToF, JEOL USA; Caltech MiniDART; LTQ, Thermo Fisher). Further details on experimental conditions and analytical methods can be found in Schilling-Fahnestock et al. (2014).

The average molar mass of SOA was estimated by taking the sum of the product of the percent-relative concentration of each compound with respect to the internal standard (dibutyl phthalate present in each filter) by each compound's molar mass. The relative concentration for each compound was obtained through the relationship of ion current intensity and concentration for DART-MS. In DART analysis, ion current intensity (*I*) is proportional to the concentration (*C*), vapor pressure (*P*_{vap}) and proton affinity (*A*): $I = AP_{\text{vap}}C$. This equation is written for both the analyte and the internal standard and then the ratio is calculated, which allows for the cancellation of the proton affinity term. Analyte vapor pressures were estimated by using proposed structures based on HR-MS data-derived formulae and known mechanisms with the EVAPORATION model (Compernelle et al., 2011). When rewritten to solve for the relative concentration of the analyte with respect to the concentration of the internal standard, the equation becomes

$$\frac{C_A}{C_{\text{IS}}} = \frac{P_{\text{vap,IS}}}{P_{\text{vap,A}}} \cdot \frac{I_A}{I_{\text{IS}}}$$

Atomic O : C ratio vs. volatility is used to represent formation and aging of SOA (Jimenez et al., 2009; Donahue et al., 2011). By analogy to Figs. 1 and 4, major oxidation products are shown in Figs. S1 and S2 in the Supplement. The markers are color-coded by molar mass. Upon gas-phase oxidation, volatility decreases and O : C ratio increases, leading to a linear correlation in O : C ratio vs. volatility for gas-phase oxidation products. Particle-phase products, however, exhibit generally lower volatility and O : C ratio as compared to gas-phase oxidation products. Consequently, the overall correlation between O : C ratio and volatility for the full spectrum of SOA products has a low coefficient of determination and wide prediction interval (Table 1, Fig. S1 in the Supplement). Figure S2 in the Supplement shows the summary of O : C ratio vs. volatility, showing that the oxidation products cover almost the full area in this 2-D space. Clear trend has found that volatile compounds have low molar mass, whereas low volatility compounds with low O : C ratio have high molar mass.

Table A1. Experimental conditions in studies identifying oxidation products, as included in Figs. 1 and 4.

	Study	Oxidants	NO	Seed
Dodecane		OH	Low/high	(NH ₄) ₂ SO ₄
Cyclododecane	This study, Schilling-Fahnestock et al. (2014)	OH	Low/high	(NH ₄) ₂ SO ₄
Hexylcyclohexane		OH	Low/high	(NH ₄) ₂ SO ₄
α -pinene	Docherty et al. (2005)	O ₃	Low	No seed
	Claeys et al. (2007)	OH	High	No seed
	Claeys et al. (2009)	OH, O ₃	High/low	(NH ₄) ₂ SO ₄ , H ₂ SO ₄ , MgSO ₄
	Kahnt et al. (2014)	O ₃	High	(NH ₄) ₂ SO ₄ , H ₂ SO ₄
	Kristensen et al. (2014)	OH, O ₃	High	(NH ₄) ₂ SO ₄ , H ₂ SO ₄ , MgSO ₄
	Zuend and Seinfeld (2012)	O ₃	Low	(NH ₄) ₂ SO ₄
Limonene	Jaoui et al. (2006)	OH, O ₃	High	No seed
	Kundu et al. (2012)	O ₃	Low	No seed
Isoprene	Surratt et al. (2006)	OH	High / low	(NH ₄) ₂ SO ₄ , H ₂ SO ₄ , no seed
	Surratt et al. (2010)	OH	High / low	(NH ₄) ₂ SO ₄ , H ₂ SO ₄ , no seed
	Lin et al (2012)	OH	High	No seed
	Lin et al. (2013)	OH	Low	(NH ₄) ₂ SO ₄ , H ₂ SO ₄ , MgSO ₄

Appendix B: Kinetic regimes for SOA formation

Figure B1 shows a classification scheme for kinetic regimes and limiting cases for SOA formation and aging. Note that the term “limiting case” is reserved for a system that is governed by a single, clearly defined limiting process; the term “kinetic regime” designates a system that is governed by a few (often only one or two) clearly defined rate-limiting processes (Berkemeier et al., 2013). The classification within the particle phase regime (right-hand side of Fig. 3) is explained in detail by Berkemeier et al. (2013). In this study, the gas-phase regime (left-hand side of Fig. 3) extends the classification scheme to SOA formation. The cases of limiting behavior arise from three criteria that are fundamental to formation and partitioning of an oxidation product: (1) the location (gas phase, particle surface, particle bulk) of the reaction leading to SOA formation; (2) the species’ saturation ratio (ratio of ambient concentration to saturation concentration) of the oxidation products; and (3) the extent of spatial heterogeneity of the gas and particle phases. Identifying kinetic regimes and limiting cases can be facilitated by an aerosol model, such as the kinetic multi-layer model for gas-particle interactions (KM-GAP) that explicitly resolves mass transport and chemical reactions in the gas and particle phases (Shiraiwa et al., 2012).

B1 Criterion 1: reaction location (gas vs. surface vs. bulk)

Where does formation of oxidation products that contribute to SOA mass predominantly occur, gas phase, particle surface or particle bulk? A two-pronged criterion can be developed. The first sub-criterion evaluates the relative con-

tribution of gas- vs. particle-phase chemistry. The gas- vs. particle-phase contribution ratio (GPCR) can be defined as ratio of the production rate of the oxidation product in the gas phase (P^g) to the total production rate in gas and particle phases ($P^g + P^p$):

$$\text{GPCR} = P^g / (P^g + P^p). \quad (\text{B1})$$

As GPCR approaches unity, an oxidation product is produced primarily in the gas phase, and as GPCR approaches zero, it is primarily produced in the particle phase.

If particle-phase chemistry dominates (GPCR ≈ 0), the surface to total particle-phase contribution ratio (STCR) is used to assess the extent to which production occurs predominantly at the surface or in the bulk. STCR can be calculated using the production rate of the oxidation product at the surface (P^s) and in the particle bulk (P^b):

$$\text{STCR} = P^s / (P^s + P^b). \quad (\text{B2})$$

If the particle-phase reaction primarily occurs at the surface, STCR approaches unity, and STCR approaches zero if the reaction occurs primarily in the bulk.

B2 Criterion 2: saturation ratio

Is mass transfer of an oxidation product through the gas or into the particle phase limiting SOA growth? After determination of the reaction location, this criterion further classifies the system based on the abundance of oxidation products at the particle surface versus in the near-surface bulk.

In the gas-phase regime, the surface saturation ratio (SSR) can be used to judge the extent to which kinetic limitation of mass transport occurs in the gas phase. With this parameter,

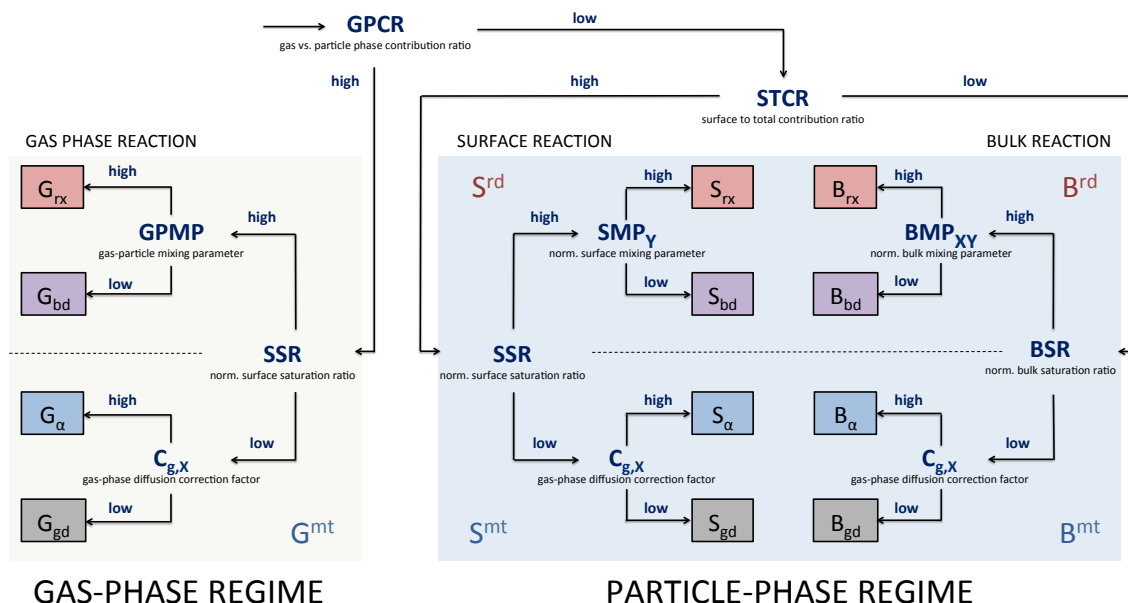


Figure B1. Decision tree for classification and distinction of limiting cases for multiphase chemical evolution of SOA. The classification is based on: (1) the location of the reaction leading to its formation, (2) its saturation ratio, and (3) its mixing parameter to assess the heterogeneity in the gas and particle phases. The resulting limiting cases are shown in the small boxes with reaction location in the gas phase (G), at the surface (S) and in the bulk (B) and limiting processes of chemical reaction (rx), bulk diffusion (bd), mass accommodation (α), and gas-phase diffusion (gd).

the surface concentration of an oxidation product Z, $[Z]_s$, is compared to its surface saturation concentration $[Z]_{s,\text{sat}}$. In the absence of reaction or diffusion into the bulk, $[Z]_{s,\text{sat}}$ is determined by the gas-phase concentration of Z, $[Z]_g$, and the rates of adsorption and desorption k_a and k_d : $[Z]_{s,\text{sat}} = k_a / k_d [Z]_g$ (Pöschl et al., 2007; Berkemeier et al., 2013). The SSR is defined as the ratio of $[Z]_s$ to its saturation concentration at adsorption equilibrium:

$$\text{SSR} = [Z]_s / [Z]_{s,\text{sat}}. \quad (\text{B3})$$

The numerical interpretation of SSR is as follows: as SSR approaches zero, the surface is starved of Z, and the system is limited by mass transfer (G^{mt} regime) either by gas-phase diffusion (G_{gd} limiting case) or surface accommodation (G_α limiting case). As SSR approaches unity, the surface is adequately supplied with Z and the system can be limited by production of Z in the gas phase (G_{rx} limiting case) or mass transport into the bulk (G_{bd} limiting case).

In the particle-phase regime, the classification step is based on SSR or the bulk saturation ratio (BSR) to distinguish between systems in the reaction-diffusion regime or the mass-transfer regime (Berkemeier et al., 2013). The BSR is defined analogously to SSR as the ratio of near-surface bulk concentration of an oxidation product to its saturation concentration.

B3 Criterion 3: mixing parameters (MPs)

Is SOA growth limited by diffusion in the gas or particle phase? Depending on the reaction location and saturation ratio, mixing parameters are used to assess the heterogeneity of the gas-particle system. One can define the surface mixing parameter (SMP), the bulk mixing parameter (BMP), the gas-phase diffusion correction factor (C_g), and the gas-particle mixing parameter (GPMP). SMP is defined as the ratio of the actual surface concentration of compound i to the maximum possible surface concentration in the case of perfect particle-phase mixing. BMP is defined using an effective reacto-diffusive length (Berkemeier et al., 2013). As an MP approaches zero, a strong concentration gradient exists and the system is limited by diffusion; as MP approaches unity, the system is well-mixed and limited by reaction.

In mass-transfer limited systems (indicated by a low SR), $C_{g,i}$ distinguishes between gas-phase diffusion limitation and accommodation limitation. $C_{g,i}$ is defined as the ratio of the concentration of compound i in the near-surface gas phase (one mean free path away from the surface) to that in the gas phase far from the particle (Pöschl et al., 2007):

$$C_{g,i} = C_i^{\text{gs}} / C_i^{\text{g}}. \quad (\text{B4})$$

As $C_{g,i}$ approaches zero, the compound i exhibits a strong concentration gradient in the gas phase and the system is classified as gas-phase diffusion limited (G_{gd} limiting case); as $C_{g,i}$ approaches unity, the system is designated as accommodation-limited (G_α limiting case).

The gas-particle mixing parameter (GPMP) measures the extent to which the gas-particle system is in quasi-equilibrium and is defined as the ratio of equilibrium gas-phase mass concentration of compound i , $C_i^{\text{g,eq}}$, to gas-phase mass concentration, C_i^{g} (far from particle), which is equivalent to the ratio of particle-phase mass concentration, C_i^{PM} , to equilibrium particle-phase mass concentration, $C_i^{\text{PM,eq}}$:

$$\text{GPMP}_i = C_i^{\text{g,eq}} / C_i^{\text{g}} = C_i^{\text{PM}} / C_i^{\text{PM,eq}}. \quad (\text{B5})$$

$C_i^{\text{g,eq}}$ and $C_i^{\text{PM,eq}}$ can be calculated using an equilibrium partitioning theory (Pankow, 1994; Donahue et al., 2006):

$$C_i^{\text{g,eq}} = C_i^* C_i^{\text{PM}} / C_{\text{Tot}}, \quad (\text{B6})$$

$$C_i^{\text{PM,eq}} = C_i^* C_{\text{Tot}} / C_i^*, \quad (\text{B7})$$

where C_i^* is the effective saturation mass concentration of compound i , and C_{Tot} is the total particle mass concentration. In the case of ideal mixing, C_i^* is equal to the gas-phase saturation mass concentration over the pure subcooled liquid (C_i^0). Note that $C_i^{\text{g,eq}}$ can be regarded as a gas-phase mass concentration just above the particle surface, C_i^{s} , when Raoult's law is strictly obeyed and C_i^{s} is in equilibrium with the whole particle (i.e., usually the case for liquid particles).

The value of GPMP determines the extent to which SOA growth is controlled by quasi-equilibrium growth or mass transport limited growth. $C_i^{\text{g}} = C_i^{\text{g,eq}}$ (or $C_i^{\text{PM}} = C_i^{\text{PM,eq}}$) at gas-particle equilibrium. The particle still grows, if C_i^{g} changes slowly and $C_i^{\text{g,eq}}$ follows C_i^{g} instantaneously (quasi-equilibrium growth) (Shiraiwa and Seinfeld, 2012; Zhang et al., 2012). If $C_i^{\text{g}} > C_i^{\text{g,eq}}$, compound i will diffuse from the gas to the particulate phase, driven by concentration or partial pressure gradient between the gas and particle phases (non-equilibrium or mass transport limited growth). Thus, the numerical interpretation of GPMP is: (1) as GPMP approaches 0, SOA growth is limited kinetically by mass transport; (2) as GPMP approaches unity, SOA growth is in quasi-equilibrium and the system is subject to the gas-phase reaction limitation case G_{rx} (the system is limited only by the gas-phase formation rate).

Note that GPMP is small for the limiting cases of G_{bd} , G_{α} , and G_{gd} . In these limiting cases, SOA growth is still sensitive to the gas-phase formation rate (as it determines the gas-phase concentration), but is limited by interfacial transport, which comprises gas-phase diffusion, surface accommodation, and surface-to-bulk transport processes. Gas-phase diffusion and surface accommodation limitation can be differentiated from surface-to-bulk transport limitation either by SSR or by comparing surface (α_{s}) and bulk (α_{b}) accommodation coefficients, each of which is resolved by KM-GAP. α_{s} is defined as the probability of a molecule sticking to the surface upon collision, whereas α_{b} is defined as the respective probability of a molecule to enter the bulk of the particle (Pöschl et al., 2007; Shiraiwa et al., 2012). If $\alpha_{\text{s}} \approx \alpha_{\text{b}}$,

then interfacial transport is not limited by surface-to-bulk exchange, and thus is limited by either gas-phase diffusion or surface accommodation; if $\alpha_{\text{s}} > \alpha_{\text{b}}$, then the interfacial transport is limited by surface-to-bulk transport (dissolution or bulk diffusion). For additional discussion of accommodation vs. surface-bulk exchange, see Appendix C in Berkemeier et al. (2013).

Appendix C: Examples of kinetic regimes and limiting cases

Here we use KM-GAP to model condensation of a semi-volatile compound generated by oxidation of a parent VOC. We assume that the parent VOC with an initial concentration of 10^{10} cm^{-3} is converted to a semi-volatile product with a first-order rate coefficient of 0.1 min^{-1} . Conversion of the first-generation product to higher generation products and particle-phase reactions need not be considered. The initial number and mass concentrations of non-volatile pre-existing particles are taken as 10^3 cm^{-3} and $0.1 \mu\text{g m}^{-3}$, respectively. The initial particle size distribution is assumed log-normal with a mean diameter of 50 nm and a standard deviation of 1.5. The required kinetic parameters for the simulation are given in Table C1. The gas-phase diffusion coefficient (D_{g}) of an oxidation product is varied between $0.01\text{--}0.05 \text{ cm}^2 \text{ s}^{-1}$ (Bilde et al., 2003; Bird et al., 2007). The surface accommodation coefficient ($\alpha_{\text{s},0}$) and bulk diffusion coefficient (D_{b}) are also varied to illustrate the different kinetic regimes and limiting cases for SOA formation in the gas-phase regime.

Figure C1 shows the results of such simulation. The temporal evolution of mass concentration of the parent VOC (black), the oxidation product in the gas phase (C^{g} , solid blue), in the near-surface gas phase (C^{gs} , dotted blue), in the particle phase (C^{PM} , red), and equilibrium gas-phase concentration ($C^{\text{g,eq}}$, dashed blue) are shown. In the simulation presented in Fig. C1a, SOA growth is limited by mass transfer, namely gas-phase diffusion and accommodation (G^{mt} regime, lying between limiting cases G_{gd} and G_{α}) up to ~ 10 s, indicated by a low surface saturation ratio (SSR) and a low gas-phase diffusion correction factor ($C_{\text{g}} = C^{\text{gs}} / C^{\text{g}} \approx 0.7$). The gas-phase concentration gradient vanishes within ~ 10 s ($C^{\text{gs}} \approx C^{\text{g}}$), and as C^{g} continues to increase due to the conversion of the parent VOC, $C^{\text{g,eq}}$ follows the change in C^{g} , essentially instantaneously, and C^{PM} increases. In this case, the gas-phase rate of formation of the oxidation product controls particle growth corresponding to the limiting case of G_{rx} (so-called quasi-equilibrium growth) (Shiraiwa and Seinfeld, 2012; Zhang et al., 2012).

In the simulation presented in Fig. C1b with a relatively low surface accommodation coefficient of 10^{-3} , a steep concentration gradient exhibits between the gas phase and the particle surface ($C^{\text{g}} \approx C^{\text{gs}} > C^{\text{g,eq}}$) during SOA growth. The system is limited by accommodation (G_{α}), as SSR is low, but C_{g} is 1. Figure C1c shows the corresponding results for

Table C1. Properties and kinetic parameters of the VOC oxidation product used in the simulations for SOA growth.

Parameter (unit)	Description	(a)	(b)	(c)	(d)
$\alpha_{s,0}$	Surface accommodation coefficient	1	10^{-3}	1	1
τ_d (s)	Desorption lifetime	10^{-6}	10^{-6}	10^{-6}	10^{-6}
C_0 ($\mu\text{g m}^{-3}$)	Saturation mass concentration	10^3	10^3	10^3	10^{-3}
D_b ($\text{cm}^2 \text{s}^{-1}$)	Bulk diffusion coefficient	10^{-5}	10^{-5}	10^{-17}	10^{-5}
D_g ($\text{cm}^2 \text{s}^{-1}$)	Gas-phase diffusion coefficient	0.01	0.05	0.05	0.01
k_g (min^{-1})	First-order gas-phase reaction rate coefficient	0.1	0.1	0.1	0.1

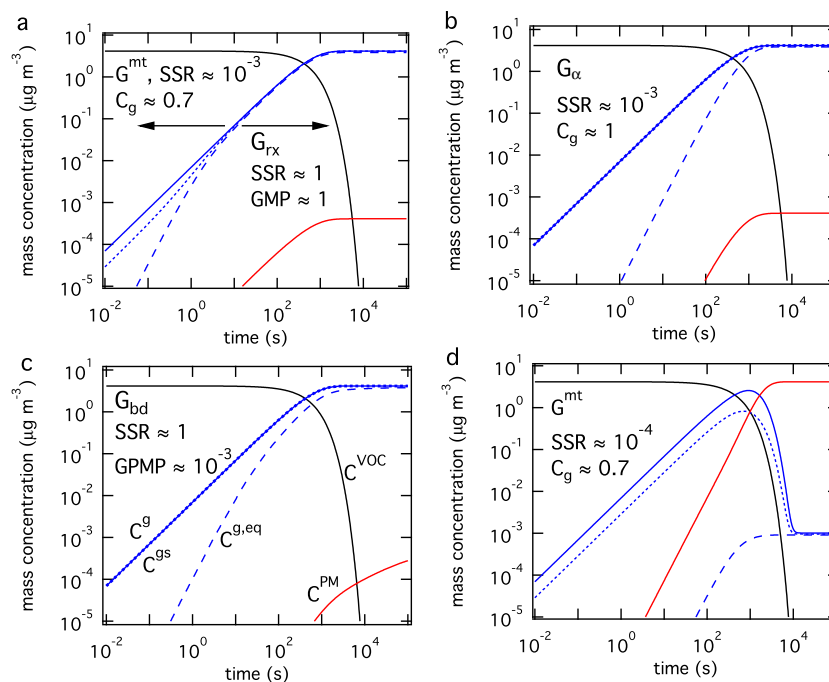


Figure C1. Temporal evolution of mass concentration of the hypothesized VOC oxidation product in the gas phase (solid blue), in the near-surface gas phase (dotted blue), in the particle phase (red), and equilibrium gas-phase concentration (dashed blue). The gas-phase mass concentration of the parent VOC is shown by the black line. For semi-volatile oxidation products with $C^* = 10^3 \mu\text{g m}^{-3}$, SOA growth is limited by (a) gas-phase reaction (G_{rx}), (b) accommodation (G_α), and (c) bulk diffusion (G_{bd}). (d) shows an exemplary simulation for LVOCs, with $C^* = 10^{-3} \mu\text{g m}^{-3}$ exhibiting kinetic limitation in the gas-particle mass transfer regime (G^{mt}).

particles in an amorphous, semi-solid state with the low bulk diffusion coefficient of $10^{-17} \text{cm}^2 \text{s}^{-1}$. In this case, particle growth is limited by surface-to-bulk transport (G_{bd}), as SSR is high and GPMP is low. Note that GPMP refers to the gap between C^g and $C^{g,eq}$. The bulk accommodation coefficient α_b is $\sim 10^{-5}$, which is much smaller than the surface accommodation coefficient α_s . Sensitivity studies with varying D_b reveal that, when $D_b < \sim 10^{-15} \text{cm}^2 \text{s}^{-1}$, the time scales for surface-bulk exchange and bulk diffusion become longer than that of gas-phase diffusion and accommodation (Shiraiwa and Seinfeld, 2012). From the Stokes–Einstein relation, this value corresponds to a viscosity of $\sim 10^7 \text{Pa s}$, which is on the same order as the viscosity of α -pinene SOA at 40% RH (relative humidity) (Renbaum-Wolff et al., 2013). Thus, SOA growth can be limited by bulk diffusion at low

RH, whereas surface accommodation becomes more important at high RH.

Figure C1d shows the simulation for gas-phase formation and partitioning of low volatility oxidation products ($C_0 = 10^{-3} \mu\text{g m}^{-3}$) into liquid particles. SSR is low over the course of particle growth, indicating persistence of a strong concentration gradient between the gas phase and the particle surface. The gas-phase diffusion correction factor (C_g) stays at 0.7 up to $\sim 10^3 \text{s}$, indicating that near-surface gas phase concentration $[Z]_{gs}$ is depleted by 30% compared to gas phase concentration $[Z]_g$ due to rapid uptake and slow gas diffusion ($D_g = 0.01 \text{cm}^2 \text{s}^{-1}$). C_g decreases substantially down to ~ 0.2 only when gas-phase formation ceases at $\sim 10^3$ – 10^4s . Overall, SOA growth is limited by mass transfer (gas-phase diffusion and accommodation;

G^{mt} regime). When a very low-bulk diffusivity is assumed ($D_b \approx 10^{-19} \text{ cm}^2 \text{ s}^{-1}$; figure not shown), SSR is close to 1 and GPMP is very low during particle growth. Thus, the system is limited by bulk diffusion (G_{bd}). Consequently, partitioning of low volatility compounds could be limited by bulk diffusion, when organic particles adopt amorphous solid state (Shiraiwa and Seinfeld, 2012; Zaveri et al., 2014).

Appendix D: Application to chamber data – dodecane photooxidation

Here we apply the classification scheme to experimental data on SOA formation from oxidation of the C_{12} alkane, dodecane ($C_{12}H_{28}$) in the Caltech environmental chamber (Yee et al., 2012). 34 ppb dodecane was oxidized by OH radicals over 20 h in the presence of dry ammonium sulfate seed particles at low concentrations of NO_x , typical of non-urban conditions. KM-GAP was used to simulate the evolution of SOA mass, the organic atomic oxygen-to-carbon (O:C) ratio, and particle-size distribution in the chamber experiments (Shiraiwa et al., 2013a). In the gas phase, SVOCs resulting from up to five generations of OH oxidation are considered. Some of the fourth generation products have been established to be multifunctional carbonyl compounds (aldehydes) that can react in the particle phase with hydroperoxide, hydroxyl, and peroxy-carboxylic acid groups, forming peroxyhemiacetal (PHA), hemiacetal, and acylperoxyhemiacetal, respectively (Docherty et al., 2005; Yee et al., 2012; Ziemann and Atkinson, 2012). The observed evolution of the particle size distribution is simulated successfully only if such particle-phase chemistry is included (Shiraiwa et al., 2013a).

Figure 5 shows the span of molar mass and gas-phase saturation concentrations over the pure subcooled liquids (C_i^0) for gas-phase oxidation products and particle-phase products of the dodecane system. The smaller symbols indicate individual products predicted in the dodecane photooxidation chemical mechanism (Yee et al., 2012) and the large solid circles indicate the surrogate compounds used in the KM-GAP simulations (Shiraiwa et al., 2013a). Upon gas-phase multi-generation oxidation, the volatility of SVOCs decreases from $\sim 10^6 \mu\text{g m}^{-3}$ (dodecane) to $\sim 1 \mu\text{g m}^{-3}$. The particle-phase products have significantly lower volatilities of $\sim 10^{-2} \mu\text{g m}^{-3}$.

Figure D1a and b show the temporal evolution of mass concentration of the first and fifth generation oxidation products in the gas phase (C^g), at the particle surface (C^s), and in the particle phase (C^{PM}). C^g is slightly higher than $C^{\text{g,eq}}$ up to ~ 5 h due to continuous generation of oxidation products in the gas phase, and eventually reaching $C^g \approx C^{\text{g,eq}}$ for both products (GPMP ≈ 1). Note that mass concentration in the near-surface gas phase (C^{gs}) is identical to C^g , indicating that gas-phase diffusion is not a limiting step. The same trend is seen for other generation products. Thus, the contribution of gas-phase semi-volatile oxidation products to SOA formation is limited by their formation in the gas phase, corresponding to the limiting case of G_{rx} .

Particle-phase products are formed by the reaction of reactive aldehydes with SVOCs in the particle phase. Simulations suggest that this reaction occurs mainly at the surface and in the near-surface bulk (Shiraiwa et al., 2013a). Aldehydes and SVOCs are both saturated in the bulk (BSR is high). A strong concentration gradient of aldehydes in the bulk is predicted, whereas SVOCs are predicted to be essentially homogeneous in the bulk ($\text{BMP}_{\text{XY}} \approx 0.5$). Bulk reaction is tightly coupled with bulk diffusion, and the system falls into the reaction-diffusion regime (SB^{rd}), particularly the traditional reacto-diffusive case ($\text{B}_{\text{trad}}^{\text{rd}}$) (Worsnop et al., 2002; Pöschl et al., 2007; Kolb et al., 2010; Berkemeier et al., 2013).

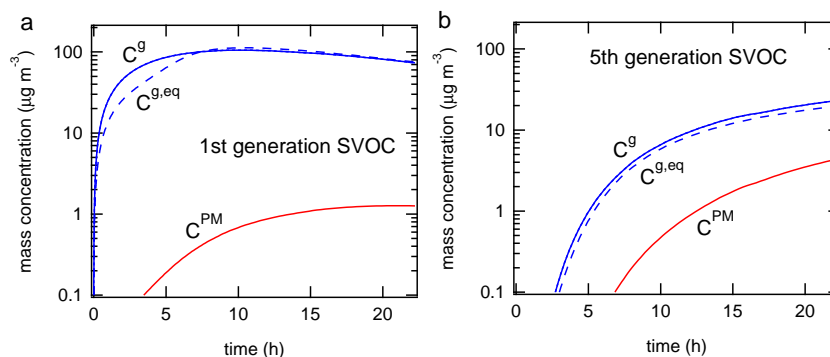


Figure D1. Modeling SOA formation from dodecane photooxidation. Temporal evolution of mass concentration of the (a) first and (b) five generation products in the gas phases (solid blue), particle phases (red), and equilibrium gas-phase mass concentration (dashed blue).

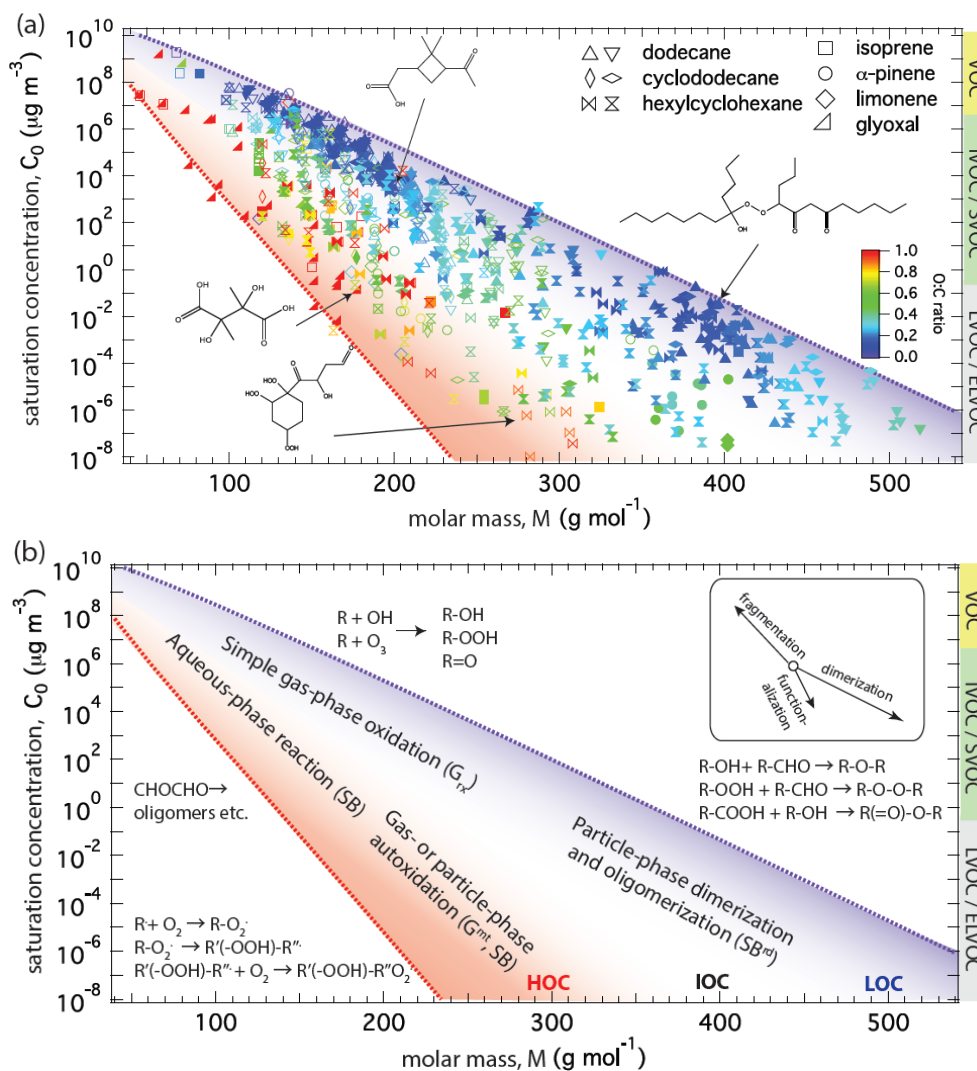


Figure D2. Alternative representation of molecular corridors (Fig. 4) displaying volatility (C_0) as a function of molar mass, which appears more straightforward to use and interpret in mechanistic studies (see Fig. 5) and for direct comparison to mass spectra. Volatility decreases as molar mass increases from left to right, and the slope $\text{dlog}C_0 / \text{d}M$ is steeper for molecules with higher O:C ratio and polarity due to stronger hydrogen bonding and evaporation enthalpy.

The Supplement related to this article is available online at doi:10.5194/acp-14-8323-2014-supplement.

Acknowledgements. This work was funded by the Max Planck Society and US National Science Foundation grant AGS-1057183. M. Shiraiwa, T. Berkemeier and U. Pöschl thank the European Commission project Pan-European gas-aerosols-climate interaction study (No. 265148, PEGASOS). M. Shiraiwa thanks the Japan Society for the Promotion of Science (JSPS) for Postdoctoral Fellowships for Research Abroad.

The service charges for this open access publication have been covered by the Max Planck Society.

Edited by: M. C. Facchini

References

- Abramson, E., Imre, D., Beranek, J., Wilson, J. M., and Zelenyuk, A.: Experimental determination of chemical diffusion within secondary organic aerosol particles, *Phys. Chem. Chem. Phys.*, 15, 2983–2991, 2013.
- Berkemeier, T., Huisman, A. J., Ammann, M., Shiraiwa, M., Koop, T., and Pöschl, U.: Kinetic regimes and limiting cases of gas uptake and heterogeneous reactions in atmospheric aerosols and clouds: a general classification scheme, *Atmos. Chem. Phys.*, 13, 6663–6686, doi:10.5194/acp-13-6663-2013, 2013.
- Bertram, A. K., Ivanov, A. V., Hunter, M., Molina, L. T., and Molina, M. J.: The reaction probability of OH on organic surfaces of tropospheric interest, *J. Phys. Chem. A*, 105, 9415–9421, 2001.
- Bilde, M., Svenningsson, B., Monster, J., and Rosenorn, T.: Even-odd alternation of evaporation rates and vapor pressures of C3–C9 dicarboxylic acid aerosols, *Environ. Sci. Technol.*, 37, 1371–1378, 2003.
- Bird, R. B., Stewart, W. E., and Lightfoot, E. N.: *Transport Phenomena*, 2nd edition, John Wiley & Sons, Inc., New York, 2007.
- Cappa, C. D. and Wilson, K. R.: Evolution of organic aerosol mass spectra upon heating: implications for OA phase and partitioning behavior, *Atmos. Chem. Phys.*, 11, 1895–1911, doi:10.5194/acp-11-1895-2011, 2011.
- Carlton, A. G., Turpin, B. J., Altieri, K. E., Seitzinger, S., Reff, A., Lim, H. J., and Ervens, B.: Atmospheric oxalic acid and SOA production from glyoxal: Results of aqueous photooxidation experiments, *Atmos. Environ.*, 41, 7588–7602, 2007.
- Chan, M. N., Nah, T., and Wilson, K. R.: Real time in situ chemical characterization of sub-micron organic aerosols using Direct Analysis in Real Time mass spectrometry (DART-MS): the effect of aerosol size and volatility, *Analyst*, 138, 3749–3757, 2013.
- Chang, E. I. and Pankow, J. F.: Prediction of activity coefficients in liquid aerosol particles containing organic compounds, dissolved inorganic salts, and water – Part 2: Consideration of phase separation effects by an X-UNIFAC model, *Atmos. Environ.*, 40, 6422–6436, 2006.
- Claeys, M., Szmigielski, R., Kourtchev, I., Van der Veken, P., Vermeylen, R., Maenhaut, W., Jaoui, M., Kleindienst, T. E., Lewandowski, M., Offenberg, J. H., and Edney, E. O.: Hydroxy-dicarboxylic acids: Markers for secondary organic aerosol from the photooxidation of alpha-pinene, *Environ. Sci. Technol.*, 41, 1628–1634, 2007.
- Claeys, M., Iinuma, Y., Szmigielski, R., Surratt, J. D., Blockhuys, F., Van Alsenoy, C., Boege, O., Sierau, B., Gomez-Gonzalez, Y., Vermeylen, R., Van der Veken, P., Shahgholi, M., Chan, A. W. H., Herrmann, H., Seinfeld, J. H., and Maenhaut, W.: Terpenylic Acid and Related Compounds from the Oxidation of alpha-Pinene: Implications for New Particle Formation and Growth above Forests, *Environ. Sci. Technol.*, 43, 6976–6982, 2009.
- Compennolle, S., Ceulemans, K., and Muller, J. F.: EVAPORATION: a new vapour pressure estimation method for organic molecules including non-additivity and intramolecular interactions, *Atmos. Chem. Phys.*, 11, 9431–9450, doi:10.5194/acp-11-9431-2011, 2011.
- Crouse, J. D., Nielsen, L. B., Jørgensen, S., Kjaergaard, H. G., and Wennberg, P. O.: Autoxidation of organic compounds in the atmosphere, *J. Phys. Chem. Lett.*, 4, 3513–3520, 2013.
- Docherty, K. S., Wu, W., Lim, Y. B., and Ziemann, P. J.: Contributions of organic peroxides to secondary aerosol formed from reactions of monoterpenes with O₃, *Environ. Sci. Technol.*, 39, 4049–4059, 2005.
- Donahue, N. M., Robinson, A. L., Stanier, C. O., and Pandis, S. N.: Coupled partitioning, dilution, and chemical aging of semivolatile organics, *Environ. Sci. Technol.*, 40, 2635–2643, 2006.
- Donahue, N. M., Epstein, S. A., Pandis, S. N., and Robinson, A. L.: A two-dimensional volatility basis set: 1. organic-aerosol mixing thermodynamics, *Atmos. Chem. Phys.*, 11, 3303–3318, doi:10.5194/acp-11-3303-2011, 2011.
- Donahue, N. M., Henry, K. M., Mentel, T. F., Kiendler-Scharr, A., Spindler, C., Bohn, B., Brauers, T., Dorn, H. P., Fuchs, H., Tillmann, R., Wahner, A., Saathoff, H., Naumann, K.-H., Möhler, O., Leisner, T., Müller, L., Reinnig, M.-C., Hoffmann, T., Salo, K., Hallquist, M., Frosch, M., Bilde, M., Tritscher, T., Barmet, P., Praplan, A. P., DeCarlo, P. F., Dommen, J., Prévôt, A. S. H., and Baltensperger, U.: Aging of biogenic secondary organic aerosol via gas-phase OH radical reactions, *P. Natl. Acad. Sci. USA*, 109, 13503–13508, 2012.
- Ehn, M., Kleist, E., Junninen, H., Petaja, T., Lonn, G., Schobesberger, S., Dal Maso, M., Trimborn, A., Kulmala, M., Worsnop, D. R., Wahner, A., Wildt, J., and Mentel, T. F.: Gas phase formation of extremely oxidized pinene reaction products in chamber and ambient air, *Atmos. Chem. Phys.*, 12, 5113–5127, doi:10.5194/acp-12-5113-2012, 2012.
- Ehn, M., Thornton, J. A., Kleist, E., Sipila, M., Junninen, H., Pullinen, I., Springer, M., Rubach, F., Tillmann, R., Lee, B., Lopez-Hilfiker, F., Andres, S., Acir, I.-H., Rissanen, M., Jokinen, T., Schobesberger, S., Kangasluoma, J., Kontkanen, J., Nieminen, T., Kurten, T., Nielsen, L. B., Jørgensen, S., Kjaergaard, H. G., Canagaratna, M., Dal Maso, M., Berndt, T., Petaja, T., Wahner, A., Kerminen, V.-M., Kulmala, M., Worsnop, D. R., Wildt, J., and Mentel, T. F.: A large source of low-volatility secondary organic aerosol, *Nature*, 506, 476–479, 2014.
- Ervens, B. and Volkamer, R.: Glyoxal processing by aerosol multiphase chemistry: towards a kinetic modeling framework of secondary organic aerosol formation in aqueous particles, *Atmos.*

- Chem. Phys., 10, 8219–8244, doi:10.5194/acp-10-8219-2010, 2010.
- Ervens, B., Turpin, B. J., and Weber, R. J.: Secondary organic aerosol formation in cloud droplets and aqueous particles (aqSOA): a review of laboratory, field and model studies, *Atmos. Chem. Phys.*, 11, 11069–11102, doi:10.5194/acp-11-11069-2011, 2011.
- Goldstein, A. H. and Galbally, I. E.: Known and unexplored organic constituents in the earth's atmosphere, *Environ. Sci. Technol.*, 41, 1514–1521, 2007.
- Hallquist, M., Wenger, J. C., Baltensperger, U., Rudich, Y., Simpson, D., Claeys, M., Dommen, J., Donahue, N. M., George, C., Goldstein, A. H., Hamilton, J. F., Herrmann, H., Hoffmann, T., Iinuma, Y., Jang, M., Jenkin, M. E., Jimenez, J. L., Kiendler-Scharr, A., Maenhaut, W., McFiggans, G., Mentel, T. F., Monod, A., Prevot, A. S. H., Seinfeld, J. H., Surratt, J. D., Szmigielski, R., and Wildt, J.: The formation, properties and impact of secondary organic aerosol: current and emerging issues, *Atmos. Chem. Phys.*, 9, 5155–5235, doi:10.5194/acp-9-5155-2009, 2009.
- Hosny, N. A., Fitzgerald, C., Tong, C., Kalberer, M., Kuimova, M. K., and Pope, F. D.: Fluorescent lifetime imaging of atmospheric aerosols: a direct probe of aerosol viscosity, *Faraday Discuss.*, 165, 343–356, 2013.
- Iinuma, Y., Boge, O., Gnauk, T., and Herrmann, H.: Aerosol-chamber study of the alpha-pinene/O₃ reaction: influence of particle acidity on aerosol yields and products, *Atmos. Environ.*, 38, 761–773, 2004.
- Iinuma, Y., Muller, C., Berndt, T., Boge, O., Claeys, M., and Herrmann, H.: Evidence for the existence of organosulfates from beta-pinene ozonolysis in ambient secondary organic aerosol, *Environ. Sci. Technol.*, 41, 6678–6683, 2007.
- Jang, M. S., Czoschke, N. M., Lee, S., and Kamens, R. M.: Heterogeneous atmospheric aerosol production by acid-catalyzed particle-phase reactions, *Science*, 298, 814–817, 2002.
- Jaoui, M., Corse, E., Kleindienst, T. E., Offenberg, J. H., Lewandowski, M., and Edney, E. O.: Analysis of secondary organic aerosol compounds from the photooxidation of *d*-limonene in the presence of NO_x and their detection in ambient PM_{2.5}, *Environ. Sci. Technol.*, 40, 3819–3828, 2006.
- Jimenez, J. L., Canagaratna, M. R., Donahue, N. M., Prevot, A. S. H., Zhang, Q., Kroll, J. H., DeCarlo, P. F., Allan, J. D., Coe, H., Ng, N. L., Aiken, A. C., Docherty, K. S., Ulbrich, I. M., Grieshop, A. P., Robinson, A. L., Duplissy, J., Smith, J. D., Wilson, K. R., Lanz, V. A., Hueglin, C., Sun, Y. L., Tian, J., Laaksonen, A., Raatikainen, T., Rautiainen, J., Vaattovaara, P., Ehn, M., Kulmala, M., Tomlinson, J. M., Collins, D. R., Cubison, M. J., Dunlea, E. J., Huffman, J. A., Onasch, T. B., Alfarra, M. R., Williams, P. I., Bower, K., Kondo, Y., Schneider, J., Drewnick, F., Borrmann, S., Weimer, S., Demerjian, K., Salcedo, D., Cottrell, L., Griffin, R., Takami, A., Miyoshi, T., Hatakeyama, S., Shimono, A., Sun, J. Y., Zhang, Y. M., Dzepina, K., Kimmel, J. R., Sueper, D., Jayne, J. T., Herndon, S. C., Trimborn, A. M., Williams, L. R., Wood, E. C., Middlebrook, A. M., Kolb, C. E., Baltensperger, U., and Worsnop, D. R.: Evolution of organic aerosols in the atmosphere, *Science*, 326, 1525–1529, 2009.
- Kahnt, A., Iinuma, Y., Blockhuys, F., Mutzel, A., Vermeylen, R., Kleindienst, T. E., Jaoui, M., Offenberg, J. H., Lewandowski, M., Böge, O., Herrmann, H., Maenhaut, W., and Claeys, M.: 2-Hydroxyterpenylic acid: An oxygenated marker compound for α -pinene secondary organic aerosol in ambient fine aerosol, *Environ. Sci. Technol.*, 48, 4901–4908, 2014.
- Kalberer, M., Sax, M., and Samburova, V.: Molecular size evolution of oligomers in organic aerosols collected in urban atmospheres and generated in a smog chamber, *Environ. Sci. Technol.*, 40, 5917–5922, 2006.
- Kampf, C. J., Waxman, E. M., Slowik, J. G., Dommen, J., Pfaffenberger, L., Praplan, A. P., Prevot, A. S. H., Baltensperger, U., Hoffmann, T., and Volkamer, R.: Effective Henry's Law Partitioning and the Salting Constant of Glyoxal in Aerosols Containing Sulfate, *Environ. Sci. Technol.*, 47, 4236–4244, 2013.
- Kolb, C. E., Cox, R. A., Abbatt, J. P. D., Ammann, M., Davis, E. J., Donaldson, D. J., Garrett, B. C., George, C., Griffiths, P. T., Hanson, D. R., Kulmala, M., McFiggans, G., Pöschl, U., Riipinen, I., Rossi, M. J., Rudich, Y., Wagner, P. E., Winkler, P. M., Worsnop, D. R., and O' Dowd, C. D.: An overview of current issues in the uptake of atmospheric trace gases by aerosols and clouds, *Atmos. Chem. Phys.*, 10, 10561–10605, doi:10.5194/acp-10-10561-2010, 2010.
- Koop, T., Bookhold, J., Shiraiwa, M., and Pöschl, U.: Glass transition and phase state of organic compounds: dependency on molecular properties and implications for secondary organic aerosols in the atmosphere, *Phys. Chem. Chem. Phys.*, 13, 19238–19255, 2011.
- Kristensen, K., Cui, T., Zhang, H., Gold, A., Glasius, M., and Surratt, J. D.: Dimer esters in α -pinene secondary organic aerosol: effect of hydroxyl radical, ozone, relative humidity and aerosol acidity, *Atmos. Chem. Phys.*, 14, 4201–4218, doi:10.5194/acp-14-4201-2014, 2014.
- Kroll, J. H. and Seinfeld, J. H.: Chemistry of secondary organic aerosol: Formation and evolution of low-volatility organics in the atmosphere, *Atmos. Environ.*, 42, 3593–3624, 2008.
- Kundu, S., Fisseha, R., Putman, A. L., Rahn, T. A., and Mazzone, L. R.: High molecular weight SOA formation during limonene ozonolysis: insights from ultrahigh-resolution FT-ICR mass spectrometry characterization, *Atmos. Chem. Phys.*, 12, 5523–5536, doi:10.5194/acp-12-5523-2012, 2012.
- Kuwata, M. and Martin, S. T.: Phase of atmospheric secondary organic material affects its reactivity, *P. Natl. Acad. Sci. USA*, 109, 17354–17359, 2012.
- Laskin, A., Laskin, J., and Nizkorodov, S. A.: Mass spectrometric approaches for chemical characterisation of atmospheric aerosols: critical review of the most recent advances, *Environ. Chem.*, 9, 163–189, 2012a.
- Laskin, J., Eckert, P. A., Roach, P. J., Heath, B. S., Nizkorodov, S. A., and Laskin, A.: Chemical Analysis of Complex Organic Mixtures Using Reactive Nanospray Desorption Electrospray Ionization Mass Spectrometry, *Anal. Chem.*, 84, 7179–7187, 2012b.
- Liggio, J., Li, S. M., and McLaren, R.: Heterogeneous reactions of glyoxal on particulate matter: Identification of acetals and sulfate esters, *Environ. Sci. Technol.*, 39, 1532–1541, 2005.
- Lim, Y. B., Tan, Y., Perri, M. J., Seitzinger, S. P., and Turpin, B. J.: Aqueous chemistry and its role in secondary organic aerosol (SOA) formation, *Atmos. Chem. Phys.*, 10, 10521–10539, doi:10.5194/acp-10-10521-2010, 2010.
- Lin, Y.-H., Zhang, Z., Docherty, K. S., Zhang, H., Budisulistiorini, S. H., Rubitschun, C. L., Shaw, S. L., Knipping, E. M., Edgerton, E. S., Kleindienst, T. E., Gold, A., and Surratt, J. D.: Isoprene Epoxydiols as Precursors to Secondary Organic Aerosol

- Formation: Acid-Catalyzed Reactive Uptake Studies with Authentic Compounds, *Environ. Sci. Technol.*, 46, 250–258, 2012.
- Lin, Y.-H., Zhang, H., Pye, H. O. T., Zhang, Z., Marth, W. J., Park, S., Arashiro, M., Cui, T., Budisulistiorini, S. H., Sexton, K. G., Vizuete, W., Xie, Y., Luecken, D. J., Piletic, I. R., Edney, E. O., Bartolotti, L. J., Gold, A., and Surratt, J. D.: Epoxide as a precursor to secondary organic aerosol formation from isoprene photooxidation in the presence of nitrogen oxides, *P. Natl. Acad. Sci. USA*, 110, 6718–6723, 2013.
- Loza, C. L., Craven, J. S., Yee, L. D., Coggon, M. M., Schwantes, R. H., Shiraiwa, M., Zhang, X., Schilling, K. A., Ng, N. L., Canagaratna, M. R., Ziemann, P. J., Flagan, R. C., and Seinfeld, J. H.: Secondary organic aerosol yields of 12-carbon alkanes, *Atmos. Chem. Phys.*, 14, 1423–1439, doi:10.5194/acp-14-1423-2014, 2014.
- McNeill, V. F., Woo, J. L., Kim, D. D., Schwier, A. N., Wannenell, N. J., Sumner, A. J., and Barakat, J. M.: Aqueous-phase secondary organic aerosol and organosulfate formation in atmospheric aerosols: A modeling study, *Environ. Sci. Technol.*, 46, 8075–8081, 2012.
- Murphy, B. N., Donahue, N. M., Robinson, A. L., and Pandis, S. N.: A naming convention for atmospheric organic aerosol, *Atmos. Chem. Phys.*, 14, 5825–5839, doi:10.5194/acp-14-5825-2014, 2014.
- Nguyen, T. B., Laskin, J., Laskin, A., and Nizkorodov, S. A.: Nitrogen-Containing Organic Compounds and Oligomers in Secondary Organic Aerosol Formed by Photooxidation of Isoprene, *Environ. Sci. Technol.*, 45, 6908–6918, 2011.
- Nguyen, T. B., Nizkorodov, S. A., Laskin, A., and Laskin, J.: An approach toward quantification of organic compounds in complex environmental samples using high-resolution electrospray ionization mass spectrometry, *Anal. Methods*, 5, 72–80, 2013.
- Offenberg, J. H., Lewandowski, M., Edney, E. O., Kleindienst, T. E., and Jaoui, M.: Influence of Aerosol Acidity on the Formation of Secondary Organic Aerosol from Biogenic Precursor Hydrocarbons, *Environ. Sci. Technol.*, 43, 7742–7747, 2009.
- Pankow, J. F.: An absorption-model of the gas aerosol partitioning involved in the formation of secondary organic aerosol, *Atmos. Environ.*, 28, 189–193, 1994.
- Perraud, V., Bruns, E. A., Ezell, M. J., Johnson, S. N., Yu, Y., Alexander, M. L., Zelenyuk, A., Imre, D., Chang, W. L., Dabdub, D., Pankow, J. F., and Finlayson-Pitts, B. J.: Nonequilibrium atmospheric secondary organic aerosol formation and growth, *P. Natl. Acad. Sci. USA*, 109, 2836–2841, 2012.
- Pfrang, C., Shiraiwa, M., and Pöschl, U.: Chemical ageing and transformation of diffusivity in semi-solid multi-component organic aerosol particles, *Atmos. Chem. Phys.*, 11, 7343–7354, doi:10.5194/acp-11-7343-2011, 2011.
- Pierce, J. R., Riipinen, I., Kulmala, M., Ehn, M., Petäjä, T., Junninen, H., Worsnop, D. R., and Donahue, N. M.: Quantification of the volatility of secondary organic compounds in ultrafine particles during nucleation events, *Atmos. Chem. Phys.*, 11, 9019–9036, doi:10.5194/acp-11-9019-2011, 2011.
- Pöschl, U., Rudich, Y., and Ammann, M.: Kinetic model framework for aerosol and cloud surface chemistry and gas-particle interactions – Part 1: General equations, parameters, and terminology, *Atmos. Chem. Phys.*, 7, 5989–6023, doi:10.5194/acp-7-5989-2007, 2007.
- Presto, A. A., Hartz, K. E. H., and Donahue, N. M.: Secondary organic aerosol production from terpene ozonolysis. 2. Effect of NO_x concentration, *Environ. Sci. Technol.*, 39, 7046–7054, 2005.
- Renbaum-Wolff, L., Grayson, J. W., Bateman, A. P., Kuwata, K., Sellier, M., Murray, B. J., Schilling, J. E., Martin, S. T., and Bertram, A. K.: Viscosity of α -pinene secondary organic material and implications for particle growth and reactivity, *P. Natl. Acad. Sci. USA*, 110, 8014–8019, 2013.
- Riipinen, I., Pierce, J. R., Yli-Juuti, T., Nieminen, T., Hakkinen, S., Ehn, M., Junninen, H., Lehtipalo, K., Petaja, T., Slowik, J., Chang, R., Shantz, N. C., Abbatt, J., Leaitch, W. R., Kerminen, V. M., Worsnop, D. R., Pandis, S. N., Donahue, N. M., and Kulmala, M.: Organic condensation: a vital link connecting aerosol formation to cloud condensation nuclei (CCN) concentrations, *Atmos. Chem. Phys.*, 11, 3865–3878, doi:10.5194/acp-11-3865-2011, 2011.
- Sareen, N., Schwier, A. N., Shapiro, E. L., Mitroo, D., and McNeill, V. F.: Secondary organic material formed by methylglyoxal in aqueous aerosol mimics, *Atmos. Chem. Phys.*, 10, 997–1016, doi:10.5194/acp-10-997-2010, 2010.
- Schilling-Fahnestock, K. A., Yee, L. D., Loza, C. L., Coggon, M. M., Schwantes, R., Zhang, X., Dalleska, N. F., and Seinfeld, J. H.: Secondary Organic Aerosol Composition from C₁₂ Alkanes, *J. Phys. Chem. A*, doi:10.1021/jp501779w, 2014.
- Schobesberger, S., Junninen, H., Bianchi, F., Lonn, G., Ehn, M., Lehtipalo, K., Dommen, J., Ehrhart, S., Ortega, I. K., Franchin, A., Nieminen, T., Riccobono, F., Hutterli, M., Duplissy, J., Almeida, J., Amorim, A., Breitenlechner, M., Downard, A. J., Dunne, E. M., Flagan, R. C., Kajos, M., Keskinen, H., Kirkby, J., Kupc, A., Kuerten, A., Kurten, T., Laaksonen, A., Mathot, S., Onnela, A., Praplan, A. P., Rondo, L., Santos, F. D., Schallhart, S., Schnitzhofer, R., Sipila, M., Tome, A., Tsagkogeorgas, G., Vehkamäki, H., Wimmer, D., Baltensperger, U., Carslaw, K. S., Curtius, J., Hansel, A., Petaja, T., Kulmala, M., Donahue, N. M., and Worsnop, D. R.: Molecular understanding of atmospheric particle formation from sulfuric acid and large oxidized organic molecules, *P. Natl. Acad. Sci. USA*, 110, 17223–17228, 2013.
- Shiraiwa, M., Ammann, M., Koop, T., and Pöschl, U.: Gas uptake and chemical aging of semisolid organic aerosol particles, *P. Natl. Acad. Sci. USA*, 108, 11003–11008, 2011.
- Shiraiwa, M., Pfrang, C., Koop, T., and Pöschl, U.: Kinetic multi-layer model of gas-particle interactions in aerosols and clouds (KM-GAP): linking condensation, evaporation and chemical reactions of organics, oxidants and water, *Atmos. Chem. Phys.*, 12, 2777–2794, doi:10.5194/acp-12-2777-2012, 2012.
- Shiraiwa, M. and Seinfeld, J. H.: Equilibration timescale of atmospheric secondary organic aerosol partitioning, *Geophys. Res. Lett.*, 39, L24801, doi:10.1029/2012GL054008, 2012.
- Shiraiwa, M., Yee, L. D., Schilling, K. A., Loza, C. L., Craven, J. S., Zuend, A., Ziemann, P. J., and Seinfeld, J. H.: Size distribution dynamics reveal particle-phase chemistry in organic aerosol formation, *P. Natl. Acad. Sci. USA*, 110, 11746–11750, 2013a.
- Shiraiwa, M., Zuend, A., Bertram, A. K., and Seinfeld, J. H.: Gas-particle partitioning of atmospheric aerosols: interplay of physical state, non-ideal mixing and morphology, *Phys. Chem. Chem. Phys.*, 15, 11441–11453, 2013b.
- Surratt, J. D., Murphy, S. M., Kroll, J. H., Ng, N. L., Hildebrandt, L., Sorooshian, A., Szmigielski, R., Vermeylen, R., Maenhaut,

- W., Claeys, M., Flagan, R. C., and Seinfeld, J. H.: Chemical composition of secondary organic aerosol formed from the photooxidation of isoprene, *J. Phys. Chem. A*, 110, 9665–9690, 2006.
- Surratt, J. D., Gomez-Gonzalez, Y., Chan, A. W. H., Vermeylen, R., Shahgholi, M., Kleindienst, T. E., Edney, E. O., Offenberg, J. H., Lewandowski, M., Jaoui, M., Maenhaut, W., Claeys, M., Flagan, R. C., and Seinfeld, J. H.: Organosulfate formation in biogenic secondary organic aerosol, *J. Phys. Chem. A*, 112, 8345–8378, 2008.
- Surratt, J. D., Chan, A. W. H., Eddingsaas, N. C., Chan, M. N., Loza, C. L., Kwan, A. J., Hersey, S. P., Flagan, R. C., Wennberg, P. O., and Seinfeld, J. H.: Reactive intermediates revealed in secondary organic aerosol formation from isoprene, *P. Natl. Acad. Sci. USA*, 107, 6640–6645, 2010.
- Trump, E. R. and Donahue, N. M.: Oligomer formation within secondary organic aerosols: equilibrium and dynamic considerations, *Atmos. Chem. Phys.*, 14, 3691–3701, doi:10.5194/acp-14-3691-2014, 2014.
- Vaden, T. D., Imre, D., Beranek, J., Shrivastava, M., and Zelenyuk, A.: Evaporation kinetics and phase of laboratory and ambient secondary organic aerosol, *P. Natl. Acad. Sci. USA*, 108, 2190–2195, 2011.
- Virtanen, A., Joutsensaari, J., Koop, T., Kannosto, J., YliPirilä, P., Leskinen, J., Mäkelä, J. M., Holopainen, J. K., Pöschl, U., Kulmala, M., Worsnop, D. R., and Laaksonen, A.: An amorphous solid state of biogenic secondary organic aerosol particles, *Nature*, 467, 824–827, 2010.
- Vogel, A. L., Äijälä, M., Corrigan, A. L., Junninen, H., Ehn, M., Petäjä, T., Worsnop, D. R., Kulmala, M., Russell, L. M., Williams, J., and Hoffmann, T.: In situ submicron organic aerosol characterization at a boreal forest research station during HUMPPA-COPEC 2010 using soft and hard ionization mass spectrometry, *Atmos. Chem. Phys.*, 13, 10933–10950, doi:10.5194/acp-13-10933-2013, 2013.
- Williams, B. J., Goldstein, A. H., Kreisberg, N. M., and Hering, S. V.: In situ measurements of gas/particle-phase transitions for atmospheric semivolatile organic compounds, *P. Natl. Acad. Sci. USA*, 107, 6676–6681, 2010.
- Worsnop, D. R., Morris, J. W., Shi, Q., Davidovits, P., and Kolb, C. E.: A chemical kinetic model for reactive transformations of aerosol particles, *Geophys. Res. Lett.*, 29, 1–4, 2002.
- Xu, L., Kollman, M. S., Song, C., Shilling, J. E., and Ng, N. L.: Effects of NO_x on the Volatility of Secondary Organic Aerosol from Isoprene Photooxidation, *Environ. Sci. Technol.*, 48, 2253–2262, 2014.
- Yee, L. D., Craven, J. S., Loza, C. L., Schilling, K. A., Ng, N. L., Canagaratna, M. R., Ziemann, P. J., Flagan, R. C., and Seinfeld, J. H.: Secondary organic aerosol formation from low-NO_x photooxidation of dodecane: evolution of multigeneration gas-phase chemistry and aerosol composition, *J. Phys. Chem. A*, 116, 6211–6230, 2012.
- Zaveri, R. A., Easter, R. C., Shilling, J. E., and Seinfeld, J. H.: Modeling kinetic partitioning of secondary organic aerosol and size distribution dynamics: representing effects of volatility, phase state, and particle-phase reaction, *Atmos. Chem. Phys.*, 14, 5153–5181, doi:10.5194/acp-14-5153-2014, 2014.
- Zhang, X., Pandis, S. N., and Seinfeld, J. H.: Diffusion-limited versus quasi-equilibrium aerosol growth, *Aerosol Sci. Technol.*, 46, 874–885, 2012.
- Zhao, R., Lee, A. K. Y., and Abbatt, J. P. D.: Investigation of Aqueous-Phase Photooxidation of Glyoxal and Methylglyoxal by Aerosol Chemical Ionization Mass Spectrometry: Observation of Hydroxyhydroperoxide Formation, *J. Phys. Chem. A*, 116, 6253–6263, 2012.
- Zhou, S., Shiraiwa, M., McWhinney, R., Pöschl, U., and Abbatt, J. P. D.: Kinetic limitations in gas-particle reactions arising from slow diffusion in secondary organic aerosol, *Faraday Discuss.*, 165, 391–406, 2013.
- Ziemann, P. J. and Atkinson, R.: Kinetics, products, and mechanisms of secondary organic aerosol formation, *Chem. Soc. Rev.*, 41, 6582–6605, 2012.
- Zuend, A. and Seinfeld, J. H.: Modeling the gas-particle partitioning of secondary organic aerosol: the importance of liquid-liquid phase separation, *Atmos. Chem. Phys.*, 12, 3857–3882, 2012, <http://www.atmos-chem-phys.net/12/3857/2012/>.

Appendices

Appendix A

Molecular Corridors and Kinetic Regimes in the Multiphase Chemical Evolution of Secondary Organic Aerosol³

³ Reproduced by permission from “Molecular corridors and kinetic regimes in the multiphase chemical evolution of secondary organic aerosol” by M. Shiraiwa, T. Berkemeier, K. A. Schilling-Fahnestock, J. H. Seinfeld, and U. Poschl. *Atmos. Chem. Phys.* **2014**, *14*, 8323-8341.

Appendix B

Size Distribution Dynamics Reveal the Importance of Particle-Phase Chemistry in Organic Aerosol Formation⁴

⁴ Reproduced by permission from “Size distribution dynamics reveal particle-phase chemistry in organic aerosol formation” by M. Shiraiwa, L. D. Yee, K. A. Schilling, C. L. Loza, J. S. Craven, A. Zuend, P. J. Ziemann, and J. H. Seinfeld. *Proc. Natl. Acad. Sci. USA* **2013**, *110*, 11746-11750.

Appendix C

The Pasadena Aerosol Characterization Observatory (PACO): Chemical and Physical Analysis of the Western Los Angeles Basin Aerosol⁵

⁵ Reproduced by permission from “The Pasadena Aerosol Characterization Observatory (PACO): chemical and physical analysis of the Western Los Angeles basin aerosol” by S. P. Hersey, J. S. Craven, K. A. Schilling, A. R. Metcalf, A. Sorooshian, M. N. Chan, R. C. Flagan, and J. H. Seinfeld. *Atmos. Chem. Phys.* **2011**, *11*, 7417-7443.

Appendix D

Effect of Chemical Structure on Secondary Organic Aerosol Formation
from C₁₂ Alkanes⁶

⁶ Reproduced by permission from “Effect of chemical structure on secondary organic aerosol formation from C₁₂ alkanes” by L. D. Yee, J. S. Craven, C. L. Loza, K. A. Schilling, N. L. Ng, M. R. Canagaratna, P. J. Ziemann, R. C. Flagan, and J. H. Seinfeld. *Atmos. Chem. Phys.* **2013**, *13*, 11121-11140.

Appendix E

Secondary Organic Aerosol Formation from Low-NO_x Photooxidation of Dodecane: Evolution of Multigeneration Gas-Phase Chemistry and Aerosol Composition⁷

⁷ Reproduced by permission from “Secondary organic aerosol formation from low-NO_x photooxidation of dodecane: Evolution of multigeneration gas-phase chemistry and aerosol composition” by L. D. Yee, J. S. Craven, C. L. Loza, K. A. Schilling, N. L. Ng, M. R. Canagaratna, P. J. Ziemann, R. C. Flagan, and J. H. Seinfeld. *J. Phys. Chem. A* **2012**, *116*, 6211-6230.

Appendix F

Secondary Organic Aerosol Formation from Biomass Burning Intermediates: Phenol and Methoxyphenols⁸

⁸ Reproduced by permission from “Secondary organic aerosol formation from biomass burning intermediates: phenol and methoxyphenols” by L. D. Yee, K. E. Kautzman, C. L. Loza, K. A. Schilling, M. M. Coggon, P. S. Chhabra, M. N. Chan, A. W. H. Chan, S. P. Hersey, J. D. Crouse, P. O. Wennberg, R. C. Flagan, J. H. Seinfeld. *Atmos. Chem. Phys.* **2013**, *13*, 8019-8043.

Appendix G

Secondary Organic Aerosol Yields of 12-Carbon Alkanes⁹

⁹ Reproduced by permission from “Secondary organic aerosol yields of 12-carbon alkanes” by C. L. Loza, J. S. Craven, L. D. Yee, M. M. Coggon, R. H. Schwantes, M. Shiraiwa, X. Zhang, K. A. Schilling, N. L. Ng, M. R. Canagaratna, P. J. Ziemann, R. C. Flagan, and J. H. Seinfeld. *Atmos. Chem. Phys.* **2014**, *14*, 1423-1439.

Appendix H

Influence of Aerosol Acidity on the Chemical Composition of Secondary Organic Aerosol from β -Caryophyllene¹⁰

¹⁰ Reproduced by permission from “Influence of aerosol acidity on the chemical composition of secondary organic aerosol from β -caryophyllene” by M. N. Chan, J. D. Surratt, A. W. H. Chan, K. Schilling, J. H. Offenberg, M. Lewandowski, E. O. Edney, T. E. Kleindienst, M. Jaoui, E. S. Edgerton, R. L. Tanner, S. L. Shaw, M. Zheng, E. M. Knipping, and J. H. Seinfeld. *Atmos. Chem. Phys.* **2011**, *11*, 1735-1751.

Appendix I

α -Pinene Photooxidation under Controlled Chemical Conditions – Part 2: SOA Yield and Composition in Low- and High-NO Environments¹¹

¹¹ Reproduced by permission from “ α -Pinene photooxidation under controlled chemical conditions – Part 2: SOA yield and composition in low- and high-NO environments” by N. C. Eddingsaas, C. L. Loza, L. D. Yee, M. Chan, K. A. Schilling, P. S. Chhabra, J. H. Seinfeld, and P. O. Wennberg. *Atmos. Chem. Phys.* **2012**, *12*, 7413-7427.

Appendix J

Analysis of Secondary Organic Aerosol Formation and Aging Using Positive Matrix Factorization of High-Resolution Aerosol Mass Spectra: Application to the Dodecane Low-NO_x System¹²

¹² Reproduced by permission from “Analysis of secondary organic aerosol formation and aging using positive matrix factorization of high-resolution aerosol mass spectra: application to the dodecane low-NO_x system” by J. S. Craven, L. D. Yee, N. L. Ng, M. R. Canagaratna, C. L. Loza, K. A. Schilling, R. L. N. Yatawelli, J. A. Thornton, P. J. Ziemann, R. C. Flagan, and J. H. Seinfeld. *Atmos. Chem. Phys.* **2012**, *12*, 11795-11817.

Appendix K

Role of Ozone in SOA Formation from Alkane Photooxidation¹³

¹³ Reproduced by permission from “Role of ozone in SOA formation from alkane photooxidation” by X. Zhang, R. H. Schwantes, M. M. Coggon, C. L. Loza, K. A. Schilling, R. C. Flagan, and J. H. Seinfeld. *Atmos. Chem. Phys.* **2014**, *14*, 1733-1753.

Appendix L

Organic Aerosol Formation from the Reactive Uptake of Isoprene Epoxydiols (IEPOX) onto Non-Acidified Inorganic Seeds¹⁴

¹⁴ Reproduced by permission from “Organic aerosol formation from the reactive uptake of isoprene epoxydiols (IEPOX) onto non-acidified inorganic seeds” by T. B. Nguyen, M. M. Coggon, K. H. Bates, X. Zhang, R. H. Schwantes, K. A. Schilling, C. L. Loza, R. C. Flagan, P. O. Wennberg, and J. H. Seinfeld. *Atmos. Chem. Phys.* **2014**, *14*, 3497-3510.

Appendix M

A Chemically Relevant Artificial Fingerprint Material for the Cross Comparison of Mass Spectrometry Techniques¹⁵

¹⁵ Reproduced by permission from “A Chemically Relevant Artificial Fingerprint Material for the Cross Comparison of Mass Spectrometry Techniques” by E. R. Sisco, J. Staymates, and K. Schilling, Submitted to *Foren. Sci. Intl.*

Appendix N

Supporting Information from “Secondary Organic Aerosol Composition from C₁₂ Alkanes”¹⁶

¹⁶ Reproduced by permission from “Secondary Organic Aerosol Composition from C₁₂ Alkanes” by K. A. Schilling, F. H. Fehsenfeld, L. D. Yee, C. L. Loza, M. M. Coggon, R. Schwantes, X. Zhang, N. F. Dalleska, J. H. Seinfeld. *J. Phys. Chem. A*, Article ASAP, DOI: 10.1021/jp501779w, 9 May 2014.

Appendix O

Supporting Information from “Chemical Composition of Toluene and Cresol Secondary Organic Aerosol”¹⁷

¹⁷ Reproduced by permission from “Chemical Composition of Toluene and Cresol Secondary Organic Aerosol: Effect of NO” by K. A. Schilling, H. Lignell, M. M. Coggon, R. H. Schwantes, X. Zhang, and J. H. Seinfeld. In submission to *Environmental Science and Technology*, 2015.

Size distribution dynamics reveal particle-phase chemistry in organic aerosol formation

Manabu Shiraiwa^{a,b}, Lindsay D. Yee^c, Katherine A. Schilling^a, Christine L. Loza^a, Jill S. Craven^a, Andreas Zuend^{a,d}, Paul J. Ziemann^e, and John H. Seinfeld^{a,c,1}

Divisions of ^aChemistry and Chemical Engineering and ^cEngineering and Applied Science, California Institute of Technology, Pasadena, CA 91125; ^eAir Pollution Research Center, University of California, Riverside, CA 92521; ^bMultiphase Chemistry Department, Max Planck Institute for Chemistry, 55128 Mainz, Germany; and ^dInstitute for Atmospheric and Climate Science, Eidgenössische Technische Hochschule Zürich, 8092 Zurich, Switzerland

Edited by Mark H. Thiemens, University of California at San Diego, La Jolla, CA, and approved June 13, 2013 (received for review April 21, 2013)

Organic aerosols are ubiquitous in the atmosphere and play a central role in climate, air quality, and public health. The aerosol size distribution is key in determining its optical properties and cloud condensation nucleus activity. The dominant portion of organic aerosol is formed through gas-phase oxidation of volatile organic compounds, so-called secondary organic aerosols (SOAs). Typical experimental measurements of SOA formation include total SOA mass and atomic oxygen-to-carbon ratio. These measurements, alone, are generally insufficient to reveal the extent to which condensed-phase reactions occur in conjunction with the multigeneration gas-phase photooxidation. Combining laboratory chamber experiments and kinetic gas-particle modeling for the dodecane SOA system, here we show that the presence of particle-phase chemistry is reflected in the evolution of the SOA size distribution as well as its mass concentration. Particle-phase reactions are predicted to occur mainly at the particle surface, and the reaction products contribute more than half of the SOA mass. Chamber photooxidation with a midexperiment aldehyde injection confirms that heterogeneous reaction of aldehydes with organic hydroperoxides forming peroxyhemiacetals can lead to a large increase in SOA mass. Although experiments need to be conducted with other SOA precursor hydrocarbons, current results demonstrate coupling between particle-phase chemistry and size distribution dynamics in the formation of SOAs, thereby opening up an avenue for analysis of the SOA formation process.

gas-particle interactions | heterogeneous chemistry | intermediate volatility organic compounds | alkane

Laboratory chamber experiments are the basis on which gas-phase photooxidation mechanisms and subsequent formation and evolution of secondary organic aerosols (SOAs) are evaluated. Despite major advances in understanding of the mechanisms of SOA formation, the long-standing question of the relative contributions of gas- vs. particle-phase routes to SOA formation and aging for the major classes of SOA-forming hydrocarbons is still unresolved (1). Photooxidation of parent hydrocarbons and subsequent multigeneration gas-phase chemistry produce an array of semivolatile organic compounds (SVOCs) that partition into the particle phase (2, 3). At the same time, particle-phase reactions involving these condensed SVOCs can lead to formation of low-volatility compounds, such as oligomers and other high molecular mass compounds (4–6). The extent to which particle-phase chemistry is important in SOA formation for each of the major classes of SOA precursors remains unclear. We show here that the evolution of the particle-size distribution, a measurement routinely made in chamber experiments of SOA formation, holds a key to evaluating the importance of particle-phase chemistry.

Current atmospheric aerosol models underpredict ambient SOA mass (1). The missing SOAs can be partly explained by intermediate volatility organic compounds (IVOCs) that may be emitted initially as primary organic aerosol but evaporate upon dilution and are subsequently oxidized in the gas phase, yielding

substantial SOA mass (7, 8). Recent modeling studies have demonstrated that IVOCs are expected to be a major precursor of SOAs in megacity outflows (9). Long-chain alkanes, mainly emitted from incomplete fuel combustion (10), constitute a substantial fraction of IVOCs. Here we use dodecane (C₁₂H₂₆), a surrogate compound for IVOCs, to study the connection between the chemical mechanism of SOA formation and the evolution of the size distribution.

Results and Discussion

Dodecane Photooxidation Experiments and Modeling. The photooxidation of dodecane and subsequent SOA formation is studied using the Caltech Environmental Chamber (11, 12). Dodecane at initial concentration of 34 parts per billion (ppb) in the presence of ammonium sulfate seed particles under dry conditions [relative humidity (RH) < 5%] was oxidized by OH radicals at low concentrations of NO_x typical of nonurban conditions. The kinetic multilayer model of gas-particle interactions in aerosols and clouds (KM-GAP) (13) is used to simulate the evolution of SOA mass, the organic atomic oxygen-to-carbon (O:C) ratio, and particle-size distribution in the chamber experiments (Fig. 1). The model treats the following processes explicitly: gas-phase diffusion, reversible adsorption, bulk diffusion, and chemical reactions in the gas and particle phases. The model also accounts for the loss of gas-phase SVOCs to the chamber Teflon wall (14, 15) based on measurements for representative compounds in separate experiments (*SI Materials and Methods, Gas-phase wall loss, Table S1 and S2*). The physical state of the particle bulk is assumed to be semisolid with an average bulk diffusivity of 10⁻¹² cm²·s⁻¹ [a typical value for a semisolid state (16) (*SI Materials and Methods*)], consistent with observations that long-chain alkane-derived SOA particles bounce moderately on the smooth plates of an inertial impactor indicating behavior between that of liquid and glassy particles (17).

In the gas phase, SVOCs resulting from up to five generations of OH oxidation are considered (Fig. 14). Fig 1B shows the span of O:C ratio and gas-phase saturation concentrations for the surrogate SVOCs based on the dodecane oxidation mechanism of Yee et al. (11). Some of the fourth generation products have been established to be multifunctional carbonyl compounds, aldehydes, and ketones. The aldehydes can react with hydroperoxide, hydroxyl, and peroxy-carboxylic acid groups, forming peroxyhemiacetal (PHA), hemiacetal, and acylperoxyhemiacetal, respectively, in the particle phase (2, 11, 18). Ketone functional

Author contributions: M.S., L.D.Y., and J.H.S. designed research; M.S., L.D.Y., K.A.S., C.L.L., and J.S.C. performed research; M.S., L.D.Y., K.A.S., C.L.L., J.S.C., A.Z., and P.J.Z. analyzed data; M.S., L.D.Y., K.A.S., and C.L.L. wrote the supplement; and M.S., and J.H.S. wrote the paper.

The authors declare no conflict of interest.

This article is a PNAS Direct Submission.

¹To whom correspondence should be addressed. E-mail: seinfeld@caltech.edu.

This article contains supporting information online at www.pnas.org/lookup/suppl/doi:10.1073/pnas.1307501110/-DCSupplemental.

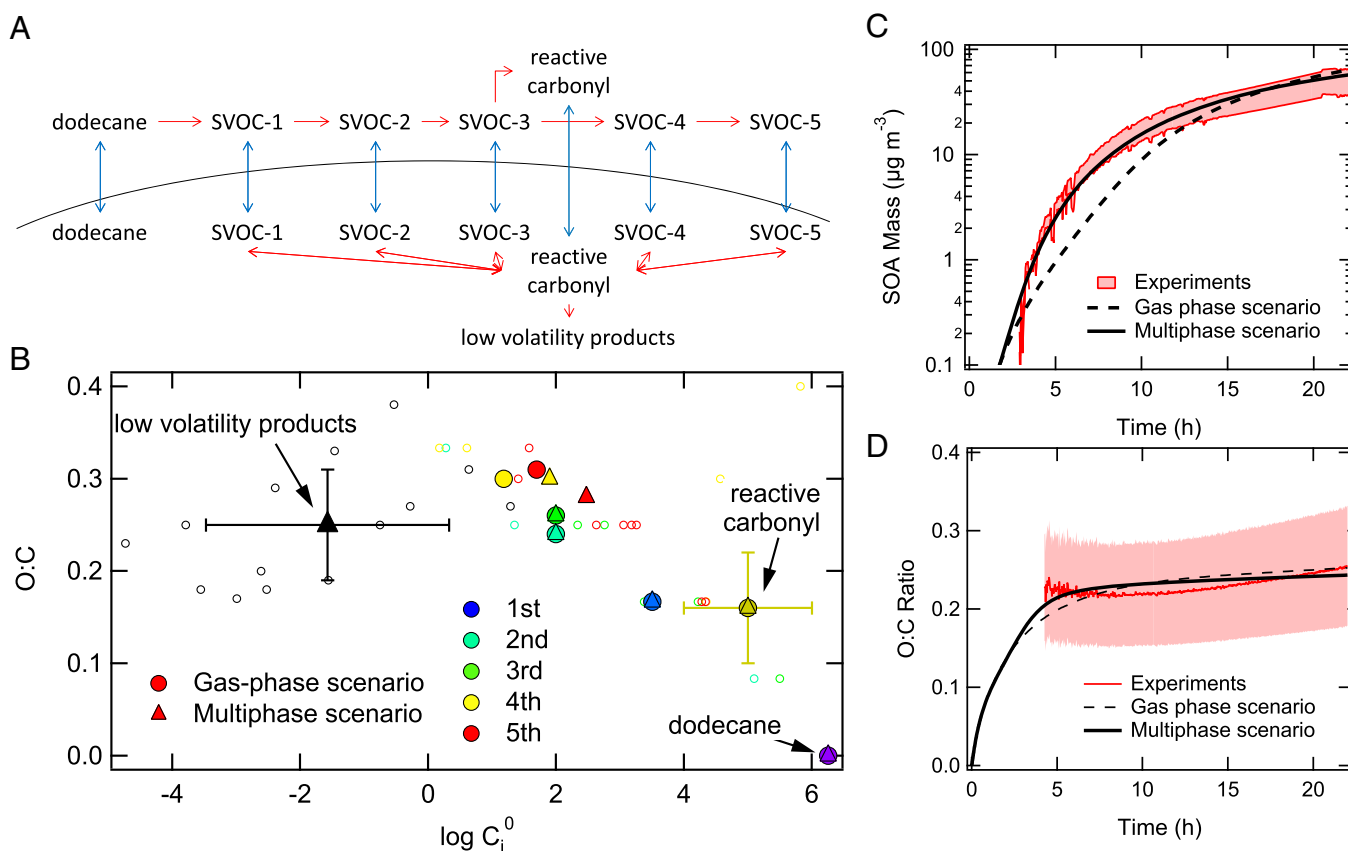


Fig. 1. Modeling secondary organic aerosol formation from dodecane photooxidation. (A) Schematic of the mass transport (blue arrows) and chemical reactions (red arrows) in the dodecane SOA system. Multigeneration of SVOCs is considered in the gas phase. The multiphase scenario includes second-order reactions (red double arrows) between reactive carbonyl and SVOCs forming low-volatility products in the particle phase. (B) O:C ratios for products of dodecane oxidation vs. their predicted gas-phase saturation concentration ($\mu\text{g}\cdot\text{m}^{-3}$) over the pure (subcooled) liquids (C_i^0). The smaller symbols indicate individual products predicted in the dodecane photooxidation chemical mechanism developed by Yee et al. (11). Color indicates the gas-phase generation in which compound is formed. These compounds include reactive carbonyl compounds (fourth generation). Black symbols indicate particle-phase products. The large solid circles and triangles indicate the surrogate SVOC compounds in the gas-phase and multiphase scenarios, respectively. Measured (red) and modeled SOA mass concentration (C) and O:C ratio (D) with the gas-phase (dashed line) and multiphase (solid line) scenarios, respectively. The upper and lower red lines in the C correspond to upper and lower bound wall loss corrections, respectively. The measured O:C ratio is subject to $\pm 30\%$ uncertainty (12).

groups can react with hydroxyl groups, catalyzed by acids, forming a variety of oligomers (4). These products have significantly lower volatility than their gas-phase precursors, as shown for PHA by the black triangles in Fig. 1B. We evaluate the potential effect of particle-phase chemistry on SOA formation by simulating two distinct scenarios. In the “multiphase” model scenario, the formation of low-volatility products arising from particle-phase chemistry is considered whereas, in the “gas-phase” scenario, only gas-phase reactions are accounted for. In the kinetic model simulations, the volatility and O:C ratio of each surrogate product are chosen to lie in the range of those of corresponding individual compounds, as shown by the large solid and triangle markers in Fig. 1B for the gas and multiphase scenarios, respectively. Note that the O:C ratios of later generation gas-phase and particle-phase products are both ~ 0.25 . Fig. 1C shows the experimental observations of SOA mass concentration for the cases of two limiting particle-wall loss corrections (19, 20): (i) wall-deposited particles are assumed to cease interaction with the gas phase (lower red line), and (ii) wall-deposited particles are assumed to continue interacting with the gas phase as if they were still suspended (upper red line). Fig. 1D shows the measured O:C ratio (12). Both scenarios, gas-phase (dashed lines) and multiphase (solid lines), are able to match the observed SOA mass concentration and O:C ratio within the experimental uncertainties, even though the gas-phase scenario

initially underestimates SOA mass for times up to ~ 10 h. This result exemplifies the ambiguity that arises in assessing the chemical routes to SOA formation based solely on SOA mass and O:C ratio.

Fig. 2A shows the measured evolution of the particle-size distribution. The mean particle diameter grows from ~ 60 nm to ~ 180 nm over ~ 20 h. The simulated size distribution for the gas-phase scenario is shown in Fig. 2B. In contrast to the observed size distribution, the gas-phase scenario predicts a broad size distribution that is a characteristic also found for quasi-equilibrium growth mechanism (21), in which the condensed SVOCs equilibrate quickly with the gas phase. When SVOCs equilibrate with the particle population, they tend, on average, to partition to larger particles because of their greater absorption capacity and the reduction in equilibrium vapor pressure over the surface compared with that over smaller particles (the Kelvin effect). By contrast, the simulated number size distribution for the multiphase scenario captures the characteristic narrowing of the measured size distribution (Figs. 2C and D, Fig. S1). The evolution of the volume size distribution is also well reproduced by the multiphase scenario (Fig. S2). Evaporation and recondensation of SVOCs tend to be inhibited in this case owing to the formation of low volatility products in the particle phase. The narrowing of the size distribution is characteristic of kinetically limited growth, in which the mass of condensing material is

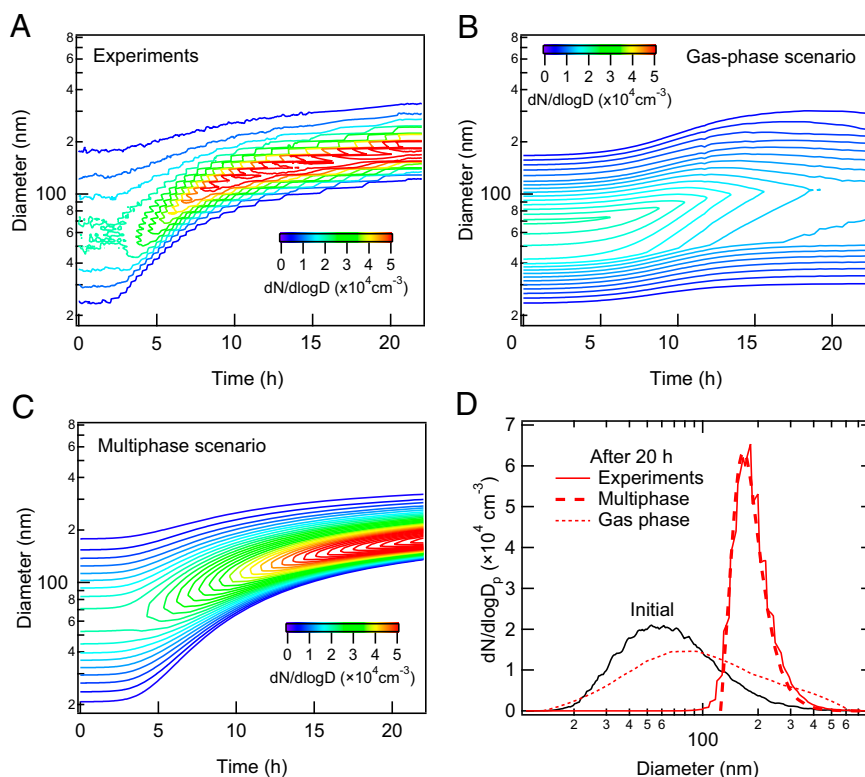


Fig. 2. Evolution of particle number size distribution. Measured (with the upper-bound wall loss correction) (A) and modeled by KM-GAP with gas-phase (B) and multiphase (C) scenarios. (D) Initial number size distribution (black) and measured (red solid line) and modeled number size distribution after 20 h in the gas-phase (dotted line) and multiphase (dashed line) scenarios.

distributed proportional to the particle surface area (21, 22). The second-order reaction rate coefficient between reactive carbonyl and SVOCs (k_{BR}), which is estimated to be $12 \text{ M}^{-1}\cdot\text{s}^{-1}$ ($2 \times 10^{-20} \text{ cm}^3\cdot\text{s}^{-1}$), is found to be the most sensitive parameter in controlling the evolution of the particle size distribution. The evolution of SOA mass and number size distribution obtained with an initial dodecane concentration of 8 ppb was also modeled well using the same parameters of the multiphase scenario (Fig. S3).

Fig. 3 shows the simulated evolution of the mass concentration ratio of oxidation products in the particle (Fig. 3A) and gas phase (Fig. 3B) in the multiphase scenario. During the first several hours, the particle phase is dominated by first- to third-generation SVOCs, which are progressively converted to higher generation SVOCs in the gas phase and low volatility products in the particle phase. The contribution of particle-phase products to the total SOA budget is predicted to exceed 60% after ~ 5 h. The dominance of low-volatility particle-phase products is consistent with previous studies, in which peroxyhemiacetals were found to be major products in SOA derived from oxidation of alkenes (1-tetradecene) (23, 24), aromatic hydrocarbons (toluene) (25, 26), and monoterpenes (α - and β -pinene) (27).

Fig. 3C shows the simulated radial profile of the production rate of low-volatility products along with the evolution of particle radius. The production rate becomes substantial, with a rate of $>2 \times 10^{17} \text{ cm}^{-3}\cdot\text{s}^{-1}$ in the surface layer after ~ 4 h when SOA mass starts growing (Fig. 1C). The particle-phase reactions are predicted to occur mainly at and near the surface, consistent with a product analysis study suggesting that PHA formation should occur mainly at the particle surface (24). Fig. 3D shows the measured evolution of gas-phase C_6 -carboxylic acid, which is a fourth-generation product and a proxy for the expected formation of aldehydes (11). Aerosol mass spectrometer (AMS)

ions at mass-to-charge ratios (m/z) of 183 and 215 are also shown, which are representative fragments from the carbonyl hydroperoxide (CARBROOH; $\text{C}_{12}\text{H}_{24}\text{O}_3$) and its derived PHA (11). The onset of gas-phase aldehyde, particle-phase PHA, SOA mass growth, and production rate of low-volatility products at ~ 4 h suggests that the formation of PHA triggers initial SOA growth.

Tridecanal Injection Experiment. To evaluate the hypothesis concerning the role of PHA production in SOA formation, we have conducted an additional chamber experiment with intentional injection of the aldehyde tridecanal (Fig. 4). Dodecane (initial concentration of 239 ppb) was photooxidized for 4 h under low- NO_x and dry conditions in the presence of ammonium sulfate seed particles, at which time chamber UV lights were turned off to halt production of OH radicals, ceasing gas-phase chemistry and SOA growth. After 6 h, injection of 9.5 ppb tridecanal into the chamber led to a rapid increase in organic mass (measured by the AMS) of $\sim 45 \mu\text{g}\cdot\text{m}^{-3}$ within 1 h. Simultaneously, the tracer ions for gas-phase CARBROOH decreased and that for particle-phase CARBROOH-derived PHA increased. The same trend was also observed for organic hydroperoxide and its derived PHA (Fig. S4). Direct analysis in real time mass spectrometry (DART-MS) spectra confirm the formation of high molecular mass compounds such as PHA and oligomers (Fig. S5 and Table S3). Note that the observed SOA growth cannot be explained by physical uptake of tridecanal, as its vapor pressure is too high ($C_0 = \sim 10^5 \mu\text{g}\cdot\text{m}^{-3}$).

As the observed particle growth is predicted to be essentially a result of the particle-phase reaction, the second-order reaction rate between tridecanal and SVOCs can be estimated to lie in the range $0.3\text{--}12 \text{ M}^{-1}\cdot\text{s}^{-1}$ (*SI Materials and Methods, Estimation of the particle-phase reaction rate coefficient*). This range is consistent with the estimated k_{BR} of $12 \text{ M}^{-1}\cdot\text{s}^{-1}$ derived from the

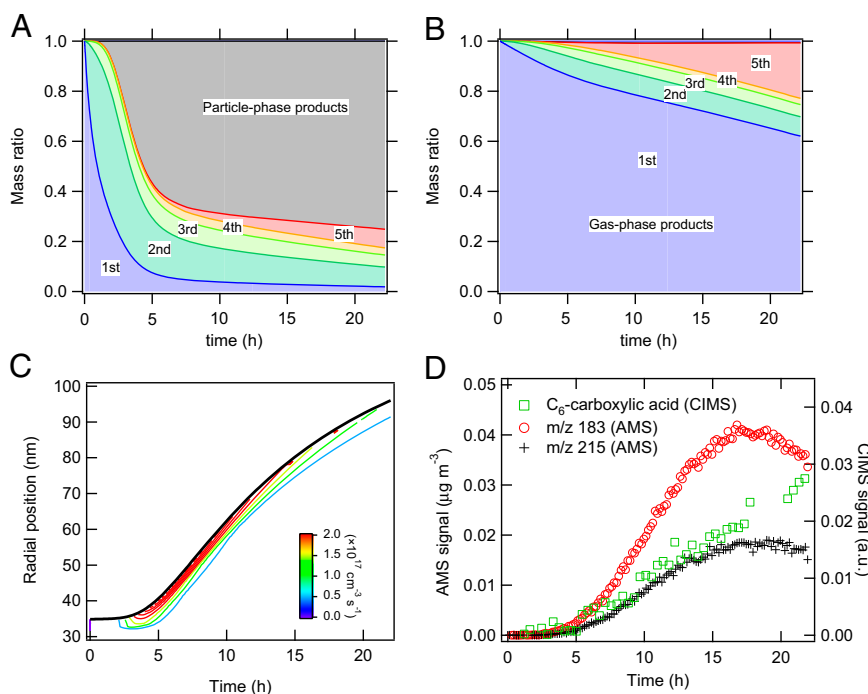


Fig. 3. Relative contribution and distribution of gas-phase and particle-phase reaction products. Mass concentration ratios of multigeneration dodecane gas-phase oxidation products (colored) and particle phase products (gray) in the particle phase (A) and the gas phase (B), modeled with the multiphase scenario. (C) Modeled radial profile of the production rate ($\text{cm}^{-3}\cdot\text{s}^{-1}$) of particle-phase products for an initially 35-nm radius particle. The solid black line indicates the evolution of the particle radius. (D) Temporal evolution of a C_6 -carboxylic acid (tracer for aldehyde/reactive carbonyl) in the gas phase monitored by the CIMS. Two characteristic tracers of peroxyhemiacetal formation in the particle phase are measured by the AMS at m/z 183 ($\text{C}_{12}\text{H}_{23}\text{O}^+$) and m/z 215 ($\text{C}_{12}\text{H}_{23}\text{O}_3^+$).

KM-GAP modeling of the dodecane photooxidation experiments. Note that literature values of k_{BR} for uncatalyzed reactions of various hydroperoxides and aldehydes in different solvents range from 10^{-4} to $0.06 \text{ M}^{-1}\cdot\text{s}^{-1}$ (18, 28). The value of k_{BR} inferred from the observations indicates that the reactions must be catalyzed (by two orders of magnitude) by the presence

of acids (4, 18, 24) generated in the low- NO_x dodecane mechanism (11). This magnitude of enhancement seems reasonable, as in the case of hemiacetal formation from acetaldehyde plus methanol, the presence of 1 M acetic acid increases the rate constants by a factor of ~ 250 (18).

Summary and Implications. The results of the current work have a number of implications for SOA models. Although the dynamics of an aerosol size distribution reflects the mechanism of growth (22, 29), we demonstrate here that it provides a key constraint in interpreting laboratory and ambient SOA formation. Aldehyde injection experiments suggest that peroxyhemiacetal formation by heterogeneous reactions between aldehydes and organic hydroperoxides can have a major impact on SOA formation. This work, although carried out specifically for the long chain alkane dodecane, is expected to be widely applicable to other major classes of SOA precursors. SOA consists of a myriad of organic compounds containing carbonyl, hydroxyl, and carboxyl groups (among other functional groups), which can generally undergo heterogeneous/multiphase reactions forming low-volatility products such as oligomers and other high molecular mass compounds (18). The importance of such a peroxyhemiacetal formation pathway depends on the reaction rate constants and concentrations of reactants as well as on particle acidity and hygroscopicity because the reactions can be acid-catalyzed (4, 30, 31) or hydration-based (32), depending on the environmental conditions and particle composition. Heterogeneous reactivity of SOA particles can be regulated by relative humidity and temperature, which will affect particle viscosity and bulk diffusivity (16, 33). If particle-phase chemistry is indeed central to SOA growth in general, the size-resolved SOA formation is better described in terms of kinetically limited condensational growth, rather than solely by thermodynamic equilibrium partitioning (22, 34). Analysis of field and laboratory data on size-distribution

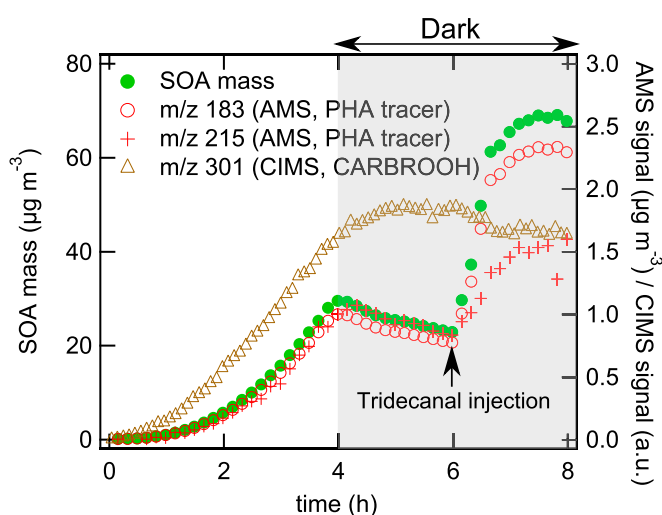


Fig. 4. Intentional aldehyde (tridecanal) injection experiments. SOA mass concentration and carbonyl hydroperoxide (CARBROOH; $\text{C}_{12}\text{H}_{24}\text{O}_3$) signal monitored by CIMS at m/z 301 and CARBROOH-derived peroxyhemiacetals monitored by the AMS at m/z 183 ($\text{C}_{12}\text{H}_{23}\text{O}^+$) and m/z 215 ($\text{C}_{12}\text{H}_{23}\text{O}_3^+$). UV lights are switched off after 4 h, and 9.5 ppb tridecanal is injected to the chamber at 6 h.

dynamics and heterogeneous chemistry for various SOA precursors and environmental conditions may lead to more robust predictions of chemical composition and particle-size distribution, with relevance to properties such as radiative forcing and cloud condensation nuclei activity.

Materials and Methods

Chamber Experiments. Experiments were carried out in the Teflon reactors in the Caltech Environmental Chamber. Aqueous H₂O₂ solution was evaporated into the chamber, followed by the atomization of an aqueous ammonium sulfate solution generating seed particles, which were subsequently dried. Liquid dodecane was evaporated into the chamber to achieve 34 ppb gas-phase mixing ratio of dodecane. After an hour of mixing, the blacklights were turned on, initiating generation of the OH radical from H₂O₂ photolysis. The gas-phase composition of oxidation products was monitored using a chemical ionization mass spectrometer (CIMS) (11). The particle-phase chemical composition, including the atomic oxygen-to-carbon (O:C) ratio of SOA, was measured by an Aerodyne high-resolution time-of-flight aerosol mass spectrometer (HR-ToF-AMS) (12). In addition, particle-phase chemical composition was analyzed offline using direct analysis in real time mass spectrometry (DART-MS). Particle number size distribution was measured using a cylindrical differential mobility

analyzer coupled to a condensation particle counter. More details are available in *SI Materials and Methods*.

Kinetic Modeling. The kinetic multilayer model of gas-particle interactions in aerosols and clouds (KM-GAP) (13) is used for simulations. For size-resolved simulations, the bin method with full-moving size structure is used. KM-GAP consists of a number of compartments and layers in which semivolatile species can undergo mass transport and chemical reactions in the gas and particle phases. The required kinetic parameters for surrogate SVOCs include the gas-phase first-order reaction rate coefficients, the surface accommodation coefficient, the molecular desorption lifetime, gas and bulk diffusion coefficients, and the second-order bulk reaction rate coefficient for the reaction of reactive carbonyl with SVOCs (Table S1 and S2). The dynamics of compound concentrations in the gas and particle phases and of the aerosol size distribution were computed by solving the mass balance, transfer, and reaction rate equations. More details are described in *SI Materials and Methods*.

ACKNOWLEDGMENTS. We thank Xuan Zhang and Matt Coggon for assistance in the experiments. This work was supported by US Department of Energy Grant DE-SC0006626 and National Science Foundation Grant AGS-1057183. M.S. is supported by a Japan Society for the Promotion of Science Postdoctoral Fellowship for Research Abroad.

- Hallquist M, et al. (2009) The formation, properties and impact of secondary organic aerosol: Current and emerging issues. *Atmos Chem Phys* 9(14):5155–5235.
- Kroll JH, Seinfeld JH (2008) Chemistry of secondary organic aerosol: Formation and evolution of low-volatility organics in the atmosphere. *Atmos Environ* 42(16):3593–3624.
- Jimenez JL, et al. (2009) Evolution of organic aerosols in the atmosphere. *Science* 326(5959):1525–1529.
- Jang MS, Czoschke NM, Lee S, Kamens RM (2002) Heterogeneous atmospheric aerosol production by acid-catalyzed particle-phase reactions. *Science* 298(5594):814–817.
- Kalberer M, et al. (2004) Identification of polymers as major components of atmospheric organic aerosols. *Science* 303(5664):1659–1662.
- Wang L, et al. (2010) Atmospheric nanoparticles formed from heterogeneous reactions of organics. *Nat Geosci* 3(4):238–242.
- Robinson AL, et al. (2007) Rethinking organic aerosols: semivolatile emissions and photochemical aging. *Science* 315(5816):1259–1262.
- Presto AA, et al. (2009) Intermediate-volatility organic compounds: A potential source of ambient oxidized organic aerosol. *Environ Sci Technol* 43(13):4744–4749.
- Lee-Taylor J, et al. (2011) Explicit modeling of organic chemistry and secondary organic aerosol partitioning for Mexico City and its outflow plume. *Atmos Chem Phys* 11(24):13219–13241.
- Schauer JJ, Kleeman MJ, Cass GR, Simoneit BRT (1999) Measurement of emissions from air pollution sources. 2. C₁ through C₃₀ organic compounds from medium duty diesel trucks. *Environ Sci Technol* 33(10):1578–1587.
- Yee LD, et al. (2012) Secondary organic aerosol formation from low-NO_x photooxidation of dodecane: Evolution of multigeneration gas-phase chemistry and aerosol composition. *J Phys Chem A* 116(24):6211–6230.
- Craven JS, et al. (2012) Analysis of secondary organic aerosol formation and aging using positive matrix factorization of high-resolution aerosol mass spectra: Application to the dodecane low-NO_x system. *Atmos Chem Phys* 12(24):11795–11817.
- Shiraiwa M, Pfrang C, Koop T, Pöschl U (2012) Kinetic multi-layer model of gas-particle interactions in aerosols and clouds (KM-GAP): Linking condensation, evaporation and chemical reactions of organics, oxidants and water. *Atmos Chem Phys* 12(5):2777–2794.
- Matsunaga A, Ziemann PJ (2010) Gas-wall partitioning of organic compounds in a Teflon film chamber and potential effects on reaction product and aerosol yield measurements. *Aerosol Sci Technol* 44(10):881–892.
- Loza CL, et al. (2010) Characterization of vapor wall loss in laboratory chambers. *Environ Sci Technol* 44(13):5074–5078.
- Shiraiwa M, Ammann M, Koop T, Pöschl U (2011) Gas uptake and chemical aging of semisolid organic aerosol particles. *Proc Natl Acad Sci USA* 108(27):11003–11008.
- Saukko E, et al. (2012) Humidity-dependent phase state of SOA particles from biogenic and anthropogenic precursors. *Atmos Chem Phys* 12(16):7517–7529.
- Ziemann PJ, Atkinson R (2012) Kinetics, products, and mechanisms of secondary organic aerosol formation. *Chem Soc Rev* 41(19):6582–6605.
- Loza CL, et al. (2012) Chemical aging of m-xylene secondary organic aerosol: Laboratory chamber study. *Atmos Chem Phys* 12(1):151–167.
- Weitkamp EA, Sage AM, Pierce JR, Donahue NM, Robinson AL (2007) Organic aerosol formation from photochemical oxidation of diesel exhaust in a smog chamber. *Environ Sci Technol* 41(20):6969–6975.
- Shiraiwa M, Seinfeld JH (2012) Equilibration timescale of atmospheric secondary organic aerosol partitioning. *Geophys Res Lett* 39:L24801.
- Riipinen I, et al. (2011) Organic condensation: A vital link connecting aerosol formation to cloud condensation nuclei (CCN) concentrations. *Atmos Chem Phys* 11(8):3865–3878.
- Tobias HJ, Docherty KS, Beving DE, Ziemann PJ (2000) Effect of relative humidity on the chemical composition of secondary organic aerosol formed from reactions of 1-tetradecene and O₃. *Environ Sci Technol* 34(11):2116–2125.
- Tobias HJ, Ziemann PJ (2000) Thermal desorption mass spectrometric analysis of organic aerosol formed from reactions of 1-tetradecene and O₃ in the presence of alcohols and carboxylic acids. *Environ Sci Technol* 34(11):2105–2115.
- Johnson D, Jenkin ME, Wirtz K, Martin-Reviejo M (2004) Simulating the formation of secondary organic aerosol from the photooxidation of toluene. *Environ Chem* 1(3):150–165.
- Sato K, Hatakeyama S, Imamura T (2007) Secondary organic aerosol formation during the photooxidation of toluene: NO_x dependence of chemical composition. *J Phys Chem A* 111(39):9796–9808.
- Docherty KS, Wu W, Lim YB, Ziemann PJ (2005) Contributions of organic peroxides to secondary aerosol formed from reactions of monoterpenes with O₃. *Environ Sci Technol* 39(11):4049–4059.
- Capouet M, et al. (2008) Modeling aerosol formation in alpha-pinene photo-oxidation experiments. *J Geophys Res Atmos* 113(D2):D02308.
- McMurry PH, Wilson JC (1982) Growth laws for the formation of secondary ambient aerosols: Implications for chemical conversion mechanisms. *Atmos Environ* 16(1):121–134.
- Zhao J, Levitt NP, Zhang R (2005) Heterogeneous chemistry of octanal and 2,4-hexadienal with sulfuric acid. *Geophys Res Lett* 32(9):L09802.
- Iinuma Y, Boge O, Gnauk T, Herrmann H (2004) Aerosol-chamber study of the alpha-pinene/O₃ reaction: Influence of particle acidity on aerosol yields and products. *Atmos Environ* 38(5):761–773.
- Zhao J, Levitt NP, Zhang R, Chen J (2006) Heterogeneous reactions of methylglyoxal in acidic media: Implications for secondary organic aerosol formation. *Environ Sci Technol* 40(24):7682–7687.
- Kuwata M, Martin ST (2012) Phase of atmospheric secondary organic material affects its reactivity. *Proc Natl Acad Sci USA* 109(43):17354–17359.
- Perraud V, et al. (2012) Nonequilibrium atmospheric secondary organic aerosol formation and growth. *Proc Natl Acad Sci USA* 109(8):2836–2841.

Supporting Information

Shiraiwa et al. 10.1073/pnas.1307501110

SI Materials and Methods

KM-GAP Model and Parameters. A kinetic multi-layer model of gas-particle interactions in aerosols and clouds (KM-GAP) (1) is used for simulations. For size-resolved simulations, the bin method with full-moving size structure is used, in which the number concentration of particles in each size bin is conserved but the single particle volumes change (2). The number of size bins is 20 in this study. Coagulation is not considered in the model, as the coagulation timescale of more than a day significantly exceeds the experimental timescale (3, 4). KM-GAP consists of multiple model compartments and layers, respectively: gas phase, near-surface gas phase, sorption layer, surface layer, and a number of bulk layers. KM-GAP treats the following processes explicitly: gas-phase diffusion, gas-surface transport (reversible adsorption), surface-bulk exchange, bulk diffusion, and a selection of chemical reactions in the gas and particle phases. Note that assumptions of instantaneous gas-particle partitioning and homogeneous mixing of the particle bulk, which are often assumed in secondary organic aerosol (SOA) modeling studies (5), were not applied. Surface and bulk layers can either grow or shrink in response to mass transport, which eventually leads to particle growth or shrinkage. Surface-bulk transport and bulk diffusion are treated as mass transport from one bulk layer to the next through first-order transport velocities, which are calculated from the bulk diffusion coefficients (1). As the experiments considered here were conducted under dry conditions, ammonium sulfate is assumed to remain in the form of crystalline seed particles on which SOA condenses. The ammonium sulfate core is represented by one bulk layer, and the organic phase is resolved with 10 bulk layers. Ideal mixing is assumed within the organic phase (mole fraction-based activity coefficients are assumed to be unity), an assumption that is reasonable for an SOA phase formed by the oxidation products of a single parent compound (here dodecane) at conditions of low water content (low relative humidity) (6). Loss of gas-phase semivolatile organic compounds (SVOCs) to the chamber wall (4, 7) is considered using a pseudo-first order gas-phase wall-loss coefficient k_w (see *Gas-phase wall loss* for determination of k_w values). Particle wall loss is not considered in the model; thus, the particle-number concentration stays constant. The dynamics of mass concentrations in the gas and particle phases and of the aerosol size distribution are computed by numerically solving the ordinary differential equations for the mass balance of each model compartment (1).

Five generations of gas-phase oxidation are considered, each generation of which is represented by a surrogate compound. Yee et al. (8) have developed the dodecane low- NO_x gas-phase chemical mechanism based on gas-phase measurements of dodecane photooxidation in conjunction with the Master Chemical Mechanism (MCM, version 3.2) (9). Yee et al. (8) estimated gas-phase saturation concentrations ($\mu\text{g}\cdot\text{m}^{-3}$) over the pure (subcooled) liquids (C_i^0) for oxidation products predicted by a detailed gas-phase chemical mechanism using the EVAPORATION (Estimation of Vapor Pressure of Organics, Accounting for Temperature, Intramolecular, and Nonadditivity effects) method (10), as shown in the open color circles in Fig. 1B. C_i^0 values for surrogate compounds are determined by varying C_i^0 over the predicted range for each generation to fit to the measured SOA mass. The first-order gas-phase reaction rate constants are summarized in Table S1, which is based on the chemical mechanism for dodecane photooxidation developed by Yee et al. (8). Concerning the branching ratio for formation of reactive car-

bonyl compounds in the fourth generation of gas-phase oxidation, a number of compounds are predicted to contain ketone and aldehyde groups by the chemical mechanism (8); thus, we chose to vary the branching ratio over the range of 0.1–0.9. For the simulations presented in Fig. 1, the value of 0.4 is taken. In the multiphase scenario, particle-phase reactions between SVOCs and reactive carbonyls are considered using the second-order bulk reaction rate coefficient (k_{BR}) as listed in Table S1. k_{BR} is assumed to be the same for all reactions. The k_{BR} value was varied to fit the model to the experimental data, resulting in a value of $k_{\text{BR}} = 2 \times 10^{-20} \text{ cm}^3\cdot\text{s}^{-1}$.

The required kinetic parameters for the SVOCs are listed in Table S2, which includes an estimate for the surface accommodation coefficient on a free substrate (α_s), the molecular desorption lifetime (τ_d), gas and bulk diffusion coefficients (D_g , D_b), and the second-order bulk reaction rate coefficient (k_{BR}) for the reaction of reactive carbonyl with SVOCs. D_g is assumed to be $0.05 \text{ cm}^2\cdot\text{s}^{-1}$ (11). Note that the sensitivity studies by varying D_g in the range of 0.02 – $0.2 \text{ cm}^2\cdot\text{s}^{-1}$ revealed that D_g is not critical for describing SOA mass and size distribution, indicating that gas-phase diffusion is not the limiting step in SOA formation. τ_d is assumed to be $1 \mu\text{s}$ (1). α_s is often assumed to be unity in organic aerosol modeling studies (12). Estimates of the accommodation coefficient of SVOC using thermodenuders have resulted in values in the range of 0.28–0.46 (13). α_s is estimated to be 0.3–0.5 by kinetic modeling (1) of evaporation data of dioctyl phthalate (14). In this study, we assume $\alpha_s = 0.5$. A sensitivity study by varying α_s in the range of 0.1–1 in the multiphase scenario revealed that SOA mass and size distribution are not especially sensitive to the value of α_s , suggesting that surface accommodation is not the limiting step in SOA growth in the present case.

Neither the bulk viscosity nor the bulk diffusivity of dodecane SOA is known. Saukko et al. (15) measured a bounce behavior of SOA particles formed from the oxidation of *n*-heptadecane (a long-chain alkane). At low relative humidity (RH), particles bounced from the plate of an inertial low-pressure impactor, indicating that they are not a liquid (of low viscosity), but the particles did not bounce with the behavior of solid or glassy particles; with a bounce fraction of ~ 0.5 , the *n*-heptadecane SOA particles are deemed to be semisolid. The typical bulk diffusivities of multifunctional organic compounds in semisolid phases range from 10^{-20} to $10^{-10} \text{ cm}^2\cdot\text{s}^{-1}$ (16, 17). We assume here that the SOA products from the *n*-dodecane oxidation have similar diffusivities as the *n*-heptadecane SOA. D_b was varied systematically over the given range to fit to the data of SOA mass and size distribution; the optimal value was found to be $10^{-12} \text{ cm}^2\cdot\text{s}^{-1}$. Note that, if the particles are assumed to be liquid with D_b in the range of 10^{-10} to $10^{-5} \text{ cm}^2\cdot\text{s}^{-1}$, indeed size distribution was not reproduced as well as in the case that the particle is assumed to be semisolid. The most sensitive parameters in fitting SOA mass are the gas-phase saturation concentrations ($\mu\text{g}\cdot\text{m}^{-3}$) for SVOCs. The second-order bulk reaction rate coefficient k_{BR} is the most critical parameter in controlling the evolution of the particle number size distribution. This finding is understood as this coefficient affects the average vapor pressures of the condensed SOA species via the conversion of higher-volatility monomers to low-volatility dimers and oligomers.

Dodecane Photooxidation Experiments. Experimental methods. Dodecane photooxidation experiments were conducted in the dual 28 m^3 Caltech Environmental Chambers (3, 18) as described in Yee et al.

(8). The extended OH exposure of more than 22 h was achieved using the experimental chamber protocol of Loza et al. (19). A gas chromatograph with flame ionization detection (GC-FID; Agilent 6890) with an HP-5 column was used to monitor the dodecane decay at 1 h time resolution. A chemical ionization mass spectrometer (CIMS) (20–22) was used for tracking the gas-phase development of several hydroperoxide species, ketones, and acids. The CIMS operated in both positive ionization mode for a mass scan range of 50–200 amu $[M \bullet (H_2O)_n \cdot H]^+$ and negative ionization mode for a mass scan range of 50–300 amu $[M \bullet CF_3O]^-$, $[M \bullet F]^-$, where M is the analyte. NO, NO_x, O₃, temperature, and RH were all monitored. NO and NO_x levels remained below 5 parts per billion (ppb), the lower detection limit of the chemiluminescence analyzer (Horiba; APNA 360), and photochemical simulations (8) confirmed that, at the sufficiently low levels of NO_x, the fate of the alkylperoxy radical (RO₂) is dominated by reaction with HO₂. Initial O₃ levels were 3 ppb, rising to 22 ppb by the end of the experiment. Temperature remained between 296 and 298 K after irradiation began, and RH remained below 5%.

A differential mobility analyzer (TSI Model 3081), coupled with a condensation particle counter (TSI Model 3010), was used for monitoring the particle-size distribution. An Aerodyne high-resolution time-of-flight aerosol mass spectrometer (HR-ToF-AMS) was operated according to protocols described in Yee et al. (8) and Craven et al. (23). Briefly, the HR-ToF-AMS (24) was operated collecting data at 1 min resolution, switching between a higher resolution, lower sensitivity “W” mode and a lower resolution, higher sensitivity “V” mode. Analysis of AMS data were performed according to analysis procedures previously described (24–27). Chamber reactors were flushed for 24 h with purified dry air before each experiment. Then 280 μL of 50% by weight aqueous H₂O₂ solution was injected into a glass trap. The glass trap was submerged in a warm water bath (35–38 °C), and the solution was evaporated by flowing 5 L·min⁻¹ of purified dry air through the trap into the chamber. This resulted in ~4 ppm H₂O₂ concentration in the chamber. A 0.015 M aqueous ammonium sulfate solution was atomized into the chamber until a seed volume of ~11 μm³·cm⁻³ was achieved. Next, 9 μL of *n*-dodecane (Sigma-Aldrich) was injected into a glass bulb and evaporated under gentle heating into a 5 L·min⁻¹ flow of purified dry air delivered to the chamber, resulting in an initial concentration of 34 ppb. After 1 h of mixing, the blacklights were turned on to initiate photooxidation.

With the same procedure, the photooxidation experiments were also conducted with an initial concentration of dodecane of 8 ppb. The AMS was not available for the 8 ppb experiments. For those experiments, the measured SOA mass and particle size distribution are modeled well using the same parameters of the multiphase scenarios for 34 ppb experiment, as shown in Fig. S3. **Particle wall loss.** The upper and lower wall loss corrections bound the amount of aerosol deposited to the Fluorinated ethylene propylene (FEP) Teflon chamber walls during an experiment. To estimate the mass growth rate of wall-deposited particles, the mass growth rate of suspended particles must be determined. We use the Aerosol Parameter Estimation (APE) model described by Pierce et al. (28) for this purpose. The APE model uses the General Dynamic Equation (29) to describe the condensation, coagulation, and wall loss of an aerosol population. The model is initialized with a suspended particle-size distribution at one time step and solves for particle wall loss parameters and a mass growth parameter, F_c (cm·s⁻¹), that produce the best match to the particle size distribution measured at the next time step. In the present case, particle wall loss rate constants are determined in separate particle wall loss experiments (18, 19, 30), and these rate constants are used directly in the model.

Once the mass growth parameters are known, they are applied to particles deposited to the walls. The aerosol General Dynamic

Equation also governs deposited particle size distribution behavior, and deposited particles are assumed not to undergo coagulation. The change in the size distribution for deposited particles is governed by

$$\frac{\partial n_w}{\partial t} = \beta(D_p)n_s(D_p,t) - F_c\omega \left[-\frac{1}{D_p^2}n_w(D_p,t) + \frac{1}{D_p} \frac{\partial n_w(D_p,t)}{\partial D_p} \right], \quad [S1]$$

where n_w is the deposited particle size distribution (cm⁻³), t is time (s), $\beta(D_p)$ is the wall loss rate constant, D_p is the particle diameter (cm), n_s is the suspended particle size distribution (cm⁻³), and ω is a parameter that describes the extent of gas-particle partitioning for deposited particles. Values for ω range from 0 to 1, with $\omega = 0$ representing no gas-particle partitioning to deposited particles whereas $\omega = 1$ describes gas-particle partitioning to deposited particles identical to that to suspended particles. Here, only the limits (0, 1) for values of ω are considered. To determine the deposited particle size distribution, Eq. S1 is solved at each size distribution time step using the value of F_c calculated from the APE model at that time step with constant ω . The wall loss corrected particle-size distribution is calculated by summing the suspended and deposited number size distributions. The wall loss corrected SOA volume concentration is calculated from the wall loss corrected size distribution. To calculate the mass of organic aerosol formed, the seed particle volume concentration is subtracted from the wall loss corrected particle volume concentration, and the resulting organic volume concentration is multiplied by a mean particle density, here 1.12 g·cm⁻³, as determined in a separate nucleation chamber experiment (seed-free), to obtain the organic mass concentration.

Gas-phase wall loss. Gas-phase SVOCs can be absorbed by the Teflon film during the experiments (4, 7). The pseudo-first order gas-phase wall loss coefficient k_w is determined from dark vapor-phase wall loss experiments. Two vapor-phase wall loss experiments were run, using 3,6-octanediol and 2-dodecanone (Sigma-Aldrich), respectively. The hydrocarbon was injected into the reactor, and then the decay was monitored by the CIMS. A first-order wall loss coefficient was calculated from the slope of $\ln C / \ln C_0$ vs. time, where C is the signal for the hydrocarbon and C_0 is the hydrocarbon signal 21 min after completion of the hydrocarbon injection (mixing time). Then 10.7 mg of 3,6-octanediol was weighed out into a glass bulb and gently heated while 5 L·min⁻¹ of dry purified air flowed through to the reactor. There was slight recondensation on the injection line, leading to incomplete delivery to the reactor. The 3,6-octanediol signal dropped by 39% over 14 h, leading to a first-order fit of $k_w = 9.6 \times 10^{-6} \text{ s}^{-1}$. For the 2-dodecanone experiment, 15.5 μL of 2-dodecanone was injected to the chamber, and its signal decayed by 14% over 22 h, resulting in $k_w = 2.2 \times 10^{-6} \text{ s}^{-1}$. Due to difficulties in handling these standards for calibration on the CIMS, the suspended concentration after injection could not be verified to match the target concentration based on the injection amount. Without a calibration factor, the presence of rapid vapor-phase wall loss as observed in Matsunaga and Ziemann (7) cannot be ruled out. If this behavior occurs during the injection or mixing period before C_0 is defined, the true rates should be higher than those calculated here. Therefore, we refer to the calculated k_w as pseudo-first order. If a confident calibration factor could be established on the CIMS, care would still need to be taken to minimize losses due to recondensation in the injection line so that these losses are not falsely attributed to rapid vapor-phase wall loss in the reactor.

For the KM-GAP simulations, k_w of SVOCs was varied between the measured values (2.2×10^{-6} to $9.6 \times 10^{-6} \text{ s}^{-1}$) assuming that all five generations of SVOCs are characterized by

the same k_w value. It is found that the value of k_w does not affect the evolution of the shape of the size distribution but can lead to a lower modeled SOA mass up to $\sim 30\%$. For the simulations of dodecane photooxidation, $k_w = 5 \times 10^{-6} \text{ s}^{-1}$ is assumed.

Tridecanal Injection Experiments. Experimental methods. The tridecanal injection experiment was run in a 24 m^3 FEP teflon (2 mil) reactor. The same gas- and particle-phase instruments as described in the photooxidation experiments in *Dodecane Photooxidation Experiments, Experimental methods* were used, except that a compact-time-of-flight aerosol mass spectrometer (C-ToF-AMS) (31) was used. Injection protocols were also the same, except loadings were modified to speed up the chemical development and to achieve an organic loading sufficient for offline filter analyses [Direct analysis in real time mass spectrometry (DART-MS)]. Then $280 \mu\text{L}$ of aqueous H_2O_2 solution (50% by weight) was injected to achieve a starting concentration of ~ 5 ppm of H_2O_2 in the reactor. The initial *n*-dodecane concentration was 239 ppb as measured by the GC-FID. Throughout the experiment, NO_x levels remained below the lower detection limit of the analyzer, temperature ranged over $21\text{--}22.5^\circ\text{C}$, and RH remained below 10%.

Photooxidation occurred during the first 4 h of the experiment. The remainder of the experiment was conducted in the dark. After 6 h from the start of irradiation, tridecanal (Sigma-Aldrich) was injected. Then 24.5 mg of tridecanal (assuming no line/wall losses) was delivered to the reactor by evaporating it under gentle heating into a flow of $5 \text{ L}\cdot\text{min}^{-1}$ of dry purified air for 30 min. Tridecanal concentration was $9.5 (\pm 2.5)$ ppb following injection, as measured by the GC-FID. Filter sampling took place after the SOA mass peaked starting at hour 9. A total sample volume of $\sim 1.9 \text{ m}^3$ (2 h at $16 \text{ L}\cdot\text{min}^{-1}$) was drawn onto a Teflon filter (47 mm diameter) and analyzed offline using DART-MS.

Estimation of the particle-phase reaction rate coefficient. Tridecanal reacts with SVOCs (e.g., organic hydroperoxides) to form peroxyhemiacetals (PHA) in the particle phase. Thus, the change of the bulk number concentration of PHA $[\text{PHA}]_b$ (cm^{-3}) can be described as follows:

$$\frac{d[\text{PHA}]_b}{dt} = k_{\text{BR,Tri}}[\text{SVOC}]_b[\text{Tri}]_b, \quad [\text{S2}]$$

where $k_{\text{BR,Tri}}$ ($\text{cm}^3\cdot\text{s}^{-1}$) is the second-order reaction rate coefficient between tridecanal and SVOCs. As the increase of the total particle mass concentration C_{tot} ($\mu\text{g}\cdot\text{m}^{-3}$) is predicted to be dominated by PHA formation in the present study, its rate of change can be described using the particle mass concentration of PHA $C_{\text{PHA}}^{\text{PM}}$ ($\mu\text{g}\cdot\text{m}^{-3}$ of air):

$$\begin{aligned} \frac{dC_{\text{tot}}}{dt} &\approx \frac{dC_{\text{PHA}}^{\text{PM}}}{dt} = \frac{M_{\text{PHA}}}{N_A} (10^6 \mu\text{g g}^{-1}) \frac{d[\text{PHA}]_b}{dt} \\ &= \frac{M_{\text{PHA}}}{N_A} (10^6 \mu\text{g g}^{-1}) k_{\text{BR,Tri}}[\text{SVOC}]_b[\text{Tri}]_b, \end{aligned} \quad [\text{S3}]$$

where M_{PHA} is the molar mass of PHA ($\sim 300\text{--}400 \text{ g}\cdot\text{mol}^{-1}$) and N_A is the Avogadro constant ($6.02 \times 10^{23} \text{ mol}^{-1}$). The factor 10^6 is for the unit conversion of g to μg . The average bulk number concentration $[\text{Tri}]_b$ (cm^{-3}) and the average particle-phase mass concentration of tridecanal $C_{\text{Tri}}^{\text{PM}}$ ($\mu\text{g}\cdot\text{m}^{-3}$) can be roughly estimated based on equilibrium gas-particle partitioning theory (32, 33) using its volatility, namely the pure component gas-phase saturation concentration $C_{\text{Tri}}^0 = 1.6 \times 10^5 \mu\text{g}\cdot\text{m}^{-3}$ (34),

$$[\text{Tri}]_b = \frac{C_{\text{Tri}}^{\text{PM}}}{M_{\text{Tri}}/N_A} (10^6 \mu\text{g g}^{-1}) \quad [\text{S4}]$$

$$C_{\text{Tri}}^{\text{PM}} = \frac{C_{\text{Tri}}^{\text{g}}}{C_{\text{Tri}}^0} C_{\text{tot}}, \quad [\text{S5}]$$

where M_{Tri} is the molar mass of tridecanal ($198 \text{ g}\cdot\text{mol}^{-1}$) and $C_{\text{Tri}}^{\text{g}}$ ($\mu\text{g}\cdot\text{m}^{-3}$) is the gas phase mass concentration of tridecanal. Note that this is an approximation as a concentration gradient can exist due to slow bulk diffusion. The initial tridecanal gas-phase number concentration was measured by the CIMS to be $9.5 (\pm 2.5)$ ppb, which corresponds to $C_{\text{Tri}}^{\text{g}} = 77 (\pm 20) \mu\text{g}\cdot\text{m}^{-3}$. $[\text{SVOC}]_b$ can be estimated assuming an average molar mass of SVOC ($\sim 200\text{--}300 \text{ g}\cdot\text{mol}^{-1}$), and a certain fraction (10–100%) of the organic particle content is reactive toward aldehydes, resulting in $[\text{SVOC}]_b \sim 10^{20}$ to 10^{21} cm^{-3} .

Based on Eq. S3, dC_{tot}/dt is constant if $[\text{SVOC}]_b$ and $[\text{Tri}]_b$ are constant. Indeed, C_{tot} increased linearly from $22 \mu\text{g}\cdot\text{m}^{-3}$ at tridecanal injection at 6 h to $61 \mu\text{g}\cdot\text{m}^{-3}$ at 6.7 h (Fig. 4 of the main text), corresponding to $dC_{\text{tot}}/dt = 0.017 \mu\text{g}\cdot\text{m}^{-3}\cdot\text{s}^{-1}$. Inserting these values in Eq. S3, $k_{\text{BR,Tri}}$ can be estimated to be 2×10^{-22} to $2 \times 10^{-20} \text{ cm}^3\cdot\text{s}^{-1}$ (or $0.12\text{--}12 \text{ M}^{-1}\cdot\text{s}^{-1}$). This value is in good agreement with the second-order reaction rate coefficient between reactive carbonyl and SVOCs (k_{BR}) estimated by KM-GAP ($12 \text{ M}^{-1}\cdot\text{s}^{-1}$) in simulating dodecane photooxidation in which different aldehydes and ketones may be relevant reactants.

DART-MS Analysis. Duplicate Teflon filters (PALL Life Sciences; 47 mm diameter, $1.0 \mu\text{m}$ pore size, Teflon membrane) were used for particle collection from the chamber upon stabilization of the aerosol volume for off-line chemical analysis. Chamber air was pulled through two stainless steel filter assemblies containing two filters for 2 h at rates of 16 and $23 \text{ L}\cdot\text{min}^{-1}$, respectively. In the standard chamber filter collection procedure, the upstream filter collected particles, and the downstream filter served to indicate whether breakthrough had occurred or whether gaseous compounds were condensing on the filters. Upon the termination of the collection period, the filters were removed from the assembly with pre-cleaned stainless steel forceps and stored in 20-mL glass vials with Teflon caps, which were sealed with Teflon tape and stored in plastic containers in a freezer maintained at a temperature of -20°C .

Filters were analyzed by direct analysis in real-time mass spectrometry (DART-MS) using a custom-built DART source (J. L. Beauchamp group, Caltech) interfaced to a Thermo LTQ ion trap mass spectrometer; positive mode ionization was used in this analysis. DART-MS is an ambient ionization method originally developed by Cody et al. (35). It achieves positive ionization through the generation of metastable triplet helium and its reaction with atmospheric water. For the final proton transfer step to occur, the analyte's proton affinity must exceed that of water. SOA samples collected on Teflon filters were analyzed by folding the filter in half with clean stainless steel forceps, and placing the folded filter so the DART stream ablated the aerosol-containing edge. Blank filters and the breakthrough test filters were analyzed as experimental controls. Data were analyzed using the Thermo proprietary software program, Xcalibur.

SOA samples were also extracted in a 1:1 mixture of GC grade heptane and acetone (vol/vol) via sonication. The extracts were dried down by a gentle stream of N_2 , then reconstituted in $150 \mu\text{L}$ of 1:1 mixture of GC grade heptane and acetone (vol/vol) for analysis by GC/MS (Varian Saturn 2200) with a programmed temperature vaporization (PTV) inlet, DB-5MS-UI column (30 m, 0.250 mm , $0.25 \mu\text{m}$; Agilent), and electron impact ionization and chemical ionization with methanol. The PTV temperature program was as follows: (i) 45°C , 0.5 min hold; (ii) $180^\circ\text{C min}^{-1}$ ramp to 300°C ; and (iii) 300°C , 46.58 min hold. The oven temperature program was as follows: (i) 65°C , 10 min hold; (ii) $10^\circ\text{C min}^{-1}$ ramp to 300°C ; and (iii) 300°C , 15 min hold.

Table S3 lists major peaks, defined by signal intensity > 5,000 counts for $m/z < 400$ Da; signal intensity > 1,000 counts for $m/z > 400$ Da. Proposed formulae are listed for the ions; matches were assigned when the theoretical mass was within 5 mDa of the measured mass. This mass spectrum was acquired using the AccuToF DART-MS, which was mass-calibrated in positive mode by using PEG-600. The ions with m/z above 400 Da that contain nitrogen may be assigned in two ways: (i) they may be nitrate-containing compounds, resulting from reaction with the background levels of NO_x in the chamber (<5 ppb); or (ii) they may be PHAs or contain peroxide groups, both of which form adducts with ammonia present in trace amounts in laboratory air, and are measured by DART-MS as ammonium adducts ($[\text{M}+17]^+$). The low level of NO_x and the lack of smaller mass organonitrates or alcohols suggest that the ammonium adduct option is more likely in this case.

The mass spectra in Fig. S5 were acquired using the experimental DART source in conjunction with the Thermo LTQ ion trap mass spectrometer with unit mass resolution. Fig. S5A shows a duplicate sample of dodecane SOA; the significant overlap with the data in Table S3 indicates similar performance across DART ion sources. Fig. S5B shows a sample of SOA from the dodecane low- NO_x photooxidation experiment where tridecanal was added in the gas phase to attempt to force oligomerization

by PHA formation. The high-resolution AccuToF DART was unavailable for use at the time of the tridecanal experiment, so only unit mass resolution data were obtained for this sample. From Fig. S5B, one can observe that different high molecular weight species were formed in the tridecanal experiment, and that the added SOA mass was not simply tridecanal condensing onto the particles (i.e., the spectrum is not dominated by m/z 199), so it must have reacted after uptake.

Fig. S6 is an extracted ion chromatogram (EIC) that compares the m/z 183 signal from the heptane/acetone extracted SOA generated in the tridecanal experiment and in the dodecane photooxidation experiment. The mass loadings for each experiment were different; more mass was on the filter for the dodecane experiment than the tridecanal experiment. The m/z 183 is the AMS tracer for PHA; because the GC/MS was run in EI mode, it has the potential to generate similar ions as the AMS. Fig. S6 demonstrates that, in the tridecanal experiment, different m/z 183-producing compounds (presumably PHA) were generated. There is more variety of m/z 183-producing compounds in the dodecane experiment EIC than in the tridecanal experiment EIC; this observation suggests that the addition of tridecanal drove the oligomer-forming reaction toward a few specific products, creating less diversity than in the dodecane experiment.

- Shiraiwa M, Pfrang C, Koop T, Pöschl U (2012) Kinetic multi-layer model of gas-particle interactions in aerosols and clouds (KM-GAP): Linking condensation, evaporation and chemical reactions of organics, oxidants and water. *Atmos Chem Phys* 12(5):2777–2794.
- Jacobson MZ (2005) *Fundamentals of Atmospheric Modeling* (Cambridge Univ. Press, Cambridge), 2nd Ed.
- Cocker DR, 3rd, Flagan RC, Seinfeld JH (2001) State-of-the-art chamber facility for studying atmospheric aerosol chemistry. *Environ Sci Technol* 35(12):2594–2601.
- Loza CL, et al. (2010) Characterization of vapor wall loss in laboratory chambers. *Environ Sci Technol* 44(13):5074–5078.
- Hallquist M, et al. (2009) The formation, properties and impact of secondary organic aerosol: Current and emerging issues. *Atmos Chem Phys* 9(14):5155–5235.
- Zuend A, Seinfeld JH (2012) Modeling the gas-particle partitioning of secondary organic aerosol: The importance of liquid-liquid phase separation. *Atmos Chem Phys* 12(9):3857–3882.
- Matsunaga A, Ziemann PJ (2010) Gas-wall partitioning of organic compounds in a Teflon film chamber and potential effects on reaction product and aerosol yield measurements. *Aerosol Sci Technol* 44(10):881–892.
- Yee LD, et al. (2012) Secondary organic aerosol formation from low- NO_x photooxidation of dodecane: Evolution of multigeneration gas-phase chemistry and aerosol composition. *J Phys Chem A* 116(24):6211–6230.
- Saunders SM, Jenkin ME, Derwent RG, Pilling MJ (2003) Protocol for the development of the Master Chemical Mechanism, MCM v3 (Part A): Tropospheric degradation of non-aromatic volatile organic compounds. *Atmos Chem Phys* 3(1):161–180.
- Compernelle S, Ceulemans K, Muller JF (2011) EVAPORATION: A new vapour pressure estimation method for organic molecules including non-additivity and intramolecular interactions. *Atmos Chem Phys* 11(18):9431–9450.
- Bilde M, Svenningsson B, Monstern J, Rosenorn T (2003) Even-odd alternation of evaporation rates and vapor pressures of C3-C9 dicarboxylic acid aerosols. *Environ Sci Technol* 37(7):1371–1378.
- Riipinen I, et al. (2011) Organic condensation: A vital link connecting aerosol formation to cloud condensation nuclei (CCN) concentrations. *Atmos Chem Phys* 11(8):3865–3878.
- Saleh R, Khlystov A, Shihadeh A (2012) Determination of evaporation coefficients of ambient and laboratory-generated semivolatile organic aerosols from phase equilibration kinetics in a thermodenuder. *Aerosol Sci Technol* 46(1):22–30.
- Vaden TD, Imre D, Beránek J, Shrivastava M, Zelenyuk A (2011) Evaporation kinetics and phase of laboratory and ambient secondary organic aerosol. *Proc Natl Acad Sci USA* 108(6):2190–2195.
- Saukko E, et al. (2012) Humidity-dependent phase state of SOA particles from biogenic and anthropogenic precursors. *Atmos Chem Phys* 12(16):7517–7529.
- Mikhailov E, Vlasenko S, Martin ST, Koop T, Pöschl U (2009) Amorphous and crystalline aerosol particles interacting with water vapor: Conceptual framework and experimental evidence for restructuring, phase transitions and kinetic limitations. *Atmos Chem Phys* 9(2):9491–9522.
- Shiraiwa M, Ammann M, Koop T, Pöschl U (2011) Gas uptake and chemical aging of semisolid organic aerosol particles. *Proc Natl Acad Sci USA* 108(27):11003–11008.
- Keywood MD, Varutbangkul V, Bahreini R, Flagan RC, Seinfeld JH (2004) Secondary organic aerosol formation from the ozonolysis of cycloalkenes and related compounds. *Environ Sci Technol* 38(15):4157–4164.
- Loza CL, et al. (2012) Chemical aging of m-xylene secondary organic aerosol: Laboratory chamber study. *Atmos Chem Phys* 12(1):151–167.
- Paulot F, et al. (2009) Isoprene photooxidation: New insights into the production of acids and organic nitrates. *Atmos Chem Phys* 9(4):1479–1501.
- St Clair JM, McCabe DC, Crounse JD, Steiner U, Wennberg PO (2010) Chemical ionization tandem mass spectrometer for the in situ measurement of methyl hydrogen peroxide. *Rev Sci Instrum* 81(9):094102–094106.
- Crounse JD, Paulot F, Kjaergaard HG, Wennberg PO (2011) Peroxy radical isomerization in the oxidation of isoprene. *Phys Chem Chem Phys* 13(30):13607–13613.
- Craven JS, et al. (2012) Analysis of secondary organic aerosol formation and aging using positive matrix factorization of high-resolution aerosol mass spectra: Application to the dodecane low- NO_x system. *Atmos Chem Phys* 12(24):11795–11817.
- DeCarlo PF, et al. (2006) Field-deployable, high-resolution, time-of-flight aerosol mass spectrometer. *Anal Chem* 78(24):8281–8289.
- Allan JD, et al. (2004) A generalised method for the extraction of chemically resolved mass spectra from Aerodyne aerosol mass spectrometer data. *J Aerosol Sci* 35(7):909–922.
- Aiken AC, DeCarlo PF, Jimenez JL (2007) Elemental analysis of organic species with electron ionization high-resolution mass spectrometry. *Anal Chem* 79(21):8350–8358.
- Aiken AC, et al. (2008) O/C and OM/OC ratios of primary, secondary, and ambient organic aerosols with high-resolution time-of-flight aerosol mass spectrometry. *Environ Sci Technol* 42(12):4478–4485.
- Pierce JR, et al. (2008) Constraining particle evolution from wall losses, coagulation, and condensation-evaporation in smog-chamber experiments: Optimal estimation based on size distribution measurements. *Aerosol Sci Technol* 42(12):1001–1015.
- Seinfeld JH, Pandis SN (2006) *Atmospheric Chemistry and Physics: From Air Pollution to Climate Change* (Wiley, New York).
- Ng NL, et al. (2007) Secondary organic aerosol formation from m-xylene, toluene, and benzene. *Atmos Chem Phys* 7(14):3909–3922.
- Drewnack F, et al. (2005) A new time-of-flight aerosol mass spectrometer (TOF-AMS): Instrument description and first field deployment. *Aerosol Sci Technol* 39(7):637–658.
- Pankow JF (1994) An absorption model of gas-particle partitioning of organic-compounds in the atmosphere. *Atmos Environ* 28(2):185–188.
- Donahue NM, Robinson AL, Stanier CO, Pandis SN (2006) Coupled partitioning, dilution, and chemical aging of semivolatile organics. *Environ Sci Technol* 40(8):2635–2643.
- Weast RC (1982) *Handbook of Chemistry and Physics* (CRC, Boca Raton, FL).
- Cody RB, Laramée JA, Durst HD (2005) Versatile new ion source for the analysis of materials in open air under ambient conditions. *Anal Chem* 77(8):2297–2302.

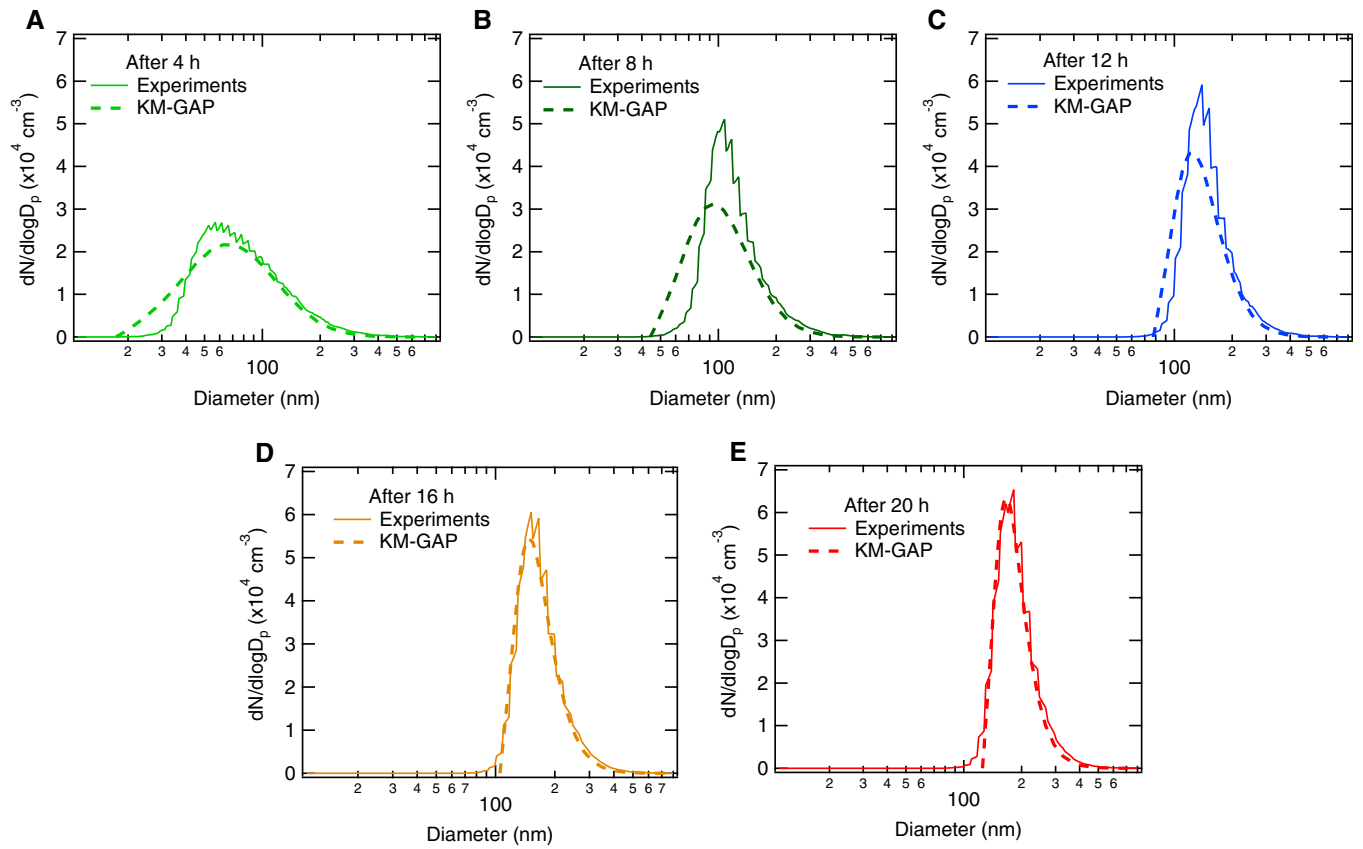


Fig. S1. Experimental (with the upper-bound wall loss correction) and modeled number size distribution ($dN/d\log D$) by KM-GAP with the multiphase scenario after (A) 4 h, (B) 8 h, (C) 12 h, (D) 16 h, and (E) 20 h.

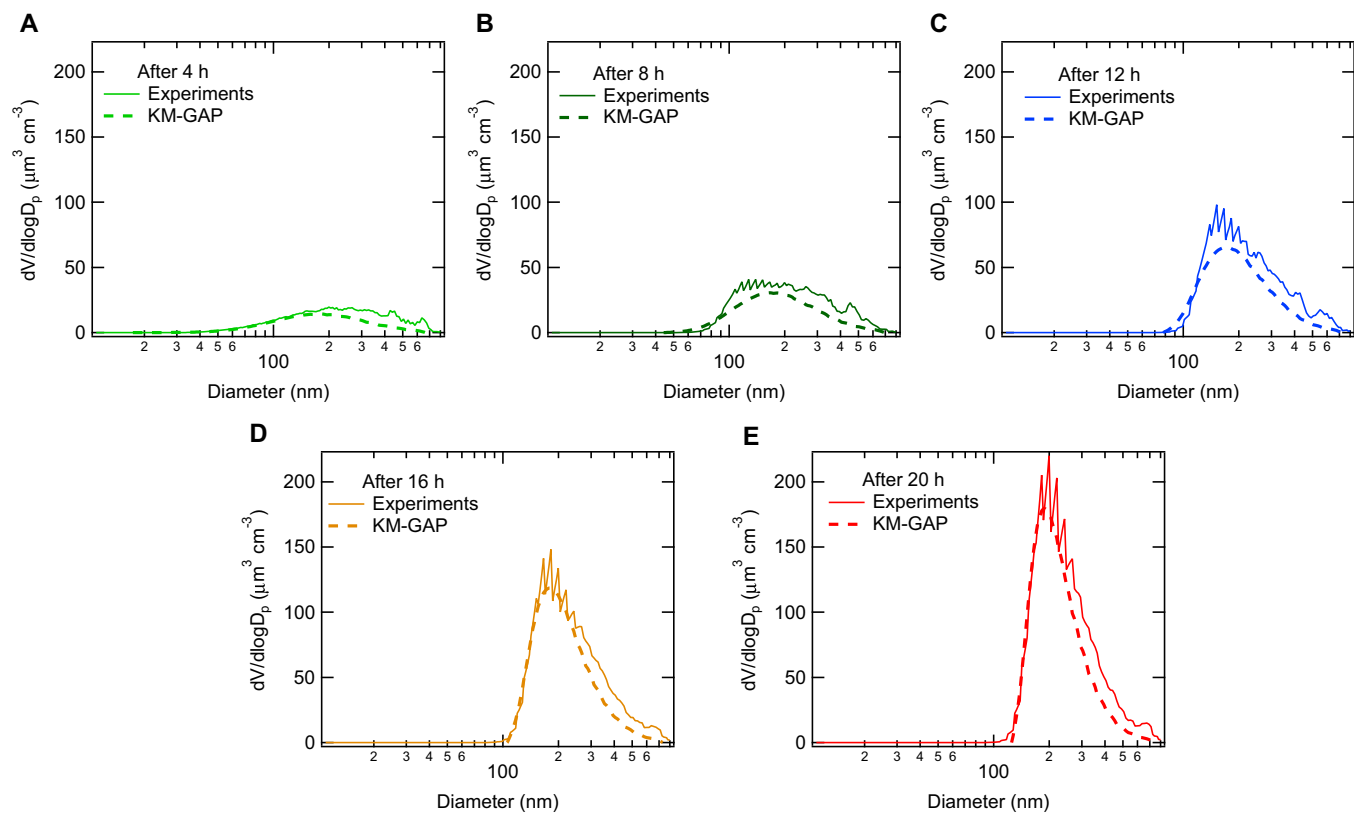


Fig. S2. Experimental (with the upper-bound wall loss correction) and modeled volume size distribution ($dV/d\log D$) by KM-GAP with the multiphase scenario after (A) 4 h, (B) 8 h, (C) 12 h, (D) 16 h, and (E) 20 h.

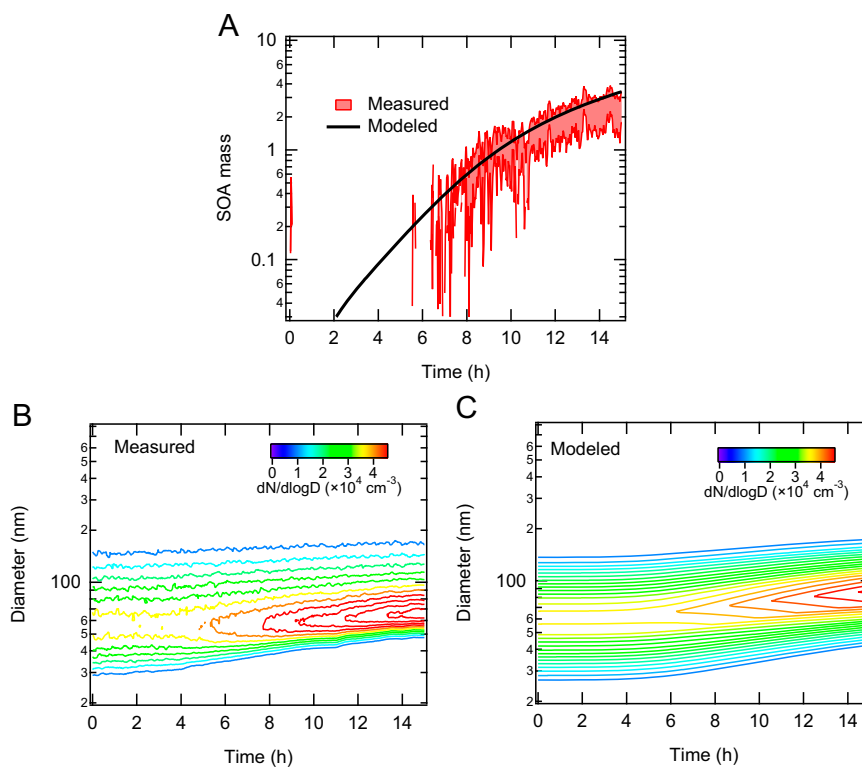


Fig. S3. Modeling SOA formation from dodecane photooxidation. Initial concentration of dodecane was 8 ppb. SOA mass and size distribution is simulated by KM-GAP using the same kinetic parameters of the multiphase scenario used for modeling photooxidation of 34 ppb dodecane (Tables S1 and S2). (A) Measured and modeled SOA mass. The extent of the red lines corresponds to upper and lower bound wall loss corrections. (B) Measured particle number size distribution with upper-bound wall loss correction. (C) Modeled particle number size distribution.

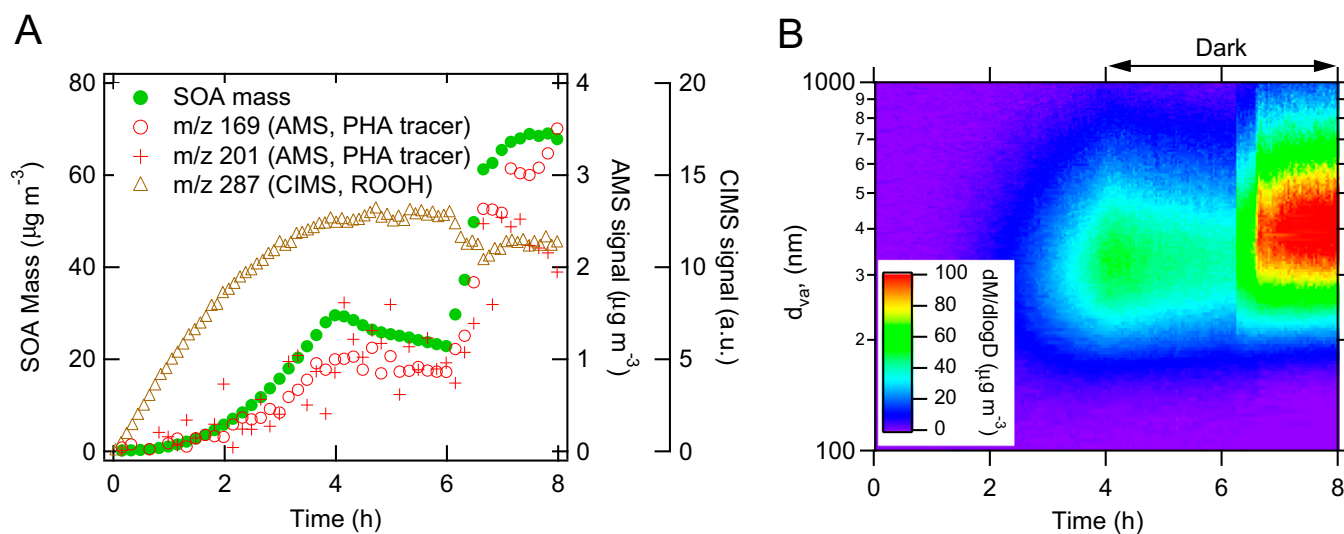


Fig. S4. Intentional aldehyde (tridecanal) injection experiments. Lights are switched off after 4 h, resulting in a net loss of SOA mass due to chamber wall deposition. After 6 h, tridecanal is injected to the chamber. (A) SOA mass, organic hydroperoxide ROOH ($\text{C}_{12}\text{H}_{26}\text{O}_2$) signal monitored by CIMS at m/z 287 and m/z 169 and m/z 201 ions measured by the C-ToF-AMS, which are tracers for ROOH-derived PHA. (B) Organic aerosol mass size distribution measured by the C-ToF-AMS, showing the growth of mean particle diameter from ~ 300 nm to ~ 400 nm due to tridecanal injection.

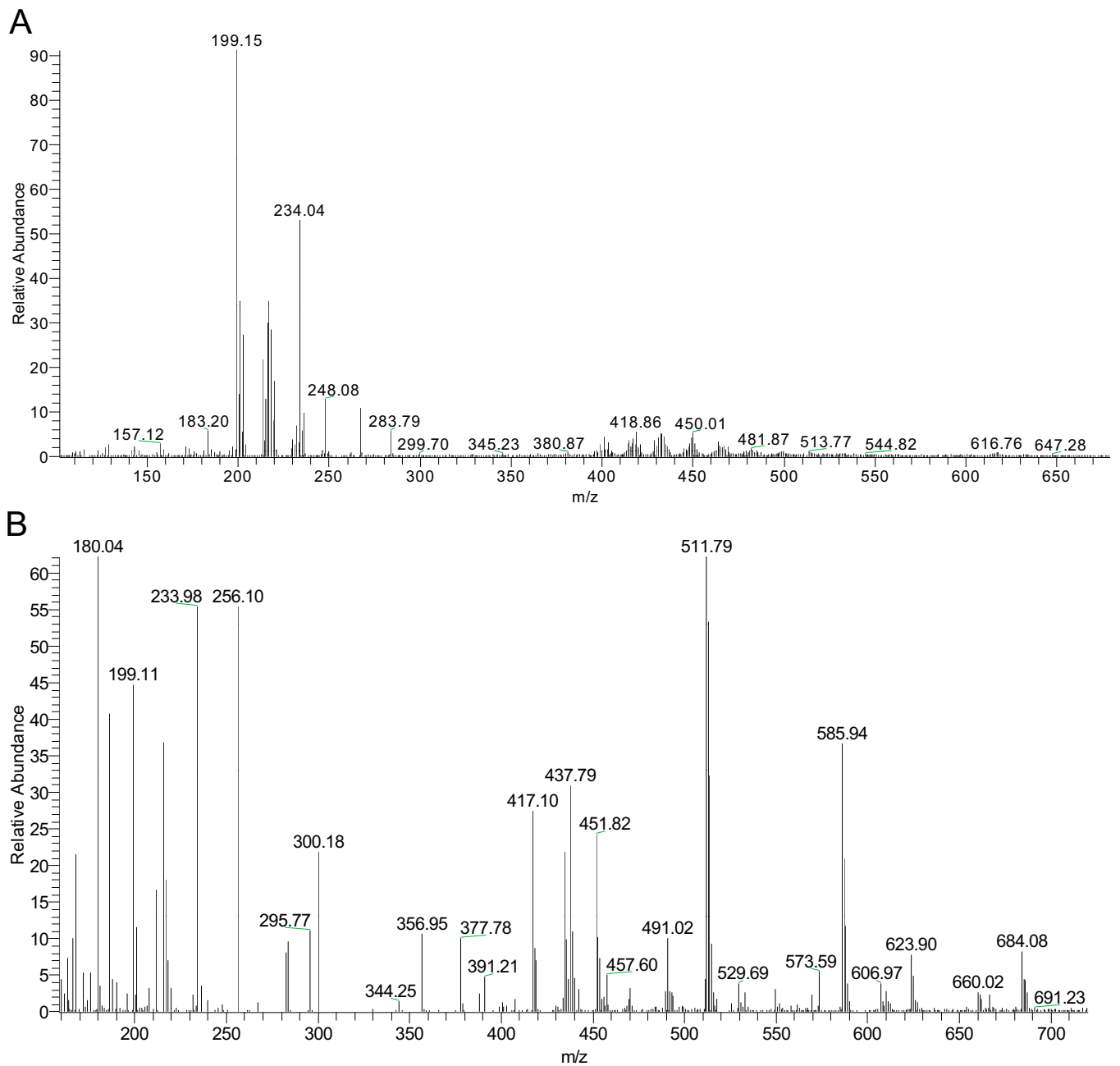


Fig. S5. DART-MS spectrum of SOA formed by photooxidation of dodecane (A) and that of SOA formed in tridecanal injection experiments (B).

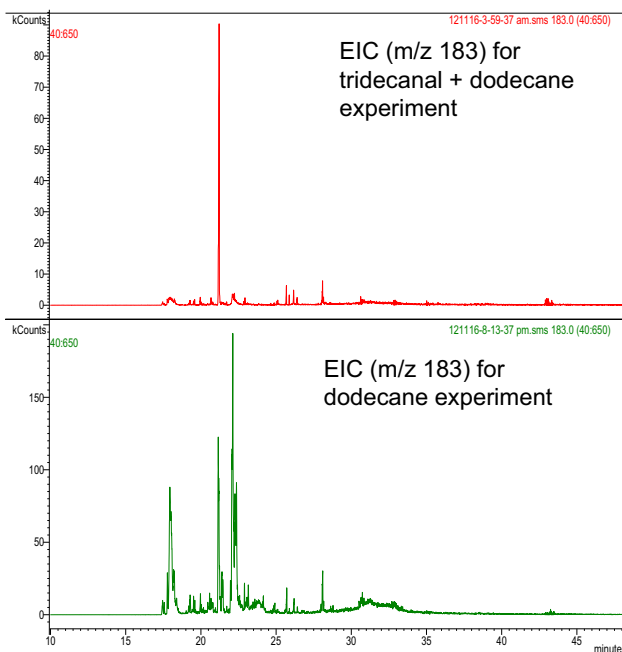


Fig. S6. Extracted ion chromatogram (EIC) that compares the m/z 183 signal from the heptane/acetone extracted SOA generated in the tridecanal experiment (*Upper*) and in the dodecane photooxidation experiment (*Lower*).

Table S1. Gas-phase and particle-phase chemistry considered in KM-GAP

Reaction	Reaction rate coefficient
Gas phase	
dodecane \rightarrow SVOC-1	$2.64 \times 10^{-5} \text{ s}^{-1}$
SVOC-1 \rightarrow SVOC-2	$1.71 \times 10^{-5} \text{ s}^{-1}$
SVOC-2 \rightarrow SVOC-3	$1.32 \times 10^{-4} \text{ s}^{-1}$
SVOC-3 \rightarrow $(1 - \beta)$ SVOC-4 + β reactive carbonyl	$1.85 \times 10^{-4} \text{ s}^{-1}$
SVOC-4 \rightarrow SVOC-5	$1.85 \times 10^{-4} \text{ s}^{-1}$
Particle phase	
SVOC-1 + reactive carbonyl \rightarrow low volatility products	$2 \times 10^{-20} \text{ cm}^3 \text{ s}^{-1}$
SVOC-2 + reactive carbonyl \rightarrow low volatility products	$2 \times 10^{-20} \text{ cm}^3 \text{ s}^{-1}$
SVOC-3 + reactive carbonyl \rightarrow low volatility products	$2 \times 10^{-20} \text{ cm}^3 \text{ s}^{-1}$
SVOC-4 + reactive carbonyl \rightarrow low volatility products	$2 \times 10^{-20} \text{ cm}^3 \text{ s}^{-1}$
SVOC-5 + reactive carbonyl \rightarrow low volatility products	$2 \times 10^{-20} \text{ cm}^3 \text{ s}^{-1}$

Gas-phase reactions are considered using the first-order conversion rate coefficients. In the multiphase scenario, particle-phase reactions are considered using the second-order reaction rate coefficient.

Table S2. Estimated kinetic parameters for the surrogate SVOCs in the KM-GAP simulations

Parameters	Description	Value
$\alpha_{s,0}$	Surface accommodation coefficient on a free substrate	0.5
τ_d	Desorption lifetime	1 μs
D_b	Bulk diffusion coefficient	$10^{-12} \text{ cm}^2 \text{ s}^{-1}$
D_g	Gas diffusion coefficient	$0.05 \text{ cm}^2 \text{ s}^{-1}$

Table S3. Major peaks in DART mass spectrum for dodecane low-NO_x SOA

<i>m/z</i> , Da	Intensity, counts	Proposed formula
127.15	6,253.34	C ₈ H ₁₅ O ⁺
141.16	9,527.53	C ₉ H ₁₇ O ⁺
155.17	9,916.25	C ₁₀ H ₁₉ O ⁺
183.19	10,1521.10	C ₁₂ H ₂₃ O ⁺
197.16	69,729.89	C ₁₂ H ₂₁ O ₂ ⁺
199.18	52,161.82	C ₁₂ H ₂₃ O ₂ ⁺
213.15	26,890.18	C ₁₂ H ₂₁ O ₃ ⁺
401.36	36,11.87	C ₂₄ H ₄₉ O ₄ ⁺
416.37	3,794.30	C ₂₄ H ₅₀ O ₄ N ⁺
430.35	4,076.51	C ₂₄ H ₄₈ O ₄ N ⁺
446.35	2,134.07	C ₂₄ H ₄₈ O ₆ N ⁺
460.34	1,223.03	C ₂₄ H ₄₆ O ₇ N ⁺

Appendix C

The Pasadena Aerosol Characterization Observatory (PACO): Chemical and Physical Analysis of the Western Los Angeles Basin Aerosol⁵

⁵ Reproduced by permission from “The Pasadena Aerosol Characterization Observatory (PACO): chemical and physical analysis of the Western Los Angeles basin aerosol” by S. P. Hersey, J. S. Craven, K. A. Schilling, A. R. Metcalf, A. Sorooshian, M. N. Chan, R. C. Flagan, and J. H. Seinfeld. *Atmos. Chem. Phys.* **2011**, *11*, 7417-7443.

The Pasadena Aerosol Characterization Observatory (PACO): chemical and physical analysis of the Western Los Angeles basin aerosol

S. P. Hersey¹, J. S. Craven², K. A. Schilling², A. R. Metcalf¹, A. Sorooshian³, M. N. Chan¹, R. C. Flagan^{1,2}, and J. H. Seinfeld^{1,2}

¹Division of Engineering and Applied Science, California Institute of Technology, Pasadena, CA, USA

²Division of Chemistry and Chemical Engineering, California Institute of Technology, Pasadena, CA, USA

³Department of Chemical and Environmental Engineering, University of Arizona, Tucson, AZ, USA

Received: 3 February 2011 – Published in Atmos. Chem. Phys. Discuss.: 18 February 2011

Revised: 16 June 2011 – Accepted: 25 June 2011 – Published: 1 August 2011

Abstract. The Pasadena Aerosol Characterization Observatory (PACO) represents the first major aerosol characterization experiment centered in the Western/Central Los Angeles Basin. The sampling site, located on the campus of the California Institute of Technology in Pasadena, was positioned to sample a continuous afternoon influx of transported urban aerosol with a photochemical age of 1–2 h and generally free from major local contributions. Sampling spanned 5 months during the summer of 2009, which were broken into 3 regimes on the basis of distinct meteorological conditions. Regime I was characterized by a series of low pressure systems, resulting in high humidity and rainy periods with clean conditions. Regime II typified early summer meteorology, with significant morning marine layers and warm, sunny afternoons. Regime III was characterized by hot, dry conditions with little marine layer influence. Regardless of regime, organic aerosol (OA) is the most significant constituent of nonrefractory submicron Los Angeles aerosol (42, 43, and 55 % of total submicron mass in regimes I, II, and III, respectively). The overall oxidation state remains relatively constant on timescales of days to weeks ($O:C = 0.44 \pm 0.08$, 0.55 ± 0.05 , and 0.48 ± 0.08 during regimes I, II, and III, respectively), with no difference in $O:C$ between morning and afternoon periods. Periods characterized by significant morning marine layer influence followed by photochemically favorable afternoons displayed significantly higher aerosol mass and $O:C$ ratio, suggesting that aqueous processes may

be important in the generation of secondary aerosol and oxidized organic aerosol (OOA) in Los Angeles. Online analysis of water soluble organic carbon (WSOC) indicates that water soluble organic mass (WSOM) reaches maxima near 14:00–15:00 local time (LT), but the percentage of AMS organic mass contributed by WSOM remains relatively constant throughout the day. Sulfate and nitrate reside predominantly in accumulation mode aerosol, while afternoon SOA production coincides with the appearance of a distinct fine mode dominated by organics. Particulate NH_4NO_3 and $(NH_4)_2SO_4$ appear to be NH_3 -limited in regimes I and II, but a significant excess of particulate NH_4^+ in the hot, dry regime III suggests less SO_4^{2-} and the presence of either organic amines or NH_4^+ -associated organic acids. C-ToF-AMS data were analyzed by Positive Matrix Factorization (PMF), which resolved three factors, corresponding to a hydrocarbon-like OA (HOA), semivolatile OOA (SV-OOA), and low-volatility OOA (LV-OOA). HOA appears to be a periodic plume source, while SV-OOA exhibits a strong diurnal pattern correlating with ozone. Peaks in SV-OOA concentration correspond to peaks in DMA number concentration and the appearance of a fine organic mode. LV-OOA appears to be an aged accumulation mode constituent that may be associated with aqueous-phase processing, correlating strongly with sulfate and representing the dominant background organic component. Periods characterized by high SV-OOA and LV-OOA were analyzed by filter analysis, revealing a complex mixture of species during periods dominated by SV-OOA and LV-OOA, with LV-OOA periods characterized by shorter-chain dicarboxylic acids (higher $O:C$ ratio), as well as appreciable amounts of nitrate- and



Correspondence to: J. H. Seinfeld
(seinfeld@caltech.edu)

sulfate-substituted organics. Phthalic acid was ubiquitous in filter samples, suggesting that PAH photochemistry may be an important SOA pathway in Los Angeles. Aerosol composition was related to water uptake characteristics, and it is concluded that hygroscopicity is largely controlled by organic mass fraction (OMF). The hygroscopicity parameter κ averaged 0.31 ± 0.08 , approaching 0.5 at low OMF and 0.1 at high OMF, with increasing OMF suppressing hygroscopic growth and increasing critical dry diameter for CCN activation (D_d). An experiment-averaged κ_{org} of 0.14 was calculated, indicating that the highly-oxidized organic fraction of aerosol in Los Angeles is appreciably more hygroscopic than previously reported in urban areas. Finally, PACO will provide context for results forthcoming from the CalNex field campaign, which involved ground sampling in Pasadena during the spring and summer of 2010.

1 Introduction

Over half the world's population lives in urban areas, and that fraction is expected to increase in coming decades (Bremner et al., 2009). There have been a number of recent coordinated studies focused on characterizing particulate air quality in major urban areas, such as Pittsburgh, PA (Pittsburgh Air Quality Study, PAQS; e.g., Pekney et al., 2006; Bein et al., 2006; Wittig et al., 2004; Cabada et al., 2004; Modey et al., 2004), Los Angeles, CA (Southern California Air Quality Study, SCAQS; e.g., Eldering et al., 1994; Watson et al., 1994; Chow et al., 1994; Turpin and Huntzicker, 1991; Southern California Ozone Study 1997, SCOS97-NARSTO; e.g., Croes and Fujita, 2003; Liu et al., 2000; Pastor et al., 2003; Hughes et al., 2002; Secondary Organic Aerosol in Riverside, SOAR; e.g., Docherty et al., 2008; Eatough et al., 2008; Denkenberger et al., 2007), Mexico City, Mexico (Megacity Initiative: Local and Global Research Observations, MILAGRO; e.g., DeCarlo et al., 2008; Stone et al., 2008; Aiken et al., 2009), and Beijing, China (Campaign of Air Quality Research in Beijing, CAREBEIJING; e.g., Matsui et al., 2009; Yue et al., 2009; van Pinxteren et al., 2009).

The Los Angeles metropolitan area, with a population of over 17 million people, has long been considered a laboratory for air quality. Once the quintessential example of classic photochemical smog, the Los Angeles area has, as a result of decades of aggressive emission controls, reached a point where 8-h US National Ambient Air Quality Standard ozone exceedances have decreased from over 200 days/year in the 1980s to 120 in 2008 (AQMD, 2010). Nonetheless, this area remains one in which particulate matter levels continue to regularly exceed air quality standards, with annual $\text{PM}_{2.5}$ averages exceeding the national standard every year from 2000–2008 in Los Angeles County (CARB, 2010).

The Los Angeles Basin is generally characterized as source-rich in its western area, with prevailing west and

southwest winds transporting emissions downwind toward the east and northeast (Lu and Turco, 1995). Three major coordinated studies have been undertaken to characterize Los Angeles air quality, in addition to ongoing work to describe facets of Los Angeles aerosol (Table 1). The majority of previous studies in the Los Angeles Basin have been centered in the downwind, eastern part of the basin, roughly 60 km east of downtown Los Angeles. The aerosol in this region is predominantly aged, with local contributions as well.

A major source of gaseous and particulate pollution in the Los Angeles area is mobile source emissions. The Los Angeles aerosol undergoes dramatic evolution from nighttime/morning periods to the photochemically active afternoon, characterized by changes in both its microphysical properties and composition. Overall, the submicron aerosol is dominated by organic aerosol (OA), which is predominantly secondary in origin (SOA), and nitrate (Docherty et al., 2008), with smaller amounts of sulfate and a minor chloride contribution. Primary marine and secondary sulfate aerosol are expected to contribute a relatively uniform loading of sulfate across the Los Angeles Basin (Watson et al., 1994). Marine sulfate is expected to be contributed by natural primary processes (biological, sea spray, bubble bursting), with anthropogenic shipping-related emissions contributing a varied and often significant loading of sulfate (Ault et al., 2010).

The Pasadena Aerosol Characterization Observatory experiment (PACO) was conducted from May–August 2009 in Pasadena, CA, in the north-central/north-western portion of the Los Angeles Basin, 16 km NE of downtown Los Angeles. Aerosol physics, composition, and hygroscopicity were measured during 54 days that spanned three distinct regimes of the annual meteorological cycle. A major forest fire occurred at the end of the sampling period, starting on 26 August and consuming over 160 000 acres of the Angeles National Forest before containment on 16 October. Named the “Station Fire”, its southernmost extent was roughly 8 km from the sampling site, and emissions from the fire impacted the sampling site with periodic heavy smoke, soot, and ash. Results from PACO sampling during the Station Fire will be presented in subsequent work.

PACO represents the first prolonged experiment aimed at characterizing the aerosol near the source-rich western/central part of the Los Angeles basin; comparisons with previous studies in downwind areas will help determine the rate of aerosol generation from Los Angeles sources, as well as the nature of aerosol transformations with downwind transport. Further, the PACO study was well-timed to precede the 2010 CalNex field campaign (<http://www.esrl.noaa.gov/csd/calnex/>).

This paper presents an overview of the PACO experiment. Aerosol number and volume distributions measured by a differential mobility analyzer (DMA) exhibit distinct diurnal patterns, and composition data from an Aerodyne Compact-Time-of-Flight Aerosol Mass Spectrometer (C-ToF AMS)

Table 1. Previous Los Angeles air quality studies and major findings relative to particulate matter.

Study	Date	Major aerosol findings
Southern California Air Quality Study (SCAQS)	Summer/fall 1987	- SOA/OA ~ 40 % in summer afternoon (Turpin and Huntzicker, 1991) - Primary vehicle exhaust is the major aerosol component near PACO sampling site (Watson et al., 1994) - 20- 32 % of PM ₁₀ is SO ₄ ²⁻ and NO ₃ ⁻ (Watson et al., 1994)
Southern California Ozone Study (SCOS97-NARSTO)	Summer 1997	- Submicron organic mode evolves during periods of intense photochemistry, coincident with maximum O ₃ (Pastor et al., 2003) - NH ₄ NO ₃ and organics added to submicron aerosol with photochemical age (Pastor et al., 2003) - NH ₃ sources in eastern basin enhance particulate NH ₄ NO ₃ (Hughes et al., 2002)
Secondary Organic Aerosol in Riverside (SOAR-1, 2)	Aug, Nov 2005	- Significant diurnal changes in organic aerosol, with species more reduced in the morning and more oxidized in the afternoon (DeCarlo et al., 2006) - Oligomers detected in aged, acidic particles (Denkenberger et al., 2007) - SOA/OA = 70- 90 % at midday and ~ 45 % during morning commute; SOAR average = 74 % (Docherty et al., 2008)
Individual studies	1999, 2001- 2002	- Complex, multi-modal GF data in Pasadena (Cocker et al., 2001) - SOA > 50 % of total PM _{2.5} in eastern basin (Sawant et al., 2004; Na et al., 2004)

indicate that these patterns are associated largely with the production of semivolatile oxidized organic species during photochemically active daytime periods. AMS-based Positive Matrix Factorization (PMF) results indicate that the character of OA in Los Angeles is overwhelmingly oxidized and secondary, and the high time resolution data allow for investigation of the daily evolution of OA components. Ultra Performance Liquid Chromatography/Electrospray Ionization Time-of-Flight High-Resolution Mass Spectrometry (UPLC/ESI-TOFMS) analysis of high-volume filter samples provides further evidence for diurnal changes in the character of OA, while thermal-optical analysis of low-volume, denuded filter samples reveals the magnitude of organic and elemental carbon in morning versus afternoon sampling periods. A particle-into-liquid sampler with offline ion chromatography analysis (PILS-IC) provides quantitative water-soluble inorganic ion composition during PACO, while a PILS coupled with online total organic carbon analysis (PILS-TOC) measured total water soluble organic carbon measurements during the third regime. Finally, trends in aerosol hygroscopicity indicate the degree to which changes in the magnitude and character of OA affect particle water uptake. PACO results are compared with previous aerosol characterization experiments in the Los Angeles Basin, with major differences attributed to regional variations in both source profiles and degree of aging.

2 Methods

Sampling was conducted on the Caltech campus in Pasadena, at 34.138° N, 118.124° W. Caltech is located in the west-

ern/central portion of the Los Angeles Basin, 8 km south of the San Gabriel Mountains and 16 km NE of downtown Los Angeles in the San Gabriel Valley. The 210 freeway is located 1.5 km north of the site, with heavy traffic between the hours of 08:00 and 09:00 LT, and then again between 15:00 and 19:00 LT. Prevailing daytime winds are from the W or SW, minimizing the impact of primary emissions from the 210 freeway at the sampling site, but overnight NW winds occasionally bring freeway emissions to Caltech. Other than this periodic impact from local primary emissions, the Pasadena aerosol is representative of transported urban particulate pollution from near the source-rich downtown area of the Los Angeles Basin.

PACO sampling took place between May and August of 2009, spanning the transition from spring to summer meteorological regimes. PACO was separated into three distinct analysis periods on the basis of meteorology, as summarized in Table 2.

2.1 Meteorology

Hourly meteorological data were downloaded from the Remote Automatic Weather Stations (RAWS) archive from the Western Regional Climate Center at the Desert Research Institute (DRI, Reno, Nevada). Data are from the Santa Fe Dam station, approximately 16 km east of the sampling site in the San Gabriel Valley, and are available online: <http://www.raws.dri.edu/cgi-bin/rawMAIN.pl?caCSFD>.

Table 2. PACO sampling regimes (2009).

Regime	Dates	Characteristics
Springtime meteorology	22 May to 12 Jun	<ul style="list-style-type: none"> - Basin impacted by a series of low pressure systems - Cutoff low brought rare springtime precipitation and cleaner atmosphere - Persistent cloudcover, unstable atmosphere - Low daytime temperatures, high RH, and limited photochemistry - High visibility with low O₃
Early summer/marine influence	18 Jun to 7 Jul	<ul style="list-style-type: none"> - Limited impact from low pressure systems - Morning marine layer eroded several hours after sunrise - Higher daytime temperatures, slightly lower RH, and photochemically active afternoons - Hazy afternoons with increased O₃
Photo-chemically active	10 Jul to 4 Aug	<ul style="list-style-type: none"> - Semi-permanent high pressure over Southern California - Little marine moisture and infrequent, quickly-eroded marine layer - High daytime temp. (often exceeding 35 °C), very low daytime RH ($\leq 15\%$), photochemically active days - Decreased visibility, high afternoon O₃

2.2 Gas-phase data

Hourly O₃, NO_x, and CO data were obtained from the California Air Resources Board's Pasadena (South Wilson) monitoring site located on the Caltech campus. Data are available online at <http://www.arb.ca.gov/adam/hourly/hourly1.php>.

2.3 Differential mobility analyzer

Particle size distribution measurements were performed with a cylindrical scanning differential mobility analyzer (TSI Model 3081) upstream from a condensation particle counter (TSI Model 3760). A logarithmic scan from a mobility diameter of 15 nm to 815 nm was completed every 237 s. The sheath and excess flows of 2.5 l min⁻¹ were used, with a 10 : 1 flow rate ratio of sheath-to-aerosol.

2.4 Aerosol mass spectrometer

An Aerodyne compact time-of-flight aerosol mass spectrometer (C-ToF-AMS; Drewnick et al., 2005; Canagaratna et al., 2007) measured aerosol composition and size information for 54 days during PACO. The AMS collects sub-micron particles via an aerodynamic lens into a particle sizing chamber, after which particles are vaporized and ionized by a heater and filament assembly. Aerosol fragments are then orthogonally extracted into an ion time-of-flight chamber where they are detected and interpreted as mass spectra. Adjustments to the AMS fragmentation table were made regularly, based on 21 filter sample periods over the course of PACO (Allan et al., 2004b). Additionally, thirteen ionization efficiency calibrations were made using ammonium nitrate solutions. The AMS sulfate measurement was compared to sulfate concentrations from the PILS-IC, resulting in an AMS collection

efficiency (CE) of 0.5. This CE is in agreement with previous ambient studies (Huffman et al., 2005; Drewnick et al., 2003; Allan et al., 2004a). AMS data were processed with the ToF-AMS Analysis Toolkit in Igor Pro 6 (Wavemetrics, Lake Oswego, OR).

2.5 Positive matrix factorization analysis

The dominant fraction of submicron nonrefractory aerosol is organic in most urban areas (Zhang et al., 2007). OA comprises a multitude of compounds, such that characterization by identification of each component is not currently possible (Schauer et al., 1996). Positive Matrix Factorization (PMF) has been used to deconvolve AMS mass spectra in order to identify classes of organic compounds that constitute OA (Paatero and Tapper, 1994; Paatero, 1997; Ulbrich et al., 2009). PMF solutions represent linear, positive combinations of mass spectra that describe variability in data, and AMS-based PMF results from most sites resolve factors whose mass spectra have characteristics of hydrocarbon-like OA (HOA) and oxygenated OA (OOA), with other factors such as biomass burning OA (BBOA) occurring in some areas (Zhang et al., 2007). OOA can often be further deconvolved into low-volatility OOA (LV-OOA) and semivolatile OOA (SV-OOA), broadly representing aged, transported, and highly oxidized OA and fresher, local, and less oxidized OA, respectively (Ng et al., 2010). AMS measurements, in conjunction with PMF analysis, allow for investigation of the diurnal evolution of OA and rapid changes in OA occurring during photochemically intense periods. Further, the combination of PMF solutions with analysis of the relative abundance of mass-to-charge (m/z) ratios 43 and 44 can be used as an aerosol aging diagnostic that allows comparison between locations (Ng et al., 2010).

For the PACO dataset, bulk AMS organic aerosol was prepared and then processed using the PMF2.exe algorithm (Paatero and Tapper, 1994). Solutions from the PMF algorithm were compared to meteorological variables and chemical tracers, as well as previously published mass spectra, using the PMF Evaluation Tool (PET Ulbrich et al., 2009). The strategic procedure for probing the PMF solution space is provided in Appendix A.

2.6 PILS-IC

A particle-into-liquid sampler coupled with off-line ion chromatography (PILS-IC, Sorooshian et al., 2006) sampled during 4-h periods (07:00–11:00 and 15:00–19:00 LT), providing quantitative measurements of inorganic and organic ions. The PILS samples ambient air through a 1 μm cut size impactor and three denuders (URG and Sunset Laboratory) designed to remove inorganic and organic gases that might bias aerosol measurements. Sampled air is then exposed to high water supersaturation in a steam chamber, where particles grow sufficiently large to be collected by inertial impaction before being delivered to vials held on a rotating carousel. Samples were collected every 30 min, and were stored at 2 $^{\circ}\text{C}$ until analysis by a dual IC system (Dionex ICS-2000). PILS-IC data from PACO are used primarily to determine collection efficiency corrections for the AMS and are not presented in detail here.

2.7 PILS-TOC

Water-soluble organic carbon (WSOC) was quantified during 12-h periods (07:00–19:00 LT) using a PILS (Brechtel Manufacturing Inc.) coupled to a Sievers Model 800 Total Organic Carbon (TOC) Analyzer (PILS-TOC). Details of this technique are described in detail by (Sullivan et al., 2004, 2006). Briefly, particles smaller than 2.5 μm in diameter are sampled by the PILS and passed immediately through an organic carbon denuder (Sunset Laboratory Inc.) to remove organic vapors. Particles are grown into droplets, collected by inertial impaction, and delivered to a TOC analyzer for quantification of WSOC, with data reported every 6 min. To account for dilution of the PILS liquid wash flow to the TOC analyzer owing to collected drops and condensation on the PILS droplet impactor, a constant dilution factor of 1.15 is assumed. This factor is based on measurements with an independent PILS system coupled to ion chromatography, a technique that can more precisely quantify the dilution factor. The reported WSOC levels are the difference between the measured and background concentrations. Contamination in the MQ water was the main component of the background levels, which were assumed to be constant between periodic background measurements. The overall measurement uncertainty is estimated to be approximately 10%. The PILS-TOC was employed during the final, photochemically active regime of PACO, from 10 July to 4 August.

2.8 Filter sampling

Both high- and low-volume filter samples were collected during 4-h sampling periods (07:00–11:00 and 15:00–19:00 LT). High-volume (12501min^{-1}) samples were collected with a Tisch TE-6001 sampler fitted with a $\text{PM}_{2.5}$ fractionator, using Whatman Quartz Microfibre Filters (cat. #1851-865). Low volume (15.91min^{-1}) samples were collected on 47 mm PALL Life Sciences Pallflex membrane filters, downstream from a Sunset Laboratory parallel-plate carbon filter denuder. Sampling was carried out according to the IMPROVE_A protocol, except that oven limitations forced filters to be pre-baked at 300 $^{\circ}\text{C}$ before sampling. Despite the lower pre-baking temperature, subsequent analysis of pre-baked filters revealed $\leq 0.01\text{ }\mu\text{g}$ of organic carbon (OC) and elemental carbon (EC). After sampling, filters were wrapped in two layers of aluminum foil and stored at $-20\text{ }^{\circ}\text{C}$ until analysis.

Low- and high- volume samples were analyzed for OC and EC via thermal-optical analysis (TOA) with a Sunset OC-EC TOA analyzer, following the IMPROVE_A temperature and calibration protocols. High volume quartz filters were also analyzed by Ultra Performance Liquid Chromatography/Electrospray Ionization Time-of-Flight High-Resolution Mass Spectrometry (UPLC/ESI-TOFMS). One-eighth of each filter was extracted with high-purity methanol under ultrasonication for 45 min. Filter extracts were filtered through a PALL Life Sciences Acrodisc CR 25-mm syringe filter (PTFE membrane, 0.2-mm pore size) into a scintillation vial. The filtered extracts were blown dry under a gentle nitrogen stream at ambient temperature. The residue was reconstituted with 50 : 50 v/v methanol with 0.1 % acetic acid and water. Blank filters were extracted and treated in the same manner as the field samples. Extracts were analyzed by a Waters ACQUITY ultra performance liquid chromatography (UPLC) system, coupled with a Waters LCT Premier TOF mass spectrometer equipped with an electrospray ionization (ESI) source, allowing for accurate mass measurements (i.e., determination of molecular formulas) to be obtained for each observed ion. Extracts were analyzed by UPLC/ESI TOFMS operated in both negative and positive ion modes. Details of operation protocols, including column information and chromatographic method for the UPLC/ESI-TOFMS are given by Surratt et al. (2008).

2.9 Hygroscopicity

Hygroscopicity measurements were carried out with the Differential Aerosol Sizing and Hygroscopicity Spectrometer Probe (DASH-SP, Brechtel Mfg), which is described by Sorooshian et al. (2008). Briefly, ambient particles pass through a nafion dryer before size-selection by a cylindrical, single-classification differential mobility analyzer (DMA). The resulting monodisperse aerosol is split into five separate flows – one providing a redundant measurement of total

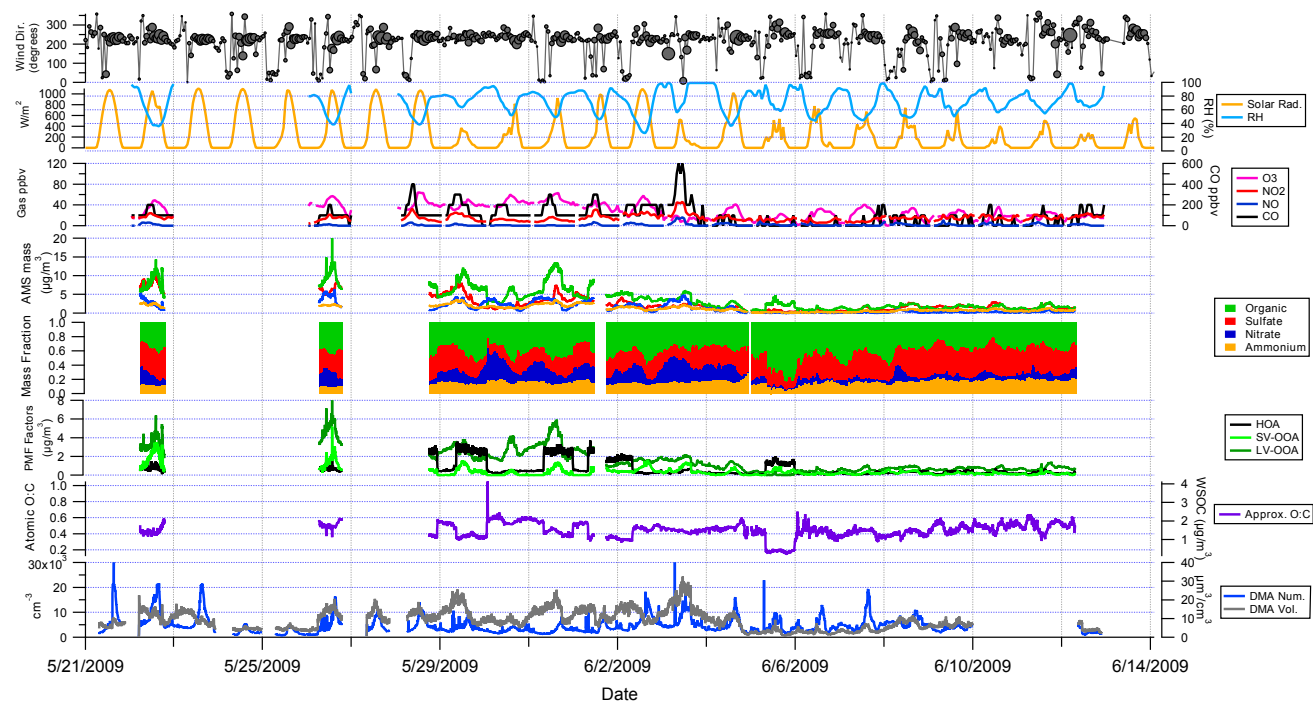


Fig. 1a. Regime I (wind direction marker size proportional to wind speed; max size = 20 km h^{-1}).

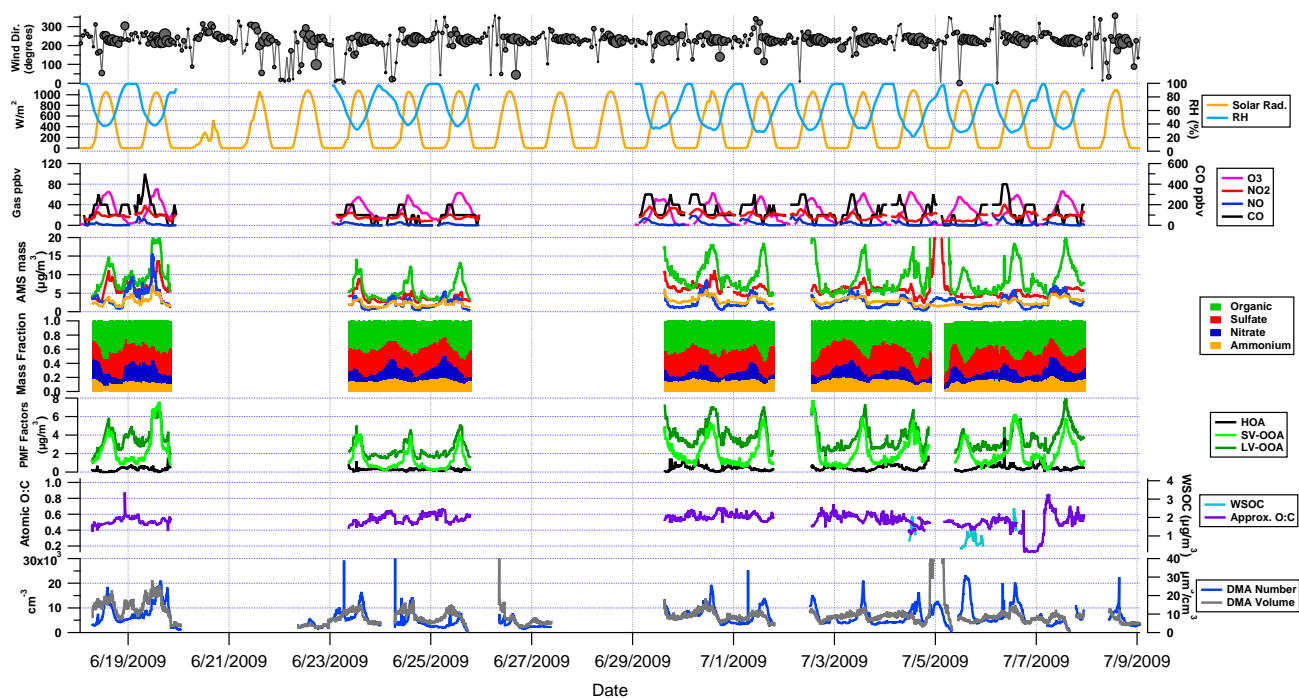


Fig. 1b. Regime II (wind direction marker size proportional to wind speed; max size = 20 km h^{-1}).

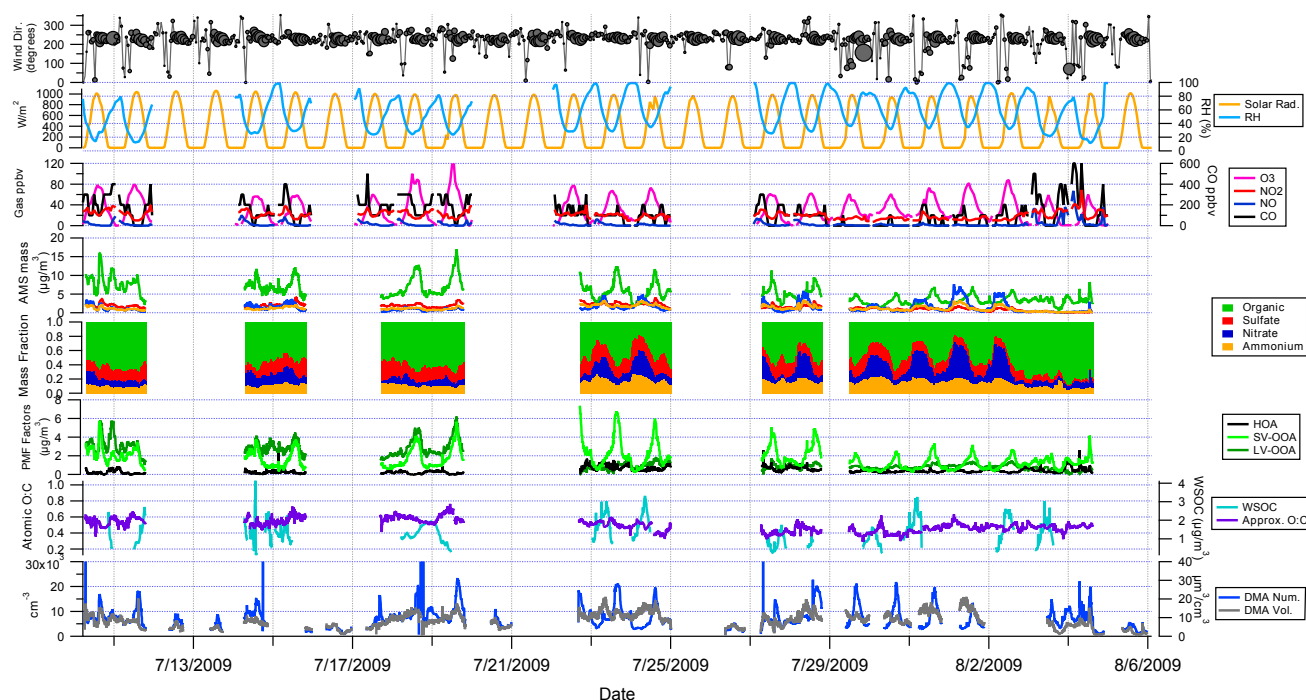


Fig. 1c. Regime III (wind direction marker size proportional to wind speed; max size = 20 km h^{-1}).

particle concentration at the DMA-selected size with a water condensation particle counter (TSI Model 3831), and the remaining four channels consisting of parallel nafion humidification chambers (Perma Pure, LLP, Model MD-070-24FS-4), followed by correspondingly humidified custom optical particle counters (OPCs). In the OPC sample volume, particles pass through a focused laser beam ($\lambda = 532 \text{ nm}$, World Star Technologies, Model TECGL-30) and scatter light in proportion to size (D_p) and refractive index (RI). Forward-scattered light is collected and focused on a photomultiplier tube, and the resulting electrical pulse is recorded by a high-speed data acquisition computer. An iterative data processing algorithm, based on laboratory calibrations with salts of known refractive indices, is used to determine the best fit on a solution surface relating electrical pulse height, size, and refractive index. The hygroscopic growth factor ($\text{GF} = D_{p,\text{wet}}/D_{p,\text{dry}}$) is corrected for the RI change caused by particulate liquid water at elevated RH.

In the current study, the DASH-SP sampled for 4-h periods (07:00–11:00 and 15:00–19:00 LT). Hygroscopicity was measured at dry sizes corresponding to $D_{p,\text{em}}$ of 150, 175, 200, and 225 nm. Multiple RH sensors in the nafion tubes and OPCs controlled RHs to dry ($\leq 8\%$), 74%, 85%, and 92%, with RH uncertainty of 1.5%. Because calculated RI varied little during sampling periods, GF calculations were made with a single RI for each sampling period, representing the average RI calculated for the entire period. The error introduced by this assumption is small, as light scattering in

the DASH is far more sensitive to size than RI. Overall uncertainty in GF calculations is calculated to be 4.5%.

3 Results and discussion

3.1 Atmospheric conditions

Figure 1a–c is a compilation of meteorological data, as well as gas- and aerosol-phase composition for regimes I, II, and III, respectively. Wind speed and direction display distinct diurnal patterns, with stagnant or very light winds from the N/NE in the overnight to early morning hours (20:00–06:00 LT) changing direction to come from the W/SW shortly after sunrise (06:00–07:00 LT). Between 06:00 and 16:00 LT, wind speed increases from 3–4 km h^{-1} to 13–15 km h^{-1} out of the W/SW before decreasing back to very light or stagnant out of the N/NE by 20:00 LT. One effect of these wind patterns is to allow local emissions to build up in the Los Angeles Basin during the nighttime and early morning hours, leading to significant carryover of aged aerosol in the background Los Angeles air, as proposed by (Blumenthal et al., 1978). When sea breezes develop, fresh emissions in source-rich areas are gradually transported from the Western Los Angeles Basin toward downwind areas in the E/NE. Situated 16 km from downtown Los Angeles, Pasadena can be considered as a receptor site that first receives transported pollution between 10:00 and 11:00 LT, after roughly 4–5 h of transport. During the afternoon hours

(13:00–18:00 LT), the sampling site receives a steady influx of air from the W/SW with photochemical age of 1–2 h. There are no significant freeways or point sources of particulate pollution in close W/SW proximity to the sampling site, and so it is expected that air sampled during PACO is representative of transported urban air in Los Angeles. A major freeway with significant diesel and gasoline mobile sources is located 1.5 km to the north of the sampling site, and so overnight N/NE winds may have periodically impacted the site with primary particulate emissions. Daytime variation in gas- and aerosol-phase composition is expected to result from three sources: (1) temporal changes in emissions from source-rich areas, (2) diurnal variations in the intensity of photochemistry, and (3) the age of transported pollution.

A clear diurnal trend is observed in RH and solar radiation, with RH increasing to near 100 % on most nights and remaining at or near saturation until sunrise. The incidence of nighttime and morning marine cloudcover was common during regimes I and II, while regime III was typically drier, with clear nighttime skies more common. Periods of more significant marine layer influence are indicated by longer periods of saturated RH and more gradual decrease in RH (and slower increase in solar radiation) after sunrise. Regime I has been classified as “springtime meteorology” due to the impact of several low pressure systems in Southern California, bringing periodic drizzle and leading to several days of cloudcover and significantly diminished solar radiation (i.e. 6 to 12 June). Daytime RH rarely fell below 50 % during regime I. Regime II exhibited the strongest summertime marine layer influence, with heavy cloudcover persisting until late morning (10:00 to 12:00 LT) nearly every day before making way for sunny, hazy afternoons with daytime RH between 25 and 40 %. Regime III observed the least marine layer influence, with many mornings of clear skies and daytime RH typically between 10 and 30 %. Despite differences in meteorology, the diurnal wind patterns described above were robust, with stagnant morning winds giving way to afternoon sea breezes and pollutant transport from the W/SW.

Gas-phase data give a sense of the atmospheric chemical environment during sampling. O_3 exhibits a strong diurnal pattern correlated with solar radiation and serves as a tracer for photochemical activity. During periods of relatively dry atmospheric conditions, the O_3 concentration peak increases in magnitude over subsequent days (see 17 to 19 July and 27 July to 2 August in regime III), suggesting that either pollutants accumulate or photochemical activity increases during periods of consistent, stable atmospheric conditions, resulting in photochemical episodes. CO and NO_x display more random behavior, exhibiting periodic peaks in concentration indicative of plumes of fresher emissions.

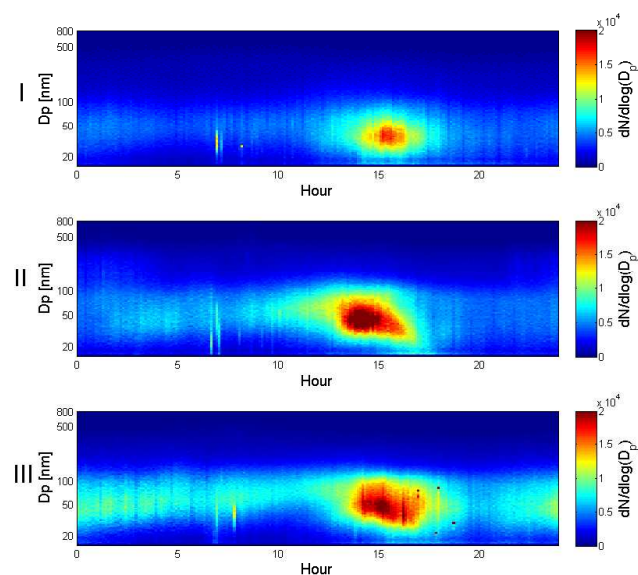


Fig. 2. Average diurnal DMA number concentrations (cm^{-3}) for regimes I, II, and III.

3.2 Aerosol composition

OC and EC mass concentrations, in addition to OC:EC ratios from representative days in each regime, are presented in Table 3. OC is higher in afternoon periods when compared with mornings in each regime (27, 18, and 4 % higher in regimes I, II, and III, respectively), while EC is lower during afternoons (7, 35, and 22 % lower in regimes I, II, and III, respectively). Further, OC:EC ratios are significantly higher during afternoon periods. These diurnal trends in OC are expected, given the importance of photochemical SOA production, and the percentage increase in OC mass between morning and afternoon periods is similar to that observed by the AMS (15, 17, and 10 % higher in regime I, II, and III, respectively). Discrepancies may arise due to the different size ranges measured by the AMS and filter sampling (upper limits of measurement are 1.0 and 2.5 μm for the AMS and filters, respectively), in addition to potential volatilization of semivolatile organics relating to the thermo-optical OC/EC analysis technique. The modest increase in OC between morning and afternoon periods during the photochemically intense regime III may indicate that significant OC existed in the background aerosol during this period. The decrease in EC observed between morning and afternoon periods suggests that primary organics are a more significant portion of the Los Angeles aerosol in the mornings, and the relatively low concentrations of EC suggest that the dominant source of organic aerosol in Los Angeles is secondary.

DMA data are presented in panel 8 of Fig. 1a–c. Diurnal patterns are evident in both DMA volume and number in all regimes. DMA volume tends to reach a maximum in the mid-to-late morning (10:00, 11:00, 08:00 LT in regime I, II, and

Table 3. OC/EC concentrations ($\mu\text{g m}^{-3}$) for representative days from each regime.

Regime	OC		EC		OC:EC	
	AM	PM	AM	PM	AM	PM
I	3.88 ± 0.32	4.92 ± 1.18	0.43 ± 0.02	0.40 ± 0.27	9.1	12.4
II	4.24 ± 0.46	5.01 ± 1.62	0.80 ± 0.31	0.52 ± 0.40	5.3	9.6
III	6.16 ± 1.40	6.41 ± 1.44	0.83 ± 0.47	0.65 ± 0.22	7.4	9.9

III, respectively), when RH is still high and particles have presumably undergone cloud processing. The early maxima in regime III underscore the absence of significant marine layer influence persisting into the late morning. On average, DMA number concentration reaches a maximum between 14:00 and 15:00 LT during each regime, roughly 3 h after transported pollution is expected to first arrive at the sampling site (Fig. 2). This indicates that increases in fine particle mass at the PACO sampling site are not the result of transport alone, but also affected by photochemical production in transported, polluted air from source-rich areas. There was no significant difference in wind patterns between regimes, so the slightly earlier peak in DMA number in regime II suggests that marine moisture and aqueous-phase processes (most prevalent in regime II) may hasten secondary aerosol production. Figure 2 indicates that appreciable concentrations of fine particles (< 100 nm) are present in late nights and early mornings (particularly in regimes II and III), possibly comprised of fresh emissions, nighttime-generated NO_3^- , or fine particle carryover residing in a shallow mixed layer.

With the exception of a high-volume filter sampler located outdoors on the roof, instruments sampled from inlets connected to a main sampling line drawing in ambient air at a 16 l per minute (1 min^{-1}) laminar flow rate. Sample flow to each instrument was supplemented with pumps to be isokinetic with flow in the main sampling line, and sample lines were designed to draw from the center of flow through the main line. Ambient air was dried by nafion driers upstream of each instrument.

The third and fourth panels of Fig. 1a–c show time traces of bulk AMS aerosol mass concentration and mass fraction, respectively, while the sixth panel shows a time trace of approximate O:C ratio, based on Aiken et al. (2008), as well as WSOC concentration from the PILS-TOC (regime III). Organics dominated the aerosol sampled during PACO, and except for short episodes in regime I, the approximate O:C ratio remained relatively constant during each regime (0.44 ± 0.08 , 0.55 ± 0.05 , and 0.48 ± 0.08 during regimes I, II, and III, respectively). Organic aerosol in regime II appears to be more oxidized than I and III, suggesting that the marine moisture and presumed aqueous processing may enhance the rate of organic oxidation in Los Angeles. From bulk AMS time traces it is evident that organics increase in

both magnitude and mass fraction each afternoon, particularly during the more photochemically active regimes II and III. It is noteworthy that there are no distinct trends in approximate O:C between mornings and afternoons (morning approximate O:C = 0.44 ± 0.08 , 0.54 ± 0.08 , and 0.49 ± 0.07 for regimes I, II, and III, respectively, while afternoon approximate O:C = 0.44 ± 0.08 , 0.53 ± 0.06 , 0.50 ± 0.08 for regimes I, II, and III, respectively). This suggests that there is little change in overall oxidation state of Los Angeles aerosol, even on timescales of weeks. It is unlikely that all organics are uniformly oxidized at all times in Los Angeles, but rather that there exists a continuum of OA oxidation, with more reduced and more oxidized ends of that continuum maintaining a relatively constant ratio for extended periods of time.

Trends in aerosol mass fraction are presented in Fig. 4. Organics dominate the Los Angeles submicron aerosol, contributing 42, 43, and 55 % of aerosol mass in regimes I, II, and III, respectively. Diurnal trends are evident in Fig. 4, with organic mass fraction increasing significantly from morning (07:00–11:00 LT) to midday (11:00–15:00 LT) to afternoon (15:00–19:00 LT) in each regime. Sulfate is a significant component in marine/moisture-influenced regimes I and II, and is a more minor component in regime III, suggesting that cloud processing and marine influence may be an important source of sulfate aerosol in Los Angeles. Nitrate contributes equal mass fractions in each regime, with a minimum in the afternoon and a maximum in the morning. Ammonium contributes a remarkably constant mass fraction to the aerosol, despite significantly less inorganic sulfate in regime III, suggesting an ammonium surplus for aerosol sampled in regime III. The significant peak in AMS masses during the early morning of 5 July (regime II) corresponds to a total submicron mass of over $200 \mu\text{g m}^{-3}$, and resulted from a myriad of fireworks displays in the area surrounding the sampling site. This plume has been removed from further analysis. Diurnal trends in bulk composition are highlighted in the top panel of Fig. 3. It is noteworthy that during the significantly marine-layer-impacted regime II, bulk organic, sulfate, nitrate, and ammonium masses are all enhanced. This is further evidence that aqueous processing associated with marine layer influence may be an important factor in generating aerosol mass in Los Angeles. Typically, organics increase in magnitude to a maximum near 14:00–15:00 LT in each

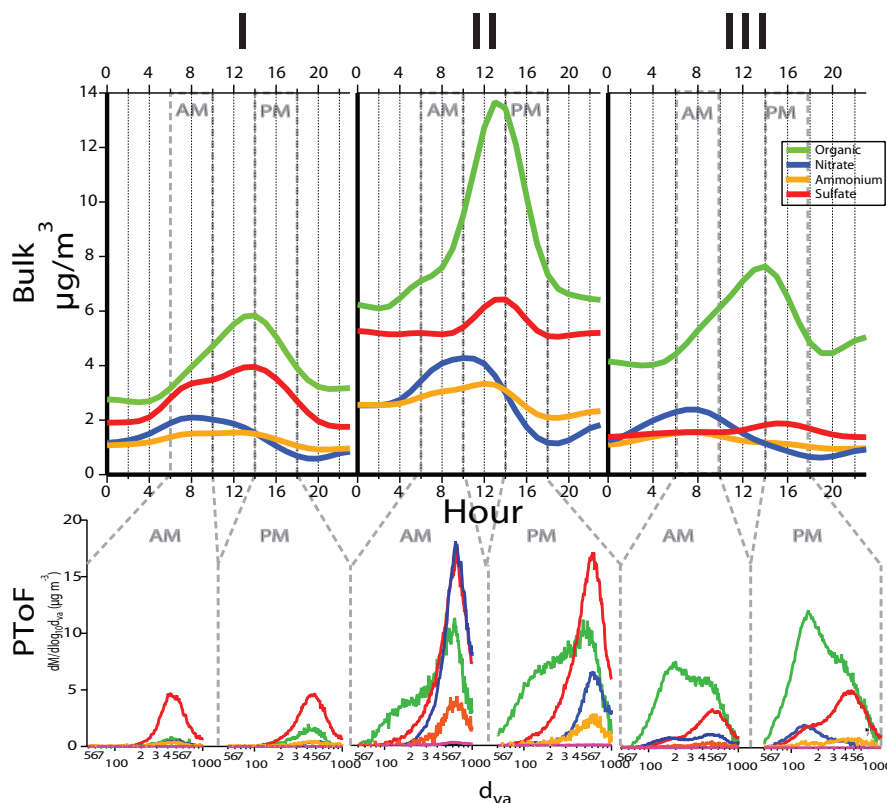


Fig. 3. Bulk AMS diurnal mass averages for regimes I, II, and III. Bottom panel shows size-resolved PToF AMS data for a representative morning and afternoon period in each regime, where morning = 07:00–11:00 LT and afternoon = 15:00–19:00 LT.

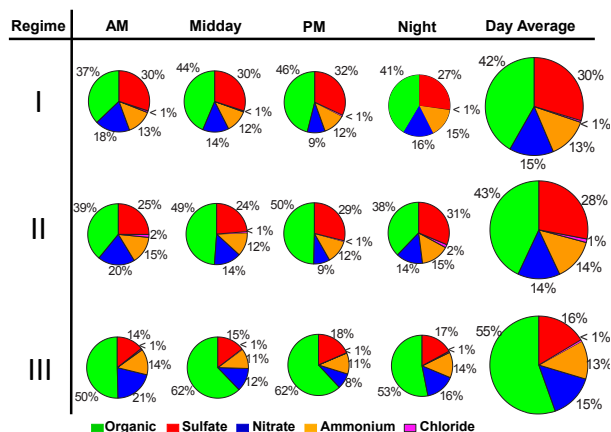


Fig. 4. AMS bulk mass fractions for AM (07:00–11:00 LT), midday (11:00–15:00 LT), PM (15:00–19:00 LT), and night (19:00–07:00 LT) for regimes I, II, and III.

regime, corresponding to a maximum in ozone, solar radiation, and DMA number – evidence of photochemical SOA production. Sulfate exhibits slight enhancements during periods of peak photochemical activity in all three regimes, but as

suggested by Kleeman et al. (1999), it appears to be predominantly a background marine species. Nitrate mass is highest in the nighttime and morning periods, likely resulting from ozone-NO_x production of HNO₃ at night and HO_x-NO_x production of HNO₃ after rush hour in the mornings. As mentioned in Sect. 3.1, there were periods of high O₃ observed during PACO, and during several of these periods there also appeared to be significantly elevated levels of aerosol nitrate during nighttime sampling (e.g. 30 July to 3 August). Further, morning peaks in aerosol nitrate varied significantly in magnitude, suggesting that there may be significant variation in the amount of gas-phase HNO₃ production from day to day.

Ammonium mass generally follows the combined trends of SO₄²⁻ and NO₃⁻, but appears to be in excess in regime III. Defining an ammonium ratio as:

$$\frac{(\text{moles of NH}_4^+ \text{ measured by AMS})}{(\text{moles of NH}_4^+ \text{ required to neutralize SO}_4^{2-} \text{ and NO}_3^-)}, \quad (1)$$

aerosol sampled in regimes I and II was found to be generally neutralized (average ammonium ratio = 0.96 ± 0.21 and 0.94 ± 0.17 for regimes I and II, respectively), while aerosol from regime III was characterized by significant ammonium excess (ammonium ratio = 1.28 ± 0.30). These

results suggest that aerosol phase NH_4NO_3 was ammonia-limited during regimes I and II, but ammonia may have been in excess during regime III. Investigating molar ratios of inorganic species, it is apparent that the role of SO_4^{2-} is significantly diminished in regime III, corresponding to the absence of marine layer influence. The ratio of NO_3^- to NH_4^+ remains relatively constant across regimes (0.32, 0.29, and 0.34 in regimes I, II, and III, respectively), while the ratio of SO_4^{2-} to NH_4^+ exhibits a marked decrease in regime III (0.42, 0.41, and 0.24 in regimes I, II, and III, respectively). The AMS has difficulty distinguishing whether NH , NH_2 , and NH_3^+ (*m/z* 15, 16, and 17, respectively) are contributed by inorganics or organic amines. One explanation for these trends is that ammonium may be chiefly inorganic during the moister, marine-layer-influenced regimes I and II, serving primarily to neutralize SO_4^{2-} and NO_3^- , while there may be an influence from organic amines in the absence of marine layer influence during regime III. While particulate amines have been observed in the particle phase, it is unclear why they would appear to be more prevalent in regime III, as amines are typically associated with cooler, moister environments. Another explanation is that the “excess” NH_4^+ may be associated with organic anions. An enhancement in acidic organic species, which would not be unexpected in a hot, dry, photochemically active regime, may lead to a corresponding enhancement in neutralizing NH_4^+ . Since the AMS does not specifically quantify organic anions, such an enhancement in both organic acids and associated NH_4^+ would lead to an increased ammonium ratio.

The bottom panel of Fig. 3 shows size-resolved PToF-AMS composition for a representative morning and afternoon period in each regime, with 9 June, 19 June, and 19 July representing regimes I, II, and III, respectively. Size-resolved data indicate that aerosol in regime I is typically internally-mixed, with the mode centered at $\sim 400\text{--}500\text{ nm}$. Afternoon PToF data from regime I indicate that photochemical organic production typically results in organics condensing on existing accumulation mode aerosol. Regime II is characterized by significantly higher aerosol mass and more complex size distributions. While there is a significant internally-mixed accumulation mode present and centered at $\sim 600\text{--}700\text{ nm}$, there is also significant aerosol mass at sizes smaller than 300 nm in both morning and afternoon sampling periods, though the mass at smaller sizes does not comprise a distinct mode. Afternoon PToF data from regime II indicate that a fine mode appears coincident with photochemistry, suggesting that fine mode aerosol is predominately comprised of secondary species. Nitrate, sulfate, and ammonium are generally confined to accumulation mode aerosol in regime II. Regime III PToF data reveal an aerosol that is dominated by organics at all sizes and is distinctly bimodal. In addition to an internally mixed accumulation mode centered at $\sim 500\text{--}600\text{ nm}$, distributions from regime III also reveal a significant fine mode centered at $\sim 100\text{--}200\text{ nm}$. The accumulation mode tends to be comprised of sulfate, nitrate,

and ammonium (in addition to organics) in the morning periods, with less nitrate in afternoons. Afternoon PToF data from regime III, like those from regime II, reveal fine-mode aerosol growth resulting from production of secondary organic species. Numerous studies have shown that the critical species for new particle formation in the atmosphere is H_2SO_4 . The extent to which the observed fine mode aerosol might have originated from the nucleation of gas-phase species during PACO is unclear. However, given the relatively large amount of pre-existing aerosol surface area, as well as the relatively low concentration of SO_2 , the precursor to H_2SO_4 , it is unlikely that new particle formation by nucleation is an important process in Los Angeles. Instead, the growth of fine-mode organics is proposed to occur by condensation of SOA on existing ultrafine primary aerosol. This tentative conclusion is contrasted with results from Pittsburgh, in which Stanier et al. (2004) found new particle formation to be an important process, strongly correlated with SO_2 concentrations. Whether condensing on nucleated sulfate or existing ultrafine primary aerosol, growth of fine mode particles in Los Angeles is predominantly due to SOA.

Figure 5 shows the hourly average for WSOC mass (top panel, representing WSOC organic mass) and % of AMS organic accounted for by WSOC (bottom panel) for regime III. A factor of 1.8 was used to convert water soluble carbon (WSOC) mass to water soluble organic mass (WSOM), within the range of factors presented by Turpin and Lim (2001), and matching the factor used by Docherty et al. (2008) for aerosol in the Los Angeles Basin. Averaged hourly data reveal a trend in WSOM, increasing from a minimum in the late evening and early morning to a maximum at 15:00 LT, corresponding to maxima in O_3 concentration, solar radiation, AMS organic, and DMA number concentration. This suggests that photochemical production of SOA in air transported from source-rich areas is a significant source of WSOM in the Los Angeles Basin. While there is a diurnal trend in WSOM, the fraction of AMS organic accounted for by WSOM is relatively constant at 0.44 ± 0.16 during regime III, with a slight enhancement between 15:00 and 19:00 LT. This suggests that while significant WSOM is photochemically generated during the course of a day, water soluble organics comprise a relatively constant percentage of organic aerosol in Los Angeles. WSOC has been found to correlate well with oxidation state of organic aerosol (e.g., Kondo et al., 2007). Given the relatively constant approximate O:C ratio observed in regime III and steady afternoon influx of polluted air on the order of 1–2 h old, the constant WSOM:AMS organic ratio is not unexpected.

3.3 PMF results

AMS data from PACO were combined into a single continuous dataset for analysis by the PMF method. PMF produced several non-unique solutions that were compared with known

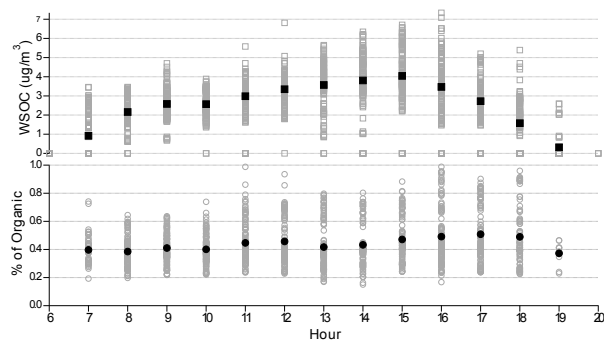


Fig. 5. WSOC magnitude (squares) and % of AMS organic (circles). Black markers represent the average over regime III.

mass spectra and external time traces in order to choose final solutions. Figure 6 presents a summary of PMF factors, while panel 6 of Fig. 1a–c represents time traces for PMF factors for regimes I, II, and III, respectively. Details of the PMF method and solution selection are presented in Appendix A.

Three factors were resolved from the PMF method, and comparisons with previously published spectra indicate that they correspond to a hydrocarbon-like organic aerosol (HOA) and semivolatile- and low-volatility-oxygenated organic aerosol (SV-OOA and LV-OOA, respectively). PMF analysis was also performed on each regime separately, to determine the sensitivity of solutions to the assumption that OA is comprised of factors with constant mass spectra. In each case (HOA, SV-OOA, and LV-OOA), the factors resolved in the bulk analysis displayed a high degree of correlation (Pearson's *R* generally on the order of 0.94–0.99 for LV-OOA, SV-OOA, and HOA) with those resolved in analysis of individual regimes. The HOA factor is closely correlated with previously published spectra from periods dominated by reduced, primary organics (Zhang et al., 2005; Lanz et al., 2007; Ulbrich et al., 2009), and has significant signal at m/z 41 and 57. The LV-OOA factor is closely correlated with previously-published OOA-1 factors and OOA-like factors observed in highly oxidizing environments (Zhang et al., 2005; Lanz et al., 2007; Ulbrich et al., 2009; Alfara et al., 2004). The SV-OOA factor is also correlated with previously-published OOA factors, but has a higher degree of correlation with previously-published factors expected to represent less-aged, less-oxidized, semivolatile oxygenated organic aerosol, or SV-OOA (Zhang et al., 2005; Lanz et al., 2007; Ulbrich et al., 2009; Bahreini et al., 2005; Alfara et al., 2004). The LV-OOA factor has a larger ratio of m/z 44 to m/z 43, an indication of a more aged, oxidized organic component (Ng et al., 2010). The SV-OOA factor, on the other hand, has a smaller m/z 44 to m/z 43 ratio. PACO PMF factors correlated closely with “standard” HOA, SV-OOA, and LV-OOA factors reported by Ng et al. (2011), based on an average of results from 15 sites.

As seen in Fig. 1a–c, the HOA factor has the character of a periodic plume source, with low background concentrations punctuated by sudden, significant increases in concentration that remain high for several hours at a time. These increases in HOA concentration occurred primarily during regime I and are typically correlated with or just following peaks in CO concentration (panel 3 in Fig. 1a–c), though the low time- and concentration-resolution of CO measurements made statistical analysis difficult. HOA is typically associated with primary organic aerosol (POA) (e.g., Ulbrich et al., 2009; Ng et al., 2010), and the only significant local source of POA is expected to be the 210 freeway, 1.5 km north of the sampling site. There appears to be a trend of HOA plumes coinciding with or immediately following periods of light winds out of the N, which suggests that the HOA-like factor may represent primary freeway emissions. It is unclear why this HOA factor does not appear during every period of light winds out of the N. Low correlation between the HOA factor and ozone ($Pr = 0.39$) suggests that HOA production is not a photochemical process, and low correlations with inorganic AMS traces ($Pr = 0.18, 0.15, 0.21,$ and 0.02 for sulfate, nitrate, ammonium, and chloride, respectively) suggest that HOA production is independent of formation of inorganic aerosol, and that HOA may comprise an externally mixed mode, separate from the accumulation mode aerosol that is typically comprised of inorganic constituents.

The more dominant LV-OOA factor is most significantly correlated with inorganic AMS traces ($Pr = 0.75, 0.46, 0.65,$ and 0.46 for sulfate, nitrate, ammonium, and chloride, respectively). As discussed in Sect. 3.2, inorganics are most prevalent in accumulation mode aerosol (rather than fine mode), and their loadings appear to be associated with significant marine layer influence in the Los Angeles Basin (e.g., regimes I and II). The high degree of correlation between LV-OOA and inorganic constituents suggests that the LV-OOA factor represents an organic component that typically resides in accumulation mode aerosol and may be associated with marine layer/cloud processing influence. The correlation between LV-OOA and ozone is relatively low ($Pr = 0.39$), indicative of an aged background organic species, as opposed to a rapidly-produced photochemical product that exhibits a distinct diurnal trend. Examining time traces for LV-OOA in Fig. 1a–c reveals that the LV-OOA factor exhibits relatively high background levels in the mornings and at night, while periodically showing moderate increases in magnitude during midday periods of photochemistry. These periodic photochemical trends in LV-OOA correspond to periods of intense photochemistry (e.g., 18–19 July), characterized by midday ozone concentrations near 80–100 ppb. This suggests that while LV-OOA appears to be the major constituent of the aged background aerosol discussed in Sect. 3.2, it can be photochemically produced on relatively short timescales during periods of intense photochemical activity. Its strong correlation with SO_4^{2-} , consistent presence during humid overnight and morning hours, coincidence

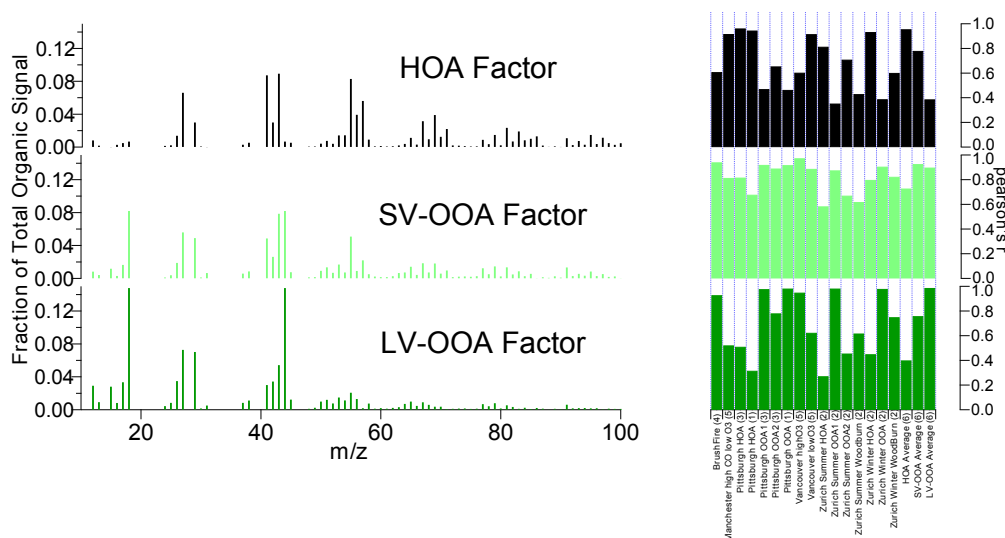


Fig. 6. Mass spectra for the three factors identified in PMF analysis (HOA, SV-OOA, and LV-OOA; left) and Pearson's R correlations of those solution mass spectra with previously reported mass spectra (1, 2, 3, 4, 5, 6: Zhang et al., 2005; Lanz et al., 2007; Ulbrich et al., 2009; Bahreini et al., 2005; Alfarrá et al., 2004; Ng et al., 2011, respectively).

with accumulation mode aerosol, and greater prevalence in moisture-impacted regimes I and II suggest that there may be significant aqueous processing sources for LV-OOA in Los Angeles.

Figure 1a–c show a regular diurnal trend in SV-OOA, with overnight minima increasing to maximum concentrations daily at approximately 14:00–15:00 LT, correlating with maxima in solar radiation, AMS organic, and DMA number concentration. The SV-OOA factor exhibits a reasonable degree of correlation with ozone ($Pr = 0.53$), suggesting that semivolatile organics are products of short-timescale photochemical oxidation of VOCs. Correlations with inorganic traces are lower than those for LV-OOA ($Pr = 0.42, 0.31, 0.45,$ and 0.19 for sulfate, nitrate, ammonium, and chloride, respectively). As discussed in Sect. 3.2, aerosol size distributions exhibit significant enhancements in fine mode aerosol in afternoon periods, with the fine mode comprised almost entirely of organics (particularly in regimes II and III). Further, SV-OOA correlates strongly with DMA number concentration ($Pr = 0.62$, vs. 0.00 and 0.33 for HOA and LV-OOA, respectively). The regular, significant enhancements in SV-OOA during peak photochemical periods, high correlation with DMA number concentration combined with lower correlations with inorganics (which typically comprise accumulation mode aerosol), and the regular appearance of fine organic modes during afternoons suggests that the SV-OOA factor is comprised of early-generation photochemical products that are chiefly responsible for the growth of fine-mode aerosol in the afternoons. Based on wind patterns discussed in Sect. 3.1, SV-OOA is proposed to consist of secondary organic products on the order of 1–2 h old, based on

the transport time from source-rich areas near downtown to the sampling site.

Traditional PMF analysis correlates LV-OOA with sulfate, since SO_4^{2-} is essentially nonvolatile, and SV-OOA with nitrate since NO_3^- is more volatile. These correlations are not necessarily based on mechanistic chemistry, but rather a similarity in volatilities. So there is no reason, on a fundamental chemical basis, that NO_3^- should correlate better with SV-OOA than with LV-OOA. That is, the routes by which semivolatile organics and NO_3^- reach the particle phase are distinctly different chemically. In the Los Angeles aerosol, these distinct pathways result in a relatively poor correlation between SV-OOA and NO_3^- . A better correlation between inorganics and LV-OOA suggests that the pathways by which they reach the aerosol phase are more similar than for SV-OOA in transported Los Angeles Aerosol.

Ng et al. (2011) applied a simple method for making real-time estimates of OA components, based on an empirical scaling factor that relates HOA and OOA (further segregated as SV-OOA and LV-OOA) to signal at fragments m/z 57 and m/z 44. HOA is estimated by $b \times (C_{57} - 0.1 \times C_{44})$, where b for PACO was found to be 14.0, compared with 13.4 (range = 8.5–19.2) for Ng et al. (2011). PACO OOA (combined SV-OOA and LV-OOA) is estimated by $c \times C_{44}$, where c was found to be 8.1 for PACO, compared with 6.6 (range = 2.9–9.0) by Ng et al. (2011). The PACO SV-OOA and LV-OOA factors are estimated by $3.3 \times C_{44}$ and $4.8 \times C_{44}$, respectively.

Figure 7 shows the mass fraction of organic accounted for by each organic component during each regime. OA in Los Angeles is overwhelmingly oxidized in nature, with LV- and

SV-OOA combined contributing 77, 92, and 86 % of OA during regimes I, II, and III, respectively. HOA contributed the largest fraction to OA during regime I, in large part due to episodically high HOA concentrations during May and early June. HOA is a minor factor during regimes II and III. SV-OOA is a major constituent of OA during periods of photochemistry, with the hot, dry, photochemically intense regime III seeing the most significant contribution of SV-OOA to OA. LV-OOA dominates in regimes I and II, which were both periods of significant marine/moisture influence and cloud processing.

3.4 Filter analysis

PMF factors are mathematical solutions that return constant mass spectra that are combined linearly to describe variability in AMS data, and it is important to compare PMF results to physical, independent characterizations of OA. For PACO, UPLC-ESI-(+ and -)-MS analysis of high-volume filter samples was performed on 9 selected filters representing periods of high HOA, SV-OOA, and LV-OOA concentrations, in order to distinguish chemical profiles associated with the PMF factors. Periods distinguished as “high SV- and LV-OOA” were chosen such that those species were the single, dominant component of OA. PACO filter sampling did not include any periods in which HOA was the isolated, dominant species, as periods distinguished as “high HOA” were also impacted by high background levels of LV-OOA.

Functional groups of interest in UPLC-ESI-(+)-TOF-MS analysis were basic nitrogen groups (i.e. amines, imines) as well as oxygen-containing moieties (i.e. carbonyls, alcohols, ethers). The complexity of the samples made complete speciation by this technique difficult, but it was possible to identify the majority of the base peaks. Non-oxygenated nitrogenous compounds likely to be amines were detected in significant concentrations and with some variety of carbon chain-length (C8–C16) in the high HOA + LV-OOA periods, as well as during morning periods in which background LV-OOA dominated the organic fraction. This suggests that amines may be an important class of organic compounds in aged, background Los Angeles aerosol. The most prominent class of compounds in all filters was oxygenated organic species, with increased variety of oxygenated species during periods of significant photochemical organic production.

UPLC-ESI-(–)-TOF-MS offered better mass spectral resolution and more complete identification of base peaks than (+)-mode, allowing for more complete chemical profiles. Phthalic acid is ubiquitous in appreciable quantities in the extractable fraction of Los Angeles OA. Phthalic acid has been identified as a significant product of poly-aromatic hydrocarbon (PAH) photochemistry (Kautzman et al., 2010), so this result suggests that PAHs may be a significant class of precursor VOCs to OA in Los Angeles. The high HOA + LV-OOA samples were characterized by appreciable quantities of nitrogen- and sulfur-containing organics (> 10 % of the

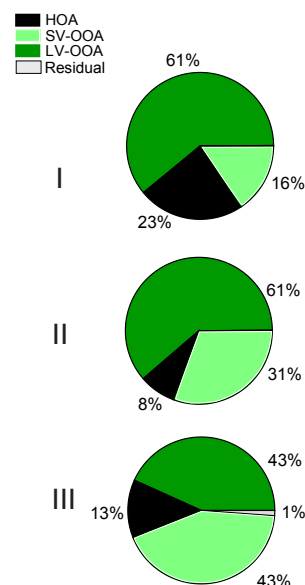


Fig. 7. Mass fraction of total organic accounted for by each PMF factor during regimes I, II, and III.

extractable, identifiable fraction), which is unique to periods in which both HOA and LV-OOA were high in magnitude. Carboxylic acids were significant during both SV- and LV-OOA periods (> 15 % of extractable, identifiable fraction), though the carboxylic acids identified during SV-OOA periods tended to be longer-chain (C7–C10, as opposed to C4–C9 for LV-OOA periods). Additionally, aerosol in LV-OOA periods tended to have a more complex chemical profile, with no single class of compounds dominating the extractable fraction identified by UPLC. This suggests that while the SV- and LV-OOA periods contain many of the same chemical compounds, LV-OOA tends to be characterized by smaller organic acids (higher O:C ratio), as well as a more complex profile of organonitrates, organosulfates, and oxidized acids. As explained in Ulbrich et al. (2009), aerosol partitioning with a bilinear PMF model is inherently limited in fitting a dynamic organic component. With a dataset as large as that represented by PACO, it is not unexpected that the organic component undergoes numerous and significant changes over the course of a single regime. Thus, two unique, constant mass spectra used to describe variability in a bilinear model may be more accurately viewed as two points on a continuum of volatility, rather than two distinct components of differing volatility. This hypothesis is supported by the commonality of compound classes identified by UPLC analysis for SV- and LV-OOA periods. The continuum of oxygenation is further illustrated in Fig. 8, a plot of m/z 44 (CO_2^+) vs. m/z 43 (mostly $\text{C}_2\text{H}_3\text{O}^+$) proposed by Ng et al. (2010) as a mass spectral diagnostic for the age of organic aerosol. It is hypothesized that LV-OOA components tend to have a higher ratio of m/z 44 to m/z 43 and represent a lower-

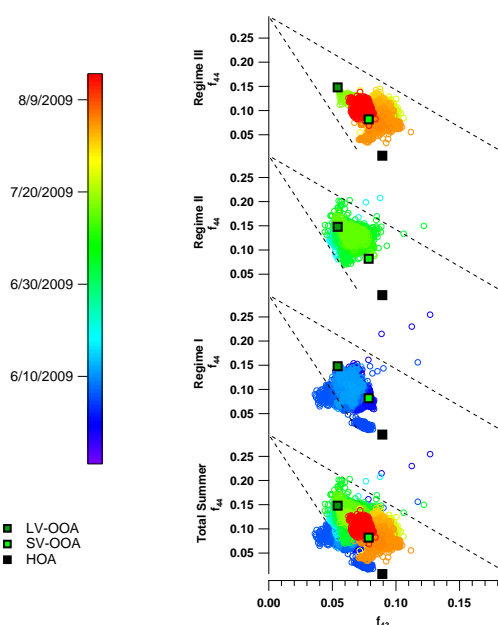


Fig. 8. f_{44} vs. f_{43} for PACO, with color scale corresponding to date. Square markers represent values for HOA, SV-OOA, and LV-OOA factors identified in PACO.

volatility, more-aged organic component with a higher degree of oxidation. Results from PACO indicate that the organic component of Los Angeles aerosol produces a continuum of f_{44} values during each regime and that the most aged organic fraction may actually be characterized by a predominance of longer-chain, oxidized monoacids, complex amines, and nitrate- and sulfate- containing organics. It is concluded that for the Los Angeles aerosol, a bilinear PMF model, with mass spectra assumed to be constant over an entire regime, is helpful in qualitatively assessing the degree of aging of the organic component, but represents a broad simplification of a dynamic organic fraction of aerosol.

3.5 Hygroscopicity

The intensity of scattered light is a strong function of particle diameter (D_p), and since aerosol water uptake largely determines particle size, it is a major variable determining the interaction of particles with radiation. Urban aerosol tends to be dominated by organic material, which is often hydrophobic, leading to overall growth factors (GFs, $D_{p,wet}/D_{p,dry}$) that are smaller than those for pure inorganic aerosol. At RH above the deliquescence RH of common inorganic aerosol constituents, the comparatively low hygroscopicity of organics tends to result in an inverse correlation between organic mass fraction and overall aerosol hygroscopicity (Shinozuka et al., 2009; Quinn et al., 2005; Hersey et al., 2009).

Because urban aerosol is, in part, an external mixture of organic and inorganic components, hygroscopic behavior is of-

ten complex, with several GF modes observed (e.g., Cocker et al., 2001; Massling et al., 2005, 2009; Swietlicki et al., 2008; Meier et al., 2009; Tiitta et al., 2010; Rose et al., 2010). The optical sizing method utilized by the DASH-SP provides rapid measurements on timescales suitable for aircraft studies, but does not allow resolution of more than two modes (a nonhygroscopic and hygroscopic mode). During PACO, two modes were typically distinguishable: a nonhygroscopic mode ($1 < GF < 1.15$ at 92 % RH) identified during morning sampling (≤ 30 % of aerosol), decreasing to very minor significance in the afternoon, in addition to a dominant hygroscopic mode that will be the focus of the rest of this section. This suggests that aerosol sampled in the morning included an appreciable fraction of nonhygroscopic particles, with afternoon photochemistry and SOA production resulting in an aerosol of more uniform, unimodal hygroscopicity. Since it was not possible to resolve multiple growth modes, GF data represent the overall subsaturated water uptake behavior for hygroscopic particles.

The DASH-SP measured GF at dry particle sizes of 150, 175, 200, and 225 nm. There was no statistically significant difference between GF at these dry sizes, and so data were averaged to give GFs representative for particles between 150 and 225 nm dry diameter. Particles sampled during morning periods (07:00–11:00 LT) were significantly more hygroscopic at 74 and 92 % than those sampled during afternoon periods (15:00–19:00 LT); morning GF averaged 1.14 ± 0.13 , 1.37 ± 0.10 , and 1.97 ± 0.45 at 74, 85, and 92 % RH, respectively, while afternoon GF averaged 1.06 ± 0.04 , 1.37 ± 0.07 , and 1.74 ± 0.20 at 74, 85, and 92 % RH, respectively. Suppressed GF at 74 and 92 % during afternoon sampling but constant GF at 85 % suggests that the hygroscopic growth curve (GF vs. RH) for morning-sampled aerosol is one with a higher GF at lower RHs, combined with a steep ascending section at RH > 85 %, suggestive of a predominantly inorganic aerosol with a small hygroscopic organic component and little nonhygroscopic aerosol.

These GF values are significantly higher than those measured during the 1987 SCAQS study in the eastern Los Angeles Basin (1.23 ± 0.08 for 200 nm particles at 90 ± 3 % RH; Zhang and McMurray, 1993), and are more consistent with the most hygroscopic mode measured in Pasadena in 1999 (1.6 at 89 % RH; Cocker et al., 2001).

Figure 9 shows GF at 74, 85, and 92 % plotted against organic mass fraction (OMF), with markers colored by sampling date and time. PACO data show a clear trend of suppressed GF with increasing organic mass fraction (Pr = -0.56 , -0.78 , -0.71 for 74, 85, and 92 %, respectively). The lowest GFs and highest values of organic mass fraction occur late in PACO, during the dry and photochemically intense regime III characterized by significant photochemical production of SV-OOA.

An increasingly popular representation of aerosol hygroscopicity is the κ parameter, developed by Petters and Kreidenweis (2007). As outlined in Shinozuka et al. (2009), one

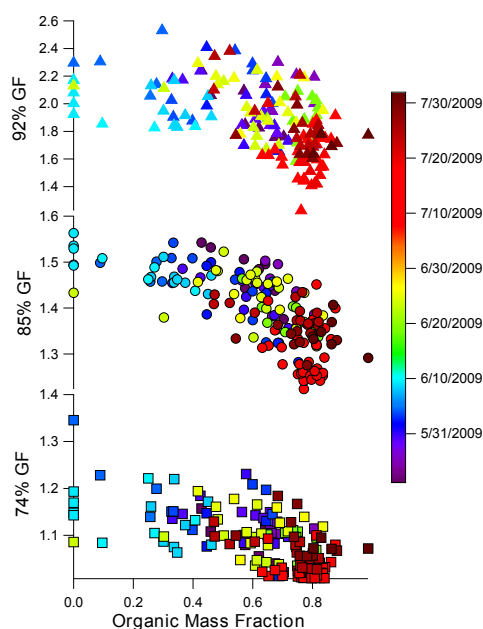


Fig. 9. GF at 74, 85, and 92 % RH plotted against organic mass fraction, with color scale corresponding to date.

can use size-resolved GF data at sub-saturated RH to solve the equation:

$$S(D) = \frac{D^3 - D_d^3}{D^3 - D_d^3(1 - \kappa)} \exp\left[\frac{4\sigma M_w}{RT\rho_w D}\right] \quad (2)$$

for κ , where S is the saturation ratio over an aqueous droplet (0.74, 0.85, or 0.92), D and D_d are the humidified and dry diameters, respectively, σ is the surface tension at the interface of air and pure water (0.072 J m^{-2}), M_w is the molecular weight of water (18 g mol^{-1}), R is the gas constant ($8.3 \text{ J mol}^{-1} \text{ K}^{-1}$), T is the temperature (298 K), and ρ_w is the density of water (1 g cm^{-3}). Because the effect of organics on surface tension is not explicitly accounted for in this model, the κ here may be regarded an “effective hygroscopicity parameter”, which includes both solute-induced water activity changes and surface tension effects (Petters and Kreidenweis, 2007; Rose et al., 2010).

Using the calculated κ values, one may estimate critical dry diameter (D_d), or the diameter above which aerosol particles activate as cloud condensation nuclei (CCN) at a given saturation ratio (S), using the following equations:

$$\kappa = \frac{4A^3}{27D_d^3 \ln^2 S} \quad (3)$$

where:

$$A = \frac{4\sigma M_w}{RT\rho_w} \quad (4)$$

Following Shinzuka et al. (2009) and assuming a supersaturation (S_c) of 0.2 %, the relationship between κ and D_d becomes:

$$D_d = \kappa^{(-1/3)} \cdot 70 \text{ nm} \quad (5)$$

Values of κ and critical dry diameter at 0.2 % supersaturation were calculated based on GFs at 85 % RH and dry particle diameter of 200 nm. Uncertainties are estimated to be 25 %, based on sizing uncertainties in the DASH-SP and RH variation in the instrument (Sorooshian et al., 2008). Figure 10 shows κ (left axis) and critical dry diameter (right axis; D_d) plotted against organic mass fraction (OMF), colored by time and date. Kappa values range from 0.15 to 0.51, with an average of 0.31 ± 0.08 , while critical diameters ranged from 87 to 131 nm, with an average of $105 \pm 10 \text{ nm}$. As with GF data, there is a clear trend of decreasing κ and increasing critical dry diameter with increasing organic mass fraction, with the lowest hygroscopicity and CCN activity occurring during regime III. Earlier periods characterized by more marine influence and higher RH exhibited more hygroscopic behavior. At low values of organic mass fraction, κ approaches that of nitrate and sulfate salts (0.53–0.67), while approaching 0.1 at high organic fraction. Cubison et al. (2008) found that CCN concentrations in eastern Los Angeles were best modeled by treating organics (including the oxidized fraction) as nonhygroscopic. GF- and CCN- derived κ values for hygroscopic organics range from 0.01 to 0.5 (Petters and Kreidenweis, 2007), with only the most hygroscopic organics (i.e. malonic acid) approaching the high end of that range. Results from PACO suggest that organics are moderately hygroscopic, with κ values on the lower end of the range cited by Petters and Kreidenweis (2007).

Shinzuka et al. (2009) presented parameterizations for calculating κ as a function of organic mass fraction for 100 nm D_p , dry aerosol in Central Mexico and the North American West Coast ($\kappa = 0.34 - 0.20 \cdot \text{OMF}$ and $\kappa = 0.47 - 0.43 \cdot \text{OMF}$, respectively), and these parameterizations are shown in Fig. 10. Overall, aerosol sampled during PACO are more hygroscopic at a given OMF than those presented in Shinzuka et al. (2009), and are parameterized as $\kappa = 0.50 - 0.29 \cdot \text{OMF}$. This suggests that the organic fraction measured by Shinzuka et al. (2009) inhibits hygroscopicity significantly more than in Los Angeles. It is possible that the organics measured in Central Mexico and off the N. American West Coast exhibit more surface-active behavior, inhibiting hygroscopic activity, or that those organics are predominantly non-hygroscopic. In order to further investigate the hygroscopicity of organics, κ calculations were combined with AMS data giving mass fractions of individual aerosol species in order to estimate a κ value for organics, κ_{org} . If the overall hygroscopicity parameter, κ is given by:

$$\kappa = \sum_{i=1}^n \kappa_i \cdot \chi_i, \quad (6)$$

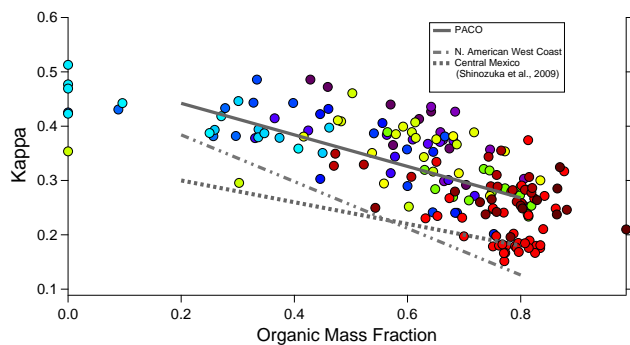


Fig. 10. κ and critical dry diameter plotted against mass fraction organic, with color scale corresponding to date; lines represent empirical parameterizations from PACO, Central Mexico, and N. American West Coast.

where n is the number of chemical constituents, i , with mole fraction χ_i and hygroscopicity parameter κ_i , then the organic hygroscopicity parameter, κ_{org} can be estimated by:

$$\kappa_{\text{org}} = \frac{\sum_{i=1}^{n_{\text{inorg}}} \kappa_i \cdot \chi_i}{\chi_{\text{org}}}, \quad (7)$$

where n_{inorg} is the number of inorganic constituents, i , with hygroscopicity parameter κ_i and mole fraction χ_i , and χ_{org} is the mole fraction of organics in the aerosol. Previous publications have assumed κ_{org} of 0.1 for “hygroscopic” organics, and 0 for “nonhygroscopic” organics (Dusek et al., 2010; Wang et al., 2010; Wex et al., 2010). Assuming κ_i for inorganics to be 0.6 and κ_i for sea salt to be 1.3 (Wex et al., 2010), Eq. (7) gives κ_{org} of 0.16 for urban background aerosol transported to the PACO sampling site. Assuming κ_i for inorganics to be 0.7 (Dusek et al., 2010) gives κ_{org} of 0.12. Taking a median κ_{org} of 0.14, it is clear that the organics measured during PACO are significantly more hygroscopic than those previously measured in urban areas. This is not unexpected, given the consistently high O:C ratios of organics and the dominance of SV-OOA and LV-OOA during all three regimes of PACO. Further, the PACO sampling site is relatively free from the influence of local sources of primary aerosol, which would have the effect of reducing κ_{org} . Given that organics dominate aerosol in most urban areas, it is potentially significant to find that organics in an important urban center such as Los Angeles would have a value of κ_{org} appreciably higher than previously calculated for urban aerosol.

4 Conclusions

A major ambient sampling experiment was conducted at a site in Pasadena, CA positioned to sample a constant afternoon influx of transported Los Angeles pollution with a photochemical age of roughly 1–2 h and generally free from the influence of local point sources. Sampling spanned 4 months during the summer of 2009, and was characterized by three distinct meteorological regimes: a “springtime” period characterized by clean conditions coincident with low pressure systems (regime I), a typical early-summer period characterized by significant morning marine layer followed by warm, photochemically active afternoons (regime II), and a late-summer period characterized by little marine layer influence, hot and dry conditions, and elevated photochemical activity (regime III).

Chemical analysis of aerosol revealed that OC dominates particulate carbon in Los Angeles (OC:EC average of 8.04), and is enhanced relative to EC by an average of 47% in the afternoon, suggesting significant SOA production. High RH during marine-layer-influenced morning sampling periods resulted in aqueous processing of aerosol particles and high aerosol volume, while drier afternoon periods saw increased aerosol number and volume due to SOA production. Maxima in aerosol volume occurred in the mid-late morning, reflecting a balance between RH-induced hygroscopic growth and SOA production. Maxima in aerosol number tended to occur near 14:00–15:00 LT, indicating that daytime photochemistry tended to generate a fine aerosol mode.

Organics are the most significant constituent of transported Los Angeles aerosol, contributing an average of 42, 43, and 55% of total submicron mass in regimes I, II, and III, respectively. Interestingly, there was no significant difference between morning and afternoon O:C ratios, suggesting that the constant influx of 1–2 h old aerosol results in an overall organic oxidation state at the sampling site varying little despite significant SOA production. Regime II, characterized by significant morning marine layer influence followed by photochemically active afternoons, displayed significantly higher aerosol mass and 15–25% higher average O:C ratio, suggesting that aqueous processes may be important in the generation of secondary aerosol and OOA in Los Angeles. Afternoons during regime II and III are characterized by the appearance of a fine organic mode, suggesting that SOA contributes significantly to growth of fine particles. It is unclear whether these fine particles are the result of sulfate nucleation and subsequent SOA growth or SOA condensation on existing primary aerosol.

Water soluble organic mass (WSOM) reaches maxima near 14:00–15:00 LT, coincident with markers for photochemistry and suggesting significant SOA contribution to WSOM. Sulfate is predominantly an accumulation mode constituent, and its magnitude appears to depend on the degree of marine influence. Nitrate is similarly a predominantly accumulation mode species, reaching maxima after morning

rush hour periods. Nighttime nitrate production is observed during periods in which maximum ozone levels indicated significant photochemical events. An ammonium ratio, defined as the moles of ammonium measured divided by the moles of ammonium required to neutralize sulfate and nitrate as $(\text{NH}_4)_2\text{SO}_4$ and NH_4NO_3 , respectively, revealed that ammonia limits particulate $(\text{NH}_4)_2\text{SO}_4$ and NH_4NO_3 in regimes I and II. An ammonium ratio of 1.28 ± 0.30 in regime III suggests that ammonium was in excess and that organic amines may have been an important constituent of submicron aerosol during this hot, dry, photochemically intense sampling period with reduced marine sulfate influence.

PMF analysis of C-ToF-AMS data resolved three factors, corresponding to HOA, SV-OOA, and LV-OOA, and correlating well with the “standard” factors presented in Ng et al. (2011). The HOA factor appears to be a periodic plume source, generally appearing during or shortly after peaks in CO concentration. SV-OOA displays a strong diurnal pattern, correlating strongly with ozone and the appearance of a fine mode (< 100 nm) in the aerosol size distribution, suggesting that these SOA products are generated on timescales of 1–2 h and tend to comprise a fine aerosol mode. LV-OOA is correlated with inorganic nitrate and sulfate and appears to be an aged carryover organic component that resides in accumulation mode aerosol, but may be generated on short timescales (1–2 h) under extremely oxidizing conditions. Its prevalence during humid overnight and morning hours and enhanced importance in moisture-influenced regimes I and II suggest that there may be significant aqueous-phase sources for LV-OOA. Overall the organic fraction of Los Angeles aerosol is overwhelmingly oxidized, with LV- and SV-OOA contributing 77, 92, and 86 % of OA in regimes I, II, and III, respectively.

Filter analysis by both (+) and (–) mode UPLC-ESI-TOF-MS reveals a complex mixture of organic compounds dominated by oxygenated species. Long (C8–C16), non-oxygenated nitrogenous compounds likely to be amines are detected during periods impacted by high concentrations of background LV-OOA, suggesting that amines may be an important constituent of aged organic aerosol in Los Angeles. Phthalic acid represents a ubiquitous, appreciable fraction of extractable OA, suggesting that PAH photochemistry may be an important pathway for SOA production in Los Angeles. Organo-nitro-sulfate species are observed during periods when aerosol appears to be a mixture of aged background species and freshly emitted particles. Carboxylic acids appear to be major contributors to both SV- and LV-OOA, with LV-OOA tending to be associated with shorter (C4–C9) carboxylic acids and thereby higher O:C ratio.

The organic fraction of transported Los Angeles aerosol is dynamic and undergoes numerous and significant changes on timescales of days to weeks, despite exhibiting consistency in the overall degree of oxidation. Many compounds are common to periods identified as distinct by PMF analysis, and PACO data suggest that Los Angeles OA is best

described as a complex, dynamic mixture of compounds that represent a continuum of oxidation. Thus, a bilinear PMF model that assumes constant mass spectra representative of classes of OA is a useful tool in qualitatively assessing the degree of OA aging and oxidation, but is a dramatic simplification of a complex organic fraction.

Finally, aerosol water uptake characteristics measured by the DASH-SP indicate that a bimodal distribution becomes more unimodal during periods of photochemical SOA production. The degree of hygroscopicity of the main hygroscopic mode is highly anti-correlated with organic mass fraction, as indicated by decreasing GF and κ , as well as increasing critical diameter with increased organic fraction. Values for κ averaged 0.31 ± 0.08 , approaching 0.5 at low OMF and 0.1 at high OMF. It appears that organics in Los Angeles inhibit hygroscopicity less than those measured in Central Mexico and off the N. American West Coast, potentially owing to less surface-active behavior or an organic fraction comprised of more water soluble species.

PACO represents the first major aerosol characterization in the Western Los Angeles Basin, and comparison with SOAR will help identify spatial variation in Los Angeles aerosol and determine the nature of aerosol evolution as it is transported from source-rich (western) to downwind (eastern) parts of Los Angeles. Further, its timing will serve to contextualize and compare forthcoming results from the CalNex field campaign, part of which involved ground sampling at the PACO site.

Appendix A

PMF analysis

PMF was initiated using 50 seed values, and then again using a range of f_{peak} values from -1 to 1 varying by 0.1 . Figures A1 and A2 show the Q/Q_{expected} values for the different solutions. The PMF results were sorted by regime, number of factors, and seed (only where it caused the solution to vary) and compared to previously published mass spectra in the AMS online Spectral Database explained in Ulbrich et al. (2009). Table A1 shows Pearson's r values comparing the PMF mass spectral profile solutions to existing mass spectra. Table A2 shows Pearson's r values comparing the PMF time series solutions to gas phase tracers, AMS inorganic tracers, PILS tracers, and WSOC. Figure A3 shows total residuals of all masses over time for solutions with different factor numbers. Figure A4 shows the scaled residuals at each mass for the presented 3 factor solution. The 2 and 4 factor solution profiles and time series contributions are shown in Figs. A5a, b.

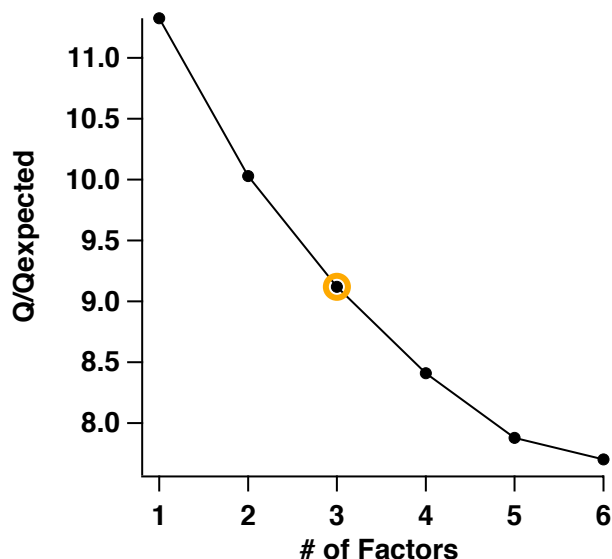


Fig. A1. Q/Q_{exp} values for varying number of factors (p values). The circled marker is the presented solution.

The difference in the total residuals was noticeable between the 1 and 2 factor solution and the 2 and 3 factor solution, but negligible between the 3 and 4 factor solution. In the 2 factor solution there is evidence of an HOA-like factor and OOA-like factor from the mass spectral comparison, but when compared to the 3 factor solution, the time series correlations with AMS inorganic and certain gas phase tracers is improved. In the 3 factor case, 3 solutions were explored, and were representative of the 50 possible solutions from the PMF results. Regarding the mass spectral profile, the seed = 6 solution was chosen since it has very strong correlations with the real mass spectra, and each of the profiles are least similar to one another (see the right hand side of Table A2) when compared to the two other 3 factor solutions. When considering the time series comparison, the seed = 6 LV-OOA like factor (factor 1) has the highest correlation with the AMS inorganic species. The p-ToF data suggests the organic profile of LV-OOA has similar particle size distributions to the AMS inorganic species (this was investigated in areas of known LV-OOA like factor and low SV-OOA like factor, since PMF was not performed on pToF data). When the afternoon sun reaches a maximum, there is another, smaller mode that is believed to be SV-OOA, without the strong inorganic signal. Also, the seed = 6 SV-OOA

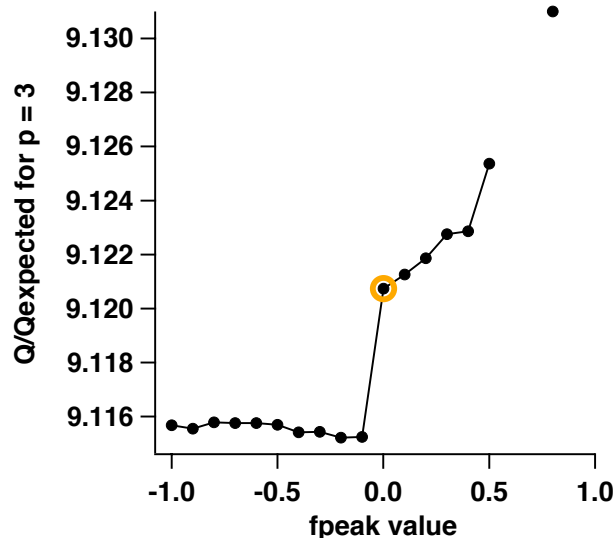


Fig. A2. Q/Q_{exp} for varying fpeak values for $p = 3$. The circled marker is the presented solution.

factor correlates best with ozone when compared to the two other solutions. The tracers for HOA were limited in this study since the resolution for the CO and NO_x were poor and the r values are very low. However, when comparing the seed = 6 and seed = 1 solutions, the correlations of the HOA-like factor to CO and NO_x are slightly larger. Additionally, the HOA-like factor was compared to m/z 57, which is higher for the seed = 6 solutions. The HOA correlations for the seed = 4 solutions are slightly higher than in the seed = 1 and seed = 6 solutions, but this solution is not as strong mass spectrally, and when comparing the tracers for the two other factors. The four factor situation provided two different solutions, representative of the 50 seeds. In addition to the residuals not changing dramatically, in the mass spectral comparison, for both solutions, two of the factors have very similar r values (factor 1 and 4 for seed 1 and factor 2 and 4 for seed 4). Also, the time series correlations are worse in the four factor solutions, when compared to the presented 3 factor solution.

Table A1. Mass spectral comparison of several PMF solutions.

Factor Number (<i>p</i>) Seed		Mass Spectra Comparison																			
		Brushfire (4)	Manchester high CO low O ₃ (5)	Pittsburgh HOA (3)	Pittsburgh HOA(1)	Pittsburgh OOA I (3)	Pittsburgh OOA II (3)	Pittsburgh OOA (1)	Urban Vancouver high O ₃ (5)	Urban Vancouver low O ₃ (5)	Zurich Summer HOA (2)	Zurich Summer OOA I (2)	Zurich Summer OOA II (2)	Zurich Summer Wood burning (2)	Zurich Winter HOA (2)	Zurich Winter OOA (2)	Zurich Winter Wood burning (2)	Factor 1	Factor 2	Factor 3	Factor 4
1	1	0.96	0.68	0.68	0.51	0.97	0.85	0.97	0.99	0.77	0.44	0.95	0.58	0.64	0.66	0.97	0.81				
1	1	0.94	0.55	0.54	0.35	0.98	0.80	0.98	0.96	0.65	0.30	0.98	0.47	0.62	0.50	0.98	0.76		0.64		
2	1	0.77	0.94	0.97	0.91	0.67	0.78	0.66	0.78	0.96	0.78	0.57	0.76	0.51	0.90	0.61	0.73	0.64			
1	1	0.92	0.50	0.49	0.29	0.98	0.77	0.98	0.94	0.60	0.25	0.98	0.44	0.61	0.42	0.98	0.74		0.56	0.56	
2	1	0.74	0.91	0.95	0.88	0.63	0.73	0.62	0.74	0.93	0.76	0.53	0.71	0.51	0.88	0.56	0.69		0.56	0.94	
3	1	0.74	0.95	0.97	0.93	0.63	0.79	0.63	0.76	0.97	0.79	0.54	0.75	0.48	0.92	0.58	0.70	0.56	0.94		
1	4	0.93	0.66	0.66	0.49	0.93	0.79	0.93	0.93	0.73	0.42	0.89	0.56	0.64	0.55	0.92	0.81		0.92	0.57	
2	4	0.92	0.51	0.50	0.30	0.98	0.78	0.98	0.95	0.61	0.26	0.99	0.45	0.61	0.44	0.98	0.74	0.92	0.39		
3	4	0.59	0.93	0.97	0.96	0.46	0.67	0.45	0.61	0.93	0.83	0.35	0.72	0.39	0.95	0.38	0.58	0.57	0.39		
1	6	0.93	0.52	0.51	0.32	0.98	0.78	0.98	0.95	0.62	0.27	0.98	0.46	0.62	0.45	0.98	0.75		0.41	0.90	
2	6	0.61	0.92	0.96	0.95	0.47	0.65	0.46	0.60	0.92	0.81	0.35	0.71	0.43	0.93	0.39	0.60	0.41		0.73	
3	6	0.94	0.81	0.82	0.68	0.92	0.89	0.92	0.97	0.89	0.58	0.88	0.67	0.62	0.80	0.91	0.82	0.90	0.73		
1	1	0.94	0.57	0.56	0.37	0.98	0.81	0.98	0.97	0.67	0.32	0.98	0.49	0.63	0.54	0.98	0.76		0.89	0.49	0.93
2	1	0.90	0.60	0.59	0.43	0.89	0.74	0.89	0.87	0.66	0.37	0.84	0.54	0.65	0.43	0.87	0.80	0.89	0.53	0.86	
3	1	0.61	0.92	0.96	0.94	0.48	0.67	0.48	0.63	0.93	0.81	0.38	0.68	0.41	0.94	0.41	0.58	0.49	0.53	0.56	
4	1	0.93	0.69	0.66	0.51	0.95	0.86	0.94	0.96	0.75	0.46	0.92	0.62	0.58	0.60	0.95	0.82	0.93	0.86	0.56	
1	4	0.90	0.60	0.59	0.43	0.89	0.74	0.89	0.87	0.66	0.37	0.85	0.54	0.65	0.43	0.88	0.80		0.89	0.53	0.87
2	4	0.94	0.57	0.56	0.37	0.98	0.81	0.98	0.97	0.67	0.32	0.98	0.49	0.63	0.54	0.98	0.76	0.89	0.49	0.93	
3	4	0.61	0.92	0.96	0.94	0.48	0.67	0.48	0.63	0.93	0.81	0.38	0.68	0.41	0.94	0.41	0.58	0.53	0.49	0.56	
4	4	0.93	0.69	0.66	0.51	0.95	0.87	0.94	0.96	0.76	0.46	0.92	0.63	0.58	0.60	0.95	0.82	0.87	0.93	0.56	

(1) Zhang, et al., 2005; (2) Lanz et al., 2007; (3) Ulbrich, et al., 2009; (4) Bahreini et al., 2005; (5) Alfarra et al., 2004

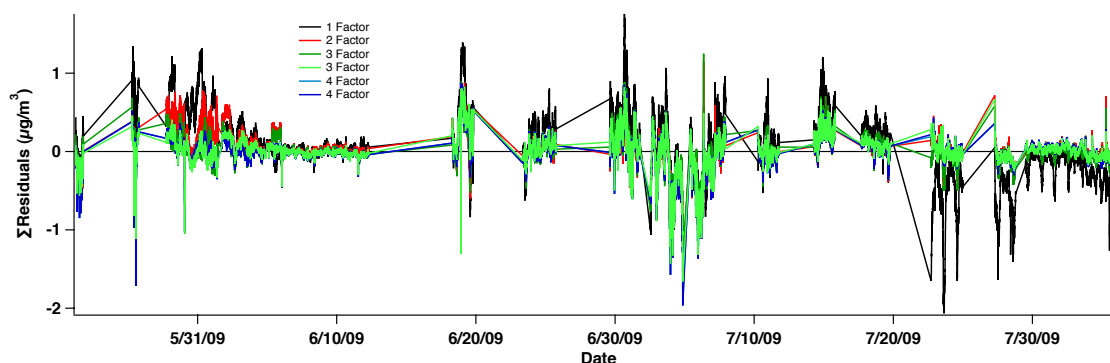
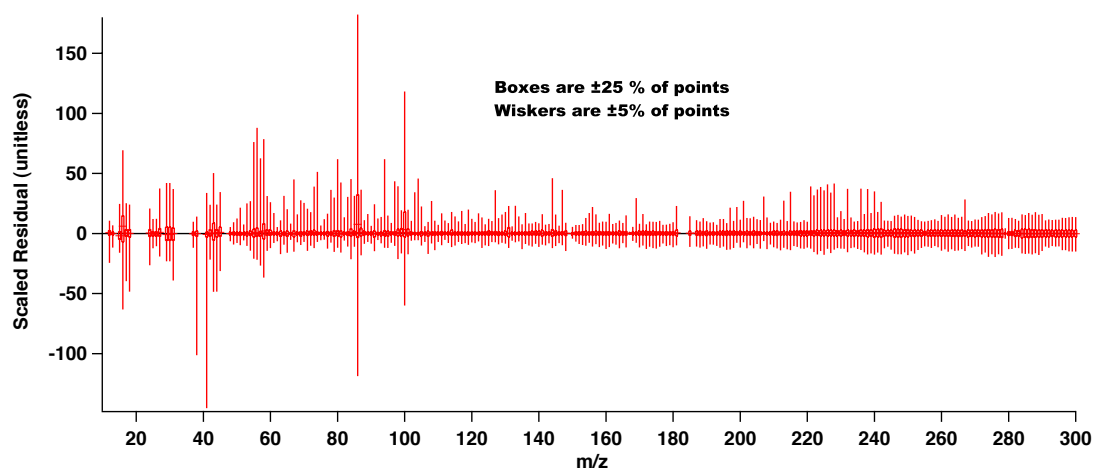
**Fig. A3.** Sum of the residuals for 1, 2, 3, and 4 factor solutions.

Table A2. Time series comparison of several PMF solutions.

Factor Number (<i>p</i>) Seed		Gas Phase Tracers			AMS Inorganic Tracers				Organic Tracers		PILS Tracers						
		Ozone	CO	NO _x	SO ₄	NO ₃	NH ₄	Chl	WSOC	org57	NH ₄	NO ₃	SO ₄	Factor 1	Factor 2	Factor 3	Factor 4
1	1	0.51	0.38	0.24	0.66	0.45	0.63	0.35	0.58	0.79	0.70	0.67	0.76				
1	1	0.46	0.33	0.14	0.73	0.45	0.64	0.43	0.53	0.54	0.74	0.69	0.79		0.51		
2	1	0.41	0.34	0.30	0.37	0.31	0.44	0.12	0.30	0.91	0.56	0.56	0.63	0.51			
1	1	0.47	0.33	0.16	0.71	0.44	0.63	0.42	0.56	0.53	0.73	0.68	0.79				
2	1	-0.06	0.15	-0.03	0.23	0.18	0.24	0.06	-0.39	0.61	0.22	0.22	0.20	-0.02	-0.02	0.73	
3	1	0.51	0.34	0.30	0.43	0.32	0.47	0.18	0.50	0.77	0.60	0.59	0.67	0.73	0.00		
1	4	0.07	0.12	-0.14	0.22	0.29	0.30	0.02	-0.19	0.22	0.10	0.25	0.14		-0.19	-0.02	
2	4	0.47	0.32	0.19	0.66	0.39	0.58	0.40	0.58	0.54	0.71	0.66	0.77	-0.19		0.64	
3	4	0.42	0.35	0.30	0.42	0.31	0.45	0.15	0.36	0.93	0.59	0.58	0.65	-0.02	0.64		
1	6	0.39	0.31	0.09	0.75	0.46	0.65	0.46	0.47	0.49	0.76	0.73	0.81		0.05	0.05	0.60
2	6	0.39	0.17	0.04	0.18	0.15	0.21	0.02	-0.29	0.70	0.16	0.17	0.14			-0.08	
3	6	0.53	0.31	0.28	0.42	0.31	0.45	0.19	0.56	0.62	0.60	0.58	0.67	0.60	-0.08		
1	1	0.43	0.30	0.15	0.71	0.39	0.58	0.43	0.53	0.52	0.73	0.66	0.79		-0.14	0.26	0.56
2	1	0.01	0.15	-0.07	0.16	0.29	0.26	0.01	-0.22	0.07	0.03	0.20	0.04	-0.14		0.06	-0.18
3	1	0.24	0.29	0.22	0.28	0.19	0.30	0.04	0.16	0.94	0.43	0.43	0.46	0.26	0.06		0.44
4	1	0.51	0.28	0.27	0.31	0.34	0.44	0.13	0.39	0.58	0.57	0.58	0.66	0.56	-0.18	0.44	
1	4	0.01	0.15	-0.07	0.16	0.29	0.26	0.01	-0.23	0.07	0.02	0.20	0.04		-0.15	0.06	-0.18
2	4	0.43	0.30	0.15	0.70	0.39	0.58	0.43	0.54	0.52	0.73	0.66	0.79	-0.15		0.26	0.56
3	4	0.24	0.29	0.22	0.27	0.19	0.30	0.04	0.16	0.94	0.43	0.43	0.46	0.06	0.26		0.43
4	4	0.51	0.28	0.27	0.31	0.34	0.44	0.13	0.39	0.58	0.57	0.58	0.66	-0.18	0.56	0.43	

**Fig. A4.** Scaled residuals for the 3 factor solution (seed = 6).

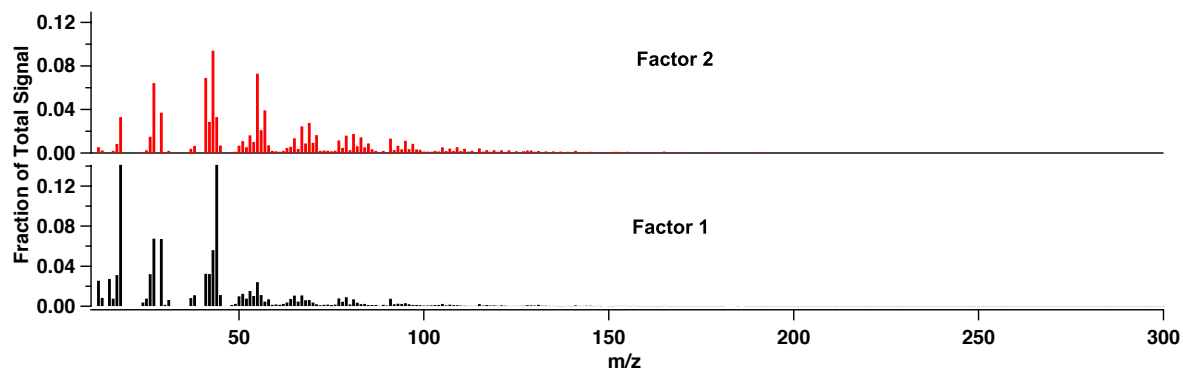


Fig. A5a. Mass spectral profiles for the 2 factor solution.

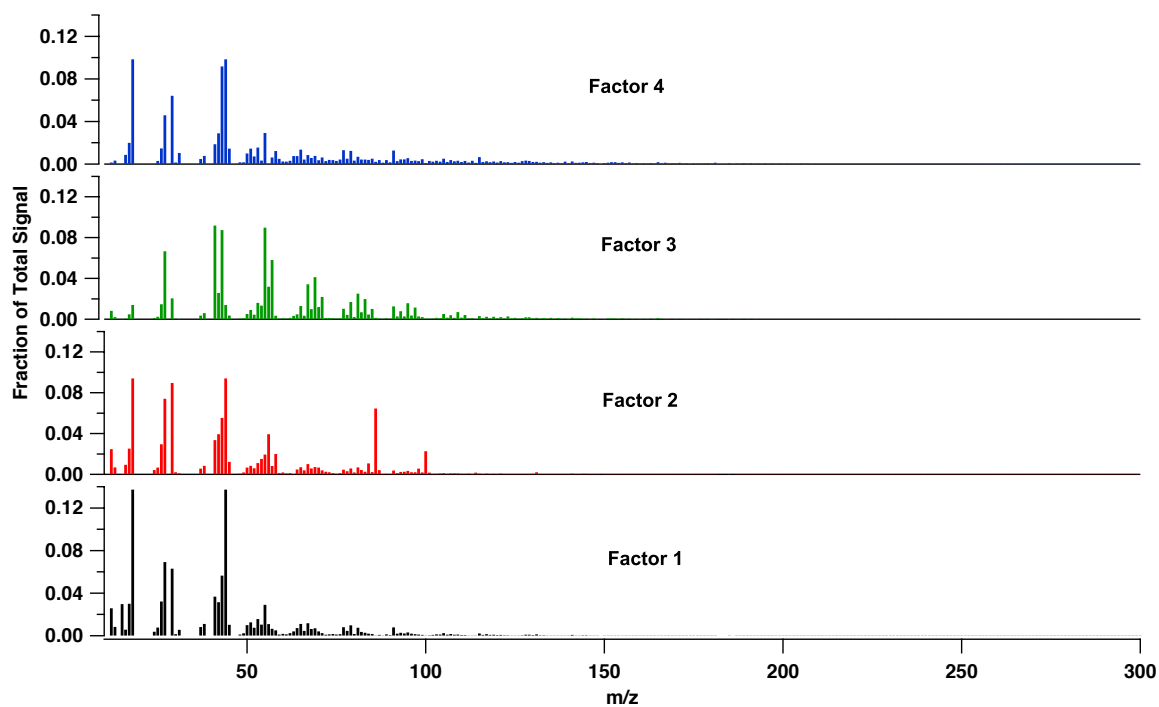


Fig. A5b. Mass spectral profiles for the 4 factor solution.

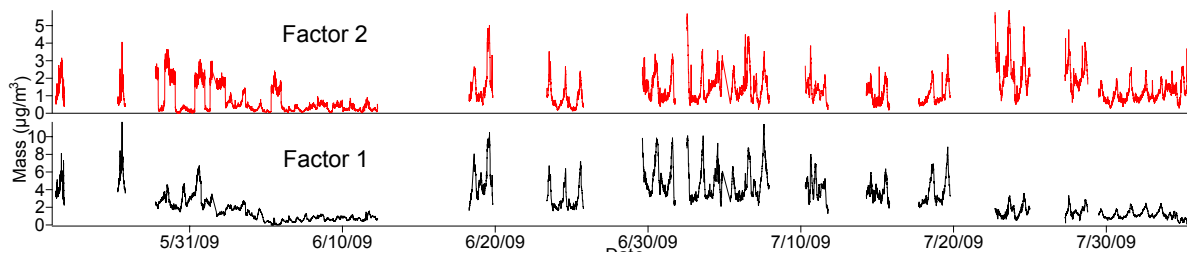


Fig. A6. Time series contributions for the 2-factor solution.

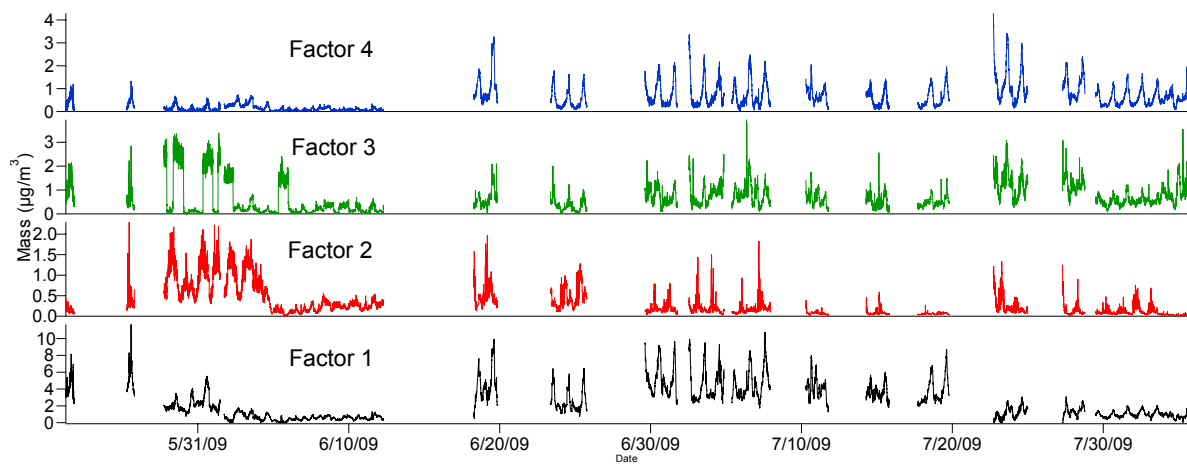


Fig. A7. Time series contributions for the 4-factor solution.

Acknowledgements. Funding was provided by the Electric Power Research Institute. The authors would like to thank Jason Surratt for his helpful comments and direction. We would also like to thank Eric Edgerton and the SEARCH network for guidance on high-volume filter sampling and for the use of a sampler during PACO.

Edited by: M. C. Facchini

References

- Aiken, A. C., DeCarlo, P. F., Kroll, J. H., Worsnop, D. R., Huffman, J. A., Docherty, K. S., Ulbrich, I. M., Mohr, C., Kimmel, J. R., Sueper, D., Sun, Y., Zhang, Q., Trimborn, A., Northway, M., Ziemann, P. J., Canagaratna, M. R., Onasch, T. B., Alfarra, M. R., Prevot, A. S. H., Dommen, J., Duplissy, J., Metzger, A., Baltensperger, U., and Jimenez, J. L.: O/C and OM/OC ratios of primary, secondary, and ambient organic aerosols with high-resolution time-of-flight aerosol mass spectrometry, *Environ. Sci. Technol.*, 42, 4478–4485, 2008.
- Aiken, A. C., Salcedo, D., Cubison, M. J., Huffman, J. A., DeCarlo, P. F., Ulbrich, I. M., Docherty, K. S., Sueper, D., Kimmel, J. R., Worsnop, D. R., Trimborn, A., Northway, M., Stone, E. A., Schauer, J. J., Volkamer, R. M., Fortner, E., de Foy, B., Wang, J., Laskin, A., Shutthanandan, V., Zheng, J., Zhang, R., Gaffney, J., Marley, N. A., Paredes-Miranda, G., Arnott, W. P., Molina, L. T., Sosa, G., and Jimenez, J. L.: Mexico City aerosol analysis during MILAGRO using high resolution aerosol mass spectrometry at the urban supersite (T0) – Part 1: Fine particle composition and organic source apportionment, *Atmos. Chem. Phys.*, 9, 6633–6653, doi:10.5194/acp-9-6633-2009, 2009.
- Alfarra, M., Coe, H., Allan, J., Bower, K., Boudries, H., Canagaratna, M., Jimenez, J., Jayne, J., Garforth, A., Li, S., and Worsnop, D. R.: Characterization of urban and rural organic particulate in the Lower Fraser Valley using two aerodyne aerosol mass spectrometers, *Atmos. Environ.*, 38, 5745–5758, 2004.
- Allan, J., Bower, K., Coe, H., Boudries, H., Jayne, J., Canagaratna, M., Millet, D., Goldstein, A., Quinn, P., Weber, R., and Worsnop, D.: Submicron aerosol composition at Trinidad Head, California, during ITCT 2K2: its relationship with gas phase volatile organic carbon and assessment of instrument performance, *J. Geophys. Res. Atmos.*, 109, D23S24, doi:10.1029/2003JD004208, 2004a.
- Allan, J., Delia, A., Coe, H., Bower, K., Alfarra, M., Jimenez, J., Middlebrook, A., Drewnick, F., Onasch, T., Canagaratna, M., Jayne, J., and Worsnop, D.: A generalised method for the extraction of chemically resolved mass spectra from aerodyne aerosol mass spectrometer data, *J. Aerosol Sci.*, 35, 909–922, doi:10.1016/j.jaerosci.2004.02.007, 2004b.
- Ault, A. P., Gaston, C. J., Wang, Y., Dominguez, G., Thiemens, M. H., and Prather, K. A.: Characterization of the single particle mixing state of individual ship plume events measured at the port of Los Angeles, *Environ. Sci. Technol.*, 44(6), 1954–1961, 2010.
- AQMD: Historic ozone air quality trends, available at: <http://www.aqmd.gov/smog/o3trend.html>, last access: August 2010, 2010.
- Bahreini, R., Keywood, M., Ng, N., Varutbangkul, V., Gao, S., Flagan, R., Seinfeld, J., Worsnop, D., and Jimenez, J.: Measurements of secondary organic aerosol from oxidation of cycloalkenes, terpenes, and m-xylene using an Aerodyne aerosol mass spectrometer, *Environ. Sci. Technol.*, 39, 5674–5688, 2005.
- Bein, K. J., Zhao, Y. J., Pekney, N. J., Davidson, C. I., Johnston, M. V., and Wexler, A. S.: Identification of sources of atmospheric PM at the Pittsburgh Supersite – Part II: Quantitative comparisons of single particle, particle number, and particle mass measurements, *Atmos. Environ.*, 40, S424–S444, 2006.
- Blumenthal, D., White, W., and Smith, T.: Anatomy of a Los Angeles smog episode: pollutant transport in the daytime sea breeze regime, *Atmos. Environ.*, 12, 893–907, 1978.
- Bremner, J., Haub, C., Lee, M., Mather, M., and Zuehlke, E.: World Population Highlights: Key Findings From PRB's 2009 World Population Data Sheet, Population Reference Bureau, available at: www.prb.org, 2009.
- Cabada, J. C., Rees, S., Takahama, S., Khlystov, A., Pandis, S. N., Davidson, C. I., and Robinson, A. L.: Mass size distributions and size resolved chemical composition of fine particulate matter at the Pittsburgh supersite, *Atmos. Environ.*, 38, 3127–3141, 2004.
- Canagaratna, M., Jayne, J., Jimenez, J., Allan, J., Alfarra, M., Zhang, Q., Onasch, T., Drewnick, F., Coe, H., Middlebrook, A., Worsnop, D. R., and Jimenez, J. L.: Chemical and microphysical characterization of ambient aerosols with the aerodyne aerosol mass spectrometer, *Mass Spectrom. Rev.*, 26, 185–222, 2007.
- CARB: iADAM Air Quality Data Statistics, California Air Resources Board, available at: <http://www.arb.ca.gov/adam/>, 2010.
- Chow, J. C., Fujita, E. M., Watson, J. G., Lu, Z. Q., Lawson, D. R., and Asbaugh, L. L.: Evaluation of filter-based aerosol measurements during the 1987 Southern California-Quality Study, *Environ. Monit. Assess.*, 30, 49–80, 1994.
- Cocker, D. R., Whitlock, N. E., Flagan, R. C., and Seinfeld, J. H.: Hygroscopic properties of Pasadena, California aerosol, *Aerosol Sci. Technol.*, 35, 637–647, 2001.
- Croes, B. E. and Fujita, E. M.: Overview of the 1997 Southern California Ozone Study (SCOS97-NARSTO), *Atmos. Environ.*, 37, S3–S26, 2003.
- Cubison, M. J., Ervens, B., Feingold, G., Docherty, K. S., Ulbrich, I. M., Shields, L., Prather, K., Hering, S., and Jimenez, J. L.: The influence of chemical composition and mixing state of Los Angeles urban aerosol on CCN number and cloud properties, *Atmos. Chem. Phys.*, 8, 5649–5667, doi:10.5194/acp-8-5649-2008, 2008.
- DeCarlo, P. F., Kimmel, J. R., Trimborn, A., Northway, M. J., Jayne, J. T., Aiken, A. C., Gonin, M., Fuhrer, K., Horvath, T., Docherty, K. S., Worsnop, D. R., and Jimenez, J. L.: Field-deployable, high-resolution, time-of-flight aerosol mass spectrometer, *Anal. Chem.*, 78, 8281–8289, 2006.
- DeCarlo, P. F., Dunlea, E. J., Kimmel, J. R., Aiken, A. C., Sueper, D., Crouse, J., Wennberg, P. O., Emmons, L., Shinzuka, Y., Clarke, A., Zhou, J., Tomlinson, J., Collins, D. R., Knapp, D., Weinheimer, A. J., Montzka, D. D., Campos, T., and Jimenez, J. L.: Fast airborne aerosol size and chemistry measurements above Mexico City and Central Mexico during the MILAGRO campaign, *Atmos. Chem. Phys.*, 8, 4027–4048, doi:10.5194/acp-8-4027-2008, 2008.
- Denkenberger, K. A., Moffet, R. C., Holecek, J. C., Rebotier, T. P., and Prather, K. A.: Real-time, single-particle measurements of oligomers in aged ambient aerosol particles, *Environ. Sci. Technol.*, 41, 5439–5446, 2007.
- Dusek, U., Frank, G. P., Curtius, J., Drewnick, F., Schneider,

- J., Kürten, A., Rose, D., Andreae, M. O., Borrmann, S., and Pöschl, U.: Enhanced organic mass fraction and decreased hygroscopicity of cloud condensation nuclei (CCN) during new particle formation events, *Geophys. Res. Lett.*, 37, L03804, doi:10.1029/2009GL040930, 2010.
- Docherty, K. S., Stone, E. A., Ulbrich, I. M., DeCarlo, P. F., Snyder, D. C., Schauer, J. J., Peltier, R. E., Weber, R. J., Murphy, S. M., Seinfeld, J. H., Grover, B. D., Eatough, D. J., and Jimenez, J. L.: Apportionment of primary and secondary organic aerosols in Southern California during the 2005 Study of Organic Aerosols in Riverside (SOAR-1), *Environ. Sci. Technol.*, 42, 7655–7662, 2008.
- Drewnick, F., Schwab, J., Högrefe, O., Peters, S., Husain, L., Diamond, D., Weber, R., and Demerjian, K.: Intercomparison and evaluation of four semi-continuous PM_{2.5} sulfate instruments, *Atmos. Environ.*, 37, 3335–3350, doi:10.1016/S1352-2310(03)00351-0, 2003.
- Drewnick, F., Hings, S., DeCarlo, P., Jayne, J., Gonin, M., Fuhrer, K., Weimer, S., Jimenez, J., Demerjian, K., Borrmann, S., and Worsnop, D.: A new time-of-flight aerosol mass spectrometer (TOF-AMS) – instrument description and first field deployment, *Aerosol Sci. Tech.*, 39, 637–658, doi:10.1080/02786820500182040, 2005.
- Eatough, D. J., Grover, B. D., Woolwine, W. R., Eatough, N. L., Long, R., and Farber, R.: Source apportionment of 1 h semi-continuous data during the 2005 Study of Organic Aerosols in Riverside (SOAR) using positive matrix factorization, *Atmos. Environ.*, 42, 2706–2719, 2008.
- Eldering, A., Cass, G. R., and Moon, K. C.: An Air monitoring network using continuous particle-size distribution monitors – connecting pollutant properties to visibility via mie scattering calculations, *Atmos. Environ.*, 28, 2733–2749, 1994.
- Hersey, S. P., Sorooshian, A., Murphy, S. M., Flagan, R. C., and Seinfeld, J. H.: Aerosol hygroscopicity in the marine atmosphere: a closure study using high-time-resolution, multiple-RH DASH-SP and size-resolved C-ToF-AMS data, *Atmos. Chem. Phys.*, 9, 2543–2554, doi:10.5194/acp-9-2543-2009, 2009.
- Huffman, J., Jayne, J., Drewnick, F., Aiken, A., Onasch, T., Worsnop, D., and Jimenez, J.: Design, modeling, optimization, and experimental tests of a particle beam width probe for the aerodyne aerosol mass spectrometer, *Aerosol Sci. Tech.*, 39, 1143–1163, doi:10.1080/02786820500423782, 2005.
- Hughes, L. S., Allen, J. O., Salmon, L. G., Mayo, P. R., Johnson, R. J., and Cass, G. R.: Evolution of nitrogen species air pollutants along trajectories crossing the Los Angeles area, *Environ. Sci. Technol.*, 36, 3928–3935, 2002.
- Kautzman, K. E., Surratt, J. D., Chan, M. N., Chan, A. W. H., Hersey, S. P., Chhabra, P. S., Dalleska, N. F., Wennberg, P. O., Flagan, R. C., and Seinfeld, J. H.: Chemical composition of gas- and aerosol-phase products from the photooxidation of naphthalene, *J. Phys. Chem. A*, 114, 913–934, 2010.
- Kleeman, M., Hughes, L., Allen, J., and Cass, G.: Source contributions to the size and composition distribution of atmospheric particles: Southern California in September 1996, *Environ. Sci. Technol.*, 33, 4331–4341, 1999.
- Kondo, Y., Miyazaki, Y., Takegawa, N., Miyakawa, T., Weber, R. J., Jimenez, J. L., Zhang, Q., and Worsnop, D. R.: Oxygenated and water-soluble organic aerosols in Tokyo, *J. Geophys. Res.*, 112, D01203, doi:10.1029/2006JD007056, 2007.
- Lanz, V. A., Alfarra, M. R., Baltensperger, U., Buchmann, B., Hueglin, C., and Prévôt, A. S. H.: Source apportionment of sub-micron organic aerosols at an urban site by factor analytical modelling of aerosol mass spectra, *Atmos. Chem. Phys.*, 7, 1503–1522, doi:10.5194/acp-7-1503-2007, 2007.
- Liu, D. Y., Prather, K. A., and Hering, S. V.: Variations in the size and chemical composition of nitrate-containing particles in Riverside, CA, *Aerosol Sci. Technol.*, 33, 71–86, 2000.
- Lu, R. and Turco, R.: Air pollutant transport in a coastal environment – II. Three-dimensional simulations over Los Angeles Basin, *Atmos. Environ.*, 29, 1499–1518, 1995.
- Massling, A., Stock, M., and Wiedensohler, A.: Diurnal, weekly, and seasonal variation of hygroscopic properties of submicrometer urban aerosol particles, *Atmos. Environ.*, 39, 3911–3922, 2005.
- Massling, A., Stock, M., Wehner, B., Wu, Z. J., Hu, M., Brüggemann, E., Gnauk, T., Herrmann, H., and Wiedensohler, A.: Size segregated water uptake of the urban submicrometer aerosol in Beijing, *Atmos. Environ.*, 43, 1578–1589, 2009.
- Matsui, H., Koike, M., Kondo, Y., Takegawa, N., Kita, K., Miyazaki, Y., Hu, M., Chang, S. Y., Blake, D. R., Fast, J. D., Zaveri, R. A., Streets, D. G., Zhang, Q., and Zhu, T.: Spatial and temporal variations of aerosols around Beijing in summer 2006: model evaluation and source apportionment, *J. Geophys. Res. Atmos.*, 114, D00G13, 2009.
- Meier, J., Wehner, B., Massling, A., Birmili, W., Nowak, A., Gnauk, T., Brüggemann, E., Herrmann, H., Min, H., and Wiedensohler, A.: Hygroscopic growth of urban aerosol particles in Beijing (China) during wintertime: a comparison of three experimental methods, *Atmos. Chem. Phys.*, 9, 6865–6880, doi:10.5194/acp-9-6865-2009, 2009.
- Modey, W. K., Eatough, D. J., Anderson, R. R., Martello, D. V., Takahama, S., Lucas, L. J., and Davidson, C. I.: Ambient fine particulate concentrations and chemical composition at two sampling sites in metropolitan Pittsburgh: a 2001 intensive summer study, *Atmos. Environ.*, 38, 3165–3178, 2004.
- Na, K., Sawant, A. A., Song, C., and Cocker, D. R.: Primary and secondary carbonaceous species in the atmosphere of Western Riverside County, California *Atmos. Environ.*, 38, 1345–1355, 2004.
- Ng, N. L., Canagaratna, M. R., Zhang, Q., Jimenez, J. L., Tian, J., Ulbrich, I. M., Kroll, J. H., Docherty, K. S., Chhabra, P. S., Bahreini, R., Murphy, S. M., Seinfeld, J. H., Hildebrandt, L., Donahue, N. M., DeCarlo, P. F., Lanz, V. A., Prévôt, A. S. H., Dinar, E., Rudich, Y., and Worsnop, D. R.: Organic aerosol components observed in Northern Hemispheric datasets from Aerosol Mass Spectrometry, *Atmos. Chem. Phys.*, 10, 4625–4641, doi:10.5194/acp-10-4625-2010, 2010.
- Ng, N. L., Canagaratna, M. R., Jimenez, J. L., Zhang, Q., Ulbrich, I. M., and Worsnop, D. R.: Real-time methods for estimating organic component mass concentrations from aerosol mass spectrometer data, *Environ. Sci. Technol.*, 45, 910–916, doi:10.1021/es102951k, 2011.
- Paatero, P.: A weighted non-negative least squares algorithm for three-way “PARAFAC” factor analysis, *Chemom. Intell. Lab. Syst.*, 38, 223–242, 1997.
- Paatero, P. and Tapper, U.: Positive matrix factorization – a nonnegative factor model with optimal utilization of error-estimates of data values, *Environmetrics*, 5, 111–126, 1994.

- Pastor, S. H., Allen, J. O., Hughes, L. S., Bhave, P., Cass, G. R., and Prather, K. A.: Ambient single particle analysis in Riverside, California by aerosol time-of-flight mass spectrometry during the SCOS97-NARSTO, *Atmos. Environ.*, **37**, S239–S258, 2003.
- Pekney, N. J., Davidson, C. I., Bein, K. J., Wexler, A. S., and Johnston, M. V.: Identification of sources of atmospheric PM at the Pittsburgh Supersite, Part I: single particle analysis and filter-based positive matrix factorization, *Atmos. Environ.*, **40**, S411–S423, 2006.
- Petters, M. D. and Kreidenweis, S. M.: A single parameter representation of hygroscopic growth and cloud condensation nucleus activity, *Atmos. Chem. Phys.*, **7**, 1961–1971, doi:10.5194/acp-7-1961-2007, 2007.
- van Pinxteren, D., Brüggemann, E., Gnauk, T., Iinuma, Y., Müller, K., Nowak, A., Achtert, P., Wiedensohler, A., and Herrmann, H.: Size- and time-resolved chemical particle characterization during CAREBeijing-2006: different pollution regimes and diurnal profiles, *J. Geophys. Res. Atmos.*, **114**, D00G09, doi:10.1029/2008JD010890, 2009.
- Quinn, P., Bates, T., Baynard, T., Clarke, A., Onasch, T., Wang, W., Rood, M., Andrews, E., Allan, J., Carrico, C., Coffman, D., and Worsnop, D. R.: Impact of particulate organic matter on the relative humidity dependence of light scattering: a simplified parameterization, *Geophys. Res. Lett.*, **32**(22), L22809, doi:10.1029/2005GL024322, 2005.
- Rose, D., Nowak, A., Achtert, P., Wiedensohler, A., Hu, M., Shao, M., Zhang, Y., Andreae, M. O., and Pöschl, U.: Cloud condensation nuclei in polluted air and biomass burning smoke near the mega-city Guangzhou, China – Part 1: Size-resolved measurements and implications for the modeling of aerosol particle hygroscopicity and CCN activity, *Atmos. Chem. Phys.*, **10**, 3365–3383, doi:10.5194/acp-10-3365-2010, 2010.
- Sawant, A. A., Na, K., Zhu, X., Cocker, K., Butt, S., Song, C., and Cocker III, D. R.: Characterization of PM_{2.5} and selected gas-phase compounds at multiple indoor and outdoor sites in Mira Loma, California, *Atmos. Environ.*, **38**, 6269–6278, 2004.
- Schauer, J. J., Rogge, W. F., Hildemann, L. M., Mazurek, M. A., and Cass, G. R.: Source apportionment of airborne particulate matter using organic compounds as tracers, *Atmos. Environ.*, **30**, 3837–3855, 1996.
- Shinozuka, Y., Clarke, A. D., DeCarlo, P. F., Jimenez, J. L., Dunlea, E. J., Roberts, G. C., Tomlinson, J. M., Collins, D. R., Howell, S. G., Kapustin, V. N., McNaughton, C. S., and Zhou, J.: Aerosol optical properties relevant to regional remote sensing of CCN activity and links to their organic mass fraction: airborne observations over Central Mexico and the US West Coast during MILAGRO/INTEX-B, *Atmos. Chem. Phys.*, **9**, 6727–6742, doi:10.5194/acp-9-6727-2009, 2009.
- Sorooshian, A., Brechtel, F., Weber, R., Corless, A., Flagan, R., and Seinfeld, J.: Modeling and characterization of a particle-into-liquid sampler (PILS), *Aerosol Sci. Technol.*, **40**, 396–409, 2006.
- Sorooshian, A., Hersey, S., Brechtel, F., Corless, A., Flagan, R., and Seinfeld, J.: Rapid, size-resolved aerosol hygroscopic growth measurements: differential aerosol sizing and hygroscopicity spectrometer probe (DASH-SP), *Aerosol Sci. Technol.*, **42**, 445–464, 2008.
- Stanier, C., Khlystov, A., and Pandis, S.: Nucleation events during the Pittsburgh Air Quality Study: description and relation to key meteorological, gas phase, and aerosol parameters special issue of aerosol science and technology on findings from the fine particulate matter supersites program, *Aerosol Sci. Technol.*, **38**, 253–264, 2004.
- Stone, E. A., Snyder, D. C., Sheesley, R. J., Sullivan, A. P., Weber, R. J., and Schauer, J. J.: Source apportionment of fine organic aerosol in Mexico City during the MILAGRO experiment 2006, *Atmos. Chem. Phys.*, **8**, 1249–1259, doi:10.5194/acp-8-1249-2008, 2008.
- Sullivan, A., Weber, R., Clements, A., Turner, J., Bae, M., and Schauer, J.: A method for on-line measurement of water-soluble organic carbon in ambient aerosol particles: results from an urban site, *Geophys. Res. Lett.*, **31**, L13105, doi:10.1029/2004GL019681, 2004.
- Sullivan, A., Peltier, R., Brock, C., De Gouw, J., Holloway, J., Warneke, C., Wollny, A., and Weber, R.: Airborne measurements of carbonaceous aerosol soluble in water over Northeastern United States: method development and an investigation into water-soluble organic carbon sources, *J. Geophys. Res.*, **111**, 1–14, 2006.
- Surratt, J., Gomez-Gonzalez, Y., Chan, A., Vermeylen, R., Shahgholi, M., Kleindienst, T., Edney, E., Offenberg, J., Lewandowski, M., Jaoui, M., Maenhaut, W., Claeys, M., Flagan, R. C., and Seinfeld, J. H.: Organosulfate formation in biogenic secondary organic aerosol, *J. Phys. Chem. A*, **112**, 8345–8378, 2008.
- Swietlicki, E., Hansson, H., Hameri, K., Svenningsson, B., Massling, A., McFiggans, G., McMurry, P., Petaja, T., Tunved, P., Gysel, M., Topping, D., Weingartner, E., Baltensperger, U., Rissler, J., Wiedensohler, A., and Kulmala, M.: Hygroscopic properties of submicrometer atmospheric aerosol particles measured with H-TDMA instruments in various environments – a review, *Tellus B*, **60**, 432–469, 2008.
- Tiitta, P., Miettinen, P., Vaattovaara, P., Joutsensaari, J., Pet, T., Virtanen, A., Raatikainen, T., Aalto, P., Portin, H., Romakkaniemi, S., Kokkolab, H., Lehtinen, E. J., Markku, K., and Laaksonena, A.: Roadside aerosol study using hygroscopic, organic and volatility TDMA: characterization and mixing state, *Atmos. Environ.*, **44**, 976–986, 2010.
- Turpin, B. J. and Huntzicker, J. J.: Secondary formation of organic aerosol in the Los-Angeles Basin – a descriptive analysis of organic and elemental carbon concentrations, *Atmos. Environ. A*, **25**, 207–215, 1991.
- Turpin, B. J. and Lim, H.-J.: Species contributions to PM_{2.5} mass concentrations: revisiting common assumptions for estimating organic mass, *Aerosol Sci. Technol.*, **35**, 602–610, 2001.
- Ulbrich, I. M., Canagaratna, M. R., Zhang, Q., Worsnop, D. R., and Jimenez, J. L.: Interpretation of organic components from Positive Matrix Factorization of aerosol mass spectrometric data, *Atmos. Chem. Phys.*, **9**, 2891–2918, doi:10.5194/acp-9-2891-2009, 2009.
- Ulbrich, I. M., Lechner, M., and Jimenez, J. L.: AMS Spectral Database, available at: <http://cires.colorado.edu/jimenez-group/AMSsd/>, 2009.
- Wang, J., Cubison, M. J., Aiken, A. C., Jimenez, J. L., and Collins, D. R.: The importance of aerosol mixing state and size-resolved composition on CCN concentration and the variation of the importance with atmospheric aging of aerosols, *Atmos. Chem. Phys.*, **10**, 7267–7283, doi:10.5194/acp-10-7267-2010, 2010.

- Watson, J. G., Chow, J. C., Lu, Z. Q., Fujita, E. M., Lowenthal, D. H., Lawson, D. R., and Ashbaugh, L. L.: Chemical mass-balance source apportionment of PM₍₁₀₎ during the Southern California Air-Quality Study, *Aerosol Sci. Technol.*, 21, 1–36, 1994.
- Wex, H., McFiggans, G., Henning, S., and Stratmann, F.: Influence of the external mixing state of atmospheric aerosol on derived CCN number concentrations, *Geophys. Res. Lett.*, 37, L10805, doi:10.1029/2010GL043337, 2010.
- Wittig, A. E., Anderson, N., Khlystov, A. Y., Pandis, S. N., Davidson, C., and Robinson, A. L.: Pittsburgh air quality study overview, *Atmos. Environ.*, 38, 3107–3125, 2004.
- Yue, D. L., Hu, M., Wu, Z. J., Wang, Z. B., Guo, S., Wehner, B., Nowak, A., Achtert, P., Wiedensohler, A., Jung, J., Kim, Y. J., and Liu, S.: Characteristics of aerosol size distributions and new particle formation in the summer in Beijing, *J. Geophys. Res. Atmos.*, 114, D00G12, doi:10.1029/2008JD010894, 2009.
- Zhang, X. and McMurray, S.: Mixing characteristics and water content of submicron aerosols measured in Los Angeles and at the Grand Canyon, *Atmos. Environ. A*, 27, 1593–1607, 1993.
- Zhang, Q., Alfarra, M., Worsnop, D., Allan, J., Coe, H., Canagaratna, M., and Jimenez, J.: Deconvolution and quantification of hydrocarbon-like and oxygenated organic aerosols based on aerosol mass spectrometry, *Environ. Sci. Technol.*, 39, 4938–4952, 2005.
- Zhang, Q., Jimenez, J. L., Canagaratna, M. R., Allan, J. D., Coe, H., Ulbrich, I., Alfarra, M. R., Takami, A., Middlebrook, A. M., Sun, Y. L., Dzepina, K., Dunlea, E., Docherty, K., DeCarlo, P. F., Salcedo, D., Onasch, T., Jayne, J. T., Miyoshi, T., Shimojo, A., Hatakeyama, S., Takegawa, N., Kondo, Y., Schneider, J., Drewnick, F., Borrmann, S., Weimer, S., Demerjian, K., Williams, P., Bower, K., Bahreini, R., Cottrell, L., Griffin, R. J., Rautiainen, J., Sun, J. Y., Zhang, Y. M., and Worsnop, D. R.: Ubiquity and dominance of oxygenated species in organic aerosols in anthropogenically-influenced Northern Hemisphere midlatitudes, *Geophys. Res. Lett.*, 34, L13801, doi:10.1029/2007GL029979, 2007.

Appendix D

Effect of Chemical Structure on Secondary Organic Aerosol Formation
from C₁₂ Alkanes⁶

⁶ Reproduced by permission from “Effect of chemical structure on secondary organic aerosol formation from C₁₂ alkanes” by L. D. Yee, J. S. Craven, C. L. Loza, K. A. Schilling, N. L. Ng, M. R. Canagaratna, P. J. Ziemann, R. C. Flagan, and J. H. Seinfeld. *Atmos. Chem. Phys.* **2013**, *13*, 11121-11140.



Effect of chemical structure on secondary organic aerosol formation from C₁₂ alkanes

L. D. Yee^{1,*}, J. S. Craven², C. L. Loza², K. A. Schilling², N. L. Ng³, M. R. Canagaratna⁴, P. J. Ziemann⁵, R. C. Flagan^{2,1}, and J. H. Seinfeld^{2,1}

¹Division of Engineering and Applied Science, California Institute of Technology, Pasadena, California, USA

²Division of Chemistry and Chemical Engineering, California Institute of Technology, Pasadena, California, USA

³School of Chemical and Biomolecular Engineering and School of Earth and Atmospheric Sciences, Georgia Institute of Technology, Atlanta, Georgia, USA

⁴Aerodyne Research, Inc., Billerica, Massachusetts, USA

⁵Air Pollution Research Center, Department of Environmental Sciences, and Environmental Toxicology Graduate Program, University of California, Riverside, California, USA

*now at: Department of Environmental Science, Policy and Management, University of California, Berkeley, California, USA

Correspondence to: J. H. Seinfeld (seinfeld@caltech.edu)

Received: 5 April 2013 – Published in Atmos. Chem. Phys. Discuss.: 24 April 2013

Revised: 17 September 2013 – Accepted: 11 October 2013 – Published: 15 November 2013

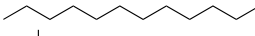
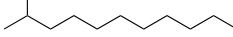
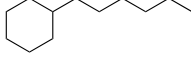
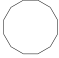
Abstract. The secondary organic aerosol (SOA) formation from four C₁₂ alkanes (*n*-dodecane, 2-methylundecane, hexylcyclohexane, and cyclododecane) is studied in the Caltech Environmental Chamber under low-NO_x conditions, in which the principal fate of the peroxy radical formed in the initial OH reaction is reaction with HO₂. Simultaneous gas- and particle-phase measurements elucidate the effect of alkane structure on the chemical mechanisms underlying SOA growth. Reaction of branched structures leads to fragmentation and more volatile products, while cyclic structures are subject to faster oxidation and lead to less volatile products. Product identifications reveal that particle-phase reactions involving peroxyhemiacetal formation from several multifunctional hydroperoxide species are key components of initial SOA growth in all four systems. The continued chemical evolution of the particle-phase is structure-dependent, with 2-methylundecane SOA formation exhibiting the least extent of chemical processing and cyclododecane SOA achieving sustained growth with the greatest variety of chemical pathways. The extent of chemical development is not necessarily reflected in the oxygen to carbon (O:C) ratio of the aerosol as cyclododecane achieves the lowest O:C, just above 0.2, by the end of the experiment and hexylcyclohexane the highest, approaching 0.35.

1 Introduction

Long-chain alkanes constitute a significant component of the unresolved complex mixture (UCM) in motor vehicle fuel sources and its combustion products (Schauer et al., 1999, 2002) and are a potential source of atmospheric secondary organic aerosol (SOA) formation (Robinson et al., 2007). However, the extent of SOA formation from atmospheric alkane photooxidation remains uncertain (Bahreini et al., 2012; Gentner et al., 2012). Each fuel type (e.g., gasoline vs. diesel) has different distributions of alkane chain length and structure in terms of straight-chain, branched, cyclic, and cyclic + branched conformations (Schauer et al., 1999, 2002; Isaacman et al., 2012; Gentner et al., 2012). This variety in structure leads to chemical differences in the processes leading to SOA formation, which have been the subject of extensive laboratory studies (Lim and Ziemann, 2005; Lipsky and Robinson, 2006; Lim and Ziemann, 2009a, b, c; Presto et al., 2009, 2010; Nakao et al., 2011; Lambe et al., 2012; Tkacik et al., 2012) and modeling efforts (Jordan et al., 2008; Pye and Pouliot, 2012; Zhang and Seinfeld, 2013; Aumont et al., 2012; Cappa et al., 2013).

Gas-phase chemical mechanisms for the OH-initiated oxidation of alkanes in the presence of NO_x have been studied (Atkinson, 1994, 1997; Atkinson and Arey, 2003; Atkinson

Table 1. C₁₂ compounds studied.

Compound	Structure	V.P. ^a @ 25 °C (atm)	$k_{\text{OH}} \times 10^{12\text{b}}$ (molec cm ⁻³ s ⁻¹)
<i>n</i> -dodecane		2.59×10^{-4}	13.9
2-methylundecane		4.1×10^{-4}	13.1
hexylcyclohexane		2.59×10^{-4}	17.4
cyclododecane		1.64×10^{-4}	14.7

^a Using EVAPORATION (Compernelle et al., 2011)^b Calculated using relative rate from *n*-dodecane k_{OH} in MCM (Jenkin et al., 1997).

et al., 2008). Many aspects of key particle-phase reactions for these species have also been explored (Aschmann et al., 2003; Dibble, 2007; Lim and Ziemann, 2009c). The prevailing level of NO_x is fundamental in atmospheric oxidation chemistry, as it controls, among other steps, the fate of the alkyl peroxy radical (RO₂) formed in the initial OH-organic reaction. The designation, high- and low-NO_x, refer to conditions in which the RO₂ fate is predominantly RO₂ + NO and RO₂ + HO₂, respectively. These cases represent idealizations of actual atmospheric conditions, but they allow isolation of the mechanistic pathways leading to SOA formation in the two cases.

We focus here on the low-NO_x oxidation mechanisms of four C₁₂ alkanes (*n*-dodecane, 2-methylundecane, hexylcyclohexane, and cyclododecane) (Table 1). The C₁₂ alkane system is a prototype for relatively long alkanes, which are characterized by side chains and cyclic structure in addition to a linear structure. The distribution of oxidation products comprise a variety of functionalizations (hydroperoxy, hydroxyl, ketone, aldehyde, carboxylic acid, and peracid). Detailed study of the C₁₂ system affords insight into the effect of alkane structure on the multigeneration gas-phase oxidation and particle-phase chemistry that leads to SOA formation.

This study builds on the previous work on the *n*-dodecane low-NO_x system (Yee et al., 2012; Craven et al., 2012) employing complementary gas- (chemical ionization mass spectrometry) and particle-phase measurements (Aerodyne high-resolution time-of-flight aerosol mass spectrometry). Those studies revealed that peroxyhemiacetals are likely major components of the organic aerosol at initial growth. This was hypothesized via comparison of time trends of key gas- and particle-phase ion tracers that showed initial SOA growth to be coincident with gas-phase aldehyde formation in the system, which can react with an available multifunctional hydroperoxide to form a peroxyhemiacetal (PHA). Of special interest in this study is the identification of and incorporation of multifunctional hydroperoxides in the aerosol via such accretion reactions as well as the chemical evolution of the aerosol as it ages.

Increasing evidence of accretion reactions observed in laboratory (Gao et al., 2004b, a; Kalberer, 2004; Surratt et al., 2010) and field measurements (Kalberer et al., 2006) suggest that these reactions are critical for understanding SOA formation chemistry (DePalma et al., 2013). PHA and peroxide formation have been observed in previous laboratory studies (Tobias et al., 2000; Tobias and Ziemann, 2000) and are relevant to consider in SOA formation from biogenics (Docherty et al., 2005; Capouet et al., 2008; Surratt et al., 2007), and aromatic systems (Johnson et al., 2005; Sato et al., 2007). Modeling studies including Capouet et al. (2008) and Johnson et al. (2005) show that parameterizations of laboratory SOA formation are improved if low volatility, high molecular weight product (PHA) formation is included. Modeling by Pye and Pouliot (2012) shows that alkanes are likely to contribute greater SOA mass concentrations than polyaromatic hydrocarbons and about half of this SOA formation could be from oligomers.

Most accretion reactions are not traditionally treated in modeling of atmospheric chemistry, mostly because the chemical pathways are not well-constrained by molecular level measurements. The current study provides measurements that elucidate PHA formation pathways in these alkane systems and data that can be used for modeling particle-phase chemical processes. For example, Shiraiwa et al. (2013) found that the observed evolution of the particle size distribution in *n*-dodecane oxidation under low-NO_x conditions could only be reasonably simulated when including kinetically-limited growth processes in the form of particle-phase reactions (i.e., PHA formation). Additional controlled studies, like those described in this work, can provide a framework for modeling additional particle-phase reactions that provide insight into the controlling processes of SOA growth.

2 Experimental section

2.1 Chamber experiments

The experiments in this study were conducted using the experimental protocols and controls as discussed in Yee et al. (2012) and Craven et al. (2012). The experiments and conditions are given in Table 2. The *n*-dodecane experiments are the same as those presented in Yee et al. (2012) and Craven et al. (2012), and are used here for additional analyses and comparisons to the other C₁₂ structures.

Experiments were conducted in the dual 28 m³ Caltech Environmental Chambers (Cocker et al., 2001; Keywood et al., 2004). The chambers were flushed for at least 24 h with dry purified air between experiments, resulting in particle number and volume concentrations < 100 cm⁻³ and < 0.1 μm³ cm⁻³, respectively. Particle number concentration and size distributions were measured using a coupled differential mobility analyzer (DMA, TSI model 3081) and condensation particle counter (TSI Model 3010). Hydroxyl radicals were generated by photolysis of H₂O₂. Experiments began with slow injection of 280 μL of a 50 % aqueous H₂O₂ solution in a glass trap submerged in a warm water bath at 35–38 °C, via a 5 L min⁻¹ flow of pure air. The chamber was then seeded with atomized 0.015 M aqueous ammonium sulfate solution to achieve a target initial seed volume of ~ 10–15 μm³ cm⁻³. Subsequently, the hydrocarbon was injected by delivering the appropriate liquid volume or solid mass amount for the desired chamber concentration into a glass bulb, gently heating the glass bulb, and flowing 5 L min⁻¹ of pure air over the hydrocarbon until evaporation was complete.

Temperature (*T*), relative humidity (RH), and concentrations of O₃, NO, and NO_x were continuously monitored. Experiments were run at temperatures ranging from 23–26 °C after an initial rise from 20 °C upon irradiation. RH remained below 10 % for all experiments except for the cyclododecane 36 h experiment in which RH rose to about 20 % in the last six hours. NO levels remained below the 5 ppbv lower detection limit of the analyzer (Horiba, APNA 360) and measured NO₂ levels remained below 7 ppbv after irradiation began.

2.2 Gas- and particle-phase measurements

Hydrocarbon concentration was continuously monitored by gas chromatograph–flame ionization detection (GC-FID) by taking 1.3 L samples of chamber air on Tenax adsorbent. The cartridge was loaded into the GC-FID (Agilent 6890N), desorbed, and injected onto an HP-5 column (15 m × 0.53 mm ID × 1.5 μm thickness, Hewlett-Packard).

Gas-phase oxidation products were monitored using a chemical ionization mass spectrometer (CIMS), consisting of a custom-modified Varian 1200 triple quadrupole mass spectrometer (Crouse et al., 2006; Paulot et al., 2009; St. Clair et al., 2010). Briefly, the instrument was operated in neg-

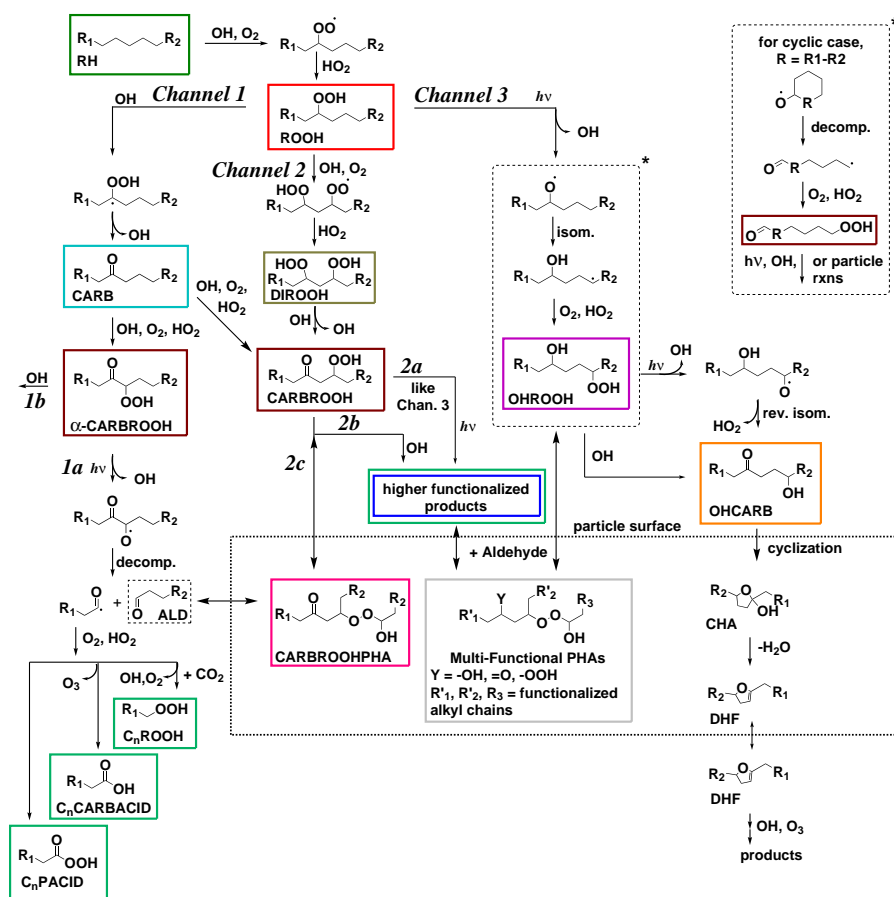
ative mode with CF₃OOCF₃ reagent gas, generating cluster products from the analyte at [X·CF₃O]⁻ and F transfer products at [X·F]⁻. The cluster product tends to occur when the analyte, X, is a hydroperoxide or weakly acidic compound. The transfer product dominates for more strongly acidic compounds. Several carboxylic acids are present in both ionizations, and are therefore reported as the sum of the two products when used. The CIMS cannot detect ketones and aldehydes in this mode unless a molecule is additionally-functionalized with hydroperoxy or sufficient acidic groups (e.g., hydroxy, carboxyl) that it is sensitive to. The negative mode mass scan range was *m/z* 50–300. Positive mode ionization utilizes water as the reagent gas and results in ion clusters of the form [X·(H₂O)_{*n*}H]⁺. The positive mode mass scan ranged from *m/z* 50 to 200. The gas-phase analyses presented here assume that the CIMS sensitivity to certain functionalized species within the same mode of operation are comparable despite differences in structure (straight, branched, cyclic + branched, cyclic).

Due to mid-project tuning shifts in the positive mode operation, the ions monitored were not those expected from the ionization of proposed products. The reported ions are those as monitored during the project, though the proposed ion assignments are reported taking the tuning shift into account. A back-calibration was performed to verify the shift in peak-centering, which typically resulted in an upwards shift by 5 amu in the range of 200–220 amu during positive mode operation. To distinguish between ions monitored in the different modes of the instrument a (+) or (–) is indicated in front of the *m/z* monitored for ions monitored in positive and negative mode operation, respectively.

An Aerodyne high-resolution time-of-flight aerosol mass spectrometer (DeCarlo et al., 2006), hereafter referred to as the AMS, was operated at 1 min resolution, switching between the lower resolution (up to ~2100 at *m/z* 200), higher sensitivity “V-mode”, and the high-resolution (up to ~4300 at *m/z* 200), lower sensitivity “W-mode”. Data analysis and calibrations were performed according to procedures previously described (Allan et al., 2004; Aiken et al., 2007, 2008; Canagaratna et al., 2007). HR-ToF-AMS data were processed with Squirrel, the ToF-AMS Unit Resolution Analysis Toolkit and PIKA (Peak Integration by Key Analysis, DeCarlo et al., 2006), the high-resolution analysis software tool (<http://cires.colorado.edu/jimenez-group/ToFAMSResources/ToFSoftware/index.html>) in Igor Pro Version 6.22A (Wavemetrics, Lake Oswego, OR). At the beginning of each experiment, an AMS sample was taken with a particle filter in-line to the chamber sample line to make corrections for air interferences (Allan et al., 2004). The adjustments to the fragmentation table proposed by Aiken et al. (2008) for organic mass at *m/z* 18 and *m/z* 28 were included. Elemental ratios were calculated using the technique outlined by Aiken et al. (2007, 2008). The C₂H₄⁺ ion at *m/z* 28 was

Table 2. Experimental conditions.

Exp.	Organic	Duration of photooxidation (h)	Initial HC (ppb _v)	[NO] ₀ (ppb _v)	[NO _x] ₀ (ppb _v)	[O ₃] ₀ (ppb _v)	Initial Seed Vol. μm ³ cm ⁻³	Δ HC (ppb _v)	Peak Organic ^a μg m ⁻³
1	<i>n</i> -dodecane	18	33.0	< LDL ^b	< LDL ^b	3.3	12.0	32.3	51.3
2	<i>n</i> -dodecane	36	34.9	< LDL ^b	< LDL ^b	2.6	11.4	33.6	62.8
3	2-methylundecane	18	27.3	< LDL ^b	< LDL ^b	4.0	16.3	22.4	not available ^c
4	2-methylundecane	36	28.9	< LDL ^b	< LDL ^b	4.2	13.6	27.6	45.6
5	hexylcyclohexane	18	16.2	< LDL ^b	< LDL ^b	2.4	10.5	15.2	34.8
6	hexylcyclohexane	36	14.9	< LDL ^b	< LDL ^b	3.8	4.2	14.4	34.4
7	cyclododecane	18	10.1	< LDL ^b	< LDL ^b	2.0	24.4	9.2	19.5 ^d
8	cyclododecane	36	11.0	< LDL ^b	< LDL ^b	3.1	14.1	10.6	30.8

^a Not corrected for particle wall loss^b Below lower detection limit (5 ppb_v)^c AMS not sampling^d Reported for end of experiment, though growth had not peaked.**Fig. 1.** General mechanism for alkanes under low-NO_x conditions. R₁ and R₂ are alkyl groups. Solid boxed compounds indicate proposed structures monitored by the CIMS in the gas-phase and/or the AMS in the particle-phase. Pathway in upper right with asterisk denotes alternative pathway for the cyclic case (R₁ and R₂ are bonded together as R).

not fit in PIKA due to strong interference from N₂⁺ and was therefore not included in the elemental ratio calculations.

Photochemical simulations of each system were performed based on that of *n*-dodecane used in Yee et al. (2012) to further define the level of NO. An initial NO

level of ≤ 1 ppb_v is consistent with $\leq 10\%$ of reactions of RO₂ being due to reaction with NO_x. This NO concentration is also consistent with the trends observed for NO_x-sensitive species such as the first generation hydroperoxide and the 1,4-hydroxycarbonyl. Multifunctional nitrate species in the CIMS spectra were not significant, supporting that the RO₂ + NO_x channels are not significant in these experiments.

3 SOA formation chemistry

3.1 Chemical mechanism leading to SOA formation

A proposed general mechanism for the photooxidation of alkanes under low-NO_x conditions (i.e., RO₂ reacts exclusively with HO₂) is presented in Fig. 1. This scheme is based on the *n*-dodecane photooxidation mechanism developed in Yee et al. (2012) generalized to the C₁₂ structures studied here. R₁ and R₂ represent alkyl groups. In the case of *n*-dodecane, R₁ and R₂ are any straight-chain alkyl groups that sum to C₇H₁₆. For 2-methylundecane, R₁ and R₂ are also alkyl groups that make up C₇H₁₆, though one side contains a methyl branch at the number 2 carbon atom. For hexylcyclohexane, R₁ is C₆H₅ and R₂ is CH₃. While the sites of oxidation are shown in the mechanism to occur between R₁ and R₂, oxidation can also occur on the R₁ and R₂ groups including the C₆H₅ ring in hexylcyclohexane. In the case of cyclododecane, R₁ and R₂ are bonded together, indicated as R in the sidebar denoted by an asterisk. Structures in a solid box indicate one isomer of a product identified by the CIMS in the gas phase or the AMS in the particle phase. Colors of boxes containing compounds are consistent with those used when comparing trends of species in later plots within a compound system. Product names within the boxes will continue to be referenced in the following discussion, tables of identified products, and figures.

Photooxidation begins with H-abstraction by OH from the parent alkane (RH) to form an alkylperoxy radical (RO₂). Under the experimental conditions, the fate of the RO₂ radical is dominated by reaction with HO₂ radical ($\geq 90\%$) to form the 1st-generation hydroperoxide (ROOH). This calculation is based on analogous photochemical simulations as presented for *n*-dodecane in Yee et al. (2012), which also demonstrate that the time constant by which RO₂ + RO₂ reactions become significant is greater than 9 days, not relevant for the current experiments. The hydroperoxide (ROOH) can then undergo reaction with OH (channels 1 and 2) or photolysis (channel 3). Along channel 1, a 2nd-generation carbonyl (CARB) is formed, followed by continued oxidation to form a 3rd-generation carbonyl hydroperoxide (CARBROOH). This CARBROOH can also be generated via channel 2, in which ROOH undergoes reaction with OH to generate a dihydroperoxide (DIROOH). In the case of channel 1 where the carbonyl hydroperoxide forms such that the functional groups are on adjacent carbons (α -

CARBROOH), photolysis of the hydroperoxy group (channel 1a) results in formation of an aldehyde (ALD) and several $< C_{12}$ fragments: peracid (C_{*n*}PACID), carboxylic acid (C_{*n*}CARBACID), and hydroperoxides (C_{*n*}ROOH). The formation of the α -CARBROOH is expected to be minor, as several other isomers would result with the hydroperoxy group located at any of several other possible positions along the carbon chain. It could be located beta to the ketone containing carbon, as shown in channel 2, or at positions greater than 2 methylene carbons away (not explicitly shown).

Along channel 2, the carbonyl hydroperoxide (CARBROOH) can undergo photolysis (channel 2a) analogous to the reactions outlined in channel 3, or react with OH (channel 2b). Channels 2a and 2b both lead to higher functionalized products. There is potential for tri-functionalized compounds (not shown) to form, a hydroxy carbonyl hydroperoxide (OHCARBROOH) to be formed along channel 2a and a dicarbonyl hydroperoxide (DICARBROOH) along channel 2b. Additional oxidation (not shown) can lead to a tricarbonyl hydroperoxide (TRICARBROOH) and hydroxy dicarbonyl hydroperoxide (OHDICARBROOH). The carbonyl hydroperoxide (CARBROOH) has a pure liquid vapor pressure ranging from 6.1×10^{-9} to 6.6×10^{-8} atm depending on structure, as estimated using the EVAPORATION method (Compernelle et al., 2011). This intermediate volatile/semivolatile organic is one of the first products that can partition to the particle phase, channel 2c.

In channel 3, photolysis of the 1st-generation hydroperoxide produces an alkoxy radical RO. The C₁₂ alkoxy radical will undergo 1,4-isomerization according to well-established mechanisms (Atkinson, 1997; Lim and Ziemann, 2005, 2009a, b). This results in the formation of a 1,4-hydroxy hydroperoxide (OHROOH), which has sufficiently low volatility to partition into the particle phase or undergo reaction with OH or photolyze. Reaction with OH can result in the formation of a carbonyl hydroperoxide (pathway not shown) or a hydroxy carbonyl. The particular carbonyl hydroperoxide and hydroxy carbonyl generated would be different isomers of the generalized CARBROOH and OHCARB shown in the mechanism. The 1,4-hydroxy carbonyl is known to undergo cyclization under an acid-catalyzed process on the particle surface to generate a cyclic hemiacetal (CHA) and dehydrate to form a dihydrofuran (DHF), which can then return to the gas phase to become further oxidized (Aschmann et al., 2003; Lim and Ziemann, 2009c).

In the case of cyclododecane where the ring strain is high enough (Benson, 1976; Lim and Ziemann, 2009a), the alkoxy radical can decompose to generate an aldehydic alkyl radical and a hydroperoxy aldehyde according to the asterisked scheme to the right-hand side (see Fig. 1). Though a C₆ ring is not considered to have ring strain (Benson, 1976; Lim and Ziemann, 2009a), hexylcyclohexane may also undergo ring opening in an analogous process, depending on the extent and position of functionalization on the ring and its alkyl chain during continued oxidation. By structure activity

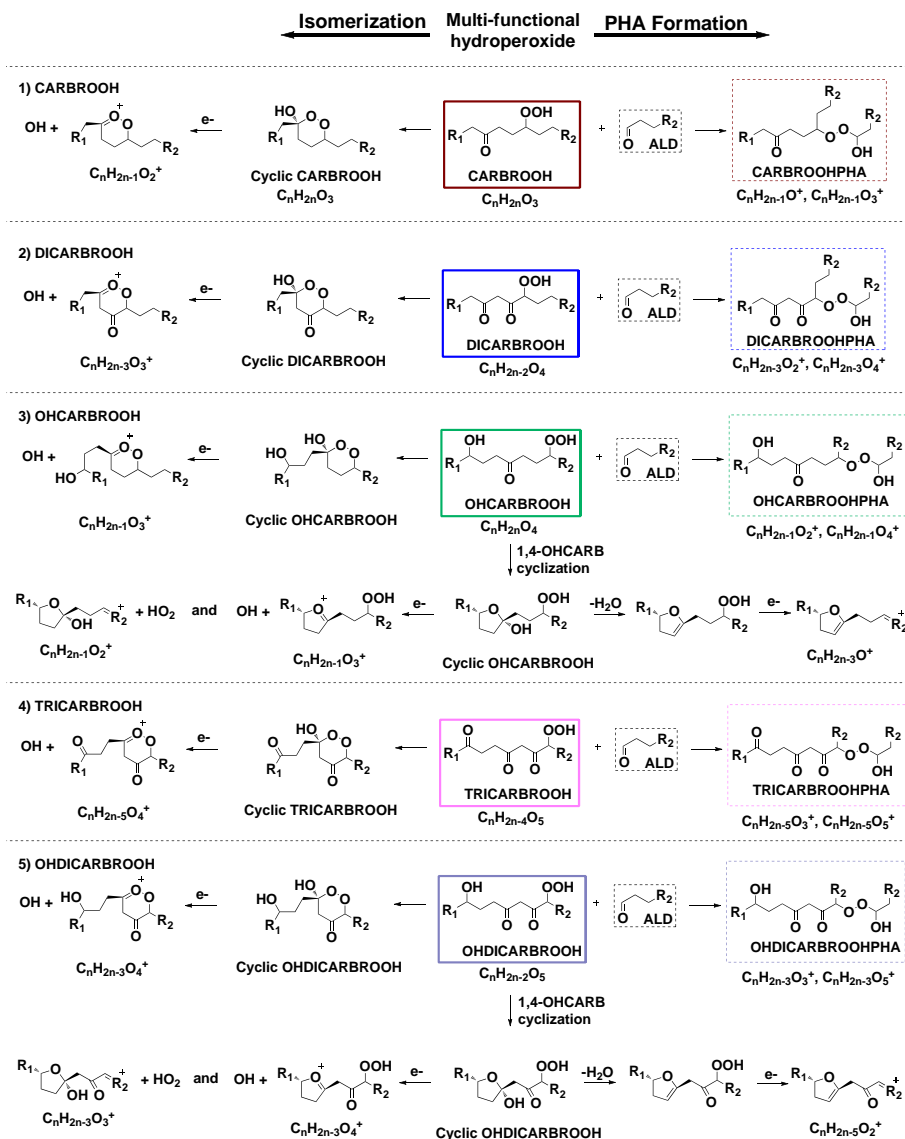


Fig. 2. General mechanism for particle-phase chemistry involving PHA formation (right-hand side) and potential isomerization (left-hand side) from higher functionalized products (solid boxed) formed along channel 2 in Fig. 1. R_1 and R_2 are alkyl groups. One isomer is shown. Dashed boxed compounds indicate PHA structures for which AMS ion tracers exist. General chemical and ion formulae for multifunctional hydroperoxides and proposed PHA and isomerization products are shown, where $n=12$. Analogous products for hexylcyclohexane and cyclododecane would have an additional degree of unsaturation.

estimations (Kwok and Atkinson, 1995), initial H-abstraction by OH should primarily take place at the secondary carbons over the branching point in an approximate 80 % to 20 % ratio. Continued oxidation will tend to favor these secondary carbon sites over the branching point, though eventually fragmentation may be induced.

Several multifunctional hydroperoxides can potentially react with the aldehydes generated in channel 1a to form peroxyhemiacetals. The carbonyl hydroperoxide PHA (CARBROOHPHA) is explicitly shown in the mechanisms (Figs. 1 and 2, scheme 1), and was proposed as a key component

of the initial SOA growth in the case of *n*-dodecane (Yee et al., 2012). Multifunctional PHAs are represented generally in Fig. 1, where Y is any functional group (-hydroxyl, -carbonyl, -hydroperoxy). The more explicit representation of expected higher functionalized products along channel 2 and their potential to form PHAs are represented along the right-hand side of Fig. 2. One isomer is shown with the expected functionalization. PHA formation from DIROOH (Fig. 1, channel 2) and OHROOH (Fig. 1, channel 3) is not explicitly shown since these tracer ions are relatively small signals compared to those of other multifunctional hydroperoxides

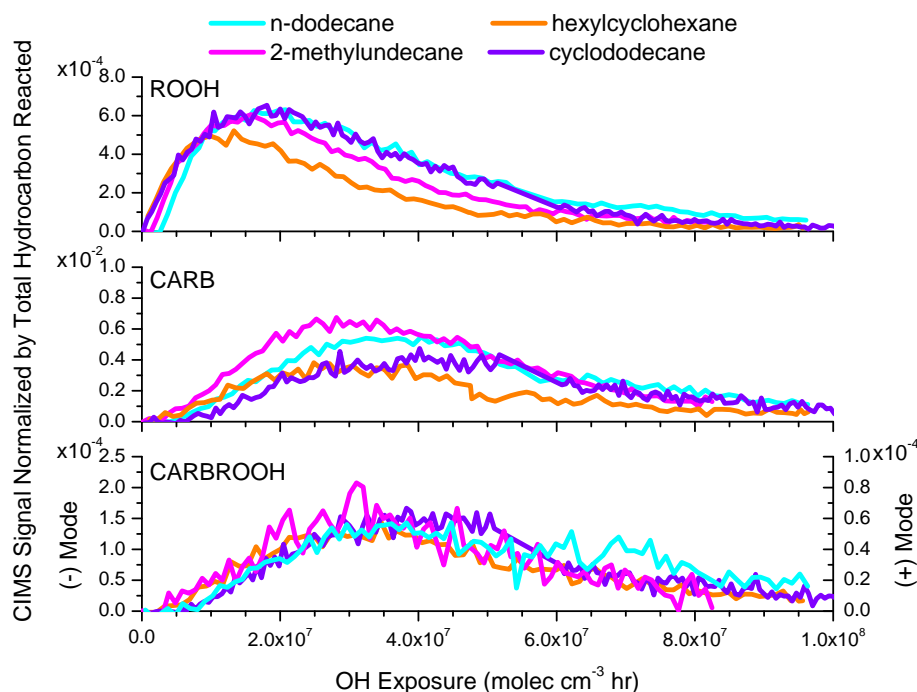


Fig. 3. Gas-phase trends of major species formed in the first three generations of photooxidation. Top panel: first-generation hydroperoxide (ROOH). Middle panel: second-generation carbonyl (CARB). Bottom panel: third-generation carbonyl hydroperoxide (CARBROOH). Note that the CARBROOH was monitored in positive mode for *n*-dodecane and 2-methylundecane (the right side axis) and in negative mode for hexylcyclohexane and cyclododecane (the left side axis).

in the AMS. Of note is the potential to generate a 2nd-generation C₁₂ hydroperoxy aldehyde in the case of cyclododecane, which is a likely candidate for participating in peroxyhemiacetal formation. Under channels 1 and 2, the CARBROOH is a 3rd-generation product, though continued reaction with OH in these channels may compete with one generation of OH reaction and photolysis to form the hydroperoxy aldehyde.

3.2 Gas- and particle-phase product identification using CIMS and AMS

Ions monitored by the CIMS and the AMS and their proposed compound assignments by system are presented in Tables 3–7. Note that because hexylcyclohexane and cyclododecane differ by one degree of unsaturation from that of 2-methylundecane and *n*-dodecane, many of the ions monitored across systems for analogous products differ by just 2 amu.

3.2.1 Gas-phase mechanism comparison

Comparisons of the several analogous gas-phase species across systems help elucidate the chemical development by structure. Associated CIMS signals are normalized by the total reacted hydrocarbon to account for differences in initial hydrocarbon loading and represented along an OH exposure

Table 3. Selected ions monitored by the CIMS for *n*-dodecane and 2-methylundecane.

Mode	Observed <i>m/z</i>	Chemical Formula	Assignment
(–)	287	C ₁₂ H ₂₆ O ₂	ROOH
(+)	223	C ₁₂ H ₂₄ O	CARB
(+)	204	C ₁₂ H ₂₄ O ₃	CARBROOH
(–)	285	C ₁₂ H ₂₄ O ₂	OHCARB
(–)	135/201	C ₆ H ₁₂ O ₂	C6CARBACID

Table 4. Selected ions monitored by the CIMS for hexylcyclohexane and cyclododecane.

Mode	Observed <i>m/z</i>	Chemical Formula	Assignment
(–)	285	C ₁₂ H ₂₄ O ₂	ROOH
(+)	221	C ₁₂ H ₂₂ O	CARB
(–)	299	C ₁₂ H ₂₂ O ₃	CARBROOH
(–)	283	C ₁₂ H ₂₂ O ₂	OHCARB
(–)	135/201	C ₆ H ₁₂ O ₂	C6CARBACID

timescale for comparison of the different systems (Fig. 3). While there are slight differences in magnitude of the curves presented, gas-phase yields are not inferred from these figures as slight variations in the CIMS sensitivity based on structure may account for this effect. Time profiles of total

Table 5. Selected ions monitored by the AMS in the *n*-dodecane and 2-methylundecane systems.

Observed <i>m/z</i>	Exact mass ion formula	Proposed assignment
183	C ₁₂ H ₂₃ O ⁺	CARBROOH + CARBROOH PHA
215	C ₁₂ H ₂₃ O ₃ ⁺	CARBROOH PHA
185	C ₁₂ H ₂₅ O ⁺	OHROOH + OHROOH PHA
217	C ₁₂ H ₂₅ O ₃ ⁺	OHROOH PHA
197	C ₁₂ H ₂₁ O ₂ ⁺	DICARBROOH + DICARBROOH PHA
229	C ₁₂ H ₂₁ O ₄ ⁺	DICARBROOH PHA + CYC. OHDICARBROOH
199	C ₁₂ H ₂₃ O ₂ ⁺	OHCARBROOH + OHCARBROOH PHA
231	C ₁₂ H ₂₃ O ₄ ⁺	OHCARBROOH PHA
201	C ₁₂ H ₂₅ O ₂ ⁺	DIROOH
211	C ₁₂ H ₁₉ O ₃ ⁺	TRICARBROOH + TRICARBROOH PHA
243	C ₁₂ H ₁₉ O ₅ ⁺	TRICARBROOH PHA
213	C ₁₂ H ₂₁ O ₃ ⁺	OHDICARBROOH + OHDICARBROOH PHA
245	C ₁₂ H ₂₁ O ₅ ⁺	OHDICARBROOH PHA

Table 6. Selected ions monitored by the AMS in the hexylcyclohexane system.

Observed <i>m/z</i>	Exact mass ion formula	Proposed assignment
179	C ₁₂ H ₁₉ O ⁺	OHCARBROOH DHF
181	C ₁₂ H ₂₁ O ⁺	CARBROOH + CARBROOH PHA
213	C ₁₂ H ₂₁ O ₃ ⁺	CARBROOH PHA
183	C ₁₂ H ₂₃ O ⁺	OHROOH + OHROOH PHA
215	C ₁₂ H ₂₃ O ₃ ⁺	OHROOH PHA
195	C ₁₂ H ₁₉ O ₂ ⁺	DICARBROOH + DICARBROOH PHA
227	C ₁₂ H ₁₉ O ₄ ⁺	DICARBROOH PHA + CYC. OHDICARBROOH
197	C ₁₂ H ₂₁ O ₂ ⁺	OHCARBROOH + OHCARBROOH PHA
229	C ₁₂ H ₂₁ O ₄ ⁺	OHCARBROOH PHA
199	C ₁₂ H ₂₃ O ₂ ⁺	DIROOH
209	C ₁₂ H ₁₇ O ₃ ⁺	TRICARBROOH + TRICARBROOH PHA
211	C ₁₂ H ₁₉ O ₃ ⁺	OHDICARBROOH + OHDICARBROOH PHA
243	C ₁₂ H ₁₉ O ₅ ⁺	OHDICARBROOH PHA

reacted hydrocarbon and the decay of H₂O₂ for each system are presented in the Supplement (Fig. S1).

The OH exposure in the system is defined as the product of the concentration of OH (molec cm⁻³) and the hours of irradiation. The OH concentration is inferred from the parent hydrocarbon decay using the known reaction rate coefficient with OH. The OH concentration over the course of an experiment is constant ($\sim 2 \times 10^6$ molec cm⁻³). Total OH exposure ranges from $\sim 8 \times 10^7$ molec cm⁻³ h to $\sim 1 \times 10^8$ molec cm⁻³ h for these experiments.

The 1st-generation hydroperoxides (ROOH) trends across systems are shown in Fig. 3, top panel. Under similar OH ex-

posures, the hexylcyclohexane hydroperoxide peaks slightly earlier than those of *n*-dodecane and cyclododecane. This is consistent with a slightly faster reaction rate coefficient for hexylcyclohexane. The 2nd-generation carbonyl (CARB) formation is compared across the systems in Fig. 3, middle panel. The trends are also consistent with faster gas-phase oxidation for hexylcyclohexane.

Most of the intermediate hydroperoxide species are best monitored in negative mode operation of the CIMS, but due to the mass scan range ending at 300 amu, alternative ions in positive mode were used to track development of some expected products. Major products such as the carbonyl

Table 7. Selected ions monitored by the AMS in the cyclododecane system.

Observed m/z	Exact mass ion formula	Proposed assignment
181	$C_{12}H_{21}O^+$	CARBROOH + CARBROOH PHA
213	$C_{12}H_{21}O_3^+$	CARBROOH PHA
183	$C_{12}H_{23}O^+$	OHROOH + OHROOH PHA
215	$C_{12}H_{23}O_3^+$	OHROOH PHA
195	$C_{12}H_{19}O_2^+$	DICARBROOH + DICARBROOH PHA
227	$C_{12}H_{19}O_4^+$	DICARBROOH PHA
197	$C_{12}H_{21}O_2^+$	OHCARBROOH + OHCARBROOH PHA
229	$C_{12}H_{21}O_4^+$	OHCARBROOH PHA
199	$C_{12}H_{23}O_2^+$	DIROOH
207	$C_{12}H_{15}O_3^+$	OH4CARBROOH
223	$C_{12}H_{15}O_4^+$	CYC. OH4CARBROOH
209	$C_{12}H_{17}O_3^+$	TRICARBROOH/4CARBROOH Ring Opened
225	$C_{12}H_{17}O_4^+$	CYC. TRICARBROOH
211	$C_{12}H_{19}O_3^+$	OHDICARBROOH/TRICARBROOH Ring Opened

hydroperoxide (CARBROOH) for the 2-methylundecane and *n*-dodecane systems were monitored at (+) m/z 204 for this reason (Table 3), while for hexylcyclohexane and cyclododecane CARBROOH was monitored at (–) m/z 299 (Table 4). Note that signal intensities should not be compared across positive and negative mode operation of the CIMS as the sensitivities differ. The CARBROOH trends in Fig. 3 (bottom panel) show similar trends across systems, though the signals are more noisy as this hydroperoxide is expected to be the first species with sufficiently low volatility to partition into the particle phase.

3.2.2 Particle-phase composition

Mass spectra (1–2 h averages) from the AMS at the time of initial growth, a period mid-experiment, and at experiment end for each system, along with a difference spectrum from end and initial growth, are presented in Figs. 4–7. The initial growth spectrum is taken at the point where the organic aerosol mass rises above the limit of detection. The limit of detection is defined as 3 standard deviations above the signal during the filter period taken before photooxidation begins. The mid-experiment average spectrum is taken at the point where the suspended organic aerosol is the highest, typically coincident with the peak of one or more AMS ion tracers of interest. The peak in suspended organic aerosol is consistent with the effects of particle wall loss and unlikely due to evaporation as the size distribution remains the same. The end spectrum is the average of the spectra during the last 1–2 h of photooxidation. The $C_xH_yO_z$ chemical formulas corresponding with the dominant exact masses are labeled in the mass spectra. Unit mass m/z is denoted here for brevity, but the re-

ported ion chemical formulas are determined from the exact mass ions.

In the $m/z < 100$ amu range, several of the dominant $C_xH_y^+$ ions are shared across all systems, though there is greater relative contribution of cycloalkyl ions compared to alkyl ions in the case of hexylcyclohexane and cyclododecane. For example, there is greater signal of the ion $C_6H_7^+$ compared to $C_6H_9^+$ for these systems compared to those of *n*-dodecane and 2-methylundecane. The highest signal is attributed to the same ions for *n*-dodecane and 2-methylundecane (Figs. 4 and 5); however, the fraction is higher for *n*-dodecane than in the 2-methylundecane case. This observation is consistent with more fragmentation in the 2-methylundecane oxidation, as compared to *n*-dodecane. 2-methylundecane oxidation also exhibits a higher fraction of $C_2H_3O^+$ in the < 100 amu range. $C_2H_3O^+$ has been proposed as an ion tracer for non-acid organic oxygenates (Chhabra et al., 2011). This ion also tends to dominate during hexylcyclohexane oxidation (Fig. 6) in the 40–45 amu ion cluster range, though it never dominates in the case of cyclododecane (Fig. 7).

In the cyclododecane system one ion tends to predominate within a cluster of ions. For example, $C_4H_7^+$ at m/z 55 dominates during initial aerosol growth (Fig. 7) in the 50–60 amu region, whereas in the *n*-dodecane system, ions at m/z 55 and m/z 57 are present at similar mass fractions (Fig. 4). At initial growth, they are reduced ions, whereas at maximum growth, the two ions are more oxidized, and the oxidized ion ($C_3H_5O^+$) at m/z 57 is higher. For cyclododecane, the m/z 55 ion also shifts from the reduced ion ($C_4H_7^+$) to the more oxidized ion ($C_3H_5O^+$) and remains predominant in the 50–60 amu range throughout the oxidation. The fraction of mass at $C_3H_5O^+$ at m/z 55 is also high for the entire

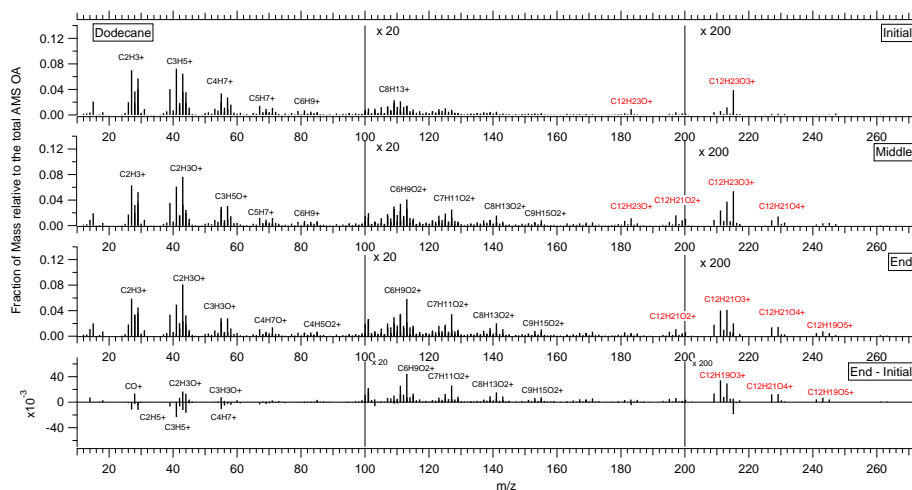


Fig. 4. High-resolution mass spectrum of SOA formed from *n*-dodecane at initial organic growth, mid-experiment, and end of experiment. The difference spectrum is also shown. m/z 101–200 are multiplied by 20, and m/z 201–300 are multiplied by 200 for visual clarity. Ions with high signal are labeled. Ion labels in red correspond with proposed ion assignments in Table 5.

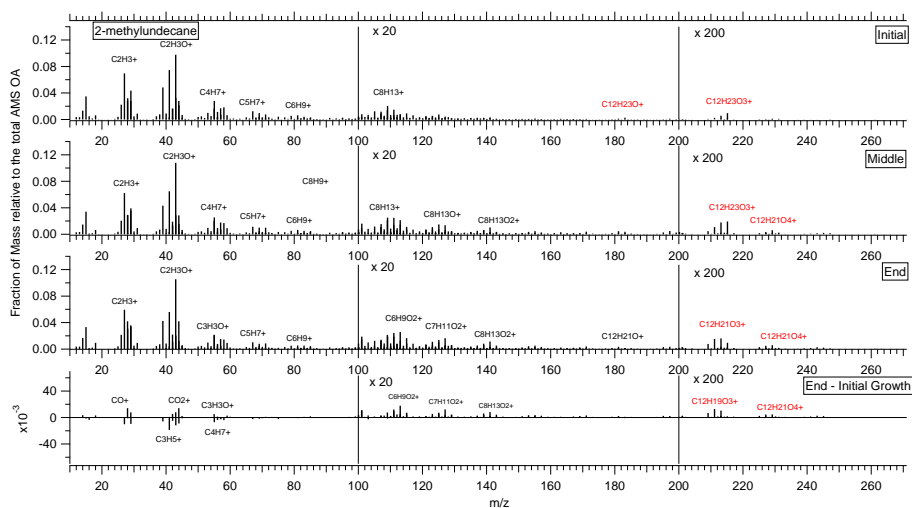


Fig. 5. High-resolution mass spectrum of SOA formed from 2-methylundecane at initial organic growth, mid-experiment, and end of experiment. The difference spectrum is also shown. m/z 101–200 are multiplied by 20, and m/z 201–300 are multiplied by 200 for visual clarity. Ions with high signal are labeled. Ion labels in red correspond with proposed ion assignments in Table 5.

duration of the hexylcyclohexane oxidation, whereas in the other systems, the reduced ion ($C_4H_7^+$) at m/z 55 is high, and then $C_3H_3O^+$ grows in.

The mass spectrum from the hexylcyclohexane system (Fig. 6) between m/z 100 and 200 amu is less discretely structured as compared to the other compounds (Figs. 4, 5, 7). Since hexylcyclohexane exhibits alkyl, cyclic, and branched features in its structure, this may be interpreted as a unique hybrid of chemical features in the aerosol spectrum.

Overall, the difference spectra in the m/z 100–300 amu region are all positive, indicating the incorporation of higher molecular weight species. The only negative differences in signal are in the m/z < 100 range and are the result of alkyl

ion fragments decreasing in AMS signals from the particle phase. Several ions in the >150 amu range have been proposed as tracers for particle-phase chemistry (Yee et al., 2012; Craven et al., 2012), as, though low in signal, they retain more molecular information than lower mass ions that are only small fragments of the original molecule. The chemical processes by which these >150 amu ions are generated may be analogous across all systems, as the structures of the spectra in this range are generally the same. That is, the prominent ions in hexylcyclohexane correspond to the prominent ions in the *n*-dodecane and 2-methylundecane cases, but tend to have one additional degree of unsaturation. This is consistent with the difference in degrees of

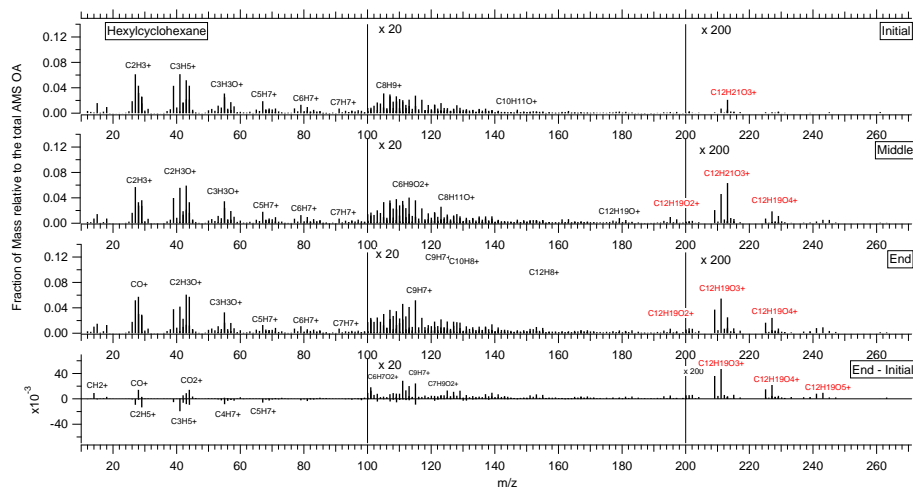


Fig. 6. High-resolution mass spectrum of SOA formed from hexylcyclohexane at initial organic growth, mid-experiment, and end of experiment. The difference spectrum is also shown. m/z 101–200 are multiplied by 20, and m/z 201–300 are multiplied by 200 for visual clarity. Ions with high signal are labeled. Ion labels in red correspond with proposed ion assignments in Table 6.

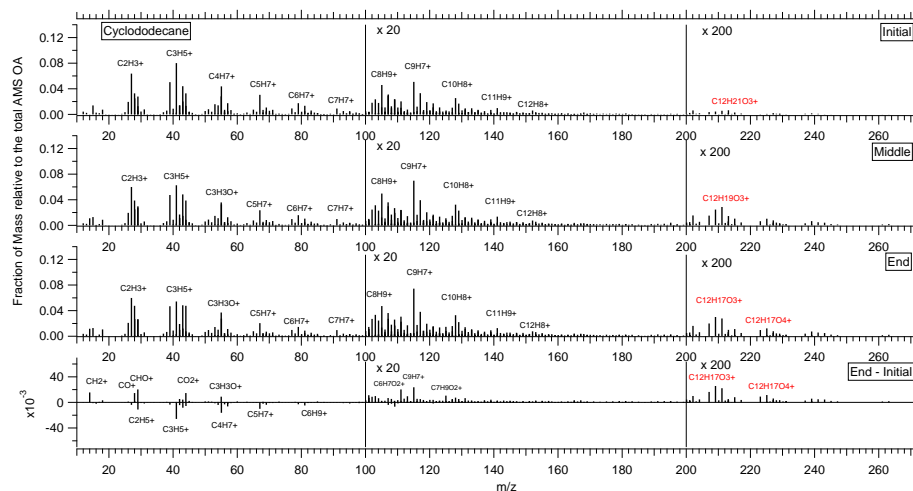


Fig. 7. High-resolution mass spectrum of SOA formed from cyclododecane at initial organic growth, mid-experiment, and end of experiment. The difference spectrum is also shown. m/z 101–200 are multiplied by 20, and m/z 201–300 are multiplied by 200 for visual clarity. Ions with high signal are labeled. Ion labels in red correspond with proposed ion assignments in Table 7.

unsaturation between the parent compounds. However, the cyclododecane peaks in this high amu region tend to be two degrees of unsaturation lower than those of *n*-dodecane. This could indicate chemical processing that results in more carbonyl group formation for the case of cyclododecane. This type of functionalization is relevant for cyclododecane along channel 3 in the gas-phase mechanism (Fig. 1), as cyclododecane can ring-open early on, generating an aldehyde. This also means that cyclododecane can form a lower vapor pressure C_{12} aldehyde that can participate in particle-phase reactions as discussed in Lim and Ziemann (2009a, b), whereas other systems form a $<C_{12}$ aldehyde along channel 1a (Fig. 1).

3.2.3 Indicators of particle-phase chemistry: peroxy-hemiacetal (PHA) formation

Yee et al. (2012) and Craven et al. (2012) proposed that several ion tracers in the $m/z > 150$ amu region differing by 32 amu could be used to track a variety of potential peroxyhemiacetals (PHAs) formed in the particle phase. Craven et al. (2012) established that general hydroperoxides (ROOH) could be monitored in the AMS at ions consistent with an $m/z [M-33]^+$, where M is the molecular weight of the hydroperoxide. This ion will be hereafter referred to as R^+ . However, the distinct pattern of similarly trending R^+ ions and those at m/z 32 amu higher suggests that this mass difference may result from the peroxide O–O bond

of a peroxyhemiacetal. We refer to this ion as ROO^+ for the following discussions. We note that because the typical vaporizer temperature in the AMS is operated at 600°C , as employed in these experiments, the signals from these $m/z > 150$ R^+ and ROO^+ ions are small. After running the experiments presented here, Craven et al. (2012) explored the effect of lowering the vaporizer temperature for the case of C_{18} hydroperoxide in the particle phase and found that greater signal from the hydroperoxide ion tracer could be achieved by doing so. This suggests that future studies exploring hydroperoxide and peroxides in the particle phase may benefit from modification of standard AMS operation. While small in signal for the current experiments, these ions are still crucial indicators of the particle-phase chemistry. These ions are listed in tables of ions monitored in the AMS along with their proposed product assignments (Tables 5–7). Since these initial studies, another *n*-dodecane experiment (Shiraiwa et al., 2013) involved intentional injection of tridecanal in the dark after an initial period of dodecane photooxidation and SOA formation to induce peroxyhemiacetal formation. Upon tridecanal injection, a corresponding decrease in signal of several hydroperoxide species occurred in the gas phase (as monitored by the CIMS) accompanied by a corresponding increase in the 32 amu difference ion pairs in the AMS, consistent with the proposed attribution to particle-phase chemistry involving peroxyhemiacetal formation.

The formation of fragments along channel 1a, specifically carboxylic acids tracked by the CIMS, is the key proxy for the presence of aldehyde in the system (since the aldehyde is not directly measured). The presence of gas-phase acid indicates that aldehyde is present in the system, and that peroxyhemiacetal formation may commence, as observed in Yee et al. (2012) for *n*-dodecane. Hence, a key comparison of the gas- and particle-phase measurements includes the time trend comparison between gas-phase acid production and particle-phase ion markers for PHA formation. In each system, the CARBROOH PHA ions grow in the particle phase when gas-phase aldehyde forms, as proxied by a measured co-product, C_6 carboxylic acid (C6CARBACID), in Fig. 8. The initial growth of organic aerosol in each of these systems is also characterized by the respective CARBROOH and CARBROOH PHA tracer ions in the AMS mass spectra. In Figs. 4 and 5, $\text{C}_{12}\text{H}_{23}\text{O}^+$ at m/z 183 and $\text{C}_{12}\text{H}_{23}\text{O}_3^+$ at m/z 215 are the dominant ions at initial growth of *n*-dodecane and 2-methylundecane SOA. For hexylcyclohexane (Fig. 6) and cyclododecane (Fig. 7), the ion at $\text{C}_{12}\text{H}_{21}\text{O}_3^+$ at m/z 213 is characteristic of initial growth. Note that there are different right-hand axes and scales for the R^+ and ROO^+ ion tracers in Fig. 8.

3.2.4 Effect of structure on PHA formation

Common for all four systems, three ions that enter the particle phase early on (within 2×10^7 molec cm^{-3} h OH exposure) are attributed to their respective CARBROOH,

OHCARBROOH, and DICARBROOH. While the R^+ ions can come from both the hydroperoxide itself and its derived PHA, the ROO^+ ion is considered to arise mostly from PHA. To understand the effect of structure on PHA formation, time trends of the fraction of the organic aerosol attributed to ROO^+ PHA tracer ions can be compared across parent structures. These analyses assume that the ionization probability and fragmentation pattern in the AMS are relatively consistent for PHAs of analogous functionality. That is, the CARBROOH PHA ionization probability is similar across the four C_{12} alkanes studied. Also, this currently assumes that there is only one hydroperoxide and its PHA (regardless of the aldehyde variety) contributing to the ROO^+ .

Figure 9 shows that the relative fraction of organic aerosol attributed to the CARBROOH PHA is approximately similar for *n*-dodecane and hexylcyclohexane, followed by 2-methylundecane and cyclododecane (top panel). For the DICARBROOH PHA (middle panel) and OHCARBROOH PHA (bottom panel), a greater fraction of the organic aerosol is attributed to PHAs in hexylcyclohexane SOA, followed by *n*-dodecane. Smaller contributions are made for the PHAs from 2-methylundecane and cyclododecane.

Hexylcyclohexane may seem like an outlier since the contribution of PHA ions generally decreases in the order of branching or cyclic character (i.e., *n*-dodecane > 2-methylundecane > cyclododecane), though it is notably higher than or on the same order of *n*-dodecane. This may be a result of hexylcyclohexane chemistry having the unique mix of many features typically individualized to the other systems. That is, while hexylcyclohexane is branched like 2-methylundecane, even if C-C scission is favored at the branch point, the presence of the cyclohexane ring means that gas-phase fragmentation can still result in preservation of the C_{12} backbone, unlike 2-methylundecane. This means certain aspects of hexylcyclohexane's chemistry will be akin to that of *n*-dodecane, supporting continued functionalization and higher MW species. While hexylcyclohexane is also cyclic in nature like cyclododecane, the hexyl-chain may still afford it many sites of reaction without the potential of disrupting the stability of the C_6 ring. In the case of cyclododecane, any reaction affects a ring-bound carbon, and as such may impact the resulting chemistry.

Generally, the fraction of organic aerosol attributed to the cyclododecane-derived PHAs is lower compared to the other systems, indicating that there may be structural biases in PHA formation. Since PHA formation relies on the intermolecular reaction of two condensing species, aldehyde and a hydroperoxide, it may be that the cyclic structure of cyclododecane hydroperoxide is less apt for this reaction, depending on the hydroperoxy group accessibility on the C_{12} ring. It may also be possible that there are competing intramolecular reactions of more highly-functionalized hydroperoxides within the C_{12} ring that are more easily facilitated. There is also trend information in Fig. 8d that shows that the R^+ and ROO^+ ions for CARBROOH PHA in

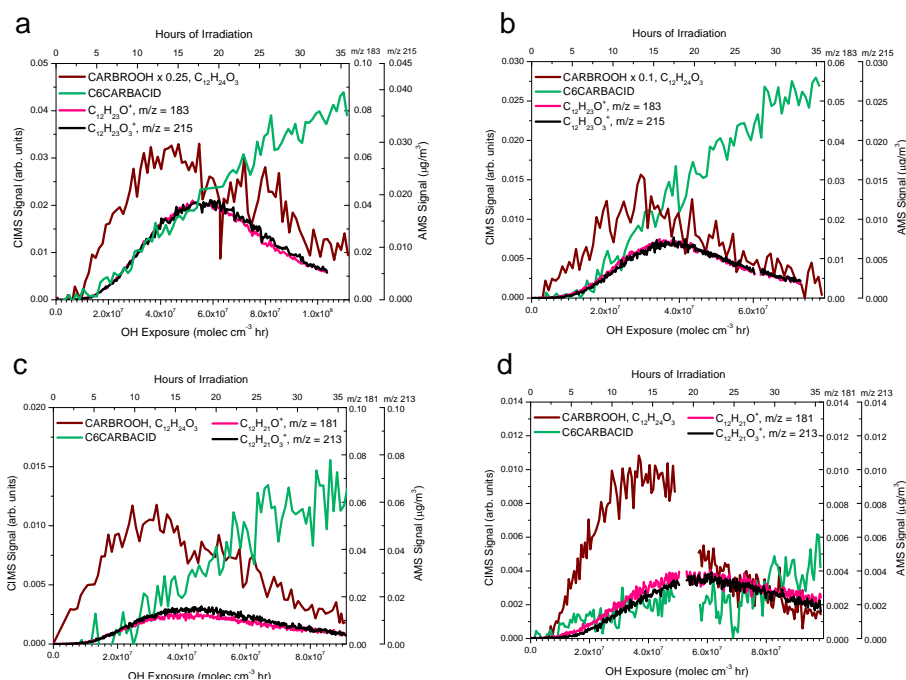


Fig. 8. Gas-phase trends of the generated carbonyl hydroperoxide (CARBROOH) and C₆ carboxylic acid (C6CARBACID) as monitored by the CIMS and the CARBROOH and its derived PHA in the particle phase for (a) *n*-dodecane, (b) 2-methylundecane, (c) hexylcyclohexane, and (d) cyclododecane. CARBROOH and its PHA are tracked by AMS ions C₁₂H₂₃O⁺ and C₁₂H₂₃O₃⁺ for *n*-dodecane and 2-methylundecane, and by C₁₂H₂₁O⁺ and C₁₂H₂₁O₃⁺ for hexylcyclohexane and cyclododecane.

cyclododecane do not trend together as tightly as compared to the other systems (Fig. 8a–c). The ROO⁺ ion lags slightly, indicating that PHA formation from the CARBROOH in cyclododecane may not form immediately with the condensation of CARBROOH.

While signal at the ROO⁺ ion for CARBROOH PHA can also potentially be derived from the OHCARBROOH cyclizing, as in Fig. 2, Scheme 3, the tight correlation of the R⁺ and ROO⁺ ions for *n*-dodecane and 2-methylundecane suggests less of a contribution from competing cyclization. Since the R⁺ ions cannot be derived from the competitive cyclization products, the majority of the signal at the ROO⁺ ion is attributed to the CARBROOH PHA form. For hexylcyclohexane and cyclododecane, however, there is slightly more deviation of the R⁺ and ROO⁺ ion trends. This may suggest that these structures may undergo intramolecular reactions that result in the variety of ions and chemical development discussed in further detail below.

3.2.5 Indicators of competitive chemistry with peroxy-hemiacetal (PHA) formation

Here, we present the general particle-phase development in terms of the multifunctional hydroperoxide/PHA R⁺ and PHA ROO⁺ proposed ion tracers for all systems (Fig. 10). In this systematic analysis going from straight-chain to branched to cyclic structures, we find that the presence of cer-

tain ions by structure and their trend information informs the need to consider intramolecular reaction as an additional fate of some of the multifunctional hydroperoxides. All ion signals have been normalized by the suspended organic aerosol to account for effects on the ion signal trend due to particle wall loss. This normalization results in large noise at periods < OH exposure of 2 × 10⁷ molec cm⁻³ h, owing to low and noisy ion and organic aerosol signals before this time.

The same tracer ions are present in both the *n*-dodecane and 2-methylundecane systems (Fig. 10a, b). C₁₂H₁₉O₃⁺ is of low signal in the 2-methylundecane and *n*-dodecane AMS spectra, though there is a greater contribution from this ion in *n*-dodecane SOA. All of these ions can potentially be explained by multifunctional hydroperoxide compounds that can carry up to four sites of functionalization and three degrees of unsaturation relative to the parent (See PHA schemes in Fig. 2 for proposed multifunctional structures and AMS ions assignments in Table 5). Generally for these acyclic systems, the CARBROOH is initially incorporated, followed by the DICARBROOH (C₁₂H₂₁O₂⁺ at *m/z* 197) and the OHCARBROOH (C₁₂H₂₃O₂⁺ at *m/z* 199). Additional chemical processing leads to incorporation of a potential OHDICARBROOH (C₁₂H₂₁O₃⁺ at *m/z* 213) and a TRICARBROOH (C₁₂H₁₉O₃⁺ at *m/z* 211). The C₁₂H₁₉O₅⁺ at *m/z* 245 is possibly the OHDICARBROOH PHA ROO⁺ ion, though the signal at this *m/z* is not sufficiently high to be

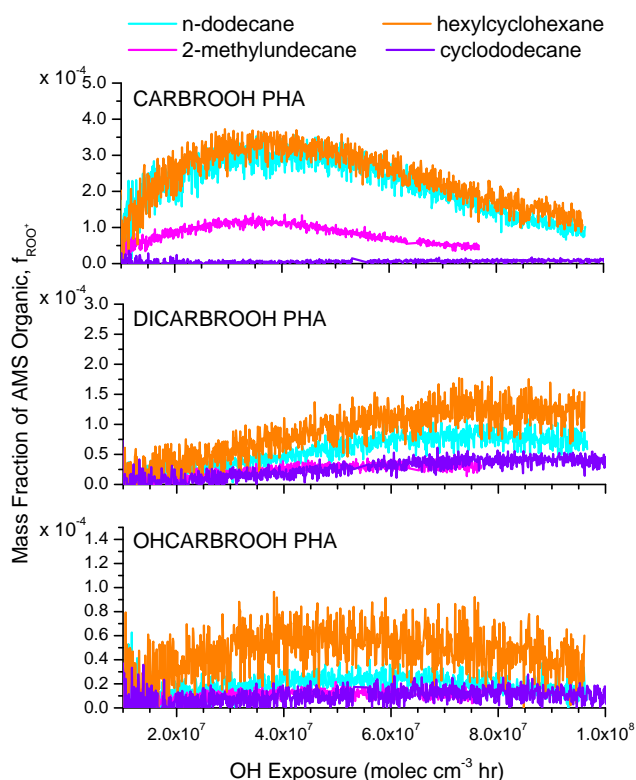


Fig. 9. Fraction of organic attributed to the corresponding ROO⁺ PHA tracer ion for (top) carbonyl hydroperoxide PHA (CARBROOH PHA), (middle) dicarbonyl hydroperoxide (DICARBROOH), and (bottom) hydroxycarbonyl hydroperoxide (OHCARBROOH).

plotted on the same scale as the R⁺ ions here. The DIROOH and OHROOH tracer ions are also not included for this reason, although tracer ions are identified in the mass spectra. Of note is the relatively earlier peaking (in terms of OH exposure) and lower relative contribution of these ions in the 2-methylundecane system as compared to their analogs in the *n*-dodecane system. This may be a result of fragmentation processes relevant for 2-methylundecane gas-phase oxidation that begin to dominate. The lower relative contribution of C₁₂H₁₉O₅⁺ for 2-methylundecane SOA as compared to *n*-dodecane SOA is also consistent with less chemical development due to gas-phase fragmentation dominating over functionalization, as well as potentially slower gas-phase oxidation since 2-methylundecane has a lower *k*_{OH} than that of *n*-dodecane. Though all of these ions for *n*-dodecane and 2-methylundecane can be explained by species involved in PHA formation mechanisms, we find that comparison of these and additional ions in the hexylcyclohexane and cyclododecane system indicate that additional chemistry is present.

For hexylcyclohexane, there is noticeably more simultaneous incorporation in the aerosol phase of such species as the CARBROOH (C₁₂H₂₁O⁺ at *m/z* 181), DICARBROOH

(C₁₂H₁₉O₂⁺ at *m/z* 195), OHCARBROOH (C₁₂H₂₁O₂⁺ at *m/z* 197), and their respective PHAs (Fig. 10c, Table 6). There is also significant contribution from an ion at C₁₂H₁₉O⁺ not explained by the PHA tracer fragmentation pattern. The presence of the C₁₂H₁₉O⁺ ion may be a result of forming an analogous hydroperoxy dihydrofuran product (Fig. 2, Scheme 3) via the OHCARBROOH undergoing 1,4 cyclization and dehydration. This ion is unique to hexylcyclohexane SOA (in terms of degrees of unsaturation achieved with little oxygen in the ion formula and prominence of the ion). The proposed reaction is consistent with the hexylcyclohexane structure undergoing another 1,4-cyclization along its C₆ branch to form a bicyclic structure (cyclohexyl and cyclic hemiacetal). The cyclic hemiacetal portion of the molecule can then dehydrate to form a dihydrofuran-like structure of higher volatility. This prominent route may therefore limit formation of lower volatility oxidation products during hexylcyclohexane oxidation. The peak of the suspended organic aerosol (Fig. 10c, OH exposure ~5 × 10⁶ molec cm⁻³ h) does follow the peak of this ion and those of the DICARBROOH, OHCARBROOH, consistent with limitations of the growth. At this point the rate of particle wall loss dominates over the rate of continued growth.

Tracer ions for these products are followed by further chemical processing also leading to the OHDICARBROOH and its PHA (C₁₂H₁₉O₃⁺ at *m/z* 211) and the OHDICARBROOH PHA (C₁₂H₁₉O₅⁺ at *m/z* 243). The *m/z* 243 ion is not shown due to low signal. The ion at *m/z* 227 C₁₂H₁₉O₄⁺ corresponds to the ROO⁺ ion for DICARBROOH PHA, though the time trend does not follow that of the R⁺ ion as closely, and may indicate another species (in combination) being responsible for the signal here. For example, in Fig. 2, Scheme 5, the OHDICARBROOH may isomerize (left reaction) via cyclization between a carbonyl and hydroperoxy group to form this ion as well. It may also undergo 1,4-cyclization involving the hydroxy and ketone groups. This presents two potentially competitive fates for the OHDICARBROOH, one to PHA formation (Scheme 5, right reaction) and the other to cyclization (Scheme 5, left and bottom reaction). Cyclization of alkoxy hydroperoxy aldehydes has been observed to be potentially competitive with PHA formation in the case of cyclic alkenes ozonolysis in the presence of alcohols (Ziemann, 2003). A similar cyclization reaction for the multifunctional carbonyl hydroperoxides can explain the presence of additional ions not expected from PHA formation.

For cyclododecane, at least two “waves” of chemical development exist in the particle phase (Fig. 10d). Initially, R⁺ ions associated with the CARBROOH, OHCARBROOH, and DICARBROOH grow in. Then, a series of ions with formulae of the form C₁₂H_{*y*}O₃⁺, with *y* = 19, 17, and 15, grow in consecutively. C₁₂H₁₉O₃⁺ at *m/z* 211 and C₁₂H₁₇O₃⁺ at *m/z* 209 could correspond with the OHDICARBROOH

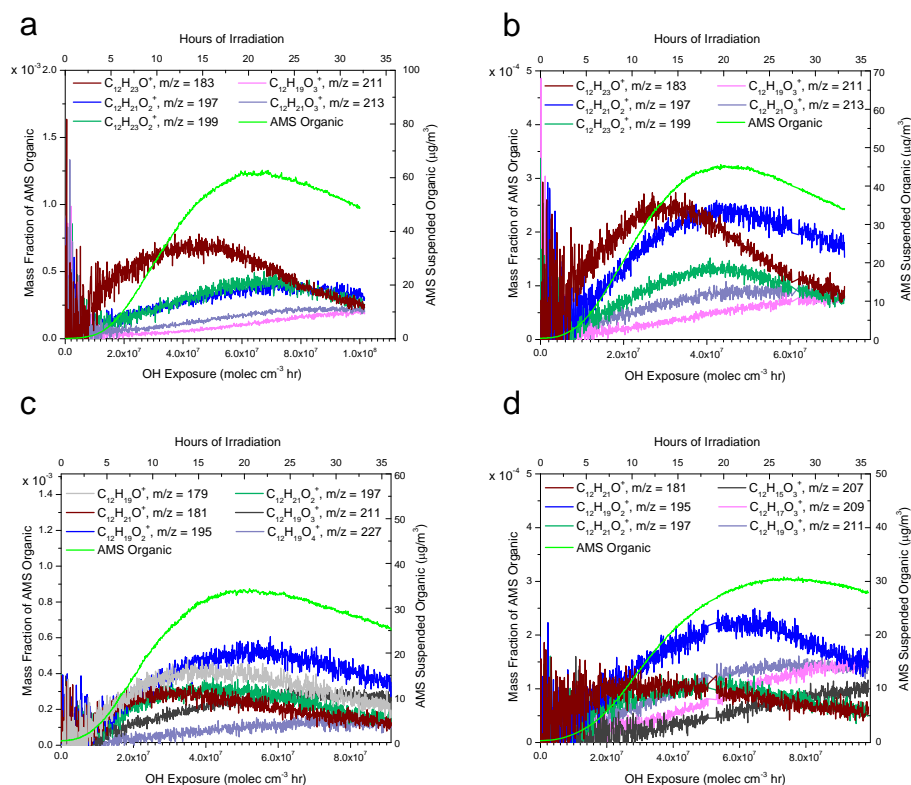


Fig. 10. Characteristic ions in (a) *n*-dodecane, (b) 2-methylundecane, (c) hexylcyclohexane, and (d) cyclododecane aerosol measured by the AMS.

and TRICARBROOH R⁺ ions, respectively. Note that the C₁₂H₁₉O₃⁺ ion can also result from a ring-opened TRICARBROOH (same as in the linear case), but where at least one of the carbonyl groups is presumably an aldehyde. The C₁₂H₁₅O₃⁺ at *m/z* 207 implies yet another step achieving one fewer degree of saturation. This was characteristic of many of the ions in the cyclododecane AMS mass spectra achieving one additional degree of unsaturation compared to that of hexylcyclohexane and two compared to the non-cyclic systems. This ion assignment is uncertain, though it could correspond with a structure containing a hydroxy, four ketone groups, and a hydroperoxy group with the ring intact (OH4CARBROOH). There may be additional cyclizations or dehydration reactions in the particle phase and/or additional ionization patterns in the AMS that may more feasibly explain the presence of this ion. This is especially relevant when considering the ions of the form C₁₂H_yO_z⁺, with *y* = 19, 17, and 15 and *z* = 3, 4, 5. For the OH4CARBROOH, TRICARBROOH, and OHDICARBROOH, the mass spectrum (Fig. 7) indicates a greater fraction of organic aerosol due to the corresponding *z* = 4 ions compared to the *z* = 5 ions. This may indicate competitive cyclization over PHA formation, as shown in Schemes 4 (TRICARBROOH) and 5 (OHDICARBROOH) of Fig. 2.

3.2.6 AMS elemental ratios

The Van Krevelen diagram, originally used for showing how O : C and H : C elemental ratios change during coal formation (Van Krevelen, 1950), has been recently utilized with HR-TOF-AMS data to aid in the interpretation of elemental ratio changes in organic aerosol formation (Heald et al., 2010; Ng et al., 2011; Chhabra et al., 2011; Lambe et al., 2011, 2012). The slopes on the diagram of O : C versus H : C can provide insight into the chemical evolution of the aerosol in terms of functional group changes. A slope of -1 for ambient and laboratory data is consistent with carboxylic acid groups without fragmentation (Heald et al., 2010). Ng et al. (2011) showed that, for aged ambient organic aerosol, the slope of -0.5 is consistent with carboxylic acid addition with fragmentation. Both of these results highlighted aerosol that was already quite oxidized, with most of the O : C values greater than 0.30. Lambe et al. (2012) presented SOA results from a potential aerosol mass (PAM) chamber in which long-chain alkane SOA O : C extended from a value of 0 to close to 1.4. The Van Krevelen slope from an O : C of 0 to approximately 0.3 was -1.3 , and for O : C values greater than 0.3 the slope became less negative with a value of -0.7 . Lambe et al. (2012) attribute this change in slope to a transition from a functionalized- to fragment-dominated regime.

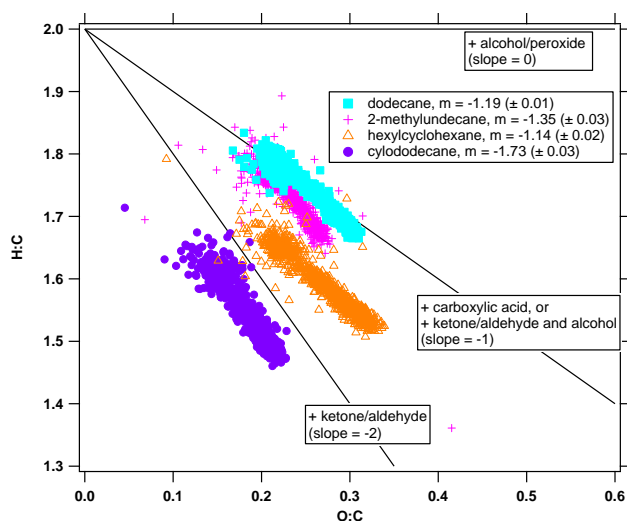


Fig. 11. Van Krevelen diagram for low- NO_x photooxidation of *n*-dodecane, 2-methylundecane, hexylcyclohexane, and cyclododecane.

The elemental ratios from the current study are shown in Fig. 11. The experimental progression for all four systems is from upper left to lower right across the Van Krevelen space. All of the compounds have $\text{O}:\text{C} < 0.3$, except for the end of the hexylcyclohexane experiment. In increasing order, the slopes are -1.73 , -1.35 , -1.19 , and -1.14 for cyclododecane, 2-methylundecane, dodecane, and hexylcyclohexane, respectively. In the presence of NO_x , Tkacik et al. (2012) found steeper slopes (approaching -2) for the same or comparable in structure alkane species, attributed to a combination of carboxylic acid addition and added ketone and alcohol moieties. This was also achieved under a much lower total OH exposure ($\sim 6 \times 10^6 \text{ molec cm}^{-3} \text{ h}$) than that used in the current experiments, providing contrast between the more efficiently (in terms of OH exposure) achieved higher $\text{O}:\text{C}$ ratios with fragmentation pathways in the presence of NO_x compared to the proposed functionalization and accretion schemes in the low- NO_x regime presented here. In comparison to the average slope of -1.3 in the $\text{O}:\text{C}$ range 0 to 0.3 from OH-initiated oxidation of alkanes in the absence of NO_x by Lambe et al. (2012), many of the systems here show comparable behavior. The fact that many do not reach an $\text{O}:\text{C}$ much higher than 0.3 with a less negative slope as observed in Lambe et al. (2012) is also consistent with these experiments remaining in the functionalized-dominated regime, and not having yet transitioned to a fragment-dominated regime.

This functionalized-dominated regime is supported by the proposed chemical mechanisms and AMS ions found in each system. Cyclododecane SOA has the slope closest to -2 , indicating a greater contribution from ketone and aldehyde groups. This is consistent with the $\text{C}_{12}\text{H}_y\text{O}_3^+$ ion series in Fig. 10d and the relatively higher degrees of unsaturation in

the cyclododecane AMS mass spectrum (Fig. 7) as compared to the other systems.

2-methylundecane SOA exhibits a lower $\text{O}:\text{C}$ than that from *n*-dodecane, supported by the lower fraction of total organic aerosol attributed to oxidized ions compared to *n*-dodecane. *n*-Dodecane achieves the second highest $\text{O}:\text{C}$ for the OH exposures in this study, and while the progression of key $> 150 \text{ amu}$ ions in this system (Fig. 10a) is more gradual, there is continued oxygenation, as observed by the presence of the $\text{C}_{12}\text{H}_{19}\text{O}_5^+$ ion. Yee et al. (2012) also found the $\text{O}:\text{C}$ range to be consistent with the $\text{O}:\text{C}$ of several of the multifunctional hydroperoxides and their derived PHAs.

The higher $\text{O}:\text{C}$ achieved for hexylcyclohexane may be a result of the generally faster chemistry seen in both the gas-phase oxidation and the particle-phase development, in which initial key ions in the particle phase (Fig. 10c) peak earlier in terms of OH exposure $< 5 \times 10^7 \text{ molec cm}^{-3} \text{ h}$ as compared to those of the other systems. This could be a result of verging on increased contribution from fragmentation processes increasing the $\text{O}:\text{C}$ or oxygenation achieved from continued oxidation.

4 Conclusions

We address here the mechanisms of formation of SOA in alkane systems under low- NO_x conditions. Special attention is given to the effect of alkane structure on SOA formation and to the molecular identifications of the oxidation products responsible for SOA growth. Aerosol formation from the photooxidation of *n*-dodecane, 2-methylundecane, hexylcyclohexane, and cyclododecane under low- NO_x conditions is initiated by the partitioning of a 2nd-generation product, the carbonyl hydroperoxide (CARBROOH), to the particle phase. It appears that this hydroperoxide is incorporated with simultaneous formation of a peroxyhemiacetal. Several other multifunctional hydroperoxides are proposed to explain characteristic ions in the AMS mass spectra for each system, suggesting that at least three additional degrees of unsaturation might be achieved for cyclododecane while functionalizing primarily via ketone/aldehyde addition.

2-methylundecane exhibits the least extent of chemical processing in the particle phase (in terms of the least variety of $\text{C}_x\text{H}_y\text{O}_z^+$ ions observed in the mass spectra) relative to the other systems, likely a result of gas-phase fragmentation that leads to a product distribution consisting of relatively higher volatility intermediates. Hexylcyclohexane exhibits rapid gas-phase oxidation and particle-phase processing reflected in the highest achieved $\text{O}:\text{C}$ (verging on 0.4). Of the systems studied, hexylcyclohexane behaves in terms of SOA chemistry as a hybrid of the other systems. It exhibits the rapid formation of functionalized semi- and low-volatility species that contribute to the particle phase, but then fragmentation processes (attributable to the branching) start to dominate and lower the relative particle mass due to

C₁₂ oxygenates. Cyclization processes analogous to cyclic hemiacetal and higher volatility dihydrofuran formation can also contribute to limitations in particle growth.

While the > 150 amu tracer ions in the AMS help to identify potential species involved in particle-phase chemistry like PHA formation, the more oxidized and functionalized the ion, the greater potential exists for multiple ionization and fragmentation schemes in the AMS. Ideally, standards of different structure but analogous functionality would be available for generating mass spectral standards that can be used to better interpret the mass spectra in this region. Ionization schemes need to be better elucidated to see if observed ions can be explained by particle-phase chemistry that involves species of cyclic structure and/or those undergoing cyclization followed by dehydration. Such schemes were proposed here to explain additional ions in the AMS not expected purely from PHA formation. This is relevant for determining the molecular identity of some of the highly oxygenated (> O₃⁺) ions that grow in the particle phase at extended OH exposures.

Evidence for additional particle-phase reactions including cyclization of multifunctional hydroperoxides exists. Intramolecular cyclization of multifunctional hydroperoxides can be competitive with the intermolecular reaction of multifunctional hydroperoxides with aldehydes to form PHAs. For the functional groups presumed to be incorporated via the gas-phase mechanisms ketone (some aldehyde for cyclododecane), hydroperoxy, and hydroxyl, it is very likely these functional groups undergo intramolecular, as well as intermolecular, reactions (including oligomer formation), depending on their relative positions on the C₁₂ backbone. This may be highly relevant for hexylcyclohexane in which the alkyl branch is sufficiently long to still cyclize and result in a bicyclic structure. Cyclododecane may ring open to form functionalized aldehydes and then cyclize again (not necessarily returning to a C₁₂ ring).

Environmental factors such as humidity, aerosol acidity, and temperature are likely to play a role in controlling these chemical transformations and ultimately impact the extent of PHA formation. The present study was conducted under dry conditions, but future study would benefit from examining the role of humidity as aqueous particles will affect partitioning of certain species. Parameterizations of 1-tetradecene ozonolysis experiments found that the organic hydroperoxides and peroxides made up the majority of the aerosol mass under humid conditions (Tobias et al., 2000). Tobias et al. (2000) also calculated using these parameterizations that, for an organic aerosol loading ~10 μg m⁻³, the generated hydroperoxides and peroxides would be expected to be completely in the particle phase. Further, aldehyde contribution to the particle phase has been found to be enhanced with aerosol acidity (Jang et al., 2002). DePalma et al. (2013) also found that dimers formed from α-pinene ozonolysis products, including a PHA, return to the monomers with increases in temperature from 298 K to 373 K. Additional simulations

in DePalma et al. (2013) also suggest that, for the PHA structure considered, the dimerization free energy is favorable for formation in the gas-phase as well as in water-, methanol-, and acetonitrile-like solutions. This was found to be unique to the PHA structure considered, as other dimerization reactions were not as broadly favorable among the different solution types. The potential for dimerization in the gas phase has implications for new particle formation as well. While the experiments employed here were seeded, and it seems that initial organic growth may be initiated by PHA incorporation to the particle phase, it has been generally assumed that PHA reactions occur in the particle phase. This is supported by simulations in Shiraiwa et al. (2013) for the case of *n*-dodecane, though it may also be that the phase of reaction depends on the precursor system and the structure of its oxidation products.

The systematic study of these C₁₂ structures lays a chemical groundwork for understanding the dynamics of particle growth concerted with particle-phase reactions (e.g., PHA formation) and sustained growth via semi-volatile and low-volatile product partitioning, followed by additional particle-phase oxidation if unhampered by fragmentation processes. Further study of the C₁₂ system should include additional isomeric configurations of branching and cyclic + branched structures to better understand the spectrum of oxidation pathways between 2-methylundecane and hexylcyclohexane and between hexylcyclohexane and cyclododecane. These structural dependencies will certainly impact the mechanisms of SOA formation and SOA yields, which can affect the representation of SOA formation from alkanes in atmospheric modeling.

Supplementary material related to this article is available online at <http://www.atmos-chem-phys.net/13/11121/2013/acp-13-11121-2013-supplement.pdf>.

Acknowledgements. This work was supported by the Office of Science (Biological and Environmental Research), US Department of Energy Grant (DE-SC 0006626), and National Science Foundation Grants AGS-1057183 and ATM-0650061. The authors acknowledge helpful discussions with John D. Crouse and Jason M. St. Clair regarding treatment of CIMS data and gas-phase data, as well as experimental assistance and discussions with Reddy L. N. Yatavelli and ManNin Chan. L. D. Yee, J. S. Craven, and C. L. Loza were supported by National Science Foundation Graduate Research Fellowships.

Edited by: J. Liggio

References

- Aiken, A. C., DeCarlo, P. F., and Jimenez, J. L.: Elemental analysis of organic species with electron ionization high-resolution mass spectrometry, *Anal. Chem.*, 79, 8350–8358, 2007.
- Aiken, A. C., Decarlo, P. F., Kroll, J. H., Worsnop, D. R., Huffman, J. A., Docherty, K. S., Ulbrich, I. M., Mohr, C., Kimmel, J. R., Sueper, D., Sun, Y., Zhang, Q., Trimborn, A., Northway, M., Ziemann, P. J., Canagaratna, M. R., Onasch, T. B., Alfarra, M. R., Prevot, A. S. H., Dommen, J., Duplissy, J., Metzger, A., Baltensperger, U., and Jimenez, J. L.: O/C and OM/OC ratio of primary, secondary, and ambient organic aerosols with high-resolution time-of-flight aerosol mass spectrometry, *Environ. Sci. Technol.*, 42, 4478–4485, 2008.
- Allan, J. D., Delia, A. E., Coe, H., Bower, K. N., Alfarra, M. R., Jimenez, J. L., Middlebrook, A. M., Drewnick, F., Onasch, T. B., Canagaratna, M. R., Jayne, J. T., and Worsnop, D. R.: A generalised method for the extraction of chemically resolved mass spectra from aerodyne aerosol mass spectrometer data, *J. Aerosol Sci.*, 35, 909–922, 2004.
- Aschmann, S. M., Arey, J., and Atkinson, R.: Kinetics and products of the gas-phase reaction of OH radicals with 5-hydroxy-2-pentanone at 296 ± 2 K, *J. Atmos. Chem.*, 45, 289–299, doi:10.1023/A:1024216900051, 2003.
- Atkinson, R.: Gas-phase tropospheric chemistry of organic compounds, *J. Phys. Chem. Ref. Data, Monogr.*, 2, 1–216, 1994.
- Atkinson, R.: Gas-phase tropospheric chemistry of volatile organic compounds. 1. Alkanes and alkenes, *J. Phys. Chem. Ref. Data*, 26, 215–290, 1997.
- Atkinson, R. and Arey, J.: Atmospheric degradation of volatile organic compounds, *Chem. Rev.*, 103, 4605–4638, doi:10.1021/cr0206420, 2003.
- Atkinson, R., Arey, J., and Aschmann, S. M.: Atmospheric chemistry of alkanes: Review and recent developments, *Atmos. Environ.*, 42, 5859–5871, doi:10.1016/j.atmosenv.2007.08.040, 2008.
- Aumont, B., Valorso, R., Mouchel-Vallon, C., Camredon, M., Lee-Taylor, J., and Madronich, S.: Modeling SOA formation from the oxidation of intermediate volatility n-alkanes, *Atmos. Chem. Phys.*, 12, 7577–7589, doi:10.5194/acp-12-7577-2012, 2012.
- Bahreini, R., Middlebrook, A. M., de Gouw, J. A., Warneke, C., Trainer, M., Brock, C. A., Stark, H., Brown, S. S., Dube, W. P., Gilman, J. B., Hall, K., Holloway, J. S., Kuster, W. C., Perrig, A. E., Prevot, A. S. H., Schwarz, J. P., Spackman, J. R., Szidat, S., Wagner, N. L., Weber, R. J., Zotter, P., and Parrish, D. D.: Gasoline emissions dominate over diesel in formation of secondary organic aerosol mass, *Geophys. Res. Lett.*, 39, L06805, doi:10.1029/2011GL050718, 2012.
- Benson, S. W.: Thermochemical kinetics, Wiley, second edn., 1976.
- Canagaratna, M., Jayne, J., Jimenez, J., Allan, J., Alfarra, M., Zhang, Q., Onasch, T., Drewnick, F., Coe, H., Middlebrook, A., Delia, A., Williams, L., Trimborn, A., Northway, M., DeCarlo, P., Kolb, C., Davidovits, P., and Worsnop, D.: Chemical and microphysical characterization of ambient aerosols with the Aerodyne aerosol mass spectrometer, *Mass Spectrom. Rev.*, 26, 185–222, doi:10.1002/mas.20115, 2007.
- Capouet, M., Mueller, J. F., Ceulemans, K., Compernelle, S., Vereecken, L., and Peeters, J.: Modeling aerosol formation in alpha-pinene photo-oxidation experiments, *J. Geophys. Res.-Atmos.*, 113, D02308, doi:10.1029/2007JD008995, 2008.
- Cappa, C. D., Zhang, X., Loza, C. L., Craven, J. S., Yee, L. D., and Seinfeld, J. H.: Application of the statistical oxidation model (SOM) to secondary organic aerosol formation from photooxidation of C₁₂ alkanes, *Atmos. Chem. Phys.*, 13, 1591–1606, doi:10.5194/acp-13-1591-2013, 2013.
- Chhabra, P. S., Ng, N. L., Canagaratna, M. R., Corrigan, A. L., Russell, L. M., Worsnop, D. R., Flagan, R. C., and Seinfeld, J. H.: Elemental composition and oxidation of chamber organic aerosol, *Atmos. Chem. Phys.*, 11, 8827–8845, doi:10.5194/acp-11-8827-2011, 2011.
- Cocker, D. R., Flagan, R. C., and Seinfeld, J. H.: State-of-the-art chamber facility for studying atmospheric aerosol chemistry, *Environ. Sci. Technol.*, 35, 2594–2601, 2001.
- Compernelle, S., Ceulemans, K., and Müller, J.-F.: EVAPORATION: a new vapour pressure estimation method for organic molecules including non-additivity and intramolecular interactions, *Atmos. Chem. Phys.*, 11, 9431–9450, doi:10.5194/acp-11-9431-2011, 2011.
- Craven, J. S., Yee, L. D., Ng, N. L., Canagaratna, M. R., Loza, C. L., Schilling, K. A., Yatavelli, R. L. N., Thornton, J. A., Ziemann, P. J., Flagan, R. C., and Seinfeld, J. H.: Analysis of secondary organic aerosol formation and aging using positive matrix factorization of high-resolution aerosol mass spectra: application to the dodecane low-NO_x system, *Atmos. Chem. Phys.*, 12, 11795–11817, doi:10.5194/acp-12-11795-2012, 2012.
- Crouse, J. D., McKinney, K. A., Kwan, A. J., and Wennberg, P. O.: Measurement of gas-phase hydroperoxides by chemical ionization mass spectrometry, *Anal. Chem.*, 78, 6726–6732, 2006.
- DeCarlo, P. F., Kimmel, J. R., Trimborn, A., Northway, M. J., Jayne, J. T., Aiken, A. C., Gonin, M., Fuhrer, K., Horvath, T., Docherty, K. S., Worsnop, D. R., and Jimenez, J. L.: Field-deployable, high-resolution, time-of-flight aerosol mass spectrometer, *Anal. Chem.*, 78, 8281–8289, 2006.
- DePalma, J. W., Horan, A. J., Hall IV, W. A., and Johnston, M. V.: Thermodynamics of oligomer formation: implications for secondary organic aerosol formation and reactivity, *Phys. Chem. Chem. Phys.*, 15, 6935–6944, doi:10.1039/C3CP44586K, 2013.
- Dibble, T. S.: Cyclization of 1,4-hydroxycarbonyls is not a homogeneous gas phase process, *Chem. Phys. Lett.*, 447, 5–9, doi:10.1016/j.cplett.2007.08.088, 2007.
- Docherty, K. S., Wu, W., Lim, Y. B., and Ziemann, P. J.: Contributions of Organic Peroxides to Secondary Aerosol Formed from Reactions of Monoterpenes with O₃, *Environ. Sci. Technol.*, 39, 4049–4059, doi:10.1021/es050228s, 2005.
- Gao, S., Keywood, M., Ng, N. L., Surratt, J., Varutbangkul, V., Bahreini, R., Flagan, R. C., and Seinfeld, J. H.: Low-molecular-weight and oligomeric components in secondary organic aerosol from the ozonolysis of cycloalkenes and alpha-pinene, *J. Phys. Chem. A*, 108, 10147–10164, 2004a.
- Gao, S., Ng, N. L., Keywood, M., Varutbangkul, V., Bahreini, R., Nenes, A., He, J. W., Yoo, K. Y., Beauchamp, J. L., Hodyss, R. P., Flagan, R. C., and Seinfeld, J. H.: Particle phase acidity and oligomer formation in secondary organic aerosol, *Environ. Sci. Technol.*, 38, 6582–6589, 2004b.
- Gentner, D. R., Isaacman, G., Worton, D. R., Chan, A. W. H., Dallmann, T. R., Davis, L., Liu, S., Day, D. A., Russell, L. M., Wilson, K. R., Weber, R., Guha, A., Harley, R. A., and Goldstein, A. H.: Elucidating secondary organic aerosol from diesel and gasoline vehicles through detailed characterization

- of organic carbon emissions, *Proc. Natl. Acad. Sci. U. S. A.*, doi:10.1073/pnas.1212272109, 2012.
- Heald, C. L., Kroll, J. H., Jimenez, J. L., Docherty, K. S., DeCarlo, P. F., Aiken, A. C., Chen, Q., Martin, S. T., Farmer, D. K., and Artaxo, P.: A simplified description of the evolution of organic aerosol composition in the atmosphere, *Geophys. Res. Lett.*, 37, L08803, doi:10.1029/2010GL042737, 2010.
- Isaacman, G., Wilson, K. R., Chan, A. W. H., Worton, D. R., Kimmel, J. R., Nah, T., Hohaus, T., Gonin, M., Kroll, J. H., Worsnop, D. R., and Goldstein, A. H.: Improved resolution of hydrocarbon structures and constitutional isomers in complex mixtures using gas chromatography-vacuum ultraviolet-mass spectrometry, *Anal. Chem.*, 84, 2335–2342, doi:10.1021/ac2030464, 2012.
- Jang, M., Czoschke, N. M., Lee, S., and Kamens, R. M.: Heterogeneous Atmospheric Aerosol Production by Acid-Catalyzed Particle-Phase Reactions, *Science*, 298, 814–817, doi:10.1126/science.1075798, 2002.
- Jenkin, M. E., Saunders, S. M., and Pilling, M. J.: The tropospheric degradation of volatile organic compounds: a protocol for mechanism development, *Atmos. Environ.*, 31, 81–104, doi:10.1016/S1352-2310(96)00105-7, 1997.
- Johnson, D., Jenkin, M., Wirtz, K., and Martin-Reviejo, M.: Simulating the formation of secondary organic aerosol from the photooxidation of aromatic hydrocarbons, *Environ. Chem.*, 2, 35–48, doi:10.1071/EN04079, 2005.
- Jordan, C. E., Ziemann, P. J., Griffin, R. J., Lim, Y. B., Atkinson, R., and Arey, J.: Modeling SOA formation from OH reactions with C8–C17 n-alkanes, *Atmos. Environ.*, 42, 8015–8026, doi:10.1016/j.atmosenv.2008.06.017, 2008.
- Kalberer, M.: Identification of polymers as major components of atmospheric organic aerosols, *Science*, 303, 1659–1662, doi:10.1126/science.1092185, 2004.
- Kalberer, M., Sax, M., and Samburova, V.: Molecular Size Evolution of Oligomers in Organic Aerosols Collected in Urban Atmospheres and Generated in a Smog Chamber, *Environ. Sci. Technol.*, 40, 5917–5922, doi:10.1021/es0525760, 2006.
- Keywood, M. D., Varutbangkul, V., Bahreini, R., Flagan, R. C., and Seinfeld, J. H.: Secondary organic aerosol formation from the ozonolysis of cycloalkenes and related compounds, *Environ. Sci. Technol.*, 38, 4157–4164, 2004.
- Kwok, E. S. and Atkinson, R.: Estimation of hydroxyl radical reaction rate constants for gas-phase organic compounds using a structure-reactivity relationship: An update, *Atmos. Environ.*, 29, 1685–1695, doi:10.1016/1352-2310(95)00069-B, 1995.
- Lambe, A. T., Onasch, T. B., Massoli, P., Croasdale, D. R., Wright, J. P., Ahern, A. T., Williams, L. R., Worsnop, D. R., Brune, W. H., and Davidovits, P.: Laboratory studies of the chemical composition and cloud condensation nuclei (CCN) activity of secondary organic aerosol (SOA) and oxidized primary organic aerosol (OPOA), *Atmos. Chem. Phys.*, 11, 8913–8928, doi:10.5194/acp-11-8913-2011, 2011.
- Lambe, A. T., Onasch, T. B., Croasdale, D. R., Wright, J. P., Martin, A. T., Franklin, J. P., Massoli, P., Kroll, J. H., Canagaratna, M. R., Brune, W. H., Worsnop, D. R., and Davidovits, P.: Transitions from functionalization to fragmentation reactions of laboratory secondary organic aerosol (SOA) generated from the OH oxidation of alkane precursors, *Environ. Sci. Technol.*, 46, 5430–5437, doi:10.1021/es300274t, 2012.
- Lim, Y. B. and Ziemann, P. J.: Products and mechanism of secondary organic aerosol formation from reactions of n-alkanes with OH radicals in the presence of NO_x, *Environ. Sci. Technol.*, 39, 9229–9236, doi:10.1021/es051447g, 2005.
- Lim, Y. B. and Ziemann, P. J.: Effects of molecular structure on aerosol yields from OH radical-initiated reactions of linear, branched, and cyclic alkanes in the presence of NO_x, *Environ. Sci. Technol.*, 43, 2328–2334, doi:10.1021/es803389s, 2009a.
- Lim, Y. B. and Ziemann, P. J.: Chemistry of secondary organic aerosol formation from OH radical-initiated reactions of linear, branched, and cyclic alkanes in the presence of NO_x, *Aerosol Sci. Technol.*, 43, 604–619, doi:10.1080/02786820902802567, 2009b.
- Lim, Y. B. and Ziemann, P. J.: Kinetics of the heterogeneous conversion of 1,4-hydroxycarbonyls to cyclic hemiacetals and dihydrofurans on organic aerosol particles, *Phys. Chem. Chem. Phys.*, 11, 8029–8039, doi:10.1039/B904333K, 2009c.
- Lipsky, E. M. and Robinson, A. L.: Effects of dilution on fine particle mass and partitioning of semivolatile organics in diesel exhaust and wood smoke, *Environ. Sci. Technol.*, 40, 155–162, 2006.
- Nakao, S., Shrivastava, M., Nguyen, A., Jung, H., and Cocker, D.: Interpretation of secondary organic aerosol formation from diesel exhaust photooxidation in an environmental chamber, *Aerosol Sci. Technol.*, 45, 964–972, doi:10.1080/02786826.2011.573510, 2011.
- Ng, N. L., Canagaratna, M. R., Jimenez, J. L., Chhabra, P. S., Seinfeld, J. H., and Worsnop, D. R.: Changes in organic aerosol composition with aging inferred from aerosol mass spectra, *Atmos. Chem. Phys.*, 11, 6465–6474, doi:10.5194/acp-11-6465-2011, 2011.
- Paulot, F., Crouse, J. D., Kjaergaard, H. G., Kroll, J. H., Seinfeld, J. H., and Wennberg, P. O.: Isoprene photooxidation: new insights into the production of acids and organic nitrates, *Atmos. Chem. Phys.*, 9, 1479–1501, 1680-7316, 2009.
- Presto, A. A., Miracolo, M. A., Kroll, J. H., Worsnop, D. R., Robinson, A. L., and Donahue, N. M.: Intermediate-volatility organic compounds: a potential source of ambient oxidized organic aerosol, *Environ. Sci. Technol.*, 43, 4744–4749, doi:10.1021/es803219q, 2009.
- Presto, A. A., Miracolo, M. A., Donahue, N. M., and Robinson, A. L.: Secondary organic aerosol formation from high-NO_x photo-oxidation of low volatility precursors: n-alkanes, *Environ. Sci. Technol.*, 44, 2029–2034, doi:10.1021/es903712r, 2010.
- Pye, H. O. T. and Pouliot, G. A.: Modeling the role of alkanes, polycyclic aromatic hydrocarbons, and their oligomers in secondary organic aerosol formation, *Environ. Sci. Technol.*, 46, 6041–6047, doi:10.1021/es300409w, 2012.
- Robinson, A. L., Donahue, N. M., Shrivastava, M. K., Weitkamp, E. A., Sage, A. M., Grieshop, A. P., Lane, T. E., Pierce, J. R., and Pandis, S. N.: Rethinking organic aerosols: Semivolatile emissions and photochemical aging, *Science*, 315, 1259–1262, 2007.
- Sato, K., Hatakeyama, S., and Imamura, T.: Secondary organic aerosol formation during the photooxidation of toluene: NO_x dependence of chemical composition, *J. Phys. Chem. A*, 111, 9796–9808, doi:10.1021/jp071419f, 2007.
- Schauer, J. J., Kleeman, M. J., Cass, G. R., and Simoneit, B. R. T.: Measurement of emissions from air pollution sources. 2. C1 through C30 organic compounds from medium

- duty diesel trucks, *Environ. Sci. Technol.*, 33, 1578–1587, doi:10.1021/es980081n, 1999.
- Schauer, J. J., Kleeman, M. J., Cass, G. R., and Simoneit, B. R. T.: Measurement of emissions from air pollution sources. 5. C1–C32 organic compounds from gasoline-powered motor vehicles, *Environ. Sci. Technol.*, 36, 1169–1180, doi:10.1021/es0108077, 2002.
- Shiraiwa, M., Yee, L. D., Schilling, K. A., Loza, C. L., Craven, J. S., Zuend, A., Ziemann, P. J., and Seinfeld, J. H.: Size distribution dynamics reveal particle-phase chemistry in organic aerosol formation, *Proc. Natl. Acad. Sci.*, 110, 11746–11750, doi:10.1073/pnas.1307501110, 2013.
- St. Clair, J. M., McCabe, D. C., Crouse, J. D., Steiner, U., and Wennberg, P. O.: Chemical ionization tandem mass spectrometer for the in situ measurement of methyl hydrogen peroxide, *Rev. Sci. Instrum.*, 81, 094102, doi:10.1063/1.3480552, 2010.
- Surratt, J. D., Kroll, J. H., Kleindienst, T. E., Edney, E. O., Claeys, M., Sorooshian, A., Ng, N. L., Offenberg, J. H., Lewandowski, M., Jaoui, M., Flagan, R. C., and Seinfeld, J. H.: Evidence for organosulfates in secondary organic aerosol, *Environ. Sci. Technol.*, 41, 517–527, times Cited: 33, 2007.
- Surratt, J. D., Chan, A. W. H., Eddingsaas, N. C., Chan, M. N., Loza, C. L., Kwan, A. J., Hersey, S. P., Flagan, R. C., Wennberg, P. O., and Seinfeld, J. H.: Reactive intermediates revealed in secondary organic aerosol formation from isoprene, *Proc. Natl. Acad. Sci. USA*, 107, 6640–6645, 2010.
- Tkacik, D. S., Presto, A. A., Donahue, N. M., and Robinson, A. L.: Secondary organic aerosol formation from intermediate-volatility organic compounds: cyclic, linear, and branched alkanes, *Environ. Sci. Technol.*, 46, 8773–8781, doi:10.1021/es301112c, 2012.
- Tobias, H. J. and Ziemann, P. J.: Thermal Desorption Mass Spectrometric Analysis of Organic Aerosol Formed from Reactions of 1-Tetradecene and O₃ in the Presence of Alcohols and Carboxylic Acids, *Environ. Sci. Technol.*, 34, 2105–2115, doi:10.1021/es9907156, 2000.
- Tobias, H. J., Docherty, K. S., Beving, D. E., and Ziemann, P. J.: Effect of Relative Humidity on the Chemical Composition of Secondary Organic Aerosol Formed from Reactions of 1-Tetradecene and O₃, *Environ. Sci. Technol.*, 34, 2116–2125, doi:10.1021/es991057s, 2000.
- Van Krevelen, D. W.: Graphical-statistical method for the study of structure and reaction processes of coal, *Fuel*, 24, 269–284, 1950.
- Yee, L. D., Craven, J. S., Loza, C. L., Schilling, K. A., Ng, N. L., Canagaratna, M. R., Ziemann, P. J., Flagan, R. C., and Seinfeld, J. H.: Secondary organic aerosol formation from low-NO_x photooxidation of dodecane: evolution of multigeneration gas-phase chemistry and aerosol composition, *J. Phys. Chem. A*, 116, 6211–6230, doi:10.1021/jp211531h, 2012.
- Zhang, X. and Seinfeld, J. H.: A functional group oxidation model (FGOM) for SOA formation and aging, *Atmos. Chem. Phys.*, 13, 5907–5926, doi:10.5194/acp-13-5907-2013, 2013.
- Ziemann, P. J.: Formation of alkoxyhydroperoxy aldehydes and cyclic peroxyhemiacetals from reactions of cyclic alkenes with O₃ in the presence of alcohols, *J. Phys. Chem. A*, 107, 2048–2060, doi:10.1021/jp022114y, 2003.

Appendix E

Secondary Organic Aerosol Formation from Low-NO_x Photooxidation of Dodecane: Evolution of Multigeneration Gas-Phase Chemistry and Aerosol Composition⁷

⁷ Reproduced by permission from “Secondary organic aerosol formation from low-NO_x photooxidation of dodecane: Evolution of multigeneration gas-phase chemistry and aerosol composition” by L. D. Yee, J. S. Craven, C. L. Loza, K. A. Schilling, N. L. Ng, M. R. Canagaratna, P. J. Ziemann, R. C. Flagan, and J. H. Seinfeld. *J. Phys. Chem. A* **2012**, *116*, 6211-6230.

Secondary Organic Aerosol Formation from Low-NO_x Photooxidation of Dodecane: Evolution of Multigeneration Gas-Phase Chemistry and Aerosol Composition

Lindsay D. Yee,[†] Jill S. Craven,[‡] Christine L. Loza,[‡] Katherine A. Schilling,[‡] Nga Lee Ng,[§] Manjula R. Canagaratna,^{||} Paul J. Ziemann,[⊥] Richard C. Flagan,^{†,‡} and John H. Seinfeld^{*,†,‡}

[†]Division of Engineering and Applied Science, California Institute of Technology, Pasadena, California 91125, United States

[‡]Division of Chemistry and Chemical Engineering, California Institute of Technology, Pasadena, California 91125, United States

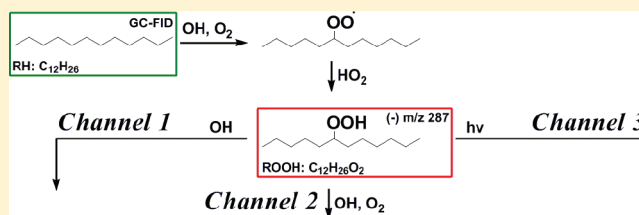
[§]School of Chemical and Biomolecular Engineering and School of Earth and Atmospheric Sciences, Georgia Institute of Technology, Atlanta, Georgia 30332, United States

^{||}Aerodyne Research, Inc., Billerica, Massachusetts 01821, United States

[⊥]Air Pollution Research Center, Department of Environmental Sciences and Environmental Toxicology Graduate Program, University of California, Riverside, California 92521, United States

S Supporting Information

ABSTRACT: The extended photooxidation of and secondary organic aerosol (SOA) formation from dodecane (C₁₂H₂₆) under low-NO_x conditions, such that RO₂ + HO₂ chemistry dominates the fate of the peroxy radicals, is studied in the Caltech Environmental Chamber based on simultaneous gas and particle-phase measurements. A mechanism simulation indicates that greater than 67% of the initial carbon ends up as fourth and higher generation products after 10 h of reaction, and simulated trends for seven species are supported by gas-phase measurements. A characteristic set of hydroperoxide gas-phase products are formed under these low-NO_x conditions. Production of semivolatile hydroperoxide species within three generations of chemistry is consistent with observed initial aerosol growth. Continued gas-phase oxidation of these semivolatile species produces multifunctional low volatility compounds. This study elucidates the complex evolution of the gas-phase photooxidation chemistry and subsequent SOA formation through a novel approach comparing molecular level information from a chemical ionization mass spectrometer (CIMS) and high *m/z* ion fragments from an Aerodyne high-resolution time-of-flight aerosol mass spectrometer (HR-ToF-AMS). Combination of these techniques reveals that particle-phase chemistry leading to peroxyhemiacetal formation is the likely mechanism by which these species are incorporated in the particle phase. The current findings are relevant toward understanding atmospheric SOA formation and aging from the “unresolved complex mixture,” comprising, in part, long-chain alkanes.



INTRODUCTION

Atmospheric chemical transformations occur through mechanisms involving free radical reactions, sunlight, and reactions in or on condensed media.¹ The formation of secondary organic aerosol (SOA) involves the multigeneration oxidation of a parent organic molecule leading to product molecules that partition between the gas and particle phases. As the parent organic is consumed, usually by reaction with the hydroxyl (OH) radical, subsequent products may also react with OH, giving rise to an evolving product distribution. As products become more functionalized with oxygen-containing moieties, their volatility decreases, and their propensity to partition into the particle phase increases.² In the gas-phase chemical cascade, both functionalization and fragmentation (C–C bond scission) reactions occur, and the interplay between these two general types of reactions, together with the progressive decrease in volatility accompanying the addition of oxygen atoms to the

parent backbone, defines the SOA formation process for a particular parent organic.³ As the SOA formation process evolves, a competition ensues between the rate of production of lower volatility species with increasing oxygen-to-carbon (O:C) atomic ratio and the increase in the SOA mass; as the mass of SOA increases, the partitioning of gas-phase products with somewhat higher volatility and somewhat lower O:C ratio is enhanced. The mass of SOA can, in some cases, reach a maximum and decrease as gas-phase fragmentation reactions convert lower volatility species into higher volatility species, leading to evaporation of the lower volatility particle-phase species in an attempt to maintain gas-particle equilibrium. In

Special Issue: A. R. Ravishankara Festschrift

Received: November 30, 2011

Revised: March 16, 2012

Published: March 16, 2012

short, the rate at which oxygens are added via successive gas-phase reactions, the relative importance of fragmentation versus functionalization reactions, and the specific decrease in volatility attending the formation of oxidized species govern the evolution of the SOA mass.

Long-chain alkanes represent an especially important class of organics with respect to SOA formation. The so-called unresolved complex mixture (UCM) is likely an important source of unaccounted for SOA formation in the atmosphere,⁴ and alkanes are a major component of that mixture.^{5,6} Low-volatility vapors from the UCM are a source of “untraditional” SOA, as they evaporate from primary organic aerosol emissions upon dilution and undergo subsequent oxidation to form SOA.⁴ Quantifying the SOA formation from long-chain alkanes will undoubtedly aid in closing the gap between observed atmospheric organic aerosol and that predicted by atmospheric models based on traditional biogenic and anthropogenic SOA precursors. SOA formation from alkane photooxidation has received study.^{7–12} Alkane–OH reaction kinetics^{13,14} and gas-phase chemistry in the presence of NO_x exhibit a product distribution that can lead to highly oxidized products.^{7,9,10} Studies of alkane oxidation under low-NO_x conditions have also been carried out.¹⁵ Importantly, owing to the relatively long lifetimes against OH reaction at typical ambient OH concentrations (on the order of 12 h to several days) and to a relatively rich information base on the kinetics and mechanisms of alkane oxidation reactions, long-chain alkanes represent an especially important class of compounds with respect to SOA formation. Finally, it is crucial to develop detailed chemical databases on the explicit pathways of SOA formation for classes of parent organics, which can serve as benchmarks for evaluation of empirical/statistical models of SOA formation.

The present work represents the first report on a comprehensive series of laboratory chamber experiments on SOA formation from long-chain alkanes. We focus here on SOA formation from dodecane under low-NO_x conditions. The low-NO_x regime of atmospheric chemistry is particularly important in the regional to remote atmosphere and is especially relevant to the chemical aging that is intrinsic to SOA formation. The key to atmospheric photooxidation chemistry is the fate of the alkyl peroxy radical (RO₂) formed after OH attack and O₂ addition. RO₂ can react with HO₂, RO₂, or NO_x, the distribution of which is critical for understanding radical propagation and sinks, as well as the pathways that lead eventually to SOA.^{16,17} In atmospheric regions of low NO_x levels, the RO₂ radical will react preferentially with HO₂ and RO₂. In such regions, HO₂ concentrations are on the order of 10⁹ molecules cm⁻³,^{18–20} and the RO₂–HO₂ reaction is competitive with the reaction of RO₂ with NO_x. Generally, under such atmospheric conditions, the RO₂–HO₂ reaction, which leads to hydroperoxides, dominates over RO₂ self-reaction. We present here the first experimental study of SOA formation from dodecane oxidation in the regime in which the fate of the dodecane peroxy radical is dominated by the RO₂ + HO₂ regime of alkyl peroxy radical chemistry. The particular focus of the present work is the multigeneration gas-phase chemistry of dodecane oxidation that leads to SOA formation. We employ chemical ionization mass spectrometry (CIMS) to track the evolution of the gas-phase oxidation products. We develop a gas-phase mechanism to describe the low-NO_x regime of chemistry. The mechanism is used to explicitly simulate four generations of gas-phase chemistry. By combining

CIMS and high-resolution time-of-flight aerosol mass spectrometer (HR-ToF-AMS) measurements, we are able to simultaneously track several semivolatiles oxidation products in the gas and particle phases. Together, these measurements provide evidence of particle-phase formation of peroxyhemiacetals (PHAs).

■ EXPERIMENTAL SECTION

Instrumentation. Experiments were conducted in the dual 28 m³ Teflon reactors in the Caltech Environmental Chamber described elsewhere.^{21,22} The reactors are flushed with clean, dry air for 24 h before a new experiment. A suite of online gas- and particle-phase instruments was used to monitor the development of the chemistry from dodecane photooxidation. The dodecane decay was monitored by taking hourly samples at 0.13 LPM of chamber air over 10 min (1.3 L total sample volume) onto a Tenax adsorbent. This was then loaded into the inlet of a gas chromatograph with flame ionization detection (GC/FID, Agilent 6890N), desorbed, and then injected onto an HP-5 column (15 m × 0.53 mm ID × 1.5 μm thickness, Hewlett-Packard). Desorption was at 270 °C for 15 min onto the column held at 30 °C. Next the oven was ramped from 30 to 280 °C at 10 °C/min and held at 280 °C for 5 min. The mass response of the detector was calibrated by spiking the Tenax cartridges with 0.5 μL of standard solution and analyzing them following the previously described method. Standard solutions of 25 mL volume each with concentrations ranging from 1 mM to 11 mM of dodecane in cyclohexane were prepared for these calibrations. The O₃ and NO_x were monitored using a standard UV absorption O₃ analyzer (Horiba, APOA 360) and a chemiluminescence NO_x analyzer (Horiba, APNA 360). During the injection period and before lights on, the temperature was around 293–294 K. After lights on, the temperature for all experiments ranged between 296 and 298 K, and relative humidity levels remained <5%.

The gas-phase chemistry was tracked using measurements from a CIMS, consisting of a modified Varian 1200 quadrupole mass spectrometer to accommodate a custom ionization region. The general operation and details of the instrument have been discussed previously.^{23–25} In negative mode operation, the use of CF₃OOCF₃ reagent gas makes the instrument ideal for measuring hydroperoxide containing compounds and acidic species, as described in studies of CF₃OOCF₃ chemistry.²⁶ For a more strongly acidic species [H·X], the transfer product is formed during ionization [H·X·F]⁻, resulting in a nominal mass-to-charge ratio, *m/z*, of [M+19]⁻, where M is the molecular weight of the analyte. For less acidic species and hydroperoxides [R], the cluster product forms [R·CF₃O]⁻, or *m/z* = [M+85]⁻. Carboxylic acids such as acetic and formic acids tend to have equal contributions to the transfer and cluster product, in which case the overall signal of a compound is considered as the sum of the two product channels. In positive mode operation, an analyte R can undergo proton transfer reaction generating an ion of the form [R·H]⁺ and/or react with *n* positively charged water clusters to form a cluster in the form of [(H₂O)_{*n*}·R·H]⁺. Hydroperoxide species tend to undergo dehydration after protonation, and are thus monitored at nominal *m/z* = [M-17]⁺.²⁷ Unfortunately, due to mass tuning shifts midproject, the positive mode *m/z*'s reported do not reflect the expected *m/z* from the clustering theory, but use of this mode of the CIMS was essential for tracking less polar compounds such as the carbonyl and, in some instances, where product *m/z*'s were out of range for the mass scan in negative

Table 1. Dodecane Low-NO_x Experiments

expt date	hrs of photooxidation	initial HC (ppb)	[NO] ₀ (ppb)	[NO _x] ₀ (ppb)	[O ₃] ₀ (ppb)	initial seed vol. (μm ³ cm ⁻³)	ΔHC (ppb)	peak organic ^a (μg cm ⁻³)
1/16/2011	18	34.2 ± 1.6	<LDL	<LDL	2.7	9.1 ± 0.3	32.0 ± 2.1	54.6
3/13/2011	36	34.9 ± 1.6	<LDL	<LDL	2.6	11.4 ± 1.5	33.6 ± 2.1	62.8
3/16/2011	18	33.0 ± 1.6	<LDL	<LDL	3.3	12.0 ± 1.2	32.3 ± 2.1	51.3

^aNot corrected for particle wall loss.

mode operation. The positive mode m/z 's are reported as monitored during the experiment, but suggested assignments were made using a back calibration of the shift of m/z , generally upward by five atomic mass units (amu) in the m/z range of interest from 200 to 220. While the CIMS is capable of measuring a diverse array of chemical species, specificity is challenged when isomers or different compounds with the same nominal MW contribute to the same m/z signal, which has unit mass resolution. In this study, many isomers are formed because there are many possible locations of hydroxyl radical attack on the starting chain. The CIMS signal at one m/z represents the summed contribution of all the isomers. Isomeric compounds in this study were mostly problematic for distinguishing the acids, in that one cannot fully distinguish the difference between a C_n peracid, C_n hydroxycarboxylic acid, and a C_{n+1} hydroperoxide, as discussed in the results section on acid formation.

Particle size distribution and number concentration measurements are made with a cylindrical differential mobility analyzer (DMA; TSI Model 3081) coupled to a condensation particle counter (TSI Model 3010). A logarithmic scan from a mobility diameter of 10 nm to 1 μm is completed every 90 s. Sheath and excess flows of 2.5 LPM were used, with a 5:1 flow rate ratio of sheath-to-aerosol (i.e., a resolving power of 5). An Aerodyne HR-ToF-AMS,^{28–30} hereafter referred to as the AMS, continuously measured submicrometer nonrefractory aerosol composition at 1 min resolution switching between the higher resolution, lower sensitivity W mode and the lower resolution, higher sensitivity V mode. A detailed discussion of the AMS method for the automated m/z calibration, mass accuracy, mass resolution of V and W modes, the high-resolution ion fitting algorithm, and ion signal integrations at the same integer mass is presented in previous work.²⁹ The AMS ions (organic) are reported with a relative ionization efficiency of 1.4.³⁰

Experimental Protocols. To maximize total OH exposure, a set of experiments was designed following phased instrument sampling protocols similar to those used in the work of Loza et al.³¹ to capture 36 h of total photooxidation while preserving reactor volume. In this study, the 36 h time series is achieved by combining data from an 18 h experiment during which all instruments are online and a 36 h experiment during which all instruments but the AMS are offline during the first 20 h of oxidation. Relative humidity and temperature were monitored for the full 36 h. Thus, the concatenated time series for many instruments (i.e., the CIMS, DMA, NO_x, and O₃ analyzers) is that of the 18 h experiment and the last 16 h of the 36 h experiment. A list of the experiments used for this study are in Table 1. The March experiments used another DMA with a lower total effective flow rate. General consistency between the AMS and CIMS measurements across the two 18 h experiments is observed (see Supporting Information, Figure S1). In the 18 h January experiment, CIMS traces for negative mode ions at $m/z > 300$ were included; the mass scan was reduced to $m/z \leq 300$ in the March experiments. The January

experiment also provided evidence for supporting alternate positive mode m/z 's used for monitoring select hydroperoxide species in the March experiments, which would otherwise be best monitored by the negative mode in the m/z range >300 (see Supporting Information, Figure S2).

Injection protocols were the same for all experiments. Two-hundred eighty microliters of a 50% by weight solution of hydrogen peroxide in water was measured using a glass syringe and injected into a glass trap. The trap was submerged in a warm water bath (~35–38 °C) while 5 LPM of the purified injection air flowed through the trap and into the chamber evaporating the hydrogen peroxide over approximately 90 min. This results in an approximate starting hydrogen peroxide concentration of 4 ppm. Next a 0.015 M aqueous ammonium sulfate solution was atomized into the chambers providing ~11 μm³/cm³ volume concentration of seed prior to lights on, as measured by the chamber DMA. Finally, 9 μL of dodecane (Sigma-Aldrich, 98% purity) was injected into a glass bulb and connected within six inches to a reactor injection port via 1/4" o.d. polytetrafluoroethylene (PTFE) tubing. This led to a 10 inch line of 1/4" o.d. PTFE internal to the reactor from the injection port to ensure injection would not be directly to the reactor wall. Using a heat gun with gentle heat, the dodecane evaporated into a flow of 5 LPM of purified injection air going into the chamber. This injection method was performed as close to the chamber as possible to prevent losses of the parent hydrocarbon during line transfer. The resulting dodecane concentration in the chamber was about 34 ppb. Each experiment's starting concentration is listed in Table 1. After loading the reactors, an hour period elapsed to allow for mixing. Then, the blacklights were turned on initiating generation of the OH radical from H₂O₂ photolysis.

Experimental Controls. A thorough discussion on characterizations of the particle-phase wall loss for longer experiments in the Caltech Environmental Chamber appears elsewhere.³¹ For this study, we estimate that by 18 and 36 h of oxidation, approximately 15% and finally 28% of the particle volume has been lost to the walls when comparing DMA suspended volume and wall loss corrected particle volume. A diagnostic dark vapor-phase wall-loss experiment was performed by injecting 60 ppb 2-dodecanone into the chamber and monitoring its decay in the dark over 22 h. Although there was an observed loss of 14% CIMS dodecanone signal over 22 h from its initial signal after injection, one cannot eliminate the possibility of immediate wall-loss or transfer loss during the injection and mixing period (~75 min total). Because handling of the standard proved difficult for establishing a confident calibration curve for the CIMS, this could not be verified. No appreciable formation of $> C_3$ acids and hydroperoxide species above the background noise from the CIMS measurements was observed, and no aerosol volume above the limit of detection (~0.6 μm³ cm⁻³) was produced by 22 h as measured by the DMA. Further investigation would be necessary for the goal of mass closure. In order to verify the fragmentation pattern of

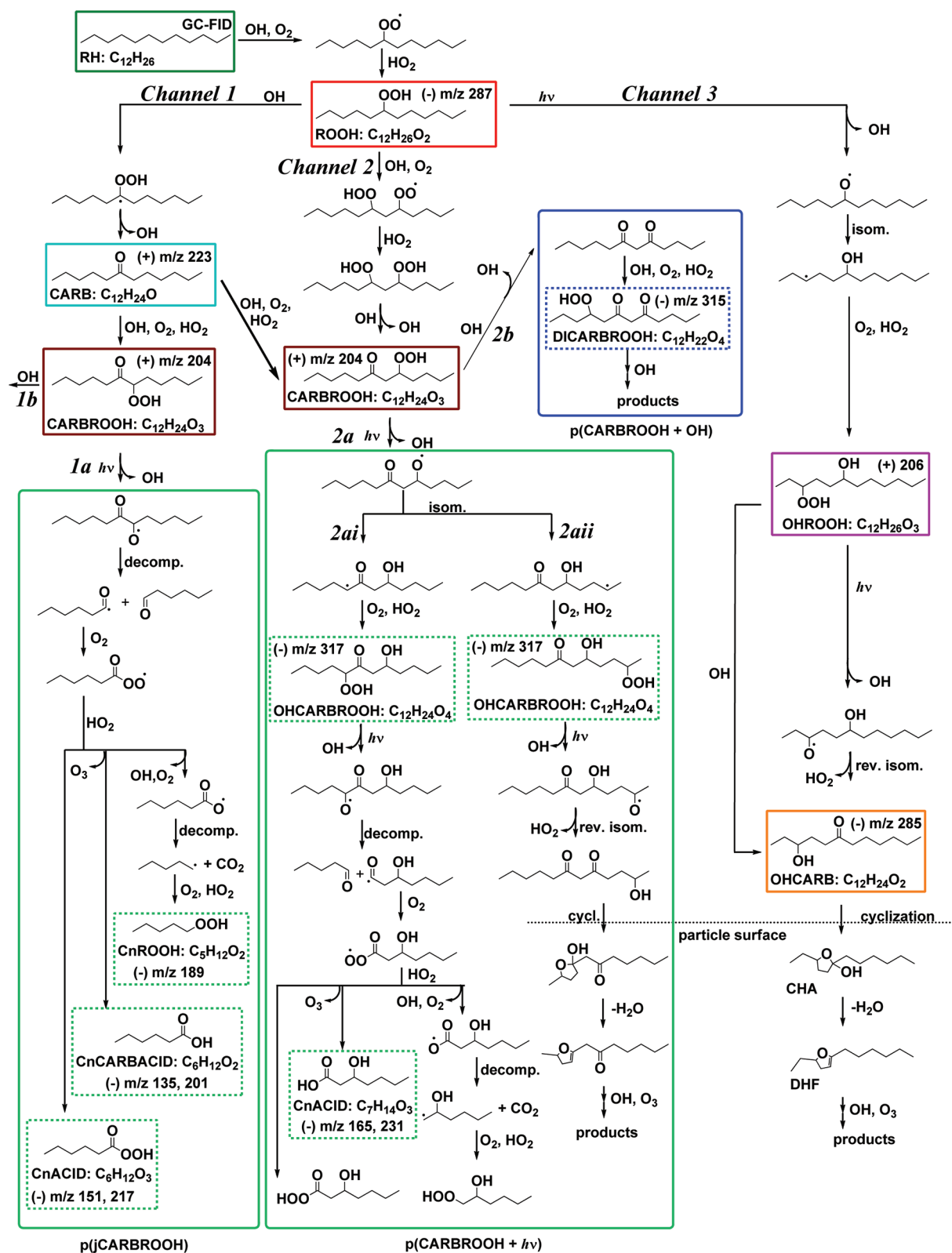


Figure 1. Dodecane low- NO_x mechanism. This scheme explicitly shows OH attack at the C_6 position; however, abstraction of other hydrogens on secondary carbons can also occur. Reaction of dodecane with OH forms a hydroperoxide (ROOH). The hydroperoxide undergoes successive reactions to generate the carbonyl hydroperoxide (CARBROOH , Channel 1 and Channel 2) or photolyzes to form the hydroxy hydroperoxide (OHROOH , Channel 3). The solid colored boxes indicate compounds or reaction pathways photochemically simulated. CIMS monitored species have m/z noted. Dashed colored boxes indicate compounds monitored by CIMS, but not explicitly simulated in the photochemical mechanism. The gray dashed line denotes a gas–particle interface where 1,4-hydroxycarbonyl (OHCARB)-like compounds reactively uptake onto the particle and cyclize to form a cyclic hemiacetal (CHA).

Table 2. Reactions Included in the Gas-Phase Photochemical Model

rxn #	reaction	<i>k</i>	ref.
1	$\text{H}_2\text{O}_2 + h\nu \rightarrow 2\text{OH}$	$j_{\text{H}_2\text{O}_2} = 2.87 \times 10^{-6} \text{ s}^{-1}$	JPL ³⁷ + chamber irradiance data
2	$\text{H}_2\text{O}_2 + \text{OH} \rightarrow \text{HO}_2 + \text{H}_2\text{O}$	$k_1 = 1.8 \times 10^{-12} \text{ cm}^3 \text{ molecule}^{-1} \text{ s}^{-1}$	JPL ³⁷
3	$\text{RH} + \text{OH} \rightarrow \text{RO}_2 + \text{H}_2\text{O}$	$k_2 = k_{\text{OH}} = 13.2 \times 10^{-12} \text{ cm}^3 \text{ molecule}^{-1} \text{ s}^{-1}$	Atkinson, 1997 ¹⁴
4	$\text{RO}_2 + \text{RO}_2 + \text{M} \rightarrow \text{pRO}_2\text{RO}_2 + \text{M}$	$k_3 = 5 \times 10^{-15} \text{ cm}^3 \text{ molec}^{-1} \text{ s}^{-1}$	Atkinson, 1997 ¹⁴
5	$\text{RO}_2 + \text{HO}_2 \rightarrow \text{ROOH} + \text{O}_2$	$k_4 = 2.16 \times 10^{-11} \text{ cm}^3 \text{ molecule}^{-1} \text{ s}^{-1}$	MCM 3.2
6	$\text{HO}_2 + \text{HO}_2 \rightarrow \text{H}_2\text{O}_2 + \text{O}_2$	$k_5 = 1.5 \times 10^{-12} \text{ cm}^3 \text{ molec}^{-1} \text{ s}^{-1}$	JPL ³⁷
7	$\text{OH} + \text{HO}_2 \rightarrow \text{H}_2\text{O} + \text{O}_2$	$k_6 = 1.1 \times 10^{-10} \text{ cm}^3 \text{ molecule}^{-1} \text{ s}^{-1}$	JPL ³⁷
8	$\text{OH} + \text{OH} \rightarrow \text{H}_2\text{O}_2$	$k_7 = 6.28 \times 10^{-12} \text{ cm}^3 \text{ molec}^{-1} \text{ s}^{-1}$	JPL ³⁷
9	$\text{ROOH} + \text{OH} \rightarrow \text{CARB}$	$k_8 = 7.4 \times 10^{-12} \text{ cm}^3 \text{ molecule}^{-1} \text{ s}^{-1}$	JPL ³⁷
10	$\text{ROOH} + h\nu \rightarrow \text{RO} + \text{OH}$	$j_{\text{ROOH}} = 2.30 \times 10^{-6} \text{ s}^{-1}$	MCM 3.2 + chamber irradiance data
11	$\text{RO} + \text{O}_2 \rightarrow \text{OHRO}_2$	$k_9 = 2.59 \times 10^{-6} \text{ cm}^3 \text{ molecule}^{-1} \text{ s}^{-1}$	MCM 3.2
12	$\text{OHRO}_2 + \text{HO}_2 \rightarrow \text{OHROOH} + \text{O}_2$	$k_{10} = k_4$	MCM 3.2
13	$\text{CARB} + \text{OH} \rightarrow \text{CARBRO}_2 + \text{H}_2\text{O}$	$k_{11} = 1.49 \times 10^{-11} \text{ cm}^3 \text{ molecule}^{-1} \text{ s}^{-1}$	MCM 3.2
14	$\text{CARBRO}_2 + \text{HO}_2 \rightarrow \text{CARBROOH}$	$k_{12} = k_4$	MCM 3.2
15	$\text{CARB} + h\nu \rightarrow \text{pjCARB}$	$j_{\text{CARB}} = 3.32 \times 10^{-7} \text{ s}^{-1}$	MCM 3.2 + chamber irradiance data
16	$\text{CARBROOH} + \text{OH} \rightarrow \text{p(CARBROOH} + \text{OH)}$	$k_{13} = 9.10 \times 10^{-11} \text{ cm}^3 \text{ molecule}^{-1} \text{ s}^{-1}$	MCM 3.2
17	$\text{CARBROOH} + h\nu \rightarrow \text{p(jCARBROOH)}$, aka $\text{p(CARBROOH} + h\nu)$	j_{ROOH}	MCM 3.2 + chamber irradiance data
18	$\text{OHROOH} + \text{OH} \rightarrow \text{OHCARB}$	$k_{14} = 4.97 \times 10^{-11} \text{ cm}^3 \text{ molecule}^{-1} \text{ s}^{-1}$	MCM 3.2
19	$\text{OHROOH} + h\nu \rightarrow \text{pjOHROOH}$	j_{ROOH}	MCM 3.2 + chamber irradiance data
20	$\text{pjOHROOH} \rightarrow \text{OHCARB} + \text{HO}_2$	$k_{15} = 2.83 \times 10^7 \text{ cm}^3 \text{ molecule}^{-1} \text{ s}^{-1}$	MCM 3.2
21	$\text{RO}_2 + \text{NO} \rightarrow 0.56 \text{ RO} + 0.44 \text{ pRONO}_2$	$k_{16} = 9.04 \times 10^{-12} \text{ cm}^3 \text{ molecule}^{-1} \text{ s}^{-1}$	MCM 3.2
22	$\text{OHRO}_2 + \text{NO} \rightarrow 0.176 \text{ OHRO} + 0.824 \text{ pOHRONO}_2$	$k_{17} = k_{16}$	MCM 3.2
23	$\text{CARBRO}_2 + \text{NO} \rightarrow \text{CARBRO}$	$k_{18} = k_{16}$	MCM 3.2
24	$\text{OHRO}_2 + \text{RO}_2 \rightarrow \text{pOHRO}_2\text{RO}_2$	$k_{19} = k_3$	MCM 3.2
25	$\text{CARBRO}_2 + \text{RO}_2 \rightarrow \text{pCARBRO}_2\text{RO}_2$	$k_{20} = k_3$	MCM 3.2
26	$\text{RO}_2 + \text{NO}_2 \rightarrow \text{pRO}_2\text{NO}_2$	$k_{21} = 9.0 \times 10^{-12} \text{ cm}^3 \text{ molecule}^{-1} \text{ s}^{-1}$	JPL ³⁷
27	$\text{OHRO}_2 + \text{NO}_2 \rightarrow \text{pOHRO}_2\text{NO}_2$	$k_{22} = k_{21}$	JPL ³⁷
28	$\text{CARBRO}_2 + \text{NO}_2 \rightarrow \text{pCARBRO}_2\text{NO}_2$	$k_{23} = k_{21}$	JPL ³⁷

hydroperoxide species in the AMS spectrum, a seeded photooxidation experiment was run with a target injection of 300 ppb octadecane ($\text{C}_{18}\text{H}_{38}$) using the experimental protocols discussed earlier. The first generation hydroperoxide ($\text{C}_{18}\text{H}_{38}\text{O}_2$) immediately partitions to the particle-phase, and a distinct AMS ion at nominal $m/z = 253$ ($\text{C}_{18}\text{H}_{37}^+$) appeared after lights on, suggesting that hydroperoxide species fragment to form ions of the form $[\text{M}-33]^+$, where M is the molecular weight of the hydroperoxide species.

■ DODECANE LOW- NO_x GAS-PHASE MECHANISM

The OH-initiated photooxidation of *n*-alkanes has been studied previously, providing a framework of well-known chemical reactions under varying NO_x conditions^{14,15} that can be extended to the case of dodecane. Such reactions are also included in the Master Chemical Mechanism 3.2 (MCM 3.2) via Web site: <http://mcm.leeds.ac.uk/MCM>.^{32,33} The reactions proposed in such previous studies in conjunction with gas-phase measurements from this study afforded the development of a mechanism for the photooxidation of dodecane under low- NO_x conditions where $\text{RO}_2 + \text{HO}_2$ chemistry dominates (see Figure 1). Reaction pathways past the carbonyl hydroperoxide (CARBROOH) along Channel 1a and Channel 2b are not included in the MCM 3.2 for dodecane. For clarity, colored boxed molecules with simple labels are those that were explicitly simulated in the photochemical mechanism and are represented in the reactions of Table 2, consistent with the color scheme comparing CIMS measurements and simulated output in Figure 2 (RH, ROOH, CARB, CARBROOH, OHROOH, and OHCARB). In some cases, a group of products was not modeled explicitly, so a reaction pathway is

boxed and labeled (p(jCARBROOH) , $\text{p(CARBROOH} + h\nu)$, and $\text{p(CARBROOH} + \text{OH})$). Boxed molecules with a dashed border indicate those that have been monitored by the CIMS including the m/z that was monitored, but they were not explicitly modeled in the photochemical mechanism (C_nROOH , $\text{C}_n\text{CARBACID}$, C_nACID , OHCARBROOH , and DICARBROOH). Reaction channels are noted with alphanumeric labels, and the labels for molecules or product channels of interest are referred to throughout the text. OH attack is explicitly shown at the C_6 carbon, although it is expected that any of the hydrogens on secondary carbons will be similarly vulnerable to abstraction by the OH radical. Using estimated structure activity relationship reaction rate constants,³⁴ OH abstraction of the hydrogens on the primary carbons would only represent two percent of the overall reaction rate of dodecane with OH. Five generations of chemistry are represented in the reaction pathways of Figure 1, with a generation defined as the OH-initiated or photolysis reaction of a stable (nonradical) compound. The mechanism provides an overview of the types of products generated from the alkyl peroxy radical RO_2 exclusively reacting with HO_2 to generate hydroperoxides, which then react with OH or undergo photolysis. While a wide variety of compounds are included in the mechanism shown in Figure 1, this mechanism is by no means exhaustive of all possible compounds formed in terms of functional group placement and molecular structure.

Low- NO_x Conditions. Under conditions in which $[\text{HO}_2] \gg [\text{RO}_2]$, and in which NO_x levels are very low, RO_2 can be expected to react exclusively with HO_2 . For the experimental conditions, the HO_2 is calculated by a photochemical model. The HO_2 concentration ($\sim 1 \times 10^{10} \text{ molecules cm}^{-3}$) exceeds

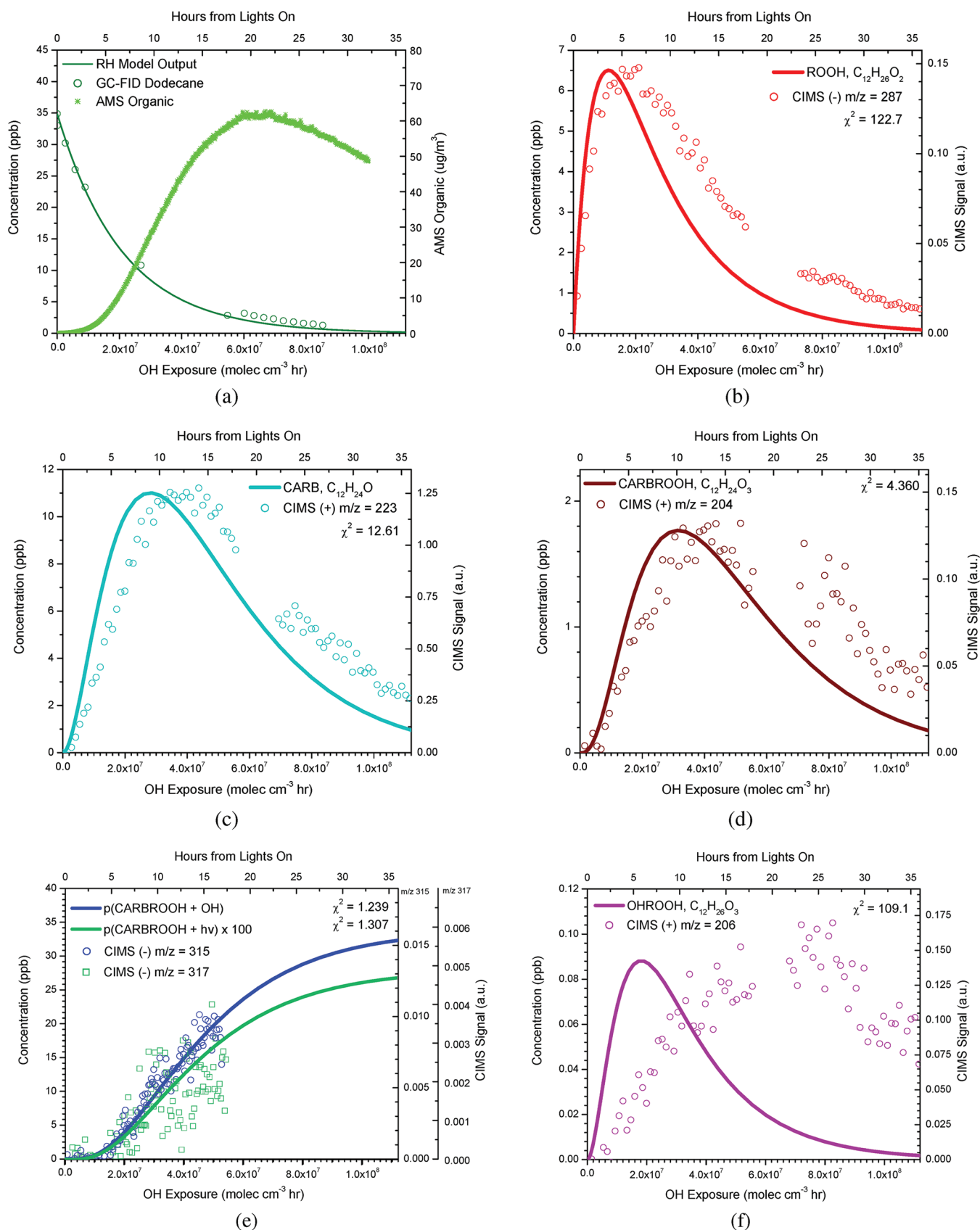


Figure 2. continued

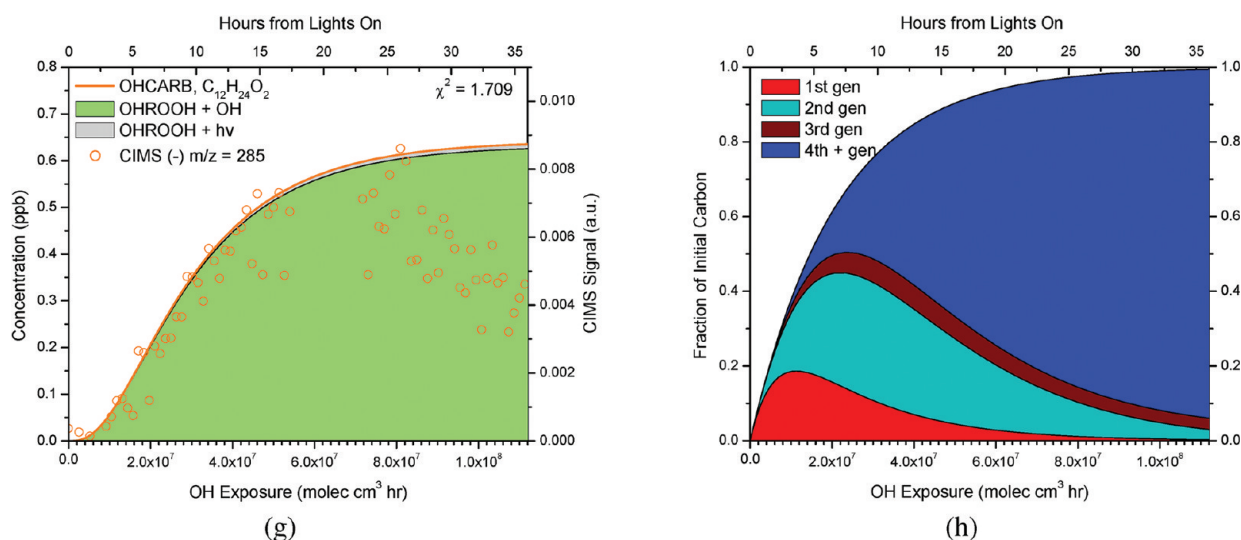


Figure 2. Simulated (curves) and observed (open circles) time evolutions of various gas-phase species from OH-initiated photooxidation of dodecane. Colors used match species outlined in the gas-phase mechanism. (a) Decay of dodecane parent hydrocarbon with suspended organic growth. (b) First-generation formation of the hydroperoxide (ROOH) monitored at (-) m/z 287. (c) Second-generation formation of the ketone (CARB) monitored at (+) m/z 223. (d) Third-generation formation of the carbonyl hydroperoxide (CARBROOH) monitored at (+) m/z 204. (e) Simulated output of remaining carbon from further oxidation of the carbonyl hydroperoxide p(CARBROOH + OH) as (-) m/z 315 or photolysis p(CARBROOH + $h\nu$) as (-) m/z 317. (f) Photolysis of the hydroperoxide (ROOH) leads to formation of a hydroxy hydroperoxide (OHROOH) monitored at (+) m/z 206. (g) Formation of the hydroxycarbonyl (OHCARB) from two sources: (1) photolysis of the hydroxy hydroperoxide (OHROOH + $h\nu$) and (2) OH reaction with the hydroxy hydroperoxide (OHROOH + OH). (h) Simulated fraction of initial carbon in the gas-phase by generation over the course of the experiment.

that of RO₂ ($\sim 1 \times 10^8$ molecules cm⁻³) by 2 orders of magnitude. The dominant route of RO₂ chemistry is reaction with HO₂ to form hydroperoxide compounds. It is important to note that what determines low-NO_x or high-NO_x conditions is not merely dependent on the HO₂ concentration itself; rather, the conditions are defined by the dynamics of NO and RO₂ and the various reaction rate constants. For example, the reaction rate constants for CH₃O₂ with HO₂, CH₃O₂, NO, and NO₂ at 298 K are 5.2×10^{-12} cm³ molecule⁻¹ s⁻¹, 3.7×10^{-13} cm³ molecule⁻¹ s⁻¹, $6.5\text{--}7.8 \times 10^{-12}$ cm³ molecule⁻¹ s⁻¹, and 3.9×10^{-12} cm³ molecule⁻¹ s⁻¹, respectively.¹⁴ On the basis of these rate constants, CH₃O₂ lifetime against reaction with these species increases in the order of NO, HO₂, NO₂, and CH₃O₂. However, sufficient concentrations of HO₂ and/or CH₃O₂ as compared with NO would shift the conditions to an effectively low-NO_x regime of chemistry, in which the relative concentrations of HO₂ and CH₃O₂ would then determine whether the low-NO_x regime is dominated by CH₃O₂ + HO₂ or shared with CH₃O₂ + CH₃O₂.

Without any addition of NO_x, a small amount of NO_x, presumably from residual nitrogen-containing acids (e.g., HONO or HNO₃) on the chamber walls, is generated upon irradiation. This phenomenon of "NO_x offgasing"³⁵ is a common observation among environmental chambers.^{35,36} In the chamber experiments to be described, the NO concentration is below the limit of detection (~ 5 ppb), and the NO₂ generated is <5 ppb. While the total generated NO_x is primarily in the form of NO₂, NO₂ cannot be calibrated directly with this technique, and there are fewer calibration points at this lower range leading to some uncertainty in the measurement. Low-NO_x conditions in the chamber are further verified by CIMS measurements of HO₂NO₂ pernitric acid (PNA), the formation of which is highly sensitive to the HO₂:NO₂ ratio. Using the CIMS sensitivity to PNA,²⁴ the PNA concentration generated upon lights on is <350 pptv. As discussed in the work of Paulot

et al.,²⁴ it is likely that the sensitivity to PNA is overestimated due to ligand exchange of H₂O₂ with the reagent ion. Using the expected HO₂ concentration generated upon irradiation, and the equilibrium constant for HO₂ + NO₂ \rightleftharpoons HO₂NO₂, 1.6×10^{-11} cm³ molec⁻¹,³⁷ the predicted NO₂ residual concentration is <1.2 ppb.

To explore possible effects of residual NO_x, the chemistry was simulated with initial concentrations of NO at 0.1 ppb, 2 ppb, and constant NO at 0.1 ppb, using all reactions in Table 2. Under these varying NO_x conditions, we estimate that $<1\%$, $<10\%$, and $<19\%$, respectively, of the dodecane reacts via RO₂ + NO_x reactions. Relative lifetimes of RO₂ against reaction with RO₂, HO₂, NO, and NO₂ for these varying NO_x conditions are provided in the Supporting Information, Table S1. The two species, the 1,4-hydroxycarbonyl (OHCARB, Figure 1) and the hydroxy hydroperoxide (OHROOH, Figure 1) that would be most affected by the presence of NO_x are shown based on NO concentration and provided in the Supporting Information, Figure S3. At NO concentration greater than 0.1 ppb, the delay seen in the CIMS measurement of the 1,4-hydroxycarbonyl is not reproduced (Supporting Information, Figure S3a). The 1,4-hydroxycarbonyl is an important intermediate in SOA formation in the presence of NO_x,^{12,38} so the presence of NO should enhance its production and contribute to initial organic growth. The observed delay in the organic growth as measured by the AMS is consistent with the absence of any appreciable NO_x in the system. Further, the presence of NO should accelerate formation of the hydroxy hydroperoxide (OHROOH) (Supporting Information, Figure S3b), causing the simulations to further deviate from the observed gas-phase measurements. These analyses support the fact that residual NO_x does not play a significant role in the overall chemistry represented and that the majority of alkoxy radical formation is not a result of RO₂ + NO chemistry. In addition, CIMS spectra show no evidence of nitrate compounds formed. Thus, the

photochemical mechanism used in the remainder of this study excludes the presence of NO_x .

Hydroperoxide Photolysis. The OH-initiated reaction of dodecane results in the formation of the peroxy radical which, upon reaction with HO_2 , rapidly produces the hydroperoxide ($\text{C}_{12}\text{H}_{26}\text{O}_2$, ROOH in Figure 1). The hydroperoxide can undergo further reaction with OH or photolyze. In the absence of an explicit photolysis rate, following MCM 3.2, the methyl hydroperoxide photolysis rate is used as a proxy for the photolysis rate of hydroperoxide species. Using absorption cross sections and quantum yields for methyl hydroperoxide (CH_3OOH)^{39,40} with the actinic flux calculated from spectral irradiance measurements in the chamber using a LICOR spectroradiometer, the expected photolysis rate constant of methyl hydroperoxide is calculated to be $j = 2.30 \times 10^{-6} \text{ s}^{-1}$. Under these experimental conditions, the C_{12} hydroperoxide is simulated in the mechanism to react with OH and undergo photolysis in branching ratios of 86% and 14%, respectively. The most likely route of photolysis is to sever the O–OH bond rather than the C–OOH bond in the hydroperoxy group,⁴¹ resulting in the formation of an alkoxy radical. In the domain of $\text{RO}_2 + \text{HO}_2$ chemistry, alkoxy radicals can be generated only via photolysis of a hydroperoxy group; there is no formation of simple alcohols, which is the same when NO_x is present.^{9,11,14,15} Along Channel 3 of the mechanism in Figure 1, the hydroperoxide photolyzes to generate the alkoxy radical. Due to the length of the carbon chain, isomerization through a 1,5-hydride shift will occur,^{9,11,15} generating a hydroxy group and leaving a radical on a secondary carbon. Reaction of this radical with O_2 followed by reaction with HO_2 leads to the hydroxy hydroperoxide ($\text{C}_{12}\text{H}_{26}\text{O}_3$) referred to as OHROOH in Figure 1, which can undergo photolysis or further reaction with OH. Under photolysis, the same reverse isomerization of the resulting hydroxy alkoxy radical occurs to form a 1,4-hydroxycarbonyl ($\text{C}_{12}\text{H}_{24}\text{O}_2$)^{9,11} referred to as OHCARB in Figure 1. On the basis of the calculated photolysis rate constant of methyl hydroperoxide as a proxy and the OH concentration lumped reaction rate constant, $k_{\text{OH}} = 9.94 \times 10^{-5} \text{ s}^{-1}$, generation of the 1,4-hydroxycarbonyl (OHCARB) via reaction with OH is the preferred pathway. The 1,4-hydroxycarbonyl is estimated to react with OH and undergo photolysis in branching ratios of 98% and 2%, respectively, according to the photochemical simulation. In the case of reaction with OH, the positions of the carbonyl and hydroxy groups would be switched from what is shown in the mechanism. This formation mechanism of the 1,4-hydroxycarbonyl (OHCARB) is also distinct from the predominant reverse isomerization mechanism when in the presence of NO_x .^{9,11,14,15} Still, an even quicker route of formation is through alkyl peroxy radical isomerization with an extrapolated isomerization rate constant of 0.03 s^{-1} at 298 K, which is applicable to the conditions of $[\text{RO}_2] < 6 \times 10^{12} \text{ molecules cm}^{-3}$ and $[\text{NO}] < 3 \times 10^9 \text{ molecules cm}^{-3}$.^{15,42,43} Since the NO concentration is only confidently known to be $< 5 \text{ ppb}$ or $1 \times 10^{11} \text{ molecules cm}^{-3}$ (the lower detection limit of our NO_x analyzer), the alkyl peroxy radical isomerization route is unconfirmed.

Hydroperoxide + OH. The hydroperoxide primarily reacts with OH, in which abstraction of the hydrogen from the hydroperoxy-containing carbon is favored.⁴¹ This leads to decomposition of the hydroperoxy group to form a carbonyl ($\text{C}_{12}\text{H}_{24}\text{O}$), resulting in recycling of OH radical (Channel 1, CARB in Figure 1). In the case in which the OH attacks another secondary carbon along the hydroperoxide chain, a

dihydroperoxide, $\text{C}_{12}\text{H}_{26}\text{O}_4$ (Channel 2 in Figure 1) may be formed. Reaction of the carbonyl or the dihydroperoxide with OH would generate the third-generation carbonyl hydroperoxide (CARBROOH), with chemical formula $\text{C}_{12}\text{H}_{24}\text{O}_3$. OH reaction with the carbonyl generally favors attack at a carbon beta from the existing carbonyl group;³⁴ however, a small fraction could occur at the α position. Depending on the relative positions of the carbonyl and hydroperoxy group, fragmentation or functionalization will occur. In the case of Channel 1, the carbonyl and hydroperoxy groups are on adjoining carbons, such that when photolysis of the hydroperoxy group generates the alkoxy radical, scission of this C–C bond is favored. Products along Channel 1a are referred to as p(jCARBROOH) in reaction 17 of Table 2. Decomposition of the carbonyl alkoxy radical leads to an acyl radical and an aldehyde. The eventual fate of the acyl radical is reaction with O_2 to generate an acyl peroxy radical, which reacts with HO_2 to generate acids (Channel 1a, CnCARBACID and CnACID) and eventually a shorter chain hydroperoxide (Channel 1a, CnROOH). While the formation of aldehydes and acids is reliant upon the formation of a less abundant form of the carbonyl hydroperoxide and its photolysis, Channel 1a serves an important role in generating aldehydes in a system with hydroperoxide species. These aldehydes can react in the particle phase to form PHAs, to be discussed later in the paper.

In the case of the carbonyl and hydroperoxy groups located beta to one another (Channel 2), photolysis (Channel 2a) or reaction with OH (Channel 2b) leads to more highly functionalized compounds than if the C_{12} backbone is fragmented as in Channel 1a. Products along Channel 2a are collectively referred to as p(CARBROOH + $h\nu$) in reaction 17 (Table 2), and products along Channel 2b are referred to as p(CARBROOH + OH) in reaction 16 (Table 2). In chemistry analogous to the photolysis route (Channel 3) of the initial hydroperoxide (ROOH), functionalization is achieved by gain of a hydroxy group through isomerization, leading to a multifunctional compound containing carbonyl, hydroxy, and hydroperoxide groups (Channel 2a). Again, the relative positions of these functional groups lead to hydroxy acids formation through photolysis (Channel 2ai, CnACID) or a 1,4-hydroxycarbonyl with an additional keto group (Channel 2aii). Consecutive OH reaction with the carbonyl hydroperoxide (CARBROOH) would lead to multiple keto groups forming from the previous hydroperoxide group (Channel 2b). However, the competitive photolysis of hydroperoxy groups leads to the variety in functionalization as in Channel 2a. Although the fate of the carbonyl hydroperoxide (CARBROOH) is likely to channel more carbon through reaction with OH (pCARBROOH + OH), (Channel 2b), the gas-phase chemistry in Channel 1a becomes important for SOA growth and will be discussed subsequently.

■ COMPARISON OF GAS-PHASE MECHANISM AND MEASUREMENTS

The dodecane–OH mechanism derived from the MCM 3.2^{32,33} (Table 2) was used to simulate the first four generations of chemistry. The simulated hydrocarbon decay agrees with GC-FID measurements of dodecane in Figure 2a. The photolysis rate for H_2O_2 was calculated using the absorption cross section and quantum yield^{39,40} with the chamber actinic flux, analogous to the calculation done for hydroperoxide species. The simple labels for compounds in Figure 1 are also used in the legend entries for the photochemical mechanism

and CIMS measurements comparisons throughout Figure 2. CIMS traces are referred to with a polarity as “(+)” or “(–)” preceding the m/z solely to indicate the ionization mode used, positive or negative, respectively. Table 3 provides a summary of the monitored CIMS ions and their suggested assignments.

Table 3. Signals Monitored by CIMS and Their Suggested Assignments

mode	m/z (s)	assignment	molecular formula
(–)	287	ROOH	$C_{12}H_{26}O_2$
(+)	223	CARB	$C_{12}H_{24}O$
(+)/(–)	204/301 ^a	CARBROOH	$C_{12}H_{24}O_3$
(+)/(–)	206/303 ^a	OHROOH	$C_{12}H_{26}O_3$
(–)	285	OHCARB	$C_{12}H_{24}O_2$
(–)	315 ^a	DICARBROOH	$C_{12}H_{22}O_4$
(–)	317 ^a	OHCARBROOH	$C_{12}H_{24}O_4$
(–)	187	C5CARBACID	$C_5H_{10}O_2$
(–)	135/201	C6CARBACID	$C_6H_{12}O_2$
(–)	149/215	C7CARBACID	$C_7H_{14}O_2$
(–)	163/229	C8CARBACID	$C_8H_{16}O_2$
(–)	177/243	C9CARBACID	$C_9H_{18}O_2$
(–)	191/257	C10CARBACID	$C_{10}H_{20}O_2$
(–)	205/271	C11CARBACID	$C_{11}H_{22}O_2$
(–)	203	C5ACID/C6ROOH	$C_5H_{10}O_3/C_6H_{14}O_2$
(–)	151/217	C6ACID/C7ROOH	$C_6H_{12}O_3/C_7H_{16}O_2$
(–)	165/231	C7ACID/C8ROOH	$C_7H_{14}O_3/C_8H_{18}O_2$
(–)	245	C8ACID/C9ROOH	$C_8H_{16}O_3/C_9H_{20}O_2$
(–)	193/259	C9ACID/C10ROOH	$C_9H_{18}O_3/C_{10}H_{22}O_2$

^aDenotes negative mode ions at $m/z > 300$ monitored in the January 18 h experiment. All other m/z 's were monitored in the January and March experiments.

The mechanism was used primarily for evaluating time profiles of expected products in the CIMS measurements. The scales for the CIMS signal and the simulated output have been adjusted for peak matching to compare the trends in Figure 2. Reduced χ^2 values are given for the fit of the simulated trace and the CIMS measurements using the maximum value for the first 18 h as the normalization parameter. The χ^2 for the simulated and measured 1,4-hydroxycarbonyl (OHCARB) is for the first 18 h since the measurement decays, but the simulation does not include a reactive sink. Vapor-phase wall loss is not treated here in the photochemical model or in correcting the gas-phase observations (for reasons described in the Experimental Section), although it is likely to play a role affecting the more highly oxidized lower volatility products formed as in other chamber studies.^{44,45} While the gas-phase chemistry represented in the mechanism generally describes the gas-phase CIMS trends for many species such as the hydroperoxide (ROOH), carbonyl (CARB), and carbonyl hydroperoxide (CARBROOH), the hydroxy hydroperoxide (OHROOH) may be subject to greater vapor-phase wall loss, contributing to some of the discrepancy between the simulated and measured trace in the beginning of the experiment. This effect is discussed further in the following section.

Mechanism and Measurement Comparison of Hydroperoxide + OH. Mechanism predictions of the hydroperoxide (ROOH) capture the trend of the CIMS measurements for the hydroperoxide (–) $m/z = 287$ (Figure 2b). At its peak, the hydroperoxide is simulated to represent about 20% of the initial carbon. While the hydroperoxide production rate is captured by the ROOH photochemical mechanism, the simulated loss is

overestimated. The loss processes for the hydroperoxide include $ROOH + OH$ and $ROOH + h\nu$. As noted, the MCM 3.2 gives an explicit reaction rate constant for a C_{12} hydroperoxide with OH, but utilizes the photolysis rate of CH_3OOH as a general photolysis rate for all hydroperoxide species. Extrapolating the photolysis rate from a C_1 to a C_{12} hydroperoxide is a source of uncertainty in the simulated trace. The simulated chemistry is more rapid than the measurements, consistent with a faster than measured production rate of the carbonyl.

The MCM 3.2 mechanism for dodecane does not include explicit reactions for formation of the dihydroperoxide (Channel 2), although evidence exists in the CIMS data at (–) $m/z = 319$ (CF_3O^- cluster) that suggests formation. The possibility of alkyl peroxy radical isomerization⁴⁶ was also considered, but this is unlikely under these experimental conditions because the $[HO_2]$ and $[OH]$ are not low enough to extend the lifetime of the alkyl peroxy radical for it to isomerize. Because the carbonyl (CARB) is not sufficiently polar to be detected in the negative mode ionization, it was monitored in positive mode at (+) $m/z = 223$. The carbonyl measurements also track the mechanism simulations, although with a slight lag (Figure 2c). The carbonyl (CARB) forms quickly, simultaneously with the hydroperoxide generation, so its peak just after 10 h represents almost a third of the initial carbon. The carbonyl hydroperoxide (CARBROOH) monitored at (+) $m/z = 204$ also times well with the model output during growth, but the gas-phase concentration remains low overall because of its many reactive sinks.

Owing to the complexity of the many later generation products, these are not represented explicitly in the mechanism, and the simulation terminates with the remaining carbon represented in further reaction of the carbonyl hydroperoxide. This includes three possible routes as discussed previously and seen in Figure 1: (1) photolysis and subsequent decomposition if the carbonyl and hydroperoxy group are vicinal (Channel 1a), (2) photolysis of the hydroperoxy group beta to the carbonyl (Channel 2a), and subsequent decomposition products (Channel 2ai) or C_{12} retaining products (Channel 2aii), and (3) continued OH reaction and functionalization of the C_{12} molecule (Channel 2b). The respective photolysis of the α -carbonyl hydroperoxide (Channel 1a) and the β -carbonyl hydroperoxide photolysis (Channel 2a) or reaction with OH (Channel 2b) are represented in the mechanism scheme in Figure 1. However, the MCM 3.2 makes no distinction between reaction rates for isomers of the carbonyl hydroperoxide, so the sum of the α -carbonyl hydroperoxide (Channel 1) and the β -carbonyl hydroperoxide (Channel 2) are implemented in the photochemical simulation as (CARBROOH). Thus, the subsequent photolysis product from the α -carbonyl hydroperoxide (Channel 1a) and the β -carbonyl hydroperoxide (Channel 2a), respectively, will produce the same time trend from the photochemical simulation (Table 2, Reaction 17), although we distinguish the alpha photolysis products (Channel 1a) as p(jCARBROOH) and the beta photolysis products (Channel 2a) as p(CARBROOH + $h\nu$) for relevant discussion on a distinct set of products formed from photolysis of each isomer. That is, acid formation (Figures 3b and 4b) is considered as p(jCARBROOH), and the multifunctional formed via Channel 2a is considered as p(CARBROOH + $h\nu$) in Figure 2e.

Note that photolysis of the β -carbonyl hydroperoxide (Channel 2ai) produces a hydroxy carbonyl hydroperoxide

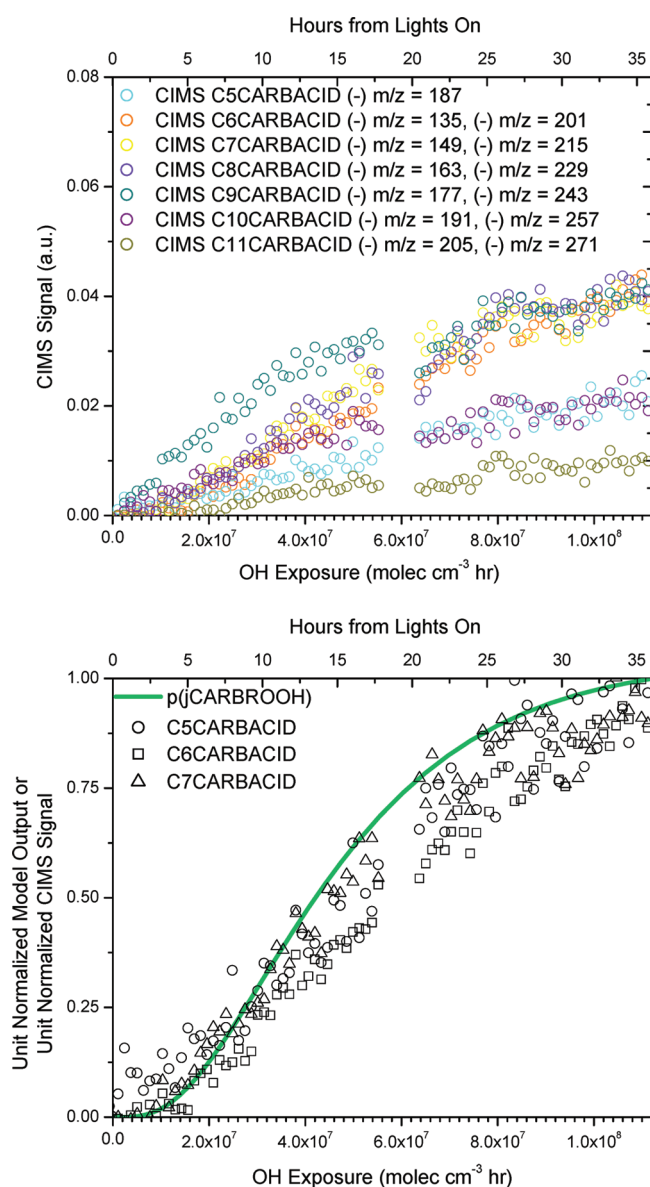


Figure 3. Carboxylic acids. (a) Series of suggested C₅ through C₁₁ carboxylic acid traces and the ions measured in CIMS negative mode ionization. (b) Representative C₅ through C₇ carboxylic acid traces on a unit normalized scale trend with modeled results for photolysis of the carbonyl hydroperoxide.

(OHCARBROOH) with the carbonyl and hydroperoxide groups vicinal. Photolysis of this multifunctional compound shows a parallel decomposition route to Channel 1a leading to hydroxy acids. Channel 2a_i retains the C₁₂ backbone, because, although it also starts with a hydroxy carbonyl hydroperoxide (OHCARBROOH), the carbonyl and hydroxy functional groups are nonvicinal to the -OOH group. Analogous to the treatment of the two carbonyl hydroperoxide (CARBROOH) isomers, these two hydroxy carbonyl hydroperoxide (OHCARBROOH) isomers are also not distinguished in the photochemical simulation; they are shown as p(CARBROOH + hν). That is, Figure 2e compares the simulated output of p(CARBROOH + hν) to the CIMS measured ion suggested for the multifunctional compound (presumably OHCARBROOH, C₁₂H₂₄O₄) at (-) m/z = 317 to represent Channel 2a. Products of the continued OH oxidation of the β-carbonyl

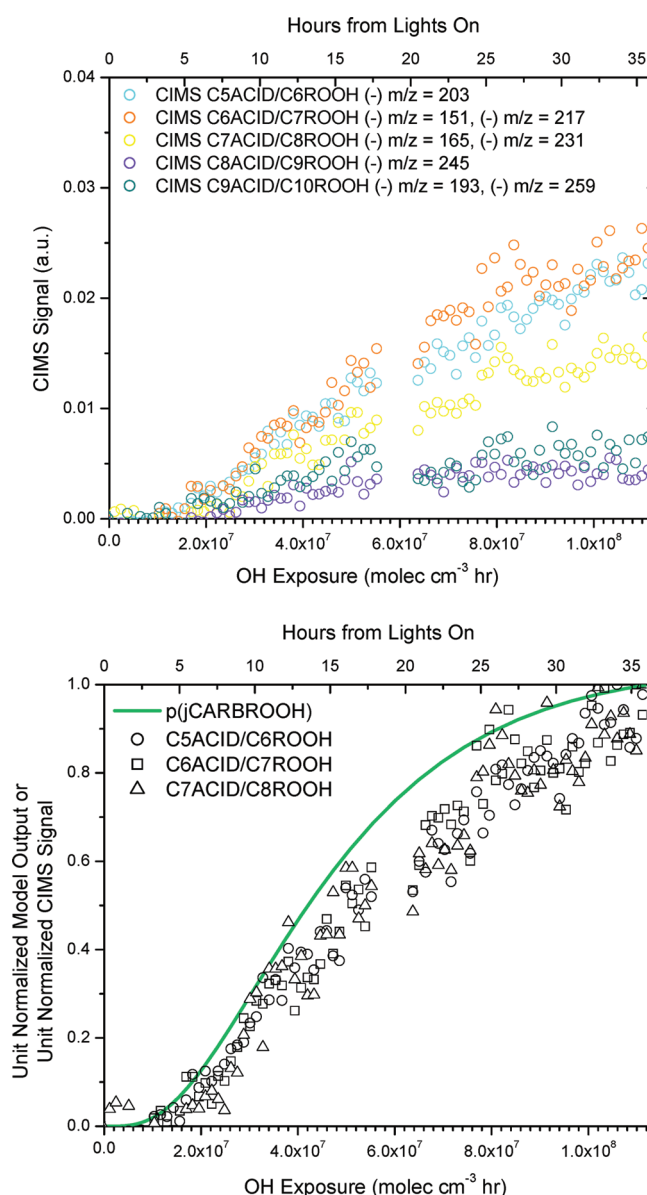


Figure 4. Acids (hydroxycarboxylic/peracid) or hydroperoxides. (a) Series of suggested C₅ through C₉ peracid and hydroxy carboxylic acid, and C₆ through C₁₀ hydroperoxide traces. Since the peracid and hydroxy carboxylic acid are the same molecular weight as a hydroperoxide with one additional carbon, the ions measured by the CIMS may have contributions from all three species. (b) Example unit normalized trends of C₅ through C₇ peracids and hydroxycarboxylic acids, and C₆ through C₈ hydroperoxides that trend with the product of carbonyl hydroperoxide photolysis from the mechanism.

hydroperoxide (Channel 2b) are simulated under p(CARBROOH + OH), which has a distinct output from that of the carbonyl hydroperoxide photolysis, represented identically in p(CARBROOH + hν) and p(jCARBROOH). Production of a possible dicarbonyl hydroperoxide (presumably DICARBROOH, C₁₂H₂₂O₄), monitored at (-) m/z = 315, represents this channel in the mechanism (Channel 2b). Note that the signals at (-) m/z = 317 and (-) m/z = 315 do not extend the full 36 h because they were not monitored for a full 36 h as described in the Experimental Section. More detailed treatment of Channel 1a is discussed subsequently relative to acid formation.

Mechanism and Measurement Comparison of Hydroperoxide Photolysis. The hydroxy hydroperoxide measurements exhibit the largest deviation of all CIMS traces from the simulated hydroxy hydroperoxide (OHROOH) (Figure 2f). While we cannot fully account for this discrepancy at the present time, it could be possible that (1) the hydroxy hydroperoxide formation is in fact slower than predicted by using the photolysis rate of a C_1 hydroperoxide for the C_{12} hydroperoxide and (2) the hydroxy hydroperoxide (OHROOH) has sufficiently low volatility that it may be lost to the chamber walls more quickly than other gas-phase compounds. We observe that the chemistry in general is actually slower than the simulation. That is, the simulated hydroperoxide (ROOH) exhibits a faster decay than that of the measurement (Figure 2b) and subsequent products (CARB, CARBROOH, and OHROOH) are simulated to rise more quickly than their individual measurements (Figure 2c,d,f). Hence, we do expect that OHROOH's actual rise will come later than that simulated. If gas-to-wall partitioning is responsible for the discrepancy, the walls may first act as a reservoir but subsequently release the hydroxy hydroperoxide back to the gas-phase as it is removed by secondary reactions, shifting the trend of the gas-phase measurement from the simulated trend. We return to the hydroxy hydroperoxide sinks in the SOA Growth section.

The 1,4-hydroxycarbonyl (OHCARB, Figure 2g) is generated from the hydroxy hydroperoxide (OHROOH, Figure 2f) in greater concentration than its precursor. As discussed earlier, the 1,4-hydroxycarbonyl may be formed via photolysis of the hydroxy hydroperoxide ($\text{OHROOH} + h\nu$) or via hydroxyl radical reaction with the hydroxy hydroperoxide ($\text{OHROOH} + \text{OH}$). The relative contributions from these sources to 1,4-hydroxycarbonyl (OHCARB) formation are shown in Figure 2g. The CIMS measurement of the 1,4-hydroxycarbonyl at $m/z = 285$ follows the simulated production despite discrepancy in the simulation and measurement for its precursor, the hydroxy hydroperoxide (OHROOH). This may suggest that the true time profile for OHROOH is not captured by the measurement. The vapor pressure of OHROOH is about 2 orders of magnitude lower than OHCARB, so one hypothesis is that the early losses of OHROOH are due to vapor-phase wall loss to the reactor walls and reaction with OH to form OHCARB. Mass closure is needed to confirm whether the measurements match the expected OHROOH distribution among losses to the wall and its oxidation to OHCARB, but it is possible that if the OHROOH is converted quickly to OHCARB via reaction with OH (lifetime ~ 2.8 h), then the trend in the CIMS measurement for OHCARB would still agree with the simulation early on as observed (Figure 2g). Although there is no explicitly simulated sink for the 1,4-hydroxycarbonyl (OHCARB), the measurement peaks sometime after 18 h. It is expected that from the difference between the gas-phase and mechanism trends, roughly 0.3 ppb of it exists in this sink.

Mechanism and Measurement Comparison of Acid Formation. Acidic species are expected to form from photolysis of a hydroperoxy group that is vicinal to another oxygen containing carbon. Photolysis of the hydroperoxy group results in an alkoxy radical vicinal to another oxygen containing carbon so decomposition ensues (see Figure 1, Channels 1a and 2ai). Depending on where in the molecule the C–C bond is severed, varying carbon length carboxylic acids (Channel 1a, CnCARBACID, $C_nH_{2n}O_2$), peracids (Channel 1a, CnACID,

$C_nH_{2n}O_3$), hydroxycarboxylic acids, (Channel 2ai, CnACID $C_nH_{2n}O_3$), and hydroxyperacids (Channel 2ai) result. Such compounds in the CIMS may appear as both the transfer ($m/z = [M + 19]^-$) and the cluster product ($m/z = [M + 85]^-$), so the traces shown are the sum of these two ions (see Figure 3 and Figure 4). In some cases, like the C_5 carboxylic acid, there were additional contributions to the cluster product ion ($m/z = 253$), so it is omitted. The C_9 carboxylic acid likely has contributions from an unidentified mass interferent since its time profile is slightly different than the others. The overall time profiles and their relative abundances are consistent with expectations that C_{11} acid production is least likely to form, as tertiary H abstraction at the end carbons is slower.³⁴ Still, distribution by carbon number would need to be confirmed after full mass quantification. When unit normalized, the carboxylic acid traces (CnCARBACID) collapse to a distinct time profile consistent with the modeled trace representing the photolysis products of the carbonyl hydroperoxide p-(jCARBROOH) in Figure 3b.

The formation of a peracid (Channel 1a, CnACID) of the same carbon number as a hydroxy carboxylic acid (Channel 2ai, CnACID) is difficult to discern, as they are isomers. Thus, these two types of acids have been referred to generally as CnACID, and this is separate from the carboxylic acids referred to as CnCARBACID. Other isomers include a hydroperoxide (Channel 1a, CnROOH) with an additional carbon. Hence, the ions monitored are generally assigned as a C_n acid or a C_{n+1} hydroperoxide in Figure 4. Still, it is more likely that the majority initial contribution to these ions stems from the peracid, as the hydroxycarboxylic acid (Channel 2ai, CnACID) is a higher generation product. Further, resulting branching ratios for the products of the acyl peroxy radical reaction with HO_2 , as discussed in Hasson et al.⁴⁷ for the case of acetyl peroxy radical ($\text{CH}_3\text{C}(\text{O})\text{O}_2$), would tend to favor peracid (via $\text{R}(\text{O})\text{O}_2 + \text{HO}_2 \rightarrow \text{R}(\text{O})\text{OOH}$) and carboxylic acid formation (via $\text{R}(\text{O})\text{O}_2 + \text{HO}_2 \rightarrow \text{R}(\text{O})\text{OH} + \text{O}_3$) routes over generation of another alkoxy radical (leading to the eventual $< C_{12}$ hydroperoxides of Channel 1a in the dodecane case). Again, on a unit normalized basis, these ion traces collapse onto the unit normalized mechanism prediction for the products of carbonyl hydroperoxide photolysis, p(jCARBROOH), consistent with this identification as peracids accompanying carboxylic acid formation (Figure 4b). While the decomposition products (i.e., acyl radical and aldehyde) in Channel 1a preceding acid formation are not explicitly modeled, the reaction of the acyl radical with O_2 is considered instantaneous, and the lifetime of an acyl peroxy radical with HO_2 is expected to be 3.7 s under low- NO_x conditions. Thus, comparison of the acid traces with p(jCARBROOH) is sufficiently close for comparison to the trend in the gas-phase measurements. While the aldehydes could not be explicitly monitored by the CIMS, the acid traces are confirmation of aldehyde formation in the gas-phase. The aldehyde will be seen to be an important gas-phase intermediate, for its role in PHA formation.

Carbon Balance. Now we discuss the fate of the initial mass of dodecane distributed among the various reaction channels in the mechanism and compare to the gas-phase measurements. More reactions are represented in the mechanism scheme of Figure 1 than are implemented in the photochemical simulation (Table 2). While the distinct product distribution from photolysis of the two isomers of the carbonyl hydroperoxide (CARBROOH) matters for the gas-phase chemistry and SOA formation, the alpha isomer is not

considered in MCM 3.2, although reactions along Channel 2a including the formation and fate of a hydroxy carbonyl hydroperoxide (OHCARBROOH) are included. As is, the photolysis rates of the carbonyl hydroperoxide (CARBROOH) isomers would be treated the same, so $p(j\text{CARBROOH})$ and $p(j\text{CARBROOH} + h\nu)$ are simulated to be the same (Table 2, Reaction 17). This prevents further explicit extension of the photochemical simulation for products along Channel 1a without further approximation of reaction rate coefficients. For carbonyl hydroperoxide (CARBROOH) reaction with OH, MCM 3.2 ends with production of the carbonyl hydroperoxy radical (CARBRO₂ in reactions 13 and 14 of Table 2); CARBRO₂ then goes back to the carbonyl hydroperoxide (CARBROOH) after reaction with HO₂ for these experimental conditions. That is, MCM 3.2 does not suggest further oxidation of CARBROOH to a dicarbonyl or to a thrice-functionalized chain (DICARBROOH), as supported by the CIMS trace monitored at $(-)$ $m/z = 315$ (DICARBROOH). Effectively, this route (Channel 2b) becomes a large carbon sink without further explicit treatment of the products. With the limitation of measurable gas-phase species beyond this point, extension of the photochemical simulation is not attempted, although the further extent of oxidation is of interest, as it will play a role in the volatilities of products and contribution to particle growth.

The simulated fraction of initial carbon over time in the various generations of products is shown in Figure 2h. After sufficient time, the majority of the carbon resides in fourth and later generation products. While fourth and later generation products represent over half of the initial carbon, the major development of this chemistry becomes apparent after the third and earlier generations peak around 2.3×10^7 molecules cm^{-3} h of total OH exposure (~ 10 h). This would correspond to almost a day of atmospheric aging, assuming an ambient OH concentration of $\sim 10^6$ molecules cm^{-3} . Thus, dodecane and other alkanes that have similarly long OH-reactive lifetimes have the potential for generating multifunctional semivolatile species over the course of a few days.

Although CIMS sensitivities to each individual compound could not be determined (see Experimental Section), we used previously determined sensitivities for compounds with similar functionality as proxies for the sensitivity of species in this mechanism. We used the previously measured sensitivity of methyl hydroperoxide (CH₃OOH)²³ for the C₁₂ hydroperoxide monitored at $(-)$ $m/z = 287$, and the previously measured sensitivity of hydroxyacetone (C₃H₆O₂)⁴⁸ for the acids and multifunctional compounds. At the end of 18 h, it is estimated that roughly 13 ppb within a factor of 2 of the simulated 31 ppb of dodecane reacted is accounted for by the CIMS negative mode ions measured. All CIMS traces shown in Figure 2 were included, except the carbonyl (CARB, Figure 2c), as it could only be monitored in positive mode, and signal intensities of this mode are not comparable to that of negative mode. Although the carbonyl hydroperoxide (CARBROOH, Figure 2d) and the hydroxy hydroperoxide (OHROOH, Figure 2f) are tracked in positive mode over 36 h, we used the signals at $(-)$ $m/z = 301$ and $(-)$ $m/z = 303$, respectively, from the 18 h January experiment for a rough carbon balance at 18 h. The acid traces shown in Figure 3a and Figure 4a were also included, although there is likely a great deal of carbon still unaccounted for in $< C_5$ acids. Other remaining carbon not accounted for by the CIMS measurements include vapor-phase wall loss (though it is expected to be small), aldehyde

formation from Channel 1a of the mechanism, and the many later generation products along Channel 2 that are not explicitly monitored by the CIMS.

SOA GROWTH

Organic growth as measured by the AMS is shown versus the dodecane decay in Figure 2a. The AMS organic trace is not corrected for particle wall-loss. The onset of growth occurs coincident with the peak of the hydroperoxide, indicating aerosol formation from higher generation oxidation products. The total suspended particle organic peaked at approximately $63 \mu\text{g m}^{-3}$ around hour 20, consistent with the development of fourth-generation gas-phase chemistry. Peak particle diameter grew from 58 nm (seed diameter) to 190 nm at the point of maximum concentration, and then to 200 nm by the end of the experiment as measured by the DMA. Further analyses and consideration of heterogeneous chemistry provide more insight into the dynamics of the aerosol growth.

Vapor Pressure Estimation. To better constrain the expected aerosol chemical makeup, vapor pressures at 298 K were estimated for an array of compounds listed in Table S2 of the Supporting Information section using the EVAPORATION (Estimation of Vapor Pressure of ORganics, Accounting for Temperature, Intramolecular, and Nonadditivity effects) method.⁴⁹ The method predicts the (subcooled) liquid pure compound vapor pressure, p^0 , taking into account intramolecular effects from the positions of functional groups on a compound. For example, the predicted p^0 for the α -carbonyl hydroperoxide is 6.58×10^{-8} atm, more than twice that of the β -carbonyl hydroperoxide, $p^0 = 2.45 \times 10^{-8}$ atm. Conversion of the pure component liquid vapor pressure to a value of C_i^0 in units of $\mu\text{g m}^{-3}$ (also in Table S2, Supporting Information) can be used to classify compounds according to previously defined volatility classes.⁵⁰ These classes in order of increasing volatility include extremely low volatility organic compounds (ELVOCs) with $C_i^* < 3 \times 10^{-4} \mu\text{g m}^{-3}$, low volatility organic compounds (LVOCs) with $3 \times 10^{-4} < C_i^* < 0.3 \mu\text{g m}^{-3}$, semivolatile organic compounds (SVOCs) with $0.3 < C_i^* < 300 \mu\text{g m}^{-3}$, intermediate volatility organic compounds (IVOCs) with $300 < C_i^* < 3 \times 10^6 \mu\text{g m}^{-3}$, and finally volatile organic compounds (VOCs) with $C_i^* > 3 \times 10^6 \mu\text{g m}^{-3}$. These volatility regimes are provided for reference in Figure 5. Note that the calculated values presented here are not the conventionally used C_i^* , since values for the activity coefficients, γ_i , are not estimated and experimental volatility measurements were not made. C_i^* is related to C_i^0 through the activity coefficient, $C_i^* = \gamma_i C_i^0$.⁵⁰

O:C Values. The O:C values for each molecule are included in the Supporting Information section, Table S2. To view the progression of the oxidation, each compound is shown in the O:C versus $\log C_i^0$ space (Figure 5). The marker colors indicate the gas-phase generation of the compound. Black markers are reserved specifically for those compounds that may participate in heterogeneous chemistry. Each compound has a letter assigned label, corresponding to the key used in Table S2. A general upward trend to the left indicates lower volatility and increasing oxygenation over time. Exceptions do occur where there is formation of second generation compounds, like the hydroxy hydroperoxide and the dihydroperoxide, of a higher O:C and lower volatility compared to later generation products. AMS measurements show that within the first 10 h of early growth, the O:C stabilizes at 0.22, after which it steadily increases to 0.30 by the end of the experiment. O:C measurements are estimated to have an uncertainty of 30%,⁵¹

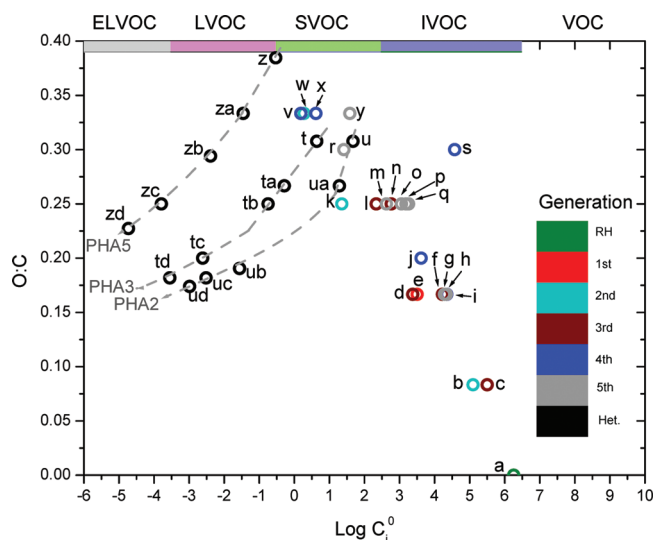


Figure 5. Span of O:C values versus log of the pure subcooled liquid vapor pressures in units of $\mu\text{g m}^{-3}$ (C_i^0) for predicted compounds from dodecane low- NO_x photooxidation. Colored markers indicate the product generation, and black markers indicate compounds thought to participate in heterogeneous chemistry. Letter data labels correspond with the compounds listed in Table S2. Regions of volatility previously defined⁵⁰ are denoted along the top axis for reference. The overall progression is upward to the left; vapor pressure drops from the starting dodecane, “a”, at $\log(C_i^0) = 6.3$ to $\log(C_i^0) = 0.19$ for $\text{C}_{12}\text{H}_{24}\text{O}_4$, “v”, and O:C increases to a max at 0.33. AMS measured O:C of 0.22–0.30 during the experiment. The gray dashed lines indicate the progression of increasing carbon length on the aldehyde that reacts with a hydroperoxy compound to form PHAs. PHA2 represents formation of the carbonyl hydroperoxide (CARBROOH) derived PHA, γ -keto- α -alkyl- α' -hydroxyalkyl peroxide (KAHAP); PHA3 the hydroxy hydroperoxide (OHROOH) derived PHA, δ -hydroxy- α -alkyl- α' -hydroxyalkyl peroxide (HAHAP); and PHA5 the hydroxycarbonyl hydroperoxide derived PHA, ϵ -hydroxy- γ -keto- α -alkyl- α' -hydroxyalkyl peroxide (HKAHAP). Increasing carbon length leads to convergence to a lower O:C and lower vapor pressure approaching the ELVOC region.

and the species shown in Figure 5 fall within the measured O:C range. The fifth-generation compounds in gray markers represent an increase in vapor pressure, owing to the formation of the hydroxy acids (Channel 2ai) and conversion of hydroperoxy groups to carbonyl groups. Only C_{10} acids are shown to condense the space and represent the bulk aerosol character. With estimated volatilities of expected gas-phase products and the measured O:C range, we investigate further the role of the semivolatiles on SOA growth.

Peroxyhemiacetal Formation. Many of the semivolatiles in Figure 5 are hydroperoxide species including (1) the second-generation hydroxy hydroperoxide (OHROOH, Channel 3; Figure 5 “k”), (2) the third-generation carbonyl hydroperoxide (CARBROOH, Channels 1 and 2; Figure 5 “n” and “l”), (3) the fourth-generation hydroxycarbonyl hydroperoxide (OHCARBROOH, Channel 2a; Figure 5, “v” and “x”), and (4) the fifth-generation dicarbonyl hydroperoxide (DICARBROOH, Channel 2b; Figure 5, “y”). Once these semivolatiles have partitioned into the particle phase, reaction with aldehydes generated from decomposition of the photolyzed α -carbonyl hydroperoxide (Channel 1a) can occur to form PHAs. A general mechanism summarizing some possible reactions for the current system is shown in Figure 6. If the first-generation hydroperoxide (ROOH) reacts with an aldehyde, an α -alkyl- α' -

hydroxyalkyl peroxide (hereafter referred to as AHAP) will be generated. If the β -carbonyl hydroperoxide (CARBROOH) reacts with an aldehyde, a γ -keto- α -alkyl- α' -hydroxyalkyl peroxide is formed (hereafter referred to as KAHAP). Similarly, if a hydroxy hydroperoxide (OHROOH) reacts with an aldehyde, a δ -hydroxy- α -alkyl- α' -hydroxyalkyl peroxide (hereafter referred to as HAHAP) will be formed. If a dicarbonyl hydroperoxide (DICARBROOH) reacts with an aldehyde, a ϵ -diketo- α -alkyl- α' -hydroxyalkyl peroxide is formed (hereafter referred to as DKAHAP). Finally, if a hydroxycarbonyl hydroperoxide (OHCARBROOH) reacts with an aldehyde, a ϵ -hydroxy- γ -keto- α -alkyl- α' -hydroxyalkyl peroxide is formed (hereafter referred to as HKAHAP). There is also the possibility of cyclization of the KAHAP, DKAHAP, or HKAHAP because of the carbonyl groups, similar to the mechanisms proposed in previous studies,^{52–54} although being isomers the cyclic and noncyclic forms would be hard to distinguish. Of course, alternative functional group placement on the compounds presented in Figure 6 is expected, and the compounds shown are examples.

PHA volatility will depend on the length of the aldehyde that originally reacted with the particle-phase incorporated hydroperoxide. Progression of the O:C and volatility of three select PHAs with increasing length of the aldehyde is marked by the series of “t” through “td” markers for HAHAP, “u” through “ud” for KAHAP, and “z” through “zd” for HKAHAP in Figure 5. The gray dotted lines are intended to guide the eye along these progressions toward lower O:C and lower vapor pressure, labeled “PHA2” for the KAHAP, “PHA3” for the HAHAP, and “PHAs” for the HKAHAP for visual clarity. PHA formation effectively converts semivolatiles into lower volatility products that approach the ELVOC region.

Evidence of PHA Formation Comparing Gas-Phase and Particle-Phase Mass Spectra. PHA formation is complex, as it involves reaction of a fourth-generation aldehyde (of varying carbon length) with second- to fifth-generation but lower vapor pressure hydroperoxy compounds at/in the particle. Figure 7 shows that aerosol growth follows after gas-phase formation of the carbonyl hydroperoxide (CARBROOH, Channels 1 and 2), but more importantly it is delayed until photolysis of the carbonyl hydroperoxide, p(jCARBROOH). The aldehydes could not be measured directly with CIMS because of their nonpolar nature, but the simulated p(jCARBROOH) can be used as a proxy for their expected formation according to Channel 1a in the mechanism. The aldehydes would precede acid formation, which is very quick after photolysis of the carbonyl hydroperoxide, when comparing the C_6 CARBACID trace with the p(jCARBROOH) trace in Figure 7. From the trends presented in Figure 7, it appears that aerosol growth is timed with aldehyde formation, making PHA formation a potential mechanism for aerosol growth. This is further supported in species-specific comparisons of the CIMS and AMS.

Comparisons of the gas-phase mechanism predictions and CIMS traces were made with selected ion fragments from the HR-ToF-AMS mass spectra. The AMS utilizes vaporization and electron impact (EI) ionization resulting in fragmentation of aerosol species, but the prevalence of high amu ($m/z > 100$) in the spectra suggests that some stable high MW ions retain more of the original backbone and functionality of the initial product molecule. The selected ions discussed are those that would result from a PHA severed at either C–O bond of the peroxide $\text{RC}_1\text{–OO–C}_2\text{R}$. Scission at $\text{C}_1\text{–O}$ results in the ion RC_1^+ .

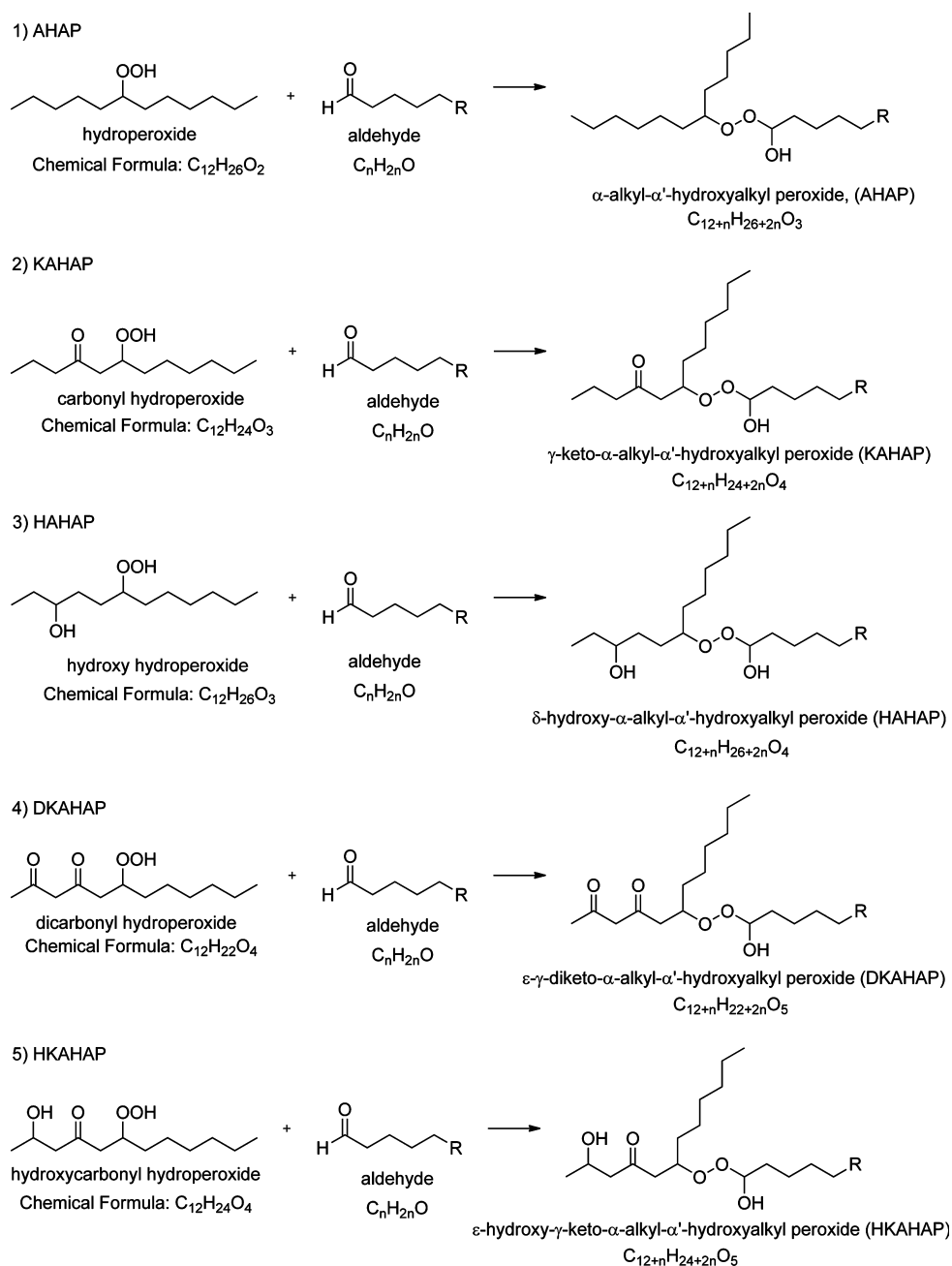


Figure 6. Scheme for forming five types of PHAs from reaction of an aldehyde of carbon length n , with various hydroperoxy compounds. (1) Reaction with a hydroperoxide generates an AHAP. (2) Reaction with a β -carbonyl hydroperoxide forms a KAHAP. (3) Reaction with a hydroxy hydroperoxide generates a HAHAP. (4) Reaction with a dicarbonyl hydroperoxide forms a DKAHAP. (5) Reaction with a hydroxycarbonyl hydroperoxide forms a HKAHAP.

Scission at C_2-O results in the ion RC_1OO^+ , 32 amu greater than the RC_1^+ ion. The RC_1^+ ion was observed in previous studies of α -substituted hydroperoxide-derived PHAs,^{52,55} although not the RC_1OO^+ , which we propose for the PHAs in this study. The hydroperoxides we discuss in this study are not α -substituted, which may be cause for the different fragmentation pattern. Note that the RC_1^+ ion would be the equivalent ion generated from a hydroperoxide compound, RC_1-OOH , by loss of the hydroperoxy group to generate the $m/z = [M-33]^+$ ion, where M = mass of the hydroperoxide, also previously observed.^{52,55} This fragmentation pathway was observed in identifying the C_{18} hydroperoxide during the standard experiment described previously in the Experimental

section. Examination of $[M-33]^+$ ions and their exact masses from this fragmentation pathway alone suggests incorporation of the gas-phase carbonyl hydroperoxide (CARBROOH), hydroxy hydroperoxide (OHROOH), and other multifunctional long chains (OHCARBROOH, DICARBROOH) into the aerosol phase. However, the predominance of their respective RC_1^+ ions trending closely with their respective RC_1OO^+ ions strongly supports that these compounds are incorporated into the aerosol phase via PHA formation. The following discussion focuses on the pairing of $m/z < 200$ ions and their $m/z > 200$ (+ 32 amu) counterparts. For simplicity, we refer to the nominal mass of an ion rather than its exact

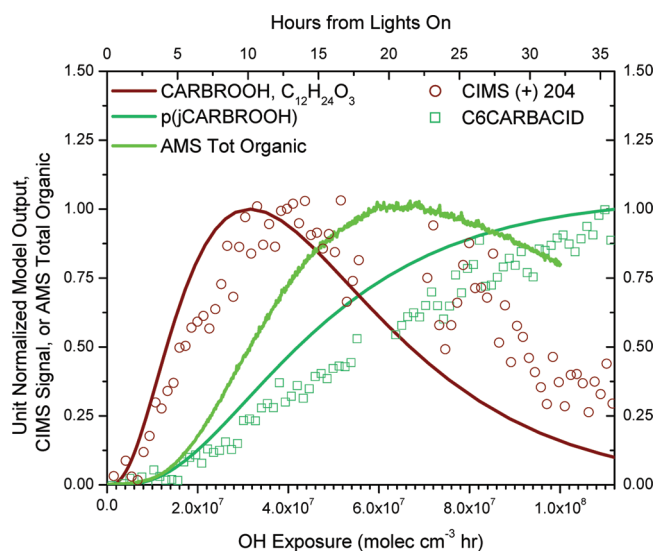


Figure 7. Aerosol growth occurs between formation of the carbonyl hydroperoxide (CARBROOH) and the onset of acid formation (observations in teal squares and simulated result, p(jCARBROOH), in teal) in the gas-phase. It is likely that initial aerosol growth can be supported by PHA formation since hydroperoxide containing species in the gas phase form within 5 h of lights on, and aldehyde formation will precede acid formation after photolysis of the carbonyl hydroperoxide.

mass, but the exact mass was used to obtain the chemical formula of the ion.

The AMS ions at $m/z = 183$ ($C_{12}H_{23}O^+$) and $m/z = 215$ ($C_{12}H_{23}O_3^+$) dominate the early SOA growth, suggesting that they may be characteristic fragments of the carbonyl hydroperoxide (CARBROOH)-derived PHA (KAHAP in Figure 6). Comparison of the simulated and measured gas-phase carbonyl hydroperoxide and AMS ions $m/z = 183$ and $m/z = 215$ is shown in Figure 8a along with the simulated gas-phase trend for photolysis of the carbonyl hydroperoxide, p(jCARBROOH) in Channel 1a. The growth of these ions in the aerosol phase is delayed from the onset of the carbonyl hydroperoxide formation in the gas phase until aldehyde formation begins, as proxied by the simulated p(jCARBROOH) trace in teal representing Channel 1a of the mechanism in Figure 1. As further reactions of the carbonyl hydroperoxide dominate, the gas-phase trace peaks and decays, followed as well by a decrease in these characteristic ions in the AMS mass spectrum. An analysis of the dynamics of the particle-phase AMS spectra will be addressed in a subsequent study.

AMS ions consistent with hydroxy hydroperoxide (OHROOH)-derived PHAs (HAHAP in Figure 6) at $m/z = 185$ ($C_{12}H_{25}O^+$) and $m/z = 217$ ($C_{12}H_{25}O_3^+$) grow in similarly with $m/z = 183$ and $m/z = 215$, although they peak later with their corresponding gas-phase trace (See Figure 8a and Figure 8b). Again, the appearance of these hydroxy hydroperoxide-derived PHA ions are contingent upon aldehyde formation as represented by the simulated p(jCARBROOH) trace in Figure 8b. If gas-to-particle partitioning was partially responsible for the simulated versus measured discrepancy for hydroxy hydroperoxide (OHROOH) Figure 2f, we would expect to see the $m/z = 185$ ion grow into the aerosol-phase before $m/z = 217$ and before aldehyde formation. That is, $m/z = 185$ growing in earlier to the aerosol-phase would indicate uptake of the hydroxy hydroperoxide (OHROOH) itself without

conversion to PHA. With little SOA at this time and no aldehyde formation, partitioning of the hydroxy hydroperoxide early on is unlikely to account for this model-measurement discrepancy. It is possible that the hydroxy hydroperoxide lingers in the gas phase before aldehyde formation and undergoes vapor-phase wall loss as discussed previously.

The incorporation of the dicarbonyl hydroperoxide (DICARBROOH, $C_{12}H_{22}O_4$) into the particle phase is tracked with the AMS ion fragment at $m/z = 197$ ($C_{12}H_{21}O_2^+$) paired with $m/z = 229$ ($C_{12}H_{21}O_4^+$) in Figure 8c but after aldehyde formation. Note that, on a unit normalized scale, the p(jCARBROOH) overlaps the p(CARBROOH + OH) trend. This implies that dicarbonyl hydroperoxide (DICARBROOH) formation is practically simultaneous with aldehyde formation, although not necessarily in the same amount. The other thrice-functionalized chain, a hydroxycarbonyl hydroperoxide (OHCARBROOH, $C_{12}H_{24}O_4$) is tracked with AMS ion fragments $m/z = 199$ ($C_{12}H_{23}O_2^+$) and $m/z = 231$ ($C_{12}H_{23}O_4^+$). The ion trace at $m/z = 199$ is within the variation of the noisy CIMS marker at $(-)$ $m/z = 317$ (Figure 8d).

Thus far, we observe that in the progression of increasing oxygenation (decreasing volatility) of the starting hydroperoxide there is less time between the gas-phase formation of a species and its incorporation into the particle phase. For example, there are a few hours between carbonyl hydroperoxide (CARBROOH) formation in the gas-phase measured by the CIMS at $(+)$ $m/z = 204$ and the growth of the derived PHA AMS ions at m/z 's 183 and 215 (Figure 8a). This is partially due to the delay in aldehyde formation. Still, once aldehyde is present, this time is significantly reduced for the delay between the hydroxy hydroperoxide (OHROOH) growth in the gas-phase measurement and its derived PHA ions (Figure 8b). While this also holds for the dicarbonyl hydroperoxide (DICARBROOH) in Figure 8c and the hydroxycarbonyl hydroperoxide (OHCARBROOH) in Figure 8d, there is a delay in the appearance of the AMS ions expected from their derived PHAs. That is, even though aldehyde is present and the thrice multifunctional compounds have been produced in the gas-phase, their incorporation as PHAs to the aerosol-phase is not timed with aldehyde formation as is the case for CARBROOH- and OHROOH-derived PHAs. This lag may be due to limiting reactant effects. That is, although the unit normalized simulations in Figure 8c suggest that DICARBROOH and aldehyde formation are practically simultaneous, it may be that the aldehyde produced is in lower quantity than the stoichiometric amount needed for reaction compared to the total semivolatile hydroperoxides available. Another possibility may be decreased reactivity of the dicarbonyl hydroperoxide (DICARBROOH) with another aldehyde since it already contains two carbonyl groups that may compete for or deactivate reaction with the hydroperoxy group, depending on their placement. Cyclization of carbonyl containing α -substituted hydroperoxides via intramolecular reaction of the carbonyl with the hydroperoxy group has been observed, setting up potential competition between cyclization and PHA formation.⁵² Further study would be required to test for deactivation effects. Steric effects due to intramolecular hydrogen bonding⁵⁶ may also play a role for compounds like the hydroxy carbonyl hydroperoxide (OHCARBROOH). A previous study on the kinetics of α -hydroxy peroxides (RCH(OH)OOR) in solution noted that tetralin hydroperoxide is more reactive to acetaldehyde over cumene

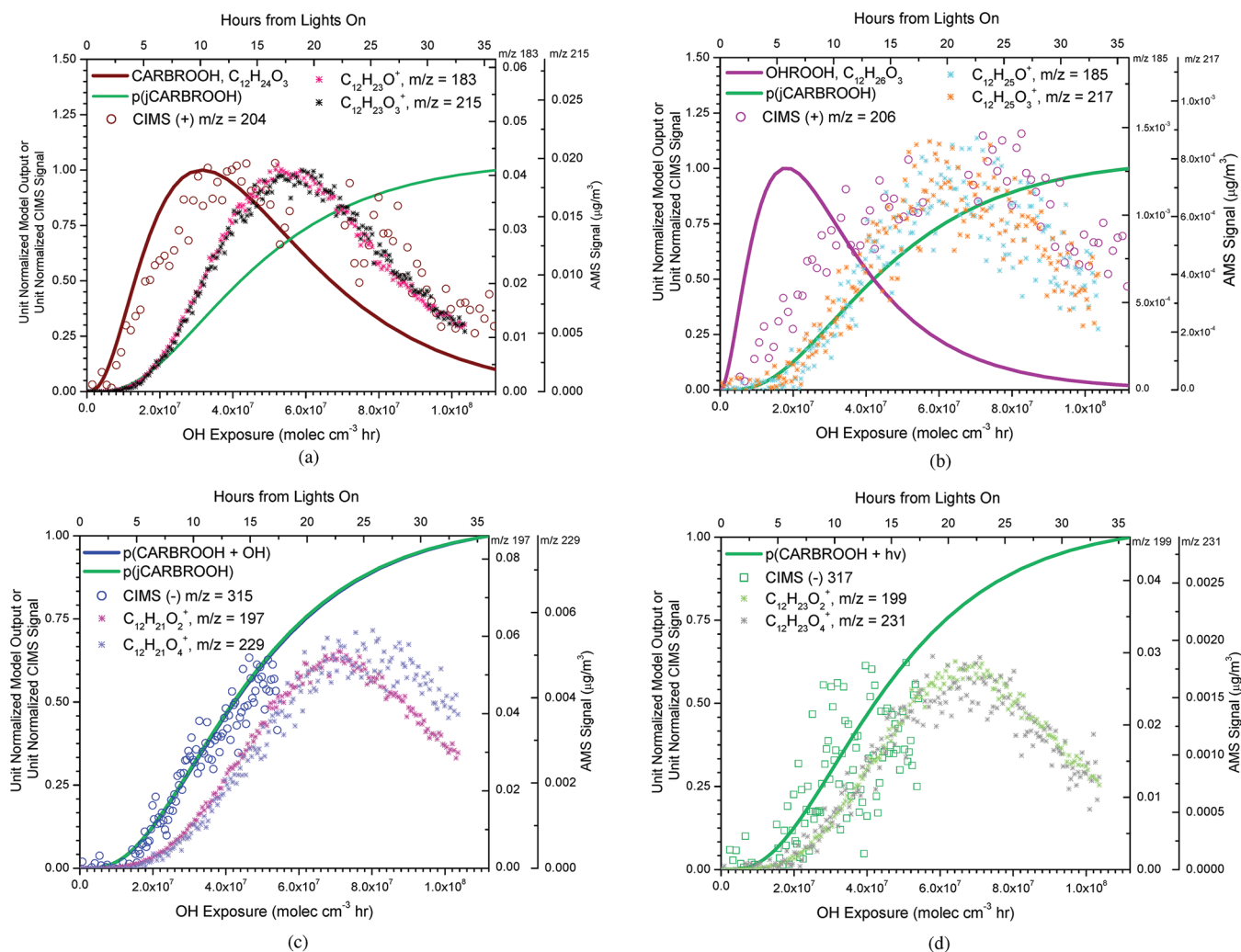


Figure 8. (a) AMS high-resolution fragments at $m/z = 183$ and $m/z = 215$ are possible characteristic fragments of the carbonyl hydroperoxide (CARBROOH)-derived PHA. (b) AMS high-resolution fragments at $m/z = 185$ and $m/z = 217$ are possible characteristic fragments of the hydroxy hydroperoxide (OHROOH)-derived PHA. (c) AMS high-resolution fragments at $m/z = 197$ and $m/z = 229$ are possible characteristic fragments of a multifunctional compound, dicarbonyl hydroperoxide (DICARBROOH)-derived PHA. (d) AMS high-resolution fragments at $m/z = 199$ and $m/z = 231$ are possible characteristic fragments of a multifunctional compound, hydroxycarbonyl hydroperoxide (OHCARBROOH) and its derived PHA.

hydroperoxide and other hydroperoxides because the peroxy group is surrounded by α -hydrogens.⁵⁶

We note that the $m/z = 183$ and $m/z = 185$ (Figure 8a,b) ion fragments may be derived from other molecules containing similar functionalities to the carbonyl hydroperoxide (CARBROOH) and hydroxy hydroperoxide (OHROOH). For example, the fourth-generation hydroxycarbonyl hydroperoxide multifunctional (OHCARBROOH, Channel 2a) shares two of its functional groups with the carbonyl hydroperoxide (CARBROOH) and two with the hydroxy hydroperoxide (OHROOH), suggesting that there may be contributions to these ion signals from later incorporation of this multifunctional compound into the particle. This is similar to the case of the dicarbonyl hydroperoxide (DICARBROOH, Channel 2b) sharing two functionalities with the carbonyl hydroperoxide (CARBROOH), so it may contribute to the signal at $m/z = 183$. However, because the $m/z = 183$ and $m/z = 185$ ions are distinct and dominant components of the initial organic growth, and since their trends do not deviate from their respective +32 amu ion partners ($m/z = 215$, $m/z = 217$) with later incorporation of the suggested ions for the multifunc-

tionals (m/z 's 197, 199, 229, and 231), they are still likely representative ion fragments from the carbonyl hydroperoxide-derived PHA (KAHAP) and the hydroxy hydroperoxide-derived PHA (HAHAP).

Particle-Phase Peroxyhemiacetal Formation. The surface matrix of an aerosol particle probably enhances PHA generation by lowering energetic barriers or chemically catalyzing the reaction at the surface,⁵⁵ similar to dihydrofuran (DHF) formation.³⁸ Still, a lower energy barrier was not sufficient to see evidence of AHAP formed from the second-generation hydroperoxide (ROOH) in the AMS spectra. Its higher vapor pressure, further reaction with OH or photolysis, as well as the delay to aldehyde formation are all likely reasons why the fate of the ROOH is purely gas-phase oxidation. The nature of the particle interface and bulk are difficult to establish when considering such heterogeneous processes in the current study, but some insights into the chemistry behind PHA formation come from the study by Antonovskii and Terent'ev.⁵⁶ First, they find that aldehydes are more likely than ketones to participate in α -hydroxy peroxide formation because they exhibit greater polarity and polarizability in their

C=O containing π bond. Hence, PHA formation from the second-generation carbonyl is not considered for this discussion. Second, they observed that the forward reaction to α -hydroxy peroxide dominated over backward dissociation when run in polar solvents (chloroform, diisopropyl ether, or hexanol). Considering earlier discussion on the characteristic of the aerosol chemistry, PHA formation may be hindered if the aerosol matrix is not sufficiently polar, as there is a large mass fraction of organic described by CH family ions. Lastly, Antonovskii and Terent'ev observed stable α -hydroxy peroxides at 20 and 40 °C, but they note that α -hydroxy peroxides are less thermally stable than the hydroperoxide. This could mean the peroxides do not survive well through the thermal vaporization (600 °C) and ionization process in the techniques here. This may possibly explain the small mass concentrations for the characteristic PHA ions relative to the total organic mass. Still, in this study we keep in mind that the aldehyde formation relies on photolysis of a well-positioned α -carbonyl hydroperoxide. So, concentration, timing, and chemistry of the aerosol all have to be in harmony to facilitate PHA formation.

Cyclic Hemiacetal Formation. The 1,4-hydroxycarbonyl (OHCARB) has been theorized³⁸ and found experimentally to heterogeneously react, isomerizing to a cyclic hemiacetal (CHA) in the particle^{9,11} or on chamber walls in an acid-catalyzed process.¹⁵ These heterogeneous reactions have been found to happen within a time frame of approximately 1 h.^{9,11,15} Conversion of the CHA to a DHF is sensitive to water vapor;⁵⁷ under low relative humidity environments, it will dehydrate to form a higher vapor pressure DHF compound that can partition back to the gas-phase and undergo further reaction with OH or O₃. A summary of these reactions is shown in Channel 3, Figure 1. Higher relative humidity conditions will slow the dehydration process, and OH reaction with the 1,4-hydroxycarbonyl (OHCARB) will more likely be its fate.⁵⁸ Under the current experimental conditions, DHF reaction with O₃ is expected to dominate after 2.5 h of irradiation when O₃ produced over time surpasses 5 ppb, the limit at which reaction with O₃ is competitive with reaction of the available OH radical ($\sim 2 \times 10^6$ molecules cm⁻³). This is based on reaction rate coefficients available in the literature on 4,5-dihydro-2-methylfuran, using $k_{\text{DHF-OH}} = 2.18 \times 10^{-10}$ molecules cm⁻³ s⁻¹ and $k_{\text{DHF-O}_3} = 3.49 \times 10^{-15}$ molecules cm⁻³ s⁻¹.⁵⁹ This provides an interesting problem to consider when thinking of the true lifecycle of the starting alkane and its ultimate generation of a higher vapor pressure unsaturated compound susceptible to oxidation and relevant for further SOA formation. Kinetic study of this heterogeneous conversion under OH radical initiated photooxidation of C₁₁–C₁₇ alkanes in the presence of NO_x suggests that the conversion to the CHA is fast in dry air, while the dehydration of the CHA to the DHF occurs on the order of ~ 15 min.¹²

CHA formation may be possible via the photolysis of the hydroperoxide (ROOH) in Channel 3 or through a fifth-generation multifunctional compound analogously cyclizing (Channel 2aii), though the resulting CHA has an extra carbonyl group as seen in Figure 1. Sufficient evidence does not exist to confirm CHA formation for this study despite low relative humidity experimental conditions. If the CHA is formed as C₁₂H₂₄O₂, an AMS fragment at $m/z = 183$ (C₁₂H₂₃O⁺) generated from loss of the –OH group⁹ is possible. However, this fragment is more appropriately assigned as a characteristic ion of the carbonyl hydroperoxide (CARBROOH)-derived

PHA instead as discussed earlier. In experiments carried out in the presence of NO_x, which are not reported here, the $m/z = 183$ ion is observed distinctly and does not pair with $m/z = 215$, making the current assignment consistent with the expected gas-phase mechanism under low-NO_x conditions. Since a distinct time trend indicating formation of the CHA in the particle-phase is not yet fully distinguished from the nominal mass at $m/z = 183$, the kinetics under the current experimental conditions cannot be modeled. On another note, the nature of the particle acidity is different than that of previous studies, as it is thought that adsorbed HNO₃ on the particle surface catalyzed the heterogeneous conversion to the DHF.^{11,12} Under these low-NO_x conditions, HNO₃ formation is not considered. While the particle character shows enhancement of acidity as tracked by the AMS ion CO₂⁺ at $m/z = 44$, there is still a large mass fraction described by the CH family ions, consistent with the many reduced fragments that could be derived from these long chain products. Considering that the simulated production of the 1,4-hydroxycarbonyl is only around 0.6 ppb in the gas-phase (without sinks) and the unclear nature of the particle acidity, if the cyclization and dehydration to the DHF does occur, the amount that formed was probably small, indiscernible in the AMS signal.

Heterogeneous Chemistry versus Gas-Phase Oxidation. We have currently considered two routes to formation of SOA through heterogeneous reactions. We see evidence of PHA formation derived from many semivolatile hydroperoxide species formed in all reaction channels, but we cannot confirm formation of the CHA from the 1,4-hydroxycarbonyl (OHCARB) at this time. Furthermore, the contributions to the SOA mass from pure gas-particle partitioning and heterogeneous chemistry of the hydroperoxide compounds to the SOA mass are unclear. To explore this, we roughly estimate the mass contributions of organic from five select semivolatiles that have been highlighted in a previous discussion: (1) carbonyl hydroperoxide (CARBROOH), (2) hydroxy hydroperoxide (OHROOH), (3) hydroxycarbonyl hydroperoxide (OHCARBROOH), (4) dicarbonyl hydroperoxide (DICARBROOH) and (5) 1,4-hydroxycarbonyl (OHCARB). Using the roughly estimated gas-phase concentrations of these species as monitored by the CIMS, the subcooled pure component liquid vapor pressure estimates (C_i^0), and the organic mass concentration from the AMS (as shown in Figure 2a), we assume that gas-particle equilibrium is established quickly so that the instantaneous contribution of each compound in the particle-phase is calculated by eq 1:

$$C_{pi} = \frac{C_{\text{org}} C_{gi}}{\gamma_i C_i^0} \quad (1)$$

where C_{pi} is the mass concentration of species i in the particle phase [$\mu\text{g m}^{-3}$], C_{org} is the mass concentration of organic aerosol in [$\mu\text{g m}^{-3}$], C_{gi} is the mass concentration of species i in the gas phase [$\mu\text{g m}^{-3}$], γ_i is the activity coefficient of species i in the bulk aerosol solution (assumed as 1 here), and C_i^0 = the subcooled pure component liquid vapor pressure of species i [$\mu\text{g m}^{-3}$].

The result of this analysis is presented in Figure 9. Note that we estimate the organic mass only up to 18 h because we utilized species monitored at $m/z \geq 300$, available only from the January experiment. We see that just under $10 \mu\text{g m}^{-3}$ of organic is expected each from the dicarbonyl hydroperoxide (DICARBROOH), carbonyl hydroperoxide (CARBROOH),

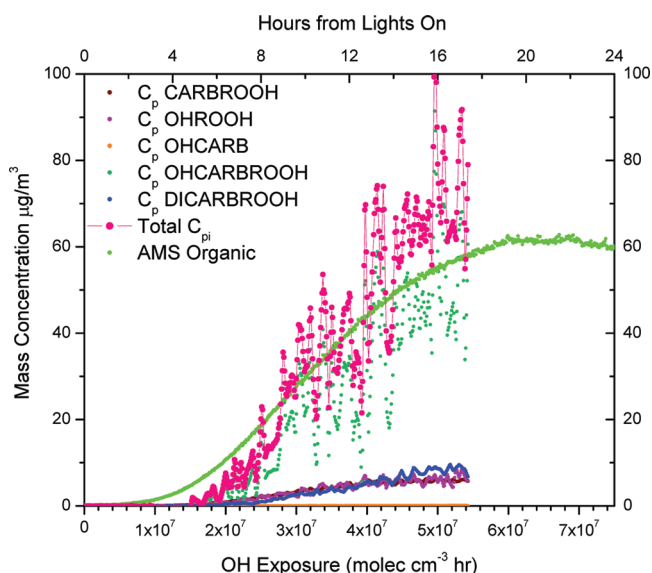


Figure 9. Rough estimate of total organic mass attributed to gas-to-particle phase partitioning from select semivolatiles (pink circles with line) as compared to the AMS organic trace (bright green). Individual contributions from each species are shown: (1) carbonyl hydroperoxide (CARBROOH, wine-colored circles), (2) hydroxy hydroperoxide (OHROOH, purple circles), (3) 1,4-hydroxycarbonyl (OHCARB, orange circles), (4) hydroxycarbonyl hydroperoxide (OHCARBROOH, teal circles), and (5) dicarbonyl hydroperoxide (DICARBROOH, blue circles).

and the hydroxy hydroperoxide (OHROOH). The 1,4-hydroxycarbonyl (OHCARB) makes negligible mass, and this is consistent with the small amount expected to form from the gas-phase chemistry and the absence of an AMS ion for the CHA. The hydroxycarbonyl hydroperoxide (OHCARBROOH) is expected to make up the majority of the organic mass ($\sim 60 \mu\text{g m}^{-3}$). The total contributions of these species to organic mass is $C_{\text{ptot}} = \sum_i C_{\text{pi}}$. Thus, partitioning from just four semivolatile hydroperoxides could explain the majority of the organic growth observed after 5 h of irradiation. However, a small amount of organic was formed previously and is not fully described by equilibrium partitioning of these semivolatiles.

The uncertainty in the estimated gas-phase concentrations could resolve the appearance of organic growth prior to significant contributions from partitioning, but based on the well-paired $m/z < 200$ and $m/z > 200$ ions that differ by 32 amu, it is overwhelmingly likely that the fragments come from the same compound (their respective PHA). These ions also begin to appear prior to 5 h with aldehyde formation in the case of the carbonyl hydroperoxide (CARBROOH) and the hydroxy hydroperoxide (OHROOH) (see Figure 8a,b). So the early gap between the measurement and estimated organic mass may be due to PHA formation initiating aerosol growth. In light of the AMS measurements of characteristic PHA ions and the estimated mass from partitioning of the same hydroperoxide semivolatiles, it is difficult to tell whether these semivolatiles would be completely in the particle-phase as PHAs or in molecular form. In addition, later more functionalized compounds may partition in without conversion to PHA formation right away, as in the lag between gas-phase aldehyde formation and PHA ion appearance observed for the hydroxycarbonyl hydroperoxide (OHCARBROOH) and for that of the dicarbonyl hydroperoxide (DICARBROOH). However, since aldehyde formation is fairly coincident with

most of the higher generation multifunctionals (OHCARBROOH, DICARBROOH) in the gas-phase, PHA formation as a mechanism for their incorporation into the particle phase cannot be ruled out. Full treatment of the kinetics of the heterogeneous chemistry require mass closure on the contribution of PHA mass to the organic present. While the AMS ions presented support PHA formation, their mass concentration signals do not account for the total mass of the derived PHA in the particle phase. Recall that the ions discussed do not include the side of the molecule that contains varying carbon lengths from the aldehyde that reacted with the hydroperoxide species. This provides a multitude of possible PHA structures. Second, being such a large molecule, PHA mass would certainly be distributed in the AMS spectrum among many possible fragmentation pathways. To truly understand these aspects, synthesis of these compounds would be required as an AMS standard to understand the full spectrum distribution.

■ ATMOSPHERIC IMPLICATIONS

Presented here is the first experimental study of SOA formation from the long-chain alkanes under low- NO_x conditions, such that $\text{RO}_2 + \text{HO}_2$ chemistry dominates the fate of the RO_2 radical. This regime of chemistry is typical of a region relatively isolated from NO_x sources and where trace VOC concentrations are too low to sustain RO_2 self-reaction. It is a challenge to simulate this chemistry in most laboratory chambers under atmospherically pristine conditions at which NO_x levels are typically tens to low hundreds of pptv. The gas-phase measurements of this study are consistent with chemistry expected for NO_x levels toward this range. Further, a regime of “slow” chemistry that lengthens the RO_2 lifetime sufficiently to allow for alkyl peroxy radical rearrangement through a 1,6-H shift is relevant to pristine conditions (ppt levels of NO_x , HO_2 , and low $[\text{OH}] \sim 1.2 \times 10^5 \text{ molecules cm}^{-3}$).⁴⁶ Achieving such conditions further challenges the design of environmental chamber studies. Although many challenges remain in simulating and spanning the range of “atmospherically relevant” conditions using environmental chambers, fundamental studies such as that described here address the fundamental chemistry in a regime relevant for closing the gap in the VOC and SOA budgets.

A myriad of compounds is formed in long-chain alkane photooxidation via functionalization and fragmentation pathways in the gas phase. For dodecane, 19 gas-phase species were monitored by the CIMS, and many compared well to a simulation with an abbreviated chemical mechanism based on the MCM 3.2. The gas-phase mechanism generally captures the observations only using four generations of explicit chemistry. Further work on empirical quantification and branching ratios of the gas-phase routes in the mechanism is needed, but was hindered for this study due to the lack of available standards and difficulties associated with experimental handling. Nonetheless, this study fundamentally captures the chemical framework representative of low initial organic loading of a longer-lived species (in terms of reaction with OH) while in the relative absence of NO_x that can be extended to alkanes of different lengths and structures. Current work is ongoing to understand the chemistry of SOA formation from other C_{12} alkanes of branched and cyclic conformations.

Mechanisms of particle formation emerge from comparison of the gas-phase mechanism and known heterogeneous chemistry. While there is evidence supporting the formation

of PHAs, confirmation of the heterogeneous conversion of the 1,4-hydroxycarbonyl to the CHA is lacking, but the amount that formed was probably small. A powerful approach to confirming direct partitioning of specific gas-phase compounds is through comparison of CIMS gas-phase time trends and corresponding characteristic ion fragments from the AMS. The paired (32 amu difference) high $m/z > 100$ AMS fragments identified were instrumental in deriving more molecular structure information in support of PHA formation. Comparisons of time trends provide insight into the chemistry of the partitioning, as seen, for example, with the decreasing delay between appearance of characteristic AMS ions and gas-phase product growth with increasing oxidation of the parent molecule. A rough estimate shows that much of the organic growth can be described by theoretical partitioning estimates of select semivolatile hydroperoxides. Still, better mass closure on the semivolatiles in the system in the gas and particle-phases could provide greater insight into the kinetic and equilibrium effects on SOA formation from dodecane.

The degree of generational development in the gas-phase photooxidation of this long-chain alkane over the extended chamber experiments is quite remarkable. While the majority of the gas-phase product distribution (almost two-thirds of the carbon) is developed within the first 20 h of photooxidation, SOA formation clearly involves the further oxidation of the third-generation carbonyl hydroperoxide, which peaks about 8 h earlier. This chemical development occurs much later than typical experimental time scales for chamber experiments, which highlights the need for simulating extended oxidation to truly capture the SOA formation process.

While the chemical composition of the gas and aerosol phases was well resolved with the techniques used in this study, challenges still exist in understanding the nature of the particle phase, as this can have profound effects on the further chemical aging of the particles.⁶⁰ This aging could be manifested in the formation of alkane-derived PHAs. In regards to time scale, the current work focuses on oxidative processes in the gas phase affecting the chemical development of the particle phase, although the possibility of photolysis or reactions with OH of the aerosol products may become more important under extended photooxidation time scales. A better understanding of these and other factors that potentially affect SOA chemical evolution might address issues such as the observed “glassy” nature of some SOA.^{61,62} Extrapolating the present study to the atmosphere suggests that (1) hydroperoxide and PHA species are likely to be in the particle phase for alkane-derived aerosol under low-NO_x conditions, and (2) with the possibility of viscous phases that affect further chemical aging in the aerosol phase, the lifetimes of these products could be extended, lending themselves to long-range transport and a more complicated assessment of the SOA life cycle.

■ ASSOCIATED CONTENT

● Supporting Information

The Supporting Information includes (1) A table with calculated lifetimes of RO₂ with RO₂, HO₂, NO, and NO₂ under varying NO_x conditions, (2) table of O:C and volatility, (3) figures on AMS and CIMS measurements across all experiments, (4) alternative positive mode ions for CIMS negative mode ions, and (5) simulations of varying NO concentration. This information is available free of charge via the Internet at <http://pubs.acs.org>.

■ AUTHOR INFORMATION

Corresponding Author

*E-mail: seinfeld@caltech.edu.

Notes

The authors declare no competing financial interest.

■ ACKNOWLEDGMENTS

This work was supported by the Office of Science (Biological and Environmental Research), U.S. Department of Energy Grant (DE-SC 0006626), and National Science Foundation Grants AGS-1057183 and ATM-0650061. We acknowledge John D. Crouse and Jason M. St. Clair for helpful discussions on CIMS data analysis, Reddy L. N. Yatavelli and ManNin Chan for useful discussions, and Andreas Zuend, Xuan Zhang, and Steve Compernelle for assistance with the vapor-pressure estimations. L.D.Y., J.S.C., and C.L.L. were supported by National Science Foundation Graduate Research Fellowships.

■ REFERENCES

- (1) Ravishankara, A. R. *Chem. Rev.* **2003**, *103*, 4505–4508.
- (2) Jimenez, J. L.; Canagaratna, M. R.; Donahue, N. M.; Prevot, A. S. H.; Zhang, Q.; Kroll, J. H.; DeCarlo, P. F.; Allan, J. D.; Coe, H.; Ng, N. L.; et al. *Science* **2009**, *326*, 1525–1529.
- (3) Kroll, J. H.; Donahue, N. M.; Jimenez, J. L.; Kessler, S. H.; Canagaratna, M. R.; Wilson, K. R.; Altieri, K. E.; Mazzoleni, L. R.; Wozniak, A. S.; Bluhm, H.; et al. *Nat. Chem.* **2011**, *3*, 133–139.
- (4) Robinson, A. L.; Donahue, N. M.; Shrivastava, M. K.; Weitkamp, E. A.; Sage, A. M.; Grieshop, A. P.; Lane, T. E.; Pierce, J. R.; Pandis, S. N. *Science* **2007**, *315*, 1259–1262.
- (5) Schauer, J. J.; Kleeman, M. J.; Cass, G. R.; Simoneit, B. R. T. *Environ. Sci. Technol.* **1999**, *33*, 1578–1587.
- (6) Schauer, J. J.; Kleeman, M. J.; Cass, G. R.; Simoneit, B. R. T. *Environ. Sci. Technol.* **2002**, *36*, 1169–1180.
- (7) Presto, A. A.; Miracolo, M. A.; Kroll, J. H.; Worsnop, D. R.; Robinson, A. L.; Donahue, N. M. *Environ. Sci. Technol.* **2009**, *43*, 4744–4749.
- (8) Presto, A. A.; Miracolo, M. A.; Donahue, N. M.; Robinson, A. L. *Environ. Sci. Technol.* **2010**, *44*, 2029–2034.
- (9) Lim, Y. B.; Ziemann, P. J. *Environ. Sci. Technol.* **2005**, *39*, 9229–9236.
- (10) Lim, Y. B.; Ziemann, P. J. *Environ. Sci. Technol.* **2009**, *43*, 2328–2334.
- (11) Lim, Y. B.; Ziemann, P. J. *Aerosol Sci. Technol.* **2009**, *43*, 604–619.
- (12) Lim, Y. B.; Ziemann, P. J. *Phys. Chem. Chem. Phys.* **2009**, *11*, 8029–8039.
- (13) Talukdar, R. K.; Mellouki, A.; Gierczak, T.; Barone, S. *Int. J. Chem. Kinet.* **1994**, *26*, 973–990.
- (14) Atkinson, R. *J. Phys. Chem. Ref. Data* **1997**, *26*, 215–290.
- (15) Atkinson, R.; Arey, J.; Aschmann, S. M. *Atmos. Environ.* **2008**, *42*, 5859–5871.
- (16) Tyndall, G. S.; Cox, R. A.; Granier, C.; Lesclaux, R.; Moortgat, G. K.; Pilling, M. J.; Ravishankara, A. R.; Wallington, T. J. *J. Geophys. Res.* **2001**, *106*, 12157–12182.
- (17) Kroll, J. H.; Seinfeld, J. H. *Atmos. Environ.* **2008**, *42*, 3593.
- (18) Lelieveld, J.; Butler, T. M.; Crowley, J. N.; Dillon, T. J.; Fischer, H.; Ganzeveld, L.; Harder, H.; Lawrence, M. G.; Martinez, M.; Taraborrelli, D.; et al. *Nature* **2008**, *452*, 737–740.
- (19) Ren, X.; Olson, J. R.; Crawford, J. H.; Brune, W. H.; Mao, J.; Long, R. B.; Chen, Z.; Chen, G.; Avery, M. A.; Sachse, G. W.; et al. *J. Geophys. Res.* **2008**, *113*, D05310.
- (20) Wolfe, G. M.; Thornton, J. A.; Bouvier-Brown, N. C.; Goldstein, A. H.; Park, J.-H.; McKay, M.; Matross, D. M.; Mao, J.; Brune, W. H.; LaFranchi, B. W.; et al. *Atmos. Chem. Phys.* **2011**, *11*, 1269–1294.
- (21) Cocker, D. R.; Flagan, R. C.; Seinfeld, J. H. *Environ. Sci. Technol.* **2001**, *35*, 2594–2601.

- (22) Keywood, M. D.; Varutbangkul, V.; Bahreini, R.; Flagan, R. C.; Seinfeld, J. H. *Environ. Sci. Technol.* **2004**, *38*, 4157–4164.
- (23) St Clair, J. M.; McCabe, D. C.; Crounse, J. D.; Steiner, U.; Wennberg, P. O. *Rev. Sci. Instrum.* **2010**, *81*, 6.
- (24) Paulot, F.; Crounse, J. D.; Kjaergaard, H. G.; Kroll, J. H.; Seinfeld, J. H.; Wennberg, P. O. *Atmos. Chem. Phys.* **2009**, *9*, 1479–1501.
- (25) Crounse, J. D.; McKinney, K. A.; Kwan, A. J.; Wennberg, P. O. *Anal. Chem.* **2006**, *78*, 6726–6732.
- (26) Huey, L. G.; Villalta, P. W.; Dunlea, E. J.; Hanson, D. R.; Howard, C. J. *J. Phys. Chem.* **1996**, *100*, 190–194.
- (27) Crutzen, P.; Williams, J.; Pöschl, U.; Hoor, P.; Fischer, H.; Warneke, C.; Holzinger, R.; Hansel, A.; Lindinger, W.; Scheeren, B.; Lelieveld, J. *Atmos. Environ.* **2000**, *34*, 1161–1165.
- (28) Jayne, J. T.; Leard, D. C.; Zhang, X.; Davidovits, P.; Smith, K. A.; Kolb, C. E.; Worsnop, D. R. *Aerosol Sci. Technol.* **2000**, *33*, 49–70.
- (29) DeCarlo, P. F.; Kimmel, J. R.; Trimborn, A.; Northway, M. J.; Jayne, J. T.; Aiken, A. C.; Gonin, M.; Fuhrer, K.; Horvath, T.; Docherty, K. S.; et al. *Anal. Chem.* **2006**, *78*, 8281–8289.
- (30) Canagaratna, M.; et al. *Mass Spectrom. Rev.* **2007**, *26*, 185–222.
- (31) Loza, C. L.; Chhabra, P. S.; Yee, L. D.; Craven, J. S.; Flagan, R. C.; Seinfeld, J. H. *Atmos. Chem. Phys. Disc.* **2011**, *11*, 24969–25010.
- (32) Jenkin, M. E.; Saunders, S. M.; Pilling, M. J. *Atmos. Environ.* **1997**, *31*, 81–104.
- (33) Saunders, S. M.; Jenkin, M. E.; Derwent, R. G.; Pilling, M. J. *Atmos. Chem. Phys.* **2003**, *3*, 161–180.
- (34) Kwok, E. S.; Atkinson, R. *Atmos. Environ.* **1995**, *29*, 1685–1695.
- (35) Carter, W. P.; Cocker, D. R. I.; Fitz, D. R.; Malkina, I. L.; Bumiller, K.; Sauer, C. G.; Pisano, J. T.; Bufalino, C.; Song, C. *Atmos. Environ.* **2005**, *39*, 7768–7788.
- (36) Wang, J.; Doussin, J. F.; Perrier, S.; Perraudin, E.; Katrib, Y.; Pangui, E.; Picquet-Varrault, B. *Atmos. Meas. Tech.* **2011**, *4*, 2465–2494.
- (37) Sander, S. P.; Abbatt, J.; Barker, J. R.; Burkholder, J. B.; Friedl, R. R.; Golden, D. M.; Huie, R. E.; Kolb, C. E.; Kurylo, M.; Moortgat, G. K.; et al., Chemical kinetics and photochemical data for use in atmospheric studies, Evaluation No. 17. JPL Publication 10-6, 2011; <http://jpldataeval.jpl.nasa.gov>.
- (38) Dibble, T. S. *Chem. Phys. Lett.* **2007**, *447*, 5–9.
- (39) Vaghjiani, G.; Ravishankara, A. *J. Geophys. Res.* **1989**, *94* (D3), 3487–3492.
- (40) Vaghjiani, G. L.; Ravishankara, A. R. *J. Chem. Phys.* **1990**, *92*, 996–1003.
- (41) Baasandorj, M.; Papanastasiou, D. K.; Talukdar, R. K.; Hasson, A. S.; Burkholder, J. B. *Phys. Chem. Chem. Phys.* **2010**, *12*, 12101–12111.
- (42) Atkinson, R. *J. Phys. Chem. Ref. Data, Monogr.* **1994**, *2*, 1–216.
- (43) Atkinson, R.; Arey, J. *Chem. Rev.* **2003**, *103*, 4605–4638.
- (44) Matsunaga, A.; Ziemann, P. *J. Aerosol Sci. Technol.* **2010**, *44*, 881–892.
- (45) Loza, C. L.; Chan, A. W. H.; Galloway, M. M.; Keutsch, F. N.; Flagan, R. C.; Seinfeld, J. H. *Environ. Sci. Technol.* **2010**, *44*, 5074–5078.
- (46) Crounse, J. D.; Paulot, F.; Kjaergaard, H. G.; Wennberg, P. O. *Phys. Chem. Chem. Phys.* **2011**, *13*, 13607–13613.
- (47) Hasson, A. S.; Tyndall, G. S.; Orlando, J. J. *J. Phys. Chem. A* **2004**, *108*, 5979–5989.
- (48) Spencer, K. M.; Beaver, M. R.; Clair, J. M. S.; Crounse, J. D.; Paulot, F.; Wennberg, P. O. *Atmos. Chem. Phys. Disc.* **2011**, *11*, 23619–23653.
- (49) Compernelle, S.; Ceulemans, K.; Müller, J.-F. *Atmos. Chem. Phys.* **2011**, *11*, 9431–9450.
- (50) Donahue, N. M.; Kroll, J. H.; Pandis, S. N.; Robinson, A. L. *Atmos. Chem. Phys. Disc.* **2011**, *11*, 24883–24931.
- (51) Aiken, A. C.; DeCarlo, P. F.; Jimenez, J. L. *Anal. Chem.* **2007**, *79*, 8350–8358.
- (52) Ziemann, P. *J. Phys. Chem. A* **2003**, *107*, 2048–2060.
- (53) Matsunaga, A.; Docherty, K. S.; Lim, Y. B.; Ziemann, P. *J. Atmos. Environ.* **2009**, *43*, 1349–1357.
- (54) Kern, W.; Spitteller, G. *Tetrahedron* **1996**, *52*, 4347–4362.
- (55) Tobias, H. J.; Ziemann, P. *J. Environ. Sci. Technol.* **2000**, *34*, 2105–2115.
- (56) Antonovskii, V. L.; Terent'ev, V. A. *J. Org. Chem. U.S.S.R. (Engl. Transl.)* **1967**, *3*, 972.
- (57) Holt, T.; Atkinson, R.; Arey, J. *J. Photochem. Photobiol., A* **2005**, *176*, 231–237.
- (58) Aschmann, S. M.; Arey, J.; Atkinson, R. *J. Atmos. Chem.* **2003**, *45*, 289–299.
- (59) Martin, P.; Tuazon, E. C.; Aschmann, S. M.; Arey, J.; Atkinson, R. *J. Phys. Chem. A* **2002**, *106*, 11492.
- (60) Ziemann, P. *J. Faraday Discuss.* **2005**, *130*, 469–490.
- (61) Virtanen, A.; Joutsensaari, J.; Koop, T.; Kannosto, J.; Yli-Pirila, P.; Leskinen, J.; Makela, J. M.; Holopainen, J. K.; Poschl, U.; Kulmala, M.; et al. *Nature* **2010**, *467*, 824–827.
- (62) Vaden, T. D.; Imre, D.; Beránek, J.; Shrivastava, M.; Zelenyuk, A. *Proc. Natl. Acad. Sci. U. S. A.* **2011**, *108*, 2190–2195.

Appendix F

Secondary Organic Aerosol Formation from Biomass Burning Intermediates: Phenol and Methoxyphenols⁸

⁸ Reproduced by permission from “Secondary organic aerosol formation from biomass burning intermediates: phenol and methoxyphenols” by L. D. Yee, K. E. Kautzman, C. L. Loza, K. A. Schilling, M. M. Coggon, P. S. Chhabra, M. N. Chan, A. W. H. Chan, S. P. Hersey, J. D. Crouse, P. O. Wennberg, R. C. Flagan, J. H. Seinfeld. *Atmos. Chem. Phys.* **2013**, *13*, 8019-8043.



Secondary organic aerosol formation from biomass burning intermediates: phenol and methoxyphenols

L. D. Yee^{1,*}, K. E. Kautzman^{2,**}, C. L. Loza², K. A. Schilling², M. M. Coggon², P. S. Chhabra^{2,***}, M. N. Chan^{1,****}, A. W. H. Chan^{2,*****}, S. P. Hersey¹, J. D. Crouse³, P. O. Wennberg^{1,3}, R. C. Flagan^{2,1}, and J. H. Seinfeld^{2,1}

¹Division of Engineering and Applied Science, California Institute of Technology, Pasadena, CA, USA

²Division of Chemistry and Chemical Engineering, California Institute of Technology, Pasadena, CA, USA

³Division of Geological and Planetary Sciences, California Institute of Technology, Pasadena, CA, USA

* now at: Department of Environmental Science, Policy and Management, University of California, Berkeley, USA

** now at: Department of Chemistry, Towson University, Towson, MD, USA

*** now at: Aerodyne Research Inc., Billerica MA, USA

**** now at: Chemical Sciences Division, Lawrence Berkeley National Laboratory, Berkeley, CA, USA

***** now at: Department of Chemical Engineering and Applied Chemistry, University of Toronto, Toronto, Canada

Correspondence to: J. H. Seinfeld (seinfeld@caltech.edu)

Received: 20 January 2013 – Published in Atmos. Chem. Phys. Discuss.: 6 February 2013

Revised: 13 June 2013 – Accepted: 20 June 2013 – Published: 21 August 2013

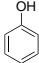
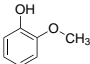
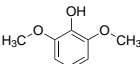
Abstract. The formation of secondary organic aerosol from oxidation of phenol, guaiacol (2-methoxyphenol), and syringol (2,6-dimethoxyphenol), major components of biomass burning, is described. Photooxidation experiments were conducted in the Caltech laboratory chambers under low-NO_x (< 10 ppb) conditions using H₂O₂ as the OH source. Secondary organic aerosol (SOA) yields (ratio of mass of SOA formed to mass of primary organic reacted) greater than 25 % are observed. Aerosol growth is rapid and linear with the primary organic conversion, consistent with the formation of essentially non-volatile products. Gas- and aerosol-phase oxidation products from the guaiacol system provide insight into the chemical mechanisms responsible for SOA formation. Syringol SOA yields are lower than those of phenol and guaiacol, likely due to novel methoxy group chemistry that leads to early fragmentation in the gas-phase photooxidation. Atomic oxygen to carbon (O:C) ratios calculated from high-resolution-time-of-flight Aerodyne Aerosol Mass Spectrometer (HR-ToF-AMS) measurements of the SOA in all three systems are ~ 0.9, which represent among the highest such ratios achieved in laboratory chamber experiments and are similar to that of aged atmospheric organic aerosol. The global contribution of SOA from intermediate volatility and semivolatile organic compounds has been shown to be substantial (Pye and Seinfeld, 2010). An approach to rep-

resenting SOA formation from biomass burning emissions in atmospheric models could involve one or more surrogate species for which aerosol formation under well-controlled conditions has been quantified. The present work provides data for such an approach.

1 Introduction

Biomass burning is a major source of atmospheric organic aerosol (OA), with contributions from both anthropogenic (biofuel, deforestation, etc.) as well as natural sources such as wildfires. Aerosol produced from biomass burning has been estimated to account for 90 % of all primary organic carbon emitted globally from combustion sources (Ito and Penner, 2005). Bond et al. (2004) estimated global annual emissions of carbonaceous aerosol due to combustion as 8.0 Tg for black carbon (BC) and 33.9 Tg organic carbon (OC). Biofuel and open burning were estimated by these authors to account, respectively, for 20 % and 42 % of BC, and 19 % and 74 %, of OC. The amount and composition of organic aerosol formed from these sources vary widely based on combustion conditions and fuel type. Measured wood smoke emissions from fireplaces, for example, depend strongly on the type of fuel consumed and can vary in magnitude by a factor of five for

Table 1. Chemical properties.

Compound	Structure	Boiling Pt. ^a (°C)	V.P. ^a @ 25 °C (mm Hg)	$k_{\text{OH}} \times 10^{11}$ (molec cm ⁻³ s ⁻¹)
Phenol		182	0.351	2.7 ± 0.25 at 25 °C (Calvert et al., 2002)
Guaiacol		205	0.13	7.53 ± 0.41 at 21 ± 2 °C (Coeur-Tourneur et al., 2010)
Syringol		261	0.00602 ^b	9.66 ± 1.11 at 21 ± 2 °C (Lauraguais et al., 2012)

^a Experimental database values within EPA (2012)^b Calculated within EPA (2012)

different fuel sources and sampling techniques (Fine et al., 2001). Particulate matter from biomass burning, including wildfires, residential wood burning, and deforestation is also of major concern for visibility, climate change and health effects (Naeher et al., 2007).

Recent studies have been devoted to measuring and chemically characterizing the gas and particle-phase emissions from biomass burning in-situ (Iinuma et al., 2010; Akagi et al., 2012) and in the laboratory (Veres et al., 2010; Iinuma et al., 2010). Understanding the fate of such emissions in the atmosphere as a plume rises and advects away from the source is a challenge to discern. One approach towards addressing this problem is to simulate the photooxidation of known biomass burning tracers in the laboratory under highly-controlled chemical conditions.

Phenols are produced from the pyrolysis of lignin, the second most abundant polymer on Earth comprising the secondary cell wall of plants. Hawthorne et al. (1989) showed that phenols and methoxyphenols account for a significant fraction of particulate matter derived from wood smoke, constituting 21 % and 45 % by mass of total aerosol, respectively. Emission rates for methoxyphenol species from biomass burning have been estimated to range from 420–900 mg kg⁻¹ fuel (Hawthorne et al., 1989; Hawthorne et al., 1992; Schauer et al., 2001). In addition to the significant emission factors of these compounds, guaiacol, which is emitted from both hard and soft wood combustion, and syringol, which is emitted primarily from soft woods, have been proposed as aerosol markers for wood combustion as well as biomarkers to determine human exposure levels (Dills et al., 2001; Simpson and Naeher, 2010).

Such phenolic compounds are used in ozonolysis and photooxidation studies to simulate the chemical fate and aerosol forming potential of such biomass burning intermediates in the atmosphere. Often these include candidate compounds such as phenol and catechol (Atkinson et al., 1992; Olariu, 2001; Olariu et al., 2002; Berndt and Boge, 2003; Tomas et al., 2003; Coeur-Tourneur et al., 2009; Iinuma et al., 2010; Nakao et al., 2011; Ofner et al., 2011). Many of these com-

pounds can also serve as model systems for understanding aerosol formation from humic substances, the role of water, and associated heterogeneous processes (Ammann et al., 2005; Nieto-Gligorovski et al., 2008; Ofner et al., 2010, 2011; Sun et al., 2010).

Still, little is known about the detailed gas-phase photooxidation mechanism of methoxyphenol compounds. Here we investigate the aerosol-forming potential of phenol and two of the most abundant methoxyphenol species, guaiacol and syringol (Table 1). Both guaiacol and phenol are intermediate volatility organic compounds; syringol has a vapor pressure 100 times less than those of phenol and guaiacol. The molecular structures are shown in Table 1 along with vapor pressures and reaction rate constants with OH.

We determine the fractional yield of secondary organic aerosol (SOA) from photooxidation of phenol, guaiacol, and syringol by OH in laboratory chamber studies under low-NO_x ([NO_x]₁₀ < 10 ppb) conditions. While NO_x is certainly present in biomass burning events at higher levels than this, we focus on the results of the low-NO_x experiments in the main text and leave discussion on the effect of NO_x in the Appendix. The atmospheric chamber experiments performed on these systems were performed under idealized chemical conditions such that specific regimes of chemistry could be isolated. That is, low-NO_x experiments resulted in the predominant fate of RO₂ radical to be reaction with HO₂, and in the high-NO_x experiments, reaction with NO_x. In the atmosphere there exists a spectrum of chemical regimes that depend on proximity to the heart of the biomass burning source. Owing to the high-NO_x experiments resulting in levels of total NO_x approaching 1 ppm (beyond typical atmospheric levels), we find the results to be chemically instructive, though not practical for use as an accurate representation of the SOA formation from these systems under atmospherically relevant NO_x conditions. For example, Iinuma et al. (2010) measured co-located NO_x to be on the order of 20 ppb.

Studies on the photooxidation mechanisms of aromatics and phenol in general find that the product distributions for aromatics chemistry are qualitatively similar in the absence

Table 2. Experimental conditions and aerosol yields.

Date (2010)	Organic	[Org] ₀ (ppb)	[Org] _f (ppb)	RH ₀ (%)	[NO ₂] ₀ (ppb)	[NO] ₀ (ppb)	Vol ₀ ^e μm ³ cm ⁻³	Vol _f ^e μm ³ cm ⁻³	Yield
1/29	guaiacol	66.3	13.4	5.6	< LDL ^d	< LDL ^d	18.2	120.0	0.49 ± 0.01
2/2	guaiacol	5.9	< LDL ^a	5.8	< LDL ^d	< LDL ^d	16.4	25.0	0.46 ± 0.03
2/4	guaiacol	12.4	< LDL ^a	5.5	< LDL ^d	< LDL ^d	13.6	31.0	0.44 ± 0.03
2/6	guaiacol	45.5	4.1	6.7	< LDL ^d	5	12.9	85.0	0.50 ± 0.02
2/11	phenol	47.6	9.9	5.7	< LDL ^d	6	16.0	58.0	0.44 ± 0.08
2/15	phenol	10.0	2.1	6.2	< LDL ^d	5	11.4	20.0	0.40 ± 0.06
2/17	phenol	73.9	14.4	< LDL ^c	< LDL ^d	< LDL ^d	12.0	32.9	0.25 ± 0.01
2/20	phenol	101.9	18.8	< LDL ^c	< LDL ^d	5	10.0	69.0	0.24 ± 0.03
3/10	syringol	185.1	< LDL ^b	< LDL ^c	7	< LDL ^d	11.0	325.0	0.37 ± 0.01
3/15	syringol	49.5	< LDL ^b	< LDL ^c	< LDL ^d	< LDL ^d	14.2	67.0	0.25 ± 0.01
3/29	syringol	112.9	< LDL ^b	< LDL ^c	9	< LDL ^d	11.7	174.0	0.34 ± 0.01

^a below CIMS lower detection limit (LDL) of 0.1 ppb for guaiacol

^b CIMS LDL = 0.5 ppb for syringol

^c RH probe LDL = 5 % RH

^d NO_x Analyzer LDL = 5 ppb

^e Vol₀ is initial seed volume; Vol_f is final volume (seed + organic aerosol), as measured by DMA

and presence of NO_x (Atkinson et al., 1992; Olariu et al., 2002; Sato et al., 2007), with noted presence of nitroaromatics generated in the presence of NO_x. Still, these products tend to have gas-phase yields less than 0.1 (Olariu et al., 2002; Berndt and Boge, 2006). Thus, the low-NO_x data presented here focus analyses on relevant gas- and particle-phase constituents in guaiacol photooxidation to elucidate the chemical mechanism involved in guaiacol SOA formation. This chemistry may best represent the chemical regime in which biomass burning emissions are transported to areas where NO_x levels have become diluted and photochemistry ensues. We also qualitatively compare the chemistry of the tested compounds to explore why syringol results in lower SOA yield compared to phenol and guaiacol. Further motivation for this work is the potential use of phenol, guaiacol, and syringol as compounds to represent biomass burning emissions in atmospheric models of organic aerosol formation. SOA products identified in the laboratory studies may also serve as markers for biomass burning in ambient aerosols.

2 Experimental section

2.1 Chamber experiments

All experiments were carried out in the Caltech dual 28 m³ Teflon chambers. Details of the facilities have been described previously (Cocker et al., 2001; Keywood et al., 2004). Before each experiment, the chambers were flushed with dried purified air RH < 5 %, NO_x < 2 ppb for > 24 h, until the particle number concentration was < 100 cm⁻³ and the volume concentration was < 0.1 μm³ cm⁻³. In all yield experiments, ammonium sulfate seed aerosol was used to promote conden-

sation of low volatility oxidation products. The seed aerosol was generated by atomization of a 0.015 M aqueous ammonium sulfate solution. Following atomization, the size distribution of the seed particles peaked at ~ 56 nm with an average number concentration of ~ 2700 cm⁻³, and a total seed volume concentration of 10–15 μm³ cm⁻³ was achieved. The hydrocarbon was introduced into the chamber by injecting a known volume of pure hydrocarbon into a glass bulb and flowing purified air over the hydrocarbon at 5 L min⁻¹ until the hydrocarbon had fully vaporized. Gentle heat was applied to the glass bulb to support evaporation of syringol (solid) into the chamber.

For these low-NO_x experiments, hydrogen peroxide (H₂O₂) was used as the OH precursor. We refer to the reaction conditions of these experiments as “low-NO_x” because there is no intentional injection of NO_x ([NO_x]₀ < 5 ppb, the lower detection limit of the NO_x analyzer). There are three hundred 40 W black lights, Sylvania 350BL, with an emission spectrum that peaks at 340–350 nm wavelength. Based on the irradiance spectrum of the lights and the absorption cross section of H₂O₂ (Sander, 2011), this results in a photolysis rate constant, $j_{\text{H}_2\text{O}_2} = 2.9 \times 10^6 \text{ s}^{-1}$. Prior to atomization of the ammonium sulfate seed, H₂O₂ was introduced by flowing 5 L min⁻¹ of purified air through a glass trap containing 280 μL of a 50 % aqueous H₂O₂ solution. The glass trap was submerged in a warm water bath maintained at 35–38 °C. This resulted in an approximate concentration of 4 ppm H₂O₂ in the chamber.

The aerosol number concentration and size distribution were measured by a differential mobility analyzer (DMA, TSI model 3081) coupled with a condensation nuclei counter (TSI, CNC-3760). After allowing all concentrations to

stabilize, irradiation was initiated. The temperature (T), relative humidity (RH), and concentrations of O_3 , NO , and NO_x were continuously monitored. Experiments were run at temperatures ranging 20–26 °C and varied within ± 2 °C. RH remained below 10 %. The lower detection limits (LDL) of the utilized analyzers are 5 % RH, 2 ppb O_3 , and 5 ppb NO_x . Table 2 summarizes the experimental conditions for the series of methoxyphenol oxidation experiments conducted.

2.2 Gas-phase measurements

2.2.1 Gas Chromatography/Flame-Ionization Detection (GC/FID)

The hydrocarbon concentration was continuously monitored by GC/FID in the phenol experiments. Chamber air was sampled into a 10 mL injection loop and injected onto a HP5 15 m \times 0.53 mm ID \times 1 μ m thickness column installed on a 6890 Agilent GC. The GC response was calibrated by dissolving a known mass of the hydrocarbon in methanol and then vaporizing a known volume of that solution into a 55 L Teflon chamber. Guaiacol and syringol measurements obtained using the GC/FID were unreliable due to condensation loss in the sample loop; thus, the hydrocarbon concentration during these experiments was monitored using Chemical Ionization Mass Spectrometry (CIMS) in negative mode operation. The LDL for phenol on the GC-FID was determined to be ~ 1 ppb from calibrations.

2.2.2 Chemical Ionization Mass Spectrometry (CIMS)

Monitoring of gas-phase oxidation products was carried out in real time by the use of a CIMS instrument. The details of this instrument are described elsewhere (St. Clair et al., 2010). The instrument operates in both negative mode, using CF_3O^- as a reagent ion, and in positive proton transfer reaction (PTR)-MS mode. Negative mode is found to be more selective towards the detection of hydroperoxides and polar molecules, particularly acids, while positive mode detects a broader range of organic compounds. Analytes in negative mode can be monitored as the cluster product $[R \cdot CF_3O]^-$ and/or as the transfer product if it is more strongly acidic $[R \cdot F]^-$, where R is the analyte. Analytes in positive mode cluster as $[R \cdot (H_2O)_n]^+$. Mass scans covering masses 50–300 amu for negative mode, and 50–200 amu for positive mode, with a total scan time of ~ 6 min were continuously repeated over the course of each experiment.

Guaiacol was monitored at the fluoride transfer product $([M + 19]^-)$, m/z 143, and the cluster product $([M + 85]^-)$, m/z 209, in negative mode operation. Syringol was also monitored at the fluoride transfer product, m/z 173, and the cluster product, m/z 239. Calibrations of guaiacol and syringol on the CIMS were performed similar to those of phenol on the GC-FID by preparing 55 L Teflon chamber standards of varying concentrations of the methoxyphenol compounds. The

LDL for guaiacol on the CIMS was established to be 100 ppt and that for syringol to be 500 ppt. While phenol was detected at both the transfer (m/z 113) and the cluster product (m/z 179), a calibration curve was not made because a photooxidation product in the phenol system interfered significantly at m/z 113.

2.3 Particle-phase measurements

2.3.1 Chamber filter sample collection, extraction, and off-line chemical characterization

A detailed description of the aerosol filter sample collection and extraction protocol for the Caltech laboratory chambers has been previously published (Surratt et al., 2008). Aerosol samples were collected on Teflon filters (PALL Life Sciences, 47 mm diameter, 1.0 μ m pore size, teflomembrane). Filter samplers employed for aerosol filter sample collection used a front and back-up filter sampling approach, in which back-up filters were collected in order to examine if aerosol breakthrough from the front filter occurred or whether evaporation of semivolatiles from the front filter occurred during sampling. In all experiments, no SOA constituents were detected on the back-up filters. Filter sampling was initiated when the aerosol volume reached its maximum (constant) value, as determined by the DMA. Lights were turned off after the filter sampling period was complete. Depending on the total volume concentration of aerosol in the chamber, the duration of filter sampling was 1.8–2.1 h, which resulted in 2.0–2.9 m³ of total chamber air sampled. Teflon filter extraction protocols in high-purity methanol (LC-MS CHROMASOLV-Grade, Sigma-Aldrich) have been described previously (Surratt et al., 2008). The resultant filter extracts were then analyzed by a Waters ACQUITY ultra performance liquid chromatography (UPLC) system, coupled with a Waters LCT Premier TOF mass spectrometer equipped with an ESI source, allowing for accurate mass measurements by UPLC/ESI-TOFMS to be obtained for each ion (Surratt et al., 2008).

Selected filter extracts from experiments were also analyzed by a Thermo Finnigan Surveyor high performance liquid chromatography (HPLC) system (pump and autosampler) coupled to a Thermo Finnigan LCQ ion trap mass spectrometer (ITMS) equipped with an ESI source, allowing for tandem MS measurements to be obtained. Data were acquired and processed using Xcalibur version 1.3 software. A Waters Atlantis T3 column (3 μ m particle size; 2.1 \times 150 mm) was employed, which is similar to the Water ACQUITY UPLC HSS column used for the UPLC/ESI-TOFMS analysis. The mobile phases consisted of 0.1 % acetic acid in water (A) and 0.1 % acetic acid in methanol (B). The applied 45 min gradient elution program was as follows: the concentration of eluent B was kept at 3 % for 4 min, then increased to 100 % in 21 min, holding at 100 % for 10 min, then decreased to 3 % in 5 min, and kept at 3 %

for 5 min. The injection volume and flow rate were 10 μL and 0.2 mL min^{-1} , respectively. The ion trap mass analyzer was operated under the following conditions: sheath gas flow (N_2), 65 arbitrary units; auxiliary gas flow (N_2), 3 arbitrary units; source voltage, -4.5 kV ; capillary voltage, -14.5 V ; tube lens offset, 7 V; capillary temperature, 200 $^\circ\text{C}$; and maximum ion injection time, 200 ms. Two scan events were used during each chromatographic run; scan event 1 was the full scan mode in which data were collected from m/z 120 to 600 in the negative ionization mode and scan event 2 was the MS2 mode in which product ions were generated from significant base peak ions observed in scan event 1. For MS2 experiments, an isolation width of 2.5 m/z units and a normalized collision energy level of 35 % were applied. The $[\text{M-H}]^-$ ion signal optimization was carried out by introducing a 1 mg mL^{-1} malic acid standard solution. Due to the on-axis ESI source that is characteristic of the LCQ ITMS instrument, a solvent delay time of 3.5 min (which diverted the column effluent from the ESI source to waste) was employed to prevent clogging by nonvolatile salts at the entrance of the capillary.

2.3.2 High-Resolution Time-of-Flight Aerosol Mass Spectrometry (HR-ToF-AMS)

Real-time aerosol mass spectra were obtained using an Aerodyne HR-ToF-AMS (DeCarlo et al., 2006). The HR-ToF-AMS was operated in a lower resolution, higher sensitivity “V-mode”, and a high-resolution “W” mode, switching between modes once every minute. The “V-mode” data were analyzed to extract sulfate, ammonium, and organic spectra according to procedures in Allan et al. (2004). Calculation of the SOA densities were achieved by comparing the particle mass distributions obtained using the particle ToF mode and the volume distributions obtained by the DMA (Bahreini et al., 2005) in nucleation (seed-free) experiments. O : C, N : C, and H : C ratios were determined from “W” mode data using the APES toolbox and applying the procedures outlined in Aiken et al. (2007) and Aiken et al. (2008). The particle-phase signal of CO^+ and the organic contribution to H_xO^+ ions were estimated as described in Aiken et al. (2008).

Particle-into-Liquid Sampler/Ion Chromatography (PILS/IC) was also employed as described in Kautzman et al. (2010) for the guaiacol experiments, though we find that $< \text{C}_6$ diacids do not constitute an important fraction of the SOA formed.

3 SOA yields

The formation of secondary organic aerosol (SOA) results from the gas-particle partitioning of low-vapor-pressure products formed in the oxidation of volatile organic compounds (VOCs). The SOA yield is defined as the ratio of

mass of organic aerosol formed, ΔM_o , to the mass of the parent organic species consumed, ΔOrg , $Y = \Delta M_o / \Delta \text{Org}$. The SOA yields for all experiments are summarized in Table 2. To calculate the mass concentration of the SOA, the SOA volumes established by DMA measurements are wall-loss corrected following procedures in Keywood et al. (2004); Ng et al. (2007) and then multiplied by the SOA density, as determined by the AMS in seed-free (nucleation) experiments. A density of 1.65 $\mu\text{g cm}^{-3}$ was determined for phenol. Guaiacol and syringol densities were determined to be 1.45 and 1.49 $\mu\text{g cm}^{-3}$, respectively. The O : C was calculated at time of maximum SOA growth for these systems and were reported in Chhabra et al. (2011). O : C values of 0.88 ± 0.27 , 0.89 ± 0.28 , and 0.97 ± 0.30 were calculated for the phenol, guaiacol, and syringol systems, respectively.

Aerosol yields as a function of organic mass for the studied systems are shown in Fig. 1. Phenol traces are denoted by square markers and are of a green shade. Guaiacol traces are denoted by circles and are of a blue shade. Triangle markers indicate the syringol experiments and are colored in various shades of purple. The error bars represent the propagated uncertainty from all parameters varying with time for each experiment. Generally, there is larger error associated with yield measurements at smaller M_o . Within a system, the yield curves generally converge within uncertainty for $M_o > 20 \mu\text{g cm}^{-3}$ and there is greater deviation for experiments with the least amount of hydrocarbon reacted within a set of loadings tested for. This may indicate the existence of chemical differences as well as equilibrium and kinetic regimes of aerosol growth that are affected by initial hydrocarbon loading.

About 80 % of the initial phenol was reacted in these experiments. Final SOA yields for phenol range 24–44 % under the experimental conditions (Fig. 1a). For phenol, the hydrocarbon measurement obtained from all gas-phase instruments displayed interferences under low- NO_x conditions, leading to a wider spread and greater uncertainty in the yield curve parameters. Still, the measured yields under low- NO_x conditions overlap with the range of 38–45 % reported by Nakao et al. (2011). Greater than 90 % of the initial guaiacol was consumed over the course of all experiments except for the higher guaiacol loading 1/29 experiment as noted in Table 2. SOA yields from guaiacol photooxidation, based on the final aerosol volume achieved, range 44–50 % (Fig. 1b). Within six hours of irradiation, the syringol levels are lower than the limit of detection and SOA yields of 25–37 % result (Fig. 1c). This range overlaps yields of 10–36 % reported for syringol photooxidation under high- NO_x (approaching 10 ppm NO) conducted by Lauraguais et al. (2012) using CH_3ONO as the OH source.

Figure 1d compares phenol, guaiacol, and syringol experiments in which approximately 300 $\mu\text{g cm}^{-3}$ of hydrocarbon precursor reacted. Phenol and guaiacol follow a similar trend and syringol aerosol is the only system that plateaus with increasing organic aerosol mass, resulting in aerosol

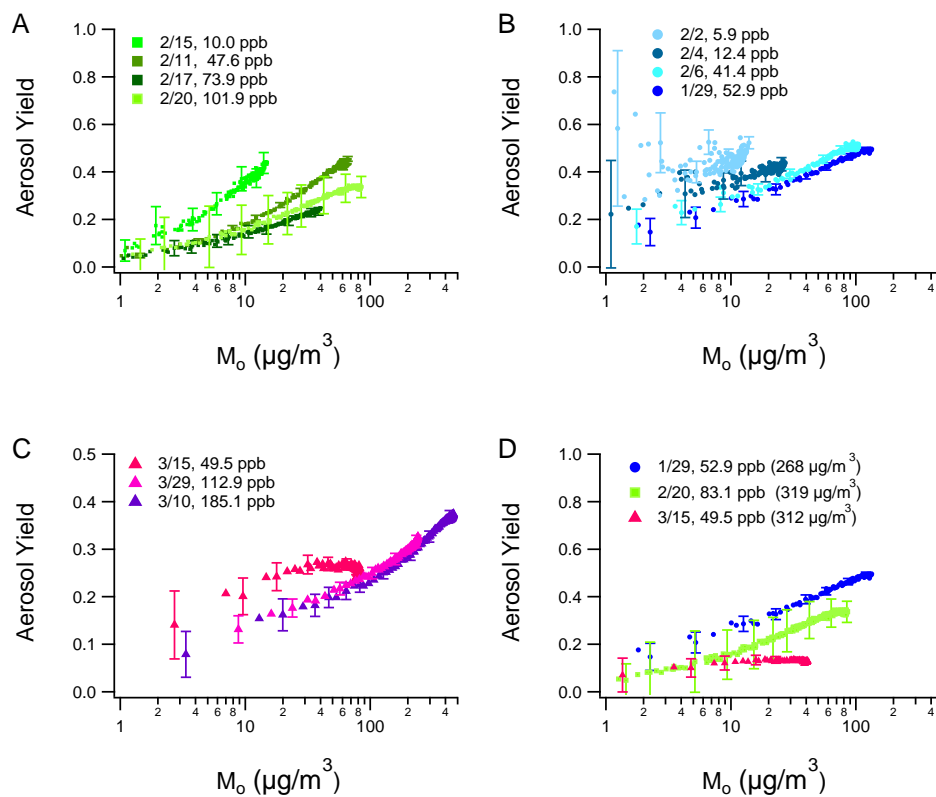


Fig. 1. Aerosol yields as a function of organic aerosol mass for (A) phenol (squares), (B) guaiacol (circles), and (C) syringol (triangles). (D) Comparison across systems for similar amounts of reacted hydrocarbon by mass concentration.

yields that are lower than those of phenol and guaiacol at $M_o > 20 \mu\text{g cm}^{-3}$.

One might expect that the relatively higher boiling point and lower vapor pressure of syringol might suggest enhanced ability of it or its photooxidation products to partition to the particle-phase, as vapor pressure is a key component in calculating the partitioning coefficient (Pankow, 1994). Syringol vapor-phase wall loss in the reactors is also believed to be minimal. Lauraguais et al. (2012) found no vapor-phase wall loss of syringol and Coeur-Tourneur et al. (2010) found negligible losses for guaiacol and related methoxy and alkyl substituted benzenes. Assuming a first-order wall loss rate, $k_w \sim 1 \times 10^{-5} \text{ s}^{-1}$, a typical rate for previously tested compounds in our chamber (Loza et al., 2010), this would lead to roughly a quarter loss of syringol to the walls over the course of the experiment. Correcting for this by lowering ΔOrg would lead to syringol SOA yields that are similar to those of guaiacol, but not significantly higher. We further explore the chemical basis for the differences in the yields after examining the gas-phase chemistry.

Most methoxyphenol experiments ended shortly after the hydrocarbon decay was complete. Though, even 4 h after 112.9 ppb syringol was completely reacted in the 3/29 experiment, there was no additional SOA growth. The type of growth observed here is typified by a mechanism involving

oxidation to form SOA either from first-generation products or sufficiently rapid low-volatility product formation over the course of the experiment from further generation reactions (Chan et al., 2007; Ng et al., 2006). We believe it to be the latter explanation in the case of methoxyphenol systems. The high-level of oxidation determined from the measured O : C ratios of the SOA are indicative of multi-generation products, which is consistent with the identified gas and aerosol products discussed below.

4 SOA formation chemistry

We present in this section an analysis of the gas-phase mechanistic chemistry involved in SOA formation based on the CIMS traces for each system along with SOA mass growth over time. All ions unless otherwise noted were monitored during negative mode operation. CIMS signals are plotted in arbitrary units (a.u.). Discussion is focused on the guaiacol system since the off-line aerosol filter analyses complement the gas-phase data. Chemical parallels are drawn between the three systems.

4.1 Gas-phase oxidation

Substituent groups such as $-\text{OH}$ and $-\text{OCH}_3$ activate more strongly the aromatic ring towards electrophilic addition of OH compared to the $-\text{CH}_3$ group. Of these groups, activation potential of the ring increases in order of $-\text{CH}_3 < -\text{OCH}_3 < -\text{OH}$. Thus, as predicted, methoxyphenol compounds react faster with OH than their methyl or unsubstituted equivalents (Coeur-Tourneur et al., 2010). Methoxy and hydroxy substituent groups tend to make OH -attack favorable at positions *ortho* and *para* to the substituents, so structures for the measured ions are proposed from chemical mechanisms assuming one of these positions of initial OH -attack. H-atom abstraction from the methoxy group is expected to be small, as this path was determined to contribute $< 4\%$ in the case of methoxybenzene (Coeur-Tourneur et al., 2010).

A generation is defined as the OH -initiated reaction of a stable (non-radical) species, and the OH exposure is calculated as the product of the OH concentration (inferred from the parent hydrocarbon decay) and the hours of irradiation. Each m/z is the sum of the signal from all isomeric structures detected by the CIMS at that ion, but are not shown explicitly in the abbreviated mechanisms and tables presented. However, from the chemical ionization method employed, we expect certain common chemical features of the proposed structures. For example, many of the transfer $[\text{M}+19]^-$ products are likely acidic (Huey et al., 1996), containing carboxylic acid groups and/or sufficient acidic hydroxyl groups (Tables 3, 4, 6).

4.2 Phenol chemistry

Initial steps of the phenol gas-phase mechanism have been elucidated elsewhere (Olariu et al., 2002; Berndt and Boge, 2003). Phenol + OH proceeds primarily with *ortho*- OH addition to the ring, O_2 addition, followed by elimination of HO_2 to form 1,2-dihydroxybenzene (catechol). In the low- NO_x phenol experiments, CIMS ions are tracked that show successive OH adduct product formation up to three generations. Quinone products are also likely, though these are not detected in negative mode operation of the current CIMS technique unless they are additionally functionalized. A list of ions monitored in this system is presented in Table 3. Representative data for the phenol low- NO_x system are shown in Fig. 2. Phenol, $\text{C}_6\text{H}_6\text{O}$, is monitored at m/z 179, a cluster product. We do not include m/z 113, the fluoride transfer product, because this signal includes interference from another compound (likely a small acid) that grows in over time. Dihydroxybenzene, $\text{C}_6\text{H}_6\text{O}_2$, is observed primarily as the fluoride transfer product m/z 129 (DHB) with less signal observed at the m/z 195 cluster product. A trace at m/z 211 indicates a third OH addition to the ring to form trihydroxybenzene (THB), $\text{C}_6\text{H}_6\text{O}_3$. These time profiles are shown along with SOA growth and phenol decay for the first nine hours

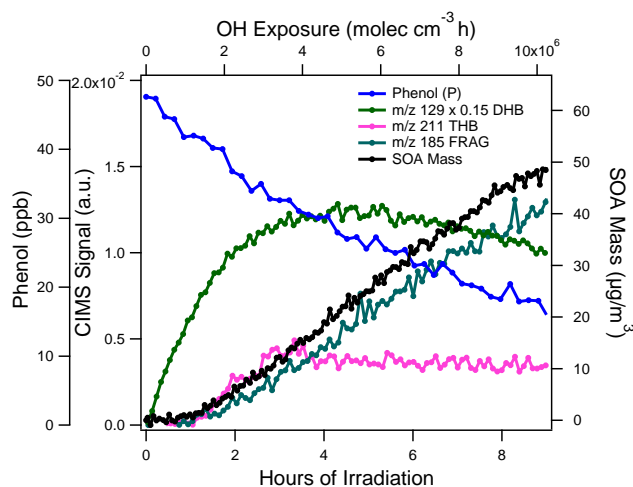
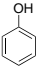
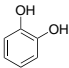
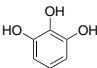
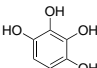
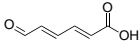
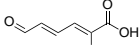
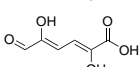
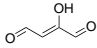
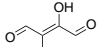


Fig. 2. Phenol low- NO_x gas-phase and particle-phase development. The signal at m/z 129 was scaled by a factor of 0.15.

of irradiation (Fig. 2). SOA growth occurs coincident with the growth of m/z 211 (THB), indicating that the transition to lower volatility products to form SOA likely occurs along the 3rd addition of OH just after $\sim 1 \times 10^6$ molec cm^{-3} h of OH exposure. This is the approximate equivalent of one hour of photooxidation in the atmosphere assuming an ambient OH concentration of $\sim 1 \times 10^6$ molec cm^{-3} . A signal at m/z 227 was observed to have a similar profile as m/z 211, and may be attributed to tetra hydroxybenzene (4HB, Table 3) and an epoxide isomer ($\text{C}_6\text{H}_6\text{O}_4$). A plateau in the profile is consistent with 4HB also contributing to the particle phase. Individual contributions from 4HB and the epoxide could not be determined from the signal at m/z 227, which was approximately one-fourth of the signal at m/z 211 (not shown for clarity). A minor amount of signal at m/z 229 is attributed to the hydroperoxide $\text{C}_6\text{H}_8\text{O}_4$.

Figure 2 also shows that the SOA is in equilibrium with m/z 185, which we propose to be the ring fragment $\text{C}_4\text{H}_4\text{O}_3$, hydroxy butenedial, that forms from the decomposition of the bicyclic radical from phenol + OH . Another dicarbonyl, $\text{C}_4\text{H}_4\text{O}_4$, is monitored at m/z 135, which could be the analogous ring fragment from dihydroxybenzene + OH . These products approach the high O:C ratios characteristic of the SOA in this system. Comparisons of the CIMS gas-phase traces and the off-line filter analyses from similar experiments performed by Nakao et al. (2011) provide additional insights. Nakao et al. (2011) utilized electrospray ionization and atmospheric pressure chemical ionization mass spectrometry (ESI/APCI-TOFMS) as well as PILS-ESI-TOFMS for analysis, though Nakao et al. (2011) noted that the PILS-ESI-TOFMS spectra may include water soluble gas-phase species because a denuder was not used. While Nakao et al. (2011) observed an exact mass match that corresponds with the bicyclic hydroperoxide from phenol ($\text{C}_6\text{H}_8\text{O}_6$) and another compound with a suggested formula $\text{C}_6\text{H}_8\text{O}_7$ using

Table 3. Proposed structures for CIMS ions in the phenol low-NO_x system. C and T indicate the cluster and transfer product, respectively.

Observed m/z	Product	Chemical Formula	Proposed Structure (one isomer shown)	Chemical Pathway
179	C	C ₆ H ₆ O		phenol
129	T ^a	C ₆ H ₆ O ₂		DHB = phenol + OH
211	C	C ₆ H ₆ O ₃		THB = DHB + OH
227	C ^b	C ₆ H ₆ O ₄		4HB = THB + OH
145	T	C ₆ H ₆ O ₃		ring opening acid
161	T	C ₆ H ₆ O ₄		ring opening acid
177	T	C ₆ H ₆ O ₅		ring opening acid
185	C ^c	C ₄ H ₄ O ₃		ring fragment
135	T ^d	C ₄ H ₄ O ₄		ring fragment

^a m/z 195 is also present as C₆H₆O₂, but is lower signal than at m/z 129

^b Signal at m/z 227 likely has an epoxide contribution as well

^c The transfer product at C₄H₄O₃ is at m/z 119, which is not monitored in low-NO_x conditions because it is the cluster product of H₂O₂

^d m/z 201 is also present as C₄H₄O₄, but is lower signal than at m/z 135

both techniques, we do not observe these products in the gas-phase with the CIMS. It is possible that these compounds are of sufficiently low volatility at this point that they are not measurable in the gas phase. The CIMS does detect ions corresponding to several < C₆ products seen in Nakao et al. (2011), including: C₄H₄O₃ at m/z 185 and C₄H₄O₄ at m/z 135 and m/z 201.

Nakao et al. (2011) also observed a series of oxygen additions, from C₆H₆O₂ to C₆H₆O₅, which are interpreted to possibly be a series of OH adduct products. Another structural possibility is that these are C₆ retaining, but ring-opened carboxylic acids that would correspond to large signals in the CIMS as transfer products: m/z 145, m/z 161, and m/z 177. From the time profiles of these CIMS ions, we predict that they are likely carboxylic acids even though the proposed chemical formulae are isomeric to the aromatic OH adducts. That is, these ion signals grow linearly with time (not shown) during the experiment duration and do not peak or plateau like their isomeric aromatic OH adducts. The peak/plateau of the signal from aromatic OH adducts is consistent with the proposed products' functionalities and potential to partition into the particle-phase, whereas these ring-opened products are of higher vapor pressure and may form throughout

the experiment during continued oxidation of the phenolic products.

The presence of these products may partially explain the absence of a strong signal from a hydroperoxide C₆H₈O₄ at m/z 229. The alkylperoxy radical preferentially isomerizes to form the bicyclic peroxy radical and decomposes from a bicyclic alkoxy radical to < C₆ fragments (often dicarbonyl) as mentioned above. However, Birdsall et al. (2010) observed evidence that the alkylperoxy radical may also participate in chemistry that regenerates OH and opens the ring (alternate route to alkoxy radical formation without first forming the bicyclic peroxy radical). This was found to be a more minor pathway also via RO₂ + HO₂ → RO + OH + O₂ for the case of toluene photooxidation. This results in an aromatic alkoxy radical and ring-opening to form methylhexadienedial, a C₇ dialdehyde (preserving the carbon backbone). Though this route was more prominent under low [O₂] conditions, Birdsall et al. (2010) also observed this product at pressures more similar to the atmosphere where bicyclic peroxy radical formation is expected to dominate and form dicarbonyl ring fragments. Thus, this ring-opening dicarbonyl pathway may also be present in this study, while minor compared to production of dicarbonyl fragments.

Table 4. Proposed structures for CIMS ions in the guaiacol low-NO_x system. C and T indicate the cluster and transfer product, respectively.

Observed m/z	Product	Chemical Formula	Proposed Structure (one isomer shown)	Chemical Pathway ^a
209	C ^b	C ₇ H ₈ O ₂		guaiacol
259	C	C ₇ H ₁₀ O ₅		(1) hydroperoxide
225	C	C ₇ H ₈ O ₃		(2) G + OH = guaiacol + OH
241	C	C ₇ H ₈ O ₄		(2) G + 2OH = guaiacol + 2OH
191	T ^c	C ₇ H ₈ O ₅		(2) G + 3OH = guaiacol + 3OH
175	T	C ₇ H ₈ O ₄		ring opening product
257	C ^d	C ₇ H ₈ O ₅		(3aii) EPOX and (2) G + 3OH
149	T	C ₅ H ₆ O ₄		(3aiii) ring fragment
187	C	C ₄ H ₆ O ₃		(3aiii) ring fragment
199	C	C ₅ H ₆ O ₃		(3aiii) ring fragment
107	T	C ₃ H ₄ O ₃		(3aiii) ring fragment
189	C	C ₃ H ₄ O ₄		(3aiii) ring fragment
243	T	C ₆ H ₆ O ₅		(3b) C ₆ bicyclic ketone
129	T ^e	C ₆ H ₆ O ₂		(4) Methoxy Loss

^a Numbers indicate correspondence with pathways outlined in mechanism (Fig. 4); ^b m/z 143 is also present as C₇H₈O₂, but is lower signal than at m/z 209; ^c Also includes signal from C₇H₈O₅ ring opening acid; ^d Includes contributions from G + 3OH along pathway 2 in Fig. 4; ^e m/z 195 is also present as C₆H₆O₂, but is lower signal than at m/z 129

Figure 3 outlines a potential mechanism employing this scheme to form these multifunctional C₆ carboxylic acids from phenol, dihydroxybenzene, and trihydroxybenzene. The difference between the products proposed here and those of Birdsall et al. (2010) is that the hydroxy group placement

results in carboxylic acid functionality. We note that depending on the hydroxy group placement on the ring, isomeric hydroxy dicarbonyl products are also likely and can contribute to these ion signals as well. OH regeneration could also come from photolysis of a hydroperoxide producing a favorable

Table 5. SOA products observed in UPLC/(-)ESI-TOFMS offline filter analysis for the guaiacol low-NO_x system.

[M-H] ⁻	Meas. Mass	Suggested Chemical Formula (M)	Error* (mDa)
189	189.0378	C ₇ H ₁₀ O ₆	-2.1
219	219.014	C ₇ H ₈ O ₈	-0.1
147	147.0266	C ₅ H ₈ O ₅	-2.6
157	157.0113	C ₆ H ₆ O ₅	-2.4
133	133.0133	C ₄ H ₆ O ₅	-2.4
149	149.0072	C ₄ H ₆ O ₆	-1.4
205	205.0327	C ₇ H ₁₀ O ₇	2.1
145	145.048	C ₆ H ₁₀ O ₄	-2.1
163	163.0233	C ₅ H ₈ O ₆	-1
203	203.0177	C ₇ H ₈ O ₇	-1.5
171	171.0279	C ₇ H ₈ O ₅	-1.4
169	169.0124	C ₇ H ₆ O ₅	-1.3
173	173.0428	C ₇ H ₁₀ O ₅	-2.2
115	115.0004	C ₄ H ₄ O ₄	-2.7
129	129.0175	C ₅ H ₆ O ₄	-1.3

* The error in the accurate mass measurements is the difference between the theoretical mass of the suggested molecular formulae and the measured mass of the ion.

alkoxy radical for ring opening, though we would not expect this to be significant on such a quick timescale that is consistent with negligible signal from the hydroperoxide. All CIMS traces for proposed ring opening acids and ring fragments share a similar trend of constant linear growth over time (not shown). Many of these trend with the aerosol mass (e.g. *m/z* 185 mentioned earlier), indicating that aerosol growth continues to proceed with the generation of ring opening and fragmentation processes.

4.3 Guaiacol chemistry

Figure 4 presents proposed oxidation pathways for the guaiacol system under low-NO_x conditions. Solid boxed structures indicate that the expected *m/z* from the chemical ionization reactions in the CIMS for that compound was detected. The *m/z* monitored is indicated, as are proposed C_xH_yO_z formulas and molecular weights. A list of ions monitored in this system is presented in Table 4. Chemical formulas shown in red indicate correspondence with a suggested C_xH_yO_z for accurate mass observations in filter data (Table 5). The particular structures in Fig. 4 indicate potential structures for the accurate mass suggested chemical formulae and the mechanism does not explicitly present all potential isomeric structures. The boxed colors correspond with the colors used for ion time traces as measured by the CIMS and included in Fig. 5.

Guaiacol gas-phase oxidation proceeds with OH addition to the ring, followed by reaction with oxygen to form an organic peroxy radical. Under the experimental conditions, the fate of this RO₂ radical is reaction with HO₂ to form a hy-

droperoxide (Fig. 4, Pathway 1), elimination of HO₂ to retain aromaticity (Fig. 4, Pathway 2), or isomerization to the bicyclic radical (Fig. 4, Pathway 3).

4.3.1 Pathway 1: RO₂ + HO₂

Despite predominant conditions of RO₂ + HO₂ chemistry, we do not observe strong signals in the CIMS measurements for potential hydroperoxides, as is similar to the case of phenol. A small trace at *m/z* 259 suggests that there is slight production of the hydroperoxide C₇H₁₀O₅. The off-line filter analysis does reveal a small contribution from a corresponding accurate mass measurement (Table 5). More significant signals in the CIMS are presented in Fig. 5, demonstrating that the preferred routes are to preserve aromaticity or involve isomerization to the bicyclic radical. This observation is consistent with previous studies on aromatic systems (Calvert et al., 2002; Bloss et al., 2005; Johnson et al., 2005; Birdsall et al., 2010).

4.3.2 Pathway 2: continuous OH addition to ring

The general chemical development of the consecutive OH addition pathways in the guaiacol low-NO_x system are tracked in Fig. 5. Figure 4, Pathway 2 is marked by *m/z* 225 on the CIMS, a cluster product for the guaiacol OH-adduct product, C₇H₈O₃ and denoted as G + OH. Successive OH addition products are monitored at 16 amu increments at *m/z* 241 and *m/z* 257, for C₇H₈O₄ denoted as G + 2OH and C₇H₈O₅ denoted as G + 3OH, respectively. The third OH adduct can be tracked at both the transfer and the cluster products, *m/z* 191 and *m/z* 257, respectively. However, *m/z* 257 includes the combined signal of rapid epoxide formation and the later formed third generation OH adduct. A signal at *m/z* 191 is predominantly the third generation OH adduct during the first 8 h until another product (likely an acid) grows in at this *m/z*. The first OH-adduct product (*m/z* 225) is short-lived due to further activation of the ring by the additional hydroxy group. Formation of C₇H₈O₄ monitored at *m/z* 241 follows promptly. The signal at *m/z* 191 (not shown) was observed to follow after *m/z* 241, indicating that third OH addition is achieved. C₇H₈O₅ is also a proposed chemical formula for a product observed in the filter analysis (Table 5), suggesting that the third OH adduct is of sufficiently low volatility to partition to the particle phase.

4.3.3 Pathway 3: isomerization to bicyclic radical

The bicyclic peroxy radical can react with HO₂ to form the bicyclic hydroperoxide C₇H₁₀O₇ (Fig. 4, Pathway 3ai), however, no evidence exists for this product in the CIMS. This is analogous with the bicyclic hydroperoxide from the phenolic case. However, if this product is formed, it already has a low vapor pressure and an O : C of 1, and would likely partition into the aerosol phase. Filter data also indicate the presence of C₇H₁₀O₇ in the particle-phase (Table 5). The majority of

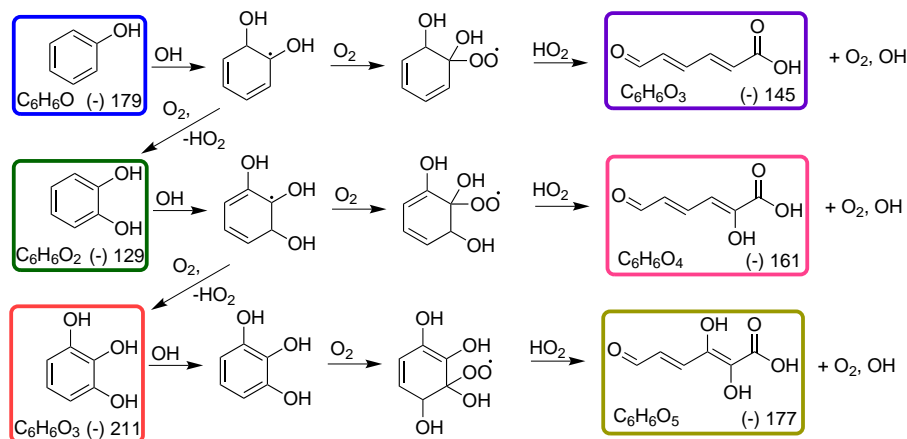


Fig. 3. Proposed pathway for gas-phase production of C_6 carboxylic acids in the phenol low- NO_x system. Boxed structures indicate that the expected m/z from the chemical ionization reactions in the CIMS for that compound was detected.

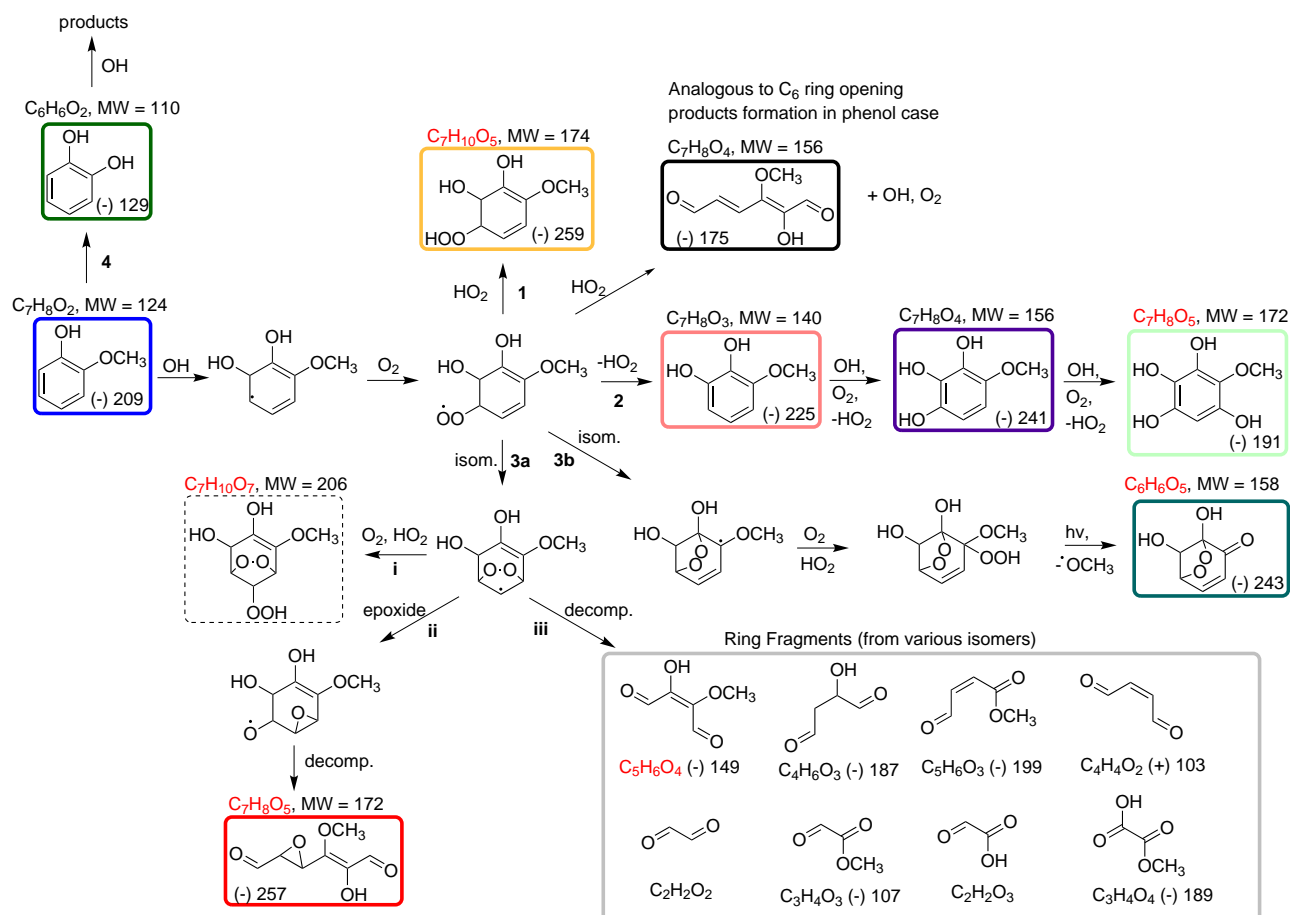


Fig. 4. Proposed mechanism for guaiacol low- NO_x oxidation. Boxed structures indicate that the expected m/z from the chemical ionization reactions in the CIMS for that compound was detected. Chemical formulae in red correspond with those proposed for the filter accurate mass aerosol measurements.

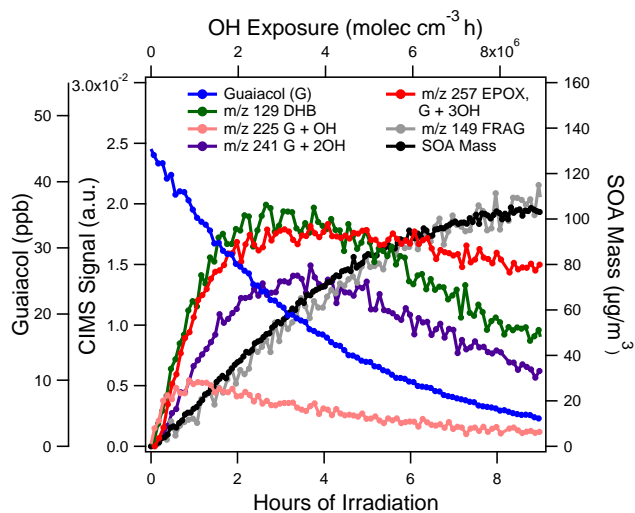


Fig. 5. Selected traces in guaiacol low- NO_x gas-phase and particle-phase development.

the filter data guaiacol products exhibit O : C ratio > 0.7 , and the average bulk O : C ratio as measured by the AMS is 0.89, so it is likely these hydroperoxide species may immediately partition and become further processed in the particle phase. Ofner et al. (2011) found O : C ratios of 0.3–1, which were attributed to products that are likely highly oxygenated benzenes and conjugated olefins.

Alternatively, the bicyclic radical can rearrange, breaking the oxygen bridge to form an epoxide and open the ring (Fig. 4, Pathway 3aii). There is evidence of a significant epoxide (EPOX) route that grows in early with the dihydroxybenzene route (Fig. 5). The epoxide is monitored at m/z 257, the cluster product of $\text{C}_7\text{H}_8\text{O}_5$ (Fig. 5), though there is some later contribution from the third generation OH adduct, as mentioned earlier. The epoxide will continue to react with OH to generate more functionalized molecules that will likely contribute to SOA formation.

The bicyclic radical can also decompose to several fragments as shown in the box in Fig. 4, Pathway 3aiii. A major fragment is observed at m/z 149, which could be the methoxy analog to the phenolic fragment, hydroxybutenedial ($\text{C}_4\text{H}_4\text{O}_3$) at m/z 185. We propose that m/z 149 is a methoxy-hydroxy-butenedial fragment, $\text{C}_5\text{H}_6\text{O}_4$. $\text{C}_5\text{H}_6\text{O}_4$ is also an accurate mass assignment for a product observed in the filter data (Table 5). The m/z 149 trace has a similar profile to the SOA mass curve, indicating that it is in equilibrium with the particle phase (Fig. 5). Other possible fragments are observed at ions indicated in the mechanism. The $< \text{C}_4$ fragments approach O : C values > 1 , and the C_4 and C_5 fragments would likely undergo further oxidation in the gas phase and then possibly contribute to the particle phase. The fate of butenedial ($\text{C}_4\text{H}_4\text{O}_2$) has been described elsewhere (Calvert et al., 2002; Bloss et al., 2005).

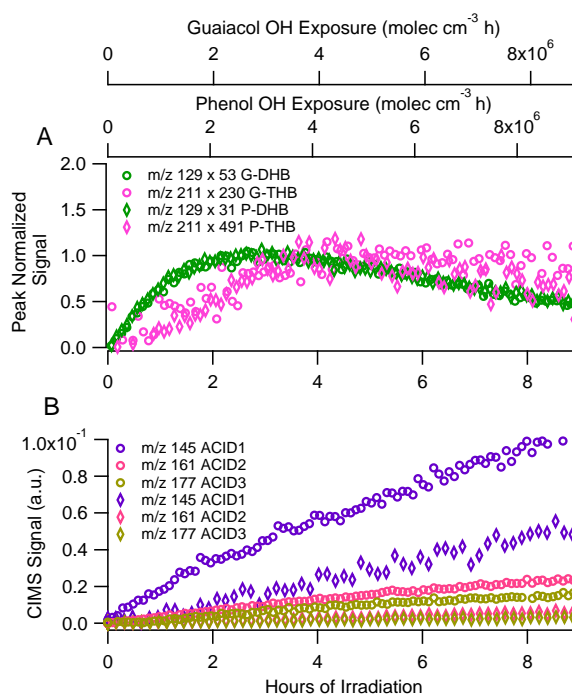


Fig. 6. Common chemical routes in the phenol and guaiacol low- NO_x systems. (A) Dihydroxybenzene routes in phenol (diamonds) and guaiacol (open circles). Each CIMS trace is normalized by the peak value. (B) Common acids in phenol (diamonds) and guaiacol (open circles).

4.3.4 Pathway 4: methoxy loss route

The early growth of a strong signal at m/z 129 (Fig. 5) and a matching time profile at m/z 195 upon irradiation suggests that dihydroxybenzene ($\text{C}_6\text{H}_6\text{O}_2$) is somehow formed from guaiacol ($\text{C}_7\text{H}_8\text{O}_3$) + OH in the gas phase. This is further supported by matching time profiles from the guaiacol and phenol systems for dihydroxybenzene (DHB) and its oxidation to trihydroxybenzene (THB) in Fig. 6a, as well as growth of the proposed C_6 ring opening acids (Fig. 6b). In the guaiacol system, the raw signal at m/z 211 includes contributions from the ^{18}O natural isotope peak of the guaiacol cluster product and trihydroxybenzene. The signal at m/z 211 has been corrected to reflect only the contribution from trihydroxybenzene (G-THB). There is negligible signal at m/z 227 in the guaiacol system, indicating that the dihydroxybenzene that is formed proceeds only to one more step of oxidation before the carbon along this route is incorporated into pathways besides continuous OH adduct formation. Rather, the carbon likely ends up in production of ring-opened acids as shown in Fig. 6b.

A trace at m/z 243 is present in the guaiacol system, though because there is negligible signal at m/z 227, it is unlikely that this ion is part of the OH adduct series from dihydroxybenzene as $\text{C}_6\text{H}_6\text{O}_5$. Still, an exact mass match for $\text{C}_6\text{H}_6\text{O}_5$ is the fourth highest product (in terms of area counts) of

constituents identified in the filter data, and m/z 243 follows the SOA trace indicating that it may be an important contributor to the particle phase. In the event that the radical placement occurs on the carbon containing the methoxy group during formation of the bicyclic radical, carbon loss may occur by removal of a methoxy group. The ether alkyl radical will react with O_2 to generate an ether alkyl peroxy radical. Collins et al. (2005) proposed that photooxidation of diisopropyl ether in the absence of NO_x (with $RO_2 + HO_2$ reactions dominating) likely resulted in the formation of hydroperoxide species that could then undergo decomposition, photolysis, or reaction with OH. Photolysis of the hydroperoxy group in the current methoxyphenol case would result in an alkoxy radical and elimination of the methoxy group to form a ketone. This leads to formation of a C_6 bicyclic ketone product as outlined in Pathway 3b of Fig. 4. The mechanism and structure for this particle-phase product remain tentative, as the proposed structure may be unstable and participate in additional condensation reactions.

4.3.5 Guaiacol aerosol-phase products

The off-line filter analysis suggests that there are additional chemical pathways for this system than those inferred from the gas-phase CIMS measurements. The top fifteen ions (by highest peak area) are presented in Table 5 along with measured masses and suggested corresponding chemical formulae. Of the suggested chemical formulae, the O : C ranges from 0.67 to 1.5. The $< C_7$ components are likely ring fragments that have undergone further oxidation to achieve such high O : C compared to those shown in Fig. 4, Pathway 3a.iii. Of the C_7 retaining products listed in Table 5, all suggested chemical formulae except $C_7H_5O_5$ can be explained by first-generation products along pathways 1, 2, 3ai, and 3a.ii (Fig. 4) and the analogous pathways in higher generation chemistry from the OH adducts. Similar structures to those proposed here have been observed previously in EI-MS analyses (Justesen, 2001). However, since many corresponding signals are not observed in the CIMS, it is also possible that a number of these highly oxygenated ($> O_5$) species may be formed in the particle phase, as evidenced in Ofner et al. (2011) for aerosol from guaiacol and catechol.

Previous study by Ofner et al. (2011) reports that the most important functional groups of generated SOA from guaiacol and catechol include carboxylic acids, carboxylic anhydrides and lactones or esters. While carboxylic acids can form as ring fragmentation products depending on the particular conformation of the bicyclic radical, the observation of carboxylic anhydrides and lactones suggests potential for additional intra- and inter-molecular reactions that may occur in the particle-phase involving the carbonyl and methoxy groups of SOA products. Ofner et al. (2011) also observe the degradation of the methoxy group during SOA formation from guaiacol, and finds this degradation to be more pronounced under wet conditions. This supports additional

chemistry (likely in the particle phase) that goes beyond the proposed gas-phase products in Fig. 4.

4.4 Syringol chemistry

The chemistry of syringol under low- NO_x conditions leads to rapid formation of a rich diversity of gas-phase products and SOA growth. Whereas at least two generations of OH oxidation of phenol are required to generate SOA, guaiacol and syringol produce SOA in the first generation. This is clear when comparing the SOA mass curves between systems in Figs. 2, 5, and 7. As expected, syringol is more reactive than guaiacol because of its additional methoxy group. Syringol is detected primarily at the transfer $[M+19]^-$, m/z 173, with some signal at the cluster product $[M+85]^-$, m/z 239. This is the opposite of guaiacol, the signal of which is found predominantly at the cluster product. This suggests that the extra methoxy group on syringol compared to guaiacol leads to an enhancement towards greater acidity to be seen predominantly at the transfer product (m/z 173). This shift is observed for many of the ions in the syringol case that are analogous to the guaiacol system. CIMS ions monitored in this system are presented in Table 6.

Syringol oxidation chemistry seems to undergo similar routes as guaiacol with analogous ions monitored by the CIMS for the following pathways: (1) hydroperoxide formation, (2) OH adduct formation up to two to three generations, and (3) epoxide and $< C_8$ ring fragment formation from decomposition of the bicyclic radical. These pathways are highlighted in Fig. 7a by selected ions at 189 and 271 for OH adducts $C_8H_{10}O_4$ (S + OH) and $C_8H_{10}O_5$ (S + 2OH), respectively, m/z 287 for the $C_8H_{10}O_6$ syringol epoxide (SE-POX), and a $C_6H_8O_5$ ring fragment (FRAG) at m/z 245. A minor contribution from the $C_8H_{12}O_6$ syringol hydroperoxide at m/z 289 was observed in the CIMS spectra and is not shown.

These routes seem to be minor, however, in comparison to those that favor immediate scission of the C_8 backbone (Fig. 7). Many of the higher signals in the CIMS are at m/z values that can only be reasonably explained by $< C_8$ molecular formulas. For example, major traces are from ions at m/z 275 (Fig. 7b), likely $C_7H_{10}O_6$. A signal was also observed in the CIMS spectra at m/z 291, possibly $C_7H_{10}O_7$, and is not shown. There is also evidence of methoxy and hydroxy exchanges and eliminations, providing even more diversity of masses in the CIMS spectra from syringol photooxidation. More detailed analyses on chemical structure would be required to confirm precise mechanisms.

For syringol, the immediate loss of carbon through novel chemical pathways (methoxy group elimination or exchange with hydroxy) is more evident in multiple routes than was observed in the case of guaiacol. Figure 8 proposes several possibilities of syringol conversion to compounds with fewer methoxy groups. Each of these pathways has representative

Table 6. Proposed structures for CIMS ions in the syringol low-NO_x system. C and T indicate the cluster and transfer product, respectively.

Observed m/z	Product	Chemical Formula	Proposed Structure (one isomer shown)	Chemical Pathway ^a
173	T ^b	C ₈ H ₁₀ O ₃		syringol
189	T	C ₈ H ₁₀ O ₄		S + OH = syringol + OH
271	C	C ₈ H ₁₀ O ₅		S + 2OH = syringol + 2OH
289	C	C ₈ H ₁₂ O ₆		hydroperoxide
225	C	C ₇ H ₈ O ₃		(a) G + OH = guaiacol + OH
211	C	C ₆ H ₆ O ₃		(b) THB = DHB + OH
209	C	C ₇ H ₈ O ₂		(c) guaiacol
129	T ^c	C ₆ H ₆ O ₂		(d) DHB = phenol + OH
205	T ^d	C ₈ H ₁₀ O ₅		ring opening product
287	C	C ₈ H ₁₀ O ₆		SEPOX
245	C	C ₆ H ₈ O ₅		ring fragment
149	T	C ₅ H ₆ O ₄		ring fragment
185	C	C ₄ H ₄ O ₃		ring fragment
203	C	C ₄ H ₆ O ₄		ring fragment
275	C	C ₇ H ₁₀ O ₆	none proposed	C ₈ scission
291	C	C ₇ H ₁₀ O ₇	none proposed	C ₈ scission

^a Letters indicate correspondence with pathways outlined in mechanism (Fig. 8).

^b m/z 239 is also present as C₈H₁₀O₃, but is lower signal than at m/z 173.

^c m/z 195 is also present as C₆H₆O₂, but is lower signal than at m/z 129.

^d Includes contributions from S + 2OH as well as ring opening product.

ions that also appear in the guaiacol case, though they are not necessarily the same mechanistically.

Analogous to the formation of dihydroxybenzene in the case of guaiacol + OH, the early growth of m/z 225 (presumably C₇H₈O₃) suggests that hydroxy guaiacol (G + OH) may form from syringol + OH (Figs. 7b, 8, Pathway a). Another possibility is the complete exchange of both methoxy groups for hydroxy groups, resulting in trihydroxybenzene (THB)

monitored at m/z 211 (Figs. 7b, 8, Pathway b). Formation of guaiacol is also evident by matching time profiles growing in at m/z 143 and 209 (Figs. 7b, 8, Pathway c). Growth of dihydroxybenzene (DHB) at m/z 129 and m/z 195 is observed later in the experiment, likely from conversion of guaiacol (Fig. 8, Pathway d). Observation of signal at m/z 257 (the guaiacol epoxide and third OH adduct) supports that there is a guaiacol channel in syringol photooxidation, and is not

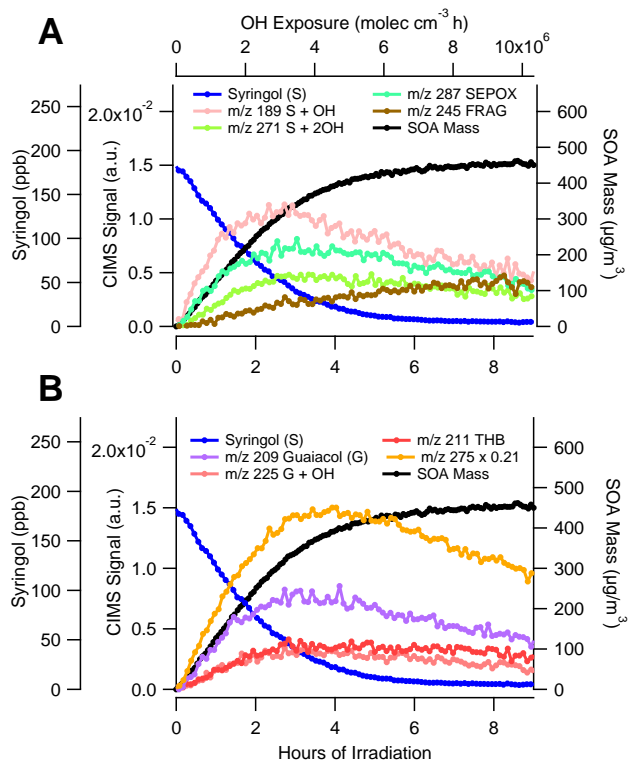


Fig. 7. Selected traces in syringol low-NO_x gas-phase and particle-phase development. **(A)** OH addition pathways. **(B)** Traces indicating methoxy loss pathways.

shown. Though a guaiacol channel exists, the coincident formation of *m/z* 225 (G + OH) and *m/z* 211 (THB) with that of guaiacol at *m/z* 209 is consistent with their direct formation from syringol + OH.

4.5 Novel chemical pathways for loss of carbon in methoxyphenol systems

We observe evidence that guaiacol and syringol OH-initiated photooxidation leads to loss of carbon, likely due to unique chemistry involving the methoxy group. While gas-phase aromatic chemistry is not completely understood (Calvert et al., 2002), we propose possible explanations for these carbon loss pathways. Carbon loss from aromatic systems has been observed previously in the gas-phase, and is thought to be a result of *ipso* addition of OH at a substituent containing ring carbon and subsequent elimination of the substituent leaving a phenolic group. This is the case for alkylbenzenes, in which Noda et al. (2009) observed phenol formation from OH-initiated photooxidation of toluene and cresol formation from xylenes. Prior, Koch et al. (2007) provided evidence that the *ipso* addition of OH is relevant for the case of hexamethylbenzene. The extent by which these processes occur in the gas-phase is still unclear, as Aschmann et al. (2010) does not observe the dealkylation as in Noda et al. (2009). Addition at the *ipso* position is generally considered to be a minor

route ($\leq 20\%$ for the alkylbenzenes studied in Noda et al., 2009), though it could be that oxy substituents may influence the favorability of this route. Raff and Hites (2006) found that brominated diphenylethers also undergo ether cleavage, proposed as a result of *ipso* addition of OH. Thus, *ipso* addition of OH in the gas-phase may be more relevant for more highly-substituted and/or more complex substituents on aromatics.

Koch et al. (2007) also pointed out several liquid-phase studies that find evidence of ether bond cleavage. Again, *ipso* addition of hydroxyl radical is cited as being responsible for ether bond cleavage (removal of an oxy substituent) and C-C cleavage (removal of a methyl substituent) in some cases. Aihara et al. (1993) studied two pathways in which 1,2-dihydroxybenzene (catechol) forms from *o*-methoxyphenols using a copper (II) – ascorbic acid-dioxygen system: hydroxyl radical attack *ipso* to the methoxy containing carbon, and H-abstraction from the methoxy group. Hydroxyl radical attack *ipso* to the methoxy containing carbon allows for loss of the methoxy (–OCH₃) group in the form of methanol (CH₃OH), removing a C atom from the parent molecule. During H-abstraction from the methoxy group, Aihara et al. (1993) propose that the OCH₂ radical reacts with the OH radical and then elimination of formaldehyde (HCHO) ensues. In isotopically labeled studies, Aihara et al. (1993) observed transformation of guaiacol to catechol and syringol to hydroxy guaiacol. They also measure yields of these products that might imply *ipso* addition of OH being a more important route than previously considered compared to *ortho*- and *para*-OH addition to the ring. This route could serve as explanation of the observed hydroxy substitutions of methoxy groups in the current systems, but they cannot be verified without measurements of methanol and formaldehyde.

While we see ions indicating that methoxy groups may convert to hydroxyl groups, we do not see evidence supporting the addition of or reversible exchange of methoxy groups to the ring. Methoxy radicals may be formed from photolysis of the C–OCH₃ bond, if we assume that this bond energy can be proxied by the bond in dimethylether (CH₃–OCH₃). This bond energy, 351.9 kJ mole⁻¹ (Luo, 2007), translates to an approximate wavelength of 340 nm, exactly where the irradiance spectrum of the light source in our atmospheric chambers peaks. In the event that methoxy radicals are formed, though, it seems unlikely that methoxy radical reaction with the methoxyphenols results in methoxy addition to the ring or replacement of a hydroxy group, especially compared to rapid reaction with O₂. Gomez et al. (2001) studied the reaction rate constants for methoxy radical with cyclohexane, cyclohexene, and 1,4-cyclohexadiene. It was found that methoxy radical reaction with these compounds is likely to result in preferential H abstraction with minor routes of addition to cyclohexene and 1,4-cyclohexadiene. This corroborates the absence of >C₇ species in the guaiacol case and >C₈ species in the syringol case.

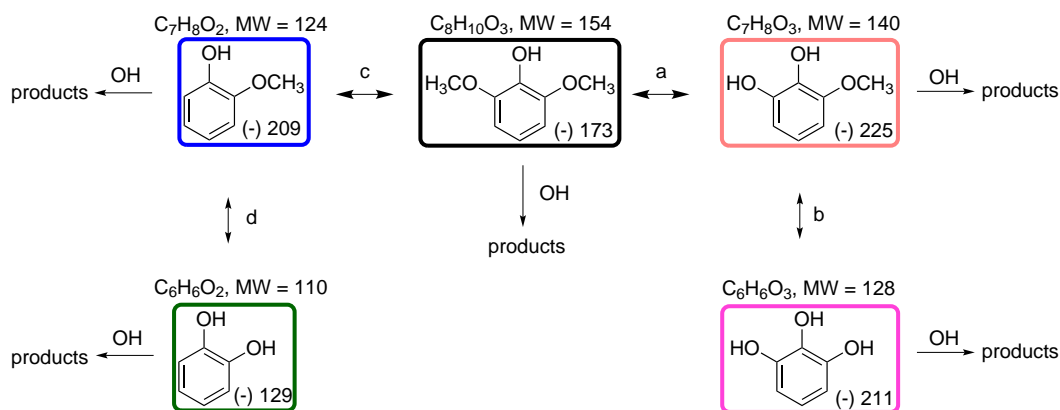


Fig. 8. Possible routes of methoxy loss in syringol gas-phase chemistry.

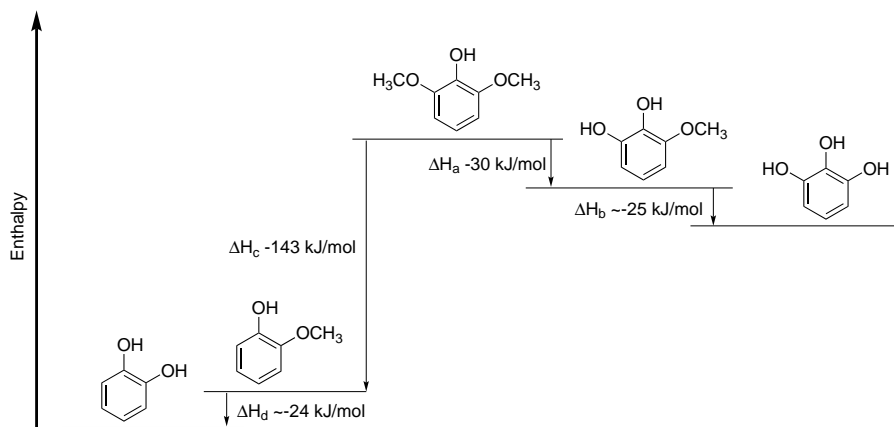


Fig. 9. Estimates of enthalpy differences between several products indicating methoxy loss.

Thermodynamic evaluation of the substituent group effects in methoxyphenols can also provide some insight. The following discussion is based on the work presented in Varfolomeev et al. (2010) that examines pairwise substitution effects, and inter- and intramolecular hydrogen bonds in methoxyphenols and dimethoxybenzenes. Varfolomeev et al. (2010) show that intramolecular hydrogen bonding plays a significant role on *ortho*-methoxy substituted phenols. This leads to *o*-methoxyphenols having a lower phenolic O–H bond dissociation energy (BDE) compared to *meta* isomers and higher than *para* isomers. This means that the phenolic O–H BDE increases in order the order 4-methoxyphenol < 2-methoxyphenol < 3-methoxyphenol. From the ab initio calculations of Varfolomeev et al. (2010), the enthalpy of formation for 2-methoxyphenol (guaiacol) is expressed below:

$$\Delta_f H_m^\circ(2\text{-methoxyphenol}) = \Delta_f H_m^\circ(\text{B}) + \Delta H(\text{H} \rightarrow \text{OH}) + \Delta H(\text{H} \rightarrow \text{OCH}_3) + (\textit{ortho}\text{-OH-OCH}_3),$$

where $\Delta_f H_m^\circ(\text{B})$ = enthalpy of formation of benzene, $\Delta H(\text{H} \rightarrow \text{OH}) = -179.0 \text{ kJ mol}^{-1}$, the increment in enthalpy for substitution of an H atom by $-\text{OH}$, $\Delta H(\text{H} \rightarrow$

$\text{OCH}_3) = -150.5 \text{ kJ mol}^{-1}$, the increment in enthalpy for substitution of an H atom by $-\text{OCH}_3$, and (*ortho*-OH–OCH₃) = 4.5 kJ mol^{-1} , the increment in enthalpy for the pairwise interactions of $-\text{OH}$ and $-\text{OCH}_3$ *ortho* to one another.

The enthalpy of formation expression begins with the base enthalpy of formation from benzene, then adds the effects of hydroxy or methoxy substitution to the ring. Finally, the pairwise interactions are added, reflecting the stabilizing intramolecular H bonding and destabilizing effect from sterics in the *ortho*-OH–OCH₃ configuration. From the comparison of the substitution effects alone, this suggests that H→OH is slightly more favorable than H→OCH₃. For example, this might support substitution of a methoxy group by a hydroxy group in the guaiacol system, as the pairwise *ortho* effect is minimal.

Assuming that the Varfolomeev et al. (2010) formulation can be extended to the case of a trisubstituted benzene, we can write an analogous expression for the case of syringol (2,6-dimethoxyphenol):

$$\begin{aligned} \Delta_f H_m^\circ(2,6\text{-dimethoxyphenol}) &= \Delta_f H_m^\circ(\text{B}) + \Delta H(\text{H} \rightarrow \text{OH}) \\ &+ 2 \times \Delta H(\text{H} \rightarrow \text{OCH}_3) + 2 \times (\textit{ortho}\text{-OH-OCH}_3) \\ &+ (\textit{meta}\text{-OCH}_3\text{-OCH}_3), \end{aligned}$$

where (*meta*-OCH₃-OCH₃) = 0.1 kJ mol⁻¹ from Varfolomeev et al. (2010).

After writing a similar expression for 3-methoxybenzene-1,2-diol (hydroxyguaiacol), the difference between the substituent effects for hydroxyguaiacol and syringol is -30 kJ mol⁻¹, in slight favor of hydroxyguaiacol. The pairwise effect of (*ortho*-OH-OH) was not calculated by Varfolomeev et al. (2010), but assuming that it is less sterically hindered compared to (*ortho*-OH-OCH₃) and is stabilized by intramolecular hydrogen bonding similar to 1,2-dimethoxybenzene, we assume it to be < 4.5 kJ mol⁻¹. Due to the combined favorability of energetics for the substituent effects and the pairwise effects, this can help explain why some of the syringol rapidly converts to hydroxyguaiacol and even trihydroxybenzene. A simplified schematic with estimated enthalpy differences using this analysis is presented in Fig. 9.

The “phenolic route”, involving OH addition at the *ortho* position to the main electron-donating substituent group has been cited as being the main channel responsible for SOA formation in many aromatic systems (Calvert et al., 2002; Johnson et al., 2005; Nakao et al., 2011). However, with the additional methoxy groups, OH attack at the alpha-unsubstituted carbons to the methoxy groups becomes competitive and changes the potential for maintaining aromaticity in the methoxyphenol systems. It is possible that the extra methoxy group in syringol inhibits OH attack that is typically favored *ortho* to the hydroxyl substituted carbon in other systems that generate SOA via this route. For the other compounds, in order to achieve the degree of oxidation of the aerosol, it appears that at least two steps of reaction are needed, but that these steps occur fairly rapidly. If subsequent OH reactions are even slower due to the extra methoxy group in the case of syringol, then conversion to SOA may not be as complete as with the other two compounds over the duration of the experiments reported here.

4.6 Chemical basis for observed yields

The AMS high-resolution spectra for the methoxyphenol systems are distinct. Initial aerosol growth in the guaiacol system is marked by the exact mass ion C₄H₃O₂⁺. Later the aerosol growth is characterized by the ions C₂H₃O⁺, and C₂H₅O₂⁺. In the case of syringol, initial growth is characterized by C₅H₂O₂⁺ and C₇H₉O₃⁺ ions, followed by C₅H₅O₄⁺, and then by C₅H₂O₄⁺ and C₂H₄O₃⁺. This suggests that guaiacol SOA is characterized by smaller carbon number and less oxygenated fragments than the case of syringol.

The characteristic ions from the AMS spectra for syringol SOA seem counter-intuitive for understanding why the sy-

ringol SOA yield is lower than that of guaiacol. Syringol has more carbon and oxygen to begin with and these ions are larger, more oxygenated fragments than in guaiacol. However, if we return to the gas-phase comparison of the characteristic trends in the guaiacol (Fig. 5) and syringol (Fig. 7) systems, one notes that many of the major products from syringol photooxidation peak later than their analogs in the guaiacol system. Further, there is no analogous peak in the guaiacol system to the *m/z* 275 unique to the syringol system. Since this is a major product of gas-phase syringol photooxidation and it peaks > 4 × 10⁶ molec cm⁻³ h of OH exposure compared to guaiacol ions that peak generally within 3 × 10⁶ molec cm⁻³ h, it acts like a gas-phase carbon reservoir. That is, the signal at *m/z* 275 is much more significant than the more efficient SOA formers at *m/z* 129 (dihydroxybenzene, not shown) and *m/z* 209 (guaiacol) in Fig. 7b.

AMS elemental analyses of SOA from these systems as reported in Chhabra et al. (2011) suggest that the majority of oxygenation is derived from organic acid functionalities: 77 % for phenol, 61 % for guaiacol, and 59 % for syringol. This is consistent with the necessity of further oxidation of ring-opened dicarbonyl fragments and ring-opened acids to explain the presence of highly oxidized species observed in the guaiacol filter analyses. Ofner et al. (2010) found that the SOA-formation process from catechol involves ring-opened carboxylic acid derivatives that are part of highly hydroxylated olefin structures, which supports the organic acid functionality observed in the current related systems. Previous study on the ozonolysis of 1,2-dihydroxybenzene showed that several carbonyls existed in both the gas and particle phases (Olariu, 2001). Carboxylic acids believed to be ring fragments, as well as muconic acid, a ring-opened C₆ dicarboxylic acid, were also identified. Muconic acid was also identified in the particle phase from benzenediol ozonolysis (Tomas et al., 2003). These results support the current observations that many dicarbonyl species in general trend with the SOA mass, suggesting that they may be semi-volatile in nature.

The decrease in oxygenation derived from organic acid functionalities from phenol to the methoxyphenol systems may reflect the oxygen reserved in OH adduct and aromatic retaining pathways, especially in the case of syringol (Fig. 8). This may also partially explain why the syringol SOA yield is lower if particle-phase acid formation from carbonyl ring fragments drives the SOA growth. At similar OH exposures, the syringol system still has not developed a carbonyl ring fragment signal that tracks well with the SOA growth, as *m/z* 185 does in the phenol system (Fig. 2) and *m/z* 149 does in the guaiacol system (Fig. 5). The *m/z* 245 fragment lags the SOA growth in the syringol system (Fig. 7a). This could be due to the lack of OH addition to the ring on syringol in critical positions that lead to SOA formation via ring-fragmentation pathways and acid formation.

Estimation of carbon oxidation state also provides some insight into the chemical evolution of the aerosol towards

incorporation of highly oxidized species. Representative time series of the carbon oxidation state, $\overline{\text{OS}}_{\text{C}}$, for the studied systems are shown in Fig. 10. Carbon oxidation state was estimated with the AMS O:C and H:C elemental analyses using the formulation presented in Kroll et al. (2011). All systems approach an $\overline{\text{OS}}_{\text{C}}$ of +0.5. This approaches the range of low-volatility oxygenated organic aerosol (Kroll et al., 2011). A delay in the rise of $\overline{\text{OS}}_{\text{C}}$ from phenol aerosol is observed, consistent with the rise in organic growth at the point of formation of trihydroxybenzene (Fig. 2). Syringol aerosol lags in oxidation in the beginning compared to guaiacol until approximately $4 \times 10^6 \text{ molec cm}^{-3} \text{ h}$ of OH exposure. This times with the peak of many of the methoxy loss products in Fig. 7b, supporting that additional oxidation is achieved once methoxy loss occurs and the syringol product distribution overlaps that of guaiacol (i.e. G + OH and THB) and the “phenolic route”. Primary organic aerosol from biomass burning was found to have an $\overline{\text{OS}}_{\text{C}}$ of -1.0 to -0.7 (Aiken et al., 2008; Kroll et al., 2011), which falls inbetween the range of $\overline{\text{OS}}_{\text{C}}$ from the three systems here. However, aged (Whistler Mountain) aerosols ranged -0.6 to $+0.6$ (Sun et al., 2009; Kroll et al., 2011), enveloping the methoxyphenols and a portion of the phenol $\overline{\text{OS}}_{\text{C}}$ evolution. In terms of average carbon oxidation state, these experiments pick up from primary organic aerosol in biomass burning and move towards the character of aged organic aerosol.

5 Atmospheric relevance

While the current experiments were conducted without the addition of NO_x , the chemistry elucidated under these low- NO_x conditions is expected to be relevant for typical atmospheric conditions. For phenol photooxidation in the presence of NO_x , Olariu et al. (2002) measured yields of 0.8 catechol (1,2-dihydroxybenzene), 0.037 1,4-benzoquinone, and 0.058 2-nitrophenol. However, according to kinetic data and yield comparisons for nitrophenol presented in Berndt and Boge (2003), it is likely that this nitro-product formation can be biased due to sufficiently high NO_2 ($\lesssim 800$ ppb) concentrations. Berndt and Boge (2003) point out that for atmospheric conditions with NO_2 of approximately 20 ppb, it is probable that phenoxy radicals also react with O_3 as well as NO and NO_2 . This would result in more minor nitrophenol yields in the atmosphere for daytime chemistry. Reaction with NO_3 should also be considered as phenolic compounds can react rapidly with trace levels of NO_3 during the day and especially at night.

Thus, because OH addition dominates over H abstraction, and subsequent O_2 addition to the OH radical adduct is rapid, it is more likely that in the atmosphere, SOA primarily forms via pathways involving higher-generation OH adducts and their respective routes to oxygenated fragments. This is consistent with the chemistry presented in this work. Though we did not observe appreciable evidence of gas-phase hydroper-

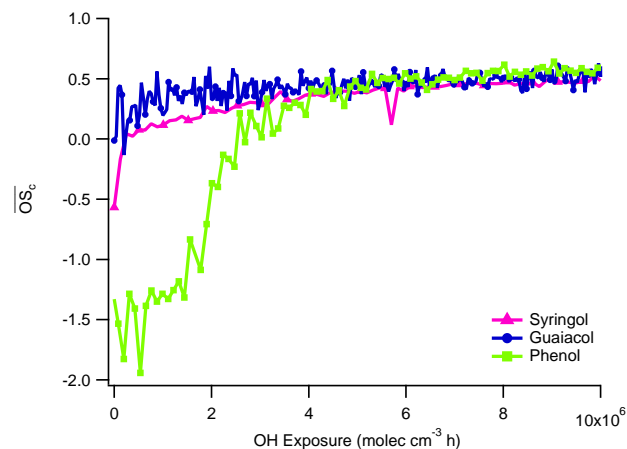


Fig. 10. Evolution of the average carbon oxidation state ($\overline{\text{OS}}_{\text{C}}$) for studied systems.

oxides, they may be rapidly incorporated into the particle phase and contribute to peroxide formation, as postulated by Johnson et al. (2005) and observed by Sato et al. (2007) for the case of toluene photooxidation. Sato et al. (2007) also find similar species in the particle-phase under $[\text{NO}]_0 = 0.2$ and 1 ppm, still citing O_2 addition to the OH-aromatic adduct as the major channel contributing to SOA formation.

In the presence of moderate NO_x , we would expect the major gas-phase species to be the same as those presented here, with only a minor contribution from nitrogen-containing products. Still, for the studied compounds, novel routes of reaction of alkylperoxy radicals under these low- NO_x conditions may still result in product distributions expected under higher NO_x conditions. First, the aromatic peroxy radicals in the studied systems may preferentially decompose to regenerate OH via novel $\text{RO}_2 + \text{HO}_2$ chemistry (Birdsall et al., 2010). This is a possible explanation for the observation of ring-opened acids in phenol and guaiacol. Second, generation of carbonyls via novel rearrangements of ether peroxy radicals (Orlando and Tyndall, 2012), relevant for guaiacol and syringol, would further make the product distributions less distinct from alkoxy radical pathways expected under high- NO_x chemistry.

These observations warrant caution when conducting experiments in the presence of NO_x for aromatic compounds, as derived aerosol yields may be based on chemistry non-representative of the atmosphere. Hence, we left discussion of the experiments conducted in the presence of NO_x for the Appendix. Klotz et al. (2002) found that at high- NO_x conditions (hundreds of ppb to ppm) one must also start to consider reactions of NO_x with the hydroxy radical adduct. At sufficiently high NO_x concentrations, the gas-phase chemistry can generate higher yields of nitroaromatics as compared to the OH aromatic adduct (Koch et al., 2007; Nishino et al., 2008). Nitroaromatics can serve to enhance aerosol yields if sufficient nitro-containing functionalities are achieved or

to act as gas-phase carbon reservoirs and depress aerosol yields. Hydroxyl groups will lead to a vapor pressure lowering more than that associated with nitro groups, but sufficient nitro groups could lead to incorporation to the particle phase. Owing to the lower OH reactivity of the molecule containing a nitro group as compared to the comparable molecule containing a hydroxyl group (Kwok and Atkinson, 1995), one might also find that more OH is necessary in the presence of NO_x to attain further gas-phase development to more highly oxidized species that contribute to SOA formation.

While the OH-initiated photooxidation of aromatics in general is complex (Calvert et al., 2002), methoxyphenols seem to follow some steps of the general mechanism developed for simpler aromatics. We have qualitatively presented gas-phase trends that give some insight into the chemistry of SOA formation. Though, more complete mechanism development would be enhanced by the availability of authentic standards to solidify mass assignments and more detailed structural information. For example, the structural identity of the ion at m/z 275 in the syringol system remains elusive. Calculation of quantitative gas-phase yields would benefit from additional kinetic data pertaining to some of the complex intermediates.

Carbon loss via the methoxy groups in guaiacol and syringol appears to be a feasible route to describe the gas-phase product distributions. While the chemistry of syringol is complex, this compound may be a better model system to represent the mixture of methoxy and phenolic compounds since it displays chemistry from both classes. Syringol, however, does not generate as much SOA as these other systems. This may be a result of the unique $\text{OCH}_3\text{--OH--OCH}_3$ pairwise effects that hinder the typical phenolic pathway responsible for SOA formation.

Future studies to investigate this effect might start with methoxyphenols of different substituted positions relative to the hydroxy group to see the effect on SOA yields. For example, using a methoxyphenol where at least one or two methoxy groups are not *ortho* to the hydroxy group would serve to further investigate the importance of OH addition *ortho* to the hydroxy group in these compounds, as 1,2-dihydroxybenzene is the major gas-phase product and SOA former from phenol. Also, 2,5-dimethoxyphenol might also indicate if OH attack is preferred at the 6-position, again *ortho* to the hydroxy group. Such studies would require more detailed analyses that provide greater structural analysis for the gas-phase products as well as unique tracers for fragmentation patterns that would clarify the chemistry.

Detailed study of the gas-phase products from the OH-initiated photooxidation of methoxybenzene might also be informative for understanding the proposed carbon loss associated with methoxy groups in the guaiacol and syringol systems. If phenol is a major product, this has implications on understanding the chemical fate of methoxyphenol-like compounds in the atmosphere. For example, Lauraguais et al. (2012) suggest that syringol is too reactive with OH (1.8 h) to

be a relevant tracer in the atmosphere for woodsmoke emissions and that it results in a very minor SOA yield. However, the chemical analyses presented in this study suggest that syringol can efficiently convert to guaiacol and hydroxylated benzenes that are longer lived in the atmosphere and potentially have larger SOA yields. This can be analogous to the isoprene photochemical cascade, where it is the products of isoprene photooxidation that have greater SOA forming potential (Kroll et al., 2006). The syringol conversion to guaiacol also has implications for using these compounds as specific tracers for fuel type (hardwood vs. softwood). Thus, care must be taken in selecting one or more surrogate species for use in modeling aerosol yields from biomass burning emissions in the atmosphere.

Appendix A

Methoxyphenol oxidation in the presence of NO_x

We present here results from the methoxyphenol experiments performed in the presence of NO_x including SOA yields and qualitative analyses of the chemical development in these systems. As mentioned in the Introduction section, the main text of this paper focuses on methoxyphenol and phenol photooxidation under idealized chemical conditions ($\text{NO}_x < 10$ ppb), such that the predominant fate of the RO_2 radical here is reaction with HO_2 . Biomass burning events certainly generate NO_x , and the authors recognize that the low- NO_x chemistry presented in the main text by no means provides the complete chemical picture of aged biomass burning plumes. A complementary set of experiments in the presence of NO_x was conducted along with the low- NO_x experiments presented earlier using the same protocols, except that HONO was used as the OH precursor instead of H_2O_2 and NO was also injected.

However, we do not focus on the results of these experiments in the main text for both technical and scientific reasons including: (1) The actual experimental conditions resulted in hundreds of ppb levels of NO_x , which are much higher than those reported for biomass burning events. For example, Iinuma et al. (2010) measured biomass burning co-located NO_x on the order of 20 ppb. Thus, the product distributions in these experiments result in favored nitro-products, but do not necessarily represent the more relevant chemical development in the atmosphere. NO_x levels can also become depleted several hours later (via NO_2 incorporation into PAN species) or with dilution via transport of a plume as observed in Akagi et al. (2012). Thus, experiments in the absence of or at levels of $\text{NO}_x < 10$ ppb (such as those presented in the main text) can still be representative of product distributions at lower NO_x levels (< 30 ppb) when methoxyphenol precursors are transported away and subsequently photooxidize. (2) Interference of HONO response on our NO_x analyzer made it more difficult to report

Table A1. Experimental conditions and aerosol yields in the presence of added NO_x.

Date (2010)	Organic	[Org] ₀ (ppb)	[Org] _f (ppb)	RH ₀ (%)	[NO ₂] ₀ ^a (ppb)	[NO] ₀ ^a (ppb)	Vol ₀ ^b μm ³ cm ⁻³	Vol _f ^b μm ³ cm ⁻³	Yield
2/3	guaiacol	14.2	0.7	< LDL ^c	447	282	12.9	27.5	0.34 ± 0.02
2/5	guaiacol	51.9	3.1	5.6	536	461	13.5	92.5	0.53 ± 0.01
3/2	guaiacol	38.0	2.0	< LDL ^c	458	295	10.5	65.4	0.46 ± 0.01
3/28	guaiacol	13.6	0.8	< LDL ^c	429	222	11.4	26.5	0.35 ± 0.02
3/31	guaiacol	55.3	4.0	< LDL ^c	518	330	13.8	86.5	0.46 ± 0.02
4/6	guaiacol	16.4	1.2	< LDL ^c	493	314	9.0	29.4	0.4 ± 0.02
4/9 ^d	guaiacol	14.2	0.5	< LDL ^c	509	315	18.7	33.5	0.35 ± 0.02
4/13 ^d	guaiacol	15.4	0.8	< LDL ^c	464	296	11.3	27.1	0.4 ± 0.02
4/15	guaiacol	35.6	3.7	< LDL ^c	526	321	10.8	55.7	0.49 ± 0.02
4/22	guaiacol	50.4	4.4	< LDL ^c	433	329	14.4	74.6	0.47 ± 0.02
2/19	phenol	14.8	1.9	< LDL ^c	443	295	14.0	32.0	0.54 ± 0.06
3/23	phenol	23.5	3.0	< LDL ^c	488	301	14.2	37.9	0.54 ± 0.06
3/6	syringol	53.1	2.4	< LDL ^c	448	286	11.9	68.0	0.3 ± 0.01
3/9	syringol	124.2	4.2	< LDL ^c	481	313	14.6	110.0	0.2 ± 0.01
3/11	syringol	92.3	2.9	< LDL ^c	469	314	12.6	73.0	0.17 ± 0.01
3/13	syringol	31.9	1.0	< LDL ^c	418	241	12.8	29.0	0.11 ± 0.01

^a Corrections for HONO interference not made; values for NO_x listed are upper limits

^b Vol₀ is initial seed volume; Vol_f is final volume (seed + organic aerosol), as measured by DMA

^c RH probe LDL = 5 % RH

^d Additional HONO injected mid-experiment

precise NO_x levels. (3) Before photooxidation commenced, we observed a likely nitro-product that formed once HONO was introduced to the reactors, presumably a reaction of methoxyphenol with HONO and/or NO_x (by-product of the HONO synthesis) in the dark to form a nitro-product. This was not observed in Lauraguais et al. (2012) for the case of syringol and CH₃ONO in the dark. While direct HONO/NO_x reaction with the methoxyphenol compounds may be of atmospheric relevance, this complicated the chemical system that we started with and made it difficult to constrain the chemistry for the observed product distributions.

A1 Methoxyphenol SOA yields in the presence of NO_x

The yield data presented here are not recommended for use in atmospheric models, as the conditions of the experiments are not representative of typical or biomass burning NO_x levels in the atmosphere. The excess of NO_x employed in these experiments likely biases the product distributions to more nitrogen-containing species, thereby affecting associated volatilities and the SOA yields. All experiment conditions and SOA yields are presented in Table A1.

For high-NO_x experiments (NO > 200 ppb initially), nitrous acid (HONO) was used as the OH precursor. HONO was prepared by adding 15 mL of 1 wt % aqueous NaNO₂ dropwise into 30 mL of 10 wt % sulfuric acid in a glass bulb. A stream of dry air was then passed through the bulb, sending HONO into the chamber. During this process NO and NO₂ formed as side products and were also introduced into the

chamber. NO/NO_x was measured with a commercial chemiluminescence NO_x monitor (Horiba, APNA-360) with lower detection limit (LDL) of 5 ppb of NO. Total starting NO_x was generally just under 800 ppb as indicated by the NO_x analyzer, and no corrections have been made for HONO interference on the analyzer.

Additional HONO was injected in two ~ 14 ppb guaiacol experiments (4/9 and 4/13) to explore the extent to which additional OH and NO_x would affect the gas-phase chemistry leading to SOA formation. Additional HONO was injected both at the mid-point of aerosol growth (4/13) and at the point where virtually all of the initial organic had been consumed (4/9). In both cases, further oxidation by OH did not lead to further aerosol formation in comparison to the guaiacol high-NO_x experiment with similar organic loading (2/3). While an enhancement of some nitrogen-containing products occurred as observed in the gas phase for the cases with additional HONO (4/9 and 4/13), this suggests that the major components of SOA formation are not likely from these particular products. In addition, there were no observations of new species in the CIMS spectra to suggest that additional OH exposure unlocks new generations of chemistry that contribute to SOA formation. These observations are consistent with the relatively rapid formation of highly oxidized, low-volatility SOA during the course of the experiment.

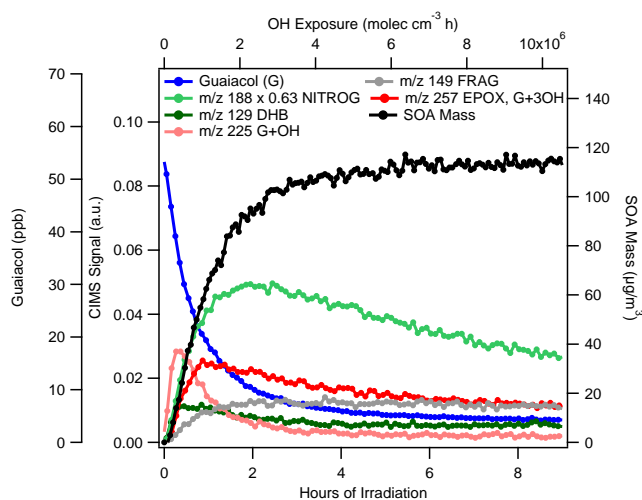


Fig. A1. Guaiacol high- NO_x gas-phase and particle-phase development.

A2 Phenol high- NO_x chemistry

Olariu et al. (2002) measured yields of 0.8 catechol (1,2-dihydroxybenzene), 0.037 1,4-benzoquinone, and 0.058 2-nitrophenol using Fourier transform infrared (FT-IR) absorption spectroscopy for phenol photooxidation in the presence of NO_x . The CIMS traces in this study are consistent with these products. We find the major signals in the CIMS at m/z 129 (dihydroxybenzene) and m/z 158 (nitrophenol). There is some signal at m/z 211 and m/z 174 indicating that trihydroxybenzene and its nitro-product are present in small amounts. However, according to the kinetic data and yield comparisons for nitrophenol presented in Berndt and Boge (2003), it is likely that nitro-product formation is favored from reaction of phenoxy radicals with NO_2 due to sufficiently high NO_2 concentrations in these experiments (max. $\text{NO}_2 \sim 500$ ppb). The relative signals in the CIMS indicated such a bias existed. Berndt and Boge (2003) point out that for atmospheric conditions with NO_2 of approximately 20 ppb, it is probable that phenoxy radicals also react with O_3 and other species. In negative mode operation, the CIMS is not sensitive to quinone products, however, there are masses in positive mode operation at m/z 109 and 127 that may be the $[\text{M}+1]^+$ and $[\text{M}+19]^+$ ions of benzoquinone. The set of C_6 ring-opened acids as proposed in Fig. 3 for low- NO_x conditions is not prevalent under high- NO_x conditions, except for the acid at m/z 145. An alkoxy radical generated from $\text{RO}_2 + \text{NO}$ results in the same acid ($\text{C}_6\text{H}_6\text{O}_3$). Signals for proposed acidic fragments at m/z 185 and m/z 201 in the low- NO_x case are also present under high- NO_x conditions.

A3 Guaiacol high- NO_x chemistry

During experiments with HONO injection, the majority of guaiacol is rapidly converted to nitroguaiacol ($\text{C}_7\text{H}_7\text{NO}_4$)

Table A2. SOA products observed in UPLC/(-)ESI-ToFMS offline filter analysis for the guaiacol high- NO_x system.

$[\text{M}-\text{H}]^-$	Meas. Mass	Suggested Chemical Formula (M)	Error* (mDa)
154	154.0121	$\text{C}_6\text{H}_5\text{NO}_4$	-1.9
170	170.0069	$\text{C}_6\text{H}_5\text{NO}_5$	-2
186	186.0023	$\text{C}_6\text{H}_5\text{NO}_6$	-1.6
199	198.9965	$\text{C}_6\text{H}_4\text{N}_2\text{O}_6$	-2.6
200	200.0182	$\text{C}_7\text{H}_7\text{NO}_6$	-1.3
184	184.0229	$\text{C}_7\text{H}_7\text{NO}_5$	-1.7

* The error in the accurate mass measurements is the difference between the theoretical mass of the suggested molecular formulae and the measured mass of the ion.

monitored at m/z 188, NITROG, in Fig. A1. Production of dihydroxybenzene and the OH adducts still occurs as seen in the low- NO_x case, as well as their nitro analogs in the high- NO_x case. However, the nitro OH adducts are formed in minor amounts. The hydroperoxide channel is negligible as expected. However, the presence of NO_x seems to favor the production of many nitrogen-containing fragments since there is a prevalence of even-numbered m/z 's < 200 in the CIMS spectra. Some of the identifications of these ions remains elusive. Additional even-numbered fragments are present, but of low signal to noise.

Table A2 lists a few of the most prevalent particle-phase products (from highest to lowest peak area). The filter data show that dihydroxybenzene with a nitro group ($\text{C}_6\text{H}_5\text{NO}_4$) is incorporated into the particle phase as well as up to two more oxygens ($\text{C}_6\text{H}_5\text{NO}_5$, $\text{C}_6\text{H}_5\text{NO}_6$). The formation of these essentially non-volatile products and rapid incorporation into the particle phase is consistent with the lack of CIMS observations for such oxygenated compounds in the guaiacol high- NO_x system. The presence of particle-phase $\text{C}_6\text{H}_4\text{N}_2\text{O}_6$ suggests that this product may be a C_6 ring fragment that undergoes additional oxidation. The C_7 products are consistent with the minimally detected gas-phase formation of nitroguaiacol OH adducts, also supporting rapid incorporation into the particle phase. One thing to note is that while the filter data suggest that the majority of particle-phase products are nitrogen containing, this may be partially biased by sensitivity of the technique for measuring such compounds. The AMS bulk analyses show that the guaiacol system N : C ratio is only 0.04 which does not match the average N : C represented by the products in Table A2. However, the AMS N : C ratio may also be biased low by uncertainties introduced if many of these species are organonitrates (Farmer et al., 2010).

A4 Syringol high- NO_x chemistry

High- NO_x syringol photooxidation is dominated primarily by m/z 275 again, and fragments (Fig. A2). The ion at m/z 203 is likely a volatile fragment and was also prominent

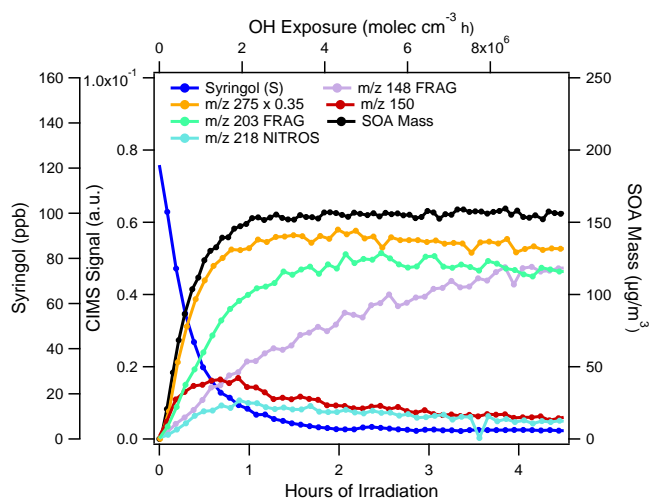


Fig. A2. Syringol high- NO_x gas-phase and particle-phase development.

in the guaiacol high- NO_x system. Nitrosyringol is a small contribution at m/z 218 (NITROS) and unidentified m/z 150 grows in and reacts quickly in a similar manner. An ion at m/z 148 growing in over time indicates the conversion of some of these initial nitro-containing products to nitrogen-containing fragments. This may also explain why the aerosol yields in the high- NO_x case appear to be slightly lower than those in the low- NO_x case. Particle-phase analyses and structure identification would be necessary to further understand if the particle phase consists mostly of $< \text{C}_8$ species.

While in the low- NO_x case one is able to distinguish some conversion of syringol to guaiacol and hydroxy guaiacol, the presence of NO_x seems to rapidly lead to incorporation of a nitro group. Nitroguaiacol species are minor species in this system. The SOA forms quickly in this case and could be due to rapid incorporation of the nitroguaiacol and nitrosyringol products into the particle phase.

A5 Chemical differences between high- NO_x and low- NO_x chemistry

In the case of guaiacol and syringol, product identifications are generally analogous for the low and high- NO_x cases, except that more nitrogen-containing species are present in the high- NO_x case. Both cases result in fragments that are often acidic and have the potential to become further oxidized. It is likely that these highly oxidized fragments are incorporated into the particle phase as observed in the filter analyses for the guaiacol low- NO_x system. If alkylperoxy radicals preferentially decompose to regenerate OH via novel $\text{RO}_2 + \text{HO}_2$ pathways as observed from aromatic peroxy radicals (Birdsall et al., 2010) or to generate carbonyls via novel rearrangements of ether peroxy radicals (Orlando and Tyndall, 2012), this further makes the product distributions less distinct from alkoxy radical pathways in high- NO_x chemistry.

In the guaiacol system, the acidic fragment traces in the CIMS have the same time profile as the SOA growth in the low- NO_x case. Under high- NO_x conditions, the SOA growth does not follow the same time profile as any of the major gas-phase products. This suggests that under the experimental conditions of OH exposure, the SOA under low- NO_x conditions may be dominated by production of more highly oxidized and lower volatility products than under high- NO_x conditions. The major difference between SOA formation in the low- and high- NO_x conditions may be attributed to the nitro-group incorporation into the ring. Comparison of the predominant first-generation product nitroguaiacol ($\text{C}_7\text{H}_7\text{NO}_4$) under high- NO_x conditions to any of the C_7 -retaining first generation products (typically $\text{O} > 5$) under low- NO_x conditions demonstrates that the low- NO_x case begins with relatively lower vapor pressure products. Though we did not observe appreciable evidence of gas-phase hydroperoxides in the low- NO_x case, they may be rapidly incorporated into the particle phase. With continued OH addition in the low- NO_x case and competing nitro-group addition in the high- NO_x case, the volatilities resulting from addition of the hydroxyl and nitro groups can rival one another. Though, hydroxyl groups will lead to a vapor pressure lowering more than that associated with nitro groups. In addition, the nitroguaiacol fate is predominantly gas-phase reaction with OH, as it does not have sufficient oxygens as represented by the majority of products observed in the filter data ($> \text{O}_4$). Owing to the lower OH reactivity of the molecule containing a nitro group as compared to the comparable molecule containing a hydroxyl group (Kwok and Atkinson, 1995), this also suggests that more OH is necessary in the high- NO_x case to attain further gas-phase development to more highly oxidized species. For example, while $\text{RO}_2 + \text{NO}$ chemistry generally leads to fragmentation, there is a tendency for at least C_6 highly oxygenated nitrogen containing species to be retained. This could be due to lack of continued OH exposure. It is also possible that the C_6 species are derived from the dihydroxybenzene route in guaiacol photooxidation, rather than $\text{RO}_2 + \text{NO}$ induced carbon-carbon cleavage.

In general, the CIMS spectra indicate there is greater signal at the fragmented acidic species compared to the ring retaining species, and these fragment traces tend to have a time profile that is in equilibrium with SOA growth. Though there are distinct nitrogen-containing products in the high- NO_x case, it is again the fragments (many at the same m/z as the low- NO_x case) and some nitrogen-containing fragment traces that seem to be in equilibrium with the particle phase. Thus, while nitrogen incorporation may occur early on in the high- NO_x cases, there is still a degree of oxygenation required for these species to be incorporated in the particle phase. This is consistent with the observation of several aerosol species in the guaiacol high- NO_x system that have chemical formulae with one nitrogen, but > 3 oxygens (more than guaiacol itself). AMS elemental analyses of SOA from these systems as reported in Chhabra et al. (2011) suggest

that the majority of oxygenation is derived from organic acid functionalities under both NO_x conditions, ranging 61–77 % for phenol and guaiacol and 54–59 % for syringol. There is a < 7 % contribution from organic nitrate groups under high-NO_x conditions. The relatively lower contribution of oxygenation from organic acid groups in the syringol system compared to phenol and guaiacol may partially explain why the syringol SOA yield is also lower. SOA formation from these compounds may be dominated by acidic species that result from ring-opening pathways, so prevention of this pathway (as evidenced by the presence of *m/z* 275 under both conditions of NO_x) in the case of syringol would hinder SOA formation.

Acknowledgements. This work was supported by the US Department of Energy grants DE-FG02-05ER63983 and DE-SC 0006626 and US Environmental Protection Agency (EPA) STAR Research Agreement No. RD-833749.

Edited by: M. Ammann

References

- Aihara, K., Urano, Y., Higuchi, T., and Hirobe, M.: Mechanistic studies of selective catechol formation from *o*-methoxyphenols using a copper(II) ascorbic-acid dioxygen system, *J. Chem. Soc. Perk. T.*, 2, 2165–2170, doi:10.1039/p29930002165, 1993.
- Aiken, A. C., DeCarlo, P. F., and Jimenez, J. L.: Elemental analysis of organic species with electron ionization high-resolution mass spectrometry, *Anal. Chem.*, 79, 8350–8358, 2007.
- Aiken, A. C., DeCarlo, P. F., Kroll, J. H., Worsnop, D. R., Huffman, J. A., Docherty, K. S., Ulbrich, I. M., Mohr, C., Kimmel, J. R., Sueper, D., Sun, Y., Zhang, Q., Trimborn, A., Northway, M., Ziemann, P. J., Canagaratna, M. R., Onasch, T. B., Alfarra, M. R., Prevot, A. S. H., Dommen, J., Duplissy, J., Metzger, A., Baltensperger, U., and Jimenez, J. L.: O/C and OM/OC ratios of primary, secondary, and ambient organic aerosols with high-resolution time-of-flight aerosol mass spectrometry, *Environ. Sci. Technol.*, 42, 4478–4485, 2008.
- Akagi, S. K., Craven, J. S., Taylor, J. W., McMeeking, G. R., Yokelson, R. J., Burling, I. R., Urbanski, S. P., Wold, C. E., Seinfeld, J. H., Coe, H., Alvarado, M. J., and Weise, D. R.: Evolution of trace gases and particles emitted by a chaparral fire in California, *Atmos. Chem. Phys.*, 12, 1397–1421, doi:10.5194/acp-12-1397-2012, 2012.
- Allan, J. D., Delia, A. E., Coe, H., Bower, K. N., Alfarra, M. R., Jimenez, J. L., Middlebrook, A. M., Drewnick, F., Onasch, T. B., Canagaratna, M. R., Jayne, J. T., and Worsnop, D. R.: A generalised method for the extraction of chemically resolved mass spectra from Aerodyne aerosol mass spectrometer data, *J. Aerosol Sci.*, 35, 909–922, 2004.
- Ammann, M., Rossler, E., Strekowski, R., and George, C.: Nitrogen dioxide multiphase chemistry: Uptake kinetics on aqueous solutions containing phenolic compounds, *Phys. Chem. Chem. Phys.*, 7, 2513–2518, 2005.
- Aschmann, S. M., Arey, J., and Atkinson, R.: Extent of H-atom abstraction from OH plus *p*-cymene and upper limits to the formation of cresols from OH plus *m*-xylene and OH plus *p*-cymene, *Atmos. Environ.*, 44, 3970–3975, doi:10.1016/j.atmosenv.2010.06.059, 2010.
- Atkinson, R., Aschmann, S. M., and Arey, J.: Reactions of hydroxyl and nitrogen trioxide radicals with phenol, cresols, and 2-nitrophenol at 296 ± 2 K, *Environ. Sci. Technol.*, 26, 1397–1403, doi:10.1021/es00031a018, 1992.
- Bahreini, R., Keywood, M. D., Ng, N. L., Varutbangkul, V., Gao, S., Flagan, R. C., Seinfeld, J. H., Worsnop, D. R., and Jimenez, J. L.: Measurements of secondary organic aerosol from oxidation of cycloalkenes, terpenes, and *m*-xylene using an Aerodyne aerosol mass spectrometer, *Environ. Sci. Technol.*, 39, 5674–5688, 2005.
- Berndt, T. and Boge, O.: Gas-phase reaction of OH radicals with phenol, *Phys. Chem. Chem. Phys.*, 5, 342–350, doi:10.1039/b208187c, 2003.
- Berndt, T. and Boge, O.: Formation of phenol and carbonyls from the atmospheric reaction of OH radicals with benzene, *Phys. Chem. Chem. Phys.*, 8, 1205–1214, doi:10.1039/B514148F, 2006.
- Birdsall, A. W., Andreoni, J. F., and Elrod, M. J.: Investigation of the role of bicyclic peroxy radicals in the oxidation mechanism of toluene, *J. Phys. Chem. A*, 114, 10655–10663, doi:10.1021/jp105467e, 2010.
- Bloss, C., Wagner, V., Bonzanini, A., Jenkin, M. E., Wirtz, K., Martin-Reviejo, M., and Pilling, M. J.: Evaluation of detailed aromatic mechanisms (MCMv3 and MCMv3.1) against environmental chamber data, *Atmos. Chem. Phys.*, 5, 623–639, doi:10.5194/acp-5-623-2005, 2005.
- Bond, T. C., Streets, D. G., Yarber, K. F., Nelson, S. M., Woo, J. H., and Klimont, Z.: A technology-based global inventory of black and organic carbon emissions from combustion, *J. Geophys. Res.-Atmos.*, 109, D14203, doi:10.1029/2003JD003697, 2004.
- Calvert, J. G., Atkinson, R., Becker, K. H., Kamens, R. M., Seinfeld, J. H., Wallington, T. J., and Yarwood, G.: *The Mechanisms of Atmospheric Oxidation of Aromatic Hydrocarbons*, Oxford University Press, Inc, New York, USA, 2002.
- Chan, A. W. H., Kroll, J. H., Ng, N. L., and Seinfeld, J. H.: Kinetic modeling of secondary organic aerosol formation: effects of particle- and gas-phase reactions of semivolatile products, *Atmos. Chem. Phys.*, 7, 4135–4147, doi:10.5194/acp-7-4135-2007, 2007.
- Chhabra, P. S., Ng, N. L., Canagaratna, M. R., Corrigán, A. L., Russell, L. M., Worsnop, D. R., Flagan, R. C., and Seinfeld, J. H.: Elemental composition and oxidation of chamber organic aerosol, *Atmos. Chem. Phys.*, 11, 8827–8845, doi:10.5194/acp-11-8827-2011, 2011.
- Cocker, D. R., Flagan, R. C., and Seinfeld, J. H.: State-of-the-art chamber facility for studying atmospheric aerosol chemistry, *Environ. Sci. Technol.*, 35, 2594–2601, 2001.
- Coeur-Tourneur, C., Tomas, A., Guilloteau, A., Henry, F., Ledoux, F., Visez, N., Riffault, V., Wenger, J. C., and Bedjanian, Y.: Aerosol formation yields from the reaction of catechol with ozone, *Atmos. Environ.*, 43, 2360–2365, doi:10.1016/j.atmosenv.2008.12.054, 2009.
- Coeur-Tourneur, C., Cassez, A., and Wenger, J. C.: Rate coefficients for the gas-phase reaction of hydroxyl radicals with 2-Methoxyphenol (guaiacol) and related compounds, *J. Phys. Chem. A*, 114, 11645–11650, doi:10.1021/jp1071023, 2010.

- Collins, E., Sidebottom, H., Wenger, J., Calvé, S. L., Melouki, A., LeBras, G., Villenave, E., and Wirtz, K.: The influence of reaction conditions on the photooxidation of diisopropyl ether, *J. Photoch. Photobiol. A*, 176, 86–97, doi:10.1016/j.jphotochem.2005.09.004, 2005.
- DeCarlo, P. F., Kimmel, J. R., Trimborn, A., Northway, M. J., Jayne, J. T., Aiken, A. C., Gonin, M., Fuhrer, K., Horvath, T., Docherty, K. S., Worsnop, D. R., and Jimenez, J. L.: Field-deployable, high-resolution, time-of-flight aerosol mass spectrometer, *Anal. Chem.*, 78, 8281–8289, 2006.
- Dills, R. L., Zhu, X. Q., and Kalman, D. A.: Measurement of urinary methoxyphenols and their use for biological monitoring of wood smoke exposure, *Environ. Res.*, 85, 145–158, 2001.
- U.S. EPA.: EPI Suite v4.11, <http://www.epa.gov/opptintr/exposure/pubs/episuitedi.htm>, 2012.
- Farmer, D. K., Matsunaga, A., Docherty, K. S., Surratt, J. D., Seinfeld, J. H., Ziemann, P. J., and Jimenez, J. L.: Response of an aerosol mass spectrometer to organonitrates and organosulfates and implications for atmospheric chemistry, *P. Natl. Acad. Sci. USA*, 107, 6670–6675, doi:10.1073/pnas.0912340107, 2010.
- Fine, P. M., Cass, G. R., and Simoneit, B. R. T.: Chemical characterization of fine particle emissions from fireplace combustion of woods grown in the northeastern United States, *Environ. Sci. Technol.*, 35, 2665–2675, 2001.
- Gomez, N., Henon, E., Bohr, F., and Devolder, P.: Rate constants for the reactions of CH₃O with cyclohexane, cyclohexene, and 1,4-cyclohexadiene: Variable temperature experiments and theoretical comparison of addition and H-abstraction channels, *J. Phys. Chem. A*, 105, 11204–11211, doi:10.1021/jp010204h, 2001.
- Hawthorne, S. B., Krieger, M. S., Miller, D. J., and Mathiason, M. B.: Collection and quantitation of methoxylated phenol tracers for atmospheric-pollution from residential wood stoves, *Environ. Sci. Technol.*, 23, 470–475, 1989.
- Hawthorne, S. B., Miller, D. J., Langenfeld, J. J., and Krieger, M. S.: PM-10 high-volume collection and quantification of semivolatile and nonvolatile phenols, methoxylated phenols, alkanes, and polycyclic aromatic-hydrocarbons from winter urban air and their relationship to wood smoke emissions, *Environ. Sci. Technol.*, 26, 2251–2262, 1992.
- Huey, L. G., Villalta, P. W., Dunlea, E. J., Hanson, D. R., and Howard, C. J.: Reactions of CF₃O- with atmospheric trace gases, *J. Phys. Chem.*, 100, 190–194, 1996.
- Inuma, Y., Böge, O., Gräfe, R., and Herrmann, H.: Methyl-Nitrocatechols: Atmospheric tracer compounds for biomass burning secondary organic aerosols, *Environ. Sci. Technol.*, 44, 8453–8459, doi:10.1021/es102938a, 2010.
- Ito, A. and Penner, J. E.: Historical emissions of carbonaceous aerosols from biomass and fossil fuel burning for the period 1870–2000, *Global Biogeochem. Cy.*, 19, GB2028, doi:10.1029/2004GB002374, 2005.
- Johnson, D., Jenkin, M., Wirtz, K., and Martin-Reviejo, M.: Simulating the formation of secondary organic aerosol from the photooxidation of aromatic hydrocarbons, *Environ. Chem.*, 2, 35–48, doi:10.1071/EN04079, 2005.
- Justesen, U.: Collision-induced fragmentation of deprotonated methoxylated flavonoids, obtained by electrospray ionization mass spectrometry, *J. Mass Spectrom.*, 36, 169–178, doi:10.1002/jms.118, 2001.
- Kautzman, K. E., Surratt, J. D., Chan, M. N., Chan, A. W. H., Hersey, S. P., Chhabra, P. S., Dalleska, N. F., Wennberg, P. O., Flagan, R. C., and Seinfeld, J. H.: Chemical composition of gas- and aerosol-phase products from the photooxidation of naphthalene, *J. Phys. Chem. A*, 114, 913–934, 2010.
- Keywood, M. D., Varutbangkul, V., Bahreini, R., Flagan, R. C., and Seinfeld, J. H.: Secondary organic aerosol formation from the ozonolysis of cycloalkenes and related compounds, *Environ. Sci. Technol.*, 38, 4157–4164, 2004.
- Klotz, B., Volkamer, R., Hurley, M., Andersen, M., Nielsen, O., Barnes, I., Imamura, T., Wirtz, K., Becker, K., Platt, U., Wallington, T., and Washida, N.: OH-initiated oxidation of benzene – Part II. influence of elevated NO_x concentrations, *Phys. Chem. Chem. Phys.*, 4, 4399–4411, doi:10.1039/b204398j, 2002.
- Koch, R., Knispel, R., Elend, M., Siese, M., and Zetzsch, C.: Consecutive reactions of aromatic-OH adducts with NO, NO₂ and O₂: benzene, naphthalene, toluene, m- and p-xylene, hexamethylbenzene, phenol, m-cresol and aniline, *Atmos. Chem. Phys.*, 7, 2057–2071, doi:10.5194/acp-7-2057-2007, 2007.
- Kroll, J. H., Ng, N. L., Murphy, S. M., Flagan, R. C., and Seinfeld, J. H.: Secondary organic aerosol formation from isoprene photooxidation, *Environ. Sci. Technol.*, 40, 1869–1877, doi:10.1021/es0524301, 2006.
- Kroll, J. H., Donahue, N. M., Jimenez, J. L., Kessler, S. H., Canagaratna, M. R., Wilson, K. R., Altieri, K. E., Mazzoleni, L. R., Wozniak, A. S., Bluhm, H., Mysak, E. R., Smith, J. D., Kolb, C. E., and Worsnop, D. R.: Carbon oxidation state as a metric for describing the chemistry of atmospheric organic aerosol, *Nat. Chem.*, 3, 133–139, doi:10.1038/nchem.948, 2011.
- Kwok, E. S. and Atkinson, R.: Estimation of hydroxyl radical reaction rate constants for gas-phase organic compounds using a structure-reactivity relationship: An update, *Atmos. Environ.*, 29, 1685–1695, doi:10.1016/1352-2310(95)00069-B, 1995.
- Lauraguais, A., Coeur-Tourneur, C., Cassez, A., and Seydi, A.: Rate constant and secondary organic aerosol yields for the gas-phase reaction of hydroxyl radicals with syringol (2,6-dimethoxyphenol), *Atmos. Environ.*, 55, 43–48, doi:10.1016/j.atmosenv.2012.02.027, 2012.
- Luo, Y. R.: *Comprehensive Handbook of Chemical Bond Energies*, CRC Press, Boca Raton, FL, 2007.
- Naeher, L. P., Brauer, M., Lipsett, M., Zelikoff, J. T., Simpson, C. D., Koenig, J. Q., and Smith, K. R.: Woodsmoke health effects: A review, *Inhal. Toxicol.*, 19, 67–106, 2007.
- Nakao, S., Clark, C., Tang, P., Sato, K., and Cocker III, D.: Secondary organic aerosol formation from phenolic compounds in the absence of NO_x, *Atmos. Chem. Phys.*, 11, 10649–10660, doi:10.5194/acp-11-10649-2011, 2011.
- Ng, N. L., Kroll, J. H., Keywood, M. D., Bahreini, R., Varutbangkul, V., Flagan, R. C., Seinfeld, J. H., Lee, A., and Goldstein, A. H.: Contribution of first- versus second-generation products to secondary organic aerosols formed in the oxidation of biogenic hydrocarbons, *Environ. Sci. Technol.*, 40, 2283–2297, 2006.
- Ng, N. L., Chhabra, P. S., Chan, A. W. H., Surratt, J. D., Kroll, J. H., Kwan, A. J., McCabe, D. C., Wennberg, P. O., Sorooshian, A., Murphy, S. M., Dalleska, N. F., Flagan, R. C., and Seinfeld, J. H.: Effect of NO_x level on secondary organic aerosol (SOA) formation from the photooxidation of terpenes, *Atmos. Chem. Phys.*, 7, 5159–5174, doi:10.5194/acp-7-5159-2007, 2007.

- Nieto-Gligorovski, L., Net, S., Gligorovski, S., Zetzsch, C., Jamoul, A., D'Anna, B., and George, C.: Interactions of ozone with organic surface films in the presence of simulated sunlight: impact on wettability of aerosols, *Phys. Chem. Chem. Phys.*, 10, 2964–2971, doi:10.1039/B717993F, 2008.
- Nishino, N., Atkinson, R., and Arey, J.: Formation of nitro products from the gas-phase OH radical-initiated reactions of toluene, naphthalene, and biphenyl: effect of NO₂ concentration, *Environ. Sci. Technol.*, 42, 9203–9209, doi:10.1021/es802046m, 2008.
- Noda, J., Volkamer, R., and Molina, M. J.: Dealkylation of Alkylbenzenes: A Significant Pathway in the Toluene, o-, m-, p-Xylene + OH Reaction, *J. Phys. Chem. A*, 113, 9658–9666, doi:10.1021/jp901529k, 2009.
- Ofner, J., Kruger, H.-U., and Zetzsch, C.: Time Resolved Infrared Spectroscopy of Formation and Processing of Secondary Organic Aerosol, *Z. Phys. Chem.*, 224, 1171–1183, doi:10.1524/zpch.2010.6146, 2010.
- Ofner, J., Krüger, H.-U., Grothe, H., Schmitt-Kopplin, P., Whitmore, K., and Zetzsch, C.: Physico-chemical characterization of SOA derived from catechol and guaiacol – a model substance for the aromatic fraction of atmospheric HULIS, *Atmos. Chem. Phys.*, 11, 1–15, doi:10.5194/acp-11-1-2011, 2011.
- Olariu, R. I., Tomas, A., Barnes, I., Bejan, I., Becker, K. H., and Wirtz, K.: Atmospheric Ozone Degradation Reaction of 1,2-Dihydroxybenzene, EUPHORE 4th Report 2001, Tech. rep., Compiled and Produced by Institute of Physical Chemistry, Bergische Universität Wuppertal, Germany, 2001.
- Olariu, R. I., Klotz, B., Barnes, I., Becker, K. H., and Mocanu, R.: FTIR study of the ring-retaining products from the reaction of OH radicals with phenol, o-, m-, and p-cresol, *Atmos. Environ.*, 36, 3685–3697, 2002.
- Orlando, J. J. and Tyndall, G. S.: Laboratory studies of organic peroxy radical chemistry: an overview with emphasis on recent issues of atmospheric significance, *Chem. Soc. Rev.*, 41, 6294–6317, doi:10.1039/c2cs35166h, 2012.
- Pankow, J.: An absorption-model of gas-particle partitioning of organic-compounds in the atmosphere, *Atmos. Environ.*, 28, 185–188, doi:10.1016/1352-2310(94)90093-0, 1994.
- Pye, H. O. T. and Seinfeld, J. H.: A global perspective on aerosol from low-volatility organic compounds, *Atmos. Chem. Phys.*, 10, 4377–4401, doi:10.5194/acp-10-4377-2010, 2010.
- Raff, J. D. and Hites, R. A.: Gas-Phase Reactions of Brominated Diphenyl Ethers with OH Radicals, *J. Phys. Chem. A*, 110, 10783–10792, doi:10.1021/jp0630222, 2006.
- Sander, S. P., Abbatt, J. P. D., Barker, J. R., Burkholder, J. B., Friedl, R. R., Golden, D. M., Huie, R. E., Kolb, C. E., Moortgat, G. K., Orkin, V. L., and Wine, P. H.: Chemical kinetics and photochemical data for use in atmospheric studies, Evaluation No. 17, JPL Publication 10-6, 2011, <http://jpldataeval.jpl.nasa.gov>, 2011.
- Sato, K., Hatakeyama, S., and Imamura, T.: Secondary organic aerosol formation during the photooxidation of toluene: NO_x dependence of chemical composition, *J. Phys. Chem. A*, 111, 9796–9808, doi:10.1021/jp071419f, 2007.
- Schauer, J. J., Kleeman, M. J., Cass, G. R., and Simoneit, B. R. T.: Measurement of emissions from air pollution sources. 3. C-1-C-29 organic compounds from fireplace combustion of wood, *Environ. Sci. Technol.*, 35, 1716–1728, 2001.
- Simpson, C. D. and Naeher, L. P.: Biological monitoring of wood-smoke exposure, *Inhal. Toxicol.*, 22, 99–103, 2010.
- St. Clair, J. M., McCabe, D. C., Crouse, J. D., Steiner, U., and Wennberg, P. O.: Chemical ionization tandem mass spectrometer for the in situ measurement of methyl hydrogen peroxide, *Rev. Sci. Instrum.*, 81, 094102, doi:10.1063/1.3480552, 2010.
- Sun, Y., Zhang, Q., Macdonald, A. M., Hayden, K., Li, S. M., Liggio, J., Liu, P. S. K., Anlauf, K. G., Leaitch, W. R., Steffen, A., Cubison, M., Worsnop, D. R., van Donkelaar, A., and Martin, R. V.: Size-resolved aerosol chemistry on Whistler Mountain, Canada with a high-resolution aerosol mass spectrometer during INTEX-B, *Atmos. Chem. Phys.*, 9, 3095–3111, doi:10.5194/acp-9-3095-2009, 2009.
- Sun, Y. L., Zhang, Q., Anastasio, C., and Sun, J.: Insights into secondary organic aerosol formed via aqueous-phase reactions of phenolic compounds based on high resolution mass spectrometry, *Atmos. Chem. Phys.*, 10, 4809–4822, doi:10.5194/acp-10-4809-2010, 2010.
- Surratt, J. D., Gómez-González, Y., Chan, A. W. H., Vermeylen, R., Shahgholi, M., Kleindienst, T. E., Edney, E. O., Offenberg, J. H., Lewandowski, M., Jaoui, M., Maenhaut, W., Claeys, M., Flagan, R. C., and Seinfeld, J. H.: Organosulfate formation in biogenic secondary organic aerosol, *J. Phys. Chem. A*, 112, 8345–8378, 2008.
- Tomas, A., Olariu, R. I., Barnes, I., and Becker, K. H.: Kinetics of the reaction of O₃ with selected benzenediols, *Int. J. Chem. Kinet.*, 35, 223–230, doi:10.1002/kin.10121, 2003.
- Varfolomeev, M. A., Abaidullina, D. I., Solomonov, B. N., Verevkin, S. P., and Emel'yanenko, V. N.: Pairwise substitution effects, inter- and intramolecular hydrogen bonds in methoxyphenols and dimethoxybenzenes. thermochemistry, calorimetry, and first-principles calculations, *J. Phys. Chem. B*, 114, 16503–16516, doi:10.1021/jp108459r, 2010.
- Veres, P., Roberts, J. M., Burling, I. R., Warneke, C., de Gouw, J., and Yokelson, R. J.: Measurements of gas-phase inorganic and organic acids from biomass fires by negative-ion proton-transfer chemical-ionization mass spectrometry, *J. Geophys. Res.*, 115, D23302, doi:10.1029/2010JD014033, 2010.

Appendix G

Secondary Organic Aerosol Yields of 12-Carbon Alkanes⁹

⁹ Reproduced by permission from “Secondary organic aerosol yields of 12-carbon alkanes” by C. L. Loza, J. S. Craven, L. D. Yee, M. M. Coggon, R. H. Schwantes, M. Shiraiwa, X. Zhang, K. A. Schilling, N. L. Ng, M. R. Canagaratna, P. J. Ziemann, R. C. Flagan, and J. H. Seinfeld. *Atmos. Chem. Phys.* **2014**, *14*, 1423-1439.



Secondary organic aerosol yields of 12-carbon alkanes

C. L. Loza¹, J. S. Craven¹, L. D. Yee², M. M. Coggon¹, R. H. Schwantes², M. Shiraiwa^{1,3}, X. Zhang², K. A. Schilling¹, N. L. Ng⁴, M. R. Canagaratna⁵, P. J. Ziemann⁶, R. C. Flagan^{1,2}, and J. H. Seinfeld^{1,2}

¹Division of Chemistry and Chemical Engineering, California Institute of Technology, Pasadena, CA, USA

²Division of Engineering and Applied Science, California Institute of Technology, Pasadena, CA, USA

³Multiphase Chemistry Department, Max Planck Institute for Chemistry, Mainz, Germany

⁴School of Chemical and Biomolecular Engineering and School of Earth and Atmospheric Sciences, Georgia Institute of Technology, Atlanta, GA, USA

⁵Aerodyne Research, Inc., Billerica, MA, USA

⁶Air Pollution Research Center, Department of Environmental Sciences, and Environmental Toxicology Graduate Program, University of California, Riverside, CA, USA

Correspondence to: J. H. Seinfeld (seinfeld@caltech.edu)

Received: 29 June 2013 – Published in Atmos. Chem. Phys. Discuss.: 7 August 2013

Revised: 13 December 2013 – Accepted: 23 December 2013 – Published: 7 February 2014

Abstract. Secondary organic aerosol (SOA) yields were measured for cyclododecane, hexylcyclohexane, *n*-dodecane, and 2-methylundecane under high-NO_x conditions, in which alkyl proxy radicals (RO₂) react primarily with NO, and under low-NO_x conditions, in which RO₂ reacts primarily with HO₂. Experiments were run until 95–100% of the initial alkane had reacted. Particle wall loss was evaluated as two limiting cases using a new approach that requires only suspended particle number-size distribution data and accounts for size-dependent particle wall losses and condensation. SOA yield differed by a factor of 2 between the two limiting cases, but the same trends among alkane precursors were observed for both limiting cases. Vapor-phase wall losses were addressed through a modeling study and increased SOA yield uncertainty by approximately 30%. SOA yields were highest from cyclododecane under both NO_x conditions. SOA yields ranged from 3.3% (dodecane, low-NO_x conditions) to 160% (cyclododecane, high-NO_x conditions). Under high-NO_x conditions, SOA yields increased from 2-methylundecane < dodecane ~ hexylcyclohexane < cyclododecane, consistent with previous studies. Under low-NO_x conditions, SOA yields increased from 2-methylundecane ~ dodecane < hexylcyclohexane < cyclododecane. The presence of cyclization in the parent alkane structure increased SOA yields, whereas the presence of branch points decreased SOA yields due to increased vapor-phase fragmentation.

Vapor-phase fragmentation was found to be more prevalent under high-NO_x conditions than under low-NO_x conditions. For different initial mixing ratios of the same alkane and same NO_x conditions, SOA yield did not correlate with SOA mass throughout SOA growth, suggesting kinetically limited SOA growth for these systems.

1 Introduction

Alkanes are emitted from combustion sources and can comprise up to 90% of anthropogenic emissions in urban areas (Rogge et al., 1993; Fraser et al., 1997; Schauer et al., 1999, 2002) and 67.5%, 56.8%, and 82.8% of the mass of diesel fuel, liquid gasoline, and non-tailpipe gasoline sources, respectively (Gentner et al., 2012). Upon atmospheric oxidation by OH and NO₃ radicals, alkanes form lower-volatility products that can condense as secondary organic aerosol (SOA). Ambient lifetimes against reaction with OH range, for example, from 0.5 days for *n*-hexadecane to 1.4 days for *n*-octane (Atkinson and Arey, 2003; Seinfeld and Pandis, 2006), allowing for the transport of alkanes from urban to rural areas.

SOA formation under high-NO_x conditions, in which alkyl proxy radicals (RO₂) react primarily with NO, has received much attention. Lim and Ziemann (2005, 2009a, c) developed a mechanism for linear, branched, and cyclic alkane

oxidation that includes the formation of multi-generation oxidation products. SOA yields, defined as mass of SOA formed divided by mass of alkane reacted, have been measured in the laboratory for C₇–C₂₅ alkanes with linear, branched, and cyclic structures (Lim and Ziemann, 2005, 2009b; Presto et al., 2010; Tkacik et al., 2012). In these studies, SOA yields are reported after 50–85 % of the alkane had reacted and may not represent the maximum possible yield. Generally, SOA yield was found to increase with increasing carbon number or the presence of a cyclic structure and decrease with branching of the carbon chain.

SOA formation under low-NO_x conditions, in which RO₂ reacts primarily with HO₂, has received less attention. Yee et al. (2012, 2013) developed an oxidation mechanism for *n*-dodecane and extended it to cyclic and branched compounds. Yee et al. (2012, 2013) also identified multiple generations of alkane oxidation products, and Craven et al. (2012) used positive matrix factorization to demonstrate continuous evolution of the chemical composition of SOA generated during 36 h of low-NO_x dodecane photooxidation. SOA yields for select linear and cyclic structures have been measured, and the same trends for carbon number and presence of a cyclic structure were observed under low-NO_x conditions as under high-NO_x conditions (Lambe et al., 2012).

Here we report SOA yields from 12-carbon alkanes with linear, cyclic, and branched structures under both high- and low-NO_x conditions. In each experiment, 95–100 % of the alkane, a greater percentage than those achieved in previous chamber studies, was oxidized to study the contribution of multi-generation products to SOA yield. Additionally, multiple alkane mixing ratios were used to assess the effect of precursor mixing ratio on gas-particle partitioning.

2 Materials and methods

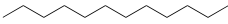
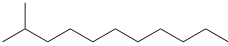
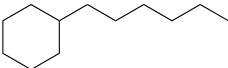

2.1 Experimental setup

Low-NO_x experiments were conducted in the Caltech dual 28 m³ Teflon chambers, details of which are given elsewhere (Cocker et al., 2001; Keywood et al., 2004). High-NO_x experiments were conducted in the Caltech dual 24 m³ Teflon chambers, located in a new facility that replaced the 28 m³ chamber facility. Most components of the old facility, including instrumentation, were moved to the new laboratory, which provides precise temperature control of the chambers (± 1 °C) and flushing at a rate approximately 3 times faster than that in the 28 m³ chamber facility. The difference in chamber volume is not expected to influence the experiment outcomes. Before each experiment, the chambers were flushed with dried, purified air for > 24 h, until the particle number concentration was < 50 cm⁻³ and the volume concentration was < 0.1 $\mu\text{m}^3 \text{cm}^{-3}$. First, hydrogen peroxide (H₂O₂, 50 % wt., Sigma Aldrich) was added to the chamber by flowing purified air over a measured volume of H₂O₂

in a glass bulb maintained at 30–35 °C. Volumes of 70 and 280 μL were used for high-NO_x and low-NO_x experiments, respectively. Next, seed particles were injected by atomizing a 0.015 M aqueous ammonium sulfate solution. *n*-Dodecane (Sigma Aldrich, 99+ % purity), 2-methylundecane (TCI, America, > 98 % purity), or hexylcyclohexane (TCI, America, > 98 % purity) was introduced into the chamber by evaporating a known alkane liquid volume with 5 L min⁻¹ of purified air. Cyclododecane (TCI, America, > 99 % purity) was introduced into the chamber by evaporating a known cyclododecane mass with 5 L min⁻¹ of purified air. During each injection, the glass bulb containing the liquid or solid alkane was heated slightly to facilitate evaporation. For high-NO_x experiments, approximately 100 ppbv NO was then added to the chamber from a 510 ppmv NO in N₂ cylinder (Air Liquide). The chamber contents were allowed to mix for 1 h before beginning irradiation with 350 nm-centered UV broadband lamps (40 W Sylvania 350BL). Different light intensities were used for low- and high-NO_x experiments corresponding to $j_{\text{NO}_2} \sim 4 \times 10^{-3} \text{ s}^{-1}$ and $\sim 6 \times 10^{-3} \text{ s}^{-1}$, respectively. To maintain high-NO_x conditions, 20 sccm of 510 ppmv NO was continuously injected into the chamber during the irradiation period. This additional ~ 21 L of N₂ has a negligible effect on chamber volume. The chamber contents were irradiated for 18 h and 30–36 h for high- and low-NO_x experiments, respectively, to achieve similar OH exposures in all experiments.

A suite of instruments was used to study the evolution of the gas and particle phases. Alkane mixing ratios were measured using a gas chromatograph with flame ionization detector (GC/FID, Agilent 6890N), equipped with a HP-5 column (15 m \times 0.53 mm ID \times 1.5 μm thickness, Agilent). Samples for injection into the GC/FID were taken by drawing 1.3 L of chamber air at a flow rate of 0.13 L min⁻³ through a glass tube packed with Tenax TA resin. The glass tube was subsequently desorbed for 10 min in the inlet of the GC/FID at 260 and 275 °C for low- and high-NO_x experiments, respectively, onto the column, held at 30 °C. After 15 min, the oven temperature was ramped at 10 °C min⁻¹ to 280 °C and held at that temperature for 5 min. The mass response of the detector was calibrated for each alkane using Tenax tubes spiked with standard solutions and analyzed using the same method as the sample tubes. Relative humidity (RH), temperature, NO, NO_x, and O₃ were continuously monitored. Alkane oxidation products were detected using a custom-modified Varian 1200 triple-quadrupole chemical ionization mass spectrometer (CIMS). Details of operation can be found elsewhere (Crounse et al., 2006; Paulot et al., 2009; Yee et al., 2012, 2013). The CIMS was operated in negative mode in which CF₃O⁻ is used as the reagent ion. CF₃O⁻ clusters with the analyte, R, forming ions [R · CF₃O]⁻ at mass-to-charge ratio (m/z) [M+85]⁻, where M is the nominal weight of R. For acidic species, the transfer product forms ions [R · F]⁻ at m/z [M+19]⁻. Some analytes can be seen in both the cluster and

Table 1. SOA precursor and aerosol properties.

Alkane	Structure	$k_{\text{OH}} \times 10^{12\text{a}}$ ($\text{cm}^3 \text{s}^{-1}$)	High- NO_x SOA density ^b (g cm^{-3})	Low- NO_x SOA density ^b (g cm^{-3})
<i>n</i> -Dodecane (Dod)		13.9 ^c	1.28 ± 0.01	1.12 ± 0.03
2-Methylundecane (Mud)		13.1 ± 0.7	1.28 ± 0.01	1.12 ± 0.03
Hexylcyclohexane (Hch)		17.4 ± 0.6	1.29 ± 0.01	1.17 ± 0.03
Cyclododecane (Cdd)		14.7 ± 0.4	1.23 ± 0.02	1.28 ± 0.03

^a Measured from a relative rate experiment at 297 K using dodecane as the reference compound. One standard deviation is given for each rate constant.

^b SOA densities were calculated during nucleation experiments by comparing the diameter of the SOA measured by the DMA to that measured by the AMS. One standard deviation is given for each value.

^c Jordan et al. (2008) for 298 K.

transfer product forms. The signal at each m/z represents the sum of signals from all isomers contributing to that m/z .

Aerosol size distribution and number concentration were measured continuously using a custom-built scanning mobility particle sizer consisting of a differential mobility analyzer (DMA, TSI, 3081) coupled to a condensation particle counter (CPC, TSI, 3010), henceforth referred to as the DMA. The DMA was operated in a closed-loop configuration with a recirculating sheath and excess flow of 2.67 L min^{-1} and a 5.4 : 1 ratio of sheath to aerosol flow rates. The column voltage was scanned either from 10 to 1000 V over 100 s or 15 to 9850 V over 45 s.

Real-time particle mass spectra were collected continuously by an Aerodyne high-resolution time-of-flight aerosol mass spectrometer (AMS, DeCarlo et al., 2006; Canagaratna et al., 2007). The AMS switched between the higher resolution, lower sensitivity “W-mode” and the lower resolution, higher sensitivity “V-mode”. AMS data were processed using the ToF-AMS Unit Resolution Analysis Toolkit, “SQUIRREL” (<http://cires.colorado.edu/jimenez-group/ToFAMSResources/ToFSoftware/index.html>), in Igor Pro Version 6.31 (Wavemetrics, Lake Oswego, OR). “V-mode” data were analyzed using fragmentation table to separate sulfate, ammonium, and organic spectra and to time-trace specific mass-to-charge ratios (Allan et al., 2004). “V-mode” and “W-mode” data were analyzed using the high-resolution spectra toolbox known as PIKA (Peak Integration by Key Analysis) to determine the chemical formulas contributing to distinct m/z ratios (DeCarlo et al., 2006). Organic ions up to m/z 305 were used to calculate elemental ratios. Craven et al. (2012) proposed formulas for organic ions with $m/z > 100$ observed for low- NO_x dodecane photooxidation SOA based on hypothesized fragmentation of products formed in the dodecane photooxidation mechanism (Yee

et al., 2012). Similar analysis was applied to identify organic ions with $m/z > 100$ for SOA from all 4 alkanes investigated here under both low- and high- NO_x conditions. Organic ions CO^+ and C_2H_4^+ were not fit in “V-mode” due to the large interference from the N_2^+ peak, and their signals were estimated from those of particle-phase CO_2^+ and C_2H_3^+ , respectively, using correlations determined from “W-mode” data, which has better resolution of the CO^+ , N_2^+ , and C_2H_4^+ peaks. The ratio of particle-phase CO^+ to CO_2^+ varied by experiment between 0.45 and 3.5, and a specific ratio was used for each experiment (see Table S1). The ratio of C_2H_4^+ to C_2H_3^+ was found to be 0.47 for SOA from dodecane, 2-methylundecane, and hexylcyclohexane and 0.40 for SOA from cyclododecane under both NO_x conditions. Additionally, the intensities of H_2O^+ , OH^+ , and O^+ were calculated from particle-phase CO_2^+ (Aiken et al., 2008). AMS data reported in this work were collected using “V-mode” and averaged over 1 h or 30 min intervals for low- or high- NO_x experiments, respectively.

Experimental OH concentrations were calculated from the measured alkane mixing ratio, the alkane concentration decay rate, estimated from the alkane mixing ratio fit to a differentiable function (typically, a 1- or 2-term exponential function), and the alkane + OH reaction rate constant. A literature OH reaction rate constant was available only for dodecane; rate constants for the other three alkanes were estimated from a relative rate experiment in which 10 ppbv of each alkane was oxidized simultaneously under low- NO_x conditions (Table 1). The measured rate constant for hexylcyclohexane is in good agreement with that calculated from structure–activity relationships (Kwok and Atkinson, 1995), $17.6 \times 10^{-12} \text{ cm}^3 \text{ molec}^{-1} \text{ s}^{-1}$, and the measured rate constants for 2-methylundecane and cyclododecane are lower than those calculated from structure–activity relationships,

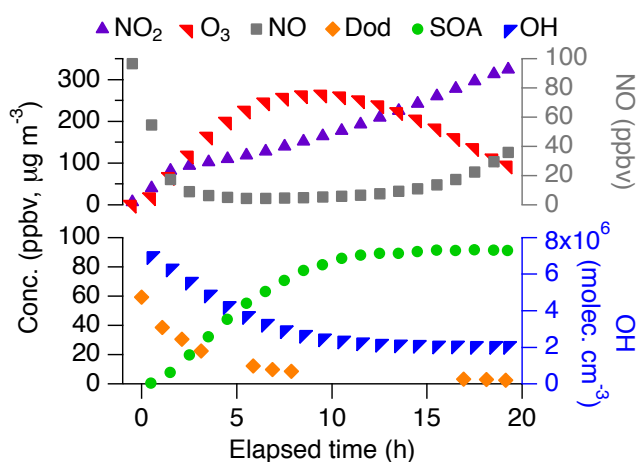


Fig. 1. Temporal trends of gas-phase species and SOA mass concentration during a typical high- NO_x experiment. On the left axis, SOA mass concentration (lower limit) is reported in $\mu\text{g m}^{-3}$, and dodecane, O_3 , and NO_2 mixing ratios are reported in ppbv. NO and OH concentrations are given on the right axis. NO_2 , O_3 , NO , SOA mass, and OH concentrations are hourly averaged. Data are shown for the 57 ppbv dodecane experiment, DH2 (see Table 2). OH concentration was calculated from the dodecane decay.

13.9×10^{-12} and $17.0 \times 10^{-12} \text{ cm}^3 \text{ molec}^{-1} \text{ s}^{-1}$, respectively. To calculate OH exposure, an interpolated OH concentration with a time resolution of 2–3 min is calculated from a fit to experimental data, as described previously, the alkane mixing ratio decay rate, and the alkane + OH reaction rate constant. The interpolated OH concentration is multiplied by the time between data points and summed to each time point to obtain OH exposure.

Photolysis of H_2O_2 under low- NO_x conditions produced a constant OH radical concentration of $(1\text{--}3) \times 10^6 \text{ molec cm}^{-3}$. Under high- NO_x conditions, OH radicals also were produced throughout the entire irradiation period, 18 h, with initial concentrations of $(0.7\text{--}3) \times 10^7 \text{ molec cm}^{-3}$ that decreased steadily to $(1\text{--}5) \times 10^6 \text{ molec cm}^{-3}$ after 18 h. In addition, reaction of HO_2 radicals with NO produced NO_2 , which photolyzed to produce O_3 . O_3 mixing ratios peaked at 200–600 ppbv approximately halfway through the experiment and then decreased as NO was continuously injected into the chamber. The variance in O_3 mixing ratio is not expected to affect SOA formation mechanisms and is discussed below. Typical vapor mixing ratios and SOA growth for a high- NO_x experiment (59 ppbv dodecane) are shown in Fig. 1.

Three oxidants, OH , O_3 , and NO_3 , were produced under high- NO_x conditions. All oxidant concentrations varied during the experiment due to the continuous addition of NO . While O_3 is not expected to react with most alkane photooxidation products, it can react with dihydrofurans, which also react with OH and NO_3 . Variation in O_3 mixing ratios amongst the experiments could influence SOA yields by af-

fecting the fate of dihydrofurans. In the present experiments, the ratios of dihydrofuran sinks were determined by comparing the lifetimes for dihydrofuran against reaction with OH , O_3 , and NO_3 at experimental conditions. Jordan et al. (2008) estimated C_{12} dihydrofuran + OH rate constants as approximately $2.4 \times 10^{-13} \text{ cm}^3 \text{ molec}^{-1} \text{ s}^{-1}$. The rate constants for C_{12} dihydrofuran + O_3 and C_{12} dihydrofuran + NO_3 were taken as 3.49×10^{-15} and $1.68 \times 10^{-10} \text{ cm}^3 \text{ molec}^{-1} \text{ s}^{-1}$, respectively, as measured for 4,5-dihydro-2-methylfuran by Martin et al. (2002). O_3 mixing ratios were measured directly, OH concentrations were calculated from the alkane mixing ratio decay, and NO_3 concentrations were estimated from a photochemical model. The lifetime for dihydrofuran against reaction with O_3 was calculated to be at least an order of magnitude less than that against reaction with OH for all experimental conditions, and the variation in O_3 mixing ratios amongst the experiments had little effect on the fate of dihydrofurans. For the highest estimated NO_3 concentration ($1 \times 10^7 \text{ molec cm}^{-3}$), the lifetime for dihydrofuran against reaction with NO_3 was comparable to that against reaction with O_3 , and at the lowest estimated concentration, the lifetime for dihydrofuran against reaction with NO_3 was an order of magnitude larger than that against reaction with OH . In an urban area such as Mexico City with maximum OH , O_3 , and NO_3 (daytime) concentrations of 4.6×10^6 , $(0.74\text{--}2.0) \times 10^{12}$, and $2.4 \times 10^7 \text{ molec cm}^{-3}$, respectively (Molina et al., 2010; Stephens et al., 2008; Volkamer et al., 2010), the estimated lifetimes for dihydrofuran against reaction with these compounds are 15 min, 2.4–6.4 min, and 4.1 min, respectively. The conditions in the present experiments produce atmospherically relevant ratios of dihydrofuran sinks. Additionally, NO_3 was not a significant sink of either the parent alkane or RO_2 radicals even at the largest estimated NO_3 mixing ratio.

2.2 SOA yield calculations

Particles deposited to the chamber walls are accounted for when calculating the mass concentration of organic aerosol formed. Particle wall-loss corrections were made using the two limiting assumptions of gas-particle partitioning (Weitkamp et al., 2007; Hildebrandt et al., 2009; Loza et al., 2012). In one limit, no suspended vapors are assumed to condense on deposited particles. This limit is termed the lower limit because it represents the smallest possible SOA mass formed during growth. In the other limit, deposited particles are assumed to interact with suspended vapors to the same extent as suspended particles. This limit is termed the upper limit because it represents the largest possible SOA mass formed during growth. A new approach to calculate both upper and lower limit wall loss solely from suspended particle number-size distribution data is described in Appendix A. This approach is an extension of the Aerosol Parameterization Estimation model (Pierce et al., 2008) to calculate both limits to particle wall-loss corrections. Total particle volume

concentration was calculated from the wall-loss corrected number-size distributions. To obtain SOA mass concentration, the seed particle volume concentration was subtracted from the total particle volume concentration, and the resulting organic particle volume concentration was multiplied by the SOA density, calculated from DMA and AMS data from a separate experiment (see Table 1).

SOA yield, Y , was calculated for both upper and lower limit SOA mass concentrations, ΔM_o ($\mu\text{g m}^{-3}$), using

$$Y = \frac{\Delta M_o}{\Delta\text{HC}}, \quad (1)$$

where ΔHC ($\mu\text{g m}^{-3}$) is the mass concentration of alkane reacted.

In addition to particle-phase wall losses, vapor-phase wall losses of 12-carbon alcohols and ketones have been observed in laboratory chambers (Matsunaga and Ziemann, 2010). If vapors condense on chamber walls instead of on particles, then SOA yields will be underestimated. Vapor wall losses were not taken into account for the yields presented here; the effect of vapor wall losses on SOA yields is discussed in Appendix B.

3 Results and discussion

For most SOA precursors, a larger initial hydrocarbon mixing ratio results in a larger source of semivolatile oxidation products, assuming that reactions occur at the same temperature and oxidizing conditions and that the vapor-phase product distributions do not vary over the range of initial hydrocarbon mixing ratios considered. The presence of more condensible products facilitates partitioning of semivolatile product species to the particle phase, leading to increased yields relative to lower mixing ratio experiments. Oxidant exposure also affects SOA yield. SOA yield increases with increasing oxidant exposure as the hydrocarbon reacts forming multiple generations of semivolatile products; however, with ever-increasing oxidation, fragmentation reactions will begin to dominate over functionalization reactions, producing volatile products that do not condense or evaporate from the condensed phase and decreasing SOA yield.

3.1 High- NO_x SOA yield measurements

Conditions for high- NO_x experiments are given in Table 2. The reported ΔM_o and yield correspond to approximately 18 h of irradiation and an OH exposure of $(6\text{--}12) \times 10^7$ molec cm^{-3} h. By this point, at least 95 % of the initial hydrocarbon had reacted. SOA growth occurred continuously as the alkane reacted. Figure 2a shows the SOA yield after approximately 18 h of irradiation as a function of hydrocarbon concentration reacted. The top and bottom of each line correspond to the upper and lower limits to the particle wall-loss correction, respectively. Experiments were

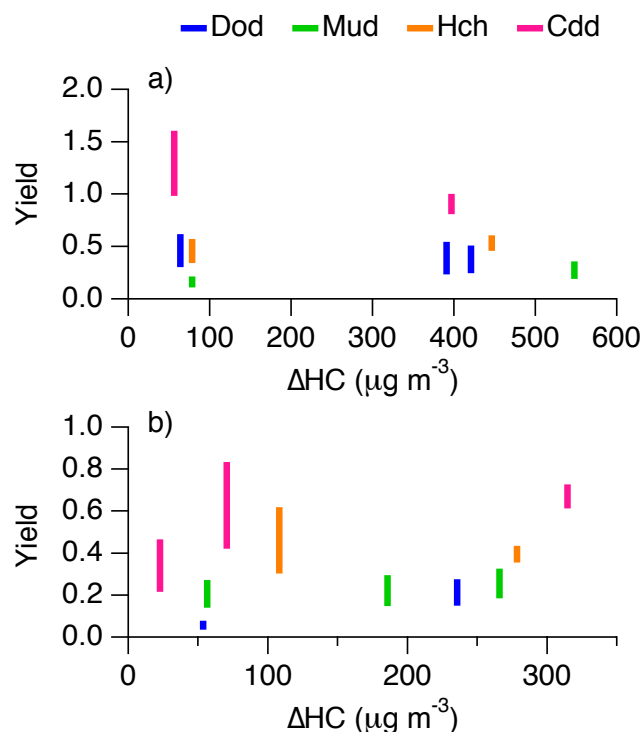


Fig. 2. SOA yield at 95–100 % of initial hydrocarbon reacted under (a) high- and (b) low- NO_x conditions. Each line shows the range between the lower limit (deposited particles do not undergo gas-particle partitioning) and upper limit (gas-particle partitioning to deposited particles is the same as that to suspended particles) SOA yields for an experiment.

run with approximately 10 ppbv ($100 \mu\text{g m}^{-3}$) or 60–80 ppbv ($400\text{--}550 \mu\text{g m}^{-3}$) initial alkane mixing ratio. In both initial alkane concentration regimes, cyclododecane produced the largest yields, while the smallest yields were observed for 2-methylundecane. Dodecane and hexylcyclohexane yields were similar. These results are consistent with the relationship between alkane structure and SOA yield observed by Lim and Ziemann (2009b) and Tkacik et al. (2012). When comparing the yields for each compound between the two initial hydrocarbon concentration regimes, no clear patterns emerge. For 2-methylundecane and hexylcyclohexane, the yield increases as initial alkane concentration increases. For dodecane and cyclododecane, the yield decreases as initial alkane concentration increases. This behavior will be discussed further in Sect. 3.4.

For cyclododecane and hexylcyclohexane, a large difference between upper and lower limit yields is observed in Fig. 2 for experiments with $\Delta\text{HC} < 100 \mu\text{g m}^{-3}$. These experiments had approximately 10 ppbv initial alkane. For experiments shown in Fig. 2 with $\Delta\text{HC} > 100 \mu\text{g m}^{-3}$, those with 60–80 ppbv initial alkane, SOA growth began soon after the onset of irradiation, increasing the suspended particle number-size distribution peak diameter to 250–350 nm.

Table 2. High-NO_x experimental details.

Expt. ^a	Alkane	Seed vol. ($\mu\text{m}^3 \text{cm}^{-3}$)	NO _o ^b (ppbv)	NO _{2,o} ^b (ppbv)	HC _o (ppbv)	ΔHC (ppbv)	ΔM_o^c ($\mu\text{g m}^{-3}$)	Yield ^c (frac.)
MH1	Mud	31.7 ± 9.5	94.1 ± 0.5	6.6 ± 0.2	11.6 ± 0.4	11.6	8.5–17	0.11–0.21
MH2	Mud	41.6 ± 12.5	97.7 ± 0.5	5.8 ± 0.2	79.6 ± 2.5	79.1	100–200	0.19–0.38
DH1	Dod	30.9 ± 9.3	93.8 ± 0.5	6.3 ± 0.2	9.7 ± 0.3	9.2	19–40	0.30–0.62
DH2	Dod	26.1 ± 7.8	96.8 ± 0.5	7.1 ± 0.2	59.2 ± 1.9	56.8	91–210	0.23–0.54
DH3	Dod	30.4 ± 9.1	96.5 ± 0.5	6.1 ± 0.2	63.6 ± 2.0	61.2	100–210	0.22–0.51
HH1	Hch	34.1 ± 10.2	101 ± 0.5	2.6 ± 0.2	11.5 ± 0.4	11.5	27–45	0.34–0.57
HH2	Hch	40.0 ± 12.0	95.4 ± 0.5	2.9 ± 0.2	65.0 ± 2.1	64.9	210–270	0.46–0.61
CH1	Cdd	38.7 ± 11.6	95.6 ± 0.5	6.8 ± 0.2	8.5 ± 0.3	8.5	56–91	0.98–1.6
CH2	Cdd	37.7 ± 11.3	93.4 ± 0.5	7.9 ± 0.2	61.0 ± 2.0	58.6	320–400	0.80–1.0

^a The first letter of each experiment identifier refers to the alkane, and the second letter refers to high- (H) or low- (L) NO_x conditions.

^b One standard deviation is reported, as measured by the instrument manufacturer.

^c The range of values listed correspond to the two limiting assumptions for suspended vapor-deposited particle gas-particle partitioning. The smaller and larger values correspond to the upper and lower partitioning limits, respectively.

During the experiments with ~ 10 ppbv initial alkane, SOA growth did not begin immediately, and the suspended particle number-size distribution peak diameter remained below 200 nm for most of the experiment. The temporal trend of suspended particle number-size distribution peak diameter for the high-NO_x cyclododecane experiments is shown in Fig. S1. In the Caltech chambers, particle wall-loss rate constants are lowest for 200–300 nm particles (Fig. S1, right panel). Typical seed particle number-size distribution peak diameters are 40–60 nm. Because particle growth is slower in ~ 10 ppbv initial alkane experiments and particles remain at a smaller diameter for longer times, more particles are lost to the wall before and during SOA growth in ~ 10 ppbv initial alkane experiments than in those with 60–80 ppbv initial alkane, owing to the size-dependence of particle wall loss. Therefore, a large difference between lower and upper limit yields is observed for the ~ 10 ppbv initial alkane experiments. The difference between upper and lower limit yields for dodecane and 2-methylundecane is similar for all ΔHC . Less overall SOA growth is observed for dodecane and 2-methylundecane; as a result, less difference is observed between the lower and upper limit yields.

SOA yields from cyclododecane were close to or greater than 1 depending on the wall-loss correction method used. SOA yields can be > 1 if most of the functionalized oxidation products generated from a non-functionalized parent hydrocarbon condense to form SOA. SOA yields > 1 have been observed previously from longifolene photooxidation under high-NO_x conditions (Ng et al., 2007a). To determine if the SOA mass produced violated mass conservation, an estimation of maximum potential SOA mass concentration was calculated assuming that all oxidation products formed from the reacted cyclododecane condensed. For the estimation, the average SOA molecular weight was calculated from the oxygen-to-carbon (O : C), hydrogen-to-carbon (H : C), and nitrogen-to-carbon (N : C) ratios measured by the AMS, as-

suming that condensed species retain 12 carbon atoms. Note that ions NO⁺ and NO₂⁺ are included in these calculations and will be discussed further in Sect. 3.4. To calculate the maximum potential SOA mass concentration, the molar concentration of cyclododecane reacted is multiplied by the average SOA molecular weight. This SOA mass concentration is then compared to the observed SOA mass concentration. For experiment CH1 (cyclododecane), the maximum potential SOA formed was $84 \mu\text{g m}^{-3}$, which is greater than the lower wall-loss limit ΔM_o but less than the upper wall-loss limit ΔM_o . For experiment CH2 (cyclododecane), the maximum potential SOA formed was $519 \mu\text{g m}^{-3}$, which is greater than both the lower and upper bound limit ΔM_o . All observed cyclododecane yields except for the upper wall-loss limit yield for CH1 do not violate mass conservation. It is likely that uncertainties in deposited particle growth rates calculated in the upper limit wall-loss correction method (see Appendix A) cause the upper limit yield for CH1 to be overestimated.

Previous studies exist of SOA yields under high-NO_x conditions for dodecane, 2-methylundecane, and cyclododecane. Lim and Ziemann (2009b) measured SOA yields for all three compounds with initial alkane mixing ratios of approximately 1 ppmv, of which 76–83 % was oxidized at the point at which yields were calculated. In the present work, yields were calculated for lower initial alkane mixing ratios with a larger fraction of the initial alkane reacted. Because higher initial alkane mixing ratio and lower extent of alkane reacted have opposite effects on SOA yield that are difficult to decouple, comparison of absolute measurements between Lim and Ziemann (2009b) and the present work are not instructive. Presto et al. (2010) reported SOA yields for dodecane oxidation for 19.1 and 57.8 ppbv initial alkane, and Tkacik et al. (2012) reported SOA yields from 2-methylundecane oxidation for a low alkane mixing ratio (initial alkane mixing ratios were not specified). Both studies parameterized yields using the volatility basis set (VBS)

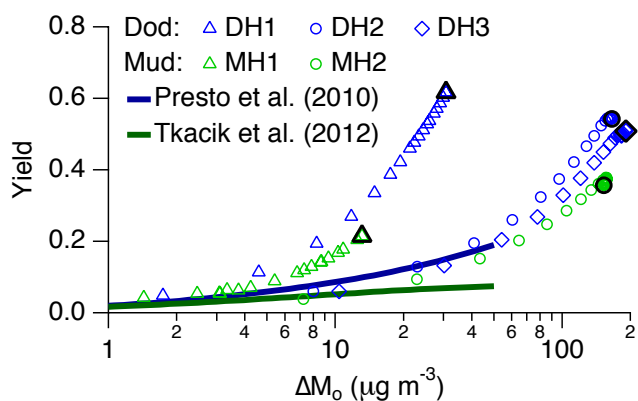


Fig. 3. Comparison of SOA yields as a function of organic aerosol mass concentration, ΔM_o , observed in the present study with those reported in previous studies. For the present study, final yields (after 95–100 % alkane reacted) are denoted by the black markers.

for $\Delta M_o < 50 \mu\text{g m}^{-3}$. A comparison of the present work to these studies is shown in Fig. 3. Both Presto et al. (2010) and Tkacik et al. (2012) report the upper limit to particle wall losses. For comparison to these previous studies, the upper limit to particle wall losses and a unit SOA density were used to calculate yields for experiments DH1, DH2, DH3, MH1, and MH2 shown in Fig. 3. The dodecane VBS parameterization presented by Presto et al. (2010) matches the higher final ΔM_o dodecane experiments, DH2 and DH3, for $\Delta M_o < 50 \mu\text{g m}^{-3}$; however, it does not match the lower final ΔM_o dodecane experiment, DH1. This discrepancy can be attributed to different OH exposure. Presto et al. (2010) achieved an OH exposure of approximately $1.2 \times 10^7 \text{ molec cm}^{-3} \text{ h}$ and did not react all of the parent alkane, whereas OH exposure in the present experiments was approximately $7 \times 10^7 \text{ molec cm}^{-3} \text{ h}$ and at $> 95\%$ of the parent alkane reacted. Similar results are observed when comparing 2-methylundecane yields from Tkacik et al. (2012) with those in the present study. The OH exposure achieved in Tkacik et al. (2012), $6 \times 10^6 \text{ molec cm}^{-3} \text{ h}$, was also lower than that achieved in the present work.

3.2 Low- NO_x SOA yield measurements

Conditions for low- NO_x experiments are presented in Table 3. ΔM_o and SOA yield measurements are reported after 30–36 h irradiation, corresponding to OH exposures of $(6\text{--}12) \times 10^7 \text{ molec cm}^{-3} \text{ h}$, for which at least 95 % of the initial alkane reacted. Figure 2b shows the SOA yield after 30–36 h irradiation, and, as for the high- NO_x data, the top and bottom of each line correspond to the upper and lower limits to the particle wall-loss correction, respectively. The highest yields are observed for cyclododecane, followed by hexylcyclohexane, with the yields for dodecane and 2-methylundecane being similar. The ordering of hexylcyclohexane, dodecane, and 2-methylundecane yields is different

from that observed under high- NO_x conditions and will be discussed further in Sect. 3.4. As with the high- NO_x yields, there are no compound-specific trends for SOA yield with initial alkane concentration.

SOA yields under low- NO_x conditions have not been reported previously for the compounds studied here. SOA yields under low- NO_x conditions have been reported for *n*-decane and *n*-pentadecane in a Potential Aerosol Mass flow reactor (Lambe et al., 2012). Lambe et al. (2012) reported maximum yields of 0.39 and 0.69 at OH exposures of 1.4×10^8 and $9.7 \times 10^7 \text{ molec cm}^{-3} \text{ h}$ and SOA concentrations of 231 and $100 \mu\text{g m}^{-3}$ for decane and pentadecane, respectively. The dodecane SOA yield is expected to lie between those for longer and shorter chain alkanes; however, the dodecane SOA yields measured in the present study (Table 3) are less than that measured for $231 \mu\text{g m}^{-3}$ decane, a much larger initial concentration than those used in the present experiments, by Lambe et al. (2012) at similar OH exposure. Lambe et al. (2012) note that the maximum SOA yield for pentadecane at $16 \mu\text{g m}^{-3}$ is 0.21, which is in much better agreement with the dodecane SOA concentrations and SOA yields in the present study.

3.3 SOA growth parameterization

In Fig. 3, it is interesting to note that different SOA yields are observed from the same alkane and ΔM_o for different initial alkane mixing ratios (e.g., at $\Delta M_o = 10 \mu\text{g m}^{-3}$, the yield from 9 ppbv dodecane, DH1, is 0.27, whereas the yield from 57–61 ppbv dodecane, DH2 and DH3, is 0.06). This trend is observed for all four compounds under both high- and low- NO_x conditions and suggests that there may be an alternative to parameterizing yields for these alkanes in terms of ΔM_o (i.e., assuming quasi-equilibrium growth).

Shiraiwa et al. (2013) predicted that the behavior of the particle size distribution during low- NO_x dodecane photooxidation is consistent with kinetically limited, rather than quasi-equilibrium, growth. Other ambient and laboratory studies also suggest that SOA growth can be kinetically limited (Riipinen et al., 2011; Perraud et al., 2012). For kinetically limited SOA growth, SOA yield should be a function of total particle surface area; however, for the same alkane and NO_x conditions and a given particle surface area, different SOA yields were observed, similar to the results presented in Fig. 3. Instead, SOA yields were parameterized by number of semivolatile organic compound (SVOC)-particle collisions. Total SVOC concentration was simulated for the case of dodecane low- NO_x photooxidation using a kinetic multi-layer model of gas-particle interactions (KM-GAP) (Shiraiwa et al., 2012; Shiraiwa and Seinfeld, 2012; Shiraiwa et al., 2013). KM-GAP explicitly resolves mass transport and chemical reactions in the gas and particle phases. The cumulative number of SVOC-particle collisions per unit chamber volume, C_{sum} , was calculated from the SVOC concentration and total particle surface area. Details of these calculations

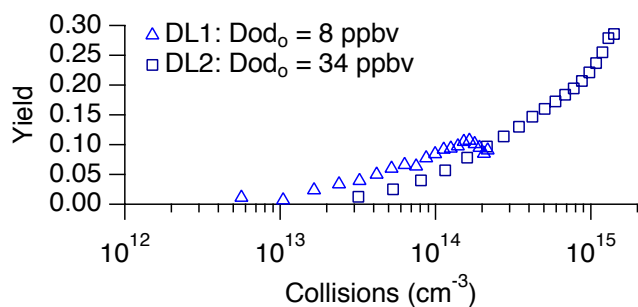
Table 3. Low-NO_x experimental details.

Expt. ^a	Alkane	Seed vol. ($\mu\text{m}^3 \text{cm}^{-3}$)	HC _o (ppbv)	ΔHC (ppbv)	ΔM_o^b ($\mu\text{g m}^{-3}$)	Yield ^b (frac.)
ML1	Mud	21.8 ± 6.5	8.5 ± 0.3	8.4	7.9–15	0.14–0.27
ML2 ^c	Mud	16.7 ± 5.0	28.9 ± 0.9	28.1	28–58	0.15–0.31
ML3	Mud	15.9 ± 4.8	40.2 ± 1.3	38.1	49–86	0.19–0.33
DL1	Dod	16.7 ± 5.0	8.2 ± 0.3	7.9	1.8–4.2	0.033–0.078
DL2 ^c	Dod	12.1 ± 3.6	34.0 ± 1.1	33.6	35–65	0.15–0.28
HL1 ^c	Hch	11.2 ± 3.4	15.6 ± 0.5	15.5	33–70	0.30–0.65
HL2	Hch	20.0 ± 6.0	41.3 ± 1.3	40.8	99–120	0.35–0.44
CL1	Cdd	18.9 ± 5.7	3.5 ± 0.1	3.4	4.9–11	0.22–0.46
CL2 ^c	Cdd	15.3 ± 4.6	10.4 ± 0.3	10.3	30–62	0.42–0.86
CL3	Cdd	21.5 ± 6.5	46.6 ± 1.5	45.1	200–230	0.61–0.73

^a The first letter of each experiment identifier refers to the alkane, and the second letter refers to high- (H) or low- (L) NO_x conditions.

^b The range of values listed corresponds to the two limiting assumptions for suspended vapor-deposited particle gas-particle partitioning. The smaller and larger values correspond to the upper and lower partitioning limits, respectively.

^c Due to chamber volume limitations, these experiments were run in two parts. The initial conditions for the two separate experiments are listed Table S2.

**Fig. 4.** SOA yield (upper limit) as a function of estimated cumulative SVOC-particle collisions per unit chamber volume for low-NO_x dodecane photooxidation experiments.

are given in Appendix C. Figure 4 shows yield as a function of C_{sum} for the dodecane low-NO_x photooxidation system. Calculations were made with a time resolution of 3 min, but hourly averaged data are displayed. The SOA yields from both experiments trend similarly with C_{sum} . This result indicates that analysis of chamber experiments for any SOA system with kinetic-flux modeling is instructive and provides an alternative to parameterizing SOA yields as a function of ΔM_o .

3.4 Aerosol chemical composition

Organonitrates have been identified previously as products from alkane high-NO_x photooxidation and are expected to be present in the particle phase (Lim and Ziemann, 2005). The AMS can detect organic nitrates as NO⁺ and NO₂⁺, but inorganic nitrates also contribute signal to these ions (Farmer et al., 2010). During the high-NO_x experiments, NO⁺ and NO₂⁺ trend with organic growth measured by the AMS. Dur-

ing this time, nitric acid is also formed from reaction of NO₂ with OH and can partition to particles and interact with the ammonium sulfate seed. The ratio of NO⁺ : NO₂⁺ observed during photooxidation experiments is higher than that from AMS ionization efficiency calibrations, in which ammonium nitrate is atomized into the AMS, indicating that the NO⁺ and NO₂⁺ signals are not likely from inorganic nitrates. Because there is evidence that the signals for NO⁺ and NO₂⁺ likely come from organonitrates in the present experiments, these ions are included when calculating the total organic mass from AMS data. According to a proposed decomposition pathway for organonitrates (Francisco and Krylowksi, 2005; Farmer et al., 2010), the oxygens in NO⁺ and NO₂⁺ are not bound directly to a carbon atom. Therefore, the ion signals at NO⁺ and NO₂⁺ were not included in elemental ratios used to calculate average carbon oxidation state.

Average carbon oxidation state, $\overline{\text{OS}}_C$ (Kroll et al., 2011) was calculated from AMS measurements for comparison of the alkane systems. SOA $\overline{\text{OS}}_C$ from each parent alkane showed similar trends with respect to initial alkane mixing ratio, NO_x conditions, and OH exposure; therefore, data only for cyclododecane are shown in Fig. 5. Under both high- and low-NO_x conditions, SOA formed from a lower initial cyclododecane mixing ratio was characterized by a higher $\overline{\text{OS}}_C$. This trend has been observed in other systems (Shilling et al., 2009) and is expected because a higher initial alkane mixing ratio increases the mixing ratios of semivolatile products, which have lower $\overline{\text{OS}}_C$ than low volatility products, in both the gas and particle phases. Under low-NO_x conditions, SOA $\overline{\text{OS}}_C$ decreases for OH exposures of 0– 2×10^7 molec cm⁻³ h and then gradually increases with increasing OH exposure. Other studies have reported similar trends for O : C formed under low-NO_x conditions (Lambe et al., 2012; Loza et al., 2012). This trend is attributed to

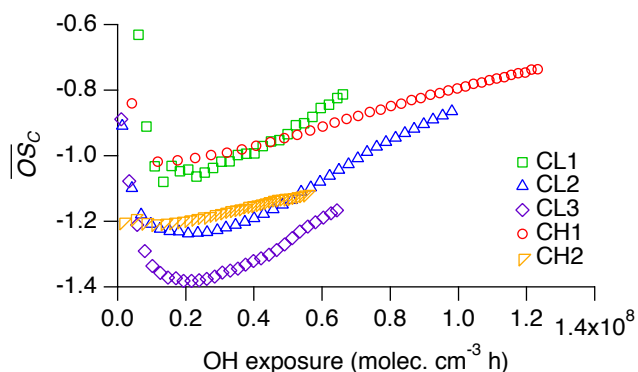


Fig. 5. SOA average carbon oxidation state as a function of OH exposure for high- and low- NO_x cyclododecane photooxidation.

initial condensation of a small amount of low-volatility oxidation products followed by condensation of semivolatile products as the SOA mass increases, and then condensation of more low-volatility products as gas-phase oxidation progresses. Under low- NO_x conditions, over 95% of the aerosol mass measured by the AMS in the present experiments comes from ions with chemical formulae of C_xH_y^+ , $\text{C}_x\text{H}_y\text{O}^+$, and $\text{C}_x\text{H}_y\text{O}_2^+$. Note that for both NO_x conditions, the ions O^+ , HO^+ and H_2O^+ are included in the mass fraction of $\text{C}_x\text{H}_y\text{O}_2^+$ ions because these concentrations of these ions are calculated from that of CO_2^+ . Initially, the contributions of ions with formula C_xH_y^+ are approximately equal to the sum of those with formulae $\text{C}_x\text{H}_y\text{O}^+$ and $\text{C}_x\text{H}_y\text{O}_2^+$, but as OH exposure increases to 2×10^7 molec cm^{-3} h, the contributions from ions with formula C_xH_y^+ begin to dominate, presumably as more semivolatile species condense. At OH exposures above 2×10^7 molec cm^{-3} h, contributions from ions with formulae $\text{C}_x\text{H}_y\text{O}^+$ and $\text{C}_x\text{H}_y\text{O}_2^+$ increase and those with formula C_xH_y^+ decrease but still comprise a majority of the organic mass. For low- NO_x alkane photooxidation, it has been suggested that peroxyhemiacetal formation triggers initial SOA growth (Yee et al., 2012, 2013; Shiraiwa et al., 2013). The hydroperoxides thought to contribute to initial peroxyhemiacetal formation, such as the carbonyl hydroperoxide, have multiple functional groups, which could explain the initial, higher $\overline{\text{OS}}_C$ values. As the particles grow, other, less functionalized oxidation products can also condense, decreasing $\overline{\text{OS}}_C$. As oxidation continued, multiple generations of gas-phase oxidation products, such as hydroxy carbonyl hydroperoxides and dicarbonyl hydroperoxides, were observed in dodecane photooxidation and proposed for cyclododecane photooxidation and also could partition to particles, increasing $\overline{\text{OS}}_C$. Although the proposed SOA products have multiple oxygen moieties, much of the carbon chain is not functionalized, and C_xH_y^+ fragments are expected to dominate the mass spectrum.

Under high- NO_x conditions, an initial decrease in $\overline{\text{OS}}_C$ was not prominent, and the increase in $\overline{\text{OS}}_C$ as OH expo-

sure increased was less when compared to that under low- NO_x conditions. When comparing high- and low- NO_x experiments with similar initial cyclododecane mixing ratio (CL2 with CH1 or CL3 with CH2), SOA formed under high- NO_x conditions has a higher $\overline{\text{OS}}_C$ during SOA growth but similar $\overline{\text{OS}}_C$ after all cyclododecane reacted. These trends indicate that less OH exposure is required to form low-volatility products under high- NO_x conditions than under low- NO_x conditions. A similar trend was observed by Presto et al. (2009), who used a thermodenuder to measure the volatility of heptadecane SOA formed under high- and low- NO_x conditions. The estimated vapor pressures of many of the condensable species produced under high- and low- NO_x dodecane photooxidation are similar (Jordan et al., 2008; Yee et al., 2012), but the experimental conditions control the rate at which these compounds are formed.

Alkane oxidation by OH generates RO_2 , which can react with NO, HO_2 , or another RO_2 . RO_2 can also react with NO_2 , but the peroxy nitrates formed quickly decompose back to RO_2 and NO_2 ; this pathway will not be considered here. In the present experiments, RO_2 reacted primarily with HO_2 under low- NO_x conditions and with NO under high- NO_x conditions. NO mixing ratio was measured directly and varied from 2–100 ppbv, and HO_2 concentration was estimated from a photochemical model as approximately 1×10^{10} cm^{-3} (Yee et al., 2012). Using RO_2 reaction rate constants from the Master Chemical Mechanism 3.2 (<http://mcm.leeds.ac.uk/MCM>; Jenkin et al., 2003; Saunders et al., 2003), the lifetimes of RO_2 reaction with NO and HO_2 are estimated as 0.04–2 and 4 s, respectively. Shorter RO_2 lifetimes under high- NO_x conditions will allow low-volatility products to form at lower OH exposures.

3.5 Effect of gas-phase fragmentation reactions on SOA yield

For a number of SOA systems, SOA yields are higher under low- NO_x conditions than under high- NO_x conditions (e.g., Song et al., 2005; Ng et al., 2007a; Eddingsaas et al., 2012). A likely explanation is that alkoxy radicals (RO) produced from the reaction of alkyl peroxy radicals (RO_2) and NO undergo fragmentation to form higher volatility species, whereas hydroperoxides produced from the reaction of RO_2 and HO_2 do not. With less fragmentation under low- NO_x conditions, the carbon chain is preserved, resulting in higher yields when compared with those observed for high- NO_x conditions. For linear alkanes with > 6 carbons, isomerization of RO is favored over fragmentation reactions or reaction with O_2 , preserving the carbon chain and producing compounds of lower volatility than fragmentation products (Lim and Ziemann, 2009a). As a result, yields under low- and high- NO_x conditions for these larger alkanes are similar, as shown in Fig. 2.

Additional trends between alkane structure, bulk SOA chemical composition, and SOA yield can be observed from

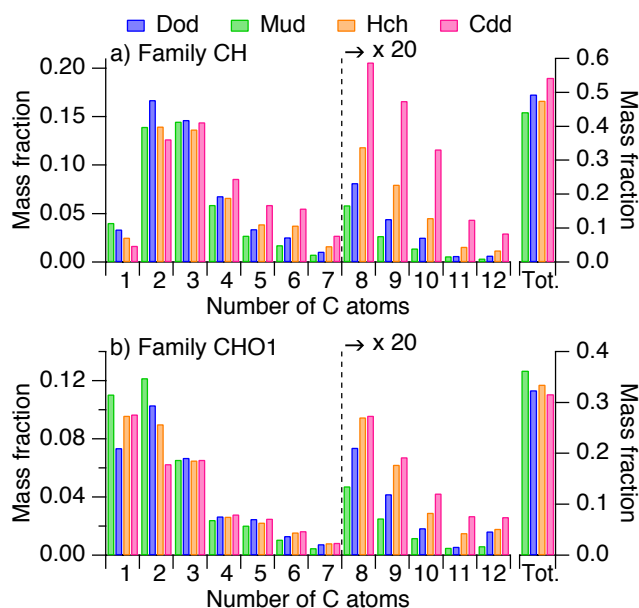


Fig. 6. Contribution of ions detected in the AMS to the bulk organic mass concentration for high- NO_x alkane photooxidation. Ions are grouped into families according to the ion atomic composition and displayed as a function of carbon atoms in the ion. Tot. is the sum over all carbon atom numbers for each family. The data represent a 30 min average of the SOA formed after 95–100% of the initial alkane had reacted. The data presented are from experiments DH2, MH2, HH2, and CH2.

the AMS mass spectra. Ions can be grouped into “families” according to their elemental composition. The mass spectra are dominated by ions in family CH, ions with formula C_xH_y^+ , and family CHO1, ions with formula $\text{C}_x\text{H}_y\text{O}^+$. Figures 6 and 7 show the contribution of ions in each family as a function of the number of carbon atoms in each ion and the total family contribution for a 30 min averaged sample obtained after 95–100% of the initial alkane mixing ratio reacted. Only data from experiments with higher alkane mixing ratio (> 50 ppbv and > 25 ppbv for high- and low- NO_x , respectively) are shown; similar trends were observed in experiments with lower initial alkane mixing ratios. In the present study, an increase in yield is characterized by larger mass fractions of ions containing nine or more carbon atoms for both families CH and CHO1. Pearson’s correlation coefficients for each carbon number are given in Tables S4 and S5 for family CH and family CHO1, respectively. Under high- NO_x conditions, the total mass fractions of family CH ions for cyclododecane and dodecane SOA are higher than those for 2-methylundecane and hexylcyclohexane SOA (Fig. 6a), and the trend is reversed for ions in family CHO1 (Fig. 6b). The same trend is not observed under low- NO_x conditions; although, compounds with a larger mass fraction of family CH ions have smaller mass fractions of family CHO1 ions. These trends provide insight into the significance of gas-

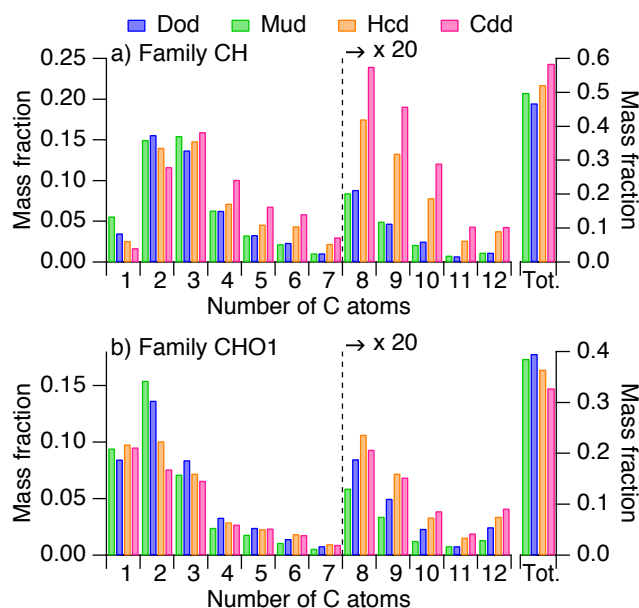


Fig. 7. Contribution of ions detected in the AMS to the bulk organic mass concentration for low- NO_x alkane photooxidation. Ions are grouped into families according to the ion atomic composition and displayed as a function of carbon atoms in the ion. Tot. is the sum over all carbon atom numbers for each family. The data represent a 60 min average of the SOA formed after 95–100% of the initial alkane had reacted. The data presented are from experiments DL2, ML2, HL2, and CL3.

phase fragmentation reactions under high- and low- NO_x conditions.

During photooxidation, the prevalence of branching in a compound is expected to lead to increased fragmentation, requiring more functionalization to produce condensable species. Greater functionalization increases the oxygen content of product molecules, thus it is reasonable that SOA from branched compounds, 2-methylundecane and hexylcyclohexane, has a higher mass fraction of family CHO1 ions than that from compounds with less branching, cyclododecane and dodecane. These trends are not as apparent under low- NO_x conditions, suggesting that the fragmentation pathway may not be as important under low- NO_x conditions as under high- NO_x conditions. It should be noted that while fragmentation occurs for cyclododecane oxidation products, it results in ring-opening, which preserves the carbon backbone and does not produce a higher-volatility species. Hexylcyclohexane is also a cyclic compound, and an alkoxy radical on the ring α to the branch point may result in ring-opening, which preserves the carbon backbone; thus, fragmentation of hexylcyclohexane will not always result in generation of species with fewer carbon atoms than the parent molecule.

Gas-phase fragmentation products from high- NO_x alkane photooxidation were detected using the CIMS (Table S3). The proposed products have been grouped into “families”

by functionality: carboxylic acid ($C_nH_{2n}O_2$), hydroxy carboxylic acid ($C_nH_{2n}O_3$), carbonyl nitrate ($C_nH_{(2n-1)}NO_4$), or hydroxynitrate ($C_nH_{(2n+1)}NO_4$), where n is the number of carbon atoms in the proposed molecule. For the CIMS ions presented here, the carbon chain is preserved as ionization occurs, whereas heating and ionization in the AMS tends to break the carbon chain, and the ions presented in Figs. 6 and 7 could come from longer chain parent molecules. Figure 8 shows the signal for each product, normalized by ΔHC for a 30 min averaged sample obtained after 95–100 % of the initial alkane mixing ratio reacted. The data are presented assuming that CIMS sensitivity is independent of n for a given family and that sensitivity is the same for all isomers (including cyclic and branched structures) for a given n and family. Mixing ratio calibrations were not performed for all species presented, and trends of ion signal with carbon number are not evaluated. Because the CIMS has unit mass resolution and can detect ions produced as transfer ($m/z = [M+19]^-$) and cluster ($m/z = [M+85]^-$) products, the signals in Fig. 8b could come from an acid or a hydroperoxide. Under high- NO_x conditions, hydroperoxide production is not expected. For almost all products shown in Fig. 8, signals in the cyclododecane experiment are lower than those for the other three alkanes, suggesting that cyclododecane oxidation products undergo little fragmentation, consistent with trends obtained from AMS data. More fragmentation of 2-methylundecane and hexylcyclohexane oxidation products is expected than for those of dodecane; however, the signal from fragmentation products for most families are similar for dodecane, 2-methylundecane, and hexylcyclohexane, suggesting that some fragmentation also occurs during dodecane high- NO_x photooxidation.

Gas-phase fragmentation reactions can also occur under low- NO_x conditions from hydroperoxide photolysis (Yee et al., 2012, 2013). Photolysis of a hydroperoxide forms an alkoxy radical, which can isomerize or decompose depending on the carbon backbone structure. For dodecane, hydroperoxide photolysis is expected to be a minor reaction pathway compared with OH oxidation. The specific case of photolysis of a hydroperoxy group adjacent to a carbonyl produces an aldehyde, which has been shown to react with hydroperoxides to form peroxyhemiacetals. Peroxyhemiacetal formation is proposed to initiate SOA growth in the alkane low- NO_x photooxidation system (Yee et al., 2012, 2013; Shiraiwa et al., 2013). In this case, fragmentation reactions depend more on the relative position of hydroperoxy and carbonyl groups than the structure of the carbon backbone.

When comparing SOA yields between low- and high- NO_x conditions for each compound (Fig. 2), three dominant trends are observed. (1) Under high- NO_x conditions, SOA yields at 95–100 % of the initial hydrocarbon reacted (i.e., the yield at the largest OH exposure for each experiment), for dodecane and cyclododecane are larger for lower initial alkane mixing ratio. (2) For hexylcyclohexane and, more notice-

ably, 2-methylundecane, SOA yields under high- NO_x conditions are higher when the initial alkane mixing ratio is higher. (3) SOA yields for dodecane and cyclododecane are higher under high- NO_x conditions than under low- NO_x conditions. Trends (1) and (2) arise from the role of fragmentation under high- NO_x conditions. At higher initial alkane mixing ratios, semivolatile species can condense preferentially to particles, whereas, for lower initial alkane mixing ratios, semivolatile species remain in the gas phase for further oxidation. For linear or cyclic compounds, further oxidation decreases compound volatility, resulting in additional SOA formation and higher SOA yields. However, for branched compounds, further oxidation results in fragmentation, leading to higher volatility species that do not condense to form additional SOA. At sufficiently high OH exposures, fragmentation will become important for all systems that form SOA (Lambe et al., 2012), but those conditions were not reached in the present experiments. Trend (3) results from differences in the extent of fragmentation under both NO_x conditions. Dodecane and 2-methylundecane have almost identical chemical structures, and one may expect these two compounds to have similar SOA yields. Under low- NO_x conditions, the SOA yields for experiments ML2 and DL2 are 15–31 % (however, the SOA yield observed in ML1 is higher than that observed in DL1), whereas under high- NO_x conditions, higher SOA yields are observed for dodecane than for 2-methylundecane (see Tables 2 and 3). High- NO_x SOA yields are greater than low- NO_x yields for unbranched compounds, but high- and low- NO_x SOA yields are similar for branched compounds as a result of enhanced fragmentation under high- NO_x conditions.

4 Conclusions

In the present study SOA yields have been measured for linear, cyclic, and branched 12-carbon alkanes under high- and low- NO_x conditions in which 95–100 % of the alkane reacted. The highest SOA yields were observed from cyclic alkanes, and the presence of branch points decreased SOA yield, primarily under high- NO_x conditions where vapor-phase fragmentation reactions were more likely to occur. Uncertainties arise in the SOA yield measurements due to particle and vapor wall losses and result in a factor of 2–3 difference between upper and lower limits to SOA yield. Recently, Gentner et al. (2012) assessed SOA formation from diesel and gasoline vehicles and noted that SOA yields for cyclic alkanes with five- and six-membered rings, which comprise 37 % of diesel and 11 % of gasoline, were not well-characterized. This study presents data for one such compound, hexylcyclohexane. Hexylcyclohexane SOA yield was similar to that of dodecane under high- NO_x conditions and greater than dodecane under low- NO_x conditions. Lim and Ziemann (2009b) measured SOA yields for two other branched-cyclic compounds, *n*-butylcyclohexane and

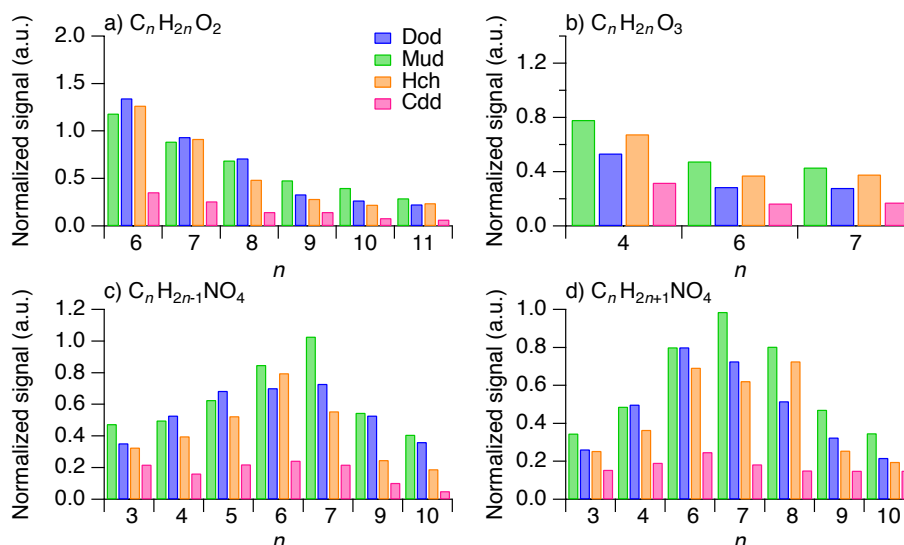


Fig. 8. Comparison of gas-phase fragmentation reaction products from high- NO_x alkane photooxidation measured by the CIMS. The signal is normalized by the mixing ratio of alkane reacted. All molecular formulae are proposed assignments. The data represent a 30 min average of gas-phase species after 95–100 % of the initial alkane had reacted. The ions monitored and their proposed chemical assignments are given in Table S3. The data presented are from experiments DH3, MH2, HH2, and CH2.

n -decylcyclohexane, under high- NO_x conditions but with initial alkane mixing ratios much higher than ambient mixing ratios, approximately 1 ppmv. The authors found that the SOA yield for butylcyclohexane was higher than that for decane, but the yield for decylcyclohexane was less than that for hexadecane. Further characterization of yields from branched-cyclic compounds is necessary to better identify trends and provide more data for models.

Although alkanes are emitted primarily in urban areas under high- NO_x oxidizing conditions, their relatively slow OH reaction rates allow for transport to rural areas with lower NO_x conditions. SOA yields measured in the present study are higher or the same under high- NO_x conditions in comparison to those measured for low- NO_x conditions. Therefore, alkanes exhibit the largest SOA formation potential in urban areas close to their sources.

Appendix A

Particle wall-loss calculations

Pierce et al. (2008) developed the Aerosol Parameter Estimation model to determine the time variance of particle wall-loss rates during an environmental chamber experiment. We have adapted this model to calculate the mass growth rate of suspended particles throughout an experiment. These mass growth rates are then applied to deposited particles to calculate lower and upper limit wall-loss corrections.

The model utilized in the current work is based on the aerosol General Dynamic Equation (Seinfeld and Pandis,

2006):

$$\frac{\partial n_s(D_p, t)}{\partial t} = \left(\frac{\partial n_s(D_p, t)}{\partial t} \right)_{\text{coag}} + \left(\frac{\partial n_s(D_p, t)}{\partial t} \right)_{\text{cond}} + \left(\frac{\partial n_s(D_p, t)}{\partial t} \right)_{\text{wl}}, \quad (\text{A1})$$

where $n_s(D_p, t)$ ($\text{cm}^{-3} \text{cm}^{-1}$) is the suspended particle number-size distribution, D_p (cm) is particle diameter, t (s) is time, and coag, cond, and wl represent the change in suspended particle size-number distribution due to coagulation, condensation, and particle-phase wall loss, respectively.

The change in the suspended particle number-size distribution due to coagulation is described by

$$\left(\frac{\partial n_s(D_p, t)}{\partial t} \right)_{\text{coag}} = \frac{1}{2} \int_0^{D_p} K \left(\left(D_p^3 - q^3 \right)^{\frac{1}{3}}, q \right) n_s \left(\left(D_p^3 - q^3 \right)^{\frac{1}{3}}, t \right) n_s(q, t) dq - n_s(D_p, t) \int_0^{\infty} K(q, D_p) n_s(q, t) dq, \quad (\text{A2})$$

where $K(D_{p1}, D_{p2})$ ($\text{cm}^3 \text{s}^{-1}$) is the coagulation coefficient for collisions of particles with diameters D_{p1} and D_{p2} (Seinfeld and Pandis, 2006). The DMA measures particle number-size distributions using discrete size bins, and the coagulation coefficient must also be discretized to be applied to these data. The change in suspended particle number-size

distribution due to coagulation becomes

$$\left(\frac{\partial n_s(D_p, t)}{\partial t}\right)_{\text{coag}} = \frac{1}{2} \sum_i \sum_j f_c(D_{pi}, D_{pj}) K(D_{pi}, D_{pj}) N(D_{pi}, t) N(D_{pj}, t) - \sum_i K(D_{pi}, D_{pk}) N(D_{pi}, t) N(D_{pk}, t), \quad (\text{A3})$$

where $f_c(D_{pi}, D_{pj})$ expresses whether the collision of a particle in size bin i with a particle in size bin j produces a particle in size bin k , bounded by diameters D_{pk-} and D_{pk+} :

$$f_c(D_{pi}, D_{pj}) = 1 \quad \text{if} \quad D_{pk-} \leq 2 \left(\left(\frac{D_{pi}}{2} \right)^3 + \left(\frac{D_{pj}}{2} \right)^3 \right)^{\frac{1}{3}} < D_{pk+} \quad (\text{A4})$$

$$f_c(D_{pi}, D_{pj}) = 0 \quad \text{otherwise.} \quad (\text{A5})$$

Particles are not allowed to form outside of the measured size range (Verheggen and Mozurkewich, 2006).

The change in suspended particle number-size distribution due to condensation is described by

$$\left(\frac{\partial n_s(D_p, t)}{\partial t}\right)_{\text{cond}} = -\frac{\partial}{\partial D_p} [I(D_p, t) n(D_p, t)], \quad (\text{A6})$$

where $I(D_p, t)$ (cm s^{-1}) is the rate of change of particle diameter as a result of condensation. Assuming spherical particles with a density ρ_p (g cm^{-3}) that is not a strong function of time,

$$I(D_p, t) = \frac{dD_p}{dt} = \frac{2 \sum J_i}{\pi D_p^2 \rho_p}, \quad (\text{A7})$$

where J_i (g s^{-1}) is the mass flux of species i to the particle. J_i is defined as

$$J_i = \frac{2\pi D_p D_i M_i}{RT} f(Kn, \alpha_i) (p_{\infty, i} - p_{s, i}), \quad (\text{A8})$$

where D_i ($\text{cm}^2 \text{s}^{-1}$) is the diffusion coefficient for species i in air, M_i (g mol^{-1}) is the molecular weight of species i , R ($\text{g cm}^2 \text{s}^{-2} \text{mol}^{-1} \text{K}^{-1}$) is the gas constant, T (K) is temperature, $f(Kn, \alpha_i)$ is a correction factor for non-continuum effects and surface accommodation effects, $p_{\infty, i}$ ($\text{g cm}^{-1} \text{s}^{-2}$) is the vapor pressure of species i in far from the particle, and $p_{s, i}$ ($\text{g cm}^{-1} \text{s}^{-2}$) is the partial pressure of species i at the surface of the particle. Substituting Eqs. (A7) and (A8) into Eq. (A6) yields

$$\left(\frac{\partial n_s(D_p, t)}{\partial t}\right)_{\text{cond}} = \frac{-4}{RT\rho_p} \left[\sum_i D_i M_i f(Kn, \alpha_i) (p_{\infty, i} - p_{s, i}) \right] \frac{\partial}{\partial D_p} \left[\frac{1}{D_p} n_s(D_p, t) \right] \quad (\text{A9})$$

Here we are assuming that ρ_p is constant with respect to D_p at a given time t . If many size bins are used to describe the particle number-size distribution, then ρ_p is likely constant over a small range of D_p , and the magnitude of the error that this assumption produces is reduced. Following Pierce et al. (2008), the unknown parameters in Eq. (A9) can be combined into a single factor, F_c ($\text{cm}^2 \text{s}^{-1}$), defined as

$$F_c = \frac{4}{RT\rho_p} \sum_i D_i M_i f(Kn, \alpha_i) (p_{\infty, i} - p_{s, i}). \quad (\text{A10})$$

Substituting F_c into Eq. (A9) and differentiating gives the final form for the change in suspended number-size distribution due to condensation:

$$\left(\frac{\partial n_s(D_p, t)}{\partial t}\right)_{\text{cond}} = -F_c \left[-\frac{1}{D_p^2} n_s(D_p, t) + \frac{1}{D_p} \frac{\partial n_s(D_p, t)}{\partial D_p} \right] \quad (\text{A11})$$

The model varies F_c to produce a number-size distribution that best fits the observed number distribution.

The change in suspend particle number-size distribution due to particle wall deposition is assumed to follow first-order kinetics with particle size-dependent rate constants, $\beta(D_p)$ (s^{-1}):

$$\left(\frac{\partial n_s(D_p, t)}{\partial t}\right)_{\text{wl}} = -\beta(D_p) n_s(D_p, t). \quad (\text{A12})$$

A theoretical determination of β is described in Crump and Seinfeld (1981) and McMurry and Rader (1985); however, parameters needed to calculate β values are difficult to quantify from theory alone for environmental chambers. Instead, β values can be determined from calibration experiments (Keyword et al., 2004; Ng et al., 2007b; Loza et al., 2012) or can be specified as unknowns in an aerosol general dynamic model (Pierce et al., 2008). The present model employs the former parameterization of β values. β values for AS particles are measured during calibration experiments in which wall deposition is the dominant process affecting the number distribution. Particles containing organics are assumed to behave the same as pure AS particles.

To implement the model, the General Dynamic Equation is solved numerically between each time step for a given experimental data set. First the General Dynamic Equation is discretized into diameter size bins corresponding to those of the measured number-size distribution. Then the model is initialized with a measured number-size distribution at time step t and a guess for the parameter F_c . The model is solved using a Dormand Price pair 4th and 5th order Runge–Kutta method to produce a number-size distribution at time step $t + 1$. The fit of the predicted to the observed number-size distributions at time step $t + 1$ is quantified using various diameter moments. The i th diameter moment is calculated as follows

$$M_i = \int_0^{\infty} D_p^i n_s(D_p) dD_p = \sum_k D_{p, k}^i N_s(D_{p, k}), \quad (\text{A13})$$

where k is the size bin and N_s (cm^{-3}) is the suspended particle number concentration. The best fit of the predicted to the observed number distribution is that which minimizes χ^2 :

$$\chi^2 = \sum_{a=1}^9 \left(\frac{M_{i(a),p} - M_{i(a),o}}{M_{i(a),o}} \right)^2, \quad (\text{A14})$$

where $i(a)$ is the set of diameter moments $[-1, -0.5, 0, 0.5, 1, 1.5, 2, 2.5, 3]$ and moment subscripts p and o are predicted and observed, respectively.

Once values for F_c have been estimated, they can be used in wall-loss corrections to parametrize the growth of particles lost to the chamber walls. The change in the deposited particle number-size distribution also is governed by the the aerosol General Dynamic Equation, but only wall loss and condensation process affect the number-size distribution:

$$\frac{\partial n_w(D_p, t)}{\partial t} = \beta(D_p) n_s(D_p, t) - F_c \omega \left[-\frac{1}{D_p^2} n_w(D_p, t) + \frac{1}{D_p} \frac{\partial n_w(D_p, t)}{\partial D_p} \right], \quad (\text{A15})$$

where $n_w(D_p, t)$ (cm^{-3}) is the deposited particle number-size distribution, and ω is a factor that describes the extent of condensation to deposited particles. ω has a value between 0 (no condensation to deposited particles) and 1 (condensation to deposited particles is the same as that to suspended particles). ω values of 0 and 1 correspond to the lower and upper limits of particle wall-loss corrections, respectively. The aerosol General Dynamic Equations for suspended and deposited particles are solved simultaneously between each time step using the previously determined value for F_c at that time step and a constant value for ω . In the current work, wall-loss corrections were calculated with $\omega = 0$ and $\omega = 1$ to evaluate the limits of condensation behavior to deposited particles.

Appendix B

Effect of vapor wall losses on SOA yields

Condensable species can partition to suspended particles, deposited particles, and the chamber walls. The SOA yields reported here account for the first two processes, but vapor wall losses are not considered. If vapors are lost to the wall instead of forming SOA, then SOA yield will be underestimated. Matsunaga and Ziemann (2010) observed vapor wall losses for alkanes, ketones, and alcohols that are relevant to compounds formed in the present systems. The extent of vapor phase wall losses in both of the Caltech chamber facilities was investigated using experiments in which a known volume of dodecanone, dodecanol, or dodecane was injected into a chamber filled with purified air. The signal for each species was monitored over a period of several

hours. Dodecane wall losses were not significant in either chamber. In the 28 m³ chamber used for low-NO_x experiments, 2-dodecanone wall losses followed first-order kinetics with a rate constant of $k_w = 2.2 \times 10^{-6} \text{ s}^{-1}$ ($\tau = 5.3$ days). In the 24 m³ chamber used for high-NO_x experiments, 2-dodecanol wall losses followed first-order kinetics with a rate constant of $k_w = 1.5 \times 10^{-6} \text{ s}^{-1}$ ($\tau = 7.7$ days). Matsunaga and Ziemann (2010) observed 20 % wall loss of 2-dodecanol in 80 min and 25 % wall loss of 2-dodecanone in 25 min, which equate to first order wall-loss rate constants of $k_w = 3.4 \times 10^{-4} \text{ s}^{-1}$ ($\tau = 49$ min) and $k_w = 9.2 \times 10^{-4} \text{ s}^{-1}$ ($\tau = 18$ min) for 2-dodecanol and 2-dodecanone, respectively; after the initial decrease, the 2-dodecanone mixing ratio remained constant for 400 min, presumably after equilibrium was achieved between the suspended vapors and those sorbed to the walls. Equilibrium was not observed for either compound in the Caltech chambers over a 22 h period, and it was not possible to detect rapid initial losses in the Caltech chambers as a result of the chamber setup and injection procedures. The time required to inject measurable mixing ratios of each compound into the chamber was at least 25 min, and because there is no active mixing in the Caltech chambers, it was necessary to wait an additional 20 min after the end of the injection for the chamber contents to mix. Rapid vapor wall losses occurring during this time period are difficult to distinguish from changes in compound mixing ratio due to injection and mixing. Finally, alkane photooxidation generates a variety of products with multiple functionalization; however, only singly-functionalized compounds were tested for wall loss. Matsunaga and Ziemann (2010) showed that vapor wall loss is a function of compound vapor pressure and structure; therefore, it is difficult to extrapolate wall-loss rates of 2-dodecanol and 2-dodecanone to all compounds formed from alkane photooxidation. In an attempt to quantify vapor wall losses, Shiraiwa et al. (2013) assumed vapor wall losses follow pseudo-first order kinetics and varied vapor wall-loss rate constants of SVOCs generated in KM-GAP simulations of dodecane low-NO_x photooxidation. Using $k_w = 9.6 \times 10^{-6} \text{ s}^{-1}$, the highest value considered, led to a decrease of the SOA mass concentration by approximately 30 %. As a result, SOA yield would increase by 30 %. The combined uncertainties of vapor and particle phase wall-loss result in a factor of 2–3 difference between the upper and lower limits to SOA yields in each system.

Appendix C

SVOC-particle collision calculations

In KM-GAP, the collision flux of SVOC at the particle surface, J_A ($\text{molec cm}^{-3} \text{ s}^{-1}$), is

$$J_A = \frac{1}{4} c_A \bar{c}_A, \quad (\text{C1})$$

where c_A is the SVOC concentration (molec cm^{-3}) and \bar{c}_A is the mean molecular speed of SVOC (cm s^{-1}). J_A can be calculated for discrete time points, i , in an experiment corresponding to particle surface area measurements. The following summation is used to calculate cumulative number of SVOC-particle collisions per unit chamber volume, C_{sum} (cm^{-3}),

$$C_{\text{sum}} = \sum_{i=1}^n J_{A,i} S_i \Delta t_i, \quad (\text{C2})$$

where n is the total number of data points, S_i is the particle surface area ($\text{cm}^2 \text{cm}^{-3}$), and Δt_i is the time between data points i and $i+1$ (s). Here the upper limit wall-loss corrected surface area concentration is used to correspond to the model, which does not simulate particle wall losses.

Supplementary material related to this article is available online at <http://www.atmos-chem-phys.net/14/1423/2014/acp-14-1423-2014-supplement.pdf>.

Acknowledgements. This work was supported by the Office of Science (Biological and Environmental Research), US Department of Energy grant DE-SC 0006626 and National Science Foundation grants AGS-1057183 and ATM-0650061. We thank M. Chan for experimental assistance and A. Matsunaga for information regarding Tenax tube preparation and sampling procedures. C. Loza, L. Yee, and J. Craven were supported by National Science Foundation Graduate Research Fellowships. Manabu Shiraiwa was supported by the Japan Society for the Promotion of Science (JSPS) Postdoctoral Fellowship for Research Abroad.

Edited by: J. B. Burkholder

References

- Aiken, A. C., DeCarlo, P. F., Kroll, J. H., Worsnop, D. R., Huffman, J. A., Docherty, K. S., Ulbrich, I. M., Mohr, C., Kimmel, J. R., Sueper, D., Sun, Y., Zhang, Q., Trimborn, A., Northway, M., Ziemann, P. J., Canagaratna, M. R., Onasch, T. B., Alfarra, M. R., Prévôt, A. S. H., Dommen, J., Duplissy, J., Metzger, A., Baltensperger, U., and Jimenez, J. L.: O/C and OM/OC ratios of primary, secondary, and ambient organic aerosols with high-resolution time-of-flight aerosol mass spectrometry, *Environ. Sci. Technol.*, 42, 4478–4485, doi:10.1021/es703009q, 2008.
- Allan, J. D., Delia, A. E., Coe, H., Bower, K. N., Alfarra, M. R., Jimenez, J. L., Middlebrook, A. M., Drewnick, F., Onasch, T. B., Canagaratna, M. R., Jayne, J. T., and Worsnop, D. R.: A generalised method for the extraction of chemically resolved mass spectra from Aerodyne aerosol mass spectrometer data, *J. Aerosol Sci.*, 35, 909–922, doi:10.1016/j.jaerosci.2004.02.007, 2004.
- Atkinson, R. and Arey, J.: Atmospheric degradation of volatile organic compounds, *Chem. Rev.*, 103, 4605–4638, doi:10.1021/cr0206420, 2003.
- Canagaratna, M., Jayne, J., Jimenez, J., Allan, J., Alfarra, M., Zhang, Q., Onasch, T., Drewnick, F., Coe, H., Middlebrook, A., Delia, A., Williams, L., Trimborn, A., Northway, M., DeCarlo, P., Kolb, C., Davidovits, P., and Worsnop, D.: Chemical and microphysical characterization of ambient aerosols with the Aerodyne aerosol mass spectrometer, *Mass Spectrom. Rev.*, 26, 185–222, doi:10.1002/mas.20115, 2007.
- Cocker, D. R., Flagan, R. C., and Seinfeld, J. H.: State-of-the-art chamber facility for studying atmospheric aerosol chemistry, *Environ. Sci. Technol.*, 35, 2594–2601, doi:10.1021/es0019169, 2001.
- Craven, J. S., Yee, L. D., Ng, N. L., Canagaratna, M. R., Loza, C. L., Schilling, K. A., Yatavelli, R. L. N., Thornton, J. A., Ziemann, P. J., Flagan, R. C., and Seinfeld, J. H.: Analysis of secondary organic aerosol formation and aging using positive matrix factorization of high-resolution aerosol mass spectra: Application to the dodecane low-NO_x system, *Atmos. Chem. Phys.*, 12, 11795–11817, doi:10.5194/acp-12-11795-2012, 2012.
- Crump, J. G. and Seinfeld, J. H.: Turbulent deposition and gravitational sedimentation of an aerosol in a vessel of arbitrary shape, *J. Aerosol Sci.*, 12, 405–415, doi:10.1016/0021-8502(81)90036-7, 1981.
- DeCarlo, P. F., Kimmel, J. R., Trimborn, A., Northway, M. J., Jayne, J. T., Aiken, A. C., Gonin, M., Fuhrer, K., Horvath, T., Docherty, K. S., Worsnop, D. R., and Jimenez, J. L.: Field-deployable, high-resolution, time-of-flight aerosol mass spectrometer, *Anal. Chem.*, 78, 8281–8289, doi:10.1021/ac061249n, 2006.
- Eddingsaas, N. C., Loza, C. L., Yee, L. D., Chan, M., Schilling, K. A., Chhabra, P. S., Seinfeld, J. H., and Wennberg, P. O.: α -pinene photooxidation under controlled chemical conditions-Part 2: SOA yield and composition in low- and high-NO_x environments, *Atmos. Chem. Phys.*, 12, 7413–7427, doi:10.5194/acp-12-7413-2012, 2012.
- Farmer, D. K., Matsunaga, A., Docherty, K. S., Surratt, J. D., Seinfeld, J. H., Ziemann, P. J., and Jimenez, J. L.: Response of an aerosol mass spectrometer to organonitrates and organosulfates and implications for atmospheric chemistry, *P. Natl. Acad. Sci. USA.*, 107, 6670–6675, doi:10.1073/pnas.0912340107, 2010.
- Francisco, M. A. and Krylowksi, J.: Chemistry of organic nitrates: Thermal chemistry of linear and branched organic nitrates, *Ind. Eng. Chem. Res.*, 44, 5439–5446, doi:10.1021/ie049380d, 2005.
- Fraser, M. P., Cass, G. R., Simoneit, B. R. T., and Rasmussen, R. A.: Air quality model evaluation data for organics. 4. C₂-C₃₆ non-aromatic hydrocarbons, *Environ. Sci. Technol.*, 31, 2356–2367, doi:10.1021/es960980g, 1997.
- Gentner, D. R., Isaacman, G., Worton, D. R., Chan, A. W. H., Dallmann, T. R., Davis, L., Liu, S., Day, D. A., Russell, L. M., Wilson, K. R., Weber, R., Guha, A., Harley, R. A., and Goldstein, A. H.: Elucidating secondary organic aerosol from diesel and gasoline vehicles through detailed characterization of organic carbon emissions, *P. Natl. Acad. Sci. USA.*, 109, 18318–18323, doi:10.1073/pnas.1212272109, 2012.
- Hildebrandt, L., Donahue, N. M., and Pandis, S. N.: High formation of secondary organic aerosol from the photo-oxidation of toluene, *Atmos. Chem. Phys.*, 9, 2973–2986, doi:10.5194/acp-9-2973-2009, 2009.
- Jenkin, M. E., Saunders, S. M., Wagner, V., and Pilling, M. J.: Protocol for the development of the Master Chemical Mechanism, MCM v3 (Part B): Tropospheric degradation of aromatic

- volatile organic compounds, *Atmos. Chem. Phys.*, 3, 181–193, doi:10.5194/acp-3-181-2003, 2003.
- Jordan, C. E., Ziemann, P. J., Griffin, R. J., Lim, Y. B., Atkinson, R., and Arey, J.: Modeling SOA formation from OH reactions with C₈–C₁₇ *n*-alkanes, *Atmos. Environ.*, 42, 8015–8026, doi:10.1016/j.atmosenv.2008.06.017, 2008.
- Keywood, M. D., Varutbangkul, V., Bahreini, R., Flagan, R. C., and Seinfeld, J. H.: Secondary organic aerosol formation from the ozonolysis of cycloalkenes and related compounds, *Environ. Sci. Technol.*, 38, 4157–4164, doi:10.1021/es035363o, 2004.
- Kroll, J. H., Donahue, N. M., Jimenez, J. L., Kessler, S. H., Canagaratna, M. R., Wilson, K. R., Altieri, K. E., Mazzoleni, L. R., Wozniak, A. S., Bluhm, H., Mysak, E. R., Smith, J. D., Kolb, C. E., and Worsnop, D. R.: Carbon oxidation state as a metric for describing the chemistry of atmospheric organic aerosol, *Nat. Chem.*, 3, 133–139, doi:10.1038/NCHEM.948, 2011.
- Kwok, E. S. and Atkinson, R.: Estimation of hydroxyl radical reaction rate constants for gas-phase organic compounds using a structure-reactivity relationship: An update, *Atmos. Environ.*, 29, 1685–1695, doi:10.1016/1352-2310(95)00069-B, 1995.
- Lambe, A. T., Onasch, T. B., Croasdale, D. R., Wright, J. P., Martin, A. T., Franklin, J. P., Massoli, P., Kroll, J. H., Canagaratna, M. R., Brune, W. H., Worsnop, D. R., and Davidovits, P.: Transitions from functionalization to fragmentation reactions of laboratory secondary organic aerosol (SOA) generated from the OH oxidation of alkane precursors, *Environ. Sci. Technol.*, 46, 5430–5437, doi:10.1021/es300274t, 2012.
- Lim, Y. B. and Ziemann, P. J.: Products and mechanism of secondary organic aerosol formation from reactions of *n*-alkanes with OH radicals in the presence of NO_x, *Environ. Sci. Technol.*, 39, 9229–9236, doi:10.1021/es051447g, 2005.
- Lim, Y. B. and Ziemann, P. J.: Chemistry of secondary organic aerosol formation from OH radical-initiated reactions of linear, branched, and cyclic alkanes in the presence of NO_x, *Aerosol Sci. Tech.*, 43, 604–619, doi:10.1080/02786820902802567, 2009a.
- Lim, Y. B. and Ziemann, P. J.: Effects of molecular structure on aerosol yields from OH radical-initiated reactions of linear, branched, and cyclic alkanes in the presence of NO_x, *Environ. Sci. Technol.*, 43, 2328–2334, doi:10.1021/es803389s, 2009b.
- Lim, Y. B. and Ziemann, P. J.: Kinetics of the heterogeneous conversion of 1,4-hydroxycarbonyls to cyclic hemiacetals and dihydrofurans on organic aerosol particles, *Phys. Chem. Chem. Phys.*, 11, 8029–8039, doi:10.1039/B904333K, 2009c.
- Loza, C. L., Chhabra, P. S., Yee, L. D., Craven, J. S., Flagan, R. C., and Seinfeld, J. H.: Chemical aging of *m*-xylene secondary organic aerosol: Laboratory chamber study, *Atmos. Chem. Phys.*, 12, 151–167, doi:10.5194/acp-12-151-2012, 2012.
- Martin, P., Tuazon, E. C., Aschmann, S. M., Arey, J., and Atkinson, R.: Formation and atmospheric reactions of 4,5-dihydro-2-methylfuran, *J. Phys. Chem. A*, 106, 11492–11501, doi:10.1021/jp021499h, 2002.
- Matsunaga, A. and Ziemann, P. J.: Gas-wall partitioning of organic compounds in a Teflon film chamber and potential effects on reaction product and aerosol yield measurements, *Aerosol Sci. Tech.*, 44, 881–892, doi:10.1080/02786826.2010.501044, 2010.
- McMurry, P. H. and Rader, D. J.: Aerosol wall losses in electrically charged chambers, *Aerosol Sci. Tech.*, 4, 249–268, doi:10.1080/02786828508959054, 1985.
- Molina, L. T., Madronich, S., Gaffney, J. S., Apel, E., de Foy, B., Fast, J., Ferrare, R., Herndon, S., Jimenez, J. L., Lamb, B., Osornio-Vargas, A. R., Russell, P., Schauer, J. J., Stevens, P. S., Volkamer, R., and Zavala, M.: An overview of the MILAGRO 2006 Campaign: Mexico City emissions and their transport and transformation, *Atmos. Chem. Phys.*, 10, 8697–8760, doi:10.5194/acp-10-8697-2010, 2010.
- Ng, N. L., Chhabra, P. S., Chan, A. W. H., Surratt, J. D., Kroll, J. H., Kwan, A. J., McCabe, D. C., Wennberg, P. O., Sorooshian, A., Murphy, S. M., Dalleska, N. F., Flagan, R. C., and Seinfeld, J. H.: Effect of NO_x level on secondary organic aerosol (SOA) formation from the photooxidation of terpenes, *Atmos. Chem. Phys.*, 7, 5159–5174, doi:10.5194/acp-7-5159-2007, 2007a.
- Ng, N. L., Kroll, J. H., Chan, A. W. H., Chhabra, P. S., Flagan, R. C., and Seinfeld, J. H.: Secondary organic aerosol formation from *m*-xylene, toluene, and benzene, *Atmos. Chem. Phys.*, 7, 3909–3922, doi:10.5194/acp-7-3909-2007, 2007b.
- Perraud, V., Bruns, E. A., Ezell, M. J., Johnson, S. N., Yu, Y., Alexander, M. L., Zelenyuk, A., Imre, D., Chang, W. L., Dabdub, D., Pankow, J. F., and Finlayson-Pitts, B. J.: Nonequilibrium atmospheric secondary organic aerosol formation and growth, *P. Natl. Acad. Sci. USA.*, 109, 2836–2841, doi:10.1073/pnas.1119909109, 2012.
- Pierce, J. R., Engelhart, G. J., Hildebrandt, L., Weitkamp, E. A., Pathak, R. K., Donahue, N. M., Robinson, A. L., Adams, P. J., and Pandis, S. N.: Constraining particle evolution from wall losses, coagulation, and condensation-evaporation in smog-chamber experiments: Optimal estimation based on size distribution measurements, *Aerosol Sci. Tech.*, 42, 1001–1015, doi:10.1080/02786820802389251, 2008.
- Presto, A. A., Miracolo, M. A., Kroll, J. H., Worsnop, D. R., Robinson, A. L., and Donahue, N. M.: Intermediate-volatility organic compounds: A potential source of ambient oxidized organic aerosol, *Environ. Sci. Technol.*, 43, 4744–4749, doi:10.1021/es803219q, 2009.
- Presto, A. A., Miracolo, M. A., Donahue, N. M., and Robinson, A. L.: Secondary organic aerosol formation from high-NO_x photo-oxidation of low volatility precursors: *n*-Alkanes, *Environ. Sci. Technol.*, 44, 2029–2034, doi:10.1021/es903712r, 2010.
- Riipinen, I., Pierce, J. R., Yli-Juuti, T., Nieminen, T., Häkkinen, S., Ehn, M., Junninen, H., Lehtipalo, K., Petäjä, T., Slowik, J., Chang, R., Shantz, N. C., Abbatt, J., Leaitch, W., Kerminen, V. M., Worsnop, D. R., Pandis, S. N., Donahue, N. M., and Kulmala, M.: Organic condensation: A vital link connecting aerosol formation to cloud condensation nuclei (CCN) concentration, *Atmos. Chem. Phys.*, 11, 3865–3878, doi:10.5194/acp-11-3865-2011, 2011.
- Rogge, W. F., Hildemann, L. M., Mazurek, M. A., Cass, G. R., and Simoneit, B. R. T.: Sources of fine organic aerosol. 3. Road dust, tire debris, and organometallic brake lining dust: roads as sources and sinks, *Environ. Sci. Technol.*, 27, 1892–1904, doi:10.1021/es00046a019, 1993.
- Saunders, S. M., Jenkin, M. E., Derwent, R. G., and Pilling, M. J.: Protocol for the development of the Master Chemical Mechanism, MCM v3 (Part A): Tropospheric degradation of non-aromatic volatile organic compounds, *Atmos. Chem. Phys.*, 3, 161–180, doi:10.5194/acp-3-161-2003, 2003.
- Schauer, J. J., Kleeman, M. J., Cass, G. R., and Simoneit, B. R. T.: Measurement of emissions from air pollution

- sources. 2. C₁ through C₃₀ organic compounds from medium duty diesel trucks, *Environ. Sci. Technol.*, 33, 1578–1587, doi:10.1021/es980081n, 1999.
- Schauer, J. J., Kleeman, M. J., Cass, G. R., and Simoneit, B. R. T.: Measurement of emissions from air pollution sources. 5. C₁–C₃₂ organic compounds from gasoline-powered motor vehicles, *Environ. Sci. Technol.*, 36, 1169–1180, doi:10.1021/es0108077, 2002.
- Seinfeld, J. H. and Pandis, S. N.: *Atmospheric Chemistry and Physics*, John Wiley and Sons, Inc., Hoboken, N.J., 2 edn., 2006.
- Shilling, J. E., Chen, Q., King, S. M., Rosenoern, T., Kroll, J. H., Worsnop, D. R., DeCarlo, P. F., Aiken, A. C., Sueper, D., Jimenez, J. L., and Martin, S. T.: Loading-dependent elemental composition of α -pinene SOA particles, *Atmos. Chem. Phys.*, 9, 771–782, doi:10.5194/acp-9-771-2009, 2009.
- Shiraiwa, M. and Seinfeld, J. H.: Equilibration timescale of atmospheric secondary organic aerosol partitioning, *Geophys. Res. Lett.*, 39, L24801, doi:10.1029/2012GL054008, 2012.
- Shiraiwa, M., Pfrang, C., Koop, T., and Pöschl, U.: Kinetic multi-layer model of gas-particle interactions in aerosols and clouds (KM-GAP): Linking condensation, evaporation and chemical reactions of organics, oxidants and water, *Atmos. Chem. Phys.*, 12, 2777–2794, doi:10.5194/acp-12-2777-2012, 2012.
- Shiraiwa, M., Yee, L. D., Schilling, K. A., Loza, C. L., Craven, J. S., Zuend, A., Ziemann, P. J., and Seinfeld, J. H.: Size distribution dynamics reveal particle-phase chemistry in organic aerosol formation, *P. Natl. Acad. Sci. USA*, 110, 11746–11750, doi:10.1073/pnas.1307501110, 2013.
- Song, C., Na, K., and Cocker, D. R.: Impact of the hydrocarbon to NO_x ratio on secondary organic aerosol formation, *Environ. Sci. Technol.*, 39, 3143–3149, doi:10.1021/es0493244, 2005.
- Stephens, S., Madronich, S., Wu, F., Olson, J. B., Ramos, R., Retama, A., and Muñoz, R.: Weekly patterns of México City's surface concentrations of CO, NO_x, PM₁₀ and O₃ during 1986–2007, *Atmos. Chem. Phys.*, 8, 5313–5325, doi:10.5194/acp-8-5313-2008, 2008.
- Tkacik, D. S., Presto, A. A., Donahue, N. M., and Robinson, A. L.: Secondary organic aerosol formation from intermediate-volatility organic compounds: Cyclic, linear, and branched alkanes, *Environ. Sci. Technol.*, 46, 8773–8781, doi:10.1021/es301112c, 2012.
- Verheggen, B. and Mozurkewich, M.: An inverse modeling procedure to determine particle growth and nucleation rates from measured aerosol size distributions, *Atmos. Chem. Phys.*, 6, 2927–2942, doi:10.5194/acp-6-2927-2006, 2006.
- Volkamer, R., Sheehy, P., Molina, L. T., and Molina, M. J.: Oxidative capacity of the Mexico City atmosphere – Part 1: A radical source perspective, *Atmos. Chem. Phys.*, 10, 6969–6991, doi:10.5194/acp-10-6969-2010, 2010.
- Weitkamp, E. A., Sage, A. M., Pierce, J. R., Donahue, N. M., and Robinson, A. L.: Organic aerosol formation from photochemical oxidation of diesel exhaust in a smog chamber, *Environ. Sci. Technol.*, 41, 6969–6975, doi:10.1021/es070193r, 2007.
- Yee, L. D., Craven, J. S., Loza, C. L., Schilling, K. A., Ng, N. L., Canagaratna, M. R., Ziemann, P. J., Flagan, R. C., and Seinfeld, J. H.: Secondary organic aerosol formation from low-NO_x photooxidation of dodecane: Evolution of multigeneration gas-phase chemistry and aerosol composition, *J. Phys. Chem. A*, 116, 6211–6230, doi:10.1021/jp211531h, 2012.
- Yee, L. D., Craven, J. S., Loza, C. L., Schilling, K. A., Ng, N. L., Canagaratna, M. R., Ziemann, P. J., Flagan, R. C., and Seinfeld, J. H.: Effect of chemical structure on secondary organic aerosol formation from C₁₂ alkanes, *Atmos. Chem. Phys.*, 13, 11121–11140, doi:10.5194/acp-13-11121-2013, 2013.

Appendix H

Influence of Aerosol Acidity on the Chemical Composition of Secondary Organic Aerosol from β -Caryophyllene¹⁰

¹⁰ Reproduced by permission from “Influence of aerosol acidity on the chemical composition of secondary organic aerosol from β -caryophyllene” by M. N. Chan, J. D. Surratt, A. W. H. Chan, K. Schilling, J. H. Offenberg, M. Lewandowski, E. O. Edney, T. E. Kleindienst, M. Jaoui, E. S. Edgerton, R. L. Tanner, S. L. Shaw, M. Zheng, E. M. Knipping, and J. H. Seinfeld. *Atmos. Chem. Phys.* **2011**, *11*, 1735-1751.

Influence of aerosol acidity on the chemical composition of secondary organic aerosol from β -caryophyllene

M. N. Chan¹, J. D. Surratt^{2,*}, A. W. H. Chan^{2,**}, K. Schilling², J. H. Offenberg³, M. Lewandowski³, E. O. Edney³, T. E. Kleindienst³, M. Jaoui⁴, E. S. Edgerton⁵, R. L. Tanner⁶, S. L. Shaw⁷, M. Zheng⁸, E. M. Knipping⁹, and J. H. Seinfeld^{1,2}

¹Division of Engineering and Applied Science, California Institute of Technology, Pasadena, California, USA

²Division of Chemistry and Chemical Engineering, California Institute of Technology, Pasadena, California, USA

³National Exposure Research Laboratory, Human Exposure Atmospheric Sciences Division, United States Environmental Protection Agency, Research Triangle Park, North Carolina, USA

⁴Alion Science and Technology, P.O. Box 12313, Research Triangle Park, North Carolina, USA

⁵Atmospheric Research and Analysis, Inc., Cary, North Carolina, USA

⁶Environmental Technologies, Tennessee Valley Authority, Muscle Shoals, Alabama, USA

⁷Electric Power Research Institute, Palo Alto, California, USA

⁸School of Earth and Atmospheric Sciences, Georgia Institute of Technology, Atlanta, Georgia, USA

⁹Electric Power Research Institute, Washington, DC, USA

* present address: Department of Environmental Sciences and Engineering, University of North Carolina at Chapel Hill, Chapel Hill, North Carolina, USA

** present address: Department of Environmental Science, Policy and Management, University of California, Berkeley, California, USA

Received: 18 November 2010 – Published in Atmos. Chem. Phys. Discuss.: 30 November 2010

Revised: 10 February 2011 – Accepted: 15 February 2011 – Published: 25 February 2011

Abstract. The secondary organic aerosol (SOA) yield of β -caryophyllene photooxidation is enhanced by aerosol acidity. In the present study, the influence of aerosol acidity on the chemical composition of β -caryophyllene SOA is investigated using ultra performance liquid chromatography/electrospray ionization-time-of-flight mass spectrometry (UPLC/ESI-TOFMS). A number of first-, second- and higher-generation gas-phase products having carbonyl and carboxylic acid functional groups are detected in the particle phase. Particle-phase reaction products formed via hydration and organosulfate formation processes are also detected. Increased acidity leads to different effects on the abundance of individual products; significantly, abundances of organosulfates are correlated with aerosol acidity. To our knowledge, this is the first detection of organosulfates and nitrated organosulfates derived from a sesquiterpene. The increase of certain particle-phase reaction products with increased acidity provides chemical evidence to support the acid-enhanced

SOA yields. Based on the agreement between the chromatographic retention times and accurate mass measurements of chamber and field samples, three β -caryophyllene products (i.e., β -nocaryophyllon aldehyde, β -hydroxynocaryophyllon aldehyde, and β -dihydroxynocaryophyllon aldehyde) are suggested as chemical tracers for β -caryophyllene SOA. These compounds are detected in both day and night ambient samples collected in downtown Atlanta, GA and rural Yorkville, GA during the 2008 August Mini-Intensive Gas and Aerosol Study (AMIGAS).

1 Introduction

Secondary organic aerosol (SOA) formation from the oxidation of biogenic precursors, such as isoprene (C₅H₈), monoterpenes (C₁₀H₁₆), sesquiterpenes (C₁₅H₂₄), and oxygenated terpenes, contributes significantly to atmospheric aerosol mass (Hallquist et al., 2009 and references therein). β -caryophyllene (C₁₅H₂₄) is one of the most reactive sesquiterpenes, with two double bonds (one endocyclic and one exocyclic), and has high reactivity towards ozone (O₃),



Correspondence to: J. H. Seinfeld
(seinfeld@caltech.edu)

hydroxyl radicals (OH), and nitrate radicals (NO₃). Shu and Atkinson (1994, 1995) estimated that under typical tropospheric conditions the lifetime of β -caryophyllene with respect to O₃ and OH reaction is 2 min and 53 min, respectively. β -caryophyllene also has a high aerosol formation potential (Griffin et al., 1999; Jaoui et al., 2003; Lee et al., 2006a, b; Ng et al., 2006; Winterhalter et al., 2009; Li et al., 2011). A range of aerosol yields (mass of SOA formed per mass of hydrocarbon reacted) has been reported (O₃: 5–46%; OH: 17–68%), depending on aerosol organic mass and experimental conditions.

Particle-phase products of β -caryophyllene ozonolysis have been extensively studied in the presence or absence of ammonium sulfate ((NH₄)₂SO₄) seed particles. A number of first-generation ozonolysis products, such as aldehydes (e.g., β -caryophyllon aldehyde and β -hydroxycaryophyllon aldehyde) and acids (e.g., β -caryophyllonic acid and β -caryophyllinic acid), have been identified (Calogirou et al., 1997; Jaoui et al., 2003; Kanawati et al., 2008; Winterhalter et al., 2009; Li et al., 2011). Ng et al. (2006) observed continued aerosol growth after all β -caryophyllene was consumed in ozonolysis and photooxidation experiments, demonstrating the importance of second- or higher-generation reactions. More recently, Li et al. (2011) showed that first-generation ozonolysis products, which still contain a double bond, can be oxidized to second-generation ozonolysis products (e.g., β -nocaryophyllon aldehyde and β -hydroxynocaryophyllon aldehyde), which represent a larger contribution to the SOA mass than first-generation ozonolysis products. β -caryophyllinic acid has been detected in both chamber and ambient aerosol samples and has been suggested as a tracer for β -caryophyllene SOA (Jaoui et al., 2007). Using the tracer-to-SOA mass fractions obtained in laboratory chamber experiments, β -caryophyllene SOA is estimated to contribute about 1–10% of the atmospheric aerosol organic mass in the southeastern and midwestern United States (Kleindienst et al., 2007; Lewandowski et al., 2008).

Chamber studies have shown that increasing aerosol acidity enhances SOA formation from the oxidation of certain biogenic hydrocarbons such as isoprene, α -pinene, and β -pinene (Kroll and Seinfeld, 2008, and references therein). Acid-catalyzed reactions (e.g., hydration, esterification, hemiacetal/acetel formation, aldol condensation) leading to the formation of higher molecular-weight compounds have been proposed to explain the enhanced SOA yields (Jang et al., 2002). When the acidity is provided by sulfuric acid (H₂SO₄), sulfate esters (or organosulfates) can form (Liggio and Li, 2006; Surratt et al., 2007a, b, 2008; Iinuma et al., 2009). By comparing mass spectrometric measurements for both laboratory-generated and ambient aerosol, Iinuma et al. (2007) and Surratt et al. (2007a, b, 2008) have reported the presence of organosulfates derived from isoprene, α -pinene, β -pinene, and limonene-like monoterpenes (e.g., myrcene) in ambient aerosol.

SOA yields are enhanced by aerosol acidity in the photooxidation of mixtures of β -caryophyllene/NO_x (Offenberg et al., 2009). In the present study, the influence of aerosol acidity on the chemical composition of β -caryophyllene SOA from β -caryophyllene photooxidation is investigated using ultra performance liquid chromatography/electrospray ionization-time-of-flight mass spectrometry (UPLC/ESI-TOFMS). Certain β -caryophyllene reaction products are shown to serve as tracers for the identification of β -caryophyllene SOA in ambient aerosol collected in downtown Atlanta (at Jefferson Street (JST)), GA and rural Yorkville (YRK), GA during the 2008 August Mini-Intensive Gas and Aerosol Study (AMIGAS).

2 Experimental section

β -caryophyllene/NO_x irradiation experiments in the presence of seed aerosol of varying acidity were carried out in a 14.5 m³ fixed volume Teflon-coated reaction chamber at 297 K and 30% RH. Details of the experiments have been given in Offenberg et al. (2009). Initial aerosol acidity was controlled by nebulizing dilute aqueous (NH₄)₂SO₄/H₂SO₄ solutions. To change the acidity of the seed aerosol, the ratio of the two liquids was changed to produce a constant aerosol sulfate concentration of 30 $\mu\text{g m}^{-3}$ across the range of resulting acidities. The reaction chamber was operated as a continuous stirred tank reactor, having a residence time of 6 h, to produce a constant, steady-state aerosol distribution. For the aerosol acidity measurement, filters were extracted by sonication for 30 min using 10 mL of distilled, deionized water in a 50 mL polypropylene vial. Once the extract cooled to room temperature, the pH of each extract was measured with a Mettler-Toledo MP220 pH meter using an InLab 413 pH electrode. Aerosol acidity is expressed as the hydrogen ion air concentrations ([H⁺]_{air}), which was calculated by dividing the measured aqueous concentration of the hydrogen ion by the volume of air collected. Table 1 summarizes the steady state concentrations of gas-phase species, aerosol acidity, and secondary organic carbon (SOC) for the experiments.

For the chemical analysis, aerosol was collected on Teflon impregnated glass fiber filters (Pall Gelman Laboratory, 47 mm diameter, Teflon impregnated). To collect sufficient aerosol mass for the analysis, about 0.7–1.0 mg was collected on each filter and the sampling air volume was about 15.4–16.3 m³. One-half of each filter was extracted with methanol (LC-MS CHROMASOLV-grade, Sigma-Aldrich) under ultrasonication for 45 min. The extract was dried under ultra-pure nitrogen gas and the residue was reconstituted with a 50:50 (v/v) solvent mixture of methanol with 0.1% acetic acid (LC-MS CHROMASOLV-grade, Sigma-Aldrich) and water with 0.1% acetic acid (LC-MS CHROMASOLV-grade, Sigma-Aldrich). Day (10:00 a.m.–06:00 p.m., local time)- and night (10:00 p.m.–06:00 a.m., local time) –

Table 1. Steady state concentrations of gas-phase species, aerosol acidity, and secondary organic carbon (SOC) for β -caryophyllene/ NO_x irradiation experiments, reproduced from Offenberg et al. (2009).

Experiment	$\Delta[\text{HC}]$ (ppmC)	$[\text{NO}]$ (ppbV)	$[\text{NO}_x\text{-NO}]$ (ppbV)	O_3 (ppbV)	$[\text{H}^+]_{\text{air}}$ (nmol m ⁻³)	SOC ($\mu\text{gC m}^{-3}$)
1	0.58	60	51	25	112	9.97
2	0.58	61	51	24	204	14.7
3	0.58	63	54	29	467	21.3
4	0.58	65	53	24	1150	34.0

segregated $\text{PM}_{2.5}$ (particulate matter with an aerodynamic diameter $<2.5 \mu\text{m}$) high-volume quartz filter samples (i.e., quartz microfibre, $20.3 \times 25.4 \text{ cm}$, Whatman) were collected from JST and YRK sites during the 2008 AMIGAS campaign was analyzed for the presence of β -caryophyllene SOA constituents. Details of the 2008 AMIGAS campaign, filter collection, and sample preparation procedures are given by Chan et al. (2010). Both chamber and field sample extracts were analyzed by UPLC/ESI-TOFMS operated in both positive and negative ion modes. Details of the UPLC/ESI-TOFMS analysis have been given in Surratt et al. (2008). All accurate mass measurements were within $\pm 5 \text{ mDa}$ of the theoretical mass associated with the proposed chemical formula for each observed ion. Owing to the lack of authentic standards or suitable surrogates, concentrations are reported as the sum of the UPLC chromatographic peak area of the ions normalized by the volume of air collected. From repeated UPLC/ESI-TOFMS measurements, the variations in the chromatographic peak areas are about 5%. The concentrations are not corrected for extraction efficiencies.

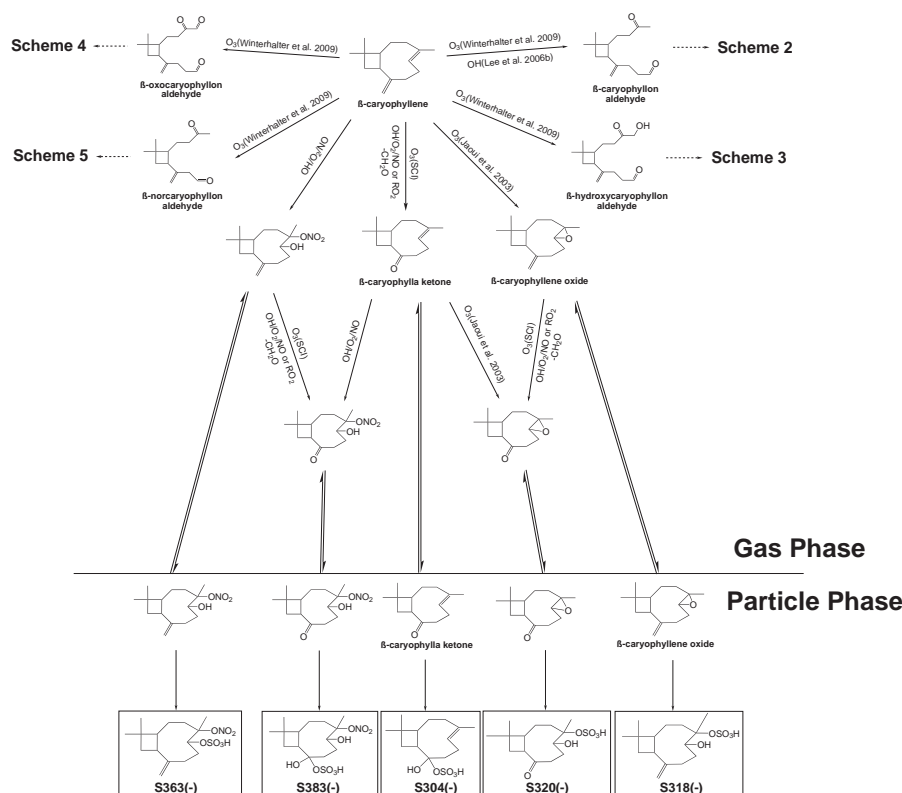
3 Results and discussion

3.1 Gas- and particle-phase reactions

In the series of β -caryophyllene photooxidation experiments, β -caryophyllene and its gas-phase products react with O_3 and OH in the presence of NO_x . Rate constants (296 K) for the reaction of β -caryophyllene with O_3 ($k_{\text{O}_3} = 1.16 \times 10^{-14} \text{ cm}^3 \text{ molecule}^{-1} \text{ s}^{-1}$) and OH ($k_{\text{OH}} = 1.97 \times 10^{-10} \text{ cm}^3 \text{ molecule}^{-1} \text{ s}^{-1}$) have been reported by Shu and Atkinson (1994, 1995). At steady state in the reaction chamber, the O_3 level was 24–29 ppb (5.93×10^{11} – $7.16 \times 10^{11} \text{ molecules cm}^{-3}$) (Table 1). The OH concentration in the chamber was not directly measured. At an assumed OH level of $10^6 \text{ molecules cm}^{-3}$, the ratio of the rates of β -caryophyllene reaction with O_3 to OH at the O_3 levels in the reaction chamber is about 36. β -caryophyllene ozonolysis is therefore likely the dominant reaction pathway in the first oxidation step. The two double bonds of β -caryophyllene have different reactivity with respect to O_3 . Nguyen et al. (2009) predicted that the rate coefficient for O_3 attack on the exocyclic double bond is less than 5% of that

for O_3 attack on the endocyclic double bond. Thus, addition of O_3 to the endocyclic double bond is likely the dominant reaction of β -caryophyllene with O_3 . Since O_3 and OH are in excess relative to β -caryophyllene in the reaction chamber, the remaining double bond (either exocyclic or endocyclic) of the first-generation products undergoes a second ozonolysis or reacts with OH, leading to second- or higher-generation products. Based on an average rate coefficient for the ozonolysis of the first-generation products ($k_{\text{O}_3} = 1.1 \times 10^{-16} \text{ cm}^3 \text{ molecule}^{-1} \text{ s}^{-1}$) reported by Winterhalter et al. (2009) at 295 K, the average lifetime of the first-generation products with respect to ozonolysis is about 3.5 to 4.2 h. Rate coefficients for the photooxidation of the first-generation products have not been reported. If the rate coefficient for the photooxidation of β -caryophyllene is used ($k_{\text{OH}} = 1.97 \times 10^{-10} \text{ cm}^3 \text{ molecule}^{-1} \text{ s}^{-1}$), as an approximation, the average lifetime of the first-generation products with respect to photooxidation is about 1.4 h at an OH level of $10^6 \text{ molecules cm}^{-3}$. Thus, the first generation products can be further oxidized in the gas phase at the residence time in the reaction chamber.

The gas-phase chemistry of β -caryophyllene in our system involves OH, O_3 , and NO_x . For clarity and simplicity, we focus on the reactions of the first-generation products of β -caryophyllene in the gas and particle phases, leading to particle-phase products detected by UPLC/ESI-TOFMS (Scheme 1). Formation mechanisms of β -caryophyllon aldehyde, β -hydroxycaryophyllon aldehyde, β -oxocaryophyllon aldehyde, and β -norcaryophyllon aldehyde from the photooxidation and ozonolysis of β -caryophyllene have been proposed (Jaoui et al., 2003; Lee et al., 2006a, b; Winterhalter et al., 2009; Li et al., 2011). Additionally, ring-retaining compounds can form (Jaoui et al., 2003; Lee et al., 2006b). For example, β -caryophyllene oxide can form from the reaction of β -caryophyllene with O_3 similar to α -pinene oxide formation (Inuma et al., 2009) and has been detected in both gas- and particle phases in the ozonolysis of β -caryophyllene (Jaoui et al., 2003). β -caryophylla ketone can form from β -caryophyllene reaction with O_3 or OH at its exocyclic double bond (Jaoui et al., 2003; Lee et al., 2006b). The first-generation ring-retaining compounds, which contain an unreacted double bond, can be further oxidized before partitioning to the particle phase.

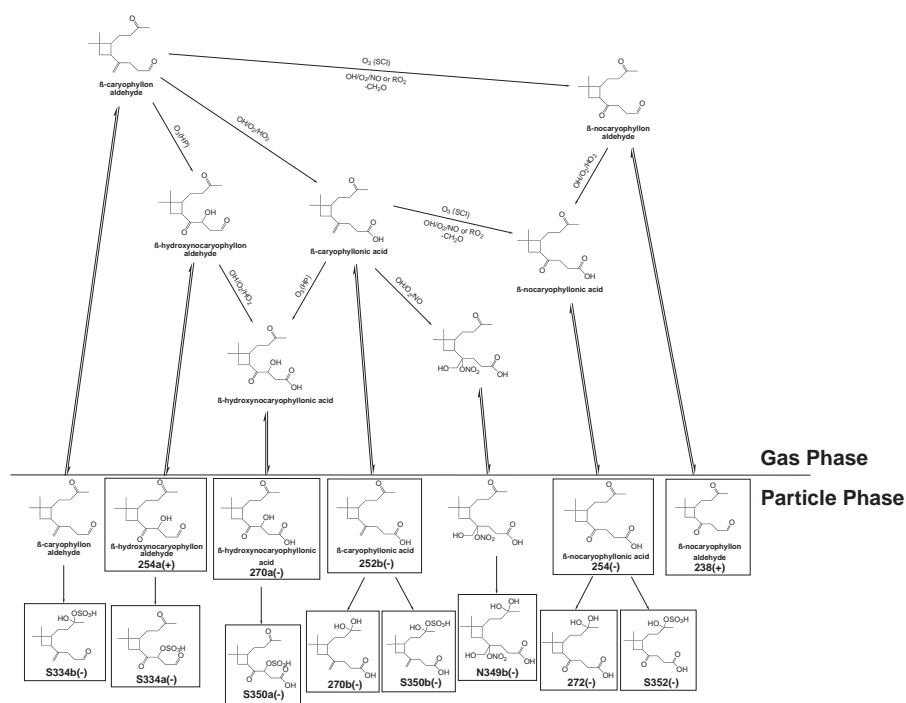


Scheme 1. Proposed reaction pathways of β -caryophyllene, leading to compounds detected by ESI in the particle phase. Boxes indicate compounds detected by ESI in the particle phase. One possible structural isomer is shown. SCI is the stabilized Criegee intermediates channel.

Schemes 2–5 show the further oxidation of the first-generation products, leading to compounds detected by ESI in the particle phase. In the presence of excess O_3 and OH , it can be assumed that the remaining double bond (exocyclic double bond) of the gas-phase products will be rapidly oxidized. Reaction of gas-phase products with O_3 generally proceeds via four channels: stabilized Criegee intermediates (CIs), isomerization, hydroperoxide, and ester channels. Detailed reaction mechanisms for these channels have been given by Jaoui et al. (2003), Winterhalter et al. (2009), and Li et al. (2011). Stabilized CIs and hydroperoxide channels are considered to explain the formation of detected compounds. The stabilized CIs can react with H_2O , NO_2 , and carbonyls. The stabilized CIs channel (SCI) here refers to the reaction between the stabilized CIs and H_2O or NO_2 to form carbonyls. For example, β -caryophyllon aldehyde and β -caryophyllonic acid undergo oxidation by O_3 on their exocyclic double bond forming β -nocaryophyllon aldehyde and β -nocaryophyllonic acid (Scheme 2). The stabilized CIs can react with carbonyls to form secondary ozonides (SOZ). Winterhalter et al. (2009) have detected the presence of SOZ in the particle phase using Fourier transform infrared spectroscopy in their β -caryophyllene ozonolysis experiments. SOZ were not detected in the particle phase in the present

study. It is possible that SOZ may decompose to form organic acids in the particle phase under acidic conditions (or during the analytical procedure) (Winterhalter et al., 2009). For the hydroperoxide channel, the CIs can rearrange via a 1,4-hydrogen shift to a vinyl hydroperoxide, which can subsequently form hydroxyl carbonyls and dicarbonyls (Winterhalter et al., 2009). The hydroperoxide channel refers to the formation of hydroxyl carbonyls. For example, β -caryophyllon aldehyde undergoes oxidation by O_3 on the exocyclic double bond forming β -hydroxynocaryophyllon aldehyde (Scheme 2).

The OH reaction with the exocyclic double bond of the gas-phase products forms alkyl radicals, followed by rapid addition of O_2 to yield peroxy radicals. In the presence of NO_x , peroxy radicals react with NO to form either alkoxy radicals plus NO_2 or organic nitrates. Alkoxy radicals can also form from the reactions between peroxy radicals. Alkoxy radicals can decompose, isomerize or react with O_2 . Here, alkoxy radicals are considered to undergo decomposition to produce a carbonyl and an alkyl radical ($CH_2OH\cdot$). For example, β -nocaryophyllon aldehyde can form from the reaction of β -caryophyllon aldehyde with OH at its exocyclic double bond (Scheme 2). Many gas-phase products have an aldehyde group. An aldehydic hydrogen atom can be



Scheme 2. Proposed reaction pathways of β -caryophyllon aldehyde, leading to compounds detected by ESI in the particle phase. Formation mechanism of β -caryophyllon aldehyde from the photooxidation and ozonolysis of β -caryophyllene (Lee et al., 2006b; Winterhalter et al., 2009). Boxes indicate compounds detected by ESI in the particle phase. One possible structural isomer is shown. SCI is the stabilized Criegee intermediates channel. HP is the hydroperoxide channel.

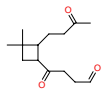
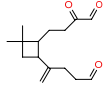
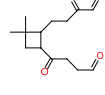
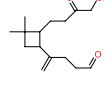
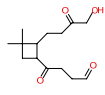
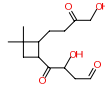
abstracted by OH to produce an acyl radical, which rapidly adds O_2 to yield an acyl peroxy radical. The reaction of acyl peroxy radicals with HO_2 forms carboxylic acid (Winterhalter et al., 2009). The acyl peroxy radicals can also react with NO and subsequently undergo decomposition or can react with NO_2 in the presence of NO_x to form peroxyacyl nitrates. The reaction of acyl peroxy radicals with HO_2 to form carboxylic acid may explain the formation of acids detected in the particle phase. For example, acyl peroxy radicals formed from the aldehydic hydrogen abstraction of β -caryophyllon aldehyde can react with HO_2 to form β -caryophyllonic acid (Scheme 2). However, it cannot be ruled out that the acids can form via other reaction pathways in the gas and particle phases. The OH abstraction of secondary or tertiary hydrogen may also occur (Jaoui et al., 2003) but is not considered here. Once the gas-phase products partition into the particle phase, they may undergo further chemical reactions. Reaction products formed via hydration and organosulfate formation have been detected in the particle phase, as discussed below.

3.2 Particle-phase β -caryophyllene products detected by UPLC/ESI-TOFMS

Tables 2–5 summarize the compounds detected by UPLC/ESI-TOFMS in both positive and negative ion

modes in the series of β -caryophyllene/ NO_x irradiation experiments. Proposed chemical structures are derived from accurate mass measurements, proposed reaction pathways, and previously identified chemical structures reported in the literature (Jaoui et al., 2003; Kanawati et al., 2008; Winterhalter et al., 2009; Li et al., 2011). Table 2 shows the compounds detected by ESI in the positive ion mode. Products having carbonyl groups can be ionized via proton attachment to form $[M+H]^+$ ions and are detected in the positive ion mode (Kanawati et al., 2008). Adducts with sodium $[M+Na]^+$ and with methanol + sodium $[M+CH_3OH+Na]^+$ are used for redundant determination of the chemical formulas of the products (Li et al., 2011). Recently, Parshintsev et al. (2008) have synthesized β -caryophyllene aldehyde and β -nocaryophyllone aldehyde. They reported that sodium adduct ions were the most abundant ions in their accurate mass measurements using ESI-TOF and could be used for identification and quantification of these two compounds in the aerosol samples by liquid chromatography–mass spectrometry. First-generation products (e.g., β -hydroxycaryophyllon aldehyde) and second-generation products (e.g., β -nocaryophyllon aldehyde, β -hydroxynocaryophyllon aldehyde, and β -dihydroxynocaryophyllon aldehyde) are detected in the particle phase.

Table 2. Compounds detected by ESI in the positive ion mode in the series of β -caryophyllene/ NO_x irradiation experiments.

ESI(+) compound	Suggested chemical formula	[M+H] ⁺ (Theoretical mass)	[M+Na] ⁺ (Theoretical mass)	[M+CH ₃ OH+Na] ⁺ (Theoretical mass)	Suggested compound ^a (Scheme)	Proposed chemical structure ^b
184(+)	C ₁₀ H ₂₆ O ₃	C ₁₀ H ₂₇ O ₃ ⁺ (185.1178)	C ₁₀ H ₁₆ O ₃ Na ⁺ (207.0997)			
238(+)	C ₁₄ H ₂₂ O ₃	C ₁₄ H ₂₃ O ₃ ⁺ (239.1647)	C ₁₄ H ₂₂ O ₃ Na ⁺ (261.1467)	C ₁₅ H ₂₆ O ₄ Na ⁺ (293.1729)	β -nocaryophyllon aldehyde ^{c, d, e} (2)	
250(+)	C ₁₅ H ₂₂ O ₃	C ₁₅ H ₂₃ O ₃ ⁺ (251.1647)	C ₁₅ H ₂₂ O ₃ Na ⁺ (273.1467)		β -oxocaryophyllon aldehyde ^d (4)	
252a(+)	C ₁₄ H ₂₀ O ₄	C ₁₄ H ₂₁ O ₄ ⁺ (253.1440)	C ₁₄ H ₂₀ O ₄ Na ⁺ (275.1259)	C ₁₅ H ₂₄ O ₅ Na ⁺ (307.1521)	β -oxonocaryophyllon aldehyde (4)	
252b(+)	C ₁₅ H ₂₄ O ₃	C ₁₅ H ₂₅ O ₃ ⁺ (253.1804)		C ₁₆ H ₂₈ O ₄ Na ⁺ (307.1885)	β -hydroxycaryophyllon aldehyde ^{c, d, e} (3)	
N253(+)	C ₁₄ H ₂₃ NO ₃	C ₁₄ H ₂₄ NO ₃ ⁺ (254.1756)	C ₁₄ H ₂₃ NO ₃ Na ⁺ (276.1576)			
254a(+)	C ₁₄ H ₂₂ O ₄	C ₁₄ H ₂₃ O ₄ ⁺ (255.1596)	C ₁₄ H ₂₂ O ₄ Na ⁺ (277.1416)	C ₁₅ H ₂₆ O ₅ Na ⁺ (309.1678)	β -hydroxynocaryophyllon aldehyde ^{c, e} (2, 3)	
254b(+)	C ₁₅ H ₂₆ O ₃		C ₁₅ H ₂₆ O ₃ Na ⁺ (277.1780)			
N267(+)	C ₁₅ H ₂₅ NO ₃	C ₁₅ H ₂₆ NO ₃ ⁺ (268.1913)	C ₁₅ H ₂₅ NO ₃ Na ⁺ (290.1732)			
268(+)	C ₁₅ H ₂₄ O ₄	C ₁₅ H ₂₅ O ₄ ⁺ (269.1753)	C ₁₅ H ₂₄ O ₄ Na ⁺ (291.1572)			
270(+)	C ₁₄ H ₂₂ O ₅	C ₁₄ H ₂₃ O ₅ ⁺ (271.1545)	C ₁₄ H ₂₂ O ₅ Na ⁺ (293.1365)	C ₁₄ H ₂₆ O ₆ Na ⁺ (325.1627)	β -dihydroxynocaryophyllon aldehyde ^e (3)	
298(+)	C ₁₅ H ₂₂ O ₆	C ₁₅ H ₂₃ O ₆ ⁺ (299.1495)	C ₁₅ H ₂₂ O ₆ Na ⁺ (321.1314)			

Labels (+): compound detected by ESI in positive ion mode; (–): compound detected by ESI in negative ion mode; N: nitrogen-containing compound; S: sulfate esters or nitroxy sulfate esters. Number represents the molecular weight of the compound. M is the compound. ^a Terpene nomenclature, Larsen et al. (1998); ^b only one possible isomer is shown for simplicity; ^c compound has been reported by Li et al. (2011); ^d compound has been reported by Winterhalter et al. (2009); ^e compound has been reported by Jaoui et al. (2003); 309(+) has been detected by the ESI in positive ion mode in this study, however, no reasonable chemical formula can be assigned.

Table 3 shows the compounds detected by ESI in negative ion mode. Products having a carboxylic acid group can be ionized via deprotonation and are detected in the negative ion mode as [M–H][–] ions. Several acids detected such as β -caryophyllonic acid, β -caryophyllinic acid, β -nocaryophyllonic acid, β -hydroxycaryophyllonic acid, β -hydroxynocaryophyllonic acid, and β -oxocaryophyllonic acid have been reported (Jaoui et al., 2003; Winterhalter et al., 2009; Li et al., 2011). Based on the

accurate mass measurements and proposed reaction pathways, three new acids (β -dihydroxycaryophyllonic acid, β -hydroxynocaryophyllonic acid, and β -oxonocaryophyllonic acid) are tentatively identified in this study. β -caryophyllinic acid and β -nocaryophyllonic acid have the same chemical formula (C₁₄H₂₂O₄) and cannot be differentiated in the accurate mass measurements, especially since our study lacked authentic standards as well as tandem MS data.

Table 3. Compounds detected by ESI in the negative ion mode in the series of β -caryophyllene/ NO_x irradiation experiments.

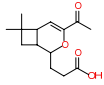
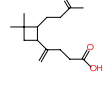
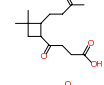
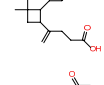
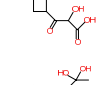
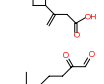
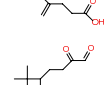
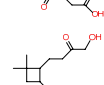
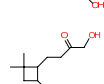
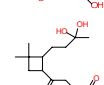
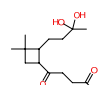
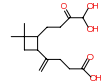
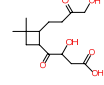
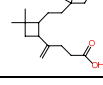
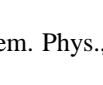
ESI(-) compound	[M-H] ⁻	Suggested chemical formula	Theoretical mass	Suggested compound ^a (Scheme)	Proposed chemical structure ^b	Detection of dimer in ESI negative ion mode
186(-)	185	C ₉ H ₁₃ O ₄ ⁻	185.0814			
216(-)	215	C ₁₀ H ₁₅ O ₅ ⁻	215.0919			
252a(-)	251	C ₁₄ H ₁₉ O ₄ ⁻	251.1283	^c		
252b(-)	251	C ₁₅ H ₂₃ O ₃ ⁻	251.1647	β -caryophyllonic acid (2) ^{c, d, e}		C ₃₀ H ₄₇ O ₆ ⁻
254(-)	253	C ₁₄ H ₂₁ O ₄ ⁻	253.1440	β -nocaryophyllonic acid (2) ^e β -caryophyllinic acid ^{c, d, e}	 	C ₂₈ H ₄₃ O ₈ ⁻
256a(-)	255	C ₁₃ H ₁₉ O ₅ ⁻	255.1232	β -hydroxynocaryophyllonic acid (5)		C ₂₆ H ₃₉ O ₁₀ ⁻
256b(-)	255	C ₁₄ H ₂₃ O ₄ ⁻	255.1596	Hydrated β -nocaryophyllonic acid (5)		
266(-)	265	C ₁₅ H ₂₁ O ₄ ⁻	265.1440	β -oxocaryophyllonic acid (4) ^e		
268a(-)	267	C ₁₄ H ₁₉ O ₅ ⁻	267.1232	β -oxonocaryophyllonic acid (4)		
268b(-)	267	C ₁₅ H ₂₃ O ₄ ⁻	267.1596	β -hydroxycaryophyllonic acid (3) ^e		
270a(-)	269	C ₁₄ H ₂₁ O ₅ ⁻	269.1389	β -hydroxynocaryophyllonic acid (2, 3) ^e		C ₂₈ H ₄₃ O ₁₀ ⁻
270b(-)	269	C ₁₅ H ₂₅ O ₄ ⁻	269.1753	Hydrated β -caryophyllonic acid (2)		
272(-)	271	C ₁₄ H ₂₃ O ₅ ⁻	271.1545	Hydrated β -nocaryophyllonic acid (2)		C ₂₈ H ₄₇ O ₁₀ ⁻
284(-)	283	C ₁₅ H ₂₃ O ₅ ⁻	283.1545	Hydrated β -oxocaryophyllonic acid (4)		C ₃₀ H ₄₇ O ₁₀ ⁻
286a(-)	285	C ₁₄ H ₂₁ O ₆ ⁻	285.1338	β -dihydroxynocaryophyllonic acid (3, 4)		C ₂₈ H ₄₃ O ₁₂ ⁻
286b(-)	285	C ₁₅ H ₂₅ O ₅ ⁻	285.1702	Hydrated β -hydroxycaryophyllonic acid (3)		C ₃₀ H ₅₁ O ₁₀ ⁻

Table 3. Continued.

ESI(-) compound	[M-H] ⁻	Suggested chemical formula	Theoretical mass	Suggested compound a (Scheme)	Proposed chemical structure b	Detection of dimer in ESI negative ion mode
294(-)	293	C ₁₇ H ₂₅ O ₄ ⁻	293.1753			C ₃₄ H ₅₁ O ₈ ⁻
312(-)	311	C ₁₃ H ₂₇ O ₈ ⁻	311.1706			
314a(-)	313	C ₁₅ H ₂₁ O ₇ ⁻	313.1287			
314b(-)	313	C ₁₆ H ₂₅ O ₆ ⁻	313.1651			
320(-)	319	C ₁₄ H ₂₃ O ₈ ⁻	319.1393			
328(-)	327	C ₁₇ H ₂₇ O ₆ ⁻	327.1808			
330a(-)	329	C ₁₆ H ₂₅ O ₇ ⁻	329.1600			
330b(-)	329	C ₁₇ H ₂₉ O ₆ ⁻	329.1964			

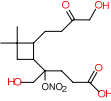
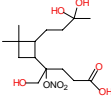
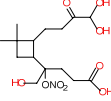
^a Terpene nomenclature, Larsen et al. (1998); ^b only one possible isomer is shown for simplicity; ^c compound has been reported by Li et al. (2011); ^d compound has been reported by Winterhalter et al. (2009); ^e compound has been reported by Jaoui et al. (2003).

β -caryophyllonic acid and β -caryophyllinic acid have traditionally been detected as first-generation products in the ozonolysis of β -caryophyllene. In the presence of OH and NO_x, β -caryophyllonic acid can form from the oxidation of β -caryophyllon aldehyde, which can form in the ozonolysis and photooxidation of β -caryophyllene (Scheme 2). β -caryophyllonic acid thus can be considered as either a first- or second-generation product. A number of other acids have been detected in this study. As shown in Schemes 2–5, many first- or higher-generation gas-phase products formed from the reaction of β -caryophyllene with O₃ and OH have an aldehyde group. In the presence of OH, the aldehydic hydrogen can be abstracted by OH, leading to an acyl peroxy radical, which reacts with HO₂ to give a carboxylic acid. This pathway could explain the formation of most of the organic acids observed in this study. However, it cannot be ruled out that the acids can form via other reaction pathways in the gas and particle phases. As shown in Tables 2 and 4, nitrogen-containing compounds have been detected by ESI in both

positive and negative ion modes. The formation of nitrogen-containing compounds may attribute to the gas-phase reactions of peroxy radicals with NO; however, heterogeneous reaction processes in the particle phase (e.g., reactions between ammonia/ammonium ions with condensed gas-phase products containing carbonyl groups) cannot be completely ruled out (Nozière et al., 2009; Bones et al., 2010) and warrants future investigation.

Particle-phase reaction products formed via hydration and organosulfate formation of gas-phase products have been detected. Condensed gas-phase products can undergo hydrolysis in the particle phase. For example, a carbonyl group of β -hydroxycaryophyllonic acid could be hydrated into a diol (Scheme 3). The hydrated gas-phase products tend to have low volatility and are preferentially present in the particle phase. Compounds having molecular weights larger than 300 Da have been detected. It is likely that these compounds are esters, which can be detected by ESI due to their stability and ionization efficiency (Camredon et al., 2010).

Table 4. Compounds detected by ESI in the negative ion mode in the series of β -caryophyllene/ NO_x irradiation experiments (Nitrogen-containing compounds).

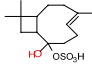
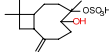
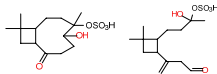
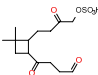
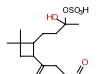
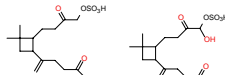
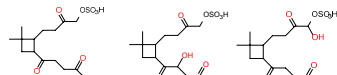
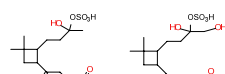
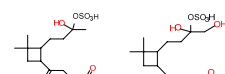
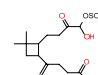
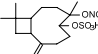
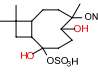
ESI(-) compound	[M-H] ⁻	Suggested chemical formula	Theoretical mass	Suggested compound (Scheme)	Proposed chemical structure ^a	Detection of dimer in ESI negative ion mode
N195(-)	194	$\text{C}_{10}\text{H}_{12}\text{NO}_3^-$	194.0817			$\text{C}_{20}\text{H}_{25}\text{N}_2\text{O}_6^-$
N345(-)	344	$\text{C}_{16}\text{H}_{26}\text{NO}_7^-$	344.1709			
N347(-)	346	$\text{C}_{15}\text{H}_{24}\text{NO}_8^-$	346.1502	(3)		$\text{C}_{30}\text{H}_{49}\text{N}_2\text{O}_{16}^-$
N349a(-)	348	$\text{C}_{14}\text{H}_{22}\text{NO}_9^-$	348.1295			$\text{C}_{28}\text{H}_{45}\text{N}_2\text{O}_{18}^-$
N349b(-)	348	$\text{C}_{15}\text{H}_{26}\text{NO}_8^-$	348.1658	(2)		
N350(-)	349	$\text{C}_{13}\text{H}_{21}\text{N}_2\text{O}_9^-$	349.1247			
N363a(-)	362	$\text{C}_{15}\text{H}_{24}\text{NO}_9^-$	362.1451	(4)		$\text{C}_{30}\text{H}_{49}\text{N}_2\text{O}_{18}^-$
N363b(-)	362	$\text{C}_{16}\text{H}_{28}\text{NO}_8^-$	362.1815			
N375(-)	374	$\text{C}_{17}\text{H}_{28}\text{NO}_8^-$	374.1815			
N546(-)	545	$\text{C}_{24}\text{H}_{37}\text{N}_2\text{O}_{12}^-$	545.2347			$\text{C}_{12}\text{H}_{18}\text{NO}_6^-$ (Monomer)

^a Only one possible isomer is shown for simplicity.

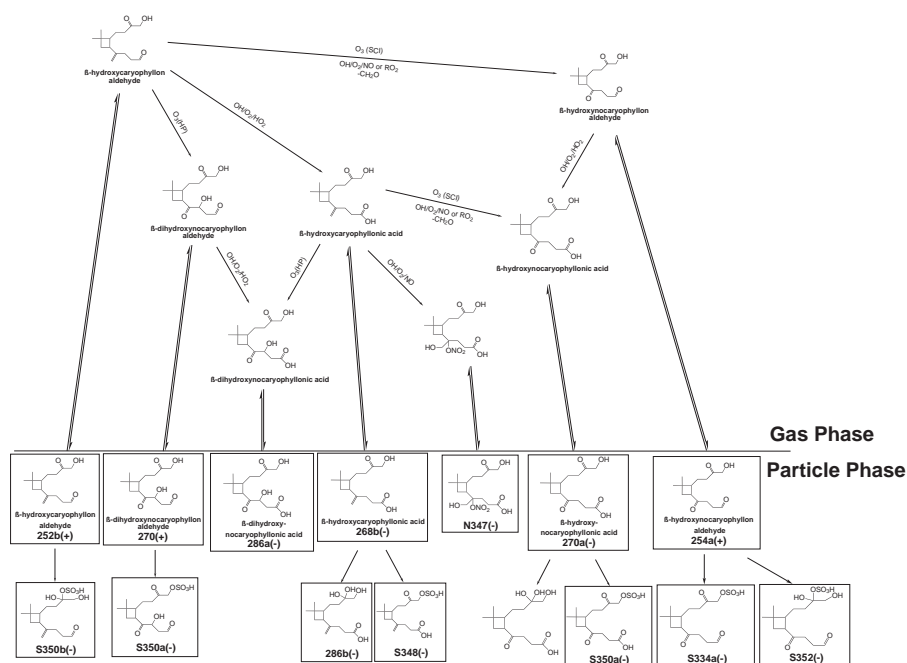
Several organosulfates, as well as two nitrated organosulfates, have been detected (Table 5). As shown in Schemes 1–5, many gas-phase products contain hydroxyl groups, carbonyl groups, epoxide groups, or a combination of these groups. Organosulfates can possibly form from the particle-phase esterification of sulfate ions with gas-phase products containing one or more hydroxyl groups; however, this reaction process has been shown to be kinetically infeasible for smaller alcohols at atmospherically relevant pH conditions (Minerath et al., 2008, 2009). Additionally, organosulfates can form from gas-phase products containing an aldehyde or a keto group. The reaction involves the electron pair of the carbonyl oxygen accepting a proton, producing the oxonium ion, and becoming susceptible to nucleophilic attack from a lone pair of electrons on one of the oxygen atoms of the sulfate ions (Surratt et al., 2007a, 2008). β -caryophyllene oxide can form in the ozonolysis of β -caryophyllene (Jaoui et al., 2003); this compound has been detected in a forested area in central Greece (Pio et al., 2001). Recent work has shown that

organosulfates can form from the reactive uptake of epoxide intermediates (Minerath et al., 2009), such as those derived from isoprene (Cole-Filipiak et al., 2010; Eddingsaas et al., 2010; Surratt et al., 2010) or from α - and β -pinene (Inuma et al., 2009). Reactive uptake of simple epoxides leading to organosulfates has been estimated to be kinetically feasible under atmospherically relevant pH conditions (Minerath et al., 2009; Cole-Filipiak et al., 2010; Eddingsaas et al., 2010). Similar to isoprene-derived epoxydiols and α - and β -pinene oxides, the sulfate ester of m/z 317 (Table 5) likely arises from the acid-catalyzed ring opening of β -caryophyllene oxide in the presence of acidic sulfate (Scheme 1). Most recently, organosulfates have also been shown to form from the irradiation of the aqueous-aerosol phase that contains sulfate (Galloway et al., 2009; Rudzinski et al., 2009; Nozière et al., 2010; Perri et al., 2010). The formation of organosulfates via sulfate radical reaction mechanisms may warrant further investigation. It is noted that isobaric organosulfates cannot be differentiated by the accurate mass measurements;

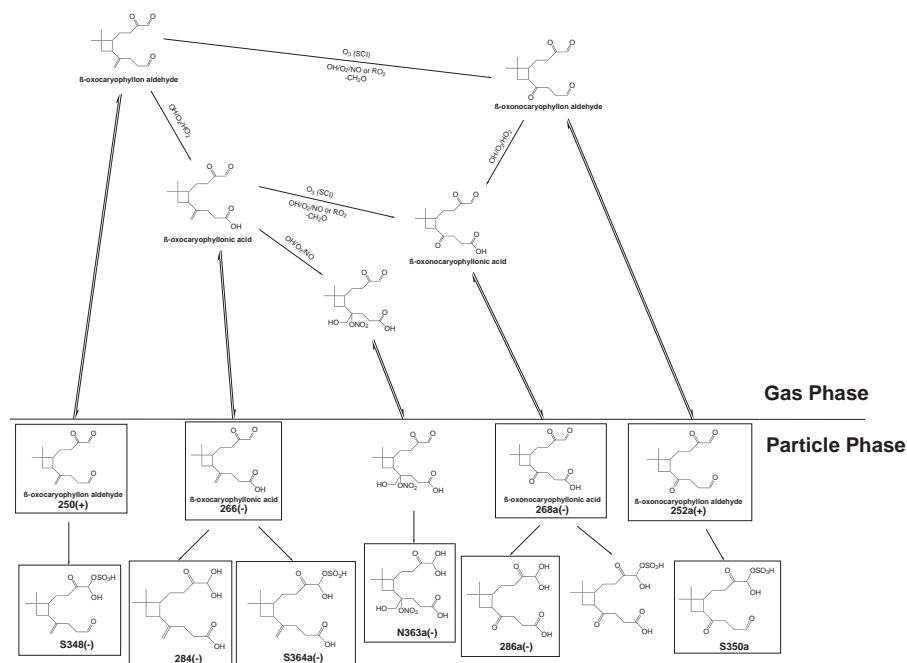
Table 5. Compounds detected by ESI in the negative ion mode in the series of β -caryophyllene/ NO_x irradiation experiments (Organosulfates).

ESI(-) compound	[M-H] ⁻	Suggested chemical formula	Theoretical mass	Suggested compound (Scheme)	Proposed chemical structure ^a
S252(-)	251	$\text{C}_9\text{H}_{15}\text{O}_6\text{S}^-$	251.0589		
S304(-)	303	$\text{C}_{14}\text{H}_{23}\text{O}_5\text{S}^-$	303.1266	(1)	
S318(-)	317	$\text{C}_{15}\text{H}_{25}\text{O}_5\text{S}^-$	317.1423	(1)	
S320(-)	319	$\text{C}_{14}\text{H}_{23}\text{O}_6\text{S}^-$	319.1215	(1), (5)	
S334a(-)	333	$\text{C}_{14}\text{H}_{21}\text{O}_7\text{S}^-$	333.1008	(2), (3)	
S334b(-)	333	$\text{C}_{15}\text{H}_{25}\text{O}_6\text{S}^-$	333.1372	(2)	
S348(-)	347	$\text{C}_{15}\text{H}_{23}\text{O}_7\text{S}^-$	347.1165	(3), (4)	
S350a(-)	349	$\text{C}_{14}\text{H}_{21}\text{O}_8\text{S}^-$	349.0957	(2), (3), (4)	
S350b(-)	349	$\text{C}_{15}\text{H}_{25}\text{O}_7\text{S}^-$	349.1321	(2), (3)	
S352(-)	351	$\text{C}_{14}\text{H}_{23}\text{O}_8\text{S}^-$	351.1114	(2), (3)	
S364a(-)	363	$\text{C}_{15}\text{H}_{23}\text{O}_8\text{S}^-$	363.1114	(4)	
S364b(-)	363	$\text{C}_{16}\text{H}_{27}\text{O}_7\text{S}^-$	363.1478		
S380(-)	379	$\text{C}_{16}\text{H}_{27}\text{O}_8\text{S}^-$	379.1427		
Nitrated Organosulfates					
S363(-)	362	$\text{C}_{15}\text{H}_{24}\text{NO}_7\text{S}^-$	362.1273	(1)	
S383(-)	382	$\text{C}_{14}\text{H}_{24}\text{NO}_9\text{S}^-$	382.1172	(1)	

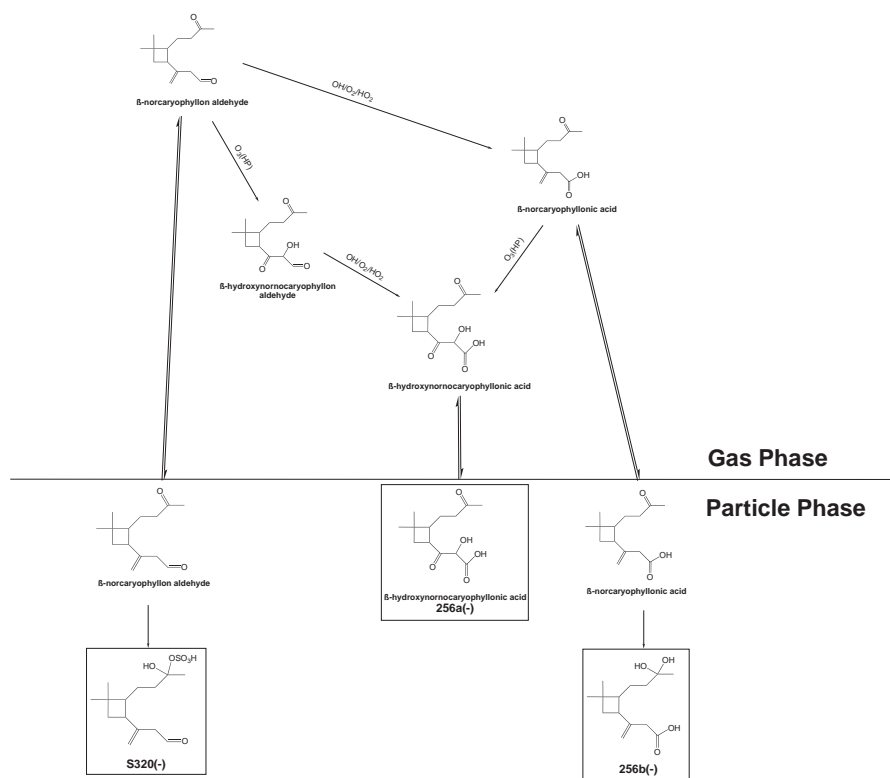
^a Only one possible isomer is shown for simplicity.



Scheme 3. Proposed reaction pathways of β -hydroxycaryophyllon aldehyde, leading to compounds detected by ESI in the particle phase. Formation mechanism of β -hydroxycaryophyllon aldehyde from the ozonolysis of β -caryophyllene (Winterhalter et al., 2009). β -14-hydroxycaryophyllon aldehyde is chosen as illustration. Boxes indicate compounds detected by ESI in the particle phase. One possible structural isomer is shown. SCI is the stabilized Criegee intermediates channel. HP is the hydroperoxide channel.



Scheme 4. Proposed reaction pathways of β -oxocaryophyllon aldehyde, leading to compounds detected by ESI in the particle phase. Formation mechanism of β -oxocaryophyllon aldehyde from the ozonolysis of β -caryophyllene (Winterhalter et al., 2009). β -14-oxocaryophyllon aldehyde is chosen as illustration. Boxes indicate compounds detected by ESI in the particle phase. One possible structural isomer is shown. SCI is the stabilized Criegee intermediates channel.



Scheme 5. Proposed reaction pathways of β -norcaryophyllon aldehyde, leading to compounds detected by ESI in the particle phase. Formation mechanism of β -norcaryophyllon aldehyde from the ozonolysis of β -caryophyllene (Winterhalter et al., 2009). Boxes indicate compounds detected by ESI in the particle phase. One possible structural isomer is shown. HP is the hydroperoxide channel.

however, further tandem MS studies, as well as synthesis of authentic standards, could elucidate these isobaric structures. Depending on the β -caryophyllene oxidation product (e.g., carbonyls or epoxides) formed, a number of chemical pathways may be leading to the formation of the organosulfates we observe.

Bonn and Moortgat (2003) and Li et al. (2011) have suggested that new particle formation can be initiated by very low volatile gas-phase products produced from β -caryophyllene ozonolysis. In the present study, some particle-phase products (first- or higher-generation products) form dimers in the mass spectra collected in the negative ion mode of ESI (e.g., for β -caryophyllonic acid (MW 252, $C_{15}H_{24}O_3$) $[2M-H]^-$ at m/z 503 ($C_{30}H_{27}O_6^-$) was detected). No dimer formation was observed for organosulfates despite relatively high signal intensity of these compounds. Although dimer formation could be potential artifacts of the ESI, the importance of dimer formation of β -caryophyllene gas-phase products to new particle formation can be noted and certainly warrants further investigation.

3.3 Influence of aerosol acidity on the β -caryophyllene SOA composition

In the series of β -caryophyllene/ NO_x irradiation experiments, the aerosol acidity ranged from 112 to 1150 nmol H^+ m^{-3} and SOA concentrations ranged from 9.97 to 34.0 $\mu g C m^{-3}$. Higher SOA concentrations were measured in the presence of increased aerosol acidity. For comparison, field measurements of aerosol acidity as $[H^+]_{air}$ have been reported (e.g., Liu et al., 1996; Pathak et al., 2003, 2004; Surratt et al., 2007b). The $[H^+]_{air}$ generally ranged from about 20 to 130 nmol H^+ m^{-3} . Aerosol acidities have also been observed to exceed 300 nmol of H^+ m^{-3} during episodes of high photochemical activity in the eastern US. For example, Liu et al. (1996) observed an aerosol acidity of up to 400 nmol of H^+ m^{-3} in particles collected from Uniontown, PA. Since changes in the aerosol acidity in the present study had no significant direct effect on the gas-phase chemistry in these series of experiments (Offenberg et al., 2009), changes in the composition of β -caryophyllene SOA at different acidities is likely attributed to the particle-phase reactions. Figures 1–5 show the concentrations of compounds detected by ESI in both positive and negative ion modes in the series of β -caryophyllene/ NO_x irradiation experiments. Different

effects of acidity on the abundance of individual compounds have been observed. For gas-phase products (Figs. 1–3) and nitrogen-containing compounds (Fig. 4) detected, some compounds (e.g., β -hydroxynocaryophyllon aldehyde, β -dihydroxynocaryophyllon aldehyde, β -oxonocaryophyllonic acid, and β -hydroxynocaryophyllonic acid) show an increase with increasing aerosol acidity, while other compounds (e.g., β -nocaryophyllon aldehyde, β -hydroxycaryophyllon aldehyde, β -caryophyllonic acid, and β -hydroxycaryophyllonic acid) exhibit a decrease at higher aerosol acidity. It is also seen that acidity has no significant effect on the concentration of some compounds (e.g., β -hydroxynocaryophyllonic acid and β -dihydroxynocaryophyllonic acid).

For particle-phase reaction products, many hydrated compounds are detected at low aerosol acidity, while a few hydrated compounds (e.g., hydrated β -caryophyllonic acid and hydrated β -nocaryophyllonic acid) are detected only at higher aerosol acidity. The concentrations of many, but not all, hydrated compounds are found to increase with increasing aerosol acidity. By contrast, hydrated β -nocaryophyllonic acid has a lower concentration at higher aerosol acidity. Different effects of aerosol acidity on the concentration of high molecular weight compounds (MW > 300 Da) are observed. Figure 5 shows that the concentration of organosulfates and nitrated organosulfates generally increases with increasing aerosol acidity, except m/z 349 and 363. The concentrations of some organosulfates increase substantially with the aerosol acidity. For example, the signal intensities for m/z 317 and 347 increase by a factor of ~ 8 at the highest aerosol acidity, as compared to the lowest aerosol acidity. Also, a larger array of organosulfates is detected under higher acidic conditions. The aerosol acidity and sulfate content determine not only the concentration of organosulfates but also the kinds of organosulfates formed. To our knowledge, this is the first detection of organosulfates and nitrated organosulfates derived from a sesquiterpene.

Although the mechanisms by which acidity affects the concentrations of individual compounds are not well understood, some observations can be made. It is found that not all particle-phase concentrations of gas-phase products increase with increasing aerosol acidity. Although gas/particle equilibrium shifts further toward the particle phase due to enhanced particle-phase reactions, the condensed gas-phase products can, as a result, react in the particle phase to form other products (e.g., hydrated compounds and sulfate esters) at an accelerated rate under acidic conditions. Because such reactions serve to convert the specific partitioning species to another compound, the enhanced gas/particle equilibrium does not necessarily lead to an increase in the particle-phase concentration of gas-phase products. Although an increase in gas/particle partitioning coefficients of gas-phase products may help to capture the acid-enhanced SOA formation in a model (Kroll and Seinfeld, 2005), increased acidity does not always lead to an increase in the particle-phase concentration of gas-phase products.

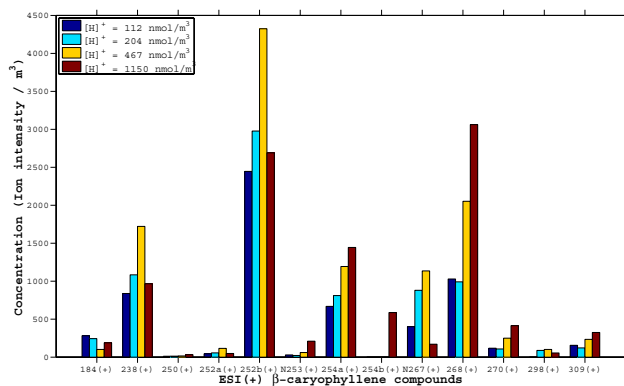


Fig. 1. Concentration of compounds detected by ESI in positive ion mode in the series of β -caryophyllene/ NO_x irradiation experiments. Chemical formulas and proposed chemical structures of these compounds are given in Table 2.

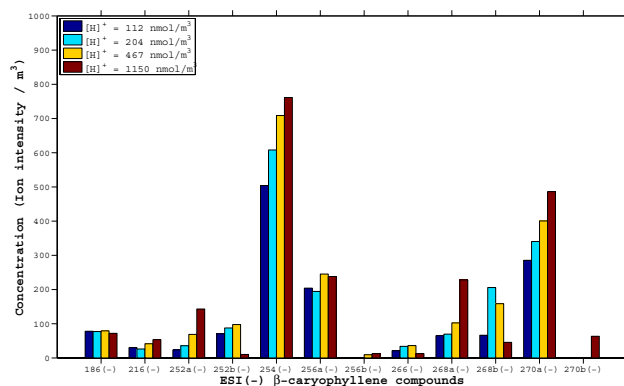


Fig. 2. Concentration of compounds detected by ESI in negative ion mode in the series of β -caryophyllene/ NO_x irradiation experiments. Chemical formulas and proposed chemical structures of these compounds are given in Table 3.

The concentrations of particle-phase reaction products formed via acid-catalyzed reactions are expected to increase with increasing aerosol acidity. However, a few hydrated gas-phase products and some higher molecular weight compounds have a lower concentration at higher aerosol acidity. It is possible that other chemical reactions (e.g., organosulfate formation processes) may become kinetically more favorable and competitive at higher aerosol acidity. Due to the complexity of chemical reactions that can potentially occur among the compounds in the particle phase, it may not be surprising to see that the acidity exhibits different effects on the concentration of particle-phase reaction products at different acidities and not all classes of particle-phase reaction products have a higher concentration at higher acidity.

Overall, increased acidity exhibits different effects on the abundance of individual compounds and does not always enhance the concentration of gas-phase and particle-phase

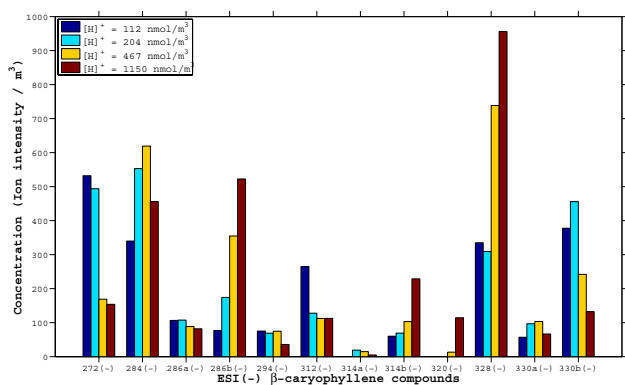


Fig. 3. Concentration of compounds detected by ESI in negative ion mode in the series of β -caryophyllene/ NO_x irradiation experiments. Chemical formulas and proposed chemical structures of these compounds are given in Table 3.

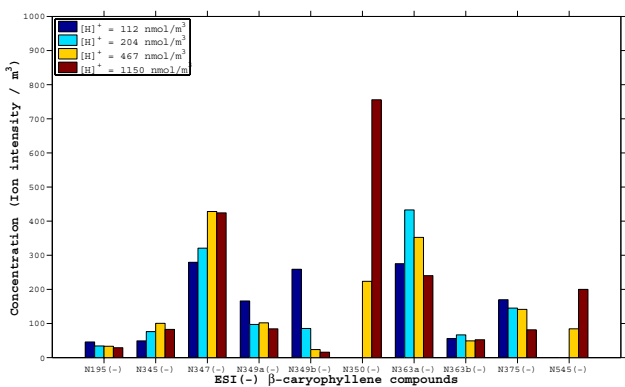


Fig. 4. Concentration of compounds detected by ESI in negative ion mode in the series of β -caryophyllene/ NO_x irradiation experiments (nitrogen-containing compounds). Chemical formulas and proposed chemical structures of these compounds are given in Table 4.

reaction products. Varying acidity also changes the product distribution. Although qualitative data are obtained for the concentrations, the relative increase in concentration of many gas-phase and particle-phase reaction products provides chemical evidence for the acid enhanced SOA formation from β -caryophyllene/ NO_x irradiation experiments.

4 Atmospheric implications

Chemical characterization of particle-phase products in the chamber samples can suggest possible chemical tracers for SOA formation from β -caryophyllene in ambient aerosol. Fine ambient aerosol collected in downtown Atlanta, GA (JST) and rural Yorkville, GA (YRK) during the AMIGAS campaign was analyzed for the presence of β -caryophyllene SOA constituents characterized from the laboratory stud-

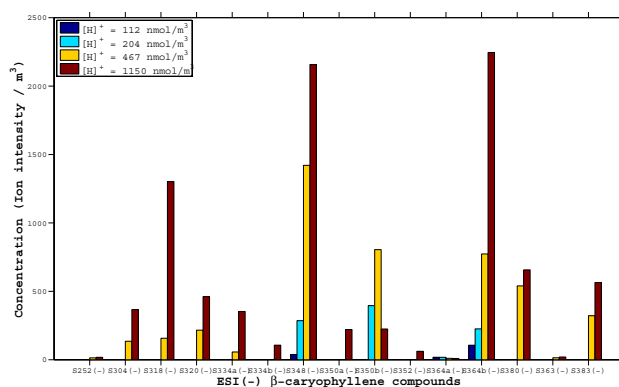


Fig. 5. Concentration of compounds detected by ESI in negative ion mode in the series of β -caryophyllene/ NO_x irradiation experiments (organosulfates and nitrated organosulfates). Chemical formulas and proposed chemical structures of these compounds are given in Table 5.

ies. As shown in Table S1, the retention time and accurate mass measurements match very well for four ions detected in both ambient and chamber samples by ESI in the positive ion mode. Three of these compounds have been tentatively identified in the present study and are β -nocaryophyllon aldehyde, β -hydroxynocaryophyllon aldehyde, and β -dihydroxynocaryophyllon aldehyde. Each of these three compounds is a second-generation ozonolysis product previously identified in β -caryophyllene ozonolysis (Li et al., 2011). As shown in Schemes 2–4, these compounds can also be produced from the reaction of β -caryophyllene with a combination of O_3 and OH . The chemical structure of the compound ($\text{C}_{15}\text{H}_{24}\text{O}_4$) is not known yet. Although the emission of β -caryophyllene drops sharply at night (Sakulyanontvittaya et al., 2008), all these compounds have been detected in most day and night samples at both sites. As shown in Table S1, based on the limited sample sizes, β -nocaryophyllon aldehyde showed a higher concentration in the nighttime samples at both JST and YRK sites. No strong diurnal variation in the concentrations was observed for the other compounds. Recently, Parshintsev et al. (2008) reported that β -nocaryophyllon aldehyde was present in ambient aerosol collected during spring 2003 at Hyytiälä, Finland. β -caryophyllon aldehyde was not detected in their ambient samples.

Gas/particle partitioning coefficients of the three aldehydes, K_p ($\text{m}^3 \mu\text{g}^{-1}$), are estimated at 297 K (Pankow, 1994). As a first approximation, the activity coefficients of the products in the particle phase are assumed to be unity and the molecular weight of the products is used as mean molecular weight in the absorbing phase. Vapor pressures are estimated at 297 K using the model developed by Pankow and Asher (2008). Saturation vapor pressure, c^* is inversely proportional to K_p ($c^* \sim 1/K_p$). The fraction F of a semivolatile compound in the particle phase can be expressed

in term of K_p as $F = MK_p/(1 + MK_p)$, where M is the amount of absorbing material ($\mu\text{g m}^{-3}$). Based on estimated gas/particle partitioning coefficients of β -nocyaryophyllon aldehyde ($K_p = 2.5 \times 10^{-3} \text{ m}^3 \mu\text{g}^{-1}$; $c^* = 400 \mu\text{g m}^{-3}$), β -hydroxynocyaryophyllon aldehyde ($K_p = 0.37 \text{ m}^3 \mu\text{g}^{-1}$; $c^* = 2.7 \mu\text{g m}^{-3}$), and β -dihydroxynocyaryophyllon aldehyde ($K_p = 54 \text{ m}^3 \mu\text{g}^{-1}$; $c^* = 0.018 \mu\text{g m}^{-3}$), a significant fraction of β -hydroxynocyaryophyllon aldehyde ($F = 0.787$) and β -dihydroxynocyaryophyllon aldehyde ($F = 0.998$) is present in the particle phase under typical organic mass loading ($M \sim 10 \mu\text{g m}^{-3}$). A small portion of β -nocyaryophyllon aldehyde ($F = 0.024$) can partition into the particle phase. The estimated saturated vapor pressures of these compounds in the present work are lower by a factor of about 2–40 than those estimated by Li et al. (2011) using a different vapor pressure estimation model.

Organosulfates detected in the laboratory-generated β -caryophyllene SOA were not observed in the ambient samples collected from the AMIGAS campaign. It is possible that the acidity of ambient aerosol is not strong enough for the formation of β -caryophyllene-derived organosulfates. As shown in Fig. 5, most organosulfates detected in the chamber samples require high aerosol acidity ($467\text{--}1150 \text{ nmol H}^+ \text{ m}^{-3}$). It is worth noting that isoprene-derived organosulfates (e.g., organosulfates of 2-methyltetrols) have been detected in these AMIGAS ambient samples (Chan et al., 2010), which were also detected in laboratory-generated isoprene SOA that employed a lower $[\text{H}^+]_{\text{air}}$ that lied between $275\text{--}517 \text{ nmol m}^{-3}$ (Surratt et al., 2007b). Although accurate mass measurements obtained in the negative ion mode show that similar molecular ions were detected in both the AMIGAS and chamber samples for some β -caryophyllene-derived acids, the chromatographic peaks of these ions in the AMIGAS samples elute at different retention times ($\Delta\text{RT} > 0.2 \text{ min}$) and may not correspond to those of the chamber samples, especially since our study lacked authentic standards and tandem MS data. The detection of β -caryophyllinic acid in ambient samples is also complicated by β -nocyaryophyllonic acid. β -caryophyllinic acid and β -nocyaryophyllonic acid have the same chemical formula ($\text{C}_{14}\text{H}_{22}\text{O}_4$) and cannot be differentiated in the accurate mass measurements.

Overall, the presence of β -caryophyllene products in ambient aerosol has been confirmed based on the agreement of chromatographic retention times and accurate mass measurements between chamber and field samples. These results suggest that the presence of β -caryophyllene products in biogenic SOA can be used as an indication of its contribution to SOA. β -nocyaryophyllon aldehyde, β -hydroxynocyaryophyllon aldehyde, and β -dihydroxynocyaryophyllon aldehyde may be good candidates for β -caryophyllene SOA tracers.

Supplementary material related to this article is available online at:

<http://www.atmos-chem-phys.net/11/1735/2011/acp-11-1735-2011-supplement.pdf>.

Acknowledgements. This work was supported by the Electric Power Research Institute and the Southern Company, Birmingham, AL. We acknowledge all members of the AMIGAS for their support during the field campaign. The US Environmental Protection Agency through its Office of Research and Development funded and collaborated in the research described here under Contract 68-D-00-206 to Alion Science and Technology. It has been subject to Agency review and approved for publication. Mention of trade names or commercial products does not constitute an endorsement or recommendation for use.

Edited by: H. Saathoff

References

- Bones, D. L., Henricksen, D. K., Mang, S. A., Gonsior, M., Bate-man, A. P., Nguyen, T. B., Cooper, W. J., and Sergey Nizkorodov, S. A.: Appearance of strong absorbers and fluorophores in limonene-O3 secondary organic aerosol due to NH_4^+ -mediated chemical aging over long time scales, *J. Geophys. Res.*, 115, D05203, doi:10.1029/2009JD012864, 2010.
- Bonn, B. and Moortgat, G. K.: Sesquiterpene ozonolysis: Origin of atmospheric new particle formation from biogenic hydrocarbons, *Geophys. Res. Lett.*, 30(11), 1585, doi:10.1029/2003GL017000, 2003.
- Calogirou, A., Kotzias, D., and Kettrup, A.: Product analysis of the gas-phase reaction of beta-caryophyllene with ozone, *Atmos. Environ.*, 31, 283–285, 1997.
- Camredon, M., Hamilton, J. F., Alam, M. S., Wyche, K. P., Carr, T., White, I. R., Monks, P. S., Rickard, A. R., and Bloss, W. J.: Distribution of gaseous and particulate organic composition during dark α -pinene ozonolysis, *Atmos. Chem. Phys.*, 10, 2893–2917, doi:10.5194/acp-10-2893-2010, 2010.
- Chan, M. N., Surratt, J. D., Claeys, M., Edgerton, E. S., Tanner, R. L., Shaw, S. L., Zheng, M., Knipping, E. M., Eddingsaas, N. C., Wennberg, P. O., and Seinfeld, J. H.: Characterization and quantification of isoprene-derived epoxydiols in ambient aerosol in the southeastern United States, *Environ. Sci. Technol.*, 44, 4590–4596, 2010.
- Cole-Filipiak, N. C., O'Connor, A. E., and Elrod, M. J.: Kinetics of the hydrolysis of atmospherically relevant isoprene-derived hydroxy epoxides, *Environ. Sci. Technol.*, 44, 6718–6723, 2010.
- Eddingsaas, N. C., VanderVelde, D. G., and Wennberg, P. O.: Kinetics and products of the acid-catalyzed ring-opening of atmospherically relevant butyl epoxy alcohols, *J. Phys. Chem. A*, 114, 8106–8113, 2010.
- Galloway, M. M., Chhabra, P. S., Chan, A. W. H., Surratt, J. D., Flagan, R. C., Seinfeld, J. H., and Keutsch, F. N.: Glyoxal uptake on ammonium sulphate seed aerosol: reaction products and reversibility of uptake under dark and irradiated conditions, *Atmos. Chem. Phys.*, 9, 3331–3345, doi:10.5194/acp-9-3331-2009, 2009.

- Griffin, R. J., Cocker, D. R., Flagan, R. C., and Seinfeld, J. H.: Organic aerosol formation from the oxidation of biogenic hydrocarbons, *J. Geophys. Res.*, 104, 3555–3567, 1999.
- Hallquist, M., Wenger, J. C., Baltensperger, U., Rudich, Y., Simpson, D., Claeys, M., Dommen, J., Donahue, N. M., George, C., Goldstein, A. H., Hamilton, J. F., Herrmann, H., Hoffmann, T., Iinuma, Y., Jang, M., Jenkin, M. E., Jimenez, J. L., Kiendler-Scharr, A., Maenhaut, W., McFiggans, G., Mentel, Th. F., Monod, A., Prévôt, A. S. H., Seinfeld, J. H., Surratt, J. D., Szmigielski, R., and Wildt, J.: The formation, properties and impact of secondary organic aerosol: current and emerging issues, *Atmos. Chem. Phys.*, 9, 5155–5236, doi:10.5194/acp-9-5155-2009, 2009.
- Iinuma, Y., Müller, C., Berndt, T., Böge, O., Claeys, M., and Herrmann, H.: Evidence for the existence of organosulfates from beta-pinene ozonolysis in ambient secondary organic aerosol, *Environ. Sci. Technol.*, 41, 6678–6683, 2007.
- Iinuma, Y., Böge, O., Kahnt, A., and Herrmann, H.: Laboratory chamber studies on the formation of organosulfates from reactive uptake of monoterpene oxides, *Phys. Chem. Chem. Phys.*, 11, 7985–7997, 2009.
- Jang, M., Czoschke, N. M., Lee, S., and Kamens, R. M.: Heterogeneous atmospheric aerosol production by acid-catalyzed particle phase reactions, *Science*, 298, 814–817, 2002.
- Jaoui, M., Leungsakul, S., and Kamens, R. M.: Gas and particle products distribution from the reaction of beta-caryophyllene with ozone, *J. Atmos. Chem.*, 45, 261–287, 2003.
- Jaoui, M., Lewandowski, M., Kleindienst, T. E., Offenber, J. H., and Edney, E. O.: Beta-caryophyllinic acid: An atmospheric tracer for beta-caryophyllene secondary organic aerosol, *Geophys. Res. Lett.*, 34, L05816, doi:10.1029/2006GL028827, 2007.
- Kanawati, B., Herrmann, F., Joniec, S., Winterhalter, R., and Moortgat, G. K.: Mass spectrometric characterization of beta-caryophyllene ozonolysis products in the aerosol studied using an electrospray triple quadrupole and time-of-flight analyzer hybrid system and density functional theory, *Rapid Commun. Mass Spectrom.*, 22, 165–186, 2008.
- Kleindienst, T. E., Jaoui, M., Lewandowski, M., Offenber, J. H., Lewis, C. W., Bhavne, P. V., and Edney, E. O.: Estimates of the contributions of biogenic and anthropogenic hydrocarbons to secondary organic aerosol at a southeastern US location, *Atmos. Environ.*, 41, 8288–8300, 2007.
- Kroll, J. H. and Seinfeld, J. H.: Representation of secondary organic aerosol laboratory chamber data for the interpretation of mechanisms of particle growth, *Environ. Sci. Technol.*, 39, 4159–4165, 2005.
- Kroll, J. H. and Seinfeld, J. H.: Chemistry of secondary organic aerosol: Formation and evolution of low-volatility organics in the atmosphere, *Atmos. Environ.*, 42, 3593–3624, 2008.
- Larsen, B. R., Lahaniati, M., Calogirou, A., and Kotzias, D.: Atmospheric oxidation products of terpenes: a new nomenclature, *Chemosphere*, 37, 1207–1220, 1998.
- Lee, A., Goldstein, A. H., Keywood, M. D., Gao, S., Varutbangkul, V., Bahreini, R., Ng, N. L., Flagan, R. C., and Seinfeld, J. H.: Gas-phase products and secondary aerosol yields from the ozonolysis of ten different terpenes, *J. Geophys. Res.*, 111(D7), D07302, doi:10.1029/2005JD006437, 2006a.
- Lee, A., Goldstein, A. H., Kroll, J. H., Ng, N. L., Varutbangkul, V., Flagan, R. C., and Seinfeld, J. H.: Gas-phase products and secondary aerosol yields from the photooxidation of 16 different terpenes, *J. Geophys. Res.*, 111(D17), D17305, doi:10.1029/2006JD007050, 2006b.
- Lewandowski, M., Jaoui, M., Offenber, J. H., Kleindienst, T. E., Edney, E. O., Sheesley, R. J., and Schauer, J. J.: Primary and secondary contributions to ambient PM in Midwestern United States, *Environ. Sci. Technol.*, 42, 3303–3309, 2008.
- Li, Y. J., Chen, Q., Guzman, M. I., Chan, C. K., and Martin, S. T.: Second-generation products contribute substantially to the particle-phase organic material produced by beta-caryophyllene ozonolysis, *Atmos. Chem. Phys.*, 11, 121–132, doi:10.5194/acp-11-121-2011, 2011.
- Liggio, J. and Li, S. M.: Organosulfate formation during the uptake of pinonaldehyde on acidic sulfate aerosols, *Geophys. Res. Lett.*, 33(13), L13808, doi:10.1029/2006GL026079, 2006.
- Liu, L.-J. S., Burton, R., Wilson, W. E., and Koutrakis, P.: Comparison of aerosol acidity in urban and semirural environments, *Atmos. Environ.*, 30, 1237–1245, 1996.
- Minerath, E. C., Casale, M. T., and Elrod, M. J.: Kinetics feasibility study of alcohol sulfate esterification reactions in tropospheric aerosols, *Environ. Sci. Technol.*, 42, 4410–4415, 2008.
- Minerath, E. C., Schultz, M. P., and Elrod, M. J.: Kinetics of the reactions of isoprene-derived epoxides in model tropospheric aerosol solutions, *Environ. Sci. Technol.*, 43, 8133–8139, 2009.
- Ng, N. L., Kroll, J. H., Keywood, M. D., Bahreini, R., Varutbangkul, V., Flagan, R. C., Seinfeld, J. H., Lee, A., and Goldstein, A. H.: Contribution of first- versus second-generation products to secondary organic aerosols formed in the oxidation of biogenic hydrocarbons, *Environ. Sci. Technol.*, 40, 2283–2297, 2006.
- Nguyen, T. L., Winterhalter, R., Moortgat, G., Kanawati, B., Peeters, J., and Vereecken, L.: The gas-phase ozonolysis of beta-caryophyllene (C₁₅H₂₄), Part 2: A theoretical study, *Phys. Chem. Chem. Phys.*, 11, 4173–4183, 2009.
- Nozière, B., Dziedzic, P., and Córdova, A.: Products and kinetics of the liquid-phase reaction of glyoxal catalyzed by ammonium ions (NH₄⁺), *J. Phys. Chem. A*, 113, 231–237, 2009.
- Nozière, B., Ekstrom, S., Alsberg, T., and Holmstrom, S.: Radical-initiated formation of organosulfates and surfactants in atmospheric aerosols, *Geophys. Res. Lett.*, 37, L05806, doi:10.1029/2009GL041683, 2010.
- Offenber, J. H., Lewandowski, M., Edney, E. O., Kleindienst, T. E., and Jaoui, M.: Influence of aerosol acidity on the formation of secondary organic aerosol from biogenic precursor hydrocarbons, *Environ. Sci. Technol.*, 43, 7742–7747, 2009.
- Pankow, J. F.: An absorption model of the gas aerosol partitioning involved in the formation of secondary organic aerosol, *Atmos. Environ.*, 28, 189–193, 1994.
- Pankow, J. F. and Asher, W. E.: SIMPOL.1: a simple group contribution method for predicting vapor pressures and enthalpies of vaporization of multifunctional organic compounds, *Atmos. Chem. Phys.*, 8, 2773–2796, doi:10.5194/acp-8-2773-2008, 2008.
- Parshintsev, J., Nurmi, J., Kilpelainen, I., Hartonen, K., Kulmala, M., and Riekkola, M. L.: Preparation of beta-caryophyllene oxidation products and their determination in ambient aerosol samples, *Anal. Bioanal. Chem.*, 390, 913–919, 2008.
- Pathak, R. K., Yao, X. H., Lau, A. K. H., and Chan, C. K.: Acidity and concentrations of ionic species of PM_{2.5} in Hong Kong,

- Atmos. Environ., 37, 1113–1124, 2003.
- Pathak, R. K., Louie, P. K. K., and Chan, C. K.: Characteristics of aerosol acidity in Hong Kong, Atmos. Environ., 38, 2965–2974, 2004.
- Perri, M. J., Lim, Y. B., Seitzinger, S. P., and Turpin, B. J.: Organosulfates from glycolaldehyde in aqueous aerosols and clouds: laboratory studies, Atmos. Environ., 44, 2658–2664, 2010.
- Pio, C., Alves, C., and Duarte, A.: Organic components of aerosols in a forested area of central Greece, Atmos. Environ., 35, 389–401, 2001.
- Rudzinski, K. J., Gmachowski, L., and Kuznietsova, I.: Reactions of isoprene and sulphony radical-anions – a possible source of atmospheric organosulphites and organosulphates, Atmos. Chem. Phys., 9, 2129–2140, doi:10.5194/acp-9-2129-2009, 2009.
- Sakulyanontvittaya, T., Duhl, T., Wiedinmyer, C., Helmig, D., Matsunaga, S., Potosnak, M., Milford, J., and Guenther, A. Monoterpene and sesquiterpene emission estimates for the United States, Environ. Sci. Technol., 42, 1623–1629, 2008.
- Shu Y. and Atkinson, R.: Rate constants for the gas phase reactions of O₃ with a series of terpenes and OH radical formation from the O₃ reactions with sesquiterpenes at 296 ± 2 K, Int. J. Chem. Kinet., 26, 1193–1205, 1994.
- Shu, Y. and Atkinson, R.: Atmospheric lifetimes and fates of a series of sesquiterpenes, J. Geophys. Res.-Atmos., 100, 7275–7281, 1995.
- Surratt, J. D., Kroll, J. H., Kleindienst, T. E., Edney, E. O., Claeys, M., Sorooshian, A., Ng, N. L., Offenberg, J. H., Lewandowski, M., Jaoui, M., Flagan, R. C., and Seinfeld, J. H.: Evidence for organosulfates in secondary organic aerosol, Environ. Sci. Technol., 41, 517–527, 2007a.
- Surratt, J. D., Lewandowski, M., Offenberg, J. H., Jaoui, M., Kleindienst, T. E., Edney, E. O., and Seinfeld, J. H.: Effect of acidity on secondary organic aerosol formation from isoprene, Environ. Sci. Technol., 41, 5363–5369, 2007b.
- Surratt, J. D., Gómez-González, Y., Chan, A. W. H., Vermeylen, R., Shahgholi, M., Kleindienst, T. E., Edney, E. O., Offenberg, J. H., Lewandowski, M., Jaoui, M., Maenhaut, W., Claeys, M., Flagan, R. C., and Seinfeld, J. H.: Organosulfate formation in biogenic secondary organic aerosol, J. Phys. Chem. A, 112, 8345–8378, 2008.
- Surratt, J. D., Chan, A. W. H., Eddingsaas, N. C., Chan, M. N., Loza, C. L., Kwan, A. J., Hersey, S. P., Flagan, R. C., Wennberg, P. O., and Seinfeld, J. H.: Reactive intermediates revealed in secondary organic aerosol formation from isoprene, P. Natl. Acad. Sci. USA, 107, 6640–6645, 2010.
- Winterhalter, R., Herrmann, F., Kanawati, B., Nguyen, T. L., Peeters, J., Vereecken, L., and Moortgat, G. K.: The gas-phase ozonolysis of beta-caryophyllene (C₁₅H₂₄), Part 1: an experimental study, Phys. Chem. Chem. Phys., 11, 4152–4172, 2009.

Appendix I

α -Pinene Photooxidation under Controlled Chemical Conditions – Part 2: SOA Yield and Composition in Low- and High-NO Environments¹¹

¹¹ Reproduced by permission from “ α -Pinene photooxidation under controlled chemical conditions – Part 2: SOA yield and composition in low- and high-NO environments” by N. C. Eddingsaas, C. L. Loza, L. D. Yee, M. Chan, K. A. Schilling, P. S. Chhabra, J. H. Seinfeld, and P. O. Wennberg. *Atmos. Chem. Phys.* **2012**, *12*, 7413-7427.



α -pinene photooxidation under controlled chemical conditions – Part 2: SOA yield and composition in low- and high-NO_x environments

N. C. Eddingsaas¹, C. L. Loza¹, L. D. Yee², M. Chan², K. A. Schilling¹, P. S. Chhabra^{1,*}, J. H. Seinfeld^{1,2}, and P. O. Wennberg^{2,3}

¹Division of Chemistry and Chemical Engineering, California Institute of Technology, Pasadena, CA, USA

²Division of Engineering and Applied Science, California Institute of Technology, Pasadena, CA, USA

³Division of Geological and Planetary Sciences, California Institute of Technology, Pasadena, CA, USA

* now at: Aerodyne Research Inc, Billerica, MA, USA

Correspondence to: N. C. Eddingsaas (eddingsa@caltech.edu)

Received: 2 March 2012 – Published in Atmos. Chem. Phys. Discuss.: 4 April 2012

Revised: 26 July 2012 – Accepted: 30 July 2012 – Published: 16 August 2012

Abstract. The gas-phase oxidation of α -pinene produces a large amount of secondary organic aerosol (SOA) in the atmosphere. A number of carboxylic acids, organosulfates and nitrooxy organosulfates associated with α -pinene have been found in field samples and some are used as tracers of α -pinene oxidation. α -pinene reacts readily with OH and O₃ in the atmosphere followed by reactions with both HO₂ and NO. Due to the large number of potential reaction pathways, it can be difficult to determine what conditions lead to SOA. To better understand the SOA yield and chemical composition from low- and high-NO_x OH oxidation of α -pinene, studies were conducted in the Caltech atmospheric chamber under controlled chemical conditions. Experiments used low O₃ concentrations to ensure that OH was the main oxidant and low α -pinene concentrations such that the peroxy radical (RO₂) reacted primarily with either HO₂ under low-NO_x conditions or NO under high-NO_x conditions. SOA yield was suppressed under conditions of high-NO_x. SOA yield under high-NO_x conditions was greater when ammonium sulfate/sulfuric acid seed particles (highly acidic) were present prior to the onset of growth than when ammonium sulfate seed particles (mildly acidic) were present; this dependence was not observed under low-NO_x conditions. When aerosol seed particles were introduced after OH oxidation, allowing for later generation species to be exposed to fresh inorganic seed particles, a number of low-NO_x products partitioned to the highly acidic aerosol. This indicates that the effect of

seed acidity and SOA yield might be under-estimated in traditional experiments where aerosol seed particles are introduced prior to oxidation. We also identify the presence of a number of carboxylic acids that are used as tracer compounds of α -pinene oxidation in the field as well as the formation of organosulfates and nitrooxy organosulfates. A number of the carboxylic acids were observed under all conditions, however, pinic and pinonic acid were only observed under low-NO_x conditions. Evidence is provided for particle-phase sulfate esterification of multi-functional alcohols.

1 Introduction

Biogenically emitted monoterpenes are important to atmospheric organic aerosol concentration and composition due to their large emission rates and high secondary organic aerosol (SOA) yields (Guenther et al., 1995; Hoffmann et al., 1997; Chung and Seinfeld, 2002; Pye et al., 2010). Of the monoterpenes, α -pinene is the most abundantly emitted. Many carboxylic acids, organonitrates, and organosulfates associated with α -pinene have been observed in aerosols both in the field and from laboratory oxidation (Kavouras et al., 1998, 1999; Yu et al., 1999b; Jaoui and Kamens, 2001; Larsen et al., 2001; Librando and Tringali, 2005; Surratt et al., 2007, 2008; Laaksonen et al., 2008; Zhang et al., 2010). A number of carboxylic acids have been used as particle-phase

tracers of α -pinene oxidation, including pinonic acid, pinic acid, 10-hydroxypinonic acid, terpenylic acid, diaterpenylic acid acetate, and 3-methyl-1,2,3-butanetricarboxylic acid (3-MBTCA). For instance, pinonic and pinic acid have been observed to be in high concentration in aerosols collected in Portugal (accounting for 18–40 % of fine particle mass), in Greece (up to 26 % of fine particle mass), as well as in high yield in Finland (Kavouras et al., 1998, 1999; Anttila et al., 2005).

In the troposphere, α -pinene is oxidized approximately equally by OH and O₃ during the daytime (Capouet et al., 2008). During the nighttime, NO₃ is the most important oxidant of α -pinene worldwide and oxidation by NO₃ can be important during the daytime under conditions of elevated NO_x (Spittler et al., 2006). After reaction with the oxidant, the peroxy radicals that are formed can react with a number of species, including HO₂, NO, NO₂ and other peroxy radicals (RO₂). Depending on the nature of the reactant with the peroxy radical, different oxidation products are produced in the gas phase. This was demonstrated in Part 1 of this series of papers (Eddingsaas et al., 2012). It was determined that pinonaldehyde is an important oxidation product under both low- and high-NO_x conditions. The formation of pinonaldehyde from low-NO_x OH oxidation implies that the reaction of α -pinene hydroxy hydroperoxy radical and HO₂ has a channel that produces an alkoxy radical and recycles OH. This type of reaction channel has been shown to be important only for acyl peroxy radicals and possibly toluene. In addition, it was demonstrated that number of organic acids formed from low-NO_x OH oxidation, including pinonic acid and pinonic peracid, are not formed from high-NO_x OH oxidation. From a modeling standpoint, it is of interest to understand how the different gas-phase reaction mechanisms influence the particle-phase composition and concentration. This understanding will improve the ability to accurately simulate the amount of aerosol produced in the oxidation of α -pinene.

In this study, we describe the SOA yield and particle phase composition from the photooxidation of α -pinene under conditions where the peroxy radical chemistry is known. We focus on OH photooxidation because particle-phase composition from ozonolysis of α -pinene has been extensively studied (Glasius et al., 1999; Yu et al., 1999a; Inuma et al., 2005; Presto et al., 2005; Ma et al., 2008; Shilling et al., 2009). The SOA composition from OH photooxidation has been much less studied and there are almost no studies examining low-NO_x conditions (Noziere et al., 1999; Ng et al., 2007a; Claeys et al., 2009). We discuss SOA composition focusing on several carboxylic acids which have been used as tracers of α -pinene oxidation. The formation of organosulfates and nitrooxy organosulfates formed from α -pinene photooxidation is also addressed. We compare SOA and gas-phase composition based on different peroxy radical reactants as well as different aerosol seed (i.e. no seed, ammonium sulfate (AS) seed, and ammonium sulfate and sulfuric acid (AS+SA) seed).

2 Experimental

Photooxidation experiments of α -pinene and pinonaldehyde were performed in the Caltech dual 28 m³ Teflon chambers. Details of the chamber facilities have been described elsewhere (Cocker et al., 2001; Keywood et al., 2004). Prior to each run, the chamber was flushed for a minimum of 24 h with dry purified air. While being flushed, the chamber was irradiated with the chamber lights for a minimum of six hours. The temperature, relative humidity, and concentrations of O₃, NO, and NO_x (NO and NO₂) were continuously monitored. In all experiments the RH was kept below 10 %. Aerosol size distribution and number concentration were measured continuously by a differential mobility analyzer (DMA, TSI model 3081) coupled to a condensation nucleus counter (TSI model 3760). Aerosol growth data were corrected for size dependent wall-loss (Keywood et al., 2004; Ng et al., 2007b).

Experiments were performed under low- and high-NO_x conditions. Under low-NO_x conditions, photolysis of hydrogen peroxide (H₂O₂) was the OH source, while for the high-NO_x experiments the photolysis of nitrous acid (HONO) or methyl nitrite (CH₃ONO) produced OH. For low-NO_x experiments, 280 μ l of 50 wt % H₂O₂ was injected into the chamber, resulting in a concentration \sim 4 ppm. Using HONO and CH₃ONO allowed the ratio of NO to NO₂ to be varied, with a lower ratio in the CH₃ONO experiments. For the remainder of this paper, the use of HONO as the OH source will be referred to as high-NO and the use of methyl nitrite will be referred to as high-NO₂ to distinguish between the relative importance of NO and NO₂.

HONO was prepared daily by dropwise addition of 15 ml of 1 wt % NaNO₂ into 30 ml of 10 wt % H₂SO₄ in a glass bulb, and then introduced into the chamber with dry air. This process produces NO and NO₂ as side products, which are also introduced to the chamber. CH₃ONO was synthesized, purified, and stored according to the procedure outlined by Taylor et al. (1980). CH₃ONO was warmed from liquid nitrogen temperatures and vaporized into an evacuated 500 ml glass bulb and introduced into the chamber with an air stream of 5 l min⁻¹. After addition of CH₃ONO, 300–400 ppb of NO was added to the chamber to suppress the formation of O₃. Determination of exact NO and NO₂ concentrations using the commercial NO_x monitor was precluded due to interferences by both HONO and CH₃ONO. While the exact NO and NO₂ concentration could not be determined, it was confirmed that greater NO₂ concentration and the ratio of NO₂ to NO is greater in the methyl nitrite experiments due to the increased gas-phase concentration of nitric acid and peroxyacyl nitrates (PANs). The gas-phase concentration of nitric acid and PANs in the methyl nitrite experiments was 1.4–2 times that in similar HONO experiments. At the start of all high-NO_x experiments the total NO_x reading (NO, NO_x, and interference from HONO or CH₃ONO) was 800 ppb and NO

concentration throughout the experiments was such that the concentration of O_3 never exceeded 5 ppb.

Experiments were performed with either no aerosol seed present, ammonium sulfate seed (AS), or ammonium sulfate plus sulfuric acid (AS+SA). The AS+SA produced a much more acidic aerosol seed. When applicable, seed particles were added to the chamber after the addition of the oxidant. Aerosol seed particles were generated by atomizing an aqueous solution of 15 mM $(NH_4)_2SO_4$ (AS) or 15 mM $(NH_4)_2SO_4$ and 15 mM H_2SO_4 (AS+SA). Upon addition of an aerosol seed, the initial aerosol number concentration was $\sim 1.8 \times 10^4 \text{ cm}^{-3}$, with a mean diameter of $\sim 60 \text{ nm}$, resulting in the initial aerosol volume of $10\text{--}15 \mu\text{m}^3 \text{ cm}^{-3}$.

Once the aerosol seed was added and stable, α -pinene was added to the chamber by transferring a known amount of α -pinene from a small glass bulb to achieve a concentration of 20–50 ppb. The mixing ratio of α -pinene was monitored with a gas chromatograph (Agilent 6890N) coupled with a flame ionization detector (GC-FID). The GC-FID was calibrated for α -pinene using a standard prepared in a 55 l Teflon bag. In photooxidation experiments where pinonaldehyde was the initial hydrocarbon, pinonaldehyde was introduced into the chamber by passing dry nitrogen over a liquid sample.

Gas-phase photooxidation products were monitored by a custom-modified Varian 1200 triple-quadrupole chemical ionization mass spectrometer (CIMS) (St. Clair et al., 2010). Details of the operation of the CIMS can be found in a number of previous reports (Crouse et al., 2006; Paulot et al., 2009a; St. Clair et al., 2010). The CIMS was operated in negative ion mode using CF_3O^- as the reagent ion, and in the positive ion mode using H_3O^+ for proton transfer mass spectrometry (PTR-MS). In negative mode, CF_3O^- is sensitive to polar and acidic compounds by either clustering with the analyte (R) resulting in an ion with a mass-to-charge ratio (m/z) $MW + 85$ ($R \cdot CF_3O^-$) or via fluorine ion transfer resulting in m/z $MW + 19$ ($HF \cdot R_{-H}^-$). The dominant ionization mechanism depends mostly on the acidity of the neutral species; highly acidic species such as nitric acid form only the fluorine transfer ion, while non-acidic species such as methyl hydrogen peroxide form only the cluster ion. This separation aids both in the determination of the structure of a molecule and in the identification of isomers. In negative mode, tandem mass spectrometry (MS/MS) was used to help identify functional groups of an analyte. In brief, a parent ion selected in the first quadrupole is exposed to an elevated pressure of N_2 resulting in collision-induced dissociation (CID) in the second quadrupole, and the resulting fragmentation ions are detected in the third quadrupole. Molecules with different functional groups have been shown to fragment differently by CID. For example, fragmentation of hydroperoxides form a characteristic anion at m/z 63 (Paulot et al., 2009b). Unfortunately, authentic standards for most compounds described here are not readily available, and thus the sensitivity of the CIMS cannot be experimentally determined. In the absence of such standards, we estimate that the sensitivity scales with

the thermal capture rate and the binding energy of the cluster ($VOC \cdot CF_3O^-$). Details on calculating the sensitivity of the CIMS to a given analyte can be found in previous publications (Paulot et al., 2009a,b).

Duplicate Teflon filters (PALL Life Sciences, 47 mm diameter, 1.0 μm pore size, Teflon membrane) were collected from each of the chamber experiments for off-line chemical analysis. Filter sampling was started when the aerosol volume reached a constant value. For the chemical analysis, each filter was extracted with methanol (LC-MS CHROMASOLV-grade, Sigma-Aldrich) under ultrasonication for 45 min. The extract was dried under ultra-pure nitrogen gas, and the residue was reconstituted with a 50 : 50 (*v/v*) solvent mixture of methanol with 0.1 % acetic acid (LC-MS CHROMASOLV-grade, Sigma-Aldrich) and water with 0.1 % acetic acid (LC-MS CHROMASOLV-grade, Sigma-Aldrich). Filter sample extracts were analyzed by ultra-performance liquid chromatography/electrospray ionization-time-of-flight mass spectrometry (UPLC/ESI-TOFMS) operated in negative ion mode. Further details of the filter collection, sample preparation procedures, and UPLC/ESI-TOFMS analysis can be found in a previous publications (Surratt et al., 2008; Chan et al., 2010).

Products having either a carboxylic acid group or that are organosulfates can be ionized via deprotonation and are detected in the negative ion mode as $[M - H]^-$ ions. All accurate mass measurements were within $\pm 5 \text{ mDa}$ of the theoretical mass associated with the proposed chemical formula. From repeated UPLC/ESI-TOFMS measurements, the variations in the chromatographic peak areas are about 5 % (Chan et al., 2011). The concentrations are not corrected for extraction efficiencies.

High-resolution time-of-flight aerosol mass spectrometry (HR-ToF-AMS) spectra were obtained for one low- NO_x experiment with AS seed and one high- NO_x experiment with AS seed. The analysis of the data has previously been reported (Chhabra et al., 2011). Both high-resolution W-mode and higher sensitivity V-mode were taken, switching between the two modes every minute. The V-mode data were analyzed using a fragmentation table that enables separation of sulfate, ammonium, and organic components and to time-trace specific mass-to-charge ratios (m/z) (Allan et al., 2004). W-mode data were analyzed using the high-resolution spectra toolbox, PIKA, to determine the chemical formulas contributing to distinct m/z (DeCarlo et al., 2006).

3 Results and discussion

In Part 1 (Eddingsaas et al., 2012), the gas-phase composition of OH photooxidation of α -pinene under low- NO_x , high-NO (HONO as the OH source), and high- NO_2 (methyl nitrite as the OH source) conditions was discussed. Under low- NO_x conditions, care was taken to ensure that reaction with HO_2 dominated the loss of the peroxy radicals. O_3 was suppressed

in all experiments so that the oxidation of α -pinene was completely dominated by OH oxidation. Here, the results of the aerosol phase growth, yield, and composition from these controlled experiments are discussed.

3.1 Aerosol growth and yield

Table 1 lists the experimental conditions of the studies, the SOA yields, and a number of other variables of interest. The SOA density used to calculate SOA mass and SOA yield were taken from previous results: 1.32 g cm^{-3} under low- NO_x conditions and 1.33 g cm^{-3} under high- NO_x conditions (Ng et al., 2007a). SOA yield is calculated cumulatively throughout the experiments as the ratio of SOA mass to the mass of α -pinene reacted. For this suite of experiments, we cannot directly relate the time-dependent aerosol growth curves (i.e. SOA mass as a function of experiment time) to yield because the OH concentration varied widely between the systems. For example, the initial OH concentration for the low- NO_x experiments was $\sim 2 \times 10^6 \text{ molecules cm}^{-3}$, while in the high-NO experiments the initial OH was approximately 3 times larger, and under high- NO_2 conditions the initial OH was an order of magnitude larger, thereby resulting in much faster oxidation of α -pinene and faster aerosol growth. In addition, under both high-NO and high- NO_2 conditions, the OH concentration declined significantly over time. The OH concentration through the experiments was determined by comparing the loss of α -pinene to a kinetic model of α -pinene OH oxidation under low- or high- NO_x conditions. Details of the model and gas phase measurements can be found in Part 1 (Eddingsaas et al., 2012). By using OH exposure (as units of OH concentration multiplied by reaction time in hours) as the coordinate system, a more direct comparison between different photooxidation systems is, however, possible.

Figure 1 shows SOA yield as a function of OH exposure from all experiments in the presence of AS seed particles. The overall yield was consistent between runs with the same OH source, but there is a systematic difference in SOA yield between the systems, decreasing as the concentration of NO increases. SOA growth under high- NO_2 conditions resembles low- NO_x SOA growth more than it does high-NO SOA growth, consistent with the hypothesis that reaction of the peroxy radicals with NO leads to reduced yields. Second, the SOA yield from high- NO_2 continued to increase after two α -pinene lifetimes. This is in contrast to the high-NO experiments where most of the aerosol growth is complete after one α -pinene lifetime. The SOA from low- NO_x photooxidation also continued to increase after two α -pinene lifetimes. This indicates that later generation oxidation products are important in determining the amount of SOA formed. As discussed in the gas-phase analysis (Eddingsaas et al., 2012), a distinct difference in the later generation oxidation products is the formation of carboxylic acids and peracids in the low- NO_x

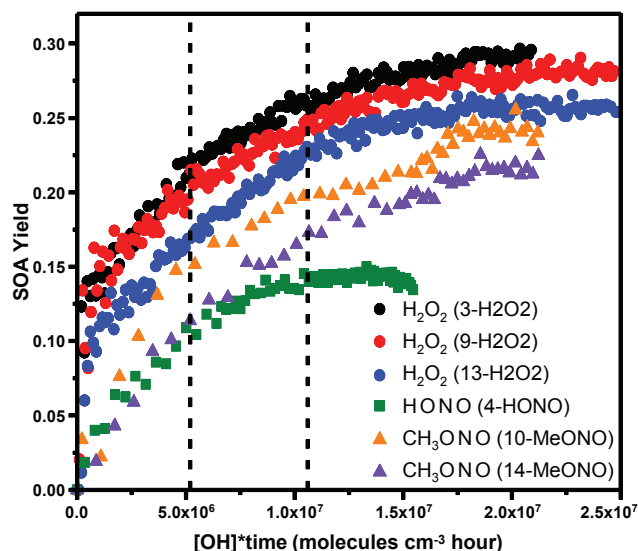


Fig. 1. SOA yield as a function of OH exposure of α -pinene from low- NO_x , high-NO, and high- NO_2 OH oxidation in the presence of ammonium sulfate seed particles. The vertical dashed lines represent one and two α -pinene lifetimes with respect to reaction with OH. The OH source and sample ID for each experiment is shown in the figure.

photooxidation. In the high- NO_2 cases, more PANs and nitric acid are formed compared to high-NO.

Illustrating that later generation oxidation products are important to SOA growth, the gas-phase time traces of first- and second-generation oxidation products are shown along with the SOA growth under all three conditions in the presence of ammonium sulfate seed in Fig. 2. Under all conditions, aerosol growth continues through the production of second-generation oxidation products. Under low- NO_x conditions, the signal for pinonaldehyde peracid and/or 10-hydroxypinonic acid is lost from the gas phase faster than pinonic acid. This is likely due to greater partitioning into the aerosol phase as a result of its lower vapor pressure. In the presence of high- NO_2 , pinonaldehyde PAN is observed to be lost from the gas phase faster than SOA growth as a result of thermal decomposition. Pinonaldehyde nitrate is lost at a faster rate when methyl nitrite is the OH source. This could be due to either higher OH exposure or aerosol uptake.

The effect of the acidity of the seed particle on SOA yield was investigated. Figure 3 shows the SOA yield as a function of OH exposure with no seed, and in the presence of either AS seed (mildly acidic) or AS + SA seed (highly acidic) in low- NO_x , high-NO, and high- NO_2 OH oxidation. From low- NO_x photooxidation with initial α -pinene concentration of $\sim 50 \text{ ppb}$, there is no difference in the aerosol growth in the presence of no, AS, or AS + SA seed. This was expected as the only difference in the gas-phase composition is that α -pinene oxide is in lower concentration in the presence of an

Table 1. SOA yields from low- and high-NO_x photooxidation of α -pinene.

Sample ID	Oxidant	Seed	Temp. (°C)	HC (ppb)	Initial Vol. ($\mu\text{m}^3 \text{cm}^{-3}$)	$\Delta\text{HC}^{\text{a}}$ ($\mu\text{g m}^{-3}$)	$\Delta\text{M}_0^{\text{b}}$ ($\mu\text{g m}^{-3}$)	SOA Yield ^c (%)
1-H2O2	H ₂ O ₂	no seed	20–23	45.0±1.0	0.9±0.3	250±6	66.8±6.0	26.7±2.5
2-HONO	HONO	no seed	20–23	50.1±1.1	0.3±.2	260±6	20.0±2.3	7.7±0.9
3-H2O2	H ₂ O ₂	AS	20–25	48.5±1.1	11.0±0.4	265±6	76.6±6.7	28.9±2.6
4-HONO	HONO	AS	20–23	52.4±1.2	12.0±0.7	258±7	37.2±3.0	14.4±1.1
5-H2O2	H ₂ O ₂	AS + SA	20–25	46.9±1.1	9.3±0.58	264±6	72.9±7.0	27.6±2.8
6-HONO	HONO	AS + SA	20–23	45.5±1.0	16.0±1.1	225±6	39.6±4.5	17.6±1.9
7-H2O2	H ₂ O ₂	no seed	20–25	19.8±0.5	0.5±0.2	109±3	40.0±3.1	36.7±3.0
8-MeONO	CH ₃ ONO	no seed	20–23	38.9±1.0	5.1±0.2	208±6	51.9±3.8	25.4±1.7
9-H2O2	H ₂ O ₂	AS	20–25	46.8±1.1	9.4±0.4	254±6	71.6±6.2	28.2±2.5
10-MeONO	CH ₃ ONO	AS	20–23	47.9±1.1	10.5±0.5	249±6	60.3±4.9	24.2±1.9
11-H2O2	H ₂ O ₂	AS + SA	20–25	46.8±1.1	8.5±0.4	256±6	70.4±6.2	27.5±2.5
12-MeONO	CH ₃ ONO	AS + SA	20–23	43.7	14	242	42.6	17.6
13-H2O2	H ₂ O ₂	AS	20–25	45.0±1.0	13.7±0.6	247±6	63.5±5.6	25.7±2.3
14-MeONO	CH ₃ ONO	AS	20–23	44.9±1	15.4±0.6	250±6	54.0±4.3	21.6±1.8

^a ΔHC : mass concentration of α -pinene reacted.

^b ΔM_0 : mass concentration of SOA.

^c SOA yield is maximum mass concentration of SOA formed divided by the mass concentration of α -pinene reacted.

acidic seed. α -pinene oxide is a minor product. This indicates that there is almost no reactive uptake occurring due to acid-catalyzed reactions and that if there are any changes in the aerosol composition, they occur within the particle phase. SOA yield was different when the initial α -pinene concentration was reduced to 20 ppb (37 % compared to 26–29 % when the initial concentration was 50 ppb). The cause of the increase in SOA yield with lower α -pinene concentration is not known.

As with low-NO_x photooxidation, there is no difference in aerosol growth under any seed conditions for high-NO₂ photooxidation. However, with high-NO, the yield does depend on seed conditions; yields increase from no seed to AS seed to AS + SA seed (increase of 22 % from AS to AS + SA seed). In the presence of AS+SA seed, the SOA yield was the same under high-NO and high-NO₂ conditions. This small increase with acidity is in contrast to low-NO_x photooxidation of isoprene where the SOA increased markedly (1000 %) (Surratt et al., 2010).

Self-nucleation under high-NO conditions did not occur until nearly one α -pinene lifetime. In contrast, nucleation occurred nearly immediately under both high-NO₂ and low-NO_x conditions. One possible explanation for the difference in behavior is that for the aerosols in the higher NO₂ case, the self-nucleated and AS seeded aerosols are more acidic than in the low-NO₂ case due to increased partitioning of nitric acid and possibly the PANs. This would result in an acidic aerosol under all conditions for the higher NO₂ experiments. When AS + SA seed is used, the particles have the same level of acidity and partitioning should be more similar. Analysis of the particle-phase composition provides more insight into the differences between the systems.

3.2 Aerosol chemical composition

Tables 2 and 3 list the UPLC peak areas for each of the carboxylic acids associated with atmospheric photooxidation of α -pinene under low-NO_x, high-NO, and high-NO₂ conditions, in the presence of either AS or AS + SA seed. Figure 4 shows the structures of the identified SOA components. The peak areas are presented both as the raw peak areas (Table 2) as well as peak areas scaled to the SOA mass loading of the low-NO_x AS seed run (Table 3), so that a weighted average of each component can be compared. Concentration calibrations were not performed and therefore the analysis is qualitative. Figure 5 shows the UPLC chromatograms from the filter samples from low-NO_x OH oxidation in the presence of AS or AS + SA seed particles along with the chromatogram from pinonaldehyde low-NO_x photooxidation, while Fig. 6 shows the UPLC chromatograms from high-NO and high-NO₂ OH oxidation in the presence of AS or AS + SA seed particles. The species of interest – pinonic acid, 10-hydroxy pinonic acid, pinic acid, terpenylic acid, 2-hydroxy terpenylic acid, diaterpenylic acid acetate, 3-MBTCA, the organosulfates and the nitrooxy organosulfates have previously been identified by UPLC/(-)ESI-TOFMS (Warnke et al., 2006; Szmigielski et al., 2007; Claeys et al., 2009), and it is these identifications that are being used to confirm the presence or absence of each species.

3.2.1 Comparison of SOA composition between low-NO_x, high-NO, and high-NO₂ OH oxidation in the presence of ammonium sulfate seed

Pinonic acid, pinic acid, and 10-hydroxy pinonic acid are only observed in substantial quantities in the aerosol phase

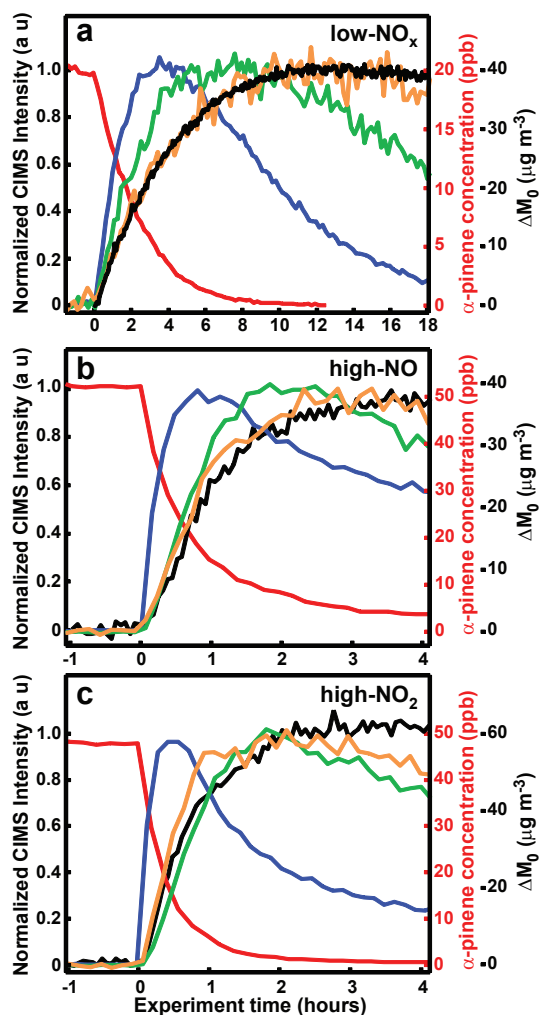


Fig. 2. Time evolution of SOA growth along with gas-phase time profile of first- and second-generation products of OH oxidation of α -pinene under (a) low-NO_x conditions (7-H₂O₂), (b) high-NO conditions (4-HONO), and (c) high-NO₂ conditions (10-MeONO). In all plots, the red line is α -pinene, blue line is pinonaldehyde, and black line is SOA growth. In (a) green is 10-hydroxy pinonic/pinonic peracid and orange is pinonic acid, (b, c) green is pinonaldehyde-PAN, and orange is pinonaldehyde nitrate.

from the low-NO_x photooxidation (Tables 2 and 3 and Fig. 5). This was expected as pinonic and 10-hydroxy pinonic acid were only observed in the gas-phase in the low-NO_x photooxidation (Eddingsaas et al., 2012). These species originate from the oxidation of pinonaldehyde as confirmed by the gas-phase data (Eddingsaas et al., 2012) as well as the UPLC chromatogram of the low-NO_x photooxidation of pinonaldehyde (Fig. 4c). Pinonic acid, pinic acid, and 10-hydroxy pinonic acid are also typical species found in SOA from the ozonolysis of α -pinene (Hoffmann et al., 1997; Ma et al., 2008; Camredon et al., 2010). Thus, it is likely that previous observation of pinonic acid, pinic acid, and 10-hydroxy

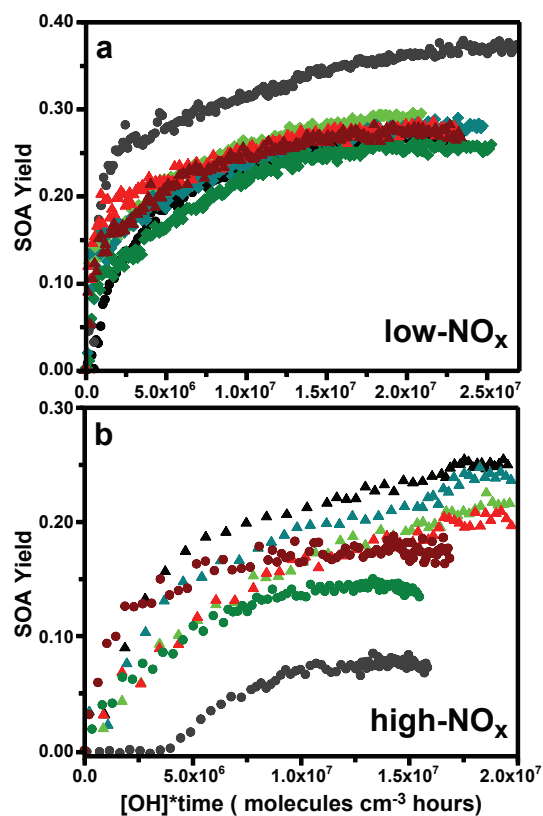


Fig. 3. SOA yield as a function of OH exposure of α -pinene OH oxidation in the presence of no (black, gray), neutral (shades of green), or acidic (shades of red) seed particles under (a) low-NO_x conditions and (b) high-NO_x conditions where photolysis of HONO (dots) or methyl nitrite (triangles) is the OH source. The sample IDs for each experiment are (a) black dots (1-H₂O₂), gray dots (7-H₂O₂), light green diamonds (3-H₂O₂), teal diamonds (9-H₂O₂), green diamonds (13-H₂O₂), red triangles (5-H₂O₂), dark red triangles (11-H₂O₂) (b) gray dots (2-HONO), black triangles (8-MeONO), green dots (4-HONO), light green triangles (10-MeONO), teal triangles (14-MeONO), dark red dots (6-HONO), and red triangles (12-MeONO). The low-NO_x experiment that resulted in greater SOA yield (gray points in panel a (7-H₂O₂)) is from 20 ppb of α -pinene, all other data is from the OH oxidation of \sim 50 ppb of α -pinene.

pinonic acid in studies of α -pinene high-NO_x photooxidation were a result of ozonolysis and not OH chemistry.

3-MBTCA is believed to be a tracer compound of α -pinene derived SOA (Szmigielski et al., 2007; Kourtchev et al., 2009; Zhang et al., 2010) and indeed it was observed here under all conditions (as well as from the low-NO_x photooxidation of pinonaldehyde). It has been proposed that 3-MBTCA is the result of further high-NO_x oxidation of pinonic acid in the gas phase (Szmigielski et al., 2007; Müller et al., 2012). A recent study by Müller et al. (2012) shows evidence of gas-phase formation of 3-MBTCA from the photooxidation of pinonic acid in the presence of NO.

Table 2. Raw peak areas from UPLC chromatograms of carboxylic acids, organosulfates, and nitrooxy organosulfates from the photooxidation of α -pinene.

SOA component ($[M - H]^-$)	H ₂ O ₂		HONO		MeONO	
	AS	AS + SA	AS	AS + SA	AS	AS + SA
2-Hydroxyterpenylic acid (187)	–	–	1918	824	2285	1509
Terpenylic acid (171)	2097	2522	911	933	1152	1255
3-methyl-1,2,3-butanetricarboxylic acid (3-MBTCA) (203)	458	702	307	337	910	1231
Diaterpenylic acid acetate (231)	318	763	1984	401	1658	1728
10-Hydroxypinonic acid (199)	2229	1760	361	426	314	662
Pinic acid (185)	1552	1469	–	–	–	–
Pinonic acid (183)	1155	1297	–	–	–	–
Sulfate of 10-hydroxy pinonic acid (279)	–	723	–	1185	–	1343
α -pinene hydroxy sulfate (249)	–	1692	–	1904	–	933
Ring opened carbonyl nitrate sulfate (310)	–	–	–	1744	–	1075
<i>m/z</i> 247.07 (C ₁₀ H ₁₅ O ₅ S)	–	–	–	3193	–	435
<i>m/z</i> 265.07 (C ₁₀ H ₁₇ O ₆ S)	–	–	–	219	–	229
<i>m/z</i> 294.06 (C ₁₀ H ₁₆ NO ₇ S)	–	–	–	1799	–	–
<i>m/z</i> 295.05 (C ₁₀ H ₁₅ O ₈ S)	–	–	–	494	–	–
<i>m/z</i> 296.04 (C ₁₀ H ₁₄ NO ₈ S)	–	–	–	108	–	–
<i>m/z</i> 328.07 (C ₁₀ H ₁₈ NO ₉ S)	–	–	–	345	–	–
<i>m/z</i> 342.05 (C ₁₀ H ₁₆ NO ₁₀ S)	–	–	–	110	–	–

Table 3. Peak areas scaled to low-NO_x AS seed SOA loading from UPLC chromatograms of carboxylic acids, organosulfates, and nitrooxy organosulfates from the photooxidation of α -pinene.

SOA component ($[M - H]^-$)	H ₂ O ₂		HONO		MeONO	
	AS	AS + SA	AS	AS + SA	AS	AS + SA
2-Hydroxyterpenylic acid (187)	–	–	4480	1426	3167	2617
Terpenylic acid (171)	2097	2451	2128	1615	1597	2177
3-methyl-1,2,3-butanetricarboxylic acid (3-MBTCA) (203)	458	682	717	583	1261	2135
Diaterpenylic acid acetate (231)	318	742	4635	695	2298	2997
10-Hydroxypinonic acid (199)	2229	1711	843	737	435	1148
Pinic acid (185)	1552	1428	–	–	–	–
Pinonic acid (183)	1155	1261	–	–	–	–
Sulfate of 10-hydroxy pinonic acid (279)	–	703	–	2051	–	2329
α -pinene hydroxy sulfate (249)	–	1645	–	3296	–	1618
Ring opened carbonyl nitrate sulfate (310)	–	–	–	3019	–	1865
<i>m/z</i> 247.07 (C ₁₀ H ₁₅ O ₅ S)	–	–	–	5527	–	755
<i>m/z</i> 265.07 (C ₁₀ H ₁₇ O ₆ S)	–	–	–	379	–	397
<i>m/z</i> 294.06 (C ₁₀ H ₁₆ NO ₇ S)	–	–	–	3114	–	–
<i>m/z</i> 295.05 (C ₁₀ H ₁₅ O ₈ S)	–	–	–	855	–	–
<i>m/z</i> 296.04 (C ₁₀ H ₁₄ NO ₈ S)	–	–	–	187	–	–
<i>m/z</i> 328.07 (C ₁₀ H ₁₈ NO ₉ S)	–	–	–	597	–	–
<i>m/z</i> 342.05 (C ₁₀ H ₁₆ NO ₁₀ S)	–	–	–	190	–	–

In the present study, however, 3-MBTCA is observed under high-NO and high-NO₂ conditions when pinonic acid is not observed and, in addition, 3-MBTCA is observed from low-NO_x photooxidation where peroxy radical reactions are dominated by reactions with HO₂. The ratio of 3-MBTCA to pinic acid in low-NO_x oxidation of α -pinene is substantially greater than from pinonaldehyde photooxidation. This is in contrast to the ratios of pinic acid, pinonic acid, and

10-hydroxypinonic acids which are very similar regardless of which initial hydrocarbon was used under low-NO_x conditions.

Terpenylic acid and diaterpenylic acid were observed in filters from all α -pinene photooxidation mechanisms, while 2-hydroxy terpenylic acid was observed only in the presence of NO_x. Under low-NO_x photooxidation, terpenylic acid is the dominant peak and is observed only as a dimer (*m/z*

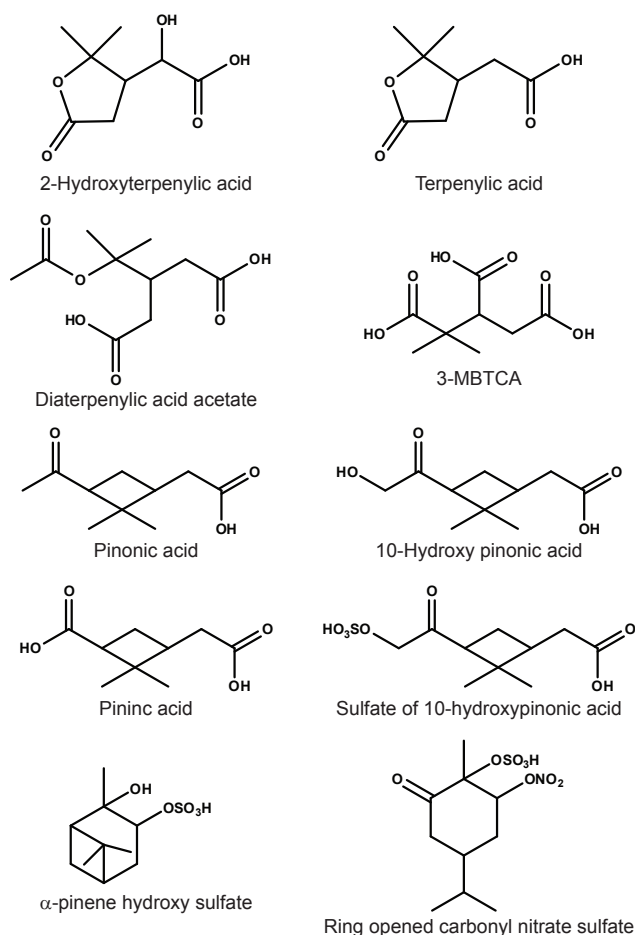


Fig. 4. Structures of identified SOA components detected by UPLC/(-)ESI-TOF.

343), while diaterpenylic acid is a minor peak. In the low- NO_x photooxidation of pinonaldehyde, terpenylic acid was observed, but it is a small contributor to the aerosol mass; diaterpenylic acid was not observed at all. There is a peak in the chromatograms for low- NO_x photooxidation of α -pinene and pinonaldehyde with a molecular ion that corresponds to 2-hydroxy terpenylic acid ($m/z = 187.06$), but it elutes much earlier than found in previous studies (Claeys et al., 2009) or in the high- NO or high- NO_2 studies here. Under high- NO and high- NO_2 photooxidation, diaterpenylic acid acetate is observed to be the dominant peak in the chromatograms. Terpenylic and 10-hydroxy terpenylic acids are also dominant peaks in the chromatograms, with their contribution to the total aerosol greater with higher NO_2 . From this analysis, it appears that terpenylic acid arises from the photooxidation of pinonaldehyde while diaterpenylic acid acetate is from some other channel of α -pinene photooxidation.

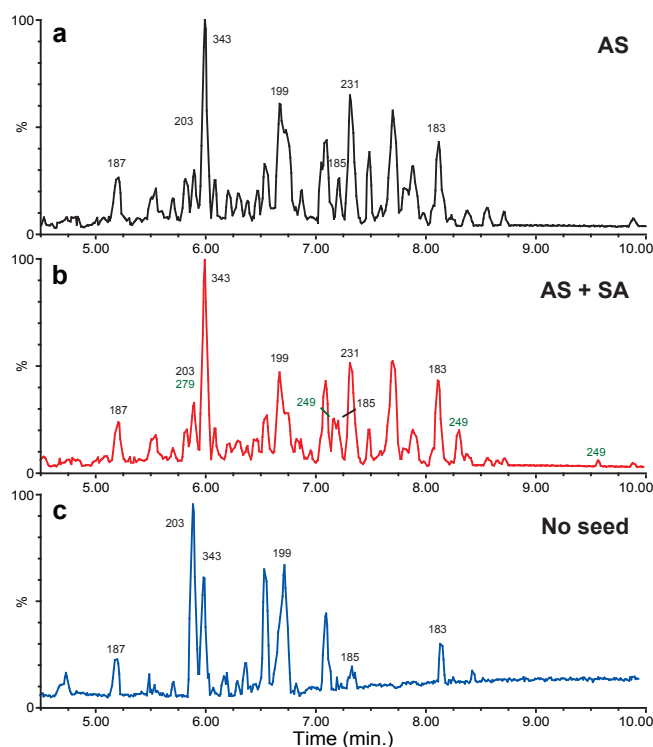


Fig. 5. UPLC/(-)ESI-TOF chromatograms from the filter samples of low- NO_x photooxidation of α -pinene or pinonaldehyde, (a) α -pinene in the presence of AS seed particles (3- H_2O_2) (b) α -pinene in the presence of AS + SA seed particles (5- H_2O_2) and (c) pinonaldehyde. Chromatographic peaks designated with black [M - H]⁻ ions are carboxylic acids and chromatographic peaks designated with green [M - H]⁻ ions are organosulfates. See Table 2 for compound names.

3.2.2 Change in SOA composition in the presence of highly acidic aerosol seed

The composition of the SOA in low- NO_x photooxidation in the presence of AS or AS + SA seed is very similar (see Tables 2 and 3 and Fig. 5). This is consistent with the fact that the SOA yield and mass loading were almost identical between these experiments. In the presence of the acidic seed, four peaks were observed that correspond to organosulfates, one with m/z 279 and three with m/z 249. The organosulfate peak at m/z 279 has been previously identified as the sulfate ester of 10-hydroxy pinonic acid and is thought to originate from the esterification of the hydroxyl group of 10-hydroxy pinonic acid (Surratt et al., 2008). Indeed, the signal for 10-hydroxy pinonic acid decreases in the presence of AS + SA seed (Table 3), while no change in peak area is observed from either pinonic or pinic acid, both of which lack a hydroxyl group. While it has been shown that for simple alcohols, sulfate esterification is too slow to be atmospherically relevant (Minerath et al., 2008), these data indicate that esterification may be sufficiently fast in more complex, acidic alcohols.

The three peaks with m/z 249 are most likely from the reactive uptake of α -pinene oxide, which was observed to be in lower concentration in the gas phase in the presence of an acidic seed. Iinuma et al. (2009) have shown that the uptake of α -pinene oxide results in the formation of three different organosulfates: 2-pinanol-3-hydrogen sulfate, 3-pinanol-2-hydrogen sulfate, and camphenol hydrogen sulfate. The SOA yield is independent of aerosol seed acidity from low- NO_x photooxidation indicating that the gas-phase yield of α -pinene oxide and the resulting organosulfates are minor components.

The SOA composition (and yield) from high- NO photooxidation is substantially different in the presence of AS + SA seed. In the presence of an acidic seed, diaterpenylic acid and 2-hydroxy terpenylic acid were greatly reduced in the aerosol while terpenylic acid was relatively unchanged (see Tables 2 and 3 and Fig. 6). A large number of organosulfates and nitrooxy organosulfates are observed. Both of the organosulfates observed in low- NO_x photooxidation are observed. The source of the m/z 249 is most likely the same, α -pinene oxide. The mechanism for the formation of the sulfate ester of 10-hydroxy pinonic acid is less clear. 10-hydroxy pinonic acid is not observed in the gas phase, is a small fraction of the particle phase mass, and its aerosol concentration is relatively unchanged in the presence of an acidic seed. In addition, 10-hydroxy pinonic acid is more prominent in low- NO_x photooxidation. However, the organosulfate associated with 10-hydroxy pinonic acid is of greater abundance in high- NO and high- NO_2 conditions than in low- NO_x conditions. The sulfate ester of 10-hydroxy pinonic acid coelutes with two other ions and therefore the peak area has greater error. However, even if the peak areas were similar, it would not be consistent with a source from 10-hydroxy pinonic acid under high- NO and high- NO_2 conditions due to the low signal. The peak is observed at the same chromatographic time under all conditions; therefore, either the organosulfates at m/z 279 are formed by different processes depending on NO concentration, or 10-hydroxy pinonic acid is not the source at all. We believe that there must be another mechanism that forms this organosulfate. The nitrooxy organosulfate ($m/z = 310$) elutes as two peaks in the chromatogram. Under high- NO and high- NO_2 conditions, two species are formed in the gas phase with molecular weight of 231 (CIMS $m/z = 316$). One of the gas-phase species was assigned to α -pinene dihydroxy nitrate as proposed in previous reports and upon sulfate esterification would produce a nitrooxy organosulfate that would produce the ion of interest (m/z 310) (Aschmann et al., 2002; Surratt et al., 2008). Thus, there is once again evidence for particle-phase sulfate esterification of a hydroxyl group in a poly-functional molecule. The largest sulfate peak was also the dominant peak in the chromatogram corresponding to m/z 247. The identification of the compound is unknown and its overall importance to the SOA yield is not known as no calibrations are available. Tables 2 and 3 list the most likely molecular formula for the ion at m/z 247, along with

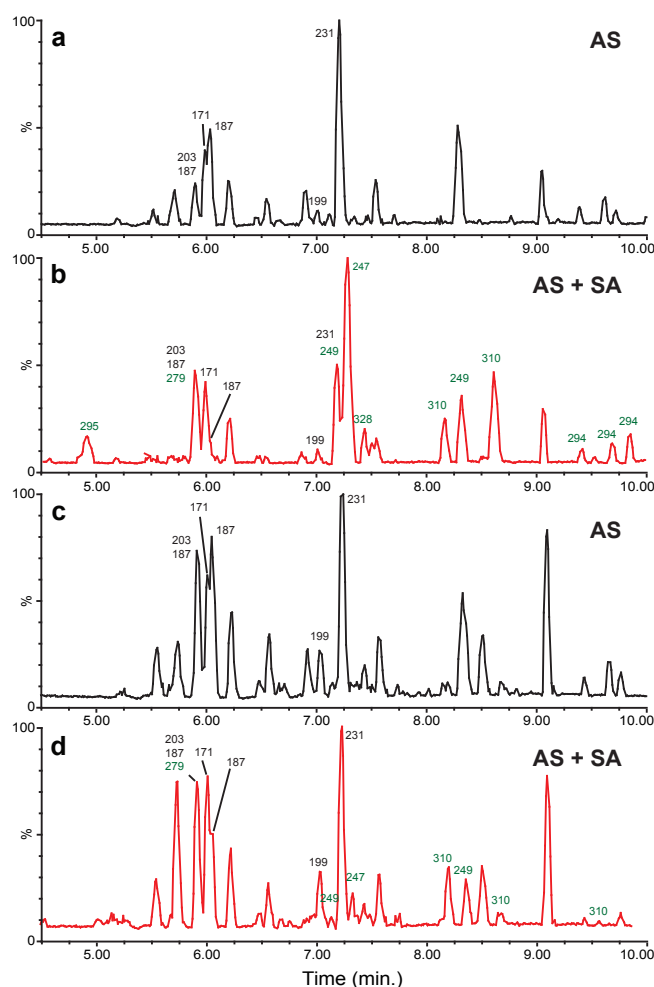


Fig. 6. UPLC/(-)ESI-TOF chromatograms from the filter samples of high- NO_x photooxidation of α -pinene. (a) HONO was the OH source, AS seed particles (4-HONO) (b) HONO was the OH source, AS + SA seed particles (6-HONO), (c) CH_3ONO was the OH source, AS seed particles (10-MeONO), and (d) CH_3ONO was the OH source, AS + SA seed particles (12-MeONO). Chromatographic peaks designated with black [M – H][–] ions are carboxylic acids and chromatographic peaks designated with green [M – H][–] ions are organosulfates and nitrooxy organosulfates. See Table 2 for compound names.

those from the other observed organosulfates and nitrooxy organosulfates.

Under high- NO_2 conditions, the addition of AS + SA rather than AS seed results in fewer new peaks in the UPLC chromatogram than under high- NO conditions. As with low- NO_x , this result is expected as the SOA yield is insensitive to aerosol acidity. As with high- NO , 2-hydroxy terpenylic acid decreases in concentration in the presence of an acidic seed; however, the concentration of diaterpenylic acid acetate is insensitive to aerosol acidity. We have no explanation for this discrepancy. All of the organosulfates and nitrooxy

organosulfates observed in high-NO₂ photooxidation are observed in high-NO photooxidation, but there are a few additional organosulfates and nitrooxy organosulfates that are unique to the high-NO case (see Tables 2 and 3 and Fig. 6).

Given that the SOA yield and growth curves are so different, it is surprising that the UPLC/(-)ESI-TOFMS data from high-NO or high-NO₂ photooxidation are remarkably similar in the presence of AS seed but substantially different with AS + SA seed (see Fig. 6). This suggests that there must be compositional differences which UPLC/(-)ESI-TOFMS is insensitive. The data also suggest that PANs may play a role in the SOA composition as the amount of PAN was the main difference observed in the gas phase.

3.2.3 Bulk SOA functionality determined by AMS

The aerosol composition in low-NO_x and high-NO₂ OH oxidation of α -pinene in the presence of AS seed particles was further analyzed by HR-ToF-AMS. A description of the results has previously been reported (Chhabra et al., 2011). In Chhabra et al. (2011) the H : C vs. O : C (Van Krevelen diagram) and the ratio of f_{44} (more oxidized species, CO₂⁺ likely from acids) to f_{43} (less oxidized species, C₂H₃O⁺) are compared over the course of the photooxidation experiments. The Van Krevelen diagram can be used to infer the bulk functionality of the organic species within the aerosol. Both the low-NO_x and high-NO₂ photooxidation of α -pinene fall along the -1 slope of the H : C vs. O : C plot (see Fig. 2 of Chhabra et al., 2011), a value indicative of either carboxylic acids and/or hydroxy carbonyls (Heald et al., 2010; Ng et al., 2011; Chhabra et al., 2011). Under both low-NO_x and high-NO₂ OH oxidation, the AMS data indicate the same bulk organic functionality while the gas-phase data show a greater quantity of carboxylic acids in the low-NO_x oxidation. Consistent with the Van Krevelen diagram, f_{44} to f_{43} is very similar between the low-NO_x and high-NO₂ experiments. f_{44} is assigned as an indicator of carboxylic acids and a higher degree of aerosol aging (Ng et al., 2011; Chhabra et al., 2011). Further analysis of AMS data indicates that carboxylic acids are a large fraction (30–40 % of the mass) of the aerosols in low-NO_x and high-NO₂ OH oxidation of α -pinene (see Table 2 of Chhabra et al., 2011).

3.3 Gas-phase composition with injection of inorganic seed after photooxidation

To study how different oxidation products interact with aerosol seed particles of different composition (acidity), experiments were performed in which α -pinene was first photooxidized, followed by introduction of an aerosol seed after the lights had been off for two hours. This results in the exposure of gas-phase compounds, formed later on in the experiment, to fresh inorganic aerosol seed particles. This type of experiment has been used previously to study the SOA produced in the low-NO_x photooxidation of isoprene (Sur-

ratt et al., 2010). Surratt et al. (2010) showed that epoxydiols formed from the photooxidation of isoprene preferentially partition to acidic aerosol by reactive uptake.

Two post-oxidation seed experiments were performed under low-NO_x and two under high-NO₂ conditions. In all experiments, aerosol self-nucleation occurred as soon as the lights were turned on so a substantial amount of aerosol had already formed. Once the oxidation products were formed, the lights were extinguished and the chamber was left in the dark for two hours followed by injection of 15–20 $\mu\text{g m}^{-3}$ of aerosol seed. For low-NO_x, this added about 50 % more aerosol volume into the chamber, while for high-NO₂ the aerosol concentration was doubled.

Figure 7 shows the aerosol growth from each of the photooxidation followed by aerosol injection experiments. Aerosol nucleation and growth occurs as soon as the lights are turned on in all experiments. The difference in SOA volume growth from self-nucleation from both low- and high-NO_x experiments is due to greater gas-phase α -pinene concentration at the beginning of each AS seed experiments compared to the AS + SA experiments. Once the lights are turned off, the aerosol mass remains constant until the addition of the inorganic seed. In the case of low-NO_x, an additional growth of $\sim 8 \mu\text{g m}^{-3}$ of SOA is observed after the addition of AS + SA seed; no growth is observed after the addition of the neutral seed. The difference in the aerosol growth is in contrast to the SOA behavior when the aerosol seed was added prior to photooxidation. Under high-NO₂ conditions, no additional SOA is formed after the addition of either neutral or acidic seed particles in the dark.

When ammonium sulfate seed was added in the dark after photooxidation under low-NO_x or high-NO₂ conditions, no change in any of the gas-phase concentrations was observed. This indicates that the gas-phase molecules were not simply in equilibrium with the total aerosol concentration. It is possible that the gas-phase species were partitioning to the wall as well as to the particles, and were at equilibrium; since the surface area of the chamber walls is two orders of magnitude larger than that of the aerosol, no loss would be observed simply due to the greater surface area. Equilibrium partitioning to the walls does not, however, seem likely as the concentration of nearly all the species in the gas phase did not change when the lights were extinguished, decreasing temperature of $\sim 5^\circ\text{C}$. If the gas-phase molecules were partitioning to the wall, it would be expected that their gas-phase concentration would drop as the temperature decreased.

The gas-phase concentration of a number of oxidation products formed under low-NO_x conditions were noticeably reduced when AS + SA seed particles were introduced after photooxidation (Fig. 8). α -pinene oxide is almost completely lost from the gas phase after introduction of the acidic seed (Fig. 8d). In addition, the highly oxidized products observed at m/z 301 and 303 decrease by $\sim 70\%$. These two compounds probably contain either two hydroperoxy groups or one hydroperoxy group and one bridging peroxy group.

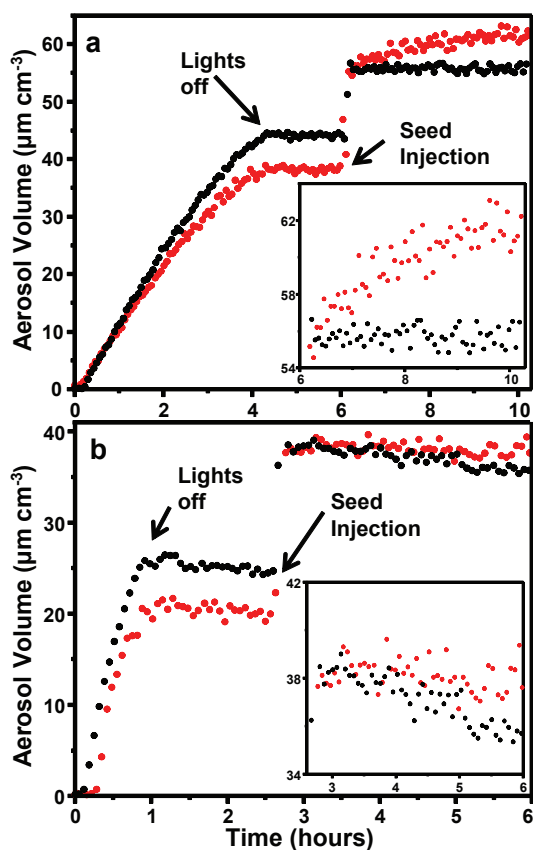


Fig. 7. Time traces of aerosol volume as a result of SOA growth from OH oxidation of α -pinene followed by injection of ammonium sulfate seed (black) or ammonium sulfate and sulfuric acid seed (red) under (a) low- NO_x and (b) high- NO_x (methyl nitrite photolysis) conditions. The difference in the quantity of self-nucleated aerosol volume growth from both (a) low- and (b) high- NO_x experiments is due to greater gas-phase α -pinene concentration at the beginning of each of the AS seed experiments compared to the AS + SA experiments.

Upon addition of the AS + SA seed, the α -pinene hydroxy hydroperoxides also decreased from the gas phase by $\sim 75\%$ (Fig. 8a). This was unexpected, as it has been shown that the hydroxy hydroperoxides formed in the photooxidation of isoprene are not lost from the gas phase due to addition of either AS or AS + SA seed particles. (Surratt et al., 2010). In addition, it was unexpected because when aerosol seed was added prior to photooxidation, the only gas-phase product observed to be in lower concentration in the presence of AS + SA seed was α -pinene oxide. It should be noted that the gas-phase mass loss was a factor of two greater than the SOA growth upon addition of AS + SA seed. It is not clear how to interpret the mass balance, as no species were observed to increase substantially in the gas phase after addition of the AS + SA seed.

The loss of additional organics upon addition of AS + SA seed after photooxidation compared to when the seed is in-

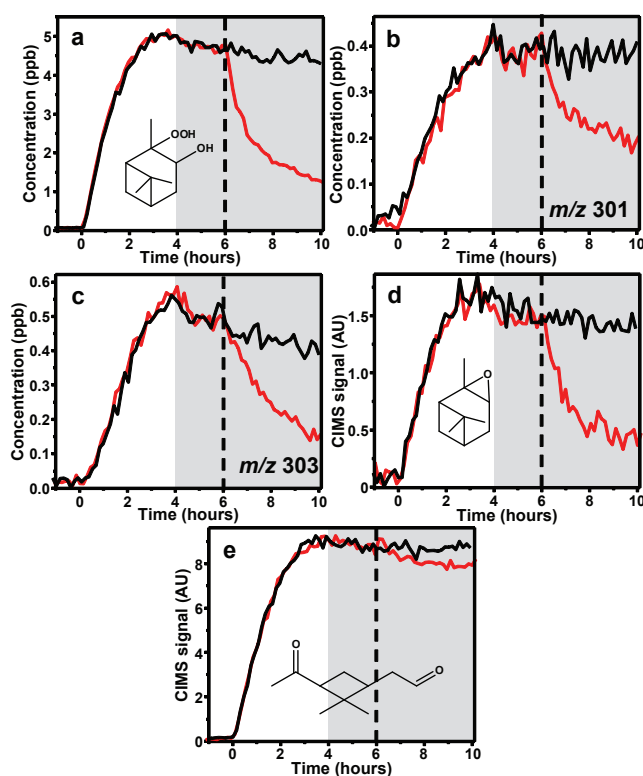


Fig. 8. CIMS traces of α -pinene OH oxidation under low- NO_x conditions, photooxidation for four hours, lights off and contents in the dark for two hours followed by injection of ammonium sulfate seed (black) or ammonium sulfate and sulfuric acid seed (red). Shaded gray area is when the chamber was dark and the dashed line indicates when aerosol seed was added.

jected prior to photooxidation may be related to the composition of the seed when exposed to a given organic. Specifically, perhaps products that are involved in self-nucleation and partition early on in the experiment coat the acidic seed resulting in a hydrocarbon surface rather than an acidic one. If this is the case, loss to the particle would be due to hydrocarbon partitioning rather than acid-catalyzed reactive uptake. Aerosol growth occurs as soon as the lights are turned on, and when a seed is present it takes only about 1.25 h before the aerosol volume has doubled. On the other hand, when the acidic seed is injected after photooxidation has occurred, the products are exposed to the acidic surface allowing reactive uptake to occur from the accumulated products.

Under high- NO_2 conditions, α -pinene oxide is substantially lost from the gas phase when the acidic seed was added (Fig. 9). Besides α -pinene oxide, there are minimal losses of other gas-phase species (Fig. 9). The observed losses include compounds that show up at m/z 215, 301, and 316. The loss of each of these is less than 25 %, as opposed to the low- NO_x case where losses were all greater than 50 %. As mentioned above, multiple species are observed at m/z 316, a first-generation product from the oxidation of α -pinene

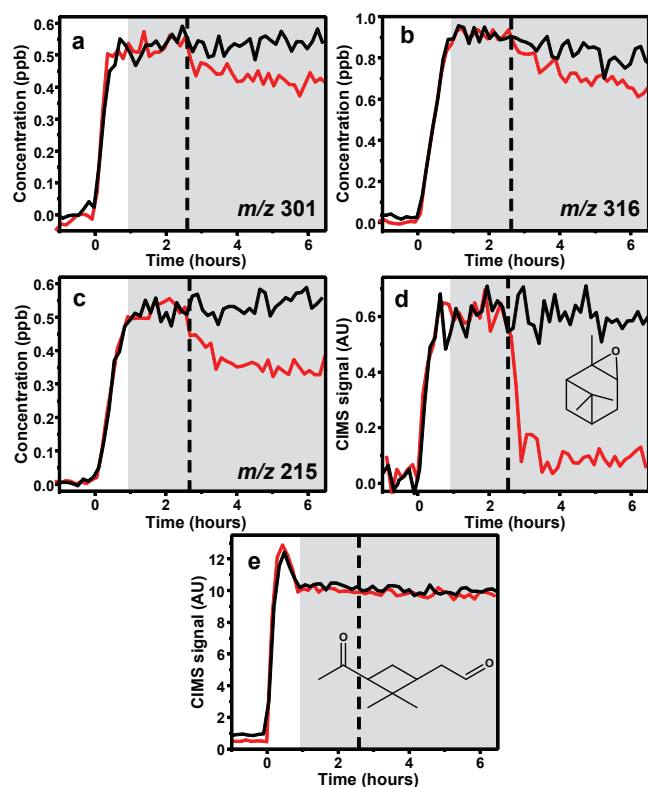


Fig. 9. CIMS traces of α -pinene OH oxidation under high- NO_x conditions, photooxidation for ~ 0.8 h, lights off and contents in the dark for ~ 2 h followed by injection of ammonium sulfate seed (black) or ammonium sulfate and sulfuric acid seed (red). Shaded gray area is when the chamber was dark and the dashed line indicates when aerosol seed was added.

(α -pinene dihydroxy nitrate) and norpinonaldehyde PAN. It is expected that if norpinonaldehyde PAN were to be lost from the gas phase upon addition of an acidic seed then pinonaldehyde PAN would as well. There is no loss of pinonaldehyde PAN from the gas phase, and therefore we conclude that the species lost from the gas phase is the α -pinene oxidation product, which we believe to be α -pinene dihydroxy nitrate. The structures of the molecules at m/z 215 and 301 are not known. Due to the small losses, it appears that under high- NO_2 conditions, acidity will play only a small or negligible effect on SOA growth, as seen in Fig. 7 where no additional growth was observed upon addition of an acidic seed. Consistent with this result, Offenberget al. (2009) saw only a modest increase in SOA yield with the increase of the aerosol acidity from high- NO_2 photooxidation of α -pinene.

4 Implications

In this study, the aerosol growth and composition from α -pinene OH oxidation were compared in low- NO , high- NO , and high- NO_2 conditions. Aerosol growth from α -pinene OH

oxidation under high- NO_2 conditions behaves more similarly to low- NO_x than high- NO aerosol growth. With low NO , aerosol growth continues well after two lifetime of α -pinene with respect to OH oxidation. This indicates that later generation oxidation products are important for SOA growth, including the products of the oxidation of pinonaldehyde, a major product of both low- and high- NO OH oxidation of α -pinene.

In high- NO conditions the SOA yield is dependent on aerosol acidity. The increase in SOA yield with acidic seed was, however, relatively small ($\sim 22\%$ increase). The composition of the gas phase in high- NO and high- NO_2 OH oxidation was identical with a few notable variations. In high- NO_2 experiments, 1.4 to 2 times greater concentrations of PANs and nitric acid were observed in the gas phase compared to the high- NO experiments. One possible explanation for the difference in SOA growth is that the aerosols formed under high- NO_2 conditions are acidic enough in the presence of a neutral seed, due to the increased nitric acid and PANs, for the SOA yield to be the same in the presence of neutral or acidic particles. Further studies on the effect of NO_2 , PANs, and nitric acid on SOA yield from high- NO_x OH oxidation of α -pinene would aid in elucidating the difference in behavior between using HONO and methyl nitrite as the OH source.

When an acidic seed was added after OH oxidation, the SOA yield under low- NO_x conditions increased with a corresponding loss of species from the gas phase. This acid effect was not observed when the aerosol seed is added prior to oxidation, perhaps due to differences in the composition of the aerosol surface. The hypothesis is that when aerosol seed particles are added prior to oxidation, the surface is coated by organics, suppressing uptake of compounds that are catalyzed by acid. This has potential implications to any system that produces a high SOA yield or systems that start with a high organic VOC concentration. In systems where the seed particles become coated with organics relatively quickly, the acid effect and therefore the SOA yield under acidic conditions might be under represented.

Organic acids are a major component of SOA in both low- and high- NO_x OH oxidation of α -pinene. While AMS data indicate that the total concentration of organic acids in SOA from low- NO_x and high- NO_2 is similar, the individual composition varies depending on the gas-phase conditions. Pinonic and pinic acid are observed in SOA only from low- NO_x OH oxidation of α -pinene. This is consistent with gas-phase data, where pinonic acid was only observed from low- NO_x conditions. It is believed that 3-MBTCA is derived from high- NO_x gas phase oxidation of pinonic acid; however, there must be other mechanism for its formation, as 3-MBTCA is observed in SOA from low- NO_x OH oxidation of α -pinene and high- NO_x OH oxidation of α -pinene where pinonic acid is not observed in the gas or aerosol phase.

Acknowledgements. This work was supported in part by Department of Energy grant DE-SC0006626 and National Science Foundation grant AGS-1057183. N. Eddingsaas was supported by the Camille and Henry Dreyfus Postdoctoral Program in Environmental Chemistry. C. Loza and L. Yee were supported by National Science Foundation Graduate Research Fellowships.

Edited by: R. McLaren

References

- Allan, J. D., Delia, A. E., Coe, H., Bower, K. N., Alfarra, M. R., Jimenez, J. L., Middlebrook, A. M., Drewnick, F., Onasch, T. B., Canagaratna, M. R., Jayne, J. T., and Worsnop, D. R.: A generalised method for the extraction of chemically resolved mass spectra from aerodyne aerosol mass spectrometer data, *J. Aerosol Sci.*, 35, 909–922, doi:10.1016/j.jaerosci.2004.02.007, 2004.
- Anttila, P., Hyotylainen, T., Heikkilä, A., Jussila, M., Finell, J., Kulmala, M., and Riekkola, M. L.: Determination of organic acids in aerosol particles from a coniferous forest by liquid chromatography-mass spectrometry, *J. Sep. Sci.*, 28, 337–346, doi:10.1002/jssc.200401931, 2005.
- Aschmann, S. M., Atkinson, R., and Arey, J.: Products of reaction of OH radicals with alpha-pinene, *J. Geophys. Res.-Atmos.*, 107, 4191, doi:10.1029/2001jd001098, 2002.
- Camredon, M., Hamilton, J. F., Alam, M. S., Wyche, K. P., Carr, T., White, I. R., Monks, P. S., Rickard, A. R., and Bloss, W. J.: Distribution of gaseous and particulate organic composition during dark α -pinene ozonolysis, *Atmos. Chem. Phys.*, 10, 2893–2917, doi:10.5194/acp-10-2893-2010, 2010.
- Capouet, M., Mueller, J. F., Ceulemans, K., Compernelle, S., Vereecken, L., and Peeters, J.: Modeling aerosol formation in alpha-pinene photo-oxidation experiments, *J. Geophys. Res.-Atmos.*, 113, D02308, doi:10.1029/2007JD008995, 2008.
- Chan, M. N., Surratt, J. D., Claeys, M., Edgerton, E. S., Tanner, R. L., Shaw, S. L., Zheng, M., Knipping, E. M., Eddingsaas, N. C., Wennberg, P. O., and Seinfeld, J. H.: Characterization and Quantification of Isoprene-Derived Epoxydiols in Ambient Aerosol in the Southeastern United States, *Environ. Sci. Technol.*, 44, 4590–4596, doi:10.1021/es100596b, 2010.
- Chan, M. N., Surratt, J. D., Chan, A. W. H., Schilling, K., Offenberg, J. H., Lewandowski, M., Edney, E. O., Kleindienst, T. E., Jaoui, M., Edgerton, E. S., Tanner, R. L., Shaw, S. L., Zheng, M., Knipping, E. M., and Seinfeld, J. H.: Influence of aerosol acidity on the chemical composition of secondary organic aerosol from β -caryophyllene, *Atmos. Chem. Phys.*, 11, 1735–1751, doi:10.5194/acp-11-1735-2011, 2011.
- Chhabra, P. S., Ng, N. L., Canagaratna, M. R., Corrigan, A. L., Russell, L. M., Worsnop, D. R., Flagan, R. C., and Seinfeld, J. H.: Elemental composition and oxidation of chamber organic aerosol, *Atmos. Chem. Phys.*, 11, 8827–8845, doi:10.5194/acp-11-8827-2011, 2011.
- Chung, S. H. and Seinfeld, J. H.: Global distribution and climate forcing of carbonaceous aerosols, *J. Geophys. Res.-Atmos.*, 107, 4407, doi:10.1029/2001JD001397, 2002.
- Claeys, M., Iinuma, Y., Szmigielski, R., Surratt, J. D., Blockhuys, F., Van Alsenoy, C., Boge, O., Sierau, B., Gomez-Gonzalez, Y., Vermeylen, R., Van der Veken, P., Shahgholi, M., Chan, A. W. H., Herrmann, H., Seinfeld, J. H., and Maenhaut, W.: Terpenylic Acid and Related Compounds from the Oxidation of alpha-Pinene: Implications for New Particle Formation and Growth above Forests, *Environ. Sci. Technol.*, 43, 6976–6982, doi:10.1021/es9007596, 2009.
- Cocker, David R., I., Flagan, R. C., and Seinfeld, J. H.: State-of-the-art chamber facility for studying atmospheric aerosol chemistry, *Environ. Sci. Technol.*, 35, 2594–2601, 2001.
- Crounse, J. D., McKinney, K. A., Kwan, A. J., and Wennberg, P. O.: Measurement of gas-phase hydroperoxides by chemical ionization mass spectrometry, *Anal. Chem.*, 78, 6726–6732, 2006.
- DeCarlo, P. F., Kimmel, J. R., Trimborn, A., Northway, M. J., Jayne, J. T., Aiken, A. C., Gonin, M., Fuhrer, K., Horvath, T., Docherty, K. S., Worsnop, D. R., and Jimenez, J. L.: Field-deployable, high-resolution, time-of-flight aerosol mass spectrometer, *Anal. Chem.*, 78, 8281–8289, doi:10.1021/ac061249n, 2006.
- Eddingsaas, N. C., Loza, C. L., Yee, L. D., Seinfeld, J. H., and Wennberg, P. O.: α -pinene photooxidation under controlled chemical conditions – Part 1: Gas-phase composition in low- and high-NO_x environments, *Atmos. Chem. Phys.*, 12, 6489–6504, doi:10.5194/acp-12-6489-2012, 2012.
- Glasius, M., Duane, M., and Larsen, B. R.: Determination of polar terpene oxidation products in aerosols by liquid chromatography-ion trap mass spectrometry, *J. Chromatogr. A*, 833, 121–135, 1999.
- Guenther, A., Hewitt, C. N., Erickson, D., Fall, R., Geron, C., Graedel, T., Harley, P., Klinger, L., Lerdau, M., Mckay, W. A., Pierce, T., Scholes, B., Steinbrecher, R., Tallamraju, R., Taylor, J., and Zimmerman, P.: A global model of natural volatile organic compound emissions, *J. Geophys. Res.-Atmos.*, 100, 8873–8892, doi:10.1029/94JD02950, 1995.
- Heald, C. L., Kroll, J. H., Jimenez, J. L., Docherty, K. S., DeCarlo, P. F., Aiken, A. C., Chen, Q., Martin, S. T., Farmer, D. K., and Artaxo, P.: A simplified description of the evolution of organic aerosol composition in the atmosphere, *Geophys. Res. Lett.*, 37, L08803, doi:10.1029/2010gl042737, 2010.
- Hoffmann, T., Odum, J. R., Bowman, F., Collins, D., Klockow, D., Flagan, R. C., and Seinfeld, J. H.: Formation of organic aerosols from the oxidation of biogenic hydrocarbons, *J. Atmos. Chem.*, 26, 189–222, 1997.
- Iinuma, Y., Boge, O., Miao, Y., Sierau, B., Gnauk, T., and Herrmann, H.: Laboratory studies on secondary organic aerosol formation from terpenes, *Faraday Discuss.*, 130, 279–294, doi:10.1039/b502160j, 2005.
- Iinuma, Y., Boge, O., Kahnt, A., and Herrmann, H.: Laboratory chamber studies on the formation of organosulfates from reactive uptake of monoterpene oxides, *Phys. Chem. Chem. Phys.*, 11, 7985–97, doi: 10.1039/B904025K, 2009.
- Jaoui, M. and Kamens, R. M.: Mass balance of gaseous and particulate products analysis from alpha -pinene/NO_x/air in the presence of natural sunlight, *J. Geophys. Res.-Atmos.*, 106, 12541–12558, 2001.
- Kavouras, I. G., Mihalopoulos, N., and Stephanou, E. G.: Formation of atmospheric particles from organic acids produced by forests, *Nature*, 395, 683–686, 1998.
- Kavouras, I. G., Mihalopoulos, N., and Stephanou, E. G.: Formation and gas/particle partitioning of monoterpenes photo-oxidation products over forests, *Geophys. Res. Lett.*, 26, 55–58, doi:10.1029/1998GL900251, 1999.

- Keywood, M. D., Varutbangkul, V., Bahreini, R., Flagan, R. C., and Seinfeld, J. H.: Secondary organic aerosol formation from the ozonolysis of cycloalkenes and related compounds, *Environ. Sci. Technol.*, 38, 4157–4164, 2004.
- Kourtchev, I., Copolovici, L., Claeys, M., and Maenhaut, W.: Characterization of Atmospheric Aerosols at a Forested Site in Central Europe, *Environ. Sci. Technol.*, 43, 4665–4671, doi:10.1021/es803055w, 2009.
- Laaksonen, A., Kulmala, M., O'Dowd, C. D., Joutsensaari, J., Vaatovaara, P., Mikkonen, S., Lehtinen, K. E. J., Sogacheva, L., Dal Maso, M., Aalto, P., Petäjä, T., Sogachev, A., Yoon, Y. J., Lihavainen, H., Nilsson, D., Facchini, M. C., Cavalli, F., Fuzzi, S., Hoffmann, T., Arnold, F., Hanke, M., Sellegri, K., Umann, B., Junkermann, W., Coe, H., Allan, J. D., Alfarra, M. R., Worsnop, D. R., Riekkola, M. -L., Hyötyläinen, T., and Viisanen, Y.: The role of VOC oxidation products in continental new particle formation, *Atmos. Chem. Phys.*, 8, 2657–2665, doi:10.5194/acp-8-2657-2008, 2008.
- Larsen, B. R., Di Bella, D., Glasius, M., Winterhalter, R., Jensen, N. R., and Hjorth, J.: Gas-phase OH oxidation of monoterpenes: Gaseous and particulate products, *J. Atmos. Chem.*, 38, 231–276, 2001.
- Librando, V. and Tringali, G.: Atmospheric fate of OH initiated oxidation of terpenes. Reaction mechanism of alpha-pinene degradation and secondary organic aerosol formation, *J. Environ. Manag.*, 75, 275–282, doi:10.1016/j.jenvman.2005.01.001, 2005.
- Ma, Y., Russell, A. T., and Marston, G.: Mechanisms for the formation of secondary organic aerosol components from the gas-phase ozonolysis of alpha-pinene, *Phys. Chem. Chem. Phys.*, 10, 4294–4312, doi:10.1039/b803283a, 2008.
- Minerath, E. C., Casale, M. T., and Elrod, M. J.: Kinetics Feasibility Study of Alcohol Sulfate Esterification Reactions in Tropospheric Aerosols, *Environ. Sci. Technol.*, 42, 4410–4415, 2008.
- Müller, L., Reinnig, M.-C., Naumann, K. H., Saathoff, H., Mentel, T. F., Donahue, N. M., and Hoffmann, T.: Formation of 3-methyl-1,2,3-butanetricarboxylic acid via gas phase oxidation of pinonic acid – a mass spectrometric study of SOA aging, *Atmos. Chem. Phys.*, 12, 1483–1496, doi:10.5194/acp-12-1483-2012, 2012.
- Ng, N. L., Chhabra, P. S., Chan, A. W. H., Surratt, J. D., Kroll, J. H., Kwan, A. J., McCabe, D. C., Wennberg, P. O., Sorooshian, A., Murphy, S. M., Dalleska, N. F., Flagan, R. C., and Seinfeld, J. H.: Effect of NO_x level on secondary organic aerosol (SOA) formation from the photooxidation of terpenes, *Atmos. Chem. Phys.*, 7, 5159–5174, doi:10.5194/acp-7-5159-2007, 2007a.
- Ng, N. L., Kroll, J. H., Chan, A. W. H., Chhabra, P. S., Flagan, R. C., and Seinfeld, J. H.: Secondary organic aerosol formation from m-xylene, toluene, and benzene, *Atmos. Chem. Phys.*, 7, 3909–3922, doi:10.5194/acp-7-3909-2007, 2007b.
- Ng, N. L., Canagaratna, M. R., Jimenez, J. L., Chhabra, P. S., Seinfeld, J. H., and Worsnop, D. R.: Changes in organic aerosol composition with aging inferred from aerosol mass spectra, *Atmos. Chem. Phys.*, 11, 6465–6474, doi:10.5194/acp-11-6465-2011, 2011.
- Noziere, B., Barnes, I., and Becker, K.-H.: Product study and mechanisms of the reactions of alpha-pinene and of pinonaldehyde with OH radicals, *J. Geophys. Res.-Atmos.*, 104, 23645–23656, doi:10.1029/1999JD900778, 1999.
- Offenberg, J. H., Lewandowski, M., Edney, E. O., Kleindienst, T. E., and Jaoui, M.: Influence of Aerosol Acidity on the Formation of Secondary Organic Aerosol from Biogenic Precursor Hydrocarbons, *Environ. Sci. Technol.*, 43, 7742–7747, doi:10.1021/es901538e, 2009.
- Paulot, F., Crouse, J. D., Kjaergaard, H. G., Kroll, J. H., Seinfeld, J. H., and Wennberg, P. O.: Isoprene photooxidation: new insights into the production of acids and organic nitrates, *Atmos. Chem. Phys.*, 9, 1479–1501, doi:10.5194/acp-9-1479-2009, 2009a.
- Paulot, F., Crouse, J. D., Kjaergaard, H. G., Kurten, A., St. Clair, J. M., Seinfeld, J. H., and Wennberg, P. O.: Unexpected epoxide formation in the gas-phase photooxidation of isoprene, *Science*, 325, 730–733, doi:10.1126/science.1172910, 2009b.
- Presto, A. A., Hartz, K. E. H., and Donahue, N. M.: Secondary organic aerosol production from terpene ozonolysis. 2. Effect of NO_x concentration, *Environ. Sci. Technol.*, 39, 7046–7054, doi:10.1021/es050400s, 2005.
- Pye, H. O. T., Chan, A. W. H., Barkley, M. P., and Seinfeld, J. H.: Global modeling of organic aerosol: the importance of reactive nitrogen (NO_x and NO₃), *Atmos. Chem. Phys.*, 10, 11261–11276, doi:10.5194/acp-10-11261-2010, 2010.
- Shilling, J. E., Chen, Q., King, S. M., Rosenoern, T., Kroll, J. H., Worsnop, D. R., DeCarlo, P. F., Aiken, A. C., Sueper, D., Jimenez, J. L., and Martin, S. T.: Loading-dependent elemental composition of α -pinene SOA particles, *Atmos. Chem. Phys.*, 9, 771–782, doi:10.5194/acp-9-771-2009, 2009.
- Spittler, M., Barnes, I., Bejan, I., Brockmann, K. J., Benter, T., and Wirtz, K.: Reactions of NO₃ radicals with limonene and α -pinene: Product and SOA formation, *Atmos. Environ.*, 40, S116–S127, 2006.
- St. Clair, J. M., McCabe, D. C., Crouse, J. D., Steiner, U., and Wennberg, P. O.: Chemical ionization tandem mass spectrometer for the in situ measurement of methyl hydrogen peroxide, *Rev. Sci. Instrum.*, 81, 094102, doi:10.1063/1.3480552, 2010.
- Surratt, J. D., Kroll, J. H., Kleindienst, T. E., Edney, E. O., Claeys, M., Sorooshian, A., Ng, N. L., Offenberg, J. H., Lewandowski, M., Jaoui, M., Flagan, R. C., and Seinfeld, J. H.: Evidence for Organosulfates in Secondary Organic Aerosol, *Environ. Sci. Technol.*, 41, 517–527, 2007.
- Surratt, J. D., Gomez-Gonzalez, Y., Chan, A. W. H., Vermeylen, R., Shahgholi, M., Kleindienst, T. E., Edney, E. O., Offenberg, J. H., Lewandowski, M., Jaoui, M., Maenhaut, W., Claeys, M., Flagan, R. C., and Seinfeld, J. H.: Organosulfate formation in biogenic secondary organic aerosol, *J. Phys. Chem. A*, 112, 8345–8378, doi:10.1021/jp802310p, 2008.
- Surratt, J. D., Chan, A. W. H., Eddingsaas, N. C., Chan, M. N., Loza, C. L., Kwan, A. J., Hersey, S. P., Flagan, R. C., Wennberg, P. O., and Seinfeld, J. H.: Reactive intermediates revealed in secondary organic aerosol formation from isoprene, *P. Natl. Acad. Sci.*, 107, 6640–6645, doi:10.1073/pnas.0911114107, 2010.
- Szmigielski, R., Surratt, J. D., Gomez-Gonzalez, Y., Van der Veken, P., Kourtchev, I., Vermeylen, R., Blockhuys, F., Jaoui, M., Kleindienst, T. E., Lewandowski, M., Offenberg, J. H., Edney, E. O., Seinfeld, J. H., Maenhaut, W., and Claeys, M.: 3-methyl-1,2,3-butanetricarboxylic acid: an atmospheric tracer for terpene secondary organic aerosol, *Geophys. Res. Lett.*, 34, L24811, doi:10.1029/2007GL031338, 2007.
- Taylor, W. D., Allston, T. D., Moscato, M. J., Fazekas, G. B., Kolzowski, R., and Takacs, G. A.: Atmospheric photo-dissociation

- lifetimes for nitromethane, methyl nitrite, and methyl nitrate, *Int. J. Chem. Kinet.*, 12, 231–240, 1980.
- Warnke, J., Bandur, R., and Hoffmann, T.: Capillary-HPLC-ESI-MS/MS method for the determination of acidic products from the oxidation of monoterpenes in atmospheric aerosol samples, *Anal. Bioanal. Chem.*, 385, 34–45, doi:10.1007/s00216-006-0340-6, 2006.
- Yu, J., Cocker, David R., I., Griffin, R. J., Flagan, R. C., and Seinfeld, J. H.: Gas-phase ozone oxidation of monoterpenes: gaseous and particulate products, *J. Atmos. Chem.*, 34, 207–258, 1999a.
- Yu, J., Griffin, R. J., Cocker, David R., I., Flagan, R. C., Seinfeld, J. H., and Blanchard, P.: Observation of gaseous and particulate products of monoterpene oxidation in forest atmospheres, *Geophys. Res. Lett.*, 26, 1145–1148, doi:10.1029/1999GL900169, 1999b.
- Zhang, Y. Y., Müller, L., Winterhalter, R., Moortgat, G. K., Hoffmann, T., and Pöschl, U.: Seasonal cycle and temperature dependence of pinene oxidation products, dicarboxylic acids and nitrophenols in fine and coarse air particulate matter, *Atmos. Chem. Phys.*, 10, 7859–7873, doi:10.5194/acp-10-7859-2010, 2010.

Appendix J

Analysis of Secondary Organic Aerosol Formation and Aging Using Positive Matrix Factorization of High-Resolution Aerosol Mass Spectra: Application to the Dodecane Low-NO_x System¹²

¹² Reproduced by permission from “Analysis of secondary organic aerosol formation and aging using positive matrix factorization of high-resolution aerosol mass spectra: application to the dodecane low-NO_x system” by J. S. Craven, L. D. Yee, N. L. Ng, M. R. Canagaratna, C. L. Loza, K. A. Schilling, R. L. N. Yatawelli, J. A. Thornton, P. J. Ziemann, R. C. Flagan, and J. H. Seinfeld. *Atmos. Chem. Phys.* **2012**, *12*, 11795-11817.



Analysis of secondary organic aerosol formation and aging using positive matrix factorization of high-resolution aerosol mass spectra: application to the dodecane low-NO_x system

J. S. Craven¹, L. D. Yee², N. L. Ng⁶, M. R. Canagaratna³, C. L. Loza¹, K. A. Schilling¹, R. L. N. Yatawelli^{4,*}, J. A. Thornton⁴, P. J. Ziemann⁵, R. C. Flagan^{1,2}, and J. H. Seinfeld^{1,2}

¹Division of Chemistry and Chemical Engineering, California Institute of Technology, Pasadena, California, USA

²Division of Engineering and Applied Science, California Institute of Technology, Pasadena, California, USA

³Aerodyne Research, Inc., Billerica, Massachusetts, USA

⁴Department of Atmospheric Sciences, University of Washington, Seattle, Washington, USA

⁵Air Pollution Research Center, Department of Environmental Sciences, and Environmental Toxicology Graduate Program, University of California, Riverside, California, USA

⁶School of Chemical and Biomolecular Engineering and School of Earth and Atmospheric Sciences, Georgia Institute of Technology, Atlanta, Georgia, USA

* current address: Cooperative Institute for Research in Environmental Sciences (CIRES), University of Colorado, Boulder, Colorado, USA

Correspondence to: J. H. Seinfeld (seinfeld@caltech.edu)

Received: 7 June 2012 – Published in Atmos. Chem. Phys. Discuss.: 6 July 2012

Revised: 26 October 2012 – Accepted: 4 December 2012 – Published: 17 December 2012

Abstract. Positive matrix factorization (PMF) of high-resolution laboratory chamber aerosol mass spectra is applied for the first time, the results of which are consistent with molecular level MOVI-HRToF-CIMS aerosol-phase and CIMS gas-phase measurements. Secondary organic aerosol was generated by photooxidation of dodecane under low-NO_x conditions in the Caltech environmental chamber. The PMF results exhibit three factors representing a combination of gas-particle partitioning, chemical conversion in the aerosol, and wall deposition. The slope of the measured high-resolution aerosol mass spectrometer (HR-ToF-AMS) composition data on a Van Krevelen diagram is consistent with that of other low-NO_x alkane systems in the same O : C range. Elemental analysis of the PMF factor mass spectral profiles elucidates the combinations of functionality that contribute to the slope on the Van Krevelen diagram.

1 Introduction

The processes by which the atmospheric oxidation of volatile organic compounds (VOCs) leads to low volatility products that partition into the aerosol phase, forming Secondary Organic Aerosol (SOA), are complex and not thoroughly understood. Gas-phase oxidation processes are key in SOA formation, but there is increasing evidence that chemistry occurring in the particle phase, as well, may be important in producing the low-volatility, oxygenated compounds that characterize SOA. Laboratory chamber studies are essential to understand the lifecycle of organics involved in the formation of SOA. In such chamber experiments, measurements of both gas- and particle-phase chemical composition provide a window into the complex chemistry of SOA formation. While measurement of the complete suite of compounds involved in SOA formation is generally not feasible, key observations can provide considerable insight into the nature of the multi-generation gas-phase oxidation that characterizes SOA formation. High-Resolution Time-of-Flight

Aerosol Mass Spectrometer (HR-ToF-AMS) measurements of aerosol composition enable derivation of a number of key SOA properties; these include the atomic oxygen-to-carbon and hydrogen-to-carbon ratios (O : C and H : C), from which one can infer the overall oxidation state of the aerosol. The full HR-ToF-AMS spectrum, over the course of SOA formation and evolution, comprises a large number of mass-to-charge ratios (m/z), which contain time-dependent information on the overall processes occurring. Positive Matrix Factorization (PMF) has proved to be a powerful procedure for analyzing HR-ToF-AMS spectra in terms of the evolution of major mass spectral factors (Lanz et al., 2007; Ulbrich et al., 2009; Aiken et al., 2009; Ng et al., 2010; Hersey et al., 2011; Fry et al., 2011). The factor profile extracts the contributions from a number of masses that are co-correlated, providing information on the time evolution of the aerosol composition that is not immediately evident from the complex aerosol spectrum. We present here the first application of PMF to HR-ToF-AMS spectra obtained in a laboratory chamber investigation of SOA formation.

The present study is part of a comprehensive investigation of SOA formation from large alkanes. Historically, alkanes have been considered a significant atmospheric component of the unresolved complex mixture (UCM) of organics (Schauer et al., 2001, 2002). With the advent of a recently developed soft ionization gas chromatography technique, the unresolved complex mixture has been characterized at the molecular level to contain *n*-alkanes, cycloalkanes, bicycloalkanes, tricycloalkanes, and steranes (Isaacman et al., 2012). Pye and Pouliot (2012) predict from the Community Multiscale Air Quality (CMAQ) model the SOA yield from alkanes and PAHs to be 20 to 30 % of that from anthropogenic hydrocarbons. In particular, the linear alkane is predicted to dominate the SOA yield for the C₁₂ alkanes. This first phase of the comprehensive investigation of alkanes focuses on high-resolution HR-ToF-AMS spectra of dodecane (C₁₂H₂₆) SOA. In conjunction with Chemical Ionization Mass Spectrometer (CIMS) measurements, and Micro-Orifice Volatilization Impactor Coupled to a Chemical Ionization Mass Spectrometer (MOVI-HRToF-CIMS), the application of PMF provides insight into the multi-generational and multi-phase processes involved in SOA formation and aging.

2 Experimental

Experiments were carried out in the Caltech environmental chamber facility, which is comprised of dual 28 m³ teflon chambers (Table 1, Cocker et al., 2001). Experiments were carried out in a low-NO_x environment with hydrogen peroxide (H₂O₂) photolysis as the OH source. For each experiment, 280 μl of 50 % wt aqueous H₂O₂ solution was evaporated into the chamber, followed by atomization of 0.015 M aqueous ammonium sulfate (AS) solution for seed particles,

which were subsequently dried. Finally, the specific volume of liquid dodecane necessary to achieve the desired gas-phase concentration was evaporated into the chamber. The oxidant, seed, and hydrocarbon mixed for 1 h prior to irradiation.

2.1 High-resolution time-of-flight aerosol mass spectrometer

In the Aerodyne high-resolution time-of-flight aerosol mass spectrometer (HR-ToF-AMS), aerosol is sampled at atmospheric pressure through an aerodynamic lens into a particle time-of-flight chamber, at the end of which the particles impact a 600 °C heater and 70 eV filament assembly where they are vaporized and ionized. The aerosol ion fragments are then orthogonally extracted into the ion time-of-flight chamber where they are sampled in either V (higher signal) or W (higher resolution) mode. For these experiments, both modes were utilized at a 1 min sequential sampling rate. The V-mode was utilized for PMF analysis, as the higher m/z values exhibit a more favorable signal-to-noise ratio; the W-mode was used for ion identification, clarification, and elemental analysis. The V-mode and W-mode can be set to measure bulk aerosol composition in which all of the particles within the transmission of the instrument (60–600 nm with 100 % transmission efficiency) are measured. This is commonly referred to as mass spec.-mode (MS-mode). The HR-ToF-AMS can also measure size-resolved chemistry by employing the particle time-of-flight-mode (PTOF-mode) in which the aerosol beam is chopped in the particle time-of-flight chamber and single particles are sized and sampled. All HR-ToF-AMS data were processed with “Squirrel”, the ToF-AMS Unit Resolution Analysis Toolkit (<http://cires.colorado.edu/jimenez-group/ToFAMSResources/ToFSoftware/index.html>), in Igor Pro Version 6.22A (Wavemetrics, Lake Oswego, OR). Adjustments to the fragmentation table were made to correct for air interferences based on measurements made at the beginning of each experiment with a particle filter in-line with the chamber sample line and the HR-ToF-AMS (Allan et al., 2004). The ToF-AMS High Resolution Analysis software tool PIKA (Peak Integration by Key Analysis) was employed for high-resolution analysis (DeCarlo et al., 2006). Elemental ratios were calculated using the technique outlined by Aiken et al. (2008) and Chhabra et al. (2010).

2.2 Chemical Ionization Mass Spectrometer

A Chemical Ionization Mass Spectrometer (CIMS) was employed for the measurement of gas-phase photooxidation products, including key intermediates contributing to the particle phase. The CIMS consists of a Varian 1200 triple quadrupole mass spectrometer that has been modified to accommodate a custom ionization region. Sample air from the environmental chamber flows at 190 sccm into a glass flow

Table 1. Experimental conditions for dodecane low-NO_x photooxidation.

Exp #	duration (h)	initial hydrocarbon conc. (ppb)	seed type	initial seed volume ($\mu\text{m}^3 \text{cm}^{-3}$)	HR-ToF-AMS mode
1	18	34	AS	9.1	MS-mode, (V and W)
2	34	34	AS	11.4	(MS-mode (V and W)
3	18	33	AS	12.0	(MS-mode (V and W)
4	18	50	AS	14.1	MS-mode (V and W), PTOF-mode (V)
5	18	300	AS	34.7	MS-mode (V and W), turned heater off

tube, where it is diluted by a factor of nine with N₂ gas. It then enters the chemical ionization region. The CIMS uses CF₃OOCF₃ reagent gas, generating cluster products at [X.CF₃O]⁻ and fluoride transfer products at [X.F]⁻, where X is the analyte. Hydroperoxide-containing species are detected as a cluster product, and strongly acidic species are primarily detected as the transfer product. More weakly acidic species can be detected as both a cluster and transfer product. In these experiments, such products were tracked with the CIMS as discussed previously (Yee et al., 2012). Additional details of the instrument and its general operation have been described elsewhere (St. Clair et al., 2010; Paulot et al., 2009; Crouse et al., 2006).

2.3 Micro-orifice volatilization impactor coupled to a high-resolution time-of-flight chemical ionization mass spectrometer

A micro-orifice volatilization impactor coupled to a high-resolution time-of-flight chemical-ionization mass spectrometer (MOVI-HRToF-CIMS) was employed. Analysis in the MOVI-HRToF-CIMS is a two-step cycle in which (i) gas-phase compounds are measured by the high-resolution TOFMS while aerosols are collected, and (ii) collected aerosols are then thermally vaporized with composition measured by the spectrometer. Chemical ionization (CI) preserves the parent ion in most cases, which, when combined with a high-resolution TOF analyzer, allows determination of the elemental composition of the molecular ions in the mass range of 17–550 *m/z* with a mass resolution of 4500 for mass to charge > 100 (Yatavelli and Thornton, 2010; Yatavelli et al., 2012).

2.4 Positive Matrix Factorization (PMF)

Positive Matrix Factorization (PMF) has emerged as a powerful technique for source apportionment of HR-ToF-AMS measurements of ambient aerosol (Paatero and Tapper, 1994; Jimenez et al., 2009; Lanz et al., 2007; Ulbrich et al., 2009; Aiken et al., 2009; Hersey et al., 2011; Ng et al., 2010; Allan, 2003; Zhang et al., 2011). Here, the application of PMF to HR-ToF-AMS spectra to investigate SOA formation in a laboratory chamber is reported for the first time. The factors are groups of ions (or fractions of ions) that

vary together in time. For chamber experiments, this variation could result from processes such as gas-particle partitioning, chemical conversion in the aerosol, or wall loss of either individual molecules, or more likely a group of molecules with similar chemical character, such as the gas-phase products from a specific generation of gas-phase oxidation. Gas-phase measurements support and the dodecane low-NO_x mechanism predicts the multi-generation production of increasingly oxidized gas-phase products, which are expected to condense at different times. The AMS-PMF time series results are compared with molecular level detail of the CIMS gas-phase and MOVI-HRToF-CIMS aerosol-phase measurements, linking the HR-ToF-AMS high time-resolution electron impact ion information to the complex aerosol molecular level composition. The PMF results are explored using the PMF Evaluation Tool Version 2.04 in Igor Pro (http://cires.colorado.edu/jimenez-group/wiki/index.php/PMF-AMS_Analysis_Guide, Ulbrich et al., 2009). The details of implementing PMF are given in the Appendix A.

3 Results

SOA formation and aging comprise a number of atmospheric processes: (1) gas-phase reactions involving the primary organic and its oxidation products that involve functionalization and fragmentation; (2) gas-particle partitioning of lower volatility products; (3) chemical reactions in the aerosol phase that can lead to even lower volatility compounds or, in some cases, fragmentation and return to the gas phase. In interpreting the results of laboratory chamber experiments, one must also consider the effect of deposition of gases and particles to the chamber walls. In the present study we seek, via a combination of HR-ToF-AMS and CIMS measurements, to evaluate both gas- and particle-phase routes to formation of oxidized compounds.

3.1 Elemental ratios

Figure 1 shows the evolution of total organic aerosol mass during the longer experiment (Table 1). The O : C and H : C elemental ratios of the aerosol provide information on the bulk chemical evolution over the course of the experiment.

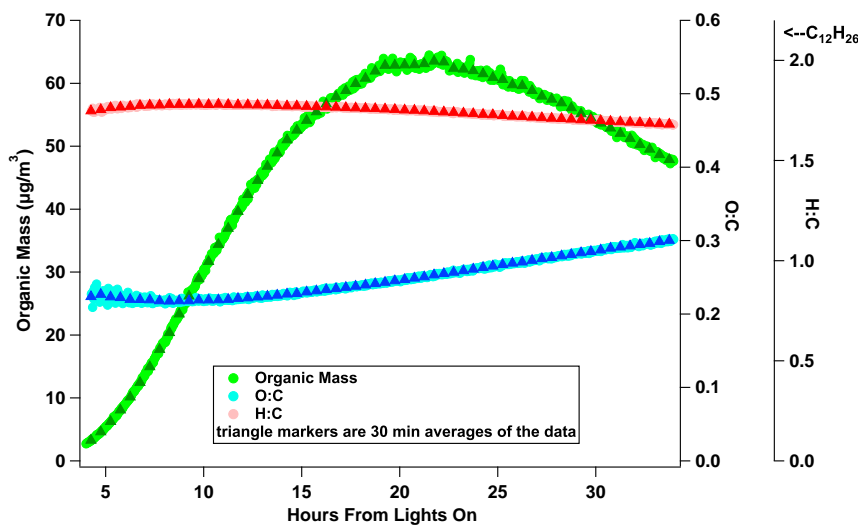


Fig. 1. Total organic aerosol mass and O : C and H : C elemental ratios for experiment 2. The $C_2H_4^+$ ion has been removed from the mass spectra due to its interference with the large signal from the N_2^+ ion. The triangles are 30 min averages of the data.

The first reliable O : C measurement yields a value near 0.22, which is consistent with the predicted early aerosol product, the C_{12} carbonyl hydroperoxide (product formula of $C_{12}H_{24}O_3$, O : C of 0.25). Upon further OH exposure, the O : C ratio grows to about 0.3. The H : C ratio is initially at 1.7, reflecting the oxidized nature of the aerosol composition at a relatively early stage of formation. The H : C ratio then increases after early growth to 1.79 and then decreases to 1.69 at 34 h. Dodecane itself has an H : C of 2.17 and an O : C of 0, so the initially high H : C and low O : C reflect the early oxidation stage of aerosol. The $C_2H_4^+$ ion was removed from the mass spectra owing to large interference with the N_2^+ ion, but with little effect on the absolute value and time trend of the elemental ratios. Individual high resolution ions provide further information on those masses in the spectrum that are driving the evolution of the aerosol chemical composition.

3.2 High-resolution ion analysis

The higher mass ions ($> m/z$ 100) in the HR-ToF-AMS spectrum provide key information regarding the low-volatility SOA constituents. Owing to the fragmentation caused by electron impact ionization, numerous ion combinations contribute to each nominal mass; the larger the mass, the greater the potential information regarding molecular detail, but the greater challenge in extracting that information. An explicit chemical mechanism of dodecane oxidation is critical in identifying individual ions, as well as patterns in the HR-ToF-AMS spectrum. A simplified schematic of the low- NO_x mechanism presented by Yee et al. (2012) is shown in Fig. 2.

At early growth, m/z 183 and m/z 215 dominate the signal for $m/z > 100$ (Figs. 3 and 4). At the outset, the only apparent ion at m/z 183 is $C_{12}H_{23}O^+$, but by the end of oxidation, $C_{10}H_{15}O_3^+$ has clearly grown in as a “left-side” neighbor to the original ion. This same type of behavior occurs for m/z 215 and, indeed, for almost all of the other masses in the spectrum. These developing patterns allow for a systematic identification of the ions at each mass. In each case, the later neighboring ion(s) have fewer carbons and more oxygens, as expected from continuous multi-generation oxidation. The unit mass resolution signals of m/z 183 and m/z 215, shown in Figs. 3 and 4, emphasize the difference in information between the unit mass and high-resolution analysis. The high resolution ions well past m/z 100 provide ion trend information (see Sect. 3.3), even if these ions do not influence the overall H : C and O : C ratios owing to small mass contributions.

3.3 Varying time trends for C_{12} ion fragments

The ions at higher m/z provide unique time traces from which inferences about the aerosol composition can be drawn. For example, the time series of C_{12} fragments in Fig. 5 shows distinct maxima during the course of the experiment. Since the parent hydrocarbon is a C_{12} molecule, the fragments shown in Fig. 5 are close to molecular level detail. The steady increase in signal of the less oxidized ion $C_{12}H_{23}O^+$ at m/z 183, followed by the increase of $C_{12}H_{21}O_2^+$ at m/z 197, and then $C_{12}H_{19}O_3^+$ at m/z 211 reflect the incorporation of increasingly oxidized products to the aerosol. The processes by which each ion reaches a maximum and then decreases are more challenging to infer. Deposition of aerosol to the chamber walls will cause the ion

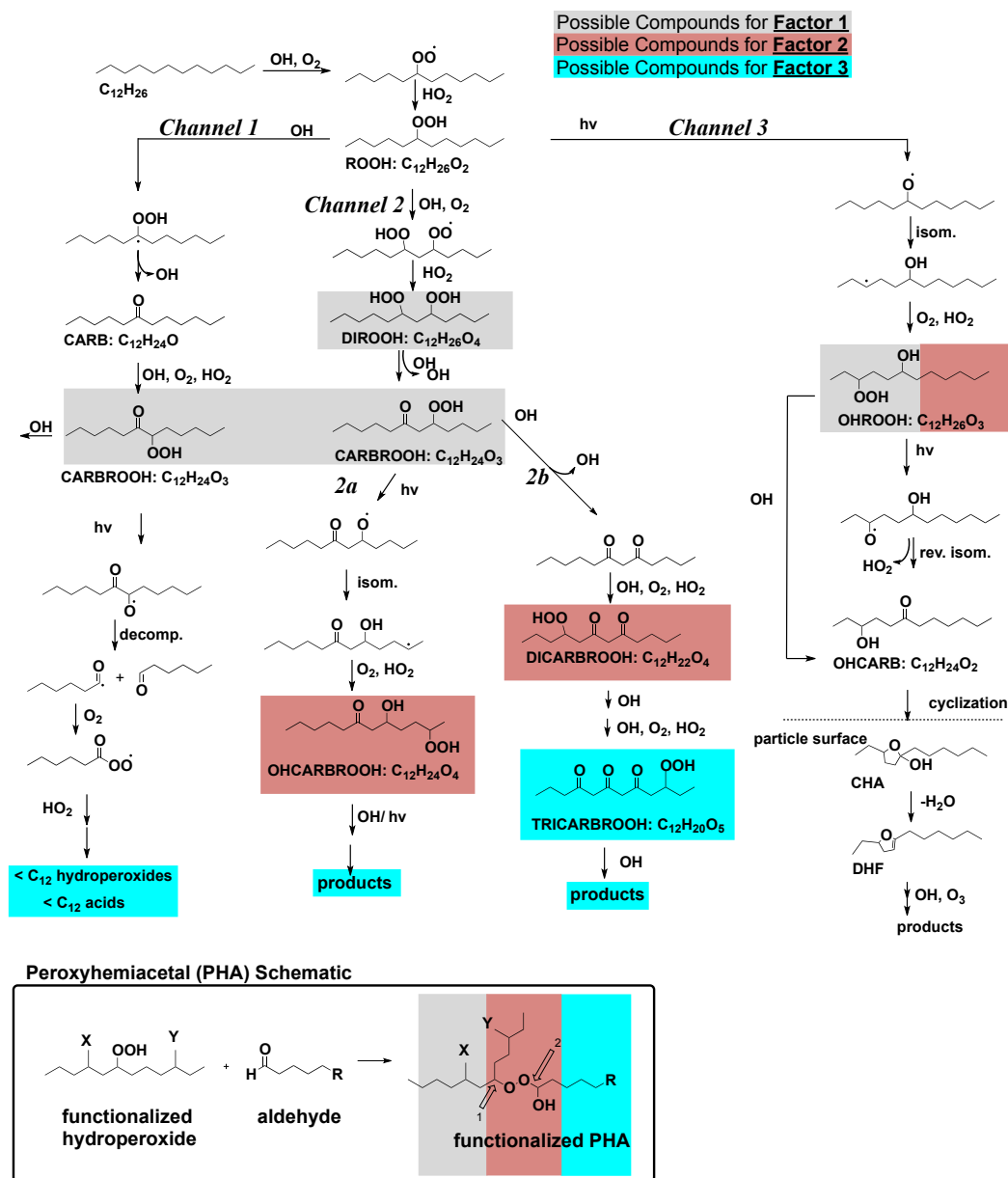


Fig. 2. Simplified chemical mechanism for dodecane photooxidation under low-NO_x, adapted from Yee et al. (2012). Shaded portions of the mechanisms are possible assignments for the PMF factors 1, 2 and 3, as discussed in Sects. 3.4 and 3.5.

signals to decrease (Sect. 3.6). A decreasing trend could also be the result of partitioning of products back to the gas-phase as their gas-phase equivalent reacts. Then, upon further oxidation in the gas-phase, the product re-condenses as a more oxidized species. Chemical conversion of the condensed products would provide another explanation for some ions to be decreasing, at the same time other ions are increasing. In electron impact ionization a particular ion fragment can be produced from two different compounds. This effect is magnified in the smaller m/z 's, for example, the C₂H₃⁺ ion

at m/z 27, which is dominant throughout the entire experiment and a common fragment for alkyl molecules.

The ions identified in the HR-ToF-AMS spectra are a linear combination of the molecules in the aerosol; positive matrix factorization is well suited for long-duration chamber experiments, especially with ions that have unique time trends. The PMF results are an attempt to rebuild the molecular trend information that is lost from electron impact ionization in the HR-ToF-AMS. The less harsh ionization methods of both the heating mode of the MOVI-HRToF-CIMS and gas-phase measurements from the CIMS provide molecular

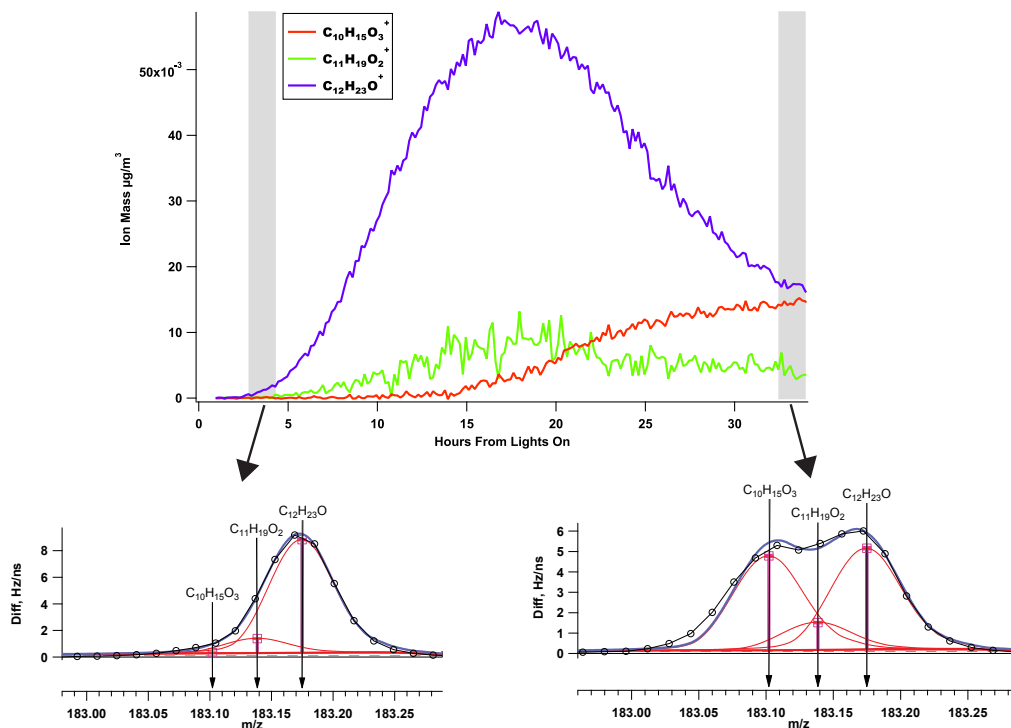


Fig. 3. Time series of ions and the raw data for “early growth” and “most oxidized growth” for m/z 183.

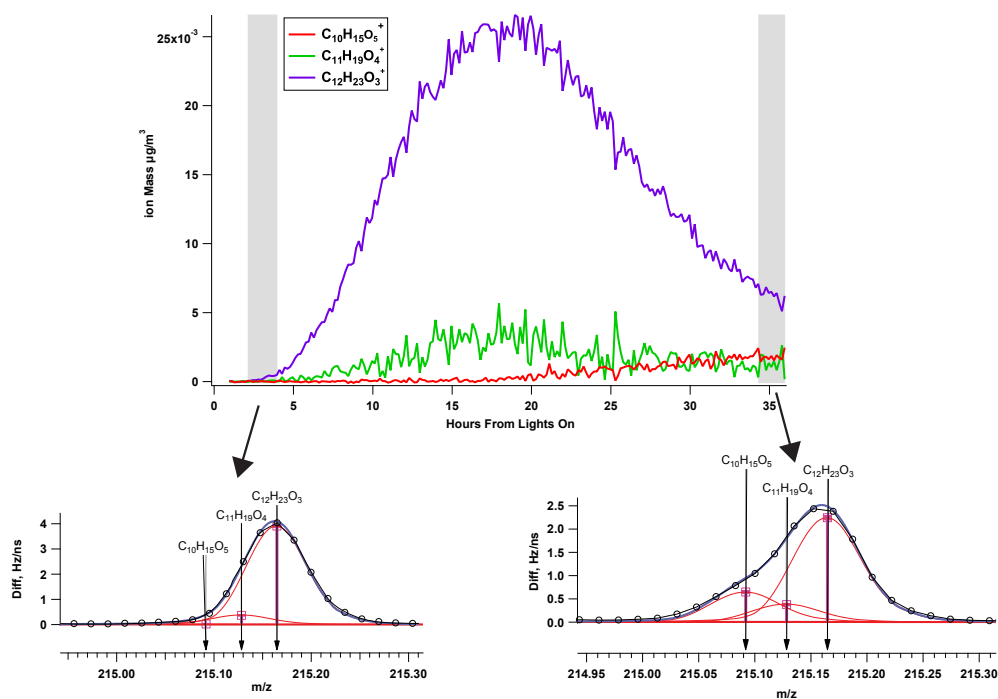


Fig. 4. Time series of ions and the raw data for “early growth” and “most oxidized growth” for m/z 215.

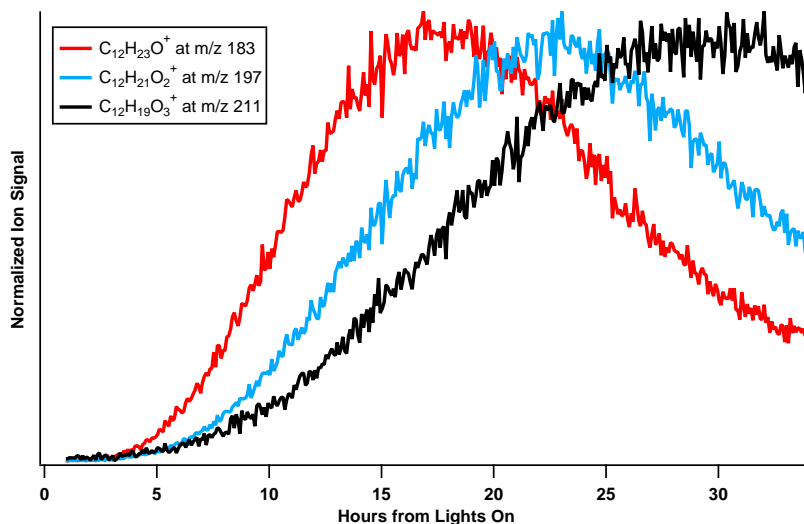


Fig. 5. C_{12} backbone ions with varying contributions of oxygen have distinct time trends over the duration of the experiment.

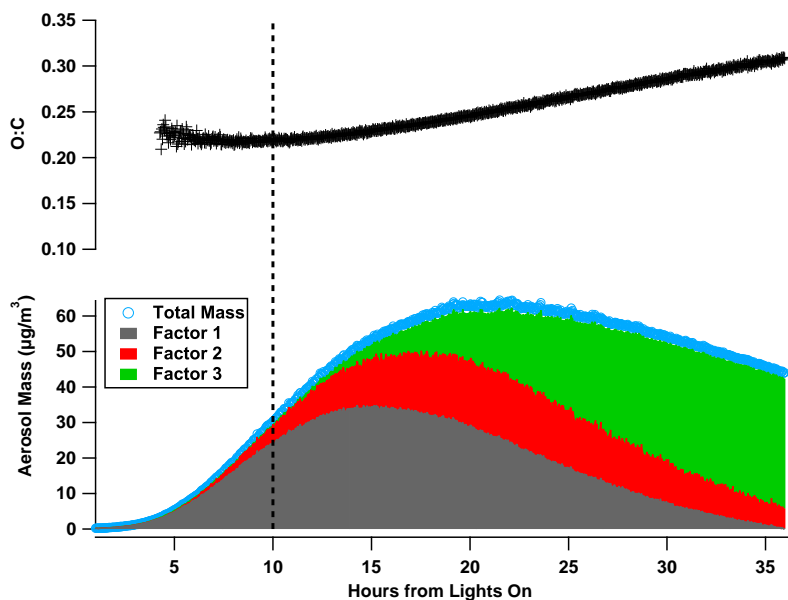


Fig. 6. Three-factor PMF solution, total organic mass, and O : C ratio. The dashed line denotes the point at which factor 3 grows in and the O : C begins to rise appreciably.

level information that the HR-ToF-AMS is unable to obtain, but to which the PMF results show similarity. From this comparison, molecular information can be inferred about the HR-ToF-AMS spectra, and how compounds fragment in the HR-ToF-AMS. Moreover, PMF results can be applied to obtain insight into the partitioning of the populations of oxidized molecules and the aerosol composition that evolves with continued oxidation.

3.4 Three-factor PMF solution

The PMF results for low- NO_x SOA formation from dodecane oxidation exhibit three distinct time traces with their correlating factor mass spectral profiles (Figs. 6 and 7). The three factor time series, shown in Fig. 6, are overlaid with the total organic loading to emphasize the relationship of each factor to the total SOA mass. The O : C ratio traces the overall oxidation state in the aerosol, and the PMF factors help explain that behavior. Factor 1, in grey, is dominant in the early aerosol growth and contains the least oxidized ions

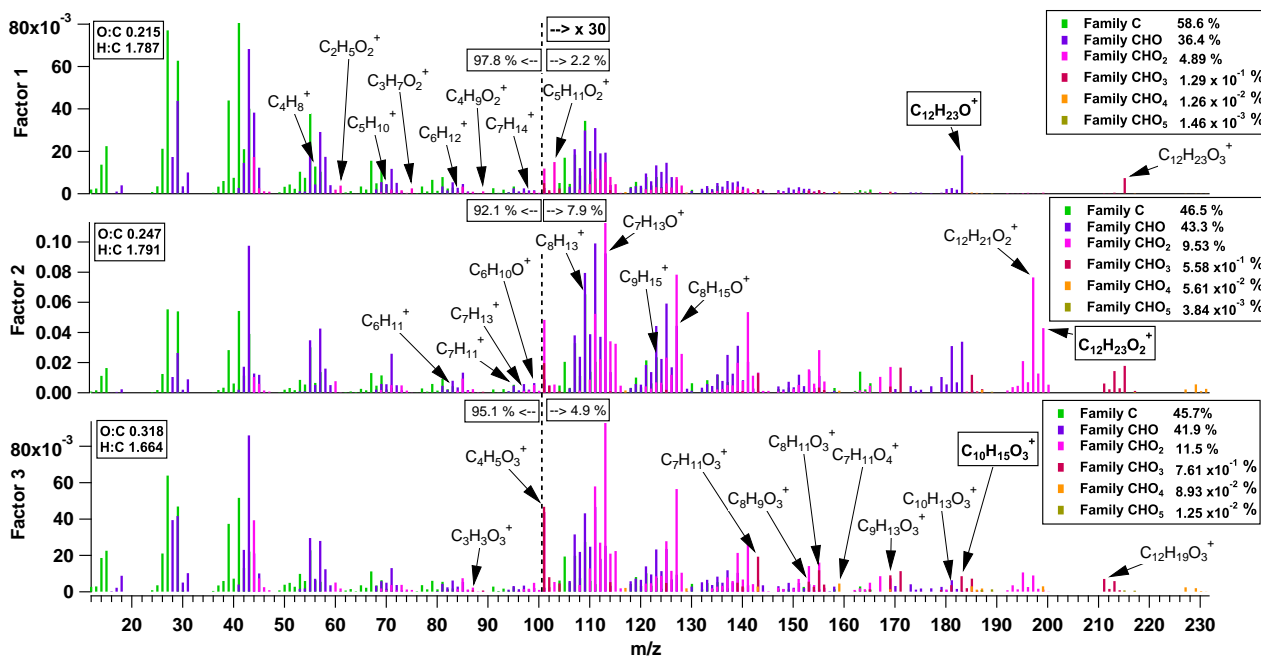


Fig. 7. The 3-factor mass spectra profiles in terms of their families. The ions past m/z 100 are multiplied by 30 to amplify signal strength.

(has the highest H:C ratio) of the factors. Factor 2 grows in next, peaks after factor 1, and then decreases. Factor 3 contains the highest contribution to the CO^+ and CO_2^+ ions and other O_2 , O_3 , O_4 , and O_5 – containing ions, explaining the steady increase in O:C over the course of the experiment. The CO_2^+ ion is the tracer for carboxylic acid in the HR-ToF-AMS (Aiken et al., 2008), which could explain the increase in O:C; however, the existence of the > 2 oxygen ion fragments indicates the O:C ratio increase could also be due to highly functionalized compounds, and not solely carboxylic acids, an observation supported by the chemical mechanism (Fig. 2) and the Van Krevelen Diagram (Sect. 3.7).

The mass spectral profiles of the factors are presented in Fig. 7, in which ions with different oxygen contents (different ion families) are highlighted by different colors. The mass percentage of each family to the total factor is presented in each factor's legend. Each factor profile has distinct, unique masses in the $> m/z$ 100 range. While it is difficult to identify an ion unique to one factor, certain ions have a higher contribution to one factor than another. Pearson's r correlation of each ion in the spectrum to each factor time series was used to identify which unique ions contribute the most to each factor. The 10 ions with the highest correlation in time with the factor profiles are tagged in the figure, with the top ion surrounded by a box. These are also listed in Table 3. The time trends of the top 3 ions correlating with each factor are displayed in Fig. 8. These ions provide the basis for identifying HR-ToF-AMS tracer ions for different generations of oxidation products. The interpretation of these factor time series and mass spectral profiles is aided by a chemical mech-

anism of dodecane oxidation, as well as comparison of time series to CIMS and MOVI-HRToF-CIMS data and individual HR-ToF-AMS ions.

3.5 Chemical interpretation of PMF solution

Factor 1 mass spectra and time series correlations with CIMS (Fig. 10) and MOVI-HRToF-CIMS (Fig. 11) ion time traces suggest that factor 1 could be C_{12} carbonyl hydroperoxide or C_{12} dihydroperoxide gas-to-particle partitioning (CAR-BROOH or DIROOH, Fig. 2, see grey shaded box) and possibly peroxyhemiacetal formation (see inset from Fig. 2). A $\text{C}_{18}\text{H}_{38}$ low- NO_x photooxidation experiment was carried out to produce a hydroperoxide standard and to understand the hydroperoxide fragmentation pattern in the HR-ToF-AMS (Fig. 9 and Table 4). The first product from $\text{C}_{18}\text{H}_{38}$ low- NO_x photooxidation is the hydroperoxide, which because of its long carbon chain, is expected to condense immediately onto the aerosol. Removal of HO_2 from the C_{18} hydroperoxide is supported by the $\text{C}_{18}\text{H}_{37}^+$ ion in the HR-ToF-AMS spectrum; this ion is considered a tracer for the C_{18} hydroperoxide. Fraser et al. (1970) also saw alkyl ions with 70 eV electronic impact ionization mass spectrometry measurements of alkyl hydroperoxides and attributed these peaks to HO_2 elimination from the hydroperoxide. The $\text{C}_3\text{H}_7\text{O}_2^+$ ion is also considered to be a tracer for the hydroperoxide-like compound since it has the highest percent difference between the $\text{C}_{18}\text{H}_{38}$ condensation spectrum before irradiation and the mass spectrum immediately after irradiation.

For dodecane, we do not expect the C_{12} hydroperoxide to partition to the particle phase, but we do expect the C_{12}

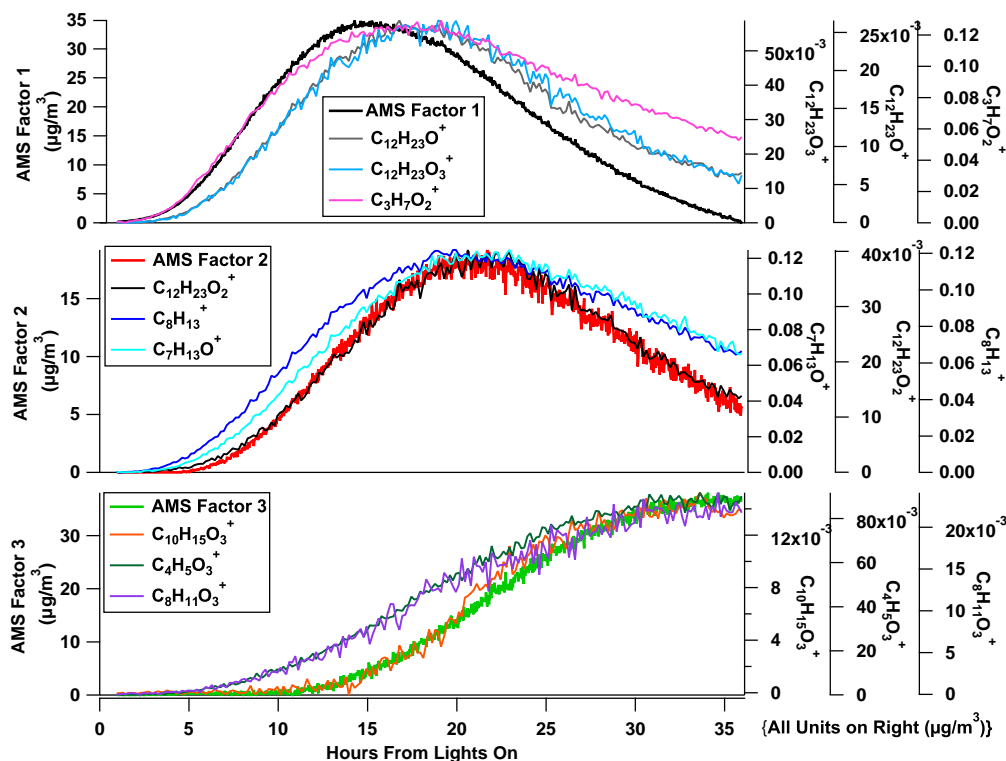


Fig. 8. Factor time series with the top three highest Pearson's r correlating HR-ToF-AMS ions.

Table 2. Ion fragments.

m/z	Ion	possible identification
169	$C_{12}H_{25}^+$	hydroperoxide, hydroperoxide-peroxyhemiacetal
201	$C_{12}H_{25}O_2^+$	hydroperoxide-peroxyhemiacetal
185	$C_{12}H_{25}O^+$	hydroxy hydroperoxide, hydroxy hydroperoxide-peroxyhemiacetal
217	$C_{12}H_{25}O_3^+$	hydroxy hydroperoxide-peroxyhemiacetal
183	$C_{12}H_{23}O^+$	carbonyl hydroperoxide, carbonyl hydroperoxide-peroxyhemiacetal
215	$C_{12}H_{23}O_3^+$	carbonyl hydroperoxide-peroxyhemiacetal
197	$C_{12}H_{21}O_2^+$	dicarbonyl hydroperoxide, dicarbonyl hydroperoxide-peroxyhemiacetal
229	$C_{12}H_{21}O_4^+$	dicarbonyl hydroperoxide-peroxyhemiacetal
199	$C_{12}H_{23}O_2^+$	hydroxy carbonyl hydroperoxide, hydroxy carbonyl hydroperoxide-peroxyhemiacetal
231	$C_{12}H_{23}O_4^+$	hydroxy carbonyl hydroperoxide-peroxyhemiacetal
211	$C_{12}H_{19}O_3^+$	tricarbonyl hydroperoxide, tricarbonyl hydroperoxide-peroxyhemiacetal
243	$C_{12}H_{19}O_5^+$	tricarbonyl hydroperoxide-peroxyhemiacetal

carbonyl hydroperoxide to partition (Yee et al., 2012). The presence of ion fragment $C_{12}H_{23}O^+$ at m/z 183 supports this explanation (Fig. 3). The $C_{12}H_{23}O_3^+$ ion at m/z 215 (a 32 m/z and O_2^+ difference from the carbonyl hydroperoxide ion) trends with the $C_{12}H_{23}O_3^+$ ion with a Pearson's r of 0.986 and is the ion with the highest correlation in the entire spectrum to $C_{12}H_{23}O^+$. A possible assignment of $C_{12}H_{23}O_3^+$

in correlation with $C_{12}H_{23}O^+$ is the peroxyhemiacetal corresponding to the carbonyl hydroperoxide (possible fragmentation at site 2 of peroxyhemiacetal, see inset in Fig. 2). Although the fragmentation of a peroxyhemiacetal standard in the HR-ToF-AMS can not be confirmed, the chemical mechanism prediction of aldehyde formation in the gas-phase and evidence for hydroperoxides in the gas- and particle-phase

Table 3. HR-ToF-AMS ions with highest Pearson's r values for $f_{\text{peak}} = 0.2$ solution.

Pearson's r with factor 1	Ion Formula	Ion Mass ($\mu\text{g m}^{-3}$)	Pearson's r with factor 2	Ion Formula	Ion Mass ($\mu\text{g m}^{-3}$)	Pearson's r with factor 3	Ion Formula	Ion Mass ($\mu\text{g m}^{-3}$)
0.888964	$\text{C}_{12}\text{H}_{23}\text{O}$	183.175	0.992157	$\text{C}_{12}\text{H}_{23}\text{O}_2$	199.17	0.978408	$\text{C}_{10}\text{H}_{15}\text{O}_3$	183.102
0.858995	$\text{C}_{12}\text{H}_{23}\text{O}_3$	215.165	0.975248	C_8H_{13}	109.102	0.970308	$\text{C}_4\text{H}_5\text{O}_3$	101.024
0.854958	$\text{C}_3\text{H}_7\text{O}_2$	75.0446	0.973654	$\text{C}_7\text{H}_{13}\text{O}$	113.097	0.95434	$\text{C}_8\text{H}_{11}\text{O}_3$	155.071
0.851494	C_6H_{12}	84.0939	0.973188	C_7H_{13}	97.1017	0.953511	$\text{C}_5\text{H}_7\text{O}_3$	115.039
0.835077	$\text{C}_5\text{H}_{11}\text{O}_2$	103.076	0.972338	$\text{C}_8\text{H}_{15}\text{O}$	127.112	0.949821	$\text{C}_9\text{H}_{13}\text{O}_3$	169.087
0.830188	$\text{C}_4\text{H}_9\text{O}_2$	89.0603	0.972216	C_7H_{11}	95.0861	0.947504	$\text{C}_7\text{H}_{11}\text{O}_3$	143.071
0.83002	C_5H_{10}	70.0782	0.970214	$\text{C}_{12}\text{H}_{21}\text{O}_2$	197.154	0.94481	$\text{C}_{12}\text{H}_{19}\text{O}_3$	211.133
0.819021	C_7H_{14}	98.1096	0.969585	C_9H_{15}	123.117	0.943721	$\text{C}_{10}\text{H}_{16}\text{O}_3$	184.11
0.812879	$\text{C}_2\text{H}_5\text{O}_2$	61.0289	0.969189	C_6H_{11}	83.0861	0.941672	$\text{C}_{10}\text{H}_{13}\text{O}_3$	181.087
0.775934	C_4H_8	56.0626	0.968232	$\text{C}_6\text{H}_{11}\text{O}$	99.081	0.939138	$\text{C}_3\text{H}_3\text{O}_3$	87.0082

suggest that peroxyhemiacetal formation or other oligomerization processes are possible.

Figure 8 shows the PMF factor time series with the top 3 correlating HR-ToF-AMS ions. The $\text{C}_3\text{H}_7\text{O}_2^+$ ion at m/z 75, which is a suggested hydroperoxide tracer (Table 4), nearly overlaps factor 1 for the first 15 h, after which the time trend of $\text{C}_3\text{H}_7\text{O}_2^+$ decays more slowly than factor 1; this is because the hydroperoxide functionalization could also have a contribution to factor 2, or later generations of oxidation products. $\text{C}_{12}\text{H}_{23}\text{O}^+$ at m/z 183 and $\text{C}_{12}\text{H}_{23}\text{O}_3^+$ at m/z 215 also have a high correlation, although these ions grow in slightly after the hydroperoxide ion at m/z 75. The difference between the individual ions trends and the PMF time trace is expected since the PMF factor represents the bulk variation of the aerosol composition over time and is not necessarily expected to exactly overlap with individual ion trends. Additionally, due to the fragmentation in the HR-ToF-AMS, single ions can contribute to multiple factors. The top 10 ions with the highest Pearson's r values for each factor show this effect (Fig. A1). The chemical interpretation of factor 1 is also supported by comparison to the CIMS gas-phase measurement of positive mode m/z 204, the suggested product being the carbonyl hydroperoxide (Fig. 10, Yee et al., 2012) as well as the MOVI-HRToF-CIMS heating-mode measurement of the $\text{C}_{12}\text{H}_{21}\text{O}_3^+$ ion, which is likely the chemical ionization product of a C_{12} dihydroperoxide (Fig. 11).

HR-ToF-AMS, CIMS, and MOVI-HRToF-CIMS measurements suggest that factor 2 represents the gas-phase partitioning of tri-functionalized products and their corresponding peroxyhemiacetals (see pink shaded boxes in Fig. 2). Factor 2 correlates highly with HR-ToF-AMS ion $\text{C}_{12}\text{H}_{23}\text{O}_2^+$ at m/z 199, which is the suggested ion tracer for the hydroxy carbonyl hydroperoxide (OHCARBROOH). Factor 2 also correlates well with the CIMS gas-phase positive mode m/z 219, which is the suggested dicarbonyl hydroperoxide product (Fig. 10) and the MOVI-HRToF-CIMS heating-mode ion $\text{C}_9\text{H}_{15}\text{O}_4^+$ (Fig. 11). The MOVI-HRToF-CIMS ion has higher oxygen content than ions trending with factor 1,

which could suggest an additional functional group from further oxidation.

Factor 3 is likely the gas-particle partitioning of multi-functional (4 or more functional groups) products, as indicated by HR-ToF-AMS ion $\text{C}_{10}\text{H}_{15}\text{O}_3^+$ at m/z 183 and $\text{C}_{12}\text{H}_{19}\text{O}_3^+$ at m/z 211 (Fig. 7), which could be the tri-carbonyl hydroperoxide product (TRICARBROOH). MOVI-HRToF-CIMS data also support the addition of a highly oxidized product to the aerosol with the ion $\text{C}_{10}\text{H}_{15}\text{O}_3^+$ trend (Fig. 11). Although the CIMS did not measure in the high m/z range necessary for identifying greater than tri-functionalized gas-phase products, the CIMS gas-phase C_8 carboxylic acid trace shows continual increase. This is consistent with factor 3 growth, the potential for acid formation in the chemical mechanism, and HR-ToF-AMS CO_2^+ ion, which could be from either acid formation or multifunctional products (Fig. 10). These results support factor 3 containing highly functionalized compounds, and acidic compounds, either from gas-to-particle partitioning of highly oxidized products or possibly from condensed chemical conversion from products in factors 1 and 2.

Factors 1 and 2 both exhibit a maximum with respect to time. A decrease after the maximum owing to wall deposition alone, addressed in Sect. 3.6, does not fully explain the decrease of these factors. The extent of evaporation of aerosol products is difficult to interpret from the gas-phase data. Other processes, such as cyclization or peroxyhemiacetal oligomerization, are possible (Tobias and Ziemann, 2000; Ziemann, 2003) but cannot be established unequivocally from HR-ToF-AMS data, as the fragments resulting from oligomerization are not unique. Masses greater than m/z 300 are observed in the MOVI-HRToF-CIMS spectra, which although difficult to assign exact elemental formulas, may suggest that products greater than C_{12} exist in the aerosol. Chemical conversion likely contributes to the decrease in factors 1 and 2 and increase in factor 3 (although gas-phase partitioning of highly oxidized compounds could also be contributing to the increase in factor 3). The percentages of mass greater than m/z 100 for factors 2 and 3 are

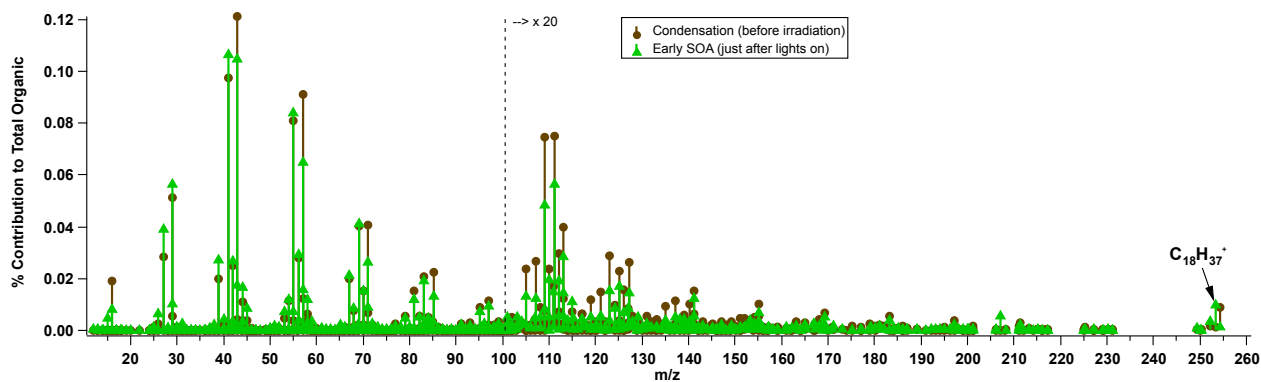


Fig. 9. Mass spectrum of octadecane condensing onto the seed before irradiation, and the relative mass spectrum just after lights on. The hypothesized octadecane-equivalent hydroperoxide fragment is marked at m/z 253.

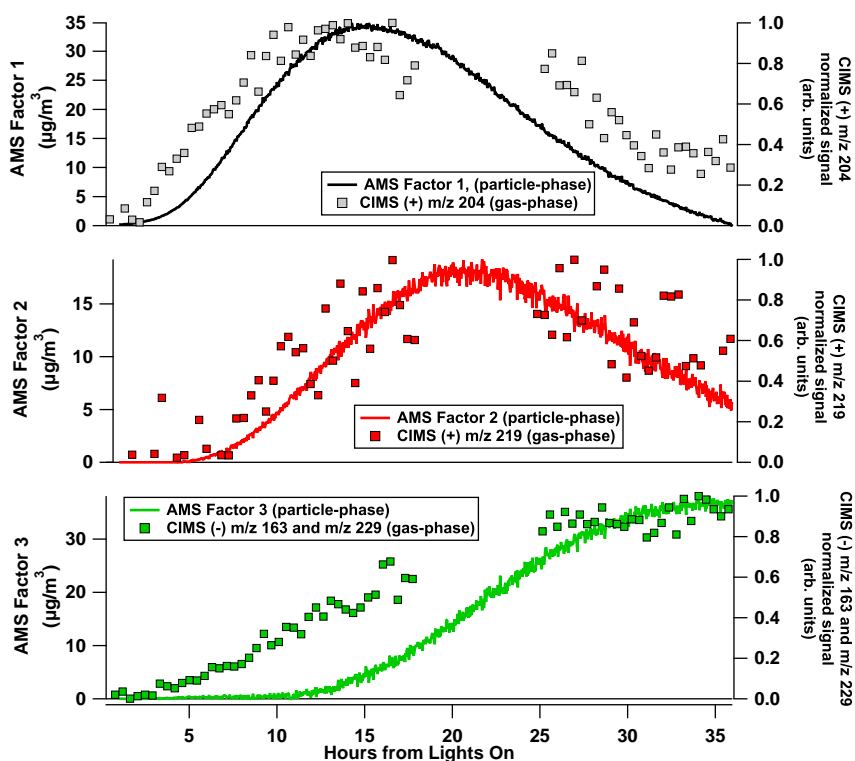


Fig. 10. Particle-phase HR-ToF-AMS factor time series with gas-phase CIMS time traces.

8 % and 5 %, respectively. The decrease of mass concentration of ions correlating with factor 2 may be a result of fragmentation in the aerosol. Molecular level identification of individual species from further MOVI-HRToF-CIMS analysis would be necessary to confirm this.

Other HR-ToF-AMS ions with 32 m/z difference that support a C_{12} functionalized hydroperoxide reacting with an aldehyde to form peroxyhemiacetal are listed in Table 2. Other 32 m/z pairs with fewer than 12 carbons exist, and may come from hydroperoxide formation in Channel 1 of the

mechanism containing fragmentation of carbon chains fewer than 12.

The proposed peroxyhemiacetal tracer ions behave differently under reduced HR-ToF-AMS temperature. In experiment 5 in Table 1, the HR-ToF-AMS 600 °C heater was turned off and only ionization (no vaporization) was used to sample the aerosol. During the time when the heater was turned off, the bulk of the organic ions decreased, since the ionization of the aerosol is contingent upon its vaporization. However, signal generated by the ions for the hypothesized

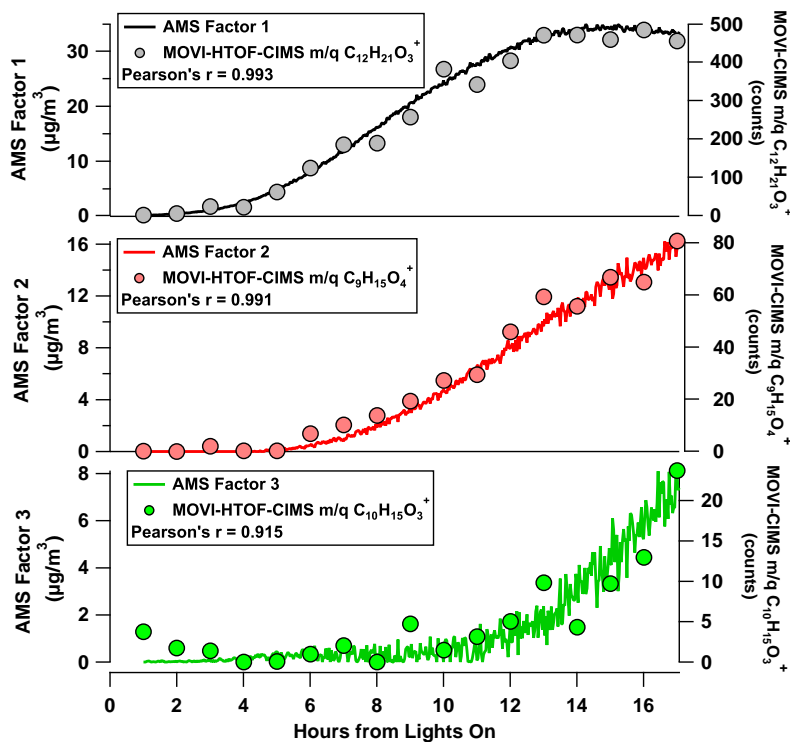


Fig. 11. Factor time series with MOVI-HRToF-CIMS heating-mode, aerosol-phase traces. Only the first 18 h of data is available for the MOVI-HRToF-CIMS data.

peroxyhemiacetal actually increased (Fig. 12). Since peroxyhemiacetals are unstable at high temperature, the decrease in temperature would stabilize peroxyhemiacetal, allowing the molecules to be more available for ionization.

It is important to note that the latter half of experiment 2 provides useful information in interpreting the chemistry of the aerosol. In the first 17 h, all of the factors show only an increase (see Figs. 11 and A1). The time trends of factors 2 and 3 look very similar in the first 17 h, but distinction becomes possible in the latter half of the experiment in which factor 2 decreases and factor 3 increases (Fig. 6). This explains perhaps why in a shorter experiment, two factors explain the data better (see Appendix A for further explanation on the effect of PMF on different lengths of experiment).

3.6 Chamber processes

Deposition of aerosol to the chamber walls decreases the suspended aerosol mass. PTOF-mode data are not available for the 34 h experiment discussed above. Experiment 4 was carried out, with a similar initial dodecane concentration, to explore the contribution from wall loss to the decrease in mass of the PMF factor time series. As expected, the average diameter of the aerosol mass distribution grew with increasing OH exposure (Fig. 13 and panel a1, a2 and a3 in Fig. 14). Since the wall loss rate is a function of diameter (Fig. 13, Loza et al., 2012), the size of the aerosol and composition

at that size are important for factor dependent wall-loss corrections. Panel b of Fig. 14 shows the PMF factors (only 2 for a shorter experiment, see Sect. A2) as a function of time. “Time 1” is early in the experiment when the mass distribution is expected to have a major contribution from factor 1. “Time 2” is at maximum growth in time of factor 1 and a large contribution from factor 2, and “Time 3” is when factor 2 has passed factor 1 in overall mass. The PMF results for the mass distributions (diameter is the independent variable now instead of time) are shown with the overall organic mass distribution to emphasize the contribution from factors 1 and 2 to each size bin (panel a1, a2, and a3 with b on Fig. 14). Since factor 1 is the first to condense onto the aerosol, some of its mass is lost more rapidly than factor 2, which condenses later onto larger particles (which are lost by deposition at a slower rate). The mass fractions of factors 1 and 2 were calculated for each size bin for 12 mass distributions; this information was used to adapt the wall deposition calculations carried out by Loza et al. (2012) for individual factor wall loss corrections.

Even with wall loss correction, factor 1 shows a decrease, while factor 2 shows an increase; the cumulative mass loss by wall deposition for factor 1 at the end of the experiment is $18 \mu\text{g m}^{-3}$, which accounts for approximately 50 % of the decrease in mass from the peak of factor 1 (panel c from Fig. 14). These results further support the hypothesis that the mass in the aerosol is undergoing chemical conversion. It is

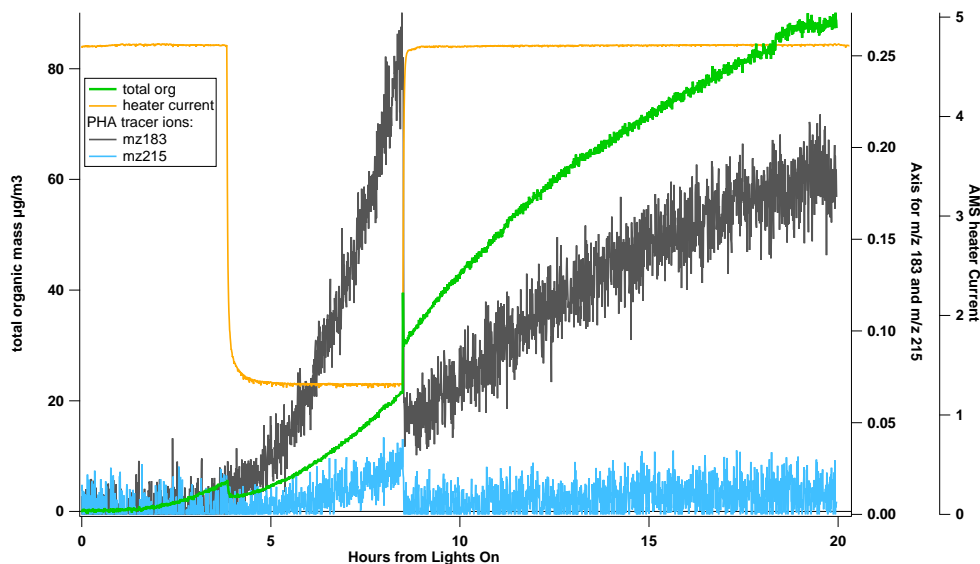


Fig. 12. Tracer ions for the carbonyl hydroperoxide increase while the bulk organic trace decreases when the 600 °C HR-ToF-AMS heater is turned off.

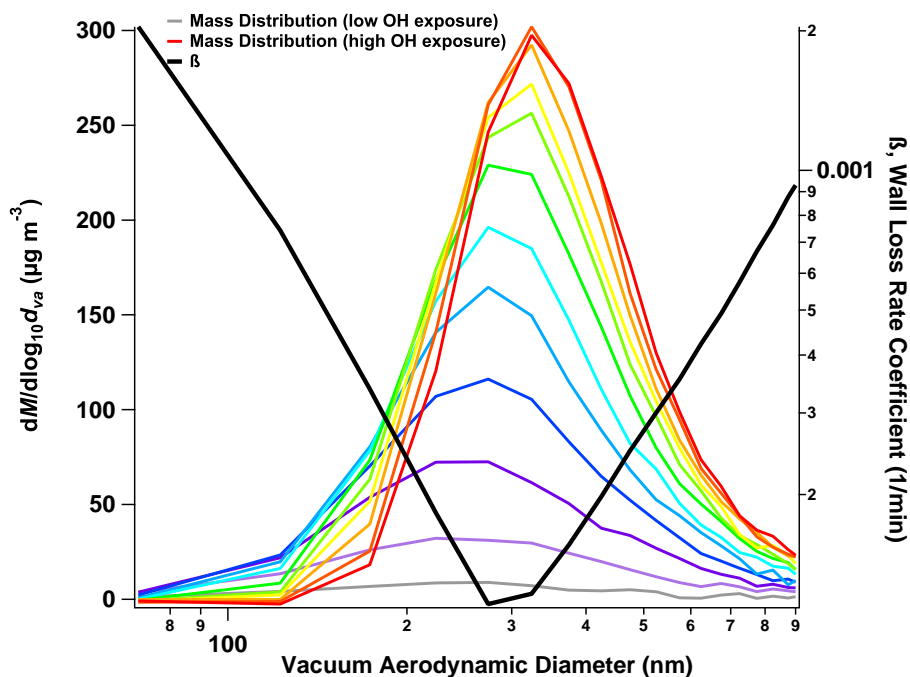


Fig. 13. The aerosol mass distribution grows from smaller diameter sizes to larger diameter sizes with increasing OH exposure (purple is low OH exposure, red is high OH exposure). The wall deposition rate coefficient is overlaid for comparison.

also important to note that the effects of wall loss on factors 1 and 2 differ as a result of the size distribution of the aerosol when the factor emerges.

3.7 Van Krevelen diagram

The Van Krevelen diagram has been used to represent the evolution of HR-ToF-AMS elemental ratios, H : C vs. O : C, for both ambient and chamber-generated organic aerosols (Heald et al., 2010; Ng et al., 2011; Chhabra et al., 2011; Lambe et al., 2011, 2012). A slope of 0 on the diagram is

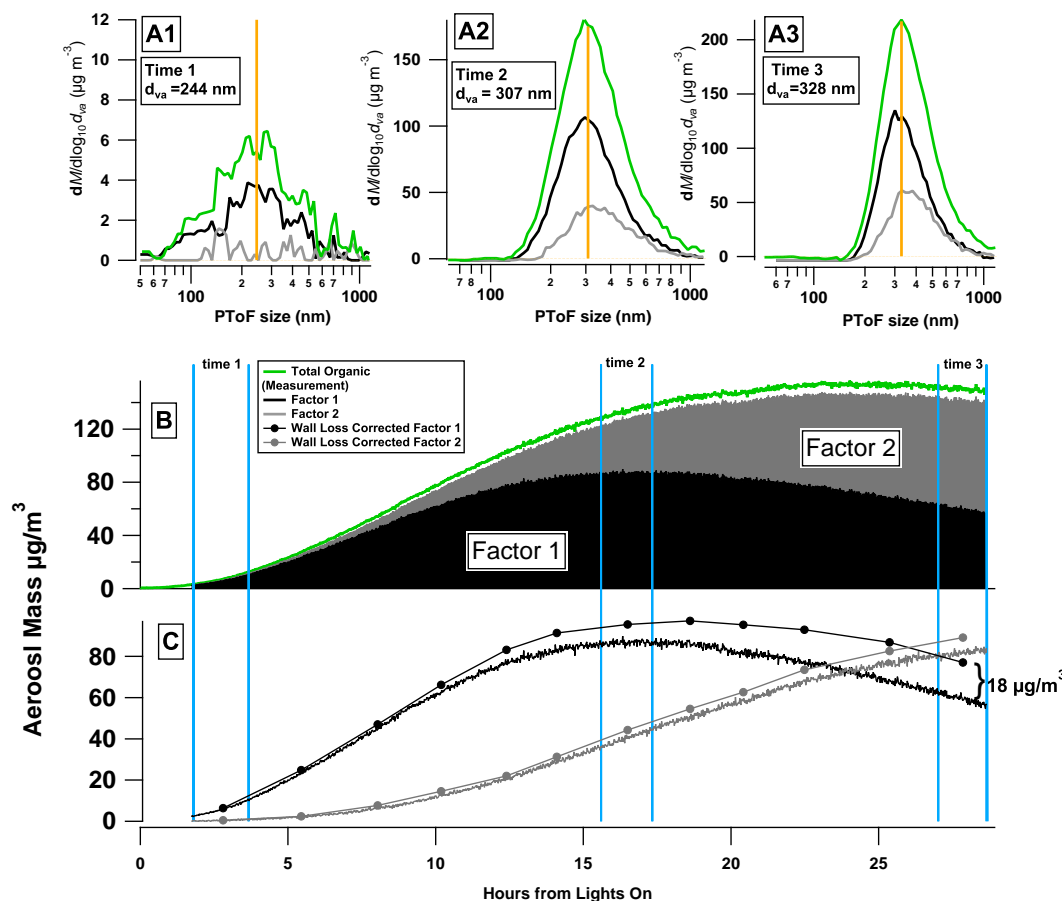


Fig. 14. Mass distributions (A1, A2 and A3) and time series (B) of total organic mass (green) broken down into 2 factors (black and grey). The average diameter for each mass distribution is highlighted by the yellow bar, and the time associated with each distribution is outlined with the two blue bars on the time series graphs. The wall-loss corrected versions of the individual factor time series are also shown (C).

consistent with peroxide or alcohol functionalization without carbon chain fragmentation. A slope of -1 is consistent with carboxylic acid or ketone/aldehyde and alcohol addition on the same carbon chain, and a slope of -2 is consistent with ketone/aldehyde addition (Van Krevelen, 1950; Heald et al., 2010). Lambe et al. (2012) report the slopes for low- NO_x photooxidation of long chain alkanes (C_{10} , C_{15} , and C_{17}) in a PAM reactor in two regimes in terms of the O : C ratio. For O : C < 0.3 , the slope is relatively steep (-1.3 ± 0.2), while for O : C > 0.3 the slope becomes less negative (-0.7 ± 0.1). Lambe et al. (2012) attribute this change in slope to a transition from functionalization to fragmentation dominated reactions. The dodecane aerosol composition data presented here lie primarily in the regime where O : C < 0.3 , with a slope of -1.16 that is consistent with Lambe et al. (2012) in this O : C range.

As discussed by Ng et al. (2011) and Lambe et al. (2012), the slope on a Van Krevelen diagram can represent a combination of several functionalities and generally requires molecular level information for further interpretation. The

PMF analysis links the HR-ToF-AMS aerosol spectrum to molecular level detail when compared to measurements from CIMS and MOVI-HRToF-CIMS. Concurrent with our chemical understanding, over 34 h of oxidation, the dodecane low- NO_x system is characterized by the addition of peroxides and ketone/aldehyde functionalization, as opposed to solely carboxylic acid formation. PMF factor 1 (black marker in Fig. 15) overlaps the bulk composition data (grey markers) near the initial growth at low OH exposure. Factor 2 (red marker in Fig. 15) has a similar H : C ratio as factor 1, but higher O : C ratio. The slope between factors 1 and 2, $m_{12} = 0.12$, is characteristic of either hydroxy or peroxide addition. We have already shown that factor 2 describes the gas-phase partitioning of hydroperoxide species (Sect. 3.5). The addition of hydroperoxide functional groups is not obvious from the bulk H : C and O : C ratios (slope = -1.16), but only from the PMF factor elemental ratios. The H : C and O : C ratios of factor 3 (green marker in Fig. 15) overlaps the data (grey markers) at the end of the experiment. The slope from factor 2 to 3, $m_{23} = -1.78$, is characteristic of

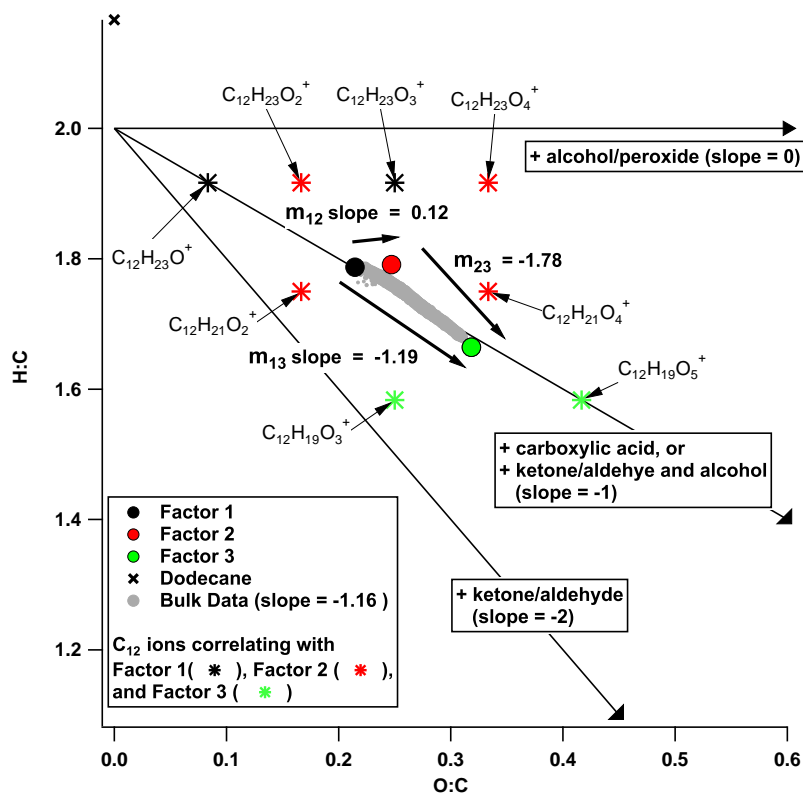


Fig. 15. Van Krevelen diagram for low- NO_x photooxidation of dodecane. HR-ToF-AMS bulk composition data are indicated by the grey markers and PMF factors 1–3 are shown by the black, red, and green circle markers. C_{12} ions, which are the ions retaining the most molecular-level detail, with high correlation to each factor are also displayed by the black, red, and green star markers.

the addition of products with carbonyl or ketone functionalization. The slope between factor 1 and 3, $m_{13} = -1.19$, is consistent with either carboxylic acid formation or ketone/aldehyde and alcohol addition to a product in factor 1. The slopes between the factor elemental ratios help indicate the combinations of functionality in the aerosol, with more clarity than one slope from the bulk elemental analysis. The C_{12} ion fragments correlating the highest with each factor and hypothesized to be mono-, di-, or tri-functionalized C_{12} hydroperoxides and/or functionalized peroxyhemiacetals are also displayed on Fig. 15.

4 Conclusions

In the present work, PMF has been applied to high-resolution chamber HR-ToF-AMS mass spectra to deduce the chemical and physical processes associated with low- NO_x dodecane SOA formation and aging. PMF untangles some of the complexity of SOA mass spectra by providing a mass spectral signature, with ion tracers, associated with a group of molecules at a distinct oxidation level. Factor 1 represents the gas-phase partitioning of initial oxidation products with two functional groups, factor 2 is the further oxidized, tri-

functionalized products incorporating into the particle phase, and factor 3 is the partitioning of extended oxidation products quadruply functionalized. All three factors could also include oligomerization processes and contributions from wall-loss.

An octadecane low- NO_x photooxidation experiment was conducted to develop a hydroperoxide standard for the HR-ToF-AMS, from which the alkyl-ion $\text{C}_{18}\text{H}_{37}^+$ at m/z 253 and $\text{C}_3\text{H}_7\text{O}_2^+$ at m/z 75 were identified as hydroperoxide ion tracers. With the PMF factor results, in combination with the SOA mechanism, CIMS, and MOVI-HRToF-CIMS measurements, the peroxyhemiacetal ion tracers were proposed, such as the $\text{C}_{12}\text{H}_{23}\text{O}^+$ at m/z 183 and $\text{C}_{12}\text{H}_{23}\text{O}_3^+$ at m/z 215 for the carbonyl hydroperoxide-peroxyhemiacetal.

The Van Krevelen diagram of the data, supported by the chemical interpretation of the dodecane low- NO_x oxidation, is consistent with the addition of peroxides and ketone/aldehyde functionalization rather than solely carboxylic acids. While the bulk experimental elemental ratios exhibit a slope of -1.16 , the change in H:C and O:C ratios from factors 1 to 2 reveals a slope of 0.12, strongly indicating hydroperoxide addition to the aerosol. The elemental ratios between factors 2 and 3 have a slope of -1.78 , indicating adding of aldehyde/carbonyl functionalization, and the slope between factor 1 and 3 is -1.19 , indicating either

Table 4. Distinct ions present in early C₁₈ SOA formation.

Ion Formula	Exact Mass	% Difference from C ₁₈ Condensation MS*	Mass Fraction in SOA Spectrum
C ₃ H ₇ O ₂	75.0446	0.99	0.0005
CO	27.9949	0.99	0.0007
CO ₂	43.9898	0.99	0.0007
C	12.0000	0.99	0.0006
C ₂ H ₂ O	42.0106	0.99	0.0017
CHO ₂	44.9977	0.99	0.0006
CH	13.0078	0.99	0.0006
CH ₃	15.0235	0.99	0.0048
C ₅ H ₃	63.0235	0.99	0.0006
C ₁₈ H ₃₇	253.2900	0.98	0.0005
C ₅ H ₇ O	83.0497	0.98	0.0024
C ₄ H ₉ O	73.0653	0.98	0.0014
C ₂ H ₃ O	43.0184	0.97	0.0174
C ₆ H ₆	78.0470	0.96	0.0014
CH ₃ O	31.0184	0.95	0.0027
C ₂ H ₂	26.0156	0.95	0.0066
C ₃ H ₇ O	59.0497	0.95	0.0036
C ₂ H ₅ O	45.0340	0.94	0.0084
C ₃ H	37.0078	0.94	0.0008
C ₄ H ₂	50.0157	0.94	0.0009
C ₃ H ₃ O	55.0184	0.94	0.0072
CHO	29.0027	0.93	0.0103
C ₄ H ₄	52.0313	0.93	0.0012
C ₂ H ₅ O ₂	61.0289	0.93	0.0007
C ₃ H ₆ O	58.0419	0.93	0.0118
C ₃ H ₄ O	56.0262	0.93	0.0010
C ₅ H ₅ O	81.0340	0.92	0.0010
C ₄ H ₅	53.0391	0.92	0.0074
C ₃ H ₄	40.0313	0.92	0.0041
C ₅ H ₁₀ O	86.0732	0.92	0.0005
C ₅ H ₁₁ O	87.0810	0.92	0.0005
C ₉ H ₇	115.0550	0.92	0.0006
C ₄ H ₆ O	70.0419	0.92	0.0019
C ₂ H ₄ O	44.0262	0.92	0.0167
C ₆ H ₈	80.0626	0.92	0.0013
C ₃ H ₂	38.0157	0.91	0.0020
C ₂ H ₃	27.0235	0.91	0.0390
C ₅ H ₅	65.0391	0.91	0.0020
C ₆ H ₁₁ O	99.0810	0.91	0.0015
C ₄ H ₇ O	71.0497	0.91	0.0089
C ₃ H ₃	39.0235	0.91	0.0271
C ₄ H ₃	51.0235	0.91	0.0016
C ₃ H ₅ O	57.0340	0.90	0.0158

* Early Oxidation MS-Condensation MS)/Condensation MS

carboxylic acid formation or aldehyde/ketone and alcohol addition. With the aid of the PMF results, the experimental data displayed on the Van Krevelen diagram can be broken down into contributions from different types of functionality.

Size-dependent composition was utilized to determine the extent of wall-loss deposition affecting factors 1 and 2. The wall deposition contributed differently to each factor, but does not entirely explain the factor mass decrease; the decrease unexplained by wall loss deposition is attributed to chemical aging of the aerosol.

The chamber photooxidation HR-ToF-AMS PMF results facilitate the interpretation of SOA chemical and physical processes by linking the bulk AMS aerosol composition data to molecular level information provided by CIMS and MOVI-HRToF-CIMS measurements.

Appendix A

SOA formation from a single source in a laboratory is characterized by smooth aerosol growth (Fig. A1); the well-behaved nature of ion signals and their associated errors is ideal for application of PMF. The size of the organic signal input matrix for PMF of experiment 2 in Table 1 is 1050 × 325. The columns of the matrix correspond to individual identified ions. High resolution stick intensities for identified ions at fractional m/z 's from 12–300 were used. AMS ion identification in the m/z 101–300 range was aided by the dodecane low-NO_x chemical mechanism, CIMS gas-phase measurements, and MOVI-CIMS aerosol measurements. Not all of the individual ions identified were included in PMF analysis, due to S/N constraints.

The ions included in PMF analysis and the solution justification are discussed here. The organic matrix was calculated using PIKA's "Open" minus "Closed" option for high-resolution ions with an average signal-to-noise ratio (S/N) greater than 0.2. Signals with a S/N between 0.2 and 2 were down-weighted by a factor of 3, as recommended by Paatero and Hopke (2003). The error matrix was calculated in PIKA in the standard way using "Open" minus "Closed" errors. The errors (σ) normalize the residuals (e) for the minimization function routine of PMF, Q ; therefore, good quantification of errors is needed. For an input matrix of $n \times m$, the PMF minimization function from Ulbrich et al. (2009), is:

$$Q = \sum_{i=1}^n \sum_{j=1}^m (e_{ij}/\sigma_{ij})^2 \quad (\text{A1})$$

Careful consideration was given when choosing the ions for PMF. Even though the ion may appear to be present in the ion fitting window in PIKA, sometimes the time trend of this ion is too noisy for PMF. Noisiness in the time trend can be introduced when there are: (a) ions that are in the shoulder of a larger ion at the same nominal mass (i.e., C₃H₃O₅⁺ is in the shoulder of the much larger ion C₈H₇O⁺ at m/z 119), (b) ions that are in the valley of two larger ions at the same nominal mass (i.e., the C₃H₇⁺ ion is in-between C₃H₃O₃⁺ and C₄H₇O₂⁺ at m/z 87), (c) ions that exhibit a strong signal in the closed spectra, but only a small signal in the difference spectra (i.e., C₁₀H₇⁺ at m/z 127), and/or (d) an ion is coincident with another ion that is expected to be there (i.e., the isotope of N₂⁺ ion and CHO⁺ ion are extremely close in exact mass). If ions like the ones mentioned above are included in PMF, then there is considerable noise in the time trend

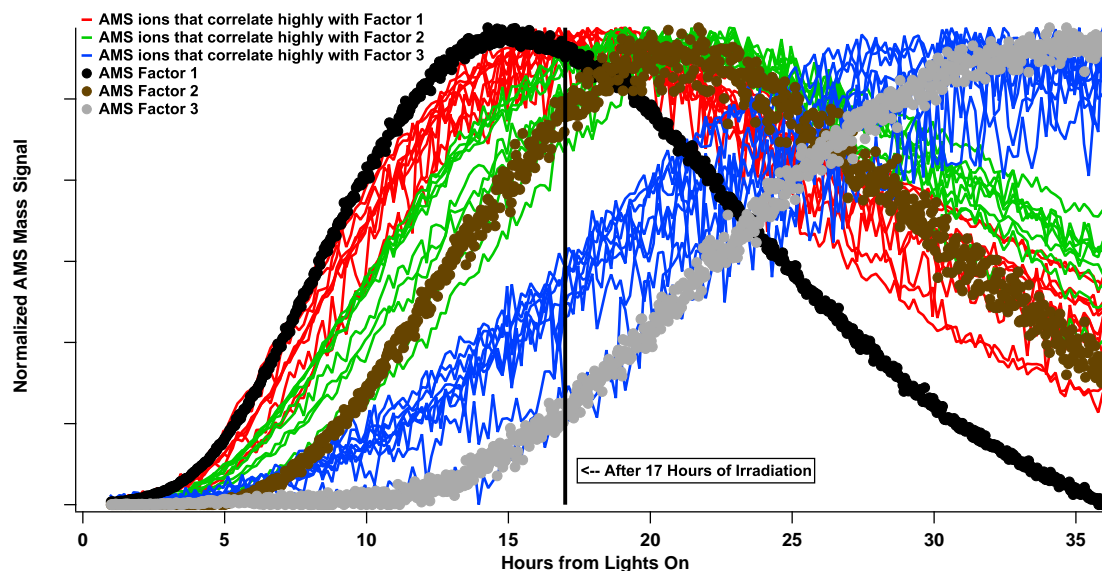


Fig. A1. Normalized mass signals from the AMS PMF factor time series are plotted with the AMS ions that have the highest correlations with those factors (ions listed in Table 3).

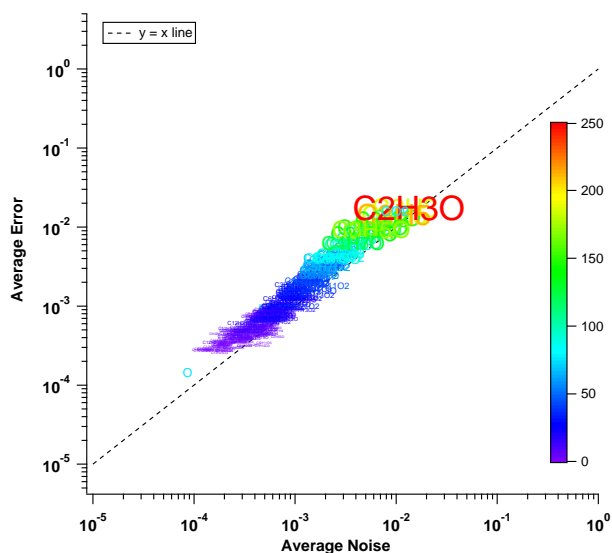


Fig. A2. Average error vs. the average noise for each ion is plotted along with the $y = x$ line. The marker is labeled by the ion it represents and is colored and sized by the S/N ratio of that ion. If the marker lies directly on the $y = x$ line, this means the calculated errors have captured the noise in the ion signal, which is critical for PMF analysis.

of Q/Q_{expected} . This noisiness results from peak fitting ions that experience large interference from other (often larger) ions, and should not be considered for PMF. An effective diagnostic to determine which ions to exclude from PMF is to calculate the S/N of each ion using the errors generated in PIKA (S/N_{error}), and then compare that to the S/N using the

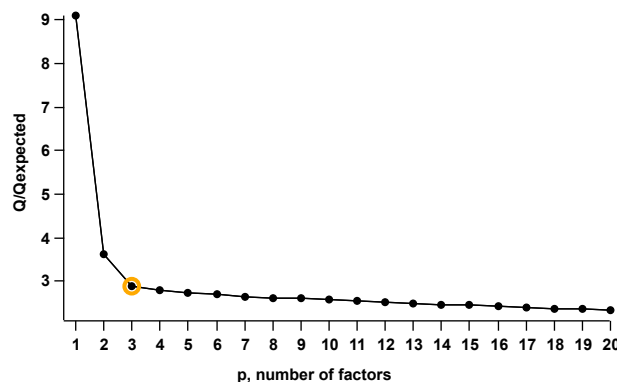


Fig. A3. Q/Q_{exp} vs. p , number of factors. The solution chosen is highlighted by the yellow circle.

observed noise (S/N_{noise}). The observed noise is calculated by smoothing the data using the binomial smoothing function in Igor (order of smoothing is chosen by user) and then subtracting the data from the smoothed data at each time point. Since the equation for errors in PIKA does not consider noise introduced by ion fitting (in the a., b., c., and d. scenarios described above), the S/N_{noise} is a good way to assess how well the ion is quantified. If S/N_{error} is much different than the S/N_{noise} , then either the ion should not be fit because it is a minor ion, or it is an ion described by a., b., c., or d. above, and should be removed from PMF analysis. Figure A2 shows the time-averaged error vs. time-averaged noise for each ion. The marker is labeled by the ion it represents and is sized and colored by its S/N . A marker lying on the $y = x$ line means that the calculated errors in PIKA captured the noisiness of

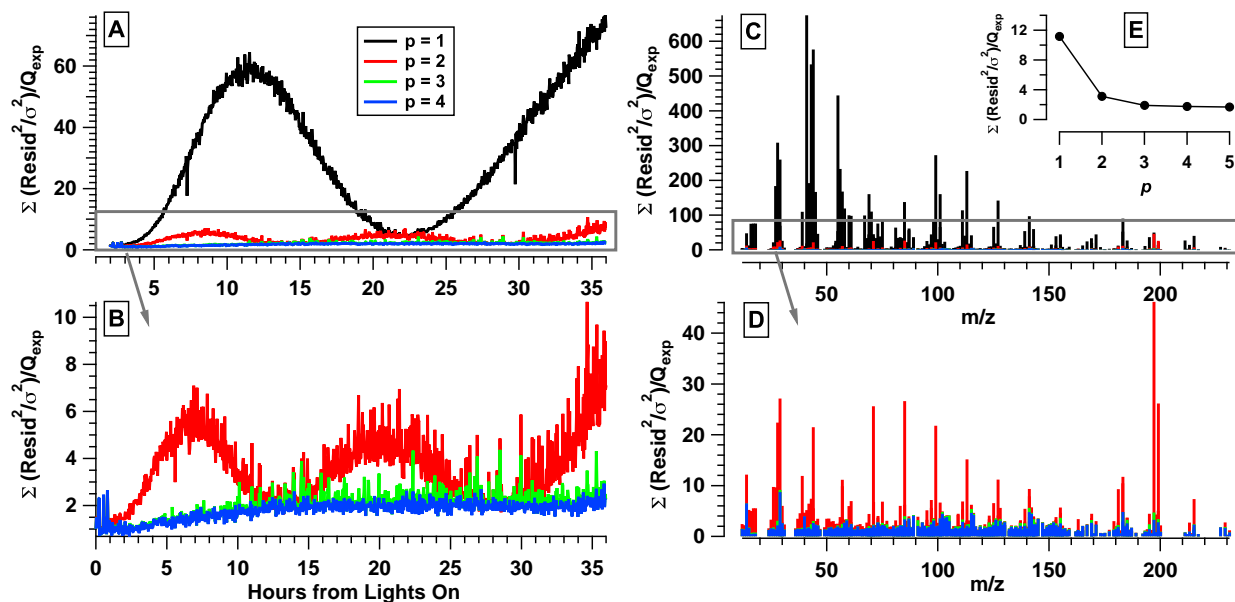


Fig. A4. The ratio of Q/Q_{expected} for $p = 1, 2, 3,$ and 4 is used as a diagnostic in determining the number of factors in PMF analysis. Time series trend of Q/Q_{expected} for $p = 1$ through $p = 4$ solutions (A) and (B) clearly show that at least three factors are needed to describe the solution. The difference between the $p = 3$ and 4 solutions is minor, with the $p = 4$ solution having the same trend as the $p = 3$, but with less noise. The Q/Q_{expected} at each m/z for $p = 1$ through $p = 4$ solutions and (C) and (D) show similar results, just for the m/z dependence. The overall time trend and m/z contributions to the Q/Q_{expected} at each factor are also presented (E).

the ion, which is essential for PMF analysis. The noisiness in the Q/Q_{expected} time trend results from some noisy ions that were selected to remain in the input PMF analysis because the time trend of the ions, albeit noisy, appears to contain useful time trend information. This must be decided by the user for each system analyzed with PMF. No smoothed or averaged data were used for PMF, albeit averaging is recommended for future chamber PMF studies (Paatero, 2012).

The optimization function, Q , for PMF involves the minimization of the scaled residual at each mass over time (Ulbrich et al., 2009). Figure A3 shows the initial decrease in Q/Q_{expected} with the addition of one factor from $p = 1$ to $p = 2$, which is expected for any data set with enough variability to run PMF. And then there is a slight decrease between $p = 2$ and $p = 3$. After $p = 3$, the decrease in Q/Q_{expected} is small and continues to decrease by the same amount with each increase in p and never flattens out. At $p = 3$, the solution has reached a point at which no additional information is gained in adding another factor. It is useful to remember that in PMF, the factor mass spectral profiles are constant, and so one has to assume that the same is true for the actual SOA. The numerous processes associated with continuous oxidation of the gas and aerosol phase may invalidate this assumption, and so this may be why the Q/Q_{expected} never flattens out. This behavior can make it difficult to select a solution. A good strategy is to examine how both specific ions and the majority of the ions are reconstructed by the fac-

torization and if individual high m/z ions (tracer ions) trend with each factor time series (see Fig. 8).

The time series of the sum of the residuals and the Q/Q_{expected} is also useful in determining a solution. Any major structure in either of these parameters would suggest that additional factors are needed to describe the data. Figure A4 shows these two parameters for the $p = 1, p = 2, p = 3$ and $p = 4$ solution for the all ion iteration of PMF. There is clear structure in both the $p = 1$ and $p = 2$ solutions, whereas the $p = 3$ and $p = 4$ solutions have a flat sum of residuals and a relatively flat and small Q/Q_{expected} . There is little difference between the $p = 3$ and $p = 4$ solutions, so the addition of another factor would not enhance the information learned from the factorization from a residual point of view. The reason why the Q/Q_{expected} has a slightly curved shape for both the $p = 3$ and $p = 4$ solutions arises from variability in the mass spectra that is beyond what is explained by the input noise. This may be a consequence of the composition of the aerosol becoming more complex, combined with the assumption of PMF that the factor must have a constant mass spectral profile (which does not hold with these systems).

Map plots were made for the $p = 2$ and $p = 3$ solutions (Figs. A5 and A6). In these plots, a red dot indicates the $\text{residual}_{ij} > \text{error}_{ij}$, a blue dot is where $\text{residual}_{ij} < -\text{error}_{ij}$, and a white dot is where $-\text{error}_{ij} < \text{residual}_{ij} < \text{error}_{ij}$. For a two factor solution (Fig. A5) there is clearly a non-random

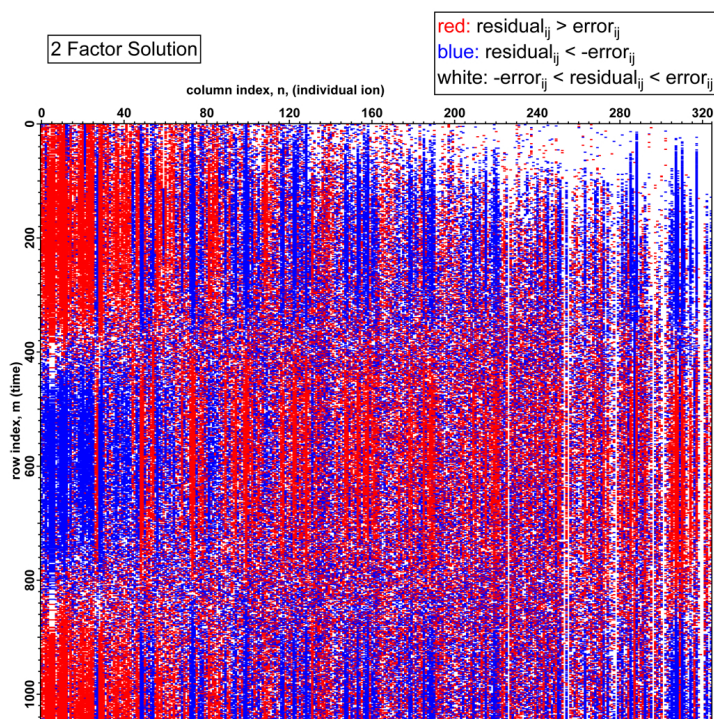


Fig. A5. The map plot for the two factor solution displays a red dot where the $\text{residual}_{ij} > \text{error}_{ij}$, a blue dot where $\text{residual}_{ij} < -\text{error}_{ij}$, and a white dot where $-\text{error}_{ij} < \text{residual}_{ij} < \text{error}_{ij}$. For a two-factor solution there is clearly a non-random pattern, indicating two factors do not adequately describe the data.

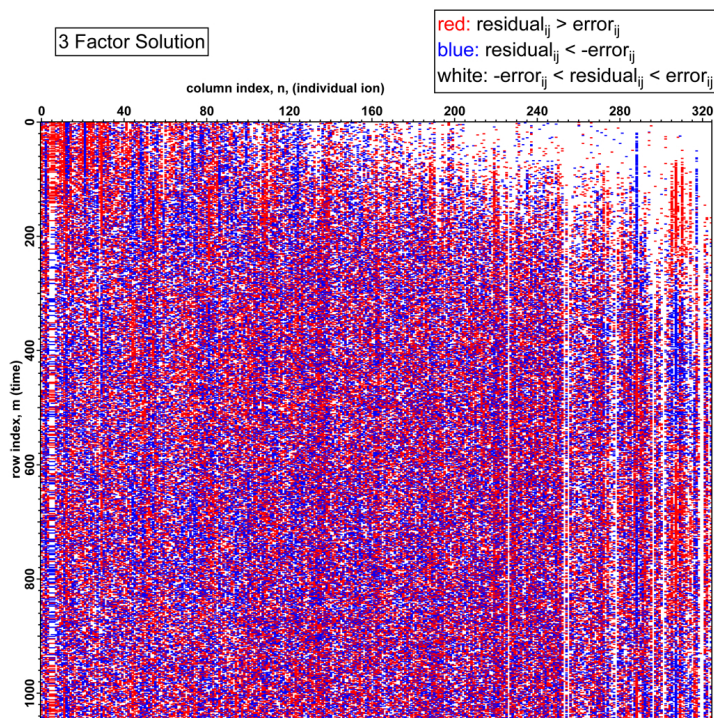


Fig. A6. The map plot, as described in Fig. A5 is shown for 3 factors. The pattern is random, indicating 3 factors describe the data variation well.

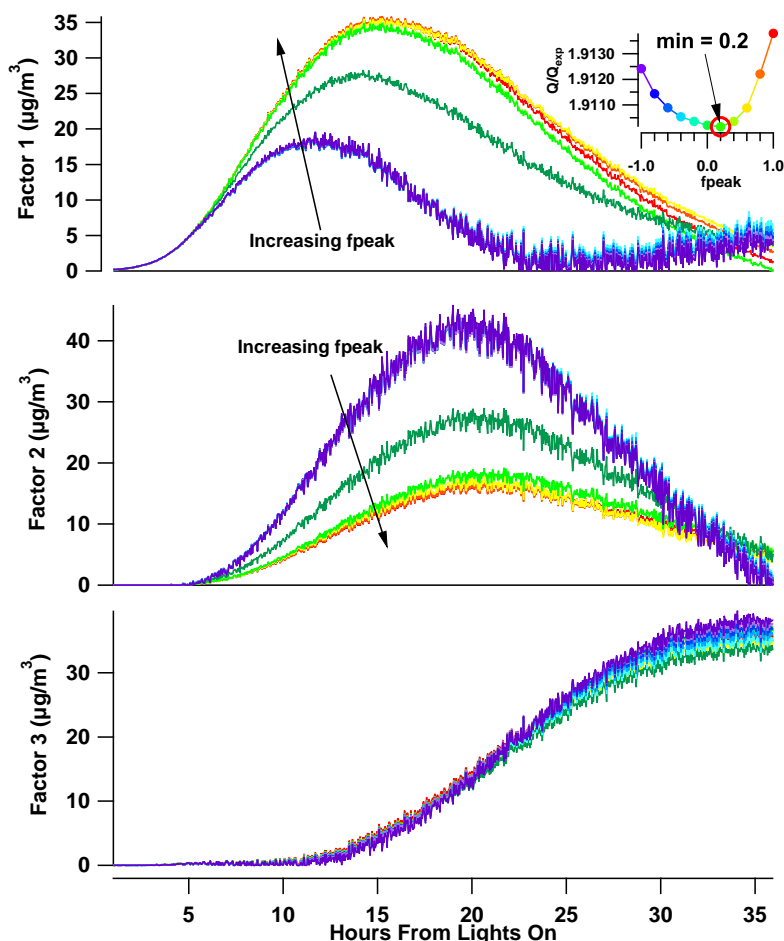


Fig. A7. The change in f_{peak} affects factors 1 and 2 more than factor 3. The increase in factor 1 explains the decrease in factor 2 when f_{peak} changes from 0 to 1. The same effect occurs when the f_{peak} changes from 0 to -1 . There is a small change in factor 3, but overall trend and magnitude remain the same for factor 3. The minimum in Q is associated with an f_{peak} of 0.2.

pattern, whereas for the 3 factor solution (Fig. A6), the pattern is random. This further supports a three factor solution.

The solution was chosen by running several iterations of PMF on the same dataset. As explained by Ulbrich et al. (2009), the PMF solution can be systematically explored by varying p , the factor number, and two other parameters, the seeds and the f_{peaks} . The 3-factor solution was uniform across many seeds, but not across f_{peaks} . Figure A7 shows the effect of f_{peak} for the three factor solution. Factor 3 shows little difference for varying solutions, however factors 1 and 2 seem to trade off mass between the different types of solutions. The minimum of Q/Q_{expected} which occurs at $f_{\text{peak}} = 0.2$ (see inset of Fig. A7) was chosen as the solution. This solution had good agreement with the time series comparison with high m/z HR-ToF-AMS molecular ion tracers (Fig. 8) and with the CIMS and MOVI-HRToF-CIMS measurements (Fig. 10). However, as emphasized by Ulbrich et al. (2009), f_{peak} does not explore all possible rotations (Paatero et al., 2002). In the current experiment, it is possible

that factor 1 time trend goes to zero, however, as indicated by the positive f_{peaks} (Fig. A7), the factor 1 decrease could also taper toward the end of 34 h and perhaps not reach zero. A longer experiment may have clarified this ambiguity, and/or comparison with aerosol molecular-level information out at this time range. If an external comparison (i.e. MOVI-CIMS molecular trace) for factor 1 did not go to zero, then it would be necessary to pull up the last few elements of the time trend of factor 1. If the increase in factor 1 at the end of the experiment did not increase Q too intensely, then the desired rotation would have been found (Paatero, 2012). Although not reported here, a full exploration of rotational ambiguity requires induced rotations, such as the example just described, by explicitly pulling individual factor elements in desired directions. For PMF2, this is described in Paatero et al. (2002).

The solution of PMF will only be as descriptive as the data matrix itself. In a chamber experiment, the initial mass spectra reflect the chemistry of early aerosol formation and are not necessarily the same as those later in the oxidation.

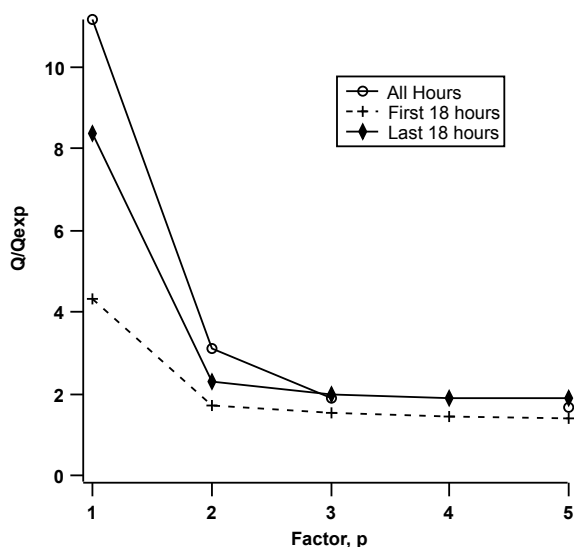


Fig. A8. Q/Q_{exp} vs. p for 3 types of solutions.

Figure A8 shows the Q/Q_{expected} versus factor number, p , for the 1 seed solution from experiment 2 for “all h”, “first 18 h”, and the “last 18 h”. For the 1 factor solution ($p = 1$), the “first 18 h” solution has the lowest Q/Q_{expected} , the “all h” solution has the highest Q/Q_{expected} , and the “last 18 h” is in between. This trend is the same for $p = 2$. The first 18 h solution is lower than the last 18 h because chemically the mass spectra are less complex at the beginning of the experiment, and $p = 1$ or $p = 2$ describes much of the data (there is less variability earlier on, in comparison to the full 34 h solution). As the oxidation progresses, the aerosol composition becomes more complex, as higher m/z oxygen-containing ions appear in the mass spectra, in addition to those observed at initial aerosol growth. For the same Q/Q_{expected} value, the last 18 h (and all h) requires more factors to describe the data to the same degree as the “first 18 h”. Three factors best describe the “all h” solution and the “last 18 h” solution since the third factor grows in at about 18 h. The “first 18 h” solution, would not “see” this third factor (since it covers only the first 18 h), so only 2 factors are necessary to describe the variability in the input data matrix.

Acknowledgements. This work was supported by US Department of Energy grant DE-SC 000 6626. Analysis of the MOVI-HRToF-CIMS data is supported by a grant to J. A. T. from the US Department of Energy (DOE-ER65318).

Edited by: M. C. Facchini

References

- Aiken, A. C., DeCarlo, P. F., Kroll, J. H., Worsnop, D. R., Huffman, J. A., Docherty, K. S., Ulbrich, I. M., Mohr, C., Kimmel, J. R., Sueper, D., Sun, Y., Zhang, Q., Trimborn, A., Northway, M., Ziemann, P. J., Canagaratna, M. R., Onasch, T. B., Alfarra, M. R., Prevot, A. S. H., Dommen, J., Duplissy, J., Metzger, A., Baltensperger, U., and Jimenez, J. L.: O/C and OM/OC Ratios of Primary, Secondary, and Ambient Organic Aerosols with High-Resolution Time-of-Flight Aerosol Mass Spectrometry, *Environ. Sci. Technol.*, 42, 4478–4485, 2008.
- Aiken, A. C., Salcedo, D., Cubison, M. J., Huffman, J. A., DeCarlo, P. F., Ulbrich, I. M., Docherty, K. S., Sueper, D., Kimmel, J. R., Worsnop, D. R., Trimborn, A., Northway, M., Stone, E. A., Schauer, J. J., Volkamer, R. M., Fortner, E., de Foy, B., Wang, J., Laskin, A., Shutthanandan, V., Zheng, J., Zhang, R., Gaffney, J., Marley, N. A., Paredes-Miranda, G., Arnott, W. P., Molina, L. T., Sosa, G., and Jimenez, J. L.: Mexico City aerosol analysis during MILAGRO using high resolution aerosol mass spectrometry at the urban supersite (T0) – Part 1: Fine particle composition and organic source apportionment, *Atmos. Chem. Phys.*, 9, 6633–6653, doi:10.5194/acp-9-6633-2009, 2009.
- Allan, J. D.: Quantitative sampling using an Aerodyne aerosol mass spectrometer 1. Techniques of data interpretation and error analysis, *J. Geophys. Res.*, 108, 4090, doi:10.1029/2002JD002358, 2003.
- Allan, J. D., Delia, A. E., Coe, H., Bower, K. N., Alfarra, M. R., Jimenez, J. L., Middlebrook, A. M., Drewnick, F., Onasch, T. B., Canagaratna, M. R., Jayne, J. T., and Worsnop, D. R.: A generalised method for the extraction of chemically resolved mass spectra from Aerodyne aerosol mass spectrometer data, *J. Aerosol Sci.*, 35, 909–922, 2004.
- Chhabra, P. S., Flagan, R. C., and Seinfeld, J. H.: Elemental analysis of chamber organic aerosol using an aerodyne high-resolution aerosol mass spectrometer, *Atmos. Chem. Phys.*, 10, 4111–4131, doi:10.5194/acp-10-4111-2010, 2010.
- Chhabra, P. S., Ng, N. L., Canagaratna, M. R., Corrigan, A. L., Russell, L. M., Worsnop, D. R., Flagan, R. C., and Seinfeld, J. H.: Elemental composition and oxidation of chamber organic aerosol, *Atmos. Chem. Phys.*, 11, 8827–8845, doi:10.5194/acp-11-8827-2011, 2011.
- Cocker, D. R., Flagan, R. C., and Seinfeld, J. H.: State-of-the-Art Chamber Facility for Studying Atmospheric Aerosol Chemistry, *Environ. Sci. Technol.*, 35, 2594–2601, 2001.
- Crounse, J. D., McKinney, K. A., Kwan, A. J., and Wennberg, P. O.: Measurement of Gas-Phase Hydroperoxides by Chemical Ionization Mass Spectrometry, *Anal. Chem.*, 78, 6726–6732, 2006.
- DeCarlo, P. F., Kimmel, J. R., Trimborn, A., Northway, M. J., Jayne, J. T., Aiken, A. C., Gonin, M., Fuhrer, K., Horvath, T., Docherty, K. S., Worsnop, D. R., and Jimenez, J. L.: Field-Deployable, High-Resolution, Time-of-Flight Aerosol Mass Spectrometer, *Anal. Chem.*, 78, 8281–8289, 2006.
- Fraser, R. T. M., Paul, N. C., and Phillips, L.: Mass spectrometry of some alkyl peroxides, *J. Chem. Soc. B*, 1970, 1278–1280, doi:10.1039/J29700001278, 1970.
- Fry, J. L., Kiendler-Scharr, A., Rollins, A. W., Brauers, T., Brown, S. S., Dorn, H.-P., Dubé, W. P., Fuchs, H., Mensah, A., Rohrer, F., Tillmann, R., Wahner, A., Wooldridge, P. J., and Cohen, R. C.: SOA from limonene: role of NO_3 in its generation and degradation, *Atmos. Chem. Phys.*, 11, 3879–3894, doi:10.5194/acp-11-

- 3879-2011, 2011.
- Heald, C. L., Kroll, J. H., Jimenez, J. L., Docherty, K. S., DeCarlo, P. F., Aiken, A. C., Chen, Q., Martin, S. T., Farmer, D. K., and Artaxo, P.: A simplified description of the evolution of organic aerosol composition in the atmosphere, *Geophys. Res. Lett.*, 37, L08803, doi:10.1029/2010GL042737, 2010.
- Hersey, S. P., Craven, J. S., Schilling, K. A., Metcalf, A. R., Sorooshian, A., Chan, M. N., Flagan, R. C., and Seinfeld, J. H.: The Pasadena Aerosol Characterization Observatory (PACO): chemical and physical analysis of the Western Los Angeles basin aerosol, *Atmos. Chem. Phys.*, 11, 7417–7443, doi:10.5194/acp-11-7417-2011, 2011.
- Isaacman, G., Chan, A. W. H., Nah, T., Worton, D. R., Ruehl, C. R., Wilson, K. R., and Goldstein, A. H.: Heterogeneous OH Oxidation of Motor Oil Particles Causes Selective Depletion of Branched and Less Cyclic Hydrocarbons, *Environ. Sci. Technol.*, 46, 10632–10640, 2012.
- Jimenez, J. L., Canagaratna, M. R., Donahue, N. M., Prévôt, A. S. H., Zhang, Q., Kroll, J. H., DeCarlo, P. F., Allan, J. D., Coe, H., Ng, N. L., Aiken, A. C., Docherty, K. S., Ulbrich, I. M., Grieshop, A. P., Robinson, A. L., Duplissy, J., Smith, J. D., Wilson, K. R., Lanz, V. A., Hueglin, C., Sun, Y. L., Tian, J., Laaksonen, A., Raatikainen, T., Rautiainen, J., Vaattovaara, P., Ehn, M., Kulmala, M., Tomlinson, J. M., Collins, D. R., Cubison, M. J., E., Dunlea, J., Huffman, J. A., Onasch, T. B., Alfarra, M. R., Williams, P. I., Bower, K., Kondo, Y., Schneider, J., Drewnick, F., Borrmann, S., Weimer, S., Demerjian, K., Salcedo, D., Cottrell, L., Griffin, R., Takami, A., Miyoshi, T., Hatakeyama, S., Shimono, A., Sun, J. Y., Zhang, Y. M., Dzepina, K., Kimmel, J. R., Sueper, D., Jayne, J. T., Herndon, S. C., Trimborn, A. M., Williams, L. R., Wood, E. C., Middlebrook, A. M., Kolb, C. E., Baltensperger, U., and Worsnop, D. R.: Evolution of Organic Aerosols in the Atmosphere, *Science*, 326, 1525–1529, 2009.
- Lambe, A. T., Onasch, T. B., Massoli, P., Croasdale, D. R., Wright, J. P., Ahern, A. T., Williams, L. R., Worsnop, D. R., Brune, W. H., and Davidovits, P.: Laboratory studies of the chemical composition and cloud condensation nuclei (CCN) activity of secondary organic aerosol (SOA) and oxidized primary organic aerosol (OPOA), *Atmos. Chem. Phys.*, 11, 8913–8928, doi:10.5194/acp-11-8913-2011, 2011.
- Lambe, A. T., Onasch, T. B., Croasdale, D. R., Wright, J. P., Martin, A. T., Franklin, J. P., Massoli, P., Kroll, J. H., Canagaratna, M. R., Brune, W. H., Worsnop, D. R., and Davidovits, P.: Transitions from Functionalization to Fragmentation Reactions of Laboratory Secondary Organic Aerosol (SOA) Generated from the OH Oxidation of Alkane Precursors, *Environ. Sci. Technol.*, 46, 5430–5437, 2012.
- Lanz, V. A., Alfarra, M. R., Baltensperger, U., Buchmann, B., Hueglin, C., and Prévôt, A. S. H.: Source apportionment of sub-micron organic aerosols at an urban site by factor analytical modelling of aerosol mass spectra, *Atmos. Chem. Phys.*, 7, 1503–1522, doi:10.5194/acp-7-1503-2007, 2007.
- Loza, C. L., Chhabra, P. S., Yee, L. D., Craven, J. S., Flagan, R. C., and Seinfeld, J. H.: Chemical aging of *m*-xylene secondary organic aerosol: laboratory chamber study, *Atmos. Chem. Phys.*, 12, 151–167, doi:10.5194/acp-12-151-2012, 2012.
- Ng, N. L., Canagaratna, M. R., Zhang, Q., Jimenez, J. L., Tian, J., Ulbrich, I. M., Kroll, J. H., Docherty, K. S., Chhabra, P. S., Bahreini, R., Murphy, S. M., Seinfeld, J. H., Hildebrandt, L., Donahue, N. M., DeCarlo, P. F., Lanz, V. A., Prévôt, A. S. H., Dinar, E., Rudich, Y., and Worsnop, D. R.: Organic aerosol components observed in Northern Hemispheric datasets from Aerosol Mass Spectrometry, *Atmos. Chem. Phys.*, 10, 4625–4641, doi:10.5194/acp-10-4625-2010, 2010.
- Ng, N. L., Canagaratna, M. R., Jimenez, J. L., Chhabra, P. S., Seinfeld, J. H., and Worsnop, D. R.: Changes in organic aerosol composition with aging inferred from aerosol mass spectra, *Atmos. Chem. Phys.*, 11, 6465–6474, doi:10.5194/acp-11-6465-2011, 2011.
- Paatero, P.: Interactive comment on *Atmos. Chem. Phys. Discuss.*, 12, 16647, 2012.
- Paatero, P. and Hopke, P. K.: Discarding or downweighting high-noise variables in factor analytic models, *Anal. Chim. Acta*, 490, 277–289, 2003.
- Paatero, P. and Tapper, U.: Positive Matrix Factorization – a Nonnegative Factor Model with Optimal Utilization of Error-Estimates of Data Values, *Environmetrics*, 5, 111–126, 1994.
- Paatero, P., Hopke, P. K., Song, X. H., and Ramadan, Z.: Understanding and controlling rotations in factor analytic models, *Chemometr. Intell. Lab.*, 60, 253–264, 2002.
- Paulot, F., Crounse, J. D., Kjaergaard, H. G., Kroll, J. H., Seinfeld, J. H., and Wennberg, P. O.: Isoprene photooxidation: new insights into the production of acids and organic nitrates, *Atmos. Chem. Phys.*, 9, 1479–1501, doi:10.5194/acp-9-1479-2009, 2009.
- Pye, H. O. T. and Pouliot, G. A.: Modeling the Role of Alkanes, Polycyclic Aromatic Hydrocarbons, and Their Oligomers in Secondary Organic Aerosol Formation, *Environ. Sci. Technol.*, 46, 6041–6047, 2012.
- Schauer, J. J., Kleeman, M. J., Cass, G. R., and Simoneit, B. R. T.: Measurement of Emissions from Air Pollution Sources. 3. C1–C29 Organic Compounds from Fireplace Combustion of Wood, *Environ. Sci. Technol.*, 35, 1716–1728, 2001.
- Schauer, J. J., Kleeman, M. J., Cass, G. R., and Simoneit, B. R. T.: Measurement of Emissions from Air Pollution Sources. 5. C1–C32 Organic Compounds from Gasoline-Powered Motor Vehicles, *Environ. Sci. Technol.*, 36, 1169–1180, 2002.
- St. Clair, J. M., McCabe, D. C., Crounse, J. D., Steiner, U., and Wennberg, P. O.: Chemical ionization tandem mass spectrometer for the in situ measurement of methyl hydrogen peroxide, *Rev. Sci. Instrum.*, 81, 094102, doi:10.1063/1.3480552, 2010.
- Tobias, H. J. and Ziemann, P. J.: Thermal Desorption Mass Spectrometric Analysis of Organic Aerosol Formed from Reactions of 1-Tetradecene and O₃ in the Presence of Alcohols and Carboxylic Acids, *Environ. Sci. Technol.*, 34, 2105–2115, 2000.
- Ulbrich, I. M., Canagaratna, M. R., Zhang, Q., Worsnop, D. R., and Jimenez, J. L.: Interpretation of organic components from Positive Matrix Factorization of aerosol mass spectrometric data, *Atmos. Chem. Phys.*, 9, 2891–2918, doi:10.5194/acp-9-2891-2009, 2009.
- Van Krevelen, D. W.: Graphical-statistical method for the study of structure and reaction processes of coal, *Fuel*, 24, 269–284, 1950.
- Yatavelli, R. L. N. and Thornton, J. A.: Particulate Organic Matter Detection Using a Micro-Orifice Volatilization Impactor Coupled to a Chemical Ionization Mass Spectrometer (MOVI-CIMS), *Aerosol Sci. Tech.*, 44, 61–74, 2010.
- Yatavelli, R. L. N., Lopez-Hilfiker, F. D., Wargo, J., Kimmel, J. R., Cubison, M. J., Bertram, T. H., Jimenez, J., Gonin, M., Worsnop, D. R., and Thornton, J. A.: Analysis of Gas and Particle-phase

- Organic Matter Using a Chemical Ionization High-Resolution Time-of-Flight Mass Spectrometer (HTOF-CIMS) Coupled to a Micro Orifice Volatilization Impactor (MOVI), *Aerosol Sci. Tech.*, 46, 1313–1327, doi:10.1080/02786826.2012.712236, 2012.
- Yee, L. D., Craven, J. S., Loza, C. L., Schilling, K. A., Ng, N. L., Canagaratna, M. R., Ziemann, P. J., Flagan, R. C., and Seinfeld, J. H.: Secondary Organic Aerosol Formation from Low-NO_x Photooxidation of Dodecane: Evolution of Multi-Generation Gas-Phase Chemistry and Aerosol Composition, *J. Phys. Chem. A*, 116, 6211–6230, 2012.
- Zhang, Q., Jimenez, J. L., Canagaratna, M. R., Ulbrich, I. M., Ng, N. L., Worsnop, D. R., and Sun, Y.: Understanding atmospheric organic aerosols via factor analysis of aerosol mass spectrometry: a review, *Anal. Bioanal. Chem.*, 401, 3045–3067, 2011.
- Ziemann, P. J.: Formation of Alkoxyhydroperoxy Aldehydes and Cyclic Peroxyhemiacetals from Reactions of Cyclic Alkenes with O₃ in the Presence of Alcohols, *J. Phys. Chem. A*, 107, 2048–2060, 2003.

Appendix K

Role of Ozone in SOA Formation from Alkane Photooxidation¹³

¹³ Reproduced by permission from “Role of ozone in SOA formation from alkane photooxidation” by X. Zhang, R. H. Schwantes, M. M. Coggon, C. L. Loza, K. A. Schilling, R. C. Flagan, and J. H. Seinfeld. *Atmos. Chem. Phys.* **2014**, *14*, 1733-1753.



Role of ozone in SOA formation from alkane photooxidation

X. Zhang¹, R. H. Schwantes¹, M. M. Coggon², C. L. Loza², K. A. Schilling², R. C. Flagan^{1,2}, and J. H. Seinfeld^{1,2}

¹Division of Engineering and Applied Science, California Institute of Technology, Pasadena, CA, USA

²Division of Chemistry and Chemical Engineering, California Institute of Technology, Pasadena, CA, USA

Correspondence to: J. H. Seinfeld (seinfeld@caltech.edu)

Received: 15 August 2013 – Published in Atmos. Chem. Phys. Discuss.: 24 September 2013

Revised: 2 January 2014 – Accepted: 9 January 2014 – Published: 14 February 2014

Abstract. Long-chain alkanes, which can be categorized as intermediate volatility organic compounds, are an important source of secondary organic aerosol (SOA). Mechanisms for the gas-phase OH-initiated oxidation of long-chain alkanes have been well documented; particle-phase chemistry, however, has received less attention. The δ -hydroxycarbonyl, which is generated from the isomerization of alkoxy radicals, can undergo heterogeneous cyclization and dehydration to form substituted dihydrofuran. Due to the presence of C=C bonds, the substituted dihydrofuran is predicted to be highly reactive with OH, and even more so with O₃ and NO₃, thereby opening a reaction pathway that is not usually accessible to alkanes. This work focuses on the role of substituted dihydrofuran formation and its subsequent reaction with OH, and more importantly ozone, in SOA formation from the photooxidation of long-chain alkanes. Experiments were carried out in the Caltech Environmental Chamber using dodecane as a representative alkane to investigate the difference in aerosol composition generated from “OH-oxidation-dominating” vs. “ozonolysis-dominating” environments. A detailed mechanism incorporating the specific gas-phase photochemistry, together with the heterogeneous formation of substituted dihydrofuran and its subsequent gas-phase OH/O₃ oxidation, is used to evaluate the importance of this reaction channel in dodecane SOA formation. We conclude that (1) the formation of δ -hydroxycarbonyl and its subsequent heterogeneous conversion to substituted dihydrofuran is significant in the presence of NO_x; (2) the ozonolysis of substituted dihydrofuran dominates over the OH-initiated oxidation under conditions prevalent in urban and rural air; and (3) a spectrum of highly oxygenated products with carboxylic acid, ester, and ether functional groups are produced from the substituted dihydrofuran chemistry, thereby affecting the average oxidation state of the SOA.

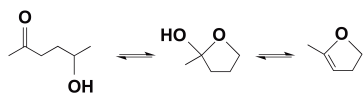
1 Introduction

Alkanes are important constituents of gasoline and vehicle emissions (Hoekman, 1992; Zielinska et al., 1996; Kirchstetter et al., 1999; Gentner et al., 2012; Jathar et al., 2013), accounting for ~50 % of volatile organic compounds (VOCs) in the urban atmosphere (Fraser et al., 1997; Schauer et al., 1999 and 2002). The unresolved complex mixture (UCM) of organics, which is potentially a significant source of secondary organic aerosol (SOA) formation in the atmosphere, has recently been shown to comprise many long-chain alkanes (Isaacman et al., 2012), which are expected to contribute to SOA formation (Robinson et al., 2007).

Laboratory chamber investigations of SOA formation from long-chain alkanes (Lim and Ziemann, 2005, 2009a, b, c; Presto et al., 2009, 2010; Miracolo et al., 2010, 2011; Craven et al., 2012; Lambe et al., 2012; Tkacik et al., 2012; Yee et al., 2012; Loza et al., 2013) provide a framework for understanding chemical mechanisms and determination of SOA yields (Jordan et al., 2008; Aumont et al., 2012 and 2013; Cappa et al., 2013; Zhang and Seinfeld, 2013). Particle-phase products from OH oxidation of alkanes contain a number of functional groups: organonitrate (–ONO₂), hydroxyl (–OH), carbonyl (–C=O), ester (–C(O)O–), and hydroperoxide (–OOH). Ambient measurements of organic aerosol composition have shown, in addition, that the carboxylic acid functional group (–C(O)OH) is closely associated with products from fossil fuel combustion sources (Liu et al., 2011; Russell et al., 2011), of which alkanes are a principal component.

Atmospheric alkanes react in daytime exclusively with OH, producing an array of peroxy radicals (RO₂). In the presence of sufficient NO, the alkoxy radical (RO) is the key product of the subsequent RO₂ reaction with NO. RONO₂

is also produced, with a branching ratio of 0.1–0.3 (Arey et al., 2001). For alkanes with carbon number ≥ 5 , the 1,5-H shift isomerization is the dominant reaction pathway for RO, producing a δ -hydroxycarbonyl, the primary fate of which is reaction with OH (Jenkin et al., 2003; Saunders et al., 2003; Bloss et al., 2005), with a lifetime of ~ 11.5 h at room temperature and a typical ambient OH concentration of 1×10^6 molecules cm^{-3} . One particular δ -hydroxycarbonyl, 5-hydroxy-2-pentanone, was found to cyclize to form the cyclic hemiacetal. The cyclic hemiacetal can subsequently lose water to form 4,5-dihydro-2-methylfuran, with an overall lifetime as short as ~ 1.1 h at 298 K (Cavalli et al., 2000; Martin et al., 2002). The presence of water vapor can, in principle, serve to convert the 4,5-dihydro-2-methylfuran back to 5-hydroxy-2-pentanone, leading to an equilibrium between these two species within several hours (Martin et al., 2002; Baker et al., 2005; Holt et al., 2005; Reisen et al., 2005):



This conversion to 4,5-dihydro-2-methylfuran is not unique to 5-hydroxy-2-pentanone and also occurs for other C_5 – C_{17} δ -hydroxycarbonyls (Lim and Ziemann, 2005, 2009a, b, c) at a rate that increases with the length of the carbon chain (Holt et al., 2005; Ziemann and Atkinson, 2012). The substituted dihydrofuran is highly reactive towards OH, O_3 , and NO_3 in the gas phase, owing to the presence of a C=C double bond. For typical ambient concentrations of OH, O_3 , and NO_3 , i.e., 2×10^6 molecules cm^{-3} (12 h average), 30 ppb (24 h average), and 5×10^8 molecules cm^{-3} (12 h average), respectively, the lifetimes of the substituted dihydrofuran with respect to reactions with these oxidants in the gas phase are 1.3 h, 7 min, and 24 s, respectively (Martin et al., 2002; Ziemann and Atkinson, 2012). Based on these estimates, ozonolysis of substituted dihydrofurans may dominate OH oxidation during daytime in the urban atmosphere.

SOA formation from long-chain alkanes involves multiple generations of OH oxidation that include functionalization (O-atom addition in forms of a variety of moieties) and fragmentation of the parent carbon backbone. These two routes can eventually lead to highly oxygenated fragments that partition into the particle phase. Two recent modeling studies of C_{12} alkanes suggest that particle-phase chemistry might play a potentially important role in the chemical composition of alkane SOA; this is inferred from the fact that simulations driven solely by gas-phase chemistry can successfully reproduce the chamber-measured SOA yield, but these fail to replicate the observed particulate O:C and H:C ratios in the absence of a particle-phase chemistry channel (Cappa et al., 2013; Zhang and Seinfeld, 2013). The extent to which particle-phase chemistry is important in alkane SOA formation has not been clearly established.

We address here the heterogeneous formation of substituted dihydrofurans and their subsequent gas-phase reaction

with ozone in SOA formation from alkanes. We present the results of a series of chamber dodecane photooxidation experiments under two reaction regimes, i.e., “OH-dominant”, in which over 70 % of substituted dihydrofurans are oxidized by OH, vs. “ O_3 -dominant”, in which 80–90 % of substituted dihydrofurans react with O_3 . Gas-phase products that are unique to the substituted dihydrofuran chemistry are identified. The impact of ozonolysis of substituted dihydrofurans on the particle-phase product distribution from the photooxidation of dodecane is investigated by comparing intensities of certain ions that are indicative of ozonolysis chemistry. We also develop a detailed mechanism with the incorporation of substituted dihydrofuran chemistry and simulate the effect of this reaction channel on SOA yield from the photooxidation of dodecane.

2 Experimental

Experiments were conducted in the new Caltech dual 24- m^3 Environmental Chamber, in which the temperature (T) and relative humidity (RH) are automatically controlled. Prior to each experiment, the Teflon chambers were flushed with clean, dry air for 24 h until the particle number concentration was < 10 cm^{-3} and volume concentration < 0.01 μm^3 cm^{-3} . Seed aerosol was injected into the chamber by atomizing 0.015 M aqueous ammonium sulfate solution to provide sufficient surface area for the partition of semivolatile products. Hydrogen peroxide (H_2O_2) was used for the OH source by evaporating 85 and 226 μL of 50 wt % aqueous solution into the chamber with 5 L min^{-1} of purified air for ~ 110 min, resulting in an approximate starting H_2O_2 concentration of 1.5 and 4 ppm, respectively, under high- and low- NO_x conditions. The 4 ppm H_2O_2 concentration employed in low- NO_x experiments creates a $\text{RO}_2 + \text{HO}_2$ dominant reaction regime. We replaced H_2O_2 with nitrous acid (HONO) as the OH source for one experiment in order to minimize the formation of ozone. HONO was prepared by dropwise addition of 15 mL of 1 wt % NaNO_2 into 30 mL of 10 wt % H_2SO_4 in a glass bulb and introduced into the chambers with 5 L min^{-1} of purified air for ~ 40 min. To minimize the vapor-phase wall loss along the injection line, 60 μL of dodecane (Sigma-Aldrich, 98 % purity) was injected into a glass bulb, which was connected directly into the Teflon chamber via a 1/4 in. inside diameter (i.d.) Swagelock to NPT fitting located on a Teflon plate. Heated 5 L min^{-1} of purified air flowed through the glass bulb into the chamber for 30 min, introducing ~ 200 ppb dodecane into the chamber. After ~ 1 h of mixing, photooxidation was initiated by irradiating the chamber with black lights with output wavelength ranging from 300 to 400 nm.

Experiments were carried out under conditions in which the peroxy radicals formed from the initial OH reaction with dodecane react either essentially exclusively with NO (so-called high NO_x) (Exp. 1, 2, 3, 4, and 5) or essentially

Table 1. Experimental conditions for the photooxidation of dodecane.

	Exp.	T_0 (K)	RH ₀ (%)	HC ₀ (ppb)	(NO) ₀ (ppb)	(NO ₂) ₀ (ppb)	(O ₃) ₀ (ppb)	Initial seed vol. ($\mu\text{m}^3 \text{m}^{-3}$)	Additional NO inj. (ppb h ⁻¹) × (h)
High NO _x ^a	1	~300	~3	208	430	576	<DL ^g	18	–
	2	~300	~3	208	287	12	~2	24	Y ^c
	3	~300	~11	206	45	33	~2	30	Y ^d
	4	~300	~20	178	38	156	~2	28	Y ^e
	5	~300	~55	214	69	30	~2	43	Y ^f
Low NO _x ^b	6	~300	~3	208	<DL	<DL	<DL	19	–
	7	~300	~3	214	<DL	<DL	32.6	25	–
	8	~300	~55	216	<DL	<DL	<DL	58	–

^a Under high-NO_x conditions, the simulated NO concentration (>5 ppb) is at least 4 orders of magnitude higher than RO₂ (<5 × 10⁷ molecules cm⁻³). Over 99% of RO₂ is predicted to react with NO.

^b Under low-NO_x conditions, the simulated HO₂ concentration (~1 × 10¹⁰ molecules cm⁻³) is ~20 times higher than RO₂ (~5 × 10⁸ molecules cm⁻³). RO₂ + HO₂ dominates the fate of RO₂.

^c NO source was controlled at 100 ppb h⁻¹ for the first 7 h of reaction and then 25 ppb h⁻¹ for the remainder of the reaction.

^d NO source was controlled at 25 ppb h⁻¹ over the course of the experiment.

^e NO source was controlled at 30 ppb h⁻¹ for the first 3 h of reaction and then 100 ppb h⁻¹ for the next 1 h of reaction and then back to 30 ppb h⁻¹ for the remainder of the reaction.

^f NO source was controlled at 50 ppb h⁻¹ over the course of the experiment.

^g Detection limits (DL) for O₃, NO, and NO₂ are 0.5 ppb, 0.4 ppb, and 0.4 ppb, respectively. H₂O₂ has an interference on the O₃ detection, increasing the O₃ monitor readout by ~2–3 ppb in the current study.

exclusively with HO₂ (so-called low NO_x) (Exp. 6, 7, and 8). For each condition, O₃-dominant vs. OH-dominant environments were generated by varying the OH source, initial NO, NO₂, and O₃ concentrations, as well as the additional NO injection rate during the irradiation period (Table 1). The ozonolysis vs. OH oxidation of substituted dihydrofuran is calculated to be equally competitive when the ratio of O₃ to OH concentration is 6.3 × 10⁴ : 1 (approximately 2.6 ppb O₃ vs. 1.0 × 10⁶ molecules cm⁻³ OH). Under low-NO_x conditions, NO, NO₂, NO_x, and O₃ were below detection limits, and no ozone formation was observed over the course of 20 h experiments. OH oxidation of dihydrofuran is dominant with average OH concentrations of 1.8 × 10⁶ and 1.5 × 10⁶ molecules cm⁻³, respectively, in Exp. 6 and 8. OH concentration is calculated by optimal fitting of the exponential decay of the GC-FID (gas chromatograph with flame ionization detection)-measured dodecane temporal profile. In order to evaluate the effect of the ozonolysis of dihydrofuran chemistry on the dodecane SOA formation under low-NO_x conditions, additional ~30 ppb of ozone was injected into the chamber before the onset of irradiation (Exp. 7). Under high-NO_x conditions, HONO was used as the OH source for the OH-dominant environment (Exp. 1). Double HONO injection was carried out in order to fully consume dodecane (before the onset and after ~3 h of irradiation). The average OH concentration is ~5.0 × 10⁶ molecules cm⁻³, whereas O₃ peaks at 8 ppb after 60 min of photooxidation and rapidly decays to ~0 ppb within 2 h. In this case, >73% of dihydrofuran is oxidized by OH over the course of Exp. 1. An O₃-dominant environment was generated by injecting NO (38–287 ppb) and NO₂ (12–156 ppb) before the onset of irradiation.

Continuous NO injection with a certain flow rate (20–100 ppb h⁻¹) was conducted over the course of experiments to reach a sufficient amount of O₃ and to maintain high-NO_x levels. Under experimental conditions in Exp. 2, 3, 4, and 5, the average OH concentrations are calculated to be 1.7 × 10⁶, 2.0 × 10⁶, 1.4 × 10⁶, and 1.3 × 10⁶ molecules cm⁻³, respectively, and the maximum O₃ mixing ratios are 20, 380, 150, and 250 ppb, respectively. As a result, ~82, ~96, ~97, and ~98% of dihydrofuran reacts with O₃ when dihydrofuran peaks after ~3 h of photooxidation. High-humidity experiments were also carried out as a set of control experiments (Exp. 4, 5, and 8) addressing the role of water vapor in the heterogeneous interconversion between δ -hydroxycarbonyls and substituted dihydrofurans.

A suite of instruments was used to investigate gas- and particle-phase chemistry. T , RH, NO, NO_x, and O₃ were continuously monitored. Dodecane concentration was monitored by taking hourly samples at ~0.13 L min⁻¹ of chamber air for 3 min onto a Tenax adsorbent, which was loaded into the inlet of a GC-FID (Agilent 6890N), desorbed at 275 °C for 13 min, and then injected onto an HP-5 column (15 m × 0.53 mm i.d. × 1.5 μm thickness, Hewlett-Packard) held at 30 °C. The oven was ramped from 30 to 275 °C at 10 °C min⁻¹ and held at 275 °C for 5 min. The retention time for dodecane is ~27.5 min. The gas-phase species were monitored using a custom-modified Varian 1200 triple-quadrupole chemical ionization mass spectrometer (CIMS) (Crouse et al., 2006; Paulot et al., 2009). In negative mode operation, CF₃O⁻ was used as the reagent ion to cluster with an analyte such as hydroperoxide or acid [R], producing [R·CF₃O]⁻ or m/z [M + 85]⁻, where M is the molecular

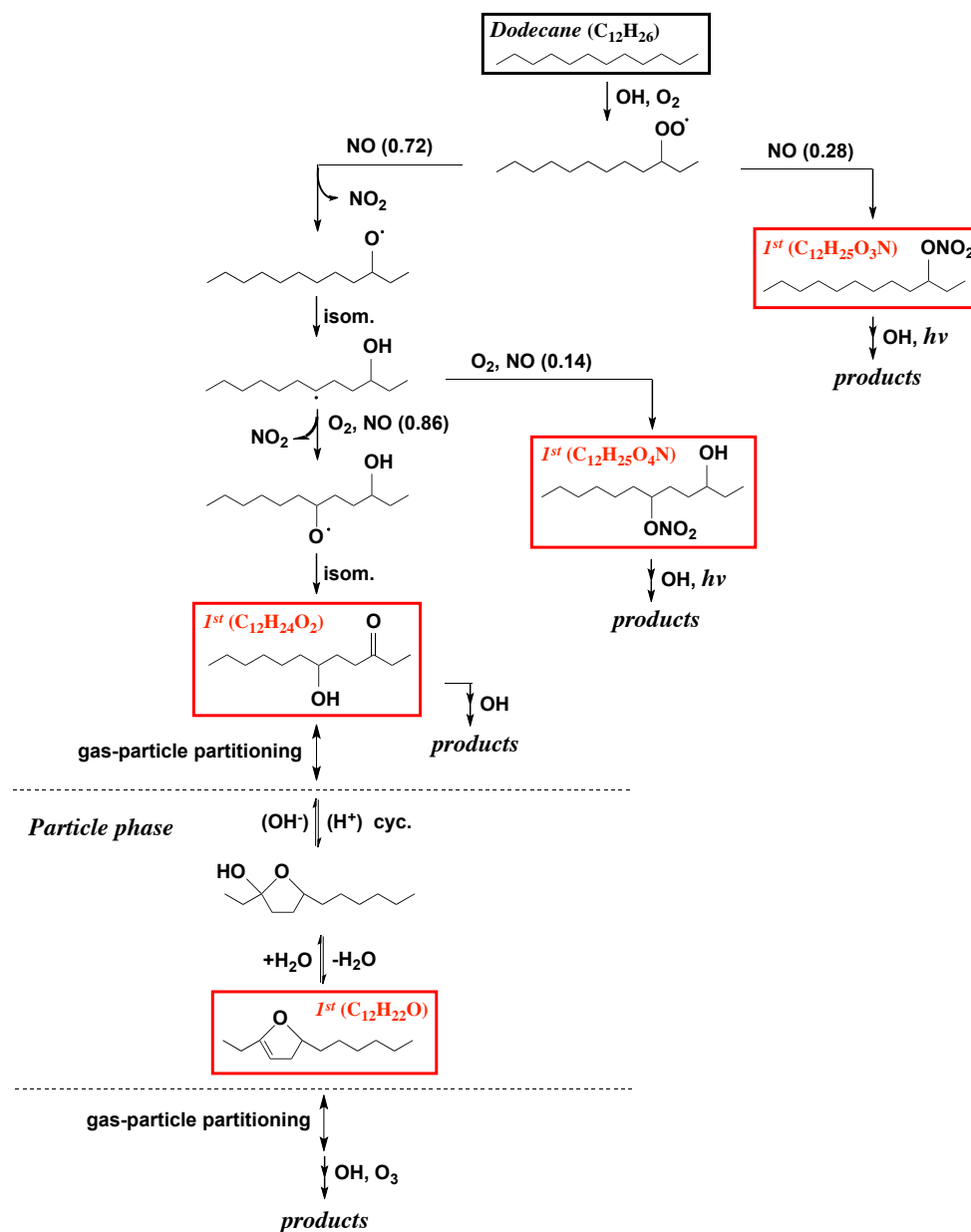


Fig. 1a. Schematic mechanism for the photooxidation of dodecane under high- NO_x conditions. Note that only first-generation products are shown here. The boxes indicate compounds and associated reaction pathways incorporated in the model simulation.

weight of the analyte. For more strongly acidic species $[H \cdot X]$, the transfer product, $[H \cdot X \cdot F]^-$ or $m/z [M+19]^-$, is formed during ionization. Carboxylic acids tend to have contributions to both the transfer and cluster product, in which case the overall signal of a compound is considered as the sum of the two product signals. In positive-mode operation, an analyte $[R]$ can undergo proton transfer reaction, producing an ion in the form of $[R \cdot H]^+$, and/or react with n positively charged water clusters to form a cluster in the form of $[(H_2O)_n \cdot R \cdot H]^+$. Positive mode is employed in this study

for tracking less polar compounds, such as the substituted dihydrofuran.

Particle size distribution and number concentration were measured by a cylindrical differential mobility analyzer (DMA, TSI Model 3081) coupled to a condensation particle counter (TSI Model 3010). The protocol for applying particle wall loss correction to DMA measured SOA growth data is described in the Supplement. Real-time particle mass spectra were collected continuously by an Aerodyne high-resolution time-of-flight aerosol mass spectrometer (DeCarlo et al., 2006; Canagaratna et al., 2007). The AMS switched

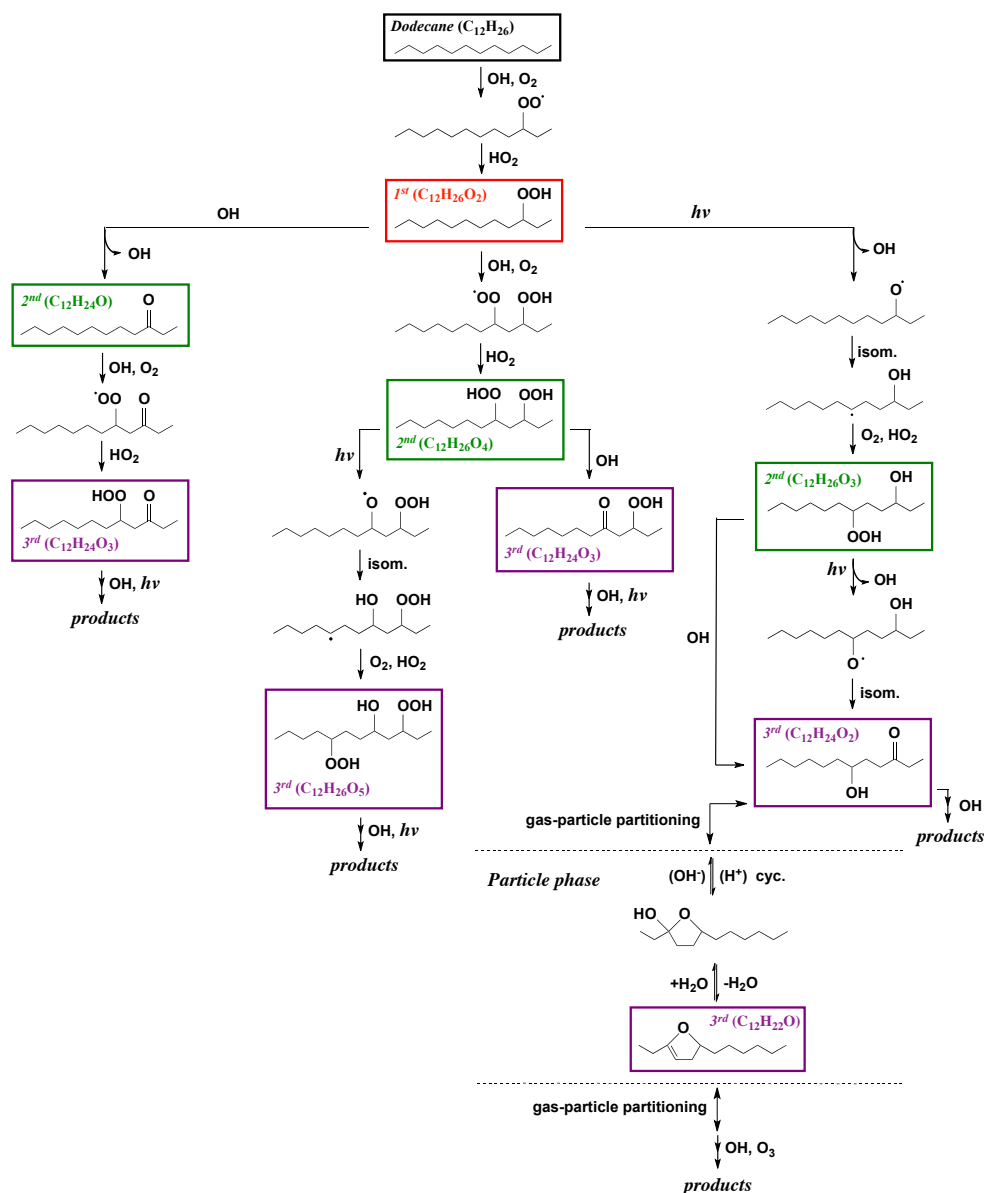


Fig. 1b. Schematic mechanism for the photooxidation of dodecane under low- NO_x conditions. Note that only the first three generations of products are shown here. The boxes indicate compounds and associated reaction pathways incorporated in the model simulation.

once every minute between the high-resolution “W mode” and the lower resolution, higher sensitivity “V mode”. The V mode was utilized for quantification, as the higher m/z values exhibit a more favorable signal-to-noise ratio. The W mode was used for ion identification and clarification. Detailed AMS data analysis protocols can be found in the Supplement.

3 Chemical mechanism

A photochemical mechanism was used to simulate the gas-phase photochemistry of NO_x , HO_x , and O_3 corresponding

to the experimental conditions. Reactions and corresponding reaction rate constants are listed in Tables S1–S3 in the Supplement. Photolysis rate constants are calculated using the irradiance spectrum measured for the chamber UV lights as well as absorption cross sections and quantum yields from Sander et al. (2011).

The kinetic scheme for the gas-phase OH-initiated oxidation of dodecane and the further OH oxidation of multi-generational products was developed primarily based on the Master Chemical Mechanism v3.2 (MCM v3.2, <http://mcm.leeds.ac.uk/MCM/>). Products identified in Lim and Ziemann (2005; 2009 a, b, c) that are not in MCM are

also included here. The kinetic scheme was incorporated in the photochemical model to estimate yields of particle-phase products generated in the chamber. A simplified flow chart illustrating the mechanism for the multigeneration gas-phase chemistry is shown in Fig. 1a, b. In general, the OH-initiated oxidation of dodecane leads to RO₂, the fate of which controls the distribution of further generation products. When sufficient NO_x is present (the concentration of NO, i.e., > 5 ppb, is at least 4 orders of magnitude higher than RO₂, i.e., < 5 × 10⁷ molecules cm⁻³), over 99 % of RO₂ reacts with NO, leading to RO or alkyl nitrate (RONO₂). The branching ratios for the production of RO and RONO₂ are obtained from Jordan et al. (2008). RO can isomerize through a 1,5-H-atom shift to a δ-hydroxyalkyl radical, react with O₂, or undergo fragmentation. The alkyl nitrate formed either undergoes photolysis or reacts with OH via H-atom abstraction from a C atom or reacts with OH via H-atom abstraction from a C atom with a -ONO₂ group attached to produce a -C=O group. The δ-hydroxyalkyl radical reacts with O₂ and then NO and undergoes another isomerization to produce a δ-hydroxycarbonyl. At sufficiently low NO_x concentrations, the simulated HO₂ concentration (~1 × 10¹⁰ molecules cm⁻³) is ~20 times higher than RO₂ (~5 × 10⁸ molecules cm⁻³). RO₂ + HO₂ dominates the fate of RO₂, producing a hydroperoxide (ROOH). Further oxidation of ROOH involves the photolysis of the -OOH group, H-atom abstraction, and the OH oxidation of a C atom with a -OOH group attached to produce a -C=O group. Products through eight generations of oxidation are included in the mechanism, although only the formation of the first three generations of products is illustrated in Fig. 1. The reaction rate constants are obtained from MCM v3.2. In the absence of specific data, the photolysis rate constants of the -OOH, -C=O, and -ONO₂ groups on the carbon backbone are assumed to be the same as those for methyl peroxide (CH₃OOH), 2-butanol (C₃H₇CHO), and *n*-propyl nitrate (*n*-CH₃ONO₂).

Cyclization and subsequent dehydration of δ-hydroxycarbonyl to substituted dihydrofuran is a heterogeneous process, including (1) gas-phase diffusion and reactive uptake of δ-hydroxycarbonyl to particles, (2) cyclization of δ-hydroxycarbonyl to cyclic hemiacetal, and (3) dehydration of cyclic hemiacetal to substituted dihydrofuran. (Atkinson et al., 2008; Lim and Ziemann, 2009c). The extent of this heterogeneous process occurring on/in particles has been predicted to predominate over chamber walls (Lim and Ziemann, 2009 c). In this study, we represent the individual steps of the conversion of δ-hydroxycarbonyl to substituted dihydrofuran by an overall first-order decay rate of 3 × 10⁻³ s⁻¹. This value is estimated by monitoring the decay of 5-hydroxy-2-pentanone using CIMS in the presence of 20 μm³ cm⁻³ (NH₄)SO₄/H₂SO₄ seeds at 3 % RH. This assumed decay rate is consistent with those rates measured in previous studies (Cavalli et al., 2000; Martin et al., 2002, Holt et al., 2005; Lim and Ziemann, 2009 c). The equilibrium

constant K ($K = [4,5\text{-dihydro-2-methylfuran}]/[5\text{-hydroxy-2-pentanone}]$) is estimated to be ~7 at 3 % RH from the CIMS measured 5-hydroxy-2-pentanone decay curve, based on the assumption that the decrease in the 5-hydroxy-2-pentanone concentration is accompanied by stoichiometric formation of the corresponding 4,5-dihydro-2-methylfuran. Note that although the proportion of the heterogeneous conversion occurring on the chamber walls is unknown, the potential contribution of chamber walls to the particle-phase production of substituted dihydrofuran has been accounted for by employing the measured overall conversion rate in the mechanism.

The substituted dihydrofuran formed evaporates rapidly due to its high volatility and undergoes reactions with OH, O₃, and NO₃ in the gas phase (Ziemann and Atkinson, 2012), with reaction rate constants of 2.18 × 10⁻¹⁰, 3.49 × 10⁻¹⁵ cm³ molecule⁻¹ s⁻¹, and 1.68 × 10⁻¹⁰ cm³ molecule⁻¹ s⁻¹, respectively (Martin et al., 2002; Atkinson et al., 2008). Reaction with NO₃ is not important under the conditions of this study. In general, the OH addition to an alkyl-substituted dihydrofuran produces either an alkyl-substituted tetrahydrofuran or a carbonyl ester; see Fig. 2a (Martin et al., 2002, Lim and Ziemann, 2005, 2009a, b, c, Jordan et al., 2008). The mechanism for the O₃ reaction with an alkyl-substituted dihydrofuran, as shown in Fig. 2b, was developed following the ozonolysis of 4,5-dihydro-2-methylfuran (Martin et al., 2002), alkyl vinyl ethers (Thiault et al., 2002; Klotz et al., 2004; Sadezky et al., 2006) and monoterpenes (Jenkin et al., 2000; Jenkin, 2004). The reaction of alkyl-substituted dihydrofuran with O₃ involves the addition of O₃ to the C=C double bond to produce an energy-rich primary ozonide, which rapidly decomposes into two excited Criegee intermediates. The energy-rich Criegee intermediates are either collisionally stabilized or decompose to yield OH (or OH+CO) and an additional α-carbonyl peroxy radical (or peroxy radical). The resulting α-carbonyl peroxy radical (or peroxy radical) can undergo the well-established reactions available for peroxy radicals; see Fig. 2b. The stabilized Criegee intermediates are predicted to react primarily with water (Martin et al., 2002), leading to 3-propoxy-nonanal (C₁₂H₂₂O₃) and 3-propoxy-nonanoic acid (C₁₂H₂₂O₃), with molar yields of 90 and 10 %, respectively. The total yield of 3-propoxy-nonanal is predicted to be 18 %, which is close to the yield of succinaldehydic acid methyl ester (23 %) from the ozonolysis of 4,5-dihydro-2-methylfuran (Martin et al., 2002).

We consider SOA formation by dodecane photooxidation, including heterogeneous formation of substituted dihydrofuran and its subsequent reaction with OH/O₃. Gas-particle equilibrium partitioning of semivolatile products is assumed. The branching ratio and vapor pressure ($P_{L,i}^0$, atm⁻¹) at 300 K (predicted by SIMPOL.1; Pankow and Asher, 2008) of each product from the OH/O₃-initiated oxidation of alkyl-substituted dihydrofuran are labeled in Fig. 2. The corresponding effective saturation concentrations

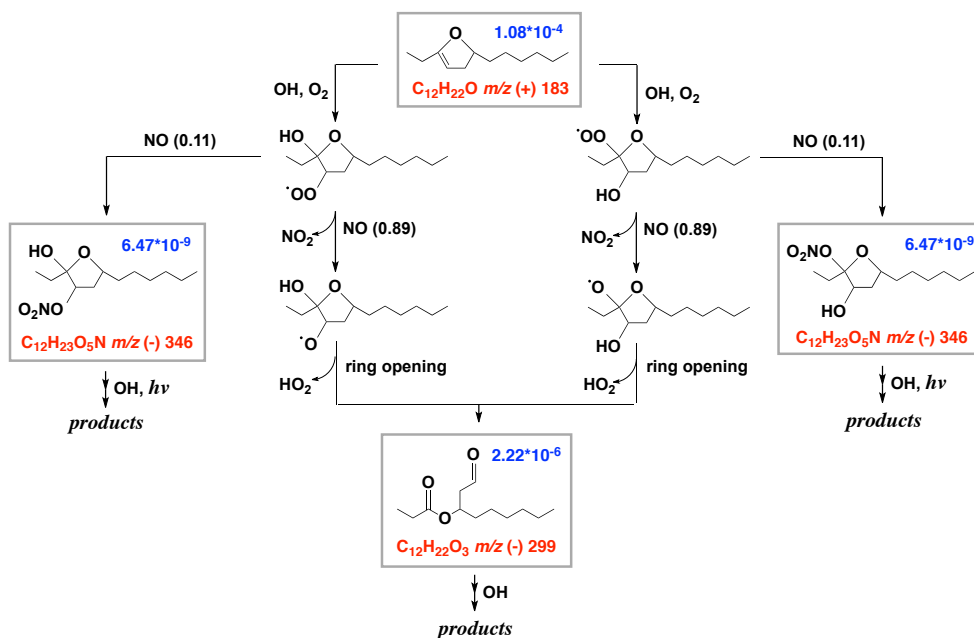


Fig. 2a. Proposed mechanism for the OH-initiated oxidation of alkyl-substituted dihydrofuran under high- NO_x conditions. The boxes indicate compounds or reaction pathways incorporated in the model simulation. CIMS monitored species have m/z noted in red. Estimated vapor pressure (atm) of each compound is indicated in blue.

($C^* = 10^6 P_{L,i}^0 \gamma_i \bar{M}_w / RT$) range from $7.0 \times 10^1 \mu\text{g m}^{-3}$ to $4.7 \times 10^4 \mu\text{g m}^{-3}$, for which approximately 0.1% ~ 41.7% of these products are in the particle phase at an organic loading of $\sim 50 \mu\text{g m}^3$. Compounds with the lowest volatility ($\sim 10^{-9}$ atm) are produced mostly from the $\text{RO}_2 + \text{NO} \rightarrow \text{RONO}_2$ reaction, the branching ratio of which ranges from 0.11 to 0.28. As a result, the total amount of organic nitrates in the particle phase is relatively high; see Fig. 9c. Compounds generated from the $\text{RO}_2 + \text{NO} \rightarrow \text{RO} + \text{NO}_2$ reaction have higher molar yields (0.72–0.89). But they are too volatile ($\sim 10^{-6}$ – 10^{-7} atm) to partition significantly into the particle phase. The stabilized Criegee intermediate reaction with water is predicted to predominate over reaction with NO/NO_2 at $\text{RH} > 3\%$. The ester containing carboxylic acid ($\text{C}_{12}\text{H}_{22}\text{O}_4$) is predicted to be present in the particle phase due to its sufficiently low volatility ($\sim 10^{-8}$ atm); see Fig. 9c.

4 Results and discussion

In this section, we seek to evaluate the impact of substituted dihydrofuran chemistry on dodecane SOA formation as follows: (1) predict the yield of alkyl-substituted dihydrofuran from the photooxidation of dodecane under both high- and low- NO_x conditions, and the fraction of alkyl-substituted dihydrofuran that reacts with O_3 in the O_3 -dominant regime (Sect. 4.1); (2) measure the time-dependent evolution of cyclic hemiacetal and alkyl-substituted dihydrofuran at 3%,

10, 20, and 50% RH (Sect. 4.2); (3) propose gas-phase products that are unique to dihydrofuran chemistry based on the CIMS speciation (Section 4.3); (4) compare particle-phase chemical composition under OH-dominant vs. O_3 -dominant environments via identifying AMS measured ions representative of dihydrofuran oxidation products (Sect. 4.4); and (5) estimate the change in SOA yield and elemental composition by incorporating the complete substituted-dihydrofuran formation and removal pathways into the dodecane SOA prediction model (Sect. 4.5).

4.1 Predicted substituted dihydrofuran formation and reaction with ozone in the dodecane system

To what extent is the formation of substituted dihydrofuran and its subsequent chemistry important in the formation of dodecane SOA? A mechanism simulation was conducted, with initial conditions similar to those employed in the chamber (Table 1), i.e., 200 ppb dodecane, 1.5 ppm H_2O_2 , 100 ppb O_3 , and 100 ppb + 30 ppb h^{-1} NO for high- NO_x conditions and 200 ppb dodecane, 4 ppm H_2O_2 , 100 ppb O_3 , and 0 ppb NO_x for low- NO_x conditions. Figure 3 shows the predicted mass distribution of δ -hydroxycarbonyl, alkyl-substituted dihydrofuran, together with other products of the same generation. δ -hydroxycarbonyl is predicted to account for > 90% total organic mass of first-generation products under high- NO_x conditions (see Fig. 3a (H)), but < 5% to the total organic mass of the third-generation products under low- NO_x conditions (see Fig. 3a (L)). Inclusion of the

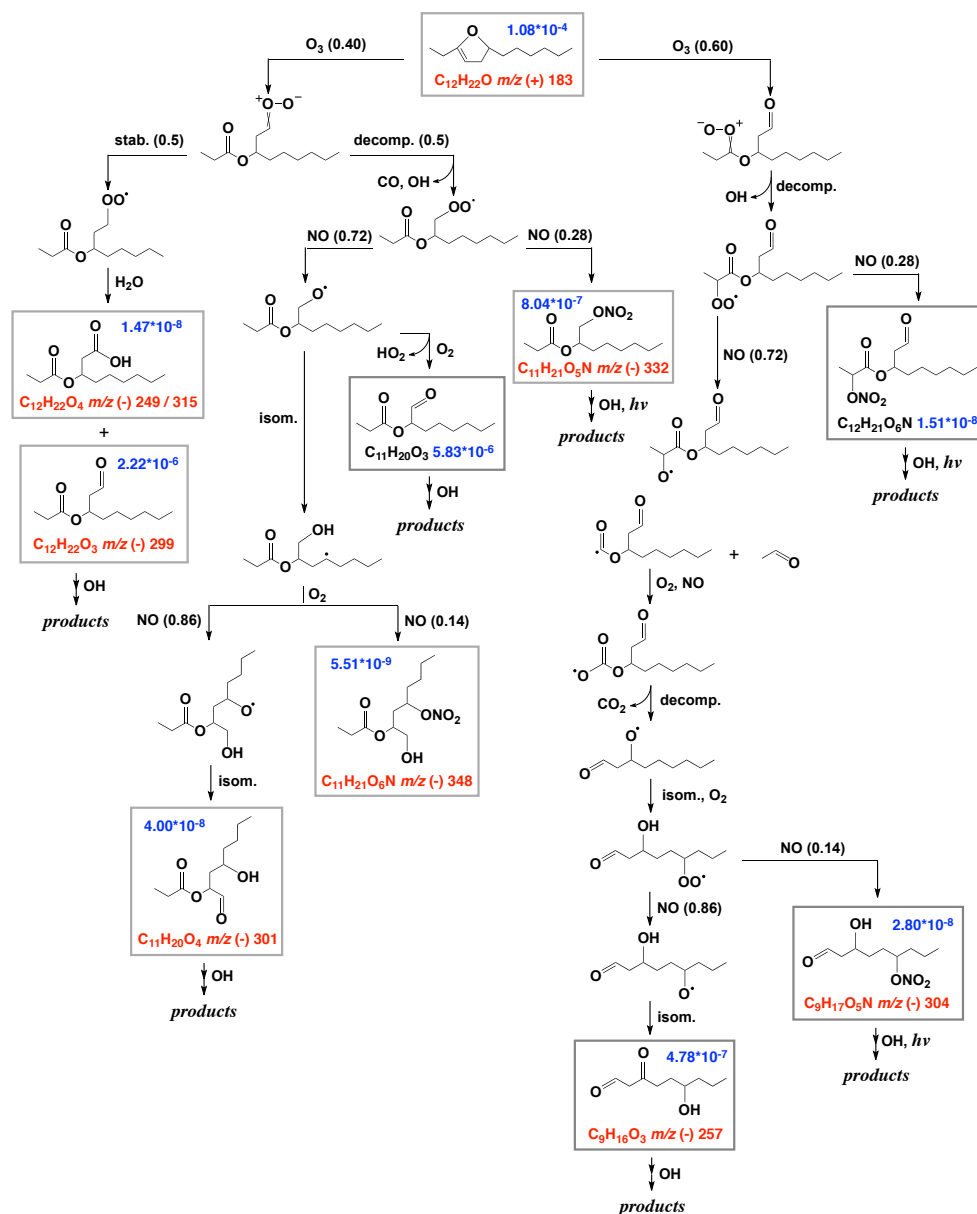


Fig. 2b. Proposed mechanism for the ozonolysis of alkyl-substituted dihydrofuran under high- NO_x conditions. The boxes indicate compounds or reaction pathways incorporated in the model simulation. CIMS monitored species have m/z noted in red. Estimated vapor pressure (atm) of each compound is indicated in blue.

heterogeneous conversion pathway from δ -hydroxycarbonyl to alkyl-substituted dihydrofuran is predicted to result in a rapid consumption of δ -hydroxycarbonyl under dry conditions, as opposed to a slow decay from OH oxidation. Alkyl-substituted dihydrofuran accounts for up to 70 % of the decay of δ -hydroxycarbonyl, as shown in Fig. 3b (H). As discussed earlier, an ozonolysis-dominant environment occurs for $\text{O}_3 > 3 \text{ ppb}$ at a typical OH concentration of $1.0 \times 10^6 \text{ molecules cm}^{-3}$. In the high- NO_x simulation case, ozone is predicted to lead to 82–98 % of the total alkyl-

substituted dihydrofuran loss over the course of photooxidation; see Fig. 3d (H).

The alkyl-substituted dihydrofuran is not the only product that contains a dihydrofuran structure in the dodecane photooxidation system. The first-generation product 3-dodecyl nitrate under high- NO_x conditions is an example. Three pathways exist that could produce semivolatile compounds containing a dihydrofuran structure from the further photochemical reaction of 3-dodecyl nitrate: (1) photolysis of the $-\text{ONO}_2$ group leads to an alkyl-substituted dihydrofuran, (2) abstraction of an H atom by OH potentially leads to an

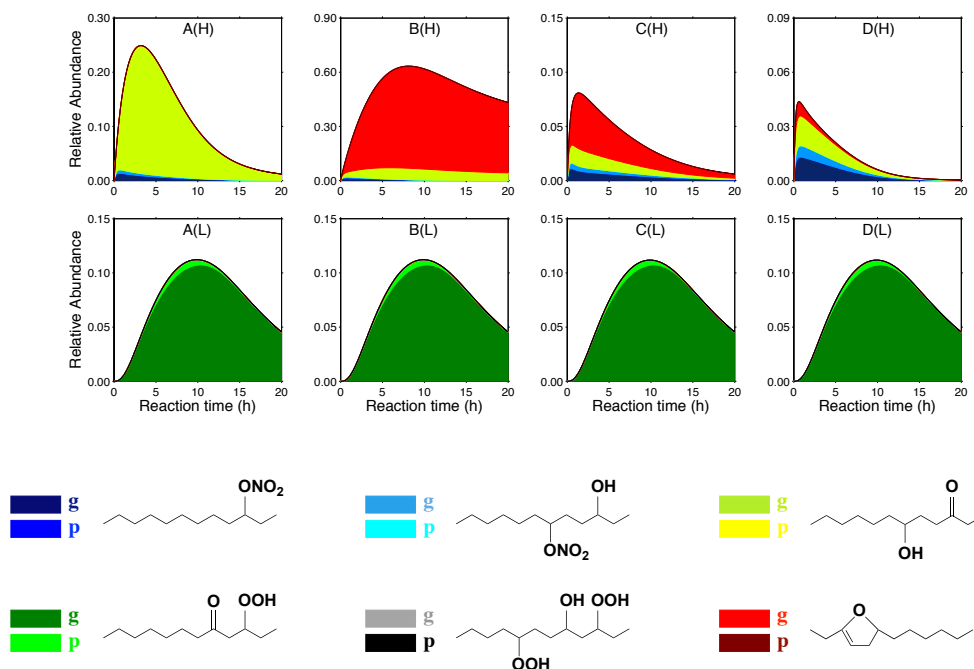


Fig. 3. Model-predicted relative abundance of δ -hydroxycarbonyl and alkyl-substituted dihydrofuran, together with other first-generation products under high-NO_x (H) and other third-generation products under low-NO_x (L) conditions in gas (g) and particle (p) phases. All the organic masses are normalized by the initial organic mass (~ 200 ppb dodecane). (A) represents the relative abundance of products without a heterogeneous alkyl-substituted dihydrofuran formation channel, (B) represents the relative abundance of products when the heterogeneous channel is incorporated into the scheme but in the absence of any sink of alkyl-substituted dihydrofuran, (C) represents the relative abundance of products when the OH oxidation is the only sink of alkyl-substituted dihydrofuran, and (D) represents the relative abundance of products using the complete gas- and particle-phase mechanism.

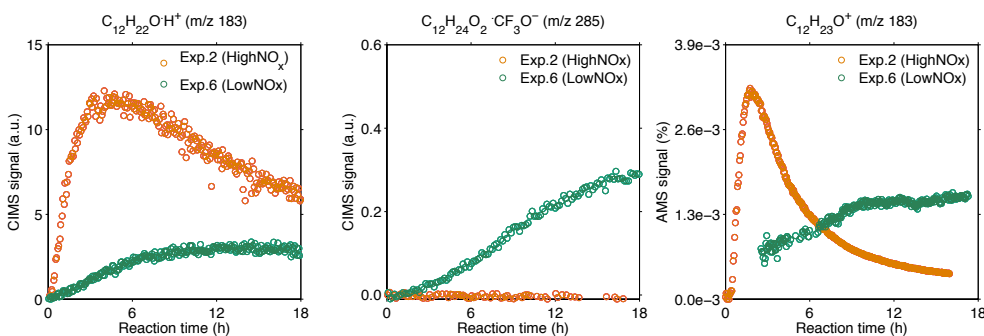


Fig. 4. Temporal profiles of ion $C_{12}H_{22}O \cdot H^+$ ($m/z = 183$) and $C_{12}H_{24}O_2 \cdot CF_3O^-$ ($m/z = 285$) measured by CIMS and ion $C_{12}H_{23}O^+$ ($m/z = 183$) measured by AMS under high- and low-NO_x conditions. Details of experimental conditions are given in Table 1.

organonitrate-substituted dihydrofuran, and (3) H-atom abstraction from a C atom with the $-ONO_2$ functional group attached and further H-atom abstraction from a C atom potentially leads to a carbonyl-substituted dihydrofuran. It is worth noting that the gas-phase ozonolysis of alkyl-substituted dihydrofuran under high-NO_x conditions contributes to most of the ozonolysis reactions because the alkyl-substituted dihydrofuran is a major first-generation product, as shown in Fig. 3b (H).

4.2 Formation of cyclic hemiacetals and alkyl-substituted dihydrofuran

CIMS measurement at (+) m/z 183 in positive mode represents the ion $C_{12}H_{22}O \cdot H^+$ generated from the proton transfer reaction with alkyl-substituted dihydrofuran ($M_w = 182$). An additional source of (+) m/z 183 is the proton transfer reaction followed by dehydration of hydroxyl dodecanone ($M_w = 200$), which is also detected as a fluoride cluster product at ($-$) m/z 285 ($C_{12}H_{24}O_2 \cdot CF_3O^-$) in negative

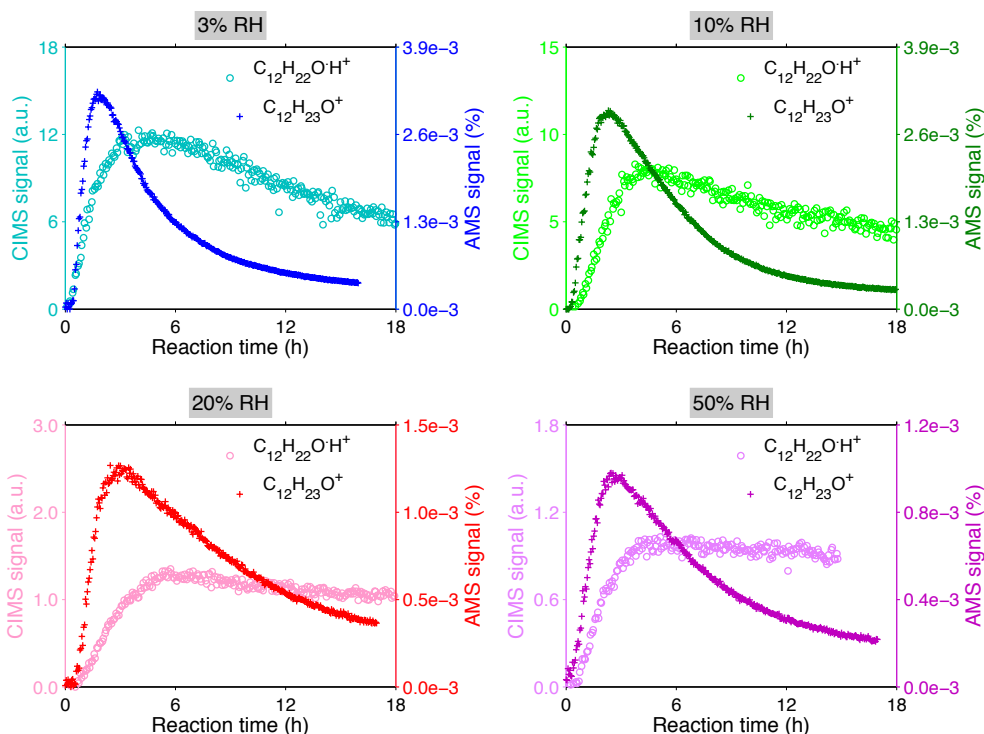


Fig. 5. Time-dependent evolution of ion $\text{C}_{12}\text{H}_{22}\text{O}\cdot\text{H}^+$ ($m/z = 183$) measured by CIMS and ion $\text{C}_{12}\text{H}_{23}\text{O}^+$ ($m/z = 183$) measured by AMS at 3, 10, 20, and 50% RH.

mode. Figure 4 shows temporal profiles of $(+)m/z$ 183 and $(-)m/z$ 285 monitored under both high- and low- NO_x conditions (Exp. 2 vs. Exp. 6). The $(+)m/z$ 183 ion was detected in each of the two experiments, but with distinct time-dependent patterns. Under high- NO_x conditions, $(+)m/z$ 183 peaks during the first 3 h of irradiation, indicating fast formation of alkyl-substituted dihydrofuran, and decays during the next 15 h of photooxidation. Under low- NO_x conditions, however, the $(+)m/z$ 183 signal eventually reaches a plateau, which is more consistent with the pattern of $(-)m/z$ 285. This behavior is consistent with the mechanism prediction that the alkyl-substituted dihydrofuran is formed in significant amounts only under high- NO_x conditions (Fig. 3b (H)). An alternative explanation for the temporal profiles of $(+)m/z$ 183 under low- NO_x conditions is that this ion is formed by dehydration of the cyclic hemiacetal following protonation in CIMS. The occurrence of a plateau could be indicative of an absence of dehydration in the particle phase due to the lack of an acid catalyst (no HNO_3 formation from $\text{NO}_2 + \text{OH}$ reaction as in the high- NO_x cases). However, based on the model prediction, cyclic hemiacetal is not likely to accumulate since the formation of its precursor, δ -hydroxycarbonyl, is a minor pathway when the $\text{RO}_2 + \text{HO}_2$ reaction is dominant and the photolysis of the resulting peroxide is not important.

The AMS measured m/z 183 ($\text{C}_{12}\text{H}_{23}\text{O}^+$) is the major characteristic ion for cyclic hemiacetal. This ion is produced by the neutral loss of OH ($M_w = 17$) from the 2 po-

sition in the cyclic hemiacetal ($M_w = 200$) during electron ionization (Gong et al., 2005; Lim and Ziemann, 2009c). In addition, the $\text{C}_{12}\text{H}_{23}\text{O}^+$ ion is suggested to be the characteristic fragment of carbonyl-hydroperoxide-derived peroxyhemiacetal (Yee et al., 2012). The temporal profiles of the $\text{C}_{12}\text{H}_{23}\text{O}^+$ ion under both high- and low- NO_x conditions (Exp. 2 vs. Exp. 6) exhibit distinct growth patterns (Fig. 4). Under high- NO_x conditions, the $\text{C}_{12}\text{H}_{23}\text{O}^+$ ion signal increases rapidly to a maximum during the first 2 h and decays over the next ~ 14 h. The temporal behavior of the $\text{C}_{12}\text{H}_{23}\text{O}^+$ ion is a result of its rapid formation, i.e., uptake of δ -hydroxycarbonyl onto particles and subsequent cyclization, and relatively slower removal, i.e., dehydration. Under low- NO_x conditions, the $\text{C}_{12}\text{H}_{23}\text{O}^+$ ion increases over the course of a 20 h experiment because of the accumulative formation of peroxyhemiacetal. During the first 3 h of irradiation under low- NO_x conditions, the organic loading is below the AMS detection limit; thus the $\text{C}_{12}\text{H}_{23}\text{O}^+$ ion signal does not appear in Fig. 4 during this period. The $\text{C}_{12}\text{H}_{23}\text{O}^+$ ion signal under low- NO_x conditions therefore potentially represents peroxyhemiacetal, since the formation of peroxides is the major reaction pathway in the $\text{RO}_2 + \text{HO}_2$ dominant regime. This is again consistent with the mechanism prediction that the formation of alkyl-substituted dihydrofuran is unimportant under low- NO_x conditions (Fig. 3b (L)).

Figure 5 shows temporal profiles of the ion $\text{C}_{12}\text{H}_{22}\text{O}\cdot\text{H}^+$ detected by CIMS and the ion $\text{C}_{12}\text{H}_{23}\text{O}^+$ detected by AMS

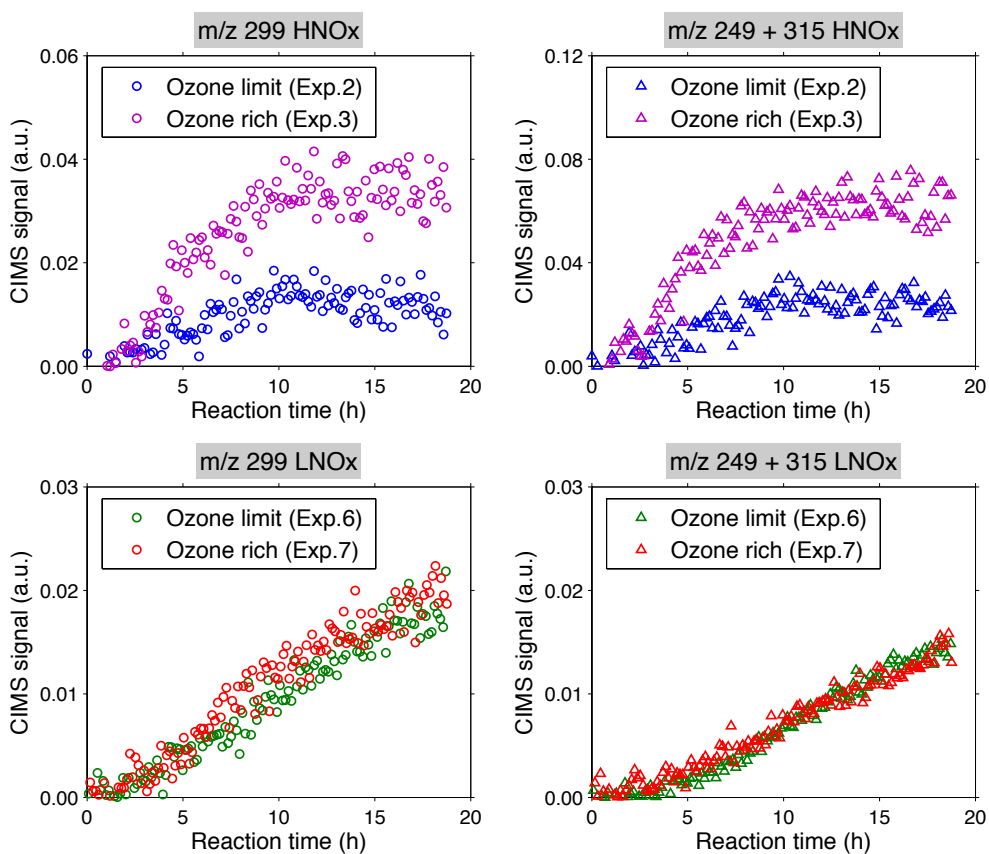


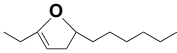
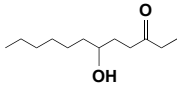
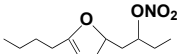
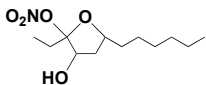
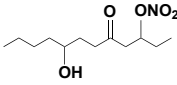
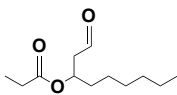
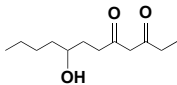
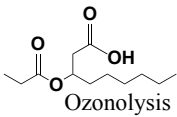
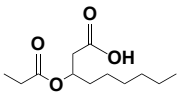
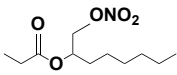
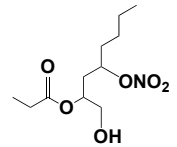
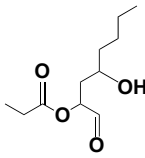
Fig. 6. Time-dependent evolution of CIMS measured signals at m/z 299, and m/z 249 and 315, as a function of O_3 levels under high- and low- NO_x conditions over the course of 20 h photooxidation.

in the presence of NO_x under varying RH. In general, the AMS ion $C_{12}H_{23}O^+$ peaks ~ 3 h earlier than the CIMS ion $C_{12}H_{22}O \cdot H^+$. The decay rates of AMS ion $C_{12}H_{23}O^+$, which is calculated by assuming first-order kinetics, are 4.02×10^{-3} , 3.06×10^{-3} , 1.71×10^{-3} , and $1.37 \times 10^{-3} \text{ s}^{-1}$ at RH of 3, 10, 20, and 50 %, respectively. Aerosol water content could slow down the formation and removal rate of AMS ion $C_{12}H_{23}O^+$, mainly because (1) water could accelerate the hydration rate, thus changing the equilibrium coefficient of the interconversion between cyclic hemiacetal and dihydrofuran, and (2) the addition of water might neutralize the particle-phase acid (e.g., HNO_3), which is thought to catalyze the cyclization of δ -hydroxycarbonyl to cyclic hemiacetal (Lim and Ziemann, 2009c). The decay rates of AMS ion $C_{12}H_{23}O^+$ are within the same order of magnitude of that measured for 5-hydroxy-2-pentanone at 3 % RH, indicating that the dehydration of cyclic hemiacetal is the rate-limiting step in the overall heterogeneous conversion process. Water vapor influences CIMS sensitivity to certain compounds in negative mode by clustering with the reagent ion CF_3O^- to form $[H_2O \cdot CF_3O]^-$. The decreasing intensity of the ion $C_{12}H_{22}O \cdot H^+$ as RH increases is likely indicative of this effect.

4.3 Products from alkyl-substituted dihydrofuran oxidation

Products unique to the alkyl-substituted dihydrofuran oxidation chemistry have been proposed based on CIMS measured m/z signals; see Table 2 for chemical structures. Authentic standards are not commercially available for these products. Compounds from the dodecane photooxidation route that share the same m/z signal with alkyl-substituted dihydrofuran oxidation products are also presented in Table 2. The CIMS signal ($-$) m/z 346 is composed of 2-nitroso-2-alkyl-3-hydroxyl-5-heptyl-tetrahydrofuran and 2-carbonyl-5-hydroxyl-2-dodecyl-nitrate. The latter is a third-generation product resulting from the further oxidation of dodecyl nitrate. The branching ratio for the addition of an $-ONO_2$ group is much lower than that for the formation of the RO radical; therefore the interference of 2-carbonyl-5-hydroxyl-2-dodecyl-nitrate in the ($-$) m/z 346 signal can be neglected. The CIMS signal ($-$) m/z 299 represents 3-propoxy-nonanal, which is a primary product from both OH oxidation and ozonolysis of alkyl-substituted dihydrofuran, and 8-hydroxy-3,5-dodecanedione, which is produced from the further oxidation of dodecyl nitrate. As discussed earlier,

Table 2. Proposed structures for CIMS ions unique to the alkyl-substituted dihydrofuran chemistry. C and T indicate the cluster and transfer product, respectively. Commercial standards are not available.

Observed m/z	Product	Chemical formula	Proposed structure	Chemical pathway	Interference
183(+)	T	$C_{12}H_{22}O$		Heterogeneous conversion	
328(-)	C	$C_{12}H_{21}NO_4$		Heterogeneous conversion	—
346(-)	C	$C_{12}H_{23}NO_5$		OH-oxidation	
299(-)	C	$C_{12}H_{22}O_3$		OH-oxidation Ozonolysis	
249(-)	T	$C_{12}H_{22}O_4$	 Ozonolysis	Ozonolysis	—
315(-)	C	$C_{12}H_{22}O_4$		Ozonolysis	—
332(-)	C	$C_{11}H_{21}O_5N$		Ozonolysis	—
348(-)	C	$C_{11}H_{21}O_6N$		Ozonolysis	—
301(-)	C	$C_{11}H_{20}O_4$		Ozonolysis	—

the formation and transformation of dodecyl nitrate is predicted to be a minor pathway, and thus the $(-)/m/z$ 299 is dominated by 3-propoxy-nonanal.

A distinct feature of proposed products from the dihydrofuran oxidation by either OH or O_3 is the formation of an ester group ($-C(O)O-$) or an ether group ($-O-$), both of which cannot be accessed from photochemical reaction pathways initiated by the OH attack on the aliphatic hydrocar-

bon. The OH oxidation channel leads solely to the formation of tetrahydrofuran and carbonyl ester. In the ozonolysis pathway, on the other hand, the reaction of stabilized Criegee intermediates with water produces one ester group containing aldehyde (3-propoxy-nonanal) and carboxylic acid (3-propoxy-nonanoic acid); see proposed structures in Table 2. From the intact C_{12} skeleton and highly oxygenated nature, these two products are consistent with CIMS signals in

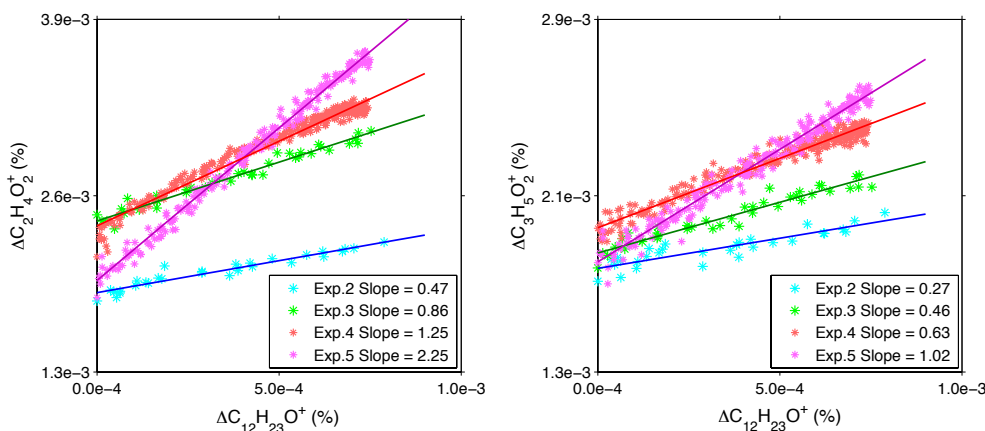


Fig. 7. Time-dependent evolution of AMS measured ion intensities of $\text{C}_2\text{H}_4\text{O}_2^+$ and $\text{C}_3\text{H}_5\text{O}_2^+$ as a function of decay of the $\text{C}_{12}\text{H}_{23}\text{O}^+$ signal.

$(-)/m/z$ 299 and $(-)/m/z$ 249 and 315 in negative mode with little interference from other products.

Figure 6 shows the temporal profiles of $(-)/m/z$ 299, as well as $(-)/m/z$ 249 and 315, under “ O_3 -limiting” (Exp. 2) and “ O_3 -rich” (Exp. 3) conditions. The decay rates of their precursor $(+)/m/z$ 183, as calculated by assuming first-order kinetics, are $1.19 \times 10^{-5} \text{ s}^{-1}$ and $1.44 \times 10^{-5} \text{ s}^{-1}$, respectively. Under O_3 -rich conditions, both species increase and eventually level off. When O_3 reaction is less competitive, the CIMS signals start to decrease after 10 h of photooxidation. Note that these three ions were also detected under low- NO_x conditions. No significant increase in their signals was observed in the O_3 -rich environment (Exp. 7), compared with the O_3 -limiting case (Exp. 6). If they were assigned the same chemical structures as those proposed under high- NO_x conditions, their growth pattern would suggest a minor formation of their precursor alkyl-substituted dihydrofuran. This can be attributed to the slowdown or even termination of the dehydration of cyclic hemiacetal in the absence of strong acid catalysis (Atkinson et al., 2008; Lim and Ziemann, 2009c).

4.4 Ozonolysis vs. OH oxidation

Carboxylic acids produce significant signals at m/z 60 and 73, specifically $\text{C}_2\text{H}_4\text{O}_2^+$ and $\text{C}_3\text{H}_5\text{O}_2^+$, in the AMS measurement (Aiken et al., 2008). The formation of these two ions, as a function of the time-dependent decay of the ion $\text{C}_{12}\text{H}_{23}\text{O}^+$, is shown under different RH conditions in Fig. 7. The largest slope of either $\Delta\text{C}_2\text{H}_4\text{O}_2^+ / \Delta\text{C}_{12}\text{H}_{23}\text{O}^+$ or $\Delta\text{C}_3\text{H}_5\text{O}_2^+ / \Delta\text{C}_{12}\text{H}_{23}\text{O}^+$ is associated with the highest RH, i.e., 50%. However, the production of $\text{C}_2\text{H}_4\text{O}_2^+$ and $\text{C}_3\text{H}_5\text{O}_2^+$ is not significant under dry conditions. Also, the changes in slopes along with changes in RH values are consistent for both ions. This indicates that the formation of the carboxylic acid functional group detected in particles is associated with the water vapor concentration in the gas phase, consistent with the reaction of the stabilized Criegee interme-

diates with water in the substituted dihydrofuran oxidation system.

Two dominant oxygen-containing ions, m/z 44 (mostly CO_2^+) and m/z 43 (C_3H_7^+ and $\text{C}_2\text{H}_3\text{O}^+$), have been widely used to characterize organic aerosol evolution in chamber and field observations. Previous studies have shown that CO_2^+ results mostly from the thermal decarboxylation of an organic acid group (Alfarra, 2004). The f_{44} (ratio of m/z 44, mostly CO_2^+ , to total signal in the component mass spectrum) axis is also considered to be an indicator of photochemical aging (Alfarra et al., 2004; Aiken et al., 2008; Kleinman et al., 2008). It has been found that increasing OH exposure increases f_{44} and decreases f_{43} (ratio of m/z 43, mostly $\text{C}_2\text{H}_3\text{O}^+$, to total signal in the component mass spectrum) for SOA generated from gas-phase alkanes (Lambe et al., 2011). The $\text{C}_2\text{H}_3\text{O}^+$ ion at m/z 43 is assumed predominantly due to nonacid oxygenates, such as saturated carbonyl groups (Ng et al., 2011). The evolution of dodecane SOA from four experiments (Table 1), characterized by different OH and O_3 exposure, and different RH levels, is shown in $f_{\text{CO}_2^+} - f_{\text{C}_2\text{H}_3\text{O}^+}$ space in Fig. 8. Overall, high- NO_x dodecane SOA lies to the lower left of the triangular region derived for ambient SOA. The relatively high organic loading (~ 200 ppb dodecane) employed in this study favors partitioning of less oxidized species, which would remain in the gas phase under atmospheric conditions. For each experiment, $f_{\text{CO}_2^+}$ decreases and $f_{\text{C}_2\text{H}_3\text{O}^+}$ increases with increasing SOA at the beginning of irradiation. After several hours of photooxidation, the trends reverse, resulting in increasing $f_{\text{CO}_2^+}$ and decreasing $f_{\text{C}_2\text{H}_3\text{O}^+}$. Curvature in $f_{\text{CO}_2^+} - f_{\text{C}_2\text{H}_3\text{O}^+}$ space has been also observed in other chamber/flow reactor studies (Kroll et al., 2009; Ng et al., 2010; Chhabra et al., 2011; Lee et al., 2011; Lambe et al., 2011). When the organic loading is small, only the highly oxygenated and least volatile species partition to the particle phase. As particles grow, more volatile and less oxidized species are able to

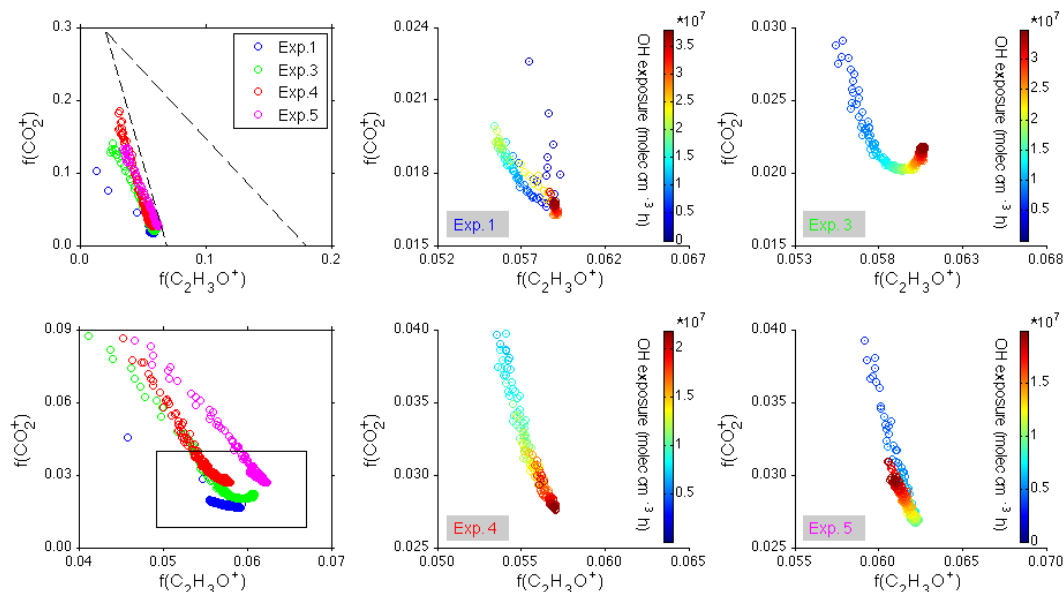


Fig. 8. SOA evolution as a function of OH exposure vs. O_3 exposure from dodecane photochemistry under high- NO_x conditions in the f_{44} vs. f_{43} space. The top-left graph shows the combination of all the data, and the bottom-left graph shows an expanded version. The other graphs show the specific behavior of each experiment: Exp. 1 corresponds to a regime in which OH oxidation of dihydrofuran is dominant. Exp. 3, 4, and 5 correspond to a regime in which ozonolysis of dihydrofuran is dominant, at 10, 20, and 50 % RH, respectively.

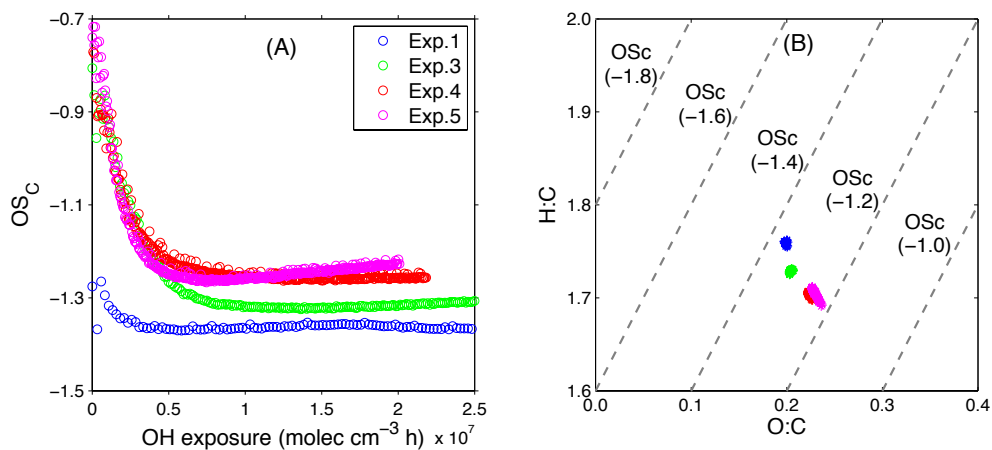


Fig. 9. (A) SOA average carbon oxidation state as a function of OH exposure from dodecane photochemistry under high- NO_x conditions. Exp. 1 corresponds to a regime in which OH oxidation of dihydrofuran is dominant. Exp. 3, 4, and 5 correspond to a regime in which ozonolysis of dihydrofuran is dominant, at 10, 20, and 50 % RH, respectively. (B) van Krevelen diagram. AMS measured O:C vs. H:C ratios for the four experiments under the OH total exposure ranging from 1.0×10^7 to 2.0×10^7 molecules cm^{-3} h. Gray dashed lines denote the average carbon oxidation state.

participate in equilibrium partitioning, leading to a decrease in $f_{CO_2^+}$. Progressive oxidation of semivolatile products in the gas phase eventually leads to multifunctionalized species contributing to the increase of $f_{CO_2^+}$.

Both O_3 - and OH-initiated oxidation of substituted dihydrofuran lead to the formation of $f_{CO_2^+}$, via the thermal decarboxylation of an organic acid group and photochemical aging, respectively. The contribution of each reaction path-

way to the intensity of $f_{CO_2^+}$ can be evaluated based on the $f_{CO_2^+} - f_{C_2H_3O^+}$ plot. As discussed in Sect. 2.1, Exp. 1 is designed as an OH-dominant case, in which it is estimated that >73 % of the dihydrofuran reacts with OH over the course of the experiment. Exp. 3, 4, and 5 were designed to be O_3 -dominant at 10 %, 20 %, and 50 % RH, respectively. Approximately 96, 97, and 98 % of substituted dihydrofuran is predicted to react with O_3 when it peaks after ~ 3 h of photooxidation in Exp. 3, 4, and 5, respectively.

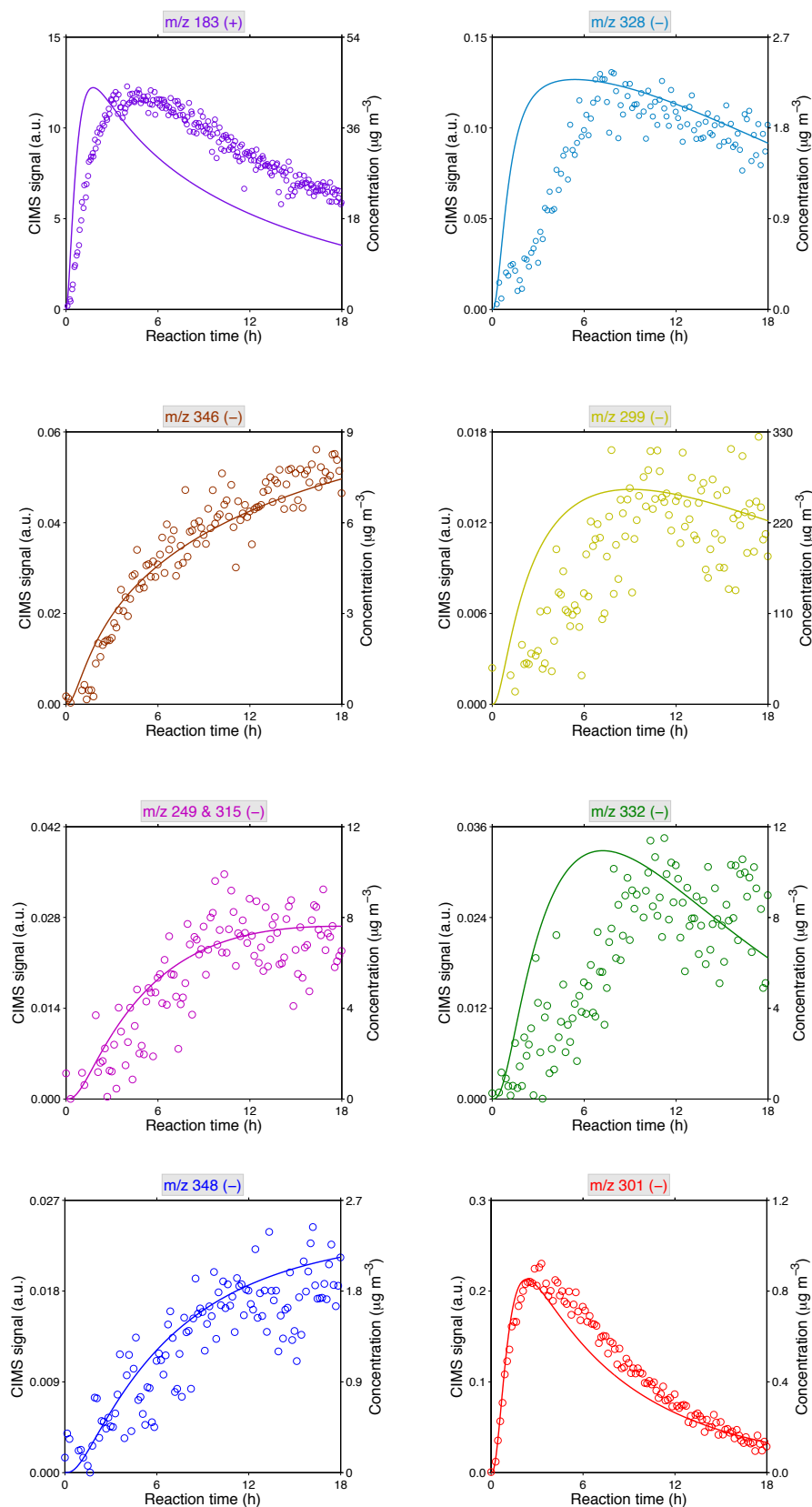


Fig. 10. Comparison of CIMS measured ions in positive and negative mode, with chemical structures proposed in Table 2, with model simulations using experimental conditions of Exp. 2.

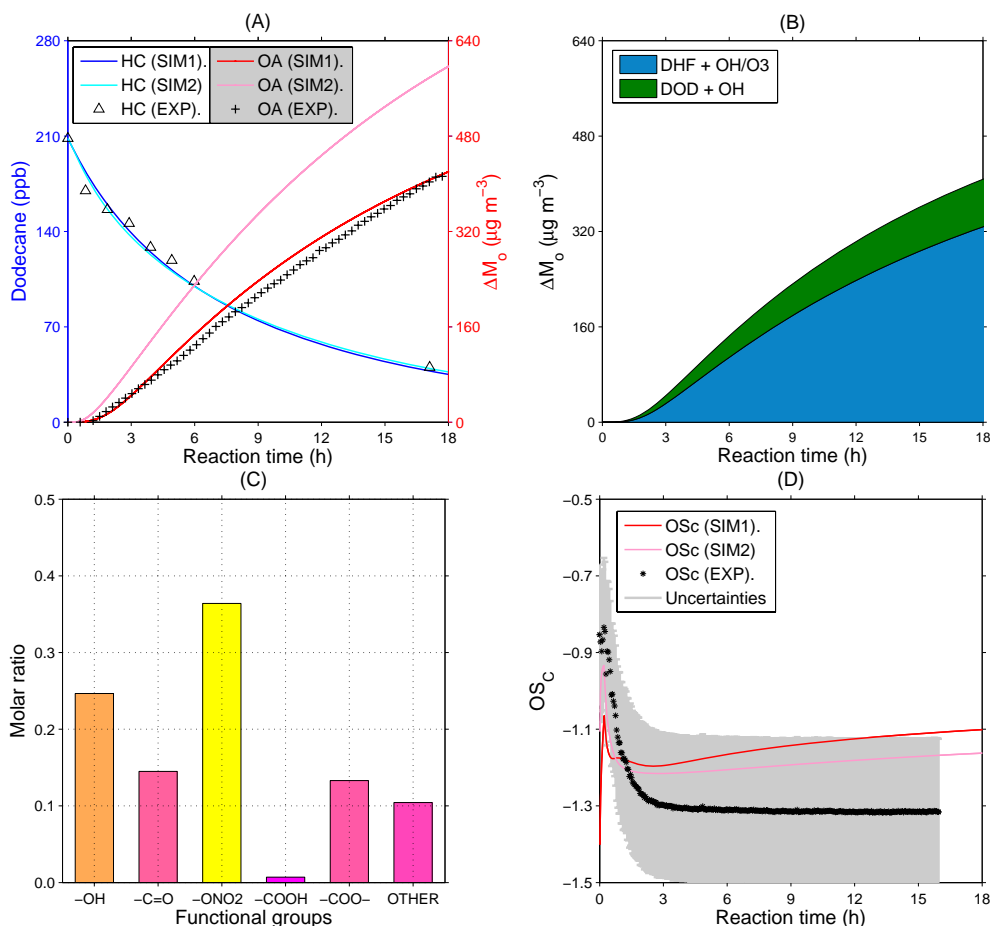


Fig. 11. (A) Comparison of the predicted dodecane decay and SOA growth with observations (Exp. 2). SIM1 represents the full mechanism simulations under initial conditions of Exp. 2. SIM2 is the simulations in the absence of the substituted dihydrofuran formation channel. (B) The contribution of dihydrofuran chemistry (DHF+OH/O₃) vs. dodecane photochemistry (DOD+OH) to the total organic mass. (C) Molar fractions of major functional groups after 3 h of photochemical reaction (when alkyl-substituted dihydrofuran peaks and organic loading is $\sim 50 \mu\text{g m}^{-3}$) as predicted by SIM1. Note that “other” includes dihydrofuran, tetrahydrofuran, and ether moieties. (D) Comparison of the predicted average carbon oxidation state with observations (Exp. 2).

As shown in Fig. 8, the intensities of $f_{\text{CO}_2^+}$ in Exp. 1, 3, 4, and 5 are 0.019, 0.020, 0.028, and 0.030, respectively, at the same OH exposure, i.e., 2×10^7 molecules cm^{-3} h. The increase in $f_{\text{CO}_2^+}$ intensities results from the increasing O₃ and RH levels in these four experiments. Overall, Exp. 1 exhibits the least intensity of $f_{\text{CO}_2^+}$ at the end of the experiment, i.e., 0.017, although the total OH exposure is the highest, i.e., 3.8×10^7 molecules cm^{-3} h. The total OH exposures for Exp. 3, 4, and 5 are 3.5×10^7 , 2.2×10^7 , and 2.1×10^7 molecules cm^{-3} h, respectively, which are less than that in Exp. 1. However, the intensities of $f_{\text{CO}_2^+}$ for these three experiments are 35–82 % higher than that in Exp. 1 at the end of experiments. In addition, the intensity of $f_{\text{CO}_2^+}$ increases along with increasing RH and O₃ exposure for these three experiments, varying from 0.023 to 0.031. The highest $f_{\text{CO}_2^+}$ intensity shown in Exp. 5 corresponds to the highest O₃ exposure and RH level, but lowest OH exposure.

The difference in elemental composition of organic particles produced from O₃-dominant vs. OH-dominant environments is also examined via the AMS measured O:C and H:C ratios in the van Krevelen plot and the time-dependent evolution of the average carbon oxidation state ($OS_C = 2 \times \text{O:C} - \text{H:C}$); see Fig. 9. In general, the OS_C values calculated fall into a region characterized by oxidized primary organic aerosol and semivolatile oxidized organic aerosol (Kroll et al., 2011). The measured O:C (~ 0.2) and H:C (~ 1.7) ratios at an OH exposure on the order of $\sim 10^7$ molecules cm^{-3} h agree with those measured for organic aerosols generated from C₁₀–C₁₇ alkanes (Lambe et al., 2011, 2012). As mentioned earlier, the four experiments (Exp. 1, 3, 4, and 5) were conducted in such a way that the total OH exposure is decreasing, whereas the total O₃ and RH exposure is increasing along with increasing experimental numbers (for example, Exp. 5 has the least

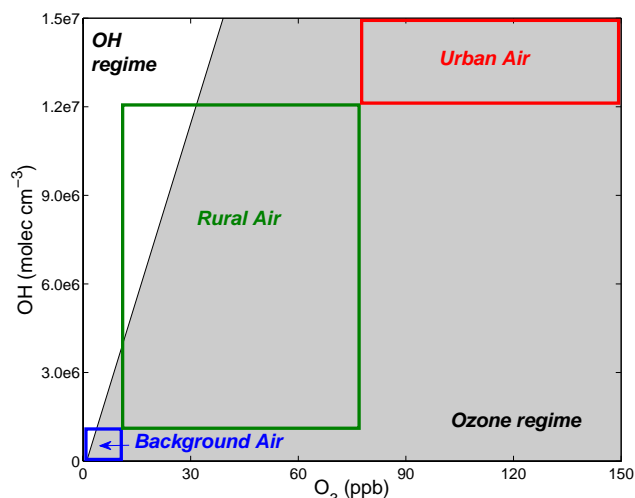


Fig. 12. Regimes of dominance of ozonolysis vs. OH oxidation of substituted dihydrofuran. Daily maximum OH concentrations vary by regions in the troposphere, i.e., 10^5 – 10^6 molecules cm^{-3} for background air, 10^6 – 10^7 molecules cm^{-3} for rural air, and $>10^7$ molecules cm^{-3} for urban air, with a global average concentration of 1×10^6 molecules cm^{-3} . Daily average surface ozone mixing ratios in rural areas are between 10 and 50 ppb, but these can exceed 100 ppb in polluted urban areas.

OH exposure but the largest O_3 and RH exposure). A clear trend observed from the van Krevelen plot is that O:C increases, whereas H:C decreases under elevated O_3 and RH levels. The effect of ozonolysis of substituted dihydrofuran chemistry on the aerosol chemical composition can be evaluated by comparing OS_C (O:C vs. H:C) for these four experiments under the same OH exposure. Consistent with our findings in $f_{\text{CO}_2^+} - f_{\text{C}_2\text{H}_3\text{O}^+}$ space, the highest OS_C is observed under the highest O_3 exposure and RH level, but lowest OH exposure (98% substituted dihydrofuran reacts with O_3 at 55% RH). With the same OH exposure, e.g., 1.5×10^7 molecules cm^{-3} h, the average carbon oxidation state increases from -1.36 in O_3 -limiting environments (Exp. 1) to -1.25 in O_3 -dominant environments (Exp. 5). In conclusion, ozonolysis of substituted dihydrofuran plays an important role in the formation of highly oxidized aerosol in alkane SOA.

4.5 Experiment and model comparison

Figure 10 shows the temporal profiles of CIMS measured ions in (+/–) mode, with structures proposed in Table 2, together with the corresponding model predictions under conditions of Exp. 2. In general, four time-dependent growth patterns are observed in experiments, which are also captured by model predictions. “Pattern 1” denotes species with rapid removal pathways, e.g., m/z 301 (–), with a proposed structure of δ -hydroxycarbonyl. In the current mechanism, the overall heterogeneous conversion rate of δ -hydroxycarbonyl

to substituted dihydrofuran is taken as $3 \times 10^{-3} \text{ s}^{-1}$. The model output is consistent with the observed time-dependent trend when this rate is used. Up to $\sim 90\%$ of m/z 301 (–) is consumed due to this rapid heterogeneous reaction pathway at 3% RH after 18 h of photooxidation. “Pattern 2” is indicative of a species that also reacts rapidly, but with a much slower consumption rate than species of pattern 1. A typical example here is m/z 183 (+), which represents the alkyl-substituted dihydrofuran. The reaction rate constants of alkyl-substituted dihydrofuran with either OH or O_3 are at least an order of magnitude higher than the generic reaction rate constant for the OH abstraction reaction, which is the dominant gas-phase pathway in the dodecane photooxidation mechanism. The simulated peak occurs ~ 2 h earlier than observations, indicating that the formation rate of alkyl-substituted dihydrofuran might be slower than the decay rate of its precursor, δ -hydroxycarbonyl, considering that fact that the acid-catalyzed dehydration process in the particle phase is the rate-limiting step. The extent to which the formation rate is slower than the decay rate, however, is unknown since the measurement of rate constants for individual steps is infeasible in this study. “Pattern 3” reflects the temporal profiles for a majority of ions here, e.g., m/z 328(–), 299(–), 249(–), 315(–), and 332(–). Compounds proposed for the above m/z can be categorized as semivolatile products. In the gas phase, they undergo functionalization or fragmentation, or partition into the particle phase as the precursors of SOA. Overall, the temporal profiles of species in pattern 3 are governed by the progressive photochemistry in the gas phase and gas–particle equilibrium partitioning. “Pattern 4”, including m/z 346 (–) and 328 (–) here, represents “non-volatile” species. Owing to their low volatilities, they will immediately partition to the particle phase once formed and the gas-phase photooxidation becomes negligible, although it might still occur via the OH attack on C atoms.

Figure 11a shows the simulated SOA growth (SIM.1) using the initial conditions in Exp. 2, together with the observed total organic aerosol mass as a function of reaction time and OH exposure. The model reproduces the chamber measured SOA yield at 3% RH when the conversion rate of $3 \times 10^{-3} \text{ s}^{-1}$ is employed to represent the heterogeneous conversion of δ -hydroxycarbonyl to dihydrofuran. A second simulation (SIM.2) was run with the complete dihydrofuran chemistry removed while other parameters were held constant. The total organic mass is $\sim 42\%$ higher as a result after 18 h of photooxidation. The formation of alkyl-substituted dihydrofuran from δ -hydroxycarbonyl is accompanied by an increase of vapor pressure from 5.36×10^{-7} to 1.08×10^{-4} atm at 300 K, as predicted by SIMPOL.1, and the total organic mass formed decreases. Although the addition of OH to the C=C double bond in the substituted dihydrofuran introduces an extra OH group, the decrease of vapor pressure owing to the addition of one OH group does not compensate for the heterogeneous conversion of both $-\text{C}=\text{O}$ and $-\text{OH}$ groups in δ -hydroxycarbonyl to an $-\text{O}-$ group in

a nonaromatic ring in dihydrofuran. The predicted average carbon oxidation state is ~ 7 – 15 % higher than observations. The overprediction is within the uncertainties in the O : C (31 %) and H : C (10 %) measurement by AMS (Aiken et al., 2008). Incorporation of the substituted dihydrofuran formation and removal pathways in the model leads to an increase in the simulated OS_C . Compared with compounds produced from dodecane photooxidation under high- NO_x conditions, products from dihydrofuran chemistry tend to have a higher O : C but lower H : C due to the formation of ether, ester, and carboxylic acid functional groups. As a result, the calculated average carbon oxidation state is higher in the presence of chemical reactions that accelerate the aerosol aging process.

5 Atmospheric implications

The importance of ozone in the SOA formation from the photooxidation of long-chain alkanes under atmospherically relevant conditions depends on two factors: (1) the relative concentration of O_3 vs. OH, and (2) the heterogeneous conversion rate of δ -hydroxycarbonyls to substituted dihydrofurans. Figure 12 shows regimes of ozonolysis vs. OH oxidation of substituted dihydrofuran corresponding to ranges of OH and O_3 concentrations. The OH-initiated oxidation of substituted dihydrofuran is predicted to dominate only under remote atmospheric conditions. Most alkane emissions occur in areas where ozone levels exceed 10 ppb, where the ozonolysis of dihydrofuran should be dominant.

Under conditions of the current study, the substituted dihydrofuran chemistry is predicted to account for > 95 % of the removal pathways of δ -hydroxycarbonyl (Fig. 1d (H)) and up to ~ 80 % of the total organic mass formed from dodecane photooxidation (Fig. 11b). This estimate sets the upper limit in terms of the contribution of substituted dihydrofuran chemistry to alkane SOA production in the actual atmosphere, where the RH is higher (50 % vs. 3 %), the ambient aerosols are less acidic, and the organic aerosol masses are lower ($\sim 10 \mu\text{g m}^{-3}$) than in the chamber experiments ($\sim 50 \mu\text{g m}^{-3}$ after 3 h of irradiation). Experimental evidence in this study shows that the heterogeneous conversion still occurs at 50 % RH, but with less efficiency (Fig. 3). The water vapor abundance at 50 % RH, however, compensates for the production of the less substituted dihydrofuran, leading to an eventually higher yield of carboxylic acids (Sect. 4.4). If the conversion of δ -hydroxycarbonyl to substituted dihydrofuran occurs efficiently in the atmosphere, this could be a source of carboxylic acid in the ambient aerosols. It has been suggested that the heterogeneous formation of substituted dihydrofuran is acid-catalyzed (Atkinson et al., 2008; Lim and Ziemann, 2009a, b, c). Aerosols generated in the chamber environment in the presence of NO_x are expected to be highly acidic due to the formation of HNO_3 . In the atmosphere, where ambient particles are less acidic or even neu-

tralized, the heterogeneous conversion of δ -hydroxycarbonyl to substituted dihydrofuran might be a minor process.

In summary, two impacts of substituted dihydrofuran chemistry on alkane SOA formation are expected. First, the SOA yield from the photooxidation of long-chain alkanes can be overpredicted without accounting for substituted dihydrofuran formation and removal pathways. Second, a substantial amount of carboxylic acid, ester, and tetrahydrofuran moieties can be produced, leading to higher O : C but much lower H : C ratios, and thus a higher oxidation state of alkane SOA in general. In this manner, the dihydrofuran chemistry can be considered as a “dehydration” channel in alkane SOA formation.

Supplementary material related to this article is available online at <http://www.atmos-chem-phys.net/14/1733/2014/acp-14-1733-2014-supplement.pdf>.

Acknowledgements. This work was supported by National Science Foundation grant AGS-1057183.

Edited by: A. Laskin

References

- Aiken, A. C., DeCarlo, P. F., and Jimenez, J. L.: Elemental analysis of organic species with electron ionization high-resolution mass spectrometry, *Anal. Chem.*, 79, 8350–8358, doi:10.1021/ac071150w, 2007.
- Aiken, A. C., Decarlo, P. F., Kroll, J. H., Worsnop, D. R., Huffman, J. A., Docherty, K. S., Ulbrich, I. M., Mohr, C., Kimmel, J. R., Sueper, D., Sun, Y., Zhang, Q., Trimborn, A., Northway, M., Ziemann, P. J., Canagaratna, M. R., Onasch, T. B., Alfarra, M. R., Prevot, A. S. H., Dommen, J., Duplissy, J., Metzger, A., Baltensperger, U., and Jimenez, J. L.: O/C and OM/OC ratios of primary, secondary, and ambient organic aerosols with high-resolution time-of-flight aerosol mass spectrometry, *Environ. Sci. Technol.*, 42, 4478–4485, 2008.
- Alfarra, M. R., Coe, H., Allan, J. D., Bower, K. N., Boudries, H., Canagaratna, M. R., Jimenez, J. L., Jayne, J. T., Garforth, A. A., Li, S. M., and Worsnop, D. R.: Characterization of urban and rural organic particulate in the lower Fraser valley using two Aerodyne aerosol mass spectrometers, *Atmos. Environ.*, 38, 5745–5758, 2004.
- Arey, J., Aschmann, S. M., Kwok, E. S. C., and Atkinson, R.: Alkyl nitrate, hydroxyalkyl nitrate, and hydroxycarbonyl formation from the NO_x -air photooxidations of C_5 – C_8 n-alkanes, *J. Phys. Chem. A.*, 105, 1020–1027, 2001.
- Atkinson, R., Arey, J., and Aschmann, S. M.: Atmospheric chemistry of alkanes: Review and recent developments, *Atmos. Environ.*, 42, 5859–5871, 2008.
- Aumont, B., Valorso, R., Mouchel-Vallon, C., Camredon, M., Lee-Taylor, J., and Madronich, S.: Modeling SOA formation from the oxidation of intermediate volatility n-alkanes, *Atmos. Chem. Phys.*, 12, 7577–7589, doi:10.5194/acp-12-7577-2012, 2012.

- Aumont, B., Camredon, M., Mouchel-Vallon, C., La, S., Ouzebidour, F., Valorso, R., Lee-Taylor, J., and Madronich, S.: Modeling the influence of alkane molecular structure on secondary organic aerosol formation, *Faraday Discuss.*, 165, 1–16, 2013.
- Bloss, C., Wagner, V., Jenkin, M. E., Volkamer, R., Bloss, W. J., Lee, J. D., Heard, D. E., Wirtz, K., Martín-Reviejo, M., Rea, G., Wenger, J. C., and Pilling, M. J.: Development of a detailed chemical mechanism (MCMv3.1) for the atmospheric oxidation of aromatic hydrocarbons, *Atmos. Chem. Phys.*, 5, 641–664, doi:10.5194/acp-5-641-2005, 2005.
- Canagaratna, M. R., Jayne, J. T., Jimenez, J. L., Allan, J. D., Alfarra, M. R., Zhang, Q., Onasch, T. B., Drewnick, F., Coe, H., Middlebrook, A., Delia, A., Williams, L. R., Trimborn, A. M., Northway, M. J., DeCarlo, P. F., Kolb, C. E., Davidovits, P., and Worsnop, D. R.: Chemical and microphysical characterization of ambient aerosols with the Aerodyne aerosol mass spectrometer, *Mass Spectrom. Rev.*, 26, 185–222, 2007.
- Cappa, C. D., Zhang, X., Loza, C. L., Craven, J. S., Yee, L. D., and Seinfeld, J. H.: Application of the Statistical Oxidation Model (SOM) to Secondary Organic Aerosol formation from photooxidation of C12 alkanes, *Atmos. Chem. Phys.*, 13, 1591–1606, doi:10.5194/acp-13-1591-2013, 2013.
- Cavalli, F., Barnes, I., and Becker, K. H.: FTIR kinetic, product, and modeling study of the OH-initiated oxidation of 1-butanol in air, *Environ. Sci. Technol.*, 36, 1263–1270, 2000.
- Chhabra, P. S., Ng, N. L., Canagaratna, M. R., Corrigan, A. L., Russell, L. M., Worsnop, D. R., Flagan, R. C., and Seinfeld, J. H.: Elemental composition and oxidation of chamber organic aerosol, *Atmos. Chem. Phys.*, 11, 8827–8845, doi:10.5194/acp-11-8827-2011, 2011.
- Craven, J. S., Yee, L. D., Ng, N. L., Canagaratna, M. R., Loza, C. L., Schilling, K. A., Yatavelli, R. L. N., Thornton, J. A., Ziemann, P. J., Flagan, R. C., and Seinfeld, J. H.: Analysis of secondary organic aerosol formation and aging using positive matrix factorization of high-resolution aerosol mass spectra: application to the dodecane low-NO_x system, *Atmos. Chem. Phys.*, 12, 11795–11817, doi:10.5194/acp-12-11795-2012, 2012.
- Crouse, J. D., McKinney, K. A., Kwan, A. J., and Wennberg, P. O.: Measurement of gas-phase hydroperoxides by chemical ionization mass spectrometry, *Anal. Chem.*, 78, 6726–6732, 2006.
- DeCarlo, P. F., Kimmel, J. R., Trimborn, A., Northway, M. J., Jayne, J. T., Aiken, A. C., Gonin, M., Fuhrer, K., Horvath, T., Docherty, K. S., Worsnop, D. R., and Jimenez, J. L.: Field-deployable, high-resolution, time-of-flight aerosol mass spectrometer, *Anal. Chem.*, 78, 8281–8289, 2006.
- Fraser, M. P., Cass, G. R., Simoneit, B. R. T., Rasmussen, R. A.: Air quality model evaluation data for organics. 4. C₂-C₃₆ non-aromatic hydrocarbons, *Environ. Sci. Technol.*, 31, 2356–2367, 1997.
- Gentner, D. R., Isaacman, G., Worton, D. R., Chan, A. W. H., Dallmann, T. R., Davis, L., Liu, S., Day, D. A., Russell, L. M., Wilson, K. R., Weber, R., Guha, A., Harley, R. A., and Goldstein, A. H.: Elucidating secondary organic aerosol from diesel and gasoline vehicles through detailed characterization of organic carbon emissions, *P. Natl. Acad. Sci. USA*, 109, 18318–18323, 2012.
- Gong, H. M., Matsunaga, A., and Ziemann, P. J.: Products and mechanism of secondary organic aerosol formation from reactions of linear alkenes with NO₃ radicals, *J. Phys. Chem. A*, 109, 4312–4324, 2005.
- Hoekman, S. K.: Speciated measurements and calculated reactivities of vehicle exhaust emissions from conventional and reformulated gasolines, *Environ. Sci. Technol.*, 26, 1206–1216, 1992.
- Holt, T., Atkinson, R., and Arey, J.: Effect of water vapor concentration on the conversion of a series of 1,4-dihydroxycarbonyls to dihydrofurans, *J. Photochem. Photobiol. A: Chem.*, 176, 231–237, 2005.
- Jathar, S. H., Miracolo, M. A., Tkacik, D. S., Donahue, N. M., Adams, P. J., and Robinson, A. L.: Secondary Organic Aerosol Formation from Photo-Oxidation of Unburned Fuel: Experimental Results and Implications for Aerosol Formation from Combustion Emissions, *Environ. Sci. Technol.*, 47, 12886–12893, 2013.
- Jenkin, M. E., Shallcross, D. E., Harvey, J. H.: Development and application of a possible mechanism for the generation of *cis*-pinic acid from the ozonolysis of α - and β -pinene, *Atmos. Environ.*, 34, 2837–2850, 2000.
- Jenkin, M. E., Saunders, S. M., Wagner, V., and Pilling, M. J.: Protocol for the development of the Master Chemical Mechanism, MCM v3 (Part B): tropospheric degradation of aromatic volatile organic compounds, *Atmos. Chem. Phys.*, 3, 181–193, 2003, <http://www.atmos-chem-phys.net/3/181/2003/>.
- Jenkin, M. E.: Modelling the formation and composition of secondary organic aerosol from α - and β -pinene ozonolysis using MCM v3, *Atmos. Chem. Phys.*, 4, 1741–1757, doi:10.5194/acp-4-1741-2004, 2004.
- Jordan, C. E., Ziemann, P. J., Griffin, R. J., Lim, Y. B., Atkinson, R., and Arey, J.: Modeling SOA formation from OH reactions with C₈-C₁₇ n-alkanes, *Atmos. Environ.*, 42, 8015–8026, 2008.
- Isaacman, G., Chan, A. W. H., Nah, T., Worton, D. R., Ruehl, C. R., Wilson, K. R., and Goldstein, A. H.: Heterogeneous OH oxidation of motor oil particles causes selective depletion of branched and less cyclic hydrocarbons, *Environ. Sci. Technol.*, 46, 10632–10640, 2012.
- Kirchstetter, T. W., Singer, B. C., Harley, R. A., Kendall, G. R., and Traverse, M.: Impact of California reformulated gasoline on motor vehicle emissions. 1. Mass emission rates, *Environ. Sci. Technol.*, 33, 318–328, 1999.
- Kleinman, L. I., Springston, S. R., Daum, P. H., Lee, Y. N., Nunnermacker, L. J., Senum, G. I., Wang, J., Weinstein-Lloyd, J., Alexander, M. L., Hubbe, J., Ortega, J., Canagaratna, M. R., and Jayne, J.: The time evolution of aerosol composition over the Mexico City plateau, *Atmos. Chem. Phys.*, 8, 1559–1575, 2008, <http://www.atmos-chem-phys.net/8/1559/2008/>.
- Klotz, B., Barnes, I., and Imamura, T.: Product study of the gas-phase reactions of O₃, OH and NO₃ radicals with methyl vinyl ether, *Phys. Chem. Chem. Phys.*, 6, 1725–1734, 2004.
- Kroll, J. H., Smith, J. D., Che, D. L., Kessler, S. H., Worsnop, D. R., and Wilson, K. R.: Measurement of fragmentation and functionalization pathways in the heterogeneous oxidation of oxidized organic aerosol, *Phys. Chem. Chem. Phys.*, 11, 8005–8014, 2009.
- Kroll, J. H., Donahue, N. M., Jimenez, J. L., Kessler, S. H., Canagaratna, M. R., Wilson, K. R., Altieri, K. E., Mazzoleni, L. R., Wozniak, A. S., Bluhm, H., Mysak, E. R., Smith, J. D., Charles, E. K., and Worsnop, D. R.: Carbon oxidation state as a metric for describing the chemistry of atmospheric organic aerosol, *Nature Chem.*, 3, 133–139, 2011.

- Lambe, A. T., Onasch, T. B., Croasdale, D. R., Wright, J. P., Martin, A. T., Franklin, J. P., Massoli, P., Kroll, J. H., Canagaratna, M. R., Brune, W. H., Worsnop, D. R., and Davidovits, P.: Transitions from functionalization to fragmentation reactions of laboratory secondary organic aerosol (SOA) generated from the OH oxidation of alkanes precursors, *Environ. Sci. Technol.*, 46, 5430–5437, 2012.
- Lee, A. K. Y., Herckes, P., Leaitch, W. R., Macdonald, A. M., and Abbatt, J. P. D.: Aqueous OH oxidation of ambient organic aerosol and cloud water organics: Formation of highly oxidized products, *Geophys. Res. Lett.*, 38, L11805, doi:10.1029/2011GL047439, 2011.
- Lim, Y. B. and Ziemann, P. J.: Products and mechanism of secondary organic aerosol formation from reactions of n-alkanes with OH radicals in the presence of NO_x, *Environ. Sci. Technol.*, 39, 9229–9236, 2005.
- Lim, Y. B. and Ziemann, P. J.: Effects of molecular structure on aerosol yields from OH radical-initiated reactions of linear, branched, and cyclic alkanes in the presence of NO_x, *Environ. Sci. Technol.*, 43, 2328–2334, 2009a.
- Lim, Y. B. and Ziemann, P. J.: Chemistry of secondary organic aerosol formation from OH radical-initiated reactions of linear, branched, and cyclic alkanes in the presence of NO_x, *Aero. Sci. Technol.*, 43, 604–619, 2009b.
- Lim, Y. B. and Ziemann, P. J.: Kinetics of the heterogeneous conversion of 1,4-hydroxycarbonyls to cyclic hemiacetals and dihydrofurans on organic aerosol particles, *Phys. Chem. Chem. Phys.*, 11, 8029–8039, 2009c.
- Liu, S., Day, D. A., Shields, J. E., and Russell, L. M.: Ozone-driven daytime formation of secondary organic aerosol containing carboxylic acid groups and alkane groups, *Atmos. Chem. Phys.*, 11, 8321–8341, doi:10.5194/acp-11-8321-2011, 2011.
- Loza, C. L., Craven, J. S., Yee, L. D., Coggon, M. M., Schwantes, R. H., Shiraiwa, M., Zhang, X., Schilling, K. A., Ng, N. L., Canagaratna, M. R., Ziemann, P. J., Flagan, R. C., and Seinfeld, J. H.: Secondary organic aerosol yields of 12-carbon alkanes, *Atmos. Chem. Phys. Discuss.*, 13, 20677–20727, doi:10.5194/acpd-13-20677-2013, 2013.
- MathWorks, MATLAB, 2002.
- Martin, P., Tuazon, E. C., Aschmann, S. M., Arey, J., and Atkinson, R.: Formation and atmospheric reaction of 4,5-dihydro-2-methylfuran, *J. Phys. Chem. A*, 106, 11492–11501, 2002.
- Miracolo, M. A., Presto, A. A., Lambe, A. T., Hennigan, C. J., Donahue, N. M., Kroll, J. H., Worsnop, D. R., and Robinson, A. L.: Photooxidation of low-volatility organics found in motor vehicle emissions: production and chemical evolution of organic aerosol mass, *Environ. Sci. Technol.*, 44, 1638–1643, 2010.
- Miracolo, M. A., Hennigan, C. J., Ranjan, M., Nguyen, N. T., Gordon, T. D., Lipsky, E. M., Presto, A. A., Donahue, N. M., and Robinson, A. L.: Secondary aerosol formation from photochemical aging of aircraft exhaust in a smog chamber, *Atmos. Chem. Phys.*, 11, 4135–4147, doi:10.5194/acp-11-4135-2011, 2011.
- Ng, N. L., Canagaratna, M. R., Zhang, Q., Jimenez, J. L., Tian, J., Ulbrich, I. M., Kroll, J. H., Docherty, K. S., Chhabra, P. S., Bahreini, R., Murphy, S. M., Seinfeld, J. H., Hildebrandt, L., Donahue, N. M., DeCarlo, P. F., Lanz, V. A., Prévôt, A. S. H., Dinar, E., Rudich, Y., and Worsnop, D. R.: Organic aerosol components observed in Northern Hemispheric datasets from Aerosol Mass Spectrometry, *Atmos. Chem. Phys.*, 10, 4625–4641, doi:10.5194/acp-10-4625-2010, 2010.
- Ng, N. L., Canagaratna, M. R., Jimenez, J. L., Chhabra, P. S., Seinfeld, J. H., and Worsnop, D. R.: Changes in organic aerosol composition with aging inferred from aerosol mass spectra, *Atmos. Chem. Phys.*, 11, 6465–6474, doi:10.5194/acp-11-6465-2011, 2011.
- Pankow, J. F. and Asher, W. E.: SIMPOL.1: a simple group contribution method for predicting vapor pressures and enthalpies of vaporization of multifunctional organic compounds, *Atmos. Chem. Phys.*, 8, 2773–2796, doi:10.5194/acp-8-2773-2008, 2008.
- Paulot, F., Crounse, J. D., Kjaergaard, H. G., Kurten, A., St. Clair, J. M., Seinfeld, J. H., and Wennberg, P. O.: Unexpected epoxide formation in the gas-phase photooxidation of isoprene, *Science*, 325, 730–733, 2009.
- Presto, A. A., Miracolo, M. A., Kroll, J. H., Worsnop, D. R., Robinson, A. L., and Donahue, N. M.: Intermediate-volatility organic compounds: a potential source of ambient oxidized organic aerosol, *Environ. Sci. Technol.* 43, 4744–4749, 2009.
- Presto, A. A., Miracolo, M. A., Donahue, N. M., and Robinson, A. L.: Secondary organic aerosol formation from high-NO_x photooxidation of low volatility precursors: n-alkanes, *Environ. Sci. Technol.* 44, 2029–2034, 2010.
- Reisen, F., Aschmann, S. M., Atkinson, R., and Arey, J.: 1, 4-Hydroxycarbonyl products of the OH radical initiated reactions of C₅–C₈ n-alkanes in the presence of NO, *Environ. Sci. Technol.*, 39, 4447–4453, 2005.
- Robinson, A. L., Donahue, N. M., Shrivastava, M. K., Weitkamp, E. A., Sage, A. M., Grieshop, A. P., Lane, T. E., Pierce, J. R., and Pandis, S. N.: Rethinking organic aerosols: semivolatile emissions and photochemical aging, *Science*, 315, 1259–1262, 2007.
- Russell, L. M., Bahadur, R., and Ziemann, P. J.: Identifying organic aerosol sources by comparing functional group composition in chamber and atmospheric particles, *Proc. Natl. Acad. Sci.*, 108, 3516–3521, 2011.
- Sadezky, A., Chaimbault, P., Mellouki, A., Römpf, A., Winterhalter, R., Le Bras, G., and Moortgat, G. K.: Formation of secondary organic aerosol and oligomers from the ozonolysis of enol ethers, *Atmos. Chem. Phys.*, 6, 5009–5024, doi:10.5194/acp-6-5009-2006, 2006.
- Sander, S. P., Abbatt, J., Barker, J. R., Burkholder, J. B., Friedl, R. R., Golden, D. M., Huie, R. E., Kolb, C. E., J., K. M., Moortgat, G. K., Orkin, V. L., and Wine, P. H.: Chemical kinetics and photochemical data for use in atmospheric studies, Evaluation No. 17. JPL Publication 10-6, Jet Propulsion Laboratory, Pasadena, <http://jpldataeval.jpl.nasa.gov>, 2011.
- Saunders, S. M., Jenkin, M. E., Derwent, R. G., and Pilling, M. J.: Protocol for the development of the Master Chemical Mechanism, MCM v3 (Part A): tropospheric degradation of non-aromatic volatile organic compounds, *Atmos. Chem. Phys.*, 3, 161–180, doi:10.5194/acp-3-161-2003, 2003.
- Schauer, J. J., Kleeman, M. J., Gass, G. R., and Simoneit, B. R. T.: Measurement of emissions from air pollution sources. 2. C₁ through C₃₀ organic compounds from medium duty diesel trucks, *Environ. Sci. Technol.*, 33, 1578–1587, 1999.
- Schauer, J. J., Kleeman, M. J., Gass, G. R., and Simoneit, B. R. T.: Measurement of emissions from air pollution sources. 5. C₁–

- C₃₂ organic compounds from gasoline-powered motor vehicles, *Environ. Sci. Technol.*, 33, 1578–1587, 1999.
- St. Clair, J. M., McCabe, D. C., Crounse, J. D., Steiner, U., and Wennberg, P. O.: Chemical ionization tandem mass spectrometer for the in situ measurement of methyl hydrogen peroxide, *Rev. Sci. Instrum.*, 81, 094102, doi:10.1063/1.3480552, 2010.
- Thiault, G., Thévenet, R., Mellouki, A., and Le Bras, G.: OH and O₃ initiated oxidation of ethyl vinyl ether, *Phys. Chem. Chem. Phys.*, 4, 613–619, 2002.
- Tkacik, D. S., Presto, A. A., Donahue, N. M., Robinson, A. M.: Secondary organic aerosol formation from intermediate-volatility organic compounds: cyclic, linear, and branched alkanes, *Environ. Sci., Technol.*, 46, 8773–8781, 2012.
- Yee, L. D., Craven, J. S., Loza, C. L., Schilling, K. A., Ng, N. L., Canagaratna, M. R., Ziemann, P. J., Flagan, R. C., and Seinfeld, J. H.: Secondary organic aerosol formation from Low-NO_x photooxidation of dodecane: evolution of multi-generation gas-phase chemistry and aerosol composition, *J. Phys. Chem. A*, 116, 6211–6230, 2012.
- Zhang, X. and Seinfeld, J. H.: A functional group oxidation model (FGOM) for SOA formation and aging, *Atmos. Chem. Phys.*, 13, 5907–5926, doi:10.5194/acp-13-5907-2013, 2013.
- Zielinska, B., Sagebiel, J. C., Harshfield, G., Gertler, A. W., Pierson, W. R.: Volatile organic compounds up to C₂₀ emitted from motor vehicles, measurement methods, *Atmos. Environ.*, 30, 2269–2286, 1996.
- Ziemann, P. J. and Atkinson, R.: Kinetics, products, and mechanisms of secondary organic aerosol formation, *Chem. Soc. Rev.*, 41, 6582–6605, 2012.

Appendix L

Organic Aerosol Formation from the Reactive Uptake of Isoprene Epoxydiols (IEPOX) onto Non-Acidified Inorganic Seeds¹⁴

¹⁴ Reproduced by permission from “Organic aerosol formation from the reactive uptake of isoprene epoxydiols (IEPOX) onto non-acidified inorganic seeds” by T. B. Nguyen, M. M. Coggon, K. H. Bates, X. Zhang, R. H. Schwantes, K. A. Schilling, C. L. Loza, R. C. Flagan, P. O. Wennberg, and J. H. Seinfeld. *Atmos. Chem. Phys.* **2014**, *14*, 3497-3510.



Organic aerosol formation from the reactive uptake of isoprene epoxydiols (IEPOX) onto non-acidified inorganic seeds

T. B. Nguyen¹, M. M. Coggon², K. H. Bates², X. Zhang¹, R. H. Schwantes¹, K. A. Schilling², C. L. Loza^{2,*}, R. C. Flagan^{2,3}, P. O. Wennberg^{1,3}, and J. H. Seinfeld^{2,3}

¹Division of Geological and Planetary Sciences, California Institute of Technology, Pasadena, California, USA

²Division of Chemistry and Chemical Engineering, California Institute of Technology, Pasadena, California, USA

³Division of Engineering and Applied Science, California Institute of Technology, Pasadena, California, USA

*currently at: 3M Environmental Laboratory, 3M Center, Building 0260-05-N-17, St. Paul, Minnesota, USA

Correspondence to: T. Nguyen (tbn@caltech.edu)

Received: 10 October 2013 – Published in Atmos. Chem. Phys. Discuss.: 28 October 2013

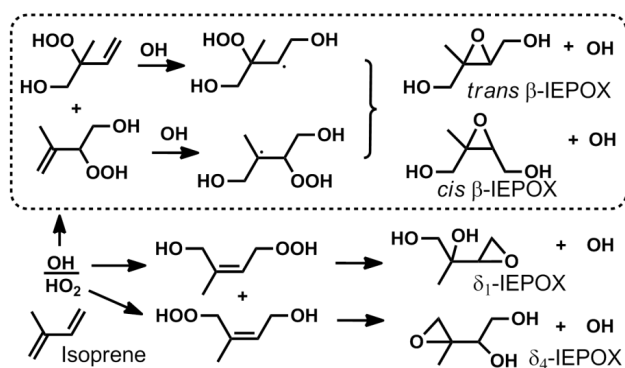
Revised: 8 February 2014 – Accepted: 18 February 2014 – Published: 8 April 2014

Abstract. The reactive partitioning of *cis* and *trans* β -IEPOX was investigated on hydrated inorganic seed particles, without the addition of acids. No organic aerosol (OA) formation was observed on dry ammonium sulfate (AS); however, prompt and efficient OA growth was observed for the *cis* and *trans* β -IEPOX on AS seeds at liquid water contents of 40–75 % of the total particle mass. OA formation from IEPOX is a kinetically limited process, thus the OA growth continues if there is a reservoir of gas-phase IEPOX. There appears to be no differences, within error, in the OA growth or composition attributable to the *cis*/*trans* isomeric structures. Reactive uptake of IEPOX onto hydrated AS seeds with added base (NaOH) also produced high OA loadings, suggesting the pH dependence for OA formation from IEPOX is weak for AS particles. No OA formation, after particle drying, was observed on seed particles where Na⁺ was substituted for NH₄⁺. The Henry's Law partitioning of IEPOX was measured on NaCl particles (ionic strength ~ 9 M) to be 3×10^7 M atm⁻¹ (–50/+100 %). A small quantity of OA was produced when NH₄⁺ was present in the particles, but the chloride (Cl⁻) anion was substituted for sulfate (SO₄²⁻), possibly suggesting differences in nucleophilic strength of the anions. Online time-of-flight aerosol mass spectrometry and offline filter analysis provide evidence of oxygenated hydrocarbons, organosulfates, and amines in the particle organic composition. The results are consistent with weak correlations between IEPOX-derived OA and particle acidity or liquid water observed in field studies, as the chemical system is nucleophile-limited and not limited in water or catalyst activity.

1 Introduction

A significant portion of the organic aerosol (OA) production from isoprene, a non-methane hydrocarbon emitted to the atmosphere in vast amounts, is attributed to the heterogeneous chemistry of isoprene epoxydiols (IEPOX) (Froyd et al., 2010; Chan et al., 2010; McNeill et al., 2012; Surratt et al., 2010; Hatch et al., 2011; Budisulistiorini et al., 2013; Pye et al., 2013). IEPOX, of which there are four isomeric forms (Scheme 1), is a second-generation low nitric oxide (NO) isoprene photooxidation product formed from the OH-oxidation of particular isomers of isoprene hydroxy hydroperoxides (Paulot et al., 2009b). The mechanism for OA production from IEPOX has been proposed as ring-opening of the epoxide group, activated by proton transfer from a strong acid such as sulfuric acid (H₂SO₄), followed by nucleophilic addition of available nucleophiles in the condensed phase, e.g., addition of water to produce tetrols, sulfate to produce organosulfates, and so on (Minerath et al., 2008; Eddingsaas et al., 2010; Surratt et al., 2010). This proposed mechanism has been corroborated by chamber investigations of particle acidity effects on OA formation (Surratt et al., 2007; Lin et al., 2012), wherein dry acidic seeds (MgSO₄ : H₂SO₄, 1 : 1) prompted strong reactive uptake behavior from epoxides (Paulot et al., 2009b), compared to negligible uptake for dry, non-acidified seeds.

Recent field data suggest that the story might be more complex than described above, as weak correlations between particle acidity and the abundance of IEPOX particle-phase tracer products were observed in Southeastern USA sites



Scheme 1 Formation of IEPOX isomers, from relevant isoprene hydroxy hydroperoxide precursors, in the low-NO photooxidation of isoprene. The expected dominant pathway is shown inside the box. The naming convention is based on Paulot et al. (2009b).

(Lin et al., 2013; Budisulistiorini et al., 2013). It should be noted that the indirect definition of “particle acidity,” which relies on charge balance of cations and anions, have several limitations and may not effectively represent the activity of H⁺ in the aqueous phase of particles in some cases (Greigore, 2013). Nevertheless, from the field observations, Lin and coworkers proposed that other factors may possibly modulate OA formation from IEPOX in conjunction with particle [H⁺]. One important distinction between previous chamber investigations, which have all been conducted under dry conditions (relative humidity, RH < 5%), and the Southeastern USA location is the prevalence of particle liquid water on the ammonium sulfate seeds. Water is a ubiquitous and abundant component of the atmosphere, therefore the effect of liquid water on the uptake of OA precursors has important implications for much of the globe. The crystalline ammonium sulfate seeds used in dry chamber experiments may not have adequate liquid water for IEPOX to partition into the aqueous phase, nor sufficient H⁺, NH₄⁺, and SO₄²⁻ activities to promote reactive uptake. Similarly, a particle with a large weight percent of H₂SO₄ may have a sizeable liquid water component, even at RH < 5%, due to the strong hygroscopicity of H₂SO₄ (Xiong et al., 1998), and the difference in reactive uptake of IEPOX may be due either to the differences in particle liquid water or the particle free acidity. In contrast, high concentrations of liquid water may cause dilution of aqueous ions, i.e., changing the acidity or ionic strength, which has been demonstrated to change the effective Henry’s Law partitioning coefficient of glyoxal (Kampf et al., 2013). Despite these important interactions, the effect of liquid water on OA formation from IEPOX has not been systematically explored in the laboratory.

We report here the reactive uptake of two isomers of IEPOX, the *cis* and *trans* β-IEPOX (Paulot et al., 2009b), which together comprise more than 97% of the isomer distribution (Bates et al., 2014). We synthesized authentic stan-

dards and observed the dark OA growth onto non-acidified and hydrated inorganic seeds at several particle liquid water concentrations. In the atmosphere, ammonium ions (NH₄⁺) are one of the most abundant components of aerosols and considerable IEPOX-derived OA are observed, even when a dominant portion of the aerosols are charge-balanced, e.g., [NH₄⁺]: 1/2 × [SO₄²⁻] or [NH₄⁺]: [NO₃⁻] ~ 1 (Lin et al., 2013). The aqueous NH₄⁺ may possibly act as catalyst for OA formation, as has been shown for a number of atmospherically important reactions (Noziere et al., 2009; Sareen et al., 2010; Ervens and Volkamer, 2010; Yu et al., 2011). We study reaction with NH₄⁺ as a potential rate-limiting mechanism for the IEPOX reaction. The role of cation and anion compositions in the seed for OA formation is studied by using ammonium sulfate, ammonium chloride, sodium sulfate, and sodium chloride seeds.

2 Materials and methods

2.1 Experimental procedures

This work utilized a newly constructed 24 m³ FEP Teflon environmental chamber specifically reserved for low-NO_x applications. The walls have not been in contact with strong acids and the chamber was operated in batch mode. Experiments were performed at room temperature (23–24 °C) and in the dark. Prior to the start of experiments, the chamber was thoroughly flushed with dry, purified air until particle concentrations are < 0.01 μg m⁻³. For humid experiments, water vapor was injected until the desired relative humidity (RH) was achieved in the chamber by flowing dry purified air over a Nafion membrane humidifier (FC200, Permapure LLC), which is kept moist by recirculating 27 °C ultrapurified (18 MΩ) water (Milli-Q, Millipore Corp). Temperature and RH were measured by a Vaisala HMM211 probe, calibrated with saturated salt solutions in the RH range of 11–95%. For RH < 11%, the water vapor content was quantified by chemical ionization mass spectrometry (Sect. 2.2.1).

Seed particles were injected by atomizing aqueous solutions (0.06 M) of ammonium sulfate ((NH₄)₂SO₄, AS), sodium chloride (NaCl), ammonium chloride (NH₄Cl), or sodium sulfate (Na₂SO₄) at 2100 hPa of air into the chamber through a ²¹⁰Po neutralizer and water trap. All inorganic seeds were injected through a 30 cm custom-built wet-wall denuder kept at 90 °C, such that the seed particles enter the chamber hydrated. Liquid water is expected to evaporate from the seed particles according to the salt’s efflorescence behavior (Lee and Hsu, 2000) at the RH of the chamber, e.g., in a dry chamber it is expected that the hydrated particles will enter the chamber fully dried. Particles were allowed to equilibrate until their volume concentrations are stable prior to organic injections.

Two isomers of isoprene epoxydiols (*cis* and *trans* β-IEPOX) were synthesized via procedures adapted from

Zhang et al. (2012) and purified with normal-phase column chromatography until the estimated purity based on nuclear magnetic resonance (NMR) of the *cis* and *trans* β -IEPOX isomers are 99 % and > 92 %, respectively. Details of the synthesis and NMR spectra are reported in Bates et al. (2014). Although the mole fractions of the impurities are low, their high volatility may lead to an over-represented abundance in the gas phase. For the *cis* isomer, we detected experimental interference from the volatile 1,4-dihydroxy-2-methyl-2-butene (a precursor used in the synthesis), comprising ~50 % of the vapor phase measured directly above a bulb of IEPOX droplets by chemical ionization mass spectrometry (CIMS, Sect. 2.2). In order to further purify before experiments were conducted, *cis* β -IEPOX droplets were purged with dry N_2 , and combined with 60 °C heating for > 8 h until the measured impurity fraction dropped below 2 % (Fig. S1 in the Supplement). After the additional purification, IEPOX was injected into the chamber by flowing a 5–8 L min⁻¹ stream of dry purified air past several droplets in a clean glass bulb heated to 60 °C for 2–4 h. The mixtures of IEPOX and seed aerosols were allowed to equilibrate for > 1 h. Most of the experimental conditions were repeated and were found to be reproducible within 15 %. We expect systematic error to dominate over the error of precision in this work.

2.2 Analytical methods

2.2.1 Chemical ionization mass spectrometry (CIMS)

Gas-phase IEPOX was measured with negative-ion chemical ionization mass spectrometry (CIMS) using CF_3O^- as the reagent ion, described in more detail previously (Crouse et al., 2006; Paulot et al., 2009a; St. Clair et al., 2010). The mass analyzer is a Varian triple-quadrupole spectrometer with unit mass resolution. Air is brought from the chamber using a 3 mm inner diameter perfluoroalkoxy (PFA) Teflon line with flow rate of 2.5 L min⁻¹. Of the total chamber flow, a 145 mL min⁻¹ analyte flow was sampled orthogonally through a glass critical orifice into the CIMS. The analyte flow was further diluted by a factor of 12 with dry N_2 to minimize the interaction of water vapor from the chamber with the reagent ion in the ion-molecule flow region. The subsequent data analysis corrects for the dilution factor. The operational pressure and temperature were kept at 35.5 hPa and 35 °C, respectively. The CIMS operated in a scanning MS mode (m/z 50–250) and tandem MS mode (MSMS). In MSMS mode, collisionally induced dissociation (CID) with 2.6 hPa of N_2 fragments analyte ions into product ions in the second quadrupole, following the ejection of neutral species. The MS cluster ion $C_5H_{10}O_3 \cdot CF_3O^-$ (m/z 203) of IEPOX was used for quantification, due to the higher signal-to-noise (S/N) of this ion compared to MSMS ions. The MSMS product ion $C_5H_9O_3 \cdot CF_2O^-$ (m/z 203 \rightarrow m/z 183), found to be unique to IEPOX in the isoprene OH-oxidation system, was used to differentiate IEPOX from the isobaric isoprene

hydroperoxide (ISOPOOH), which has been documented to yield mainly m/z 63 and a negligible amount of m/z 183 upon CID (Paulot et al., 2009b). ISOPOOH (m/z 203 \rightarrow m/z 63), was not expected, nor observed, during IEPOX injections.

CIMS calibrations of *cis* and *trans* β -IEPOX were performed by separately atomizing dilute (1–3 mM) solutions of each isomer with equimolar concentrations of hydroxyacetone, used as an internal standard, into the chamber through a 15 cm PFA Teflon transfer line for a few hours. During synthesis, NMR analysis showed that IEPOX was stable in water solution for many hours if no acid was present, so decay of IEPOX in the atomizer solution was not expected over the course of the calibration experiment. Toluene was used as a tracer to obtain the exact volume of the Teflon bag for each calibration experiment. A measured volume of toluene (6 μ L) was injected into a clean glass bulb with a microliter syringe (Hamilton) and quantitatively transferred into the chamber with a 5 L min⁻¹ stream of dry purified air. The gas-phase toluene was monitored by commercial gas chromatograph with flame-ionization detector (GC-FID, Hewlett-Packard 6890N) using a calibrated HP-5 column (15 m, 0.53 mm i.d.). The initial chamber temperature was 35 °C, and the temperature was ramped until 45 °C or until no increase of IEPOX signal was observed in the CIMS. The atomized solution was weighed before and after atomization. Each sensitivity determination was repeated at least twice. The sensitivities of the IEPOX isomers were calculated from the ratio of the normalized ion counts (with respect to the reagent ion signal) to the number of atomized moles. Small amounts of nucleated organic aerosols were observed in the chamber from the atomization, as measured by a scanning mobility particle sizer (Sect. 2.2.3) and that volume concentration was subtracted from the theoretical moles of IEPOX (corrections of < 1 %). Based on their calculated dipole moments and average polarizability, the *cis* isomer was expected to have a sensitivity of ~1.6 times greater than the *trans* isomer (Paulot et al., 2009b), and we found the sensitivity of the *cis* isomer to be a factor of 1.8 greater than the *trans* isomer in the MS mode. The difference between the two ratios is within the error of the sensitivity determination.

Additionally, several mixing ratios of water vapor were introduced into the CIMS ion-molecule region to measure the water dependence of the IEPOX detection. Water vapor was quantified by Fourier-transform infrared spectroscopy (FT-IR, Nicolet Magna-IR 560) with a 19 cm pathlength quartz cell. Spectral fitting was performed using the HITRAN spectral database (Rothman et al., 2009) and the nonlinear fitting software NLM4 developed by Griffith (1996). In the low-RH range, outside the calibration limit of the membrane RH probe, the CIMS water ions $H_2O \cdot ^{13}CF_3O^-$ (m/z 104) and $(H_2O)_2 \cdot CF_3O^-$ (m/z 121) were used to quantify water vapor concentration in the chamber after calibration of water vapor with FT-IR. These ions provide excellent sensitivity to water and linearity in the 20–3500 ppm range in the CIMS

ion molecule flow region (corresponding to 1–100 % RH in the chamber at 24 °C, before CIMS dilution). No water dependence in the detection of the IEPOX ions was observed within the range of water vapor observed by CIMS.

In order to quantify the gas-phase concentrations of IEPOX, the CIMS signal was corrected to account for the RH-dependent wall losses of IEPOX. The interactions of IEPOX with chamber walls have not been previously characterized, although those of its C₄ analog have been reported (Loza et al., 2010). IEPOX wall loss experiments were conducted at RH = 3 %, 46 %, and 69 %, as described in Section 2.1, continuously for 5–10 h. Figure S2 shows that the wall losses of IEPOX on non-acidic walls were negligibly small ($\sim 0.4\% \text{ h}^{-1}$ at RH 69 %), within the error of CIMS measurements.

2.2.2 Aerosol mass spectrometry (AMS)

Online particle composition was measured with a high-resolution time-of-flight aerosol mass spectrometer (ToF-AMS, Aerodyne Research Inc.). The ToF-AMS was operated in V mode ($R \sim 2000$ at m/z 200) and W mode ($R \sim 3000$ – 4000 at m/z 200). Prior to experiments, the ToF-AMS ionization efficiency was calibrated using size-selected 350 nm ammonium nitrate particles. The ToF-AMS monitored the content of ammonium (NH_4^+), sulfate (SO_4^{2-}) and other non-refractory ions throughout the course of the experiment. The ammonium to sulfate ratio did not change over the course of the experiment. Gas interferences and elemental ratios were calculated using the fragmentation tables developed by Allan et al. (2004) and Aiken et al. (2008). Data were analyzed in IGOR Pro 6.31 (WaveMetrics, Inc.) using the SQUIRREL v 1.51H and PIKA v 1.10H analysis toolkits. Total concentration of organics ($\mu\text{g m}^{-3}$) was calculated by summing the nitrate-equivalent masses of each high-resolution ion correlated with the organic fraction from the V-mode data.

Particles were sampled through a 130 cm Nafion membrane diffusion drier (MD-110, Permapure LLC) to avoid flow obstructions from wet particles over time, at a flow rate of 0.084 L min^{-1} . It is expected that drying the particles may introduce particle or organic line losses in the drier tube and change the particle bounce characteristics on the AMS vaporizer plate. These perturbations may be corrected by applying a collection-efficiency (CE) factor. It was demonstrated that organic aerosol particles with higher water content have very low bounce probability, which corresponds to a CE of unity (Matthew et al., 2008; Docherty et al., 2013). Comparatively, dry particles have much lower CE (~ 0.25 for pure, dry AS) due to the high bounce rate. The CE of IEPOX-derived organic aerosol-coated particles was calculated by measuring the mass concentrations of organics, sulfate, and ammonium of the wet particles without a drier, wherein CE was assumed to be unity and line losses assumed to be negligible, and comparing with measurements made through a drier. We observe a CE of 0.75 for all conditions in this work,

which is consistent with the collection efficiency of organic aerosols measured previously (Docherty et al., 2013). Further, it is expected that drying particles, relevant to the hydration/evaporation cycles of aerosols in nature, may lead to enhanced interactions between organic and inorganic compounds (De Haan et al., 2011; Nguyen et al., 2012), irreversibly forming OA.

2.2.3 Particle size and number concentration

Particle size and number concentrations were measured with a scanning mobility particle sizer (SMPS), comprised of a custom-built differential mobility analyzer (DMA) coupled to a commercial butanol-based condensation particle counter (CPC, TSI Inc.). The SMPS particle size measurement was calibrated with polystyrene latex (PSL) spheres. The particles entering the chamber have a static polydisperse distribution, with peak dry particle diameter distributions in the range of 50–100 nm. The sample air flow was not dried in humid experiments. Particle mass concentrations were corrected for RH- and size-dependent wall losses. The mass concentration of particles typically ranged from 65 – $90 \mu\text{g m}^{-3}$ for all experiments, using a particle density of 1.2 g cm^{-3} .

For AS-based experiments, the particle liquid water content was calculated based on the size-dependent hygroscopicity of AS (Biskos et al., 2006; Hu et al., 2010). For each particle diameter bin measured by SMPS, a theoretical dry diameter was calculated based on size-dependent literature growth factor data at the RH of the experiment. The difference in the wet (measured) and dry (calculated) integrated area of the mass distribution yielded the liquid water concentration in g m^{-3} . Similarly, the percent of liquid water content is calculated as $\% \text{ LWC} = 100\% \times (\text{V}_{\text{wet}} - \text{V}_{\text{dry}}) / \text{V}_{\text{wet}}$, using the predicted wet and dry diameters.

Particle wall loss characterizations were performed for AS seeds at RH = 3 %, 20 %, 50 %, and 80 % prior to the start of the experimental series to correctly quantify the mass concentrations of particles as a function of time. It was assumed that the loss rates of AS were representative for particles of different composition. Seed aerosols were atomized into the dry or humid chambers in the dark, allowed to stabilize, and particle size and number concentrations were measured for $> 12 \text{ h}$. The particle correction method that accounts for wall loss has been discussed in detail previously (Loza et al., 2012).

2.2.4 Filter collection and analysis

Offline OA composition analysis was performed by ultra-high performance liquid chromatography time-of-flight electrospray ionization mass spectrometry (UPLC/ESI-ToFMS). Aerosol samples were collected onto Teflon membrane filters (Millipore, $1 \mu\text{m}$ pore), pulled at a 20 L min^{-1} flow through an activated charcoal denuder to remove the volatile and semivolatile components. Each filter was extracted with

methanol (Fisher, Optima grade, $\geq 99.9\%$) by ultrasonication for 15 min in a 20 mL scintillation vial. The filtered extracts were blown dry under a gentle stream of ultra-high-purity N_2 . The residue was reconstituted with 150 μL of 50 : 50 v/v acetonitrile (Fisher Optima grade, $\geq 99.9\%$) and water (Milli-Q).

Extracts were analyzed by a Waters Xevo G2-S UPLC/ESI-ToF-MS equipped with an Acquity CSH C_{18} column (1.7 μm , 2.1×100 mm). The solvents used for gradient elution were acetonitrile (Fisher Optima grade, $\geq 99.9\%$) and water with a 0.1 % formic acid spike (solvent “A”). The flow rate was held at 0.5 mL min^{-1} . Accurate mass correction was completed by a lock spray of leucine enkephalin ($0.61 \text{ ng } \mu\text{L}^{-1}$ in 50 : 50 v/v acetonitrile/water with 0.1 % formic acid). The ESI source was operated in negative mode, where most analytes are ionized by deprotonation and measured as $[M-H]^-$. Ionic molecular formulas were determined from accurate masses (mass resolution of 60 000 at m/z 400) using the elemental composition tool in Mass Lynx. Control filters (no particles) and laboratory controls (seeds only) were analyzed in the same manner.

3 Results and Discussion

3.1 Reactive uptake of *cis* and *trans* β -IEPOX onto ammonium sulfate seeds

3.1.1 Liquid water content of seeds

Figure 1 shows the time profile for the organic aerosol (OA) growth corresponding to reactive uptake of the *trans* β -IEPOX onto ammonium sulfate (AS) seeds at two RH conditions, dry (LWC $\sim 0\%$) and RH 57 % (LWC $\sim 55\%$). The traces shown in Fig. 1 are representative of uptake behavior for both isomers on the experimental timescale. For RH conditions above the ammonium sulfate (AS) efflorescence point tested in this work ($E_{RH} \sim 35\%$, (Biskos et al., 2006)), prompt and efficient OA growth onto AS seeds was observed for both IEPOX isomers. No OA growth was observed when the AS seeds were dry, in good agreement with other reports (Lin et al., 2012, Surratt et al., 2010).

The OA growth from IEPOX did not halt after the end of the gas-phase injection period (Fig. 1, solid black line), even after periods of > 2 h (Fig. S3, top panel). This behavior is indicative of a non-equilibrium process, as the addition of nucleophiles is not reversible after the rate-limiting step of IEPOX activation (Eddingsaas et al., 2010). The formation of low-volatility compounds should continue as long as a reservoir of gas-phase IEPOX is available. The series of expected reactions leading to the formation of ring-opening products (ROP) is shown below, illustrated using a general proton donor (AH) and nucleophile (Nu).

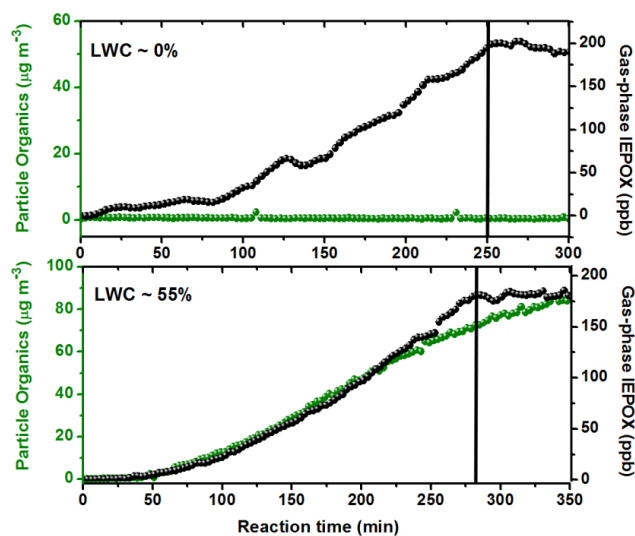
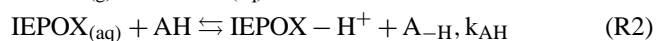
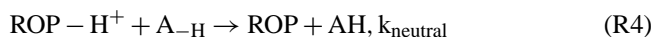
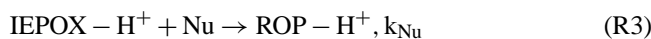


Fig. 1. Typical uptake experiment results as a function of time, shown for *trans* isomer, at dry (top) and humid (bottom) conditions with the corresponding percent of liquid water content (LWC). The solid black line indicates when IEPOX injection stopped and the mixture was allowed to equilibrate. Double y axes correspond to traces of the same color.



For a solution with low AH and Nu activity, the equilibrium accommodation of IEPOX into the aqueous phase, described by the Henry’s Law coefficient of IEPOX (K_H), can be measured in isolation. Henry’s Law may not be an appropriate description of the IEPOX reactive uptake experiments performed on the liquid water of suspended aerosols, as the aerosol water layers represent highly non-ideal solutions and the OA formation is kinetically limited. The OA formation mechanism may include contributions from reactions other than Reactions (1–4). To a first-order approximation, total OA mass formed from gas-phase reactive uptake of IEPOX will be a function of aqueous IEPOX concentration, nucleophile activity, and catalyst activity.

For the sake of comparison between experiments, it is useful to have a metric that includes the ratio of OA formed to gas-phase IEPOX injected and accounts for the variability in the size and number of injected seeds between experiments, which is reflected by the calculated aerosol water at different RH. We define here a reactive partitioning coefficient ($\Phi_{\text{OA}/\text{IEPOX}}$), calculated similarly to an effective Henry’s Law coefficient, and thus having the same units (Seinfeld and Pandis, 2006):

$$\Phi_{\text{OA}/\text{IEPOX}} = (C_{\text{OA}} / C_{\text{IEPOX}}) / [10^{-6} \cdot R \cdot T \cdot P_{\text{LWC}}], \quad (1)$$

where $(C_{\text{OA}} / C_{\text{IEPOX}})$ is the mass concentration ratio of the IEPOX-derived organic aerosol (dried), measured by ToF-AMS, and the gas-phase IEPOX, measured by negative-ion

Table 1. Summary of results from representative reactive uptake experiments onto ammonium sulfate seeds. Mean results from Lin et al. (2012) are shown for comparison.

Exp. index	IEPOX isomer	Seed composition	RH (%)	Particle pH*	Seed ($\mu\text{g m}^{-3}$)	P_{LWC} (g m^{-3})	$C_{\text{OA}}/C_{\text{IEPOX}}$	$\Phi_{\text{OA/IEPOX}}$ (M atm^{-1})
1	cis	$(\text{NH}_4)_2\text{SO}_4$	3	–	70	$<1 \times 10^{-6}$	5.04×10^{-4}	–
2	cis	$(\text{NH}_4)_2\text{SO}_4$	42	3.67	91	3.74×10^{-5}	0.102	1.15×10^8
3	cis	$(\text{NH}_4)_2\text{SO}_4$	50	3.74	92	4.79×10^{-5}	0.118	1.01×10^8
4	cis	$(\text{NH}_4)_2\text{SO}_4$	86	3.90	81	5.68×10^{-5}	0.179	4.00×10^7
5	trans	$(\text{NH}_4)_2\text{SO}_4$	2	–	65	$<1 \times 10^{-6}$	4.74×10^{-4}	–
6	trans	$(\text{NH}_4)_2\text{SO}_4$	39	3.65	82	3.44×10^{-5}	0.090	1.06×10^8
7	trans	$(\text{NH}_4)_2\text{SO}_4$	57	3.77	89	4.64×10^{-5}	0.095	8.44×10^7
8	trans	$(\text{NH}_4)_2\text{SO}_4$	81	3.88	88	6.14×10^{-5}	0.115	7.66×10^7
9	trans	$(\text{NH}_4)_2\text{SO}_4 + \text{NaOH}$, pH=7	70	~ 5.5	84	5.33×10^{-5}	0.090	6.89×10^7
Lin et al. (2012)	cis	$\text{MgSO}_4 + \text{H}_2\text{SO}_4$ (1 : 1)	<5	~ -10	48	$1.62 \times 10^{-5**}$	0.058	1.47×10^8

* Modeled pH using E-AIM and AIOMFAC models (the value from (Lin et al., 2012) is a_{molality} -based pH), see text (Sect. 3.1.2).

** Based on hygroscopicity of H_2SO_4 at RH 5 %, assumed growth factor 1.15, Xiong et al. (1998).

CIMS, P_{LWC} is the liquid water content of the inorganic aerosols prior to IEPOX introduction (g m^{-3}), R is the ideal gas constant ($\text{atm L mol}^{-1} \text{K}^{-1}$), T is the temperature (K), and 10^{-6} is a conversion factor ($\text{m}^3 \text{cm}^{-3}$). $\Phi_{\text{OA/IEPOX}}$ includes the contribution from Henry's Law equilibrium partitioning of IEPOX (Reaction R1), and thus is an upper limit for the effective Henry's Law constant.

We observe that $\Phi_{\text{OA/IEPOX}}$ was not time-dependent when both IEPOX and OA were increasing, as the ratio $C_{\text{OA}}/C_{\text{IEPOX}}$ stabilized when OA grew in response to gas-phase IEPOX (Fig. S3) but increased after IEPOX injection stopped. The stabilized ratio is used for $\Phi_{\text{OA/IEPOX}}$ calculations to compare between experiments. P_{LWC} did not have a significant time dependence due to a stable particle volume distribution before IEPOX gas-phase injections. The uncertainties in the accuracy of the $\Phi_{\text{OA/IEPOX}}$ and K_{H} measurements were estimated to be -50% and $+100\%$, compounded from the uncertainties in the calculated CIMS sensitivities, liquid water fraction, AMS organic mass determinations, and other measurements.

A summary of $\Phi_{\text{OA/IEPOX}}$ and other values is given in Table 1 for all AS-based uptake experiments. Figure 2 shows $\Phi_{\text{OA/IEPOX}}$, as a function of particle liquid water, for the *cis* and *trans* β -IEPOX uptake onto hydrated AS. A trend of decreasing $\Phi_{\text{OA/IEPOX}}$ with increasing LWC was reproducibly observed, despite the uncertainty range in the $\Phi_{\text{OA/IEPOX}}$ determinations. The suppression of $\Phi_{\text{OA/IEPOX}}$ as a function of added water is likely due to dilution. For example, high aerosol sulfate concentrations may cause a “salting-in” effect for IEPOX, or other water-soluble organic compounds (Kampf et al., 2013), which is inversely proportional to water content. Higher water may also reduce the $[\text{H}^+]$, although the dependence of the reaction on catalyst concentrations is not expected to be high. Additionally, higher P_{LWC} dilutes the aqueous IEPOX and nucleophile concentrations in the aerosol liquid water, which reduce the rate of the chemical reaction as these species are direct reagents. The dilution ef-

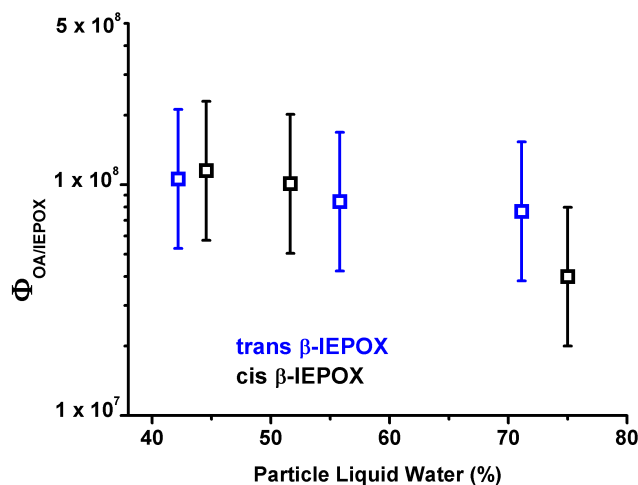


Fig. 2. Reactive partitioning coefficients ($\Phi_{\text{OA/IEPOX}}$) during the gas-phase IEPOX injection phase for the *trans* and *cis* isomers as a function of the particle liquid water concentration. Error bars indicate experimental uncertainty as described in the text.

fect from increasing the pure water fraction at a fixed ion content (moles of NH_4^+ and SO_4^{2-}) is in contrast to a modeled increase in OA mass in areas with high “anthropogenic water”, in other words, mixtures of water-soluble compounds found in urban regions (Carlton and Turpin, 2013). In the atmosphere, the partitioning of anthropogenic gases like NH_3 and SO_2 will simultaneously impact aqueous acidity and inorganic concentration and thus may lead to enhanced OA formation in areas with higher P_{LWC} .

3.1.2 Particle acidity

As the decrease of $\Phi_{\text{OA/IEPOX}}$ with increasing liquid water content may be due to more than one factor, an experiment was carried out to isolate the effect of pH. In experiment 9 (Table 1), the AS solution was neutralized with a strong base

(NaOH) until the atomizer solution reached pH = 7. Solutions of AS without additives had pH \sim 5.5 before atomization because, although no strong acid was present, H^+ is expected to be present in small quantities based on the dissociation equilibria of inorganics, such as the bisulfate/sulfate dissociation, and dissolution of CO_2 . An enhancement in the acidity of the particle may result from a smaller volume of water in the particle and/or through loss of NH_3 upon atomization. In the case of a fully hydrated AS particle, the pH in the particle is predicted to be pH \sim 4 using the E-AIM Model (Clegg et al., 1998), and modeled pH values in the particle for all AS-based experiments are shown in Table 1. As the pH values of the particles in this work are derived using inorganic models, the values obtained may include any uncertainties inherent in the models, including uncertainties in the gas/particle partitioning of NH_3 , hygroscopicity of salts, and/or acid dissociation equilibria. When the RH is below the deliquescence point of AS, the pH was estimated by calculating a concentration factor from the P_{LWC} at the lower RH. It is expected that atomization will also lead to slightly lower pH for the base-neutralized atomizer solution, so the particle may have pH < 7. However, adding NaOH above neutralization to counter this effect may induce side reactions such as base-catalyzed epoxide opening and OH^- nucleophilic addition (Solomons and Fryhle, 2004). NaOH is not explicitly treated in the E-AIM and AIOMFAC (Zuend et al., 2008) inorganic models, therefore, it was assumed that atomization of the AS + NaOH solution may lead to, at most, the same enhancement factor that occurred for the pH of the pure AS solutions.

Figure 3 shows that $\Phi_{OA/IEPOX}$ for the *trans* β -IEPOX + AS system decreases slightly as pH is increased, reaching a plateau above pH \sim 4. We note that any perceived change is within the error of the measurement, however, it is clear that the trend of $\Phi_{OA/IEPOX}$ with pH is minor. These results differ from those of Eddingsaas et al. (2010), who observed a linear increase of epoxide reaction rate with H^+ activity. Eddingsaas et al. (2010) used H_2SO_4/Na_2SO_4 solutions, and thus the differences in observations may be entirely due to the high NH_4^+ activity in the AS particles employed in this work. The data suggest that when $[H^+]$ is small, NH_4^+ may activate reactions leading to OA formation, similarly to its catalytic activity toward glyoxal (Noziere et al., 2009), methylglyoxal (Sareen et al., 2010), and other carbonyls (Nguyen et al., 2013; Bones et al., 2010). Interestingly, pH > 4 is the range where NH_4^+ catalysis is most efficient. This is demonstrated by a stable reactivity of the NH_4^+ -catalyzed reaction to generate brown carbon from limonene SOA at pH 4–9, but a sharp decline of reactivity below pH 4 (Nguyen et al., 2012). As the H^+ and NH_4^+ ions are reactive toward organics in low-moderate and moderate-high pH ranges, respectively, the resulting pH dependence may appear to be weak in AS-containing seeds. The dual reactivities of H^+ and NH_4^+ to-

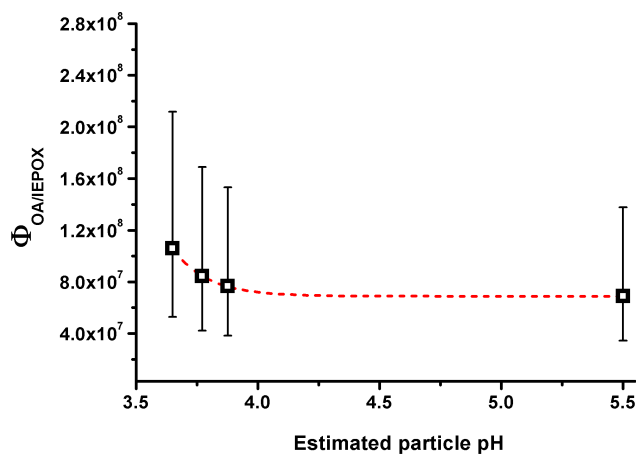


Fig. 3. $\Phi_{OA/IEPOX}$ for the *trans* β -IEPOX isomer as a function of the modeled particle pH.

ward IEPOX is expected to be important in nature, as NH_4^+ -based seeds are abundant.

In comparison, the $MgSO_4:H_2SO_4$ particles at RH < 5% in the work of Lin et al. (2012) are strongly acidic. These particles are predicted to have a non-negligible amount of water due to the large hygroscopicity of H_2SO_4 – and indeed, acidity in particles is not a useful concept if water is not present. At RH = 0–5%, pure H_2SO_4 particles have a growth factor of 1.1–1.2 (Xiong et al., 1998). Assuming a growth factor of 1.15, and taking into consideration the inorganic seed mass concentration, we calculated P_{LWC} for the mean results in Lin et al. (2012), shown in Table 1. The AIOMFAC Model (Zuend et al., 2008; Zuend et al., 2011) was used to estimate the pH based on the molal activity of H^+ in the $MgSO_4:H_2SO_4$ (1 : 1) particle. The calculated pH is \sim –10 and the corresponding mean $\Phi_{OA/IEPOX}$ is $\sim 1.5 \times 10^8$ M atm $^{-1}$ for *cis* β -IEPOX (the *trans* isomer was not studied). $\Phi_{OA/IEPOX}$ for the acidic $MgSO_4$ seeds is slightly higher than, but within the error of, the $\Phi_{OA/IEPOX}$ values for non-acidified AS seeds when a small amount of water is present (RH \sim 40%). This comparison is meant to be qualitative and subject to uncertainty because the experiments were not performed under the same conditions. Nevertheless, the comparison shows that a solution of high H^+ activity and a solution of high NH_4^+ activity may both lead to a relatively similar reactive uptake coefficient. As $[NH_4^+] \gg [H^+]$ in the particles in this work, a similar $\Phi_{OA/IEPOX}$ would also suggest that $k_{NH_4^+} \ll k_{H^+}$ if the observed rate coefficient for Reaction (2) is defined as $k_{obs} = k_{AH} \cdot [AH]$. Eddingsaas et al. (2010) estimated $k_{H^+} \sim 5 \times 10^{-2} M^{-1} s^{-1}$ and Cole-Filipiak et al. (2010) determined $k_{H^+} = 3.6 \times 10^{-2} M^{-1} s^{-1}$ for IEPOX.

3.2 Molecular picture of OA formation from IEPOX

3.2.1 Cation and anion substitutions

To further investigate the role of NH_4^+ in IEPOX ring-opening reactions at near-neutral conditions, NH_4^+ was replaced by a cation that cannot act as a proton donor (Na^+). As isomer structure appears to be unimportant for uptake, only the *trans* isomer was used for this portion of the study. Further, many nucleophiles present in the atmosphere are known to add to the protonated epoxide to give the beta-hydroxy ring-opening product, for example: H_2O (Solomons and Fryhle, 2004), SO_4^{2-} ions (Cavdar and Saracoglu, 2009), NH_3 or amines (Clayden et al., 2001), and halide ions (Clayden et al., 2001). Thus, SO_4^{2-} was substituted by Cl^- to study the anion (or nucleophile) effect.

Hydrated particles of AS ($(\text{NH}_4)_2\text{SO}_4$), sodium sulfate (Na_2SO_4), ammonium chloride (NH_4Cl), and sodium chloride (NaCl) were introduced into the chamber in separate experiments, followed by the introduction of *trans* β -IEPOX. The mixtures were allowed to equilibrate for 3.5–6 h. The RH range for these reactions is 60–85 %, chosen at a point well above their respective efflorescence RH (Martin, 2000), so that each seed would contain a considerable fraction of liquid water. The particle size distributions for each seed type were polydisperse and unimodal, with hydrated mobility diameters in the range of 15–600 nm and with 60–120 nm peak diameters. It is expected that the hydrated particles were spherical. The size-dependent hygroscopicities of AS and NaCl are well-studied, however, the calculations of liquid water content for other seed types are subject to error based on the method we described due to limited literature data. Therefore, we opt to present results based only on the $C_{\text{OA}}/C_{\text{IEPOX}}$ for the comparison of inorganic seed compositions.

OA formation after particle drying, as detected by ToF-AMS, is negligible for both sodium salts (NaCl and Na_2SO_4). The OA mass did not grow in response to the addition of IEPOX for the Na^+ -based particles (Fig. S4). Figure 4 shows the average stabilized ratios of OA formed with respect to *trans* β -IEPOX injected for the four inorganic salts used in this work. The atomizer solution pH for Na^+ -based seeds was also ~ 5.5 , a typical pH for a water solution in equilibrium with CO_2 (Reuss, 1977). The large difference in reactivity of IEPOX on Na_2SO_4 vs. $(\text{NH}_4)_2\text{SO}_4$ seeds may be attributed primarily to NH_4^+ activity, although there will be some differences in $[\text{H}^+]$ for the NH_4^+ -based and Na^+ -based seeds due to the slight dissociation of $\text{NH}_4^+ \rightleftharpoons \text{NH}_3$. Additionally, in light of the weak pH dependence for AS solutions, it appears likely that NH_4^+ activity is an important factor in suppressing OA formation on Na_2SO_4 seed particles. The results show that equilibrium partitioning of IEPOX, i.e., any condensed-phase mass formed from unreacted IEPOX, onto salty solutions is not competitive with reactive partitioning for OA formation.

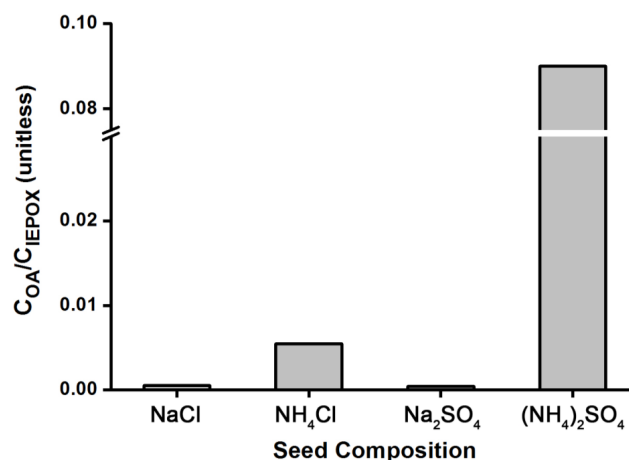


Fig. 4. Ratio of organic aerosol produced to gas-phase *trans* β -IEPOX injected for seeds of various compositions (RH 60–85 %).

For the ammonium salts, NH_4Cl produced an order of magnitude lower mean $C_{\text{OA}}/C_{\text{IEPOX}}$ ratio than $(\text{NH}_4)_2\text{SO}_4$, after an approximate 2h delay (Fig. S4). The modeled pH, using E-AIM, for both ammonium salt systems is similar (pH ~ 4 –4.5), and thus, the difference in reactivity may be attributed to the nucleophilic activity of Cl^- compared to SO_4^{2-} . Interestingly, Minerath et al. (2009) showed that acid-catalyzed ring-opening products of an epoxide with Cl^- may be more efficient than SO_4^{2-} . In that study, sulfuric acid was added to the NaCl + epoxide aqueous solution, which provide sulfate and bisulfate ions to the solution. Therefore, the results may not be directly comparable to this work. If Cl^- can be a good nucleophile in aqueous solutions of IEPOX when coupled with NH_4^+ catalysis, we may expect to observe organochloride products. There was no evidence of organochloride-derived accurate mass fragments in ToF-AMS data for the NH_4Cl reactive uptake organics. Further, gas-phase organochlorides were not observed by the CIMS. It is possible that organochlorides are produced but are easily hydrolyzed in the aerosol liquid water due to the relatively good leaving group ability of Cl^- , i.e., the hydrolysis behavior of organochlorides is more similar to that of tertiary organonitrates than that of organosulfates (Darer et al., 2011). It is also possible that organochlorides are preferentially evaporated in the diffusion drier because they might be more volatile than organosulfates or polyols. In both situations, but more so the latter, the total organic mass from the NH_4Cl experiments would be underestimated by ToF-AMS. Although we did not quantify tetrols and other polyols in this work, it is expected that they are present in substantial quantities because they are the thermodynamically preferred products in the epoxide ring-opening reactions.

3.2.2 Henry's Law constant

Although ToF-AMS did not observe OA formation for experiments using sodium salts (NaCl and Na₂SO₄) after particle drying, the wall-loss-corrected SMPS data (not dried) showed a minor and stable change in particle volume upon injection of IEPOX into the chamber with hydrated NaCl or Na₂SO₄ seeds (Fig. S5a, shown for NaCl). It is likely that the dissolved but unreacted IEPOX was removed from the condensed phase upon particle drying, which would lead to no observed OA mass in the ToF-AMS data throughout the duration of the experiment. The reversibility OA formation on the hydrated seeds indicates equilibrium-partitioning of IEPOX into the aerosol liquid water. The ratio of dissolved OA to injected IEPOX (Fig. S5b) reached a steady-state value at the end of the IEPOX injection period. Because NH₄⁺ is not present, and [H⁺] is not expected to be considerable in the aqueous phase, Reactions (R2) and (R4) are unimportant for this system. Further, in experiments using NaCl seeds, where the nucleophilicity of the solution is weaker, we are able to neglect the contribution of Reaction (R3), thereby isolating the equilibrium partitioning of IEPOX (Reaction R1).

We estimate the Henry's Law coefficient (K_H) for the equilibrium partitioning of IEPOX into a briny liquid (NaCl ~9 M ionic strength) representative of atmospheric aerosol to be 3×10^7 (−50/+100%) M atm^{−1}. The K_H in a solution of NaCl may be different than the value in pure water, due to complex aqueous interactions of Cl[−] and Na⁺ with water-soluble organics. As an example, the Henry's Law constant for glyoxal was measured to be $K_H = (4.19 \pm 0.87) \times 10^5$ M atm^{−1} in pure water, 1.90×10^6 M atm^{−1} in a 0.05 M NaCl solution, and 8.50×10^5 M atm^{−1} in a 4.0 M NaCl solution at 298 K (Ip et al., 2009). Ip et al. (2009) attributed the increase in K_H for NaCl solutions at low ionic strengths (compared to water) to hydrogen bonding interactions of Cl[−] and OH groups and the decrease at high ionic strength to a “salting-out” effect. The K_H value for IEPOX has not been experimentally determined in the past; however, the range of K_H has been estimated using the HENRYWIN model (EPA, 2008) by several studies. For example, Eddingsaas et al. (2010) estimated $K_H = 2.7 \times 10^6$ M atm^{−1} using a bond contribution method, and $K_H = 2.9 \times 10^{10}$ M atm^{−1} using a group contribution method in version 4.0 of the model. The empirical K_H value reported here is within range of both estimations – closer to the bond contribution method estimate. These results provide a critical constraint in the partitioning coefficient, significantly decreasing the error associated with using K_H in a quantitative manner (from 4 orders of magnitude to a factor of two).

3.2.3 Organic composition

A full analysis of the OA composition is outside the scope of this work. The reader is referred elsewhere for a discussion

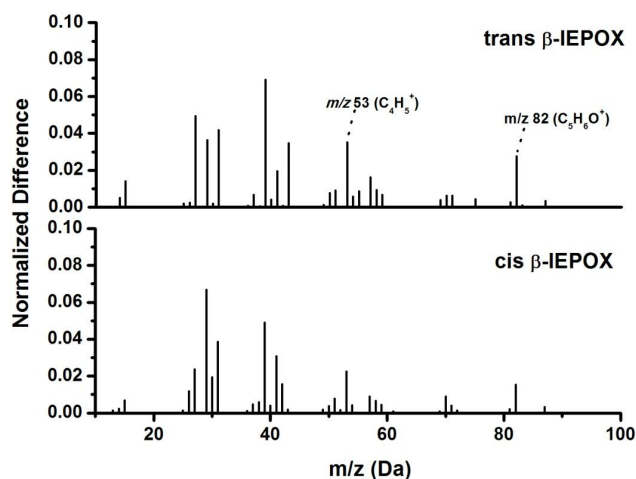


Fig. 5. ToF-AMS normalized difference spectra (composition at peak OA growth minus composition during seed injection), showing the organic composition of the OA produced by reactive uptake of the *trans* and *cis* isomers. Select nominal mass ions previously suggested to be IEPOX-derived OA tracers are labeled.

of the formation of oxygenated hydrocarbons, for example, tetrols and alkenetriols and organosulfates in the aqueous reaction of IEPOX catalyzed by acidic sulfate (Eddingsaas et al., 2010, Surratt et al., 2010). Although strong acid is absent in the systems studied in this work, we observe many similarities in the IEPOX-derived OA composition compared to the existing chamber and field results. For example, organosulfate products are abundant when hydrated AS seeds are used. The dominant ion observed in negative ion mode UPLC/ESI-ToFMS for AS uptake was C₅H₁₁SO₇[−] (Fig. S6), corresponding to the ring-opening trihydroxy organosulfate product of IEPOX. Derivatization was not performed in this work to detect tetrols. Organosulfate fragments were also observed in ToF-AMS (CSO family of fragments, not shown).

IEPOX-derived OA formed under near-neutral conditions in this work have ToF-AMS spectra similar to those of OA observed in the field. The suggested tracers for IEPOX-derived organics, m/z 53 (mostly C₄H₅⁺) and m/z 82 (mostly C₅H₆O⁺) (Lin et al., 2012, Robinson et al., 2011, Budisulistiorini et al., 2013), were observed in uptake experiments using both isomers. These mass fragments were proposed to originate from the electron-impact (EI) ionization of furan-derived molecules that were suggested to be formed from the acid-catalyzed rearrangement of IEPOX (Lin et al., 2013). Although mass fragments produced by EI may have multiple sources, in the pure system used in this study, m/z 82 was found to be a good tracer for IEPOX-derived OA. Figure 5 shows the difference between mass spectra at the end of the experiment and those at the time period prior to organic injection, corresponding to the organic fraction of the OA formed from the uptake of both isomers. The spectral ion distributions are very similar to each other

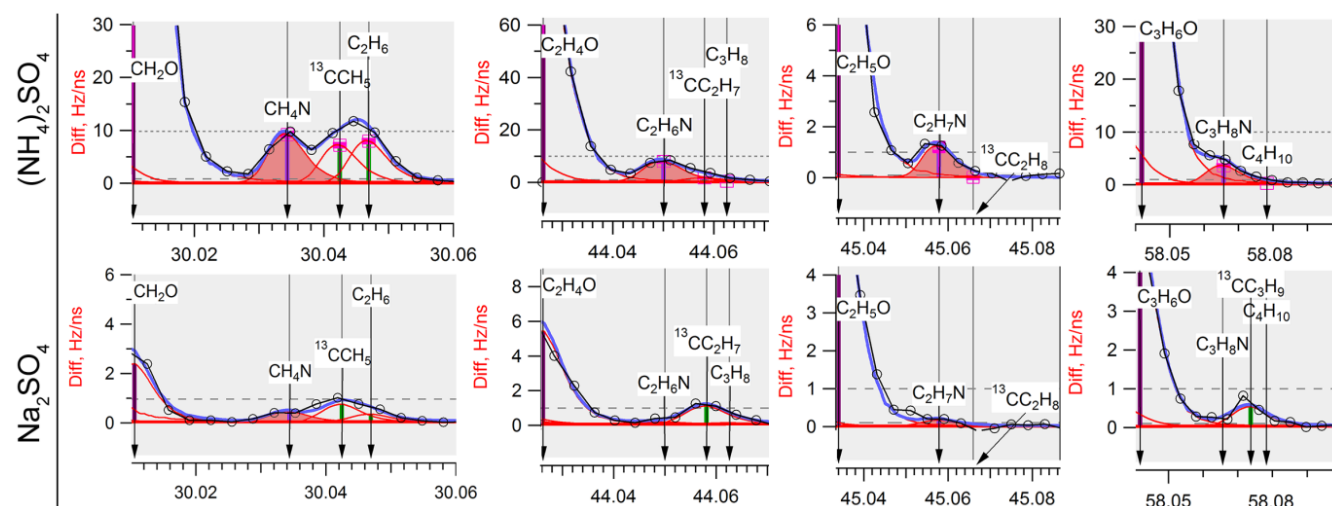


Fig. 6. ToF-AMS difference spectra (open minus closed chopper) showing organic nitrogen (amine) fragments from the reactive uptake of *trans* β -IEPOX onto AS vs. Na_2SO_4 seeds. Similar fragments were observed for *cis* β -IEPOX using NH_4^+ -based seeds and not observed in Na^+ -based seeds.

and m/z 53 and m/z 82 constituted a substantial fraction of the total ion intensity. The ion abundance of tracer fragments increased in accordance with the growth of OA mass (Fig. S7). As m/z 53 (C_4H_5^+) is a reduced fragment, it is also linked to hydrocarbon-like organics in chamber studies and may not be unique to IEPOX-derived OA. m/z 53 was observed in all experiments, including those that used Na^+ -based seeds. However, m/z 82 is abundant only when NH_4^+ -based seeds were used, supporting the suggestion that it can be formed through the EI fragmentation of an IEPOX-derived ring-opening product in ToF-AMS.

A unique aspect of the NH_4^+ -catalyzed ring-opening reaction of IEPOX is the minor possibility of nucleophilic addition by NH_3 , instead of reforming NH_4^+ after neutralizing the addition of another nucleophile. Figure 6 shows ion peaks for organic fragments containing C-N bonds observed in ToF-AMS data from the uptake of *trans* β -IEPOX onto AS vs. Na_2SO_4 seeds. The same C-N fragments were observed in *cis* β -IEPOX experiments using AS. These C-N fragments were not initially present in the AS seeds, and grow linearly following the introduction of IEPOX. Individual C-N fragments correlate well (Fig. S8, linear fit $R^2 = 0.69\text{--}0.88$) with the m/z 82 IEPOX-derived OA tracer fragment ($\text{C}_5\text{H}_6\text{O}^+$), suggesting that the reaction of IEPOX is responsible for the presence of these amines. Comparatively, C-N type fragments were negligible or non-existent in uptake experiments from Na^+ -based seeds. The identification of amines is tentative; however, to the best of our knowledge, this is the first suggestion of amine formation from IEPOX. As organic nitrogen compounds also give rise to non-nitrogenous mass fragments in ToF-AMS, it is not possible to estimate a mass concentration for the amines in this work. However, the C-N family of fragments comprised approximately 10% of the

$\text{C}_5\text{H}_6\text{O}^+$ signal, an indication that amine formation may not be negligible. The formation of organic nitrogen from the IEPOX + NH_4^+ reaction has important implications in the atmosphere as the ring-opening reaction of epoxides with amines should be more efficient than with NH_3 (Azizi and Saidi, 2005). Further investigations may provide more insight on the source of organic nitrogen from the atmospheric reactions of epoxides.

4 Summary and atmospheric implications

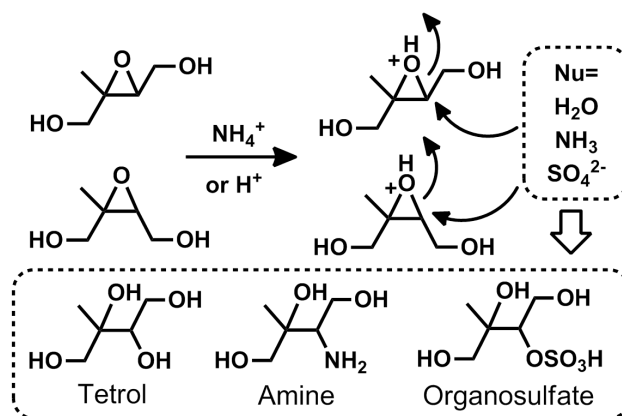
It was demonstrated here that the conversion of IEPOX to organic aerosol (OA) depends on the coupled relationship between the inorganic composition and liquid water content of the particle (P_{LWC}). The inorganic composition governs the catalyst and nucleophile characteristics, and P_{LWC} provides a reaction medium for the partitioning of IEPOX and controls the activities of all the aqueous components. The weak dependence on pH and the strong dependence on nucleophile activity and particle liquid water suggest that the IEPOX reactions in hydrated ammonium salts are nucleophile-limited, rather than catalyst-limited.

We showed that the equilibrium partitioning (Reaction 1) and the rate-limiting step of IEPOX activation (Reaction 2) do not proceed in the absence of liquid water; however, increasing the pure water content does not necessarily increase the reactive partitioning coefficient due to various dilution effects. When the inorganic particle is hydrated, the OA conversion is then determined by the catalyst and nucleophile activities. The rate of OA formation incorporates both Reactions (R2) and (R3), as illustrated by the cation and anion substitution case studies. In the hydrated Na_2SO_4 experiment, there was high activity of a relatively

good nucleophile, but a good catalyst was absent. Therefore, the formation of OA, i.e., the ring-opening product, was not observed because the equilibrium of Reaction (R2) favors IEPOX_(aq). The aqueous IEPOX mass that partitioned from the gas phase (K_H) onto the hydrated Na⁺-based seeds was removed from the condensed phase following the evaporation of water. In the hydrated NH₄Cl experiment, there was high activity of a good catalyst but possibly a poorer nucleophile than sulfate ion. A smaller quantity of OA formed because the rate of Reaction (R3) was slow, which was further supported by the observed 2 h delay in OA formation. Only when P_{LWC} , NH₄⁺ activity, and SO₄²⁻ activity are all significant, as in the case of hydrated (NH₄)₂SO₄ seeds, is the OA formation efficient and prompt. The OA mass formed from IEPOX uptake onto 1:1 MgSO₄:H₂SO₄ seeds (RH < 5 %) from previous studies may also be explained in terms of these conditions, as P_{LWC} (~30 %), catalyst (H⁺) activity and nucleophile (SO₄²⁻) activity were all sufficiently high in the particle.

In the atmosphere, relationships of water-soluble OA with P_{LWC} may be different and more difficult to interpret compared to laboratory studies because an increase in the P_{LWC} of atmospheric particles is often accompanied by the co-partitioning of water-soluble organic and inorganic compounds. The abundance of water-soluble organic compounds in the Southeast USA has been observed to be proportional to the liquid water contents of particles (Hennigan et al., 2008, 2009, Carlton and Turpin, 2013). In contrast, a weak correlation of modeled P_{LWC} with the abundance of IEPOX-derived OA tracers has also been observed, in the same geographical region (Budisulistiorini et al., 2013). The results of this work may not be directly comparable to field observations, however, they do not necessarily conflict. Particles may experience multiple hydration/evaporation cycles in the atmosphere, and the majority of particles likely contain liquid water at some point during their long lifetimes. The OA produced from IEPOX reactive uptake onto AS is irreversible (not removed from particle drying in this work), and depending on whether it had been sampled in the atmosphere before or after an evaporation cycle, the apparent correlation of IEPOX-derived OA with P_{LWC} would be different. Consequently, systematic studies in the laboratory are important for elucidating observations from the field.

Our results offer an alternate explanation to the abundance of IEPOX-derived OA tracers when the free H⁺ acidity in particles is modeled to be low (Lin et al., 2013). It has been suggested that the reason for the weak correlation with acidity is the reaction of an acidic seed particle with IEPOX to form organosulfates, which affects the particle acidity over time (Budisulistiorini et al., 2013). We show here that particle acidity does not appear to be important for the IEPOX + AS system if particle liquid water is present, in that highly acidic seeds and weakly acidic AS seeds both have high potential to form OA from IEPOX reactive partitioning. The apparent correlation between OA mass from IEPOX and P_{LWC} ,



Scheme 2 Addition of weak nucleophiles in the aqueous NH₄⁺ – and H⁺-catalyzed ring opening of IEPOX to form low-volatility organic compounds.

ammonium or acidity may be weak whenever water or catalyst concentrations are not limited; thus, in regions with high AS loading and RH, there should be a higher correlation with sulfate. This result would suggest that the OA formation process from IEPOX is insensitive to changes in the degree of neutralization of the particles in many AS-dominated areas, including the Southeast USA. The typical [NH₄⁺] is several orders of magnitude larger than [H⁺] in atmospheric particles, making it very likely to activate the IEPOX ring-opening reaction. Current models consider only H⁺ and HSO₄⁻ activity (McNeill et al., 2012, Pye et al., 2013), likely owing to the lack of experimental data describing the NH₄⁺-initiated reaction with IEPOX, for example, kinetic coefficients like $k_{NH_4^+}$. Future experimental and modeling studies should consider the NH₄⁺ activity of a particle, in addition to the H⁺ and HSO₄⁻ activity, for a more-accurate representation of OA formation from IEPOX.

An updated reaction mechanism appears in Scheme 2, in which NH₄⁺ and H⁺ are shown to donate a proton to the epoxide oxygen, followed by nucleophilic addition to form oxygenated hydrocarbons, ammonia (or amines), and organosulfates. The ability of NH₄⁺ to catalyze a nucleophilic addition reaction is not unprecedented, as NH₄⁺ can protonate aldehydes to facilitate nucleophilic addition (Noziere et al., 2009), and the high ring strain of an epoxide should provide an even greater thermodynamic motivation for the reaction. Indeed, due to the strain of epoxides, ring opening is chemically facile and may be promoted by a wide range of aqueous chemical species and conditions common in atmospheric aerosols, in addition to H⁺ and NH₄⁺. For example, Lewis acids such as iron (Fe³⁺) (Iranpoor and Salehi, 1994) and copper (Cu²⁺) (Muzart and Riahi, 1992) ions may be even stronger catalysts. Furthermore, the reaction may proceed with no added catalyst, for example, in the presence

of amines (Azizi and Saidi, 2005) or even hot water (60 °C) (Wang et al., 2008). The nucleophiles for these reactions may be water, amines or ammonia, thiols, sulfate ions, nitrate ion, halide ions, carboxylic acids, and alcohols (Iranpoor et al., 1996, Jacobsen et al., 1997, Clayden et al., 2001). Because of the diversity in the composition of atmospheric aerosols and fog/cloud droplets (Graedel and Weschler, 1981), the distribution of IEPOX-derived products in nature may be more complex and varied than currently believed.

Supplementary material related to this article is available online at <http://www.atmos-chem-phys.net/14/3497/2014/acp-14-3497-2014-supplement.pdf>.

Acknowledgements. This research was supported by the National Science Foundation (NSF) grants AGS-1057183 and AGS-1240604. TBN acknowledges funding from the NSF Postdoctoral Research Fellowship program, award AGS-1331360, and from the Foster and Coco Stanback Postdoctoral Fellowship. We are grateful for research support provided by the Brian Stoltz Group at Caltech for the syntheses of the β -IEPOX isomers, with special acknowledgement to Dr. Nathan Bennett. We thank Dr. Nathan Dalleska, director of the Caltech Environmental Analysis Center (EAC), for his assistance with the UPLC/ESI-ToFMS analyses.

Edited by: V. F. McNeill

References

- Aiken, A. C., Decarlo, P. F., Kroll, J. H., Worsnop, D. R., Huffman, J. A., Docherty, K. S., Ulbrich, I. M., Mohr, C., Kimmel, J. R., Sueper, D., Sun, Y., Zhang, Q., Trimborn, A., Northway, M., Ziemann, P. J., Canagaratna, M. R., Onasch, T. B., Alfarra, M. R., Prevot, A. S. H., Dommen, J., Duplissy, J., Metzger, A., Baltensperger, U., and Jimenez, J. L.: O/C and OM/OC ratios of primary, secondary, and ambient organic aerosols with high-resolution time-of-flight aerosol mass spectrometry, *Environ. Sci. Technol.*, 42, 4478–4485, 2008.
- Allan, J. D., Delia, A. E., Coe, H., Bower, K. N., Alfarra, M. R., Jimenez, J. L., Middlebrook, A. M., Drewnick, F., Onasch, T. B., and Canagaratna, M. R.: A generalised method for the extraction of chemically resolved mass spectra from aerodyne aerosol mass spectrometer data, *J. Aerosol. Sci.*, 35, 909–922, 2004.
- Azizi, N. and Saidi, M. R.: Highly chemoselective addition of amines to epoxides in water, *Org. Lett.*, 7, 3649–3651, 2005.
- Bates, K. H., Crounse, J. D., St. Clair, J. M., Bennett, N. B., Nguyen, T. B., Seinfeld, J. H., Stoltz, B. M., and Wennberg, P. O.: Gas phase production and loss of isoprene epoxydiols. *J. Phys. Chem. A*, 118, 1237–1246, doi:10.1021/jp4107958, 2014.
- Biskos, G., Paulsen, D., Russell, L. M., Buseck, P. R., and Martin, S. T.: Prompt deliquescence and efflorescence of aerosol nanoparticles, *Atmos. Chem. Phys.*, 6, 4633–4642, 10, <http://www.atmos-chem-phys.net/6/4633/10/5194/acp-6-4633-2006>, 2006.
- Bones, D. L., Henricksen, D. K., Mang, S. A., Gonsior, M., Bate-man, A. P., Nguyen, T. B., Cooper, W. J., and Nizkorodov, S. A.: Appearance of strong absorbers and fluorophores in limonene-O₃ secondary organic aerosol due to NH₄⁺-mediated chemical aging over long time scales, *J. Geophys. Res.*, 115, D05203, doi:10.1029/2009jd012864, 2010.
- Budisulistiorini, S. H., Canagaratna, M. R., Croteau, P. L., Marth, W. J., Baumann, K., Edgerton, E. S., Shaw, S. L., Knipping, E. M., Worsnop, D. R., Jayne, J. T., Gold, A., and Surratt, J. D.: Real-time continuous characterization of secondary organic aerosol derived from isoprene epoxydiols in downtown Atlanta, Georgia, using the Aerodyne aerosol chemical speciation monitor, *Environ. Sci. Technol.*, 47, 5686–5694, 2013.
- Carlton, A. G. and Turpin, B. J.: Particle partitioning potential of organic compounds is highest in the Eastern US and driven by anthropogenic water, *Atmos. Chem. Phys.*, 13, 10203–10214, doi:10.5194/acp-13-10203-2013, 2013.
- Cavdar, H., and Saracoglu, N.: Ring opening of epoxides with NaHSO₄: Isolation of β -hydroxy sulfate esters and an effective synthesis for trans-diols, *Tetrahedron*, 65, 985–989, 2009.
- Chan, M. N., Surratt, J. D., Claeys, M., Edgerton, E. S., Tanner, R. L., Shaw, S. L., Zheng, M., Knipping, E. M., Eddingsaas, N. C., Wennberg, P. O., and Seinfeld, J. H.: Characterization and quantification of isoprene-derived epoxydiols in ambient aerosol in the southeastern united states, *Environ. Sci. Technol.*, 44, 4590–4596, 2010.
- Clayden, J., Greeves, N., Warren, S., and Wothers, P.: *Organic chemistry*, Oxford University Press, 386 pp., ISBN 978-380-319-850346-850340, 2001.
- Clegg, S. L., Brimblecombe, P., and Wexler, A. S.: Thermodynamic model of the system H⁺–NH₄⁺–SO₄²⁻–NO₃–H₂O at tropospheric temperatures, *J. Phys. Chem. A*, 102, 2137–2154, 1998.
- Cole-Filipiak, N. C., O'Connor, A. E., and Elrod, M. J.: Kinetics of the hydrolysis of atmospherically relevant isoprene-derived hydroxy epoxides, *Environ. Sci. Technol.*, 44, 6718–6723, 2010.
- Crounse, J. D., McKinney, K. A., Kwan, A. J., and Wennberg, P. O.: Measurement of gas-phase hydroperoxides by chemical ionization mass spectrometry, *Anal. Chem.*, 78, 6726–6732, 2006.
- Darer, A. I., Cole-Filipiak, N. C., O'Connor, A. E., and Elrod, M. J.: Formation and stability of atmospherically relevant isoprene-derived organosulfates and organonitrates, *Environ. Sci. Technol.*, 45, 1895–1902, 2011.
- De Haan, D. O., Hawkins, L. N., Kononenko, J. A., Turley, J. J., Corrigan, A. L., Tolbert, M. A., and Jimenez, J. L.: Formation of nitrogen-containing oligomers by methylglyoxal and amines in simulated evaporating cloud droplets, *Environ. Sci. Technol.*, 45, 984–991, 2011.
- Docherty, K. S., Jaoui, M., Corse, E., Jimenez, J. L., Offenberg, J. H., Lewandowski, M., and Kleindienst, T. E.: Collection efficiency of the aerosol mass spectrometer for chamber-generated secondary organic aerosols, *Aerosol Sci. Technol.*, 47, 294–309, 2013.
- Eddingsaas, N. C., VanderVelde, D. G., and Wennberg, P. O.: Kinetics and products of the acid-catalyzed ring-opening of atmospherically relevant butyl epoxy alcohols, *J. Phys. Chem. A*, 114, 8106–8113, 2010.
- EPA: Estimation programs interface for microsoft windows xp v4.0, US EPA, 2008.
- Ervens, B. and Volkamer, R.: Glyoxal processing by aerosol multi-phase chemistry: towards a kinetic modeling framework of sec-

- ondary organic aerosol formation in aqueous particles, *Atmos. Chem. Phys.*, 10, 8219–8244, doi:10.5194/acp-10-8219-2010, 2010.
- Froyd, K. D., Murphy, S. M., Murphy, D. M., de Gouw, J. A., Eddingsaas, N. C., and Wennberg, P. O.: Contribution of isoprene-derived organosulfates to free tropospheric aerosol mass, *Proc. Natl. Acad. Sci.*, 107, 21360–21365, doi:10.1073/pnas.1012561107, 2010.
- Graedel, T. E. and Weschler, C. J.: Chemistry within aqueous atmospheric aerosols and raindrops, *Rev. Geophys.*, 19, 505–539, 1981.
- Gregoire, P.: Implications of ambient ammonia on aerosol acidity and reactive nitrogen measurements, MS, Department of Chemistry, University of Toronto, Toronto, Ontario, Canada, 82 pp., 2013.
- Griffith, D. W. T.: Synthetic calibration and quantitative analysis of gas-phase FT-IR spectra, *Appl. Spectrosc.*, 50, 59–70, 1996.
- Hatch, L. E., Creamean, J. M., Ault, A. P., Surratt, J. D., Chan, M. N., Seinfeld, J. H., Edgerton, E. S., Su, Y., and Prather, K. A.: Measurements of isoprene-derived organosulfates in ambient aerosols by aerosol time-of-flight mass spectrometry – Part 2: Temporal variability and formation mechanisms, *Environ. Sci. Technol.*, 45, 8648–8655, 2011.
- Hennigan, C. J., Bergin, M. H., Dibb, J. E., and Weber, R. J.: Enhanced secondary organic aerosol formation due to water uptake by fine particles, *Geophys. Res. Lett.*, 35, L18801, doi:10.1029/2008GL035046, 2008.
- Hennigan, C. J., Bergin, M. H., Russell, A. G., Nenes, A., and Weber, R. J.: Gas/particle partitioning of water-soluble organic aerosol in Atlanta, *Atmos. Chem. Phys.*, 9, 3613–3628, doi:10.5194/acp-9-3613-2009, 2009.
- Hu, D., Qiao, L., Chen, J., Ye, X., Yang, X., Cheng, T., and Fang, W.: Hygroscopicity of inorganic aerosols: Size and relative humidity effects on the growth factor, *Aerosol. Air. Qual. Res.*, 10, 255–264, 2010.
- Ip, H. S. S., Huang, X. H. H., and Yu, J. Z.: Effective Henry's law constants of glyoxal, glyoxylic acid, and glycolic acid, *Geophys. Res. Lett.*, 36, L01802, doi:10.1029/2008gl036212, 2009.
- Iranpoor, N. and Salehi, P.: Highly efficient, regio- and stereoselective alcoholysis of epoxides catalyzed with iron (iii) chloride, *Synthesis*, 1994, 1152–1154, 1994.
- Iranpoor, N., Tarrian, T., and Movahedi, Z.: FeCl₃ · 6H₂O supported on SiO₂ catalysed ring opening of epoxides with alcohols, acetic acid, water, chloride, bromide and nitrate ions, *Synthesis*, 1996, 1473–1476, 1996.
- Jacobsen, E. N., Kakiuchi, F., Konsler, R. G., Larrow, J. F., and Tokunaga, M.: Enantioselective catalytic ring opening of epoxides with carboxylic acids, *Tetrahedron Lett.*, 38, 773–776, 1997.
- Kampf, C. J., Waxman, E. M., Slowik, J. G., Dommen, J., Pfaffenberger, L., Praplan, A. P., Prévôt, A. S. H., Baltensperger, U., Hoffmann, T., and Volkamer, R.: Effective Henry's law partitioning and the salting constant of glyoxal in aerosols containing sulfate, *Environ. Sci. Technol.*, 47, 4236–4244, 2013.
- Lee, C.-T. and Hsu, W.-C.: The measurement of liquid water mass associated with collected hygroscopic particles, *J. Aerosol. Sci.*, 31, 189–197, 2000.
- Lin, Y.-H., Zhang, Z., Docherty, K. S., Zhang, H., Budisulistiorini, S. H., Rubitschun, C. L., Shaw, S. L., Knipping, E. M., Edgerton, E. S., Kleindienst, T. E., Gold, A., and Surratt, J. D.: Isoprene epoxydiols as precursors to secondary organic aerosol formation: Acid-catalyzed reactive uptake studies with authentic compounds, *Environ. Sci. Technol.*, 46, 250–258, 2012.
- Lin, Y.-H., Knipping, E. M., Edgerton, E. S., Shaw, S. L., and Surratt, J. D.: Investigating the influences of SO₂ and NH₃ levels on isoprene-derived secondary organic aerosol formation using conditional sampling approaches, *Atmos. Chem. Phys.*, 13, 8457–8470, doi:10.5194/acp-13-8457-2013, 2013.
- Loza, C. L., Chan, A. W. H., Galloway, M. M., Keutsch, F. N., Flagan, R. C., and Seinfeld, J. H.: Characterization of vapor wall loss in laboratory chambers, *Environ. Sci. Technol.*, 44, 5074–5078, 2010.
- Loza, C. L., Chhabra, P. S., Yee, L. D., Craven, J. S., Flagan, R. C., and Seinfeld, J. H.: Chemical aging of m-xylene secondary organic aerosol: laboratory chamber study, *Atmos. Chem. Phys.*, 12, 151–167, doi:10.5194/acp-12-151-2012, 2012.
- Martin, S. T.: Phase transitions of aqueous atmospheric particles, *Chem. Rev.*, 100, 3403–3453, 2000.
- Matthew, B. M., Middlebrook, A. M., and Onasch, T. B.: Collection efficiencies in an Aerodyne aerosol mass spectrometer as a function of particle phase for laboratory generated aerosols, *Aerosol. Sci. Technol.*, 42, 884–898, 2008.
- McNeill, V. F., Woo, J. L., Kim, D. D., Schwier, A. N., Wannell, N. J., Sumner, A. J., and Barakat, J. M.: Aqueous-phase secondary organic aerosol and organosulfate formation in atmospheric aerosols: A modeling study, *Environ. Sci. Technol.*, 46, 8075–8081, 2012.
- Minerath, E. C., Casale, M. T., and Elrod, M. J.: Kinetics feasibility study of alcohol sulfate esterification reactions in tropospheric aerosols, *Environ. Sci. Technol.*, 42, 4410–4415, 2008.
- Minerath, E. C., Schultz, M. P., and Elrod, M. J.: Kinetics of the reactions of isoprene-derived epoxides in model tropospheric aerosol solutions, *Environ. Sci. Technol.*, 43, 8133–8139, 2009.
- Muzart, J. and Riahi, A.: Palladium- and light-enhanced ring-opening of oxiranes by copper chloride, *J. Organomet. Chem.*, 433, 323–336, 1992.
- Nguyen, T. B., Lee, P. B., Updyke, K. M., Bones, D. L., Laskin, J., Laskin, A., and Nizkorodov, S. A.: Formation of nitrogen- and sulfur-containing light-absorbing compounds accelerated by evaporation of water from secondary organic aerosols, *J. Geophys. Res.*, 117, D01207, doi:10.1029/2021JD016944, 2012.
- Nguyen, T. B., Laskin, A., Laskin, J., Nizkorodov, S. A.: Brown carbon formation from ketoaldehydes of biogenic monoterpenes, *Faraday Discuss.*, 165, 473–494, 2013.
- Noziere, B., Dziedzic, P., and Cordova, A.: Products and kinetics of the liquid-phase reaction of glyoxal catalyzed by ammonium ions (NH₄⁺), *J. Phys. Chem. A*, 113, 231–237, 2009.
- Paulot, F., Crounse, J. D., Kjaergaard, H. G., Kroll, J. H., Seinfeld, J. H., and Wennberg, P. O.: Isoprene photooxidation: new insights into the production of acids and organic nitrates, *Atmos. Chem. Phys.*, 9, 1479–1501, doi:10.5194/acp-9-1479-2009, 2009a.
- Paulot, F., Crounse, J. D., Kjaergaard, H. G., Kurten, A., St. Clair, J. M., Seinfeld, J. H., and Wennberg, P. O.: Unexpected epoxide formation in the gas-phase photooxidation of isoprene, *Science*, 325, 730–733, 2009b.
- Pye, H. O. T., Pinder, R. W., Piletic, I. R., Xie, Y., Capps, S. L., Lin, Y.-H., Surratt, J. D., Zhang, Z., Gold, A., Luecken, D. J., Hutzell, W. T., Jaoui, M., Offenberg, J. H., Kleindienst, T. E., Lewandowski, M., and Edney, E. O.: Epoxide pathways improve

- model predictions of isoprene markers and reveal key role of acidity in aerosol formation. *Environ. Sci. Technol.*, 47, 11056–11064, 2013.
- Reuss, J.: Chemical and biological relationships relevant to the effect of acid rainfall on the soil-plant system, *Water Air Soil Pollut.*, 7, 461–478, 1977.
- Robinson, N. H., Hamilton, J. F., Allan, J. D., Langford, B., Oram, D. E., Chen, Q., Docherty, K., Farmer, D. K., Jimenez, J. L., Ward, M. W., Hewitt, C. N., Barley, M. H., Jenkin, M. E., Rickard, A. R., Martin, S. T., McFiggans, G., and Coe, H.: Evidence for a significant proportion of Secondary Organic Aerosol from isoprene above a maritime tropical forest, *Atmos. Chem. Phys.*, 11, 1039–1050, doi:10.5194/acp-11-1039-2011, 2011.
- Rothman, L. S., Gordon, I. E., Barbe, A., Benner, D. C., Bernath, P. F., Birk, M., Boudon, V., Brown, L. R., Campargue, A., and Champion, J.-P.: The HITRAN 2008 molecular spectroscopic database, *J. Quant. Spectrosc. Rad. Transf.*, 110, 533–572, 2009.
- Sareen, N., Schwier, A. N., Shapiro, E. L., Mitroo, D., and McNeill, V. F.: Secondary organic material formed by methylglyoxal in aqueous aerosol mimics, *Atmos. Chem. Phys.*, 10, 997–1016, doi:10.5194/acp-10-997-2010, 2010.
- Seinfeld, J. H. and Pandis, S. N.: *Atmospheric chemistry and physics: From air pollution to climate change*, Wiley, 2006.
- Solomons, T. W. G. and Fryhle, C. B.: *Organic chemistry*, 8 ed., John Wiley & Sons, Inc., Hoboken, NJ, 1255 pp., 2004.
- St. Clair, J. M., McCabe, D. C., Crouse, J. D., Steiner, U., and Wennberg, P. O.: Chemical ionization tandem mass spectrometer for the in situ measurement of methyl hydrogen peroxide, *Rev. Sci. Instrum.*, 81, 094102–094106, 2010.
- Surratt, J., Chan, A. W. H., Eddingsaas, N. C., Chan, M., Loza, C. L., Kwan, A. J., Hersey, S. P., Flagan, R. C., Wennberg, P. O., and Seinfeld, J. H.: Reactive intermediates revealed in secondary organic aerosol formation from isoprene, *Proc. Natl. Acad. Sci.*, 107, 6640–6645, 2010.
- Surratt, J. D., Lewandowski, M., Offenberg, J. H., Jaoui, M., Kleindienst, T. E., Edney, E. O., and Seinfeld, J. H.: Effect of acidity on secondary organic aerosol formation from isoprene, *Environ. Sci. Technol.*, 41, 5363–5369, 2007.
- Wang, Z., Cui, Y.-T., Xu, Z.-B., and Qu, J.: Hot water-promoted ring-opening of epoxides and aziridines by water and other nucleophiles, *J. Org. Chem.*, 73, 2270–2274, 2008.
- Xiong, J. Q., Zhong, M., Fang, C., Chen, L. C., and Lippmann, M.: Influence of organic films on the hygroscopicity of ultrafine sulfuric acid aerosol, *Environ. Sci. Technol.*, 32, 3536–3541, 1998.
- Yu, G., Bayer, A. R., Galloway, M. M., Korshavn, K. J., Fry, C. G., and Keutsch, F. N.: Glyoxal in aqueous ammonium sulfate solutions: Products, kinetics and hydration effects, *Environ. Sci. Technol.*, 45, 6336–6342, 2011.
- Zhang, Z., Lin, Y. H., Zhang, H., Surratt, J. D., Ball, L. M., and Gold, A.: Technical note: Synthesis of isoprene atmospheric oxidation products: Isomeric epoxydiols and the rearrangement products cis- and trans-3-methyl-3,4-dihydroxytetrahydrofuran, *Atmos. Chem. Phys.*, 12, 8529–8535, doi:10.5194/acp-12-8529-2012, 2012.
- Zuend, A., Marcolli, C., Luo, B. P., and Peter, T.: A thermodynamic model of mixed organic-inorganic aerosols to predict activity coefficients, *Atmos. Chem. Phys.*, 8, 4559–4593, doi:10.5194/acp-8-4559-2008, 2008.
- Zuend, A., Marcolli, C., Booth, A. M., Lienhard, D. M., Soonsin, V., Krieger, U. K., Topping, D. O., McFiggans, G., Peter, T., and Seinfeld, J. H.: New and extended parameterization of the thermodynamic model aiomfac: Calculation of activity coefficients for organic-inorganic mixtures containing carboxyl, hydroxyl, carbonyl, ether, ester, alkenyl, alkyl, and aromatic functional groups, *Atmos. Chem. Phys.*, 11, 9155–9206, doi:10.5194/acp-11-9155-2011, 2011.

Appendix M

A Chemically Relevant Artificial Fingerprint Material for the Cross Comparison of Mass Spectrometry Techniques¹⁵

¹⁵ Reproduced by permission from “A Chemically Relevant Artificial Fingerprint Material for the Cross Comparison of Mass Spectrometry Techniques” by E. R. Sisco, J. Staymates, and K. Schilling, Submitted to *Foren. Sci. Intl.*

A Chemically Relevant Artificial Fingerprint Material for the Cross Comparison of Mass Spectrometry Techniques

Edward Sisco^{a,*}, Jessica Staymates^a, Katherine Schilling^b

^aNational Institute of Standards and Technology
Materials Measurement Science Division
100 Bureau Drive
Gaithersburg, MD, 20899 USA

E-mail / Phone: edward.sisco@nist.gov / +1-301-975-2093
E-mail / Phone: jessica.staymates@nist.gov / +1-301-975-5436

^bDivision of Chemistry and Chemical Engineering
California Institute of Technology
Pasadena, CA, 91125 USA

E-mail: kschilling@caltech.edu

* Corresponding Author

Research was conducted at the National Institute of Standards & Technology

Acknowledgements: The authors would like to thank Matthew Staymates for his work on the artificial fingerprint stamp. This work was supported by the Science and Technology Explosives Division of the U.S. Department of Homeland Security under interagency agreement HSHQDC-12-X-0024 with the National Institute of Standards and Technology.

Disclaimer: Certain commercial equipment, instruments, or materials are identified in this document. Such identification does not imply recommendation or endorsement by the National Institute of Standards and Technology, nor does it imply that the products identified are necessarily the best available for the purpose.

Abstract

The development of a chemically relevant artificial fingerprint material as well as a preliminary method for artificial fingerprint deposition for mass spectrometric analysis and chemical imaging is presented. The material is an emulsified combination of artificial eccrine and sebaceous components designed to mimic the chemical profile of a latent fingerprint. In order to deposit this material in a manner that resembles a latent fingerprint, an artificial fingerprint stamp, created using 3-D printing, was used. Development of this material was spurred by the inability to cross-compare mass spectrometric techniques using real fingerprint deposits because of their inherent heterogeneity. To determine how well this material mimicked the chemical composition of actual fingerprint deposits, ambient ionization mass spectrometry and secondary ion mass spectrometry techniques were used to compare the signatures of the artificial and real fingerprint deposits. Chemical imaging comparisons of the artificial fingerprints across different imaging platforms are also presented as well a comparison using fingerprint development agents. The use of a material such as this may provide a way to compare the capabilities of different techniques in analyzing a sample as complex as a fingerprint as well as providing a method to create fingerprints with controlled amounts of exogenous material for research and technique validation purposes.

Keywords

Latent Fingerprints, Mass Spectrometry, Chemical Imaging

Introduction

Fingerprint analysis in a forensic setting has traditionally focused on understanding the structure and formation of fingerprint ridges, as well as establishing methods for the cross-comparison of fingerprint deposits. Additionally, research has also focused on how to locate invisible, or latent, fingerprints and make them visible using various developing agents. However, with the recent proliferation of sophisticated analytical techniques into the forensic science community, the chemical structure and makeup of latent fingerprint deposits has begun to be investigated [1–7]. One pitfall of evaluating and cross-comparing the techniques that study the chemical make-up of fingerprint deposits is the inherent variability in the chemical signature from one individual to another. Chemical signatures of an individual's fingerprint have been shown to be altered by factors such as diet, gender, age, medical conditions, application of cosmetics or lotion, and frequency of hand washing [1,2,7–10]. Because of this variability, as the chemical makeup of fingerprint deposits is probed further, and more techniques are developed to understand the chemistry in the deposits, there is a need to establish a fingerprint deposit with a known and reproducible chemical makeup. Furthermore, when it is of interest to examine fingerprints contaminated with potentially hazardous material, such as explosives and narcotics, an artificial fingerprint would allow for mitigation of hazards from direct contact by providing a method to create artificial fingerprints doped with these hazardous materials.

Though fingerprint deposits do vary amongst the population and even the individual, there are a number of components, and classes of components that are found in a large majority of fingerprints. Fingerprint deposits are generally composed of two different types of secretions – eccrine and sebaceous[2]. Eccrine secretions, also known as sweat, are secreted by the eccrine glands, located on the fingers and palms of the hands, and have been found to contain 98 % to 99

% water by mass [1,2]. The additional 1 % to 2 % by mass of the eccrine excretion has been found to contain numerous inorganic and organic compounds. Major groups within these classes of compounds include inorganic salts, amino acids, and proteins [1,2,10,11]. Other trace compound classes which are found in eccrine secretions include lipids, enzymes, immunoglobins, and vitamins as well as pharmaceuticals and metabolites [12–14]. Over four hundred individual compounds have been identified and associated with the eccrine secretions [2].

The second major type of secretion present in a fingerprint is the sebaceous secretion, also known as sebum. Sebum is secreted by the sebaceous glands located next to hair follicles [4]. Sebum components are commonly broken down into five classes of organic components: glycerides and free fatty acids, wax esters, cholesterol, squalene, and cholesterol esters [1,2]. Free fatty acids and glycerides are the most abundant component of sebum in adults, accounting for over 50 % by mass. Squalene, cholesterol, and cholesterol esters are found at lower weight percentages, typically below 10 % by mass, in adults but can have significantly higher proportions in the sebum of children. Additional, trace level components in sebaceous secretions include compounds such as phospholipids, alkanes, piperidines, and ketones [1,2,5,15,16].

Since the composition of a fingerprint deposit is variable and can contain hundreds of different compounds and salts, it would be extremely difficult to replicate the entire chemical composition of such a material. However, as the chemical composition of these deposits are probed and evaluated by a number of different analytical techniques, there is currently no way to accurately cross-compare techniques. Therefore, the material discussed herein aims to provide an artificial deposit which can be used to evaluate and cross-compare techniques using a

reproducible material with a composition that is known – instead of relying on actual fingerprint deposits of unknown chemical makeup.

Areas of research which can be explored using this material include providing a standard platform for the cross-comparison of chemical imaging techniques, understanding the chemical changes in fingerprints as a function of time and environment, determining the chemical processes responsible for visualization of latent fingerprints, and providing a material to be used to represent a complex matrix in the detection of other compounds such as metabolites or exogenous components. Also, since the substance is made in-house, the chemical composition can be altered to remove, add, or change the concentration of individual components if desired, allowing for the inclusion or exclusion of components which could be useful in a number of different applications, such as trace contraband detection. While previous studies have been completed to create artificial sweat and sebum [17,18], these works have mainly focused on cosmetic applications, and have not focused on incorporating both excretion types into one inclusive material.

The development of this material was focused on the chemicals that are present in fingerprints at concentrations that can be detected by a number of different analytical techniques such as secondary ion mass spectrometry (SIMS) [19–21], atmospheric ionization mass spectrometry (AI-MS) [22–26], and gas chromatography mass spectrometry (GC/MS) [10,27]. From an extensive literature search and analysis of the chemical compositions of actual fingerprints, a list of the prevalent and readily detected fingerprint constituents was established and used as a basis for development of the material along with cross-comparison on these platforms with actual fingerprint deposits. This work outlines the method for the production of the artificial fingerprint material, as well as the production of artificial fingerprint stamps used to

create artificial fingerprint deposits. A comparison of chemical signature of the material to actual fingerprints is then presented using both AI-MS and SIMS techniques. In addition to a chemical comparison, a comparison of chemical images produced by these techniques is presented, highlighting how the material can be used to analyze samples that are and are not doped with additional material. A brief comparison on the ability to develop artificial fingerprints using traditional development techniques is also presented.

Materials and Methods

Emulsion Development

To prepare the sweat solution, the components listed in Table 1 (total of 19) were dissolved into 990 mL of deionized water, in a 1000 mL volumetric flask. These compounds represented two of the three major classes of eccrine components; inorganic salts and amino acids. Proteins were not incorporated into the artificial eccrine material because of their low concentration and infrequent use as a target component in mass spectrometric fingerprint analysis, though they could easily be incorporated if desired. The sample was then sonicated for fifteen minutes to ensure complete mixing. After sonication, the solution was balanced to a pH of 5.5, the approximate pH of sweat [12], using 5 M NaOH and 12 M HCl (Sigma-Aldrich, St. Louis, MO, USA). The solution was then brought to volume, with deionized water, and sonicated for an additional fifteen minutes.

[Insert Table 1 near here]

To create the sebum, the 23 chemicals were used (Table 2), incorporating compounds from each of the five major classes present in sebaceous secretions. The sebum was produced by mixing the chemicals listed in Table 2 in a 20 mL amber vial using sonication. The heat

produced from sonication (which raised the temperature of the mixture to approximately 35 °C) was sufficient to liquefy all solid components and allow for complete mixing.

[Insert Table 2 near here]

The goal of this work was to create a single fingerprint material which incorporated the major components of both eccrine and sebaceous secretions. In order to accomplish this, an emulsion of the artificial eccrine and sebaceous secretions was produced by adding equal amounts, by weight, of the artificial eccrine and sebaceous materials. Additionally an emulsifying agent, Steareth-20, (Sigma-Aldrich) was added at 0.5 % by mass to ensure homogeneity. The emulsion was then sonicated for fifteen minutes. Steareth-20 is an emulsifying agent commonly found in cosmetics and hand creams and is an exogenous material that has been detected in real fingerprint deposits [28]. The final, 1:1 eccrine-sebum emulsion had the consistency of a cosmetic lotion, allowing it to be easily applied to surfaces, fingers, or artificial fingerprint stamps. If a dilute emulsion was desired, the material could be diluted in water or an organic solvent such as methanol.

Artificial Fingers

Artificial fingerprint deposits were produced by pipetting a known amount of the emulsified mixture (2 μ L to 5 μ L) onto a glass slide. If the fingerprint was doped, 5 μ g of the dopant (RDX, lead, barium, or antimony) were also pipetted onto the glass slide. A fingerprint stamp, details on the construction of which are presented elsewhere [29], was wiped over the fingerprint material to load the finger with the emulsion and then subsequently pressed down onto the surface of interest to produce a fingerprint. Real fingerprints were prepared by loading

the finger with sebaceous material by rubbing the forehead, followed by deposition onto the surface of interest, allowing for enough sebaceous material to be present for analysis.

SIMS Operating Parameters:

In order to compare the chemical signature of the artificial fingerprint material to that of actual fingerprints, three different mass spectrometry techniques, secondary ion mass spectrometry (SIMS), desorption electrospray ionization mass spectrometry (DESI-MS), and laser desorption ionization mass spectrometry (LDI-MS) were used. The SIMS system that was used was a Cameca ims-4f (Gennevilliers Cedex, France) coupled with an IonOptika (Hampshire, England) C₆₀ primary ion source. Preparation of samples for analysis by SIMS was completed by depositing the sample onto 2.54 cm circular silicon wafers. Analysis of the samples was completed on a CAMECA ims-4f (Madison, WI, USA) equipped with an IonOptika C₆₀ primary ion source (Gennevilliers Cedex, France). Instrument parameters included a primary ion accelerating voltage of 10 keV, a 500 μm x 500 μm raster, a 250 μm x 250 μm imaging field, and a primary ion current of approximately 1x10⁻¹⁰ A. Mass spectrum parameters included a scan range of 0 *m/z* to 600 *m/z* with 1800 cycles at an integration time of 0.1 s/cycle. Both positive and negative secondary ion scans were completed.

DESI-MS Operating Parameters:

DESI-MS analysis was completed by depositing fingerprints directly onto double sided tape (Scotch, 3M) that was mounted to a clean glass microscope slide. The ionization source used was a Prosolia DESI source (Indianapolis, IN, USA) coupled to an ABSciex 4000 Q Trap mass spectrometer (Framington, MA, USA). Source parameters included a spray voltage of ±4000 V, N₂ carrier gas at a pressure of 5.5 bar, an incidence angle of approximately 40 °, and a solvent flow rate of 4.6 μL/min. The solvent used was a 50 : 50 methanol : water mixture. Mass

spectrometer parameters included an inlet temperature of 200 °C and a scan range of 100 m/z to 800 m/z , at one second per scan, with 30 scans summed. Both positive and negative ion mass spectra were collected.

DESI-MS Imaging Parameters:

The DESI-MS analyses incorporated an ABSciex (Framington, MA, USA) QTrap 4000 mass spectrometer coupled with a ProSolia (Indianapolis, IN, USA) DESI source. Detailed parameters on the mass spectral imaging procedures can be found elsewhere [22,25]. Briefly, instrumental parameters identical to those in the above reference were used, however, in this instance the sample was scanned, at a rate of 350 $\mu\text{m}/\text{sec}$, in a perpendicular motion with respect to the mass spectrometer inlet. A small scan window (275 m/z – 290 m/z) was collected every 0.285 sec so that 100 μm x 100 μm pixels of data were collected. After each row was scanned, the sample was translated back to the home position and the next row (100 μm deeper than the previous) was scanned. In this configuration every line corresponded to a data file and every pixel to a single MS scan. The combined data was then transformed from the native ABSciex file type to a readable single file which was opened in MSiReader [30].

LDI-MS Operating & Imaging Parameters:

The LDI-MS analyses incorporated an ABSciex (Framington, MA, USA) QTrap 4000 mass spectrometer coupled with a MassTech (Columbia, MD, USA) AP-MALDI source. LDI-MS analysis was completed by depositing fingerprints directly onto Non-Focus Array Plates (Hudson Surface Technology, Old Tappan, NJ, USA). Source parameters included an Nd:Yag laser (355 nm wavelength) with a laser attenuation of 75 %, a laser repetition rate of 150 Hz, and an applied plate voltage of ± 3000 V. Mass spectrometer parameters included an inlet

temperature of 150 °C and a scan range of 30 m/z to 600 m/z , at two seconds per scan, with 30 scans summed. Both positive and negative ion mass spectra were collected.

Imaging procedures for the LDI-MS experiment are nearly identical to those of the DESI-MS setup. Differences included a scan rate of 0.420 $\mu\text{m}/\text{sec}$ and a mass spectral window of 30 m/z – 40 m/z for the potassium ion scan or a split scan ranges of 120 m/z – 130 m/z , 135 m/z – 145 m/z , and 204 m/z – 214 m/z for the scan of lead, barium, and antimony. In all instances, the total scan time per pixel was 0.217 s.

Fingerprint Developing Procedures:

Latent prints deposited on glass microscope slides were developed using black fingerprint powder (Regular Silk Black Powder) and fluorescent (YELLOWescent Fluorescent Fingerprint Powder) fingerprint powders (Sirchie Co., Youngsville, NC, USA). Latent prints deposited on bond paper (Navigator premium multipurpose ultrabright) were developed using solutions of ninhydrin or 1,2-indanedione. To prepare the ninhydrin working solution, 5 g of ninhydrin (Evident Crime Scene Products, Union Hall, VA, USA) was mixed into 45 mL ethanol (Fisher Chemical, Pittsburgh, PA, USA), 2 mL ethyl acetate (Fisher Chemical, Pittsburgh, PA, USA), and 5 mL glacial acetic acid (Sigma-Aldrich); to this solution, 1 L of Novec™ HFE7100 (3M, St. Paul, MN, USA) was added for the final dilution step. The 1,2-indanedione working solution was prepared by dissolving 2 g of 1,2-indanedione (Sirchie Co.) in 70 mL ethyl acetate and mixing with 930 mL Novec™ HFE7100 (3M). These working solutions were applied individually to the bond paper by spraying the surface until it was thoroughly wetted. After air-drying, the papers were placed in a drying oven at 90 °C for 20 minutes.

Latent prints deposited on clear packing tape (Scotch Brand, 3M) were developed using cyanoacrylate or gentian violet. To develop with superglue, the tapes were hung in a 0.05 m^3

cabinet with 150 mg cyanoacrylate (Adhesive Systems RP100, Frankfort, IL, USA) in an aluminum dish on a hot plate heated to 110 °C. The tapes were allowed to fume for 10 minutes, and the cabinet was vented for 10 additional minutes prior to opening. After development with cyanoacrylate, the developed prints were rinsed with a methanol-based solution of rhodamine 6G for enhanced visualization. The rhodamine 6G working solution consisted of 5 mg rhodamine 6G (Sigma-Aldrich) in 500 mL methanol (Fisher Chemical). The gentian violet working solution was prepared by adding 1 g gentian violet to 1 L distilled water. The tapes were dipped into a shallow bath of gentian violet working solution, and then rinsed with a gentle stream of water.

Results and Discussion

Comparison of the Chemical Signatures of Real and Artificial Fingerprints

To compare the chemical signatures of the artificial material to actual fingerprint deposits, chemical analysis of both sample types was completed using SIMS, DESI-MS, and LDI-MS. These three techniques highlighted that the artificial material was chemically similar, though not chemically identical, to actual fingerprint deposits.

Figure 1 illustrates the chemical similarities between the actual fingerprint and emulsion when analyzed by SIMS in negative ionization mode. SIMS provides the benefit of simultaneous analysis of organic and inorganic constituents within a sample without changing instrumental parameters. Furthermore, the use of the C₆₀ cluster ion source provided low fragmentation of molecules because of the dispersed energy of the primary ion cluster upon impact. This produced a mass spectrum dominated by molecular ion peaks, not fragment ions. The negative ion SIMS mass spectra (Figure 1) highlighted the comparison of the anionic species present in the samples as well as several amino acids and fatty acids. The make-up of the longer chain fatty

acids (mass range 200 m/z to 350 m/z) was nearly identical with the exception of heptadecanoic acid ($[M-H]^-$, 269 m/z), present in actual fingerprints but not in the artificial material. The amino acid signature (mass range 70 m/z to 150 m/z) was also similar between the actual fingerprint and the artificial material. The positive ion mass spectrum (Figure 2) provided information predominantly on the inorganics, such as sodium and potassium, and several other organic components such as amino acids, cholesterol, and squalene that were found in both the actual fingerprint and the artificial emulsion. Like the negative ion SIMS spectra, the positive ion spectral comparison between the actual and artificial fingerprint deposits showed excellent agreement, indicating similar chemical composition. The major difference in the positive ion SIMS spectra, was the presence of additional peaks present in the 200 m/z to 600 m/z range of the artificial material. Those peaks were attributed to the emulsifying agent, Steareth-20.

[Insert Figures 1 & 2 near here]

A comparison of the chemical compositions via negative ion DESI-MS was also completed (Figure 3). Like SIMS, the DESI-MS comparison further strengthened the chemical similarity between the actual and artificial materials. Since DESI-MS analysis was completed under ambient conditions, detection of semi-volatile components such as short chain length and unsaturated fatty acids was easily accomplished. The inorganic profile of the fingerprint, however, could not be probed in this configuration. Stronger peaks for the glycerides, present in the range beyond 400 m/z , could be seen in the artificial material spectrum and was likely due to a higher mass of sample deposited onto the sampling surface than that of the actual fingerprint deposit.

[Insert Figure 3 near here]

LDI-MS, utilizing a high in-source collision induced dissociation voltage, provided a method to observe the inorganic fraction of a fingerprint under ambient conditions, and also illustrated a high degree of agreement between the real and artificial fingerprint deposits (Figure 4). Overall, the mass spectrometric techniques highlighted the close resemblance of the chemical composition of the sebum-sweat emulsion to the composition of actual fingerprint deposits.

[Insert Figure 4 near here]

Chemical Imaging Comparison

Another emerging area of fingerprint analysis is the chemical imaging of these deposits in order to obtain spatial information regarding the constituents in the fingerprints. Several different mass spectral techniques, namely SIMS [19,20,20,21] and ambient ionization based techniques [6,23,25,26,31–33], have been shown to be capable of resolving the fingerprint ridges and valleys of deposited fingerprints. There are a number of potential benefits of being able to obtain such information, including age dating of fingerprint deposits, determination of deposition order [6], and the capability to complete simultaneous biometric and chemical analysis. In order to compare these many techniques, however, the same, or approximately the same, fingerprint should be used to truly examine metrics such as spatial resolution, spatial detection limits, and quality of the obtained chemical images. To highlight how this material, and corresponding stamp, could be used to fill this role, artificial fingerprints were deposited onto double sided tape and MALDI plates for chemical imaging by DESI-MS and LDI-MS respectively. Both doped and non-doped fingerprints were deposited. Fingerprints analyzed by DESI-MS were doped with cyclotrimethylenetrinitramine (RDX), while fingerprint analyzed by LDI-MS were doped with a combination of lead, barium, and antimony. The images that were obtained, as well as an

optical image of the starting deposited, are highlighted in Figure 5. It was evident from these images that both techniques were capable of resolving fingerprint ridges and valleys. Furthermore, as is highlighted in Figure 5C and 5F, it was possible for these techniques to detect and spatially resolve both the endogenous and exogenous components of a fingerprint. While this demonstration highlights the capability of this material to be used as a chemical imaging comparison tool, future work will focus on completing cross-comparisons of imaging techniques to truly understand the strengths and weaknesses of particular techniques in completing this type of complicated analysis.

Latent Fingerprint Development Comparison

In order to evaluate the ability of the artificial material to be developed in a manner similar to actual fingerprints, artificial fingerprints, using the ballistics gelatin stamps, were deposited onto surfaces, next to actual fingerprints and subjected to a number of different latent fingerprint development techniques. The techniques chosen included black powder, fluorescent powder, cyanoacrylate fuming followed by rhodamine 6G treatment, gentian violet, ninhydrin, and 1,2-indandione. The first three techniques were explored because of their widespread use in the field as physical developers. Gentian violet was tested because it reacts with the sebaceous components of fingerprints while ninhydrin and 1,2-indandione were chosen to test the reaction with amino acids [2]. Figure 6 illustrates the results of developing both the real and artificial fingerprints with each of the development techniques. Using all of the techniques listed, artificial fingerprints were able to be developed, indicating proper reaction with the chemical agents for techniques like ninhydrin and gentian violet. To understand if the detail created by the artificial fingerprints was less than those created by actual fingerprints, the real and artificial fingerprints were examined by a certified latent fingerprint examiner, from the Defense Forensic

Science Center (Fort Gillem, Georgia, USA) and the quality of the artificial fingerprint was determined to equal to or better than that of the real fingerprint in all cases. This indicates that the ability to use the artificial material as a method to study fingerprint development is possible. Current work is now focusing on expanding the range of developing agents tested as well as the ability of aged artificial fingerprints to develop in a similar manner to aged actual fingerprints.

[Insert Figure 6 near here]

Conclusions

A chemically relevant artificial fingerprint material has been established. Unlike prior work to create such a material, this method combined artificial sebaceous and eccrine secretions using an emulsification process to produce a material that contains major components of both secretions at chemically relevant concentrations and pH compared to real fingerprints pre-loaded with sebum. Chemical signatures of the actual and artificial fingerprint deposits were shown to widely agree and, though not identical, were similar enough to be used as a test material either for broad chemical detection capabilities or as an imaging standard. Another benefit of this material was that it was made in-house which allowed for the ability to incorporate additional materials to create a doped fingerprint (Figure 5). It is believed that this material has a wide range of potential applications including a standard for cross comparison of chemical analysis and chemical imaging of fingerprints, a material to evaluate new or existing visual developing agents (Figure 6), and a background matrix to supply realistic test materials for trace contraband detection. Current work is now focusing on developing a way to better quantify a method of doping the material, understanding the stability of the material, understanding how the material ages, evaluating the efficacy of developing techniques, exploring ways to enhance the precision

of fingerprint deposits to create a more reproducible artificial fingerprint and fingerprint stamp, and completing a true cross-comparison of mass spectral imaging techniques.

References

- [1] Girod A, Ramotowski R, Weyermann C. Composition of fingermark residue: A qualitative and quantitative review, *Forensic Sci. Int.* 2012;223:10–24.
- [2] Lee H. *Advances in Fingerprint Technology*. 2nd ed. Boca Raton (FL): CRC Press; 2001.
- [3] Archer NE, Charles Y, Elliott JA, Jickells S. Changes in the lipid composition of latent fingerprint residue with time after deposition on a surface. *Forensic Sci. Int.* 2005;154:224–239.
- [4] Jacobsen E, Billings JK, Frantz RA, Kinney CK, Stewart ME, Downing DT. Age-Related Changes in Sebaceous Wax Ester Secretion Rates in Men and Women. *J Investig Dermatol.* 1985;85:483–485.
- [5] Antoine KM, Mortazavi S, Miller AD, Miller LD. Chemical Differences Are Observed in Children's Versus Adults' Latent Fingerprints as a Function of Time. *J. Forensic Sci.* 2010;55: 513–518.
- [6] Bright NJ, Webb RP, Bleay S, Hinder S, Ward NI, Watts JF, et al. Determination of the Deposition Order of Overlapping Latent Fingerprints and Inks Using Secondary Ion Mass Spectrometry. *Anal Chem.* 2012;84(9):4083 - 4087.
- [7] Hemmila A, McGill J, Ritter D. Fourier Transform Infrared Reflectance Spectra of Latent Fingerprints: A Biometric Gauge for the Age of an Individual. *J. Forensic Sci.* 2008;53:369–376.
- [8] Mong GM, Petersen CE, Clauss TRW. *Advanced Fingerprint Analysis Project Fingerprint Constituents*. 1999. Available from: <http://www.osti.gov/bridge/servlets/purl/14172-SQLzxx/webviewable/>.
- [9] Boddis AM, Russell DA. Simultaneous development and detection of drug metabolites in latent fingermarks using antibody–magnetic particle conjugates. *Anal. Methods.* 2011;3:519–523.
- [10] Croxton RS, Baron MG, Butler D, Kent T, Sears VG. Variation in amino acid and lipid composition of latent fingerprints. *Forensic Sci. Int.* 2010;199:93–102.
- [11] Asbaugh DR. *Quantitative and Qualitative Friction Ridge Analysis: An Introduction to Basic and Advanced Ridgeology*. Boca Raton (FL): CRC Press; 1999.
- [12] Parnas J, Flachs H, Gram L, Wuurtz-Jørgensen A. Excretion of antiepileptic drugs in sweat. *Acta Neurol. Scand.* 2009;58:197–204.
- [13] Barnes AJ, Smith ML, Kacinko SL, Schwilke EW, Cone EJ, Moolchan ET, et al. Excretion of Methamphetamine and Amphetamine in Human Sweat Following Controlled Oral Methamphetamine Administration. *Clin. Chem.* 2008;54:172–180.
- [14] De La Torre R, Pichini S. Usefulness of Sweat Testing for the Detection of Cannabis Smoke. *Clin. Chem.* 2004;50:1961–1962.
- [15] Downing DT, Strauss JS, Pochi PE. Variability in the Chemical Composition of Human Skin Surface Lipids. *J. Invest. Dermatol.* 1969;53:322–327.
- [16] Wolstenholme R, Bradshaw R, Clench MR, Francese S. Study of latent fingermarks by matrix-assisted laser desorption/ionisation mass spectrometry imaging of endogenous lipids. *Rapid Commun. Mass Spectrom.* 2009;23:3031–3039.
- [17] Stefaniak AB, Harvey CJ, Wertz PW. Formulation and stability of a novel artificial sebum under conditions of storage and use. *Int. J. Cosmet. Sci.* 2010;32:347–355.
- [18] Wertz PW. Human synthetic sebum formulation and stability under conditions of use and storage. *Int. J. Cosmet. Sci.* 2009;31:21–25.
- [19] Bailey MJ, Jones BN, Hinder S, Watts J, Bleay S, Webb RP. Depth profiling of fingerprint and ink signals by SIMS and MeV SIMS. *Nucl. Instrum. Methods Phys. Res. Sect. B Beam Interact. Mater. At.* 2010;268:1929–1932.
- [20] Szyrkowska MI, Czerski K, Rogowski J, Paryjczak T, Parczewski A. ToF-SIMS application in the visualization and analysis of fingerprints after contact with amphetamine drugs. *Forensic Sci. Int.* 2009;184:e24–26.

- [21] Sisco E, Demoranville LT, Gillen G. Evaluation of C60 secondary ion mass spectrometry for the chemical analysis and imaging of fingerprints. *Forensic Sci. Int.* 2013;231:263–269.
- [22] Forbes TP, Brewer TM, Gillen G. Desorption electro-flow focusing ionization of explosives and narcotics for ambient pressure mass spectrometry. *Analyst.* 2013;138:5665–5673.
- [23] Ifa DR, Manicke NE, Dill AL, Cooks RG. Latent fingerprint chemical imaging by mass spectrometry. *Science.* 2008;321:805.
- [24] Eberlin LS, Liu X, Ferreira CR, Santagata S, Agar NYR, Cooks RG. Desorption Electrospray Ionization then MALDI Mass Spectrometry Imaging of Lipid and Protein Distributions in Single Tissue Sections. *Anal Chem.* 2011;83:8366–8371.
- [25] Forbes TP, Sisco E. Chemical imaging of artificial fingerprints by desorption electro-flow focusing ionization mass spectrometry. *Analyst.* 2014;139:2982–2985.
- [26] Forbes TP, Sisco E, Mass Spectrometry Detection and Imaging of Inorganic and Organic Explosive Device Signatures Using Desorption Electro-Flow Focusing Ionization. *Anal. Chem.* 2014;86:7788–7797.
- [27] Croxton RS, Baron MG, Butler D, Kent T, Sears VG. Development of a GC-MS Method for the Simultaneous Analysis of Latent Fingerprint Components. *J. Forensic Sci.* 2006;51:1329–1333.
- [28] Frujtier-Pölloth C. Safety assessment on polyethylene glycols (PEGs) and their derivatives as used in cosmetic products. *Toxicology.* 2005;214:1–38.
- [29] Staymates JL, Orandi S, Staymates ME, Gillen G. Method for combined biometric and chemical analysis of human fingerprints. *Int. J. Ion Mobil. Spectrom.* 2014;17:69–72.
- [30] Robichaud G, Garrard KP, Barry JA, Muddiman DC. MSiReader: An Open-Source Interface to View and Analyze High Resolving Power MS Imaging Files on Matlab Platform. *J. Am. Soc. Mass Spectrom.* 2013;24:718–721.
- [31] Bailey MJ, Ismail M, Bleay S, Bright N, Elad ML, Cohen Y, et al. Enhanced imaging of developed fingerprints using mass spectrometry imaging. *Analyst.* 2013;138:6246.
- [32] Miki A, Katagi M, Kamata T, Zaitzu K, Tatsuno M, Nakanishi T, et al. MALDI-TOF and MALDI-FTICR imaging mass spectrometry of methamphetamine incorporated into hair. *J. Mass Spectrom.* 2011;46:411–416.
- [33] Mirabelli MF, Chramow A, Cabral EC, Ifa DR, Analysis of sexual assault evidence by desorption electrospray ionization mass spectrometry. *J. Mass Spectrom.* 2013;48:774–778.

Tables

Chemical	Amount (mg)
Inorganic Salts	
Potassium Chloride ¹	1,400
Sodium Chloride ¹	1,300
Sodium Bicarbonate ¹	250
Ammonium Hydroxide ¹	175
Magnesium Chloride ¹	40
Amino Acids	
Serine ²	275
Glycine ²	135
Ornithine ²	110
Alanine ²	80
Aspartic Acid ²	40
Threonine ²	40
Histidine ²	40
Valine ²	30
Leucine ²	30
Other Components	
Lactic Acid ¹	1,900
Urea ¹	500
Pyruvic Acid ¹	20
Acetic Acid ³	5
Hexanoic Acid ¹	5

Table 1. Components and amounts used to create artificial sweat. Superscripts indicate the chemical supplier. Suppliers included ¹Sigma-Aldrich (St. Louis, MO, USA), ²Carolina Chemicals (Burlington, NC, USA), and ³J.T. Baker (Center Valley, PA, USA).

Chemical	Amount (mg)	Chemical	Amount (mg)
Free Fatty Acids		Triglycerides	
Hexanoic Acid ^{1*}	50	Triolein ^{1*}	275
Heptanoic Acid ^{1*}	50	Tricaprylin ⁴	20
Octanoic Acid ^{1*}	50	Tricaprin ⁴	20
Nonanoic Acid ^{1*}	50	Trilaurin ⁴	20
Dodecanoic Acid ¹	50	Trimyristin ⁴	20
Tridecanoic Acid ¹	50	Tripalmitin ⁴	20
Myristic Acid ¹	50	Other Components	
Pentadecanoic Acid ¹	50	Squalene ^{3*}	120
Palmitic Acid ¹	55	Cholesterol ¹	30
Stearic Acid ²	55	Cholesterol n-Decanoate ¹ (Cholesterol Ester)	40
Arachidic Acid ¹	50		
Linoleic Acid ^{3*}	55	Cetyl Palmitate ¹ (Wax Ester)	155
Oleic Acid ^{1*}	55		

Table 2. Components and amounts used to create artificial sebum. Superscripts indicate the chemical supplier. Suppliers included ¹Sigma-Aldrich (St. Louis, MO, USA), ²KIC (New Paltz, NY, USA), ³Fluka (Buchs, Switzerland), and ⁴Supelco (Bellefonte, PA, USA). Compounds with an asterisk (*) were liquid at room temperature.

Figure Captions

Figure 1. Negative secondary ion SIMS mass spectral comparison of an actual fingerprint (top / black) to the artificial fingerprint emulsion (bottom / grey). Select peaks of interest are numbered with their assignments listed.

Figure 2. Positive secondary ion SIMS mass spectral comparison of an actual fingerprint (black) to the artificial fingerprint emulsion (grey). Select peaks of interest are numbered with their assignments listed. Peaks with arrows indicate those produced from the emulsifying agent, Steareth-20.

Figure 3. Negative ion DESI-MS mass spectral comparison of an actual fingerprint to the artificial fingerprint emulsion. Select peaks of interest are numbered with their assignments listed.

Figure 4. Positive LDI-MS mass spectral comparison of an actual fingerprint (black) to the artificial fingerprint emulsion (grey). Select peaks of interest are numbered with their assignments listed.

Figure 5. Examples of chemical imaging of artificial fingerprints by mass spectrometry. An optical pictograph of the artificial fingerprint deposit (A.) along with LDI-MS examples (B. & C.) and a DESI-MS example (D. – F.). The LDI-MS image (B.) is of the potassium ion distribution ($39\ m/z$, K^+) while image (C.) highlights an expanded overlay image of an artificial fingerprint doped with lead (blue, $208\ m/z$), barium (red, $138\ m/z$), and antimony (green, $121\ m/z$). The DESI-MS example highlights a fingerprint (D., oleic acid, $281\ m/z$, $[M-H]^-$) doped with RDX (E., $284\ m/z$ $[M+NO_3]$). An overlay of the two signals is shown in (F.) (red and green representing the oleic acid and RDX signals respectively). In all images, a brighter color indicates higher peak intensity.

Figure 6. Comparison of real (top) and artificial (bottom) fingerprints developed using black fingerprint powder (A.), fluorescent fingerprint powder (B.), cyanoacrylate fuming followed by treatment with rhodamine 6G (C.), crystal violet (D.), 1,2-indanedione (E.), and ninhydrin (F.). For these comparisons a ballistics gelatin copy of the actual finger was used instead of the 3-D printed mold.

Appendix N

Supporting Information from “Secondary Organic Aerosol Composition from C₁₂ Alkanes”¹⁶

¹⁶ Reproduced by permission from “Secondary Organic Aerosol Composition from C₁₂ Alkanes” by K. A. Schilling, F. H. Fehsenfeld, L. D. Yee, C. L. Loza, M. M. Coggon, R. Schwantes, X. Zhang, N. F. Dalleska, J. H. Seinfeld. *J. Phys. Chem. A*, Article ASAP, DOI: 10.1021/jp501779w, 9 May 2014.

Supplemental Information

Secondary Organic Aerosol Composition from C₁₂ Alkanes

Katherine A. Schilling Fahnstock[†], Lindsay D. Yee^{†,1}, Christine L. Loza^{‡,2}, Matthew M. Coggon, Rebecca Schwantes, Xuan Zhang, Nathan F. Dalleska[‡], John H. Seinfeld^{†,‡}*

[†]Division of Chemistry and Chemical Engineering, California Institute of Technology,
Pasadena, California 91125, United States

[‡]Division of Engineering and Applied Science, California Institute of Technology, Pasadena,
California 91125, United States

Overview of Supplemental Information

This supplemental section contains further information on our DART-MS method validation; our GC/MS methods; and a review of the equations used to relate the DART-MS signal to ion abundance.

DART-MS Analysis

The use of DART-MS to enable the detection of low-volatility species is well-established in literature; its application to SOA is recent, however. A common mass calibrant for DART-MS are polypropylene or polyethylene glycols. We have analyzed polypropylene glycol by (+)-DART-MS using the same method we used to analyze SOA (Figure S1). Dipropylene glycol has, as calculated using the EVAPORATION model, a vapor pressure of 5.9×10^{-6} atm; as shown in Figure S1, the highest polymer of polypropylene glycol measured by us was the 10-mer, with a calculated vapor pressure of 6.8×10^{-20} atm.

DART-MS is routinely used to identify pharmaceuticals and drugs such as ibuprofen (calculated P_{vap} of 0.11 atm), cocaine (calculated P_{vap} of 1.4×10^{-3} atm), and heroin (calculated P_{vap} of 5.6×10^{-7} atm). We reproduced a test of this nature in Figure S2, also conducted with the same method as used to analyze SOA in the manuscript.

These standards demonstrate the viability of DART-MS for the analysis of compounds spanning a broad range of volatilities and structures. Works cited in the manuscript (Cody et al., Harris et al., etc.) illustrate the utility of DART-MS in the analysis of many classes of compounds and are part of the literature foundation for the application of DART-MS to the qualitative and quantitative analysis of organic compounds.

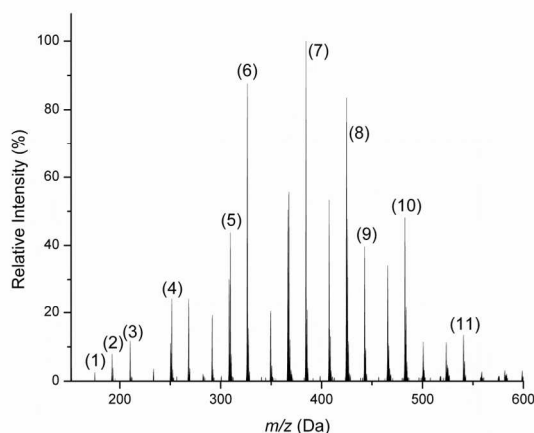


Figure S1: (+)-DART mass spectrum of polypropylene glycol ($\text{H}[\text{OCH}(\text{CH}_3)\text{CH}_2]_n\text{OH}$). Labeled peaks indicate: (1) $n=2$, $[\text{M}+\text{NH}_4]^+$; (2) $n=3$, $[\text{M}+\text{H}]^+$; (3) $n=3$, $[\text{M}+\text{NH}_4]^+$; (4) $n=4$, $[\text{M}+\text{H}]^+$; (5) $n=5$, $[\text{M}+\text{H}]^+$; (6) $n=5$, $[\text{M}+\text{NH}_4]^+$; (7) $n=6$, $[\text{M}+\text{NH}_4]^+$; (8) $n=7$, $[\text{M}+\text{H}]^+$; (9) $n=7$, $[\text{M}+\text{H}_3\text{O}]^+$; (10) $n=8$, $[\text{M}+\text{H}]^+$; (11) $n=10$, $[\text{M}+\text{H}]^+$.

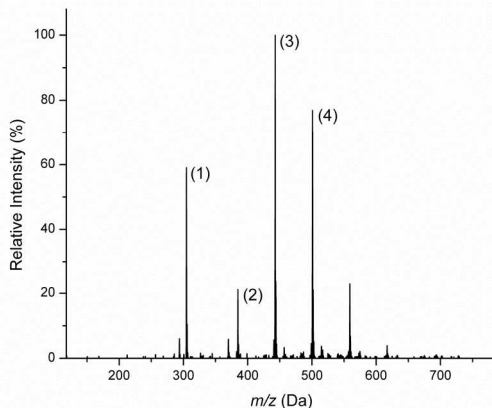


Figure S2: (+)-DART mass spectrum of the surface of a randomly chosen five-dollar bill. Labeled peaks are assigned as: (1) cocaine, $[M+H]^+$; (2) heroin, $[M+H]^+$; (3) (1R,9S)-1-acetoxy-N-acetyl-1,9-dihydro-anhydronorcarceine (major alkaloidal impurity in heroin), $[M+H]^+$; (4) N-acetylanhydronorcarceine or N-acetylnorcotinine (major isobaric alkaloidal impurities in heroin), $[M+H]^+$.

We detect peroxide standards as ammonium adducts, as well as proton- and ammonium-bound dimers and trimers, and hydronium adducts (Figure S3a). The complexation with ammonium occurs with all forms of peroxides, including acyl, alkyl, and cyclic peroxides. Adding 18-crown-6 introduces an ammonium ion sink, removing the major ionization pathway for peroxides of all kinds. Tert-butyl peroxybenzoate was analyzed as shown in Figure S3a; in Figure S3b, 18-crown-6 is co-introduced into the DART stream with t-butyl peroxybenzoate, and nearly none of the peroxide is detected. Figure S3b demonstrates the effectiveness of 18-crown-6 at complexing with ammonium ions in the DART stream and thereby halting peroxide detection. Cumene hydroperoxide is commercially available at 80% purity. We did test it, but the interferences from these impurities (methylstyrene, acetophenone, and cumyl alcohol, along with some unidentified high-concentration impurities) lead to less clear and lower quality mass spectra.

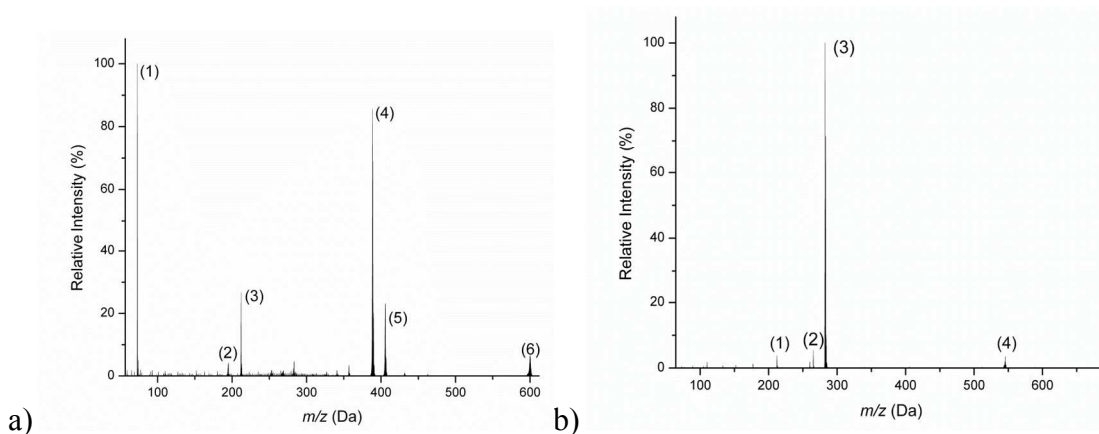


Figure S3: (a) (+)-DART mass spectrum of t-butyl peroxybenzoate. Labeled peaks are assigned as: (1) $tBuO^+$; (2) protonated t-butyl peroxybenzoate, $[M+H]^+$; (3) $[M+NH_4]^+$; (4) $[2M+H]^+$; (5) $[2M + NH_4]^+$; (6) $[3M+NH_4]^+$. (b) (+)-DART mass spectrum of t-butyl peroxybenzoate + 0.2

mM 18-crown-6 in methanol. Labeled peaks are assigned as: (1) [t-butyl peroxybenzoate + NH_4]⁺; (2) [18-crown-6 + H]⁺; (3) [18-crown-6] + NH_4]⁺; (4) [2(18-crown-6) + NH_4]⁺.

GC/MS Analysis Details: Accounting for Thermally Labile Analytes

Molecular decomposition in the GC is difficult to account for in unknown samples, so we studied it with standards. We optimized instrumental methods to reduce sample degradation to the lowest possible level for both GC/MS and DART-MS analysis. We analyzed standards by both GC/MS and DART-MS to assess the instrument's performance with different classes of expected compounds; these standards included aldehydes, ketones, alcohols, carboxylic acids, 1,4-hydroxyketones, furans, dihydrofurans, amines, and hydroperoxides. DART-MS did not produce significant dehydration of alcohols or hydroperoxides. We focused then on minimizing dehydration in our GC/MS analyses.

We used a programmed temperature vaporization (PTV) inlet, instead of a standard split/splitless inlet, to achieve the softest possible volatilization of analytes for GC/MS. PTV injectors are capable of transferring many thermally labile compounds intact onto the column for separation and of concentrating a larger volume of a complex mixture of trace organic species. The most advanced deactivation coatings for both the column (Agilent DB5-MSUI) and inlet liner (Restek Sky liners) were used to prevent loss and tailing of active hydrogen-containing species. We used Agilent's DB-5 column test mix (Agilent, P/N 200-0185) to assess instrument performance, especially peak shape and tailing that would indicate degrading separatory ability for active hydrogen-containing species. The DB-5 standard test mix contained n-tetradecane, n-tridecane, 1-undecanol, 1,6-hexanediol, 2-ethylhexanoic acid, 4-chlorophenol, dicyclohexylamine, and 1-methylnaphthalene.

These measures to reduce artifactual dehydration were effective because we were able to observe in GC/CI-MS data dehydration steps occurring due to protonation by the methanol reagent gas (see new Supplemental Figure S4). In addition to water loss, nitric acid loss is another possible method artifact. We did not detect nitric acid loss or formation during analysis. We would have been able to detect nitric acid (63 amu) by DART and GC/MS, had it formed, but it was not observed.

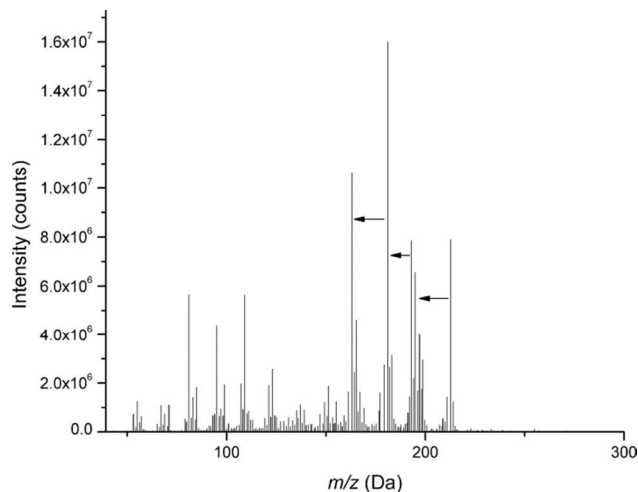


Figure S4: Chemical ionization mass spectrum at 22.73 min during GC/MS runs of SOA derived from dodecane low-NO photooxidation with ammonium sulfate seed. Arrows indicate water loss (-18 Da).

Equations for Calculating Weighting Factors from DART-MS

Relationship between Ion Current Intensity and Concentration, written for an Analyte, i :

$$(1) \quad I_i = A_i P_{vap,i} C_i$$

Ratio of Equation 1 Written for an Analyte, i , and the Internal Standard (IS):

$$(2) \quad \frac{I_i}{I_{IS}} = \frac{A_i P_{vap,i} C_i}{A_{IS} P_{vap,IS} C_{IS}}$$

Solving Equation 2 for Ratio of Concentrations, $\frac{C_i}{C_{IS}}$:

$$(3) \quad \frac{C_i}{C_{IS}} = \frac{P_{vap,IS}}{P_{vap,i}} \frac{I_i}{I_{IS}}$$

Expressing the Sum of the Relative Concentrations of All Analytes, i , for a Given SOA

Sample:

$$(4) \text{ Total concentration of SOA components} = \sum_i \frac{C_i}{C_{IS}}$$

Finding Percent Contribution (w) of Each Analyte, i :

$$(5) w = \frac{\frac{c_A}{c_{IS}}}{\sum_i \frac{c_i}{c_{IS}}} * 100\%$$

Obtaining the Mean Molecular Weight (M_w) of a Given SOA Sample Containing i Analytes, using a Weighted Average Formula and the Percent Contribution as the Weighting Factor:

$$(6) \text{Mean } M_w = \sum_i w M_{w,i}$$

Experiment:

Dodecane Low NO, (NH₄)₂SO₄, dryMean M_w (g
mol⁻¹)

429.01

M _w	P _{vap} (atm)	C _A /C _{IS}	Compound Class	SMILES String
100.16	1.35E-02	1.01E-06	ketone	CCCC(=O)CC
106.17	1.14E-02	2.43E-06	alcohol	CCCC(C)O
120.19	3.73E-03	8.34E-06	alcohol	CCCCC(C)O
126.20	3.73E-03	1.13E-05	dihydrofuran	CCCC1CC=C(C)O1
128.22	3.71E-03	1.70E-05	ketone	CCCCCC(=O)CC
130.23	1.45E-03	2.64E-05	alcohol	CCCCCC(O)CC
132.20	3.99E-04	3.25E-05	ketone	CCCCCC(C)=O
134.22	4.42E-03	3.91E-06	alcohol	CCCCCC(C)O
136.19	7.66E-04	4.36E-05	furan	CC\C=C\C1=CC=C(C)O1
138.21	1.22E-03	3.42E-05	furan	CCCCC1=CC=C(C)O1
140.23	1.21E-03	6.44E-05	aldehyde	CCCC\C=C\C=O
142.24	4.73E-04	2.03E-04	ketone	CCCCCCC(C)=O
144.21	1.31E-04	3.32E-04	alcohol	CCCCCCC(C)O
148.25	3.99E-04	3.10E-05	alcohol	CCCCCCC(C)O
150.18	3.21E-05	6.13E-04	furan	CC1=CC=C(C\C=C\O)O1
152.24	1.01E-04	2.42E-04	ketone	CCCC\C=C\C=C\C(C)=O
154.25	1.01E-04	5.90E-04	ketone	CCCCC\C=C\C(C)=O
156.27	1.55E-04	6.45E-04	ketone	CCCCCCCC(C)=O
158.29	4.27E-05	1.07E-03	alcohol	CCCCCCCC(C)O
160.26	4.73E-04	3.82E-05	ketone	CCCCCCCC(C)=O
162.27	1.31E-04	3.51E-04	alcohol	CCCCCCCC(C)O
166.26	3.32E-05	4.37E-04	aldehyde	CCCCC\C=C\C=C\C=O
168.28	3.32E-05	1.54E-03	aldehyde	CCCCCCCC\C=C\C=O
170.30	5.06E-05	1.17E-03	aldehyde	CCCCCCCCC=O
172.27	2.72E-06	1.53E-02	hydroxycarbonyl	CCCCCCC(O)CC=O
176.26	2.68E-05	5.00E-04	furan	CC\C=C\C=C\C1=CC=C(CC)O1
178.28	2.68E-05	1.42E-03	furan	CCCC\C=C\C1=CC=C(CC)O1
180.29	2.68E-05	3.74E-03	furan	CCCCCCC1=CC=C(CC)O1
164.20	4.08E-06	6.60E-02	dihydrofuran	CCC1=CCC(O1)C(=O)CCC=N
182.31	4.24E-05	6.86E-04	dihydrofuran	CCCCCCC1CC=C(CC)O1
183.25	9.93E-07	1.03E+00	dihydrofuran	CCC1=CCC(O1)C(O)CCC=N
184.32	1.65E-05	7.62E-03	ketone	CCCCCCCC(=O)CCC
186.21	2.77E-06	2.19E-02	furan	C=CC1=CC=C(O1)C1=CC=C(O1)C=C
190.24	2.77E-06	5.83E-03	furan	CCC1=CC=C(CC2=CC=C(C)O2)O1
192.26	1.98E-06	5.88E-03	furan	CCC\C=C\C(=O)C1=CC=C(CC)O1
193.25	6.26E-07	1.03E-01	furan	CC1=CC=C(O1)C(=O)CCCC=N
194.27	3.01E-06	5.32E-03	furan	CCCCC(=O)C1=CC=C(CC)O1
195.26	6.26E-07	6.65E-01	furan	CC1=CC=C(O1)C(=O)CCCC=N
196.29	1.71E-06	2.85E-02	furan	CCCCC(=O)CC1=CC=C(CC)O1
180.25	1.33E-06	5.27E-01	furan	CC1=CCC(O1)C(=O)CCCC=N
198.31	2.75E-06	3.25E-02	ketone	CCCCCCCC(=O)CC(=O)CC
199.29	4.35E-08	1.21E+01	imine	CCCC(O)CC(=O)CCCC=N
200.32	2.91E-07	1.93E-01	hydroxycarbonyl	CCCCC(O)CC(=O)CCCC
208.26	6.96E-07	1.18E-01	furan	CCCC(=O)CC(=O)C1=CC=C(CC)O1
210.27	1.48E-06	3.11E-02	dihydrofuran	CCCC(=O)CC(=O)C1CC=C(CC)O1
211.26	2.99E-08	5.24E+00	dihydrofuran	CC1CC=C(O1)C(=O)CC(O)CCC=N
212.29	3.79E-07	6.22E-02	ketone	CCCCC(=O)CC(=O)CC(=O)CC
196.29	7.27E-06	3.73E-02	furan	CCCCCCC(=O)C1CC=C(C)O1
214.31	4.84E-08	7.20E-01	hydroxycarbonyl	CCCCC(O)CC(=O)CC(=O)CC
216.32	2.06E-09	5.40E+01	hydroxycarbonyl	CCCCC(O)CC(=O)CC(O)CC
218.34	1.97E-10	1.61E+02	alcohol	CCCCC(O)CC(O)CC(O)CC
224.26	2.24E-07	4.81E-02	dihydrofuran	CCC(=O)CC(=O)CC(=O)C1CC=C(C)O1
226.27	1.60E-08	7.31E-01	ketone	CCC(=O)CC(=O)CCCC(=O)CC(C)=O
228.29	2.11E-09	2.18E+01	hydroxycarbonyl	CCC(=O)CC(=O)CCCC(O)CC(C)=O
230.30	1.01E-10	5.26E+02	hydroxycarbonyl	CCC(=O)CC(O)CCCC(O)CC(C)=O
242.32	1.98E-07	6.34E-02	ester	C\C=C\C=C\C=C\C(=O)O\C=C\C=C\C=C\C=C
244.29	4.72E-12	2.32E+03	hydroxycarbonyl	CCC(=O)CC(O)CC(=O)CC(O)CC(C)=O
230.31	6.05E-07	2.16E-02	ester	CC\C=C\C=C\C=C\C(=O)O\C=C\C=C\C=C
282.47	2.11E-08	1.69E+00	ester	CCCCCCCCOC(=O)\C=C\CCCCC

286.41	4.60E-10	2.47E+01	acid anhydride	CCCCCCCC(=O)OC(=O)CCCC(O)CCC
382.63	1.07E-11	9.98E+02	ether	CCCCCCCC(=O)C(CCC)OC(CCCC)C(=O)CCCCC
394.60	1.76E-12	5.92E+03	ether	CCCCCCCC(=O)C(CCC)OC(CCCC)C(=O)CC1CC=C(C)O1
396.61	1.91E-12	6.04E+03	ether	CCCCCCCC(=O)C(CCC)OC(CCCC)C(=O)CC(=O)CCCC
398.63	1.89E-13	1.12E+05	ether	CCCCCCCC(=O)C(CCC)OC(CCCC)C(=O)CC(O)CCCC
400.64	9.06E-15	3.07E+06	ether	CCCCCCCC(=O)C(CCC)OC(CCCC)C(O)CC(O)CCCC
410.60	5.30E-14	6.86E+05	ether	CCCCCCC(O)CC(=O)C(CC)OC(CC)C(=O)CCCC1=CCC(C)O1
412.61	3.36E-14	5.35E+05	ether	CCCCCCCC(=O)C(CC)OC(CCC)C(=O)CC(=O)CC(O)CCC
414.63	1.85E-15	1.42E+07	ether	CCCCCCCC(O)C(CC)OC(CCC)C(=O)CC(=O)CC(O)CCC
398.63	2.54E-13	9.93E+04	ether	CCCCCCCC(O)C(CC)OC(CCC)C(=O)CC(=O)CCCC
416.64	1.03E-16	3.73E+08	ether	CCCCCCCC(O)C(CC)OC(CCC)C(=O)CC(O)C(O)CCCC
426.59	8.14E-15	3.73E+08	peroxyhemiacetal	CCCCCCC(=O)CC(=O)C(CC)OC(CCC)C(=O)CC(O)C(=O)CCCC
412.61	3.02E-13	3.97E+04	ether	CCCCCCCC(O)(CCC)OOC(CCC1CC=C(CC)O1)C(=O)CC
430.63	1.50E-17	2.74E+09	peroxyhemiacetal	CCCCCCC(O)CC(=O)C(CC)OC(CCC)C(=O)CC(O)C(O)CCCC
414.63	2.19E-13	3.73E+08	peroxyhemiacetal	CCCCCCCC(O)(CCC)OOC(CCC)C(=O)CC(=O)CCCC
426.59	6.15E-14	2.65E+05	peroxyhemiacetal	CCCCC(=O)CC(=O)C(CCC)OOC(O)(CCCC)CC1CC=C(CC)O1
428.61	5.68E-14	2.73E+05	peroxyhemiacetal	CCCCC(=O)CC(=O)C(CCC)OOC(O)(CCCC)CC1CCC(CC)O1
442.59	2.71E-15	7.92E+06	peroxyhemiacetal	CCCCC(=O)CC(=O)C(CCC)OOC(O)(CCC(C)=O)CC1CCC(CC)O1
444.61	4.86E-16	2.54E+07	peroxyhemiacetal	CCCCC(=O)CC(=O)C(CCC)OOC(O)(CCC(C)O)CC1CCC(CC)O1

Experiment:

Dodecane High NO, (NH₄)₂SO₄, dryMean M_w
(g mol⁻¹) 495.33

M _w	P _{vap} (atm)	C _A /C _{IS}	Compound Class	SMILES String
112.17	1.13E-02	5.14E-05	dihydrofuran	CCC1CC=C(C)O1
114.19	4.42E-03	6.36E-05	ketone	CCCC(=O)CCC
122.17	2.34E-03	9.59E-05	furan	C\C=C\C1=CC=C(C)O1
124.18	2.34E-03	1.51E-04	furan	CCCC1=CC=C(C)O1
126.20	3.71E-03	1.17E-04	dihydrofuran	CCCC1CC=C(C)O1
128.22	4.42E-03	7.95E-05	ketone	CCCCC(=O)CCC
130.23	3.99E-04	2.55E-04	alcohol	CCCCCCC(O)C
132.20	1.55E-05	1.37E-02	alcohol	CCCCC(O)C(C)O
134.18	5.42E-07	5.47E-01	alcohol	CCC(O)C(O)C(C)O
136.15	3.77E-09	9.64E+01	alcohol	CC(O)C(O)C(O)CO
138.21	7.66E-04	7.52E-04	furan	CCCCC1=CC=C(C)O1
139.20	2.37E-04	9.53E-04	dihydrofuran	CC1=CCC(CCC=N)O1
140.23	1.21E-03	7.55E-04	dihydrofuran	CCCCC1CC=C(C)O1
141.21	7.07E-05	3.34E-03	ketone	CC(=O)CCCCC=N
142.20	7.07E-05	5.17E-03	ketone	CC(=O)CCCCC=O
144.21	7.40E-06	1.14E-02	hydroxycarbonyl	CC(=O)CCCCCO
146.23	6.80E-07	9.53E-02	alcohol	CC(O)CCCCCO
148.16	3.46E-08	3.75E+00	hydroxycarbonyl	CC(O)C(O)C(O)CC=O
150.13	3.46E-08	1.08E+01	hydroxycarbonyl	OCC(O)C(O)C(O)C=O
151.17	6.09E-05	1.52E-03	furan	CC1=CC=C(O1)C(=O)CC=N
152.24	2.51E-04	2.10E-03	furan	CCCCC1=CC=C(CC)O1
153.18	1.30E-04	1.33E-03	dihydrofuran	CC1=CCC(O1)C(=O)CC=N
154.25	3.97E-04	1.90E-03	dihydrofuran	CCCCC1CC=C(CC)O1
155.20	9.29E-06	2.59E-02	dihydrofuran	CC1=CCC(O1)C(O)CC=N
156.27	1.55E-04	1.80E-03	ketone	CCCCCCC(=O)CC
158.24	8.33E-06	9.93E-03	hydroxycarbonyl	CCC(O)CCCCC=O
160.21	1.80E-07	1.28E+00	hydroxycarbonyl	CC(O)CCCC(O)CC=O
162.14	8.20E-08	6.69E+00	hydroxycarbonyl	CC(O)C(=O)C(O)C(O)C=O
163.22	1.60E-05	5.72E-03	furan	CC1=CC=C(C\C=C\CC=N)O1
164.25	8.19E-05	5.41E-03	furan	CCC\C=C\C1=CC=C(C)O1
165.24	1.60E-05	6.05E-03	furan	CC1=CC=C(CCCCC=N)O1
166.26	8.19E-05	5.57E-03	furan	CCCCCCC1=CC=C(C)O1
167.25	2.53E-05	5.27E-03	dihydrofuran	CC1=CCC(CCCCC=N)O1
168.28	1.30E-04	5.40E-03	dihydrofuran	CCCCCCC1CC=C(C)O1
169.18	4.24E-06	2.73E-02	ketone	CC(=O)CC(=O)CC(=O)CC=N
170.25	7.56E-06	3.52E-02	ketone	CC(=O)CCCCCCC=O
174.24	5.90E-08	1.04E+00	hydroxycarbonyl	CCC(O)CCC(O)CCC=O
176.26	2.68E-05	6.97E-03	furan	CCCC1=CC=C(O1)\C=C\C=C\C
178.28	2.68E-05	1.70E-02	furan	CCC\C=C\C1=CC=C(CCC)O1
179.22	1.60E-05	6.95E-03	furan	CC1=CC=C(C\C=C\CC=N)O1
180.29	2.68E-05	4.99E-02	furan	CCCCCCC1=CC=C(CC)O1
181.24	8.81E-07	2.23E-01	imine	CCCC(=O)CC(=O)C\C=C\C=N
182.31	4.24E-05	5.81E-02	dihydrofuran	CCCCCCC1CC=C(CC)O1
183.21	2.35E-08	1.43E+01	furan	CC(O)C1=CC=C(O1)C(O)CC=N
184.28	8.40E-06	3.39E-02	ketone	CCCCCCC(=O)CC(C)=O
190.24	1.12E-06	1.47E-01	furan	C\C=C\C=C\C(=O)CC1=CC=C(C)O1
192.26	1.12E-06	7.29E-01	furan	CCC\C=C\C(=O)CC1=CC=C(C)O1
193.25	6.26E-07	3.16E-01	furan	CC1=CC=C(O1)C(=O)CCCC=N
194.27	1.71E-06	1.02E+00	furan	CCCCC(=O)CC1=CC=C(C)O1
196.29	2.71E-06	1.01E+00	dihydrofuran	CCCCC(=O)CC1CC=C(C)O1
197.28	3.66E-07	1.44E+00	imine	CC(=O)CC(=O)CCCCC=N
198.31	8.08E-07	2.04E+00	ketone	CCCCC(=O)CCCC(C)=O
200.32	2.91E-07	5.92E-01	hydroxycarbonyl	CCCCC(=O)CCCC(C)O
206.24	6.25E-07	2.57E-01	furan	CCC(=O)C(=O)\C=C\C1=CC=C(CC)O1
207.27	8.41E-07	8.17E-02	furan	CCC(=N)C(=O)CCC1=CC=C(CC)O1
208.26	8.41E-07	8.90E-01	furan	CCC(=O)C(=O)CCC1=CC=C(CC)O1
209.29	8.41E-07	2.60E-01	imine	CCC(=N)C(=O)CCC1CC=C(CC)O1
210.27	1.33E-06	1.42E+00	dihydrofuran	CCC(=O)C(=O)CCC1CC=C(CC)O1

212.29	8.16E-08	9.80E+00	dihydrofuran	CCC(=O)CC(O)CC1CC=C(CC)O1
214.31	4.84E-08	7.85E+00	hydroxycarbonyl	CCCCC(O)CC(=O)CC(=O)CC
224.26	8.56E-09	2.57E+01	furan	CC(O)CC(=O)CC(=O)CC1=CC=C(C)O1
225.29	4.60E-10	1.93E+02	furan	CC(O)CC(O)CC(=N)CC1=CC=C(C)O1
226.27	4.85E-08	1.22E+01	ketone	CCCC(=O)CC(=O)CC(=O)CC(=O)CC
227.30	7.28E-10	3.10E+02	imine	CC(O)CC(O)CC(=N)CC1CC=C(C)O1
228.29	7.28E-10	3.66E+02	dihydrofuran	CC(O)CC(O)CC(=O)CC1CC=C(C)O1
229.28	2.21E-10	4.58E+02	imine	CCCC(=O)CC(=O)CC(O)CC(O)C=N
230.30	1.01E-10	2.36E+03	hydroxycarbonyl	CC(O)CC(O)CC(=O)CCCC(C)=O
231.29	8.39E-12	1.10E+04	imine	CCCC(=O)CC(O)CC(O)CC(O)C=N
240.26	5.93E-09	1.12E+01	ketone	CCC(=O)CC(=O)CC(=O)CC(=O)CC(C)=O
225.29	4.85E-08	5.96E+00	imine	CCCC(=O)CC(=O)CC(=O)CC(=N)CC
242.27	8.54E-10	3.32E+02	hydroxycarbonyl	CCC(O)CC(=O)CC(=O)CC(=O)CC(C)=O
243.30	4.73E-11	4.79E+04	imine	CCC(=N)CC(=O)CC(=O)CC(O)CC(C)O
244.29	4.73E-11	8.23E+03	hydroxycarbonyl	CCC(=O)CC(=O)CC(=O)CC(O)CC(C)O
245.32	1.12E-07	5.78E+00	nitrate	CCCCCCC(=O)CC(CCC)O[N+][[O-]]=O
246.35	1.00E-07	1.23E+00	ether	CCC1=CC=C(COC\C=C\C=C\C=C\C)O1
255.27	1.16E-08	1.22E+01	nitrate	CCC(CC(=O)CC1=CC=C(CC)O1)O[N+][[O-]]=O
256.30	1.42E-09	4.61E+01	acid anhydride	CCCC(=O)CCC(=O)OC(=O)CCC(=O)CC
257.29	5.48E-09	1.28E+02	nitrate	CCC(CC(O)CC1=CC=C(CC)O1)O[N+][[O-]]=O
258.27	1.08E-11	1.31E+04	hydroxycarbonyl	CC(O)C(O)CC(=O)CC(=O)CC(=O)CC(C)=O
259.30	8.67E-09	8.41E+01	nitrate	CCC(CC(O)CC1=CCC(CC)O1)O[N+][[O-]]=O
260.29	5.29E-13	2.07E+05	hydroxycarbonyl	CC(O)C(O)CC(O)CC(=O)CC(=O)CC(C)=O
261.32	1.97E-09	1.15E+02	nitrate	CCCCC(O)CC(=O)CC(CC)O[N+][[O-]]=O
263.33	2.19E-10	6.77E+02	nitrate	CCCCC(O)CC(O)CC(CC)O[N+][[O-]]=O
234.34	2.07E-12	9.64E+10	alcohol	CCCCC(O)CC(O)CC(O)C(C)O
271.27	4.55E-10	1.28E+02	nitrate	CCC1=CC=C(CC(=O)CC(O[N+][[O-]]=O)C(C)O)O1
273.29	6.53E-11	3.50E+03	nitrate	CCC1=CC=C(CC(O)CC(O[N+][[O-]]=O)C(C)O)O1
274.31	5.72E-10	1.29E+02	acid anhydride	CCCC(O)CCC(=O)OC(=O)CCC(=O)CC
275.30	1.38E-10	1.73E+03	nitrate	CCC1CC=C(CC(CC(O)C(C)O)O[N+][[O-]]=O)O1
289.28	8.51E-11	7.28E+02	nitrate	CCC1CC=C(CC(O[N+][[O-]]=O)C(O)C(=O)C(C)O)O1
290.31	4.52E-14	1.29E+06	acid anhydride	CC(O)CC(=O)CCC(=O)OC(=O)CCC(O)C(C)O
291.30	1.30E-12	6.08E+04	nitrate	CC(O)C(O)CC(CC1CC=C(O1)C(C)O)O[N+][[O-]]=O
292.33	1.11E-14	7.59E+06	acid anhydride	CCC(O)CCC(=O)OC(=O)CCC(O)C(O)C(C)O
304.30	2.58E-13	4.44E+05	acid anhydride	CCC(O)C(=O)CC(=O)OC(=O)CCC(O)C(=O)C(C)O
306.40	3.58E-10	2.08E+02	ester	CCCCC1=CC=C(CCC(=O)OCC2CC=C(CC)O2)O1
308.42	5.66E-10	1.35E+02	ester	CCCCC1CC=C(CCC(=O)OCC2CC=C(CC)O2)O1
325.41	3.51E-10	2.02E+02	nitrate	CC\C=C\CC(C\C=C\C)OCCC1CC=C(CC)O1)O[N+][[O-]]=O
439.59	5.75E-14	1.01E+06	nitrate ether	CCCCC(OC(CCC1=CCC(CC)O1)C(CC)O[N+][[O-]]=O)C1CC=C(CC)O1
457.61	8.80E-16	1.20E+08	ether	CCCCC(=O)CCC(OC(C(O)CCCC)C1CC=C(CC)O1)C(CC)O[N+][[O-]]=O
459.62	1.54E-16	6.06E+08	ether	CCCCC(=O)CCC(OC(CCCC(=O)CC)C(O)CCCC)C(CC)O[N+][[O-]]=O
471.59	2.07E-17	3.62E+09	ether	CCC(O)CC(O)C(OC(CCC1=CCC(CC)O1)C(CC)O[N+][[O-]]=O)C1=CCC(CC)O1
473.61	8.07E-18	8.78E+09	ether	CCC(O)CC(O)C(CCCC(=O)CC)OC(CCC1=CCC(CC)O1)C(CC)O[N+][[O-]]=O
414.63	1.65E-16	4.50E+08	ether	CCCCC(=O)CCC(CCC)OC(CCCC(=O)CC)C(O)CC(O)CC
490.64	9.29E-16	1.04E+08	nitrate ether	CCCCC(CCC(CC)O[N+][[O-]]=O)OC(CCC(=O)CCCC)C(CC)O[N+][[O-]]=O
504.62	4.54E-17	1.91E+09	nitrate ether	CCCCC(=O)CCC(OC(CCCC(=O)CC)CCC(CC)O[N+][[O-]]=O)C(CC)O[N+][[O-]]=O
506.64	1.64E-17	4.75E+09	nitrate ether	CCCCC(=O)CCC(OC(CCCC(O)CC)CCC(CC)O[N+][[O-]]=O)C(CC)O[N+][[O-]]=O
518.60	7.67E-18	1.16E+10	nitrate ether	CCCCC(=O)CCC(OC(CCCC(=O)CC)CCC(CC)O[N+][[O-]]=O)C(O[N+][[O-]]=O)C(C)=O

Experiment:

Cyclododecane Low NO, (NH₄)₂SO₄, dryMean M_w
(g mol⁻¹) 384.52

M _w	P _{vap} (atm)	C _A /C _S	Compound Class	SMILES String
110.16	7.17E-03	1.97E-05	furan	CCC1=CC=C(C)O1
116.16	2.38E-04	1.11E-04	hydroxycarbonyl	CCC(O)CCC=O
118.13	3.32E-05	1.82E-03	hydroxycarbonyl	CC(O)C(O)C(C)=O
120.10	2.60E-07	5.20E-01	hydroxycarbonyl	OCC(O)C(O)C=O
122.17	2.34E-03	3.09E-05	furan	C\C=C\C1=CC=C(C)O1
124.18	2.34E-03	1.98E-05	furan	CCCC1=CC=C(C)O1
126.16	7.24E-04	2.50E-05	dihydrofuran	CC1=CCC(CC=O)O1
128.17	2.16E-04	1.29E-04	ketone	CC(=O)CCCC=O
129.16	2.38E-04	1.77E-04	hydroxycarbonyl	CCCC(O)CC=O
130.19	7.79E-05	5.15E-04	hydroxycarbonyl	CCCC(O)CC=O
132.16	1.69E-06	1.24E-01	hydroxycarbonyl	CC(O)CC(O)CC=O
133.19	8.32E-04	3.96E-05	imine	CCCC(O)C=N
134.13	3.85E-07	6.52E-01	hydroxycarbonyl	CC(O)C(O)C(O)C=O
118.18	3.14E-04	8.90E-05	hydroperoxide	CCCCCOO
136.10	8.14E-11	1.70E+03	carboxylic acid	OCC(O)C(O)C(O)=O
120.10	7.02E-06	2.84E-03	hydroperoxide	CC(O)C(OO)C=O
138.21	7.66E-04	7.47E-05	furan	CCCCC1=CC=C(C)O1
140.23	1.21E-03	3.74E-05	dihydrofuran	CCCCC1CC=C(C)O1
146.19	1.98E-06	5.20E-02	hydroxycarbonyl	CC(O)CCCC(O)C=O
130.19	2.72E-04	9.77E-04	hydroxycarbonyl	CCCCC(O)C=O
149.23	1.03E-04	2.58E-04	hydroxycarbonyl	CCCCCOO
150.22	2.51E-04	6.86E-04	furan	CC\C=C\C1=CC=C(CC)O1
152.24	2.51E-04	6.09E-04	furan	CCCCC1=CC=C(CC)O1
153.25	3.97E-04	4.95E-05	dihydrofuran	CCCCC1CC=C(CC)O1
154.25	3.97E-04	2.49E-04	dihydrofuran	CCCCC1CC=C(CC)O1
156.23	3.66E-05	1.31E-03	dihydrofuran	CCC(O)CC1CC=C(C)O1
156.27	1.55E-04	2.52E-04	ketone	CCCCC(=O)CCCC
158.24	8.33E-06	7.30E-03	hydroxycarbonyl	CCCCC(=O)CC(O)CC
160.21	3.23E-07	5.33E-01	hydroxycarbonyl	CCCCC(O)C(O)CC=O
160.24	2.55E-05	2.54E-02	imine	CCCCC(O)CC=N
161.22	2.55E-05	3.93E-03	hydroxycarbonyl	CCCCC(O)CC=O
162.25	5.32E-05	1.52E-02	hydroperoxide	CCCCC(CC)OO
163.22	1.60E-05	7.43E-03	furan	CCC1=CC=C(O1)\C=C\CC=N
164.25	8.19E-05	2.46E-03	furan	CCC\C=C\C1=CC=C(CC)O1
166.26	1.30E-04	7.00E-04	dihydrofuran	CCCCC1CC=C(CC)O1
168.28	1.30E-04	6.48E-04	dihydrofuran	CCCCC1CC=C(CC)O1
170.30	5.06E-05	7.98E-04	aldehyde	CCCCCCCCC=O
173.26	5.90E-08	3.93E-01	alcohol	CCCC(O)CC(O)CC=N
174.20	8.82E-09	8.50E+00	hydroxycarbonyl	OC(CCC=O)CC(O)CC=O
176.17	5.53E-10	3.01E+02	hydroxycarbonyl	OC(CC=O)C(O)C(O)CC=O
177.20	4.48E-10	6.04E+01	imine	CCC(O)C(O)C(O)C(O)C=N
178.28	2.68E-05	2.28E-02	furan	CCCC\C=C\C1=CC=C(CC)O1
179.26	5.23E-06	1.83E-02	furan	CCCCC1=CC=C(CCC=N)O1
180.29	2.68E-05	6.15E-02	furan	CCCCCCC1=CC=C(CC)O1
181.28	8.27E-06	3.27E-02	dihydrofuran	CCC1=CCC(CCCCC=N)O1
182.31	4.24E-05	6.33E-03	dihydrofuran	CCCCC1CC=C(CC)O1
184.32	1.65E-05	8.95E-03	ketone	CCCCC(=O)CCCC
186.30	8.90E-07	4.34E-02	hydroxycarbonyl	CCCCC(O)CCCC=O
190.24	1.31E-09	5.40E+01	hydroxycarbonyl	CC(O)CCCC(O)CC(O)C=O
192.26	1.12E-06	2.44E-01	furan	CCCC(=O)\C=C\C1=CC=C(CC)O1
193.29	3.01E-06	1.38E-02	furan	CCCCC1=CC=C(O1)C(=N)CCC
194.27	1.71E-06	3.86E-01	furan	CCCC(=O)CCC1=CC=C(CC)O1
195.26	5.23E-06	1.79E-02	furan	CCC1=CC=C(CCCCC=N)O1
196.29	2.71E-06	5.57E-01	furan	CCCC(=O)CCC1CC=C(CC)O1

197.32	8.08E-07	2.55E-01	imine	CCCCC(=O)CCC(=N)CCC
198.31	2.75E-06	1.71E-01	ketone	CCCCCCC(=O)CC(=O)CCC
199.29	4.35E-08	3.43E+00	hydroxycarbonyl	OC(CCCCCC=O)CCC=N
205.30	3.63E-07	5.28E-02	hydroperoxide	CCCC(CCCCC=O)OO
206.19	4.72E-12	4.15E+03	hydroxycarbonyl	OC(CC(O)C(O)C(O)CC=O)C=O
208.26	2.84E-07	3.08E-01	furan	CCC1=CC=C(CCC(=O)CC(C)=O)O1
210.27	4.49E-07	7.11E-01	furan	CCC1=CCC(CCC(=O)CC(C)=O)O1
211.26	2.52E-09	1.97E+01	imine	CCC1=CC=C(CC(O)C(O)CC=N)O1
212.29	1.20E-07	2.45E+00	ketone	CCCCC(=O)CCC(=O)CC(C)=O
213.28	3.98E-09	1.44E+01	imine	CCC1=CCC(CC(O)C(O)CC=N)O1
214.31	4.84E-08	4.24E+00	hydroxycarbonyl	CCCCC(O)CCC(=O)CC(C)=O
220.27	2.60E-13	9.08E+04	hydroxycarbonyl	OCCCC(O)C(O)CC(O)CCC=O
226.27	1.76E-08	3.27E+00	dihydrofuran	CCC1=CCC(O1)C(O)CC(=O)CC(C)=O
228.29	9.90E-09	1.02E+01	hydroxycarbonyl	CCCCC(=O)C(O)CC(=O)CC(C)=O
230.30	6.12E-10	1.01E+02	hydroxycarbonyl	CCCCC(O)C(O)CC(=O)CC(C)=O
256.25	1.82E-10	1.54E+02	hydroxycarbonyl	CC(=O)CC(=O)CC(O)C(=O)CC(=O)CC(C)=O
234.34	7.16E-12	5.69E+03	alcohol	CCCCCCC(O)C(O)C(O)C(O)CC
282.42	8.55E-09	4.36E+00	acid anhydride	CCCCCCCC(=O)OC(=O)CCC\C=C\CCC
284.48	2.11E-08	2.53E+00	ester	CCCCCCCCCO(=O)CCCCCCCC
344.54	2.82E-13	1.13E+05	ester	CCCCCCCCC(=O)OCCC(O)CCCC(O)CCC
376.58	2.15E-12	5.48E+04	peroxyhemiacetal	OC1(CC\C=C\CCCC\C=C\1)OOC1CCCCC\C=C\CC1
390.56	2.92E-14	3.62E+06	ether	O=CCCCC(CCC(=O)CCC=O)OC1CC\C=C\CCCC\C=C\1
391.60	2.15E-12	1.61E+04	peroxyhemiacetal	OC1(CC\C=C\CCCC\C=C\1)OOC1CC\C=C\CCC\C=C\CC1

Experiment:

Cyclododecane High NO, (NH₄)₂SO₄, dryMean M_w
(g mol⁻¹) 458.38

M _w	P _{vap} (atm)	C _A /C _{is}	Compound Class	SMILES String
112.17	1.13E-02	5.51E-05	dihydrofuran	CCC1CC=C(C)O1
122.17	2.34E-03	3.17E-04	furan	C\C=C\C1=CC=C(C)O1
124.18	2.34E-03	3.41E-04	furan	CCCC1=CC=C(C)O1
125.13	6.60E-04	5.68E-04	imine	C=CC(=O)C(=O)CC=N
126.20	3.71E-03	2.69E-04	dihydrofuran	CCC1CC=C(CC)O1
128.17	4.45E-04	1.67E-03	dihydrofuran	CC(O)C1=CCC(C)O1
130.19	7.79E-05	2.85E-02	hydroxycarbonyl	CCCC(=O)CC(C)O
132.16	3.02E-06	1.33E+00	hydroxycarbonyl	CC(O)C(O)CC(C)=O
133.15	3.85E-07	3.03E+00	imine	CC(O)C(O)C(O)C=N
115.15	2.38E-04	1.49E-02	hydroxycarbonyl	CC(O)CCCC=O
117.17	4.73E-05	1.52E-02	hydroxycarbonyl	CCCC(O)C(C)O
136.19	7.66E-04	1.56E-03	alcohol	CCC1=CC=C(O1)\C=C\C
137.14	5.51E-04	8.81E-04	furan	CC1=CC=C(O1)C(=O)C=N
138.21	7.66E-04	2.22E-03	furan	CCCC1=CC=C(CC)O1
139.15	1.17E-03	4.15E-04	dihydrofuran	CC1=CCC(O1)C(=O)C=N
140.09	5.67E-05	2.07E-02	ketone/aldehyde	O=CC(=O)\C=C\C(=O)C=O
142.11	8.59E-05	8.63E-03	ketone/aldehyde	O=CC(=O)CCC(=O)C=O
144.21	2.55E-05	4.23E-02	hydroxycarbonyl	CC(O)CCCCC=O
146.14	3.64E-07	7.67E+00	hydroxycarbonyl	OC(CC=O)CC(O)C=O
147.17	6.86E-08	6.51E+00	imine	CC(O)CC(O)C(O)C=N
148.21	2.51E-04	1.36E-02	furan	CCC1=CC=C(O1)\C=C\C=C
131.15	1.69E-06	4.10E-01	hydroxycarbonyl	CC(O)CC(O)CC=O
150.22	2.51E-04	5.99E-03	furan	CC\C=C\C1=CC=C(CC)O1
151.12	7.22E-05	1.01E-02	furan	N=CC1=CC=C(O1)C(=O)C=O
152.24	2.51E-04	6.29E-03	furan	CCCCC1=CC=C(C)O1
153.14	9.22E-06	5.35E-02	furan	OC(C=O)C1=CC=C(O1)C=N
154.21	7.74E-05	1.32E-02	furan	CCC1=CCC(CCC=O)O1
156.23	2.31E-05	5.83E-02	ketone/aldehyde	CCC(=O)CCCCC=O
158.24	8.33E-06	5.44E-01	hydroxycarbonyl	CCC(O)CCCCC=O
159.19	1.19E-07	7.01E+00	imine	CC(O)C(=O)CC(O)CC=N
160.21	3.23E-07	2.24E+01	hydroxycarbonyl	CCCC(O)C(O)CCC=O
161.20	6.17E-09	2.38E+02	imine	CC(O)C(O)CC(O)CC=N
162.23	8.19E-05	6.69E-02	furan	CCC1=CC=C(O1)\C=C\C=C\C
163.22	1.05E-05	9.89E-02	imine	CCC1=CC=C(C\C=C\C=N)O1
164.25	8.19E-05	4.13E-02	furan	CC\C=C\C1=CC=C(CC)O1
165.24	1.60E-05	4.62E-02	imine	CCC1=CC=C(CCCC=N)O1
166.26	8.19E-05	2.31E-02	furan	CCCCC1=CC=C(CC)O1
167.25	2.53E-05	3.23E-02	imine	CCC1=CCC(CCCC=N)O1
168.28	1.30E-04	8.36E-03	dihydrofuran	CCCCC1CC=C(CC)O1
170.30	5.06E-05	1.01E-02	ketone/aldehyde	CCCCCCCC(=O)CC
172.27	1.90E-05	4.09E-02	hemiacetal	CCCCC1CCC(O)(CC)O1
174.20	3.71E-03	7.35E-04	dihydrofuran	CCC1CC=C(CC)O1
175.23	4.00E-09	1.36E+02	imine	CCC(O)CC(O)CC(O)C=N
176.26	2.68E-05	1.98E-01	furan	CC\C=C\C1=CC=C(O1)\C=C\C
177.25	5.23E-06	2.69E-01	imine	CCC1=CC=C(C\C=C\C=N)O1
178.28	2.68E-05	3.94E-01	furan	CCC\C=C\C1=CC=C(CC)O1
179.18	2.85E-06	1.63E+00	imine	CC(=O)C1=CC=C(O1)C(=O)CC=N
180.29	2.68E-05	1.39E+00	furan	CCCCC1=CC=C(CC)O1
181.19	5.74E-06	1.12E+00	dihydrofuran	CC(=O)C1=CCC(O1)C(=O)CC=N
182.31	4.24E-05	9.83E-02	dihydrofuran	CCCCC1CC=C(CC)O1
184.28	3.91E-06	4.80E-01	dihydrofuran	CCCC(O)CC1CC=C(CC)O1
188.27	1.93E-08	3.39E+01	hydroxycarbonyl	CC(O)CC(O)CCCCC=O
190.24	6.59E-10	5.20E+03	hydroxycarbonyl	CCC(O)CCC(O)C(O)CC=O
191.23	2.71E-06	3.58E-01	nitrate	CCCC(CC(O)CC)O[N+](=O)[O-]
192.26	1.12E-06	7.01E+00	furan	CCC(=O)\C=C\C1=CC=C(CC)O1
193.29	1.71E-06	1.03E+00	imine	CCC(=N)CCCC1=CC=C(CC)O1
194.27	1.71E-06	1.38E+01	furan	CCCC(=O)CC1=CC=C(CC)O1
195.31	2.71E-06	1.73E+00	imine	CCC(=N)CCCC1CC=C(CC)O1
196.29	2.71E-06	8.73E+00	dihydrofuran	CCCC(=O)CC1CC=C(CC)O1
197.32	8.08E-07	4.38E+00	imine	CCC(=N)CCCCC(=O)CC
198.31	8.08E-07	4.63E+00	ketone/aldehyde	CCCCC(=O)CCCCC(=O)CC
200.28	4.35E-08	3.65E+01	hydroxycarbonyl	CCC(O)CCCC(=O)CCC=O
205.25	1.38E-11	1.78E+04	imine	CCC(O)CC(O)CC(O)C(O)C=N
206.24	2.11E-07	7.72E+00	furan	CCC1=CC=C(O1)\C=C\C(=O)CC(C)=O
207.23	2.56E-08	2.94E+01	nitrate	CCC(O)C(CCC(C)O)O[N+](=O)[O-]

208.26	2.84E-07	3.02E+01	furan	CCC(=O)CC(=O)CC1=CC=C(CC)O1
209.25	1.46E-07	1.43E+01	imine	CCCC1=CC=C(O1)C(O)C(=O)CC=N
210.27	4.49E-07	4.04E+01	dihydrofuran	CCC(=O)CC(=O)CC1CC=C(CC)O1
211.26	2.31E-07	1.42E+01	imine	CCCC1=CCC(O1)C(O)C(=O)CC=N
212.29	8.16E-08	2.18E+02	dihydrofuran	CCC(=O)CC(O)CC1CC=C(CC)O1
213.28	5.32E-09	5.70E+02	imine	CCCC1=CCC(O1)C(O)C(O)CC=N
214.31	1.42E-08	1.46E+02	hydroxycarbonyl	CCC(=O)CCCC(O)CC(=O)CC
222.24	1.11E-07	7.27E+00	furan	CCC1=CC=C(O1)C(=O)CC(=O)CC(C)=O
223.27	6.06E-07	6.69E-01	imine	CCCC1=CCC(O1)C(=O)C(=O)CC=N
224.26	6.18E-09	6.11E+02	furan	CCC1=CC=C(O1)C(=O)CC(O)CC(C)=O
225.29	4.60E-10	2.87E+03	imine	CCC1=CC=C(CC(O)CC(O)CC=N)O1
226.27	1.32E-08	8.33E+02	dihydrofuran	CCC1=CCC(O1)C(=O)CC(O)CC(C)=O
227.26	5.55E-07	4.49E+00	nitrate	CCC(CCCC1=CC=C(C)O1)O[N+](O)=O
228.29	2.11E-09	5.96E+03	hydroxycarbonyl	CCC(=O)CC(O)CC(=O)CC(=O)CC
229.23	6.66E-08	5.74E+01	nitrate	CCC1=CC=C(CC(O[N+](O)=O)C(C)O)O1
230.30	1.01E-10	1.29E+04	hydroxycarbonyl	CCCC(=O)CC(O)CC(=O)CC(O)CC
238.28	1.96E-15	2.09E+08	alcohol	CC(O)CC(O)CC(O)C(O)C(O)C(O)C(O)
239.22	3.93E-10	1.35E+03	nitrate	CCC(O)C(O)C(O)CC(C)O[N+](O)=O
240.26	5.84E-10	2.00E+03	furan	CCC1=CC=C(O1)C(O)CC(=O)C(O)C(C)=O
241.29	1.82E-07	2.00E+01	nitrate	CCC(CCCC1=CC=C(CC)O1)O[N+](O)=O
242.27	7.71E-12	2.69E+05	furan	CC(O)C(O)CC(=O)CC1=CC=C(O1)C(C)O
243.30	2.87E-07	1.14E+01	nitrate	CCCC(CC1CC=C(CC)O1)O[N+](O)=O
244.29	1.22E-11	1.01E+05	dihydrofuran	CC(O)C(O)CC(=O)CC1CC=C(O1)C(C)O
293.32	1.56E-13	1.19E+07	nitrate	CCCC(O)C(O[N+](O)=O)C(O)CC(O)CC(=O)CC
255.27	1.16E-08	7.49E+01	nitrate	CCC(=O)CC(CC1=CC=C(CC)O1)O[N+](O)=O
257.29	1.83E-08	8.62E+01	nitrate	CCC(=O)CC(CC1CC=C(CC)O1)O[N+](O)=O
259.30	1.97E-09	8.41E+02	nitrate	CCC(=O)CCCC(CC(=O)CC)O[N+](O)=O
261.32	1.97E-09	1.31E+03	nitrate	CCC(O)CCCC(CC(=O)CC)O[N+](O)=O
266.29	7.99E-17	3.21E+09	hydroxycarbonyl	CC(O)C(O)C(O)CC(O)CC(O)CC(O)C=O
271.27	2.20E-09	2.74E+02	nitrate	CCC(=O)CC(CC1CC=C(O1)C(C)=O)O[N+](O)=O
273.29	9.74E-10	1.57E+03	nitrate	CCC(O)CC(CC1CC=C(O1)C(C)=O)O[N+](O)=O
275.30	9.70E-10	4.72E+02	nitrate	CCC(O)CC(CCCC(=O)C(C)=O)O[N+](O)=O
287.27	1.57E-09	1.76E+02	nitrate	CCCC(=O)C(O[N+](O)=O)C(=O)CC(=O)CC(=O)CC
289.28	5.88E-11	9.18E+03	nitrate	CCCC(=O)C(O[N+](O)=O)C(=O)CC(O)CC(=O)CC
290.32	1.19E-08	5.73E+01	nitrate	CCCC(O[N+](O)=O)\C=C\CC(CCC)O[N+](O)=O
306.36	1.05E-15	4.55E+08	ester	CCC(O)CC(O)CC(=O)OC(C)CC(O)C(O)CC=O
370.53	4.17E-14	4.88E+06	ester	CCCCCCC(=O)CCCC(=O)OC(C)CC(=O)CC(O)CCCC
372.55	3.39E-12	1.04E+05	ether	CCCCCCC(OC(CCC)\C=C\CC1=CC=C(C)O1)C1=CC=C(C)O1
374.57	3.39E-12	1.61E+05	ether	CCCCCCC(OC(CCC)CCCC1=CC=C(C)O1)C1=CC=C(C)O1
376.58	5.36E-12	1.08E+05	ether	CCCCCCC(OC(CCC)CCCC1=CC=C(C)O1)C1CC=C(C)O1
378.55	4.45E-12	2.36E+05	ether	CCCCC(=O)C(OC(CCC)CCCC1CC=C(C)O1)C1CC=C(C)O1
386.53	5.80E-13	7.92E+05	ether	CCCCC(=O)C(OC(CCC)\C=C\CC1=CC=C(C)O1)C1=CC=C(C)O1
388.55	5.80E-13	1.40E+06	ether	CCCCC(=O)C(OC(CCC)CCCC1=CC=C(C)O1)C1=CC=C(C)O1
390.56	9.19E-13	8.88E+05	ether	CCCCC(=O)C(OC(CCC)CCCC1CC=C(C)O1)C1=CC=C(C)O1
392.58	9.19E-13	3.14E+06	ether	CCCCC(=O)C(OC(CCC)CCCC1CC=C(C)O1)C1=CC=C(C)O1
402.53	1.15E-13	3.51E+06	ether	CCCCC(=O)C(OC(CCC)C(=O)CCC1=CC=C(C)O1)C1=CC=C(C)O1
404.55	1.82E-13	4.35E+06	ether	CCCCC(=O)C(OC(CCC)C(=O)CCC1=CC=C(C)O1)C1CC=C(C)O1
406.56	2.88E-13	3.72E+06	ether	CCCCC(=O)C(OC(CCC)C(=O)CCC1CC=C(C)O1)C1CC=C(C)O1
408.58	5.70E-14	9.90E+06	ether	CCCCC(=O)C(OC(CCC)C(O)CCC1CC=C(C)O1)C1CC=C(C)O1
420.55	1.66E-15	3.23E+08	ether	CCCC(OC(CCC(=O)CC(C)O)C1CC=C(C)O1)C(=O)CCC1=CC=C(C)O1
422.56	2.63E-15	1.46E+09	ether	CCCC(OC(CCC(=O)CC(C)O)C1CC=C(C)O1)C(=O)CCC1CC=C(C)O1
437.58	3.63E-14	1.27E+07	nitrate ether	CCCC(CCCC1=CC=C(C)O1)OC(CCCC(C)O[N+](O)=O)C1CC=C(C)O1
439.59	5.75E-14	3.19E+07	nitrate ether	CCCC(CCCC1CC=C(C)O1)OC(CCCC(C)O[N+](O)=O)C1CC=C(C)O1
453.58	9.85E-15	5.07E+07	nitrate ether	CCCC(CCCC1CC=C(C)O1)OC(C1CC=C(C)O1)C(=O)CCCC(C)O[N+](O)=O
455.59	2.26E-15	2.55E+08	nitrate ether	CCCC(CCCC1CC=C(C)O1)OC(C(O)CCCC(C)O[N+](O)=O)C1CC=C(C)O1
471.59	2.77E-17	6.05E+10	nitrate ether	CCCC(OC(C(O)CCCC(C)O[N+](O)=O)C1CC=C(C)O1)C(O)CCC1CC=C(C)O1
488.62	2.38E-15	1.33E+08	nitrate ether	CCCCCCC(O[N+](O)=O)C(CCC)OC(CCCC(C)O[N+](O)=O)C1CC=C(C)O1

Experiment:

Hexylcyclohexane Low NO, (NH₄)₂SO₄, dryMean M_w
(g mol⁻¹) 310.49

M _w	P _{vap} (atm)	C _A /C _{is}	Compound Class	SMILES String
98.15	4.28E-03	7.14E-06	ketone/aldehyde	O=C1CCCCC1
114.14	6.62E-04	3.30E-05	ketone/aldehyde	O=CCCCCC=O
116.16	2.38E-04	4.17E-05	hydroxycarbonyl	CCC(O)CCC=O
118.13	1.85E-05	9.14E-04	hydroxycarbonyl	CC(O)CC(O)C=O
120.10	4.58E-05	1.21E-03	hydroperoxide	CCC(O)C(OO)=O
122.17	1.45E-03	1.97E-05	ketone/aldehyde	O=CCC1CC=CC=C1
124.18	1.45E-03	3.53E-05	ketone/aldehyde	O=CCC1CC=CCC1
126.20	1.45E-03	5.30E-05	ketone/aldehyde	O=CCC1CCCCC1
128.17	4.68E-04	3.44E-05	hydroxycarbonyl	O=CC1(O)CCCCC1
130.19	1.25E-05	1.00E-03	alcohol	CC1(O)C(O)CCCC1
132.16	1.35E-08	3.09E+00	alcohol	OC1C(O)CC(O)CC1
134.13	3.85E-07	2.40E-01	hydroxycarbonyl	CC(O)C(O)C(O)C=O
135.12	6.51E-07	1.57E-02	imine	CC(OO)C(OO)C=N
136.10	6.51E-07	8.82E-02	hydroperoxide	CC(OO)C(OO)C=O
137.23	2.99E-04	2.67E-05	imine	N=CCCC1=CCCCC1
138.21	2.99E-04	3.00E-04	ketone/aldehyde	O=CCCC1=CCCCC1
139.11	6.44E-04	1.49E-05	imine	C=CC(C(C(C=N)=O)=O)=O
140.18	7.11E-04	5.39E-05	ketone/aldehyde	O=CC(C1CCCCC1)=O
142.20	8.90E-05	1.51E-04	hydroxycarbonyl	O=CC(O)C1CCCCC1
144.21	9.26E-06	1.05E-03	alcohol	CC(O)C1(O)CCCCC1
146.19	3.17E-08	7.98E-01	alcohol	CC1(O)C(O)CC(O)CC1
148.16	3.46E-08	2.08E+00	hydroxycarbonyl	CC(O)C(O)C(O)CC=O
149.15	3.46E-08	2.36E-01	imine	CC(O)C(OO)C(O)C=N
150.13	3.46E-08	1.05E+00	hydroperoxide	CC(O)C(OO)C(O)C=O
152.24	9.77E-05	5.16E-04	ketone/aldehyde	O=CCCCC1=CCCCC1
154.21	7.86E-05	7.47E-04	ketone/aldehyde	O=CCC(C1CCCCC1)=O
156.23	8.33E-06	1.59E-03	hydroxycarbonyl	O=CCC(O)C1CCCCC1
158.24	3.03E-06	1.15E-02	alcohol	CCC(O)C1(O)CCCCC1
159.12	3.72E-06	3.77E-02	hydroxycarbonyl	CC(O)C(C(C(O)C=O)=O)=O
161.11	2.92E-07	6.39E-02	imine	N=CC(C(O)C(OO)C=O)=O
162.14	8.20E-08	6.02E+00	hydroxycarbonyl	CC(O)C(O)C(C(O)C=O)=O
163.17	1.37E-09	4.41E+01	imine	CC(O)C(O)C(O)C(O)C=N
164.16	1.37E-09	6.21E+01	hydroxycarbonyl	CC(O)C(O)C(O)C(O)C=O
165.15	2.23E-09	5.00E+00	imine	CC(OO)C(O)C(OO)C=N
166.13	2.23E-09	1.88E+01	hydroperoxide	CC(OO)C(O)C(OO)C=O
167.27	5.06E-05	1.02E-03	ketone/aldehyde	O=CCCCC1CCCCC1
170.21	1.02E-05	1.35E-03	hydroxycarbonyl	O=CCC(C1(O)CCCCC1)=O
174.20	1.06E-08	1.53E+00	hydroxycarbonyl	O=CC(O)C1(O)C(O)CCCC1
175.12	2.58E-07	4.59E-01	hydroperoxide	CC(O)C(C(OO)C(C=O)=O)=O
177.16	5.36E-09	3.57E+00	imine	CC(O)C(C(OO)C(O)C=N)=O
178.14	5.36E-09	7.59E+01	hydroperoxide	CC(O)C(OO)C(C(O)C=O)=O
179.17	8.66E-11	6.09E+02	imine	CC(O)C(OO)C(O)C(O)C=N
180.29	1.05E-05	9.55E-02	ketone/aldehyde	CCCC(CCC1=CCCCC1)=O
181.24	9.60E-06	1.38E-02	imine	N=CCC(C(C1CCCCC1)=O)=O
182.31	1.65E-05	7.37E-03	ketone/aldehyde	CCCC(CCC1CCCCC1)=O
183.21	1.17E-07	1.22E-01	imine	N=CC(CC(C1)(O)CCCC1)=O
184.28	1.53E-06	2.03E-02	hydroxycarbonyl	O=CCCCC1(O)CCCCC1
186.25	3.53E-08	2.37E-01	hydroxycarbonyl	O=CCC(O)CC1(O)CCCCC1
190.20	2.70E-12	7.88E+03	hydroxycarbonyl	O=CCC1(O)C(O)CC(O)CC1O
191.18	2.19E-13	3.58E+04	imine	N=CC1(O)C(O)C(O)C(O)CC1O
192.17	2.19E-13	9.77E+05	hydroxycarbonyl	O=CC1(O)C(O)C(O)C(O)CC1O
193.16	4.75E-10	6.19E+01	imine	CC(OO)C(OO)C(C(O)C=N)=O
194.14	7.26E-09	1.01E+02	hydroperoxide	CC(OO)C(O)C(C(O)C=O)=O
195.17	4.77E-11	1.96E+03	imine	CC(OO)CC(OO)C(OO)C=N
196.29	8.13E-06	9.68E-02	ketone/aldehyde	CCCC(C(CC1CCCCC1)=O)=O
197.28	2.55E-07	3.77E-01	imine	N=CCC(CCC1(O)CCCCC1)=O
198.31	5.01E-07	3.81E-01	hydroxycarbonyl	CCCC(CCC1(O)CCCCC1)=O
199.29	1.16E-08	2.09E+00	imine	N=CCC(O)CCC1(O)CCCCC1
200.32	5.92E-08	3.12E-01	alcohol	CCCC(O)CCC1(O)CCCCC1
206.19	1.95E-14	6.33E+05	hydroxycarbonyl	O=CCC1(O)C(O)C(O)C(O)CC1O
207.14	1.02E-11	7.12E+02	imine	CC(OO)C(OO)C(C(O)C=N)=O
208.17	1.35E-14	4.64E+06	hydroxycarbonyl	O=CC1(O)C(O)CC(O)C(OO)C1O

209.15	3.11E-11	3.28E+02	imine	CC(OO)C(C(OO)C(OO)C=N)=O
210.14	3.11E-11	1.26E+04	hydroperoxide	CC(OO)C(C(OO)C(OO)C=O)=O
211.26	1.42E-07	3.80E-01	imine	N=CCC(C(O)C(C1CCCC1)=O)=O
212.29	4.84E-08	5.98E+00	hydroxycarbonyl	CC(O)CC(CC(C1CCCC1)=O)=O
195.19	4.77E-11	8.14E+02	imine	CCC(OO)C(OO)C(OO)C=N
196.31	2.75E-06	2.72E-02	ketone/aldehyde	CCCC(CC(C1CCCC1)=O)=O
198.34	2.91E-07	3.83E-02	hydroxycarbonyl	CCCC(O)CC(C1CCCC1)=O
224.26	3.47E-07	5.59E-02	ketone/aldehyde	CC(C(C(CC(C1CCCC1)=O)=O)=O)=O
226.27	4.65E-08	1.66E+00	hydroxycarbonyl	CC(C(O)C(CC(C1CCCC1)=O)=O)=O
209.21	2.89E-13	4.51E+04	imine	CC(O)C(O)C(OO)C(O)C(O)C=N
228.29	2.77E-09	3.67E+01	hydroxycarbonyl	CC(O)CC(CC(C1(O)CCCC1)=O)=O
229.32	4.34E-11	4.21E+02	imine	CC(O)CC(CC(O)C1(O)CCCC1)=N
230.30	8.61E-11	2.70E+02	hydroxycarbonyl	CC(O)CC(O)CC(C1(O)CCCC1)=O
220.24	3.61E-13	9.97E+03	hydroxycarbonyl	O=CC(O)C(O)C1(OO)CCC(O)CC1
222.16	4.13E-15	1.07E+06	hydroperoxide	O=CC1(OO)C(O)C(OO)C(CC1O)=O
242.27	1.61E-09	7.69E+00	hydroperoxide	CC(CC(CC(C1(OO)CCCC1)=O)=O)=O
226.30	5.40E-08	1.51E-01	hydroxycarbonyl	CC(CC(CC(C1(O)CCCC1)=O)=O)=O
244.29	1.82E-11	5.33E+02	hydroperoxide	CC(CC(O)CC(C1(OO)CCCC1)=O)=O
228.32	3.13E-09	1.45E+01	hydroperoxide	CC(CCCC(C1(OO)CCCC1)=O)=O
246.30	8.51E-13	1.01E+04	hydroperoxide	CC(O)CC(CC(O)C1(OO)CCCC1)=O
252.40	1.16E-08	2.80E-01	hydroxycarbonyl dimer	O=C(C(O)CC1CCCC1)CC2CCCC2
254.37	4.74E-10	6.96E+00	hydroxycarbonyl dimer	O=C(C(C1CCCC1)O)CC2(O)CCCC2
259.30	6.86E-12	6.89E+02	imine	CCC(C(CC(OO)C1(OO)CCCC1)=O)=N
261.32	7.41E-11	8.19E+01	imine	CCC(C(CC(O)C1(OO)CCCC1)=O)=N
263.33	1.40E-11	2.61E+02	hydroperoxide	CCCC(CC(OO)C1(OO)CCCC1)=O
264.41	2.11E-09	2.11E+00	hydroxycarbonyl dimer	O=C(/C=C/CC1(O)CCCC1)CC2CCCC2
275.19	6.32E-16	5.65E+06	hydroperoxide	O=CCC(C(C1(OO)C(OO)CC(CC1O)=O)=O)=O
277.23	3.30E-15	1.01E+06	imine	N=CCC(C(C1(OO)C(OO)CC(OO)CC1)=O)=O
280.23	5.14E-17	8.13E+07	hydroperoxide	O=CCC(O)C(C1(OO)C(OO)CC(OO)CC1)=O
282.25	8.80E-19	5.79E+09	hydroperoxide	O=CCC(O)C(O)C1(OO)C(OO)CC(OO)CC1
292.24	3.40E-16	1.54E+07	hydroperoxide	O=C(CCC=O)C(C1(OO)C(OO)CC(OO)CC1)=O
294.30	6.88E-17	7.42E+07	hydroperoxide	CCC(O)C(OO)CC(C1(OO)CCC(OO)CC1)=O
296.27	2.88E-19	1.49E+10	hydroperoxide	OC(CCC=O)C(O)C1(OO)C(OO)CC(OO)CC1
304.21	6.86E-17	6.61E+07	hydroperoxide	O=C(C(CC=O)=O)C(C1(OO)C(OO)CC(CC1O)=O)=O
306.22	8.67E-18	4.68E+08	hydroperoxide	O=C(C(CC=O)=O)C(C1(OO)C(OO)CC(O)CC1O)=O
308.20	2.94E-18	1.80E+09	hydroperoxide	O=C(CC=O)C(C1(OO)C(OO)CC(OO)C(O)C1O)=O
310.21	4.21E-20	1.62E+11	hydroperoxide	O=C(CC=O)C(C1(OO)C(OO)CC(OO)C(O)C1O)=O
312.23	1.61E-20	2.31E+11	hydroperoxide	O=C(CC=O)C(O)C1(OO)C(OO)CC(OO)C(OO)C1
318.37	2.60E-14	1.75E+05	peroxyhemiacetal	OC(OOC(C1(O)CCCC1)=O)CC2(OO)CCCC2
320.38	1.84E-15	1.99E+06	peroxyhemiacetal	OC(OOCC1(OO)CCCC1)CC2(OO)CCCC2
322.49	7.97E-12	4.25E+02	hydroxycarbonyl dimer	O=C(C(CCCC1CCCC1)O)CCC(C2CCCC2)=O
324.46	1.78E-13	2.56E+04	hydroxycarbonyl dimer	O=C(C(CC(O)C1CCCC1)O)CCC(C2CCCC2)=O
326.48	1.62E-13	2.52E+04	hydroxycarbonyl dimer	O=C(C(CC1(OO)CCCC1)O)CCCCC2CCCC2
334.50	1.33E-12	2.73E+03	hydroxycarbonyl dimer	O=C(/C=C/CC1(O)CCCC1)CCCC(C2CCCC2)=O
336.52	2.61E-12	1.26E+03	hydroxycarbonyl dimer	O=C(C(CCCC1CCCC1)O)CCC(C2CCCC2)=O
326.46	1.31E-13	2.71E+04	hydroxycarbonyl dimer	O=C(C(O)C(CC1CCCC1)=O)CCC2(OO)CCCC2
326.54	2.53E-12	1.85E+03	ether	OC(OCCCCC1(O)CCCC1)CC2CCCC2
350.50	1.34E-13	2.82E+04	hydroxycarbonyl dimer	O=C(C(O)CCC(C1CCCC1)=O)CCC(C2CCCC2)=O
360.58	5.43E-11	8.13E+01	ether	CC(C(OC(CCC)/C=C/C1CCCC1)C/C=C/C2CCCC2)=O
362.60	5.43E-11	1.41E+02	ether	CC(C(OC(CCC)CCC1CCCC1)C/C=C/C2CCCC2)=O
366.54	1.14E-14	3.27E+05	ether	O=C(C(O)CCCC1(O)CCCC1)CCCC(C2CCCC2)=O
374.57	5.47E-13	1.00E+04	ether	CCC(OC(CC)/C=C/C(C1CCCC1)=O)/C=C/C(C2CCCC2)=O
376.58	7.35E-13	1.06E+04	ether	CCC(OC(CC)CCC(C1CCCC1)=O)/C=C/C(C2CCCC2)=O
378.60	9.89E-13	9.68E+03	ether	CCC(OC(CC)CCC(C1CCCC1)=O)CCC(C2CCCC2)=O
380.61	6.13E-13	8.02E+03	ether	CCC(OC(CC)CCC(C1CCCC1)=O)CCC2(O)CCCC2
388.55	2.06E-13	1.67E+04	ether	CCC(OC(CC)/C=C/C(C1CCCC1)=O)C(CC(C2=CCCC2)=O)=O
390.56	2.63E-13	3.09E+04	ether	CCC(OC(CC)CCC(C1CCCC1)=O)C(CC(C2=CCCC2)=O)=O
392.58	5.29E-13	2.87E+04	ether	CCC(OC(CC)CCC(C1CCCC1)=O)C(CC(C2CCCC2)=O)=O
394.60	9.88E-14	1.86E+05	ether	CCC(OC(CC)CCC(C1CCCC1)=O)C(CCC2(O)CCCC2)=O
396.61	2.28E-14	4.77E+05	ether	CCC(OC(CC)CCCC1(O)CCCC1)C(CCC2(O)CCCC2)=O
404.55	9.79E-14	3.30E+04	ether	CCC(OC(CC)CC(C1CCCC1)=O)C(CC(C2=CCCC2)=O)=O
406.56	1.91E-13	4.73E+04	ether	CCC(OC(CC)CC(C1CCCC1)=O)C(CC(C2CCCC2)=O)=O
408.58	4.34E-14	3.47E+05	ether	CCC(OC(CC)CC(C1CCCC1)=O)C(CCC2(O)CCCC2)=O
410.60	6.46E-14	1.93E+05	peroxyhemiacetal	CCC(OOC(CC)(O)CC(CC1CCCC1)=O)C(CCC2CCCC2)=O
394.63	9.88E-14	1.18E+05	ether	CCC(OC(CC)CC(C1(O)CCCC1)=O)C(CCC2CCCC2)=O
396.61	2.28E-14	3.64E+05	ether	CCC(OC(CC)CCCC1(O)CCCC1)C(CCC2(O)CCCC2)=O
422.56	2.83E-15	1.78E+06	ether	CC(C(OC(CC)CC(C1(O)CCCC1)=O)C(CC(C2CCCC2)=O)=O)=O

424.58	1.05E-14	6.20E+05	peroxyhemiacetal	<chem>CCC(OOC(CC)(O)CC(CC1CCCCC1)=O)C(CC(C2CCCCC2)=O)=O</chem>
408.61	1.83E-14	4.97E+05	ether	<chem>CC(C(OC(CC)CC(CC1(O)CCCCC1)=O)C(CCC2CCCCC2)=O)=O</chem>
426.59	1.01E-15	6.84E+06	peroxyhemiacetal	<chem>CCC(OOC(CC)(O)CC(CC1(O)CCCCC1)=O)C(CCC2CCCCC2)=O</chem>
410.63	6.46E-14	1.51E+05	peroxyhemiacetal	<chem>CCC(OOC(CC)(O)CC(CC1CCCCC1)=O)C(CCC2CCCCC2)=O</chem>
424.61	1.05E-14	7.37E+05	peroxyhemiacetal	<chem>CCC(OOC(CC)(O)CC(CC1CCCCC1)=O)C(CC(C2CCCCC2)=O)=O</chem>
426.63	1.05E-14	7.80E+05	peroxyhemiacetal	<chem>CCC(OOC(CC)(O)CC(CC1CCCCC1)=O)C(CC(C2CCCCC2)=O)=O</chem>
440.61	7.93E-16	6.30E+06	peroxyhemiacetal	<chem>CCC(OOC(CC)(O)CC(CC1CCCCC1)=O)C(CC(C2(O)CCCCC2)=O)=O</chem>
459.62	1.76E-17	2.03E+08	peroxyhemiacetal	<chem>CCC(OOC(CC)(O)CC(CC1(O)CCCCC1)=O)CCC(C2(O)CCCCC2)=O</chem>

Experiment:

Hexylcyclohexane High NO, (NH₄)₂SO₄, dryMean M_w (g mol⁻¹)
418.06

M _w	P _{vap} (atm)	C _A /C _{IS}	Compound Class	SMILES String
98.15	4.28E-03	2.18E-05	ketone/aldehyde	O=C1CCCCC1
100.16	1.35E-02	4.29E-06	ketone/aldehyde	CCCCCC=O
110.16	1.83E-03	8.07E-05	ketone/aldehyde	O=CC1=CCCCC1
116.16	2.38E-04	1.04E-04	hydroxycarbonyl	CCC(O)CCC=O
118.13	1.85E-05	2.11E-03	hydroxycarbonyl	CC(O)CC(O)C=O
102.16	2.55E-03	4.41E-06	hydroxycarbonyl	CCCC(C=O)O
122.08	2.59E-06	3.04E-02	hydroxycarbonyl	O=C(O)C(O)C=O
124.18	9.14E-04	9.00E-05	ketone/aldehyde	O=CCC1=CCCCC1
126.16	3.24E-04	2.96E-04	ketone/aldehyde	O=CC1CCCCC1=O
128.17	3.24E-04	2.94E-04	ketone/aldehyde	O=CC1CCCCC1=O
130.14	1.17E-05	3.25E-03	hydroxycarbonyl	CC(CC(O)CC=O)=O
132.16	1.69E-06	5.74E-02	hydroxycarbonyl	CC(O)CC(O)CC=O
133.15	3.85E-07	1.24E-01	imine	CC(O)C(O)C(O)C=N
134.13	3.85E-07	4.98E-01	hydroxycarbonyl	CC(O)C(O)C(O)C=O
118.16	1.85E-05	2.72E-03	hydroxycarbonyl	CC(O)CC(O)C=O
118.15	1.85E-05	7.53E-03	hydroxycarbonyl	CC(O)CC(O)C=O
120.14	3.81E-08	1.33E+00	imine	CC(O)C(O)C(O)=N
138.17	3.34E-04	5.99E-04	ketone/aldehyde	O=CC(C1=CCCCC1)=O
139.11	1.44E-05	3.82E-03	imine	O=C(C1=O)CC(C1=O)=N
140.18	7.11E-04	1.22E-04	ketone/aldehyde	O=CC(C1CCCCC1)=O
141.13	2.84E-04	8.77E-05	imine	CC(CC(C(C=N)=O)=O)=O
142.15	1.24E-05	3.10E-03	hydroxycarbonyl	O=CC1(O)CCC(CC1)=O
144.17	1.60E-06	1.73E-02	hydroxycarbonyl	O=CC1(O)CCC(O)CC1
146.19	5.52E-07	1.61E-01	hydroxycarbonyl	CC(O)CC(O)CCC=O
147.17	1.26E-07	1.94E-01	imine	CCC(O)C(O)C(O)C=N
148.11	6.18E-09	2.91E+01	hydroxycarbonyl	OC1C(C=O)OC(O)C1O
149.15	8.82E-10	5.12E+01	imine	N=CC(O)C(O)C(O)CO
132.17	7.39E-09	1.97E+01	alcohol	OC1CC(O)CC(O)C1
133.16	3.85E-07	1.57E-01	imine	CC(O)C(O)C(O)C=N
134.10	8.83E-09	2.10E+01	hydroxycarbonyl	O=C(O)C(O)C(O)C=O
153.18	3.75E-05	1.19E-03	imine	N=CC(C1CCCCC1=O)=O
154.25	1.55E-04	9.92E-04	ketone/aldehyde	O=CCCCC1CCCCC1
155.15	5.52E-06	5.54E-03	imine	N=CC1(O)C(CCCC1=O)=O
156.18	9.24E-05	3.80E-04	hydroxycarbonyl	O=CC(C1(O)CCCCC1)=O
158.20	2.12E-06	3.72E-02	hydroxycarbonyl	O=CC(O)C1(O)CCCCC1
159.19	1.35E-08	1.98E+00	imine	N=CC1(O)C(O)CCCC1O
160.17	7.35E-09	3.60E+01	hydroxycarbonyl	O=CC1(O)CCC(O)CC1O
144.20	1.60E-06	4.55E-02	hydroxycarbonyl	O=CC1(O)CCC(O)CC1
162.14	8.20E-08	4.60E+00	hydroxycarbonyl	CC(O)C(O)C(C(O)C=O)=O
146.17	7.07E-06	1.20E-02	hydroxycarbonyl	CCC(O)C(C(O)C=O)=O
163.15	3.67E-13	5.46E+05	alcohol	OC1C(O)C(O)CC(O)C1O
147.15	2.89E-09	1.88E+01	imine	CC(C(O)C(O)C(O)=N)=O
166.26	3.20E-05	6.67E-03	ketone/aldehyde	O=CCCCC1=CCCCC1
183.16	4.74E-08	1.35E+00	imine	N=CC(C1C(CC(O)CC1=O)=O)=O
168.24	2.57E-05	5.72E-03	ketone/aldehyde	O=CCC(CC1CCCCC1)=O
170.25	2.72E-06	1.37E-02	hydroxycarbonyl	O=CCC(O)CC1CCCCC1
171.22	1.93E-07	1.39E-01	hydroxycarbonyl	O=CCC(O)C1(O)CCCCC1
173.21	1.06E-08	2.01E+00	imine	N=CC(O)C1(O)CCCCC1O
174.20	1.06E-08	8.38E+00	hydroxycarbonyl	O=CC(O)C1(O)CCCCC1O
158.23	2.12E-06	2.82E-02	hydroxycarbonyl	O=CC(O)C1(O)CCCCC1
176.12	1.89E-09	2.33E+02	hydroxycarbonyl	CC(O)C(C(O)C(C(O)=O)=O)=O
160.20	1.35E-08	1.81E+01	hydroxycarbonyl	O=CC1(O)C(O)CCCC1O
160.10	1.26E-07	1.32E+01	hydroxycarbonyl	O=C(O)C(C(C(O)C=O)=O)=O
161.17	9.17E-05	3.05E-03	nitrate	CCC(O[N+](=O)[O-])CCC=O
180.29	1.05E-05	9.37E-02	ketone/aldehyde	CCCC(CCC1=CCCCC1)=O
181.19	7.43E-08	2.22E+00	imine	N=CCC(C1CC(CCC1=O)=O)=O

182.26	8.40E-06	3.50E-02	ketone/aldehyde	O=CCC(CCC1CCCCC1)=O
183.21	9.55E-07	5.30E-02	imine	N=CCC(C1(O)CCCCC1)=O
184.28	8.90E-07	8.14E-02	hydroxycarbonyl	O=CCC(O)CCC1CCCCC1
186.25	3.53E-08	6.48E-01	hydroxycarbonyl	O=CCC(O)CC1(O)CCCCC1
187.24	9.50E-10	2.30E+01	imine	N=CCC(O)C1(O)CCCCC1O
188.22	3.96E-10	7.41E+01	hydroxycarbonyl	O=CCCC1(O)C(O)CCCC1O
189.21	4.56E-11	1.11E+03	imine	OC1(C(O)C=N)C(O)CCCC1O
190.24	2.70E-12	7.27E+04	hydroxycarbonyl	O=CCC1(O)C(O)CC(O)CC1O
174.23	1.06E-08	8.97E+00	hydroxycarbonyl	O=CC(O)C1(O)CCCCC1O
192.26	9.59E-07	5.94E-01	ketone/aldehyde	C/C=C/C(CC(C1=CCCCC1)=O)=O
176.20	3.03E-11	6.18E+03	hydroxycarbonyl	O=CC1(O)C(O)CC(O)CC1O
194.27	1.29E-06	1.30E+00	ketone/aldehyde	CCCC(CC(C1=CCCCC1)=O)=O
195.22	4.69E-07	7.03E-01	imine	N=CCC(C(C1CCCCC1)=O)=O
196.29	2.75E-06	2.90E-01	ketone/aldehyde	CCCC(CC(C1CCCCC1)=O)=O
197.23	1.37E-06	1.06E-01	imine	N=CCC(C(C1(O)CCCCC1)=O)=O
198.31	5.01E-07	4.63E-01	hydroxycarbonyl	CCCC(CCC1(O)CCCCC1)=O
199.25	4.63E-08	1.22E+00	imine	N=CCC(C(O)C1(O)CCCCC1)=O
200.28	1.16E-08	3.87E+00	hydroxycarbonyl	O=CCCC(O)CC1(O)CCCCC1
203.24	3.70E-11	5.93E+02	imine	N=CC(O)C(O)C1(O)CCCCC1O
186.27	3.53E-08	6.17E-01	hydroxycarbonyl	O=CCC(O)CC1(O)CCCCC1
188.25	9.50E-10	6.62E+01	hydroxycarbonyl	O=CCC(O)C1(O)CCCCC1O
206.19	9.67E-14	1.29E+06	hydroxycarbonyl	O=CC(O)C1(O)C(O)CC(O)CC1O
190.23	2.45E-11	3.09E+03	hydroxycarbonyl	O=CC(O)C1(O)C(O)CC(O)CC1
208.26	1.88E-07	2.16E+00	ketone/aldehyde	CC(CC(CC(C1=CCCCC1)=O)=O)=O
209.25	5.98E-08	2.39E+00	imine	N=CCC(CC(C1CCCCC1)=O)=O
210.27	3.79E-07	1.84E+00	ketone/aldehyde	CC(CC(CC(C1CCCCC1)=O)=O)=O
211.26	1.65E-07	9.02E-01	imine	N=CCC(CC(C1(O)CCCCC1)=O)=O
212.29	8.32E-08	6.09E+00	hydroxycarbonyl	CC(CC(CCC1(O)CCCCC1)=O)=O
213.28	3.43E-09	2.92E+01	imine	N=CCC(CC(O)C1(O)CCCCC1)=O
214.31	6.76E-09	1.19E+01	hydroxycarbonyl	CCCC(CC(O)C1(O)CCCCC1)=O
215.29	1.33E-10	2.61E+02	imine	N=CCC(O)CC(O)C1(O)CCCCC1
220.31	4.88E-08	4.29E-01	hydroxycarbonyl dimer	O=C(C(O)C1=CCCCC1)C2=CCCCC2
221.17	4.07E-12	9.40E+03	nitrate	O=CC1(O[N+])([O-])=O)C(O)CC(O)CC1O
222.24	8.83E-13	6.71E+04	hydroxycarbonyl	O=CCCC1(O)C(O)CC(O)CC1O
205.14	1.94E-06	2.38E-02	nitrate	CC(O)C(C(C(O[N+])([O-])=O)C=O)=O
224.26	1.96E-08	9.08E+00	ketone/aldehyde	CC(CC(CC(C1CCCCC1)=O)=O)=O
225.24	2.96E-09	3.29E+01	imine	N=CCC(CC(C1(O)CCC(CC1)=O)=O)=O
226.27	5.40E-08	7.24E+00	hydroxycarbonyl	CC(CC(CC(C1(O)CCCCC1)=O)=O)=O
227.26	9.42E-09	1.11E+01	imine	OC1(CCCCC1)C(CC(C(O)C=N)=O)=O
228.29	1.12E-09	1.75E+02	hydroxycarbonyl	CC(CC(CC(O)C1(O)CCCCC1)=O)=O
229.28	1.72E-07	4.50E-01	nitrate	O=CCCCC1(O[N+])([O-])=O)CCCCC1
230.30	1.38E-11	2.35E+03	hydroxycarbonyl	CCCC(CCC1(O)C(O)CCCC1O)=O
214.32	6.76E-09	3.68E+00	hydroxycarbonyl	CCCC(CC(O)C1(O)CCCCC1)=O
236.36	2.84E-07	8.62E-02	ketone/aldehyde	O=C(C1CCCCC1)=O)CC2CCCCC2
237.26	1.11E-08	5.31E+00	imine	CC(CC(C(C1CCCCC1)=O)=O)=O)=N
238.28	1.11E-08	4.33E+00	hydroxycarbonyl	OC(C(CC(CC(C)=O)=O)=O)C1=CCCCC1
239.27	4.79E-09	1.69E+01	imine	CC(CC(CC(C1(O)CCCCC1)=O)=O)=O)=N
240.26	4.79E-09	1.55E+01	hydroxycarbonyl	CC(CC(CC(C1(O)CCCCC1)=O)=O)=O)=O
241.29	3.30E-10	9.55E+02	imine	CC(C(CC(O)C(C1(O)CCCCC1)=O)=O)=N
242.27	3.30E-10	4.28E+02	hydroxycarbonyl	CC(CC(CC(C1(O)CCCCC1O)=O)=O)=O
243.30	3.91E-11	3.23E+03	imine	CC(C(CC(O)C(O)C1(O)CCCCC1)=O)=N
244.29	3.91E-11	1.40E+03	hydroxycarbonyl	CC(C(CC(O)C(O)C1(O)CCCCC1)=O)=O
245.32	1.55E-08	3.65E+00	nitrate	CCCC(O)CCC1(O[N+])([O-])=O)CCCCC1
246.30	3.09E-14	9.32E+05	hydroxycarbonyl	CCCC(CCC1(O)C(O)CC(O)CC1O)=O
248.32	2.50E-15	1.04E+07	hydroxycarbonyl	CCCC(O)CCC1(O)C(O)CC(O)CC1O
252.35	2.15E-08	1.08E+00	hydroxycarbonyl dimer	OC(C(C1CCCCC1)=O)=O)C2CCCCC2
236.25	3.05E-16	6.84E+07	hydroxycarbonyl	O=CC(O)C(O)C1(O)C(O)CC(O)CC1O
254.33	6.87E-11	3.52E+02	hydroxycarbonyl	O=C(C1(O)CCCCC1O)C2CC(CCC2)=O
255.27	5.92E-12	1.38E+04	imine	CC(CC(CC(C1(O)CC(CCC1O)=O)=O)=O)=N
256.30	2.09E-10	1.68E+02	hydroxycarbonyl	O=C(C(CC(CC(C)=O)=O)O)C1(O)CCCCC1

257.29	9.31E-09	1.39E+01	nitrate	CCC(CC(CC1(O[N+](O-))=O)CCCC1)=O
258.31	7.54E-12	6.99E+03	hydroxycarbonyl	O=C(C(CC(CC(O)C)=O)O)C1(O)CCCC1
259.30	9.87E-10	7.92E+01	nitrate	CCC(CC(O)CC1(O[N+](O-))=O)CCCC1=O
260.33	5.96E-13	7.43E+04	hydroxycarbonyl	O=C(C(CC(O)CC(O)C)O)C1(O)CCCC1
261.32	1.10E-10	5.28E+02	nitrate	CCC(O)CC(O)CC1(O[N+](O-))=O)CCCC1
262.39	2.60E-09	1.57E+01	hydroxycarbonyl dimer	OC(C(CC1=CCCC1)=O)CCC2=CCCC2
264.41	4.12E-09	8.20E+00	hydroxycarbonyl dimer	OC(C(CC1=CCCC1)=O)CCC2CCCC2
266.29	7.99E-17	6.66E+08	hydroxycarbonyl	CC(O)C(O)C(O)CC(O)CC(O)CC(O)C=O
270.24	1.57E-12	1.08E+04	hydroxycarbonyl	CC(CC(CC(C1(O)C(CC(C1O)=O)=O)=O)=O)=O
254.27	6.10E-20	7.41E+11	alcohol	CC(O)C(O)C1(O)C(O)C(O)C(O)C1O
272.34	2.80E-13	1.24E+05	hydroxycarbonyl dimer	O=C(C(C1(O)CCC(O)CC1)O)C2(O)CCCC2
273.29	1.07E-10	7.37E+02	nitrate	CC(CC(CCC1(O[N+](O-))=O)CCCC1O)=O
274.36	5.75E-14	7.64E+05	ether	OC(OC1(O)CCC(O)CC1)CC2(O)CCCC2
275.30	4.12E-12	1.25E+04	nitrate	CC(O)CC(CCC1(O[N+](O-))=O)CCCC1O)=O
276.37	7.44E-14	7.31E+05	ether	OC(OC(O)CCC(O)CC)CC1(O)CCCC1
277.36	4.30E-09	6.47E+00	nitrate ether	CCCCC(O[N+](O-))=O)C(OCCCC)O
280.41	8.55E-09	3.03E+00	acid anhydride	O=C(OC(CCC1CCCC1)=O)CC2CCCC2
284.40	1.86E-12	9.67E+03	hydroxycarbonyl dimer	O=C(C(O)CC1(O)CCCC1)CC2(O)CCCC2
285.38	1.00E-08	1.31E+00	nitrate ether	O=[N+](OC1(CCCCC1)CCOCC2CCCC2)[O-]
286.41	9.85E-13	2.09E+04	hydroxycarbonyl dimer	O=C(C(O)CC(O)CCCC)CC1(O)CCCC1
287.36	3.88E-08	5.97E-01	nitrate ether	O=[N+](OC1(COCC2CCCC2)CCCC1)[O-]
288.38	3.24E-14	1.02E+06	hydroxycarbonyl dimer	CCC(O)C(O)CC(C(O)CCC1(O)CCCC1)=O
289.33	2.21E-11	1.58E+03	nitrate hydroxycarbonyl dimer	O=C(C(O)CC(O)CCC)C1(O[N+](O-))=O)CCCC1
290.36	3.19E-16	1.78E+08	nitrate hydroxycarbonyl dimer	OC1(C(O)CCCC1)COCC2(O)CCC(O)CC2O
292.37	4.17E-16	1.15E+08	ether	CCCC(O)C(O)COCC1(O)CCC(O)CC1O
294.39	6.61E-10	8.72E+01	acid anhydride	O=C(C1CCCC1)OC(CC(CC2CCCC2)=O)=O
278.32	2.62E-16	2.13E+08	acid anhydride	CC(O)C(O)C(C(O)C(O)C1(O)CCCC1O)=O
298.42	2.71E-11	6.72E+02	ester	O=C(OCCCC1(O)CCCC1)CC2(O)CCCC2
299.39	4.08E-13	4.77E+04	ester	O=C(OCCC1(O)CCCC1O)CC2(O)CCCC2
302.41	1.14E-14	3.51E+06	ether	OC(OCCC1(O)CCCC1O)CC2(O)CCCC2
304.30	4.97E-16	8.51E+07	acid anhydride	O=C(OC(CC(CC(O)C)=O)=O)C1(O)C(O)CCCC1O
306.40	4.74E-16	1.03E+08	ether	OC1(CCCOCC(O)C(O)C(O)CC)C(O)CCCC1
289.39	7.37E-10	3.09E+01	nitrate hydroxycarbonyl dimer	CCCCC(C(O)CC(O[N+](O-))=O)CCCC)=O
308.42	2.16E-10	1.63E+02	acid anhydride	O=C(OC(CCC1CCCC1)=O)CC(C2CCCC2)=O
310.43	8.47E-11	3.37E+02	acid anhydride	O=C(OC(CCC1CCCC1)=O)CCC2(O)CCCC2
312.45	8.85E-12	2.24E+03	ester	O=C(OCCCC1(O)CCCC1)CCC2(O)CCCC2
314.42	1.33E-13	1.84E+05	ester	O=C(OCCC1(O)CCCC1)CCC2(O)CCCC2O
316.44	5.10E-15	6.51E+06	ether	OC(COCCC1(O)CCCC1)CC2(O)CCCC2O
318.32	3.04E-17	1.34E+09	acid anhydride	O=C(OC(C1(O)C(O)CCCC1O)=O)C2(O)C(O)CCCC2
302.43	8.59E-15	4.45E+06	ether	OC1(CCOCCC2(O)CCCC2O)CCCC1O
322.40	5.12E-19	7.09E+10	ether	CC(O)CC(O)CC(O)COCC1(O)C(O)CCCC1O
324.42	5.41E-13	5.29E+04	ester	O=C(OCCC(CC1(O)CCCC1)=O)CC2CCCC2=O
326.43	3.98E-13	5.68E+04	ester	O=C(OCCC(CC1(O)CCCC1)=O)CC2(O)CCCC2
330.42	1.08E-17	2.25E+09	hydroxycarbonyl dimer	O=C(C(CC1(O)CCCC1O)O)CCC2(O)CCCC2O
332.35	5.28E-18	6.22E+09	acid anhydride	O=C(OC(CC1(O)C(O)CCCC1)=O)C2(O)C(O)CCCC2O
334.32	1.16E-19	2.80E+11	acid anhydride	O=C(OC(C1(O)C(O)CCCC1O)=O)C2(O)C(O)CCCC2O
335.46	2.31E-11	1.43E+03	acid anhydride	O=C(OC(CCC1CCCC1)=O)CC(CC2CCCC2)=O
338.44	2.14E-12	1.58E+04	acid anhydride	O=C(OC(CCC1(O)CCCC1)=O)CC(CC2CCCC2)=O
340.46	2.09E-13	1.52E+05	acid anhydride	O=C(OC(CCC1(O)CCCC1)=O)CC(O)CC2CCCC2
342.48	1.87E-14	1.59E+06	ester	OC1(CC(O)CCOC(CCC2(O)CCCC2)=O)CCCC1
344.49	7.27E-16	3.90E+07	ether	OC1(CC(O)CCOCC(O)CC2(O)CCCC2)CCCC1
346.46	9.27E-16	3.01E+07	ether	CCC(O)C(OC(C(CC)=O)C(O)C)C(O)CC1(O)CCCC1
348.48	1.45E-13	1.94E+05	hydroxycarbonyl dimer	O=C(C(O)CC(CC1CCCC1)=O)CCC(CC2=CCCC2)=O
350.50	7.55E-12	4.29E+03	acid anhydride	O=C(OC(CCC1CCCC1)=O)CC(CCC2CCCC2)=O
352.47	3.93E-13	1.53E+05	acid anhydride	O=C(OC(CCC1(O)CCCC1)=O)CCCC(C2CCCC2)=O
354.49	1.25E-13	2.75E+05	acid anhydride	O=C(OC(CCC1(O)CCCC1)=O)CCCC2(O)CCCC2
355.48	2.35E-11	9.95E+02	ester	O=C(OCCC1CCCC1)CCCC2(O[N+](O-))=O)CCCC2
356.50	6.10E-15	6.23E+06	ester	O=C(OCCC(O)CC1(O)CCCC1)CCCC2(O)CCCC2
358.52	1.74E-16	1.86E+08	ether	OC(OCCC(O)CC1(O)CCCC1)CCCC2(O)CCCC2
360.54	1.42E-12	2.31E+04	ester	O=C(OCCCCC(CC1=CCCC1)=O)CCCC2=CCCC2

362.51	9.80E-13	3.02E+04	ester	<chem>O=C(OCCC(CC(C1CCCCC1)=O)=O)CCCC2=CCCCC2</chem>
364.48	7.52E-17	4.47E+08	ester	<chem>CCCCC(OCCC(O)CC(O)COCCC(O)C(O)CC)=O</chem>
351.46	1.06E-11	2.37E+03	ester	<chem>O=C(OCC(C(C1CCCCC1)=O)=O)CC(C2CCCCC2)=O</chem>
366.45	2.03E-19	1.56E+11	ether	<chem>OC1(CCC(O)OCC(O)C2(O)C(O)CCCC2)C(O)CCCC1</chem>
368.51	1.39E-14	4.76E+06	ester	<chem>O=C(OCCC(CC1(O)CCCCC1)=O)CCCC2(O)CCCCC2</chem>
370.53	2.00E-15	1.79E+07	ester	<chem>O=C(OCCC(O)CC1(O)CCCCC1)CCCCC2(O)CCCCC2</chem>
371.52	3.21E-13	7.87E+04	imine ether	<chem>O=C(CC(COC(C=N)CCC1=CCCCC1)=O)/C=C/C2=CCCCC2</chem>
372.50	3.56E-17	1.40E+09	ester	<chem>O=C(OCCC(O)CC1(O)CCCCC1)CC(O)CC2(O)CCCCC2</chem>
373.54	3.65E-13	7.57E+04	imine ester	<chem>O=C(OC(C(C=N)CCC1=CCCCC1)CCCC(C2=CCCCC2)=O</chem>
374.57	3.34E-13	1.72E+05	ether	<chem>CCC(OC(C)CCC(C1=CCCCC1)=O)C(CC(C2CCCCC2)=O)=O</chem>
310.49	6.55E-11	5.98E+02	ether	<chem>O=C(COCCCCC1(O)CCCCC1)C2CCCCC2</chem>
378.55	5.11E-13	5.76E+04	ether	<chem>CCC(OC(C=O)CC(C1CCCCC1)=O)CC(C2CCCCC2)=O</chem>
384.51	2.05E-17	1.47E+09	hydroxycarbonyl dimer	<chem>O=C(C(O)CCCC1(O)CCCCC1)CCC(C(O)C2(O)CCCCC2)=O</chem>
386.49	2.65E-18	1.70E+10	acid anhydride	<chem>O=C(OC(CCCC1(O)CCCCC1O)=O)CCCC2(O)CCCCC2O</chem>
387.52	3.78E-15	6.96E+06	nitrate ether	<chem>OC1CCCC(CCCOCCCCC2(O)CCCCC2)(O[N+][O-])=O)C1</chem>
370.50	7.47E-18	8.08E+09	hydroxycarbonyl dimer	<chem>O=C(C(O)CC(C1(O)CCCCC1)=O)CC(O)CC2(O)CCCCC2</chem>
389.54	4.76E-14	6.88E+05	imine ester	<chem>N=CC(OC(CC(CCCC1=CCCCC1)=O)=O)CCC(C2CCCCC2)=O</chem>
390.56	1.06E-13	5.25E+05	ether	<chem>CCC(OC(C(C)=O)CC(C1CCCCC1)=O)CC(C2=CCCCC2)=O</chem>
391.55	5.04E-14	6.01E+05	imine ether	<chem>CCC(OC(CC=N)CC(C1CCCCC1)=O)CC(C(C2CCCCC2)=O)=O</chem>
392.58	1.47E-13	3.44E+05	ether	<chem>CCC(OC(CC(C(C)=O)=O)C1CCCCC1)CC(C2CCCCC2)=O</chem>
394.60	1.02E-13	2.99E+05	ether	<chem>CCC(OC(CC(C(C)=O)=O)C1CCCCC1)CCCC2(O)CCCCC2</chem>
400.52	7.76E-14	3.46E+05	ether	<chem>CC(C(OC(CC/C=C/C)=O)C1=CCCCC1)C(C(C2=CCCCC2)=O)=O)=O</chem>
402.53	9.55E-14	4.07E+05	ether	<chem>CC(C(OC(CC(CCC)=O)C1=CCCCC1)C(C(C2=CCCCC2)=O)=O)=O</chem>
403.56	5.90E-14	5.34E+05	imine ether	<chem>CC(C(OC(CC(C(C)=N)=O)C1=CCCCC1)C(C(C2CCCCC2)=O)=O</chem>
404.55	1.51E-13	3.92E+05	ether	<chem>CC(C(OC(CC(CCC)=O)C1CCCCC1)C(C(C2=CCCCC2)=O)=O)=O</chem>
388.53	2.47E-20	1.28E+12	hydroxycarbonyl dimer	<chem>O=C(C(O)C(O)CCC1(O)CCCCC1)CC(O)C(O)C2(O)CCCCC2</chem>
406.56	2.39E-13	2.96E+05	ether	<chem>CC(C(OC(CC(CCC)=O)C1CCCCC1)C(C(C2CCCCC2)=O)=O)=O</chem>
407.60	1.08E-12	3.67E+04	nitrate ether	<chem>CCC(OC(CCC)CCC1(O[N+][O-])=O)CCCCC1)/C=C/C2=CCCCC2</chem>
408.58	1.83E-14	2.12E+06	ether	<chem>CC(C(OC(CC(CCC)=O)C1CCCCC1)C(C(C2(O)CCCCC2)=O)=O</chem>
417.55	8.46E-24	3.53E+15	imine ether	<chem>CC(C(OC(C(C)=N)CC(C1CCCCC1)=O)C(C(C2=CCCCC2)=O)=O)=O</chem>
418.53	8.46E-24	4.29E+15	hydroxycarbonyl dimer	<chem>O=C(C(O)CC(O)CC1(O)CCCCC1O)CC(O)CC(O)C2(O)CCCCC2</chem>
419.56	4.30E-14	8.84E+05	imine ether	<chem>CC(C(OC(C(C)=N)CC(C1CCCCC1)=O)C(C(C2CCCCC2)=O)=O)=O</chem>
420.55	4.30E-14	1.32E+06	ether	<chem>CC(C(OC(C(C)=O)CC(C1CCCCC1)=O)C(C(C2CCCCC2)=O)=O)=O</chem>
421.58	1.02E-14	3.41E+06	imine ether	<chem>CC(C(OC(C(C)=N)CC(C1CCCCC1)=O)C(C(O)CC2CCCCC2)=O)=O</chem>
422.56	1.02E-14	4.38E+06	ether	<chem>CC(C(OC(C(C)=O)CC(C1CCCCC1)=O)C(C(O)CC2CCCCC2)=O)=O</chem>
423.59	4.85E-16	7.94E+07	imine ether	<chem>CC(O)C(OC(C(C)=N)CC(C1CCCCC1)=O)C(C(O)CC2CCCCC2)=O</chem>
424.58	4.85E-16	6.89E+07	ether	<chem>CC(O)C(OC(C(C)=O)CC(C1CCCCC1)=O)C(C(O)CC2CCCCC2)=O</chem>
433.55	7.70E-16	3.55E+07	imine ether	<chem>CC(C(OC(C(C)=O)CC(C1)CCCC1=N)=O)C(C(C2CCCCC2)=O)=O)=O</chem>
434.53	7.70E-16	3.34E+07	ether	<chem>CC(C(OC(C(C)=O)CC(C1)CCCC1=O)=O)C(C(C2CCCCC2)=O)=O)=O</chem>
435.56	9.83E-17	3.28E+08	imine ether	<chem>CC(O)C(OC(C(C)=O)CC(C1)CCCC1=N)=O)C(C(C2CCCCC2)=O)=O</chem>
436.55	9.83E-17	2.89E+08	ether	<chem>CC(O)C(OC(C(C)=O)CC(C1)CCCC1=O)=O)C(C(C2CCCCC2)=O)=O</chem>
437.58	1.61E-17	2.57E+09	imine ether	<chem>CC(O)C(OC(C(C)=O)CC(O)C(C1)CCCC1=N)C(C(C2CCCCC2)=O)=O</chem>
438.56	5.79E-16	5.92E+07	ether	<chem>CC(C(OC(C(C)=O)CC(O)C1CCCCC1)C(C(O)C2CCCCC2)=O)=O</chem>
439.59	2.60E-17	1.73E+09	imine ether	<chem>CC(O)C(OC(C(C)=N)CC(O)C1CCCCC1)C(C(O)C2CCCCC2)=O)=O</chem>
441.61	5.26E-19	6.55E+10	imine ether	<chem>CC(O)C(OC(C(C)=N)CC(O)C1CCCCC1)C(C(O)C(O)C2CCCCC2)=O</chem>
449.54	3.97E-15	6.40E+06	imine ether	<chem>CC(C(OC(C(C)=N)C(C1CCCCC1)=O)C(C(O)C(C2CCCCC2)=O)=O)=O</chem>
451.56	1.49E-16	2.19E+08	imine ether	<chem>CC(C(OC(C(C)=N)C(C1(O)CCCCC1)=O)C(C(O)C(C2CCCCC2)=O)=O)=O</chem>
453.58	6.04E-18	7.55E+09	imine ether	<chem>CC(O)C(OC(C(C)=N)C(C1(O)CCCCC1)=O)C(C(O)C(C2CCCCC2)=O)=O</chem>
455.59	2.30E-19	1.58E+11	imine ether	<chem>CC(O)C(OC(C(C)=N)C(C1(O)CCCCC1)=O)C(C(O)CC2(O)CCCCC2)=O</chem>
467.56	2.46E-18	1.24E+10	imine ether	<chem>CC(C(OC(C(C)=O)=N)C(C1(O)CCCCC1)=O)C(C(O)CC2(O)CCCCC2)=O)=O</chem>
469.58	6.20E-17	5.32E+08	nitrate ether	<chem>CCC(OC(C(C)=O)C(C1(O)CCCCC1)=O)CC(C2(O[N+][O-])=O)CCCCC2)=O</chem>
471.59	8.33E-18	3.12E+09	nitrate ether	<chem>CCC(OC(C(C)=O)C(C1(O)CCCCC1)=O)CC(O)CC2(O[N+][O-])=O)CCCCC2</chem>
486.61	6.25E-16	3.54E+07	nitrate ether	<chem>CCC(OC(C(C)=O)CCC1(O[N+][O-])=O)CCCCC1)CCCC2(O[N+][O-])=O)CCCCC2</chem>
502.61	1.10E-17	1.74E+09	nitrate ether	<chem>CCC(OC(C(C)=O)CCC1(O[N+][O-])=O)CCCCC1)CC(O)CC2(O[N+][O-])=O)CCCCC2</chem>

Appendix O

Supporting Information from “Chemical Composition of Toluene and Cresol Secondary Organic Aerosol”¹⁷

¹⁷ Reproduced by permission from “Chemical Composition of Toluene and Cresol Secondary Organic Aerosol: Effect of NO” by K. A. Schilling, H. Lignell, M. M. Coggon, R. H. Schwantes, X. Zhang, and J. H. Seinfeld. In submission to *Environmental Science and Technology*, 2015.

1 ***Supporting Information:***

2 Chemical Composition of Toluene and Cresol Secondary Organic Aerosol: Effect of NO_x Level

3 Katherine A. Schilling[†], Hanna Lignell[†], Matthew M. Coggon[†], Rebecca Schwantes[‡], Xuan Zhang[‡], John
4 H. Seinfeld^{*†‡}

5 [†]Division of Chemistry and Chemical Engineering, California Institute of Technology, Pasadena,
6 California 91125, United States

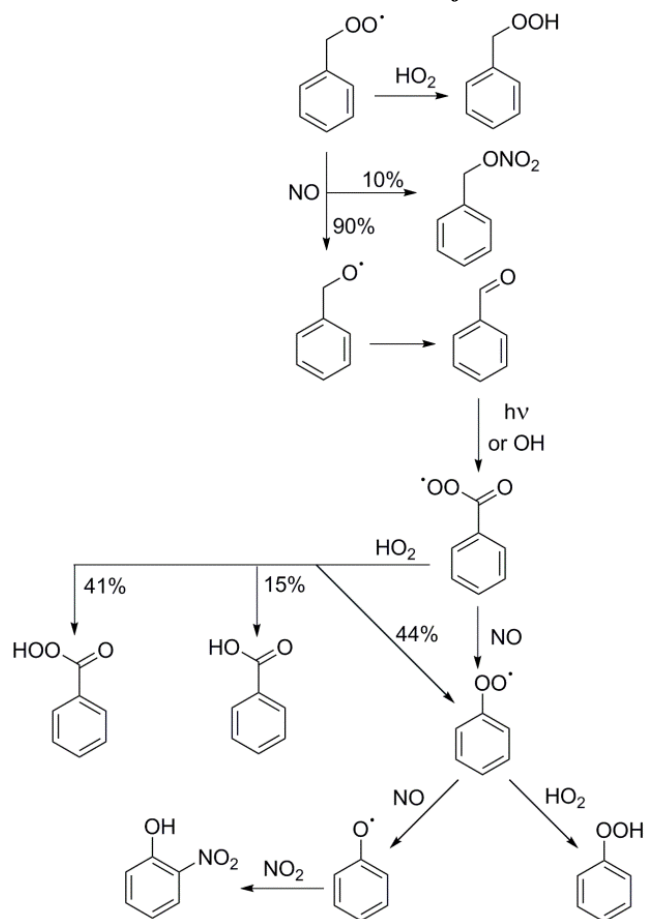
7 [‡]Division of Engineering and Applied Science, California Institute of Technology, Pasadena, California
8 91125, United States

9 ***Environmental Chamber Experimental Details***

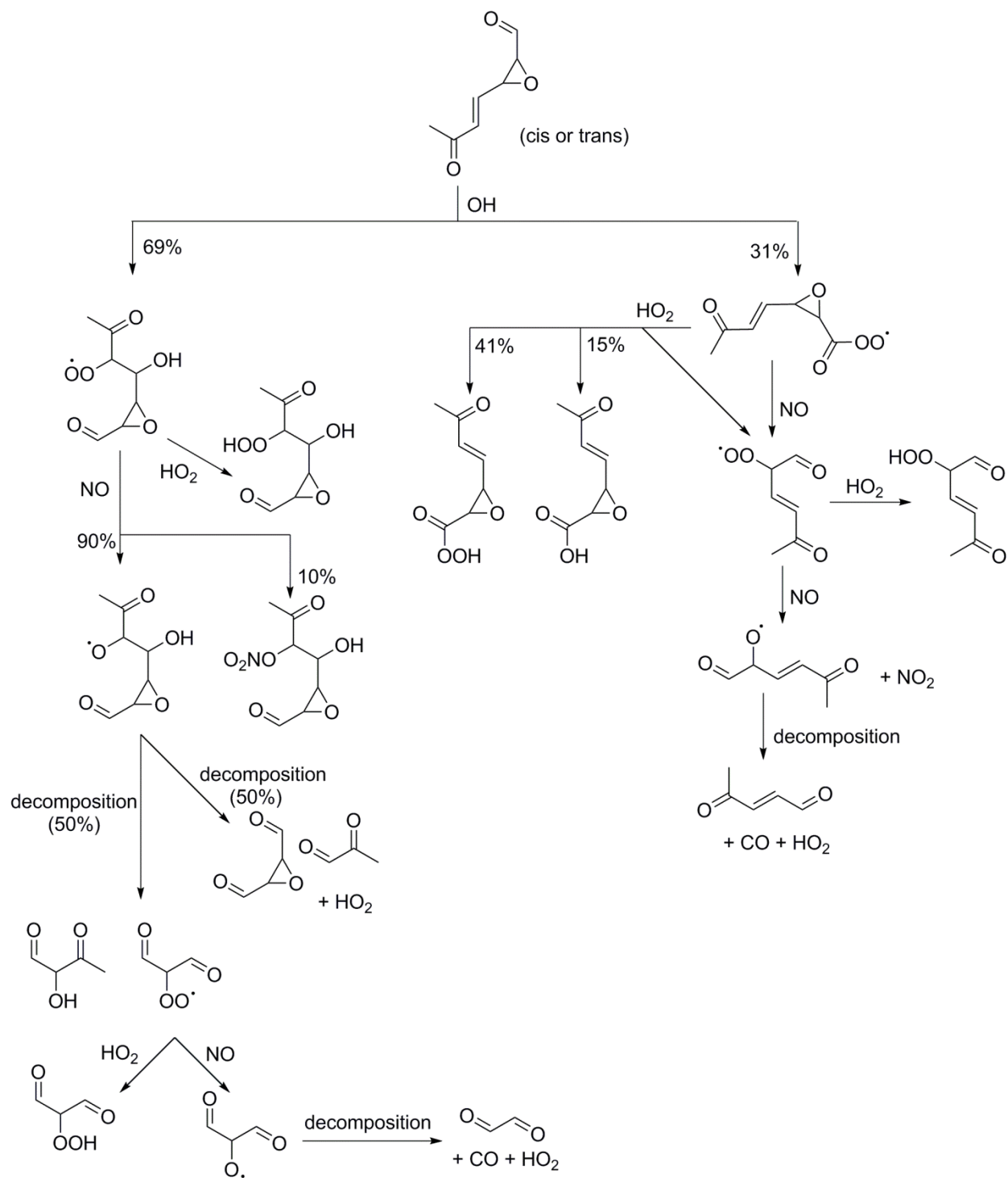
10 Hydroxyl radicals were produced through the photolysis of hydrogen peroxide (50% weight
11 solution, Sigma Aldrich), which was introduced into the environmental chamber using filtered
12 air flowing at 5 L min⁻¹ through a glass trap immersed in a 35 °C water bath over the course of
13 1.5 to 2 h. The environmental chamber black lights' peak wavelength is 350 nm. To minimize
14 self-reaction of peroxy radicals (RO₂+RO₂) and promote the reaction of peroxy radicals with
15 HO₂ radicals (RO₂+HO₂) under low-NO conditions, 220 μL of H₂O₂ solution was injected to
16 reach a concentration of 4 ppm. Under high-NO conditions, 110 μL of H₂O₂ solution was
17 injected to reach a concentration of 2 ppm; less H₂O₂ was necessary to achieve a dominant
18 RO₂+NO regime. For high-NO conditions, an initial injection of 100 ppb was performed prior to
19 the initiation of photooxidation, and a continuous flow of 50 ppb h⁻¹ was used to maintain an
20 RO₂+NO-dominant regime throughout the course of the experiment. Seed aerosol was produced
21 by the atomization of aqueous solutions of inorganic salts. Ammonium sulfate (>99.9%, Sigma
22 Aldrich), sodium chloride (>99%, Sigma Aldrich), sodium sulfate (>99%, Sigma Aldrich), and
23 magnesium sulfate (>99%, Sigma Aldrich) with sulfuric acid (18 M, Sigma Aldrich) were used
24 in seed aerosol preparations. Ammonium sulfate was prepared at a concentration of 0.015 M for

25 the majority of experiments, and at a concentration of 0.06 M for a high seed surface area
 26 experiment; the rest of the seed solutions were prepared at concentrations of 0.03 M.

27 **Master Chemical Mechanism for non-Cresol Pathways for Toluene Photooxidation**



28
 29 **Figure S1.** MCM mechanism for the gas-phase oxidation of the benzyl peroxy radical under low- and
 30 high-NO conditions.¹



31

32 **Figure S2.** MCM mechanism for the gas-phase oxidation of the toluene-derived epoxy muconaldehyde
 33 under low- and high-NO conditions.¹

34

35

36 **DART-HR-MS Analysis of SOA Collected by Filtration**

37 *Standards & Sampling Material*

38 A mass calibrant and independent quality assurance quality control (QA/QC) compounds
39 were run with each sample set to ensure mass accuracy to within 5 mDa. The mass calibrant
40 used for positive mode was polyethylene glycol (average molecular weight of 600 amu, PEG-
41 600; Acros Organics, Geel, Belgium) which was dissolved in methanol. The independent
42 QA/QC compound used is reserpine, which was purchased from Sigma-Aldrich, which was
43 diluted in methanol. The mass calibrant for negative mode was a mixture of fatty acids including
44 (at approximately 100 µg per fatty acid): hexanoic acid, octanoic acid, decanoic, acid,
45 dodecanoic acid, myristic acid, palmitic acid, stearic acid, eicosanoic acid, docosanoic acid, and
46 tetracosanoic acid; dissolved in 2 mL of hexane. An individual sample of hexadecanoic acid was
47 sampled as a QA/QC compound.

48 Tweezers were used to introduce the samples into the DART gas stream. Before analysis,
49 the tweezers were rinsed with acetone, and were introduced into the gas stream to vaporize any
50 contaminants which may have been present on them.

51 A ~1 cm strip was cut from each sample substrate for testing. The cutting was tested in
52 triplicate, with each sampling being from a different are of the substrate.

53 *Development of Mass Calibration Mixtures*

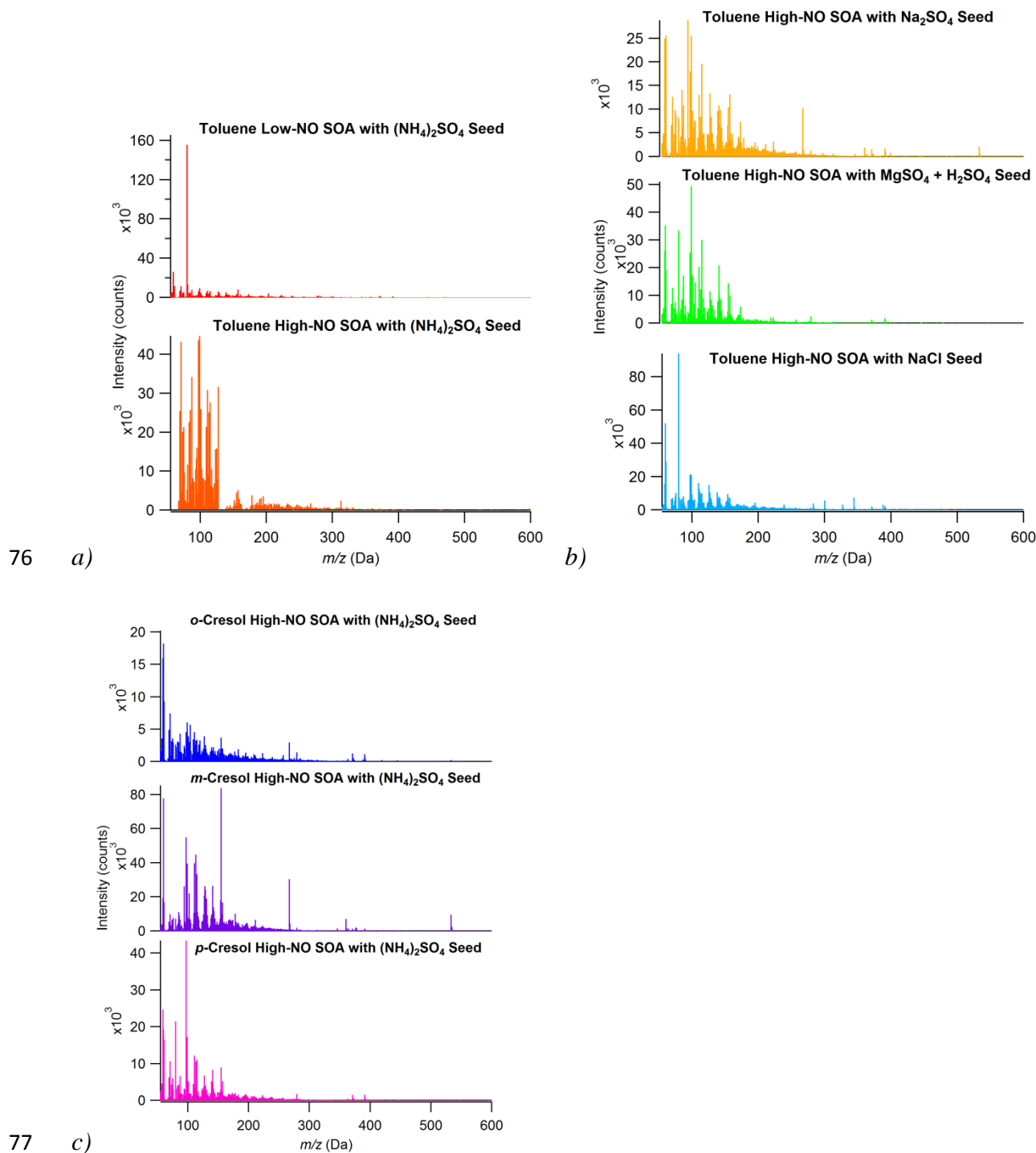
54 In these studies, a solution of PEG-600 (50 µL in 10 mL of methanol) was used to
55 calibrate the mass spectrometer for each run. PEG-600 provided a series of $[M+H]^+$ and
56 $[M+H_3O]^+$ ions in positive mode, allowing for tuning peaks in the range of 61-679 Da. In
57 negative mode $[M+OH]^-$ peaks were used, providing a tuning range of 75-675 Da. Acceptable
58 calibration was determined if the calibration Mass Center software produced a residual value of

59 $>9 \times 10^{-12}$. To ensure proper calibration, a solution of reserpine (5 mg in 10 mL of methanol) or
60 linoleic acid (20 μ L in 10 mL of methanol) was analyzed subsequent to the PEG-600 in every
61 sample run. Reserpine produces a protonated molecule peak at 609.281 Da in positive mode.
62 Linoleic acid, which produces a deprotonated molecule peak at 279.232 Da was used in negative
63 mode to ensure accurate calibration. Calibration was deemed sufficient if the mass of the above
64 listed peaks fell within ± 0.005 Da of the theoretical value.

65 *Parameters for AccuTOF-DART*

66 The instrument which was used in the study was a JEOL (Tokyo, Japan) AccuTOF™
67 mass spectrometer (JMS-T100LC) coupled with an IonSense (Saugus, MA, USA) DART®
68 source. Ultra-pure helium was used as the ionizing gas with a flow rate of 1.75 L min⁻¹. For all
69 analyses, the DART® source was set to a needle voltage of ± 3.5 kV. Electrode 1 and electrode 2
70 voltages were both set to ± 150 V. Mass spectrometer settings include: an orifice 1 voltage of
71 ± 20 V, orifice 2 voltage of ± 5 V, a ring lens voltage of ± 5 V, a peaks voltage of 1500 V, a mass
72 range of 50 – 1500 m/z at 0.5 seconds per scan. A helium gas stream temperature of 325 °C was
73 also employed.

74

75 **DART-HR-MS Mass Spectra for Toluene and o-, m-, and p-Cresol SOA**78 **Figure S3.** (+)-DART-HR-MS mass spectra for toluene and cresol SOA.

79

80

81 *Measured Chemical Compositions for Toluene and o-, m-, and p-Cresol SOA*

82 Table S1: Chemical composition measured by (+)-DART-HR-MS of toluene SOA generated under low-
 83 NO conditions with (NH₄)₂SO₄ seed. Abundance is defined as ((C_A/C_{IS})/Σ(C_A/C_{IS})).

<i>m/z</i> (Da)	Abundance	C	H	N	O	Category	Smiles	P _{vap} (atm)
59.0491	1.21E-12	3	6		1	C _x H _y O ₁	CC(C)=O	3.87E-01
61.0284	4.71E-11	2	4		2	C _x H _y O ₂	CC(O)=O	4.49E-03
71.0491	2.94E-12	4	6		1	C _x H _y O ₁	CC=CC=O	8.30E-02
73.0648	5.62E-13	3	4		2	C _x H _y O ₂	CC(C=O)=O	1.90E-01
75.0441	1.49E-11	3	6		2	C _x H _y O ₂	CC(CO)=O	6.92E-03
80.0495	1.18E-10	5	5	1		C _x H _y N	C1=NC=CC=C1	2.63E-02
85.0284	3.99E-11	4	4		2	C _x H _y O ₂	O=CC=CC=O	3.42E-03
87.0441	2.79E-11	4	6		2	C _x H _y O ₂	O=CCCC=O	6.19E-03
97.0284	1.64E-11	5	4		2	C _x H _y O ₂	O=CC1=CC=CO1	7.54E-03
99.0441	2.02E-10	5	6		2	C _x H _y O ₂	CC(C=CC=O)=O	1.12E-03
101.0597	6.31E-12	5	8		2	C _x H _y O ₂	CC1CCC(O1)=O	2.17E-02
111.0441	7.8E-11	6	6		2	C _x H _y O ₂	O=CC1=CC=C(C)O1	2.46E-03
115.0390	2.89E-07	5	6	3		C _x H _y O ₃	CC(C=CC(O)=O)=O	5.26E-07
123.0441	1.03E-08	7	6	2		C _x H _y O ₂	O=C(C=C1)C=C(C)C1=O	8.12E-06
125.0597	3.64E-08	7	8	2		C _x H _y O ₂	CC1=C(O)C=CC=C1O	2.29E-06
127.0390	3.8E-07	6	6	3		C _x H _y O ₃	O=CC1=C(O)C=C(C)O1	5.26E-07
129.0546	2.22E-07	6	8	3		C _x H _y O ₃	O=CC1=CCC(O1)(O)C	5.26E-07
139.0390	2.67E-07	7	6	3		C _x H _y O ₃	O=C1C(C)=CC(C(O)=C1)=O	5.26E-07
141.0546	1.58E-05	7	8	3		C _x H _y O ₃	CC1=C(O)C=CC(O)=C1O	5.77E-09
143.0339	2.73E-05	6	6	4		C _x H _y O ₄	O=C(O)C=CC=CC(O)=O	3.29E-09
155.0339	1.33E-05	7	6	4		C _x H _y O ₄	O=C1C(C)=C(O)C(C(O)=C1)=O	8.26E-09
157.0495	0.007994	7	8	4		C _x H _y O ₄	CC1=C(O)C(O)=CC(O)=C1O	2.35E-11
173.0445	0.991948	7	8	5		C _x H _y O ₅₊	CC1=C(O)C(O)=C(O)C(O)=C1O	8.99E-14
195.1380	3.06E-07	10	18	2		C _x H _y O ₂	O=C(OCC(C)=O)C1=CC=CC=C1O	2.29E-07

84

85 Table S2: Chemical composition measured by (+)-DART-HR-MS of toluene SOA generated under high-
 86 NO conditions with (NH₄)₂SO₄ seed. Abundance is defined as ((C_A/C_{IS})/Σ(C_A/C_{IS})). Compounds marked with
 87 an asterisk (*) indicate they are also detected in *o*-cresol SOA.

<i>m/z</i> (Da)	Abundance	C	H	N	O	Category	Smiles	P _{vap} (atm)
69.0692	4.17E-10	4	4		1	C _x H _y O ₁	O1C=CC=C1	2.05E-01
71.0487	1.75E-09	4	6		1	*C _x H _y O ₁	CC=CC=O	8.30E-02
72.0485	1.79E-06	3	5	1	1	C _x H _y NO ₁	C=CC(N)=O	9.20E-06
73.0635	3.55E-10	3	4		2	C _x H _y O ₂	CC(C=O)=O	1.90E-01
75.0433	1.03E-08	3	6		2	*C _x H _y O ₂	CC(CO)=O	6.92E-03
76.0395	1.34E-01	2	5	1	2	C _x H _y NO ₂	NCC(O)=O	2.42E-10
80.0496	6.62E-10	5	5	1		*CHN	C1=NC=CC=C1	2.63E-02
83.0838	1.14E-09	5	6		1	C _x H _y O ₁	CC1=CC=CO1	6.70E-02
85.0297	2.53E-08	4	4		2	*C _x H _y O ₂	O=CC=CC=O	3.42E-03
87.0439	1.86E-08	4	6		2	*C _x H _y O ₂	O=CCCC=O	6.19E-03
89.0581	4.26E-08	4	8		2	*C _x H _y O ₂	O=CCCCO	6.48E-04

91.0540	2.13E-06	3	6	3	C _x H _y O ₃	OC(C(O)=O)C	1.13E-05	
93.0391	2.57E-09	6	4	1	C _x H _y O ₁	C12=C(O2)C=CC=C1	1.39E-02	
95.0815	2.67E-08	6	6	1	C _x H _y O ₁	OC1=CC=CC=C1	2.02E-03	
96.0480	4.19E-05	5	5	1	1	C _x H _y NO ₁	O=C1C=CC=CN1	3.38E-07
97.0327	3.15E-07	5	4	2	C _x H _y O ₂	O=C1C=CC(C1)=O	4.67E-04	
99.0453	1.10E-08	5	6	2	C _x H _y O ₂	CC1=CCC(O1)=O	1.37E-02	
100.0452	8.82E-05	4	5	1	2	C _x H _y NO ₂	O=C(N1)CCC1=O	4.71E-07
101.0576	4.06E-08	4	4	3	C _x H _y O ₃	O=C1CCC(O1)=O	2.15E-03	
102.0896	1.90E-09	4	7	1	2	C _x H _y NO ₂	O=C(OCC)C=N	1.89E-02
103.0428	5.81E-08	4	6	3	C _x H _y O ₃	O=C1C(O)CCO1	4.80E-04	
104.0371	8.01E-10	3	5	1	3	C _x H _y NO ₃	C=CC(ON(=O)=O)	2.60E-02
105.0228	1.23E-05	3	4	4	C _x H _y O ₄	OCC(C(O)=O)=O	2.22E-06	
107.0655	1.41E-08	7	6	1	C _x H _y O ₁	O=CC1=CC=CC=C1	1.83E-03	
109.1014	1.09E-07	7	8	1	C _x H _y O ₁	OC1=C(C)C=CC=C1	6.61E-04	
110.0612	2.73E-08	6	7	1	1	C _x H _y NO ₁	OC1=CC=C(C)N=C1	7.24E-04
111.0475	2.84E-07	6	6	2	C _x H _y O ₂	O=CC=CC=CC=O	3.66E-04	
112.0432	4.35E-08	5	5	1	2	C _x H _y NO ₂	O=C(N1)C=C(C)C1=O	7.03E-04
113.0534	1.72E-07	6	8	2	C _x H _y O ₂	O=CCCC=CC=O	4.92E-04	
114.0581	1.46E-06	5	7	1	2	C _x H _y NO ₂	OC(C1=NCCC1)=O	2.57E-05
115.0418	1.41E-07	6	10	2	C _x H _y O ₂	O=CCCCCC=O	6.62E-04	
117.0570	1.86E-07	5	8	3	C _x H _y O ₃	O=C1C(C)CC(O)O1	1.91E-04	
118.0527	1.73E-09	4	7	1	3	C _x H _y NO ₃	O=C(O)C(O)CC=N	8.50E-03
119.0670	7.35E-07	4	6	4	C _x H _y O ₄	OC(C(O)C=O)C=O	2.68E-05	
123.0470	1.89E-06	7	6	2	C _x H _y O ₂	O=CC1=C(O)C=CC=C1	2.77E-05	
124.0470	6.62E-08	6	5	1	2	C _x H _y NO ₂	O=N(C1=CC=CC=C1)O	2.87E-04
125.0675	2.32E-05	7	8	2	C _x H _y O ₂	CC1=C(O)C=CC=C1O	2.29E-06	
126.0564	2.28E-05	6	7	1	2	C _x H _y NO ₂	OC1=NC(O)=CC(C)=C1	1.15E-06
127.0431	3.29E-03	6	6	3	C _x H _y O ₃	OC1=C(O)C=CC=C1O	3.24E-08	
138.0429	1.49E-04	7	7	1	2	C _x H _y NO ₂	CC1=C(N(O)=O)C=CC=C1	6.57E-09
139.0281	2.72E-05	7	6	3	C _x H _y O ₃	OC1=CC=CC=C1C(O)=O	5.80E-08	
140.0237	1.55E-09	6	5	1	3	C _x H _y NO ₃	O=N(OC1=CC=CC=C1)O	9.08E-04
141.0431	3.54E-04	7	8	3	C _x H _y O ₃	OC1=C(O)C(C)=CC=C1O	1.06E-08	
147.0526	4.17E-05	5	6	5	C _x H _y O ₅₊	O=C(O)C(CCC(O)=O)=O	3.95E-08	
154.0417	9.18E-04	7	7	1	3	C _x H _y NO ₃	CC1=C(O)C(ON(=O)=O)=CC=C1O	6.57E-09
155.0286	1.07E-01	7	6	4	C _x H _y O ₄	O=C(O)C1=C(O)C=CC(O)=C1	1.41E-10	
157.0420	7.29E-01	7	8	4	C _x H _y O ₄	CC1=C(O)C(O)=CC(O)=C1O	2.35E-11	
159.0583	3.45E-03	7	10	4	C _x H _y O ₄	CC(C=O)C(O)=C(O)C=CO	2.82E-09	
184.0624	1.99E-02	7	4	1	5	C _x H _y NO ₅₊	OC1=C(C(O)=O)C=C([N+][O-])=O)C=C1	1.24E-10
199.0941	1.30E-03	7	6	2	5	C _x H _y N ₂ O _z	CC1=C(O)C([N+][O-])=O)CC([N+][O-])=O)C1	3.95E-09

88

89 Table S3: Chemical composition measured by (+)-DART-HR-MS of toluene SOA generated under high-
90 NO conditions with Na₂SO₄ seed. Abundance is defined as ((C_A/C_{IS})/Σ(C_A/C_{IS})).

<i>m/z</i> (Da)	Abundance	C	H	N	O	Category	Smiles	P _{vap} (atm)
61.0295	2.32E-11	2	4		2	C _x H _y O ₂	CC(O)=O	4.49E-03
69.0690	1.45E-13	4	4		1	C _x H _y O ₁	O1C=CC=C1	2.05E-01
70.0295	6.73E-14	3	3	1	1	C _x H _y NO ₁	C1=NC=CO1	1.03E-01
71.0483	7.34E-13	4	6		1	C _x H _y O ₁	CC=CC=O	8.30E-02
72.0465	1.05E-09	3	5	1	1	C _x H _y NO ₁	C=CC(N)=O	9.20E-06
73.0622	1.50E-13	4	8		1	C _x H _y O ₁	C1CCCO1	2.05E-01

74.0586	1.62E-09	3	7	1	1	C _x H _y NO ₁	C1=NCCO1	9.20E-06
75.0435	8.82E-12	3	6		2	C _x H _y O ₂	CCC(O)=O	4.49E-03
76.0392	1.39E-04	2	5	1	2	C _x H _y NO ₂	NCC(O)=O	2.42E-10
80.0493	1.53E-12	5	5	1		CHN	C1=NC=CC=C1	2.00E-02
83.0817	5.12E-13	5	6		1	C _x H _y O ₁	CC1=CC=CO1	6.70E-02
85.0290	1.94E-11	4	4		2	C _x H _y O ₂	O=CC=CC=O	3.42E-03
87.0424	1.08E-11	4	6		2	C _x H _y O ₂	O=CCCC=O	6.19E-03
89.0399	1.90E-09	3	4		3	C _x H _y O ₃	OC(C(O)=O)C	1.13E-05
93.0408	8.61E-13	6	4		1	C _x H _y O ₁	C12=C(O2)C=CC=C1	1.39E-02
95.0667	1.55E-11	6	6		1	C _x H _y O ₁	OC1=CC=CC=C1	2.02E-03
97.0319	2.33E-10	5	4		2	*C _x H _y O ₂	O=C1C=CC(C1)=O	4.67E-04
98.0499	1.18E-11	4	5	2	1	C _x H _y N ₂ O _z	O=C(N1)CCC1=O	2.15E-03
99.0449	8.68E-12	5	6		2	*C _x H _y O ₂	CC1=CCC(O1)=O	1.37E-02
100.0424	7.35E-08	4	5	1	2	*C _x H _y NO ₂	O=C(N1)CCC1=O	4.71E-07
101.0288	2.73E-11	4	4		3	C _x H _y O ₃	O=C1CCC(O1)=O	2.15E-03
102.0563	1.28E-12	4	7	1	2	*C _x H _y NO ₂	O=C(OCC)C=N	1.89E-02
103.0419	5.57E-11	4	6		3	C _x H _y O ₃	O=C1C(O)CCO1	4.80E-04
104.0360	1.19E-12	3	5	1	3	*C _x H _y NO ₃	C=CC(ON(=O)=O)	2.60E-02
105.0208	1.54E-08	3	4		4	C _x H _y O ₄	OCC(C(O)=O)=O	2.22E-06
107.0623	5.40E-12	7	6		1	C _x H _y O ₁	O=CC1=CC=CC=C1	1.83E-03
110.0604	2.01E-11	6	7	1	1	C _x H _y NO ₁	OC1=CC=C(C)N=C1	7.24E-04
111.0463	1.81E-10	6	6		2	*C _x H _y O ₂	O=CC=CC=CC=O	3.66E-04
113.0461	1.24E-10	6	8		2	*C _x H _y O ₂	O=CCCC=CC=O	4.92E-04
114.0550	1.22E-09	5	7	1	2	*C _x H _y NO ₂	OC(C1=NCCCC1)=O	2.57E-05
115.0409	1.90E-11	5	6		3	C _x H _y O ₃	O=C1C=C(OC)CO1	4.48E-03
117.0539	1.61E-10	5	8		3	C _x H _y O ₃	O=C1C(C)CC(O)O1	1.91E-04
118.0517	2.29E-12	4	7	1	3	*C _x H _y NO ₃	CC=CC(ON(=O)=O)	8.50E-03
121.0767	1.18E-09	7	4		2	C _x H _y O ₂	O=C(C=C1C)C=CC1=O	8.12E-06
123.0461	1.07E-09	7	6		2	*C _x H _y O ₂	O=CC1=C(O)C=CC=C1	2.77E-05
126.0555	2.00E-08	6	7	1	2	*C _x H _y NO ₂	OC1=NC(O)=CC(C)=C1	1.15E-06
127.0423	2.32E-06	6	6		3	C _x H _y O ₃	OC1=C(O)C=CC=C1O	3.24E-08
128.0388	2.01E-10	5	5	1	3	C _x H _y NO ₃	CC1=CC(N(O)=O)=CO1	1.44E-04
129.0534	1.48E-06	6	8		3	C _x H _y O ₃	OC1=C(O)C=CC=C1O	3.24E-08
130.0518	9.07E-11	5	7	1	3	C _x H _y NO ₃	CC1OC=C(N(O)=O)C1	2.27E-04
131.0391	7.73E-11	5	6		4	C _x H _y O ₄	O=C1CC(OC)C(O1)=O	3.64E-04
132.0622	3.95E-11	5	9	1	3	C _x H _y NO ₃	CC1OCC(N(O)=O)C1	3.60E-04
133.0524	4.59E-11	5	8		4	C _x H _y O ₄	O=C1CC(OC)C(O1)=O	3.64E-04
138.0557	3.23E-06	7	7	1	2	*C _x H _y NO ₂	CC1=C(N(O)=O)C=CC=C1	6.57E-09
139.0415	5.49E-07	7	6		3	*C _x H _y O ₃	OC1=C(C=O)C(O)=CC=C1	9.59E-08
141.0544	5.51E-06	7	8		3	C _x H _y O ₃	OC1=C(O)C(C)=CC=C1O	1.06E-08
142.0516	3.42E-11	6	7	1	3	C _x H _y NO ₃	O=N(OC1=CC=CC=C1)O	9.08E-04
143.0370	1.59E-05	6	6		4	C _x H _y O ₄	O=C(O)C=CC=CC(O)=O	3.29E-09
145.0509	9.26E-06	6	8		4	C _x H _y O ₄	O=C(O)C=CC=CC(O)=O	3.29E-09
146.0484	1.13E-08	5	7	1	4	C _x H _y NO ₄	O=CC(O)C(N=O)CC=O	1.35E-06
147.0545	4.03E-06	8	6	2	1	C _x H _y N ₂ O _z	O=C(C)NC1=CC=CC=C1	3.04E-09
148.0586	2.25E-07	5	9	1	4	C _x H _y NO ₄	O=CC(O)C(N=O)CCO	4.04E-08
149.0337	9.22E-08	7	4	2	2	C _x H _y NO ₂	CC1=CC(N=O)=CC(N=O)=C1	2.01E-07
152.0686	1.23E-09	8	9	1	2	C _x H _y NO ₂	OC1=CC=C(NC(C)=O)C=C1	1.44E-05
153.0611	1.10E-07	7	8	2	2	C _x H _y N ₂ O _z	CC1=CC(N=O)=CC(N=O)=C1	2.01E-07
154.0511	4.70E-06	7	7	1	3	C _x H _y NO ₃	CC1=C(O)C(ON(=O)=O)=CC=C1O	6.57E-09
155.0397	4.21E-04	7	6		4	*C _x H _y O ₄	O=C(O)C1=C(O)C=CC(O)=C1	1.41E-10

157.0504	2.76E-03	7	8	4	*C _x H _y O ₄	CC1=C(O)C(O)=CC(O)=C1O	2.35E-11	
158.0487	6.11E-09	6	7	1	4	C _x H _y NO ₄	OC1=CC(ON(O)=O)=CC=C1	4.33E-06
159.0467	3.90E-09	10	6	2		C _x H _y O ₂	O=C(C1=C2C=CC=C1)C=CC2=O	8.12E-06
160.0607	3.60E-09	6	9	1	4	C _x H _y NO ₄	OC1=CC(ON(O)=O)=CC=C1	4.33E-06
161.0475	1.93E-06	6	8	5		C _x H _y O ₅₊	O=CC(O)C(O)C(O)=CC=O	1.34E-08
164.0597	2.75E-07	5	9	1	5	C _x H _y NO ₅₊	O=CC(O)C(N(O)=O)CCO	4.04E-08
165.0593	6.84E-10	9	8	3		C _x H _y O ₃	O=CC1=C(OC)C=CC=C1OC	2.10E-05
167.0682	9.11E-10	9	10	3		C _x H _y O ₃	O=CC1=C(OC)C=CC=C1OC	2.10E-05
168.0610	1.52E-09	8	9	1	3	C _x H _y NO ₃	CC1=C(OC)C=CC(N(O)=O)=C1	1.00E-05
169.0591	5.32E-06	7	8	2	3	C _x H _y N ₂ O _z	CC1=C(O)C(N=O)=CC(N=O)=C1	3.95E-09
170.0479	3.85E-07	7	7	1	4	C _x H _y NO ₄	OC1=CC(ON(O)=O)=CC=C1C	5.93E-08
171.0431	3.72E-09	11	6	2		C _x H _y O ₂	O=C(C1=C2C=CC(C)=C1)C=CC2=O	8.12E-06
172.0585	1.18E-08	7	9	1	4	C _x H _y NO ₄	OC1=CC(ON(O)=O)=CC=C1C	1.42E-06
173.0473	4.21E-01	7	8	5		C _x H _y O ₅₊	CC1=C(O)C(O)=C(O)C(O)=C1O	8.99E-14
174.0686	1.24E-08	7	11	1	4	C _x H _y NO ₄	OC1=CC(ON(O)=O)=CC=C1C	1.42E-06
175.0654	1.98E-01	7	10	5		C _x H _y O ₅₊	CC1=C(O)C(O)=C(O)C(O)=C1O	8.99E-14
177.0571	2.56E-09	10	8	3		C _x H _y O ₃	O=CC1=C(OC=C)C=CC=C1OC	6.85E-06
178.0703	4.31E-08	6	11	1	5	C _x H _y NO ₅₊	O=CCC(ON(O)=O)CCCCO	4.69E-07
179.0706	1.88E-09	10	10	3		C _x H _y O ₃	O=CC1=C(OC=C)C=CC=C1OC	6.85E-06
180.0679	3.71E-09	9	9	1	3	C _x H _y NO ₃	CC1=C(OC=C)C=CC(N(O)=O)=C1	3.28E-06
181.0651	6.06E-09	8	8	2	3	C _x H _y N ₂ O _z	O=C(C)NC1=CC=C(N(O)=O)C=C1	2.05E-06
183.0784	8.72E-09	8	10	2	3	C _x H _y N ₂ O _z	CC1=CC=C(N(O)=O)C=C1NC=O	2.05E-06
184.0623	1.10E-09	8	9	1	4	C _x H _y NO ₄	CC1=CC=C(ON(O)=O)C=C1OC	1.00E-05
185.0631	8.24E-08	7	8	2	4	C _x H _y N ₂ O _z	CC1=CC(N(O)=O)=CC(N(O)=O)=C1	2.01E-07
186.0504	6.43E-08	6	7	3	4	C _x H _y N ₂ O _z	CC1=NC(N(O)=O)=CC(N(O)=O)=C1	2.01E-07
187.0626	1.52E-01	8	10	5		C _x H _y O ₅₊	CC1=C(O)C(O)=C(O)C(O)=C1OC	8.99E-14
188.0608	1.39E-06	7	9	1	5	C _x H _y NO ₅₊	CC1=C(O)C(ON(O)=O)=CC=C1O	6.57E-09
189.0518	2.83E-06	6	8	2	5	C _x H _y N ₂ O _z	OC1=C(N(O)=O)C=CC(N(O)=O)=C1	9.29E-09
190.0713	1.84E-06	7	11	1	5	C _x H _y NO ₅₊	CC1=C(O)C(ON(O)=O)=CC=C1O	6.57E-09
192.0828	1.81E-06	7	13	1	5	C _x H _y NO ₅₊	CC1=C(O)C(ON(O)=O)=CC=C1O	6.57E-09
193.0737	3.33E-02	7	12	6		C _x H _y O ₅₊	CC(C(C(O)C1O)O)=C(O)C1O	3.18E-13
194.0700	1.10E-04	6	11	1	6	C _x H _y NO ₅₊	OC1=C(O)C(ON(O)=O)=CC=C1O	9.39E-11
196.0650	3.21E-09	9	9	1	4	C _x H _y NO ₄	CC1=CC=C(ON(O)=O)C=C1OC=C	3.28E-06
199.0618	1.91E-01	9	10	5		C _x H _y O ₅₊	CC1=C(O)C(O)=C(O)C(O)=C1OC=C	8.99E-14
202.0709	5.01E-08	8	11	1	5	C _x H _y NO ₅₊	CC1=C(O)C=C(ON(O)=O)C=C1OC	1.52E-07
267.1719	5.15E-06	14	22	2	3	C _x H _y NO ₃	CC(OC(N=O)=CCCC(C)C=O)C=CCCC	9.81E-09

91

92 Table S4: Chemical composition measured by (+)-DART-HR-MS of toluene SOA generated under high-
 93 NO conditions with NaCl seed. Abundance is defined as $((C_A/C_{IS})/\sum(C_A/C_{IS}))$.

<i>m/z</i> (Da)	Abundance	C	H	N	O	Category	Smiles	P _{vap} (atm)
71.0486	1.33E-10	4	6	1		C _x H _y O ₁	CC=CC=O	8.30E-02
74.0597	1.01E-06	3	7	1	1	C _x H _y NO ₁	C1=NCCO1	9.20E-06
75.0442	2.41E-09	3	6	2		C _x H _y O ₂	CCC(O)=O	4.49E-03
76.0391	5.36E-02	2	5	1	2	C _x H _y NO ₂	NCC(O)=O	2.42E-10
80.0497	6.17E-09	5	5	1		CHN	C1=NC=CC=C1	2.00E-02
83.0607	6.29E-10	4	6	2		CHN	C1N=CC=NC1	2.00E-02
84.0450	2.61E-10	4	5	1	1	C _x H _y NO ₁	C1=CNC=CO1	3.35E-02
85.0308	3.85E-09	4	4	2		C _x H _y O ₂	O=CC=CC=O	3.42E-03

10

86.0582	2.06E-10	4	7	1	1	C _x H _y NO ₁	C1=CNC=CO1	3.35E-02
87.0447	2.06E-09	4	6		2	C _x H _y O ₂	O=CCCC=O	6.19E-03
88.0405	2.93E-02	3	5	1	2	C _x H _y NO ₂	OC(C=CN)=O	2.42E-10
94.0654	3.57E-10	6	7	1		CHN	CC1=NC=CC=C1	2.00E-02
95.0628	4.11E-10	5	6	2		CHN	CC1=NC=CN=C1	2.00E-02
96.0460	6.69E-09	5	5	1	1	C _x H _y NO ₁	OC1=CC=CN=C1	1.32E-03
97.0644	1.92E-08	6	8		1	C _x H _y O ₁	OC1=CC=CC=C1	2.02E-03
98.0612	1.03E-08	5	7	1	1	C _x H _y NO ₁	OC1=CC=CN=C1	1.32E-03
99.0459	2.33E-09	5	6		2	C _x H _y O ₂	CC1=CCC(O)=O	1.37E-02
100.0420	3.18E-05	4	5	1	2	C _x H _y NO ₂	O=C(N)CCC1=O	4.71E-07
102.0570	5.40E-10	4	7	1	2	C _x H _y NO ₂	O=C(OCC)C=N	1.89E-02
104.0364	3.44E-10	3	5	1	3	C _x H _y NO ₃	C=CC(ON(=O)=O)	2.60E-02
110.0612	2.92E-08	6	7	1	1	C _x H _y NO ₁	OC1=CC=C(C)N=C1	7.24E-04
112.0424	6.50E-07	5	5	1	2	C _x H _y NO ₂	OC(C1=NCCC1)=O	2.57E-05
113.0574	4.26E-08	6	8		2	C _x H _y O ₂	O=CCCC=CC=O	4.92E-04
114.0567	5.26E-07	5	7	1	2	C _x H _y NO ₂	OC(C1=NCCC1)=O	2.57E-05
117.0574	3.87E-08	5	8		3	C _x H _y O ₃	O=C1C(C)CC(O)O1	1.91E-04
118.0520	9.87E-10	4	7	1	3	C _x H _y NO ₃	CC=CC(ON(=O)=O)	8.50E-03
126.0565	1.82E-05	6	7	1	2	C _x H _y NO ₂	OC1=NC(O)=CC(C)=C1	1.15E-06
129.0563	3.77E-04	6	8		3	C _x H _y O ₃	OC1=C(O)C=CC=C1O	3.24E-08
130.0528	3.47E-08	5	7	1	3	C _x H _y NO ₃	CC1OC=C(N(O)=O)C1	2.27E-04
138.0563	2.37E-03	7	7	1	2	C _x H _y NO ₂	CC1=C(N(O)=O)C=CC=C1	6.57E-09
139.0474	2.14E-07	6	6	2	2	C _x H _y N ₂ O _z	CC1=NC=CC(N(O)=O)=C1	7.43E-05
141.0580	1.50E-03	7	8		3	C _x H _y O ₃	OC1=C(O)C(C)=CC=C1O	1.06E-08
142.0522	1.24E-08	6	7	1	3	C _x H _y NO ₃	O=N(OC1=CC=CC=C1)O	9.08E-04
143.0435	3.93E-06	5	6	2	3	C _x H _y N ₂ O _z	OC1C=C(N(O)=O)C=NC1	2.82E-06
149.0560	1.14E-09	9	8		2	C _x H _y O ₂	O=C(OC=C)C1=CC=CC=C1	6.19E-03
152.0717	6.51E-07	8	9	1	2	C _x H _y NO ₂	OC1=CC=C(NC(C)=O)C=C1	1.44E-05
153.0670	4.77E-05	7	8	2	2	C _x H _y N ₂ O _z	CC1=CC(N=O)=CC(N=O)=C1	2.01E-07
154.0521	2.33E-03	7	7	1	3	C _x H _y NO ₃	CC1=C(O)C(ON(=O)=O)=CC=C1O	6.57E-09
155.0446	2.44E-05	6	6	2	3	C _x H _y N ₂ O _z	OC1=C(C)N=CC(N(O)=O)=C1	7.09E-07
156.0636	1.41E-03	7	9	1	3	C _x H _y NO ₃	CC1=C(O)C(ON(=O)=O)=CC=C1O	6.57E-09
157.0529	6.31E-01	7	8		4	C _x H _y O ₄	CC1=C(O)C(O)=CC(O)=C1O	2.35E-11
159.0688	2.68E-01	7	10		4	C _x H _y O ₄	CC1=C(O)C(O)=CC(O)=C1O	2.35E-11
168.0675	8.15E-07	8	9	1	3	C _x H _y NO ₃	CC1=C(OC)C=CC(N(O)=O)=C1	1.00E-05
171.0670	9.92E-03	8	10		4	C _x H _y O ₄	CC1=C(C(O)=CC(O)=C1O)OC	8.36E-10
173.0544	9.91E-08	6	8	2	2	C _x H _y N ₂ O _z	CC1=NC=CC(N(O)=O)=C1	7.43E-05
175.0777	1.91E-07	11	10		2	C _x H _y O ₂	O=C(OC=CC=C)C1=CC=CC=C1	3.34E-05
178.0718	1.44E-05	6	11	1	5	C _x H _y NO ₅₊	O=CCC(ON(O)=O)CCCO	4.69E-07

94

95 Table S5: Chemical composition measured by (+)-DART-HR-MS of toluene SOA generated under high-
 96 NO conditions with MgSO₄ + H₂SO₄ seed. Abundance is defined as ((C_A/C_{IS})/∑(C_A/C_{IS})).

<i>m/z</i> (Da)	Abundance	C	H	N	O	Category	Smiles	P _{vap} (atm)
61.02876	3.43E-11	2	4		2	C _x H _y O ₂	CC(O)=O	4.49E-03
71.04839	1.51E-12	4	6		1	C _x H _y O ₁	O1C=CC=C1	8.30E-02
73.06233	3.63E-13	3	3		2	C _x H _y O ₂	CC(C=O)=O	1.90E-01
74.0596	5.85E-09	3	7	1	1	C _x H _y NO ₁	C1=NCCO1	9.20E-06
75.04341	9.47E-12	3	6		2	C _x H _y O ₂	CC(CO)=O	6.92E-03
76.03938	1.19E-04	2	5	1	2	C _x H _y NO ₂	NCC(O)=O	2.42E-10

80.0496	1.34E-11	5	5	1	CHN	C1=NC=CC=C1	2.00E-02
83.08333	9.88E-13	5	6	1	C _x H _y O ₁	CC1=CC=CO1	6.70E-02
85.0292	2.84E-11	4	4	2	C _x H _y O ₂	O=CC=CC=O	3.42E-03
86.05703	7.81E-13	4	7	1 1	C _x H _y NO ₁	C1=CNC=CO1	3.35E-02
87.04151	3.74E-11	4	6	2	C _x H _y O ₂	O=CCCC=O	6.19E-03
88.04571	9.27E-05	3	5	1 2	C _x H _y NO ₂	O=C(C)C(N)=O	2.42E-10
89.05108	7.44E-11	4	8	2	C _x H _y O ₂	O=CCCCO	6.48E-04
91.05025	2.63E-09	3	6	3	C _x H _y O ₃	OC(C(O)=O)C	1.13E-05
94.0651	1.68E-11	6	7	1	C _x H _y O ₁	OC1=CC=CC=C1	2.02E-03
95.06317	2.40E-11	6	6	1	C _x H _y O ₁	OC1=CC=CC=C1	2.02E-03
97.03422	6.88E-10	5	4	2	C _x H _y O ₂	O=C1C=CC(C1)=O	4.67E-04
98.05791	3.85E-08	5	7	1 4	C _x H _y NO ₄	O=CC(O)C(N=O)CC=O	1.35E-06
99.04468	3.19E-11	5	6	2	C _x H _y O ₂	CC1=CCC(O1)=O	1.37E-02
100.0442	1.61E-07	4	5	1 2	C _x H _y NO ₂	O=C(N1)CCC1=O	4.71E-07
101.0258	8.45E-11	4	4	3	C _x H _y O ₃	O=C1CCC(O1)=O	2.15E-03
102.0737	2.18E-12	4	7	1 2	C _x H _y NO ₂	O=C(OCC)C=N	1.89E-02
103.0407	1.26E-10	4	6	3	C _x H _y O ₃	O=C1C(O)CCO1	4.80E-04
104.0359	2.18E-12	3	5	1 3	C _x H _y NO ₃	C=CC(ON(=O)=O)	2.60E-02
105.02	5.93E-08	3	4	4	C _x H _y O ₄	OCC(C(O)=O)=O	2.22E-06
107.0572	1.27E-11	7	6	1	C _x H _y O ₁	O=CC1=CC=CC=C1	1.83E-03
109.101	9.78E-11	7	8	1	C _x H _y O ₁	OC1=C(C)C=CC=C1	6.61E-04
111.0455	6.79E-10	6	6	2	C _x H _y NO ₂	O=N(C1=CC=CC=C1)O	2.87E-04
112.0433	6.16E-11	5	5	1 2	C _x H _y NO ₂	O=C(N1)C=C(C)C1=O	7.03E-04
113.0481	3.49E-10	6	8	2	C _x H _y O ₂	O=CCCC=CC=O	4.92E-04
114.0694	3.42E-09	5	7	1 2	C _x H _y NO ₂	OC(C1=NCCC1)=O	2.57E-05
115.0403	3.93E-10	6	10	2	C _x H _y O ₂	O=CCCCCC=O	6.62E-04
117.0548	5.00E-10	5	8	3	C _x H _y O ₃	O=C1C(C)CC(O)O1	1.91E-04
118.0522	3.53E-12	4	7	1 3	C _x H _y NO ₃	CC=CC(ON(=O)=O)	8.50E-03
119.0361	2.08E-09	4	6	4	C _x H _y O ₄	OC(C(O)C=O)C=O	2.68E-05
123.0442	2.00E-09	7	6	2	C _x H _y O ₂	O=CC1=C(O)C=CC=C1	2.77E-05
125.0584	3.20E-08	7	8	2	C _x H _y O ₂	CC1=C(O)C=CC=C1O	2.29E-06
126.0558	2.39E-08	6	7	1 2	C _x H _y NO ₂	OC1=NC(O)=CC(C)=C1	1.15E-06
127.0416	4.51E-06	6	6	3	C _x H _y O ₃	OC1=C(O)C=CC=C1O	3.24E-08
128.0372	4.58E-10	5	5	1 3	C _x H _y NO ₃	CC1=CC(N(O)=O)=CO1	1.44E-04
129.054	3.04E-06	6	8	3	C _x H _y O ₃	OC1=C(O)C=CC=C1O	3.24E-08
130.0524	1.32E-10	5	7	1 3	C _x H _y NO ₃	CC1OC=C(N(O)=O)C1	2.27E-04
131.0374	1.92E-10	5	6	4	C _x H _y O ₄	O=C1CC(OC)C(O1)=O	3.64E-04
133.0506	1.35E-10	5	8	4	C _x H _y O ₄	O=C1CC(OC)C(O1)=O	3.64E-04
139.0409	9.50E-07	7	6	3	C _x H _y O ₃	OC1=C(C=O)C(O)=CC=C1	9.59E-08
140.0378	5.64E-11	6	5	1 3	C _x H _y NO ₃	O=N(OC1=CC=CC=C1)O	9.08E-04
141.0547	1.91E-05	7	8	3	C _x H _y O ₃	OC1=C(O)C(C)=CC=C1O	1.06E-08
142.0519	8.72E-11	6	7	1 3	C _x H _y NO ₃	O=N(OC1=CC=CC=C1)O	9.08E-04
143.0382	3.29E-05	6	6	4	C _x H _y O ₄	O=C(O)C=CC=CC(O)=O	3.29E-09
145.0507	1.53E-05	6	8	4	C _x H _y O ₄	O=C(O)C=CC=CC(O)=O	3.29E-09
149.0345	1.95E-07	7	4	2 2	C _x H _y N ₂ O ₂	CC1=C(N=O)C=CC=C1N=O	2.01E-07
154.0507	6.40E-06	7	7	1 3	C _x H _y NO ₃	CC1=C(O)C(ON(=O)=O)=CC=C1O	6.57E-09
155.0365	1.09E-03	7	6	4	C _x H _y O ₄	O=C(O)C1=C(O)C=CC(O)=C1	1.41E-10
157.0503	4.57E-03	7	8	4	C _x H _y O ₄	CC1=C(O)C(O)=CC(O)=C1O	2.35E-11
158.0485	9.14E-09	6	7	1 4	C _x H _y NO ₄	OC1=CC(ON(O)=O)=CC=C1	4.33E-06
159.0442	2.65E-03	7	10	4	C _x H _y O ₄	CC1=C(O)C(O)=CC(O)=C1O	2.35E-11
161.0502	2.13E-06	6	8	5	C _x H _y O ₅₊	O=CC(O)C(O)C(O)=CC=O	1.34E-08

167.0706	6.93E-09	9	10	3	C _x H _y O ₃	CC1=C(OC(C)=O)C=CC=C1O	4.72E-06	
169.0593	1.92E-07	7	8	2	3	C _x H _y N ₂ O _z	CC1=CC(N=O)=CC(N=O)=C1	2.01E-07
170.0476	5.90E-07	7	7	1	4	C _x H _y NO ₄	OC1=CC(ON(O)=O)=CC=C1C	5.93E-08
171.0454	7.52E-10	6	6	2	4	C _x H _y N ₂ O _z	CC1=NC=CC(N(O)=O)=C1	7.43E-05
172.0564	1.56E-08	7	9	1	4	C _x H _y NO ₄	OC1=CC(ON(O)=O)=CC=C1C	1.42E-06
173.0465	7.45E-01	7	8	5	C _x H _y O ₅₊	CC1=C(O)C(O)=C(O)C(O)=C1O	8.99E-14	
175.0647	2.47E-01	7	10	5	C _x H _y O ₅₊	CC1=C(O)C(O)=C(O)C(O)=C1O	8.99E-14	
185.0866	7.10E-05	9	12	4	C _x H _y O ₄	CC1=CC(O)=C(C(O)=C1OCC)O	3.70E-10	

97

98 Table S6: Chemical composition measured by (+)-DART-HR-MS of *o*-cresol SOA generated under high-
 99 NO conditions with (NH₄)₂SO₄ seed. Abundance is defined as ((C_A/C_{IS})/Σ(C_A/C_{IS})).

<i>m/z</i> (Da)	Abundance	C	H	N	O	Category	Smiles	P _{vap} (atm)
59.04897	1.04E-07	3	6		1	C _x H _y O ₁	CC(C)=O	3.87E-01
71.04891	2.65E-07	4	6		1	C _x H _y O ₁	O=CC(C)=C	8.30E-02
73.06351	8.76E-08	4	8		1	C _x H _y O ₁	CC(CC)=O	1.27E-01
75.04392	2.15E-06	3	6		2	C _x H _y O ₂	CCC(O)=O	4.49E-03
80.04964	3.34E-07	5	5	1		CHN	C1=NC=CC=C1	0.02
85.03067	4.04E-06	4	4		2	C _x H _y O ₂	O=CC=CC=O	3.42E-03
87.04418	2.56E-06	4	6		2	C _x H _y O ₂	O=CCCC=O	6.19E-03
89.05853	8.10E-06	4	8		2	C _x H _y O ₂	O=CCCCO	6.48E-04
93.0419	9.58E-06	5	4		2	C _x H _y O ₂	O=C1C=CC(C1)=O	4.67E-04
97.03836	1.07E-05	4	4	2	1	C _x H _y N ₂ O _z	O=C(N1)CCC1=O	2.15E-03
99.04724	1.81E-06	5	6		2	C _x H _y O ₂	CC1=CCC(O1)=O	1.37E-02
100.0428	2.30E-02	4	5	1	2	C _x H _y NO ₂	O=C(N1)CCC1=O	4.71E-07
101.0582	1.21E-06	5	8		2	C _x H _y O ₂	O=C1CCCCO1	1.37E-02
102.0582	6.09E-07	4	7	1	2	C _x H _y NO ₂	O=C(OCC)C=N	1.89E-02
104.036	5.92E-07	3	5	1	3	C _x H _y NO ₃	C=CC(ON(=O)=O)	2.60E-02
107.0699	5.86E-04	4	10		3	C _x H _y O ₃	OCCOCCO	8.37E-06
110.0621	6.62E-06	6	7	1	1	C _x H _y NO ₁	OC1=CC=C(C)N=C1	0.000724
111.048	5.43E-05	6	6		2	C _x H _y O ₂	O=CC=CC=CC=O	3.66E-04
112.0444	2.62E-04	5	5	1	2	C _x H _y NO ₂	OC(C1=NCCC1)=O	2.57E-05
113.0577	2.97E-05	6	8		2	C _x H _y O ₂	O=CCCC=CC=O	4.92E-04
114.0575	3.56E-04	5	7	1	2	C _x H _y NO ₂	OC(C1=NCCC1)=O	2.57E-05
115.0445	2.96E-06	5	6		3	C _x H _y O ₃	O=C1C=C(OC)CO1	4.48E-03
117.0619	2.04E-03	4	8	2	2	C _x H _y N ₂ O _z	ON=C(C)C(C)=NO	3.30E-06
118.0519	8.54E-07	4	7	1	3	C _x H _y NO ₃	CC=CC(ON(=O)=O)	8.50E-03
119.0665	5.11E-06	5	10		3	C _x H _y O ₃	CCOC(C(C)O)=O	9.92E-04
123.0476	3.20E-04	7	6		2	C _x H _y O ₂	O=CC1=C(O)C=CC=C1	2.77E-05
125.0725	4.62E-02	6	8	2	1	C _x H _y N ₂ O _z	CC1=NC(N(O)=O)=CC(N(O)=O)=C1	2.01E-07
126.0569	5.51E-03	6	7	1	2	C _x H _y NO ₂	OC1=NC(O)=CC(C)=C1	1.15E-06
127.0443	6.47E-01	6	6		3	C _x H _y O ₃	OC1=C(O)C=CC=C1O	3.24E-08
128.0661	4.40E-04	6	9	1	2	C _x H _y NO ₂	N=CCC=C(O)CC=O	2.00E-05
129.0592	3.33E-01	6	8		3	C _x H _y O ₃	OC1=C(O)C=CC=C1O	3.24E-08
130.0532	2.76E-05	5	7	1	3	C _x H _y NO ₃	CC1OC=C(N(O)=O)C1	2.27E-04
132.0652	1.14E-05	5	9	1	3	C _x H _y NO ₃	CC1OCC(N(O)=O)C1	3.60E-04
136.0604	1.73E-06	4	9	1	4	C _x H _y NO ₄	O=N(O)OCCC(O)C	1.84E-03
138.0569	7.55E-01	7	7	1	2	C _x H _y NO ₂	CC1=C(N(O)=O)C=CC=C1	6.57E-09
139.0457	1.29E-01	7	6		3	C _x H _y O ₃	OC1=C(C=O)C(O)=CC=C1	9.59E-08
140.0655	4.97E-05	7	9	1	2	C _x H _y NO ₂	CC(C=CC1)=CC1N(O)=O	1.49E-04

141.0624	1.01E+00	6	8	2	2	$C_xH_yN_2O_z$	<chem>OC1=C(N(O)=O)C=CC(N(O)=O)=C1</chem>	9.29E-09
142.0521	8.14E-06	6	7	1	3	$C_xH_yNO_3$	<chem>O=N(OC1=CC=CC=C1)O</chem>	9.08E-04
143.0724	3.27E+00	7	10		3	$C_xH_yO_3$	<chem>CC(C=O)C(O)=C(O)C=CO</chem>	2.82E-09
144.0658	5.37E-04	6	9	1	3	$C_xH_yNO_3$	<chem>OC1CC(N(O)=O)CC=C1</chem>	6.86E-06
145.054	2.06E+00	6	8		4	$C_xH_yO_4$	<chem>O=C(O)C=CC=CC(O)=O</chem>	3.29E-09
147.0693	2.70E-02	6	10		4	$C_xH_yO_4$	<chem>O=CCC(O)C(O)CC=O</chem>	1.48E-07
149.0301	5.43E-04	8	4		3	$C_xH_yO_3$	<chem>O=C1C2=CC=CC=C2C(O1)=O</chem>	1.55E-05
152.0727	3.31E-04	8	9	1	2	$C_xH_yNO_2$	<chem>OC1=CC=C(NC(C)=O)C=C1</chem>	1.44E-05
153.0922	2.81E-04	9	12		2	$C_xH_yO_2$	<chem>CC1=C(OCC)C(O)=CC=C1</chem>	3.01E-05
154.055	1.21E+00	7	7	1	3	$C_xH_yNO_3$	<chem>CC1=C(O)C(ON(=O)=O)=CC=C1O</chem>	6.57E-09
155.0409	1.17E+02	7	6		4	$C_xH_yO_4$	<chem>O=C(O)C1=C(O)C=CC(O)=C1</chem>	1.41E-10
156.0622	1.10E+00	7	9	1	3	$C_xH_yNO_3$	<chem>CC1=C(O)C(ON(=O)=O)=CC=C1O</chem>	6.57E-09
157.0534	4.41E+02	7	8		4	$C_xH_yO_4$	<chem>CC1=C(O)C(O)=CC(O)=C1O</chem>	2.35E-11
158.052	1.50E-03	6	7	1	4	$C_xH_yNO_4$	<chem>OC1=CC(ON(O)=O)=CC=C1</chem>	4.33E-06
159.1065	1.32E-05	8	14		3	$C_xH_yO_3$	<chem>CC(C)C(OC(C(C)C)=O)=O</chem>	5.01E-04
160.0636	9.29E-04	6	9	1	4	$C_xH_yNO_4$	<chem>OC1=CC(ON(O)=O)=CC=C1</chem>	4.33E-06
161.0699	2.03E-03	9	8	2	1	$C_xH_yN_2O_z$	<chem>OC1=CC=C(C2=NC=CN2)C=C1</chem>	1.89E-06
162.0724	5.26E-01	6	11	1	4	$C_xH_yNO_4$	<chem>N=CC(O)C(O)C(O)CC=O</chem>	7.54E-09
164.065	1.21E-04	9	9	1	2	$C_xH_yNO_2$	<chem>O=C(C)C1=NC(C(C)=O)=CC=C1</chem>	3.06E-05
167.072	3.50E-04	9	10		3	$C_xH_yO_3$	<chem>O=CC1=C(OC)C=CC=C1OC</chem>	2.10E-05
168.0662	5.40E-04	8	9	1	3	$C_xH_yNO_3$	<chem>CC1=C(OC)C=CC(N(O)=O)=C1</chem>	1.00E-05
169.0824	9.86E-04	9	12		3	$C_xH_yO_3$	<chem>CC1=C(OC)C=C(O)C=C1OC</chem>	7.56E-06
171.0693	7.12E+03	7	6		5	$C_xH_yO_{5+}$	<chem>OC1=C(C=O)C(O)=CC(O)=C1O</chem>	9.84E-13
172.0635	3.57E-03	7	9	1	4	$C_xH_yNO_4$	<chem>OC1=CC(ON(O)=O)=CC=C1C</chem>	1.42E-06
174.0764	2.89E-03	7	11	1	4	$C_xH_yNO_4$	<chem>OC1=CC(ON(O)=O)=CC=C1C</chem>	1.42E-06
175.0752	6.61E-04	11	10		2	$C_xH_yO_2$	<chem>CC1=C(OC=CC(C)=O)C=CC=C1</chem>	6.85E-06
178.0689	9.50E-03	6	11	1	5	$C_xH_yNO_{5+}$	<chem>O=CCC(ON(O)=O)CCCO</chem>	4.69E-07
179.0758	1.04E-03	10	10		3	$C_xH_yO_3$	<chem>OC(C1=C(OC)C=CC=C1OC)=C</chem>	4.94E-06
180.0687	1.40E-03	9	9	1	3	$C_xH_yNO_3$	<chem>CC1=C(OC=C)C=CC(N(O)=O)=C1</chem>	3.28E-06
185.0965	4.52E-04	13	12		1	$C_xH_yO_1$	<chem>CC1=CC(OC2=CC=CC=C2)=CC=C1</chem>	1.11E-05
187.0794	6.88E-03	12	10		2	$C_xH_yO_2$	<chem>OC(C=C1)=CC=C1OC2=CC=CC=C2</chem>	5.11E-07
189.0916	5.78E-03	12	12		2	$C_xH_yO_2$	<chem>OC1C=CC(OC2=CC=CC=C2)=CC1</chem>	5.11E-07
190.0757	5.01E-01	7	11	1	5	$C_xH_yNO_{5+}$	<chem>CC1=C(O)C(ON(O)=O)=CC=C1O</chem>	6.57E-09
193.0865	7.73E-04	11	12		3	$C_xH_yO_3$	<chem>CC1=C(OCC(CC=O)=O)C=CC=C1</chem>	5.72E-06
195.1377	2.02E-04	12	18		2	$C_xH_yO_2$	<chem>CC(OC1=CC=CC=C1OC(C)C)C</chem>	4.38E-05
196.0688	1.27E-03	9	9	1	4	$C_xH_yNO_4$	<chem>CC1=CC=C(ON(O)=O)C=C1OC=C</chem>	3.28E-06
197.074	4.48E-01	12	8	2	1	$C_xH_yN_2O_z$	<chem>N=CC1=CC=C(N=C1)C2=CC=C(O)C=C2</chem>	1.07E-08
198.0689	1.11E-03	9	11	1	4	$C_xH_yNO_4$	<chem>CC1=CC=C(C=C1OCC)ON(O)=O</chem>	3.28E-06
199.1665	8.32E-05	12	22		2	$C_xH_yO_2$	<chem>CC(OC1C(OC(C)C)=CCCC1)C</chem>	6.94E-05
201.0986	3.15E-01	12	12	2	1	$C_xH_yN_2O_z$	<chem>N=CC1=CC=C(N=C1)C2=CC=C(O)C=C2</chem>	1.07E-08
205.0858	1.40E-02	12	12		3	$C_xH_yO_3$	<chem>CC1=C(OCC(C=CC=O)=O)C=CC=C1</chem>	3.04E-07
215.1248	1.07E+00	11	18		4	$C_xH_yO_4$	<chem>CC1CC(O)C=CC1OC(O)CCC=O</chem>	3.11E-09
217.137	4.15E-02	13	16	2	1	$C_xH_yN_2O_z$	<chem>N=CC1=CC=C(N=C1)C2=CC=C(OC)C=C2</chem>	7.57E-08
221.1425	2.19E-02	10	20		5	$C_xH_yO_{5+}$	<chem>O1CCOCCOCCOCCOCC1</chem>	1.79E-07
225.078	3.56E+01	11	12		5	$C_xH_yO_{5+}$	<chem>OC1=C(OCC)C(OC=C)=C(C=O)C(O)=C1</chem>	1.17E-10
227.1329	5.83E+00	12	18		4	$C_xH_yO_4$	<chem>CC1=CC(O)C=CC1OC(O)CCCC=O</chem>	6.42E-10
231.1549	5.48E+00	12	22		4	$C_xH_yO_4$	<chem>CC1CC(O)CCC1OC(O)CCCC=O</chem>	4.71E-10
233.1337	5.06E+02	11	20		5	$C_xH_yO_{5+}$	<chem>CC1CC(O)CC(O)C1OC(O)CCC=O</chem>	4.68E-12
371.3153	5.63E+02	22	42		4	$C_xH_yO_4$	<chem>CC1CCCCC1OCCCO(C)CCCCOC2CCCCC2C</chem>	5.58E-12

101 Table S7: Chemical composition measured by (+)-DART-HR-MS of *m*-cresol SOA generated under
 102 high-NO conditions with (NH₄)₂SO₄ seed. Abundance is defined as ((C_A/C_{IS})/Σ(C_A/C_{IS})).

<i>m/z</i> (Da)	Abundance	C	H	N	O	Category	Smies	P _{vap} (atm)
71.0487	2.70E-15	4	6		1	C _x H _y O ₁	CC=CC=O	8.30E-02
73.0626	5.43E-16	4	8		1	C _x H _y O ₁	C1CCCO1	2.05E-01
74.0597	1.56E-11	3	7	1	1	C _x H _y NO ₁	C1=NCCO1	9.20E-06
75.0440	1.81E-14	3	6		2	C _x H _y O ₂	CC(CO)=O	6.92E-03
76.0392	6.53E-07	2	5	1	2	C _x H _y NO ₂	NCC(O)=O	2.42E-10
80.0494	7.16E-15	5	5	1		CHN	C1=NC=CC=C1	2.00E-02
84.0450	3.37E-15	4	5	1	1	C _x H _y NO ₁	C1=CNC=CO1	3.35E-02
85.0295	8.64E-14	4	4		2	C _x H _y O ₂	O=CC=CC=O	3.42E-03
86.0598	6.42E-15	4	7	1	1	C _x H _y NO ₁	C1=CNC=CO1	3.35E-02
87.0431	3.81E-14	4	6		2	C _x H _y O ₂	O=CCCC=O	6.19E-03
90.0516	1.03E-13	3	7	1	2	C _x H _y NO ₂	OC1NCOC1	1.18E-03
94.0657	2.70E-14	6	7	1		CHN	CC1=NC=CC=C1	2.00E-02
95.0584	9.68E-15	5	6	2		CHN	CC1=NC=CN=C1	2.00E-02
97.0637	7.92E-13	6	8		1	C _x H _y O ₁	OC1=CC=CC=C1	2.02E-03
98.0617	3.64E-13	5	7	1	1	C _x H _y NO ₁	OC1=CC=CN=C1	1.32E-03
99.0454	6.84E-14	5	6		2	C _x H _y O ₂	CC1=CCC(O1)=O	1.37E-02
102.0563	2.52E-14	4	7	1	2	C _x H _y NO ₂	O=C(OCC)C=N	1.89E-02
104.0366	6.23E-15	3	5	1	3	C _x H _y NO ₃	C=CC(ON(=O)=O)	2.60E-02
105.0209	5.22E-11	3	4		4	C _x H _y O ₄	OCC(C(O)=O)=O	2.22E-06
110.0614	3.04E-13	6	7	1	1	C _x H _y NO ₁	OC1=CC=C(C)N=C1	7.24E-04
111.0462	2.47E-12	6	6		2	C _x H _y O ₂	O=CC=CC=CC=O	3.66E-04
112.0446	4.10E-13	5	5	1	2	C _x H _y NO ₂	O=C(N1)C=C(C)C1=O	7.03E-04
113.0580	2.64E-12	6	8		2	C _x H _y O ₂	O=CCCC=CC=O	4.92E-04
114.0572	1.96E-11	5	7	1	2	C _x H _y NO ₂	OC(C1=NCCC1)=O	2.57E-05
115.0411	1.67E-13	5	6		3	C _x H _y O ₃	O=C1C=C(OC)CO1	4.48E-03
116.0694	1.15E-11	5	9	1	2	C _x H _y NO ₂	O=C(O)C1CCCN1	2.57E-05
117.0567	1.20E-12	5	8		3	C _x H _y O ₃	O=C1C(C)CC(O)O1	1.91E-04
118.0521	1.73E-14	4	7	1	3	C _x H _y NO ₃	CC=CC(ON(=O)=O)	8.50E-03
123.0467	6.09E-12	7	6		2	C _x H _y O ₂	O=CC1=C(O)C=CC=C1	2.77E-05
125.0607	8.60E-11	7	8		2	C _x H _y O ₂	CC1=C(O)C=CC=C1O	2.29E-06
126.0565	1.94E-10	6	7	1	2	C _x H _y NO ₂	OC1=NC(O)=CC(C)=C1	1.15E-06
127.0425	1.74E-08	6	6		3	C _x H _y O ₃	OC1=C(O)C=CC=C1O	3.24E-08
128.0698	3.72E-10	6	9	1	2	C _x H _y NO ₂	OC(C1)=NC(O)=CC1C	1.82E-06
129.0567	1.76E-08	6	8		3	C _x H _y O ₃	OC1=C(O)C=CC=C1O	3.24E-08
130.0552	1.17E-12	5	7	1	3	C _x H _y NO ₃	CC1OC=C(N(O)=O)C1	2.27E-04
131.0367	1.33E-12	5	6		4	C _x H _y O ₄	O=C1CC(OC)C(O1)=O	3.64E-04
132.0653	6.15E-13	5	9	1	3	C _x H _y NO ₃	CC1OCC(N(O)=O)C1	3.60E-04
133.0538	3.02E-13	5	8		4	C _x H _y O ₄	O=C1CC(OC)C(O1)=O	3.64E-04
137.0568	7.11E-10	7	8	2	1	C _x H _y N ₂ O _z	CC1=CC(N=O)=CC(N=O)=C1	2.01E-07
138.0561	2.86E-08	7	7	1	2	C _x H _y NO ₂	CC1=C(N(O)=O)C=CC=C1	6.57E-09
139.0450	5.45E-09	7	6		3	C _x H _y O ₃	OC1=CC=CC=C1C(O)=O	5.80E-08
140.0669	2.95E-12	7	9	1	2	C _x H _y NO ₂	CC1=C(CCC=C1)N(O)=O	9.39E-05
141.0555	6.23E-08	7	8		3	C _x H _y O ₃	OC1=C(O)C(C)=CC=C1O	1.06E-08
142.0527	3.79E-13	6	7	1	3	C _x H _y NO ₃	O=N(OC1=CC=CC=C1)O	9.08E-04
143.0381	1.05E-07	6	6		4	C _x H _y O ₄	O=C(O)C=CC=CC(O)=O	3.29E-09
144.0652	1.49E-13	6	9	1	3	C _x H _y NO ₃	O=N(O)OC1=CCCC=C1	9.08E-04
145.0524	5.45E-08	6	8		4	C _x H _y O ₄	O=C(O)C=CC=CC(O)=O	3.29E-09

148.0622	3.35E-09	5	9	1	4	C _x H _y NO ₄	O=CC(O)C(N=O)CCO	4.04E-08
149.0476	1.73E-06	5	8		5	C _x H _y O ₅₊	OC1OC(CO)=C(O)C1O	6.50E-11
151.0858	2.33E-11	8	10	2	1	C _x H _y N ₂ O _z	CC(N=O)=CC=CC=CC=N	6.43E-06
152.0710	9.80E-12	8	9	1	2	C _x H _y NO ₂	OC1=CC=C(NC(C)=O)C=C1	1.44E-05
153.0667	1.37E-09	7	8	2	2	C _x H _y N ₂ O _z	CC1=CC(N=O)=CC(N=O)=C1	2.01E-07
154.0536	7.58E-08	7	7	1	3	C _x H _y NO ₃	CC1=C(O)C(ON(=O)=O)=CC=C1O	6.57E-09
155.0361	1.46E-05	7	6		4	C _x H _y O ₄	O=C(O)C1=C(O)C=CC(O)=C1	1.41E-10
157.0509	1.86E-05	7	8		4	C _x H _y O ₄	CC1=C(O)C(O)=CC(O)=C1O	2.35E-11
159.0669	5.58E-08	7	10		4	C _x H _y O ₄	CC(C=O)C(O)=C(O)C=CO	2.82E-09
160.0631	3.10E-11	6	9	1	4	C _x H _y NO ₄	OC1=CC(ON(O)=O)=CC=C1	4.33E-06
161.0498	9.42E-09	6	8		5	C _x H _y O ₅₊	O=CC(O)C(O)C(O)=CC=O	1.34E-08
162.0737	2.94E-11	6	11	1	4	C _x H _y NO ₄	OC1CCCC(ON(O)=O)C1	4.00E-06
163.0712	8.11E-08	5	10	2	4	C _x H _y N ₂ O _z	COC(C(NC(N)=O)CO)=O	1.33E-09
164.0553	4.88E-09	5	9	1	5	C _x H _y NO ₅₊	O=CC(O)C(N(O)=O)CCO	4.04E-08
165.0657	5.21E-11	8	8	2	2	C _x H _y N ₂ O _z	O=C(C)NC1=CC=C(N(O)=O)C=C1	2.05E-06
167.0714	9.28E-12	9	10		3	C _x H _y O ₃	O=CC1=C(OC)C=CC=C1OC	2.10E-05
168.0673	1.65E-11	8	9	1	3	C _x H _y NO ₃	CC1=C(OC)C=CC(N(O)=O)=C1	1.00E-05
169.0612	8.22E-08	7	8	2	3	C _x H _y N ₂ O _z	CC1=C(N=O)C=C(N=O)C=C1O	3.04E-09
170.0557	1.09E-09	6	7	3	3	C _x H _y N ₂ O _z	CC1=NC(N(O)=O)=CC(N(O)=O)=C1	2.01E-07
171.0610	2.56E-07	8	10		4	C _x H _y O ₄	CC1=C(C(O)=CC(O)=C1O)OC	8.36E-10
172.0642	1.22E-10	7	9	1	4	C _x H _y NO ₄	OC1=CC(ON(O)=O)=CC=C1C	1.42E-06
173.0568	1.71E-08	6	8	2	4	C _x H _y N ₂ O _z	OC1=C(N(O)=O)C=CC(N(O)=O)=C1	9.29E-09
174.0765	1.21E-10	7	11	1	4	C _x H _y NO ₄	OC1=CC(ON(O)=O)=CC=C1C	1.42E-06
177.0664	3.25E-10	9	8	2	2	C _x H _y N ₂ O _z	O=C1N=C(N)OC1C2=CC=CC=C2	3.86E-07
178.0682	6.02E-10	6	11	1	5	C _x H _y NO ₅₊	O=CCC(ON(O)=O)CCCO	4.69E-07
179.0709	1.72E-11	10	10		3	C _x H _y O ₃	O=CC1=C(OC=C)C=CC=C1OC	6.85E-06
180.0678	4.63E-11	9	9	1	3	C _x H _y NO ₃	CC1=C(OC=C)C=CC(N(O)=O)=C1	3.28E-06
181.0752	6.52E-10	7	8	2	2	C _x H _y N ₂ O _z	CC1=C(N=O)C=C(N=O)C=C1	2.01E-07
183.0726	8.08E-11	8	10	2	3	C _x H _y N ₂ O _z	CC1=CC=C(N(O)=O)C=C1NC=O	2.05E-06
185.0754	4.00E-07	9	12		4	C _x H _y O ₄	CC1=C(OCC)C(O)=CC(O)=C1O	2.73E-10
190.0737	1.71E-08	7	11	1	5	C _x H _y NO ₅₊	CC1=C(O)C(ON(O)=O)=CC=C1O	6.57E-09
195.0857	9.68E-01	7	14		6	C _x H _y O ₅₊	OC1C(O)C(O)C(O)C(O)C1CO	1.85E-16
197.0738	1.61E-08	12	8	2	1	C _x H _y N ₂ O _z	N=CC1=CC=C(N=C1)C2=CC=C(O)C=C2	1.07E-08
198.0744	4.30E-11	9	11	1	4	C _x H _y NO ₄	CC1=CC=C(ON(O)=O)C=C1OC=C	3.28E-06
207.0737	1.57E-09	10	10	2	3	C _x H _y N ₂ O _z	OC1=C2C=C(OC)C(OC)=CC2=NC=N1	6.61E-08
209.0813	4.07E-06	11	12		4	C _x H _y O ₄	CC1=C(OC=CC=C)C(O)=CC(O)=C1O	2.92E-11
223.0799	3.17E-02	8	14		7	C _x H _y O ₅₊	OC1C(O)C(O)C(O)C(O)C1COC=O	4.14E-15

103

104 Table S8: Chemical composition measured by (+)-DART-HR-MS of *p*-cresol SOA generated under high-
 105 NO conditions with (NH₄)₂SO₄ seed. Abundance is defined as ((C_A/C_{IS})/Σ(C_A/C_{IS})).

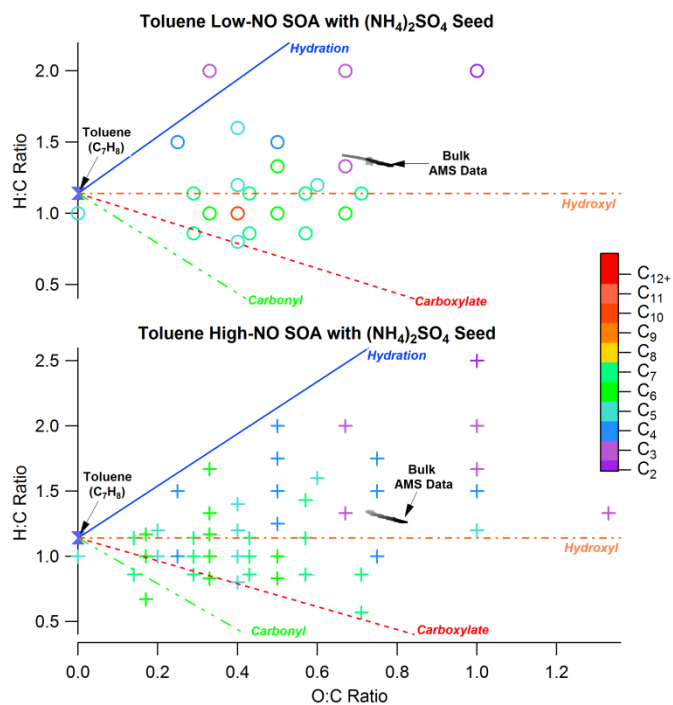
<i>m/z</i> (Da)	Abundance	C	H	N	O	Category	Smiles	P _{vap} (atm)
71.0490	1.75E-13	4	6		1	C _x H _y O ₁	CC=CC=O	8.30E-02
73.0637	3.50E-14	4	8		1	C _x H _y O ₁	C1CCCO1	2.05E-01
75.0440	1.08E-12	3	6		2	C _x H _y O ₂	CC(CO)=O	6.92E-03
80.0499	1.28E-12	5	5	1		CHN	C1=NC=CC=C1	2.00E-02
85.0306	2.65E-12	4	4		2	C _x H _y O ₂	O=CC=CC=O	3.42E-03
87.0443	1.73E-12	4	6		2	C _x H _y O ₂	O=CCCC=O	6.19E-03
94.0656	2.04E-13	6	7	1		CHN	CC1=NC=CC=C1	2.00E-02
97.0654	3.17E-11	6	8		1	C _x H _y O ₁	OC1=CC=CC=C1	2.02E-03

99.0464	1.94E-12	5	6		2	C _x H _y O ₂	CC1=CCC(O1)=O	1.37E-02
101.0584	1.62E-12	5	8		2	C _x H _y O ₂	CC=CCC(O)=O	6.19E-03
110.0618	1.01E-11	6	7	1	1	C _x H _y NO ₁	N=CC=CC=CC=O	3.66E-04
111.0469	5.29E-11	6	6		2	C _x H _y O ₂	O=CC=CC=CC=O	3.66E-04
113.0585	3.87E-11	6	8		2	C _x H _y O ₂	O=CCCC=CC=O	4.92E-04
114.0581	2.80E-10	5	7	1	2	C _x H _y NO ₂	OC(C1=NCCC1)=O	2.57E-05
115.0418	3.60E-12	5	6		3	C _x H _y O ₃	O=C1C=C(OC)CO1	4.48E-03
123.0472	2.32E-10	7	6		2	C _x H _y O ₂	O=CC1=C(O)C=CC=C1	2.77E-05
125.0630	2.77E-09	7	8		2	C _x H _y O ₂	CC1=C(O)C=CC=C1O	2.29E-06
126.0566	4.35E-09	6	7	1	2	C _x H _y NO ₂	OC1=NC(O)=CC(C)=C1	1.15E-06
129.0572	3.91E-11	6	8		3	C _x H _y O ₃	O=C1C(C)CC(O)O1	1.91E-04
138.0559	5.08E-07	7	7	1	2	C _x H _y NO ₂	CC1=C(N(O)=O)C=CC=C1	6.57E-09
141.0562	4.05E-07	7	8		3	C _x H _y O ₃	OC1=C(O)C=CC=C1O	3.24E-08
142.0533	5.07E-12	6	7	1	3	C _x H _y NO ₃	O=N(OC1=CC=CC=C1)O	9.08E-04
143.0420	5.47E-11	5	6	2	3	C _x H _y N ₂ O _z	N=CC(C(O)C(C=O)=N)=O	1.14E-04
145.0531	9.91E-07	6	8		4	C _x H _y O ₄	O=C(O)C=CC=CC(O)=O	3.29E-09
149.0304	2.55E-08	7	4	2	2	C _x H _y N ₂ O _z	CC1=C(N=O)C=CC=C1N=O	2.01E-07
154.0544	7.72E-07	7	7	1	3	C _x H _y NO ₃	CC1=C(O)C(ON(=O)=O)=CC=C1O	6.57E-09
155.0384	1.11E-04	7	6		4	C _x H _y O ₄	O=C(O)C1=C(O)C=CC(O)=C1	1.41E-10
157.0515	4.04E-04	7	8		4	C _x H _y O ₄	CC1=C(O)C(O)=CC(O)=C1O	2.35E-11
159.0630	1.34E-06	7	10		4	C _x H _y O ₄	CC(C=O)C(O)=C(O)C=CO	2.82E-09
167.0660	2.20E-10	9	10		3	C _x H _y O ₃	O=CC1=C(OC)C=CC=C1OC	2.10E-05
171.0619	5.39E-06	8	10		4	C _x H _y O ₄	CC1=C(C(O)=CC(O)=C1O)OC	8.36E-10
173.0514	2.24E-08	6	8	2	4	C _x H _y N ₂ O _z	CC1=NC(N(O)=O)=CC(N(O)=O)=C1	2.01E-07
175.1008	1.53E-06	8	14		4	C _x H _y O ₄	CC(C(OC)C(CC1O)O)=C1O	2.42E-09
178.0700	7.86E-09	6	11	1	5	C _x H _y NO ₅₊	O=CCC(ON(O)=O)CCCO	4.69E-07
179.0726	5.02E-10	10	10		3	C _x H _y O ₃	O=CC1=C(OC=C)C=CC=C1OC	6.85E-06
183.0803	1.89E-09	8	10	2	3	C _x H _y N ₂ O _z	CC1=CC=C(N(O)=O)C=C1NC=O	2.05E-06
191.0814	5.50E-08	10	10	2	2	C _x H _y N ₂ O _z	OC1=C2C=C(OC)C(OC)=CC2=NC=N1	6.61E-08
193.0883	7.05E-10	11	12		3	C _x H _y O ₃	CC1=C(OCC(CC=O)=O)C=CC=C1	5.72E-06
195.1313	1.92E-06	7	8	2	4	C _x H _y N ₂ O _z	CC1=C(N=O)C=C(N=O)C=C1O	3.04E-09
199.0679	5.07E-10	8	10	2	4	C _x H _y N ₂ O _z	CC(N=O)=CC=CC=CC=N	6.43E-06
207.0769	4.86E-08	10	10	2	3	C _x H _y N ₂ O _z	OC1=C2C=C(OC)C(OC)=CC2=NC=N1	6.61E-08
209.0831	1.23E-04	11	12		4	C _x H _y O ₄	CC1=C(OC=CC=C)C(O)=CC(O)=C1O	2.92E-11
223.0787	9.99E-01	8	14		7	C _x H _y O ₅₊	OC1C(O)C(O)C(O)C(O)C1COC=O	4.14E-15

106

107

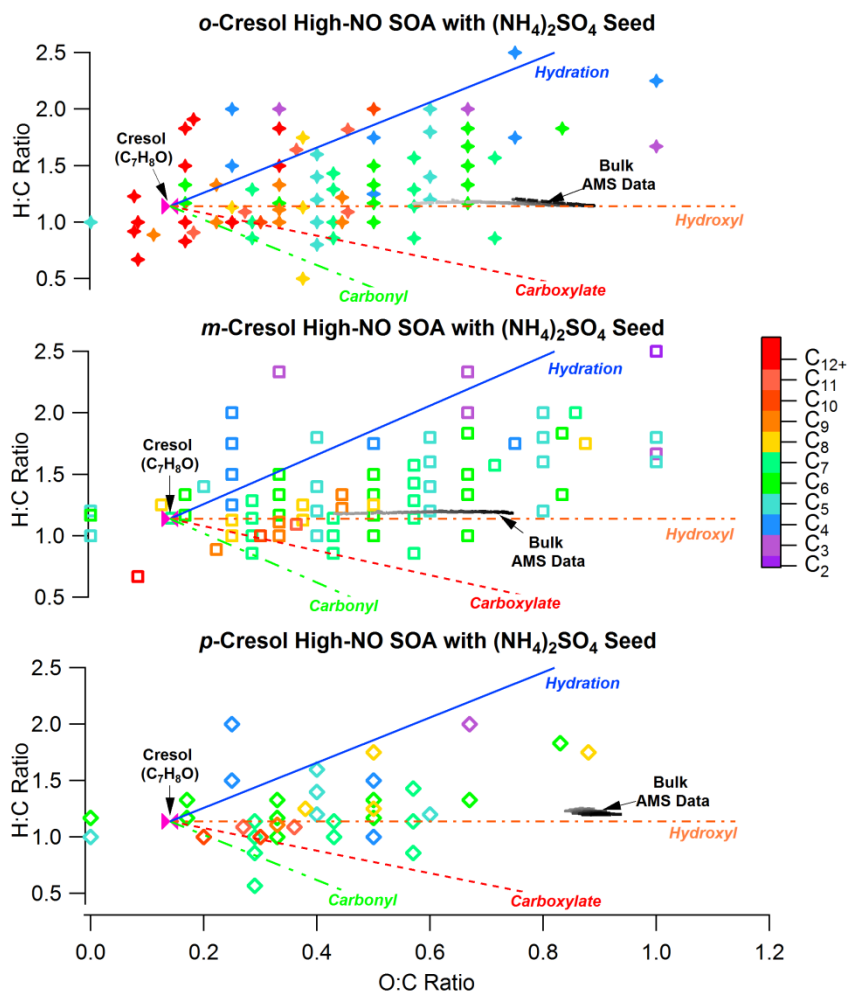
108 **Annotated van Krevelen Diagrams of DART-HR-MS and HR-AMS Data for Toluene and Cresol**
 109 **SOA**



110

111 **Figure S4.** Chemical composition of toluene SOA produced under low- and high-NO conditions
 112 with $(\text{NH}_4)_2\text{SO}_4$ seed, as measured by offline DART-HR-MS, are displayed in van Krevelen
 113 space. Data markers are colored by the molecular formula carbon number and sized by the
 114 logarithm of the mixing ratio for each molecular formula. The bulk SOA H:C and O:C elemental
 115 ratios derived from HR-AMS measurements are shown in grayscale.

116



117

118 **Figure S5.** Chemical composition of cresol SOA produced under high-NO conditions with
 119 $(\text{NH}_4)_2\text{SO}_4$ seed, as measured by offline DART-HR-MS, are displayed in van Krevelen space.
 120 Data markers are colored by the molecular formula carbon number and sized by the logarithm of
 121 the mixing ratio for each molecular formula. The bulk SOA H:C and O:C elemental ratios
 122 derived from HR-AMS measurements are shown in grayscale.

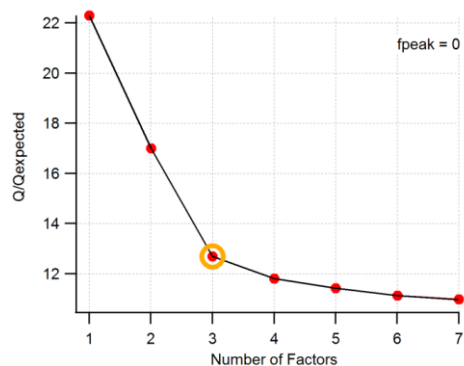
123

124 *PMF Analysis Details*

125 Positive matrix factorization (PMF) was performed on AMS data collected from toluene
 126 and *o*-cresol high-NO experiments. PMF analysis was conducted in two ways. First, each
 127 experiment was analyzed separately to explore the number of factors that could explain the
 128 variations in AMS spectra for a single experimental condition. Second, the data from each

129 experiment was combined into a unified PMF analysis to determine if common factors could be
130 resolved from toluene and o-cresol SOA formation. The results from both analyses were
131 compared to assess the reliability of using PMF on a unified dataset. The same factors were
132 resolved with both methods. The following discussion focuses on the PMF solution for the
133 unified toluene and o-cresol SOA dataset.

134 PMF analysis was performed using the PMF evaluation tool v. 2.04 in Igor Pro V6.36.
135 The organic signal matrix and corresponding errors were calculated via the procedures outlined
136 by Ulbrich et al.² Organic fragments with an average signal-to-noise ratio (SNR) lower than 0.2
137 were removed from analysis. Fragments with an average SNR between 0.2 and 2 were down-
138 weighted by increasing their corresponding errors by a factor of 3 as recommended by Paatero
139 and Hopke.³ The time series of the remaining ion fragments were analyzed for significant trends.
140 Ion fragments with time series trends that did not change significantly from the average
141 background signal ($< 3\sigma$) were removed from analysis. The PMF solution space was explored for
142 seven factors with 1-10 seeds and $-1 < f_{peak} < 1$. The number of factors was chosen to minimize the
143 goodness of fit parameter, $Q/Q_{expected}$.

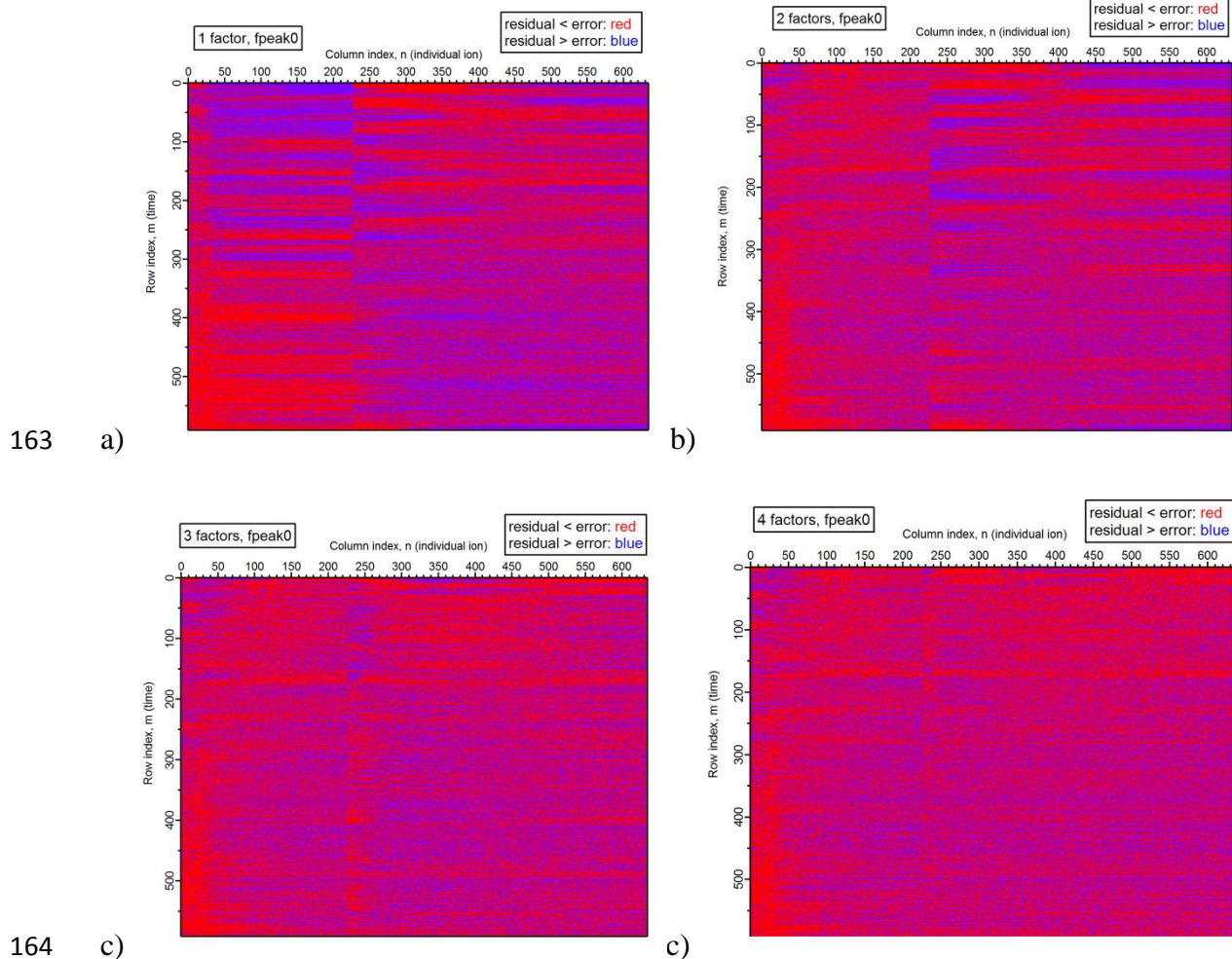


144
145 **Figure S6.** $Q/Q_{expected}$ vs. the number of factors. The chosen solution is highlighted by the yellow
146 circle.

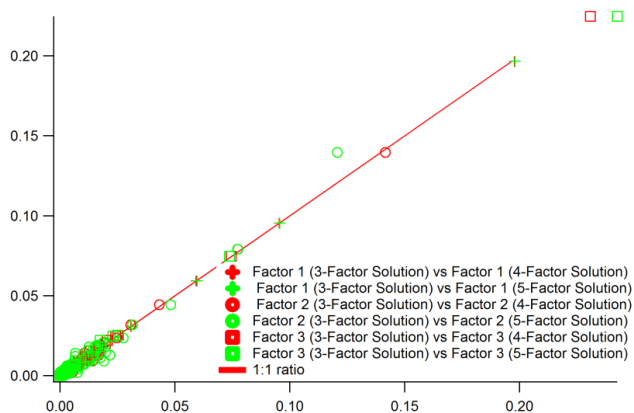
147 Figure S6 demonstrates that solutions with factor spaces > 3 , do not change significantly
148 with respect to $Q/Q_{expected}$. As discussed by Craven et al., a sufficient number of factors is
149 determined when the solution does not drastically improve with an increase in the number of
150 factors fit to the data.⁴

151 Figures S7 and S8 further justify the choice of a 3-factor solution. Figure S8 visualizes
152 the solution optimization by plotting the absolute residual: error ratio as a function of m/z and
153 time. Pixels with a ratio < 1 are colored red whereas those with a ratio > 1 are colored blue. Data
154 are sufficiently fit when no clear structure is observed, or subsequent factors do not improve the
155 randomness of the pixels. A one-factor fit exhibits clear structure in the solution space, indicating
156 that additional factors are needed to explain the variation in the data. This structure disappears
157 when three factors are fit to the data, and no clear improvement is seen when four or more
158 factors are fitted, suggesting that a three-factor solution is sufficient to capture data variation. As
159 discussed by Craven et al., these factors in chamber studies represent time series of groups or
160 fractions of ions that can be connected to different events like gas-particle partitioning and
161 specific generations of gas-phase oxidation.⁴

162



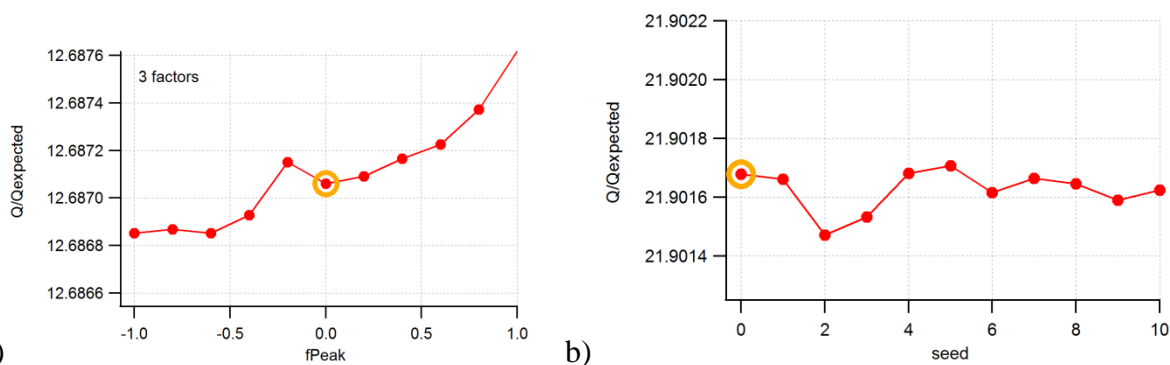
165 **Figure S7.** Maps for the one (panel a), two (panel b), three (panel c), and four (panel d) factor
 166 solutions. A red dot symbolizes where the $\text{residual}_{ij} > \text{error}_{ij}$. A blue dot symbolizes where the
 167 $\text{residual}_{ij} < -\text{error}_{ij}$.



169 **Figure S8.** Comparisons of factors 1, 2, and 3 mass spectra between three-factor and four- or five-factor
 170 solutions.

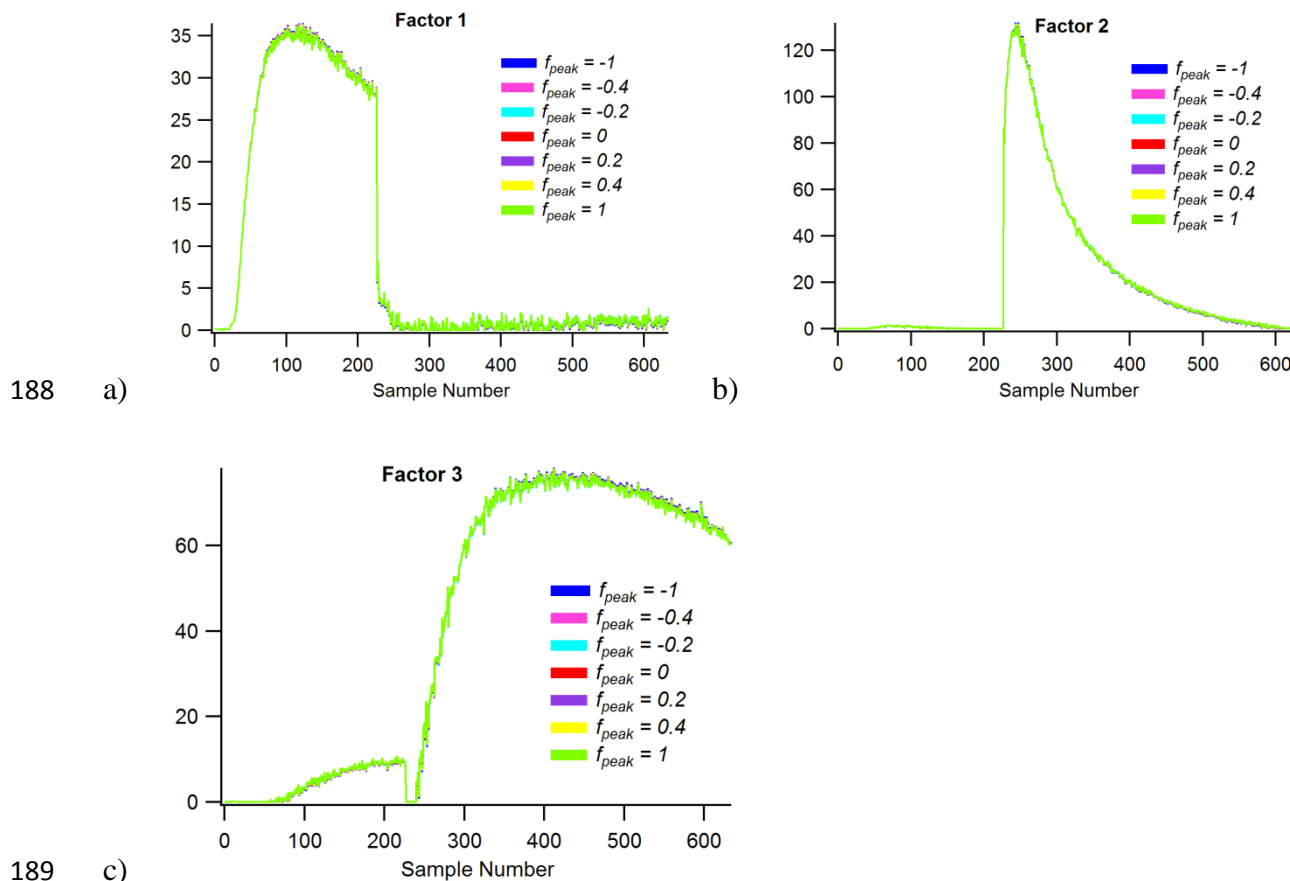
171 Figure S8 reiterates the conclusions drawn from Figure S7. When the mass spectra of a 3-
 172 factor solution are compared to those of 4 and 5-factor solutions, we find that factors 1, 2, and 3
 173 do not change significantly with increasing factor spaces. Thus, the resolved factors are robustly
 174 resolved in higher factor spaces without significant splitting or reallocation of information
 175 amongst factors 1, 2, and 3.

176 For a given number of factors, there could be multiple solutions that yield an equal fit. To
 177 investigate the robustness of the 3-factor solution, one may explore how the solution changes as
 178 a function of seed and f_{peak} .⁴ A detailed discussion about solution robustness in field
 179 measurement data is provided in Coggon et al.⁵ In the solution discussed here, $Q/Q_{expected}$ was
 180 relatively uniform over all explored seed and f_{peak} values (Figure S9).



181 a) **Figure S9.** $Q/Q_{expected}$ vs. f_{peak} values (panel a) and vs. seed number (panel b).
 182

183 This can be further verified by studying how the factor profiles vary as a function of f_{peak} .
 184 In Figure S10, we compare a 3-factor solution at $f_{peak} = 0$, seed = 0 to the same factor space at all
 185 other f_{peak} values. In general, the studied systems change very little with respect to f_{peak} ,
 186 suggesting that the solution at $f_{peak} = 0$, seed = 0 exhibits little rotational ambiguity and thus, it is
 187 sufficiently robust within the range of explored parameters.

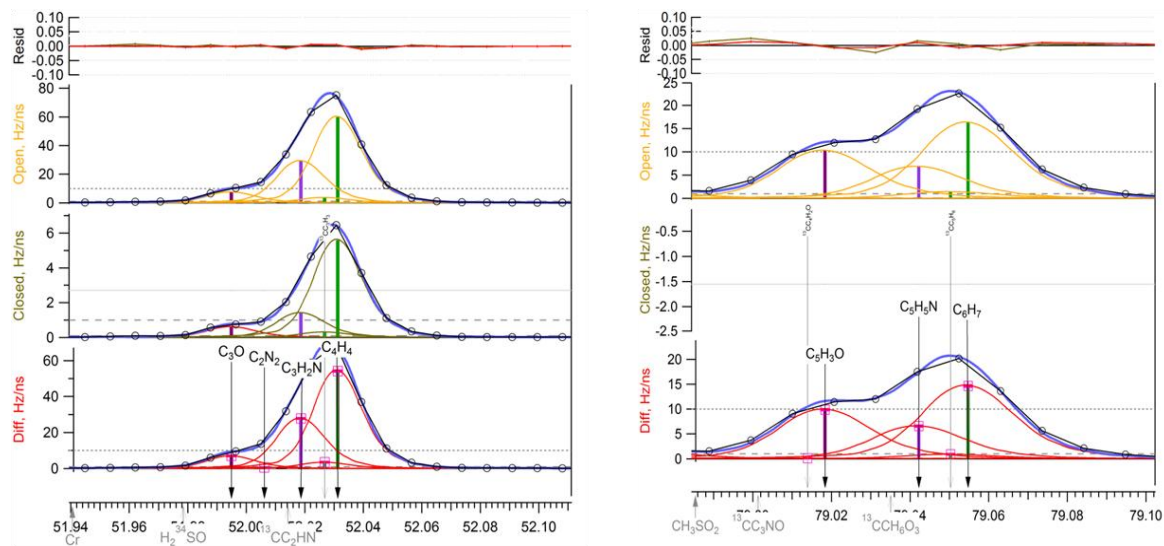


190 **Figure S10.** Factor profiles for a 3-factor solution with varying f_{peak} values. Factor 1 is shown in
 191 panel (a). Factor 2 is shown in panel (b). Factor 3 is shown in panel (c).

192

193 HR-AMS Data Supporting Pyridine Identification

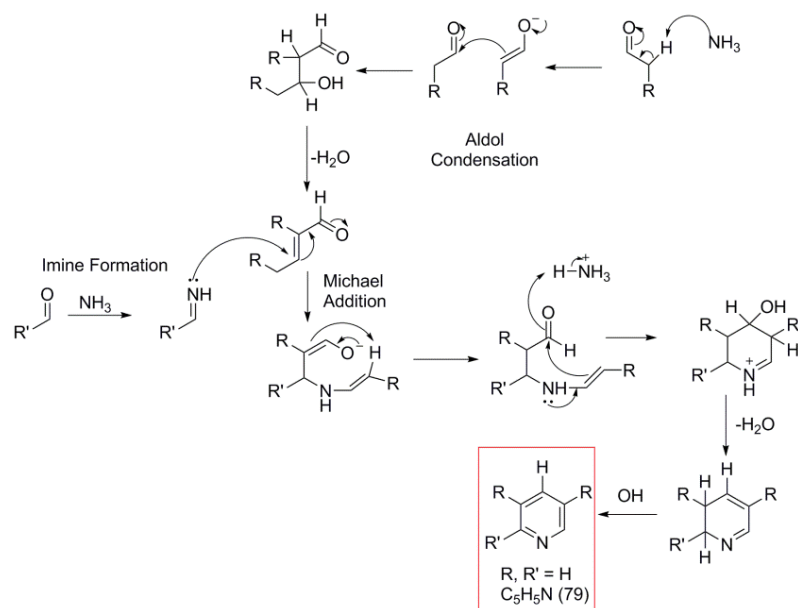
194 Pyridine is in both the ammonium sulfate-seeded and the nucleation case, and it is found in both
 195 DART-HR-MS and HR-AMS measurements. We speculate that ammonia is present in the
 196 chamber in some capacity, perhaps originating from ammonium sulfate deposited on the
 197 chamber walls; we have no means to monitor for ammonia in the gas phase.



198

199 **Figure S11.** High-resolution mass spectra of the molecular ion and major fragment of pyridine,
 200 by HR-AMS.

201 Pyridine forms a molecular ion ($C_5H_5N^+$, m/z 79) and a fragment ion ($C_3H_2N^+$, m/z 52) under EI-
 202 MS conditions; both were found by HR-AMS analysis (Figure S11). The most probable
 203 mechanism for pyridine formation under seeded conditions in a photooxidizing environment is
 204 one analogous to the traditional Chichibabin synthesis (Figure S12).⁶



205

206 **Figure S12.** Variation of Chichibabin synthesis of pyridine, proposed for toluene low-NO SOA
 207 with ammonium sulfate seed aerosol.

208 **Supporting Information References**

- 209 1. Jenkin, M. E.; Saunders, S. M.; Wagner, V.; Pilling, M. J. Protocol for the Development
210 of the Master Chemical Mechanism, MCM v3 (Part B): Tropospheric Degradation of Aromatic
211 Volatile Organic Compounds. *Atmos. Chem. Phys.* **2003**, *3*, 181-193.
- 212 2. Ulbrich, I. M.; Canagaratna, M. R.; Zhang, Q.; Worsnop, D. R.; Jimenez, J. L.
213 Interpretation of Organic Components from Positive Matrix Factorization of Aerosol Mass
214 Spectrometric data. *Atmos. Chem. Phys.* **2009**, *9*, 2891-2918.
- 215 3. Paatero, P., Hopke, P. K. Discarding or Downweighting High-Noise Variables in Factor
216 Analytic Models. *Anal. Chim. Acta* **2003**, *490*, 277-289.
- 217 4. Craven, J. S.; Yee, L. D.; Ng, N. L.; Canagaratna, M. R.; Loza, C. L.; Schilling, K. A.;
218 Yatavelli, R. L. N.; Thornton, J. A.; Ziemann, P. J.; Flagan, R. C.; Seinfeld, J. H. Analysis of
219 Secondary Organic Aerosol Formation and Aging Using Positive Matrix Factorization of High-
220 Resolution Aerosol Mass Spectra: Application to the Dodecane Low-NO_x System. *Atmos. Chem.*
221 *Phys.* **2012**, *12*, 11795-11817.
- 222 5. Coggon, M. M.; Sorooshian, A.; Wang, Z.; Craven, J. S.; Metcalf, A. R.; Lin, J. J.;
223 Nenes, A.; Jonsson, H. H.; Flagan, R. C.; Seinfeld, J. H. Observations of Continental Biogenic
224 Impacts on Marine Aerosol and Clouds Off the Coast of California. *J. Geophys. Res. Atmos.*
225 **2014**, *119*, 6724-6748.
- 226 6. Weiss, M. Acetic Acid - Ammonium Acetate Reactions: An Improved Chichibabin
227 Pyridine Synthesis. *J. Am. Chem. Soc.* **1952**, *74*, 200-202.

228

229

230